SPERM DIFFERENTIATION AND SPERMATOZOA FUNCTION: MECHANISMS, DIAGNOSTICS, AND TREATMENT - VOLUME II

EDITED BY: Tomer Avidor-Reiss, Tzviya Zeev-Ben-Mordehai and Chih-kuan Tung

PUBLISHED IN: Frontiers in Cell and Developmental Biology

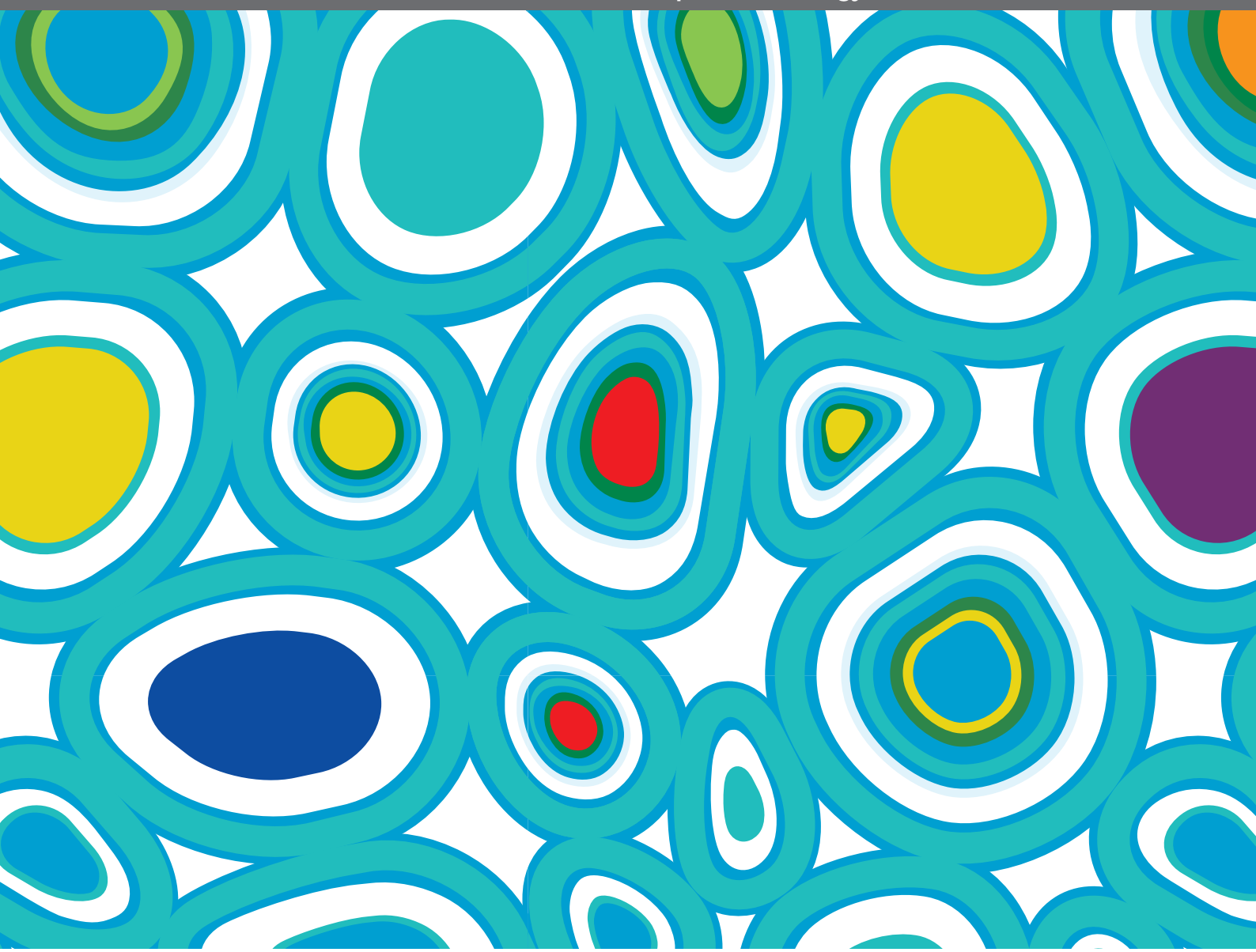

frontiers Research Topics

Frontiers eBook Copyright Statement

The copyright in the text of individual articles in this eBook is the property of their respective authors or their respective institutions or funders. The copyright in graphics and images within each article may be subject to copyright of other parties. In both cases this is subject to a license granted to Frontiers.

The compilation of articles constituting this eBook is the property of Frontiers.

Each article within this eBook, and the eBook itself, are published under the most recent version of the Creative Commons CC-BY licence. The version current at the date of publication of this eBook is CC-BY 4.0. If the CC-BY licence is updated, the licence granted by Frontiers is automatically updated to the new version.

When exercising any right under the CC-BY licence, Frontiers must be attributed as the original publisher of the article or eBook, as applicable.

Authors have the responsibility of ensuring that any graphics or other materials which are the property of others may be included in the CC-BY licence, but this should be checked before relying on the CC-BY licence to reproduce those materials. Any copyright notices relating to those materials must be complied with.

Copyright and source acknowledgement notices may not be removed and must be displayed in any copy, derivative work or partial copy which includes the elements in question.

All copyright, and all rights therein, are protected by national and international copyright laws. The above represents a summary only. For further information please read Frontiers' Conditions for Website Use and Copyright Statement, and the applicable CC-BY licence.

ISSN 1664-8714
ISBN 978-2-88976-609-3
DOI 10.3389/978-2-88976-609-3

About Frontiers

Frontiers is more than just an open-access publisher of scholarly articles: it is a pioneering approach to the world of academia, radically improving the way scholarly research is managed. The grand vision of Frontiers is a world where all people have an equal opportunity to seek, share and generate knowledge. Frontiers provides immediate and permanent online open access to all its publications, but this alone is not enough to realize our grand goals.

Frontiers Journal Series

The Frontiers Journal Series is a multi-tier and interdisciplinary set of open-access, online journals, promising a paradigm shift from the current review, selection and dissemination processes in academic publishing. All Frontiers journals are driven by researchers for researchers; therefore, they constitute a service to the scholarly community. At the same time, the Frontiers Journal Series operates on a revolutionary invention, the tiered publishing system, initially addressing specific communities of scholars, and gradually climbing up to broader public understanding, thus serving the interests of the lay society, too.

Dedication to Quality

Each Frontiers article is a landmark of the highest quality, thanks to genuinely collaborative interactions between authors and review editors, who include some of the world's best academicians. Research must be certified by peers before entering a stream of knowledge that may eventually reach the public - and shape society; therefore, Frontiers only applies the most rigorous and unbiased reviews.
Frontiers revolutionizes research publishing by freely delivering the most outstanding research, evaluated with no bias from both the academic and social point of view. By applying the most advanced information technologies, Frontiers is catapulting scholarly publishing into a new generation.

What are Frontiers Research Topics?

Frontiers Research Topics are very popular trademarks of the Frontiers Journals Series: they are collections of at least ten articles, all centered on a particular subject. With their unique mix of varied contributions from Original Research to Review Articles, Frontiers Research Topics unify the most influential researchers, the latest key findings and historical advances in a hot research area! Find out more on how to host your own Frontiers Research Topic or contribute to one as an author by contacting the Frontiers Editorial Office: frontiersin.org/about/contact

SPERM DIFFERENTIATION AND SPERMATOZOA FUNCTION: MECHANISMS, DIAGNOSTICS, AND TREATMENT - VOLUME II

Topic Editors:
Tomer Avidor-Reiss, University of Toledo, United States
Tzviya Zeev-Ben-Mordehai, Utrecht University, Netherlands
Chih-kuan Tung, North Carolina Agricultural and Technical State University, United States

Citation: Avidor-Reiss, T., Zeev-Ben-Mordehai, T., Tung, C.-K., eds. (2022). Sperm Differentiation and Spermatozoa Function: Mechanisms, Diagnostics, and Treatment - Volume II. Lausanne: Frontiers Media SA. doi: 10.3389/978-2-88976-609-3

Table of Contents

05 ***Linking Phospho-Gonadotropin Regulated Testicular RNA Helicase (GRTH/DDX25) to Histone Ubiquitination and Acetylation Essential for Spermatid Development During Spermiogenesis***
Raghuveer Kavarthapu, Rajakumar Anbazhagan, Ashish K. Sharma, Joseph Shiloach and Maria L. Dufau

17 ***Functional Analysis of Hydrolethalus Syndrome Protein HYLS1 in Ciliogenesis and Spermatogenesis in* Drosophila**
Yanan Hou, Zhimao Wu, Yingying Zhang, Huicheng Chen, Jinghua Hu, Yi Guo, Ying Peng and Qing Wei

32 ***The Impact of Di-2-Ethylhexyl Phthalate on Sperm Fertility***
Liliya Gabelev Khasin, John Della Rosa, Natalie Petersen, Jacob Moeller, Lance J. Kriegsfeld and Polina V. Lishko

46 ***Mating to Intact, but Not Vasectomized, Males Elicits Changes in the Endometrial Transcriptome: Insights From the Bovine Model***
Sandra Recuero, José María Sánchez, Yentel Mateo-Otero, Sandra Bagés-Arnal, Michael McDonald, Susanta K. Behura, Thomas E. Spencer, David A. Kenny, Marc Yeste, Pat Lonergan and Beatriz Fernandez-Fuertes

61 ***From Sperm Motility to Sperm-Borne microRNA Signatures: New Approaches to Predict Male Fertility Potential***
Maíra Bianchi Rodrigues Alves, Eneiva Carla Carvalho Celeghini and Clémence Belleannée

77 ***Male Decapacitation Factor SPINK3 Blocks Membrane Hyperpolarization and Calcium Entry in Mouse Sperm***
Lucia Zalazar, Cintia Stival, Anabella R. Nicolli, Gerardo A. De Blas, Dario Krapf and Andreina Cesari

90 ***Red LED Light Acts on the Mitochondrial Electron Chain of Donkey Sperm and Its Effects Depend on the Time of Exposure to Light***
Jaime Catalán, Marion Papas, Lina Trujillo-Rojas, Olga Blanco-Prieto, Sebastián Bonilla-Correal, Joan E. Rodríguez-Gil, Jordi Miró and Marc Yeste

108 ***Role of Phosphorylated Gonadotropin-Regulated Testicular RNA Helicase (GRTH/DDX25) in the Regulation of Germ Cell Specific mRNAs in Chromatoid Bodies During Spermatogenesis***
Rajakumar Anbazhagan, Raghuveer Kavarthapu, Steven L. Coon and Maria L. Dufau

122 ***Genes Regulating Spermatogenesis and Sperm Function Associated With Rare Disorders***
Emma Linn, Lillian Ghanem, Hanisha Bhakta, Cory Greer and Matteo Avella

139 ***High Efficiency RNA Extraction From Sperm Cells Using Guanidinium Thiocyanate Supplemented With Tris(2-Carboxyethyl)Phosphine***
Martin Roszkowski and Isabelle M. Mansuy

150 ***Fluorescence-Based Ratiometric Analysis of Sperm Centrioles (FRAC) Finds Patient Age and Sperm Morphology Are Associated With Centriole Quality***
Katerina A. Turner, Emily L. Fishman, Mariam Asadullah, Brooke Ott, Patrick Dusza, Tariq A. Shah, Puneet Sindhwani, Nagalakshmi Nadiminty, Emanuela Molinari, Pasquale Patrizio, Barbara S. Saltzman and Tomer Avidor-Reiss

166 ***Genetic Defects in* DNAH2 *Underlie Male Infertility With Multiple Morphological Abnormalities of the Sperm Flagella in Humans and Mice***
Jae Yeon Hwang, Shoaib Nawaz, Jungmin Choi, Huafeng Wang, Shabir Hussain, Mehboob Nawaz, Francesc Lopez-Giraldez, Kyungjo Jeong, Weilai Dong, Jong-Nam Oh, Kaya Bilguvar, Shrikant Mane, Chang-Kyu Lee, Christopher Bystroff, Richard P. Lifton, Wasim Ahmad and Jean-Ju Chung

182 ***Essential Role of CFAP53 in Sperm Flagellum Biogenesis***
Bingbing Wu, Xiaochen Yu, Chao Liu, Lina Wang, Tao Huang, Gang Lu, Zi-Jiang Chen, Wei Li and Hongbin Liu

196 ***Modelling Motility: The Mathematics of Spermatozoa***
Eamonn A. Gaffney, Kenta Ishimoto and Benjamin J. Walker

213 ***Conserved Mechanism of Bicarbonate-Induced Sensitization of CatSper Channels in Human and Mouse Sperm***
Juan J. Ferreira, Pascale Lybaert, Lis C. Puga-Molina and Celia M. Santi

227 ***Microtubule Organizing Centers Contain Testis-Specific γ-TuRC Proteins in Spermatids of Drosophila***
Elham Alzyoud, Viktor Vedelek, Zsuzsánna Réthi-Nagy, Zoltán Lipinszki and Rita Sinka

238 ***Tex13a Optimizes Sperm Motility* via *Its Potential Roles in mRNA Turnover***
Yinchuan Li, Panpan Mi, Xue Chen, Jiabao Wu, Xiaohua Liu, Yunge Tang, Jinmei Cheng, Yingying Huang, Weibing Qin, C. Yan Cheng and Fei Sun

247 ***Loss of Profilin3 Impairs Spermiogenesis by Affecting Acrosome Biogenesis, Autophagy, Manchette Development and Mitochondrial Organization***
Naila Umer, Lena Arévalo, Sharang Phadke, Keerthika Lohanadan, Gregor Kirfel, Dominik Sons, Denise Sofia, Walter Witke and Hubert Schorle

267 ***Bicarbonate-Stimulated Membrane Reorganization in Stallion Spermatozoa***
Paula Piccolo Maitan, Elizabeth G. Bromfield, Romy Hoogendijk, Miguel Ricardo Leung, Tzviya Zeev-Ben-Mordehai, Chris H. van de Lest, Jeroen W. A. Jansen, Bart Leemans, José Domingos Guimarães, Tom A. E. Stout, Bart M. Gadella and Heiko Henning

284 ***TMPRSS12 Functions in Meiosis and Spermiogenesis and Is Required for Male Fertility in Mice***
Jingjing Zhang, Xinli Zhou, Danyang Wan, Li Yu, Xu Chen, Tong Yan, Zhu Wu, Meimei Zheng, Feng Zhu and Hui Zhu

frontiers in Cell and Developmental Biology

ORIGINAL RESEARCH
published: 15 May 2020
doi: 10.3389/fcell.2020.00310

Linking Phospho-Gonadotropin Regulated Testicular RNA Helicase (GRTH/DDX25) to Histone Ubiquitination and Acetylation Essential for Spermatid Development During Spermiogenesis

*Raghuveer Kavarthapu[1], Rajakumar Anbazhagan[1], Ashish K. Sharma[2], Joseph Shiloach[2] and Maria L. Dufau[1]**

[1] Section on Molecular Endocrinology, Division of Developmental Biology, Eunice Kennedy Shriver National Institute of Child Health and Human Development, National Institutes of Health, Bethesda, MD, United States, [2] Biotechnology Core Laboratory, National Institute of Diabetes and Digestive and Kidney Diseases, National Institutes of Health, Bethesda, MD, United States

OPEN ACCESS

Edited by:
Tomer Avidor-Reiss, University of Toledo, United States

Reviewed by:
Maria Eugenia Teves, Virginia Commonwealth University, United States
Jianqiang Bao, Anhui Provincial Hospital Hefei, China

***Correspondence:**
Maria L. Dufau
dufaum@mail.nih.gov

Specialty section:
This article was submitted to Cell Growth and Division, a section of the journal Frontiers in Cell and Developmental Biology

Received: *04 March 2020*
Accepted: *08 April 2020*
Published: *15 May 2020*

Citation:
Kavarthapu R, Anbazhagan R, Sharma AK, Shiloach J and Dufau ML (2020) Linking Phospho-Gonadotropin Regulated Testicular RNA Helicase (GRTH/DDX25) to Histone Ubiquitination and Acetylation Essential for Spermatid Development During Spermiogenesis. Front. Cell Dev. Biol. 8:310. doi: 10.3389/fcell.2020.00310

GRTH/DDX25 is a testicular RNA helicase expressed in germ cells that plays a crucial role in completion of spermatogenesis. Previously, we demonstrated a missense mutation ($R^{242}H$) of GRTH gene in Japanese infertile patients (5.8%) with non-obstructive azoospermia. This mutation upon expression in COS-1 cells revealed absence of the 61 kDa phosphorylated GRTH in cytoplasm and the presence of the 56 kDa non-phosphorylated GRTH in the nucleus. GRTH knock-in (KI) mice carrying the human GRTH ($R^{242}H$) mutation, lack phosphorylated GRTH, and sperm due to failure of round spermatid elongation during spermiogenesis. To determine the impact of phosphorylated GRTH on molecular events/pathways participating in spermatid development during spermiogenesis, we analyzed transcriptome profiles obtained from RNA-Seq of germ cells from KI and WT mice. RNA-Seq analysis of 2624 differentially expressed genes revealed 1404 down-regulated and 1220 up-regulated genes in KI mice. Genes relevant to spermatogenesis, spermatid development and spermatid differentiation were significantly down-regulated. KEGG enrichment analysis showed genes related to ubiquitin-mediated proteolysis and protein processing in endoplasmic reticulum pathway genes were significantly down-regulated while the up-regulated genes were found to be involved in Focal adhesion and ECM-receptor interaction pathways. Real-Time PCR analysis confirmed considerable reduction in transcripts of ubiquitination related genes *Ube2j1*, *Ube2k*, *Ube2w*, *Rnf8*, *Rnf133*, *Rnf138, Cul3* and increased expression of *Ccnd2*, *Col1a*, *Lamb1*, *Cav1*, *Igf1*, *Itga9* mRNA's in KI mice compared to WT. Also, marked reduction in protein expression of UBE2J1, RNF8, RNF138 (ubiquitination network), MOF (histone acetyltransferase), their modified Histone substrates (H2AUb, H2BUb) and H4Ac, H4K16Ac were observed in KI mice. GRTH-IP mRNA binding studies revealed that *Rnf8* and *Ube2J1* mRNAs from WT mice associated with GRTH protein and the binding is greatly impaired in the KI mice.

Immunohistochemistry analysis showed significantly reduced expression of RNF8, MOF, H4Ac and H4K16Ac in round spermatids of KI mice. Absence of phosphorylated GRTH impairs UBE2J1, RNF8 and MOF-dependent histone ubiquitination and acetylation essential for histone replacement, chromatin condensation and spermatid elongation during spermiogenesis.

Keywords: phospho-GRTH/DDX25, spermatogenesis, round spermatids, histones, ubiquitination, acetylation

INTRODUCTION

Gonadotropin-regulated testicular RNA helicase (GRTH/DDX25) belongs to DEAD-box protein family of RNA helicases explicitly found in the testis and is transcriptionally regulated by gonadotropins via paracrine androgen action (Tang et al., 1999; Sheng et al., 2003; Dufau and Tsai-Morris, 2007; Dufau and Kavarthapu, 2019). GRTH/DDX25 is expressed in Leydig cells, meiotic spermatocytes and haploid spermatids (Sheng et al., 2003; Dufau and Tsai-Morris, 2007; Dufau and Kavarthapu, 2019). It is involved in multiple functions as a post-transcriptional controller of specific genes in germ cells during spermatogenesis. In germ cells GRTH is an integral constituent of messenger ribonuclear protein complex, that transports specific mRNAs from the nucleus to cytoplasmic sites including chromatoid bodies for storage prior to their translation during spermatogenesis. Chromatoid bodies (CB) are non-membranous organelles residing in the cytoplasm of round spermatids (RS) where specific mRNAs are stored and later processed during spermiogenesis (Tsai-Morris et al., 2004b; Dufau and Tsai-Morris, 2007; Dufau and Kavarthapu, 2019). We have shown that GRTH binds to actively translating polyribosomes, where may play an important role in translation of specific genes in germ cells like transition proteins (TP1/TP2), protamines (PRM1/PRM2), phosphoglycerate kinase and testicular angiotensin converting enzyme (Sheng et al., 2006; Sato et al., 2010; Tsai-Morris et al., 2012). The GRTH gene with TATA-less promotor has many transcriptional start sites and it is transcriptionally regulated by Sp1/Sp3 (Tsai-Morris et al., 2004a). We have previously reported two forms of GRTH protein in germ cells, a 61 kDa phosphorylated species exclusively found in the cytoplasm and a 56 kDa non-phosphorylated species in the nucleus. The 61 kDa phosphorylated GRTH (p-GRTH) protein in the cytoplasm participates in shuttling of specific mRNAs in and out of the CB and also associates with polyribosomes for translation. The 56 kDa non-p-GRTH protein is involved in the export of mRNAs from nucleus to cytoplasm (Sheng et al., 2006; Dufau and Tsai-Morris, 2007) and has also being proposed to participate in transcriptional events of Drosha-DGCR8 complex (Dai et al., 2011).

GRTH knock-out mice are infertile with complete loss of elongating spermatids (ES) and sperm due to spermatogenic arrest at step 8. In the RS of these null mice, the size of the CB was markedly reduced indicating either decrease or loss of mRNAs essential for progression of spermiogenesis (Tsai-Morris et al., 2004b; Sheng et al., 2006). GRTH is the only member of the DEAD-box helicase family known to be transcriptionally up-regulated by gonadotropins (luteinizing hormone/human chorionic gonadotropin). In Leydig cells, luteinizing hormone through stimulation of androgen production induces GRTH transcription in an autocrine manner through an androgen responsive element present in the proximal region of the GRTH gene (Tsai-Morris et al., 2010; Villar et al., 2012). In germ cells, where GRTH expression is both cell- and stage-specific, paracrine actions of androgen via its receptors in Sertoli cells increase transcription of GRTH in germ cells (Kavarthapu et al., 2013).

Our previous studies identified a missense heterozygous mutation of Arg to His at position 242 ($R^{242}H$) in GRTH gene in 5.8% of Japanese men with non-obstructive azoospermia (Tsai-Morris et al., 2007). *In vitro* experiments performed by overexpressing the human mutant GRTH construct in COS-1 cells revealed the loss of the cytoplasmic 61 kDa p-GRTH species, while maintaining the expression of 56 kDa non-phospho form (Tsai-Morris et al., 2007). Also, we established that GRTH was phosphorylated by Protein Kinase A (Sheng et al., 2006). Subsequently, we created transgenic GRTH Knock-In (KI) mice bearing the hGRTH gene with the $R^{242}H$ mutation which lack the 61 kDa cytoplasmic p-GRTH form (Kavarthapu et al., 2019). Homozygous GRTH-KI mice are infertile with absence of mature sperm due to failure of RS to elongate while exhibited normal mating behavior. In these KI mice loss of p-GRTH has significant effects on the levels of mRNA and protein of TP2, PRM2 and TSSK6 (Kavarthapu et al., 2019). To understand mechanistically the impact of p-GRTH on the round spermatids elongation process we investigated differential expression of genes and compared transcriptome profiles obtained from germ cells of KI and WT using Illumina RNA-Seq. This study indicates the essential role of p-GRTH/DDX25 in UBE2J1 and RNF8 dependent histone modification during spermiogenesis.

MATERIALS AND METHODS

Animals and Preparation of Germ Cells

The generation of GRTH-KI mice carrying human GRTH gene with $R^{242}H$ mutation were described previously (Kavarthapu et al., 2019). Homozygous KI mice were obtained by crossing heterozygous KI male mice either with heterozygous or homozygous KI female mice. KI mice were genotyped using two primers sets, KI-F1/KI-R1 and KI-F2/KI-R2 (**Supplementary Table S1**) to detect targeted and mice GRTH alleles, respectively. Transgenic animals were maintained at 22°C in a pathogen free, light controlled environment with an alternating light–dark cycle. All animal studies were performed as per the guidelines of National Institute of Child Health and Human Development Animal Care and Use Committee. Germ cells were prepared

individually from five mice (45 days old) each for WT and KI by collagenase-trypsin dispersion. Testes were decapsulated and the seminiferous tubules were treated with collagenase in M199 medium containing 0.1% bovine serum albumin (BSA) for 15 min. The collagenase treated tubules were minced and incubated in M199 with 0.1% BSA and 0.1% trypsin for 15 min at 35°C in rotation at 100 rpm to obtain dispersed cell suspension. After trypsin treatment 0.02% of trypsin inhibitor (Sigma) was added to the sample and filtered through 300 μm mesh strainer and glass wool and then passed through 100 and 40 μm cell strainer (Millipore) to obtain germ cell fraction (spermatogonia, spermatocytes and spermatids) which was pelleted and washed with cold PBS for total RNA isolation.

Total RNA Preparation and Library Construction for RNA-Seq

Total RNA was prepared from germ cells isolated from WT and KI testis using Qiagen RNeasy mini kit (Qiagen, CA). RNA concentration and quality were evaluated using the Agilent 2100 Bioanalyzer system (Agilent Technologies, CA, United States). mRNA was then extracted from total RNA using oligo (dT) method and RNA-Seq library was constructed according to a standard protocol provided by Illumina. Sequencing was performed for a paired-end 150 bp on the Illumina HiSeq 2500 by Novogene Bioinformatics Institute (Beijing, China). The raw RNA-seq reads have been deposited to the NCBI[1] GEO database with GEO accession number GSE145047.

Transcriptome Analysis and Identification of Differential Gene Expression

RNA-seq reads were first trimmed for adapters and then aligned to mouse mm10 reference genome sequences using STAR in Patek Flow online software[2] for next-generation sequencing analysis. The aligned reads were quantitated to Partek E/M (mm10 RefSeq_v91) annotation model to obtain gene counts. Principal component analysis (PCA) was done on gene counts to determine the variability in the data set. Differentially expressed genes (DEGs) between WT and KI conditions were generated with DESeq2 (fold change ≤ -1.5 or ≥ 1.5; $P < 0.05$, FDR < 0.05) in Partek Flow.

Protein-Protein Interaction (PPI) Network Analysis

STRING[3] is the online database used for known and predicted protein-protein interactions to analyze the interaction relationships between proteins in our study. To visualize the interactions among the down-regulated DEGs, STRING tool was used to construct a PPI network with a interacting confidence scores of >0.4 designated as the cutoff. Cytoscape 3.7.2 software was employed to analyze the PPI network by Network Analyzer plugin. cytoHubba plugin in cytoscape was used to extract the top 20 hub genes from the PPI network based on maximal clique centrality (MCC) algorithm.

Enrichment Analysis of DEGs

To identify biological functional of DEGs, Gene Ontology (GO) enrichment analysis was done, and the data was visualized using DAVID[4] online tool. GO functional analysis of DEGs were sub-divided into three groups: biological process (BP), molecular function (MF) and cellular component (CC). A *P*-value of less than 0.05 and gene count >5 was set as the cutoff. KEGG pathway analysis was carried out on up-regulated and down-regulated DEGs separately using clusterProfiler package in R-Studio 3.6.1 to identify the crucial pathways with *P*-value < 0.05.

Real-Time PCR Analysis for the Validation of RNA-Seq Results

Real-time quantitative reverse transcription PCR (qRT-PCR) was used to validate the DEGs obtained from RNA-Seq analysis. Total RNA (1 μg) prepared for RNA-Seq library was Reverse transcribed using the SuperScript III first-strand synthesis SuperMix (ThermoFisher Scientific, MA). qRT-PCR was then performed with Fast SYBR green master mix in a final volume of 20 μL. All PCR reactions were done in triplicates in a 7500 Fast Real-Time PCR machine (Applied Biosystems, CA). Cycle threshold (Ct) values were normalized to β-actin as reference gene, and Relative quantification of transcripts was performed using the comparative $2^{-\Delta\Delta Ct}$ method. The primer sets used in this analysis are available in **Supplementary Table S1**.

Western Blot Analysis

Total protein lysates from testis of WT and KI mice were extracted using RIPA lysis buffer (Upstate, Temecula, CA, United States) containing Halt protease and phosphatase inhibitor cocktail (ThermoFisher Scientific, MA, United States). The supernatants of lysates centrifuged at 2,500 *g* for 5 min were used to estimate the protein concentration by the Bradford assay (Bio-Rad Laboratories, CA, United States). These lysates (100 μg) were resolved in 4–12% Bis-Tris gel (Invitrogen) and transferred onto nitrocellulose membrane using Iblot 2 (ThermoFisher Scientific, MA, United States). Membranes blocked with 5% skimmed milk powder in PBS were incubated with the corresponding primary antibodies (**Supplementary Table S2**) at 1:1000 dilution. After the incubation of primary antibodies and washing steps, the membranes were incubated with the respective secondary antibodies conjugated with poly-HRP at 1:2000 dilution. Immunosignals were detected by a Tanon High-sig ECL Western Blotting Substrate system (ABclonal, MA, United States).

Immunohistochemistry

Paraformaldehyde fixed cross-sections were deparaffinized and rehydrated in a graded series of ethyl alcohol and distilled water. Antigen retrieval for 10 min was performed using

[1]https://www.ncbi.nlm.nih.gov/geo

[2]http://www.partek.com/partek-flow/

[3]https://string-db.org/

[4]http://david.abcc.ncifcrf.gov/

Tris-EDTA buffer pH 9.0 before blocking with horse serum. The slides were incubated overnight at 4°C with 1:250 dilution of primary antibodies of RNF8, MYST/MOF, H4-Ac, H4K16-Ac, and Ube2J1 or rabbit IgG isotype control. Subsequently, sections were incubated secondary antibody conjugated with horseradish peroxidase polymer for 1 h. (Invitrogen, Frederick, MD, United States). After washing the sections with PBS, diaminobenzidine as chromagen and hydrogen peroxide as substrate were added to develop the brown color for visualization. Then the sections were counterstained with hematoxylin.

Immunoprecipitation (IP) of GRTH-RNA Complex From Testis

Total protein extracts (0.5 mg) isolated from germ cells of WT and GRTH-KI mice using RIPA lysis buffer (Upstate, Temecula, CA, United States) were initially incubated with 50 μl of protein A/G Plus-agarose beads and 1 μg of rabbit IgG in IP binding buffer (ThermoFisher Scientific, MA) with gentle agitation for 30 min at 4°C. Supernatants were incubated with 4 μg affinity-purified anti-GRTH rabbit polyclonal antibody for overnight at 4°C to co-immunoprecipitate the GRTH-ribonucleoprotein complex. 50 μl of protein A-agarose beads was added and incubated for 2 h at 4°C. The GRTH-ribonucleoprotein complex bound to protein A-agarose was washed three times with IP binding buffer. The RNA from this GRTH-ribonucleoprotein complex was isolated by phenol/chloroform/isoamyl alcohol (25:24:1, v/v; Invitrogen). First-strand cDNA was prepared using SuperScript III first-strand synthesis kit (ThermoFisher Scientific, MA) and Real-Time PCR was performed with Fast SYBR green using specific set of primers for RNF8 and UBE2J1 (**Supplementary Table S1**) in a 7500 Fast Real-Time PCR machine (Applied Biosystems, CA, United States).

Statistical Analysis

Data was analyzed using Prism 8.0 statistical software (GraphPad Software Inc, San Diego, CA, United States). Differences between KI and WT groups were determined by two-tailed Students *t*-test. The error bars represent the standard error mean (SEM) with $P < 0.05$ was considered statistically significant.

RESULTS

Summary of RNA-Seq Data

We initially performed RNA-Seq to analyze the transcriptomes of mouse germ cells from KI and WT groups. In total, we obtained 93 and 111.2 million reads from RNA-Seq libraries made from the KI and WT mice germ cells, respectively. The average read quality (Phred33 score) was 35.8 and more than 95% of reads could be mapped to the mice reference genome (**Supplementary Table S3**). Separation of the KI and WT genotypes was evident in the Hierarchically clustered heatmap shown in the expression profiles of DEGs (**Figure 1A**). PCA analysis revealed clustering of five biological replicates in each group clearly demonstrated the differences between KI and WT (**Figure 1B**).

Identification of Differentially Expressed Genes (DEGs) and Functional Variation

The gene count data was used to analyze differences in gene expression by DESeq2. A total of 2624 DEGs were identified, including 1220 significantly up-regulated and 1404 significantly down-regulated genes between KI and WT groups (**Supplementary Table S4**). Volcano plot for DEGs are shown in **Figure 1C**. To further analyze and classify the biological function of DEGs, we performed GO functional analysis using DAVID software and KEGG pathway enrichment analysis was done using R-studio. GO analysis of DEGs were sub-divided into three categories: biological process (BP), cellular component (CC) and molecular function (MF) and only significant GO terms with *P*-value <0.05 were considered. (**Supplementary Tables S5, S6**). Top 10 (down-regulated and up-regulated) gene-enriched GO terms were identified and shown in **Figure 2**. In the BP group, the down-regulated DEGs (**Figure 2A**) are mainly enriched in spermatogenesis, male gamete generation and spermatid development, and up-regulated DEGs (**Figure 2B**) are mainly enriched in regulation of cellular component movement, cell adhesion and cell migration/motility. KEGG pathway enrichment analysis of DEGs revealed that majority of the downregulated genes were associated with protein processing in endoplasmic reticulum and ubiquitin mediated proteolysis pathways (**Supplementary Table S7**). KEGG analysis also showed genes significantly up-regulated in KI mice involved in ECM-receptor interaction, Carbon metabolism, Focal adhesion pathways (**Supplementary Table S7**). Top 10 KEGG pathways (down-regulated and up-regulated) were identified by analyzing significantly DEGs which were shown as dot plots in **Figures 2C,D**.

PPI Network Construction and Analysis

The STRING plugin app in Cytoscape was used to analyze the DEGs involved in spermatogenesis and ubiquitin-proteasome pathway (UPP) to construct a PPI network. The PPI network show 77 nodes/proteins and 247 edges/interactions, with a local clustering coefficient of 0.502 and has a PPI enrichment *P*-value $<1.0e^{-16}$ (**Figure 3A**). Using network analyzer app in cytoscape we analyzed the different network parameters for each node. Based on degree value different sizes are assigned to nodes, while darker edges represent higher string database score indicating stronger degree of interactions with other proteins. Using cytoHubba plugin in Cytoscape, we identified top 20 Hub genes representing higher degree of connectivity between nodes (**Figure 3B**). For example, Hub genes (CUL3, UBE2K, UBE2Q2, UBE2J1) with higher degree value means highly connected network. The two modules with key hub genes (red and orange nodes) in the PPI network are interconnected to each other by KLHL10 essential for spermatogenesis process and CUL3 involved in UPP (**Figure 3B**). This connection is significant as it has been shown experimentally that these two proteins KLHL10 and CUL3 directly interact with each other (Wang et al., 2006).

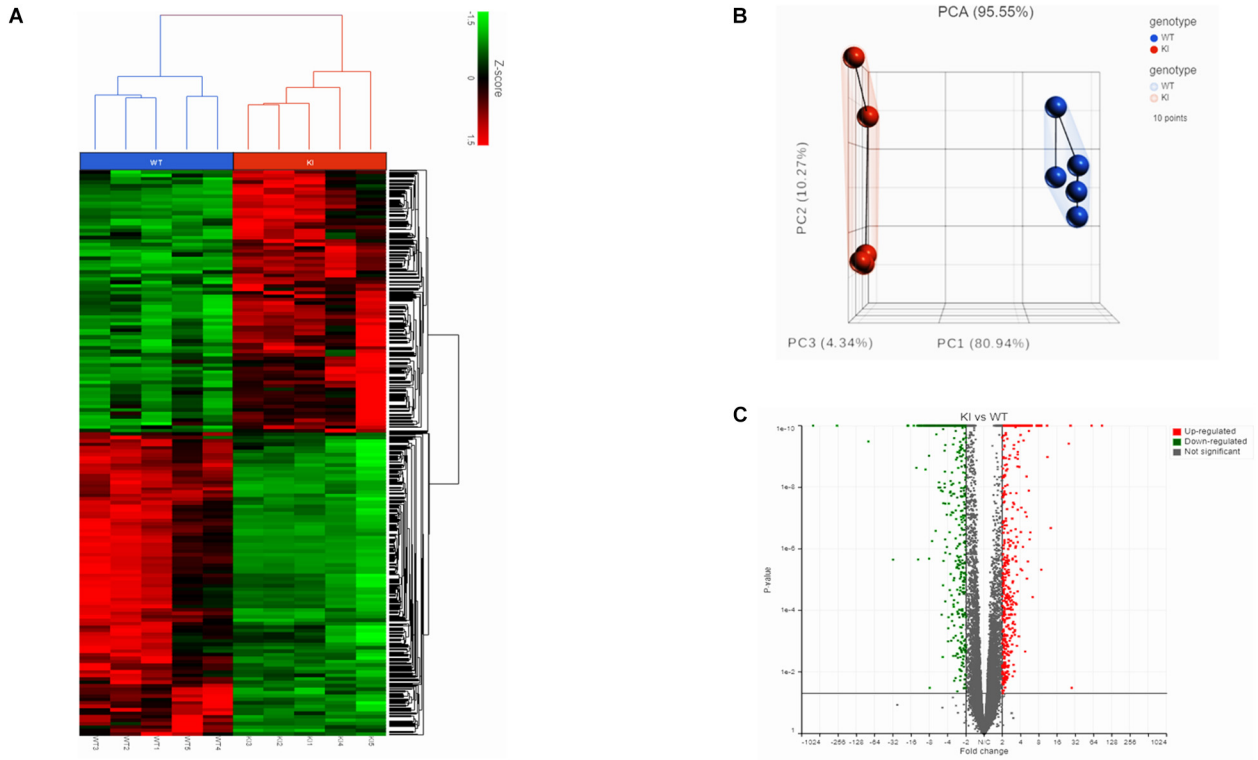

FIGURE 1 | Transcriptome analysis of germ cells from KI and WT mice. **(A)** Hierarchical clustered heatmap showing the expression patterns of significantly (fold change ≤−1.5 or ≥1.5; $p < 0.05$) DEGs. The red boxes indicate the up-regulated genes, and the green boxes indicates down-regulated genes. Colored bar represents the expression levels. **(B)** PCA plot showing clustered samples based on the KI and WT genotype. Each point represents replicate sample for each genotype. **(C)** Volcano plot (fold change vs *P*-value) showing 2624 DEGs from KI and WT group ($n = 5$ per group). Red dots represent up-regulated genes and green dots down-regulated genes in KI vs WT.

Validation of DEGs Using qRT-PCR

To further confirm and validate the transcriptome results from the RNA-seq analysis, genes relevant to spermatogenesis and UPP enriched in functional analysis were selected, and their expression levels were confirmed by qRT-PCR analysis. The results from qRT-PCR indicated that transcripts of *Tnp2*, *Prm2*, *Tssk6*, and *Klhl10* involved in spermatogenesis process and transcripts of *Ube2j1*, *Ube2k*, *Ube2w*, *Rnf8*, *Rnf138*, *Rnf133*, and *Cul3* that participate in UPP were downregulated in KI group consistent with RNA-seq results (**Figure 4A**). The upregulated genes like *Col1a*, *Lamb1*, *Cav1*, *Ccnd2*, *Itga9*, and *Igf1* crucial for focal adhesion and ECM-receptor interaction pathways were found to have increased levels of their transcripts in KI compared to WT (**Figure 4A**). Overall, the qRT-PCR results displayed high correlation with those obtained by RNA-Seq analysis.

Validation of Enriched Pathway Genes Using Western Blotting

In addition to transcript levels, we wanted to confirm the protein levels of genes that were down-regulated in the qRT-PCR analysis. The protein levels of selected UPP genes UBE2J1, RNF8, RNF133, RNF138, and other prerequisite factors MOF/MYST-1, H2B-Ub, H2A-Ub, H4-Ac, and H4K16-Ac that are implicated during spermiogenesis were drastically reduced in KI compared to WT (**Figure 4B**) indicating that p-GRTH impacts genes which are essential in the spermatid elongation process regulating the expression of genes involved in the UPP. The protein levels of up-regulated transcripts COL1a, CCND2 were increased in KI compared to WT (**Figure 4B**).

Loss of p-GRTH in KI Mice Impairs Binding of *Ube2J1* and *Rnf8* mRNA's to GRTH Protein

Previous studies from our lab have shown that GRTH protein binds to specific germ cell mRNAs (*Tp2*, *Prm2* and *Pgk2)* at cytoplasmic sites for storage in CB and later participates in translational process (Sheng et al., 2006; Kavarthapu et al., 2013). It was of interest to learn whether GRTH associates to *Ube2J1* and *Rnf8* mRNAs, two key genes of the UPP pathway, and how these were impacted in KI mice which lacks p-GRTH. The GRTH-IP mRNA binding studies revealed that *Ube2J1* and *Rnf8* mRNAs from WT mice associated with GRTH protein and the binding is abolished in the KI mice (**Figure 5**).

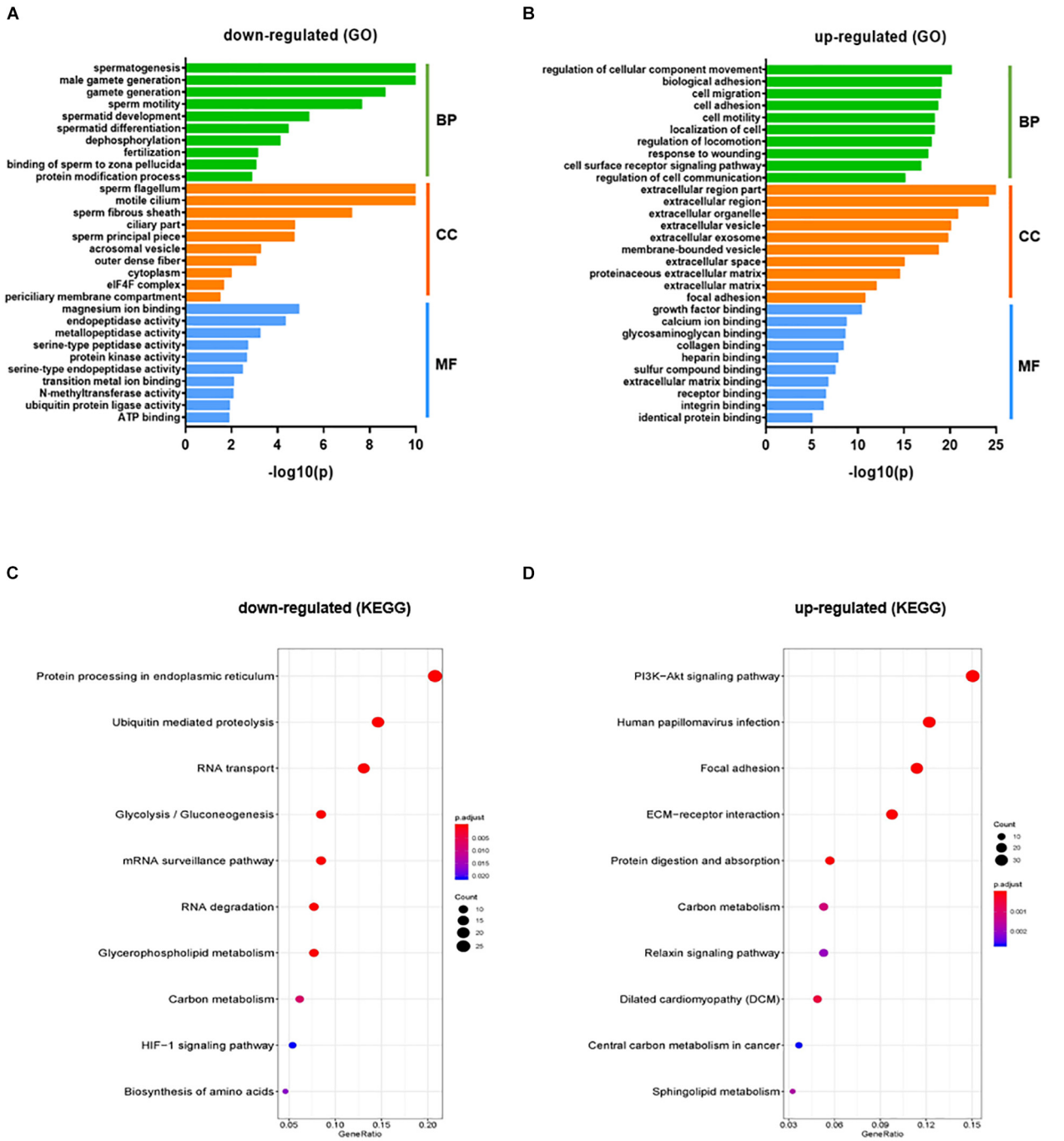

FIGURE 2 | GO and KEGG pathway enrichment analysis of DEGs. GO functional analysis (Top 10 GO terms) for down-regulated DEGs **(A)** and up-regulated DEGs **(B)** in KI vs WT mice were grouped into different functional categories: biological process (BF), cellular component (CC) and molecular function (MF).
(B) Representative dot plot of top 10 significantly ($P < 0.05$) enriched KEGG pathways for down-regulated **(C)** and up-regulated genes **(D)**. The *x*-axis represents gene ratio = count/set size. Dot size represents the number of genes and the color bar represents the padj-value.

IHC Analysis of Genes Involved in Spermatid Elongation Process

We selected UBE2J1, RNF8, MOF/MYST-1, H4-Ac, and H4K16-Ac genes that are relevant to spermatid elongation process for IHC analysis to elucidate their expression pattern in germ cells during spermiogenesis. In WT mice UBE2J1 expression was exclusively noticed in ES of step 10 and gradually intensified in condensing spermatids of steps 12 to 13 of spermiogenesis

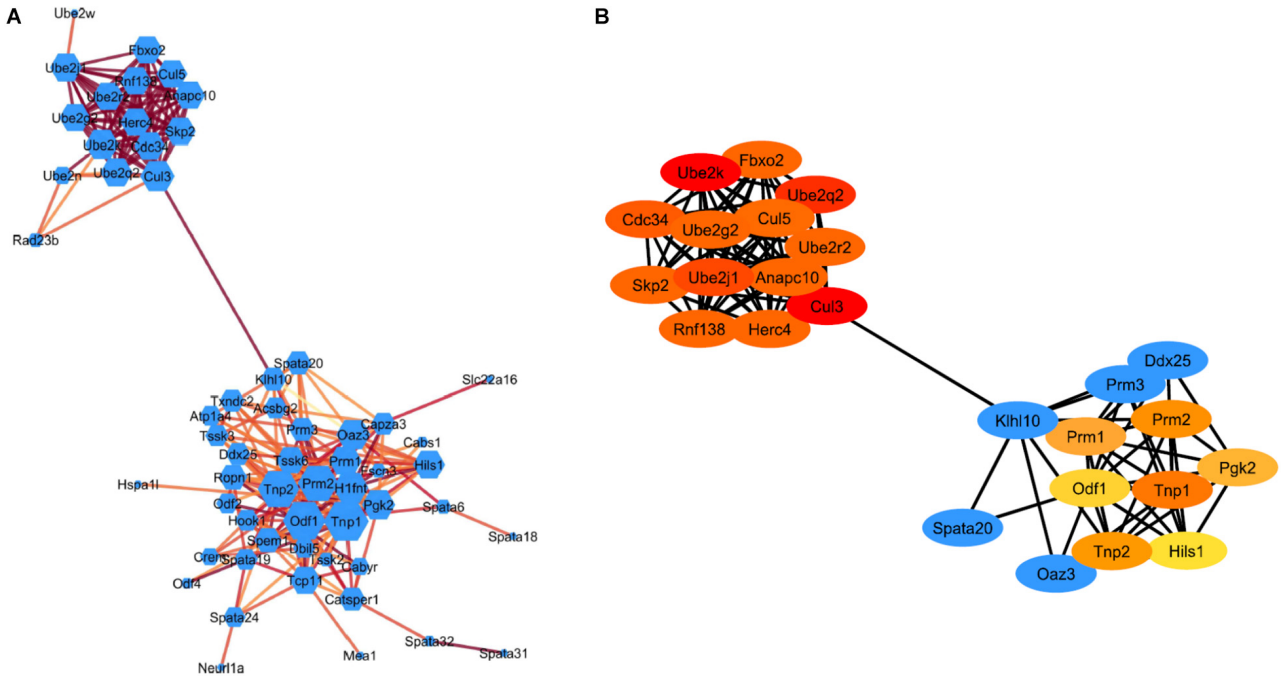

FIGURE 3 | STRING protein-protein interaction network. **(A)** Visualization of the PPI network of identified down-regulated DEGs from spermatogenesis process and UPP pathway. Colored nodes represent genes/proteins. Edges represent the protein-protein associations. Node size indicates node degree value and Edge color represents stringdb score. Darker edges mean higher stringdb score **(B)** Visualization of the top 20 hub genes from the PPI network using the cytoHubba plugin in Cytoscape software. Red to yellow colored nodes represents genes with high to low PPI degree scores.

(**Figure 6**). There was no expression of UBE2J1 in KI mice compared to WT mice (**Figure 6**). RNF8 and MOF expression was observed in spermatocytes, RS and ES of WT mice (**Figure 7A**). While their expression was abundant in round spermatids of WT mice, in KI mice was drastically reduced. As the RS elongate and chromatin starts condensing in later stages (stage XII), RNF8 expression was observed in the nucleus of ES of step 12 in WT mice. While in KI mice seminiferous tubule at stage XII, we found RS that fail to elongate and the RNF8 signal in these germ cells was very weak (**Figure 7A**). MOF/MYST1 also showed similar expression patterns with much higher signals in nucleus of spermatocytes, RS and ES of WT mice while merely low to negligible expression in germ cells of KI mice (**Figure 7B**). Acetylation of H4 observed in the nucleus of round spermatids was dramatically reduced in KI mice compared to WT (**Figure 7C**). Similar expression pattern was observed for the specific acetylation of H4 at K16 residue (**Figure 7D**).

DISCUSSION

In this study, we examined genome-wide transcriptome profiles of germ cells isolated from GRTH-KI and WT mice testis using RNA-Seq. We used homozygous KI mice with $R^{242}H$ mutation in GRTH gene with resulting loss of p-GRTH to further understand its role in spermatid development during spermiogenesis by analyzing the DEGs from RNA-Seq. Previously we have shown that homozygous KI mice are infertile and lack ES and mature sperm due to arrest of round spermatids of step 8 that fail to elongate in the process of spermatogenesis. Absence of p-GRTH in KI mice had a profound impact on spermatid development indicated by abnormal acrosome formation in round spermatids which later undergo apoptosis forming multinucleated giant spermatids. The RNA-Seq analysis of transcriptome of germ cells in KI vs WT mice revealed DEGs related to ECM-receptor interaction and focal adhesion pathways were up-regulated. Genes like collagen, integrins, laminins and others involved in focal adhesion and ECM-receptor interaction pathways play a crucial role in junction dynamics in the seminiferous epithelium regulating cell-matrix interactions and cell-cell adhesion and cell migration (Siu and Cheng, 2004). We believe that these facilitate aggregation/clumping of round spermatid together and formation of giant multi-nucleated germ cells as observed in our histological studies in KI mice (Kavarthapu et al., 2019). We found several DEGs related to spermatogenesis, spermatid development and UPP were downregulated. Of note is that in germ cells of KI mice there was a dramatic reduction in UPP proteins (UBE2J1 and RNF8) essential for chromatin remodeling during spermiogenesis. This study using the KI mice model demonstrated that loss of p-GRTH impairs UBE2J1 and RNF8 dependent histone modifications hampering initial stages of spermatid elongation process.

During spermiogenesis, round spermatids go through 16 steps of development with subsequent characteristics variations in cell morphology and nuclear condensation as characterized by development of elongating, condensing, and condensed

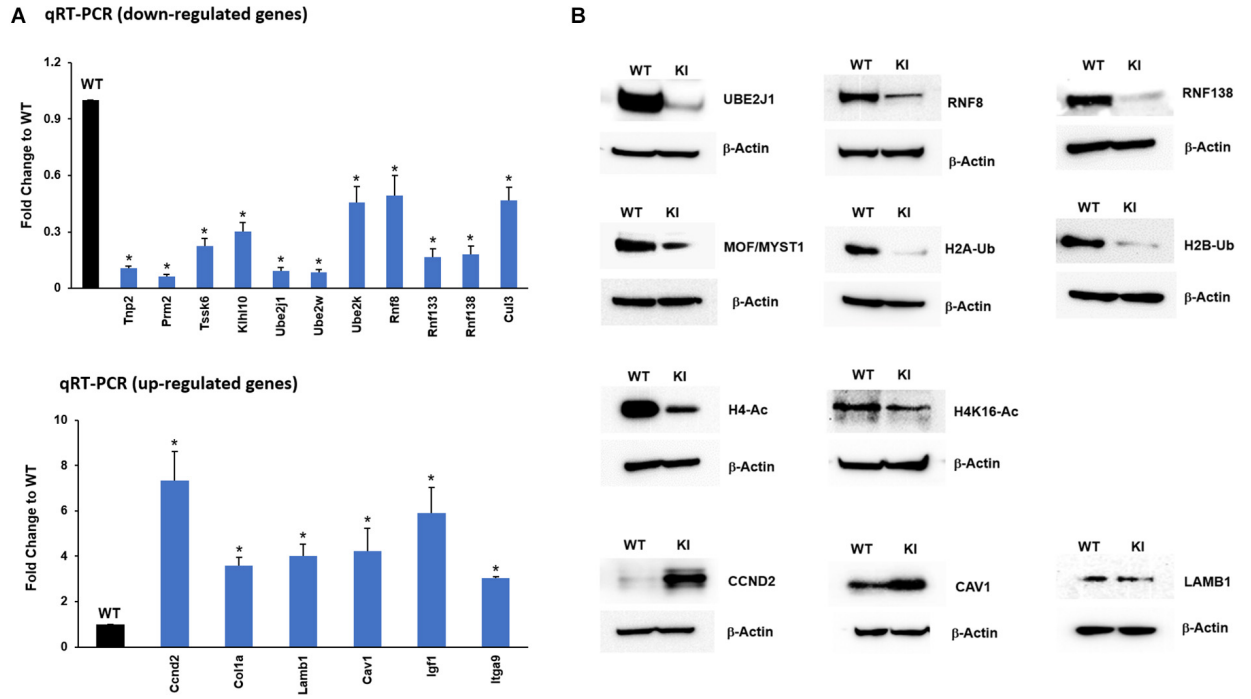

FIGURE 4 | RNA-Seq data validation by qRT-PCR and Western blot. **(A)** Expression of selected up-regulated and down-regulated genes from the RNA-seq data was measured by qRT-PCR relative to actin in KI vs WT mice. Histograms represent the fold change expression between KI and WT group. Means ± SEM were determined from three sets of qRT-PCR experiments with each sample run in triplicates. *P*-values were calculated by two-tailed Students *t*-test (asterisks indicates $P < 0.05$). **(B)** Western blots showing the protein expression of UBE2J1, RNF8, RNF138, MOF/MYST1, H2A/B-Ub (Ubiquitinated Histone 2A/B), H4-Ac (Acetylated Histone 4), H4K16-Ac, CCND2, CAV1, and LAMB1 in KI and WT mice.

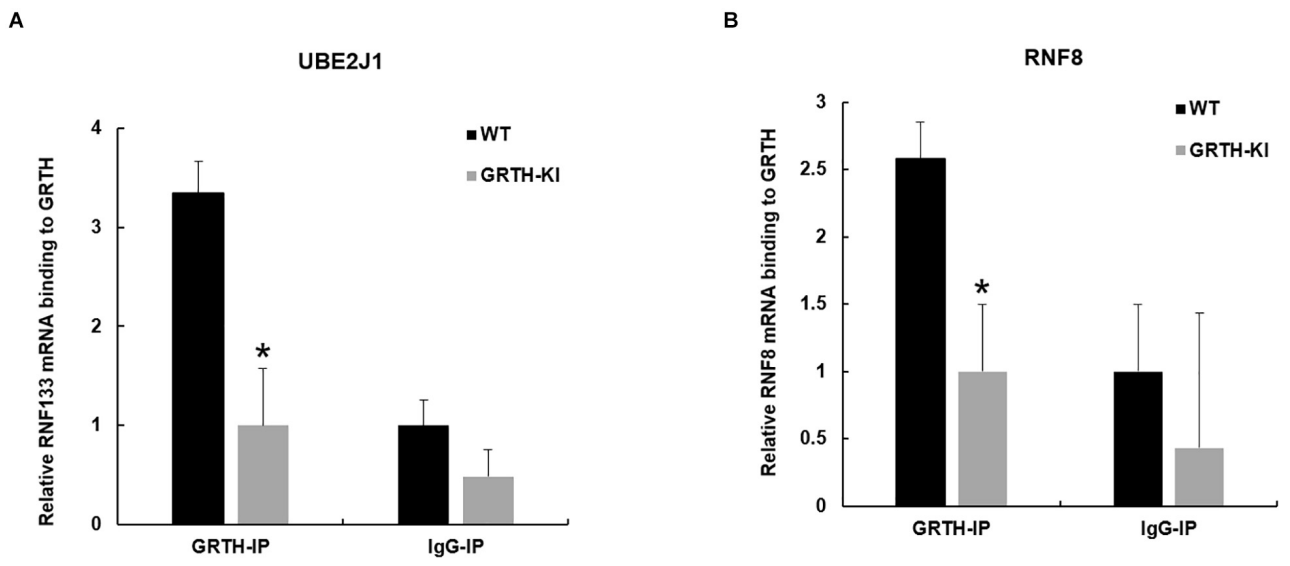

FIGURE 5 | Binding of GRTH protein to *Ube2j1* and *Rnf8* mRNA in KI vs WT mice. Relative mRNA binding of *Ube2J1* **(A)**, and *Rnf8* **(B)** to GRTH protein in WT and KI mice. Statistical analysis was done using two-tailed Students *t*-test (*indicates $P < 0.05$) and data represents mean ± SEM of two independent experiments in triplicates.

spermatids. RS of steps 1–8 possess round-shaped cells with preponderant nuclei packed with basic histone proteins and are in a state of active transcription. The step 8 RS exhibit distinct cap shaped acrosome (Russell et al., 1990; Hecht, 1998). Histone acetylation that leads to histone replacement later occurs in RS of step 8 prior to the initiation of nuclear elongation

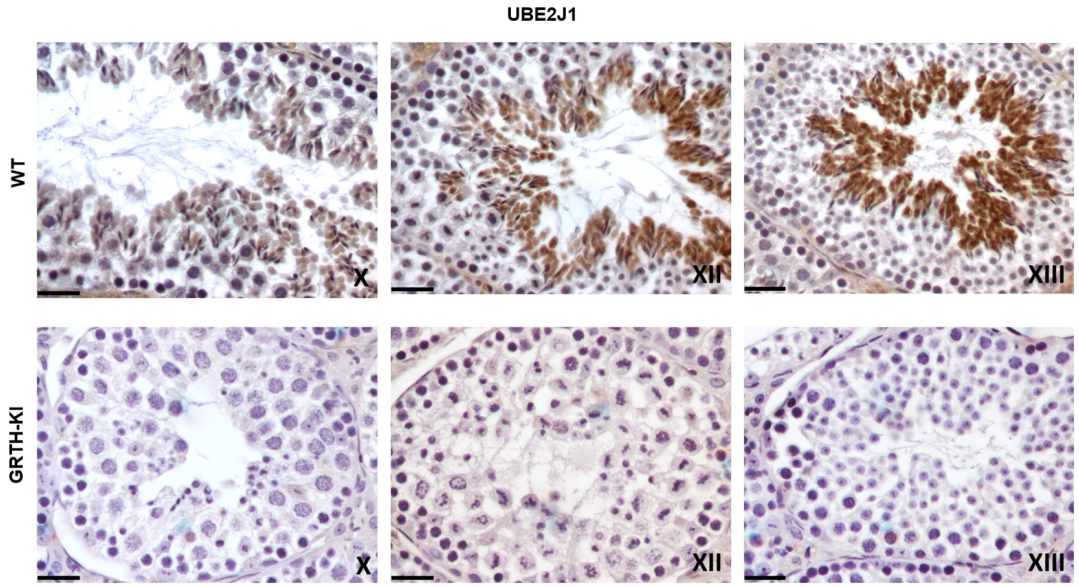

FIGURE 6 | IHC analysis of UBE2J1 in seminiferous tubules of WT and KI mice. UBE2J1 expression is localized (DAB signal) specifically in ES of stage X, XII, XIII of spermatogenesis. The signal intensity was gradually increased from stage X to XIII in WT.

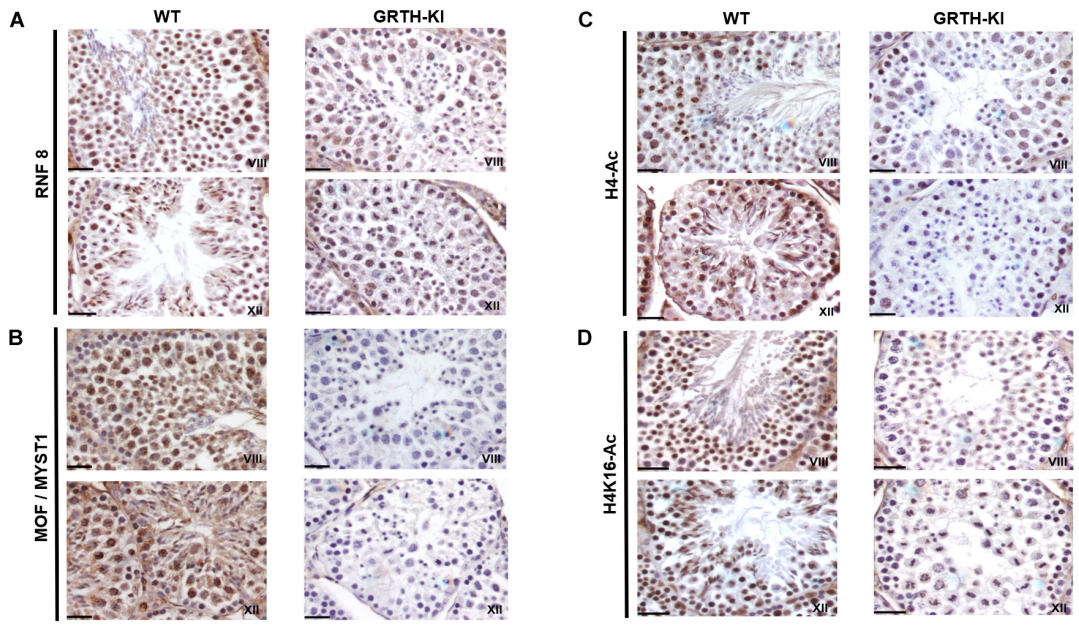

FIGURE 7 | IHC analysis of RNF8, MOF/MYST1, H4-Ac and H4K16-Ac in seminiferous tubules of WT and KI mice. RNF8 **(A)**, MOF/MYST1 **(B)**, H4-Ac **(C)**, and H4K16-Ac **(D)** expression are noticed more significantly in the nucleus of RS (stage VIII) and ES (stage XII) in seminiferous tubules of WT mice while their expression are not observed in the RS of KI mice.

(Hazzouri et al., 2000; Shirakata et al., 2014). ES of steps 9–11 show hyperacetylation of histones, nuclear elongation and concurrent extension of the acrosome. Replacement of histones by TNP1, TNP2 and subsequently by PRM1 and PRM2 occurs in the condensing spermatids of steps 12–14 (Bao and Bedford, 2016). Condensed spermatids of steps 15,16 also known as spermatozoa display a typical hook type morphology and are ready to be released into the lumen of seminiferous tubules. TSSK6, HSP90 and γH2AX are among other genes shown to play an important role in chromatin remodeling and condensation of spermatids during spermiogenesis (Jha et al., 2017). In this study, functional analysis of DEGs showed that genes (*Tnp1/2, Prm1/2, Tssk3/4/6, Hsp90, Klhl10*) mainly associated with biological process, such as spermatogenesis, male gamete

generation and spermatid development were significantly down-regulated in KI mice. This is consistent with previous studies demonstrating complete loss of TNP2 and PRM2 and TSSK6 protein expression in KI compared to WT (Kavarthapu et al., 2019). Further, the KEGG pathways analysis of down-regulated DEGs are mainly enriched in protein processing in endoplasmic reticulum and ubiquitin-proteasome pathways. Further, using STRING database we analyzed and constructed PPI network of down-regulated DEGs showing two significant modules with key hub genes belonging to spermatogenesis process and UPP. Moreover, these two modules are interconnected by KLHL10 and CUL3 proteins. CUL3 (Cullin3) is a Core component of cullin-RING-based E3 ubiquitin-protein ligase complex which interacts with substrate-specific adapter KLHL10 and functions specifically in the testis to mediate protein during spermiogenesis (Wang et al., 2006). Mutations in KLHL10 gene have been associated with oligospermia in some infertile males (Yatsenko et al., 2006). Haploinsufficiency of KLHL10 causes infertility in male mice devoid of ES due to failure of RS elongation after step 8 precisely similar morphology observed in our KI model (Yan et al., 2004; Wang et al., 2006).

Histone ubiquitination and acetylation play a crucial role in chromatin remodeling essential for development of spermatids during spermiogenesis (Baarends et al., 1999a,b; Rathke et al., 2014; Sheng et al., 2014). H2A is highly ubiquitinated in the XY bodies of pachytene spermatocytes in meiotic phase I. Ubiquitinated H2A and H2B are also abundantly found in ES and play important roles in chromatin remodeling during spermiogenesis (Baarends et al., 1999a; Sheng et al., 2014). Histone hyperacetylation mediated by specific histone acetyltransferases (HATs) like MOF/MYST1 and TIP60 during spermiogenesis facilitate histone replacement (Taipale et al., 2005; Thomas et al., 2007). E2 ubiquitin-conjugating enzyme UBE2J1 and ubiquitin E3 ligase RNF8 are part of an E2/E3 ubiquitin ligase complex shown to play an important role in spermatid development during spermiogenesis (Lu et al., 2010; Koenig et al., 2014). UBE2J1 KO mice are sterile with major defect in spermatid differentiation, resulting in male sterility acting as a key player in the elongation of spermatids (Koenig et al., 2014). Several testis-specific E3 ubiquitin ligases are known to be involved in wide-ranging molecular events during spermiogenesis including organelle turnover, protein turnover and quality and chromatin remodeling (Hou et al., 2012). RNF8 mediated H2A/H2B ubiquitination shown to be essential for histone hyperacetylation and important for histone removal at post-meiotic stage of germ cells (Lu et al., 2010). Furthermore, it has been shown that RNF8-dependent histone ubiquitination controls H4K16 acetylation by regulating association of MOF on the chromatin, which could be a crucial step for histone removal in the early ES (Lu et al., 2010; Ma et al., 2011).

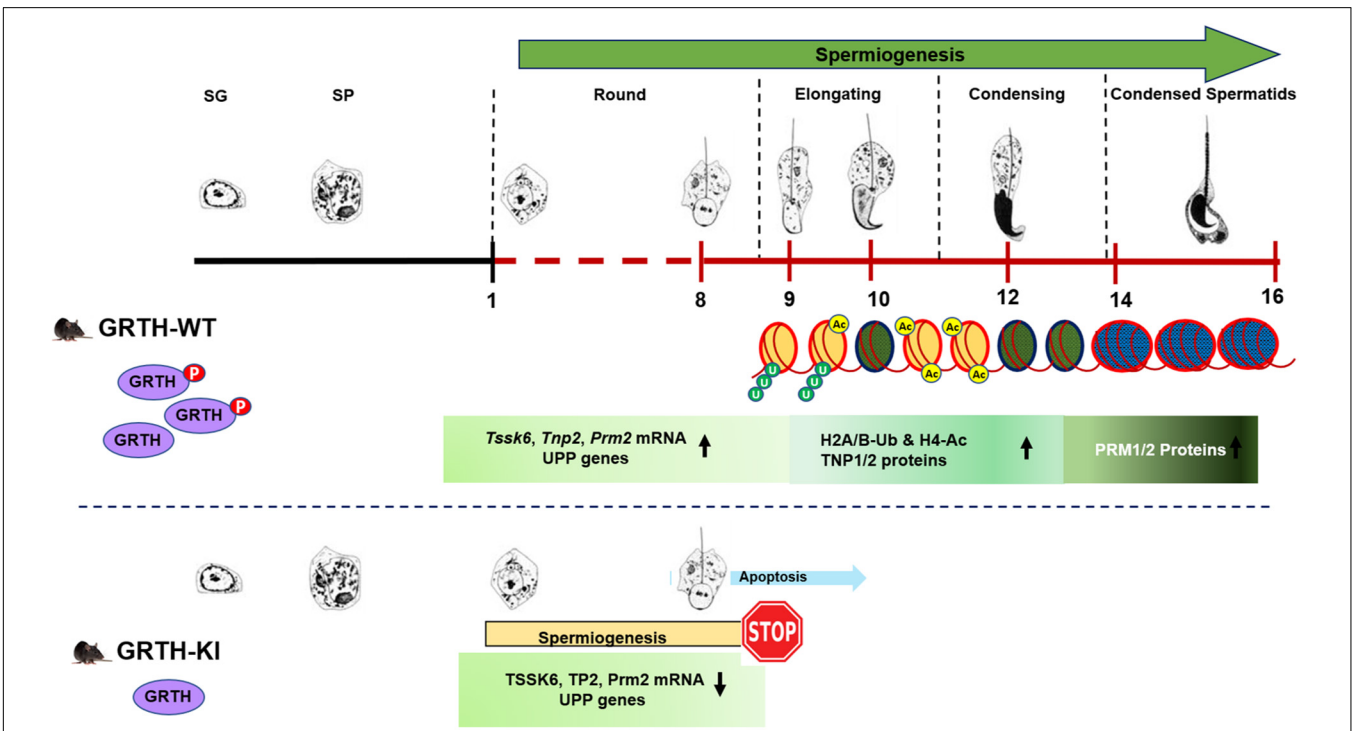

FIGURE 8 | Role of p-GRTH in histone ubiquitination and acetylation essential for round spermatid during spermiogenesis. Schematic diagram showing progression of mice spermiogenesis where germ cells undergo 16 different steps of development. In WT mice during the process of spermiogenesis in RS we observed increased and stable expression of Tssk6, Tnp2, Prm2, and UPP mRNAs until ready for translation in step 9 of RS. During spermatid elongation histones undergo ubiquitination (H2A/B-Ub) and acetylation (H4-Ac) resulting in their removal and replacement with transition proteins and protamines making the chromatin more compact/condensed. Of note is that in KI mice loss of p-GRTH has direct impact on expression of UPP genes required for ubiquitination and subsequent acetylation which impairs round spermatids to elongation.

In our study, genes related to the UPP were significantly down-regulated (**Figure 4A**). Although there was no differential expression of RNF8 in our RNA-Seq data, we found marked reduction in transcript levels of RNF8 and UBE2J1, and their proteins are barely detectable in KI mice. This consequently led to impair ubiquitination of H2A and H2B which is evident by the negligible expression of H2A-Ub and H2B-Ub proteins in Western blots. Further, the marked reduction in the association of p-GRTH protein with *Ube2j1* and *Rnf8* mRNA's may affect their translation as p-GRTH is known to associate with polyribosomes of germ cell specific genes during spermiogenesis (Sheng et al., 2006). We also found reduced expression of MOF in KI mice which facilitates acetylation of H4 during initial stages of spermatid elongation. Further, as expected these low levels of MOF hampered the acetylation of H4 and specifically of H4K16 which is evident by the significant reduction of their expression in the nucleus of RS and ES in our IHC analysis. Taken together our studies indicate that the complete impairment of spermatid development in KI mice lacking p-GRTH, is linked to the deficit on the expression of UBE2J1 and RNF8. These, in turn consequently disrupted the chain of events involving H2A/H2B ubiquitination and H4 acetylation for subsequent histone removal and replacement with transition proteins followed by protamines during spermiogenesis (**Figure 8**).

DATA AVAILABILITY STATEMENT

The RNA-Seq raw data files (KI and WT samples) in this study have been submitted to the NCBI (https://www.ncbi.nlm.nih.gov/geo) Gene Expression Omnibus (GEO accession number GSE145047). All other RNA-Seq results analyzed during this study are included in this article and its supplementary files.

ETHICS STATEMENT

The animal study was reviewed and approved by National Institute of Child Health and Human Development Animal Care and Use Committee.

AUTHOR CONTRIBUTIONS

RK and MD conceived and planned the experiments. RK and RA performed the experiments, analyzed the data. MD and RK discussed the results and wrote the manuscript. AS and JS contribute with RNA-Seq data analysis.

FUNDING

This work was supported by the National Institutes of Health Intramural Research Program through the *Eunice Kennedy Shriver* National Institute of Child Health and Human Development.

SUPPLEMENTARY MATERIAL

The Supplementary Material for this article can be found online at: https://www.frontiersin.org/articles/10.3389/fcell.2020.00310/full#supplementary-material

REFERENCES

Baarends, W. M., Hoogerbrugge, J. W., Roest, H. P., Ooms, M., Vreeburg, J., Hoeijmakers, J. H., et al. (1999a). Histone ubiquitination and chromatin remodeling in mouse spermatogenesis. *Dev. Biol.* 207, 322–333. doi: 10.1006/dbio.1998.9155

Baarends, W. M., Roest, H. P., and Grootegoed, J. A. (1999b). The ubiquitin system in gametogenesis. *Mol. Cell. Endocrinol.* 151, 5–16.

Bao, J., and Bedford, M. T. (2016). Epigenetic regulation of the histone-to-protamine transition during spermiogenesis. *Reproduction* 151, R55–R70. doi: 10.1530/REP-15-0562

Dai, L., Tsai-Morris, C. H., Sato, H., Villar, J., Kang, J. H., Zhang, J., et al. (2011). Testis-specific miRNA-469 up-regulated in gonadotropin-regulated testicular RNA helicase (GRTH/DDX25)-null mice silences transition protein 2 and protamine 2 messages at sites within coding region: implications of its role in germ cell development. *J. Biol. Chem.* 286, 44306–44318. doi: 10.1074/jbc.M111.282756

Dufau, M. L., and Kavarthapu, R. (2019). Gonadotropin regulation testicular RNA helicase, two decades of studies on its structure function and regulation from its discovery opens a window for development of a non-hormonal oral male Contraceptive. *Front. Endocrinol.* 10:710. doi: 10.3389/fendo.2019.00710

Dufau, M. L., and Tsai-Morris, C. H. (2007). Gonadotropin-regulated testicular helicase (GRTH/DDX25): an essential regulator of spermatogenesis. *Trends Endocrinol. Metab.* 18, 314–320. doi: 10.1016/j.tem.2007.09.001

Hazzouri, M., Pivot-Pajot, C., Faure, A. K., Usson, Y., Pelletier, R., Sèle, B.l, et al. (2000). Regulated hyperacetylation of core histones during mouse spermatogenesis: involvement of histone deacetylases. *Eur. J. Cell Biol.* 79, 950–960. doi: 10.1078/0171-9335-00123

Hecht, N. B. (1998). Molecular mechanisms of male germ cell differentiation. *Bioessays* 20, 555–561. doi: 10.1007/s00018-004-4034-y

Hou, X., Zhang, W., Xiao, Z., Gan, H., Lin, X., Liao, S., et al. (2012). Mining and characterization of ubiquitin E3 ligases expressed in the mouse testis. *BMC Genomics* 13:495. doi: 10.1186/1471-2164-13-495

Jha, K. N., Tripurani, S. K., and Johnson, G. R. (2017). TSSK6 is required for γH2AX formation and the histone-to-protamine transition during spermiogenesis. *J. Cell. Sci.* 130, 1835–1844. doi: 10.1242/jcs.202721

Kavarthapu, R., Anbazhagan, R., Raju, M., Morris, C. T., Pickel, J., and Dufau, M. L. (2019). Targeted knock-in mice with a human mutation in GRTH/DDX25 reveals the essential role of phosphorylated GRTH in spermatid development during spermatogenesis. *Hum. Mol. Genet.* 28, 2561–2572. doi: 10.1093/hmg/ddz079

Kavarthapu, R., Tsai-Morris, C. H., Fukushima, M., Pickel, J., and Dufau, M. L. (2013). A 5'-flanking region of gonadotropin-regulated testicular RNA helicase (GRTH/DDX25) gene directs its cell-specific androgen regulated gene expression in testicular germ cells. *Endocrinology* 154, 2200–2207. doi: 10.1210/en.2012-2230

Koenig, P. A., Nicholls, P. K., Schmidt, I., Hagiwara, M., Maruyama, T., Frydman, G. H., et al. (2014). The E2 ubiquitin-conjugating enzyme UBE2J1 is required for spermiogenesis in mice. *J. Biol. Chem.* 289, 34490–34502. doi: 10.1074/jbc.M114.604132

Lu, L. Y., Wu, J., Ye, L., Gavrilina, G. B., Saunders, T. L., and Xiaochun, Y. (2010). RNF8-dependent histone modifications regulate nucleosome removal during spermatogenesis. *Dev. Cell* 18, 371–384. doi: 10.1016/j.devcel.2010.01.010

Ma, T., Keller, J. A., and Yu, X. (2011). RNF8-dependent histone ubiquitination during DNA damage response and spermatogenesis. *Acta Biochim. Biophys. Sin.* 43, 339–345. doi: 10.1093/abbs/gmr016

Rathke, C., Baarends, W. M., and Awe, S. (2014). Renkawitz-Pohl R. chromatin dynamics during spermiogenesis. *Biochim. Biophys. Acta* 1839, 155–168. doi: 10.1016/j.bbagrm.2013.08.004

Russell, L. D., Ettlin, R. A., Sinha, H. A. P., and Clegg, E. D. (1990). *Mammalian Spermatogenesis Histological and Histopathological Evaluation of the Testis*, eds L. D. Russell, R. A. Ettlin, H. A. P. Sinha, and E. D. Clegg (St. Louis: Cache River Press), 1–40.

Sato, H., Tsai-Morris, C. H., and Dufau, M. L. (2010). Relevance of gonadotropin-regulated testicular RNA helicase (GRTH/DDX25) in the structural integrity of the chromatoid body during spermatogenesis. *Biochim. Biophys. Acta* 1803, 534–543. doi: 10.1016/j.bbamcr.2010.02.004

Sheng, K., Liang, X., Huang, S., and Xu, W. (2014). The role of histone ubiquitination during spermatogenesis. *Biomed. Res. Int.* 2014:870695.

Sheng, Y., Tsai-Morris, C. H., and Dufau, M. L. (2003). Cell-specific and hormone-regulated expression of gonadotropin-regulated testicular RNA helicase gene (GRTH/Ddx25) resulting from alternative utilization of translation initiation codons in the rat testis. *J. Biol. Chem.* 278, 27796–27803. doi: 10.1074/jbc.M302411200

Sheng, Y., Tsai-Morris, C. H., Gutti, R., Maeda, Y., and Dufau, M. L. (2006). Gonadotropin-regulated testicular RNA helicase (GRTH/Ddx25) is a transport protein involved in gene-specific mRNA export and protein translation during spermatogenesis. *J. Biol. Chem.* 281, 35048–35056. doi: 10.1074/jbc.M605086200

Shirakata, Y., Hiradate, Y., Inoue, H., Sato, E., and Tanemura, K. (2014). Histone H4 modification during mouse spermatogenesis. *J. Reprod. Dev.* 60, 383–387. doi: 10.1262/jrd.2014-018

Siu, M. K., and Cheng, C. Y. (2004). Extracellular matrix: recent advances on its role in junction dynamics in the seminiferous epithelium during spermatogenesis. *Biol. Reprod.* 71, 375–391. doi: 10.1095/biolreprod.104.028225

Taipale, M., Re, A. S., Richter, K., Vilar, A., Lichter, P., Imhof, A., et al. (2005). hMOF histone acetyltransferase is required for histone H4 lysine 16 acetylation in mammalian cells. *Mol. Cell. Biol.* 25, 6798–6810. doi: 10.1128/MCB.25.15.6798-6810.2005

Tang, P. Z., Tsai-Morris, C. H., and Dufau, M. L. (1999). A novel gonadotropin-regulated testicular RNA helicase. A new member of the dead-box family. *J. Biol. Chem.* 274, 37932–37940. doi: 10.1074/jbc.274.53.37932

Thomas, T., Loveland, K. L., and Voss, A. K. (2007). The genes coding for the MYST family histone acetyltransferases, Tip60 and Mof, are expressed at high levels during sperm development. *Gene Expr. Patterns* 7, 657–665. doi: 10.1016/j.modgep.2007.03.005

Tsai-Morris, C. H., Koh, E., Sheng, Y., Maeda, Y., Gutti, R., Namiki, M., et al. (2007). Polymorphism of the GRTH/DDX25 gene in normal and infertile Japanese men: a missense mutation associated with loss of GRTH phosphorylation. *Mol. Hum. Reprod.* 13, 887–892. doi: 10.1093/molehr/gam065

Tsai-Morris, C. H., Lei, S., Jiang, Q., Sheng, Y., and Dufau, M. L. (2004a). Genomic organization and transcriptional analysis of gonadotropin-regulated testicular RNA helicase–GRTH/DDX25 Gene. *Gene* 331, 83–94. doi: 10.1016/j.gene.2004.02.004

Tsai-Morris, C. H., Sato, H., Gutti, R., and Dufau, M. L. (2012). Role of gonadotropin regulated testicular RNA helicase (GRTH/Ddx25) on polysomal associated mRNAs in mouse testis. *PLoS One* 7:e32470. doi: 10.1371/journal.pone.0032470

Tsai-Morris, C. H., Sheng, Y., Gutti, R., Li, J., Pickel, J., and Dufau, M. L. (2010). Gonadotropin-regulated testicular RNA helicase (GRTH/DDX25) gene: cell-specific expression and transcriptional regulation by androgen in transgenic mouse testis. *J. Cell. Biochem.* 109, 1142–1147. doi: 10.1002/jcb.22493

Tsai-Morris, C. H., Sheng, Y., Lee, E., Lei, K. J., and Dufau, M. L. (2004b). Gonadotropin-regulated testicular RNA helicase (GRTH/Ddx25) is essential for spermatid development and completion of spermatogenesis. *Proc. Natl. Acad. Sci. U.S.A.* 101, 6373–6378. doi: 10.1073/pnas.0401855101

Villar, J., Tsai-Morris, C. H., Dai, L., and Dufau, M. L. (2012). Androgen-induced activation of gonadotropin-regulated testicular RNA helicase (GRTH/Ddx25) transcription: essential role of a nonclassical androgen response element half-site. *Mol. Cell. Biol.* 32, 1566–1580. doi: 10.1128/MCB.06002-11

Wang, S., Zheng, H., Esaki, Y., Kelly, F., and Yan, W. (2006). Cullin3 is a KLHL10-interacting protein preferentially expressed during late spermiogenesis. *Biol. Reprod.* 74, 102–108. doi: 10.1095/biolreprod.105.045484

Yan, W., Ma, L., Burns, K. H., and Matzuk, M. M. (2004). Haploinsufficiency of kelch-like protein homolog 10 causes infertility in male mice. *Proc. Natl. Acad. Sci. U.S.A.* 101, 7793–7798. doi: 10.1073/pnas.0308025101

Yatsenko, A. N., Roy, A., Chen, R., Ma, L., Murthy, L. J., Yan, W., et al. (2006). Non-invasive genetic diagnosis of male infertility using spermatozoal RNA: KLHL10 mutations in oligozoospermic patients impair homodimerization. *Hum. Mol. Genet.* 15, 3411–3419. doi: 10.1093/hmg/ddl417

Conflict of Interest: The authors declare that the research was conducted in the absence of any commercial or financial relationships that could be construed as a potential conflict of interest.

Copyright © 2020 Kavarthapu, Anbazhagan, Sharma, Shiloach and Dufau. This is an open-access article distributed under the terms of the Creative Commons Attribution License (CC BY). The use, distribution or reproduction in other forums is permitted, provided the original author(s) and the copyright owner(s) are credited and that the original publication in this journal is cited, in accordance with accepted academic practice. No use, distribution or reproduction is permitted which does not comply with these terms.

frontiers in Cell and Developmental Biology

ORIGINAL RESEARCH
published: 21 May 2020
doi: 10.3389/fcell.2020.00301

Functional Analysis of Hydrolethalus Syndrome Protein HYLS1 in Ciliogenesis and Spermatogenesis in *Drosophila*

*Yanan Hou[1], Zhimao Wu[1,2,3], Yingying Zhang[1,2,3], Huicheng Chen[1,2,3], Jinghua Hu[4], Yi Guo[4], Ying Peng[4,5] and Qing Wei[1]**

[1] Laboratory for Reproductive Health, Institute of Biomedicine and Biotechnology, Shenzhen Institutes of Advanced Technology, Chinese Academy of Sciences (CAS), Shenzhen, China, [2] Chinese Academy of Sciences Key Laboratory of Insect Developmental and Evolutionary Biology, Chinese Academy of Sciences Center for Excellence in Molecular Plant Sciences, Institute of Plant Physiology and Ecology, Chinese Academy of Sciences, Shanghai, China, [3] University of Chinese Academy of Sciences, Beijing, China, [4] Department of Biochemistry and Molecular Biology, Mayo Clinic, Rochester, MN, United States, [5] Institute of Medicine and Pharmaceutical Sciences, Zhengzhou University, Zhengzhou, China

OPEN ACCESS

Edited by:
Tomer Avidor-Reiss, University of Toledo, United States

Reviewed by:
Timothy L. Megraw, Florida State University, United States
Giuliano Callaini, University of Siena, Italy

***Correspondence:**
Qing Wei
qing.wei@siat.ac.cn

Specialty section:
This article was submitted to Cell Growth and Division, a section of the journal Frontiers in Cell and Developmental Biology

Received: *19 February 2020*
Accepted: *07 April 2020*
Published: *21 May 2020*

Citation:
Hou Y, Wu Z, Zhang Y, Chen H, Hu J, Guo Y, Peng Y and Wei Q (2020) Functional Analysis of Hydrolethalus Syndrome Protein HYLS1 in Ciliogenesis and Spermatogenesis in Drosophila. Front. Cell Dev. Biol. 8:301. doi: 10.3389/fcell.2020.00301

Cilia and flagella are conserved subcellular organelles, which arise from centrioles and play critical roles in development and reproduction of eukaryotes. Dysfunction of cilia leads to life-threatening ciliopathies. HYLS1 is an evolutionarily conserved centriole protein, which is critical for ciliogenesis, and its mutation causes ciliopathy–hydrolethalus syndrome. However, the molecular function of HYLS1 remains elusive. Here, we investigated the function of HYLS1 in cilia formation using the *Drosophila* model. We demonstrated that *Drosophila* HYLS1 is a conserved centriole and basal body protein. Deletion of HYLS1 led to sensory cilia dysfunction and spermatogenesis abnormality. Importantly, we found that *Drosophila* HYLS1 is essential for giant centriole/basal body elongation in spermatocytes and is required for spermatocyte centriole to efficiently recruit pericentriolar material and for spermatids to assemble the proximal centriole-like structure (the precursor of the second centriole for zygote division). Hence, by taking advantage of the giant centriole/basal body of *Drosophila* spermatocyte, we uncover previously uncharacterized roles of HYLS1 in centriole elongation and assembly.

Keywords: HYLS1, ciliogenesis, ciliary gate, PCL, centriole elongation, spermatogenesis

INTRODUCTION

Centrioles are small cylindrical cellular organelles typically composed of ninefold symmetric triplet microtubules, which perform two important functions, building centrosome and templating cilia (Bettencourt-Dias and Glover, 2007; Nigg and Stearns, 2011; Conduit et al., 2015). Centrioles recruit pericentriolar material (PCM) to form centrosomes that function as the microtubule-organizing center to organize the mitotic/meiotic spindles. In quiescent cells, centrioles dock to the cell membrane to function as basal bodies to initiate the biogenesis of cilia. Cilia are critical sensory or motile organelles that regulate development and reproduction of eukaryotes

(Goetz and Anderson, 2010; Bettencourt-Dias et al., 2011; Malicki and Johnson, 2017; Anvarian et al., 2019). Dysfunction of cilia results in dozens of human genetic diseases, collectively termed ciliopathies (Hildebrandt et al., 2011; Reiter and Leroux, 2017).

In vertebrates, only the mother centriole, but not the daughter centriole, has the ability to form cilia, because only the mother centriole has distal appendage (DA) structures, which is critical for ciliogenesis initiation by mediating centrioles membrane docking. During ciliogenesis, DAs are converted into transition fibers (TFs), one of the conspicuous structures at the cilia base. In invertebrates, such as *Caenorhabditis elegans* (*C. elegans*) and *Drosophila*, centrioles lack DAs, but TFs, at least functional homologous structures, are formed during ciliogenesis. Transition fibers, together with the transition zone (TZ), act as the ciliary gate to control the ciliary protein entry in the context of cilia (Reiter et al., 2012; Takao and Verhey, 2016; Garcia-Gonzalo and Reiter, 2017). The TZ functions as a diffusion barrier to gate the ciliary compartment (Reiter et al., 2012; Garcia-Gonzalo and Reiter, 2017), whereas the TF promotes the import of ciliary proteins. FBF1 is the key TF protein that mediates the entry of ciliary proteins, including intraflagellar transport (IFT) complexes, which are essential for ciliary axonemal elongation (Wei et al., 2013, 2015; Yang et al., 2018). Despite that great progress has been made in understanding the molecular components of DA/TF and their function in ciliogenesis, how such appendages are uniquely assembled from the distal end of mother centriole remains largely as an unsolved mystery (Tanos et al., 2013; Ye et al., 2014; Yang et al., 2018).

Hydrolethalus syndrome (HLS) is a rare recessive lethal inherited disorder that causes serious defects in fetal development and results in birth defects, with its causal gene HYLS1 first identified in 2005 (Mee et al., 2005). Its function was first studied in detail using *C. elegans* as a model organism. Dammermann et al. (2009) found that HYLS1 is a centriole protein that is recruited to the outer centriole wall via direct interaction with the core centriolar protein SAS-4/CPAP. Unexpectedly, HYLS1 is dispensable for centriole assembly, cell division, and embryonic viability in worm, but it is specifically involved in cilia formation in *C. elegans* (Dammermann et al., 2009). Subsequently, we demonstrated that HYLS1 mediates ciliogenesis by regulating the formation of the ciliary gate, plays a major role in recruiting the TF protein FBF1, and plays a minor role in TZ assembly (Wei et al., 2016).

Because of the degeneration of basal bodies after ciliogenesis in *C. elegans* (Sharma et al., 2016), our understanding of how HYLS1 regulates the ciliary gate is limited. Here we sought to address this question using the *Drosophila* model organism. We showed that HYLS1 is a conserved centriole and basal body protein, which is required for ciliogenesis and spermatogenesis in *Drosophila*. Deletion of HYLS1 compromised the localization of ciliary gate proteins in both sensory cilia and spermatocyte cilia. Importantly, by taking advantage of the giant centriole (GC)/basal body in spermatocytes, an excellent model to visualize the dynamic change from centriole to basal body conversion, we found that HYLS1 is critical for the elongation of the GC. In addition, we found that fly HYLS1 is required for efficient PCM components recruitment in spermatocyte and the proximal centriole-like structure (PCL) formation in spermatids. Our findings reveal novel roles of HYLS1 in centriole elongation and assembly during *Drosophila* spermatogenesis, suggesting that the abnormal ciliary gating associated with *hyls1* mutation may arise as a consequential outcome from HYLS1-related distal centriole assembly defects.

RESULTS

Drosophila HYLS1 Is a Conserved Centriole and Basal Body Protein

Reciprocal protein homology queries using BLAST identified CG42231 as the only annotated gene in *Drosophila* genome with significant homology comparing with mammalian HYLS1 (**Supplementary Figure S1**). Because CG42231 has never been studied, we named it as HYLS1 hereafter and used genetic manipulations to study its function.

To determine if the centriole/basal body localization of HYLS1 is conserved in *Drosophila*, we created transgenic flies expressing a green fluorescent protein (GFP) tagged HYLS1 transgene and generated the anti-HYLS1 antibody. The antibody was validated by the following facts: anti-HYLS1 staining showed similar localization pattern as HYLS1-GFP (**Figure 1** and **Supplementary Figure S2**); the staining signal was completely lost in *hyls1* deletion mutants (**Figure 3D**). As demonstrated by both HYLS1-GFP and anti-HYLS1 staining, HYLS1 colocalized with the centrosome marker γ-tubulin or ANA1 in early syncytial stage embryos of *Drosophila* (**Figure 1A** and **Supplementary Figure S2A**), indicating that it is indeed a centriole protein. In *Drosophila*, only Type I monodendritic sensory neurons of the peripheral nervous system (PNS) and sperm cells are ciliated. Type I sensory neurons include external sensory (Es) and chordotonal (Ch) neurons (Jarman, 2002; Boekhoff-Falk, 2005; Kernan, 2007). In both types of ciliated neurons, co-staining of HYLS1-GFP or anti-HYLS1 with the ciliary marker 21A6/EYS (Vieillard et al., 2015) showed that HYLS1 localized to the cilia base (**Figure 1B** and **Supplementary Figure S2B**). By colabeling ectopic HYLS1-GFP with the centriole marker ANA1, we observed that HYLS1 completely overlapped with ANA1 in both the distal centriole and the proximal centriole (**Figure 1B**).

In sperm cells, centrioles and basal bodies undergo dynamic changes during spermatogenesis (Fabian and Brill, 2012; Jana et al., 2016; Vieillard et al., 2016; Lattao et al., 2017; **Figure 2A**). In spermatogonia, centrioles are devoid of appendage structures required for ciliogenesis. In early spermatocytes, centrioles start to accumulate components required for ciliogenesis at their tips. During spermatocyte maturation, paired centrioles dock to the plasma membrane and convert to basal bodies, and then cilium-like structures arise from both the mother and daughter centrioles. Of note, at this stage, paired centrioles/basal bodies elongate dramatically and form GCs/basal bodies with a characteristic V-shaped structure; therefore, it is an attractive model to study the centriole to basal body conversion. In round spermatids, flagellar axonemes start to elongate; cilium-like structures together with ring centriole progressively migrate

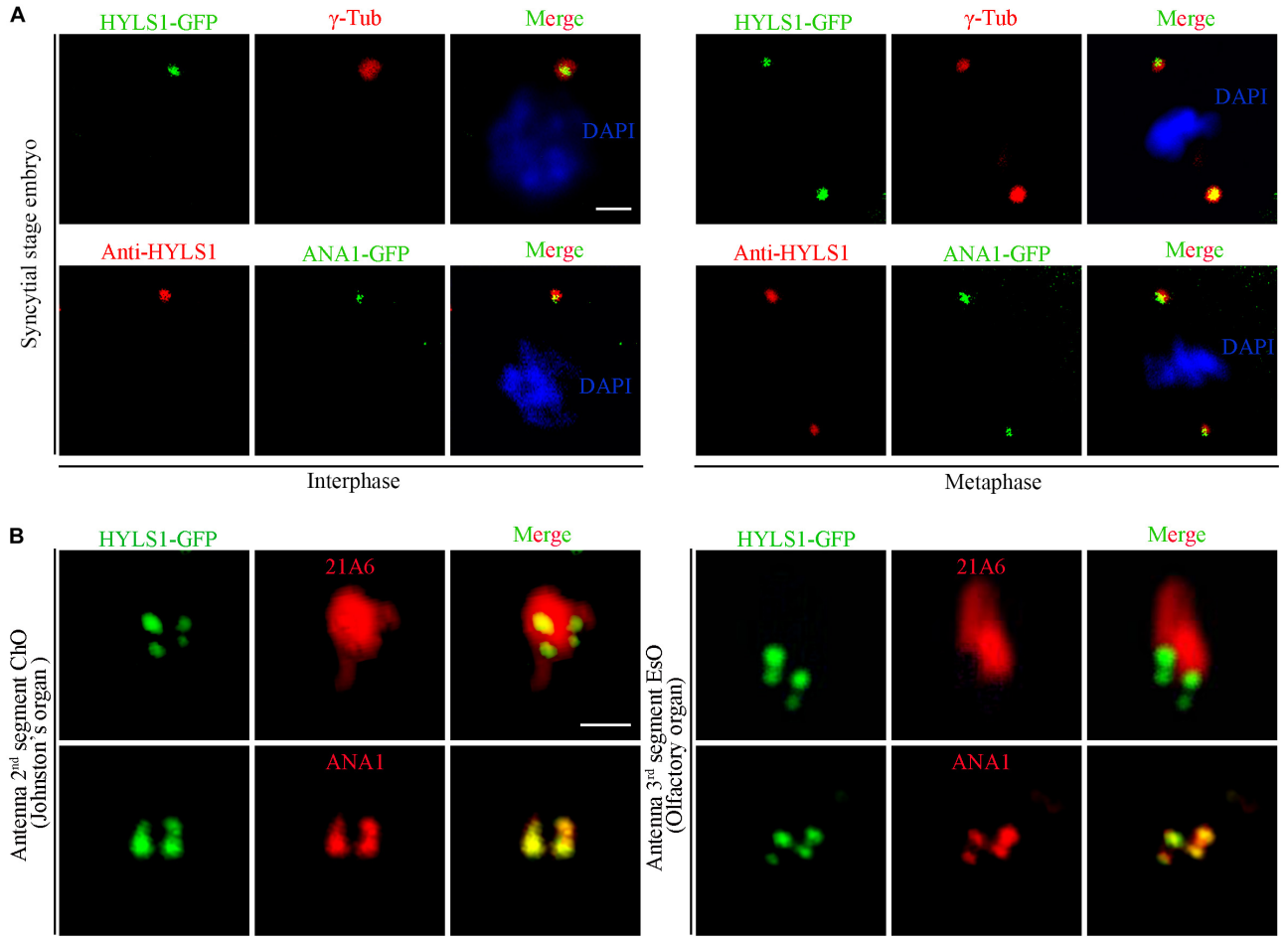

FIGURE 1 | *Drosophila* HYLS1 localizes to centrioles in embryos and basal bodies in sensory cilia. **(A)** In early syncytial stage embryos, GFP-tagged HYLS1 localizes to centrosome labeled by γ-tubulin and centriolar protein ANA1 in both interphase and metaphase. Blue channel in the merged panel represents DNA stained by DAPI. Scale bars: 2 μm. **(B)** Representative images illustrate that HYLS1 is localized to the ciliary base in sensory neurons of both chordotonal organ (ChO) and external sensory organ (EsO). ANA1 is a centriolar protein; 21A6/Eys indicates the base of the sensory cilia. Scale bars: 1 μm.

away from basal bodies. We observed that HYLS1 localized to the centriole in spermatogonia and the basal body in spermatocytes and spermatids, as demonstrated by both HYLS1-GFP and anti-HYLS1 staining (**Figure 2B** and **Supplementary Figure S2C**). In spermatocytes, HYLS1 colocalized with γ-tubulin along the whole elongated basal body. In spermatids, HYLS1 presented only at the basal body; no HYLS1 can be detected at the migrated ring centriole marked by UNC (the putative homolog of centriole distal end protein OFD1). Three-dimensional structured illumination microscopy (3D-SIM) showed that HYLS1 localized in a distinctive domain below the TF protein CG5964/FBF1 and the TZ protein MKS1 (**Figure 2C**). Taken together, we conclude that HYLS1 is a conserved centriole and basal body protein in *Drosophila*.

Drosophila HYLS1 Is Required for Sensory Responses

To understand the function of HYLS1 in *Drosophila*, we employed the CRISPR/Cas9-based genome editing technique to delete most of the second exon of HYLS1 and generated an *hyls1* deletion mutant *hyls1*^{56} (**Figures 3A,B**). We identified this allele by genomic polymerase chain reaction (PCR) (**Figure 3C**), and subsequent sequence analysis revealed it bears a 206 bp deletion in the second exon of *hyls1* gene, leading to a predicted reading frame shift. Because only the first 38 amino acids (aa) of the very N-terminus of HYLS1 are predicted to be translated followed shortly by a *de novo* stop codon (**Figure 3B**), *hyls1*^{56} is likely a null allele. Such assertion was confirmed by a complete loss of endogenous HYLS1 immunofluorescence signal from the basal body in *hyls1* mutants (**Figure 3D**).

Of note, another gene, *chiffon*, which is involved in DNA replication and histone acetylation (Landis and Tower, 1999; Torres-Zelada et al., 2019), is in the intron between the exon 1 and exon 2 of *hyls1*. *chiffon* has four annotated isoforms: RB and RD have no shared exons with *hyls1* and encode the same 1,695-aa protein; RE encodes the shortest protein of 576 aa residing within RB/RD; RA encodes a 1,711-aa protein. The extra 30-aa C-terminus of RA is encoded by a quite short exon shared

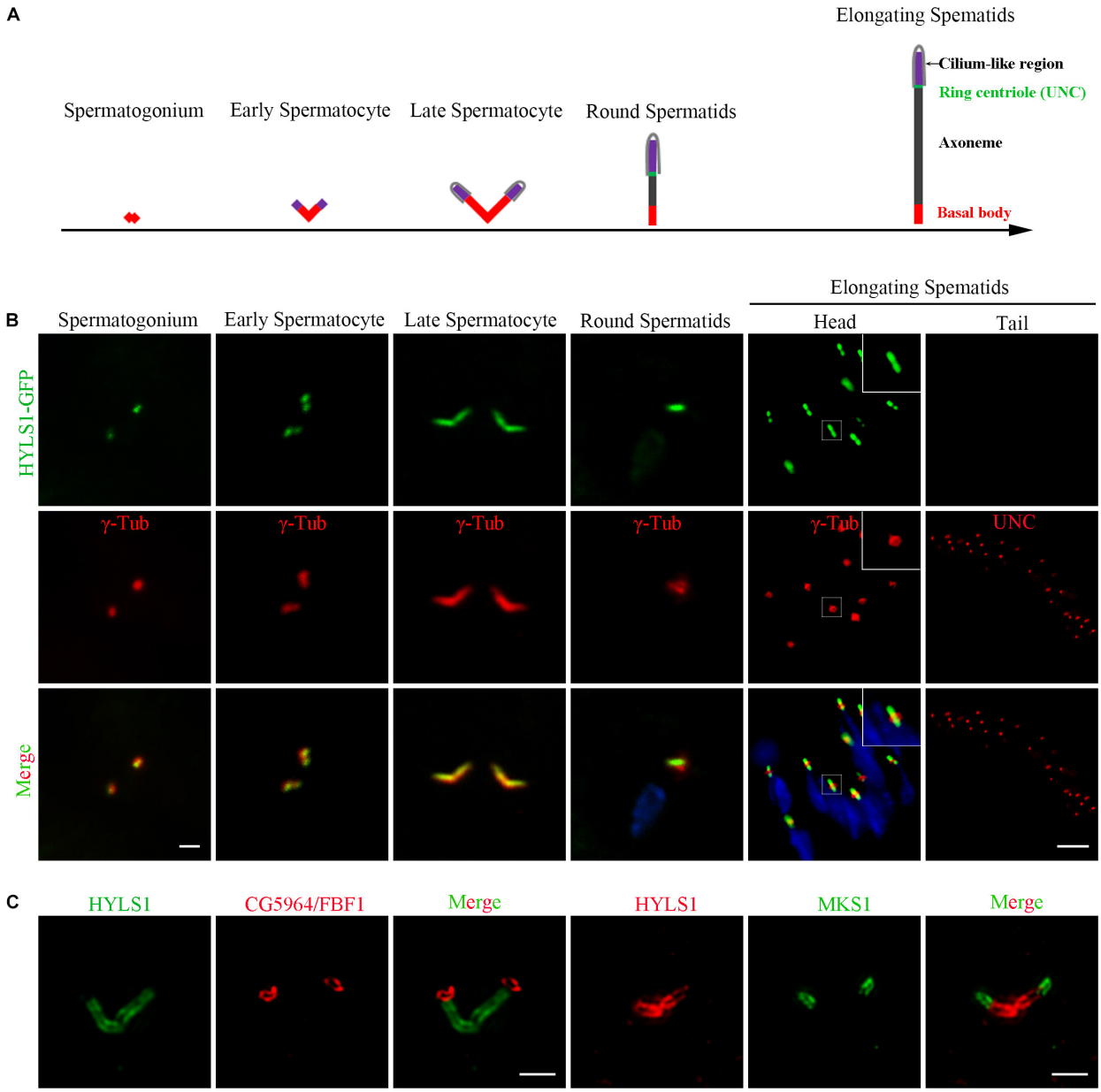

FIGURE 2 | *Drosophila* HYLS1 is a conserved centriole and basal body protein during spermatogenesis. **(A)** Schematic illustration of the dynamic behavior of centrioles during spermatogenesis (see text for details). **(B)** GFP-tagged HYLS1 colocalizes with the centrosome marker γ-tubulin in both spermatogonium and spermatocyte stages. Scale bar: 1 μm. In elongating spermatids, HYLS1 is remained as a basal body protein (magnified region from a head of elongating spermatids, bar: 5 μm), and no HYLS1 migrates to the ring centriole labeled by UNC (bar: 10 μm). Blue channel in the merged panel represents DNA from mature spermatids. **(C)** 3D-SIM images show that HYLS1 distributes along the entire centrioles and below the transition fiber marker FBF1/CG5964 (left) and the transition zone marker MKS1 (right), indicating that HYLS1 is not a TF or TZ component. Scale bars: 1 μm.

with part of exon 2 of *hyls1*, which is deleted in our *hyls1*^{56} mutants (**Supplementary Figure S3**). As the 1,695-aa protein is fully functional (Torres-Zelada et al., 2019), our mutant should not affect the function of chiffon. Such conclusion was further supported by the fact that our *hyls1*^{56} mutant flies are viable and females are fertile, whereas deletion of CHIFFON results in female infertility and adult lethality (Landis and Tower, 1999; Torres-Zelada et al., 2019).

hyls1^{56} mutants show moderately uncoordinated phenotype (**Supplementary Videos S1**, **S2**), a phenotype usually associated with cilia mutants. Interestingly, the uncoordinated phenotype was fully rescued by expression of a WT *hyls1* transgene in neurons driven by *elav*-GAL4, confirming that HYLS1 is the gene responsible for behavior defects in *hyls1*^{56} mutants (**Supplementary Video S3**).

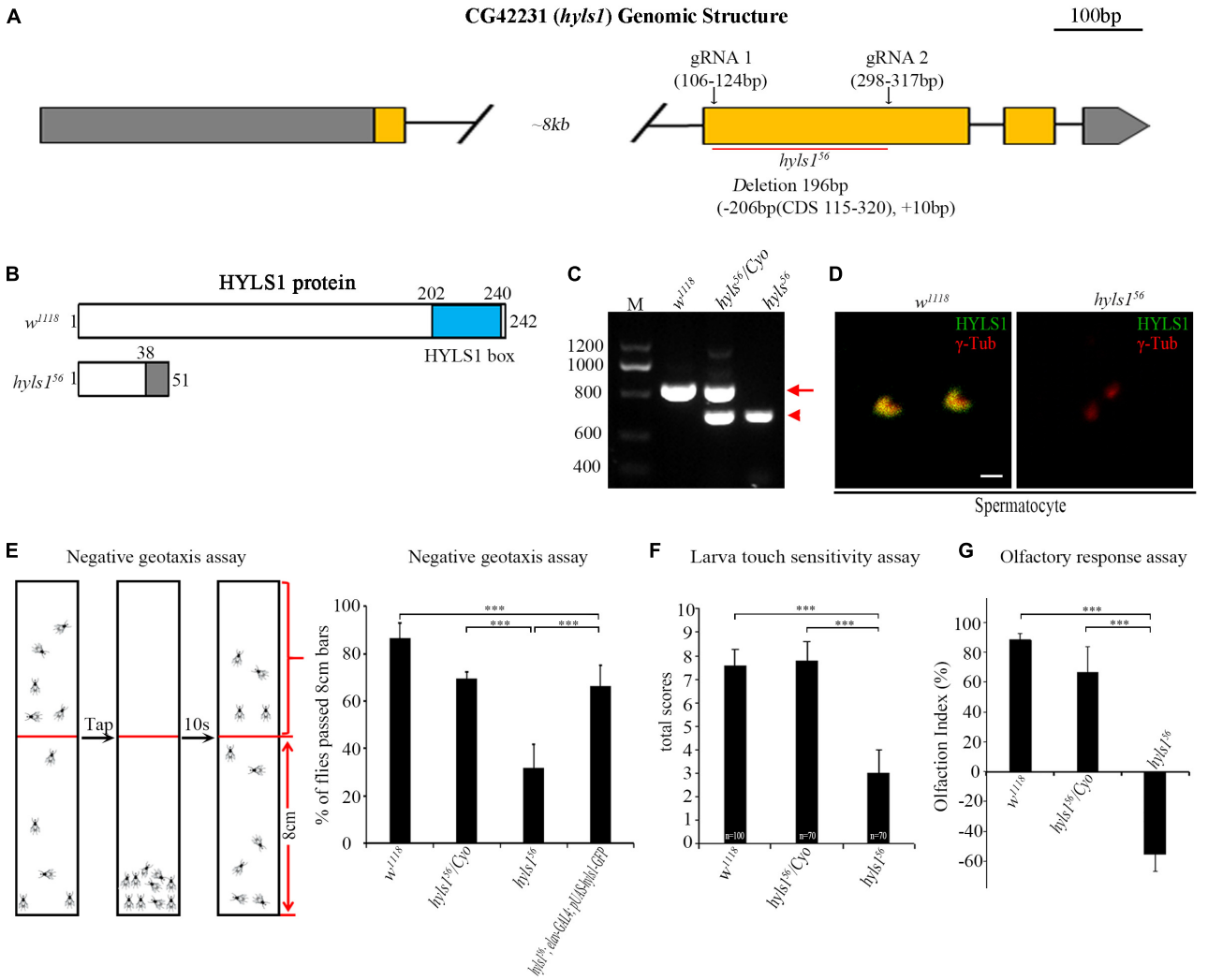

FIGURE 3 | *Drosophila* HYLS1 is required for sensory responses. **(A)** Generation of an *hyls1* null mutant. Diagram shows the genomic region of *Drosophila hyls1* (*CG42231*). CRISPR/Cas9 system was used to create the null mutant *hyls1*^{56}. *hyls1*^{56} has a 206-bp nucleotides deletion and an extra 10-bp nucleotides insertion between the targeting sites of gRNA1 and gRNA2 in the second exon. **(B)** Diagram compares the wild-type HYLS1 protein versus the predicted truncated protein. HYLS1 is a 242-residue-long protein, containing a conserved HYLS1 box at its C terminus. *hyls1*^{56} encodes a small, C-terminus truncated protein. **(C)** Genotyping of *hyls1* mutants by PCR, primers are listed in **Supplementary Table S1**. The size of amplicon from *hyls1*^{wt} is 768 bp (arrow), whereas from *hyls1*^{56} is only of 572 bp (arrowhead). **(D)** Immunostaining by anti-HYLS1 and anti–γ-tubulin confirmed that HYLS1 is lost in the spermatocyte centrosome of *hyls1*^{56} mutants. **(E)** *hyls1*^{56} mutants show reduced climbing ability. The percentage of *hyls1*^{56} flies that passed the 8-cm bars is significantly lower than that in both wild-type and heterozygous *hyls1*^{56}/*Cyo* flies. Expression of HYLS1 in PNS neurons with elav-GAL4 rescued the defective phenotype. **(F)** Compared with controls, *hyls1*^{56} homozygous larvae present touch sensitivity defects. Numbers of tested larvae are indicated in the plot. **(G)** Mutation in *hyls1* causes defective olfactory response. Error bars represent mean with SEM. n.s., $p > 0.05$; ***$p \leq 0.001$ (Student's *t*-test). Scale bar: 1 μm.

First, we examined the cilium ultrastructure of JO in *hyls1* mutants using transmission electron microscopy. JO is composed of a various number of scolopidia. A scolopidium usually consists of two neurons with cilia residing on the dendrite tip. In WT, two axonemes are present in the cross section of a scolopidium. However, in *hyls1* mutants, missing axoneme was observed (**Supplementary Figure S4**), indicating that a subset of cilia is truncated in *hyls1* mutants.

As cilia are essential for sensory response in neurons, we then examined the sensory abilities of *hyls1* mutants with a series of behavioral assays. Negative geotaxis has been well characterized in flies, governed by ciliated sensory organs, which are responsible for gravity perception and locomotor coordination (Kernan, 2007). Wild-type flies climb upward against gravity, after tapping down to the bottom of a tube; most of them move back toward the top in a few seconds. On the contrary, most *hyls1* mutants stayed at the bottom of the testing tube after tapping, indicating that negative geotaxis behavior is significantly affected in *hyls1* mutants (**Figure 3E**). Accordingly, climbing defect was effectively rescued by expression of a WT *hyls1* transgene in neurons driven by *elav*-GAL4, confirming that HYLS1 is indeed responsible for negative

geotaxis defect in mutant flies. To test the mechanosensory capabilities of *hyls1* mutants, we performed touch sensitivity assay and found the response to touch in larva of *hyls1* mutants was also severely impaired (**Figure 3F**). Moreover, we conducted the Y-maze assay to assess the olfactory sensitivity of *hyls1* mutants. As expected, *hyls1* is required for normal chemical sensation because *hyls1* mutants have serious defects in attraction by grape juice. Instead, it seems that *hyls1* mutants reject grape juice (**Figure 3G**). This result indicates that not only the normal olfactory response is disturbed, but also the response pathway also undergoes some changes, which may be due to simultaneous defects in the transport of certain membrane proteins and/or signal molecules that promote or inhibit olfactory function. Altogether, these behavioral assays demonstrate that HYLS1 is required for neuron sensory response in *Drosophila*.

Drosophila HYLS1 Is Required for Protein Trafficking in Sensory Cilia

It has been reported that HYLS1 is required for the function and formation of ciliary gate (Wei et al., 2016). Therefore, we first examined the localization of ciliary soluble proteins (IFT components) and membrane protein (IAV) in cilia of $hyls1^{56}$ mutants. Axonemes of auditory cilia in the second antennal segment are longer, which are more suitable for cilia study. As expected, we observed that compared with WT, the ciliary level of IFT-B components IFT52 and NOMPB (the ortholog of human IFT88) and the IFT-A components REMPA (the ortholog of human IFT140) was significantly reduced in auditory cilia of $hyls1^{56}$ mutants (**Figure 4B**). These observations were further confirmed by our quantitative analysis of the signal intensity of these IFT proteins or the ratio of IFT protein intensity to the actin intensity in the associated scolopidia (**Figure 4C** and **Supplementary Figure S5**). Accordingly, the amount of ciliary membrane receptor IAV was also dramatically reduced in sensory cilia of $hyls1^{56}$ mutants (**Figures 4B,C**). These results indicate that deletion of HYLS1 compromised the entry of ciliary proteins.

Then, we determined ciliary gate formation in $hyls1^{56}$ mutants by examining the localization of ciliary gate proteins. The TZ, together with TFs, forms the ciliary gate (Reiter et al., 2012; Takao and Verhey, 2016; Garcia-Gonzalo and Reiter, 2017). As shown in **Figure 5**, the signals of TZ protein MKS1 and MKS6 were dramatically reduced in $hyls1^{56}$ mutants compared to WT, although they were still able to target to the basal body. Transition fiber structures have been observed at the base of sensory cilia in *Drosophila* (Jana et al., 2018). FBF1 is the key TF protein mediating the ciliary protein entry in nematodes and mammals. Its *Drosophila* homolog is encoded by CG5964, and we have characterized CG5964 as a functional TF protein in *Drosophila* (Y.H., unpublished results). Interestingly, consistent with what we have reported in *C. elegans*, CG5964 was completely lost or only minimally retained in sensory cilia in *hyls1* mutant flies (**Figure 5**). Taken together, our results suggest that HYLS1 is involved in the function and formation of the ciliary gate in *Drosophila*.

HYLS1 Is Essential for Giant Centriole Elongation in Spermatocytes

Next, we examined the role of HYLS1 in spermatocyte cilia, which have no IFT and only contain conserved TZ proteins (Han et al., 2003; Sarpal et al., 2003; Williams et al., 2011). Although TF structures have not been observed in spermatocyte cilia (Riparbelli et al., 2012; Jana et al., 2018), CG5964 is indeed localized to a distinct region corresponding to the TF, at the tip of centriole and below the TZ. Consistent with what we observed in sensory cilia, the signal intensities of CG5964 and TZ proteins MKS1 and MKS6 were significantly reduced in spermatocyte cilia of *hyls1* mutants compared to WT (**Figure 6A**). And again, CG5964 is more sensitive to HYLS1 deletion. In approximately 30% of cilia, CG5964 was completely lost.

Surprisingly, we observed that, compared with WT that has a large V-shaped centriole pair, the centrioles in *hyls1* mutant spermatocytes were significantly shorter, as indicated by the centriole marker ANA1/CEP295 (**Figure 6B**). This phenotype is specific to the centriole elongation, because TZ proteins can still be recruited to the tip of growing centrioles throughout spermatocytes development. To further confirm the role of HYLS1 in regulating centriole elongation, we measured the distance between two TZ protein dots associated with a given pair of centrioles. As expected, the results showed that the mean distance between two protein dots in *hyls1* mutants was significantly shorter than that in WT (**Figure 6C**).

As a centriole protein, how could HYLS1 regulate the localization of TF/TZ proteins? One possible explanation is that HYLS1 regulates the elongation/assembly of the distal centriole where TF/TZ are localized. However, no supportive evidence has been reported. Our observations provide the strong evidence for this hypothesis. We suggest that defects in centriole elongation contribute to defects in TZ and TF in *hyls1* mutants. Without proper HYLS1-dependent centriole growth and structural remodeling, TF and TZ can be formed but with significant abnormalities (such as decreased localization of TF and TZ proteins).

Drosophila HYLS1 Is Required for PCM Recruitment in Spermatocytes and PCL Formation in Spermatids

In addition to the short centrioles, we observed that the signal of γ-tubulin was dramatically reduced in centrosomes in spermatocytes of *hyls1* mutants compared to WT (**Figure 7A**). Because γ-tubulin is a PCM component, we examined the level of another PCM component CNN. Compared with WT, the amount of CNN was significantly decreased in interphase in *hyls1* mutant cells as well (**Figure 7B**). Pericentriolar material enlarges in meiosis, and its component CNN is robustly recruited to the centrosome. Quantification of the CNN signal revealed that the recruitment of CNN around HYLS1-negative meiotic centrosomes was significantly less robust comparing with WT (**Figure 7C**). All these results collectively indicated that HYLS1 is involved in PCM recruitment in spermatocytes.

Drosophila spermatids have two centrioles: one is a typical centriole (GC), and the other one is an atypical centriole (PCL)

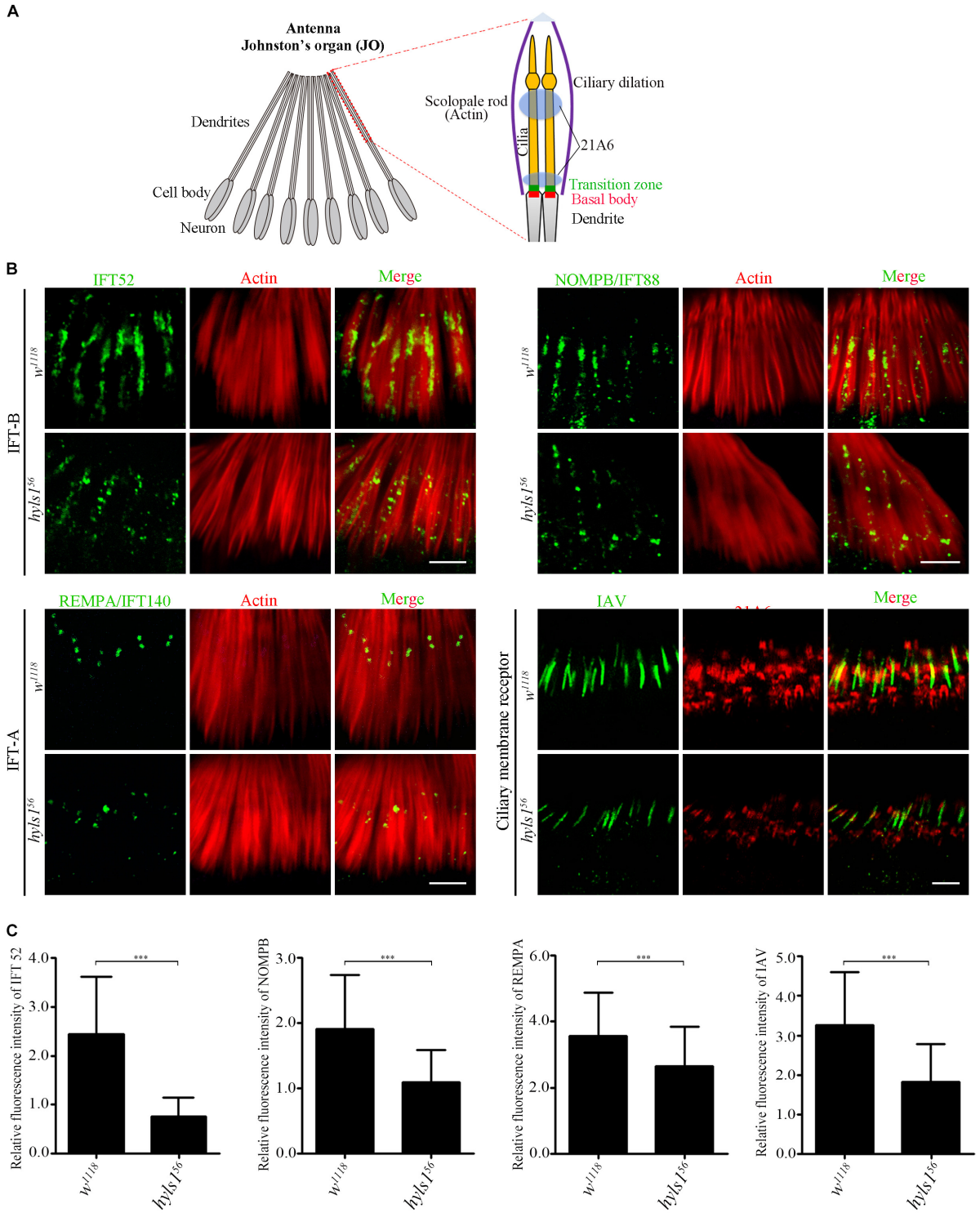

FIGURE 4 | HYLS1 is required for the entry of ciliary proteins in *Drosophila*. **(A)** Schematic view of the Johnston's organ (JO) at the second antennae segment. JO is a specialized chordotonal organ (ChO), which is composed of a various of scolopidia. A scolopidia consists of two Ch neurons and several accessory cells. Ch neurons bear cilia from their dendrite tip; details of the ciliary region of a single scolopidia are illustrated on the right panel. Actin marks scolopale rods, which enclosed the cilia, and 21A6 labels the scolopale lumen around the proximal end of the cilia and the region below the ciliary dilation. **(B)** HYLS1 is required for the ciliary entry of IFT components in *Drosophila*. The ciliary signal intensities of IFT-B components IFT52 and NOMPB/IFT88, IFT-A protein REMPA/IFT140, and ciliary membrane protein IAV are significantly reduced in *hyls1* mutants. Bars: 5 μm. **(C)** Quantifications of relative fluorescence intensities of IFT52 (control $n = 89$; $hyls1^{56}$ $n = 85$), NOMPB (control $n = 91$; $hyls1^{56}$ $n = 53$), REMPA (control $n = 148$; $hyls1^{56}$ $n = 125$), and IAV (control $n = 132$; $hyls1^{56}$ $n = 132$) in WT and *hyls1* mutants. Error bars represent ± s.d., n.s., $p > 0.05$; ***$p \leq 0.001$ (Student's *t*-test). Scale bars: 2 μm. "n" is the number of cilia examined.

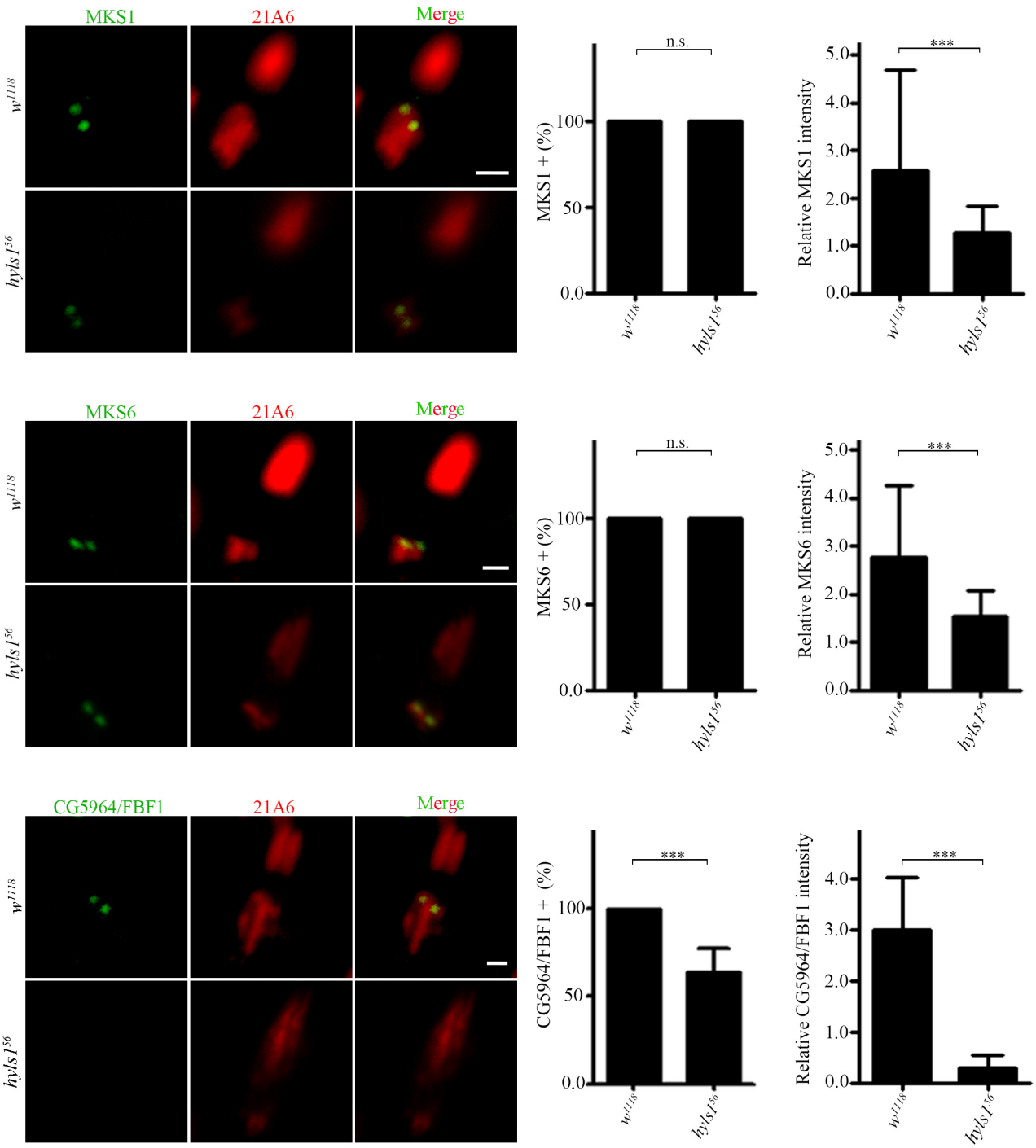

FIGURE 5 | HYLS1 is required for the proper localization of ciliary gate proteins in sensory cilia in *Drosophila*. Representative images of ciliary gate proteins MKS1 (control n = 115; $hyls1^{56}$ n = 70), MKS6 (control n = 69; $hyls1^{56}$ n = 105), and CG5964 (control n = 98; $hyls1^{56}$ n = 59) in WT and *hyls1* mutants. Corresponding quantifications of relative fluorescence intensities were shown in the right panel. Error bars represent ± s.d., n.s., $p > 0.05$; ***$p \leq 0.001$ (Student's *t*-test). Scale bars: 2 μm. "n" is the number of cilia examined.

adjacent to the distal part of GC (Blachon et al., 2009). Both centrioles are required for zygote mitosis (Gottardo et al., 2015; Khire et al., 2016). Strikingly, we observed that, in addition to the short typical centriole, PCL was often lost in *hyls1* mutant spermatids. We confirmed this result by using two PCL marker proteins ANA1 and POC1 (**Figure 7D**). It is not likely that HYLS1 is a PCL protein, as we did not observe that HYLS1 localizes to PCL (**Figure 2B** and **Supplementary Figure S2B**). Given the fact

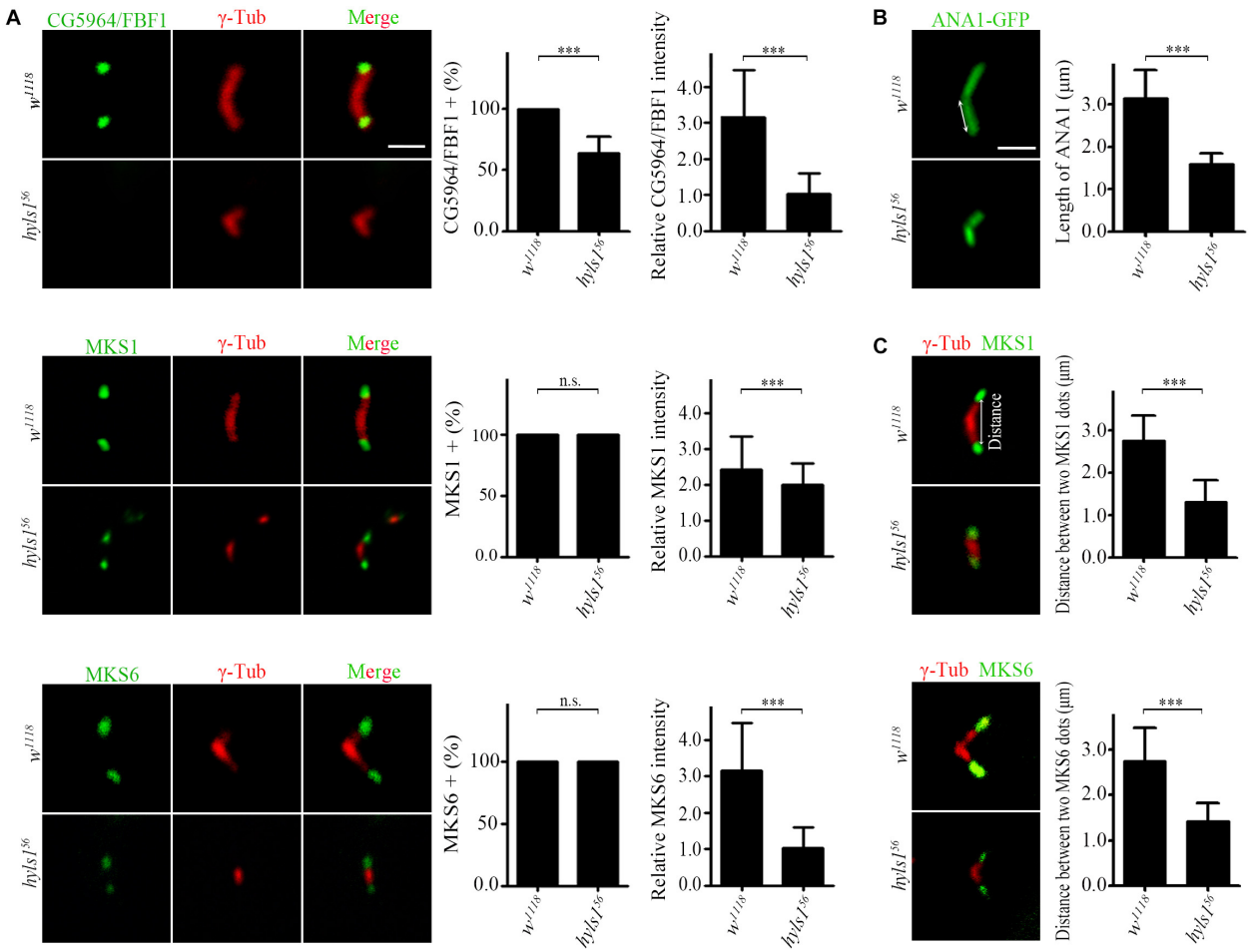

FIGURE 6 | HYLS1 is essential for giant centriole elongation in spermatocytes. **(A)** In *hyls1*, CG5964 partially failed to be recruited to centriole tips in spermatocytes (control $n = 87$; $hyls1^{56}$ $n = 57$; upper), and reduced signal intensities of MKS1 ($n = 143$; $hyls1^{56}$ $n = 76$; middle) and MKS6 (control $n = 103$; $hyls1^{56}$ $n = 98$; lower) were observed. **(B)** Representative micrographs of meiosis II centrioles stained by ANA1-GFP (right) in testes from control and *hyls1* mutants. Quantification of centriole length was shown in the right panel. **(C)** Deletion of HYLS1 leads to shorter distance between two transition zone dots associated with V-shaped centrioles (upper, MKS1; lower, MKS6). The relative distance between two signal dots (double-headed arrow) was quantified in the right panel. Scale bars: 2 μm. For all charts, error bars represent ± s.d.; statistical analysis was done with paired Student's *t*-test, n.s., $p > 0.05$; ***$p \leq 0.001$.

that PCL is adjacent to the distal part of GC, it is tempting to speculate that PCL formation depends on centriole distal part; loss of PCL in *hyls1* mutants may be caused by the defects in centriole elongation.

Taken together, our results indicate that HYLS1 is required for centriole elongation and assembly in *Drosophila* sperm cells.

HYLS1 Is Required for Spermatogenesis in *Drosophila*

To determine if HYLS1 is required for spermatogenesis, we examined sperm production. In *hyls1* mutants, mature sperms were accumulated in the seminal vesicles and were motile; no visible abnormalities were observed. Colabeling of DNA and α-tubulin in spermatocyte cyst showed that spermatids elongate in *hyls1* mutants. Surprisingly, in wild type, 64 flagella tightly associate with each other to form a well-organized bundle, whereas in *hyls1* mutants, nuclei were dispersed, and the bundled organization of spermatids was severely disordered (**Figure 8A**). When examining the sperm flagella axonemal ultrastructure by electron microscopy, we frequently observed incomplete and broken axonemal in *hyls1* mutants (32.5%; $n = 471$; **Figure 8B**; red arrow), and 8 of 19 (42.15%) cysts had 63 or fewer spermatids, whereas all control cysts possessed 64 spermatids (**Figure 8B**). Considering that sperm flagella formation is independent of IFT in *Drosophila*, we speculated that the role of HYLS1 in basal body might directly contribute to defects in spermatogenesis.

Although only moderate sperm defects in *hyls1* mutants, homozygous *hyls1* males are completely infertile (**Figure 8C**). No zygotes derived from *hyls1* mutant males could successfully develop into larvae even when homozygous mutant males were mated to wild-type (w^{1118}) females (**Figure 8D**). Male fertility can be fully rescued by a ubiquitously expressed WT *hyls1* transgene (*Ubq-hyls1-GFP*), but not by restricted rescue of HYLS1 in neurons (*elav-GAL4; pUAS-hyls1-GFP*), indicating that infertility

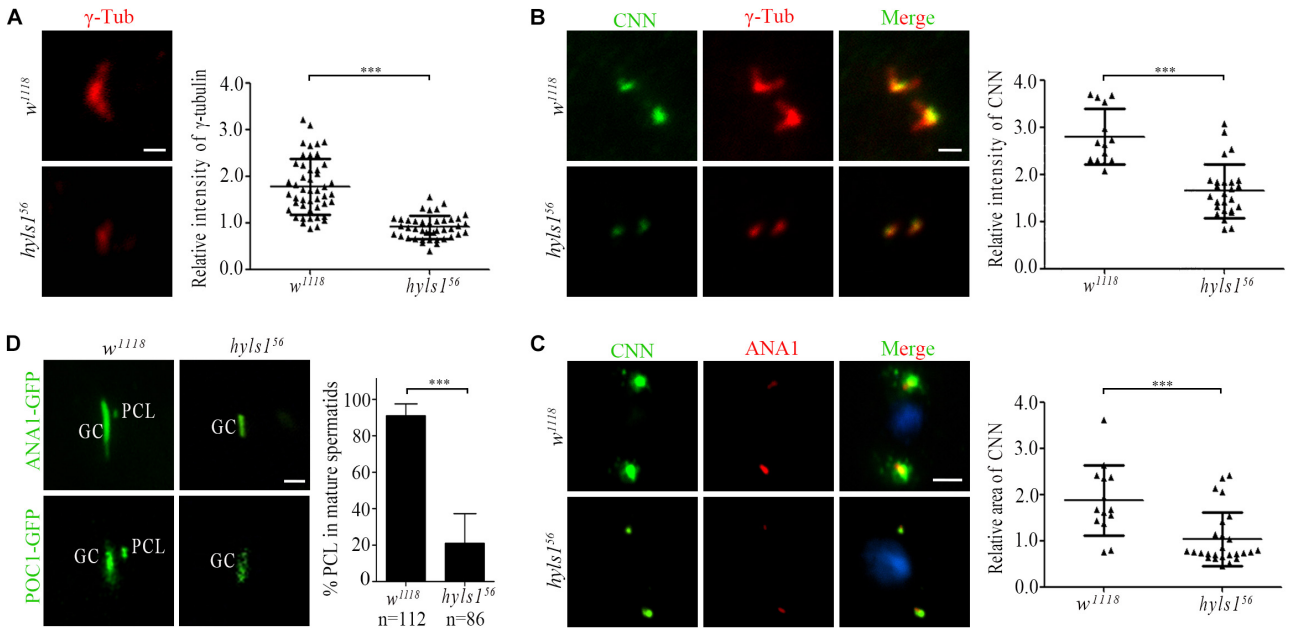

FIGURE 7 | *Drosophila* HYLS1 is required for PCM recruitment in spermatocytes and PCL formation in spermatids. **(A)** γ-Tubulin signal was significantly reduced in spermatocyte centriole in *hyls1*^{56}. Quantification data of the relative signal intensity are shown in the right panel. **(B)** HYLS1 is required for recruitment of PCM protein CNN in interphase of spermatocyte. The right panel shows the quantification of relative centrosome fluorescence intensities of CNN in controls and *hyls1* mutants. **(C)** Images of CNN signal and corresponding quantification data (right panel) in metaphase of meiosis in controls and *hyls1* mutants. Blue channel in all panels represents DNA from meiotic chromosomes. **(D)** Deletion of HYLS1 results in abnormal PCL formation indicated by ANA1-GFP and POC1-GFP. GC, giant centriole; PCL, proximal centriole-like structure. Scale bars: 1 μm (A, B, D), 5 μm **(C)**. Scattered plots with mean and SD are shown. n.s., $p > 0.05$; ***$p \leq 0.001$ (Student's *t*-test).

is not likely due to the impaired sensory or courtship capacity but owing to defects in spermatogenesis and/or embryogenesis after fertilization (**Figure 8C**). Further studies revealed that the development of embryos fathered by *hyls1*^{56} was dramatically delayed and arrested at the early cleavage stage of *Drosophila* embryos. Nearly 85% embryos have more than 32 nuclei in 1-hour-old control embryos, whereas no embryos with more than 32 nuclei were observed in 1-hour-old *hyls1* embryos (**Figure 8E**). Because both GC and PCL of spermatids are required for zygote mitosis, it is tempting to speculate that defects in GC and PCL may also contribute to embryonic development arrest in paternal *hyls1* mutants. Of note, female *hyls1* flies were partial fertile, and the phenotype was fully rescued by expressing a *Ubq-hyls1-GFP* transgene but not a *pUAS-hyls1-GFP* only in nervous system (**Figure 8C**), suggesting that maternal HYLS1 may also play a role in embryogenesis. More works will be needed to understand the role of HYLS1 in embryogenesis in the future.

DISCUSSION

Here we investigated the function of HYLS1 in ciliogenesis and spermatogenesis in *Drosophila*. We demonstrated that the centriole/basal body localization of HYLS1 and its role in ciliary function are highly conserved in *Drosophila*. More importantly, by taking advantage of the GC in *Drosophila* spermatocytes, we demonstrated that *Drosophila* HYLS1 is required for centriole elongation during spermatogenesis.

Although conventional TF structures observed in mammalian cells may not be conserved in *C. elegans* and *Drosophila*, the presence of conserved components suggests that, at least, alternative functional homologous structures should exist (Ye et al., 2014; Yang et al., 2018). In both *C. elegans* and *Drosophila*, HYLS1 is required for the localization of key TF protein FBF1. As a centriole protein, how could HYLS1 regulate the localization of a TF protein? One highly possible explanation is that HYLS1 regulates the elongation of the distal centriole required for TFs anchoring. However, short or degenerated basal body limited the analysis of centriole elongation during centriole to basal body conversion in sensory cilia in both *C. elegans* and *Drosophila*. Remarkably, by taking advantages of the GC in *Drosophila* spermatocytes, we do observe that HYLS1 promotes centriole elongation. Our observation leads us to propose that HYLS1 is required for distal centriole elongation and recruiting distal centriole proteins to build a specialized construction stage to support the *de novo* assembly of TFs. Without HYLS1, such stage is compromised, which has direct structural and functional consequences toward the associated appendages made at the distal tip of growing centriole. Although our model is largely based on observations made on the growth of specialized centrioles (*Drosophila* spermatocytes GCs), we speculate similar HYLS1-dependent distal centriole extension process is a general prerequisite for cilia

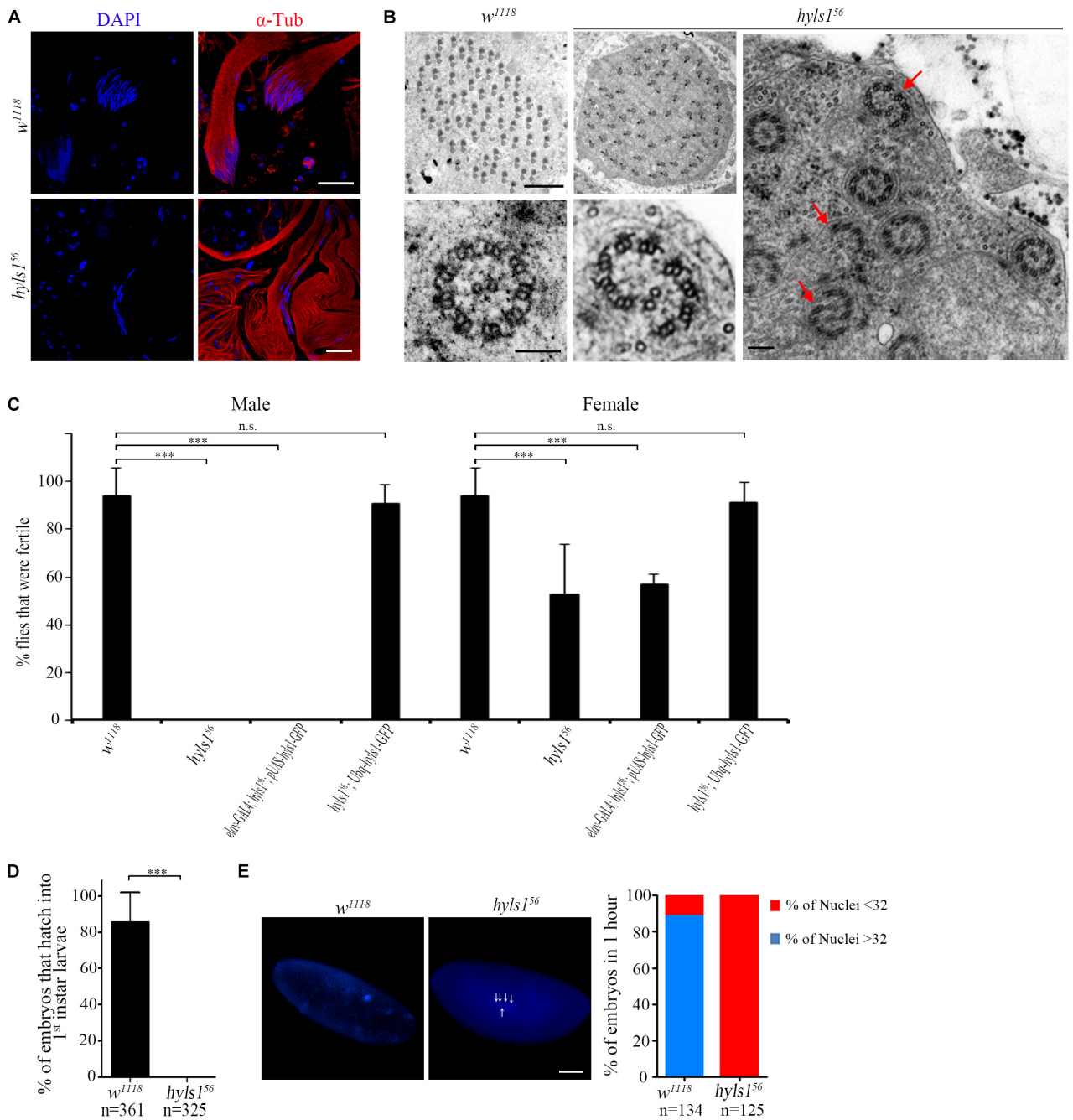

FIGURE 8 | HYLS1 is required for spermatogenesis in *Drosophila*. **(A)** Cysts of elongating spermatids in wild-type (upper) and *hyls1* mutant (lower) testis stained by nuclei marker DAPI (blue) and sperm flagellar marker α-tubulin (red). Nuclei were clustered in WT cysts but were abnormally dispersed in *hyls1*^{56} mutants. **(B)** Ultrastructure of sperm flagellar axoneme of WT and *hyls1*^{56} mutants showed that the spermatids in the *hyls1*^{56} cyst were irregularly arranged, and some axonemes were incomplete or broken (red arrows). **(C)** *hyls1*^{56} males are completely infertile. Introduction of HYLS1 in neurons driven by elav-Gal4 could not rescue the male fertility. Fertility is fully recovered with global HYSL1 rescue (*Ubq-hyls1-GFP*). Mutations in *hyls1* also affected female fertility. **(D,E)** HYLS1 is essential for embryogenesis. Embryos fathered by *hyls1* mutant failed to develop into larva **(D)** and were arrested in the early development stage **(E)**. Scale bars: 20 μm in **(A)**, 2 μm in (**B** left), 100 nm in (**B** right), 100 μm in **(E)**. Error bars represent ± s.d., n.s., $p > 0.05$; ***$p \leq 0.001$ (paired Student's *t*-test).

formation based on the mother centriole. Verification of such generalization calls for further refinement of super-resolution molecular imaging techniques to resolve the full dynamics of cilia formation.

What is the possible role of HYLS1 in centriole elongation or assembly? It has been reported that HYLS1 interacts with the core centriolar protein SAS-4 (Dammermann et al., 2009). Because SAS-4 binds tubulin and is essential for centriole elongation and

assembly, it is highly possible that HYSL1 functions through SAS-4 to regulate centriole elongation. In addition, SAS-4 cooperates with CEP120 and SPICE1 to regulate centriole elongation (Comartin et al., 2013; Lin et al., 2013); it is also possible that HYLS1 serves as a critical mediator bridging interactions between SAS-4 and other regulators of centriole elongation. Of note, SAS-4 is also required for PCM assembly (Gopalakrishnan et al., 2011, 2012; Zheng et al., 2014). It is also possible that HYLS1 functions through SAS-4 to regulate PCM recruitment. It will be interesting to test all these hypotheses in the future.

In *C. elegans*, HYLS1 is not required for centriole assembly and centrosome function (Dammermann et al., 2009). In *Drosophila*, the development of *hyls1* mutant is grossly normal, suggesting that HYLS1 may be also dispensable for centriole and centrosome function in tissues other than sperm cells. In both *C. elegans* and *Drosophila*, centrioles are short and lack of appendage structures and probably lack of distal structures found in vertebrate centrioles. Because the distal part of the mammalian centriole is usually not important for centriole duplication and assembly, but is critical for ciliogenesis, it is tempting to speculate that HYLS1 mainly plays a role in the elongation or assembly of the centriole distal part. In conclusion, our finding advances understanding on HYLS1 function and suggests that not only cilia but also the HYLS1-dependent centrosome remodeling may directly contribute to the pathogenesis of human HLS.

MATERIALS AND METHODS

Fly Stocks

All flies were cultured on standard media at 18°C or 25°C. w^{1118} was used as wild-type fly. The following flies were obtained from Bloomington Drosophila Stock Center: *elav-GAL4* (BS458; BDSC). Mks1-GFP and Mks6-GFP strains were described previously (Vieillard et al., 2016) and were gifts from Bénédicte Durand. IAV-GFP, RempA-YFP, and NompB-GFP were gifts from Seok Jun Moon (Park et al., 2013). All the other following transgenes were generated in the laboratory: *Ubq-hyls1-GFP*, *pUAS-hyls1-GFP*, *Ubq-ana1-GFP*, *Ubq-cnn-GFP*, *Ubq-poc1-GFP*, *CG5964-GFP*, *unc-GFP*, and *ift52-GFP*.

Transgenic *Drosophila* Lines

To generate ubiquitin-driven transgenic lines, promoter of ubiquitin was inserted into the *Hin*dIII site of the pJFRC2 vector[1] first, and then CDS sequences of HYLS1, POC1B, and CNN-PA were cloned into the *Not*I–*Bam*HI site of the pJFRC2 plasmid in frame with the downstream GFP sequence. To make *CG5964-GFP*, *unc-GFP* and *ift52-GFP* transgenic lines, their coding, and upstream regulatory sequences were amplified from genomic DNA and then cloned into the *Hin*dIII–*Bam*HI site of the pJFRC2 plasmid in frame with the downstream GFP sequence.

To get *pUAS-hyls1-GFP* flies, full-length HYLS1 CDS was cloned into *Not*I–*Bam*HI digested pJFRC14 vector.

All vectors were injected into *Drosophila* embryos by the Core Facility of *Drosophila* Resource and Technology, SIBCB, CAS. The resulting transgenic flies were selected according to standard procedure.

All GFP signals in colabeling immunofluorescence assay were stained with anti-GFP.

All DNA fragments used were amplified from genomic DNA by us. All CDS fragments were amplified from cDNA reverse transcribed from our own extracted total RNA. All primers used are listed in **Supplementary Table S1**.

Generation of *hyls1* Mutant

We used the CRISPR/Cas9 technique to generate the *hyls1* knockout mutants. Two gRNAs were selected using Target Finder website[2], gRNA 1: 5′-CGCAAGCTCATCAAGCATGAGG-3′ and gRNA 2: 5′-CTTAAGGAGCGCTCCGATGGTGG-3′. gRNA sequences were separately cloned into a modified pEASY-Blunt vector with a U6.3 promoter. Two gRNA plasmids were collectively injected into vasa:Cas9 embryos, and deletion lines were screened with genomic PCR and were outcrossed five times to wild-type flies (w^{1118}).

Immunofluorescence and Microscopy

Embryo Staining

Embryos were dechorionated in 50% bleach for 5 min to remove chorion, and vitelline membranes were gently stripped under the stereomicroscope and then fixed in a mixture of heptane and 4% formaldehyde (1:1) for 30 min with shaking. The fixed embryos were washed in phosphate-buffered saline (PBS) and blocked with 3% bovine serum albumin (BSA) in PBS-T (PBS 1 × + 0.1% Triton X-100) for 1 h and then incubated with primary antibodies for 24 h at 4°C. The samples were then washed three times with PBS-T for 15 min each and then incubated with secondary antibodies for 3 h at room temperature. After washing three times with PBS-T, embryos were then mounted on slides.

Whole-Mount Antennae Staining

Antennae from pupal or 1- or 2-days-old flies were dissected in PBS-T (PBS 1 × + 0.3% Triton) and then fixed in 4% paraformaldehyde in PBS-T for 1 h at room temperature. The fixed antennae were then incubated in blocking solution (PBS 1 × + 0.1% BSA + 0.1% Triton X-100) for 1 h and stained with primary antibody for 48 h and then secondary antibodies for 24 h.

Testis Squashes Staining

Testes from young males (1 or 2 days old) or pupae were dissected in PBS and then were squished between cover glass and microscopy slide. After squashing, the samples were snap-frozen in liquid nitrogen, and then the coverslips were removed off, and the slides were immersed immediately into methanol for 10 min at –20°C and sequentially in acetone for 10 min at –20°C. Slides were washed in PBS-T and blocked with 3% BSA in PBS-T for 1 h and then were incubated with primary antibodies overnight at 4°C and secondary antibodies for 3 h at room temperature. Lastly, testes were mounted and examined using fluorescence microscopy.

[1] https://www.addgene.org/26214/

[2] http://targetfinder.flycrispr.neuro.brown.edu/

Antibodies

The following primary antibodies were used: mouse anti–γ-tubulin (1:500; Sigma-Aldrich, St. Louis, MO, United States), mouse anti–α-tubulin (1:500; Santa Cruz Biotechnology, Dallsa, TX, United States), mouse anti-GFP (1:500; Roche, Basel, Switzerland), rabbit anti-GFP (1:500; Abcam, Cambridge, United Kingdom), mouse 22C10 (1:200; DSHB), mouse 21A6 (1:200; DSHB), iFluor^{TM} 555 Phalloidin (1:200; Yeasen, Shanghai, China). The following secondary antibodies were used: goat anti–mouse Alexa Fluor 488 or Alexa Fluor 594 or goat anti–rabbit Alexa Fluor 488 or Alexa Fluor 594.

Generation of *Drosophila* HYLS1 Antibody

All the work of generation of HYLS1 antibody is done by YOUKE Biotech, Shanghai, China. Briefly, His-tagged full-length HYLS1 protein was expressed in *Escherichia coli* and purified as immunogen. Antisera were raised in two rabbits and purified by protein G beads; 1:200 dilution was used for immunofluorescence assay.

Microscopy

Samples were imaged using either the fluorescence microscopy (Nikon Eclipse Ti, Nikon, Japan) or the confocal microscopy (Olympus FV1000a, Olympus, Japan) with a 100 × /NA 1.45 oil immersion objective. For super resolution imaging, samples mounted in ProLong^{TM} Diamond Antifade Mountant (Invitrogen, Carlsbad, CA, United States) were imaged using a 3D-SIM (Delta Vision OMX SR, GE Healthcare, Chicago, IL, United States).

Quantification of Fluorescence Intensity

To minimize the staining variation between mutant and control, both samples were prepared and stained at the same time and mounted on a same slide, and fluorescence images were obtained under the same microscopic conditions and settings. The fluorescence intensity was measured using Nikon NIS-Elements software, and background fluorescence was subtracted.

Transmission Electron Microscopy

Dissected fly antennae and testes were immediately held in 2.5% glutaraldehyde for at least 24 h before postfixation in OsO_4. Then samples were dehydrated in alcohol and then embedded in epoxy resin. Sections of (∼70 nm) of samples were cut in Ultracut S ultramicrotome, collected on Formvar-coated copper grids, and stained with uranyl acetate and lead citrate. Samples were imaged with H-7650 electron microscope (Hitachi, Japan) at 80 KV.

Fertility Ratio Assay

For male fertility ratio assay, virgin w^{1118} females and mutant males are crossed. For female fertility ratio assay, mutant females and w^{1118} males are crossed. Before testing, virgin females and newly enclosed males were separately collected and held in room temperature for 3–4 days. In each test, a single male was mated individually with a single virgin female for 4 days at 25°C. Crosses with dead flies were eliminated from the test. Fertility ratio was quantified.

24 h Embryo Development Assay and Larval Hatching

Virgins and males of 3–4 days were placed in a mating chamber at 25°C to lay eggs. Parents were removed until more than 80 embryos were laid, and embryos were cultured at room temperature for 3 days. The percent of hatched eggs was counted. Experiments were repeated at least three times.

Negative Geotaxis Assay (Climbing Assay)

Climbing assay was performed as described previously (Chen et al., 2015). Briefly, 10 flies were transferred as a group to a fresh food vial the day before the test. Just before the experiment, flies were transferred into a 20-cm-long clear testing vial. During the test, flies were gently tapped down to the vial bottom; the flies climbing above the 8-cm mark were counted after 10 s. After the test, flies were given 1 min to recover, repeated 10 times. At least five groups of flies were assessed.

Larva Touch Assay

Larva touch assay was performed as previously described (Chen et al., 2015). Briefly, 10 larvae as a group were gently touched one by one on their head segments with a human hair. According to the response of the larva to the touch, a score was assigned: 0 for the larva showed no response; 1 for the larva showed hesitation with ceased movement; 2 for the larva that showed anterior contract; 3 for one full wave of body contraction; and 4 for the larva that showed two or more full waves of body contractions. Each group was tested four times, and the four scores were added up to a total score; at least five groups of larvae were assayed.

Olfactory Response Assay

Olfactory response was tested by using the Y-maze assay as described (Simonnet et al., 2014). Briefly, before testing, 10 flies as a group were starved for 16–18 h at 25°C in a glass tube. Just before the test, a small filter paper with odorant or corresponding solvent was placed into the two trap vials, respectively, and flies were loaded into the loading vial. Olfactory index was calculated after 24 h. At least five groups of flies were tested each experiment.

DATA AVAILABILITY STATEMENT

The datasets generated for this study are available on request to the corresponding author.

AUTHOR CONTRIBUTIONS

QW and YH designed the study and analyzed the data. YH performed the experiments. ZW, YZ, and HC assisted the experiments and performed the SIM imaging. YP, YG, and JH assisted the experiments and provide some reagents. QW, YP, and YH wrote the manuscript. All authors discussed the results and commented on the manuscript.

FUNDING

This work was supported by National Natural Science Foundation of China (31671549 and 31871357) to QW, and National Natural Science Foundation Youth Project of China (31802009) to YH.

ACKNOWLEDGMENTS

We thank Dr. Bénédicte Durand, Dr. Chul Hoon Kim, the BDSC and Tsinghua *Drosophila* Stock Center for fly stocks. We thank Wu Wei, Core Facility of *Drosophila* Resource and Technology, SIBCB, CAS for transgenic *Drosophila*.

SUPPLEMENTARY MATERIAL

The Supplementary Material for this article can be found online at: https://www.frontiersin.org/articles/10.3389/fcell.2020.00301/full#supplementary-material

FIGURE S1 | Alignment of human HYLS1, mice HYLS1 and *Drosophila* CG42231. Conserved amino acids are highlighted, and the conserved HYLS1 box is underlined. *Hs*: *Homo sapiens*; *Mm*: *Mus musculus*; *Dm*: *Drosophila melanogaster*. Red * stands for the mutation site of hydrolethalus syndrome.

FIGURE S2 | HYLS1 is a conserved centriole and basal body protein. **(A)** HYLS1 localizes to centrosomes in syncytial stage embryos. **(B)** Endogenous HYLS1 localizes to cilia base in sensory neurons. HYLS1 colocalizes with basal body marker γ-tubulin and is detected at the ciliary base of external sensory organ marked by 21A6. 21A6 indicates the cilium base. **(C)** Localization of endogenous HYLS1 in centriole and basal body during spermatogenesis. Blue channel in the merged panel represents DNA from mature spermatids. Bars: 2 μm.

FIGURE S3 | Structural map of *hyls1* gene and *chiffon* gene. *chiffon* gene (CG5813, blue) overlaps with *hyls1* gene (CG42231, blue) and shares a common promoter, but differs in their open reading frames and codes different proteins. The coding sequences (black boxes), untranslated nucleotides (gray boxes), and introns (lines) are respectively illustrated to *chiffon* and *hyls1*. There are four annotated splice isoforms for *chiffon*: RA encodes a 1711-aa protein from two exons spanning a ∼1.1 kb intron; RB and RD encode 1695-aa proteins from a single ∼5 kb exon; RE encodes a 576-aa protein from a shorter exon within RB/RD. Deleted regions in *hyls1* and *chiffon-RA* are illustrated by black lines. gRNA editing to *hyls1* enabled the deletion of the last C-terminal 30 amino acids of CHIFFON-RA, including the stop codon (from 5043 bp to the 5136 bp).

FIGURE S4 | Ultrastructure of the chordotonal cilia in WT and *hyls1* mutants. In WT, two axonemes are usually present in the cross section of a scolopidium. However, in *hyls1* mutants, missing axonemes is observed. Red arrow, normal axoneme. Green arrow, abnormal axoneme. Scale bars: 1 μm.

FIGURE S5 | Quantification of IFT protein intensity relative to Actin intensity in the associated scolopidia in WT and *hyls1* mutants. Compare to WT, the ratios of IFT52 intensity/Actin intensity (control $n = 35$; $hyls1^{56}$ $n = 35$), NOMPB intensity/Actin intensity (control $n = 35$; $hyls1^{56}$ $n = 26$) and REMPA intensity/Actin intensity (control $n = 31$; $hyls1^{56}$ $n = 20$) were significantly reduced in *hyls1* mutants. Error bars represent ± s.d., $^{*}p < 0.05$; $^{***}p \leq 0.001$ (Student's *t*-test). "n" is the number of cilia examined.

TABLE S1 | Primers used in this paper.

VIDEO S1 | Heterozygous $hyls1^{56}/Cyo$ presented normal climbing activities.

VIDEO S2 | $hyls1^{56}$ null mutant flies showed climbing defect.

VIDEO S3 | Uncoordinated phenotype in $hyls1^{56}$ was rescued by introduction of a WT *hyls1* transgene in neurons driven by *elav*-GAL4.

REFERENCES

Anvarian, Z., Mykytyn, K., Mukhopadhyay, S., Pedersen, L. B., and Christensen, S. T. (2019). Cellular signalling by primary cilia in development, organ function and disease. *Nat. Rev. Nephrol.* 15, 199–219. doi: 10.1038/s41581-019-0116-9

Bettencourt-Dias, M., and Glover, D. M. (2007). Centrosome biogenesis and function: centrosomics brings new understanding. *Nat. Rev. Mol. Cell Biol.* 8, 451–463. doi: 10.1038/nrm2180

Bettencourt-Dias, M., Hildebrandt, F., Pellman, D., Woods, G., and Godinho, S. A. (2011). Centrosomes and cilia in human disease. *Trends Genet.* 27, 307–315.

Blachon, S., Cai, X. Y., Roberts, K. A., Yang, K., Polyanovsky, A., Church, A., et al. (2009). A proximal centriole-like structure is present in *Drosophila* spermatids and can serve as a model to study centriole duplication. *Genetics* 182, 133–144. doi: 10.1534/genetics.109.101709

Boekhoff-Falk, G. (2005). Hearing in *Drosophila*: development of Johnston's organ and emerging parallels to vertebrate ear development. *Dev. Dyn.* 232, 550–558. doi: 10.1002/dvdy.20207

Chen, J. V., Kao, L. R., Jana, S. C., Sivan-Loukianova, E., Mendonca, S., Cabrera, O. A., et al. (2015). Rootletin organizes the ciliary rootlet to achieve neuron sensory function in *Drosophila*. *J. Cell. Biol.* 211, 435–453. doi: 10.1083/jcb.201502032

Comartin, D., Gupta, G. D., Fussner, E., Coyaud, E., Hasegan, M., Archinti, M., et al. (2013). CEP120 and SPICE1 cooperate with CPAP in centriole elongation. *Curr. Biol.* 23, 1360–1366. doi: 10.1016/j.cub.2013.06.002

Conduit, P. T., Wainman, A., and Raff, J. W. (2015). Centrosome function and assembly in animal cells. *Nat. Rev. Mol. Cell. Biol.* 16, 611–624. doi: 10.1038/nrm4062

Dammermann, A., Pemble, H., Mitchell, B. J., McLeod, I., Yates, J. R. III, Kintner, C., et al. (2009). The hydrolethalus syndrome protein HYLS-1 links core centriole structure to cilia formation. *Genes Dev.* 23, 2046–2059. doi: 10.1101/gad.1810409

Fabian, L., and Brill, J. A. (2012). *Drosophila* spermiogenesis: big things come from little packages. *Spermatogenesis* 2, 197–212. doi: 10.4161/spmg.21798

Garcia-Gonzalo, F. R., and Reiter, J. F. (2017). Open sesame: how transition fibers and the transition zone control ciliary composition. *CSH Perspect. Biol.* 9:a028134. doi: 10.1101/cshperspect.a028134

Goetz, S. C., and Anderson, K. V. (2010). The primary cilium: a signalling centre during vertebrate development. *Nat Rev Genet.* 11, 331–344. doi: 10.1038/nrg2774

Gopalakrishnan, J., Chim, Y. C., Ha, A., Basiri, M. L., Lerit, D. A., Rusan, N. M., et al. (2012). Tubulin nucleotide status controls Sas-4-dependent pericentriolar material recruitment. *Nat. Cell Biol.* 14, 865–873. doi: 10.1038/ncb2527

Gopalakrishnan, J., Mennella, V., Blachon, S., Zhai, B., Smith, A. H., Megraw, T. L., et al. (2011). Sas-4 provides a scaffold for cytoplasmic complexes and tethers them in a centrosome. *Nat. Commun.* 2:359. doi: 10.1038/ncomms1367

Gottardo, M., Callaini, G., and Riparbelli, M. G. (2015). Structural characterization of procentrioles in *Drosophila* spermatids. *Cytoskeleton* 72, 576–584. doi: 10.1002/cm.21260

Han, Y. G., Kwok, B. H., and Kernan, M. J. (2003). Intraflagellar transport is required in *Drosophila* to differentiate sensory cilia but not sperm. *Curr. Biol.* 13, 1679–1686. doi: 10.1016/j.ydbio.2011.06.028

Hildebrandt, F., Benzing, T., and Katsanis, N. (2011). Ciliopathies. *N. Engl. J. Med.* 364, 1533–1543.

Jana, S. C., Bettencourt-Dias, M., Durand, B., and Megraw, T. L. (2016). *Drosophila melanogaster* as a model for basal body research. *Cilia* 5:22. doi: 10.1186/s13630-016-0041-5

Jana, S. C., Mendonca, S., Machado, P., Werner, S., Rocha, J., Pereira, A., et al. (2018). Differential regulation of transition zone and centriole proteins contributes to ciliary base diversity. *Nat. Cell. Biol.* 20, 928–941. doi: 10.1038/s41556-018-0132-1

Jarman, A. P. (2002). Studies of mechanosensation using the fly. *Hum. Mol. Genet.* 11, 1215–1218. doi: 10.1093/hmg/11.10.1215

Kernan, M. J. (2007). Mechanotransduction and auditory transduction in *Drosophila*. *Pflugers Arch.* 454, 703–720. doi: 10.1007/s00424-007-0263-x

Khire, A., Jo, K. H., Kong, D., Akhshi, T., Blachon, S., Cekic, A. R., et al. (2016). Centriole remodeling during spermiogenesis in *Drosophila*. *Curr. Biol.* 26, 3183–3189. doi: 10.1016/j.cub.2016.07.006

Landis, G., and Tower, J. (1999). The *Drosophila* chiffon gene is required for chorion gene amplification, and is related to the yeast Dbf4 regulator of DNA replication and cell cycle. *Development* 126, 4281–4293.

Lattao, R., Kovacs, L., and Glover, D. M. (2017). The centrioles, centrosomes, basal bodies, and cilia of *Drosophila melanogaster*. *Genetics* 206, 33–53. doi: 10.1534/genetics.116.198168

Lin, Y. N., Wu, C. T., Lin, Y. C., Hsu, W. B., Tang, C. J., Chang, C. W., et al. (2013). CEP120 interacts with CPAP and positively regulates centriole elongation. *J. Cell. Biol.* 202, 211–219. doi: 10.1083/jcb.201212060

Malicki, J. J., and Johnson, C. A. (2017). The cilium: cellular antenna and central processing unit. *Trends Cell Biol.* 27, 126–140. doi: 10.1016/j.tcb.2016.08.002

Mee, L., Honkala, H., Kopra, O., Vesa, J., Finnila, S., Visapaa, I., et al. (2005). Hydrolethalus syndrome is caused by a missense mutation in a novel gene HYLS1. *Hum. Mol. Genet.* 14, 1475–1488. doi: 10.1093/hmg/ddi157

Nigg, E. A., and Stearns, T. (2011). The centrosome cycle: centriole biogenesis, duplication and inherent asymmetries. *Nat. Cell. Biol.* 13, 1154–1160. doi: 10.1038/ncb2345

Park, J., Lee, J., Shim, J., Han, W., Lee, J., Bae, Y. C., et al. (2013). dTULP, the *Drosophila melanogaster* homolog of tubby, regulates transient receptor potential channel localization in cilia. *PLoS Genet.* 9:e1003814. doi: 10.1371/journal.pgen.1003814

Reiter, J. F., Blacque, O. E., and Leroux, M. R. (2012). The base of the cilium: roles for transition fibres and the transition zone in ciliary formation, maintenance and compartmentalization. *EMBO Rep.* 13, 608–618. doi: 10.1038/embor.2012.73

Reiter, J. F., and Leroux, M. R. (2017). Genes and molecular pathways underpinning ciliopathies. *Nat. Rev. Mol. Cell. Biol.* 18, 533–547. doi: 10.1038/nrm.2017.60

Riparbelli, M. G., Callaini, G., and Megraw, T. L. (2012). Assembly and persistence of primary cilia in dividing *Drosophila* spermatocytes. *Dev Cell.* 23, 425–432. doi: 10.1016/j.devcel.2012.05.024

Sarpal, R., Todi, S. V., Sivan-Loukianova, E., Shirolikar, S., Subramanian, N., Raff, E. C., et al. (2003). *Drosophila* KAP interacts with the kinesin II motor subunit KLP64D to assemble chordotonal sensory cilia, but not sperm tails. *Curr. Biol.* 13, 1687–1696. doi: 10.1016/j.cub.2003.09.025

Sharma, A., Aher, A., Dynes, N. J., Frey, D., Katrukha, E. A., Jaussi, R., et al. (2016). Centriolar CPAP/SAS-4 imparts slow processive microtubule growth. *Dev Cell.* 37, 362–376. doi: 10.1016/j.devcel.2016.04.024

Simonnet, M. M., Berthelot-Grosjean, M., and Grosjean, Y. (2014). Testing *Drosophila* olfaction with a Y-maze assay. *J. Vis. Exp.* 88:51241. doi: 10.3791/51241

Takao, D., and Verhey, K. J. (2016). Gated entry into the ciliary compartment. *Cell. Mol. Life Sci.* 73, 119–127. doi: 10.1007/s00018-015-2058-0

Tanos, B. E., Yang, H. J., Soni, R., Wang, W. J., Macaluso, F. P., Asara, J. M., et al. (2013). Centriole distal appendages promote membrane docking, leading to cilia initiation. *Genes Dev.* 27, 163–168. doi: 10.1101/gad.207043.112

Torres-Zelada, E. F., Stephenson, R. E., Alpsoy, A., Anderson, B. D., Swanson, S. K., Florens, L., et al. (2019). The *Drosophila* Dbf4 ortholog Chiffon forms a complex with Gcn5 that is necessary for histone acetylation and viability. *J. Cell. Sci.* 132:jcs214072. doi: 10.1242/jcs.214072

Vieillard, J., Duteyrat, J. L., Cortier, E., and Durand, B. (2015). Imaging cilia in *Drosophila melanogaster*. *Methods Cell Biol.* 127, 279–302.

Vieillard, J., Paschaki, M., Duteyrat, J. L., Augiere, C., Cortier, E., Lapart, J. A., et al. (2016). Transition zone assembly and its contribution to axoneme formation in *Drosophila* male germ cells. *J. Cell Biol.* 214, 875–889. doi: 10.1083/jcb.201603086

Wei, Q., Ling, K., and Hu, J. (2015). The essential roles of transition fibers in the context of cilia. *Curr. Opin. Cell Biol.* 35, 98–105. doi: 10.1016/j.ceb.2015.04.015

Wei, Q., Xu, Q. W., Zhang, Y. X., Li, Y. J., Zhang, Q., Hu, Z., et al. (2013). Transition fibre protein FBF1 is required for the ciliary entry of assembled intraflagellar transport complexes. *Nat. Commun.* 4:2750. doi: 10.1038/ncomms3750

Wei, Q., Zhang, Y., Schouteden, C., Zhang, Y., Zhang, Q., Dong, J., et al. (2016). The hydrolethalus syndrome protein HYLS-1 regulates formation of the ciliary gate. *Nat. Commun.* 7:12437. doi: 10.1038/ncomms12437

Williams, C. L., Li, C., Kida, K., Inglis, P. N., Mohan, S., Semenec, L., et al. (2011). MKS and NPHP modules cooperate to establish basal body/transition zone membrane associations and ciliary gate function during ciliogenesis. *J. Cell Biol.* 192, 1023–1041. doi: 10.1083/jcb.201012116

Yang, T. T., Chong, W. M., Wang, W. J., Mazo, G., Tanos, B., Chen, Z., et al. (2018). Super-resolution architecture of mammalian centriole distal appendages reveals distinct blade and matrix functional components. *Nat. Commun.* 9:2023. doi: 10.1038/s41467-018-04469-1

Ye, X., Zeng, H. Q., Ning, G., Reiter, J. F., and Liu, A. M. (2014). C2cd3 is critical for centriolar distal appendage assembly and ciliary vesicle docking in mammals. *Proc. Natl. Acad. Sci. U.S.A.* 111, 2164–2169. doi: 10.1073/pnas.1318737111

Zheng, X., Gooi, L. M., Wason, A., Gabriel, E., Mehrjardi, N. Z., Yang, Q., et al. (2014). Conserved TCP domain of Sas-4/CPAP is essential for pericentriolar material tethering during centrosome biogenesis. *Proc. Natl. Acad. Sci. U.S.A.* 111, E354–E363. doi: 10.1073/pnas.1317535111

Conflict of Interest: The authors declare that the research was conducted in the absence of any commercial or financial relationships that could be construed as a potential conflict of interest.

Copyright © 2020 Hou, Wu, Zhang, Chen, Hu, Guo, Peng and Wei. This is an open-access article distributed under the terms of the Creative Commons Attribution License (CC BY). The use, distribution or reproduction in other forums is permitted, provided the original author(s) and the copyright owner(s) are credited and that the original publication in this journal is cited, in accordance with accepted academic practice. No use, distribution or reproduction is permitted which does not comply with these terms.

frontiers in Cell and Developmental Biology

ORIGINAL RESEARCH
published: 30 June 2020
doi: 10.3389/fcell.2020.00426

The Impact of Di-2-Ethylhexyl Phthalate on Sperm Fertility

*Liliya Gabelev Khasin[1], John Della Rosa[1,2], Natalie Petersen[1], Jacob Moeller[3], Lance J. Kriegsfeld[3,4,5,6] and Polina V. Lishko[1,3]**

[1] Department of Molecular & Cell Biology, University of California, Berkeley, Berkeley, CA, United States, [2] Department of Chemistry, University of California, Berkeley, Berkeley, CA, United States, [3] Graduate Group in Endocrinology, University of California, Berkeley, Berkeley, CA, United States, [4] Department of Integrative Biology, University of California, Berkeley, Berkeley, CA, United States, [5] Department of Psychology, University of California, Berkeley, Berkeley, CA, United States, [6] Helen Wills Neuroscience Institute, University of California, Berkeley, Berkeley, CA, United States

A growing number of studies point to reduced fertility upon chronic exposure to endocrine-disrupting chemicals (EDCs) such as phthalates and plasticizers. These toxins are ubiquitous and are often found in food and beverage containers, medical devices, as well as in common household and personal care items. Animal studies with EDCs, such as phthalates and bisphenol A have shown a dose-dependent decrease in fertility and embryo toxicity upon chronic exposure. However, limited research has been conducted on the acute effects of these EDCs on male fertility. Here we used a murine model to test the acute effects of four ubiquitous environmental toxins: bisphenol A (BPA), di-2-ethylhexyl phthalate (DEHP), diethyl phthalate (DEP), and dimethyl phthalate (DMP) on sperm fertilizing ability and pre-implantation embryo development. The most potent of these toxins, di-2-ethylhexyl phthalate (DEHP), was further evaluated for its effect on sperm ion channel activity, capacitation status, acrosome reaction and generation of reactive oxygen species (ROS). DEHP demonstrated a profound hazardous effect on sperm fertility by producing an altered capacitation profile, impairing the acrosome reaction, and, interestingly, also increasing ROS production. These results indicate that in addition to its known chronic impact on reproductive potential, DEHP also imposes acute and profound damage to spermatozoa, and thus, represents a significant risk to male fertility.

Keywords: endocrine-disrupting chemicals (EDC), di-2-ethylhexyl phthalate (DEHP), phthalates, spermatozoa, capacitation, embryo development, acrosome reaction, reactive oxygen species (ROS)

OPEN ACCESS

Edited by:
Tomer Avidor-Reiss, The University of Toledo, United States

Reviewed by:
Xi-Feng Zhang, Wuhan Polytechnic University, China
Myung-Geol Pang, Chung-Ang University, South Korea

***Correspondence:**
Polina V. Lishko
lishko@berkeley.edu

Specialty section:
This article was submitted to Cell Growth and Division, a section of the journal Frontiers in Cell and Developmental Biology

Received: *10 March 2020*
Accepted: *07 May 2020*
Published: *30 June 2020*

Citation:
Khasin LG, Della Rosa J, Petersen N, Moeller J, Kriegsfeld LJ and Lishko PV (2020) The Impact of Di-2-Ethylhexyl Phthalate on Sperm Fertility. Front. Cell Dev. Biol. 8:426. doi: 10.3389/fcell.2020.00426

INTRODUCTION

Phthalates and plasticizers are synthetic chemicals that are utilized to make plastic more flexible. They are known to act as endocrine-disrupting chemicals (EDC) (Rudel et al., 2003; Hunt et al., 2009), which are ubiquitous in food and beverage containers, as well as coatings of pills, medical tubing (Green et al., 2005; Hauser and Calafat, 2005) and plastic packaging (Muncke, 2011). Phthalates and plasticizers are bound to plastic polymers by non-covalent bonds, and thus, easily leak into the environment (Pearson and Trissel, 1993). The main routes of exposure to these substances are ingestion, inhalation, dermal absorption, or intravenous medication administration (Hauser and Calafat, 2005; Meeker et al., 2009). Consequently, the vast majority of the population

is exposed to these toxins on a daily basis. Low micromolar concentrations of certain EDCs in human urine, sweat and plasma have been associated with an increased rate of miscarriages and compromised male and female fertility (Lovekamp and Davis, 2001; Duty et al., 2003; Hauser et al., 2006; Svechnikova et al., 2007; Burdorf et al., 2011; Toft et al., 2012; Wang et al., 2012; Bloom et al., 2015; Patel et al., 2015; Brehm and Flaws, 2019).

In the present study, we evaluated the reproductive outcomes of acute exposure to four omnipresent EDCs – Bisphenol A (BPA), dimethyl phthalate (DMP), diethyl phthalate (DEP) and Di-ethyl hexyl phthalate (DEHP). BPA, a plasticizer manufactured in large volumes for the production of polycarbonate plastics and epoxy resins, is used to line food and beverage storage containers, coat water supply pipes and is also a component of dental fillings. The aforementioned exposure routes lead to detectable levels of BPA in human serum (Vandenberg et al., 2007), urine (Calafat et al., 2005; Hauser et al., 2007), adipose tissue (Fernandez et al., 2007) and breast milk (Sun et al., 2004). Numerous studies have shown that chronic exposure to BPA alters fertility in both males and females (Zota et al., 2014; Zhou et al., 2017).

Phthalates are similarly produced in large volumes and are used as plasticizing agents. Phthalates can be grouped into two broad categories: low-molecular-weight and high-molecular-weight phthalates. The low-molecular-weight phthalates, such as DEP and DMP, are commonly found in cosmetics and personal care products, respectively. Specifically, DEP is utilized as a solvent and a fixative in fragrances. Studies have shown that chronic exposure to DEP may lead to multigenerational effects on reproductive health in both male and female rats (Fujii et al., 2005). The second most common low-molecular-weight phthalate is DMP. DMP is used primarily as an insect repellent, resulting in extensive exposure due to generous application to exposed skin and clothing. A recent study in mice found that chronic exposure to DMP triggers changes in the levels of serum hormone that lead to increased rates of ovarian granulosa cell death (Mei et al., 2019).

The high-molecular-weight phthalates, such as Di-ethyl hexyl phthalate (DEHP), are used in construction materials and numerous polyvinyl chloride (PVC) products. DEHP is one of the most commonly used phthalates (Wang et al., 2019) and is of primary interest regarding its disrupting impact on fertility. In fact, 98% of the US population test positive for DEHP and its metabolites (Api, 2001; Zota et al., 2016). Despite numerous reports on its toxicity, DEHP is still widely used in consumer products and in a number of medical devices, such as blood bags, infusion tubes, nasogastric tubes, peritoneal dialysis bags, and urological catheters. Patients who undergo frequent hemodialysis, catheterization or massive blood transfusions are at particular risk for DEHP toxicity and are exposed to doses as high as 168 mg/day (Kavlock et al., 2002). Several human studies have demonstrated the profound effects of prolonged exposure to DEHP on both male and female fertility (Burdorf et al., 2011; Pan et al., 2011; Sumner et al., 2019).

The majority of studies on EDC's impact on reproductive health, including those mentioned above, evaluated the toxic effects of chronic exposure to phthalates and plasticizers. However, little is known about the reproductive outcomes of short exposure to such EDCs.

In the present study, we assessed the effects of acute exposure to BPA, DMP, DEP, and DEHP. Out of the four EDCs tested, DEHP demonstrated the strongest effect on male fertility by significantly altering the maturation process sperm undergoes, also known as capacitation, as well as inhibiting acrosome reaction, and triggering excessive reactive oxygen species (ROS) production. Altogether these changes led to sperm inability to fertilize eggs. These results suggest that DEHP can directly affect sperm fertility and is therefore detrimental to male reproductive health.

RESULTS

Murine Embryo Development Is Impacted by DMP, BPA, DEP, and DEHP

Exposure to phthalates could either damage sperm directly or impair pre-implantation embryo development after fertilization occurs. To test the susceptibility of pre-implanted embryos to DEHP, DMP, DEP, and BPA, naturally derived zygotes were harvested and subjected to 0, 1, 2, and 10 μM of each EDC as outlined in the methods section. The ability of the pre-implantation embryo to progress toward the blastocyst stage was recorded on day 5 post-fertilization (**Figure 1** and **Supplementary Figure S1**), and the respective survival rate was calculated as described in methods. While all four tested compounds did not affect pre-implantation development at the lower concentrations (up to 2 μM), we found that at 10 μM, all four chemicals effectively prevented blastocyst formation ($p < 0.05$; **Figures 1A–H** and **Supplementary Tables S1A–D**). All controls have been performed with either vehicle control (0.1% ethanol) or EDC-free media. No significant differences were observed among control conditions (**Supplementary Table S2**).

In vitro Fertilization Is Affected by DEHP

To explore the direct effect of DEHP, DMP, DEP, and BPA on sperm fertilizing ability, *in vitro* fertilization (IVF) assays were carried out. Mouse sperm were capacitated in phthalate-supplemented media as described in methods by exposing sperm to different concentrations (0, 1, 2, and 10 μM) of EDCs, and 60–90 min post-exposure, sperm was introduced to healthy murine eggs. The fertilization rate was calculated and presented as the percentage of embryos that reached the morula or blastula stage on day 5 post-fertilization ($p < 0.05$; **Figures 2A–H**, **Supplementary Figure S2**, and **Supplementary Tables S3A–D**). As shown in **Figure 2**, all tested concentrations of DEP and DMP did not produce any effect on sperm fertilizing ability and subsequent blastocyst formation, while 10 μM BPA had a minimal, but not a statistically significant impact on early embryo development (**Figures 2C,D** and **Supplementary Figure S2**). The most damaging effect to blastocyst formation was observed with DEHP (**Figures 2G,H**). While spermatozoa retained their fertilization potential at 1 μM, a significant decrease in embryo progression to blastulae was found already at

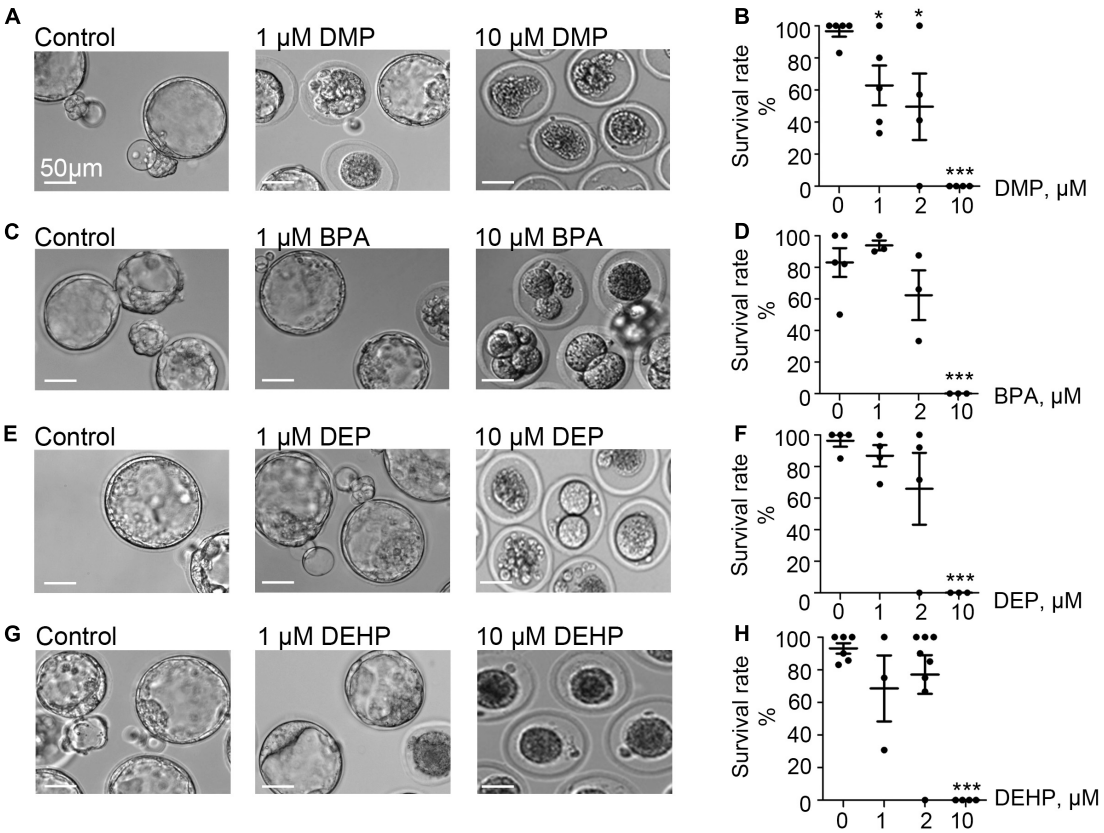

FIGURE 1 | Murine embryo development is impacted by DMP, BPA, DEP and DEHP. *In vitro* embryo development on day 5 post fertilization. Panels **(A,C,E,G)** are representative images of blastocysts previously exposed at the zygote stage to 0, 1, or 10 μM of the indicated EDC for 20 h. The subsequent embryo culture was done in the absences of the indicated EDC. **(A)** Shown are representative images of DMP-exposed embryos. **(B)** The survival rate of DMP exposed zygotes was calculated based on the percentage of embryos that have reached the morula or blastocyst stage. **(C)** Representative images of embryos previously exposed to BPA. **(D)** The survival rate of BPA exposed zygotes was calculated as in **(B)**. **(E)** Representative images of embryos previously exposed to DEP. **(F)** The survival rate of DEP exposed zygotes was calculated as in **(B)**. **(G)** Representative images of embryos previously exposed to DEHP. **(H)** The survival rate of DEHP- exposed zygotes was calculated as in **(B)**. Data are means ± S.E.M. Asterisk indicates a statistical difference between control embryos and embryos exposed to EDCs. $^{*}P \leq 0.05$, $^{**}P < 0.01$, $^{***}P < 0.001$. Scale bars for all images are 50 μm.

2 μM (74.95 ± 5.459% in control vs. 47.68 ± 9.68% in 2 μM). Moreover, at 10 μM of DEHP, almost no blastocyst formation was observed (**Figures 2G,H**). All controls have been done with either 0.1% ethanol as a vehicle control or EDC-free media, and no significant differences were detected between the control conditions (**Supplementary Table S4**).

DEHP Prevents Fertilization

The acute exposure to DEHP may either affect sperm ability to fertilize the egg or may permit fertilization but subsequently inhibit the zygotic division. To distinguish between these two scenarios, sperm fertility was assessed by recording pronuclei formation 9 h post IVF. As shown in **Figure 3**, in the presence of 10 μM DEHP, a 92.76% reduction in pronuclei formation was detected compared to untreated control. Values were calculated based on pooled data from three independent experiments and represent a total of 19 zygotes out of 25 eggs in the control conditions, versus 2 zygotes out of 36 eggs in the presence of DEHP (**Supplementary Table S5**). These results indicate that even short exposure to DEHP modifies sperm physiology making spermatozoa unable to penetrate the zona pellucida.

Murine CatSper Is Not Affected by DEHP

Since DEHP has demonstrated the most substantial effect on sperm fertility among all tested EDCs, we further explored which sperm functions were directly affected by exposure to this phthalate. Once deposited inside the female reproductive tract, mammalian spermatozoa must undergo a final maturation step, i.e., capacitation, to become competent to fertilize the egg (Austin, 1951; Yanagimachi, 1994). This process results in the removal of non-covalently attached glycoproteins, depletion of cholesterol, and other steroids (Davis, 1981), as well as the removal of adherent seminal plasma proteins (Chang, 1957). These physiological changes alter sperm membrane potential and make the cell competent to undergo a change in motility, known as hyperactivation, trigger the acrosome reaction and prepare spermatozoa for fertilization. Hyperactivation is characterized by calcium influx into the sperm flagellum via the calcium

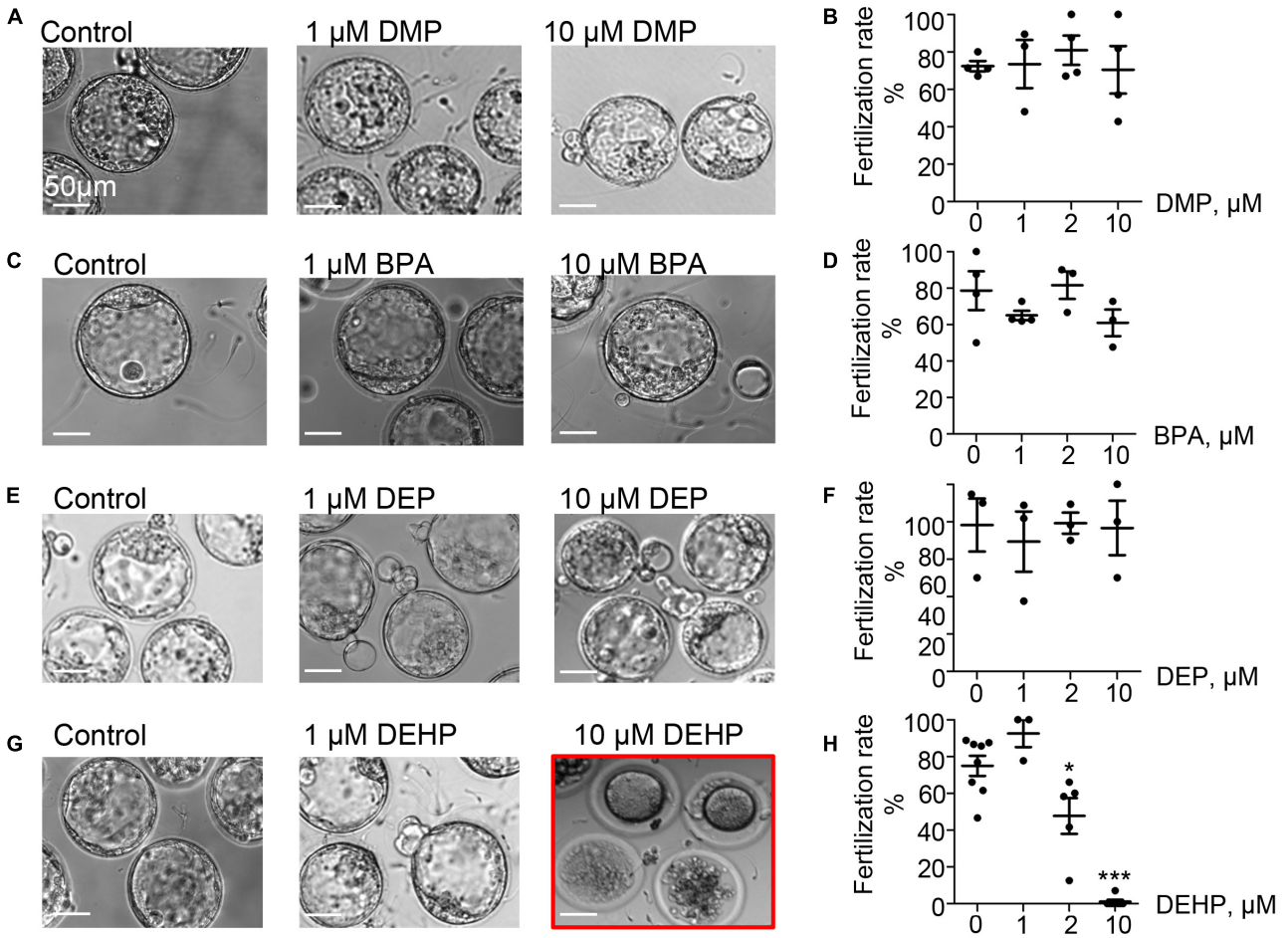

FIGURE 2 | Fertilization rate of murine eggs exposed to EDCs treated spermatozoa. Panels **(A,C,E,G)** are representative images of blastocysts obtained after murine eggs were introduced to sperm previously exposed to 0, 1, or 10 μM of the indicated EDC. Subsequent embryo culturing was done in the absences of EDCs, and the images were taken on day 5 post insemination. **(A)** Shown are representative images of blastocysts obtained after murine eggs were introduced to sperm previously exposed to DMP. **(B)** Percentage of eggs that were fertilized by DMP- treated sperm and were able to reach morula or blastocyst stage. **(C)** Representative images of embryos obtained after IVF with BPA-treated spermatozoa. **(D)** The percentage of eggs fertilized by BPA-treated sperm was calculated as in **(B)**. **(E)** Representative images of embryos obtained after IVF with DEP-treated sperm. **(F)** The percentage of eggs fertilized by DEP-treated sperm was calculated as in **(B)**. **(G)** Representative images of embryos obtained after IVF with DEHP-treated sperm. **(H)** The percentage of eggs fertilized by DEHP-treated sperm was calculated as in **(B)**. Data are means ± S.E.M. Asterisk indicates a statistical difference between control embryos and embryos exposed to EDCs. $^{*}P < 0.05$, $^{**}P < 0.01$, $^{***}P < 0.001$. Scale bars for all images are 50 μm.

channel- CatSper (Ren et al., 2001; Carlson et al., 2003) and is defined as an asymmetrical flagellar beat that is required for penetration through the viscous luminal fluids of the female reproductive tract and the protective vestments of the egg. CatSper deficiency, as well as its suppression by environmental toxins, has been previously linked to male infertility (Ren et al., 2001; Qi et al., 2007; Schiffer et al., 2014; Tamburrino et al., 2014). To investigate whether murine CatSper is also affected by DEHP, we used murine sperm patch-clamp technique (Kirichok et al., 2006). As shown in **Supplementary Figures S3A,B**, the application of 10 μM DEHP did not alter CatSper currents. Since previous studies on several EDCs reported that phthalates impact human CatSper at micromolar concentrations (Schiffer et al., 2014), we also tested DEHP at a higher dose (**Supplementary Figures S3A,B**). However, at either 10 or 100 μM concentration, no significant changes in monovalent CatSper currents were observed. This indicates that DEHP affects sperm cells through a CatSper-independent mechanism.

DEHP Alters Sperm Capacitation and ROS Production

Another hallmark of capacitation is the phosphorylation of sperm proteins on tyrosine residues (Salicioni et al., 2007; Visconti, 2009). Previous reports on the capacitation of murine sperm demonstrate a time-dependent increase in the phosphorylation of tyrosine residues in proteins with the molecular weight of 40—170 kDa (Visconti et al., 1995a; Naz and Rajesh, 2004; Sepideh et al., 2009; Visconti, 2009). This modification allows sperm to hyperactivate, undergo the acrosome reaction

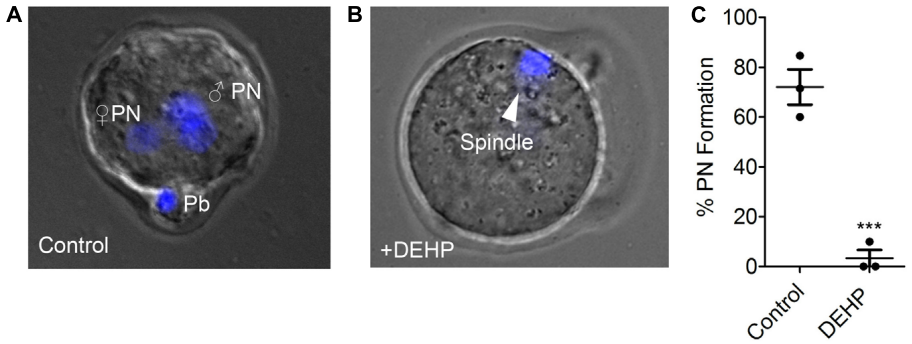

FIGURE 3 | Pronuclei formation after *in vitro* fertilization by DEHP-treated sperm. Pronuclear formation was assessed 9 h after IVF; genomic DNA staining was done with DAPI. **(A)** Representative image of a successfully fertilized egg with two pronuclei (PN) and a polar body (Pb). The egg was inseminated with sperm treated with vehicle control solution. **(B)** Shown are representative images of unfertilized eggs following an IVF with sperm that was treated with 10 μM DEHP. The arrowhead indicates the position of the second metaphase spindle. **(C)** Percentage of fertilized eggs with PN detected. Each data point represents the mean of one of the three independent experiments ± S.E.M. *** indicates statistical significance ($P < 0.005$). The total number of eggs: 25 (control), 36 (+10 μM DEHP).

and interact with the zona pellucida (Nassar et al., 1999; Naz and Rajesh, 2004). To test the effect of DEHP on sperm tyrosine phosphorylation, caudal epididymal spermatozoa were incubated in a capacitating medium containing either 10 μM DEHP or vehicle control. Subsequently, tyrosine phosphorylation was assessed by a western blot using a monoclonal anti-phosphotyrosine antibody (anti-PY) (EMD Millipore). As shown in **Figures 4A,B**, DEHP markedly alters sperm capacitation-associated tyrosine phosphorylation kinetics, by expediting the process within the first 60 min of exposure, followed by a complete reversal after 120 min of incubation. Specifically, at the 60-min time point, a 150% increase in the global tyrosine phosphorylation was detected in DEHP treated spermatozoa in comparison to the control condition. As capacitation progressed, the detected levels of the global tyrosine phosphorylation increased in the control samples. However, in the DEHP treated samples, the levels of detected phosphotyrosine significantly dropped. Specifically, at the 120-min time point, the detected levels of phosphoproteins were 59% lower in the control. The most striking changes in phosphorylation were observed at the regions that correspond to 75, 95, 170, and 270 kDa (**Supplementary Figure S4**). The 75, 95, and 170 kDa molecular weight proteins were previously reported to have important roles in sperm fertility (Naz and Rajesh, 2004; Sepideh et al., 2009). In addition, immunocytochemistry experiments using the same anti-PY antibody, revealed that the increased protein phosphorylation caused by DEHP is primarily localized to the mid-piece region of sperm (**Figure 4C**). According to previous reports, during the normal capacitation process, the sperm midpiece is undergoing more robust tyrosine phosphorylation in comparison to other parts of the flagellum (Alvau et al., 2016), and it appears that DEHP exacerbates this process. To further assess the global changes in sperm tyrosine phosphorylation induced by DEHP, flow cytometry analysis was performed using anti-PY labeled with CF647 dye (Biotium). As shown in **Figure 4D**, a significant increase in overall fluorescence was observed in DEHP treated cells resulting in 1.5- ± 0.2-fold increase in global fluorescence.

The mid-piece region of sperm flagellum harbors mitochondria- an organelle known to generate ROS. Interestingly, DEHP increases ROS generation in various cells and tissues, including hepatocytes, adipocytes, and testis (Kasahara et al., 2002; Schaedlich et al., 2018; Huang et al., 2019). However, DEHP's ability to alter sperm ROS production has not been studied. To detect ROS production, a chemiluminescence assay was employed, a commonly described technique to detect ROS in semen (Ochsendorf et al., 1994; Williams and Ford, 2005; Agarwal et al., 2008). The levels of ROS production were assessed in caudal sperm capacitated in the presence or absence of 10 and 100 μM DEHP after 60 min of exposure. A significant increase in ROS production was detected in all treated samples in comparison to vehicle-treated controls (**Figure 5A**). We found that already at 10 μM of DEHP, a maximal ROS production was achieved, and no further increase was detected at 100 μM. Since excessive ROS production is known to be cytotoxic to sperm, exposure to DEHP may lead to impaired sperm fertilizing capacity.

The Acrosome Reaction in Capacitated Spermatozoa Is Inhibited by DEHP

The acrosome reaction is the fusion of the sperm plasma membrane with the outer acrosomal membrane. It is vital for fertilization, as only acrosome-reacted spermatozoa can fuse with the egg (Avella and Dean, 2011). According to previous reports, increased levels of ROS production result in excessive peroxidation of the sperm acrosomal membrane (Zalata et al., 2004), impairing acrosomal exocytosis and sperm-egg fusion (Aitken and Clarkson, 1987; Griveau et al., 1995; Ichikawa et al., 1999). While there is a debate over the physiological triggers for the acrosome reaction and the exact site of acrosomal exocytosis, it is well accepted that the acrosome reaction is required for sperm fertility. Therefore, we have explored whether DEHP can alter the spontaneous acrosome reaction. We found that incubation with 10 μM DEHP, decreased the percentage of spontaneous acrosome reaction. In control samples, the detected rates of acrosome

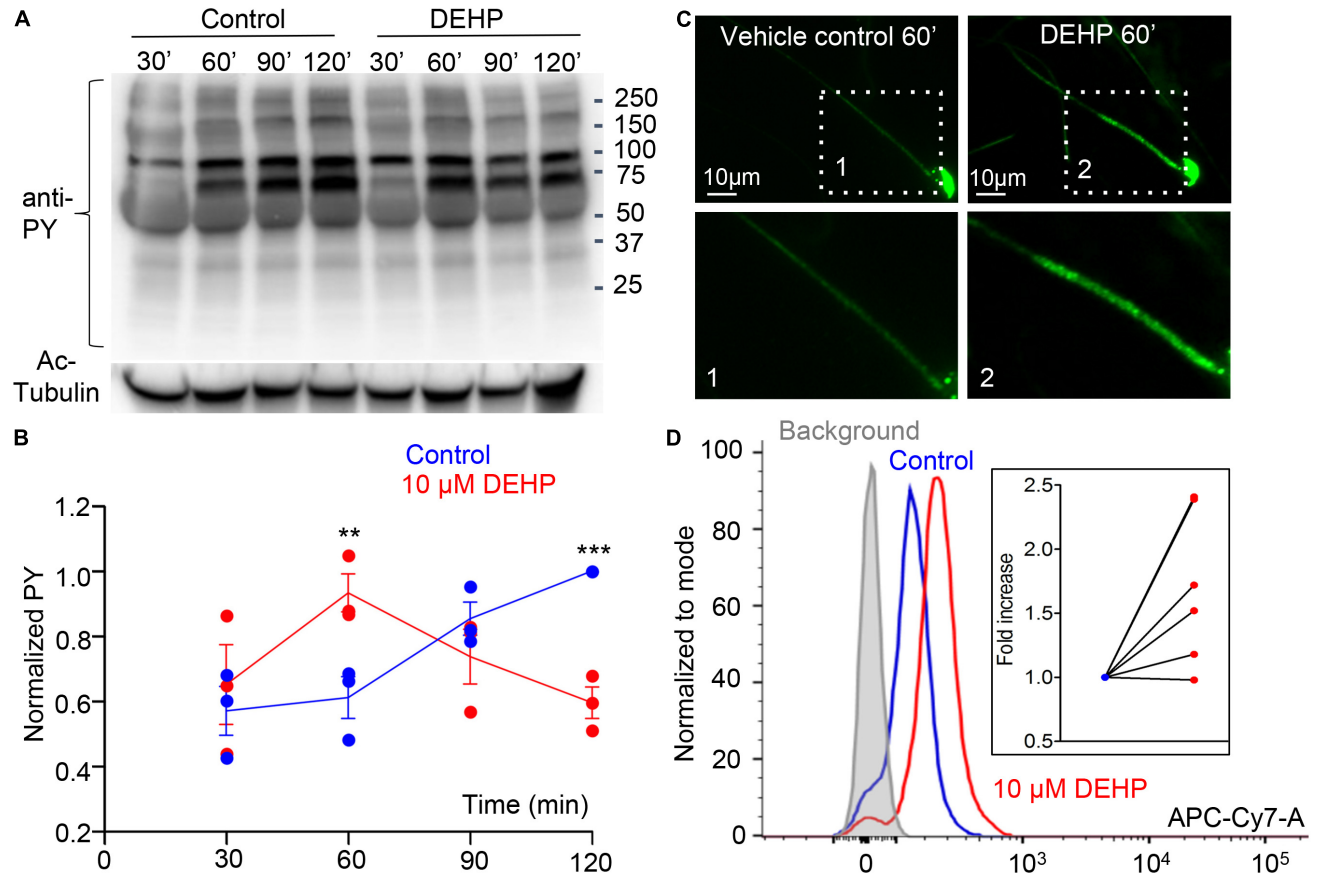

FIGURE 4 | Capacitation-associated tyrosine phosphorylation of murine sperm is altered in the presence of DEHP. **(A)** Representative western blot image shows the time course of protein tyrosine phosphorylation under capacitating conditions in the presence or absence of 10 μM DEHP. DEHP was added to the media immediately before the start of the capacitation process. Sperm lysates were obtained at the indicated times (30, 60, 90, and 120 min) and subjected to SDS-PAGE immunoblotting. Tyrosine phosphorylation was detected with a monoclonal phospho-tyrosine (PY) antibody. Acetylated-tubulin (Ac-Tubulin) was used as a loading control. **(B)** Levels of relative tyrosine phosphorylation obtained as total densities extracted from **(A)** and normalized to the densities of the loading control. Each data point represents the mean of one of the three independent experiments. **(C)** Immunofluorescent localization of tyrosine phosphorylated proteins as visualized by PY antibody. Increased phosphorylation detected after 60 min of capacitation in the mid-piece region of spermatozoa in DEHP- treatment group (right panels) as compared to control untreated spermatozoa (left panels). Lower panels represent insets from the corresponding region of interests indicated on the upper panels by dashed rectangular. **(D)** A representative flow cytometry data showing an increase in global tyrosine phosphorylation in 10 μM DEHP- treated spermatozoa (red) at 60 min of capacitation compared to the vehicle control (blue). Tyrosine phosphoproteins were detected using a CF 647 dye conjugated to an anti-PY antibody. Inset: fold increase in mean fluorescent intensity normalized to mode as detected by the flow cytometer compared to control conditions. Data are means ± S.E.M. ** indicates statistical significance ($P < 0.01$) between control spermatozoa and spermatozoa exposed to 10 μM DEHP. *** indicates statistical significance ($P < 0.001$).

reacted cells were 20.95 ± 0.62%, whereas in DEHP treated samples, the rates dropped to 8.28 ± 1.24% (**Figures 5B–D**).

To summarize, these results indicate that acute DEHP exposure stimulates excessive ROS production in sperm, as well as trigger altered tyrosine phosphorylation and inhibits the acrosome reaction. Consequently, these changes negatively affect sperm physiology and impact their fertility.

DISCUSSION

Exposure to EDCs poses a significant risk to reproductive health and fetal development (Hannon et al., 2016; Brehm et al., 2018). In this study, we assessed the effects of acute exposure to four omnipresent EDC's – BPA, DEHP, DMP, and DEP on sperm fertility and early embryo development. While it is well documented that chronic exposure to these compounds can affect both male and female fertility (Latini et al., 2006; vom Saal et al., 2008; Kay et al., 2014; Wu et al., 2014; Patel et al., 2015), the effects of short exposure are less clear. To assess the impact of the chosen EDCs on sperm fertility and pre-implantation embryo development, we employed *in vitro* embryo development and IVF studies. Of all tested EDC's DEHP had the most profound impact on fertilization and sperm fertility. While it is known that chronic exposure to DEHP impairs sperm motility and chromatin DNA stability (Pant et al., 2011; Sumner et al., 2019), its acute effect on sperm fertilizing capacity has not been elucidated. Here, we sought to investigate the impact of

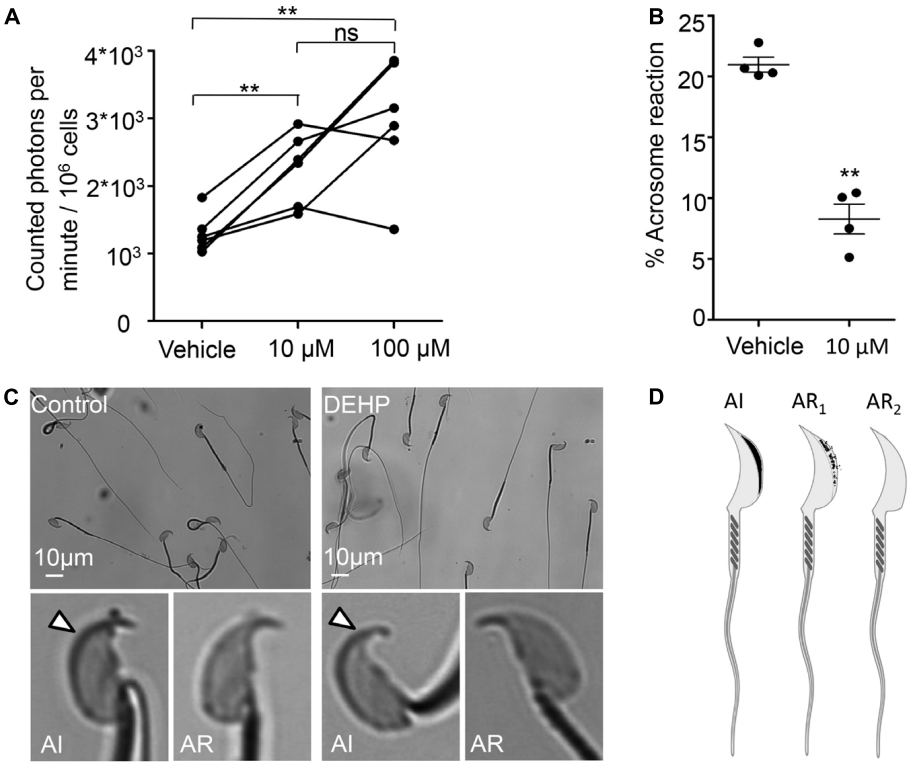

FIGURE 5 | DEHP increases ROS production and decreases spontaneous acrosome reaction in capacitated sperm cells. **(A)** Luminol-dependent chemiluminescence assay showed increased rates of ROS production in sperm treated with 10 and 100 μM DEHP in comparison to the vehicle control (0 μM DEHP). Connected dots represent spermatozoa extracted from the same mouse (a total of six mice were used for this experiment). Each sample was divided into three aliquots and subjected to different conditions. A minimum of $1.35*10^6$ sperm cells/mL was used per condition. **(B)** Percentage of spontaneously acrosome-reacted spermatozoa subjected to 10 μM DEHP or vehicle control (0.1% ethanol) during capacitation. Each data point represents the mean of one of four independent experiments. A minimum of 500 cells was evaluated per experiment. **(C)** Acrosome-reacted (AR) and acrosome-intact (AI) spermatozoa in control and 10 μM DEHP. Arrowheads point at intact acrosome caps. "AI" cells have bright blue staining on the dorsal region of the acrosome. "AR" cells have patchy or absent staining. **(D)** Diagram showing acrosome-reacted (two distinct patterns are indicated as AR1 or partially reacted, and AR2 as fully reacted) and acrosome-intact (AI) spermatozoa. Images were produced using Biorender.com. Data are means ± S.E.M. ** indicates statistical significance ($P < 0.01$) between control spermatozoa and spermatozoa exposed to 10 μM DEHP.

short exposure to DEHP on sperm fertility and the mechanisms by which this EDC exhorts its effects.

Upon absorption, DEHP is distributed throughout the body by the circulatory system. The majority of DEHP is quickly hydrolyzed by the liver into various metabolites, which have been linked to altered fertility and DNA damage in sperm (Hauser et al., 2007). However, a portion of DEHP is stored un-metabolized in the adipose tissue- which acts as a reservoir for lipophilic EDCs (Tanaka et al., 1975; Regnier and Sargis, 2014). Hormonal and neuronal signals regulating the fat tissue can trigger an abrupt release of lipophilic EDCs to the systemic circulation (Regnier and Sargis, 2014). There are two main ways in which sperm can encounter un-metabolized DEHP: via abrupt release from adipose tissue or through release from medical devices, such as a urological catheter- making unmetabolized DEHP a prominent threat to sperm fertility.

Di-2-ethylhexyl phthalate exposure has been previously linked to increased ROS production in somatic cells and oocytes (Ambruosi et al., 2011; Kim et al., 2013; Wu et al., 2014; Tripathi et al., 2019). However, its impact on ROS overproduction in sperm was not elucidated. Here we show that acute exposure to DEHP triggers excessive ROS generation, leading to oxidative damage and ultimately sperm infertility.

While minor ROS generation naturally takes place during early sperm capacitation, this process must be tightly regulated. Mild ROS production triggers an increase in intracellular cAMP, resulting in the activation of Protein Kinase A (PKA). PKA, in turn, carries out a series of controlled tyrosine phosphorylation events in a time-dependent manner (Aitken et al., 1995; Leclerc et al., 1997). Interestingly, certain EDCs such as BPA have been shown to up-regulate PKA's activity leading to an altered phosphorylation pattern downstream of PKA (Rahman et al., 2015). Since mature spermatozoa are transcriptionally and translationally silent cells, post-translational protein modifications such as tyrosine phosphorylation play an essential role in sperm maturation process and their ability to fertilize an egg (Naz and Rajesh, 2004). Unwarranted ROS production leads to over-phosphorylation which significantly alters the maturation process of sperm

(Villegas et al., 2003; Donà et al., 2011). Moreover, an excess of ROS is cytotoxic to sperm due to their limited antioxidant capacity and their high content of polyunsaturated long-chain fatty acids in the plasma membrane (Jones et al., 1979; Alvarez and Storey, 1982; Aitken and Clarkson, 1987).

Di-2-ethylhexyl phthalate-treated sperm cells had altered capacitation with aberrantly fast tyrosine phosphorylation within the first 60 min of capacitation. This differs from the gradual increasing protein phosphorylation pattern that was observed in the control condition and previously reported in the literature (Visconti et al., 1995b; Piehler et al., 2006). The detected increase in tyrosine phosphorylation was localized primarily to the mid-piece region of sperm, the flagellar compartment where mitochondria are located. Mitochondrial respiration produces a significant amount of ROS, this process, if unregulated, can damage sperm genomic DNA, lipid and protein structures, and subsequently impair sperm integrity and fertility. Previous reports show that DEHP exposed oocytes and somatic cells produce an excessive amount of ROS via mitochondrial-derived ROS (Rosado-Berrios et al., 2011; Wu et al., 2014; Roth, 2018). However, it has not been shown that DEHP affects spermatozoa in a similar manner. In fact, several EDCs were suggested to affect sperm fertility via CatSper-related mechanism (Schiffer et al., 2014). Here, we show that while murine CatSper was not sensitive to DEHP exposure, this phthalate indeed triggers excessive ROS production and subsequently impairs sperm fertility.

An additional effect of excessive oxidative stress on spermatozoa is lipid peroxidation. Spermatozoa are extremely susceptible to lipid peroxidation due to their high concentration of long- chain polyunsaturated fatty acids (Jones et al., 1979; Alvarez and Storey, 1982; Aitken and Clarkson, 1987; Aitken et al., 2006; Wathes et al., 2007). Alteration of the lipid structure due to peroxidation in sperm leads to a decrease in membrane fluidity (Sikka, 2001; Zalata et al., 2004; Cocuzza et al., 2007; Chen et al., 2013) causing decreased motility and altered acrosome reaction (Aitken and Clarkson, 1987; Griveau et al., 1995; Ichikawa et al., 1999; Zalata et al., 2004). The acrosome reaction is an important step during fertilization in order to expose sperm-egg recognition elements (Inoue et al., 2005). Murine sperm begin to undergo the acrosome reaction in the upper isthmus (La Spina et al., 2016), the part of the oviduct that connects the uterine with the ampulla. Thus, mouse fertile sperm are acrosome-reacted prior to reaching the ampulla, the site of fertilization and before encountering the eggs (Jin et al., 2011). In fact, most acrosome-intact spermatozoa are unable to fertilize the egg and swim away from the zona pellucida (Jin et al., 2011). Thus, sperm ability to undergo the AR at the end of capacitation is highly important for sperm fertility (Yanagimachi, 2011). Here we find that DEHP significantly inhibits the acrosome reaction in capacitated sperm. As a result, DEHP-exposed sperm were largely acrosome-intact and therefore unable to fertilize murine eggs. This explains the reduced levels of fertilization that were observed in IVF and the absence of pronuclei formation. These results indicate that, in addition to its chronic impact on reproductive potential, DEHP also imposes acute damage to sperm by affecting its ability to fertilize and thereby represent a risk to male fertility.

MATERIALS AND METHODS

Animal Care

C57BL6 mice were purchased from Jackson Laboratory, Bar Harbor, ME, United States, or Harlan Laboratories (Indianapolis, IN, United States). The mice were kept in a room with controlled light (14 h light and 10 h darkness) and temperature (23 ± 0.5°C); 50–60% humidity. The mice were fed a standard chow diet (PicoLab Rodent diet 20 and LabDiet, 5053) and hyper-chlorinated water *ad libitum*. BPA, DEHP, DMP, and DEP (Sigma-Aldrich, St. Louis, MO, United States) were dissolved in ethanol (Sigma-Aldrich). Phthalates were used at a final concentration of 1, 2, and 10 μM. The concentration range of 1–10 μM for tested EDC's was chosen based on previously reported phthalate concentrations linked to female infertility and on studies that evaluated DEHP plasma concentration in patients who undergo hemodialysis (Nassberger et al., 1987; Reddy et al., 2006). Vehicle controls were performed at the highest concentration.

Embryo Collection From Natural Mating

Four- to-16- week-old female mice were super- ovulated by the standard procedure previously described (Hoogenkamp and Lewing, 1982). Briefly, 5 IU of pregnant mare serum gonadotropin (PMSG; EMD Millipore) were administered via intraperitoneal injection (i.p.) at 14:30. Forty-eight hours later, 5 IU of human chorionic gonadotropin (hCG; EMD Millipore) were injected. At the time of hCG injection, each female mouse was placed in an individual cage with one proven breeder (3–10 months old). The following morning, female mice were inspected for vaginal plugs. 20 h after hCG administration, embryos were dissected out from the oviducts. The isolated oocyte-cumulus complexes were placed in pre-warmed 50 μL droplet of Hyaluronidase (80 IU/mL) (LifeGlobal) and were gently pipetted up and down repeatedly in a fine glass pipette until the oocytes were partially denuded. The oocytes were then transferred to a pre-warmed M2 media (Zenith Biotech) supplemented with 4 mg/mL BSA (Sigma-Aldrich) and washed in 4–5 droplets until all the corona cells were removed. Zygotes from each individual mouse were randomly allocated to different culture conditions for 20 h of incubation. Since the tested EDCs show low water solubility and high oil solubility, the standard culture of embryos under oil could not be employed. Thus, we cultured the embryos in 500 μL KSOM (Zenith Biotech) ± EDCs at different concentrations for 20 h in 4-well dishes (*Nunc*™, Sigma-Aldrich) without oil. At the end of the 20 h incubation, the two cell embryos were briefly washed and allocated to culture dishes, containing 10 μL droplets of KSOM (Zenith Biotech) supplemented with 1 mg/mL BSA (Sigma-Aldrich) overlaid with embryo-suitable light mineral oil (Millipore) in 5% CO_2 and 37°C. Successful development was considered as morula or blastocyst – the final stage of embryonic development before implantation. To calculate the rate of embryo survival, we

counted the number of embryos that developed to the morula or blastocyst stage and divided this number by the total number of the zygotes that were harvested.

In vitro Fertilization

To investigate the influence of EDCs exposure on spermatozoa's ability to fertilize eggs, *in vitro* fertilization (*IVF*) experiments were conducted. *IVF* was performed as previously described (Vergara et al., 1997) with a few modifications. Eggs were recovered from 4 to 16-week-old female mice by superovulation as described above. 13 h after hCG injection, the female mice were euthanized, and the oviducts were dissected out. The cumulus masses were isolated from the ampulla region of the oviduct, and incubated in HTF medium (Embryomax, Specialty Media, Millipore MR-070-D), 5% CO_2, 37°C for 30 min prior to insemination. Sperm was obtained from a mature C57BL male mouse just before egg harvest. Spermatozoa were recovered by removing the caudae epididymis and placing each cauda separately in a petri dish containing pre-warmed HTF with or without EDCs. The tissue was cut five to six times, and sperm was allowed to swim out into the medium for 20–30 min. The cauda was then removed, and the resultant sperm suspension was left for an additional 30–60 min in the media at 37°C in 5% CO_2 to capacitate. Total time of capacitation was 60–90 min.

Four well plates were used for fertilization. Each well was filled with 700 μL of HTF. Sperm was added to each well to a final concentration of 210,000 spermatozoa/mL. Subsequently, the cumulus masses were added to the fertilization dish; care was taken to avoid carry-over of excessive amounts of solution to maintain sperm concentrations. Since the cumulus masses were obtained around the time of ovulation, they were highly compact, making it difficult to quantify the exact number of eggs in each mass. To ensure similar numbers of eggs in each tested condition, two-three cumulus masses were added to each fertilization well. Dishes were placed in the incubator and maintained at 37°C in 5% CO_2 for 4h. After that time, eggs were washed to remove excess sperm and then cultured in 10 μL droplets of KSOM supplemented with 1 mg/mL BSA and overlaid with embryo-tested light mineral oil in 5% CO_2 and 37°C. To assess the rates of successful fertilization, the number of morula or blastocyst embryos produced by IVF on day 5 post insemination was counted and then divided by the number of eggs that were initially used for insemination.

Electrophysiology

Sperm was collected as previously reported (Wennemuth et al., 2003). Giga-ohm seals between the patch pipette and mouse spermatozoa were formed at the cytoplasmic droplet. Seals were formed in HS solution comprising the following (in mM): 130 NaCl, 5 KCl, 1 $MgSO_4$, 2 $CaCl_2$, 5 glucose, 1 sodium pyruvate, 10 lactic acid, 20 HEPES, pH 7.4 adjusted with NaOH. Transition into the whole-cell mode was performed by applying short (1 ms) 499–611 mV voltage pulses, combined with light suction. Access resistance was 15–25 MΩ. Cells were stimulated every 5 s. Data were sampled at 2–5 kHz and filtered at 1 kHz. Pipettes (15–20 MΩ) for whole-cell patch-clamp recordings of monovalent CatSper currents were filled with the following (in mM): 130 Cs-methanesulfonate, 70 HEPES/MES, 3 EGTA, 2 EDTA, 0.5 Tris-HCl, pH 7.4 adjusted with CsOH. Bath divalent-free solution for recording of monovalent CatSper currents contained the following (in mM): 140 Cs-methanesulfonate, 40 HEPES/MES, 1 EDTA, pH 7.4 adjusted with CsOH. HS solution was used to record baseline current while measuring monovalent CatSper currents. 1 μL/mL EtOH (vehicle control), 10 μM or 100 μm DEHP were added to the bath solution right before electrophysiology experiments. $CaCl_2$ was added to this solution in accordance with WinMAXC version 2.05 (C. Patton, Stanford University) to obtain the required free Ca^{2+} concentration.

Capacitation of Spermatozoa in the Presence of 10 μM DEHP to Test the Level of Tyrosine Phosphorylation

Spermatozoa collection and the assessment of protein tyrosine phosphorylation was performed as previously outlined (Visconti et al., 1995a), with a few modifications. Spermatozoa were recovered by removing the cauda epididymis and placing it into a Petri dish containing HTF with either 1 μL/mL ethanol or 10 μM DEHP. The tissue was cut five to six times, and sperm was allowed to swim out for 15–20 min at 37°C in 5% CO_2. The cauda was then removed, and spermatozoa suspension was further incubated at 37°C in 5% CO_2. Sperm samples were collected after 30, 60, 90, and 120 min of capacitation and placed into a clean tube. After each sample collection, the sample was centrifuged at 21,000 × *g* for 1 min. The supernatant was discarded, and the cellular pellet was resuspended in 25 μL of 2× Laemmli sample buffer (Bio-Rad) (Laemmli, 1970). The sample was then boiled for 5 min at 95°C and centrifuged at 21,000 × *g* for 1 min. Supernatants were transferred to clean tubes, β-mercapto-ethanol was added (to a final concentration of 2.5%), and the sample was heated again to 95°C for 1 min. 20 μL of the total crude cell lysate from each sample was loaded onto a 4–20% gradient Tris-HCl Criterion SDS-PAGE (Bio-Rad). After transfer to polyvinylidene fluoride membrane, blots were blocked in 0.1% PBS-Tween20 (Fisher Scientific) with 3% IgG-free BSA blocking solution for 1 h and incubated with anti-phosphotyrosine antibody, clone 4G10 (Millipore, 05-321) at a dilution of 1:2000 in 1% IgG-free BSA blocking solution overnight at +4°C. The membrane was then washed three times in PBST and probed with a secondary horseradish peroxidase-conjugated antibody (Abcam) at a dilution of 1:15,000 in 1× PBST. After subsequent washing, the membrane was developed with an ECL SuperSignal West Pico kit (Pierce) according to the manufacturer's instructions. After detection, the membrane was stripped and re-probed with mouse tubulin-alpha ab-2 (Sigma-Aldrich), 1:5000 dilution. To quantify the global changes in tyrosine phosphorylation, rectangular boxes were drawn around each lane of the western blots' images. Each lane's optical density was normalized. First, the detected signals were normalized to the loading control, acetylated tubulin. Subsequently, each lane was normalized to the control lane at 120 min of capacitation.

Spontaneous Acrosome Reaction in the Presence of 10 μM DEHP in Capacitated Spermatozoa

Assessment of the acrosomal status was done as previously reported (Larson and Miller, 1999) with a few adjustments. In summary, the right and left caudae epididymides were surgically removed. One cauda was placed in HTF medium supplemented with 1 μl/mL ethanol while the second one was placed in HTF medium containing 10 μM DEHP. Each cauda was cut five to six times, and sperm were allowed to swim out for 15–20 min at 37°C in 5% CO_2. The cauda was then removed, and the resultant spermatozoa suspension was left to capacitate for 60 min. On average, the concentration of sperm in each condition was 2–5 × 10 cells/mL. After 60 min of capacitation, spermatozoa suspension was transferred to clean microtubes and centrifuged at 300 × *g* for 5 min at room temperature. The cells were then fixed in 4% PFA in 1X PBS for 15 min. At the end of fixation, an equal volume of 0.1 M ammonium acetate was added. The microfuges were centrifuged at 800 × *g* for 5 min. The supernatant was removed, and sperm cells were resuspended in the remaining 100 μL. 30 μL of sperm suspension was spotted onto non-charged microscope slides and gently spread out with a glass pipette. The samples were allowed to air-dry for 15 min. Subsequently, the slides were washed in Milli-Q water followed by a methanol wash, and then Milli-Q water again, each wash step was done for 5 min. The slides were subsequently submerged in Coomassie brilliant blue (Sigma-Aldrich) solution for 2 min (0.11 g Coomassie brilliant blue, 20 mL water, 25 mL Methanol, and 5 mL glacial acetic acid). Next, the slides were rinsed in Milli-Q water to remove excess Coomassie and mounted with Mowiol mounting medium (Millipore). After the cells were mounted, the acrosomal status was immediately assessed to avoid diffusion of the stain. Acrosome intact cells had bright blue staining on the dorsal region of the acrosome. Acrosome reacted cells had patchy or absent staining. 500 sperm cells per condition (100–200 cells per slide, 3–5 slides per condition) were assessed.

Flow Cytometry

Spermatozoa was capacitated in the presence of either 10 μM DEHP or vehicle control. To detect phosphotyrosine residues in capacitated sperm by flow cytometry we followed the methodology previously outlined (Barbonetti et al., 2008), with few modifications. Sperm aliquots (3×10^6) were taken at 60 min of capacitation and fixed in 3.7% PFA in 1 × PBS for 10 min at room temperature. To remove the PFA, the cells were centrifuged at 500 × *g* for 10 min. The supernatant was removed, and the cellular pellet was resuspended in 1 × PBS. The cells were washed twice. Next, the cells were permeabilized in 0.1% Triton X-100 for 10 min at RT. Non-specific binding sites were blocked by 0.1% BSA in PBST for 30 min at RT. To detect phosphotyrosine, we conjugated an anti-phosphotyrosine antibody clone 4G10 with a CF 647 dye (Mix-n-Stain™ Antibody Labeling Kit, Biotium), as per the manufacturer's instructions. To label the cells, sperm were incubated with 10 μg/ml of the conjugated antibody in PBS with 0.1% BSA for 1 h at RT. Labeled spermatozoa were then washed in PBS and resuspended in 250 μL PBS for flow cytometric analysis. 10,000 cells per sample were analyzed. Sperm fluorescence was quantified using the BD LSR Fortessa flow cytometer equipped with an argon laser tuned far red spectrum. flow cytometry analysis was performed with the aid of a positive and a negative control for each experiment. FlowJo™ Software was used for data analysis. The region of interest was selected based on sperm forward scatter (FSC, relative cell size) and side scatter (SSC, cell internal complexity) to eliminate cellular debris.

ROS Production Detection by Chemiluminescence Assay

Spermatozoa were recovered by removing both caudae epididymides and placing them into a 30 mm Petri dish containing HS media. Cells were allowed to swim out for 15–20 min. Subsequently, the sperm suspension was equally divided between three Eppendorf tubes and spun down at 300 × *g* for 7 min. After the removal of the supernatant, the cells were resuspended in an equal volume of HTF containing either ethanol or DEHP. The control tube contained 1 μL/mL ethanol and the treatment tube contained either 10 μM or a 100 μM DEHP. The suspensions were then capacitated at 37°C in 5% CO_2 for 60 min. Detection of reactive oxygen species generated by sperm cells was done using the chemiluminescent agent – luminol following a previously described procedure (Saleh and Agarwal, 2002; Agarwal et al., 2008). The chemiluminescent probe, luminol (Sigma-Aldrich, A8511-5G.) was freshly prepared before each experiment. After 60 min of capacitation, the samples were spun down at 300 × *g* for 7 min and resuspended in 125 μM luminol in DPBS. Negative control, test sample, and positive control were prepared. 100 μL of 30% hydrogen peroxide solution was added to the positive control. A 100 μL aliquot of the cell suspension was taken from each sample for sperm count. The samples were then taken for Chemiluminescence measurements using the Lumicycle 32 (Actimetrics, Inc., Wilmette, IL, United States). The luminometer measured Chemiluminescence at 37°C for 5 min. ROS production was expressed as counted photons per minute (CPM)/10^6 sperm. Data were recorded using Actimetrics Lumicycle Data Collection software and analyzed using the Actimetrics Lumicycle Analysis program.

Statistical Analyses

For statistical analyses used in the manuscript the GraphPad Prism 5 software (GraphPad Software, Inc., La Jolla, CA, United States) was used. Unpaired *t*-test was used to determine statistical significance for embryo survival, *IVF* and Chemiluminescence experiments, and assigning $p \leq 0.05$ as the limit. Paired *t*-test was used for the AR, PY and flow cytometry experiments. All results are shown with the standard error of the mean. The significance of changes are indicated as follows: $^{*}p \leq 0.05$, $^{**}p \leq 0.01$, $^{***}p \leq 0.001$.

DATA AVAILABILITY STATEMENT

All datasets generated for this study are included in the article/**Supplementary Material**.

ETHICS STATEMENT

All experiments were performed in accordance with NIH guidelines for animal research and approved by UC Berkeley Animal Care and Use Committee (AUP 2015-07-7742), with every effort made to minimize suffering for the animals.

AUTHOR CONTRIBUTIONS

LGK and PL conceived the project, designed the experiments, and wrote the manuscript. LGK performed all studies, data acquisition, and analysis for the manuscript. JD helped with acrosome reaction, tyrosine phosphorylation, chemiluminescence, and flow cytometry studies. NP assisted with flow cytometry experiments. JM and LJK helped with lumicycle and data analysis of luminol studies. All authors discussed the results and commented on the manuscript.

FUNDING

This work was supported by March of Dimes Basil O'Connor Starter Scholar Research Award #5FY13-204, Pew Biomedical Scholars Award, Chau Hoi Shuen Foundation Women in Science Program Award, and Packer Wentz Endowment Will (to PL), as well as Male Contraceptive Initiative grant to LGK and Summer Research Fellowship to JD.

ACKNOWLEDGMENTS

We thank Dr. Andrew Modzelewski for his valuable advice and technical assistance with embryo work, and Monika Haoui for the help with manuscript editing.

SUPPLEMENTARY MATERIAL

The Supplementary Material for this article can be found online at: https://www.frontiersin.org/articles/10.3389/fcell.2020.00426/full#supplementary-material

FIGURE S1 | Murine embryo survival post exposure to 2 μM of tested EDCs. *In vitro* embryo development on day 5 post fertilization. **(A)** Representative images of blastocysts previously exposed at the zygote stage to 2 μM DEP for 20 h. **(B)** Representative images of blastocysts previously exposed at the zygote stage to 2 μM DMP for 20 h. Scale bars are 50 μm.

FIGURE S2 | Fertilization rate of murine eggs exposed to spermatozoa treated with 2 μM of tested EDCs. **(A)** Representative images of blastocysts obtained after murine eggs were introduced to sperm previously exposed 2 μM DEP. **(B)** Representative images of blastocysts obtained after murine eggs were introduced to sperm previously exposed 2 μM DMP. **(C)** Representative images of blastocysts obtained after murine eggs were introduced to sperm previously exposed 2 μM BPA. Scale bars are 50 μm.

FIGURE S3 | Murine CatSper is not affected by DEHP. **(A)** Representative monovalent whole-cell CatSper currents ($I_{CatSper}$) recorded from a murine spermatozoon in the absence (black) and presence of 10 μM (blue) and 100 μM DEHP (red). $I_{CatSper}$ were activated by a voltage ramp from −80 to +80 mV from a holding potential of 0 mV. Voltage protocol is shown above the currents. The panel on the right shows the main conducting ion of the pipette and bath solutions. **(B)** Averaged $I_{CatSper}$ densities recorded from murine epididymal spermatozoa in the absence and presence of DEHP. Data are means ± S.E.M. An average of 3 independent experiments is shown.

FIGURE S4 | Representative dot plot of side (SSC-A) versus forward (FSC-A) scatter showing flow-cytometry data obtained for sperm. **(A)** The region of interest demarcated by solid lines was selected to eliminate cellular debris. **(B–F)** Representative flow cytometry histograms from five independent experiments. Mean fluorescence intensities (MFI) normalized to mode show an increase in global tyrosine phosphorylation in 10 μM DEHP treated spermatozoa (red) at 60 min of capacitation compared to the vehicle control (blue). The background fluorescence detected in unstained spermatozoa is shown in gray. Tyrosine phosphoproteins were detected using a CF 647 dye conjugated to anti-PY (monoclonal antibody).

FIGURE S5 | Time course of capacitation-associated tyrosine phosphorylation of specific sperm proteins is altered by exposure to DEHP. Levels of relative tyrosine phosphorylation obtained from each of the four protein bands at the corresponding molecular weights: 75, 95, 170, and 270 kDa. **(A)** The density of the 75 kDa protein band was normalized to the densities of the loading control, followed by normalization to the control at 120 min. Each data point represents the average of one of the three independent experiments. **(B)** The 95 kDa protein band normalized as in **(A)**. **(C)** The 170 kDa protein band normalized as in **(A)**. **(D)** The 270 kDa protein band normalized as in **(A)**. Normalization to the control band at 120 min was chosen as the strongest physiological phosphorylation signal.

TABLE S1 | (A–D) Murine embryo development after 20 h exposure to DMP, BPA, DEP, or DEHP. Embryo development was assessed on day 5 post fertilization. The column "progression to blastocyst stage per experiment, %" represents the percentage of embryos that reached blastocyst or morula stage. This number was calculated by dividing the number of all embryos that reached blastocyst or morula stage to the number of all collected zygotes per each experiment. Zygotes were obtained from naturally mated super-ovulated females. Each condition was assessed by 3–8 independent experiments. **(A)** Embryo development after 20 h exposure to DMP at 0, 1, 2, and 10 μM and subsequent embryo culture in DMP-free media. **(B)** Embryo development after 20 h exposure to the indicated concentration of BPA and subsequent culture in BPA-free media. **(C)** Embryo development after 20 h exposure to the indicated concentration of DEP and subsequent culture in DEP-free media. **(D)** Embryo development after 20 h exposure to the indicated concentration of DEHP and subsequent culture in DEHP-free media.

TABLE S2 | The development of murine zygotes isolated from naturally mated super-ovulated females and after their exposure to 0.1% ethanol for 20 h in the culture media. Embryo development was assessed on day 5 post fertilization and represents the percentage of embryos that reached blastocyst or morula stage. This number was calculated by dividing the number of all embryos that reached blastocyst or morula stage by the number of all collected zygotes per experiment.

TABLE S3 | (A–D) Development of *in vitro* fertilized mouse embryos obtained after murine eggs were introduced to the sperm previously exposed to DMP, BPA, DEP, or DEHP for 60–90 min. Embryo development was assessed on day 5 post fertilization. The "Progression to the blastocyst stage per experiment, %" column represents the percentage of embryos that reached blastocyst or morula stage. This number was calculated by dividing the number of all embryos that reached blastocyst or morula stage to the number of all collected and inseminated eggs per each experiment. Each condition was assessed by 3–5 independent experiments. **(A)** *In vitro* embryo development after eggs insemination with 0, 1, 2, or 10 μM DMP-treated sperm **(B)** *In vitro* embryo development after eggs were inseminated with spermatozoa previously exposed to the indicated concentration of BPA. **(C)** *In vitro* embryo development after eggs were inseminated with the spermatozoa treated with corresponding concentrations of DEP. **(D)** *In vitro* embryo development after murine eggs were inseminated with spermatozoa treated with corresponding concentrations of DEHP.

TABLE S4 | Development of embryos derived from the murine eggs that were subjected to *in vitro* fertilization (IVF) with murine sperm previously exposed to 0.1% ethanol for 60–90 min. Embryo development was assessed on the day 5 post IVF and represents the percentage of embryos that reached blastocyst or morula stage. This number was calculated by dividing the number of all embryos

that reached blastocyst or morula stage to the number of all collected eggs per each independent experiment.

TABLE S5 | Effect of 10 μM DEHP on fertilization and pronuclei formation. Pronucleus (PN) formation was assessed 9 h after egg insemination with sperm cells previously exposed to 10 μM DEHP. Three independent experiments were carried out.

TABLE S6 | Assessment of the global tyrosine phosphorylation by flow cytometry. Tyrosine phosphoproteins were detected by flow cytometry using a CF 647 dye conjugated to anti-PY antibody. Five independent experiments were carried out. Sperm concentrations were normalized between all conditions for each experiment. Values are mean fluorescence intensity (MFI) detected in the APC-Cy7-A channel normalized to mode. A ratio of the normalized detected MFI in the 10 μM DEHP-treated sperm cells vs. the vehicle control was used to calculate the fold increase in global fluorescence.

TABLE S7 | Detection of reactive oxygen species (ROS) in murine spermatozoa treated with DEHP compared with vehicle control. The luminol-dependent chemiluminescence assay was used to detect ROS production. Six independent experiments were carried out. A minimum of $1.35*10^6$ sperm cells/mL were used per condition. ROS production was expressed as counted photons per minute (CPM)/10^6. Each row represents an individual experiment. For each experiment, sperm concentrations were normalized between all conditions.

REFERENCES

Agarwal, A., Cocuzza, M., Abdelrazik, H., and Sharma, R. K. (2008). *Oxidative Stress Measurement in Patients with Male or Female Factor Infertility*. Trivandrum: Transworld Research Network.

Aitken, R. J., and Clarkson, J. S. (1987). Cellular basis of defective sperm function and its association with the genesis of reactive oxygen species by human spermatozoa. *J. Reprod. Fertil.* 81, 459–469. doi: 10.1530/jrf.0.0810459

Aitken, R. J., Paterson, M., Fisher, H., Buckingham, D. W., and Van Duin, M. (1995). Redox regulation of tyrosine phosphorylation in human spermatozoa and its role in the control of human sperm function. *J. Cell Sci.* 108, 2017–2025.

Aitken, R. J., Wingate, J. K., De Iuliis, G. N., Koppers, A. J., and Mclaughlin, E. A. (2006). Cis-unsaturated fatty acids stimulate reactive oxygen species generation and lipid peroxidation in human spermatozoa. *J Clin Endocrinol Metab* 91, 4154–4163. doi: 10.1210/jc.2006-1309

Alvarez, J. G., and Storey, B. T. (1982). Spontaneous lipid peroxidation in rabbit epididymal spermatozoa: its effect on sperm motility. *Biol. Reprod.* 27, 1102–1108. doi: 10.1095/biolreprod27.5.1102

Alvau, A., Battistone, M. A., Gervasi, M. G., Navarrete, F. A., Xu, X., Sánchez-Cárdenas, C., et al. (2016). The tyrosine kinase FER is responsible for the capacitationassociated increase in tyrosine phosphorylation in murine sperm. *Development* 143, 2325–2333. doi: 10.1242/dev.136499

Ambruosi, B., Filioli Uranio, M., Sardanelli, A. M., Pocar, P., Martino, N. A., Paternoster, M. S., et al. (2011). Correction: *in vitro* acute exposure to DEHP affects oocyte meiotic maturation, energy and oxidative stress parameters in a large animal model. *PLoS One* 6:e27452. doi: 10.1371/journal.pone.0027452

Api, A. M. (2001). Toxicological profile of diethyl phthalate: a vehicle for fragrance and cosmetic ingredients. *Food Chem. Toxicol.* 39, 97–108. doi: 10.1016/S0278-6915(00)00124-1

Austin, C. R. (1951). Observations on the penetration of the sperm in the mammalian egg. *Aust. J. Sci. Res. B* 4, 581–596. doi: 10.1071/bi9510581

Avella, M. A., and Dean, J. (2011). Fertilization with acrosome-reacted mouse sperm: implications for the site of exocytosis. *Proc. Natl. Acad. Sci. U.S.A.* 108, 19843–19844. doi: 10.1073/pnas.1118234109

Barbonetti, A., Vassallo, M. R. C., Cinque, B., Antonangelo, C., Sciarretta, F., Santucci, R., et al. (2008). Dynamics of the global tyrosine phosphorylation during capacitation and acquisition of the ability to fuse with oocytes in human spermatozoa1. *Biol. Reprod.* 79, 649–656. doi: 10.1095/biolreprod.108.06999.00145.x8254

Bloom, M. S., Whitcomb, B. W., Chen, Z., Ye, A., Kannan, K., and Buck Louis, G. M. (2015). Associations between urinary phthalate concentrations and semen quality parameters in a general population. *Hum. Reprod.* 30, 2645–2657. doi: 10.1093/humrep/dev219

Brehm, E., and Flaws, J. A. (2019). Transgenerational effects of endocrine-disrupting chemicals on Male and female reproduction. *Endocrinology* 160, 1421–1435. doi: 10.1210/en.2019-00034

Brehm, E., Rattan, S., Gao, L., and Flaws, J. A. (2018). Prenatal exposure to Di(2-Ethylhexyl) phthalate causes long-term transgenerational effects on female reproduction in mice. *Endocrinology* 159, 795–809. doi: 10.1210/en.2017-03004

Burdorf, A., Brand, T., Jaddoe, V. W., Hofman, A., Mackenbach, J. P., and Steegers, E. A. P. (2011). The effects of work-related maternal risk factors on time to pregnancy, preterm birth and birth weight: the seneration R study. *Occup. Environ. Med.* 68, 197–204. doi: 10.1136/oem.2009.046516

Calafat, A. M., Kuklenyik, Z., Reidy, J. A., Caudill, S. P., Ekong, J., and Needham, L. L. (2005). Urinary concentrations of bisphenol A and 4-Nonylphenol in a human reference population. *Environ. Health Perspect.* 113, 391–395. doi: 10.1289/ehp.7534

Carlson, A. E., Westenbroek, R. E., Quill, T., Ren, D., Clapham, D. E., Hille, B., et al. (2003). CatSper1 required for evoked Ca2+ entry and control of flagellar function in sperm. *Proc. Natl. Acad. Sci. U.S.A.* 100, 14864–14868. doi: 10.1073/pnas.2536658100

Chang, M. C. (1957). A detrimental effect of seminal plasma on the fertilizing capacity of sperm. *Nature* 179, 258–259. doi: 10.1038/179258a0

Chen, S. J., Allam, J. P., Duan, Y. G., and Haidl, G. (2013). Influence of reactive oxygen species on human sperm functions and fertilizing capacity including therapeutical approaches. *Arch. Gynecol. Obstet.* 288, 191–199. doi: 10.1007/s00404-013-2801-4

Cocuzza, M., Sikka, S. C., Athayde, K. S., and Agarwal, A. (2007). Clinical relevance of oxidative stress and sperm chromation damage in male infertility: an evidence based analysis. *Int. Braz. J. Urol.* 33, 603–621. doi: 10.1590/S1677-55382007000500002

Davis, B. K. (1981). Timing of fertilization in mammals: sperm cholesterol/phospholipid ratio as a determinant of the capacitation interval. *Proc. Natl. Acad. Sci. U.S.A.* 78, 7560–7564. doi: 10.1073/pnas.78.12.7560

Donà, G., Fiore, C., Andrisani, A., Ambrosini, G., Brunati, A., Ragazzi, E., et al. (2011). Evaluation of correct endogenous reactive oxygen species content for human sperm capacitation and involvement of the NADPH oxidase system. *Hum. Reprod.* 26, 3264–3273. doi: 10.1093/humrep/der321

Duty, S. M., Silva, M. J., Barr, D. B., Brock, J. W., Ryan, L., Chen, Z., et al. (2003). Phthalate exposure and human semen parameters. *Epidemiology* 14, 269–277. doi: 10.1097/01.ede.0000059950.11836.16

Fernandez, M. F., Arrebola, J. P., Taoufiki, J., Navalón, A., Ballesteros, O., Pulgar, R., et al. (2007). Bisphenol-A and chlorinated derivatives in adipose tissue of women. *Reprod. Toxicol.* 24, 259–264. doi: 10.1016/j.reprotox.2007.06.007

Fujii, S., Yabe, K., Furukawa, M., Hirata, M., Kiguchi, M., and Ikka, T. (2005). A two-generation reproductive toxicity study of diethyl phthalate (DEP) in rats. *J. Toxicol. Sci.* 30, S97–S116. doi: 10.2131/jts.30.S97

Green, R., Hauser, R., Calafat, A. M., Weuve, J., Schettler, T., Ringer, S., et al. (2005). Use of di(2-ethylhexyl) phthalate-containing medical products and urinary levels of mono(2-ethylhexyl) phthalate in neonatal intensive care unit infants. *Environ. Health Perspect.* 113, 1222–1225. doi: 10.1289/ehp.7932

Griveau, J. F., Renard, P., and Le Lannou, D. (1995). Superoxide anion production by human spermatozoa as a part of the ionophore-induced acrosome reaction process. *Int. J. Androl.* 18, 67–74. doi: 10.1111/j.1365-2605.1995.tb00388.x

Hannon, P. R., Niermann, S., and Flaws, J. A. (2016). Acute exposure to Di(2-Ethylhexyl) phthalate in adulthood causes adverse reproductive outcomes later in life and accelerates reproductive aging in female mice. *Toxicol. Sci.* 150, 97–108. doi: 10.1093/toxsci/kfv317

Hauser, R., and Calafat, A. M. (2005). Phthalates and human health. *Occup. Environ. Med.* 62, 806–818. doi: 10.1136/oem.2004.017590

Hauser, R., Meeker, J. D., Duty, S., Silva, M. J., and Calafat, A. M. (2006). Altered semen quality in relation to urinary concentrations of phthalate monoester and oxidative metabolites. *Epidemiology* 17, 682–691. doi: 10.1097/01.ede.0000235996.89953.d7

Hauser, R., Meeker, J. D., Singh, N. P., Silva, M. J., Ryan, L., Duty, S., et al. (2007). DNA damage in human sperm is related to urinary levels of phthalate

monoester and oxidative metabolites. *Hum. Reprod.* 22, 688–695. doi: 10.1093/humrep/del428

Hoogenkamp, H., and Lewing, P. (1982). Superovulation in mice in relation to their age. *Vet. Q.* 4, 47–48. doi: 10.1080/01652176.1982.9693838

Huang, Y., Wu, C., Ye, Y., Zeng, J., Zhu, J., Li, Y., et al. (2019). The increase of ROS caused by the interference of DEHP with JNK/p38/p53 pathway as the reason for hepatotoxicity. *Int. J. Environ. Res. Public Health* 16:356. doi: 10.3390/ijerph16030356

Hunt, P. A., Susiarjo, M., Rubio, C., and Hassold, T. J. (2009). The bisphenol a experience: a primer for the analysis of environmental effects on mammalian reproduction1. *Biol. Reprod.* 81, 807–813. doi: 10.1095/biolreprod.109.077008

Ichikawa, T., Oeda, T., Ohmori, H., and Schill, W. B. (1999). Reactive oxygen species influence the acrosome reaction but not acrosin activity in human spermatozoa. *Int. J. Androl.* 22, 37–42. doi: 10.1046/j.1365-2605.1999.00145.x

Inoue, N., Ikawa, M., Isotani, A., and Okabe, M. (2005). The immunoglobulin superfamily protein Izumo is required for sperm to fuse with eggs. *Nature* 434, 234–238. doi: 10.1038/nature03362

Jin, M., Fujiwara, E., Kakiuchi, Y., Okabe, M., Satouh, Y., Baba, S. A., et al. (2011). Most fertilizing mouse spermatozoa begin their acrosome reaction before contact with the zona pellucida during in vitro fertilization. *Proc. Natl. Acad. Sci. U.S.A.* 108, 4892–4896. doi: 10.1073/pnas.1018202108

Jones, R., Mann, T., and Sherins, R. (1979). Peroxidative breakdown of phospholipids in human spermatozoa, spermicidal properties of fatty acid peroxides, and protective action of seminal plasma. *Fertil. Steril.* 31, 531–537. doi: 10.1016/S0015-0282(16)43999-3

Kasahara, E., Sato, E. F., Miyoshi, M., Konaka, R., Hiramoto, K., Sasaki, J., et al. (2002). Role of oxidative stress in germ cell apoptosis induced by di(2-ethylhexyl)phthalate. *Biochem. J.* 365, 849–856. doi: 10.1042/BJ20020254

Kavlock, R., Boekelheide, K., Chapin, R., Cunningham, M., Faustman, E., Foster, P., et al. (2002). NTP center for the evaluation of risks to human reproduction: phthalates expert panel report on the reproductive and developmental toxicity of di(2-ethylhexyl) phthalate. *Reprod. Toxicol.* 16, 529–653. doi: 10.1016/S0890-6238(02)00032-1

Kay, V. R., Bloom, M. S., and Foster, W. G. (2014). Reproductive and developmental effects of phthalate diesters in males. *Crit. Rev. Toxicol.* 44, 467–498. doi: 10.3109/10408444.2013.875983

Kim, J. H., Park, H. Y., Bae, S., Lim, Y.-H., and Hong, Y.-C. (2013). Diethylhexyl phthalates is associated with insulin resistance via oxidative stress in the elderly: a panel study. *PLoS One* 8:e71392. doi: 10.1371/journal.pone.007 1392

Kirichok, Y., Navarro, B., and Clapham, D. E. (2006). Whole-cell patch-clamp measurements of spermatozoa reveal an alkaline-activated Ca2+ channel. *Nature* 439, 737–740. doi: 10.1038/nature04417

La Spina, F. A., Puga Molina, L. C., Romarowski, A., Vitale, A. M., Falzone, T. L., Krapf, D., et al. (2016). Mouse sperm begin to undergo acrosomal exocytosis in the upper isthmus of the oviduct. *Dev. Biol.* 411, 172–182. doi: 10.1016/j.ydbio.2016.02.006

Laemmli, U. K. (1970). Cleavage of structural proteins during the assembly of the head of bacteriophage T4. *Nature* 227, 680–685. doi: 10.1038/227680a0

Larson, J. L., and Miller, D. J. (1999). Simple histochemical stain for acrosomes on sperm from several species. *Mol. Reprod. Dev.* 52, 445–449. doi: 10.1002/(sici)1098-2795(199904)52:4<445::aid-mrd14>3.0.co;2-6

Latini, G., Del Vecchio, A., Massaro, M., Verrotti, A., and De Felice, C. (2006). Phthalate exposure and male infertility. *Toxicology* 226, 90–98. doi: 10.1016/j.tox.2006.07.011

Leclerc, P., De Lamirande, E., and Gagnon, C. (1997). Regulation of protein-tyrosine phosphorylation and human sperm capacitation by reactive oxygen derivatives. *Free Radic. Biol. Med.* 22, 643–656. doi: 10.1016/S0891-5849(96)00379-6

Lovekamp, T. N., and Davis, B. J. (2001). Mono-(2-ethylhexyl) phthalate suppresses aromatase transcript levels and estradiol production in cultured rat granulosa cells. *Toxicol. Appl. Pharmacol.* 172, 217–224. doi: 10.1006/taap.2001.9156

Meeker, J. D., Calafat, A. M., and Hauser, R. (2009). Urinary metabolites of di(2-ethylhexyl) phthalate are associated with decreased steroid hormone levels in adult men. *J. Androl.* 30, 287–297. doi: 10.2164/jandrol.108.006403

Mei, Y., Rongshuang, M., Ruizhi, Z., Hongyuan, H., Qiyue, T., and Shu-hua, Z. (2019). Effects of dimethyl phthalate (DMP) on serum sex hormone levels and apoptosis in C57 female mice. *Int. J. Endocrinol. Metab.* 17:e82882.

Muncke, J. (2011). Endocrine disrupting chemicals and other substances of concern in food contact materials: an updated review of exposure, effect and risk assessment. *J. Steroid Biochem. Mol. Biol.* 127, 118–127. doi: 10.1016/j.jsbmb.2010.10.004

Nassar, A., Mahony, M., Morshedi, M., Lin, M. H., Srisombut, C., and Oehninger, S. (1999). Modulation of sperm tail protein tyrosine phosphorylation by pentoxifylline and its correlation with hyperactivated motility. *Fertil. Steril.* 71, 919–923. doi: 10.1016/S0015-0282(99)00013-8

Nassberger, L., Arbin, A., and Ostelius, J. (1987). Exposure of patients to phthalates from polyvinyl chloride tubes and bags during dialysis. *Nephron* 45, 286–290. doi: 10.1159/000184165

Naz, R. K., and Rajesh, P. B. (2004). Role of tyrosine phosphorylation in sperm capacitation / acrosome reaction. *Reprod. Biol. Endocrinol.* 2:75. doi: 10.1186/1477-7827-2-75

Ochsendorf, F. R., Thiele, J., Fuchs, J., Schüttau, H., Freisleben, H. J., Buslau, M., et al. (1994). Chemiluminescence in semen of infertile men. *Andrologia* 26, 289–293. doi: 10.1111/j.1439-0272.1994.tb00804.x

Pan, G., Hanaoka, T., Yu, L., Na, J., Yamano, Y., Hara, K., et al. (2011). Associations between hazard indices of di-n-butylphthalateand di-2-ethylhexylphthalate exposure and serum reproductive hormone levels among occupationally exposed and unexposed Chinese men. *Int. J. Androl.* 34, e397–e406. doi: 10.1111/j.1365-2605.2011.01201.x

Pant, N., Pant, A., Shukla, M., Mathur, N., Gupta, Y., and Saxena, D. (2011). Environmental and experimental exposure of phthalate esters: the toxicological consequence on human sperm. *Hum. Exp. Toxicol.* 30, 507–514. doi: 10.1177/0960327110374205

Patel, S., Zhou, C., Rattan, S., and Flaws, J. A. (2015). Effects of endocrine-disrupting chemicals on the Ovary1. *Biol. Reprod.* 93, 1–9. doi: 10.1095/biolreprod.115.130336

Pearson, S. D., and Trissel, L. A. (1993). Leaching of diethylhexyl phthalate from polyvinyl chloride containers by selected drugs and formulation components. *Am. J. Hosp. Pharm.* 50, 1405–1409. doi: 10.1093/ajhp/50.7.1405

Piehler, E., Petrunkina, A. M., Ekhlasi-Hundrieser, M., and Töpfer-Petersen, E. (2006). Dynamic quantification of the tyrosine phosphorylation of the sperm surface proteins during capacitation. *Cytometry. A* 69, 1062–1070. doi: 10.1002/cyto.a.20338

Qi, H., Moran, M. M., Navarro, B., Chong, J. A., Krapivinsky, G., Krapivinsky, L., et al. (2007). All four CatSper ion channel proteins are required for male fertility and sperm cell hyperactivated motility. *Proc. Natl. Acad. Sci. U.S.A.* 104, 1219–1223. doi: 10.1073/pnas.0610286104

Rahman, M. S., Kwon, W.-S., Lee, J.-S., Yoon, S.-J., Ryu, B.-Y., and Pang, M.-G. (2015). Bisphenol-A affects male fertility via fertility-related proteins in spermatozoa. *Sci. Rep.* 5:9169. doi: 10.1038/srep09169

Reddy, B. S., Rozati, R., Reddy, B. V. R., and Raman, N. V. V. S. S. (2006). Association of phthalate esters with endometriosis in Indian women. *BJOG* 113, 515–520. doi: 10.1111/j.1471-0528.2006.00925.x

Regnier, S. M., and Sargis, R. M. (2014). Adipocytes under assault: environmental disruption of adipose physiology. *Biochim. Biophys. Acta* 1842, 520–533. doi: 10.1016/j.bbadis.2013.05.028

Ren, D., Navarro, B., Perez, G., Jackson, A. C., Hsu, S., Shi, Q., et al. (2001). A sperm ion channel required for sperm motility and male fertility. *Nature* 413, 603–609. doi: 10.1038/35098027

Rosado-Berrios, C. A., Vélez, C., and Zayas, B. (2011). Mitochondrial permeability and toxicity of diethylhexyl and monoethylhexyl phthalates on TK6 human lymphoblasts cells. *Toxicol. In Vitro* 25, 2010–2016. doi: 10.1016/j.tiv.2011.08.001

Roth, Z. (2018). Symposium review: reduction in oocyte developmental competence by stress is associated with alterations in mitochondrial function1. *J. Dairy Sci.* 101, 3642–3654. doi: 10.3168/jds.2017-13389

Rudel, R. A., Camann, D. E., Spengler, J. D., Korn, L. R., and Brody, J. G. (2003). Phthalates, alkylphenols, pesticides, polybrominated diphenyl ethers, and other endocrine-disrupting compounds in indoor air and dust. *Environ. Sci. Technol.* 37, 4543–4553. doi: 10.1021/es0264596

Saleh, R. A., and Agarwal, A. (2002). Oxidative stress and male infertility: from research bench to clinical practice. *J. Androl.* 23, 737–752. doi: 10.1002/j.1939-4640.2002.tb02324.x

Salicioni, A. M., Platt, M. D., Wertheimer, E. V., Arcelay, E., Allaire, A., Sosnik, J., et al. (2007). Signalling pathways involved in sperm capacitation. *Soc. Reprod. Fertil. Suppl.* 65, 245–259.

Schaedlich, K., Gebauer, S., Hunger, L., Beier, L.-S., Koch, H. M., Wabitsch, M., et al. (2018). DEHP deregulates adipokine levels and impairs fatty acid storage in human SGBS-adipocytes. *Sci. Rep.* 8:3447. doi: 10.1038/s41598-018-21800-4

Schiffer, C., Müller, A., Egeberg, D. L., Alvarez, L., Brenker, C., Rehfeld, A., et al. (2014). Direct action of endocrine disrupting chemicals on human sperm. *EMBO Rep.* 15, 758–765. doi: 10.15252/embr.201438869

Sepideh, J., Reza, S. M., Mahdi, A. M., Azadeh, E. H., Naser, A., Niknam, L., et al. (2009). Tyrosine phosphorylation pattern in sperm proteins isolated from normospermic and teratospermic men. *J. Reprod. Infertil.* 10, 185–191.

Sikka, S. (2001). Relative impact of oxidative stress on male reproductive function. *Curr. Med. Chem.* 8, 851–862. doi: 10.2174/0929867013373039

Sumner, R. N., Tomlinson, M., Craigon, J., England, G. C. W., and Lea, R. G. (2019). Independent and combined effects of diethylhexyl phthalate and polychlorinated biphenyl 153 on sperm quality in the human and dog. *Sci. Rep.* 9:3409. doi: 10.1038/s41598-019-39913-9

Sun, Y., Irie, M., Kishikawa, N., Wada, M., Kuroda, N., and Nakashima, K. (2004). Determination of bisphenol A in human breast milk by HPLC with column-switching andfluorescence detection. *Biomed. Chromatogr.* 18, 501–507. doi: 10.1002/bmc.345

Svechnikova, I., Svechnikov, K., and Söder, O. (2007). The influence of di-(2-ethylhexyl) phthalate on steroidogenesis by the ovarian granulosa cells of immature female rats. *J. Endocrinol.* 194, 603–609. doi: 10.1677/JOE-07-0238

Tamburrino, L., Marchiani, S., Minetti, F., Forti, G., Muratori, M., and Baldi, E. (2014). The CatSper calcium channel in human sperm: relation with motility and involvement in progesterone-induced acrosome reaction. *Hum. Reprod.* 29, 418–428. doi: 10.1093/humrep/det454

Tanaka, A., Adachi, T., Takahashi, T., and Yamaha, T. (1975). Biochemical studies on phthalic esters I. Elimination, distribution and metabolism of di-(2-ethylhexyl)phthalate in rats. *Toxicology* 4, 253–264. doi: 10.1016/0300-483X(75)90105-5

Toft, G., Jönsson, B. A. G., Lindh, C. H., Jensen, T. K., Hjollund, N. H., Vested, A., et al. (2012). Association between pregnancy loss and urinary phthalate levels around the time of conception. *Environ. Health Perspect.* 120, 458–463. doi: 10.1289/ehp.1103552

Tripathi, A., Pandey, V., Sahu, A. N., Singh, A., and Dubey, P. K. (2019). Di-(2-ethylhexyl) phthalate (DEHP) inhibits steroidogenesis and induces mitochondria-ROS mediated apoptosis in rat ovarian granulosa cells. *Toxicol. Res.* 8, 381–394. doi: 10.1039/c8tx00263k

Vandenberg, L. N., Hauser, R., Marcus, M., Olea, N., and Welshons, W. V. (2007). Human exposure to bisphenol A (BPA). *Reprod. Toxicol.* 24, 139–177. doi: 10.1016/j.reprotox.2007.07.010

Vergara, G. J., Irwin, M. H., Moffatt, R. J., and Pinkert, C. A. (1997). In vitro fertilization in mice: strain differences in response to superovulation protocols and effect of cumulus cell removal. *Theriogenology* 47, 1245–1252. doi: 10.1016/S0093-691X(97)00104-0

Villegas, J., Kehr, K., Soto, L., Henkel, R., Miska, W., and Sánchez, R. (2003). Reactive oxygen species induce reversible capacitation in human spermatozoa. *Andrologia* 35, 227–232. doi: 10.1046/j.1439-0272.2003.00564.x

Visconti, P. E. (2009). Understanding the molecular basis of sperm capacitation through kinase design. *Proc. Natl. Acad. Sci. U.S.A.* 106, 667–668. doi: 10.1073/pnas.0811895106

Visconti, P. E., Bailey, J., Moore, G., Pan, D., Olds-Clarke, P., and Kopf, G. (1995a). Capacitation of mouse spermatozoa I. Correlation between the capacitation state and protein tyrosine phosphorylation. *Development* 121, 1129–1137.

Visconti, P. E., Moore, G., Bailey, J., Leclerc, P., Connors, S., Pan, D., et al. (1995b). Capacitation of mouse spermatozoa. II. Protein tyrosine phosphorylation and capacitation are regulated by a cAMP-dependent pathway. *Development* 121, 1139–1150.

vom Saal, F. S., Parmigiani, S., Palanza, P. L., Everett, L. G., and Ragaini, R. (2008). The plastic world: sources, amounts, ecological impacts and effects on development, reproduction, brain and behavior in aquatic and terrestrial animals and humans. *Environ. Res.* 108, 127–130. doi: 10.1016/j.envres.2008.03.008

Wang, W., Craig, Z., Basavarajappa, M. S., Hafner, K. S., and Flaws, J. A. (2012). Mono-(2-Ethylhexyl) phthalate induces oxidative stress and inhibits growth of mouse ovarian antral follicles1. *Biol. Reprod.* 87:152. doi: 10.1095/biolreprod.112.102467

Wang, Y., Zhu, H., and Kannan, K. (2019). A review of biomonitoring of phthalate exposures. *Toxics* 7:21. doi: 10.3390/TOXICS7020021

Wathes, D. C., Abayasekara, D. R., and Aitken, R. J. (2007). Polyunsaturated fatty acids in male and female reproduction. *Biol. Reprod.* 77, 190–201. doi: 10.1095/biolreprod.107.060558

Wennemuth, G., Carlson, A. E., Harper, A. J., and Babcock, D. F. (2003). Bicarbonate actions on flagellar and Ca2+-channel responses: initial events in sperm activation. *Development* 130, 1317–1326. doi: 10.1242/dev.00353

Williams, A. C., and Ford, W. C. L. (2005). Relationship between reactive oxygen species production and lipid peroxidation in human sperm suspensions and their association with sperm function. *Fertil. Steril.* 83, 929–936. doi: 10.1016/j.fertnstert.2004.11.031

Wu, Y., Li, K., Zuo, H., Yuan, Y., Sun, Y., and Yang, X. (2014). Primary neuronal-astrocytic co-culture platform for neurotoxicity assessment of di-(2-ethylhexyl) phthalate. *J. Environ. Sci.* 26, 1145–1153. doi: 10.1016/S1001-0742(13)60504-5

Yanagimachi, R. (1994). Fertility of mammalian spermatozoa: its development and relativity. *Zygote* 2, 371–372. doi: 10.1017/S0967199400002240

Yanagimachi, R. (2011). Mammalian sperm acrosome reaction: where does it begin before fertilization? *Biol. Reprod.* 85, 4–5. doi: 10.1095/biolreprod.111.092601

Zalata, A. A., Ahmed, A. H., Allamaneni, S. S. R., Comhaire, F. H., and Agarwal, A. (2004). Relationship between acrosin activity of human spermatozoa and oxidative stress. *Asian J. Androl.* 6, 313–318.

Zhou, W., Fang, F., Zhu, W., Chen, Z. J., Du, Y., and Zhang, J. (2017). Bisphenol A and Ovarian reserve among infertile women with polycystic Ovarian syndrome. *Int. J. Environ. Res. Public Health* 14:18. doi: 10.3390/ijerph14010018

Zota, A. R., Calafat, A. M., and Woodruff, T. J. (2014). Temporal trends in phthalate exposures: findings from the National Health and Nutrition Examination Survey, 2001-2010. *Environ. Health Perspect.* 122, 235–241. doi: 10.1289/ehp.1306681

Zota, A. R., Phillips, C. A., and Mitro, S. D. (2016). Recent fast food consumption and bisphenol A and phthalates exposures among the U.S. population in NHANES, 2003–2010. *Environ. Health Perspect.* 124, 1521–1528. doi: 10.1289/ehp.1510803

Conflict of Interest: The authors declare that the research was conducted in the absence of any commercial or financial relationships that could be construed as a potential conflict of interest.

Copyright © 2020 Khasin, Della Rosa, Petersen, Moeller, Kriegsfeld and Lishko. This is an open-access article distributed under the terms of the Creative Commons Attribution License (CC BY). The use, distribution or reproduction in other forums is permitted, provided the original author(s) and the copyright owner(s) are credited and that the original publication in this journal is cited, in accordance with accepted academic practice. No use, distribution or reproduction is permitted which does not comply with these terms.

frontiers in Cell and Developmental Biology

ORIGINAL RESEARCH
published: 10 July 2020
doi: 10.3389/fcell.2020.00547

Mating to Intact, but Not Vasectomized, Males Elicits Changes in the Endometrial Transcriptome: Insights From the Bovine Model

*Sandra Recuero[1], José María Sánchez[2], Yentel Mateo-Otero[1], Sandra Bagés-Arnal[2], Michael McDonald[2], Susanta K. Behura[3], Thomas E. Spencer[3], David A. Kenny[4], Marc Yeste[1], Pat Lonergan[2] and Beatriz Fernandez-Fuertes[1]**

[1] Biotechnology of Animal and Human Reproduction (TechnoSperm), Department of Biology, Institute of Food and Agricultural Technology, University of Girona, Girona, Spain, [2] School of Agriculture and Food Science, University College Dublin, Dublin, Ireland, [3] Division of Animal Sciences, University of Missouri, Columbia, MO, United States, [4] Animal and Bioscience Research Centre, Teagasc Grange, Meath, Ireland

OPEN ACCESS

Edited by:
Tomer Avidor-Reiss, The University of Toledo, United States

Reviewed by:
Susan S. Suarez, Cornell University, United States
John J. Bromfield, University of Florida, United States

***Correspondence:**
Beatriz Fernandez-Fuertes
beatriz.fernandez@udg.edu

Specialty section:
This article was submitted to Cell Growth and Division, a section of the journal Frontiers in Cell and Developmental Biology

Received: *05 May 2020*
Accepted: *10 June 2020*
Published: *10 July 2020*

Citation:
Recuero S, Sánchez JM, Mateo-Otero Y, Bagés-Arnal S, McDonald M, Behura SK, Spencer TE, Kenny DA, Yeste M, Lonergan P and Fernandez-Fuertes B (2020) Mating to Intact, but Not Vasectomized, Males Elicits Changes in the Endometrial Transcriptome: Insights From the Bovine Model. Front. Cell Dev. Biol. 8:547. doi: 10.3389/fcell.2020.00547

An appropriate female reproductive environment is essential for pregnancy success. In several species, including mice, pigs and horses, seminal plasma (SP) components have been shown to modulate this environment, leading to increased embryo viability and implantation. Due to the characteristics of mating in the aforementioned species, SP comes into direct contact with the uterus. However, it is questionable whether any SP reaches the uterus in species that ejaculate inside the vagina, such as humans and cattle. Hence, we hypothesized that sperm, perhaps acting as a vehicle for SP factors, play a more important role in the modulation of the maternal uterine environment in these species. In addition, changes elicited by SP and/or sperm may originate in the vagina and propagate to more distal regions of the female reproductive tract. To test these hypotheses, a bovine model in which heifers were mated to intact or vasectomized bulls or were left unmated was used. RNA-sequencing of endometrial samples collected 24 h after mating with a vasectomized bull did not reveal any differentially expressed genes (DEGs) in comparison with control samples. However, the endometrium of heifers mated with intact bulls exhibited 24 DEGs when compared to heifers mated with vasectomized bulls, and 22 DEGs when compared to unmated control heifers. The expression of a set of cytokines (*IL6*, *IL1A*, *IL8,* and *TNFA*) and candidate genes identified in the endometrial RNA-sequencing (*PLA2G10*, *CX3CL1*, *C4BPA*, *PRSS2*, *BLA-DQB,* and *CEBPD*) were assessed by RT-qPCR in the vagina and oviductal ampulla. No differences in expression of these genes were observed between treatments in any region. However, mating to both intact and vasectomized bulls induced an increase in *IL1A* and *TNFA* expression in the vagina compared to the oviduct. These data indicate that sperm, but not secretions from the accessory glands alone, induce modest changes in endometrial gene expression after natural mating in cattle. However, it is not clear whether this effect is triggered by inherent sperm proteins or SP proteins bound to sperm surface at the time of ejaculation.

Keywords: seminal plasma, cattle, endometrium, transcriptome, maternal environment

INTRODUCTION

Embryonic loss is a major contributor to pregnancy failure in livestock species and humans, ranging from 20 to 40% (Macklon et al., 2002; Wiltbank et al., 2016). Most of these losses occur before implantation, highlighting the importance of this period that encompasses such critical events as the first embryonic cleavage divisions; embryonic genome activation; blastocyst formation and hatching; conceptus development; and the preparation of the endometrium to interact with the embryonic trophectoderm (Diskin and Morris, 2008; Niakan et al., 2012; Sandra et al., 2017). Many factors are involved in implantation failure, but in mice and pigs there is growing evidence of a role for the maternal immune system and its regulation by seminal plasma (SP) (Gangnuss et al., 2004; O'Leary et al., 2004, 2006; Song et al., 2016; Glynn et al., 2017).

Seminal plasma is a complex fluid resulting from the secretions of the testes, epididymides and accessory sex glands (in the bull: ampullae, seminal vesicles, prostate and bulbourethral glands). Although it is difficult to accurately calculate the precise contribution of each organ and gland to the final composition of this fluid, vasectomy in the bull by removal of a portion of each vas deferens and therefore removing the contribution of the epididymides, does not appear to significantly affect SP volume (Alexander et al., 1971), indicating a more prominent role of the accessory sex glands. However, vasectomy does lead to a reduction in amino acids in the bull ejaculate (Alexander et al., 1971), and to slight modifications in the proteome of human SP (Batruch et al., 2011). Traditionally, SP has been viewed as a mere vehicle for sperm that nourishes and supports these cells in the female reproductive tract. However, mounting evidence demonstrates an emerging role for SP components in the modulation of the endometrial and oviductal environment, which results in improved fertility and embryo survival and development (reviewed in Bromfeld, 2016; Morgan and Watkins, 2020). Exposure to SP in mice (Schjenken et al., 2015; Song et al., 2016; Glynn et al., 2017), as well as in pigs (O'Leary et al., 2004, 2006) and mares (Tunon et al., 2000; Palm et al., 2008; Fedorka et al., 2017), induces the expression of several endometrial cytokines, leading to leukocyte recruitment to the uterus. This migration of immune cells was thought to solely serve the purpose of clearing microorganisms and excess sperm (Pandya and Cohen, 1985; Thompson et al., 1992). However, it is now thought that the endometrial cytokine and chemokine cascade induced by SP is important to facilitate maternal tolerance toward paternal antigens (reviewed in Robertson, 2007). Indeed, in mice, mating drives the expansion of $CD4^+CD25^+$ T regulatory cells (Robertson et al., 2009; Shima et al., 2015), which can suppress or modulate the immune response of other cells (Sakaguchi et al., 2001). The increase in $CD4^+CD25^+$ is not observed when females are mated to vasectomized or seminal-vesicle-excised males, suggesting that this expansion is driven by secretions from the male accessory glands (Robertson et al., 2009). This effect likely explains why mating increases maternal tolerance toward paternal major histocompatibility complex (MHC) antigens (Robertson et al., 2009), which improves the ability of the semi-allogenic embryo to implant and develop normally in this species (Bromfield et al., 2014; Watkins et al., 2018). In addition to modifying the uterine environment, transcervical infusion of SP in pigs has been shown to modulate ovarian function by increasing corpora lutea (CL) weight and progesterone synthesis (O'Leary et al., 2006), which is essential for creating an appropriate uterine environment for the developing embryo. Moreover, in horses, a pivotal role of SP in protecting spermatozoa from neutrophil phagocytosis in the uterus has been suggested, improving fertility in this environment (Troedsson et al., 2002; Alghamdi et al., 2004).

Due to characteristics of mating in rodents, pigs and horses, SP reaches the uterus and can therefore interact directly with the endometrium (Hunter, 1981; Dean et al., 2011). It is not clear, however, whether any SP reaches the uterus in species that ejaculate intravaginally and in which the volume of the ejaculate is relatively low, such as cattle or humans. It is possible that in those species, SP has an indirect effect on the endometrial environment and/or that sperm act as vehicles for the transport of SP components to more distal regions of the reproductive tract. In this sense, the bovine model could be more appropriate than rodents or pigs in understanding the regulatory properties of SP in the maternal environment of women.

In vitro studies in humans have demonstrated the potential of SP to induce expression of cytokines and chemokines in vaginal, cervical and endometrial epithelial cell cultures (Gutsche et al., 2003; Sharkey et al., 2007, 2012a; Remes Lenicov et al., 2012). While gene expression changes and leukocyte recruitment have been described in the human cervix after unprotected, but not condom-protected, coitus (Sharkey et al., 2012b), there is currently no evidence of SP-induced changes in the endometrium *in vivo*.

In cattle, the expression of several inflammatory mediators (such as colony-stimulating factor 2 – *CSF2*, interleukins 1B, 6, 17A and 8 - *IL1B*, *IL6*, *IL17A*, *IL8*; Prostaglandin-endoperoxide synthase 2 – *PTGS2*, and transforming growth factor beta 1 – *TGF-B1*) in uterine horns ipsi- and contralateral to the CL was modified after SP infusion into the uterus, in the absence or presence of sperm (Ibrahim et al., 2019). Despite this, uterine infusion of SP at the time of artificial insemination (AI) does not increase pregnancy rate in heifers or cows (Odhiambo et al., 2009; Ortiz et al., 2019). As mentioned above, it is questionable whether SP reaches the uterus during mating in cattle, so results obtained from the infusion of SP into the uterus may not be representative of physiological conditions. Indeed, recently it has been shown that infusion of SP into the vagina, but not into the uterus, modifies endometrial levels of epidermal growth factor (Badrakh et al., 2020), which highlights the importance of considering the ejaculate deposition site in natural conception in these studies. We recently reported a modest increase in conceptus length in embryos that developed from Day 7 to Day 14 in the uterus of heifers mated to a vasectomized bull in comparison to unmated heifers (Mateo-Otero et al., 2020). However, exposure of heifers to vasectomized bulls prior to AI failed to increase pregnancy rates (Pfeiffer et al., 2012). In addition, although bulls that had their seminal vesicles resected exhibited reduced semen volume, there was no apparent effect on their subsequent fertility (Shah et al., 1968). Together with recent work from our group, demonstrating

a deleterious effect of bull SP on endometrial RNA integrity due to the presence of a seminal RNase (Fernandez-fuertes et al., 2019), the literature seems to suggest that SP does not play a significant role in pregnancy establishment in cattle.

Based on these data, we hypothesized that in species that ejaculate inside the vagina, changes in the female reproductive environment begin in this region and then propagate to more distal regions, such as the uterus and/or the oviduct. Also, because of the lack of direct contact with the seminal fluid, sperm probably play a more important role in the modulation of the uterine environment in these species. In order to test these hypotheses, RNA-sequencing analysis of endometrial samples was carried out following natural mating of heifers with vasectomized (whose ejaculate lack sperm and epididymal and testicular fluid) or intact (that ejaculate sperm and SP) bulls. In addition, the expression of a set of interesting candidate genes was assessed in the vagina and oviductal ampulla, with the aim of determining the effects of sperm and accessory gland secretions from the most proximal region of the female reproductive tract (vagina) to the distal region where gamete interaction takes place (oviductal ampulla).

MATERIALS AND METHODS

Unless otherwise stated, all chemicals and reagents were sourced from Sigma-Aldrich (Arklow, Ireland).

Animals

All experimental procedures involving animals were approved by the Animal Research Ethics Committee of University College Dublin and licensed by the Health Products Regulatory Authority (HPRA), Ireland, in accordance with Statutory Instrument No. 543 of 2012 (under Directive 2010/63/EU on the Protection of Animals used for Scientific Purposes). For the duration of the study, all animals were housed in groups of 10–15, independent of treatment, and managed identically in terms of feeding and husbandry routines.

Vasectomy was carried out by removing approximately 5 cm of both vasa deferentia. This procedure took place 5–6 months prior to the trial. Vasectomized bulls underwent semen evaluation to confirm the lack of sperm and all ran as teasers for oestrus detection with 25 cows/heifers each during the breeding season preceding the study. Intact bulls underwent a breeding soundness evaluation prior to the study. Neither intact and vasectomized bulls had access to females for at least 5 months before the trial, nor during it (apart from the controlled mating to the experimental heifers).

Experimental Design

Estrous cycles of crossbreed beef heifers (Angus and Holstein-Friesian cross; n = 28) were synchronized using an 8-day intravaginal device (PRID® Delta, 1.55 g progesterone, Ceva Santé Animale, Libourne, France), together with a 2 mL intramuscular injection of a synthetic gonadotrophin releasing hormone (Ovarelin®, equivalent to 100 μg Gonadorelin, Ceva Santé Animale) administered on the day of PRID insertion. One day prior to PRID removal, all heifers received a 5 mL intramuscular injection of prostaglandin F2 alpha (Enzaprost®, equivalent to 25 mg of Dinoprost, Ceva Santé Animale) to induce luteolysis. Only heifers observed in standing estrus were used (n = 22). Heifers were blocked by weight and randomly allocated to one of three treatments (**Figure 1**): (1) mated to an intact bull (n = 7), (2) mated to a vasectomized bull (n = 8), or (3) left unmated (control; n = 7). Between 0 to 6 h after estrus detection, heifers were separated from the group and placed in a pen (one at a time) with one of three vasectomized Holstein Friesian bulls, or one of two intact Holstein Friesian bulls (**Supplementary Table 1**). Once the bull mounted and intromission was confirmed, the heifers were returned to the group. Bulls were allowed to mate no more than twice per day and the experiment was carried out over three consecutive days.

Tissue Collection

All heifers were slaughtered in a commercial abattoir 24 h (±6 h) after mating and their reproductive tracts were recovered. The ovaries were examined to determine the site of the preovulatory or freshly ovulated follicle (**Supplementary Figure 1**). Endometrial tissue samples were obtained from intercaruncular areas of the base of uterine horn ipsilateral to the preovulatory or freshly ovulated follicle. In cattle, the uterine glands are located in the intercaruncular areas of the endometrium, while the caruncular areas are aglandular. These glands are responsible for the secretion of the histotroph, which will nurture the developing embryo, and drive the maternal signals of implantation (Kelleher et al., 2019; Spencer et al., 2019). In addition, epithelial sections of anterior vagina and whole sections of the ampulla of the ipsilateral oviduct were obtained. Immediately after tissue collection, each sample was snap frozen in liquid nitrogen and stored at −80°C.

Experiment 1: Seminal Plasma Effects on the Endometrial Transcriptome

RNA Extraction

For total mRNA extraction, samples were first homogenized in Trizol reagent (Invitrogen, Carlsbad, CA, United States) using a steel bead and the Qiagen tissue lyzer (2 × 120 s at maximum speed). On-column RNA purification was performed using the Qiagen RNeasy kit (Qiagen, Crawley, Sussex, United Kingdom) per the manufacturer's instructions. The quantity of RNA was determined using the Nano Drop 1000 spectrophotometer (Thermo Fisher Scientific, Dublin, Ireland). Prior to endometrial RNA sequencing analysis, the RNA quality was assessed by the Agilent Bioanalyzer (Agilent Technologies, Cork, Ireland). Only samples that exhibited a minimum RNA integrity number (RIN) of 8 were used in this experiment (n = 6 heifers in each experimental group).

RNA Sequencing Analysis

RNA library preparation and sequencing were performed by the University of Missouri DNA Core Facility as described previously by Moraes et al. (2018). The raw sequences (fastq) were subjected

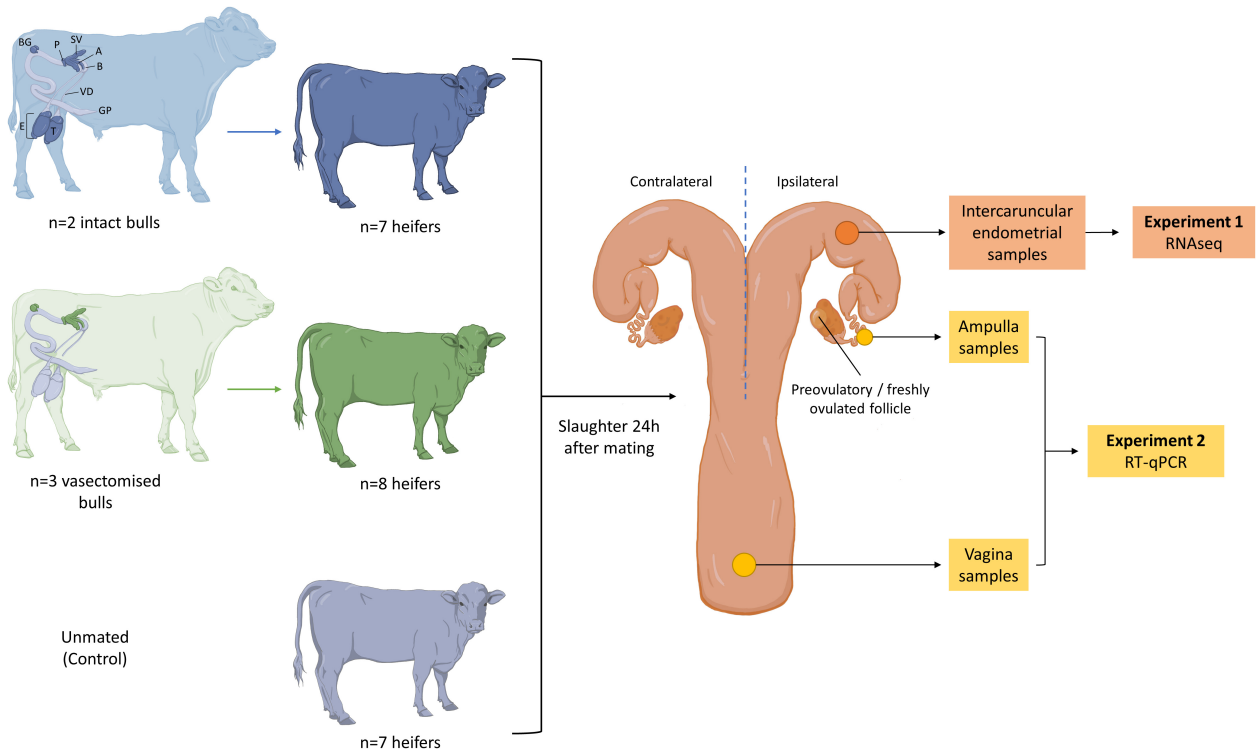

FIGURE 1 | Summary of the experimental design. Only heifers observed in standing estrus were mated with (1) an intact bull (blue; *n* = 7), (2) a vasectomized bull (green; *n* = 8) or (3) left unmated (gray; *n* = 7). A schematic representation of the male reproductive tract is shown, and the structures that contribute to the ejaculate in each case are highlighted (T, testis; E, epididymis; GP, glans penis; VD, vas deferens; B, bladder; A, ampulla; SV, seminal vesicle; P, prostate; BG, bulbourethral gland). Heifers were slaughtered 24 h after mating and their reproductive tracts were recovered. Endometrial samples were obtained from the base of the ipsilateral uterine horn to perform RNA sequencing (Experiment 1). Samples from ampulla and vagina were obtained to assess the expression of a set of genes (*PLA2G10*, *CX3CL1*, *C4BPA*, *PRSS2*, *BLA-DQB*, *CEBPD*, *IL1A*, *IL6*, *TNFA,* and *IL8*) by RT-qPCR (Experiment 2).

to quality trimming control using fqtrim[1]. Then, the quality reads were mapped to the bovine reference genome UMD3.1 using Hisat2 mapper (Kim et al., 2015). Read counts mapping to each gene were determined from the binary alignment map files of the samples using FeatureCounts (Liao et al., 2014). Differential expression analysis between different sample groups was performed using edgeR robust (Zhou et al., 2014).

For the annotated DEGs, the gene ontology analysis was performed using PANTHER[2].

Experiment 2: Seminal Plasma Effects on Gene Expression in the Vagina and Oviduct

RNA Extraction and cDNA Synthesis

Total mRNA extraction was carried out as described above. For each sample, cDNA was prepared from approximately 100 ng of total mRNA using the High Capacity cDNA Reverse Transcription Kit (Thermo Fisher Scientific) according to the manufacturer's instructions. The cDNA obtained was diluted using RNase- and DNase-free water in a final concentration of 5 ng/mL and in a total volume of 100 μL. The diluted cDNA samples were stored at −20°C for subsequent analysis. As some samples were lost during the management of the experiment, the number of samples per group varies for the vagina region: $n = 6$ heifers in the control group, $n = 5$ in the intact group and $n = 7$ in the vasectomized group. For the ampulla region, there were $n = 7$ individuals in each experimental group (control, intact, and vasectomized). In addition, the RNA quality was assessed by the Agilent Bioanalyzer (Agilent Technologies, Cork, Ireland) (RIN = 7.81 ± 0.29; mean ± standard error of the mean, SEM).

Genes of Interest Selection for Expression Analysis

In order to determine SP effects on gene expression in vagina and oviduct regions, a set of genes (*IL1A*, *IL6*, *TNFA,* and *IL8*) were selected based on the literature. These genes were inflammatory mediators expression of which was reported to be modified by SP exposure in cattle and other species (O'Leary et al., 2004; Sharkey et al., 2012b; Schjenken et al., 2015; Introini et al., 2017; Ibrahim et al., 2019). Moreover, expression of some genes (*PLA2G10*, *CX3CL1*, *C4BPA*, *PRSS2*, *BLA-DQB,* and *CEBPD*) found differentially expressed in RNA-sequencing analysis of endometrium samples was also interrogated. The selection of these genes as interesting targets was based on literature searching (Wedel and Lömsziegler-Heitbrock, 1995; Blom et al., 2004;

[1]https://ccb.jhu.edu/software/fqtrim/
[2]pantherdb.org

Hannan et al., 2004; Tapia et al., 2008; Hayashi et al., 2017; Neupane et al., 2017; Pinto De Melo et al., 2017; Tríbulo et al., 2018) and GO term analysis.

Quantitative Real-Time PCR Analysis

All primers were designed using Primer Blast software[3] (**Supplementary Table 2**). Briefly, RT-qPCR assays were performed per duplicate in a total volume of 20 μL, containing 10 μL FastStart Universal SYBR Green Master (Roche Diagnostics Ltd., West Sussex, United Kingdom), 1.2 μL forward and reverse primer mix (300 nM final concentration), 5.6 μL nuclease-free water and 2 μL cDNA template on the ABI Prism 7500 Real-Time PCR System (Life Technologies). A total of 40 cycles were performed with the following thermo-cycling conditions for each cycle: 50°C for 2 min, 95°C for 10 min followed by 95°C for 15 s, 60°C for 1 min, 95°C for 30 s and 60°C for 15 s. The melt curve was also included to ensure specificity of amplification. The specificity of all targets was confirmed by the presence of a single sharp peak in the melt curve. A total of eight potential reference genes [Glyceraldehyde 3-Phosphate Dehydrogenase (*GAPDH*), Actin Cytoplasmic 1 (*ACTB*), 60S Ribosomal Protein L18 (*RPL18*), Peptidyl-Prolyl *Cis-Trans* Isomerase A (*PPIA*), 14-3-3 Protein Zeta/Delta (*YWHAZ*), RING Finger Protein 11 (*RNF11*), Histone H3.3 (*H3F3A*), Succinate Dehydrogenase Complex Subunit A Flavoprotein Variant (*SDHA*)] were analyzed using the geNorm function with the qbase + package (Biogazelle, Zwijnaarde, Belgium) to identify the best reference genes. Due to the high variability between samples, a total of four reference genes were selected: *RNF11, H3F3A, YWHAZ,* and *GADPH*, which were the most stably expressed (average geNorm $M \leq 0.5$).

Primer efficiency was carried out for the genes of interest, and RT-qPCR of 1:4 dilutions of a cDNA mix from a representative pool of samples were analyzed. The presence of a single sharp peak in the melt curve as well as the standard curve was used to confirm primer specificity. The threshold cycle (Ct) for each sample was automatically calculated using the default settings within the SDS software (SDS 1.4, ABI). In order to obtain the relative expression values of the genes of interest, $2^{-\Delta\Delta CT}$ method was used (Livak and Schmittgen, 2001). For each individual, the expression of the genes of interest was firstly normalized to the average of housekeeping genes previously selected (*RNF11, H3F3A, YWHAZ,* and *GADPH*) with the following formula: $\Delta Ct = Ct_{\text{gene of interest}} - Ct_{(RNF11+H3F3A+YWHAZ+GADPH)/4}$. The values of $\Delta\Delta Ct$ were calculated normalizing the results to the mean across all individuals, including both tissue regions (vagina and ampulla), per each gene of interest. The subsequent statistical analysis was performed using ΔCt values whereas the results are represented as $2^{-\Delta\Delta CT}$.

Results expressed as ΔCT were analyzed with IBM SPSS 25.0 for Windows (Armonk; New York, NY, United States). Data were checked for normal distribution (Shapiro–Wilk test) and homoscedasticity (Levene test) to confirm that parametric assumptions were fulfilled. When these premises were not, data (x) were linearly transformed using the square root ($\sqrt{x}$) and arcsine of the square root (arcsin $\sqrt{x}$). Thereafter, data (transformed or not depending on the case) were analyzed by a two-way ANOVA followed by a Sidak *post hoc* test for pair-wise comparisons. The expression of five genes (*CX3CL1*, *PLA2G10*, *TNFA*, *IL6,* and *CXCL8*), even after linear transformation, did not match parametric assumptions. For this reason, Scheirer–Ray–Hare and Mann–Whitney tests were used as non-parametric alternatives. In all cases, the significance level was established at $P \leq 0.05$.

[3]https://www.ncbi.nlm.nih.gov/tools/primer-blast/

RESULTS

Ovary Status

At the time of sample collection (24 ± 6 h after mating), a total of 13 heifers had a freshly ovulated follicle on their ovary, while the remaining animals exhibited a pre-ovulatory follicle (see **Supplementary Table 1** and **Supplementary Figure 1**). In the control group, three animals had ovulated and four exhibited a pre-ovulatory follicle. Regarding the heifers mated with vasectomized bulls, fresh ovulation was found in six animals and only two presented a pre-ovulatory follicle. While in the intact group, four ovulations and three preovulatory follicles were observed. The proportion of animals that had a fresh ovulation was balanced across treatments for subsequent gene expression analysis.

Effects of Seminal Plasma on the Endometrial Transcriptome

Sequencing of endometrial samples of heifers recovered 24 h after mating to intact bulls revealed a total of 22 differentially expressed genes (DEGs) compared with contemporary unmated animals (**Table 1** and **Supplementary File 1**). Of those DEGs, 12 were up-regulated and 10 down-regulated [False discovery rate (FDR) < 0.05]. Some of the genes that exhibited the lowest expression (logFC < -2) were serine protease 2 (*PRSS2*), complement C9 (*C9*), oxytocin/neurophysin I prepropeptide (*OXT*), a novel gene encoding for carbonic anhydrase 1 (ENSBTAG00000036116) and an uncharacterized novel gene (ENSBTAG00000050072). On the other hand, the genes with greater transcript abundance (logFC > 2) levels were coiled-coil domain containing 196 (*CCDC196*), solute carrier family 24 member 2 (*SLC24A2*), UDP glucuronosyltransferase family 2-member A1 complex locus (*UGT2A1*) and interferon gamma inducible protein 47 (*IFI47*). In contrast, the endometrium of heifers exposed only to SP (by mating with a vasectomized bull) did not exhibit DEGs compared with the control group. Comparison of endometrial transcriptomes of intact and vasectomized groups revealed a total of 24 DEGs, 18 up-regulated and 6 down-regulated (**Table 2** and **Supplementary File 1**) (FDR < 0.05). Amongst these, MHC, class II, DQ beta (*BOLA-DQB*), GSG1 like (*GSG1L*), potassium voltage-gated channel subfamily E regulatory subunit 1 (*KCNE1*) and the novel gene previously mentioned (ENSBTAG00000050072) were those that displayed lower logFC values (logFC < −2). In contrast, higher levels of expression (logFC > 2) were exhibited by interleukin

17F (*IL17F*), complement component 4 binding protein alpha (*C4BPA*), the aforementioned *IFI47* and *UGT2A1*, and a novel gene (ENSBTAG00000052851) which has been predicted to code for a protein containing an Ig-like domain.

Three DEGs (*UGT2A1*, *IFI47* and the novel gene ENSBTAG00000050072) were found to be common of DEGs detected between the intact group and the control and those detected when comparing the intact and vasectomized groups.

Gene Ontology (GO) Terms of DEGs

For the annotated genes in each comparison, the GO terms are shown in **Figure 2**. For the molecular function category, the main represented GO term was "catalytic activity" in the intact group compared with control or vasectomized samples (**Figure 2A**). "Cellular process" and "metabolic process" were the most represented terms for the biological process category in intact samples compared with the control (**Figure 2B**). Compared with the vasectomized group in the same category, in addition to "cellular process," "response to stimulus" was the most represented term (**Figure 2B**). In regard to pathway category, comparing the intact group with the control, all the terms represented were related to vascular regulation (**Figure 2D**). In contrast, compared with the vasectomized bull treatment group, the represented terms referred to immunity modulation and amino acid biosynthesis (**Figure 2D**). "Hydrolase" and "receptor" were the most represented protein class terms among the differentially regulated genes in the endometrium exposed to sperm and SP compared with the control samples (**Figure 2C**). On the other hand, compared with vasectomized samples, the most represented protein class terms were "cytoskeletal protein" and "immunity protein" (**Figure 2C**).

Effects of Seminal Plasma on Gene Expression in the Vagina and Oviduct

Based on the results obtained from the endometrial RNA-sequencing, we were interested in studying whether gene expression changes are more dramatic at the site of semen deposition (the vagina), and whether these changes can propagate to more distal regions (the oviductal ampulla). Thus, six DEGs from the sequencing analysis were selected (*PLA2G10*, *CX3CL1*, *C4BPA*, *PRSS2*, *BLA-DQB,* and *CEBPD*) based on evidence of their reproductive function found in the literature (Wedel and Lömsziegler-Heitbrock, 1995; Blom et al., 2004; Hannan et al., 2004; Tapia et al., 2008; Hayashi et al., 2017; Neupane et al., 2017; Pinto De Melo et al., 2017; Tríbulo et al., 2018), as well as their GO terms. In addition to these, *IL6*, *IL1A*, *TNFA,* and *IL8* expression was also assessed, as these are genes that have been observed to be regulated by SP in several species (O'Leary et al., 2004; Sharkey et al., 2012b; Schjenken et al., 2015; Introini et al., 2017; Ibrahim et al., 2019).

Differences in relative expression of *CEBPD* ($P < 0.01$; **Figure 3F**) and *IL8* ($P < 0.05$ in the control group and $P < 0.01$ in the intact and vasectomized groups; **Figure 3J**) between regions were observed in all groups, being up-regulated in the vagina in comparison with the ampulla, whereas *CX3CL1* was down-regulated in the vagina compared with the ampulla, only in the control group ($P < 0.01$; **Figure 3B**). In addition, *TNFA* ($P < 0.05$ in the intact group and $P < 0.01$ in the vasectomized group; **Figure 3I**) and *IL1A* ($P < 0.05$; **Figure 3H**) were up-regulated in the vagina compared with the ampulla in heifers that had been mated to an intact or a vasectomized bull, but not in unmated heifers. The remaining genes did not exhibit region-specific changes (**Figures 3A**,**C–E**,**G**). Conversely, when relative abundance of these genes was compared between treatment groups, no differences were detected ($P > 0.05$). It is also important to note that for many genes, especially those related to inflammation, there was considerable variability between animals.

DISCUSSION

The main findings of this study are: (1) mating to an intact bull induces subtle changes in the endometrial transcriptome; however, (2) these transcriptomic changes are not observed in heifers mated to vasectomized bulls; (3) expression of *PLA2G10*, *CX3CL1*, *C4BPA*, *PRSS2*, *BLA-DQB*, *CEBPD*, *IL1A*, *IL6*, *TNFA,* and *IL8* in the vagina and ampulla did not differ between treatments; and (4) *TNFA* and *IL1A* exhibited regional differences between vagina and ampulla of heifers mated to intact or vasectomized bulls.

Seminal plasma is a complex fluid the composition of which is determined by the size, storage capacity, and secretory output of different organs of the male reproductive tract, which in the bull include: testes, epididymides, ampullae of the vasa deferentia, seminal vesicles, prostate and bulbourethral glands. After completion of spermatogenesis, sperm enter the epididymis bathed in fluid produced by the rete testis, which will be absorbed in its majority by the epididymal epithelium (Amann et al., 1974). However, secreted factors of epididymal and/or testicular origin are found in the ejaculate. This is evidenced by studies comparing ejaculates before and after vasectomy, which show lower concentration of amino acids in bulls (Alexander et al., 1971), and proteins in humans (Batruch et al., 2011), after the procedure. Despite this, vasectomy does not lead to a decrease in bull ejaculate volume (Alexander et al., 1971), indicating a more prominent role of the male accessory glands in the production of SP components. It is challenging to precisely calculate the contribution of each gland to the final fluid volume and composition (Seidel and Foote, 1970); however, vesiculectomy (excision of the seminal vesicles) in the bull leads to a more than 50% decrease in ejaculate volume, together with a reduction in total protein and ion concentrations (chloride, potassium, calcium, sodium), lower sperm motility, viability and morphology, and increased pH (Faulkner et al., 1968; Alexander et al., 1971).

Growing evidence exists for a role of SP in the modulation of cellular and molecular events in the maternal tract of several species during early pregnancy (Gangnuss et al., 2004; O'Leary et al., 2004, 2006; Bromfeld, 2016; Song et al., 2016; Glynn et al., 2017; Morgan and Watkins, 2020). However, most of the *in vivo* evidence comes from pigs and mice, species in which SP reaches the uterus (Gangnuss et al., 2004; O'Leary et al., 2004, 2006;

TABLE 1 | List of differentially expressed genes (FDR < 0.05) in endometrial samples of heifers mated with intact bulls compared with unmated heifers.

Ensembl acc. number	Gene name	Gene description	logFC
ENSBTAG00000014234	*CCDC196*	Coiled-coil domain containing 196	8.63
ENSBTAG00000043972	*SLC24A2*	Solute carrier family 24 member 2	4.15
ENSBTAG00000004040	*UGT2A1*	UDP glucuronosyltransferase family 2 member A1 complex locus	3.11
ENSBTAG00000003529	*ASAH2*	*N*-acylsphingosine amidohydrolase 2	2.82
ENSBTAG00000015727	*IFI47*	Interferon gamma inducible protein 47	2.62
ENSBTAG00000049426	*STARD2*	Phosphatidylcholine transfer protein	1.72
ENSBTAG00000037929	*ADAM28*	ADAM-like, decysin 1	1.42
ENSBTAG00000019636	*SCARA5*	Scavenger receptor class A member 5	1.06
ENSBTAG00000017722	*F5*	Coagulation factor V	0.99
ENSBTAG00000019625	*EHHADH*	Enoyl-CoA hydratase and 3-hydroxyacyl CoA dehydrogenase	0.83
ENSBTAG00000008735	*VASH1*	Vasoinhibin 1	0.77
ENSBTAG00000001728	*IGSF10*	Immunoglobulin superfamily member 10	0.72
ENSBTAG00000046307	*CEBPD*	CCAAT enhancer binding protein delta	−0.86
ENSBTAG00000011079	*C18H19orf48*	Chromosome 18 C19orf48 homolog	−0.92
ENSBTAG00000007101	*F3*	Coagulation factor III, tissue factor	−1.04
ENSBTAG00000051812	*CA1L*	Carbonic anhydrase 1-like	−2.45
ENSBTAG00000008026	*OXT*	Oxytocin/neurophysin I prepropeptide	−2.76
ENSBTAG00000039446	*PI3L*	Elafin-like	−2.78
ENSBTAG00000036116	*CA1*	Carbonic anhydrase 1	−3.39
ENSBTAG00000016149	*C9*	Complement C9	−4.08
ENSBTAG00000050072		Novel gene	−4.99
ENSBTAG00000021565	*PRSS2*	Serine protease 2	−6.05

FDR, false discovery rate; logFC, logarithm of fold change.

TABLE 2 | List of differentially expressed genes (FDR < 0.05) in endometrial samples of heifers mated with intact bulls compared with heifers mated with vasectomized bulls.

Ensembl acc. number	Gene name	Gene description	logFC
ENSBTAG00000052851		Novel gene	4.57
ENSBTAG00000016835	*IL17F*	Interleukin 17F	4.50
ENSBTAG00000032884	*TNP2*	Transition protein 2	3.78
ENSBTAG00000019132	*DMP1*	Dentin matrix acidic phosphoprotein 1	3.34
ENSBTAG00000015727	*IFI47*	Interferon gamma inducible protein 47	3.18
ENSBTAG00000009876	*C4BPA*	Complement component 4 binding protein alpha	2.78
ENSBTAG00000004040	*UGT2A1*	UDP glucuronosyltransferase family 2 member A1 complex locus	2.47
ENSBTAG00000037539		Vascular cell adhesion molecule 1-like	1.81
ENSBTAG00000021764	*GLRB*	Glycine receptor beta	1.62
ENSBTAG00000002214	*TAT*	Tyrosine aminotransferase	1.38
ENSBTAG00000026779	*LYZ*	Lysozyme	1.32
ENSBTAG00000000601	*COL11A2*	Collagen type XI alpha 2 chain	1.14
ENSBTAG00000019588	*BLA-DQB*	MHC class II antigen	1.11
ENSBTAG00000034338	*C15H11orf88*	Chromosome 15 C11orf88 homolog	1.10
ENSBTAG00000021526	*RPRM*	Reprimo, TP53 dependent G2 arrest mediator homolog	1.05
ENSBTAG00000033429	*FAM229B*	Family with sequence similarity 229 member B	0.94
ENSBTAG00000024869	*CX3CL1*	C-X3-C motif chemokine ligand 1	0.78
ENSBTAG00000021522	*PLA2G10*	Group 10 secretory phospholipase A2	0.72
ENSBTAG00000012703	*GLO1*	Glyoxalase I	−0.49
ENSBTAG00000008147	*MICAL1*	Microtubule associated monooxygenase, calponin and LIM domain containing 1	−0.50
ENSBTAG00000001150	*KCNE1*	Potassium voltage-gated channel subfamily E regulatory subunit 1	−2.51
ENSBTAG00000004607	*GSG1L*	GSG1 like	−4.61
ENSBTAG00000050072		Novel gene	−4.94
ENSBTAG00000021077	*BOLA-DQB*	Major histocompatibility complex, class II, DQ beta	−5.05

FDR, false discovery rate; logFC: logarithm of fold change.

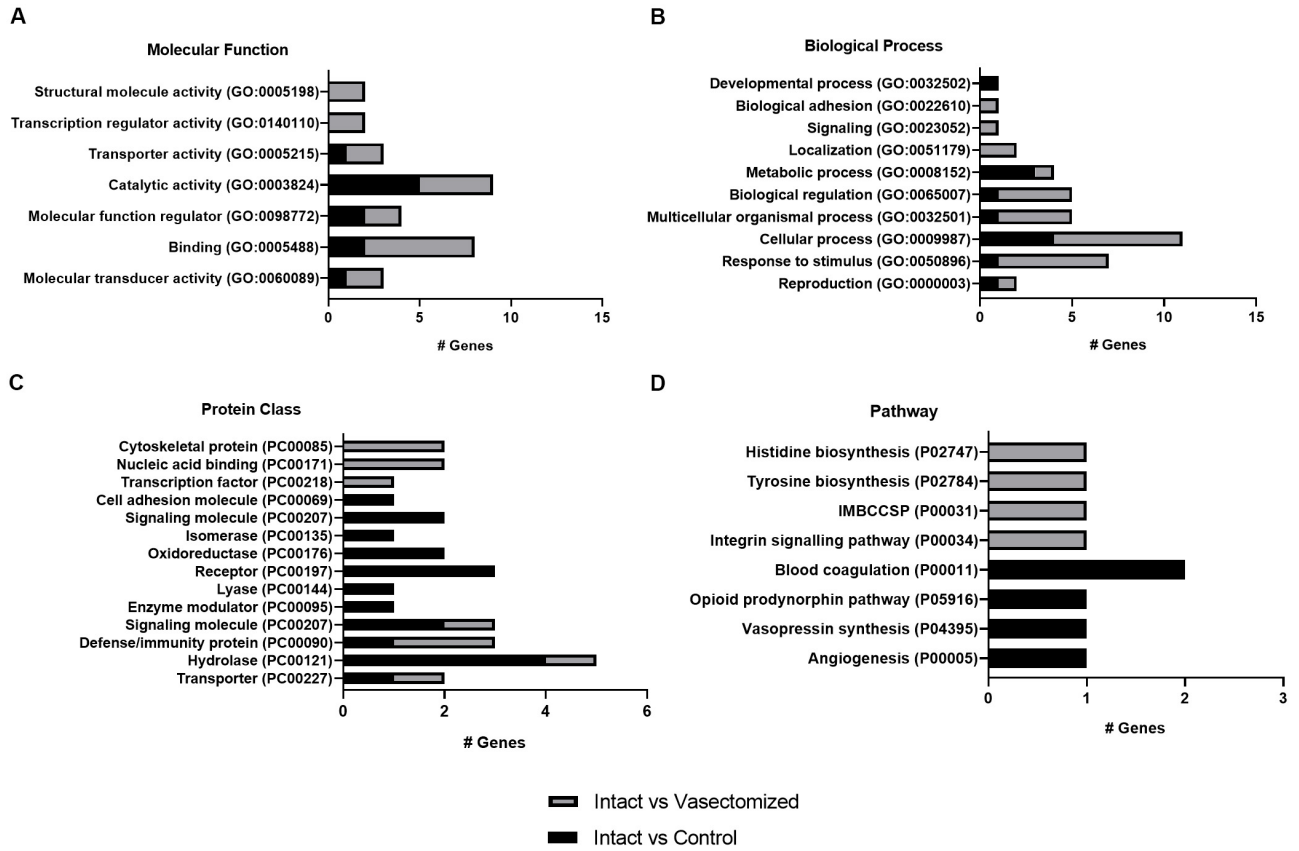

FIGURE 2 | (A–D) Representation of GO terms for annotated DEGs in each comparison. The main categories: **(A)** molecular function, **(B)** biological process, **(C)** protein class, and **(D)** pathway were represented. IMBCCSP, inflammation mediated by chemokine and cytokine signaling pathway.

Bromfield et al., 2014; Song et al., 2016; Glynn et al., 2017). Because of the relatively low volume of ejaculate in men (an average of 3.7 mL, Cooper et al., 2009) and bulls (around 5 mL), and the fact that the ejaculate is deposited in the vagina, it is questionable whether any SP reaches the uterus. Therefore, it is not clear whether this fluid has a critical role in the modulation of the uterine environment in these species. At the time of ejaculation, however, sperm come into contact with SP, leading to proteins binding tightly to the sperm plasma membrane (Pini et al., 2016). For example, seminal vesicle-derived Binder of Sperm Proteins (BSP) −1, −3, and −5 (previously called PDC-109 or BSP-A1/A2, BSP-A3 and BSP-30 kDa respectively), which make up approximately 50% of total protein in SP (Nauc and Manjunath, 2000), bind to sperm and play important roles during capacitation (Manjunath and Thérien, 2002) and formation of the sperm oviductal reservoir (Gwathmey et al., 2003, 2006). Thus, it is possible that in intravaginal ejaculators, sperm can act as a vehicle of SP proteins that interact with the reproductive epithelium to induce changes in the maternal environment. Indeed, bull sperm has been shown to interact with endometrial cells and induce a proinflammatory response *in vitro* (Elweza et al., 2018; Ezz et al., 2019).

To address this lack of basic knowledge, this study aimed to determine the effects of bovine SP and sperm exposure during natural mating on the endometrial transcriptome. Additionally, gene expression changes were assessed at the site of semen deposition (vagina) and the distal region where gamete interaction takes place (the oviductal ampulla) to determine whether SP-induced changes can propagate throughout the female reproductive tract.

In the present study, heifers were mated between 0 and 6 h after seen in standing estrus. Average time from estrus onset to ovulation is 27 h (Walker et al., 1996; Valenza et al., 2012; Randi et al., 2018). Thus, some animals had ovulated by the time of sample collection (24 ± 6 h after mating) whereas the rest exhibited a pre-ovulatory follicle. Ovulation and estrous cycle are orchestrated by an accurate hormonal regulation, and under this regulation, the endometrium experiments functional and morphological changes (Arai et al., 2013). In order to avoid any possible confounding factors due to ovulation having occurred or not, the number of ovulated and non-ovulated heifers that were analyzed by RNA-sequencing and RT-qPCR was balanced between treatments.

Strikingly, when heifers were exposed to SP in the absence of sperm and testicular and epididymal secretions (i.e., mated to a vasectomized bull) the endometrial RNA-sequencing analysis did not reveal any DEGs in comparison with samples from unmated animals. Conversely, the endometrial transcriptome of heifers

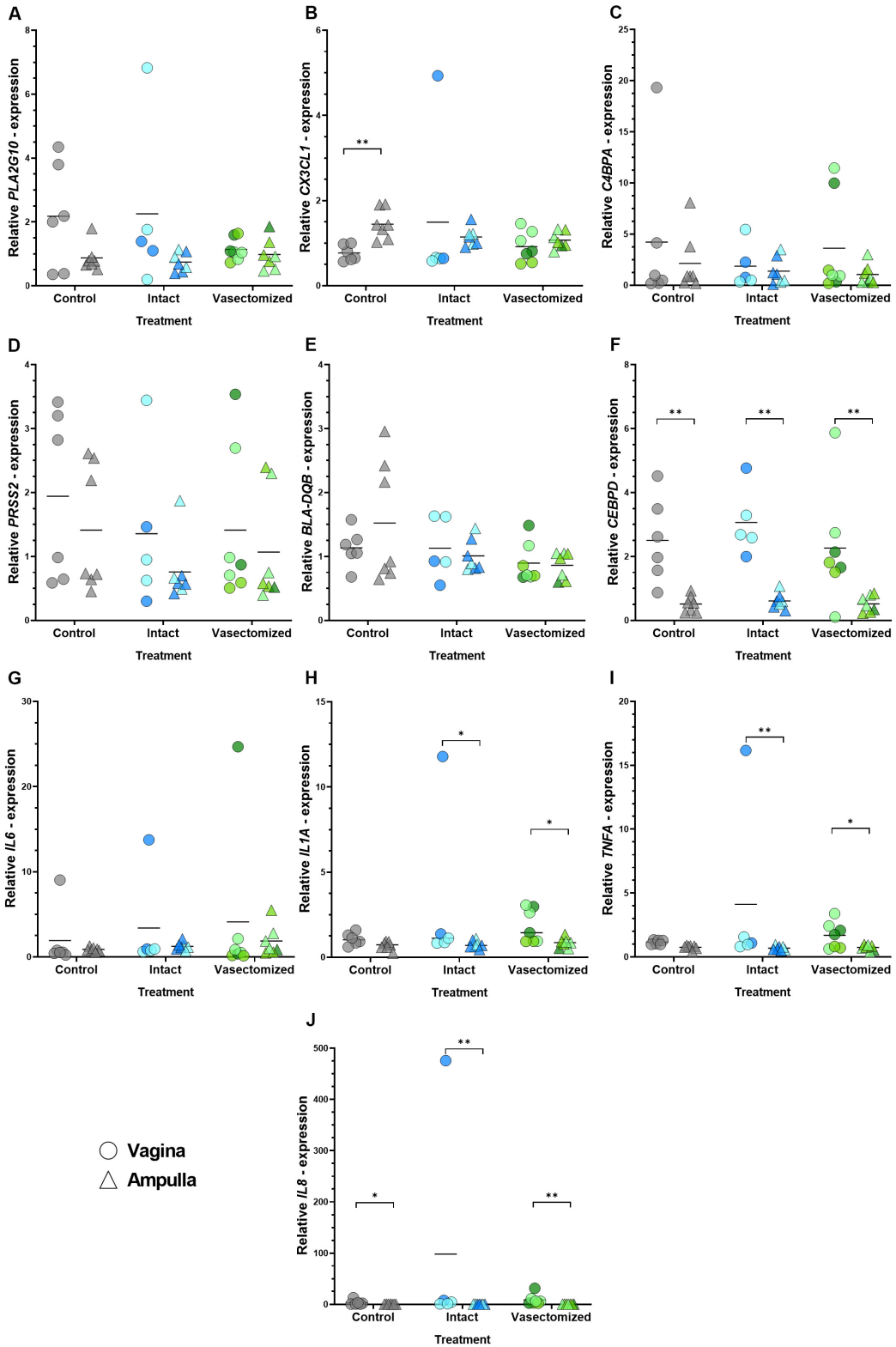

FIGURE 3 | (A–J) Relative expression values of all the genes assessed: **(A)** *PLA2G10*, **(B)** *CX3CL1*, **(C)** *C4BPA*, **(D)** *PRSS2,* **(E)** *BLA-DQB*, **(F)** *CEBPD*, **(G)** *IL6*, **(H)** *IL1A*, **(I)** *TNFA*, **(J)** *IL8* in the vagina (circles) and oviductal ampulla (triangle) in the different experimental groups (control, intact or vasectomized). Each circle/triangle refers to an individual heifer. Different color shades within groups correspond to the bull that was mated to that particular heifer, blue for intact group (n = 2 bulls) and green for vasectomized group (n = 3). Bars represent the mean of relative expression values and asterisks indicate significant (*$P < 0.05$, **$P < 0.01$) differences.

mated to intact bulls differed from the control and vasectomized groups, exhibiting differential regulation of a small number of genes that may play a role in bovine fertility. Although, these results could be due to SP reaching the uterus in both treatments, but only testicular of epididymal factors inducing a response; it is more likely that, in cattle, SP does not reach the uterus in the 24 h following natural mating, at least in the absence of a vehicle, such as sperm.

When compared with control endometrial samples, endometrium obtained from heifers mated to an intact bull exhibited up-regulation of 12 genes and down-regulation of 10 genes. Amongst these genes regulated by mating, some have been shown to participate in tissue remodeling, an important step preparing endometrium to embryo implantation. The gene coding for scavenger receptor class A, member 5 (*SCARA5)*, which participates in innate immunity (Jiang et al., 2006) was up-regulated. This gene has also been observed to be up-regulated in the endometrium of cows at day 20 of pregnancy (Mansouri-Attia et al., 2009), and has been proposed to play a role in the regulation of histotroph secretion and tissue remodeling, two critical processes for embryo implantation (Vitorino Carvalho et al., 2019). Additionally, serine protease 2 (*PRSS2*), which also participates in tissue remodeling by type 1 collagen degradation, was down-regulated by exposure to SP and sperm at mating. Interestingly, this gene is up-regulated in the endometrium of repeat breeder cows, those that are cycling normally and without clinical abnormalities but that fail to conceive after at least two successive inseminations (Hayashi et al., 2017). Mating to an intact bull also affected genes involved in cell proliferation, such as CCAAT enhancer binding protein delta (*CEBPD*), which was found to be down-regulated in the endometrium of heifers mated with intact bulls. This gene belongs to the C/EBP leucine-zipper transcription factor family involved in fat and hematopoietic progenitor cells differentiation (Wedel and Lömsziegler-Heitbrock, 1995). Another member of this family, CEBPB, has been identified as a regulator of proliferative events during decidualization in mice (Mantena et al., 2006). In regard to modulation of innate immunity, the gene coding for component 9 of complement system (*C9*) was down-regulated in the endometrium of heifers mated with intact bulls. The C9 component participates in the final steps of the complement cascade, in the formation of membrane attack complex (MAC), which mediates the formation of channels in the target cell membrane, leading to cell lysis and death (Janeway et al., 2001). Despite its importance, the function of the complement system in the context of reproduction is not well known. For instance, complement regulatory proteins have been found in bull sperm surface, such as CD59 (Byrne et al., 2012), which prevents the formation of MAC (Janeway et al., 2001). These complement regulatory proteins were also identified in human and mouse sperm and they have been proposed to play a role protecting sperm in the female tract (Harris et al., 2006). Moreover, mating with an intact bull resulted in a down-regulation of endometrial oxytocin (*OXT*). In cattle, high levels of OXT have been reported to impair embryo survival by promoting uterine secretion of prostaglandin $F_{2\alpha}$ ($PGF_{2\alpha}$), which induces luteolysis and consequently a drop in progesterone (Lemaster et al., 1999). Although endometrial OXT production has been observed also in mares (Bae and Watson, 2003), it is not known the locally effect of the OXT secreted by the endometrium during early pregnancy in cattle.

When comparing endometrial samples from heifers mated to intact bulls to those from heifers mated to vasectomized bulls, 18 genes were found to be up-regulated and four down-regulated. Amongst the up-regulated genes, literature on *CX3CL1*, *VCAM1-like*, *C4BPA*, *PLA2G10*, *IFI47*, *IL17F* and *BLA-DQB* suggest different roles of these genes in early pregnancy in different species. The chemokine CX3CL1 (C-X3-C motif chemokine ligand 1) has been identified as a potential bovine embryokine (Tríbulo et al., 2018). In addition, CX3CL1 induces recruitment of leukocytes during early pregnancy (Hannan et al., 2004), and also promotes trophoblast migration in women (Hannan et al., 2006). With importance for implantation, VCAM1 has been shown to be involved in the adhesion of the bovine conceptus to the endometrium (Bai et al., 2014). Further, in women with unexplained infertility the endometrial expression of *VCAM1* at the peri-implantation stage was significantly lower than control women (Konac et al., 2009). Additionally, the mRNA levels of complement component 4-binding protein alpha (*C4BPA*), a key inhibitor of the complement system (Blom et al., 2004), were increased during the implantation window in women (Tapia et al., 2011), but decreased in women which suffered repeated implantation failure and unexplained recurrent spontaneous abortion (Lee et al., 2007; Tapia et al., 2008). Although cattle and human implantation differs significantly, in both the time at which it takes place (around day 9 in humans and starting at day 21 in cattle) and the structure of the placenta (hemochorial in humans and epitheliochorial in bovine), it is likely that the up-regulation of *C4BPA* and *VCAM1* induced by exposure to SP and sperm during mating regulates peri-implantation events in cattle. On the other hand, group 10 secretory phospholipase A2 (*PLA2G10*), which was up-regulated in intact group samples, belongs to phospholipase A2 enzyme family, which is known to participate in inflammatory processes and to catalyze the release of arachidonic acid from phospholipids, needed to prostaglandin production (reviewed in Capper and Marshall, 2001). In addition, this gene has been associated with fertility in beef cattle (Neupane et al., 2017), and it was found highly down-regulated in the uterus of cows with negative energy balance (Wathes et al., 2009) which typically have lower pregnancy rates.

From an immunological point of view, the expression of interferon gamma inducible protein 47 (*IFI47*) was also found to be up-regulated in the endometrium of heifers mated with intact bulls in comparison with those mated to vasectomized bulls. Although its function in the uterus has not been defined, *IFI47* mRNA was more abundant in the endometrium of high fertility heifers compared to heifers classified as infertile (Minten et al., 2013). In addition, *IFI47* was up-regulated in the endometrium of heifers 13 days after embryo transfer (Spencer et al., 2013), probably under stimulation of interferon-tau secreted by the conceptus. Another immune-related gene up-regulated by mating with intact bulls is interleukin 17 F (*IL17F*), a cytokine produced by T helper 17 lymphocytes (reviewed in Iwakura et al., 2011). A similar response in expression of *IL17A*

was observed by Ibrahim et al. (2019). Both IL17A and IL17F share biological functions; indeed, both are highly homologous, can bind to the same receptor and moreover, can be secreted as heterodimers or homodimers (reviewed in Iwakura et al., 2011). Ibrahim et al. (2019) observed increased levels of *IL17A* after exposing endometrial cell cultures to SP and sperm or sperm alone, but not SP in the absence of sperm. Also, up-regulation of *IL17A* took place in *vivo*, after uterine infusion of semen (a combination of SP and sperm) but not SP alone (Ibrahim et al., 2019). Together with the data obtained in the present study, this suggests that regulation of *IL17* expression in the bovine endometrium is mediated by sperm action, not SP. This is interesting to note as, in mice, mating to a vasectomized male induces a similar increase in endometrial *IL17A* expression than mating with an intact male (Song et al., 2016). This gives weight to our hypothesis that in species that ejaculate intravaginally, sperm play a more important role than SP in regulation of the female reproductive environment. Moreover, the endometrial up-regulation of *IL17A* in bovine explants has been shown to be exclusively regulated by elongated Day 15 conceptuses, but not by interferon-tau, which is the main signal of pregnancy recognition in cattle, suggesting a role in the embryo – endometrium crosstalk during early pregnancy in cattle (Sánchez et al., 2019). During pregnancy, the maternal immune system must tolerate the presence of an embryo that expresses paternal antigens. The increase in endometrial *IL17* expression observed after mating in the aforementioned studies is reflective of an increase in the population of T helper 17 lymphocytes (Song et al., 2016), which probably participate in the establishment of this maternal tolerance toward paternal antigens. Another mechanism of maternal tolerance driven by male factors seems to be the regulation of the MHC. In the present study, mating to an intact bull elicited down-regulation of Bovine Lymphocyte antigen (referred to as MHC in other species) class II, DQ beta (*BOLA-DQB*), consistent with its down-regulation in pregnant heifers after natural breeding (Dickinson et al., 2018). Conversely, another MHC class II member, *BLA-DQB* was up-regulated in endometrial samples of heifers mated with intact bulls. Indeed, a list of genes of MHC class II family members, including *BLA-DQB* and *BOLA-DQB*, have been associated with reproductive performance in cattle (Pinto De Melo et al., 2017).

The lack of a response to mating with a vasectomized bull, together with the discovery of genes that were regulated by mating to intact bulls, led to the analysis of tissues that have direct contact with seminal fluid (i.e., the vagina). The ejaculation site during natural conception is an important factor to take into consideration since a recent study has shown that SP infusion into the vagina, but not into the uterus, could influence the levels of endometrial epidermal growth factor (Badrakh et al., 2020), which has been associated with fertility restoration in repeat breeder cows (Katagiri and Takahashi, 2006). In this sense, we were also interested in studying how far into the reproductive tract these changes could be observed, so gene expression analysis in the oviductal ampulla was also undertaken. Based on the sequencing results, genes identified as possible key regulators of uterine environment and pregnancy success (*PLA2G10*, *CX3CL1*, *C4BPA*, *PRSS2*, *BLA-DQB,* and *CEBPD*) were selected. In addition, the expression of inflammatory mediators regulated by SP components in other species (*IL1A*, *IL6*, *TNFA,* and *IL8*; O'Leary et al., 2004; Sharkey et al., 2012b; Schjenken et al., 2015; Introini et al., 2017; Ibrahim et al., 2019) was also analyzed. However, no difference between treatments was observed in the expression of any gene in the vagina or the oviduct. These results are not consistent with data in other species: in the mouse, *Il6* was reduced in the oviduct of females mated to males that had undergone a vesiculectomy with or without a vasectomy (Bromfield et al., 2014); while in the pig, natural mating induces up-regulation of *CEBPD* in the ampulla (Alvarez-Rodriguez et al., 2019); finally, in human cervix, an increase in *IL1A*, *IL6* and *IL8* is observed after coitus (Sharkey et al., 2012b). It is important to highlight, however, that the heifers in the present study had been estrous synchronized (both mated and control animals) with an intravaginal device that was removed 48 h prior to sample collection. Although all the animals were managed under the same conditions, the resulting manipulation could have had an impact on the inflammatory status of the vagina. Indeed, a higher dispersion within group is observed in the expression of inflammatory genes in the vagina, than in the ampulla region. This is especially noticeable in the intact group, were one heifer exhibits very high expression of *CX3CL1, IL6, IL1A, TNFA*, and *IL8*. Despite the lack of treatment effect, some genes were shown to be differentially expressed between tissues. A higher expression of *CX3CL1* was found in the ampulla compared with the vagina in control samples. In women, CXCL3 is present throughout the oviduct and, interestingly, its receptor was found in ejaculated sperm (Zhang et al., 2004). Conversely, *CEBPD* and *IL8* were found up-regulated in the vagina samples compared with ampulla in all treatments. On the one hand, the expression of *CEBPD* is a crucial factor during inflammatory acute-phase response, under regulation of a range of cytokines and other inflammatory agents (reviewed in Ramji and Foka, 2002) and, on the other hand, IL8 is well known to be a potent neutrophil chemoattractant (Leonard and Yoshimura, 1990). Therefore, a higher basal expression of both genes in the vagina compared with the ampulla might be expected since this tissue has contact with the outside and, thus, is more prone to environmental/external contaminants.

Interestingly, *IL1A* and *TNFA* were more highly expressed in vagina than in the ampulla tissue of heifers mated either to intact or vasectomized bulls, while control heifers did not exhibit this region-specific difference, suggesting a modulatory role induced by mating. In human exposure of ectocervical explants to SP resulted in the increase of *IL1A* and *TNFA* expression levels (Introini et al., 2017). Further, unprotected vaginal coitus, but not condom protected, induced the expression of *IL1A* in women (Sharkey et al., 2012b). However, in our study, the mechanical stimulus of mating cannot be ruled out.

CONCLUSION

The lack of changes in the endometrial transcriptome and in the expression of selected genes in the vagina and oviduct after mating to a vasectomized male do not support a role of SP (in

the absence of sperm nor testicular and epididymal secretions) in regulating early pregnancy and uterine environment in cattle. Rather, the subtle changes in the transcriptome of the endometrium and the vagina seem to be elicited by sperm. These data indicate that, in species that ejaculate intravaginally, sperm play a more critical role in the modulation of the female environment. This is most apparent when looking at regulation of *IL17*, which is driven by SP in mice (Song et al., 2016) and by sperm in cattle. However, further research is needed to elucidate the role of inherent sperm proteins or SP proteins that attach to sperm at ejaculation.

DATA AVAILABILITY STATEMENT

Gene expression data are publicly available at the Dryad Digital Repository (https://doi.org/10.5061/dryad.s7h44j14r).

ETHICS STATEMENT

The animal study was reviewed and approved by the Animal Research Ethics Committee of University College Dublin, Ireland and licensed by the Health Products Regulatory Authority (HPRA), Ireland, in accordance with Statutory Instrument No. 543 of 2012 (under Directive 2010/63/EU on the Protection of Animals used for Scientific Purposes).

AUTHOR CONTRIBUTIONS

SR carried out the laboratory work, analyzed the results, and wrote the draft. YM-O contributed to the laboratory work and the analysis of results. BF-F, JS, SB-A, MM, and DK carried out the animal work, including handling of bulls and heifers, estrus detection, mating and sample collection. SB and TS performed the RNA library preparation and sequencing analysis. MY performed the statistical analysis of the data. BF-F created the illustrations for **Figure 1**. PL, JS, MY, and BF-F contributed to the critical revision of the manuscript. BF-F, PL, and JS designed the study. All authors read and approved the final manuscript.

FUNDING

This work was funded by the EU Horizon 2020 Marie Skłodowska-Curie (No. 792212) and Science Foundation Ireland (Grant No. 16/IA/4474). The funders had no role in study design, data collection and analysis, decision to publish, or preparation of the manuscript.

ACKNOWLEDGMENTS

The authors thank the farm staff at Teagasc Grange for their important collaboration and patience. The authors acknowledge the excellent implication of several colleagues for their assistance during sample collection and processing, especially Mary Wade, Dr. Clio Maicas, and Dr. John A. Browne. The authors also thank Dr. Isabel Barranco, Ariadna Delgado-Bermúdez, and Marc Llavanera for their help during data analysis and elaboration of some figures.

SUPPLEMENTARY MATERIAL

The Supplementary Material for this article can be found online at: https://www.frontiersin.org/articles/10.3389/fcell.2020.00547/full#supplementary-material

REFERENCES

Alexander, F. C. M., Zemjanis, R., Graham, E. F., and Schmehl, M. L. (1971). Semen characteristics and chemistry from bulls before and after seminal vesiculectomy and after vasectomy. *J. Dairy Sci.* 54, 1530–1535. doi: 10.3168/jds.S0022-0302(71)86059-9

Alghamdi, A. S., Foster, D. N., and Troedsson, M. H. T. (2004). Equine seminal plasma reduces sperm binding to polymorphonuclear neurophils (PMN's) and improves the fertility of fresh semen inseminated into inflamed uteri. *Reproduction* 127, 593–600. doi: 10.1530/rep.1.00096

Alvarez-Rodriguez, M., Atikuzzaman, M., Venhoranta, H., Wright, D., and Rodriguez-Martinez, H. (2019). Expression of immune regulatory genes in the porcine internal genital tract is differentially triggered by spermatozoa and seminal plasma. *Int. J. Mol. Sci.* 20, 1–20. doi: 10.3390/ijms20030513

Amann, R. P., Kavanaugh, J. F., Griel, L. C., and Voglmayr, J. K. (1974). Sperm production of holstein bulls determined from testicular spermatid reserves, after cannulation of rete testis or vas deferens, and by daily ejaculation. *J. Dairy Sci.* 57, 93–99. doi: 10.3168/jds.S0022-0302(74)84836-8

Arai, M., Yoshioka, S., Tasaki, Y., and Okuda, K. (2013). Remodeling of bovine endometrium throughout the estrous cycle. *Anim. Reprod. Sci.* 142, 1–9. doi: 10.1016/j.anireprosci.2013.08.003

Badrakh, D., Yanagawa, Y., Nagano, M., and Katagiri, S. (2020). Effect of seminal plasma infusion into the vagina on the normalization of endometrial epidermal growth factor concentrations and fertility in repeat breeder dairy cows. *J. Reprod. Dev.* 66, 149–154. doi: 10.1262/jrd.2019-148

Bae, S. E., and Watson, E. D. (2003). A light microscopic and ultrastructural study on the presence and location of oxytocin in the equine endometrium. *Theriogenology* 60, 909–921. doi: 10.1016/S0093-691X(02)01362-6

Bai, R., Bai, H., Kuse, M., Ideta, A., Aoyagi, Y., Fujiwara, H., et al. (2014). Involvement of VCAM1 in the bovine conceptus adhesion to the uterine endometrium. *Reproduction* 148, 119–127. doi: 10.1530/REP-13-0655

Batruch, I., Lecker, I., Kagedan, D., Smith, C. R., Mullen, B. J., Grober, E., et al. (2011). Proteomic analysis of seminal plasma from normal volunteers and post-vasectomy patients identifies over 2000 proteins and candidate biomarkers of the urogenital system. *J. Proteome Res.* 10, 941–953. doi: 10.1021/pr100745u

Blom, A. M., Villoutreix, B. O., and Dahlbäck, B. (2004). Complement inhibitor C4b-binding protein – Friend or foe in the innate immune system? *Mol. Immunol.* 40, 1333–1346. doi: 10.1016/j.molimm.2003.12.002

Bromfeld, J. J. (2016). A role for Seminal plasma in modulating pregnancy outcomes in domestic species. *Reproduction* 152, R223–R232. doi: 10.1530/REP-16-0313

Bromfield, J. J., Schjenken, J. E., Chin, P. Y., Care, A. S., Jasper, M. J., and Robertson, S. A. (2014). Maternal tract factors contribute to paternal seminal fluid impact on metabolic phenotype in offspring. *Proc. Natl. Acad. Sci. U.S.A.* 111, 2200–2205. doi: 10.1073/pnas.1305609111

Byrne, K., Leahy, T., Mcculloch, R., Colgrave, M. L., and Holland, M. K. (2012). Comprehensive mapping of the bull sperm surface proteome. *Proteomics* 12, 3559–3579. doi: 10.1002/pmic.201200133

Capper, E. A., and Marshall, L. A. (2001). Mammalian phospholipases A2: mediators of inflammation, proliferation and apoptosis. *Prog. Lipid Res.* 40, 167–197. doi: 10.1016/S0163-7827(01)00002-9

Cooper, T. G., Noonan, E., von Eckardstein, S., Auger, J., Baker, H. W. G., Behre, H. M., et al. (2009). World health organization reference values for human semen characteristics. *Hum. Reprod. Update* 16, 231–245. doi: 10.1093/humupd/dmp048

Dean, M. D., Findlay, G. D., Hoopmann, M. R., Wu, C. C., MacCoss, M. J., Swanson, W. J., et al. (2011). Identification of ejaculated proteins in the house mouse (Mus domesticus) via isotopic labeling. *BMC Genomics* 12:306. doi: 10.1186/1471-2164-12-306

Dickinson, S. E., Griffin, B. A., Elmore, M. F., Kriese-Anderson, L., Elmore, J. B., Dyce, P. W., et al. (2018). Transcriptome profiles in peripheral white blood cells at the time of artificial insemination discriminate beef heifers with different fertility potential. *BMC Genomics* 19:129. doi: 10.1186/s12864-018-4505-4

Diskin, M. G., and Morris, D. G. (2008). Embryonic and early foetal losses in cattle and other ruminants. *Reprod. Domest. Anim.* 43, 260–267. doi: 10.1111/j.1439-0531.2008.01171.x

Elweza, A. E., Ezz, M. A., Acosta, T. J., Talukder, A. K., Shimizu, T., Hayakawa, H., et al. (2018). A proinflammatory response of bovine endometrial epithelial cells to active sperm in vitro. *Mol. Reprod. Dev.* 85, 215–226. doi: 10.1002/mrd.22955

Ezz, M. A., Marey, M. A., Elweza, A. E., Kawai, T., Heppelmann, M., Pfarrer, C., et al. (2019). TLR2/4 signaling pathway mediates sperm-induced inflammation in bovine endometrial epithelial cells in vitro. *PLoS ONE* 14:e0214516. doi: 10.1371/journal.pone.0214516

Faulkner, L. C., Hopwood, M. L., and Wiltbank, J. N. (1968). Seminal vesiculectomy in bulls. II. Seminal characteristics and breeding trials. *J. Reprod. Fertil.* 16, 179–182. doi: 10.1530/jrf.0.0160179

Fedorka, C. E., Scoggin, K. E., Woodward, E. M., Squires, E. L., Ball, B. A., and Troedsson, M. H. T. (2017). The effect of select seminal plasma proteins on endometrial mRNA cytokine expression in mares susceptible to persistent mating-induced endometritis. *Reprod. Domest. Anim.* 52, 89–96. doi: 10.1111/rda.12813

Fernandez-fuertes, B., Sánchez, J. M., Bagés-arnal, S., Mcdonald, M., Yeste, M., and Lonergan, P. (2019). Species-specific and collection method-dependent differences in endometrial susceptibility to seminal plasma-induced RNA degradation. *Sci. Rep.* 9, 1–12. doi: 10.1038/s41598-019-51413-4

Gangnuss, S., Sutton-McDowall, M. L., Robertson, S. A., and Armstrong, D. T. (2004). Seminal plasma regulates corpora lutea macrophage populations during early pregnancy in mice. *Biol. Reprod.* 71, 1135–1141. doi: 10.1095/biolreprod.104.027425

Glynn, D. J., Heng, K., Russell, D. L., Sharkey, D. J., Robertson, S. A., Anand-Ivell, R., et al. (2017). Male seminal relaxin contributes to induction of the post-mating cytokine response in the female mouse uterus. *Front. Physiol.* 8:422. doi: 10.3389/fphys.2017.00422

Gutsche, S., von Wolff, M., Strowitzki, T., and Thaler, C. J. (2003). Seminal plasma induces mRNA expression of IL-1β, IL-6 and LIF in endometrial epithelial cells in vitro. *Mol. Hum. Reprod.* 9, 785–791. doi: 10.1093/molehr/gag095

Gwathmey, T. M., Ignotz, G. G., Mueller, J. L., Manjunath, P., and Suarez, S. S. (2006). Bovine seminal plasma proteins PDC-109, BSP-A3, and BSP-30-kDa share functional roles in storing sperm in the oviduct. *Biol. Reprod.* 75, 501–507. doi: 10.1095/biolreprod.106.053306

Gwathmey, T. M., Ignotz, G. G., and Suarez, S. S. (2003). PDC-109 (BSP-A1/A2) promotes bull sperm binding to oviductal epithelium *in vitro* and may be involved in forming the oviductal sperm reservoir. *Biol. Reprod.* 69, 809–815. doi: 10.1095/biolreprod.102.010827

Hannan, N. J., Jones, R. L., Critchley, H. O. D., Kovacs, G. J., Rogers, P. A. W., Affandi, B., et al. (2004). Coexpression of fractalkine and its receptor in normal human endometrium and in endometrium from users of progestin-only contraception supports a role for fractalkine in leukocyte recruitment and endometrial remodeling. *J. Clin. Endocrinol. Metab.* 89, 6119–6129. doi: 10.1210/jc.2003-031379

Hannan, N. J., Jones, R. L., White, C. A., and Salamonsen, L. A. (2006). The chemokines, CX3CL1, CCL14, and CCL4, promote human trophoblast migration at the feto-maternal interface. *Biol. Reprod.* 74, 896–904. doi: 10.1095/biolreprod.105.045518

Harris, C. L., Mizuno, M., and Morgan, B. P. (2006). Complement and complement regulators in the male reproductive system. *Mol. Immunol.* 43, 57–67. doi: 10.1016/j.molimm.2005.06.026

Hayashi, K. G., Hosoe, M., Kizaki, K., Fujii, S., Kanahara, H., Takahashi, T., et al. (2017). Differential gene expression profiling of endometrium during the mid-luteal phase of the estrous cycle between a repeat breeder (RB) and non-RB cows. *Reprod. Biol. Endocrinol.* 15:20. doi: 10.1186/s12958-017-0237-6

Hunter, R. H. F. (1981). Sperm transport and reservoirs in the pig oviduct in relation to the time of ovulation. *J. Reprod. Fertil.* 63, 109–117. doi: 10.1530/jrf.0.0630109

Ibrahim, L. A., Rizo, J. A., Fontes, P. L. P., Lamb, G. C., and Bromfield, J. J. (2019). Seminal plasma modulates expression of endometrial inflammatory meditators in the bovine. *Biol. Reprod.* 100, 660–671. doi: 10.1093/biolre/ioy226

Introini, A., Boström, S., Bradley, F., Gibbs, A., Glaessgen, A., Tjernlund, A., et al. (2017). Seminal plasma induces inflammation and enhances HIV-1 replication in human cervical tissue explants. *PLoS Pathog.* 13:e1006492. doi: 10.1371/journal.ppat.1006492

Iwakura, Y., Ishigame, H., Saijo, S., and Nakae, S. (2011). Functional specialization of interleukin-17 family members. *Immunity* 34, 149–162. doi: 10.1016/j.immuni.2011.02.012

Janeway, C. A. Jr., Travers, P., Walport, M., and Shlomchik, M. (2001). *Immunobiology: The immune System in Health and Disease*, 5th Edn. New York, NY: Garland Science.

Jiang, Y., Oliver, P., Davies, K. E., and Platt, N. (2006). Identification and characterization of murine SCARA5, a novel class A scavenger receptor that is expressed by populations of epithelial cells. *J. Biol. Chem.* 281, 11834–11845. doi: 10.1074/jbc.M507599200

Katagiri, S., and Takahashi, Y. (2006). Potential relationship between normalization of endometrial epidermal growth factor profile and restoration of fertility in repeat breeder cows. *Anim. Reprod. Sci.* 95, 54–66. doi: 10.1016/j.anireprosci.2005.09.001

Kelleher, A. M., DeMayo, F. J., and Spencer, T. E. (2019). Uterine glands: developmental biology and functional roles in pregnancy. *Endocr. Rev.* 40, 1424–1445. doi: 10.1210/er.2018-00281

Kim, D., Langmead, B., and Salzberg, S. L. (2015). HISAT: a fast spliced aligner with low memory requirements. *Nat. Methods* 12, 357–360. doi: 10.1038/nmeth.3317

Konac, E., Alp, E., Onen, H. I., Korucuoglu, U., Biri, A. A., and Menevse, S. (2009). Endometrial mRNA expression of matrix metalloproteinases, their tissue inhibitors and cell adhesion molecules in unexplained infertility and implantation failure patients. *Reprod. Biomed. Online* 19, 391–397. doi: 10.1016/s1472-6483(10)60174-5

Lee, J., Oh, J., Choi, E., Park, I., Han, C., Kim, D. H., et al. (2007). Differentially expressed genes implicated in unexplained recurrent spontaneous abortion. *Int. J. Biochem. Cell Biol.* 39, 2265–2277. doi: 10.1016/j.biocel.2007.06.012

Lemaster, J. W., Seals, R. C., Hopkins, F. M., and Schrick, F. N. (1999). Effects of administration of oxytocin on embryonic survival in progestogen supplemented cattle. *Prostaglandins Other Lipid Mediat.* 57, 259–268. doi: 10.1016/S0090-6980(99)00007-6

Leonard, E. J., and Yoshimura, T. (1990). Neutrophil attractant/activation protein-l (NAP-l [Interleukin-8]). *Am. J. Respir. Cell Mol. Biol.* 2, 479–486. doi: 10.1165/ajrcmb/2.6.479

Liao, Y., Smyth, G. K., and Shi, W. (2014). FeatureCounts: an efficient general purpose program for assigning sequence reads to genomic features. *Bioinformatics* 30, 923–930. doi: 10.1093/bioinformatics/btt656

Livak, K. J., and Schmittgen, T. D. (2001). Analysis of relative gene expression data using real-time quantitative PCR and the 2(-Delta Delta C(T)) Method. *Methods* 25, 402–408. doi: 10.1006/meth.2001.1262

Macklon, N. S., Geraedts, J. P. M., and Fauser, B. C. J. M. (2002). Conception to ongoing pregnancy: the "black box" of early pregnancy loss. *Hum. Reprod. Update* 8, 333–343. doi: 10.1093/humupd/8.4.333

Manjunath, P., and Thérien, I. (2002). Role of seminal plasma phospholipid-binding proteins in sperm membrane lipid modification that occurs during capacitation. *J. Reprod. Immunol.* 53, 109–119. doi: 10.1016/S0165-0378(01)00098-5

Mansouri-Attia, N., Aubert, J., Reinaud, P., Giraud-Delville, C., Taghouti, G., Galio, L., et al. (2009). Gene expression profiles of bovine caruncular and intercaruncular endometrium at implantation. *Physiol. Genomics* 39, 14–27. doi: 10.1152/physiolgenomics.90404.2008

Mantena, S. R., Kannan, A., Cheon, Y. P., Li, Q., Johnson, P. F., Bagchi, I. C., et al. (2006). C/EBPβ is a critical mediator of steroid hormone-regulated cell proliferation and differentiation in the uterine epithelium and stroma. *Proc. Natl. Acad. Sci. U.S.A.* 103, 1870–1875. doi: 10.1073/pnas.0507261103

Mateo-Otero, Y., Sánchez, J. M., Recuero, S., Bagés-Arnal, S., Mcdonald, M., Kenny, D., et al. (2020). Effect of exposure to seminal plasma through natural mating in cattle on conceptus length and gene expression. *Front. Cell Dev. Biol.* 8:341. doi: 10.3389/fcell.2020.00341

Minten, M. A., Bilby, T. R., Bruno, R. G. S., Allen, C. C., Madsen, C. A., Wang, Z., et al. (2013). Effects of fertility on gene expression and function of the bovine endometrium. *PLoS ONE* 8:e067444. doi: 10.1371/journal.pone.0069444

Moraes, J. G. N., Behura, S. K., Geary, T. W., Hansen, P. J., Neibergs, H. L., and Spencer, T. E. (2018). Uterine influences on conceptus development in fertility-classified animals. *Proc. Natl. Acad. Sci. U.S.A.* 115, E1749–E1758. doi: 10.1073/pnas.1721191115

Morgan, H. L., and Watkins, A. J. (2020). The influence of seminal plasma on offspring development and health. *Semin. Cell Dev. Biol.* 97, 131–137. doi: 10.1016/j.semcdb.2019.06.008

Nauc, V., and Manjunath, P. (2000). Radioimmunoassays for bull seminal plasma proteins (BSP-A1/-A2, BSP-A3, and BSP-30-Kilodaltons), and their quantification in seminal plasma and sperm1. *Biol. Reprod.* 63, 1058–1066. doi: 10.1095/biolreprod63.4.1058

Neupane, M., Geary, T. W., Kiser, J. N., Burns, G. W., Hansen, P. J., Spencer, T. E., et al. (2017). Loci and pathways associated with uterine capacity for pregnancy and fertility in beef cattle. *PLoS ONE* 12:e0188997. doi: 10.1371/journal.pone.0188997

Niakan, K. K., Han, J., Pedersen, R. A., Simon, C., and Pera, R. A. R. (2012). Human pre-implantation embryo development. *Development* 139, 829–841. doi: 10.1242/dev.060426

Odhiambo, J. F., Poole, D. H., Hughes, L., DeJarnette, J. M., Inskeep, E. K., and Dailey, R. A. (2009). Pregnancy outcome in dairy and beef cattle after artificial insemination and treatment with seminal plasma or transforming growth factor beta-1. *Theriogenology* 72, 566–571. doi: 10.1016/j.theriogenology.2009.04.013

O'Leary, S., Jasper, M. J., Robertson, S. A., and Armstrong, D. T. (2006). Seminal plasma regulates ovarian progesterone production, leukocyte recruitment and follicular cell responses in the pig. *Reproduction* 132, 147–158. doi: 10.1530/rep.1.01119

O'Leary, S., Jasper, M. J., Warnes, G. M., Armstrong, D. T., and Robertson, S. A. (2004). Seminal plasma regulates endometrial cytokine expression, leukocyte recruitment and embryo development in the pig. *Reproduction* 128, 237–247. doi: 10.1530/rep.1.00160

Ortiz, W. G., Rizo, J. A., Carvalheira, L. R., Ahmed, B. M. S., Estrada-Cortes, E., Harstine, B. R., et al. (2019). Effects of intrauterine infusion of seminal plasma at artificial insemination on fertility of lactating Holstein cows. *J. Dairy Sci.* 102, 6587–6594. doi: 10.3168/jds.2019-16251

Palm, F., Walter, I., Budik, S., Kolodziejek, J., Nowotny, N., and Aurich, C. (2008). Influence of different semen extenders and seminal plasma on PMN migration and on expression of IL-1β, IL-6, TNF-α and COX-2 mRNA in the equine endometrium. *Theriogenology* 70, 843–851. doi: 10.1016/j.theriogenology.2008.04.054

Pandya, I. J., and Cohen, J. (1985). The leukocytic reaction of the human uterine cervix to spermatozoa. *Fertil. Steril.* 43, 417–421. doi: 10.1016/S0015-0282(16)48442-6

Pfeiffer, K. E., Binversie, J. A., Rhinehart, J. D., and Larson, J. E. (2012). Exposure of beef females to the biostimulatory effects of bulls with or without deposition of seminal plasma prior to AI. *Anim. Reprod. Sci.* 133, 27–34. doi: 10.1016/j.anireprosci.2012.06.011

Pini, T., Leahy, T., Soleilhavoup, C., Tsikis, G., Labas, V., Combes-Soia, L., et al. (2016). Proteomic investigation of ram spermatozoa and the proteins conferred by seminal plasma. *J. Proteome Res.* 15, 3700–3711. doi: 10.1021/acs.jproteome.6b00530

Pinto, De Melo, T., De Camargo, G. M. F., De Albuquerque, L. G., and Carvalheiro, R. (2017). Genome-wide association study provides strong evidence of genes affecting the reproductive performance of Nellore beef cows. *PLoS ONE* 12:e0178551. doi: 10.1371/journal.pone.0178551

Ramji, D. P., and Foka, P. (2002). CCAAT/enhancer-binding proteins: structure, function and regulation. *Biochem. J.* 365, 561–575. doi: 10.1042/BJ20020508

Randi, F., McDonald, M., Duffy, P., Kelly, A. K., and Lonergan, P. (2018). The relationship between external auditory canal temperature and onset of estrus and ovulation in beef heifers. *Theriogenology* 110, 175–181. doi: 10.1016/j.theriogenology.2018.01.001

Remes Lenicov, F., Rodriguez Rodrigues, C., Sabatté, J., Cabrini, M., Jancic, C., Ostrowski, M., et al. (2012). Semen promotes the differentiation of tolerogenic dendritic cells. *J. Immunol.* 189, 4777–4786. doi: 10.4049/jimmunol.1202089

Robertson, S. A. (2007). Seminal fluid signaling in the female reproductive tract: lessons from rodents and pigs. *J. Anim. Sci.* 85, 36–44. doi: 10.2527/jas.2006-578

Robertson, S. A., Guerin, L. R., Bromfield, J. J., Branson, K. M., Ahlström, A. C., and Care, A. S. (2009). Seminal fluid drives expansion of the CD4+CD25+ T regulatory cell pool and induces tolerance to paternal alloantigens in mice1. *Biol. Reprod.* 80, 1036–1045. doi: 10.1095/biolreprod.108.074658

Sakaguchi, S., Sakaguchi, N., Shimizu, J., Yamazaki, S., Sakihama, T., Itoh, M., et al. (2001). Immunologic tolerance maintained by CD25+ CD4+ regulatory T cells: their common role in controlling autoimmunity, tumor immunity, and transplantation tolerance. *Immunol. Rev.* 182, 18–32. doi: 10.1034/j.1600-065X.2001.1820102.x

Sánchez, J. M., Mathew, D. J., Behura, S. K., Passaro, C., Charpigny, G., Butler, S. T., et al. (2019). Bovine endometrium responds differentially to age-matched short and long conceptuses†. *Biol. Reprod.* 101, 26–39. doi: 10.1093/biolre/ioz060

Sandra, O., Charpigny, G., Galio, L., and Hue, I. (2017). Preattachment embryos of domestic animals: insights into development and paracrine secretions. *Annu. Rev. Anim. Biosci.* 5, 205–228. doi: 10.1146/annurev-animal-022516-022900

Schjenken, J. E., Glynn, D. J., Sharkey, D. J., and Robertson, S. A. (2015). TLR4 signaling is a major mediator of the female tract response to seminal fluid in mice1. *Biol. Reprod.* 93, 1–13. doi: 10.1095/biolreprod.114.125740

Seidel, G., and Foote, R. (1970). Compartmental analysis bovine of sources of the ejaculate. *Biol. Reprod.* 2, 189–196. doi: 10.1095/biolreprod2.2.189

Shah, B. A., Hopwood, M. L., and Faulkner, L. C. (1968). Seminal vesiculectomy in bulls. I. Seminal biochemistry. *J. Reprod. Fertil.* 16, 171–177. doi: 10.1530/jrf.0.0160171

Sharkey, D. J., Macpherson, A. M., Tremellen, K. P., Mottershead, D. G., Gilchrist, R. B., and Robertson, S. A. (2012a). TGF-β mediates proinflammatory seminal fluid signaling in human cervical epithelial cells. *J. Immunol.* 189, 1024–1035. doi: 10.4049/jimmunol.1200005

Sharkey, D. J., Tremellen, K. P., Jasper, M. J., Gemzell-Danielsson, K., and Robertson, S. A. (2012b). Seminal fluid induces leukocyte recruitment and cytokine and chemokine mRNA expression in the human cervix after coitus. *J. Immunol.* 188, 2445–2454. doi: 10.4049/jimmunol.1102736

Sharkey, D. J., Macpherson, A. M., Tremellen, K. P., and Robertson, S. A. (2007). Seminal plasma differentially regulates inflammatory cytokine gene expression in human cervical and vaginal epithelial cells. *Mol. Hum. Reprod.* 13, 491–501. doi: 10.1093/molehr/gam028

Shima, T., Inada, K., Nakashima, A., Ushijima, A., Ito, M., Yoshino, O., et al. (2015). Paternal antigen-specific proliferating regulatory T cells are increased in uterine-draining lymph nodes just before implantation and in pregnant uterus just after implantation by seminal plasma-priming in allogeneic mouse pregnancy. *J. Reprod. Immunol.* 108, 72–82. doi: 10.1016/j.jri.2015.02.005

Song, Z. H., Li, Z. Y., Li, D. D., Fang, W. N., Liu, H. Y., Yang, D. D., et al. (2016). Seminal plasma induces inflammation in the uterus through the γδT/IL-17 pathway. *Sci. Rep.* 6, 1–8. doi: 10.1038/srep25118

Spencer, T. E., Forde, N., Dorniak, P., Hansen, T. R., Romero, J. J., and Lonergan, P. (2013). Conceptus-derived prostaglandins regulate gene expression In the endometrium prior to pregnancy recognition In ruminants. *Reproduction* 146, 377–387. doi: 10.1530/REP-13-0165

Spencer, T. E., Kelleher, A. M., and Bartol, F. F. (2019). Development and function of uterine glands in domestic animals. *Annu. Rev. Anim. Biosci.* 7, 125–147. doi: 10.1146/annurev-animal-020518-115321

Tapia, A., Gangi, L. M., Zegers-Hochschild, F., Balmaceda, J., Pommer, R., Trejo, L., et al. (2008). Differences in the endometrial transcript profile during the receptive period between women who were refractory to implantation and those who achieved pregnancy. *Hum. Reprod.* 23, 340–351. doi: 10.1093/humrep/dem319

Tapia, A., Vilos, C., Marín, J. C., Croxatto, H. B., and Devoto, L. (2011). Bioinformatic detection of E47, E2F1 and SREBP1 transcription factors as potential regulators of genes associated to acquisition of endometrial receptivity. *Reprod. Biol. Endocrinol.* 9, 1–14. doi: 10.1186/1477-7827-9-14

Thompson, L. A., Barratt, C. L. R., Bolton, A. E., and Cooke, I. D. (1992). The leukocytic reaction of the human uterine cervix. *Am. J. Reprod. Immunol.* 28, 85–89. doi: 10.1111/j.1600-0897.1992.tb00765.x

Tríbulo, P., Siqueira, L. G. B., Oliveira, L. J., Scheffler, T., and Hansen, P. J. (2018). Identification of potential embryokines in the bovine reproductive tract. *J. Dairy Sci.* 101, 690–704. doi: 10.3168/jds.2017-13221

Troedsson, M. H. T., Alghamdi, A. S., and Mattisen, J. (2002). Equine seminal plasma protects the fertility of spermatozoa in an inflamed uterine environment. *Theriogenology* 58, 453–456. doi: 10.1016/S0093-691X(02)00862-2

Tunon, A.-M., Katila, T., Magnusson, U., Nummijärvi, A., and Rodriguez-Martinez, H. (2000). T-cell distribution in two different segments of the equine. *Theriogenology* 54, 835–841. doi: 10.1016/s0093-691x(00)00395-2

Valenza, A., Giordano, J. O., Lopes, G., Vincenti, L., Amundson, M. C., and Fricke, P. M. (2012). Assessment of an accelerometer system for detection of estrus and treatment with gonadotropin-releasing hormone at the time of insemination in lactating dairy cows. *J. Dairy Sci.* 95, 7115–7127. doi: 10.3168/jds.2012-5639

Vitorino Carvalho, A., Eozenou, C., Richard, C., Forde, N., Healey, G. D., Giraud-Delville, C., et al. (2019). Bovine scavenger receptor class A (SR-A) exhibit specific patterns of regulation in the endometrium during the oestrous cycle and early pregnancy. *Reprod. Fertil. Dev.* 31, 1078–1090. doi: 10.1071/RD18411

Walker, W. L., Nebel, R. L., and McGilliard, M. L. (1996). Time of ovulation relative to mounting activity in dairy cattle. *J. Dairy Sci.* 79, 1555–1561. doi: 10.3168/jds.S0022-0302(96)76517-7

Wathes, D. C., Cheng, Z., Chowdhury, W., Fenwick, M. A., Fitzpatrick, R., Morris, D. G., et al. (2009). Negative energy balance alters global gene expression and immune responses in the uterus of postpartum dairy cows. *Physiol. Genomics* 39, 1–13. doi: 10.1152/physiolgenomics.00064.2009

Watkins, A. J., Dias, I., Tsuro, H., Allen, D., Emes, R. D., Moreton, J., et al. (2018). Paternal diet programs offspring health through sperm- and seminal plasma-specific pathways in mice. *Proc. Natl. Acad. Sci. U.S.A.* 115, 10064–10069. doi: 10.1073/pnas.1806333115

Wedel, A., and Lömsziegler-Heitbrock, H. W. (1995). The C/EBP family of transcription factors. *Immunobiology* 193, 171–185. doi: 10.1016/S0171-2985(11)80541-3

Wiltbank, M. C., Baez, G. M., Garcia-Guerra, A., Toledo, M. Z., Monteiro, P. L. J., Melo, L. F., et al. (2016). Pivotal periods for pregnancy loss during the first trimester of gestation in lactating dairy cows. *Theriogenology* 86, 239–253. doi: 10.1016/j.theriogenology.2016.04.037

Zhang, Q., Shimoya, K., Temma, K., Kimura, T., Tsujie, T., Shioji, M., et al. (2004). Expression of fractalkine in the Fallopian tube and of CX3CR1 in sperm. *Hum. Reprod.* 19, 409–414. doi: 10.1093/humrep/deh085

Zhou, X., Lindsay, H., and Robinson, M. D. (2014). Robustly detecting differential expression in RNA sequencing data using observation weights. *Nucleic Acids Res.* 42:e91. doi: 10.1093/nar/gku310

Conflict of Interest: The authors declare that the research was conducted in the absence of any commercial or financial relationships that could be construed as a potential conflict of interest.

Copyright © 2020 Recuero, Sánchez, Mateo-Otero, Bagés-Arnal, McDonald, Behura, Spencer, Kenny, Yeste, Lonergan and Fernandez-Fuertes. This is an open-access article distributed under the terms of the Creative Commons Attribution License (CC BY). The use, distribution or reproduction in other forums is permitted, provided the original author(s) and the copyright owner(s) are credited and that the original publication in this journal is cited, in accordance with accepted academic practice. No use, distribution or reproduction is permitted which does not comply with these terms.

frontiers in Cell and Developmental Biology

REVIEW
published: 21 August 2020
doi: 10.3389/fcell.2020.00791

From Sperm Motility to Sperm-Borne microRNA Signatures: New Approaches to Predict Male Fertility Potential

Maíra Bianchi Rodrigues Alves[1,2], *Eneiva Carla Carvalho Celeghini*[2] *and Clémence Belleannée*[1]*

[1] CHU de Québec Research Center (CHUL), Department of Obstetrics, Gynecology and Reproduction, Faculty of Medicine, Université Laval, Quebec City, QC, Canada, [2] Department of Animal Reproduction, Universidade de São Paulo, Pirassununga, Brazil

In addition to the paternal genome, spermatozoa carry several intrinsic factors, including organelles (e.g., centrioles and mitochondria) and molecules (e.g., proteins and RNAs), which are involved in important steps of reproductive biology such as spermatogenesis, sperm maturation, oocyte fertilization and embryo development. These factors constitute potential biomarkers of "viable sperm" and male fertility status and may become major assets for diagnosing instances of idiopathic male infertility in both humans and livestock animals. A better understanding of the mechanism of action of these sperm intrinsic factors in the regulation of reproductive and developmental processes still presents a major challenge that must be addressed. This review assembles the main data regarding morpho-functional and intrinsic sperm features that are associated with male infertility, with a particular focus on microRNA (miRNA) molecules.

Keywords: infertility, diagnosis, spermatozoa, semen, intrinsic factors, ncRNAs, human, cattle

OPEN ACCESS

Edited by:
Tzviya Zeev-Ben-Mordehai, Utrecht University, Netherlands

Reviewed by:
Myung-Geol Pang, Chung-Ang University, South Korea
Brett Nixon, The University of Newcastle, Australia

***Correspondence:**
Clémence Belleannée
Clemence.Belleannee@crchudequebec.ulaval.ca

Specialty section:
This article was submitted to Cell Growth and Division, a section of the journal Frontiers in Cell and Developmental Biology

Received: *26 May 2020*
Accepted: *28 July 2020*
Published: *21 August 2020*

Citation:
Alves MBR, Celeghini ECC and Belleannée C (2020) From Sperm Motility to Sperm-Borne microRNA Signatures: New Approaches to Predict Male Fertility Potential. Front. Cell Dev. Biol. 8:791. doi: 10.3389/fcell.2020.00791

INTRODUCTION

Male fertility potential relies on several physical, endocrine, and genetic factors, which underlie the production of fully functional spermatozoa as well as their successful arrival at the site of fertilization. Impairment of these male reproductive functions accounts for half of the infertility issues that couples face during their reproductive age (Agarwal et al., 2015; Zegers-Hochschild et al., 2017). While male infertility diagnosis is mainly based on physical characteristics, hormonal analysis, and use of the traditional spermogram, its etiology remains unexplained in more than 30% of patients (Irvine, 1998; Agarwal et al., 2015). Thus, the design of novel customized diagnostic tools to fully assess male fertility potential and male infertility etiology is a necessity. Furthermore, an improved method to assess male fertility potential would be a major asset to the livestock industry, since this parameter constitutes a serious economic challenge in this field. Research performed on sperm samples from humans, livestock animals and rodents recently questioned the definition of the sperm cell as a simple carrier of the paternal genome. From this, it now appears that the spermatozoon is a well-differentiated cell that carries a widely diverse signature of specific organelles and molecules, that could vary according to male fertility potential, and be transferred to

the oocyte at the time of fertilization. This contemporary view of the sperm cell opens potential new avenues concerning the development of a novel generation of diagnostic tools. In this review, we will delineate structural, morpho-functional and intrinsic sperm features, and comment on their contribution to the post-fertilization processes. The detection of sperm microRNAs (miRNAs) as a predictor of male fertility potential will be discussed with regard to its possible applications in both clinic and industry.

"HEALTHY SPERM" CONCEPT: STRUCTURAL, MORPHO-FUNCTIONAL AND INTRINSIC FEATURES

While sperm quality is a key determinant of male fertility potential, the discrimination between a high- and low-quality sperm sample is challenging. Indeed, this relies on a broad spectrum of sperm features (Amann and Hammerstedt, 1993). According to this concept, "healthy spermatozoa" also referred to as "viable spermatozoa" should possess the ability to reach the fertilization site, bind to and fertilize the oocytes, and properly contribute to initiation of early embryo development (Krawetz, 2005). These abilities are strictly dependent on specific structural, morpho-functional, and intrinsic features (**Figure 1**).

Structural Sperm Features

Spermatozoa are the most differentiated cells of the organism and display particular features related to their main function: the delivery of paternal DNA to the oocyte (Krawetz, 2005). In this regard, spermatozoa are composed of two main parts: a head to carry and protect the genome, and a tail or flagellum to propel the cell to the site of fertilization (**Figure 2**).

Within the **sperm head** is a limited quantity of cytoplasm, highly condensed DNA, and a well-delimited acrosome. A substantial portion of the cytoplasm is lost during the final steps of spermatogenesis, specifically during spermiogenesis, the process during which round spermatids differentiate into elongated spermatids and then spermatozoa (Gadea et al., 2013). The remaining cytoplasm from intercellular bridges, called the cytoplasmic droplet, is lost during sperm transit through the epididymis (Cooper and Yeung, 2003). During spermiogenesis, the sequential replacement of histones by transitional proteins and then by protamines within sperm chromatin triggers genome condensation (Zini and Agarwal, 2011; Gadea et al., 2013). The acrosome, located at the top of the head, contains specific enzymes that promote specific functions trailing sperm capacitation and acrosome reaction: (1) exposure of acrosome zona pellucida binding proteins during sperm capacitation; (2) sperm ability to cross cumulus cells that surrounds the oocytes, (3) sperm binding to zona pellucida and acrosome reaction, and (4) migration of IZUMO1 protein from the outer acrosomal membrane to the equatorial segment of sperm surface to ensure its binding to JUNO receptor on the oocyte (Satouh et al., 2012; Bianchi et al., 2014). Since acrosome reacted sperm retain the ability to penetrate the zona pellucida, the previous paradigm supporting the role of enzymes released during acrosome reaction in the digestion of the zona pellucida has been revisited in different species (Hirohashi and Yanagimachi, 2018).

The **sperm tail** (or flagellum) includes the neck, midpiece, principal piece and terminal piece. The sperm centrioles are important to early embryo development and are localized in the sperm neck (Avidor-Reiss and Fishman, 2019). The axoneme, located internally along the entire flagellum, is composed of nine peripheral doublets and two central single microtubules (9 + 2 structure) integrated by the intraflagellar transport (IFT) system. Surrounding the axoneme, there is the outer dense fibers (ODF) and mitochondria in the sperm midpiece and the fibrous sheath (FS), formed by nine bundles of fibers of different lengths, in the principal piece (Inaba, 2003). Depending on species, approximately 22–75 mitochondria are present in the midpiece to produce enough energy necessary for a spermatozoon to transit along the female reproductive tract and to reach the fertilization site in the oviduct (Song and Lewis, 2008). All of these sperm structural characteristics are essential to ensure the ability of spermatozoa to cross the muco-cervical and uterine barriers and reach the oviduct, where they bind to and penetrate the oocyte to deliver their DNA content.

Morpho-Functional Sperm Features

Morpho-functional sperm attributes are capable of modulating male fertility potential and are tightly related to the structural sperm features. Parameters such as **sperm motility/kinetics, morphological abnormalities, integrity of plasma and acrosome membranes, mitochondrial activity production of reactive oxygen species (ROS), DNA fragmentation** and **capacitation status** are included in this group and usually are associated with male fertility (**Table 1** and **Figure 3**). Thus, assessment of these parameters is essential to determine male fertility potential: evaluation of a higher number of morpho-functional attributes establishes the highest relationship with male fertility (Amann and Hammerstedt, 1993). A high proportion of **morphological abnormalities** – referred to as teratozoospermia – including, e.g., spermatozoa with large, small or piriform heads as well as coiled-tails, is associated with reproductive dysfunctions (Gillan et al., 2008). This common cause of male infertility is routinely assessed by light microscopic analysis of semen in fertility clinics.

Several other techniques are currently available to assess sperm morpho-functional attributes. **Sperm motility, kinetics, vigor and hyperactivation levels**, are morpho-functional features classically assessed by light microscopy or computer-assisted sperm analysis (i.e., CASA) (Vincent et al., 2012). In addition, since sperm motility requires a substantial amount of energy produced by **mitochondrial activity** (Piomboni et al., 2012), high fertility samples usually present with high mitochondrial membrane potential. This feature can be assessed by fluorescence microscopy and flow cytometric approaches mainly using the JC-1 fluorescent probe, which forms J-aggregates when mitochondria are active

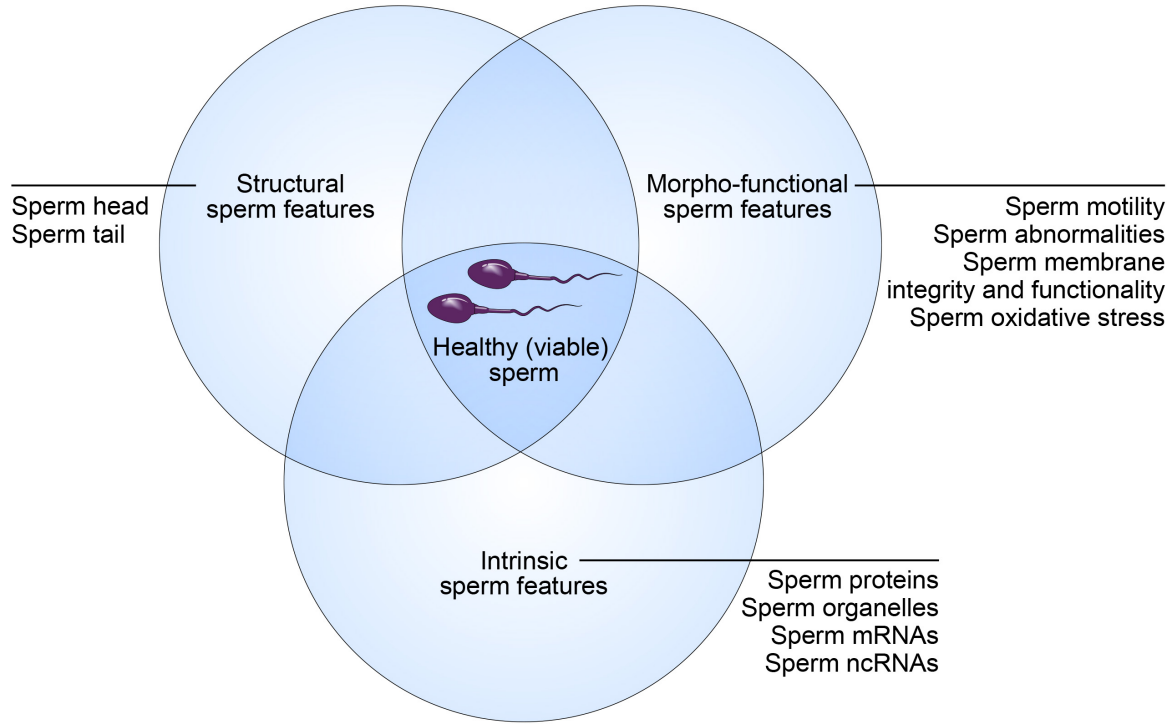

FIGURE 1 | Concept of "healthy (viable) sperm." Male fertility potential relies on structural, morpho-functional, and intrinsic sperm features that shape equally the concept of "healthy (viable) sperm."

and polarized; in this situation, more JC-1 monomers enter the spermatozoa and aggregate to generate red fluorescence (Gillan et al., 2005; Celeghini et al., 2007). In addition to energy production, mitochondria also produce large quantities of ROS that promote oxidative stress and damage to sperm membranes and DNA. Therefore, **ROS quantification** in sperm cells is also an important morpho-functional feature that can be assessed by fluorescence microscopy, flow cytometry and molecular/biochemical assays using fluorescent probes. Such assays include BODIPY, which measures the susceptibility of sperm to lipid peroxidation, CellROX Deep Red®, which stains ROS present in sperm cells, and measurement of malondialdehyde concentration (produced during lipid peroxidation) using the TBARS (Thiobarbituric acid reactive substances) assay (Aitken et al., 2007; Celeghini et al., 2019). In addition, since damage to the sperm membranes and DNA impairs sperm capacitation and early embryo development, both **plasma and acrosome membrane as well as DNA integrity** should be evaluated by fluorescence microscopy or flow cytometric approaches. Propidium iodide fluorescent probes and fluorescent lectin from *Pisum sativum* can be used to assess plasma and acrosome membrane damage (Celeghini et al., 2007), respectively, as well as SCSA® (Sperm Chromatin Structure Assay) to detect the susceptibility of sperm to DNA fragmentation (Evenson and Wixon, 2006). Post-sperm **capacitation status** could be assessed using the combination of Hoechst 33258/chlortetracycline fluorescence probes and is proposed to predict litter size and fertility success in pigs (Kwon et al., 2015).

While the assessment of these features is essential to determine male fertility potential, based on data from human clinics, about 30% of sperm samples presenting with satisfactory morpho-functional features (**Figure 3**) are still unable to fertilize the oocytes or to trigger early embryo development. Recent advances in analyses of sperm molecular and subcellular content suggested that intrinsic factors may participate to early embryo development and, consequently, could be potential targets for the assessment of male fertility potential.

Intrinsic Sperm Features

In addition to the paternal DNA, the spermatozoon carries numerous molecules and organelles, which constitute a growing focus of interest in fundamental research. Among these intrinsic factors, **sperm centrioles, sperm mitochondria, sperm proteins,** and **sperm RNAs** are particularly interesting with respect to their potential contribution to the post-fertilization process (**Figure 4**). As shown in **Figure 2**, sperm **centrioles** are localized in the sperm neck while sperm **mitochondria** are arranged in the midpiece. Since mature spermatozoa possess a minimal amount of cytoplasm and a nucleus with highly condensed DNA that prevents transcription, the presence of **proteins** and **RNAs** in sperm cells is limited. However, several proteins and ribonucleic acid molecules are likely acquired by the maturing spermatozoa during spermatogenesis and their transit through the epididymis and post-ejaculatory journey (Boerke et al., 2007).

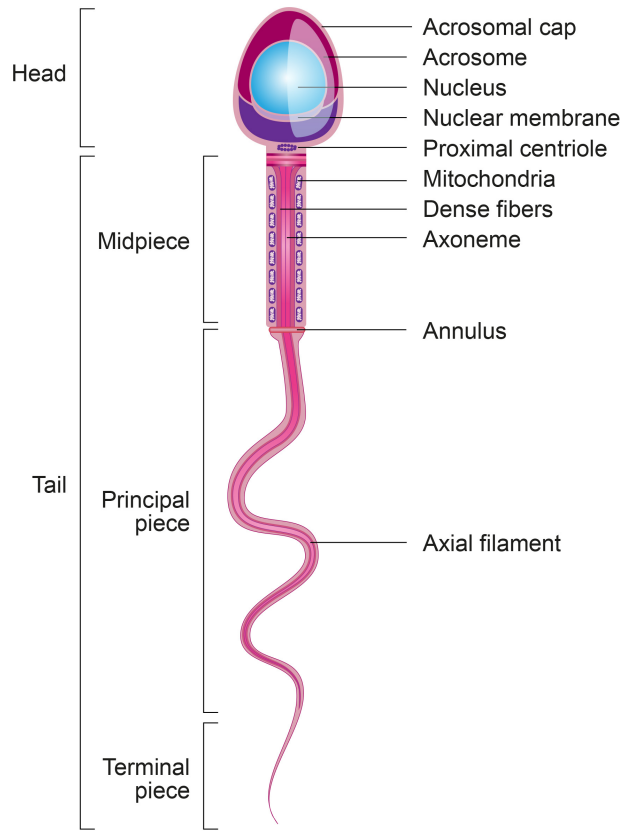

FIGURE 2 | Structural sperm features. Spermatozoa are composed of two main parts: head and tail (or flagellum). The sperm head is constituted basically by the acrosome and nucleus. The sperm tail includes: the neck that contains mainly the proximal centriole; the midpiece which is composed by mitochondria, outer dense fibers (ODF) and axoneme; principal piece containing the fibrous sheath and axoneme; and terminal piece.

RNAS SPECIES ARE MAJOR SPERM INTRINSIC FACTORS

microRNAs and Other Sperm RNA Species

Sperm RNAs were first described in the 1970s in murine and bovine spermatozoa (Betlach and Erickson, 1973; Paul and Duerksen, 1975). Given the limited quantity of cytoplasm and high level of sperm DNA condensation, this finding has been questioned as RNAs were potentially providing from mitochondria or contamination from somatic cells (Krawetz, 2005). In that regards, the roles and the origin of sperm RNAs remain to be determined (Ostermeier et al., 2004; Krawetz, 2005).

Four different RNA species can be distinguished in spermatozoa (Boerke et al., 2007): (1) mRNAs that are remnants from the spermatogenesis process with no known function in the oocyte (e.g., protamine-2 encoding RNA, Ziyyat, 2001); (2) mRNAs that originate from spermatogenesis with a potential function in the oocytes (e.g., PLCζ encoding RNA, Saunders et al., 2002); (3) mRNAs classified as "foreign" RNAs as a result of their acquisition by sperm during passage through the epididymis and by the contact with the fluids coming from the accessory sexual glands (e.g., clusterin encoding RNA, Hermo et al., 1994); and (4) non-coding RNAs (ncRNAs) that are acquired during the late steps of spermatogenesis or during post-testicular sperm maturation with a potential function at the time of fertilization (e.g., miRNAs and tRNA derived fragments, Sharma et al., 2016; Yuan et al., 2016). Among RNA species present in spermatozoa, ribosomal RNAs and mitochondrial RNAs (mtRNAs) are the most abundant, followed by ncRNAs. In contrast to somatic cells that comprise approximately 10 pg of RNA, mature spermatozoa carry around a 1,000-fold lower RNA content (Odia et al., 2018).

In addition to mRNAs, other sperm-borne RNA species, including miRNAs have been associated with sperm cell fertility status and early embryo development (Liu et al., 2012). The central dogma of molecular biology supports that genes are transcribed in the form of mRNAs, which in turn are translated into proteins, with the exception of structural RNAs such as ribosomal RNA (Mattick, 2001). Advancements in molecular biology and studies on the human genome have revealed that only 2% of all genes actually encode proteins (Mattick, 2001). In addition, many genomic sequences that were first described as "junk DNA" due to the fact that they did not encode proteins and had no apparent function, now appear to play an important role as post-transcriptional modulators. In this context, a large group of RNAs called non-coding RNAs (ncRNAs) has been identified in spermatozoa, including miRNAs (Wightman et al., 1993).

MicroRNAs are ∼18–22-nucleotide sequences that modulate gene expression following their pairing with the untranslated region (3′UTR) of target transcripts (Ambros, 2004; Bartel, 2004). The biosynthesis of miRNAs is performed in the cell nucleus with the generation of primary miRNA transcripts (pri-miRNA) and then precursor miRNAs (pre-miRNA), which are transported to the cytoplasm. In the cytoplasm, the hairpin structure is cleaved by Dicer, resulting in small double-stranded transcripts. The miRNA double strand is then transferred to Argonaut proteins, which bind to the mature miRNA also called guide-miRNA. This complex promotes gene silencing through translational inhibition or cleavage of mRNA (Ambros, 2004; Bartel, 2004). Such cleavage is common in plants and occurs when the pairing between the miRNA and 3′UTR region is perfect. On the other hand, an imperfect pairing implies the blockade of translation machinery on that particular mRNA without degradation—the most common process in animals (Bartel, 2004, 2018).

Of interest is that miRNAs either act in the cell where they are transcribed or in target cells through an intercellular communication mechanism (Raposo and Stoorvogel, 2013). Extracellular vesicles are important mediators of this communication. Exosomes comprise a population of small (40–160 nm) extracellular vesicles derived from intracellular multivesicular bodies carrying diverse bioactive molecules, including miRNAs, mRNAs and proteins (Raposo and Stoorvogel, 2013). Once exosomes are released into the extracellular environment, they can be internalized by recipient target cells (Raposo and Stoorvogel, 2013).

TABLE 1 | Correlation between sperm morpho-functional attributes and male fertility.

Sperm morpho-functional attribute	Definition	Required equipment	Correlation with fertility	References
Sperm subjective motility	Maximum percentage of sperm cells with movement	Light field optical microscope, preferably with phase contrast	$r = 0.53$ ($P < 0.01$) ([1]60 to 90-day non-return)	Correa et al., 1997
			$r = 0.67$ ($P = 0.03$) ([1]56-day non-return)	Gillan et al., 2008
Computer assisted sperm analysis (CASA)	Percentage of sperm with motility and measurement of different sperm kinetic features	Light field optical microscope, with phase contrast coupled to a computer	WOB[2]: $r = 0.57$ ($P < 0.05$) ([1]56-day non-return)	Morrell et al., 2018
			$r = 0.67$ ($P = 0.03$) ([1]56-day non-return)	Gillan et al., 2008
			VSL[3]: $r = -0.34$ ($P < 0.05$) ([1]56-day non-return)	Sellem et al., 2015
			ALH[4] and progressive motility presented r^2 of 0.68	Farrell et al., 1998
			ALH[4], BCF[5], LIN[6], VAP[7] and VSL[3] presented r^2 of 0.98	Farrell et al., 1998
Sperm morphological abnormalities	Percentage of cells that present with form defects, often called abnormal cell percentage (Blom, 1973)	Light field optical microscope preferably with differential interference contrast	$r = -0.59$ ($P = 0.01$) ([1]60 to 90-day non-return)	Correa et al., 1997
			$r = -0.76$ ($P < 0.05$) ([1]56-day non-return)	Gillan et al., 2008
			$r = -0.62$ ($P < 0.05$) ([1]56-day non-return)	Morrell et al., 2018
IPIAH[8]	Percentage of IPIAH[8] sperm	Fluorescence microscopy or flow cytometry	High IPIAH[8] (44.5%): 64.7% of pregnancy rate[9] Low IPIAH[8] (8.5%): 36.2% of pregnancy rate[9]	Oliveira et al., 2014
ROS	Percentage of sperm cells producing ROS	Fluorescence microscopy or flow cytometry	High ROS (10.63%): low fertility rates Low ROS (6.11%): high fertility rates	Celeghini et al., 2019
DNA fragmentation	Percentage of sperm cells with DNA fragmentation	Fluorescence microscopy or flow cytometry	$r = -0.56$ ($P < 0.01$)	Morrell et al., 2018
Capacitation status	Percentage of acrosome-reacted spermatozoa	Fluorescence microscopy or flow cytometry	$r = 0.37$ ($P < 0.05$) ([1]litter size)	Kwon et al., 2015

[1]Fertility measurement; [2]wobble (%); [3]progressive velocity (μm/s); [4]lateral head amplitude (μm); [5]beat cross frequency (Hz); [6]linearity (%); [7]path velocity (μm/s); [8]spermatozoa with intact plasma and acrosome membranes and high mitochondrial membrane potential; [9]ultrassonography exam 30 days after insemination.

Exosomes are released from different internal organs of the male reproductive tract, including the epididymis (epididymosomes) and prostate (prostasomes) (Sullivan and Saez, 2013). Epididymosomes play a key role during cellular communication that promotes sperm maturation during spermatozoa passage into the microenvironment of the epididymis (Belleannée, 2015).

In general, miRNAs are post-transcriptional regulators that play important roles in physiological processes and their impairment results in different pathologies. These molecules have been shown to have great importance in the regulation of spermatogenesis (Papaioannou et al., 2009; Kotaja, 2014) and sperm maturation during sperm passage through the epididymis (Björkgren et al., 2012; Jerczynski et al., 2016; Sipilä and Björkgren, 2016) as shown in **Figure 5**. With the knowledge that miRNAs are very stable, conserved bioactive molecules derived from the different internal organs of the male reproductive tract, they could be considered potent fertility biomarkers. In light of these findings, sperm cells have gained the status of gametes that are not only responsible for transporting genetic material, but also as contributors to the activation of the oocyte and the cellular structure and molecular components of the zygote as shown in **Figure 5**.

miRNAs and Spermatogenesis

Spermatogenesis is a well-organized process that culminates in the production of sperm cells. Conditional knock-out of the miRNA processing enzyme Dicer1 in Sertoli cells triggers male infertility due to the absence of sperm in the lumen of the seminiferous tubules and spermatogenesis disorders (Papaioannou et al., 2009; Zimmermann et al., 2014), suggesting that the biogenesis of small non-coding RNA is important to spermatogenesis. Indeed, each cell type of the seminiferous tubule has a different miRNA profile that plays an important role in proliferation and differentiation (Hayashi et al., 2008; Smorag et al., 2012). In pigs, miR-26a has been shown to inhibit proliferation and to promote apoptosis in Sertoli cells, thus impairing sperm production (Ran et al., 2018). In mice, miR−221 and

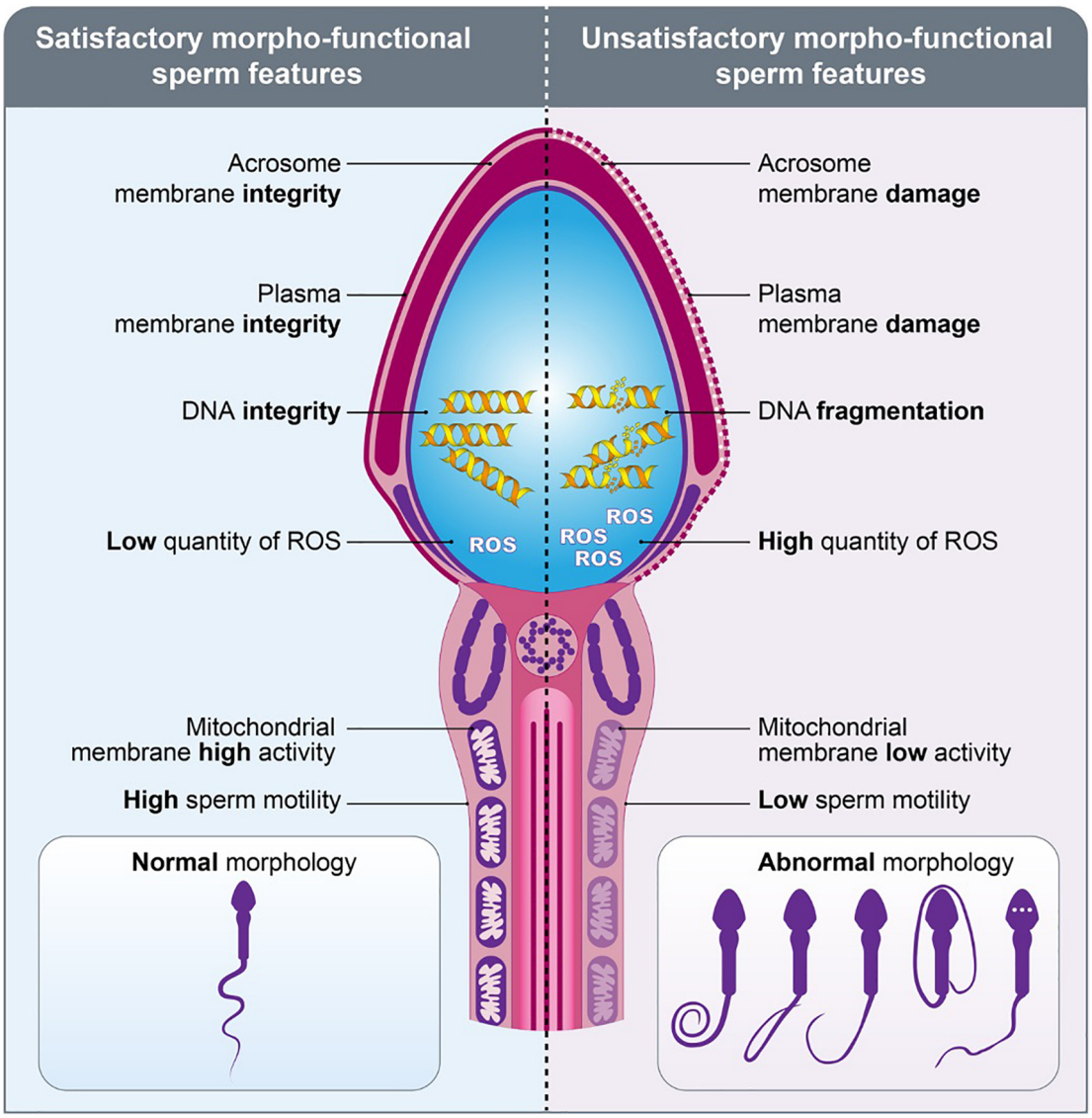

FIGURE 3 | Morpho-functional sperm features. Schematic figure representing the spermatozoa with satisfactory **(left)** and unsatisfactory **(right)** morpho-functional features. Sperm acrosome membrane integrity, sperm plasma membrane integrity, sperm DNA integrity, low quantity of ROS, sperm mitochondrial membrane high activity, high sperm motility and normal sperm morphology characterize the satisfactory morpho-functional sperm features. Sperm acrosome membrane damage, sperm plasma membrane damage, sperm DNA fragmentation, high quantity of ROS, sperm mitochondrial membrane low activity, low sperm motility and abnormal sperm morphology characterize the unsatisfactory morpho-functional sperm features.

miR−290 regulate the proliferation of spermatogonia and primary spermatocytes (Smorag et al., 2012). In addition, miR−203 modulates spermatocyte meiosis and the miR−34 family regulates the formation of spermatids (Smorag et al., 2012). In humans, pigs and mice, the miR−34 family is also important in the regulation of spermatogenesis (Bouhallier et al., 2010; Zimmermann et al., 2014). Thus, miRNAs such as miR−26a, miR−221, miR−290, miR−203, and the miR−34 have been proposed to contribute to spermatozoa production (**Figure 5**), as their dysregulation results in disturbances in spermatogenesis and consequently a decrease in male fertility potential.

miRNAs and Sperm Maturation

Once produced in the testis, spermatozoa must pass through the epididymis to acquire their motility and oocyte-fertilizing ability. During their passage through the different epididymal segments, spermatozoa come into contact with different repertoires of ncRNAs, transcripts and proteins that are released from the epithelium of the epididymis mostly via epididymosomes (Sullivan et al., 2007; Belleannée et al., 2013; Sullivan, 2015; Reilly et al., 2016; Sharma et al., 2018). The transfer of proteins and other contents from epididymosomes to spermatozoa has been proposed to occur via the dynamin 1 mechanoenzyme following the tethering of epididymosomes to specific sperm

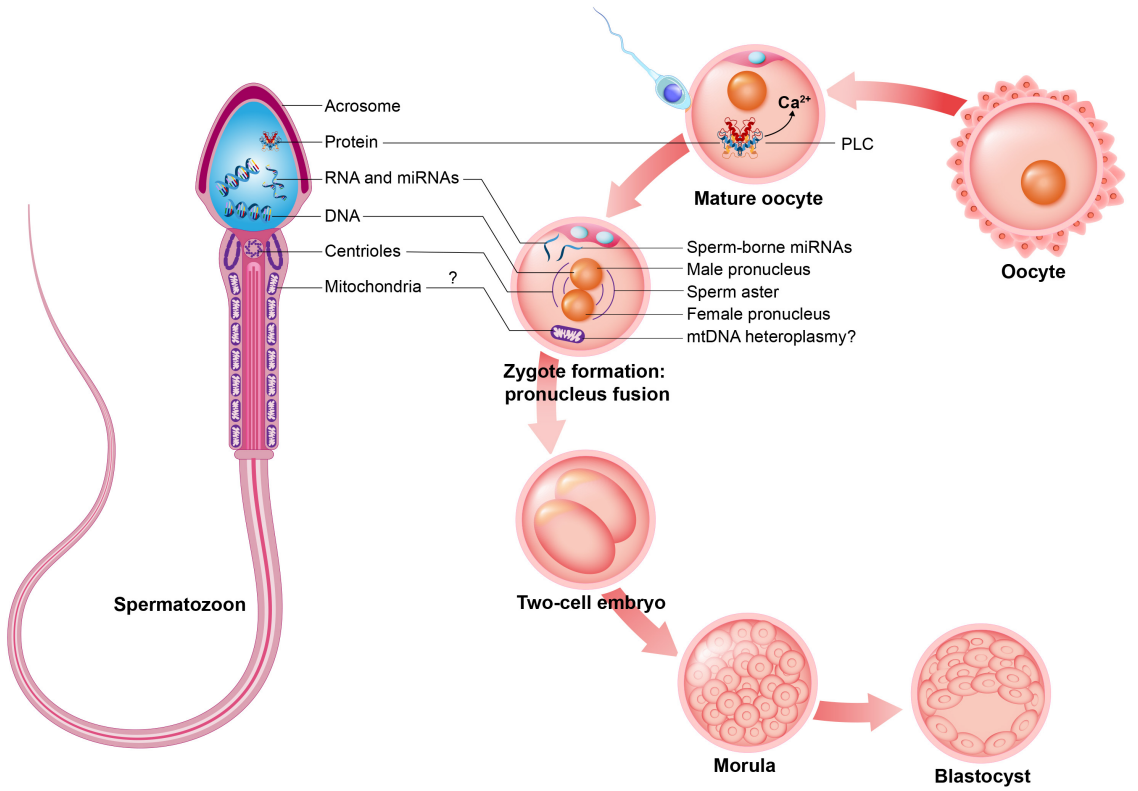

FIGURE 4 | Intrinsic sperm features. Spermatozoon contributes early embryo development during mature oocyte fertilization, zygote formation and embryo cleavage potentially with intrinsic sperm features such as: sperm proteins (e.g., PLCζ, to promote oocyte activation); sperm RNAs and microRNAs (miRNAs); sperm DNA, to generate male pronucleus; sperm centrioles, to form sperm aster; and may contribute sperm mitochondria, promoting mtDNA heteroplasmy.

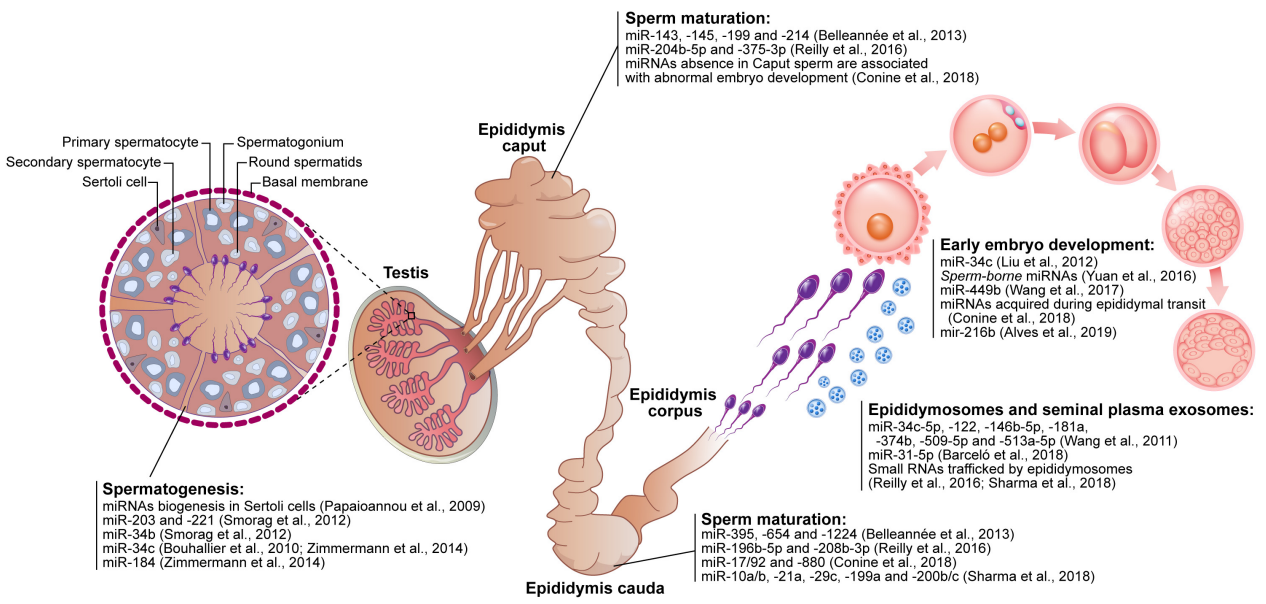

FIGURE 5 | Schematic figure demonstrating the contribution of microRNAs (miRNAs) in the reproductive events. The sperm-related-miRNAs molecules display functions in spermatogenesis (testis), sperm maturation (epididymis *caput*, *corpus,* and *cauda*), sperm and seminal plasma interaction (e.g., epididymosomes) as well as modulating early embryo development.

receptors located in the post-acrosomal region and the fusion of epididymosomes with the sperm membrane (Zhou et al., 2019). In mice, sperm miRNAs present in the sperm are altered along the epididymis (**Figure 5**), showing that the sperm miRNA content is dynamic even following spermatogenesis (Nixon et al., 2015).

Conditional knock-out mice for the *Dicer* enzyme in principal cells of the epididymis dysregulated the differentiation process (Björkgren et al., 2012). Thus, biogenesis of ncRNAs seems to be important in the regulation of epididymal epithelium, sperm maturation and fertility. While miR-10a/b, −21a, −29c, −196b−5p, −199a, −200b/c, and −208b−3p accumulate in spermatozoa during passage through the epididymis, miR−204b−5p and miR−375−3p are more abundant in spermatozoa from the *caput* and *corpus* of the epididymis (Reilly et al., 2016; Sharma et al., 2018). Epididymosomes also display different miRNA profiles and traffic small RNAs to spermatozoa (Sharma et al., 2018), including miR−143, −145, −199, and −214 that are more abundant in epididymosomes present in the *caput* of the bovine epididymis, and miR−395, −654, and −1224 that are more abundant in epididymosomes from the *cauda* (Belleannée et al., 2013). In men with reproductive abnormalities, miRNAs present in seminal plasma (miR−34c−5p, −122, −146b−5p, −181a, −374b, −509−5p, and −513a−5p) decreased in abundance in men presenting with azoospermia (absence of spermatozoa in the ejaculate) and increased in abundance in men presenting with asthenozoospermia (decreased sperm motility) (Wang et al., 2011). Although studies have shown the importance of miRNAs along the epididymis, further work is required to show how miRNAs are able to regulate sperm maturation during passage of spermatozoa through the epididymis and how regulation of motility acquisition and the ability of the sperm to become fertile occur.

CONTRIBUTION OF SPERM INTRINSIC FACTORS TO POST-FERTILIZATION PROCESSES

For many years it was postulated that sperm cells had the exclusive function of transporting genetic material to the oocyte. However, at the end of the 20th century, this sole contribution was challenged by the fact that specific sperm intrinsic factors, including sperm centrioles, sperm proteins, ribonucleic acids and mitochondrial DNA (mtDNA) could contribute to fertilization and/or early embryo development (**Figure 6**).

Contribution of the Sperm Centriole to Embryo Development

Centrioles are cytoplasmic structures involved in cell division and in the formation of cilia and flagella (Avidor-Reiss and Fishman, 2019). While spermatozoa present with centrioles arranged in the neck of their tail (**Figure 2**), mature oocytes lack centrioles (Simerly et al., 2018). Therefore, sperm-derived centrioles ensure the formation of sperm aster and centrosome in the fertilized oocyte, which bring the female and male pronuclei into close proximity and promote syngamy (Simerly et al., 1995; Schatten and Sun, 2009), as shown in **Figure 4**. Thus, centrioles are organelles that ensure proper embryonic development. In addition, the proper formation of the sperm aster is an important factor related to male fertility. For instance, large and well organized sperm aster formations in human spermatozoa correlate with samples that present with high fertility, while small and disorganized sperm aster formations correlate with low fertility samples (Navara et al., 1997). Therefore, beyond the transmission of the centrioles by the sperm cells, the quality of the sperm-borne centrioles is also important to embryo development. It has recently been shown that sperm from non-rodent mammals are responsible for transmitting a second atypical centriole to oocyte (Fishman et al., 2018). This centriole potentially forms the sperm aster and centrosome in the oocytes and, together with the first centriole, supports the fusion between the female and male pronucleus.

The Questioned Contribution of Sperm Mitochondrial DNA to Embryo Paternal Inheritance

Mitochondria are peculiar organelles that possess a specific DNA type: mtDNA. This organelle is essentially responsible for energy production, which is important to the cell's activity. During spermatogenesis, sperm mitochondria change from a conventional to a condensed form that ensures more efficient energy production (Amaral et al., 2013). While some mitochondria are lost during spermatogenesis, between 22 and 75 mitochondria remain in the midpiece of the mature spermatozoon depending on species (**Figure 2**) (Bahr and Engler, 1970; Song and Lewis, 2008). Although spermatic mitochondria also contain mtDNA, the current paradigm is that the embryo exclusively possesses maternal mitochondria and, consequently, mitochondrial diseases are only inherited from the mother (Hecht et al., 1984). However, the inheritance of paternal mtDNA was suggested following the discovery of a high level of mtDNA heteroplasmy, i.e., mix of maternal and paternal mitochondrial genome, in mouse (Gyllensten et al., 1991) and human (17 individuals) (Luo et al., 2018) as schematized in **Figure 4**. These findings open new research avenues to better understand mitochondrial disease inheritance. However, further studies are necessary to confirm this potential paradigm shift.

Contribution of Sperm Proteins to Oocyte Activation

While mature spermatozoa are transcriptionally inactive upon their entrance to the epididymis, their proteome is dynamic due to the acquisition of proteins from the surrounding fluid, the cleavage of others from the sperm surface, and the rearrangement of acrosomal proteins during sperm capacitation. These proteins ensure diverse functions at different stages including: **sperm maturation**, e.g., the glioma pathogenesis-related 1-like protein 1 (GLiPr1L1) that is acquired by spermatozoa and participates in the binding of sperm cells to zona pellucida (Caballero et al., 2012); **tagging of sperm sub-populations to ensure heterogeneity**, e.g., the sperm binding protein 1 (ELSPBP1) that discriminates dead spermatozoa (D'Amours et al., 2012); and

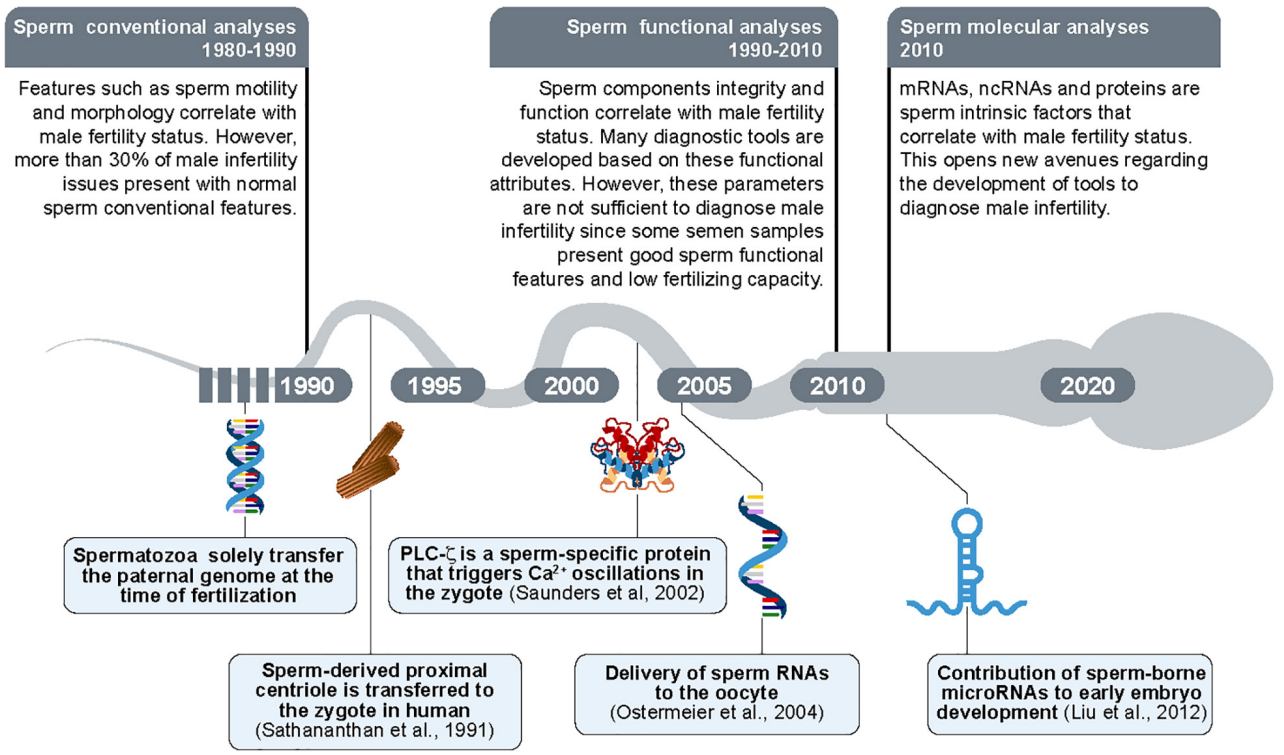

FIGURE 6 | Timeline of the new findings regarding sperm morpho-functional and intrinsic features. The paternal DNA was considered as the sole intrinsic sperm feature transferred from spermatozoon to oocyte until 1990s. In parallel, the sperm evaluation was limited to sperm conventional analyses (sperm motility and sperm morphology/abnormalities). Proximal centrioles were then shown to be transmitted by sperm to the oocytes during fertilization for the first time in 1991 (Sathananthan et al., 1991). The sperm-borne PLCζ protein was shown as a promotor of oocyte activation in 2002 (Saunders et al., 2002). The delivery of RNAs molecules was then revealed as transferred from sperm to the oocyte in 2004 (Ostermeier et al., 2004). In parallel, the sperm evaluation was updated to sperm functional analyses (e.g., sperm plasma membrane integrity). In 2010s, small sperm-borne RNAs molecules (microRNAs/miRNAs) were shown as important to early embryo development (Liu et al., 2012) potentially constituting a new group of sperm analyses composed by evaluation of molecular targets.

sperm ability to bind to the oocyte, e.g., Spermadhesin AWN (AWN) that promotes sperm binding to oocyte's zona pellucida during fertilization (Kwon et al., 2014).

In addition to these proteins, sperm cells also acquire proteins during the final steps of spermatogenesis that are important to **oocyte activation**, e.g., the sperm-specific WW domain-binding protein (PAWP) and phospholipase C zeta (PLCζ) (Saunders et al., 2002; Wu et al., 2007). Among these spermatic proteins, PLCζ is an important player during fertilization, since it triggers intracellular calcium impulses required for oocyte activation (Saunders et al., 2002; Kashir et al., 2010). As a result of these impulses, and once fertilized, the metaphase II mature oocyte is able to resume and progress through meiotic division. This ensures the formation of female and male pronuclei, followed by syngamy (**Figure 4**). The presence of these proteins in spermatozoa positively correlates with male fertility (Saunders et al., 2002; Aarabi et al., 2014).

Contribution of Sperm RNA Species to Embryo Development

Sperm RNAs

The detection of sperm-borne RNAs, including *clusterin* and *AKAP4,* in embryos raised questions regarding their potential contribution to the molecular regulation of embryonic development (Ostermeier et al., 2004). The discovery of zygote transcripts originating exclusively from spermatozoa opened new avenues into the investigation of sperm RNAs and their importance to embryo development (Ostermeier et al., 2005; Jodar et al., 2013). Most sperm RNAs are transcribed and then stored or inactivated in spermatozoa during spermiogenesis. During this stage of spermatogenesis, histones are replaced by protamines in sperm DNA, changing the shape of nucleosomes to a toroid structure with high sperm nuclear condensation culminating in gene expression silencing. However, 1% of histones in mice and 10–15% of histones in humans and cattle remain in the form of nucleosomes in spermatozoa (Samans et al., 2014). The remaining nucleosomes in human and bovine spermatozoa are located in similar promoter regions, indicating transcriptional conservation of specific genes related to early embryonic development (Samans et al., 2014). Even if the presence of RNAs is now accepted in spermatozoa, there is no evidence showing that RNAs can be transcribed from DNA in mature spermatozoa. Most of the RNAs present in sperm cells are thus potentially acquired during spermatogenesis as well as during passage through the epididymis.

Even though sperm cells possess limited quantities of sperm RNAs, sperm-borne RNAs have been associated with many relevant reproductive processes and several correlate with fertility potential in the bull, including AK1 (adenylate kinase 1; R^2 = 0.90), IB (integrin β5, R^2 = 0.95), NGF (R^2 = 0.47), TIMP (tissue inhibitor of metalloproteinases, R^2 = 0.39), SNRPN (small nuclear ribonucleoprotein polypeptide N, R^2 = 0.71) and PLCζ (phospholipase C, R^2 = 0.69) (Kasimanickam et al., 2012). Similarly, the presence of 415 transcripts out of 24,000, were found in different proportions between bovine spermatozoa presenting with high or low fertility potential (Feugang et al., 2010). In human sperm cells, ANXA2 (Annexin A2), BRD2 (Bromodomain Containing 2), OAZ3 (Ornithine Decarboxylase Antizyme 3), PRM1 (Protamine 1) and PRM2 (Protamine 2) transcripts were present in lower amounts in sperm cells with low motility (Jodar et al., 2013).

Sperm miRNAs

Until embryonic gene activation, i.e., when the embryo begins to transcribe its newly formed genome, embryo development relies on the expression of maternal transcripts originating from the oocyte and, to a lesser extent, from spermatozoa. MicroRNAs are also delivered by gametes to the embryos. Until activation of the embryonic genome the abundance of miRNA transcripts present in the embryo decreases until embryonic gene activation begins (Tang et al., 2007). Murine embryos produced from *Dicer* enzyme knock-out oocytes fail to undergo the first cell division, demonstrating the importance of the miRNAs or other ncRNAs contributed by the female gamete during early embryonic development (Tang et al., 2007). Similarly, murine embryos generated with normal oocytes and *Dicer* or *Drosha* enzyme knock-out spermatozoa showed decreased development rates, which recovered following the replacement of miRNAs (Yuan et al., 2016). In addition, the inhibition of miR-34c, which is exclusively delivered by sperm to the embryo in mice (Liu et al., 2012), but not in cattle (Tscherner et al., 2014), prevents the first cleavage (Liu et al., 2012). Sperm-borne miR−449b overexpression in cloned embryos is associated with enhanced cleavage rates at the 8-cell stage and lower rates of apoptosis in the blastocyst (Wang et al., 2017). Sperm-borne miR−216b was recently shown to be present at higher abundance in spermatozoa from low fertility bulls and is associated with a reduced first cleavage rate as well as a reduced number of cells in blastocysts (Alves et al., 2019). In parallel, the RNAs that are acquired by spermatozoa during epididymal transit were shown to be essential for embryo implantation and development in mice (Conine et al., 2018, 2019). Thus, despite the decrease in miRNA levels until activation of the embryonic genome, proper embryo development potentially relies on miRNAs delivered by the gametes (**Figure 5**).

Contribution of Small Non-coding RNAs to Transgenerational Inheritance of Traits

The transgenerational inheritance of traits concerns the transmission of characteristics from the parents to the offspring, i.e., heritable phenotype, without altering the DNA sequence (Weinhold, 2006). Following advances in the field of epigenetics, i.e., the study of inheritance that is not based on DNA sequence, but on how the DNA sequence is utilized, miRNAs transmitted by spermatozoa at the time of fertilization are considered epigenetic factors that have some effects on the offspring.

Environmental conditions such as toxicant exposure (Schuster et al., 2016), mental stress (Rodgers et al., 2013), alcohol consumption (Rompala et al., 2018), and low protein or high fat diet (Sharma et al., 2016) are considered principal modulators of epigenetic markers by promoting alterations in the sperm "epigenome." Rodgers et al. (2015) identified nine miRNAs that had altered abundance in the sperm cells from mice submitted to chronic stress. Surprisingly, the injection of these nine miRNAs into embryos of non-stressed parents recapitulated the effects observed in parents undergoing chronic stress (Rodgers et al., 2015). In a similar manner, regulation of another group of ncRNAs in sperm cells, the tRNA-derived fragments, was dependent on the diet of the sire and this influenced the offspring phenotype (Sharma et al., 2016). These studies show that sperm-borne ncRNAs potentially own epigenetic influence. However, further studies are necessary in order to explain the mechanism of action of these molecules in the offspring.

LINKING MIRNAS TO MALE (IN)FERTILITY STATUS

Since miRNAs play an important role in the physiological processes related to spermatogenesis, sperm maturation and early embryonic development (**Figure 5**), these molecules have the potential to modulate sperm morpho-functional features as well as male fertility ability. In that regards, different miRNA profiles have been associated with different sperm quality levels and fertility phenotypes from animal models and human clinical samples as listed in **Table 2**.

Functional studies have been carried out in knock-out mouse models to determine the contribution of individual miRNAs to male fertility (Comazzetto et al., 2014; Wu et al., 2014). For instance, simultaneous deletion of miR34b/c and miR−449 triggered male infertility following the impairment of spermatogenesis, motile ciliogenesis, and sperm maturation (Comazzetto et al., 2014; Wu et al., 2014). While targeted deletion is essential to unravel the function of specific miRNAs *in vivo*, phenotypic effects are rarely observed after invalidation of a single miRNA-encoding gene due to compensatory functions of related miRNAs. These functional approaches were complemented by several correlative studies performed in large mammals and humans.

Within livestock animals, bulls that presented satisfactory sperm quality and history of distinct fertility (high *vs.* low fertility) displayed different profiles of sperm miRNAs that are summarized in **Table 2** (Fagerlind et al., 2015; Alves et al., 2019; Menezes et al., 2019). Similarly, spermatozoa from boar featuring low motility and a high percentage of abnormalities, displayed a higher abundance of the miRNAs: let−7a, let−7d, let−7e, and miR−22; and lower abundance of miR−15b (Curry et al., 2011) compared with spermatozoa presenting with normal features. In addition, Capra et al. (2017) sorted spermatozoa

TABLE 2 | Sperm miRNAs associated with different infertility issues in porcine, human, bovine and mouse.

miRNAs	Abundance	Phenotype associate	Specie	References
let-7a	Down-regulated	Low abnormalities	Porcine	Curry et al., 2011
let-7a-5p	Down-regulated	High fertility	Human	Salas-Huetos et al., 2016
let-7d	Down-regulated	Low abnormalities/High motility	Porcine	Curry et al., 2011
let-7e	Down-regulated	Low abnormalities/High motility	Porcine	Curry et al., 2011
let-7f-5p	Down-regulated	High fertility	Human	Salas-Huetos et al., 2016
miR-9-3p	Down-regulated	High fertility	Human	Salas-Huetos et al., 2016
miR-15a	Down-regulated	High fertility	Bovine	Menezes et al., 2019
miR-15b	Up-regulated	Low abnormalities	Porcine	Curry et al., 2011
miR-15b	Down-regulated	Oligoasthenozoospermic	Human	Abu-Halima et al., 2013
miR-16	Down-regulated	Oligoasthenozoospermic	Human	Abu-Halima et al., 2013
miR-17-5p	Up-regulated	High motility sperm	Bovine	Capra et al., 2017
miR-19a	Down-regulated	Oligoasthenozoospermic	Human	Abu-Halima et al., 2013
miR-19b-3p	Down-regulated	High fertility	Bovine	Fagerlind et al., 2015
miR-20a-5p	Up-regulated	High motility sperm	Bovine	Capra et al., 2017
miR-22	Down-regulated	Low abnormalities	Porcine	Curry et al., 2011
miR-22-3p	Down-regulated	High fertility	Human	Salas-Huetos et al., 2016
miR-26a-5p	Up-regulated	High motility sperm	Bovine	Capra et al., 2017
miR-27a-5p	Down-regulated	High fertility	Bovine	Fagerlind et al., 2015
miR-29b	Down-regulated	High fertility	Bovine	Menezes et al., 2019
miR-30b-5p	Down-regulated	High fertility	Human	Salas-Huetos et al., 2016
miR-30d-3p	Down-regulated	High fertility	Human	Salas-Huetos et al., 2016
miR-33b	Up-regulated	High fertility	Bovine	Alves et al., 2019
miR-34a-5p	Up-regulated	High fertility	Human	Salas-Huetos et al., 2016
miR-34b	Down-regulated	Oligoasthenozoospermic	Human	Abu-Halima et al., 2013
miR-34c	Up-regulated	High fertility	Mouse	Liu et al., 2012
miR-34c-5p	Down-regulated	Oligoasthenozoospermic	Human	Abu-Halima et al., 2013
miR-34c-3p	Down-regulated	High fertility	Bovine	Fagerlind et al., 2015
miR-93-3p	Down-regulated	High fertility	Human	Salas-Huetos et al., 2016
miR-103a-3p	Down-regulated	High fertility	Human	Salas-Huetos et al., 2016
miR-122	Down-regulated	Oligoasthenozoospermic	Human	Abu-Halima et al., 2013
miR-122-5p	Down-regulated	High motility sperm	Bovine	Capra et al., 2017
miR-126-5p	Up-regulated	High fertility	Bovine	Alves et al., 2019
miR-127	Down-regulated	Capacitated sperm	Porcine	Li et al., 2018
miR-130b-5p	Down-regulated	High fertility	Human	Salas-Huetos et al., 2016
miR-132-5p	Down-regulated	High fertility	Human	Salas-Huetos et al., 2016
miR-145-5p	Down-regulated	High fertility	Human	Salas-Huetos et al., 2016
miR-148b-3p	Down-regulated	High fertility	Bovine	Fagerlind et al., 2015
miR-149-3p	Down-regulated	High fertility	Human	Salas-Huetos et al., 2016
miR-151-3p	Up-regulated	Capacitated sperm	Porcine	Li et al., 2018
miR-152	Down-regulated	Capacitated sperm	Porcine	Li et al., 2018
miR-181a-3p	Down-regulated	High fertility	Human	Salas-Huetos et al., 2016
miR-184	Down-regulated	High motility sperm	Bovine	Capra et al., 2017
miR-193b-5p	Down-regulated	High fertility	Human	Salas-Huetos et al., 2016
miR-205	Up-regulated	High fertility	Bovine	Alves et al., 2019
miR-208a	Up-regulated	High fertility	Human	Salas-Huetos et al., 2016
miR-212-3p	Up-regulated	High fertility	Human	Salas-Huetos et al., 2016
miR-216b	Down-regulated	High fertility	Bovine	Alves et al., 2019
miR-222-5p	Down-regulated	High fertility	Human	Salas-Huetos et al., 2016
miR-296-5p	Down-regulated	High fertility	Human	Salas-Huetos et al., 2016
miR-320a	Down-regulated	High fertility	Bovine	Fagerlind et al., 2015
miR-324-3p	Up-regulated	High fertility	Human	Salas-Huetos et al., 2016

(Continued)

TABLE 2 | Continued

miRNAs	Abundance	Phenotype associate	Specie	References
miR-339a	Down-regulated	High fertility	Bovine	Alves et al., 2019
miR-339-5p	Down-regulated	High fertility	Human	Salas-Huetos et al., 2016
miR-340-3p	Down-regulated	High fertility	Human	Salas-Huetos et al., 2016
miR-346	Down-regulated	High fertility	Human	Salas-Huetos et al., 2016
miR-365a-3p	Down-regulated	High fertility	Human	Salas-Huetos et al., 2016
miR-432-3p	Down-regulated	High fertility	Human	Salas-Huetos et al., 2016
miR-449a	Down-regulated	Oligoasthenozoospermic	Human	Abu-Halima et al., 2013
miR-483-5p	Up-regulated	High fertility	Human	Salas-Huetos et al., 2016
miR-486-5p	Down-regulated	High motility sperm	Bovine	Capra et al., 2017
miR-487a	Down-regulated	High fertility	Human	Salas-Huetos et al., 2016
miR-491-5p	Up-regulated	High fertility	Human	Salas-Huetos et al., 2016
miR-500	Up-regulated	High fertility	Bovine	Alves et al., 2019
miR-502-5p	Down-regulated	High fertility	Bovine	Fagerlind et al., 2015
miR-505	Up-regulated	High fertility	Bovine	Alves et al., 2019
miR-517-5p	Down-regulated	High fertility	Human	Salas-Huetos et al., 2016
miR-518d-5p	Down-regulated	High fertility	Human	Salas-Huetos et al., 2016
miR-518f-3p	Up-regulated	High fertility	Human	Salas-Huetos et al., 2016
miR-520c-3p	Down-regulated	High fertility	Human	Salas-Huetos et al., 2016
miR-520d-3p	Up-regulated	High fertility	Human	Salas-Huetos et al., 2016
miR-526b-5p	Down-regulated	High fertility	Human	Salas-Huetos et al., 2016
miR-532	Up-regulated	High fertility	Bovine	Alves et al., 2019
miR-542-5p	Up-regulated	High fertility	Bovine	Alves et al., 2019
miR-543	Down-regulated	High fertility	Human	Salas-Huetos et al., 2016
miR-552	Down-regulated	High fertility	Human	Salas-Huetos et al., 2016
miR-564	Up-regulated	High fertility	Human	Salas-Huetos et al., 2016
miR-573	Down-regulated	High fertility	Human	Salas-Huetos et al., 2016
miR-596	Down-regulated	High fertility	Human	Salas-Huetos et al., 2016
miR-622	Down-regulated	High fertility	Human	Salas-Huetos et al., 2016
miR-636	Up-regulated	High fertility	Human	Salas-Huetos et al., 2016
miR-644a	Down-regulated	High fertility	Human	Salas-Huetos et al., 2016
miR-659-3p	Down-regulated	High fertility	Human	Salas-Huetos et al., 2016
miR-708-5p	Up-regulated	High fertility	Human	Salas-Huetos et al., 2016
miR-744-5p	Down-regulated	High fertility	Human	Salas-Huetos et al., 2016
miR-766-3p	Down-regulated	High fertility	Human	Salas-Huetos et al., 2016
miR-935	Down-regulated	High fertility	Human	Salas-Huetos et al., 2016
miR-942	Down-regulated	High fertility	Human	Salas-Huetos et al., 2016
miR-1249	Down-regulated	High fertility	Bovine	Fagerlind et al., 2015
miR-1254	Up-regulated	High fertility	Human	Salas-Huetos et al., 2016
miR-1285	Down-regulated	Capacitated sperm	Porcine	Li et al., 2018
miR-1296	Down-regulated	High fertility	Human	Salas-Huetos et al., 2016
miR-1298	Down-regulated	High fertility	Human	Salas-Huetos et al., 2016
miR-1973	Up-regulated	Asthenozoospermic	Human	Abu-Halima et al., 2013
miR-1973	Down-regulated	Oligoasthenozoospermic	Human	Abu-Halima et al., 2013

according to their motility and showed that miR−17−5p, −20a−5p, −26a−5p, −122−5p, −184, and −486−5p were differently displayed between the two subpopulations (Capra et al., 2017). Capacitated and non-capacitated spermatozoa also appeared to show different miRNAs profiles. For instance, Li et al. (2018) showed that miR−127, −151−3p, −152, −1285 were differently expressed in *in natura* (fresh) compared to capacitated boar sperm (Li et al., 2018). Based on that sperm miRNAs features, variation in expression of miRNAs associated with economically important infertility issues might open avenues to the development of selection programs in livestock animals. Targeting seminal miRNAs candidates as non-invasive biomarkers for male infertility could thus have profound economic impact on livestock industry.

In humans, sperm miRNA profiles from fertile and infertile men accompanied or not by morpho-functional sperm alterations have been extensively investigated. In that regards, men with reproductive disorders presented different sperm miRNA profiles compared with normospermic control individuals: *asthenozoospermia* (low sperm motility) was

associated with higher abundance of 50 sperm miRNAs, among then hsa-miR−34b, −122, and −1973, and lower abundance of 27 sperm miRNAs; *oligoasthenozoospermia* (low sperm concentration and low sperm motility) was associated with higher abundance of 42 miRNAs (hsa-miR−15b, −16, −19a, −34b, −34c−5p, −122, −449a e −1973 were the most abundant) and lower abundance of 44 miRNAs (Abu-Halima et al., 2013); *teratozoospermia* (abnormal sperm morphology) was associated with the downregulation of six miRNAs (hsa-miR−151−5p, −935, −125a−3p, −132−5p, −320b, −195−5p) (Salas-Huetos et al., 2015). On the other hand, the sperm miRNA profile of men who presented normal semen quality (normozoospermic), but had a different fertility performance (fertile *vs.* infertile) showed that 57 miRNAs were presented at a different abundance between the groups. Among these miRNAs miR-15b−5p and 34a−5p, were related to pathways linked to embryonic development and chromatin remodeling (Salas-Huetos et al., 2016). Correlations were also observed between sperm miRNA content and assisted reproductive technology (ART) outcomes. For instance, the study from Cui et al. (2015) indicated that the proportion of good quality embryos obtained after 3 days post-ICSI positively correlated with the amount of hsa-miR−34c found in spermatozoa (Cui et al., 2015). While several confounding factors might be considered before drawing extrapolative conclusions, some spermatic miRNAs may thus become predictive biomarker of defective spermatozoa and ART outcome. Tentative explanations have been proposed regarding the molecular mechanism involved in these correlative observations between sperm miRNA profiles and fertility levels. For instance, hsa-miR−27a that is increased in asthenoteratozoospermic patients regulates the post-transcriptional expression of the Cysteine-Rich Secretory Protein2 (CRISP2), which encodes for a protein playing a role in sperm motility, acrosome reaction and gamete fusion (Zhou et al., 2017).

Overall, the different studies performed on human clinical samples as well as on animal models have shown that different profiles of sperm miRNA content can be observed according to sperm morpho-functional features and fertility status. Extracellular miRNAs correlated with male infertility issues are also retrieved in seminal plasma (Barceló et al., 2018), which encompasses secretions from the different internal organs of the male reproductive tract. While both spermatic and extracellular RNA could be used as molecular targets for the non-invasive diagnosis of male infertility and reproductive system diseases, a better understanding of miRNA-mediated regulation of reproductive functions is needed.

FINAL CONSIDERATIONS

In summary, sperm cells should display specific factors to fulfill the "healthy sperm" concept, including proper morpho-functional features in addition to intrinsic factors. While sperm cell morpho-functional attributes are not always sufficient to predict male fertility potential, spermatozoa carry different factors, including organelles (centrioles, mitochondria) and molecules (proteins, RNAs, ncRNAs), which are involved in important steps of reproductive biology, e.g., spermatogenesis, sperm maturation, fertilization and embryo development. These factors constitute potential biomarkers of "healthy sperm" and male fertility status and may become major assets for diagnosing instances of idiopathic male infertility in both humans and livestock animals. A better understanding of the mechanism of action of these sperm intrinsic factors in the regulation of reproductive and developmental processes still presents a major challenge that must be addressed.

AUTHOR CONTRIBUTIONS

CB, MA, and EC wrote the manuscript and designed the figures. All the authors revised the manuscript.

FUNDING

We are grateful to the São Paulo Research Foundation (FAPESP) and the Natural Sciences and Engineering Research Council of Canada for financing the studies by the authors described in this review (MA was funded by FAPESP Grants #2015/09154-6 and #2016/23243-4. EC was funded by FAPESP Grant #2016/05395-1. CB was the recipient of an NSERC discovery grant).

REFERENCES

Aarabi, M., Balakier, H., Bashar, S., Moskovtsev, S. I., Sutovsky, P., Librach, C. L., et al. (2014). Sperm content of postacrosomal WW binding protein is related to fertilization outcomes in patients undergoing assisted reproductive technology. *Fertil. Steril.* 102, 440–447. doi: 10.1016/j.fertnstert.2014.05.003

Abu-Halima, M., Hammadeh, M., Schmitt, J., Leidinger, P., Keller, A., Meese, E., et al. (2013). Altered microRNA expression profiles of human spermatozoa in patients with different spermatogenic impairments. *Fertil. Steril.* 99, 1249.e16–1255.e16. doi: 10.1016/j.fertnstert.2012.11.054

Agarwal, A., Mulgund, A., Hamada, A., and Chyatte, M. R. (2015). A unique view on male infertility around the globe. *Reprod. Biol. Endocrinol.* 13, 1–9. doi: 10.1186/s12958-015-0032-1

Aitken, R. J., Wingate, J. K., De Iuliis, G. N., and McLaughlin, E. A. (2007). Analysis of lipid peroxidation in human spermatozoa using BODIPY C11. *MHR Basic Sci. Reprod. Med.* 13, 203–211. doi: 10.1093/molehr/gal119

Alves, M. B. R., de Arruda, R. P., De Bem, T. H. C., Florez-Rodriguez, S. A., Sá Filho, M. F., de Belleannée, C., et al. (2019). Sperm-borne miR-216b modulates cell proliferation during early embryo development via K-RAS. *Sci. Rep.* 9, 1–14. doi: 10.1038/s41598-019-46775-8

Amann, R. P., and Hammerstedt, R. H. (1993). In vitro evaluation of sperm quality: an opinion. *J. Androl.* 14, 397–406. doi: 10.1002/j.1939-4640.1993.tb03247.x

Amaral, A., Lourenço, B., Marques, M., and Ramalho-Santos, J. (2013). Mitochondria functionality and sperm quality. *Reproduction* 146, 163–174. doi: 10.1530/REP-13-0178

Ambros, V. (2004). The functions of animal microRNAs. *Nature* 431, 350–355. doi: 10.1038/nature02871

Avidor-Reiss, T., and Fishman, E. L. (2019). It takes two (centrioles) to tango. *Reproduction* 157, R33–R51. doi: 10.1530/REP-18-0350

Bahr, G. F., and Engler, W. F. (1970). Considerations of volume, mass, DNA, and arrangement of mitochondria in the midpiece of bull spermatozoa. *Exp. Cell Res.* 60, 338–340. doi: 10.1016/0014-4827(70)90526-4

Barceló, M., Mata, A., Bassas, L., and Larriba, S. (2018). Exosomal microRNAs in seminal plasma are markers of the origin of azoospermia and can predict the presence of sperm in testicular tissue. *Hum. Reprod.* 33, 1087–1098. doi: 10.1093/humrep/dey072

Bartel, D. P. (2004). MicroRNAs: genomics, biogenesis, mechanism, and function. *Cell* 116, 281–297. doi: 10.1016/S0092-8674(04)00045-5

Bartel, D. P. (2018). Metazoan MicroRNAs. *Cell* 173, 20–51. doi: 10.1016/j.cell.2018.03.006

Belleannée, C. (2015). Extracellular microRNAs from the epididymis as potential mediators of cell-to-cell communication. *Asian J. Androl.* 17, 730–736.

Belleannée, C., Calvo, É, Caballero, J., and Sullivan, R. (2013). Epididymosomes convey different repertoires of microRNAs throughout the bovine epididymis. *Biol. Reprod.* 89:30. doi: 10.1095/biolreprod.113.110486

Betlach, C., and Erickson, R. (1973). A unique RNA species from maturing mouse spermatozoa. *Nature* 242, 114–115. doi: 10.1038/242114a0

Bianchi, E., Doe, B., Goulding, D., and Wright, G. J. (2014). Juno is the egg Izumo receptor and is essential for mammalian fertilization. *Nature* 508, 483–487. doi: 10.1038/nature13203

Björkgren, I., Saastamoinen, L., Krutskikh, A., Huhtaniemi, I., Poutanen, M., and Sipilä, P. (2012). Dicer1 ablation in the mouse epididymis causes dedifferentiation of the epithelium and imbalance in sex steroid signaling. *PLoS One* 7:e38457. doi: 10.1371/journal.pone.0038457

Blom, E. (1973). The ultrastructure of some characteristic sperm defects and a proposal for a new classification of the bull spermiogram. *Nord. Vet. Med.* 25, 383–391.

Boerke, A., Dieleman, S. J., and Gadella, B. M. (2007). A possible role for sperm RNA in early embryo development. *Theriogenology* 68(Suppl. 1), S147–S155. doi: 10.1016/j.theriogenology.2007.05.058

Bouhallier, F., Allioli, N., Lavial, F., Chalmel, F., Perrard, M.-H., Durand, P., et al. (2010). Role of miR-34c microRNA in the late steps of spermatogenesis. *RNA* 16, 720–731. doi: 10.1261/rna.1963810

Caballero, J., Frenette, G., Amours, O., Belleannée, C., Lacroix-Pepin, N., Robert, C., et al. (2012). Bovine sperm raft membrane associated Glioma Pathogenesis-Related 1-like protein 1 (GliPr1L1) is modified during the epididymal transit and is potentially involved in sperm binding to the zona pellucida. *J. Cell. Physiol.* 227, 3876–3886. doi: 10.1002/jcp.24099

Capra, E., Turri, F., Lazzari, B., Cremonesi, P., Gliozzi, T. M., Fojadelli, I., et al. (2017). Small RNA sequencing of cryopreserved semen from single bull revealed altered miRNAs and piRNAs expression between High- and Low-motile sperm populations. *BMC Genomics* 18:14. doi: 10.1186/s12864-016-3394-7

Celeghini, E. C. C., Alves, M. B. R., de Arruda, R. P., de Rezende, G. M., Florez-Rodriguez, S. A., and de Sá Filho, M. F. (2019). Efficiency of CellROX deep red ® and CellROX orange ® fluorescent probes in identifying reactive oxygen species in sperm samples from high and low fertility bulls. *Anim. Biotechnol.* [Epub ahead of print].

Celeghini, E. C. C., de Arruda, R. P., de Andrade, A. F. C., Nascimento, J., and Raphael, C. F. (2007). Practical techniques for bovine sperm simultaneous fluorimetric assessment of plasma, acrosomal and mitochondrial membranes. *Reprod. Domest. Anim.* 42, 479–488. doi: 10.1111/j.1439-0531.2006.00810.x

Comazzetto, S., Di Giacomo, M., Rasmussen, K. D., Much, C., Azzi, C., Perlas, E., et al. (2014). Oligoasthenoteratozoospermia and Infertility in Mice Deficient for miR-34b/c and miR-449 Loci. *PLoS Genet.* 10:e1004597. doi: 10.1371/journal.pgen.1004597

Conine, C. C., Sun, F., Song, L., Rivera-Pérez, J. A., and Rando, O. J. (2018). Small RNAs gained during epididymal transit of sperm are essential for embryonic development in mice. *Dev. Cell* 46, 470.e3–480.e3. doi: 10.1016/j.devcel.2018.06.024

Conine, C. C., Sun, F., Song, L., Rivera-Pérez, J. A., and Rando, O. J. (2019). MicroRNAs absent in caput sperm are required for normal embryonic development. *Dev. Cell* 50, 7–8. doi: 10.1016/j.devcel.2019.06.007

Cooper, T. G., and Yeung, C.-H. (2003). Acquisition of volume regulatory response of sperm upon maturation in the epididymis and the role of the cytoplasmic droplet. *Microsc. Res. Tech.* 61, 28–38. doi: 10.1002/jemt.10314

Correa, J. R., Pace, M. M., and Zavos, P. M. (1997). Relationships among frozen-thawed sperm characteristics assessed via the routine semen analysis, sperm functional tests and fertility of bulls in an artificial insemination program. *Theriogenology* 48, 721–731. doi: 10.1016/S0093-691X(97)00296-3

Cui, L., Fang, L., Shi, B., Qiu, S., and Ye, Y. (2015). Spermatozoa micro ribonucleic acid–34c level is correlated with intracytoplasmic sperm injection outcomes. *Fertil. Steril.* 104, 312.e1–317.e1. doi: 10.1016/j.fertnstert.2015.05.003

Curry, E., Safranski, T. J., and Pratt, S. L. (2011). Differential expression of porcine sperm microRNAs and their association with sperm morphology and motility. *Theriogenology* 76, 1532–1539. doi: 10.1016/j.theriogenology.2011.06.025

D'Amours, O., Frenette, G., Bordeleau, L.-J., Allard, N., Leclerc, P., Blondin, P., et al. (2012). Epididymosomes transfer epididymal sperm binding protein 1 (ELSPBP1) to dead spermatozoa during epididymal transit in bovine. *Biol. Reprod.* 87, 1–11. doi: 10.1095/biolreprod.112.100990

Evenson, D. P., and Wixon, R. (2006). Clinical aspects of sperm DNA fragmentation detection and male infertility. *Theriogenology* 65, 979–991. doi: 10.1016/j.theriogenology.2005.09.011

Fagerlind, M., Stalhammar, H., Olsson, B., and Klinga-Levan, K. (2015). Expression of miRNAs in bull spermatozoa correlates with fertility rates. *Reprod. Domest. Anim.* 50, 587–594. doi: 10.1111/rda.12531

Farrell, P. B., Presicce, G. A., Brockett, C. C., and Foote, R. H. (1998). Quantification of bull sperm characteristics measured by computer-assisted sperm analysis (CASA) and the relationship to fertility. *Theriogenology* 49, 871–879. doi: 10.1016/S0093-691X(98)00036-3

Feugang, J. M., Rodriguez-Osorio, N., Kaya, A., Wang, H., Page, G., Ostermeier, G. C., et al. (2010). Transcriptome analysis of bull spermatozoa: implications for male fertility. *Reprod. Biomed. Online* 21, 312–324. doi: 10.1016/j.rbmo.2010.06.022

Fishman, E. L., Jo, K., Nguyen, Q. P. H., Kong, D., Royfman, R., Cekic, A. R., et al. (2018). A novel atypical sperm centriole is functional during human fertilization. *Nat. Commun.* 9:2210. doi: 10.1038/s41467-018-04678-8

Gadea, J., Parrington, J., Kashir, J., and Coward, K. (2013). "The male reproductive tract and spermatogenesis," in *Textbook of Clinical Embryology*, eds K. Coward and D. Wells (Cambridge: Cambridge University Press), 18–26. doi: 10.1017/cbo9781139192736.005

Gillan, L., Evans, G., and Maxwell, W. M. C. (2005). Flow cytometric evaluation of sperm parameters in relation to fertility potential. *Theriogenology* 63, 445–457. doi: 10.1016/j.theriogenology.2004.09.024

Gillan, L., Kroetsch, T., Chis Maxwell, W. M., and Evans, G. (2008). Assessment of in vitro sperm characteristics in relation to fertility in dairy bulls. *Anim. Reprod. Sci.* 103, 201–214. doi: 10.1016/j.anireprosci.2006.12.010

Gyllensten, U., Wharton, D., Josefsson, A., and Wilson, A. C. (1991). Paternal inheritance of mitochondrial DNA in mice. *Nature* 352, 255–257. doi: 10.1038/352255a0

Hayashi, K., Chuva de Sousa Lopes, S. M., Kaneda, M., Tang, F., Hajkova, P., Lao, K., et al. (2008). MicroRNA biogenesis is required for mouse primordial germ cell development and spermatogenesis. *PLoS One* 3:e0001738. doi: 10.1371/journal.pone.0001738

Hecht, N. B., Liem, H., Kleene, K. C., Distel, R. J., and Ho, S. (1984). Maternal inheritance of the mouse mitochondrial genome is not mediated by a loss or gross alteration of the paternal mitochondrial DNA or by methylation of the oocyte mitochondrial DNA. *Dev. Biol.* 102, 452–461. doi: 10.1016/0012-1606(84)90210-0

Hermo, L., Oka, R., and Morales, C. R. (1994). Secretion and endocytosis in the male reproductive tract: a role in sperm maturation. *Int. Rev. Cytol.* 154, 106–189. doi: 10.1016/S0074-7696(08)62199-3

Hirohashi, N., and Yanagimachi, R. (2018). Sperm acrosome reaction: its site and role in fertilization. *Biol. Reprod.* 99, 127–133. doi: 10.1093/biolre/ioy045

Inaba, K. (2003). Molecular architecture of the sperm flagella: molecules for motility and signaling. *Zool. Sci.* 20, 1043–1056. doi: 10.2108/zsj.20.1043

Irvine, D. S. (1998). Epidemiology and aetiology of male infertility. *Hum. Reprod.* 13, 33–38. doi: 10.1093/humrep/13.1.33

Jerczynski, O., Lacroix-Pépin, N., Boilard, E., Calvo, E., Bernet, A., Fortier, M. A., et al. (2016). Role of Dicer1-dependent factors in the paracrine regulation of epididymal gene expression. *PLoS One* 11:e0163876. doi: 10.1371/journal.pone.0163876

Jodar, M., Selvaraju, S., Sendler, E., Diamond, M. P., and Krawetz, S. A. (2013). The presence, role and clinical use of spermatozoal RNAs. *Hum. Reprod. Update* 19, 604–624. doi: 10.1093/humupd/dmt031

Kashir, J., Heindryckx, B., Jones, C., De Sutter, P., Parrington, J., and Coward, K. (2010). Oocyte activation, phospholipase C zeta and human infertility. *Hum. Reprod. Update* 16, 690–703. doi: 10.1093/humupd/dmq018

Kasimanickam, V., Kasimanickam, R., Arangasamy, A., Saberivand, A., Stevenson, J. S., and Kastelic, J. P. (2012). Association between mRNA abundance of functional sperm function proteins and fertility of Holstein bulls. *Theriogenology* 78, 2007–2019. doi: 10.1016/j.theriogenology.2012.07.016

Kotaja, N. (2014). MicroRNAs and spermatogenesis. *Fertil. Steril.* 101, 1552–1562. doi: 10.1016/j.fertnstert.2014.04.025

Krawetz, S. A. (2005). Paternal contribution: new insights and future challenges. *Nat. Rev. Genet.* 6, 633–642. doi: 10.1038/nrg1654

Kwon, W.-S., Rahman, M., Lee, J.-S., Kim, J., Yoon, S.-J., Park, Y.-J., et al. (2014). A comprehensive proteomic approach to identifying capacitation related proteins in boar spermatozoa. *BMC Genomics* 15:897. doi: 10.1186/1471-2164-15-897

Kwon, W.-S., Rahman, M. S., Lee, J.-S., You, Y.-A., and Pang, M.-G. (2015). Improving litter size by boar spermatozoa: application of combined H33258/CTC staining in field trial with artificial insemination. *Andrology* 3, 552–557. doi: 10.1111/andr.12020

Li, Y., Li, R. H., Ran, M. X., Zhang, Y., Liang, K., Ren, Y. N., et al. (2018). High throughput small RNA and transcriptome sequencing reveal capacitation-related microRNAs and mRNA in boar sperm. *BMC Genomics* 19:1–12. doi: 10.1186/s12864-018-5132-9

Liu, W., Pang, R. T. K., Chiu, P. C. N., Wong, B. P. C., Lao, K., and Lee, K. (2012). Sperm-borne microRNA-34c is required for the first cleavage division in mouse. *Proc. Natl. Acad. Sci. U.S.A.* 109, 490–494. doi: 10.1073/pnas.1110368109

Luo, S., Valencia, C. A., Zhang, J., Lee, N.-C., Slone, J., Gui, B., et al. (2018). Biparental Inheritance of Mitochondrial DNA in Humans. *Proc. Natl. Acad. Sci. U.S.A.* 115, 13039–13044. doi: 10.1073/pnas.1810946115

Mattick, J. S. (2001). Non-coding RNAs: the architects of eukaryotic complexity. *EMBO Rep.* 2, 986–991. doi: 10.1093/embo-reports/kve230

Menezes, E. S. B., Badial, P. R., El Debaky, H., Husna, A. U., Ugur, M. R., Kaya, A., et al. (2019). Sperm miR-15a and miR-29b are associated with bull fertility. *Andrologia* 52:e13412. doi: 10.1111/and.13412

Morrell, J. M., Valeanu, A. S., Lundeheim, N., and Johannisson, A. (2018). Sperm quality in frozen beef and dairy bull semen. *Acta Vet. Scand.* 60, 1–10. doi: 10.1186/s13028-018-0396-2

Navara, C. S., Hewitson, L. C., Simerly, C. R., Sutovsky, P., and Schatten, G. (1997). The implications of a paternally derived centrosome during human fertilization: consequences for reproduction and the treatment of male factor infertility. *Am. J. Reprod. Immunol.* 37, 39–49. doi: 10.1111/j.1600-0897.1997.tb00191.x

Nixon, B., Stanger, S. J., Mihalas, B. P., Reilly, J. N., Anderson, A. L., Tyagi, S., et al. (2015). The MicroRNA signature of mouse spermatozoa is substantially modified during epididymal maturation. *Biol. Reprod.* 93, 1–20. doi: 10.1095/biolreprod.115.132209

Odia, M., Swanson, G., and Krawetz, S. A. (2018). A history of why fathers' RNA matters. *Biol. Reprod.* 99, 147–159. doi: 10.1093/biolre/ioy007

Oliveira, B. M., Arruda, R. P., Thomé, H. E., Maturana Filho, M., Oliveira, G., Guimarães, C., et al. (2014). Fertility and uterine hemodynamic in cows after artificial insemination with semen assessed by fluorescent probes. *Theriogenology* 82, 767–772. doi: 10.1016/j.theriogenology.2014.06.007

Ostermeier, G. C., Goodrich, R. J., Diamond, M. P., Dix, D. J., and Krawetz, S. A. (2005). Toward using stable spermatozoal RNAs for prognostic assessment of male factor fertility. *Fertil. Steril.* 83, 1687–1694. doi: 10.1016/j.fertnstert.2004.12.046

Ostermeier, G. C., Miller, D., Huntriss, J. D., Diamond, M. P., and Krawetz, S. A. (2004). Reproductive biology: delivering spermatozoan RNA to the oocyte. *Nature* 429:2603. doi: 10.1038/nature02602

Papaioannou, M. D., Pitetti, J. L., Ro, S., Park, C., Aubry, F., Schaad, O., et al. (2009). Sertoli cell Dicer is essential for spermatogenesis in mice. *Dev. Biol.* 326, 250–259. doi: 10.1016/j.ydbio.2008.11.011

Paul, J., and Duerksen, J. D. (1975). Chromatin-associated RNA content of heterochromatin and euchromatin. *Mol. Cell. Biochem.* 9, 9–16. doi: 10.1007/BF01731728

Piomboni, P., Focarelli, R., Stendardi, A., Ferramosca, A., and Zara, V. (2012). The role of mitochondria in energy production for human sperm motility. *Int. J. Androl.* 35, 109–124. doi: 10.1111/j.1365-2605.2011.01218.x

Ran, M., Weng, B., Cao, R., Li, Z., Peng, F., Luo, H., et al. (2018). miR-26a inhibits proliferation and promotes apoptosis in porcine immature Sertoli cells by targeting the PAK2 gene. *Reprod. Domest. Anim.* 53, 1375–1385. doi: 10.1111/rda.13254

Raposo, G., and Stoorvogel, W. (2013). Extracellular vesicles: exosomes, microvesicles, and friends. *J. Cell Biol.* 200, 373–383. doi: 10.1083/jcb.201211138

Reilly, J. N., McLaughlin, E. A., Stanger, S. J., Anderson, A. L., Hutcheon, K., Church, K., et al. (2016). Characterisation of mouse epididymosomes reveals a complex profile of microRNAs and a potential mechanism for modification of the sperm epigenome. *Sci. Rep.* 6, 1–15. doi: 10.1038/srep31794

Rodgers, A. B., Morgan, C. P., Bronson, S. L., Revello, S., and Bale, T. L. (2013). Paternal stress exposure alters sperm MicroRNA content and reprograms offspring HPA stress axis regulation. *J. Neurosci.* 33, 9003–9012. doi: 10.1523/JNEUROSCI.0914-13.2013

Rodgers, A. B., Morgan, C. P., Leu, N. A., and Bale, T. L. (2015). Transgenerational epigenetic programming via sperm microRNA recapitulates effects of paternal stress. *Proc. Natl. Acad. Sci. U.S.A.* 112, 13699–13704. doi: 10.1073/pnas.1508347112

Rompala, G. R., Simons, A., Kihle, B., and Homanics, G. E. (2018). Paternal preconception chronic variable stress confers attenuated ethanol drinking behavior selectively to male offspring in a pre-stress environment dependent manner. *Front. Behav. Neurosci.* 12:257. doi: 10.3389/fnbeh.2018.00257

Salas-Huetos, A., Blanco, J., Vidal, F., Godo, A., Grossmann, M., Pons, M. C., et al. (2015). Spermatozoa from patients with seminal alterations exhibit a differential micro-ribonucleic acid profile. *Fertil. Steril.* 104, 591–601. doi: 10.1016/j.fertnstert.2015.06.015

Salas-Huetos, A., Blanco, J., Vidal, F., Grossmann, M., Pons, M. C., Garrido, N., et al. (2016). Sperm from normozoospermic fertile and infertile individuals convey a distinct miRNA cargo. *Andrology* 4, 1–9. doi: 10.1111/andr.12276

Samans, B., Yang, Y., Krebs, S., Sarode, G. V., Blum, H., Reichenbach, M., et al. (2014). Uniformity of nucleosome preservation pattern in mammalian sperm and Its connection to repetitive DNA elements. *Dev. Cell* 30, 23–35. doi: 10.1016/j.devcel.2014.05.023

Sathananthan, A. H., Kola, I., Osborne, J., Trounson, A., Ng, S. C., Bongso, A., et al. (1991). Centrioles in the beginning of human development. *Proc. Natl. Acad. Sci. U.S.A.* 88, 4806–4810. doi: 10.1073/pnas.88.11.4806

Satouh, Y., Inoue, N., Ikawa, M., and Okabe, M. (2012). Visualization of the moment of mouse sperm-egg fusion and dynamic localization of IZUMO1. *J. Cell Sci.* 125, 4985–4990. doi: 10.1242/jcs.100867

Saunders, C. M., Larman, M. G., Parrington, J., Cox, L. J., Royse, J., Blayney, L. M., et al. (2002). PLC ζ: a sperm-specific trigger of Ca 2 + oscillations in eggs and embryo development. *Development* 3544, 3533–3544.

Schatten, H., and Sun, Q.-Y. (2009). The role of centrosomes in mammalian fertilization and its significance for ICSI. *Mol. Hum. Reprod.* 15, 531–538. doi: 10.1093/molehr/gap049

Schuster, A., Skinner, M. K., and Yan, W. (2016). Ancestral vinclozolin exposure alters the epigenetic transgenerational inheritance of sperm small noncoding RNAs. *Environ. Epigenet.* 2:dvw001. doi: 10.1093/eep/dvw001

Sellem, E., Broekhuijse, M. L. W. J., Chevrier, L., Camugli, S., Schmitt, E., Schibler, L., et al. (2015). Use of combinations of in vitro quality assessments to predict fertility of bovine semen. *Theriogenology* 84, 1447.e5–1454.e5. doi: 10.1016/j.theriogenology.2015.07.035

Sharma, U., Conine, C. C., Shea, J. M., Boskovic, A., Derr, A. G., Bing, X. Y., et al. (2016). Biogenesis and function of tRNA fragments during sperm maturation and fertilization in mammals. *Science* 351, 391–396. doi: 10.1126/science.aad6780

Sharma, U., Sun, F., Conine, C. C., Reichholf, B., Kukreja, S., Herzog, V. A., et al. (2018). Small RNAs are trafficked from the epididymis to developing mammalian sperm. *Dev. Cell* 46, 481–494. doi: 10.1016/j.devcel.2018.06.023

Simerly, C., Manil-Ségalen, M., Castro, C., Hartnett, C., Kong, D., Verlhac, M. H., et al. (2018). Separation and loss of centrioles from primordidal germ cells to mature oocytes in the mouse. *Sci. Rep.* 8, 1–17. doi: 10.1038/s41598-018-31222-x

Simerly, C., Wu, G.-J., Zoran, S., Ord, T., Rawlins, R., Jones, J., et al. (1995). The paternal inheritance of the centrosome, the cell's microtubule-organizing center, in humans, and the implications for infertility. *Nat. Med.* 1, 47–52. doi: 10.1038/nm0195-47

Sipilä, P., and Björkgren, I. (2016). Segment-specific regulation of epididymal gene expression. *Reproduction* 152, R91–R99. doi: 10.1530/REP-15-0533

Smorag, L., Zheng, Y., Nolte, J., Zechner, U., Engel, W., and Pantakani, D. V. K. (2012). MicroRNA signature in various cell types of mouse spermatogenesis: evidence for stage-specifically expressed miRNA-221, -203 and -34b-5p mediated spermatogenesis regulation. *Biol. Cell* 104, 677–692. doi: 10.1111/boc.201200014

Song, G. J., and Lewis, V. (2008). Mitochondrial DNA integrity and copy number in sperm from infertile men. *Fertil. Steril.* 90, 2238–2244. doi: 10.1016/j.fertnstert.2007.10.059

Sullivan, R. (2015). Epididymosomes: a heterogeneous population of microvesicles with multiple functions in sperm maturation and storage. *Asian J. Androl.* 17, 726–729. doi: 10.4103/1008-682X.155255

Sullivan, R., Frenette, G., and Girouard, J. (2007). Epididymosomes are involved in the acquisition of new sperm proteins during epididymal transit. *Asian J. Androl.* 9, 483–491. doi: 10.1111/j.1745-7262.2007.00281.x

Sullivan, R., and Saez, F. (2013). Epididymosomes, prostasomes, and liposomes: their roles in mammalian male reproductive physiology. *Reproduction* 146, R21–35. doi: 10.1530/REP-13-0058

Tang, F., Kaneda, M., O'Carroll, D., Hajkova, P., Barton, S. C., Sun, Y. A., et al. (2007). Maternal microRNAs are essential for mouse zygotic development. *Genes Dev.* 21, 644–648. doi: 10.1101/gad.418707

Tscherner, A., Gilchrist, G., Smith, N., Blondin, P., Gillis, D., and LaMarre, J. (2014). MicroRNA-34 family expression in bovine gametes and preimplantation embryos. *Reprod. Biol. Endocrinol.* 12:85. doi: 10.1186/1477-7827-12-85

Vincent, P., Underwood, S. L., Dolbec, C., Bouchard, N., Kroetsch, T., and Blondin, P. (2012). Bovine semen quality control in artificial insemination centers. *Anim. Reprod.* 9, 153–165.

Wang, C., Yang, C., Chen, X., Yao, B., Yang, C., Zhu, C., et al. (2011). Altered profile of seminal plasma microRNAs in the molecular diagnosis of male infertility. *Clin. Chem.* 57, 1722–1731. doi: 10.1373/clinchem.2011.169714

Wang, M., Gao, Y., Qu, P., Qing, S., Qiao, F., Zhang, Y., et al. (2017). Sperm-borne miR-449b influences cleavage, epigenetic reprogramming and apoptosis of SCNT embryos in bovine. *Sci. Rep.* 7, 1–12. doi: 10.1038/s41598-017-13899-8

Weinhold, B. (2006). Epigenetics: the science of change. *Environ. Health Perspect.* 114, 160–167.

Wightman, B., Ha, I., and Ruvkun, G. (1993). Posttranscriptional regulation of the heterochronic gene lin- 14 by lin-4 mediates temporal pattern formation in *C. elegans*. *Cell* 75, 855–862. doi: 10.1016/0092-8674(93)90530-4

Wu, A. T. H., Sutovsky, P., Manandhar, G., Xu, W., Katayama, M., Day, B. N., et al. (2007). PAWP, a sperm-specific WW domain-binding protein, promotes meiotic resumption and pronuclear development during fertilization. *J. Biol. Chem.* 282, 12164–12175. doi: 10.1074/jbc.M609132200

Wu, J., Bao, J., Kim, M., Yuan, S., Tang, C., Zheng, H., et al. (2014). Two miRNA clusters, miR-34b/c and miR-449, are essential for normal brain development, motile ciliogenesis, and spermatogenesis. *Proc. Natl. Acad. Sci. U.S.A.* 111, E2851–E2857. doi: 10.1073/pnas.1407777111

Yuan, S., Schuster, A., Tang, C., Yu, T., Ortogero, N., Bao, J., et al. (2016). Sperm-borne miRNAs and endo-siRNAs are important for fertilization and preimplantation embryonic development. *Development* 143, 635–647. doi: 10.1242/dev.131755

Zegers-Hochschild, F., Adamson, G. D., Dyer, S., Racowsky, C., De Mouzon, J., Sokol, R., et al. (2017). The international glossary on infertility and fertility care, 2017. *Hum. Reprod.* 32, 1786–1801. doi: 10.1093/humrep/dex234

Zhou, J.-H., Zhou, Q.-Z., Yang, J.-K., Lyu, X.-M., Bian, J., Guo, W.-B., et al. (2017). MicroRNA-27a-mediated repression of cysteine-rich secretory protein 2 translation in asthenoteratozoospermic patients. *Asian J. Androl.* 19:591. doi: 10.4103/1008-682X.185001

Zhou, W., Stanger, S. J., Anderson, A. L., Bernstein, I. R., De Iuliis, G. N., McCluskey, A., et al. (2019). Mechanisms of tethering and cargo transfer during epididymosome-sperm interactions. *BMC Biol.* 17:1–18. doi: 10.1186/s12915-019-0653-5

Zimmermann, C., Romero, Y., Warnefors, M., Bilican, A., Borel, C., Smith, L. B., et al. (2014). Germ cell-specific targeting of DICER or DGCR8 reveals a novel role for endo-siRNAs in the progression of mammalian spermatogenesis and male fertility. *PLoS One* 9:e107023. doi: 10.1371/journal.pone.0107023

Zini, A., and Agarwal, A. (2011). *Sperm Chromatin*. New York, NY: Springer.

Ziyyat, A. (2001). Differential gene expression in pre-implantation embryos from mouse oocytes injected with round spermatids or spermatozoa. *Hum. Reprod.* 16, 1449–1456. doi: 10.1093/humrep/16.7.1449

Conflict of Interest: The authors declare that the research was conducted in the absence of any commercial or financial relationships that could be construed as a potential conflict of interest.

Copyright © 2020 Alves, Celeghini and Belleannée. This is an open-access article distributed under the terms of the Creative Commons Attribution License (CC BY). The use, distribution or reproduction in other forums is permitted, provided the original author(s) and the copyright owner(s) are credited and that the original publication in this journal is cited, in accordance with accepted academic practice. No use, distribution or reproduction is permitted which does not comply with these terms.

frontiers in Cell and Developmental Biology

ORIGINAL RESEARCH
published: 30 September 2020
doi: 10.3389/fcell.2020.575126

Male Decapacitation Factor SPINK3 Blocks Membrane Hyperpolarization and Calcium Entry in Mouse Sperm

Lucia Zalazar[1†], Cintia Stival[2†], Anabella R. Nicolli[1], Gerardo A. De Blas[3], Dario Krapf[2] and Andreina Cesari[1,4*]*

[1] Instituto de Investigaciones Biológicas (IIB), Consejo Nacional de Investigaciones Científicas y Técnicas (CONICET), Universidad Nacional de Mar del Plata, Mar del Plata, Argentina, [2] Laboratory of Cell Signal Transduction Networks, Instituto de Biologia Molecular y Celular de Rosario (IBR), Consejo Nacional de Investigaciones Científicas y Técnicas (CONICET), Universidad Nacional de Rosario, Rosario, Argentina, [3] Instituto de Histología y Embriología de Mendoza (IHEM), Consejo Nacional de Investigaciones Científicas y Técnicas (CONICET), Universidad Nacional de Cuyo, National Scientific and Technical Research Council, Mendoza, Argentina, [4] Escuela Superior de Medicina, Universidad Nacional de Mar del Plata, Mar del Plata, Argentina

OPEN ACCESS

Edited by:
Tomer Avidor-Reiss, University of Toledo, United States

Reviewed by:
Haim Breitbart, Bar-Ilan University, Israel
Barbara Barboni, University of Teramo, Italy
Bart Gadella, Utrecht University, Netherlands

***Correspondence:**
Dario Krapf
krapf@ibr-conicet.gov.ar
Andreina Cesari
acesari@mdp.edu.ar

[†] *These authors have contributed equally to this work*

Specialty section:
This article was submitted to Cell Growth and Division, a section of the journal Frontiers in Cell and Developmental Biology

Received: *22 June 2020*
Accepted: *10 September 2020*
Published: *30 September 2020*

Citation:
Zalazar L, Stival C, Nicolli AR, De Blas GA, Krapf D and Cesari A (2020) Male Decapacitation Factor SPINK3 Blocks Membrane Hyperpolarization and Calcium Entry in Mouse Sperm. Front. Cell Dev. Biol. 8:575126. doi: 10.3389/fcell.2020.575126

Mammalian sperm acquire ability to fertilize through a process called capacitation, occurring after ejaculation and regulated by both female molecules and male decapacitation factors. Bicarbonate and calcium present in the female reproductive tract trigger capacitation in sperm, leading to acrosomal responsiveness and hyperactivated motility. Male decapacitating factors present in the semen avert premature capacitation, until detached from the sperm surface. However, their mechanism of action remains elusive. Here we describe for the first time the molecular basis for the decapacitating action of the seminal protein SPINK3 in mouse sperm. When present in the capacitating medium, SPINK3 inhibited Src kinase, a modulator of the potassium channel responsible for plasma membrane hyperpolarization. Lack of hyperpolarization affected calcium channels activity, impairing the acquisition of acrosomal responsiveness and blocking hyperactivation. Interestingly, SPINK3 acted only on non-capacitated sperm, as it did not bind to capacitated cells. Binding selectivity allows its decapacitating action only in non-capacitated sperm, without affecting capacitated cells.

Keywords: decapacitation factor, sperm capacitation, membrane potential hyperpolarization, fertilization, SPINK3

INTRODUCTION

After testicular ejaculation, mammalian sperm transit the female reproductive tract where they undergo a series of biochemical and physiological modifications in order to gain fertilization competence. These changes, known as capacitation (Austin, 1951; Chang, 1951), can also be promoted in culture medium containing Ca^{2+}, HCO_3^-, energy sources, and a cholesterol acceptor such as BSA (Zalazar et al., 2012; Assis et al., 2013), mimicking an *in vivo* environment. Capacitation is a highly complex process in which influx of HCO_3^- and Ca^{2+} plays a key role, acting on the atypical adenylyl cyclase sAC (aka ADCY10) (Hess et al., 2005; Stival et al., 2016). The activity of this cyclase increases intracellular cAMP concentration which promotes the direct activation of the Ser/Thr kinase Protein Kinase A (PKA), orchestrating different signaling cascades downstream

(Aitken and Nixon, 2013). Its activation is involved in: membrane potential (*Em*) hyperpolarization and acquisition of acrosomal responsiveness, flagellar hyperactivation, intracellular alkalization, and phosphorylation of sperm proteins in Tyr residues, among other known effects (Puga Molina et al., 2018). Even though these processes differ in their kinetics, all of them involve phosphorylation cascades initiated by PKA. In this regard, we have recently shown that PKA activity is necessary for Src activation, which in turn leads to *E*m hyperpolarization and acrosomal responsiveness in mouse sperm (Stival et al., 2015).

In order for fertilization to succeed, capacitation must be highly time-controlled and synchronized with ovulation. Ejaculation prompts contact of spermatozoa with components of the seminal plasma. Some of these components have been proposed to bind to sperm and promote decapacitating activity (i.e., prevent capacitation), either negatively regulating or delaying capacitation. Detaching of these molecules allows capacitation to proceed. The protein SPINK3 (Serine Protease Inhibitor Kazal type 3) has been proposed as one of these decapacitation factors (Ou et al., 2012; Zalazar et al., 2012). SPINK3 is a 6 kDa protein with a well-characterized function as an inhibitor of trypsin-like serine proteases (Ohmuraya et al., 2012; Assis et al., 2013). However, among different functions ascribed to this protein, it has been found to reduce intracellular calcium increase ($[Ca^{2+}]i$) that normally occurs upon capacitation (Coronel et al., 1992; Zalazar et al., 2012). The molecular mechanism underlying this effect is unknown. SPINK3 is secreted mainly by seminal vesicles into the seminal fluid where it adheres to the sperm surface (Chen et al., 1998) before entering the female duct (Ou et al., 2012). It has been hypothesized that decapacitating factors should detach from sperm for capacitation to proceed. Our results using the mouse model, showed that when sperm were challenged with SPINK3 and then exposed to capacitating conditions, capacitation failed to occur. Although phosphorylation of PKA substrates was not abolished, Src activation was impaired with the consequent lack of hyperpolarization. Accordingly, acrosomal responsiveness was not acquired. Calcium influx was also inhibited, and sperm did not acquire hyperactivation. Our data indicate that SPINK3 blocked both *Em* hyperpolarization and CatSper-dependent Ca^{2+} uptake, affecting the onset of capacitation. Supporting these results, sperm recovered from the uterus after mating showed binding of SPINK3 localized to the apical portion of the head and to the principal piece. Altogether, these results shed light on the molecular mechanism by which the seminal protein SPINK3 prevents premature capacitation in murine sperm.

RESULTS

SPINK3 Inhibits the Acquisition of Acrosomal Responsiveness Associated With Capacitation

We have previously shown that the recombinant protein SPINK3 reduced acrosomal responsiveness in mouse sperm when added at the beginning of capacitation (Zalazar et al., 2012). Thus, in order to discard a blockade on the exocytotic mechanism *per se*, we added SPINK3 before or after capacitation. As shown in **Figure 1A**, when physiologically relevant SPINK3 concentrations (Dematteis et al., 2008; Samanta et al., 2018) were added to capacitating media from the beginning, induction of acrosome reaction (AR) with progesterone was impaired in a concentration dependent manner. Treatment with 13 μM SPINK3 showed complete AR blockade. On the other hand, when SPINK3 was added to capacitated sperm (i.e., after 60 min of incubation in capacitating medium), sperm underwent AR upon stimulation with progesterone (**Figure 1B**). These results suggest that SPINK3 inhibitory effect on AR is the consequence of sperm not achieving the capacitated state and therefore, not being able to acquire acrosome responsiveness.

SPINK3 Disrupts Membrane Hyperpolarization Associated With Capacitation

Since hyperpolarization of the plasma membrane potential (E*m*) has been proven to be necessary and sufficient for sperm to acquire acrosome responsiveness (De La Vega-Beltran et al., 2012), we hypothesized that SPINK3 was affecting this E*m* shift. The study of *Em* was performed on a fluorimeter using the probe $DISC_3(5)$ (Ritagliati et al., 2018a; Stival et al., 2015). The presence of SPINK3 in the capacitation medium significantly blocked sperm plasma membrane hyperpolarization in a concentration dependent manner (**Figure 2A**).

The tyrosine kinase Src activates during capacitation, and is necessary to achieve hyperpolarization of mouse sperm, modulating the K^+ channel Slo3 (Stival et al., 2015). Thus, we analyzed whether Src activity was being affected by SPINK3. The activity of Src can be monitored by the phosphorylation status of its Tyr416, which is autophosphorylated upon activation. As shown in **Figure 2B**, phosphorylation of Tyr416 was not observed under the presence of SPINK3, arising as the molecular cause of the lack of hyperpolarization and acrosomal responsiveness.

Considering that PKA activity is upstream of Src activation (Stival et al., 2016), we hypothesized that SPINK3 effect on Src activation was due to decreased PKA activity. PKA can be easily monitored by western-blot assessment of phosphorylated PKA substrates (Krapf et al., 2010). As shown in **Figure 2C**, when SPINK3 was present in the medium, the overall pattern of phosphorylated PKA substrates remained comparable to that of the capacitation control, indicating that PKA activity was not substantially affected by the presence of SPINK3. In addition, no effect was observed on the phosphorylation status of tyrosine residues (**Figure 2D**), used for many years as a hallmark of sperm capacitation. These data portraits a situation where PKA is active, while Tyr416-Src phosphorylation is impaired by SPINK3 (1 μM and above) (**Figure 2B**), standing as a plausible cause for the absence of hyperpolarization.

Some evidence suggests that *Em* hyperpolarization is part of a complex mechanism of regulation (González-Martínez, 2003; Fraire-Zamora and González-Martínez, 2004; Del Carmen Neri-Vidaurri et al., 2006) in which interplay with calcium influx has

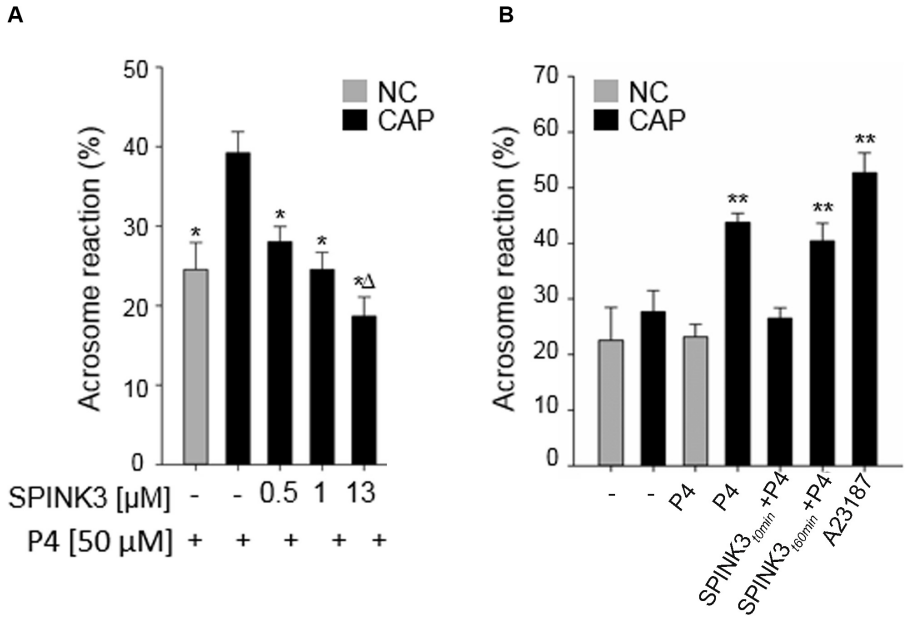

FIGURE 1 | Effect of SPINK3 on acrosome reaction (AR). **(A)** Different SPINK3 concentrations were added at the beginning of the incubation time in either non-capacitating (NC, gray bars) or capacitating (CAP, black bars) medium (60 min at 37°C). AR was induced by 50 μM progesterone ("P4") (data represent mean ± SE; $n = 3$). *$p < 0.05$ respect to control Progesterone-induced capacitated cells; Δ$p < 0.05$ compared to 1 μM SPINK3 treatment. **(B)** SPINK3 (13 μM) was added either at the beginning ($SPINK3_{t0\ min}$ + P4) or at the end of capacitation ($SPINK3_{t60\ min}$ + P4). Progesterone (50 μM) was always added after capacitation was completed (data represent mean ± S.E.; $n = 8$); **$p < 0.05$ with respect to cells treated with SPINK3 at the beginning of capacitation (SPINK3 + P4).

been proposed (Orta et al., 2019). Therefore, the assessment of the effect of SPINK3 on intracellular calcium levels was pursued.

SPINK3 Impairs Intracellular Calcium Increase During Capacitation

Considering that SPINK3 affected signaling events conducive to capacitation associated hyperpolarization, we investigated whether intracellular calcium increase was affected by SPINK3. By using a single-cell imaging approach, we studied SPINK3 effect on intracellular calcium exerted by BSA, which is known to induce CatSper-mediated Ca^{2+} entry (Xia and Ren, 2009). CatSper is a sperm-specific calcium channel with a key role in the acquisition of fertilization competence. Cells were loaded with the calcium sensitive probe Fluo3-AM, and equilibrated in medium supplemented with $NaHCO_3$. Upon addition of BSA, there was an increase of intracellular calcium signal of living cells. Even though the influx of Ca^{2+} was noticeable 20 s after BSA addition, the highest signal intensities were reached after 60 s post-stimuli (**Figure 3A**, upper panel), as previously reported (Ren and Xia, 2010). About half of the living sperm analyzed in control conditions exhibited a positive response to stimulus (**Figure 3B**), as expected from the high heterogeneity of sperm populations (Movie S1). When sperm were pre-incubated with SPINK3, the increase in calcium signal upon BSA induction was significantly inhibited (**Figure 3A** second panel, **Figures 3B,C** and **Supplementary Movie S2**) compared to untreated cells. Basal $[Ca^{2+}]i$ was not affected by pre-incubation of sperm with SPINK3 considering the ratio between treated/non-treated cells (1.06 ± 0.4). As a second approach, the effect of SPINK3 over CatSper Ca^{2+} entry was addressed by means of depolarization coupled to alkalization (K8.6 solution treatment), in order to elicit a CatSper-dependent $[Ca^{2+}]i$ increase in mouse sperm (Xia et al., 2007). K8.6 did not promote intracellular Ca^{2+} increase in non-capacitated ("NC") cells incubated with SPINK3, as evidenced by the reduction in the percentage of responsive cells and in the amount of the calcium intensity (**Figure 3A** fourth panel, **Figures 3B,C** middle panel). However, SPINK3 failed to inhibit this response in capacitated sperm ("CAP") when challenged with K8.6 (**Figures 3B,C** middle panel). These results indicated that SPINK3 was affecting calcium entry through CatSper channel only when present from the beginning of capacitation. To rule out the possible role of the purinergic P2X receptor channels (Navarro et al., 2011), non-capacitated sperm where exposed to 2.5 mM ATP either in the presence or absence of SPINK3. Both conditions showed normal calcium response (**Figure 3A** last two panels and **Figures 3B,C** right panels). In addition, spermatozoa showed normal response to BSA when incubated in the presence of Verapamil, an L-type calcium channel blocker (i.e., does not affect CatSper) (**Figure 3A** third panel and **Figures 3B,C** left panels). These data indicate that SPINK3 blocked calcium influx presumably through CatSper channels.

In order to analyze the effect of SPINK3 on CatSper opening, cells were capacitated in either the presence or absence of SPINK3 and then loaded with $DISC_3(5)$ (Kirichok et al., 2006; Carlson et al., 2009; López-González et al., 2014; Ritagliati et al., 2018b; Stival et al., 2018; Torres-Flores et al., 2011). After fluorescence stabilization, calcium was chelated with 3.5 mM

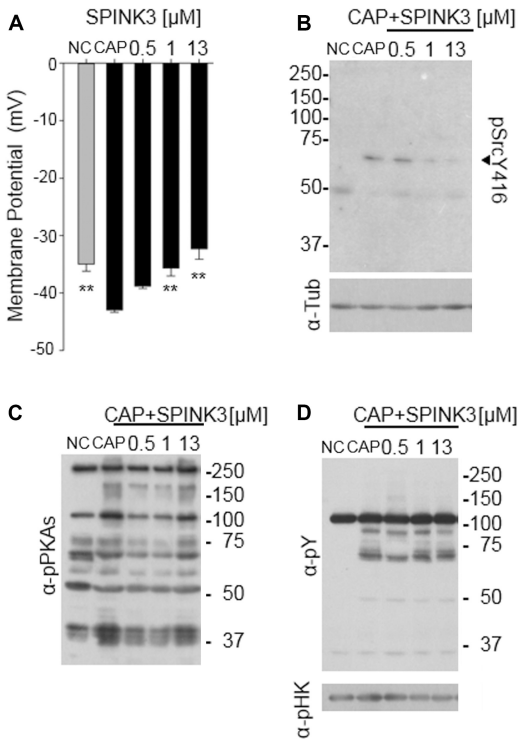

FIGURE 2 | Effect of SPINK3 on sperm membrane potential (*Em*) and associated pathways. **(A)** *Em* measurements of $DISC_3(5)$-loaded sperm, incubated for 60 min in non-capacitating (NC, gray bar) or capacitating (CAP, black bars) conditions containing the specified SPINK3 concentrations. Data represent mean ± S.E., $n = 4$, ** values significantly different ($p < 0.01$) compared to CAP; **(B,C)** after sperm incubations as detailed in **(A)**, western blot analyses were performed with anti pSrcY416 antibodies **(B)** (clone D49G4), further stripped and re-probed with anti-tubulin (α-Tub) antibodies. Alternatively, western blot analyses were performed with anti-pPKAs (clone 100G7E) **(C)**, further stripped and re-probed with anti-pTyr (α-pY) (clone 4G10) **(D)**. Western blot analyses are representative of experiments repeated at least three times. p-hexokinase (116 kDa, α-pHK) detected with anti-pY, is showed as loading control.

EGTA (Bers et al., 1994; Ritagliati et al., 2018b) allowing sodium to permeate through CatSper. The increase in fluorescence after addition of EGTA indicates the magnitude of depolarization caused by sodium influx, and correlates to the extent of CatSper opening. As shown in **Figure 4**, treatment with 13 μM SPINK3 effectively blocked EGTA-induced depolarization. Recent evidence suggests that CatSper could be stimulated by PKA in mouse sperm (Stival et al., 2018; Orta et al., 2019). Thus, cells treated with SPINK3 were also incubated in the presence of the cAMP permeable-analog 8Br-cAMP to directly activate PKA, and consequently CatSper. However, EGTA-induced depolarization could not be rescued by directly activating PKA with 8Br-cAMP, further substantiating that SPINK3 effect is not due to PKA downregulation.

SPINK3 Binds to Non-capacitated Cells

SPINK3 negatively regulates hyperpolarization presumed to be driven by SLO3 potassium channels (Santi et al., 2010) and also, either directly or indirectly, CatSper channels. Considering that both SLO3 and CatSper locate exclusively to the principal piece of the flagellum (Navarro et al., 2007; Chung et al., 2014; Hwang et al., 2019), we studied whether recombinant SPINK3 binds to this region. Sperm from cauda epididymis incubated under non-capacitating conditions in the presence of recombinant SPINK3, showed SPINK3 binding to the principal piece and head. However, after *in vitro* capacitation, sperm failed to bind to exogenously added SPINK3 (**Figure 5A**). Lack of SPINK3 binding to capacitated sperm was not due to BSA masking because both capacitated and non-capacitated sperm were incubated with BSA and further washed before SPINK3 addition. As a control, non-capacitated cells exposed to BSA still bound SPINK3 (**Figure 5A**). This *ex vivo* experiment was replicated by an *in vivo* approach, to assess the binding of endogenous SPINK3 to naturally deposited sperm in females, after matting. Immediately after coitus, sperm were recovered from the female uterus and analyzed for the presence of SPINK3. Under these conditions, a strong signal was observed in the sperm principal piece. Worth noticing, control sperm derived from the cauda epididymis that were never in contact with endogenous SPINK3, showed no immunofluorescence signal (**Figure 5B**).

SPINK3 Inhibits Acquisition of Hyperactivation

Hyperactivation is a functional change in the sperm movement pattern, associated to capacitation and described as a relatively progressive motion with high-amplitude flagellar bending (Yanagimachi, 1970). Calcium is essential for hyperactivation of mouse sperm (Carlson et al., 2003). Therefore, the effect of SPINK3 on acquisition of hyperactivation was evaluated. While no statistically significant differences were observed in total motility upon supplementation of capacitating media with SPINK3 (Zalazar et al., 2012), hyperactivation was impaired by 1 μM SPINK3 and above (**Figure 6A**). No effect of SPINK3 was observed on hyperactivation when SPINK3 was added to already capacitated sperm (**Figure 6B**). This result further substantiates the role of SPINK3 as a protein that prevent acquisition of fertilizing competence by impairing hyperpolarization and dysregulation of calcium entry.

DISCUSSION

Sperm leave the male body through ejaculation, as part of a complex suspension where seminal proteins are found. Among these proteins, decapacitation factors are important constituents of semen, but still poorly understood (Araki et al., 2015). One of these factors is the protein SPINK3, present in the seminal vesicles at a concentration of approximately 11 μM (Coronel et al., 1992). SPINK3 is known as a serine protease inhibitor Kazal type 3. Upon secretion by the seminal vesicle, SPINK3 binds to ejaculated sperm (Chen et al., 1998; Zalazar et al., 2012) until it apparently detaches in the uterus during ovulation (Ou et al., 2012). Similarly, other decapacitation factors with protease inhibitory activity have been described with a similar behavior (Lin et al., 2008; Li et al., 2010). Increasing

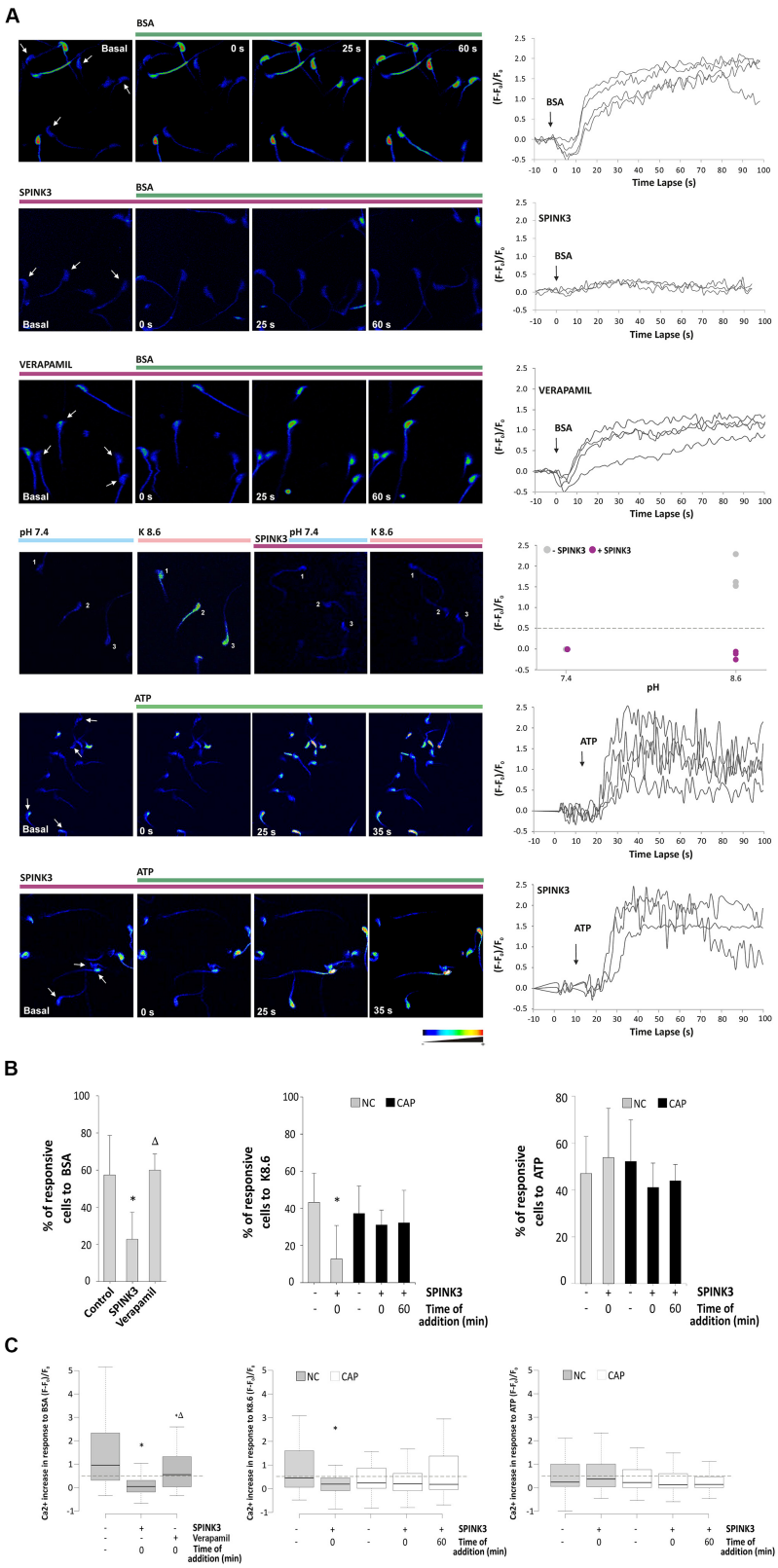

FIGURE 3 | Effect of SPINK3 on $[Ca^{2+}]i$ during sperm capacitation. Non-capacitated sperm loaded with Fluo-3 AM were exposed to 13 μM SPINK3 or 100 μM verapamil for 15 min. After washing with fresh media, cells were smeared on laminin-coated slides and basal calcium signal (F_0) was monitored before any stimulus

(Continued)

FIGURE 3 | Continued
was applied. Single-cell fluorescence (F) was monitored and recorded. **(A)** Representative pseudocolor images of calcium concentration in the head of control cells. Different stimuli (BSA, K8.6 medium or ATP) were added to test an intracellular calcium increase (green bar). Graph on right panels show representative images for calcium fluctuations, obtained as the fluorescence change $(F - F_0)/F_0$. **(B)** Percentages of sperm that increased at least 1.5-fold the calcium intensity compared to the basal signal after stimulus. Capacitated (CAP) or non-capacitated (NC) sperm were treated as indicated (left panel, BSA: $n = 12$, 822 cells, $^*p < 0.05$ with respect to control, $\Delta p < 0.05$ with respect to SPINK3; middle panel K8.6: $n = 3$, 430 cells, $^*p < 0.05$ with respect to control; right panel: ATP: $n = 3$, 410 cells, $^*p < 0.05$ with respect to control). **(C)** Fluorescence intensity after 60 s of stimulus expressed as $(F - F_0)/F_0$, where F is the fluorescence intensity at time t and F_0 is the mean basal fluorescence. The dotted line indicates the threshold lay out from which a significant increase in calcium uptake in the sperm head (positive response) was considered. Outliers were excluded from the graphical representation. Capacitated or non-capacitated sperm were treated as indicated (left panel, BSA: $n = 12$, 822 cells, $^*p < 0.05$ with respect to control, $\Delta p < 0.05$ with respect to SPINK3; middle panel K8.6: $n = 3$, 430 cells, $^*p < 0.05$ with respect to control; right panel: ATP: $n = 3$, 410 cells, $^*p < 0.05$ with respect to control).

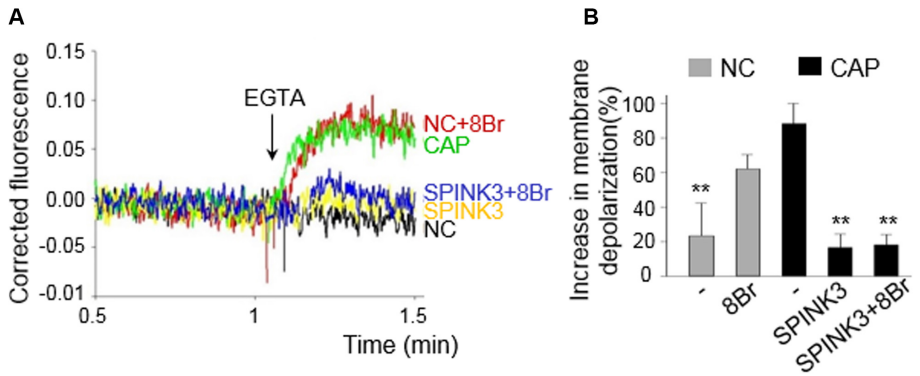

FIGURE 4 | Effect of SPINK3 on Sodium-dependent depolarization induced by EGTA. CatSper opening was indirectly assessed by membrane potential (*Em*) recordings, and following the magnitude of the EGTA-induced depolarization. Capacitated (CAP) or non-capacitated (NC) sperm were loaded with 1 μM $DISC_3(5)$ during *Em* recordings. **(A)** Representative traces are shown for all conditions assayed: CAP (green), NC (black), CAP + 13 μM SPINK3 (yellow); NC + 1 mM 8Br-cAMP (red); CAP + 13 μM SPINK3 + 1 mM 8Br-cAMP (blue). **(B)** The increase in membrane depolarization is expressed as $(F - F_0)/F_0 \times 100$, where F_0 is the mean value before EGTA addition, and F represents the $DISC_3(5)$ signal after addition of EGTA. $^{**}p < 0.01$ with respect to CAP.

evidence ascribes to SPINK3 functions other than a protease inhibitor, e.g., growth factor for regeneration of pancreatic acinar cells and cell proliferation during early embryogenesis (Ohmuraya et al., 2005, 2006). Although SPINK3 lacks calcium-binding domains that could act as Ca^{2+} chelator (Marchler-Bauer and Bryant, 2004; de Castro et al., 2006; Mazumder et al., 2014), it has been described as a Calcium Transport Inhibitory protein (CalTrIn) because it could reduce intracellular calcium content in sperm (Coronel et al., 1992; Zalazar et al., 2012). Our manuscript shows that SPINK3 is capable of impairing sperm membrane hyperpolarization and calcium influx through CatSper when present during capacitation at physiologically relevant concentrations, substantiating the molecular basis of its action as a decapacitating factor. However, no protease target for SPINK3 inhibitory action has been identified.

The mechanisms that regulate hyperpolarization of the sperm plasma membrane during capacitation are poorly understood. Using knock-out mouse models it was observed that sperm lacking the sperm-specific K^+ channel SLO3 do not undergo hyperpolarization during capacitation. We have previously shown that activation of the tyrosine kinase Src is necessary for hyperpolarization of the mouse sperm plasma membrane (Stival et al., 2015), as it modulates SLO3 function. Thus, the fact that SPINK3 prevented activation of Src, substantiates the hypothesis that SPINK3 prevents hyperpolarization through lack of SLO3 opening. Hyperpolarization was shown to be required for exocytosis of the sperm acrosome (De La Vega-Beltran et al., 2012). In this regard, the inhibition of acrosome responsiveness by SPINK3 could be explained by the lack of hyperpolarization. Accordingly, sperm lacking SLO3 do not undergo acrosome reaction when stimulated (Chávez et al., 2013).

Two types of Ca^{2+} channels have been reported to be present in mouse sperm flagellum; the sperm-specific voltage-dependent CatSper channel (at the principal piece) and P2X receptor channels (purinergic Ca^{2+} channels, at the midpiece). However, only CatSper was shown to be active during capacitation (reviewed by Lishko and Mannowetz, 2018). The fact that Ca^{2+} cytoplasmic increase was abrogated by SPINK3, suggests that normal function of CatSper is being impaired by SPINK3. It has been proposed that the elevation of Ca^{2+} necessary to hyperactivate the sperm is primarily driven by an interplay of CatSper and SLO3 channels (Navarro et al., 2007; Zeng et al., 2011, 2013). However, the functional relationship between the two channels has not yet been completely demonstrated. Activation of CatSper by SLO3 appears to be indirect and may involve a voltage-dependent change in intracellular pH (Kirichok et al., 2006; Chávez et al., 2013). Our data indicate that when SPINK3 is present since the beginning of capacitation, Ca^{2+} influx through CatSper is impaired. This conclusion is supported by the following evidence: (a) BSA fails to elicit intracellular Ca^{2+} increase when SPINK3 is present; (b) SPINK3 does not abolish Ca^{2+} increase when sperm are prompted with ATP,

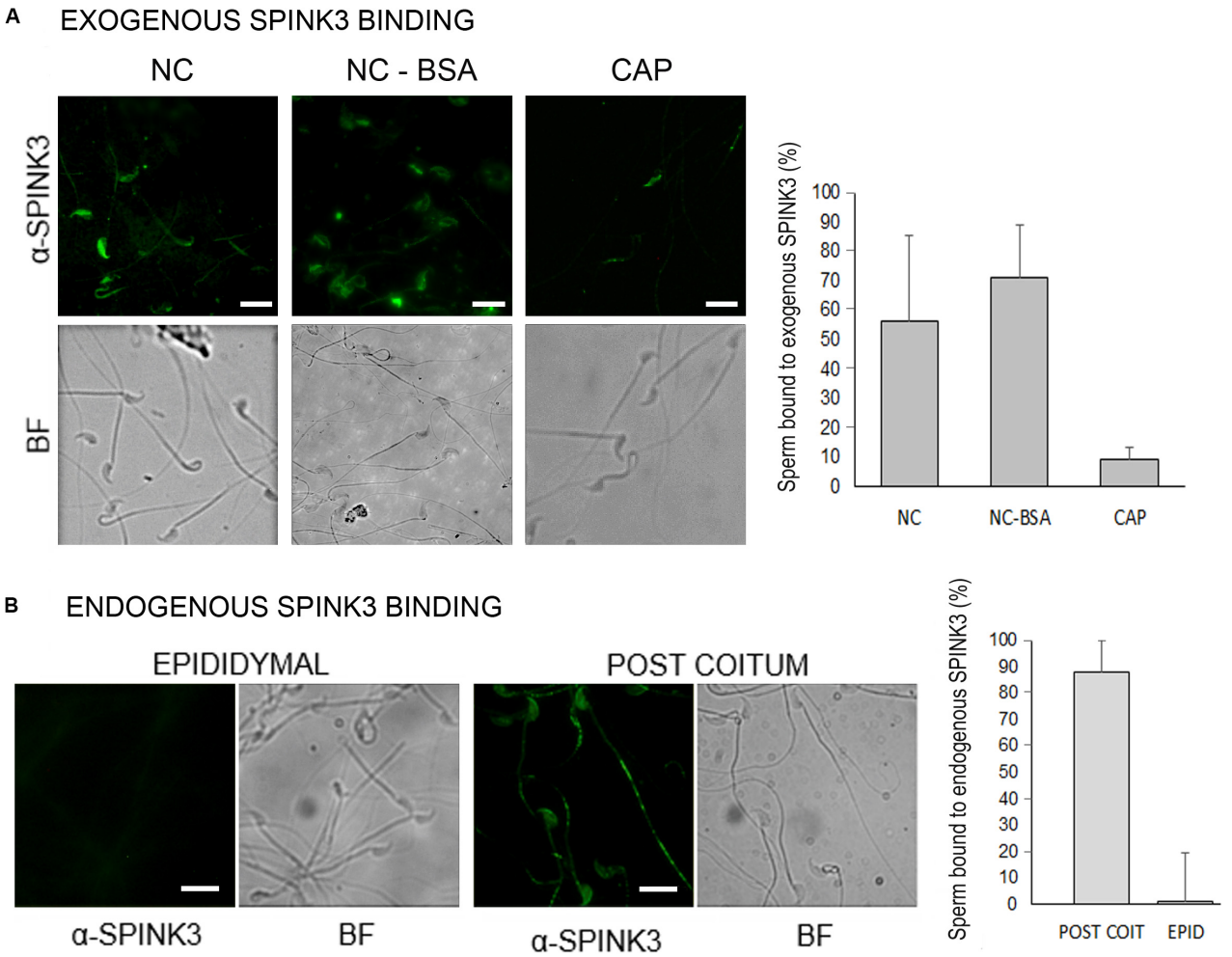

FIGURE 5 | Distribution of SPINK3 on capacitated and non-capacitated sperm. **(A)** Caudal sperm were incubated in non-capacitating (NC) or capacitating (CAP) conditions and then treated with recombinant SPINK3 (13 μM, "exogenous SPINK3") for 15 min, washed and fixed. As a control of BSA blocking effect, a NC + BSA condition was included. SPINK3 was immunodetected as detailed in Methods. **(B)** Sperm recovered from the uterus of synchronized females immediately after coitus or from the male epididymis (negative control of cells that were not in contact with seminal vesicle secretions) were fixed. Then, native SPINK3 ("endogenous SPINK3") was immunodetected. For **(A,B)** left panel shows representative pseudocolor images and bright fields (BF), and right panel shows percentage of positive immunoreactive cells. Scale bar = 10 μM.

suggesting that P2X channels are not involved, (c) Ca^{2+} increase caused by alkalization/depolarization triggered by K8.6 solution is affected by the presence of SPINK3, and (d) SPINK3 decreases the depolarization induced by monovalent ions influx when EGTA is added to the extracellular media. Whether SPINK3 affects calcium entry through an indirect effect on SLO3 appears as a plausible explanation, although a direct effect cannot be discarded, based on the effect seen by SPINK3 on K8.6 prompted sperm. Further supporting a possible direct effect, SPINK3 effect on CatSper could not be rescued by directly activating PKA with 8Br-cAMP, substantiating that SPINK3 effect is not due to PKA downregulation. It should be noted that cAMP analogs could also act directly on CatSper, through extracellular binding (Wang et al., 2020).

Calcium influx mediated by CatSper is required for essential sperm functions, including hyperactivation (Lishko and Mannowetz, 2018). In this regard, SPINK3 also affected the acquisition of the hyperactivated motility. However, SPINK3 affected neither progesterone-induced acrosome reaction nor hyperactivation when added after capacitation has been completed. This might reflect the lack of SPINK3 binding to capacitated sperm, as supported by our immunofluorescence data. Single-cell analysis showed that $[Ca^{2+}]i$ increase observed when sperm were prompted with different stimuli was not homogeneous throughout the population; half of the sperm were responsive to BSA stimulus and among them, half of these cells were not affected by the presence of SPINK3. The existence of sperm sub-populations was already described (Buffone et al., 2004; Sousa et al., 2011; Cisneros-Mejorado et al., 2014), and was therefore not surprising. In this regard, SPINK3 could not bind equally to all spermatozoa, as seen by immunofluorescence

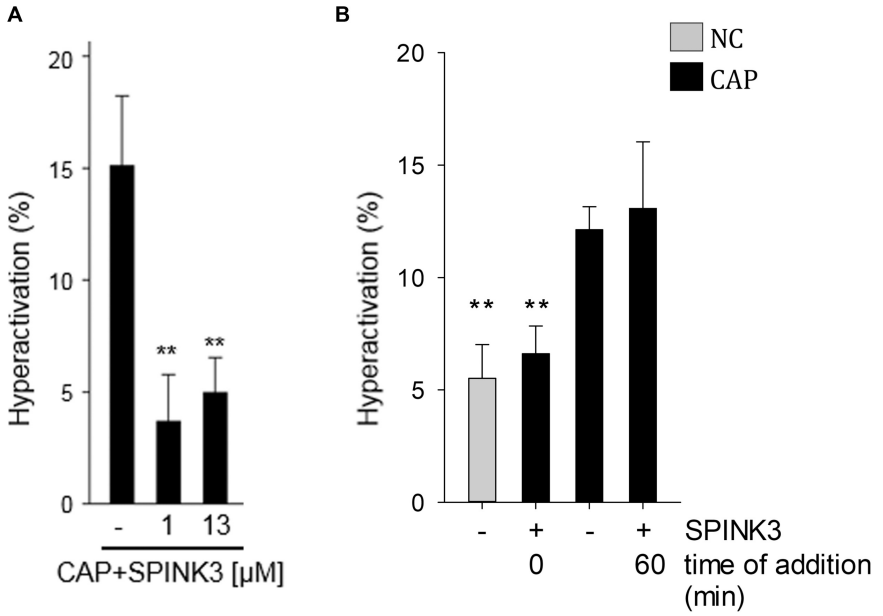

FIGURE 6 | Effect of SPINK3 on hyperactivation. **(A)** Mouse sperm were incubated in the absence or presence of different SPINK3 concentrations in medium that supports capacitation (CAP). Hyperactivation was analyzed using a Hamilton Thorne IVOS CASA system (data represents mean ± SE, $n = 3$; $^{**}p < 0.01$ with respect to CAP control). **(B)** Sperm were incubated under non-capacitating (NC) or capacitating (CAP) medium for 75 min, and 1 μM SPINK3 was added either since the beginning (0 min) or at the end (60 min) of the capacitation period (data represents mean ± S.E.M., $n = 3$; $^{**}p < 0.01$ with respect to CAP control).

assays probably due to different degrees of sperm epididymal maturation. In addition to different maturational status, a selective binding mechanism of SPINK3 to non-capacitated cells over capacitated sperm would evidence its role as decapacitating factor. Therefore, SPINK3 could allow triggering of capacitation at proper timing while not affecting cells that have already initiated capacitation.

In conclusion, this work presents molecular insights into the decapacitating effect exerted by the seminal plasma protein SPINK3 on mouse sperm. Its presence in the capacitation medium prevented both acquisition of hyperactivation and acrosomal responsiveness and inhibits the acquisition of sperm hyperpolarization associated to sperm capacitation. This effect involves a deficient Ca^{2+} uptake through CatSper, which altogether stands out as the main mechanism for its decapacitation effect. Thus, sperm encounter SPINK3 during ejaculation, preventing off-site capacitation. Whether the environment of the female tract contributes to SPINK3 detachment, allowing capacitation to proceed still needs to be addressed.

MATERIALS AND METHODS

Reagents

Secondary antibodies were from Cell Signaling Technologies, Fluo-3 AM and Pluronic acid F127 from Invitrogen, United States. Laminin was acquired from BD. All other chemicals and reagents were analytical grade and obtained either from Merck or Sigma-Aldrich.

Animals

BalbC and C57-BL mice (*Mus musculus*) were maintained at 22°C with a photoperiod of 12 h light: 12 h darkness, food and water *ad libitum*. Sexually mature (2–3 months old) male mice were euthanized by cervical dislocation or by CO_2, inhalation, and sperm from caudal epididymides were removed. All procedures were in agreement with the local Ethics Committee of the National University of Mar del Plata (RD 225/16), as well as the Animal Care and Use Committee of the National University of Rosario (RD 7298/532), following the National Institutes of Health Guide for the Care and Use of Laboratory Animals[1].

Heterologous Expression of Recombinant SPINK3

The cDNA encoding the mature SPINK3 from *Mus musculus* (NCBI ID: NM 009258.5) was cloned into the pET-24b (+) (Novagen, United States) expression vector. Overexpression of SPINK3 was performed in *Escherichia coli* Rosetta cells (Novagen, United States) and the recombinant protein was purified to apparent homogeneity by a HiTrap IMAC HP (GE Healthcare Life Sciences, United States) affinity chromatography as was described in a previous work Assis et al. (2013). Purified recombinant protein was dialyzed against phosphate buffer saline (PBS, 10 mM phosphate buffer, 137 mM NaCl and 2.7 mM KCl pH 7.4).

[1]http://grants.nih.gov/grants/olaw/Guide-for-the-Care-and-Use-of-Laboratory-Animals.pdf

Sperm Preparation

Cauda epididymides were immersed in HM medium (Modified Krebs Ringer medium without bicarbonate: 25 mM Hepes, 109 mM NaCl, 14.77 mM KCl, 1.19 mM $MgSO_4$, 5.6 mM glucose, 21.18 mM sodium lactate, 1.19 mM KH_2PO_4, 1.2 mM sodium pyruvate and 1.7 mM $CaCl_2$; pH 7.4) placed in culture dishes on a warm plate at 37°C. The tissues were minced with scissors to allow the sperm dispersion into the media. After 10 min, tissue debris were removed, and caudal non-capacitated sperm were washed with fresh HM medium by mild centrifugation. For capacitation, 25 mM $NaHCO_3$ and 3 mg/ml BSA (HMB) was added, and sperm incubated in an atmosphere of 5% CO_2 at 37°C for 90 min, at 7.5 × 10^6 cells/ml, as indicated in the corresponding assays. In cases where capacitation was performed in the presence of either 0.5, 1, or 13 μM SPINK3, the peptide was added to the sperm suspension from the beginning of the incubation time (t_0) or after capacitation (t_{60}), as indicated in each experiment.

Time Lapse Single-Cell Imaging

Non-capacitated sperm (10 × 10^6 cells/ml) were loaded with 10 μM Fluo-3 AM (Invitrogen United States, Molecular Probes F1242) and 0.02% (v/v) pluronic acid (Invitrogen, United States) as a surfactant at 37°C for 30 min in HM medium. After incubation, sperm were washed by centrifugation (3 × 700 × *g*, 5 min) to remove unincorporated dye. To evaluate the effect of different compounds, sperm were pre-incubated during 15 min in non-capacitating medium at 37°C in the presence or absence of 13 μM SPINK3. Unless indicated, the assay was performed with non-capacitated spermatozoa. As a control, cells were treated with 100 μM Verapamil (a L-type calcium channel blocker). Cells from an aliquot of each treatment were adhered onto a chamber with a slide previously covered with laminin (100 μg/ml, BD Biosciences) to ensure the head sperm adherence to the glass. HM medium supplemented with 25 mM $NaHCO_3$ was added to the chamber and basal fluorescence was monitored under confocal microscope (excitation 488 nm; emission 526 nm, Nikon C1SiR) at 400 x magnification. A stimulus of BSA (3 mg/ml final concentration) or extracellular ATP (2.5 mM, Pharmacia, United States) was applied, and changes in calcium signal were video recorded throughout the process at the times indicated. At specified times, 10 μM A23187 was added to identify responsive cells. Fluorescence signal intensity was quantified at the head of sperm with beating flagella by using ImageJ 1.43 free software (National Institutes of Health, Bethesda, Maryland, United States)[2]. Data were normalized using the equation $(F - F_0)/F_0$, where F is the fluorescence intensity at time t and F_0 is the mean fluorescence taken during the control period (initial 10 s) before the addition of either BSA or ATP. Then, total series of $(F - F_0)/F_0$ plotted vs. time as well as the percentage of positive response to stimulus. Threshold to consider a significant increase in calcium uptake was as previously reported (Xia and Ren, 2009). For alkalization assay, cells were incubated under the appropriate conditions and seeded onto laminin coated slides in a perfusion chamber. The chamber was filled with HM medium supplemented with 25 mM $NaHCO_3$ (pH 7.4) and basal fluorescence was monitored. The increase in calcium after a change in the pH by addition of K8.6 solution (135 mM KCl, 5 mM NaCl, 2 mM $CaCl_2$, 1 mM $MgCl_2$, 10 mM glucose, 10 mM lactic acid, 1 mM sodium pyruvate, 30 mM HEPES, pH 8.6 (Wennemuth et al., 2000) was evaluated. Data were normalized using the equation $(F - F_0)/F_0$, where F is the fluorescence intensity after addition of K8.6 medium and F_0 is the basal fluorescence. Cells that increased at least 1.5-fold the calcium intensity after K8.6 medium were quantified.

[2]http://imagej.nih.gov/ij/

Immunolocalization of SPINK3

For detection of recombinant SPINK3 binding to capacitated or non-capacitated sperm, caudal sperm were obtained in HM. After washing, cells were incubated either in HM (NC), HM plus 3% BSA (NC-BSA) or HMB (CAP) for 60 min. Then, sperm were washed (700 x g, 10 min) with PBS and incubated with or without 13 μM recombinant SPINK3 for 15 min, washed, fixed with 4% (v/v) formaldehyde solution and placed onto glass slides. Sperm were blocked in PBS plus 3% (w/v) BSA for 1 h, and then incubated overnight with anti-SPINK1 antibody (1:50, Sigma-Aldrich, HPA027498, this antibody reacts against SPINK3 (Zalazar et al., 2012) in blocking solution. Thereafter, slides were gently washed and incubated for 2 h with both anti-rabbit IgG Alexa Fluor 555 conjugated (1:1,000, Thermo Fisher Scientific). Slides were washed, mounted with Glicerol:PBS (9:1) and observed under 480/525 nm filter on a microscope: Nikon Eclipse T2000. The specificity of the antibody was assessed in samples without SPINK3, and secondary antibody control was performed by incubating without the respective primary antibodies. For the detection of endogenous SPINK3, sperm were recovered from the uterus of synchronized females immediately after coitus or from the male epididymis (negative control of cells that were not in contact with seminal vesicle secretions), washed (700 × *g*, 10 min) with PBS and fixed with 4% (v/v) formaldehyde solution. Immunolocalization assay was performed as was previously described by using anti-SPINK1 antibody (1:50, Sigma-Aldrich, HPA027498) and anti- rabbit IgG Alexa Fluor 488 (1:1,000, Thermo Fisher Scientific, A11070).

Evaluation of Acrosome Reaction (AR)

Caudal sperm were capacitated in HMB medium for 60 min, with or without SPINK3. For induced AR, sperm were incubated with 50 μM progesterone (Zalazar et al., 2012) or 10 μM A23187 (Sigma-Aldrich, United States) for 15 min after 60 min capacitation. To evaluate the effect of SPINK3 over AR once capacitation was completed, cells were capacitated at 37°C for 1 h without SPINK3 and thereafter SPINK3 was added for 15 min before progesterone induction of AR. Cells were fixed with 4% (v/v) formaldehyde solution in PBS and washed with 100 mM ammonium acetate (pH 9). The acrosomal status was evaluated according to the *Coomassie Brilliant Blue* (CBB) G-250 staining technique (Bendahmane et al., 2002). Briefly, sperm were placed and smeared onto glass slides and stained with a 0.22% (w/v) CBB G-250 solution prepared in 50% (v/v) methanol and 10% (v/v) acetic acid. The slides

were washed with distilled water, dried, smeared on glycerol: PBS (9:1) and observed under a light microscope at 400 x magnification by two independent observers. A blue stain over the sperm head dorsal and/or ventral edge was visualized in spermatozoa with intact acrosome, whereas no stain was observed in spermatozoa with reacted acrosome. Spermatozoa that lost their acrosomes were quantified as a percentage over 200–400 cells per replicate.

SDS-PAGE and Immunoblotting

Samples were prepared as described previously (Ritagliati et al., 2018b). Briefly, sperm were collected after treatments by centrifugation, washed in 1 ml of TBS, resuspended in Laemmli sample buffer without β-mercaptoethanol, and boiled for 3 min. After centrifugation, 5% (v/v) β-mercaptoethanol was added to the supernatants and boiled again for 5 min. Protein extracts equivalent to 1–2 $\times$ 10^6 spermatozoa per lane were subjected to SDS-PAGE and electro-transferred to PVDF membranes (Bio-Rad) at 250 mA for 60 min on ice. Membranes were blocked with 5% (w/v) fat free milk in TBS containing 0.1% (v/v) Tween-20 (T-TBS). For anti-pY and anti-pPKA immunodetections, membranes were blocked with 3% (w/v) BSA (Sigma) in T-TBS. Antibodies were diluted in T-TBS as follows: 1/10,000 for anti-pY (clone 4G10 Millipore), 1/5,000 for anti-pPKA (clone 100G7E Cell Signaling Technology), 1/10,000 for anti-tubulin (clone E7, Hybridoma bank), anti 1/2,000 pSrcY416 (Cell Signaling Technology clone D49G4). Secondary antibodies were diluted 1/10,000 in T-TBS and developed using an enhanced chemiluminescence detection kit (ECL plus, Amersham, GE Healthcare) according to the manufacturer's instructions. When necessary, PVDF membranes were stripped at 60°C for 15 min in 2% (w/v) SDS, 0.74% (v/v) β-mercaptoethanol, 62.5 mM Tris, pH 6.5, and washed 6 $\times$ 5 min in T-TBS. In all experiments, molecular masses were expressed in kDa. Western blots showed in the manuscript are representative of at least three replicates.

Membrane Potential Assay in Cell Populations

After sperm treatment, cells were collected by centrifugation (700 $\times$ g, 5 min) and concentration was adjusted to 2.7 $\times$ 10^6 sperm/ml. Then, sperm were loaded with 1 μM of the membrane potential-sensitive dye $DISC_3(5)$ (Molecular Probes) for 5 min. No mitochondrial un-couplers were used because their contribution to the resting potential has been determined to be insignificant (Chávez et al., 2013). The sperm were transferred to a gently stirred cuvette at 37°C, and the fluorescence was monitored with a Varian Cary Eclipse fluorescence spectrophotometer at 620/670 nm excitation/emission wavelengths. Recordings were initiated when steady-state fluorescence was reached and calibration was performed at the end of each measure by adding 1 μM valinomycin and sequential additions of KCl as previously described (Ritagliati et al., 2018a). Sperm *Em* was obtained from the initial fluorescence (measured as arbitrary fluorescence units) by linearly interpolating it in the theoretical *Em* values for the calibration curve against arbitrary fluorescence units of each trace. This internal calibration for each determination compensates for variables that influence the absolute fluorescence values.

Sodium Dependent Depolarization Induced by EGTA as a Measure of Calcium Channels Activity

For experiments where EGTA-induced depolarization was assessed, extracellular Ca^{2+} was chelated using EGTA allowing sodium ions influx through CatSper to occur (Kirichok et al., 2006). The magnitude of the depolarization caused by Na^+ (present in the culture media) influx relates to the extent of the channel opening. Cells were incubated during capacitation as required, and then loaded with 1 μM $DISC_3(5)$. Fluorescence was recorded as detailed above. Calcium was chelated with 3.5 mM EGTA to a free calcium value of 138 nM (MaxChelator) (Patton et al., 2004). The fluorescence change was presented as $(F - F_0)/(F_0)$, where F represents fluorescence intensity after EGTA addition, F_0 is the mean of 1 min of acquisition before addition of EGTA (Stival et al., 2018).

Sperm Motility Analysis

Sperm suspensions were loaded so as to form a 40 μM depth chamber slide and placed on a Hamilton Thorne IVOS CASA analyzer (Hamilton Thorne Research, Beverly, MA), at 37°C. Parameters used were as follows: 30 frames acquired, frame rate of 60 Hz, minimum cell size of 4 pixels, low average path velocity cutoff of 10 mm/s, static head size of 0.43–2.43, static head intensity of 0.53–1.52, and static head elongation lower than 100. At least 10 microscopy fields corresponding to a minimum of 200 sperm were analyzed in each experiment. Hyperactivated sperm were classified as such when presenting; Curvilinear Velocity (VCL) $\geq$271 μM/s, Linearity (LIN) <50% and Amplitude of Lateral Head displacement (ALH) >7 μM.

Statistical Analysis

Data from all experiments were analyzed by GLMM (generalized linear mixed effect model) to determine statistical significance between treatments and control (Zuur et al., 2009). Data associated to cell percentages were analyzed through models with binomial distribution, whereas fluorescence intensities were analyzed by models with Gaussian error distribution. In both cases, normality of residuals was assessed by plotting theoretical quantiles vs. standardized residuals (Q–Q plots). Homogeneity of variance was evaluated by plotting residuals vs. fitted values. A *post-hoc* analysis was conducted with the "lsmeans" package (Lenth, 2016). All analyses were performed using R software version 3.3.3[3], with the "lme4" package for binomial models and the "nlme" package for Gaussian models (Pinheiro et al., 2017). For all analyses, statistically significant differences were determined at p <0.05. Graph bars indicate mean ± SE.

[3]https://CRAN.R-project.org/package=nlme

DATA AVAILABILITY STATEMENT

All datasets generated for this study are included in the article/**Supplementary Material**.

ETHICS STATEMENT

The animal study was reviewed and approved by the Ethics Committee of the National University of Mar del Plata (RD 225/16), as well as the Animal Care and Use Committee of the National University of Rosario (RD 7298/532).

AUTHOR CONTRIBUTIONS

AC and DK contributed to the conceptualization of the study, supervision, and project administration. LZ, CS, GD, and AN contributed to the design and development of the methodology. AC, DK, LZ, and CS contributed to the writing – reviewing and editing of the manuscript. All the co-authors were involved in the formal analysis, validation, and visualization of the results.

FUNDING

This research was supported by grants from the National Scientific and Technical Research Council (CONICET, Argentina, PIP 11220130100273 awarded to AC), and from ANPCyT (PICT 2015-3164 and PICT 2017-3217 awarded to DK; PICT 2015-3682 awarded to AC).

ACKNOWLEDGMENTS

We would like to thank D. Villamonte, C. Sosa, J. Ibañez, and J. P. Busalmen for their support on the single cell time lapse assay, M. Greco for the assistance in western blotting, and P. E. Meretta for statistical analyses.

SUPPLEMENTARY MATERIAL

The Supplementary Material for this article can be found online at: https://www.frontiersin.org/articles/10.3389/fcell.2020.575126/full#supplementary-material

MOVIE S1 | Time course of the Ca^{2+} fluorescence changes with BSA stimulus. Non-capacitated sperm were loaded with Fluo-3 AM and smeared onto laminin coated slides. Basal calcium signal was monitored for 10 s after addition of BSA stimulus had been applied.

MOVIE S2 | Time course of the Ca^{2+} fluorescence changes with BSA stimulus in the presence of SPINK3. Non-capacitated sperm were loaded with Fluo-3 AM and incubated with 13 μM SPINK3 during 15 min at 37°C before being smeared onto laminin coated slides. Basal calcium signal was monitored for 10 s after addition of BSA stimulus had been applied.

REFERENCES

Aitken, R. J., and Nixon, B. (2013). Sperm capacitation: a distant landscape glimpsed but unexplored. *Mol. Hum. Reprod.* 19, 785–793. doi: 10.1093/molehr/gat067

Araki, N., Trencsényi, G., Krasznai, Z. T., Nizsalóczki, E., Sakamoto, A., Kawano, N., et al. (2015). Seminal vesicle secretion 2 acts as a protectant of sperm sterols and prevents ectopic sperm capacitation in mice1. *Biol. Reprod.* 92, 8–10.

Assis, D., Zalazar, L., Juliano, M., Castro, R., and Cesari, A. (2013). Novel inhibitory activity for serine protease inhibitor kazal Type-3 (Spink3) on human recombinant kallikreins. *Protein Pept. Lett.* 20, 1098–1107. doi: 10.2174/0929866511320100003

Austin, C. R. (1951). Observations on the penetration of the sperm in the mammalian egg. *Aust. J. Sci. Res. B.* 4, 581–596. doi: 10.1071/bi9510581

Bendahmane, M., Zeng, H. T., and Tulsiani, D. R. P. (2002). Assessment of acrosomal status in rat spermatozoa: Studies on carbohydrate and non-carbohydrate agonists. *Arch. Biochem. Biophys.* 404, 38–47. doi: 10.1016/s0003-9861(02)00278-3

Bers, D. M., Patton, C. W., and Nuccitellid, R. (1994). A practical guide to the preparation of Ca2+buffers. *Methods Cell Biol.* 99, 1–26. doi: 10.1016/b978-0-12-374841-6.00001-3

Buffone, M. G., Doncel, G. F., Briggiler, C. I. M., Vazquez-Levin, M. H., and Calamera, J. C. (2004). Human sperm subpopulations: relationship between functional quality and protein tyrosine phosphorylation. *Hum. Reprod.* 19, 139–146. doi: 10.1093/humrep/deh040

Carlson, A. E., Burnett, L. A., del Camino, D., Quill, T. A., Hille, B., Chong, J. A., et al. (2009). Pharmacological targeting of native CatSper channels reveals a required role in maintenance of sperm hyperactivation. *PLoS One* 4:e6844. doi: 10.1371/journal.pone.0006844

Carlson, A. E., Westenbroek, R. E., Quill, T., Ren, D., Clapham, D. E., Hille, B., et al. (2003). CatSper1 required for evoked Ca2+ entry and control of flagellar function in sperm. *Proc. Natl. Acad. Sci. U.S.A.* 100, 14864–14868. doi: 10.1073/pnas.2536658100

Chang, M. C. (1951). Fertilizing capacity of spermatozoa deposited into the fallopian tubes. *Nature* 168, 697–698. doi: 10.1038/168697b0

Chávez, J. C., de la Vega-Beltrán, J. L., Escoffier, J., Visconti, P. E., Treviño, C. L., Darszon, A., et al. (2013). Ion permeabilities in mouse sperm reveal an external trigger for SLO3-dependent hyperpolarization. *PLoS One* 8:e60578. doi: 10.1371/journal.pone.00060578

Chen, L.-Y., Lin, Y.-H., Lai, M.-L., and Chen, Y.-H. (1998). Developmental profile of a caltrin-Like protease inhibitor, P12, in mouse seminal vesicle and characterization of its binding sites on sperm surface1. *Biol. Reprod.* 59, 1498–1505. doi: 10.1095/biolreprod59.6.1498

Chung, J. J., Shim, S. H., Everley, R. A., Gygi, S. P., Zhuang, X., and Clapham, D. E. (2014). Structurally distinct Ca2+ signaling domains of sperm flagella orchestrate tyrosine phosphorylation and motility. *Cell* 157, 808–822. doi: 10.1016/j.cell.2014.02.056

Cisneros-Mejorado, A., Hernández-Soberanis, L., Islas-Carbajal, M. C., and Sánchez, D. (2014). Capacitation and Ca2+ influx in spermatozoa: role of CNG channels and protein kinase G. *Andrology* 2, 145–154. doi: 10.1111/j.2047-2927.2013.00169.x

Coronel, C., Winnica, D., Novella, M., and Lardy, H. (1992). Purification, structure, and characterization of caltrin proteins from seminal vesicle of the rat and mouse. *J. Biol. Chem.* 267, 20909–20915.

de Castro, E., Sigrist, C. J. A., Gattiker, A., Bulliard, V., Langendijk-Genevaux, P. S., Gasteiger, E., et al. (2006). ScanProsite: detection of PROSITE signature matches and ProRule-associated functional and structural residues in proteins. *Nucleic Acids Res.* 34, W362–W365.

De La Vega-Beltran, J. L., Sánchez-Cárdenas, C., Krapf, D., Hernandez-González, E. O., Wertheimer, E., Treviño, C. L., et al. (2012). Mouse sperm membrane potential hyperpolarization is necessary and sufficient to prepare sperm for the acrosome reaction. *J. Biol. Chem.* 287, 44384–44393. doi: 10.1074/jbc.m112.393488

Del Carmen Neri-Vidaurri, P., Torres-Flores, V., and González-Martínez, M. T. (2006). A remarkable increase in the pHi sensitivity of voltage-dependent

calcium channels occurs in human sperm incubated in capacitating conditions. *Biochem. Biophys. Res. Commun.* 343, 105–109. doi: 10.1016/j.bbrc.2006.02.095

Dematteis, A., Miranda, S. D., Novella, M. L., Maldonado, C., Ponce, R. H., Maldera, J. A., et al. (2008). Rat caltrin protein modulates the acrosomal exocytosis during sperm capacitation1. *Biol. Reprod.* 79, 493–500. doi: 10.1095/biolreprod.107.067538

Fraire-Zamora, J. J., and González-Martínez, M. T. (2004). Effect of intracellular pH on depolarization-evoked calcium influx in human sperm. *Am. J. Physiol. Cell Physiol.* 287, C1688–C1696.

González-Martínez, M. T. (2003). Induction of a sodium-dependent depolarization by external calcium removal in human sperm. *J. Biol. Chem.* 278, 36304–36310. doi: 10.1074/jbc.m304479200

Hess, K. C., Jones, B. H., Marquez, B., Chen, Y., Ord, T. S., Kamenetsky, M., et al. (2005). The "soluble" adenylyl cyclase in sperm mediates multiple signaling events required for fertilization. *Dev. Cell* 9, 249–259. doi: 10.1016/j.devcel.2005.06.007

Hwang, J. Y., Mannowetz, N., Zhang, Y., Everley, R. A., Gygi, S. P., Bewersdorf, J., et al. (2019). Dual sensing of physiologic pH and Calcium by EFCAB9 regulates sperm motility. *Cell* 177, 1480–1494. doi: 10.1016/j.cell.2019.03.047

Kirichok, Y., Navarro, B., and Clapham, D. E. (2006). Whole-cell patch-clamp measurements of spermatozoa reveal an alkaline-activated Ca2+ channel. *Nature* 439, 737–740. doi: 10.1038/nature04417

Krapf, D., Arcelay, E., Wertheimer, E. V., Sanjay, A., Pilder, S. H., Salicioni, A. M., et al. (2010). Inhibition of Ser/Thr phosphatases induces capacitation-associated signaling in the presence of Src kinase inhibitors. *J. Biol. Chem.* 285, 7977–7985. doi: 10.1074/jbc.m109.085845

Lenth, R. V. (2016). Least-squares means: the R package lsmeans. *J. Stat. Softw.* 69, 1–33.

Li, S.-H., Lu, C.-H., Li, R. K.-K., Hwu, Y.-M., Chen, Y.-J., Chang, W.-C., et al. (2010). SERPINE2, a serine protease inhibitor extensively expressed in adult male mouse reproductive tissues, may serve as a murine sperm decapacitation factor. *Biol. Reprod.* 84, 514–525. doi: 10.1095/biolreprod.110.085100

Lin, M. H., Lee, R. K. K., Hwu, Y. M., Lu, C. H., Chu, S. L., Chen, Y. J., et al. (2008). SPINKL, a Kazal-type serine protease inhibitor-like protein purified from mouse seminal vesicle fluid, is able to inhibit sperm capacitation. *Reproduction* 136, 559–571. doi: 10.1530/rep-07-0375

Lishko, P. V., and Mannowetz, N. (2018). CatSper: a unique calcium channel of the sperm flagellum. *Curr. Opin. Physiol.* 2, 109–113. doi: 10.1016/j.cophys.2018.02.004

López-González, I., Torres-Rodríguez, P., Sánchez-Carranza, O., Solís-López, A., Santi, C. M., Darszon, A., et al. (2014). Membrane hyperpolarization during human sperm capacitation. *Mol. Hum. Reprod.* 20, 619–629. doi: 10.1093/molehr/gau029

Marchler-Bauer, A., and Bryant, S. H. (2004). CD-Search: protein domain annotations on the fly. *Nucleic Acids Res.* 32, W327–W331.

Mazumder, M., Padhan, N., Bhattacharya, A., and Gourinath, S. (2014). Prediction and analysis of canonical EF hand loop and qualitative estimation of Ca2+ binding affinity. *PLoS One* 9:e96202. doi: 10.1371/journal.pone.0096202

Navarro, B., Kirichok, Y., and Clapham, D. E. (2007). KSper, a pH-sensitive K+ current that controls sperm membrane potential. *Proc. Natl. Acad. Sci. U.S.A.* 104, 7688–7692. doi: 10.1073/pnas.0702018104

Navarro, B., Miki, K., and Clapham, D. E. (2011). ATP-activated P2X2 current in mouse spermatozoa. *Proc. Natl. Acad. Sci. U.S.A.* 108, 14342–14347. doi: 10.1073/pnas.1111695108

Ohmuraya, M., Hirota, M., Araki, K., Baba, H., and Yamamura, K. I. (2006). Enhanced trypsin activity in pancreatic acinar cells deficient for serine protease inhibitor Kazal type 3. *Pancreas* 33, 104–106. doi: 10.1097/01.mpa.0000226889.86322.9b

Ohmuraya, M., Hirota, M., Araki, M., Mizushima, N., Matsui, M., Mizumoto, T., et al. (2005). Autophagic cell death of pancreatic acinar cells in serine protease inhibitor Kazal type 3-deficient mice. *Gastroenterology* 129, 696–705. doi: 10.1016/j.gastro.2005.05.057

Ohmuraya, M., Sugano, A., Hirota, M., Takaoka, Y., and Yamamura, K. I. (2012). Role of intrapancreatic SPINK1/Spink3 expression in the development of pancreatitis. *Front. Physiol.* 3:126. doi: 10.3389/fphys.2012.00126

Orta, G., De La Vega-Beltran, J. L., Martín-Hidalgo, X. D., Santi, C. M., Visconti, P. E., and Darszon, X. A. (2019). CatSper channels are regulated by protein kinase A. *J. Biol. Chem.* 293, 16830–16841. doi: 10.1074/jbc.ra117.001566

Ou, C. M., Tang, J. B., Huang, M. S., Sudhakar Gandhi, P. S., Geetha, S., Li, S. H., et al. (2012). The mode of reproductive-derived Spink (serine protease inhibitor Kazal-type) action in the modulation of mammalian sperm activity. *Int. J. Androl.* 35, 52–62. doi: 10.1111/j.1365-2605.2011.01159.x

Patton, C., Thompson, S., and Epel, D. (2004). Some precautions in using chelators to buffer metals in biological solutions. *Cell Calcium* 35, 427–431. doi: 10.1016/j.ceca.2003.10.006

Pinheiro, J., Bates, D., DebRoy, S., and Sarkar, D. (2017). *nlme: Linear and Nonlinear Mixed Effects Models. R Package Version 3.1-131.*

Puga Molina, L. C., Luque, G. M., Balestrini, P. A., Marín-Briggiler, C. I., Romarowski, A., and Buffone, M. G. (2018). Molecular basis of human sperm capacitation. *Front. Cell Dev. Biol.* 6:72. doi: 10.3389/fcell.2018.00072

Ren, D., and Xia, J. (2010). Calcium signaling through CatSper channels in mammalian fertilization. *Physiology* 25, 165–175. doi: 10.1152/physiol.00049.2009

Ritagliati, C., Baro Graf, C., Stival, C., and Krapf, D. (2018a). Regulation mechanisms and implications of sperm membrane hyperpolarization. *Mech. Dev.* 154, 33–43. doi: 10.1016/j.mod.2018.04.004

Ritagliati, C., Luque, G. M., Stival, C., Baro Graf, C., Buffone, M. G., and Krapf, D. (2018b). Lysine acetylation modulates mouse sperm capacitation. *Sci. Rep.* 8:13334.

Samanta, L., Parida, R., Dias, T. R., and Agarwal, A. (2018). The enigmatic seminal plasma: a proteomics insight from ejaculation to fertilization. *Reprod. Biol. Endocrinol.* 16:41.

Santi, C. M., Martínez-López, P., de la Vega-Beltrán, J. L., Butler, A., Alisio, A., Darszon, A., et al. (2010). The SLO3 sperm-specific potassium channel plays a vital role in male fertility. *FEBS Lett.* 584, 1041–1046. doi: 10.1016/j.febslet.2010.02.005

Sousa, A. P., Amaral, A., Baptista, M., Tavares, R., Campo, P. C., Peregrín, P. C., et al. (2011). Not all sperm are equal: functional mitochondria characterize a subpopulation of human sperm with better fertilization potential. *PLoS One* 6:e18112. doi: 10.1371/journal.pone.0018112

Stival, C., La Spina, F. A., Graf, C. B., Arcelay, E., Arranz, S. E., Ferreira, J. J., et al. (2015). Src kinase is the connecting player between Protein Kinase A (PKA) activation and hyperpolarization through SLO3 potassium channel regulation in mouse sperm. *J. Biol. Chem.* 290, 18855–18864. doi: 10.1074/jbc.m115.640326

Stival, C., Puga Molina, L. D. C., Paudel, B., Buffone, M. G., Visconti, P. E., and Krapf, D. (2016). Sperm capacitation and acrosome reaction in mammalian sperm. *Adv. Anat. Embryol. Cell Biol.* 220, 93–106. doi: 10.1007/978-3-319-30567-7_5

Stival, C., Ritagliati, C., Xu, X., Gervasi, M. G., Luque, G. M., Graf, C. B., et al. (2018). Disruption of protein kinase A localization induces acrosomal exocytosis in capacitated mouse sperm. *J. Biol. Chem.* 293, 9435–9447. doi: 10.1074/jbc.ra118.002286

Torres-Flores, V., Picazo-Juárez, G., Hernández-Rueda, Y., Darszon, A., and Gonzlez-Martínez, M. T. (2011). Sodium influx induced by external calcium chelation decreases human sperm motility. *Hum. Reprod.* 26, 2626–2635. doi: 10.1093/humrep/der237

Wang, T., Young, S., Tüttelmann, F., Röpke, A., Krallmann, C., Kliesch, S., et al. (2020). Shedding light on the control of CatSper Ca2+ channels by cAMP and chemicals used to probe cAMP signaling. *bioRxiv* [Preprint], doi: 10.1101/2020.02.10.942029

Wennemuth, G., Westenbroek, R. E., Xu, T., Hille, B., and Babcock, D. F. (2000). Ca(v)2.2 and *Ca(v)*2.3 (N- and R-type) Ca2+ channels in depolarization-evoked entry of Ca2+ into mouse sperm. *J. Biol. Chem.* 275, 21210–21217. doi: 10.1074/jbc.m002068200

Xia, J., Reigada, D., Mitchell, C. H., and Ren, D. (2007). CATSPER channel-mediated Ca2+ entry into mouse sperm triggers a tail-to-head propagation. *Biol. Reprod.* 77, 551–559. doi: 10.1095/biolreprod.107.061358

Xia, J., and Ren, D. (2009). The BSA-induced Ca(2+) influx during sperm capacitation is CATSPER channel-dependent. *Reprod. Biol. Endocrinol.* 7:119.

Yanagimachi, R. (1970). The movement of golden hamster spermatozoa before and after capacitation. *J. Reprod. Fertil.* 23, 193–196. doi: 10.1530/jrf.0.0230193

Zalazar, L., Saez Lancellotti, T. E. E., Clementi, M., Lombardo, C., Lamattina, L., De Castro, R., et al. (2012). SPINK3 modulates mouse sperm physiology through the reduction of nitric oxide level independently of its trypsin inhibitory activity. *Reproduction* 143, 281–295. doi: 10.1530/rep-11-0107

Zeng, X. H., Navarro, B., Xia, X. M., Clapham, D. E., and Lingle, C. J. (2013). Simultaneous knockout of slo3 and catsper1 abolishes all alkalization- and voltage-activated current in mouse spermatozoa. *J. Gen. Physiol.* 142, 305–313. doi: 10.1085/jgp.201311011

Zeng, X. H., Yang, C., Kim, S. T., Lingle, C. J., and Xia, X. M. (2011). Deletion of the Slo3 gene abolishes alkalizationactivated K+ current in mouse spermatozoa. *Proc. Natl. Acad. Sci. U.S.A.* 108, 5879–5884. doi: 10.1073/pnas.1100240108

Zuur, A. F., Leno, E. N., Walker, N., Saveliev, A. A., and Smith, G. M. (2009). *Mixed Effects Models and Extensions in Ecology with R*, 1st Edn, New York, NY: Springer.

Conflict of Interest: The authors declare that the research was conducted in the absence of any commercial or financial relationships that could be construed as a potential conflict of interest.

Copyright © 2020 Zalazar, Stival, Nicolli, De Blas, Krapf and Cesari. This is an open-access article distributed under the terms of the Creative Commons Attribution License (CC BY). The use, distribution or reproduction in other forums is permitted, provided the original author(s) and the copyright owner(s) are credited and that the original publication in this journal is cited, in accordance with accepted academic practice. No use, distribution or reproduction is permitted which does not comply with these terms.

frontiers in Cell and Developmental Biology

ORIGINAL RESEARCH
published: 07 December 2020
doi: 10.3389/fcell.2020.588621

Red LED Light Acts on the Mitochondrial Electron Chain of Donkey Sperm and Its Effects Depend on the Time of Exposure to Light

Jaime Catalán[1,2,3], Marion Papas[1], Lina Trujillo-Rojas[1], Olga Blanco-Prieto[1], Sebastián Bonilla-Correal[1], Joan E. Rodríguez-Gil[1], Jordi Miró[1†] and Marc Yeste[2,3†]*

[1] Unit of Animal Reproduction, Department of Animal Medicine and Surgery, Faculty of Veterinary Medicine, Autonomous University of Barcelona, Bellaterra, Spain, [2] Biotechnology of Animal and Human Reproduction (TechnoSperm), Institute of Food and Agricultural Technology, University of Girona, Girona, Spain, [3] Unit of Cell Biology, Department of Biology, Faculty of Sciences, University of Girona, Girona, Spain

OPEN ACCESS

Edited by:
Tomer Avidor-Reiss,
University of Toledo, United States

Reviewed by:
Jorge G. Farias,
University of La Frontera, Chile
Alberto Darszon,
National Autonomous University of Mexico, Mexico
Ana Josefa Soler,
University of Castilla La Mancha, Spain
Felipe Martínez-Pastor,
Universidad de León, Spain

***Correspondence:**
Marc Yeste
marc.yeste@udg.edu

[†]These authors share senior authorship

Specialty section:
This article was submitted to Cell Growth and Division, a section of the journal Frontiers in Cell and Developmental Biology

Received: 29 July 2020
Accepted: 17 November 2020
Published: 07 December 2020

Citation:
Catalán J, Papas M, Trujillo-Rojas L, Blanco-Prieto O, Bonilla-Correal S, Rodríguez-Gil JE, Miró J and Yeste M (2020) Red LED Light Acts on the Mitochondrial Electron Chain of Donkey Sperm and Its Effects Depend on the Time of Exposure to Light. Front. Cell Dev. Biol. 8:588621. doi: 10.3389/fcell.2020.588621

This work aimed to investigate how stimulation of donkey sperm with red LED light affects mitochondrial function. For this purpose, freshly diluted donkey semen was stimulated with red light for 1, 5, and 10 min, in the presence or absence of oligomycin A (Omy A), a specific inhibitor of mitochondrial ATP synthase, or FCCP, a specific disruptor of mitochondrial electron chain. The results obtained in the present study indicated that the effects of red LED light on fresh donkey sperm function are related to changes in mitochondria function. In effect, irradiation of donkey sperm resulted in an increase in mitochondrial membrane potential (MMP), the activity of cytochrome C oxidase and the rate of oxygen consumption. In addition, in the absence of oligomycin A and FCCP, light-stimulation augmented the average path velocity (VAP) and modified the structure of motile sperm subpopulations, increasing the fastest and most linear subpopulation. In contrast, the presence of either Omy A or FCCP abolished the aforementioned effects. Interestingly, our results also showed that the effects of red light depend on the exposure time applied, as indicated by the observed differences between irradiation protocols. In conclusion, our results suggest that exposing fresh donkey sperm to red light modulates the function of their mitochondria through affecting the activity of the electron chain. However, the extent of this effect depends on the irradiation pattern and does not exclude the existence of other mechanisms, such as those related to thermotaxis.

Keywords: sperm, red light stimulation, mitochondrial function, donkey, oligomycin A, FCCP

INTRODUCTION

In recent years, the use and development of artificial insemination (AI) in equine species has grown considerably (Canisso et al., 2008; Crowe et al., 2008; Squires, 2009), and is currently being considered as the basis of modern equine reproduction worldwide (Pagl et al., 2006; Kowalczyk et al., 2019). However, while a significant number of previous studies have described

and characterized the semen of domestic horses, studies on donkey sperm are scarce (Miró and Papas, 2018; Catalán et al., 2020a). In addition to this, at present, the most of European donkey breeds are in danger of extinction, which added to a mounting world demand for new donkey uses (milk, cosmetics or skin production, oncotherapy, silviculture, rural tourism. . .). For these reasons, the interest in developing studies to improve the reproductive performance in this species has increased (Miró et al., 2020). At this respect, it is worth noting that while both horses and donkeys are phylogenetically close species, they show important reproductive differences, and not only do their sperm vary in motility and morphology but also on how they interact with the female endometrium (Miró and Papas, 2018). Be that as it may, the fact that AI has been largely developed in the horse over the last years has fostered the application of those techniques in the donkey, which necessarily entails the need of developing methods, protocols or procedures aimed at optimizing sperm survival and fertilizing capacity, as in the horse (Loomis, 2006; Varner, 2016).

Irradiation of sperm with red light (laser and LED) has been demonstrated to jointly increase sperm motility and mitochondrial activity in sheep, cattle, pigs, donkeys and horses (Iaffaldano et al., 2016; Siqueira et al., 2016; Yeste et al., 2016; Catalán et al., 2020a,b,c). These effects seem, however, to rely upon the light-stimulation pattern, species and other factors, since while it has also been found to increase the *in vivo* fertilizing ability in pigs (Yeste et al., 2016; Blanco-Prieto et al., 2019), its use in separate farms around the world brings significant differences (Blanco-Prieto et al., 2019). In addition, the literature remains inconsistent on how irradiation affects sperm function and, at present, the mechanisms underlying that impact on mammalian spermatozoa remain largely unknown (reviewed in Yeste et al., 2018). Hence, further studies aimed at addressing the machinery that potentially guides the response of sperm to red light in separate species are warranted. In this context, the donkey could be an interesting model since previous studies have demonstrated that irradiation affects some sperm parameters in this species (Catalán et al., 2020a).

At present, three mechanisms have been suggested as being related to the response of sperm to red light (Yeste et al., 2018). The first hypothesizes that irradiation is linked to thermotaxis, via its interaction with specific members of the Transient Receptor Potential (TRP) family. While the TRP family is a highly heterogeneous class of plasma membrane receptors, only those belonging to vanilloid TRP (TRPV), ankyrin TRP (TRPA), and melastanin TRP (TRPM) subfamilies have been reported to be involved in the control of thermotaxis (Vriens et al., 2014). Remarkably, ion channels are crucial during sperm capacitation (Lishko et al., 2012; Singh and Rajender, 2014; Sun et al., 2017; Mundt et al., 2018), and TRPV4 has been linked to the thermotactic response both in mouse (Hamano et al., 2016) and human sperm (Mundt et al., 2018). A second potential mechanism envisages the participation of opsins, which are coupled to a G-protein (transducin) and also reside in the plasma membrane of mammalian sperm (Pérez-Cerezales et al., 2015). The different members of this family of proteins (melanopsin, encephalopsin, rhodopsin, and neuropsin) appear to work as thermosensitizers rather than light-sensitive intracellular proteins (photosensitizers), via canonical phospholipase C (PLC) and cyclic nucleotide pathways (cAMP/cGMP; Pérez-Cerezales et al., 2015). In effect, opsins, especially melanopsin and rhodopsin, are involved, along with the aforementioned TRPV proteins, in the sperm response to thermotaxis (Zheng, 2013; Pérez-Cerezales et al., 2015; Roy et al., 2020). Interestingly, a recent study has demonstrated that rhodopsin and melanopsin trigger a different signaling pathway but, unlike vision, both types of opsin coexist in the same sperm cells (Roy et al., 2020). The third hypothesis considers the role of endogenous photosensitizers, particularly cytochromes residing in the mitochondria (Yeste et al., 2018). It is widely known that cytochromes are an essential component of the mitochondrial electron chain and control oxidative phosphorylation, generation of reactive oxygen species and apoptosis (Ortega-Ferrusola et al., 2009). Cytochromes have a heme group, which not only accepts and donates electrons (Kessel, 1982; Pottier and Truscott, 1986), but is sensitive to light. However, not all cytochromes react against the same wavelengths (Lynch and Copeland, 1992). Thus, whereas cytochrome P450, which is also present in the endoplasmic reticulum of somatic cells, has its highest absorption peak at 450 nm, cytochrome C, which forms the complex IV of the mitochondrial electron chain, has two peaks at 610–630 nm and 660–680 nm (Lynch and Copeland, 1992). However, and despite unpublished data supporting the relevance of mitochondria in pig sperm (Blanco-Prieto et al., personal communication), one should not rule out that more than one of these hypothetical mechanisms could be involved in the sperm response to red light, as well as that the potential influence of light on the conformation of other proteins might also be implied in that response (Yeste et al., 2018).

Against this background, the objective of this study was to determine if the previously reported effects of light stimulation in donkey sperm (Catalán et al., 2020a) are related to changes caused by the action of light on mitochondrial function, since this is one of the hypothetical mechanisms of action. Our hypothesis is that the effects of irradiating donkey sperm with red-light are driven by changes in mitochondrial function. For this reason, freshly diluted donkey semen was irradiated with red light for 1, 5, and 10 min, in the presence/absence of Omy A, a specific inhibitor of the mitochondrial ATP synthase activity, or FCCP, which acts as a disruptor of the electron chain function. If mitochondria are involved in the sperm response to irradiation, utilizing these two effectors should affect the impact from red light. In addition, the use of both oligomycin A and FCCP should allow elucidating the exact part of the mitochondrial electron chain that is involved in the sperm response to light, and should also contribute to shed light onto the different effects between species.

MATERIALS AND METHODS

Animals, Semen Samples, and Ethics

Eight ejaculates, each coming from a separate jackass, were used. Animals were allocated to individual paddocks at the Equine Reproduction Service, Autonomous University of Barcelona

(Bellaterra, Cerdanyola del Vallès, Spain). This is an EU-approved semen collection center (Authorization code: ES09RS01E) that operates under strict protocols of animal welfare and health control. Jackasses were adult, healthy and of proven fertility, and were fed grain forage, straw and hay, with water being provided *ad libitum*.

Ejaculates were collected through a Hannover artificial vagina (Minitüb GmbH, Tiefenbach, Germany) and an in-line nylon mesh filter to remove the gel fraction. Upon collection, gel-free semen was diluted 1:5 (v:v) with Kenney extender (Kenney et al., 1975), previously preheated to 37°C. Thereafter, a conventional spermiogram, based on total ejaculate volume, sperm concentration (Neubauer chamber, Paul Marienfeld GmbH, and Co. KG; Lauda-Königshofen, Germany), motility (Computer Assisted Semen Analysis, CASA), morphology (eosin-nigrosin staining) and plasma membrane integrity (SYBR14/PI), was performed. All samples were confirmed to be above the standard thresholds ($\geq$70% of total motility and SYBR14$^+$/PI$^-$ sperm and $\geq$ 70% morphologically normal sperm).

All jackasses used in this study were semen donors and no manipulation to animals, apart from semen collection in the authorized center, was made. The animal study was reviewed and approved by the Ethics Committee for Animal and Human Experimentation (CEEAH) of our institution (Autonomous University of Barcelona; authorization code: CEEAH 1424).

Experimental Design

Prior to light-stimulation, sperm concentration was adjusted to 30 $\times$ 10^6 spermatozoa/mL with Kenney extender using a Neubauer chamber (Paul Marienfeld GmbH & Co. KG; Lauda-Königshofen, Germany). Following this, each semen sample was split into separate aliquots of 1.5 mL that were subjected to three red light irradiation protocols with an air-refrigerated red LED light system (PhastBlue®, IUL, S.L.; Barcelona, Spain; wavelength range: 620–630 nm; intensity per sample: 35.05 W/m^2). These three protocols consisted of exposing sperm to red light for 1 min (P1), 5 min (P5) or 10 min (P10). In all cases, the temperature within the PhastBlue® system was maintained at 20°C $\pm$ 0.1°C. The control consisted of 1.5 mL tubes kept at 20°C in the dark for 10 min. In addition to the aforementioned, semen samples were also exposed to the same three protocols (i.e., P1, P5, and P10) or non-exposed (control), in the presence of either 5 μM oligomycin A or 5 μM FCCP. In order to achieve a maximal effect of both Omy A and FCCP, these two molecules were added to semen samples 10 min prior to exposure to red light. Following exposure to red light, sperm motility was evaluated through a computer-assisted sperm analysis system (CASA); sperm membrane integrity, mitochondrial membrane potential (MMP), and intracellular ROS and calcium levels were determined through flow cytometry; O_2 consumption rate; intracellular ATP levels and total cytochrome C oxidase (CCO) activity were also assessed. In the case of intracellular ATP levels and total CCO activity, samples were first centrifuged at 2,000 $\times$ *g* and 20°C for 30 s; the resulting pellets were immediately frozen by plunging them into liquid N_2. Samples were stored at −80°C until use.

Sperm Motility

As indicated above, sperm motility was evaluated using a CASA system (Integrated Sperm Analysis System V1.0; Proiser S.L.; Valencia, Spain). For this purpose, samples were incubated in a water bath at 38°C for 5 min prior to analysis. Five microliter of each sperm sample was placed onto a Makler chamber (Sefi Medical Instruments; Haifa, Israel) previously warmed at 38°C. Samples were observed under a 10 $\times$ negative phase-contrast objective (Olympus BX41 microscope; Olympus Corporation, Tokyo, Japan), and at least 1,000 sperm cells were counted per analysis. In each evaluation, percentages of total (TMOT) and progressively motile spermatozoa (PMOT) were recorded along with the following kinetic parameters: curvilinear velocity (VCL, μm/s), which is the mean path velocity of the sperm head along its actual trajectory; straight-line velocity (VSL, μm/s), which is the mean path velocity of the sperm head along a straight line from its first to its last position; average path velocity (VAP, μm/s), which is the mean velocity of the sperm head along its average trajectory; percentage of linearity (LIN,%), which is the quotient between VSL and VCL multiplied by 100; percentage of straightness (STR,%), which is the quotient between VSL and VAP multiplied by 100; percentage of oscillation (WOB,%), which is the quotient between VAP and VCL multiplied by 100; mean amplitude of lateral head displacement (ALH, μm), which is the mean value of the extreme side-to-side movement of the sperm head in each beat cycle; and frequency of head displacement (BCF, Hz), which is the frequency at which the actual sperm trajectory crosses the average path trajectory (Hz).

Settings of the CASA system were those recommended by the manufacturer: frames/s: 25 images captured per second; particle area $>$ 4 and $<$ 75 μm^2; connectivity: 6; minimum number of images to calculate the ALH: 10. Cut-off values were VAP $\geq$ 10 μm/s for TMOT, and STR $\geq$ 75% for PMOT. In addition, individual kinematic parameters (VSL, VCL, VAP, LIN, STR, and BCF) were used to determine motile sperm subpopulations. Three replicates were evaluated before calculating the corresponding mean $\pm$ SD.

Flow Cytometry

Flow cytometry was used to determine plasma membrane integrity, MMP, and intracellular levels of superoxides, peroxides and calcium, following the recommendations set by the International Society for Advancement of Cytometry (ISAC; Lee et al., 2008). In all analyses, sperm concentration was previously adjusted to 1 $\times$ 10^6 spermatozoa/mL in a final volume of 500 μL, and three technical replicates were evaluated. Samples were examined using a Cell Laboratory QuantaSC cytometer (Beckman Coulter, Fullerton, CA, United States), and the sheath flow rate was set at 4.17 μL/min. Electronic volume (EV) and side scatter (SS) were recorded in a log-linear mode (EV/SS dot plots) for 10,000 events per replicate. The analyzer threshold was adjusted on the EV channel to exclude subcellular debris (particle diameter $<$ 7 μm) and cell aggregates (particle diameter $>$ 12 μm). When required, compensation was used to minimize fluorescence spill-over into a different channel. Information on all events was collected in List-mode Data files (EV, SS, FL1, FL2, and FL3) and processed

using the Cell Lab QuantaSC MPL Analysis Software (version 1.0; Beckman Coulter). In all assessments, data were corrected using the procedure described by Petrunkina et al. (2010), based on the percentage of debris particles ($SYBR14^-/PI^-$) determined through SYBR14/PI staining. Fluorochromes were purchased from Molecular Probes® (Invitrogen®, Thermo Fisher Scientific, Waltham, MA, United States) and diluted with dimethyl sulfoxide (DMSO).

Plasma Membrane Integrity

Sperm membrane integrity was assessed using the LIVE/DEAD Sperm Viability Kit (SYBR14/PI; Molecular Probes, Thermo Fisher Scientific), according to the protocol described by Garner and Johnson (1995) and adapted to donkey spermatozoa. In brief, samples were first incubated with SYBR14 (final concentration: 100 nM) at 38°C for 10 min, and then with PI (final concentration: 12 μM) at 38°C for 5 min. Three sperm populations were distinguished: (i) viable spermatozoa emitting green fluorescence ($SYBR14^+/PI^-$), which appeared on the right side of the lower half of FL1/FL3 dot plots; (ii) non-viable spermatozoa emitting red fluorescence ($SYBR14^-/PI^+$), which appeared on the left side of the upper half of FL1/FL3 dot plots; and (iii) non-viable spermatozoa emitting both green and red fluorescence ($SYBR14^+/PI^+$), which appeared on the right side of the upper half of FL1/FL3 dot plots. Non-stained particles ($SYBR14^-/PI^-$), which appeared on the left side of the lower half of FL1/FL3 dot plots, had similar EV/SS distributions than spermatozoa and were considered as non-DNA, debris particles. Percentages of non-stained particles were used to correct the percentages of double-negative sperm populations in the other assessments. Spill-over of FL1- into FL3-channel was compensated (2.45%).

Mitochondrial Membrane Potential

Mitochondrial membrane potential was determined through incubation with JC1 (5,5′,6,6′-tetrachloro-1,1′,3,3′tetraethyl−benzimidazolylcarbocyanine iodide; final concentration: 0.5 μM) at 38°C for 30 min in the dark. At low MMP, JC1 remains as a monomer ($JC1_{mon}$) emitting green fluorescence, which is detected through FL1. At high MMP, JC1 forms aggregates ($JC1_{agg}$) emitting orange fluorescence, which is collected through FL2. Three sperm populations were distinguished: (i) spermatozoa with green-stained mitochondria (low MMP); (ii) spermatozoa with heterogeneous mitochondria stained both green and orange in the same cell (intermediate MMP); and (iii) spermatozoa with orange-stained mitochondria (high MMP). Ratios between $JC1_{agg}$ (FL2) and $JC1_{mon}$ (FL1) fluorescence for each of these sperm populations were also evaluated. Spill-over of FL1- into FL2-channel was compensated (68.50%). Percentages of debris particles found in SYBR14/PI staining ($SYBR14^-/PI^-$) were subtracted from those of spermatozoa with low MMP, and percentages of all sperm populations were recalculated.

Analysis of Intracellular ROS Levels: H_2O_2 and $\cdot O_2^-$

Intracellular ROS levels were determined through two oxidation sensitive fluorescent probes: 2′,7′-dichlorodihydrofluorescein diacetate (H_2DCFDA) and hydroethidine (HE), which detect hydrogen peroxide (H_2O_2) and superoxide anion ($\cdot O_2^-$), respectively (Murillo et al., 2007). Sperm were counterstained with PI (H_2DCFDA) or YO-PRO-1 (HE), following a protocol modified from Guthrie and Welch (2006).

With regard to peroxides, spermatozoa were incubated with H_2DCFDA (final concentration: 200 μM) and PI (final concentration: 12 μM) at room temperature for 30 min in the dark. H_2DCFDA is a stable, cell-permeable, non-fluorescent probe that, in the presence of H_2O_2, is deesterified and converted into 2′,7′-dichlorofluorescein (DCF). Fluorescence of DCF and PI were measured through FL1 and FL3 detectors, respectively. Four sperm populations were distinguished: (i) viable spermatozoa with low levels of peroxides (DCF^-/PI^-); (ii) viable spermatozoa with high levels of peroxides (DCF^+/PI^-); (iii) non-viable spermatozoa with low levels of peroxides (DCF^-/PI^+); and (iv) non-viable spermatozoa with high levels of peroxides (DCF^+/PI^+). Percentages of debris particles found in SYBR14/PI staining ($SYBR14^-/PI^-$) were subtracted from those of viable spermatozoa with low levels of peroxides (DCF^-/PI^-), and percentages of all sperm populations were recalculated. Spill-over of FL1- into the FL3-channel was compensated (2.45%). Data are shown as corrected percentages of viable spermatozoa with high levels of peroxides (DCF^+/PI^-), and geometric mean of DCF^+-fluorescence intensity in the DCF^+/PI^- sperm population.

As far as superoxides are concerned, samples were incubated with HE (final concentration: 4 μM) and YO-PRO-1 (final concentration: 25 nM) at room temperature for 30 min in the dark (Guthrie and Welch, 2006). Hydroethidine diffuses freely through plasma membrane and converts into ethidium (E^+) in the presence of superoxide anions ($\cdot O_2^-$) (Zhao et al., 2003). Fluorescence of ethidium (E) was detected through FL3 and that of YO-PRO-1 was detected through FL1. Four sperm populations were distinguished: (i) viable spermatozoa with low levels of superoxides (E^-/YO-PRO-1^-); (ii) viable spermatozoa with high levels of superoxides (E^+/YO-PRO-1^-); (iii) non-viable spermatozoa with low levels of superoxides (E^-/YO-PRO-1^+); and (iv) non-viable spermatozoa with high levels of superoxides (E^+/YO-PRO-1^+). Percentages of debris particles found in SYBR14/PI staining ($SYBR14^-/PI^-$) were subtracted from those of viable spermatozoa with low levels of superoxides (E^-/YO-PRO-1^-), and percentages of all sperm populations were recalculated. Spill-over of FL3-into the FL1-channel was compensated (5.06%). Data are shown as corrected percentages of viable spermatozoa with high levels of superoxides (E^+/YO-PRO-1^-), and geometric mean of E^+-fluorescence intensity in the E^+/YO-PRO-1^- sperm population.

Intracellular Calcium Levels

Previous studies found that Fluo3 mainly stains mitochondrial calcium in pig sperm (Yeste et al., 2015). For this reason, we combined this fluorochrome with PI (Fluo3/PI), as described by Kadirvel et al. (2009). Four sperm populations were identified: (i) viable spermatozoa with low levels of intracellular calcium ($Fluo3^-/PI^-$); (ii) viable spermatozoa with high levels of intracellular calcium ($Fluo3^+/PI^-$); (iii) non-viable spermatozoa

with low levels of intracellular calcium ($Fluo3^-/PI^+$); and (iv) non-viable spermatozoa with high levels of intracellular calcium ($Fluo3^+/PI^+$). FL3 spill-over into the FL1-channel (28.72%) and FL1 spill-over into the FL3-channel (2.45%) were compensated.

Determination of Intracellular ATP Levels

Intracellular ATP levels were determined following the protocol set by Chida et al. (2012). Immediately after light-stimulation, 1-mL semen aliquots were centrifuged at 17°C for 30 s; pellets were plunged into liquid N_2, and frozen pellets were subsequently stored at −80°C for a maximum of 3 weeks. Pellets were then resuspended in 300 μL ice-cold 10 mM 2-[4-(2-hydroxyethyl)piperazin-1-yl]ethanesulfonic acid (HEPES) buffer containing 250 mM sucrose (pH was adjusted to 7.4), and subsequently sonicated (10 kHz, 20 pulses; Bandelin Sonopuls HD 2070; Bandelin Electronic GmbH and Co., Berlin, Germany). During this process, tubes were kept on ice to avoid specimen heating. Next, samples were centrifuged at 1,000× g and 4°C for 10 min, supernatants were harvested for further use and pellets were discarded. Twenty μL of supernatant was used to determine total protein content, and the remaining volume was mixed with 300 μL ice-cold 10% (v:v) trichloroacetic acid and held at 4°C for 20 s. Samples were subsequently centrifuged at 1,000 × *g* and 4°C for 30 s, and supernatants were carefully separated from the pellet and again centrifuged at 1,000 × *g* and 4°C for 10 min. Supernatants were mixed with two volumes of 1 M Tris-acetate buffer (pH = 7.75), and the resulting suspension was used to determine the ATP content using the Invitrogen® ATP Determination Kit (Thermo Fisher Scientific, Waltham, United States; catalog number: A22066). Determinations of ATP content were carried out with an Infinite F200 fluorimeter (TECAN®), using 96-wells microplates for fluorescence-based assays (Invitrogen®). Data were normalized against the total protein content determined with the Bradford method (Bradford, 1976) using a commercial kit (Bio-Rad laboratories; Hercules, CA, United States).

Determination of O_2 Consumption Rate

Determination of O_2 consumption rate was performed through the SensorDish® Reader (SDR) system (PreSens Gmbh; Regensburg, Germany). After light-stimulation, 1 mL of each sperm sample was transferred onto an Oxodish® OD24 plate (24 wells/plate). Plates were sealed with Parafilm®, placed within the SDR system, and incubated at 37°C (controlled atmosphere) for 2 h. During that time, O_2 concentration was recorded in each well at a rate of one reading/min. Data were exported to an Excel file and final O_2 consumption rate was normalized against the total number of viable spermatozoa per sample, which was determined through flow cytometry ($SYBR14^+/PI^-$ spermatozoa) as described above.

Determination of Cytochrome C Oxidase Activity

The CCO activity was determined in mitochondria-enriched sperm fractions, as described in Mclean et al. (1993). Briefly, 1-mL sperm aliquots, previously irradiated with red light, were centrifuged at 1,000 × *g* and 17°C for 30 s. The resulting pellets were immediately plunged into liquid N_2 and stored for 3 weeks. Pellets were resuspended in 500 μL ice-cold PBS and sonicated (10 kHz, 20 pulses; Bandelin Sonopuls HD 2070). Thereafter, 500 μL Percoll® (concentration: 1.055 mg/mL in PBS) at 4°C was placed onto each sperm homogenate. Samples were centrifuged at 3,000 × *g* and 10°C for 45 min and the mitochondria-enriched fraction was carefully harvested with a micropipette and transferred into a new 1.5 mL tube. Samples were again centrifuged at 12,000 × *g* and 20°C for 2 min and the resulting pellets were resuspended in 100 μL PBS at 20°C. These mitochondria-enriched suspensions were split into two separate aliquots. The first one was used to determine CCO activity using a commercial kit (Cytochrome C Oxidase Assay Kit; Sigma-Aldrich; catalog number CYTOCOX1). Enzyme activity was normalized against the total protein content. Therefore, the other aliquot (10 μL) was used to determine total protein content through a commercial kit (Bio-Rad laboratories) based on the Bradford method (Bradford, 1976).

Statistical Analysis

Statistical analyses were conducted using a statistical package (SPSS® Ver. 25.0 for Windows; IBM Corp., Armonk, NY, United States). Data were first tested for normal distribution (Shapiro-Wilk test) and homogeneity of variances (Levene test) and, if required, they were transformed with arcsin $\sqrt{x}$. The effects of irradiating donkey with red light and the presence of oligomycin A/FCCP were tested on sperm motility parameters, percentages of spermatozoa with an intact plasma membrane ($SYBR14^+/PI^-$), spermatozoa with high and intermediate MMP, viable spermatozoa with high intracellular calcium levels ($Fluo3^+/PI^-$), viable spermatozoa with high superoxide levels (E^+/YO-PRO-1^-), and viable spermatozoa with high peroxide levels (DCF^+/PI^-); geometric mean fluorescence intensities (GMFI) of $JC1_{agg}$, $Fluo3^+$, E^+ and DCF^+; $JC1_{agg}/JC1_{mon}$ GMFI-ratios; intracellular levels of ATP; O_2 consumption rate; and cytochrome C oxidase activity were evaluated through two-way analysis of variance (ANOVA; factor 1: irradiation protocol; factor 2: presence/absence of Omy A or FCCP) followed by *post hoc* Sidak test for pair-wise comparisons.

Motile sperm subpopulations were determined through the protocol described in Luna et al. (2017). In brief, individual kinematic parameters (VCL, VSL, VAP, LIN, STR, WOB, ALH, and BCF) recorded for each sperm cell were used as independent variables in a Principal Component Analysis (PCA). Kinematic parameters were sorted into PCA components and the obtained matrix was subsequently rotated using the Varimax method with Kaiser normalization. As a result, each spermatozoon was assigned a regression score for each of the new PCA components and these values were subsequently used to run a two-step cluster analysis based on the log-likelihood distance and the Schwarz Bayesian Criterion. Four sperm subpopulations were identified and each individual spermatozoon was assigned to one of these subpopulations (SP1, SP2, SP3, or SP4). Following this, percentages of spermatozoa belonging to each subpopulation were calculated per sample and used to determine

the effects of irradiation and Omy A/FCCP on the distribution of motile sperm subpopulations through two-way ANOVA followed by Sidak test.

In all analyses, the level of significance was set at $P \leq 0.05$. Data are shown as mean ± standard deviation (SD), median and interquartile range (i.e., Q1 and Q3).

RESULTS

Effects of Red Light Stimulation on Plasma Membrane Integrity in the Presence or Absence of Either Omy A or FCCP

Irradiating donkey sperm with red light did not affect sperm membrane integrity, as no significant differences between the control and light-stimulation protocols were observed with regard to the percentages of membrane-intact spermatozoa ($SYBR14^+/PI^-$; **Figure 1**), neither did the presence of Omy A or FCCP alter that parameter.

Effects of Red Light Stimulation on Sperm Motility in the Presence or Absence of Either Omy A or FCCP

As shown in **Figure 2**, percentages of TMOT (**Figure 2A**) and PMOT (**Figure 2B**) did not differ between non-irradiated and irradiated sperm samples, in the presence/absence of either Omy A or FCCP. Moreover, the presence of Omy A or FCCP, irrespective of irradiation/non-irradiation, led to a significant ($P < 0.05$) decrease in total (**Figure 2A**) and progressive (**Figure 2B**) sperm motility.

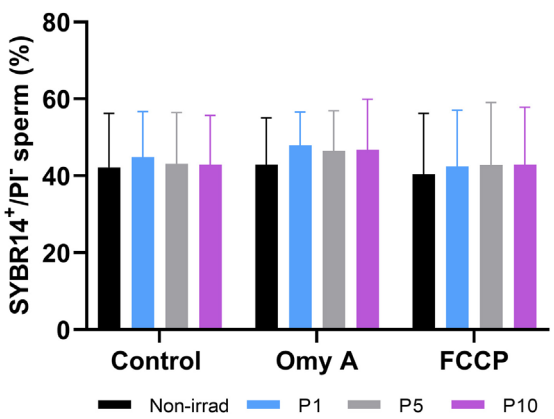

FIGURE 1 | Effects of light-stimulation on the percentages of membrane-intact sperm ($SYBR14^+/PI^-$) in the presence/absence of Omy A or FCCP. No significant differences between non-irradiated and irradiated sperm in the presence/absence of oligomycin A or FCCP were observed, nor between samples in the presence of Omy A or FCCP and the treatment without the two disruptors for a given light-stimulation protocol (i.e., control, P1, P5, or P10). Data are shown as mean ± SD from eight separate experiments.

Regarding the effects of light-stimulation on sperm kinetic parameters (**Table 1**), irradiation for 5 min and 10 min significantly ($P < 0.05$) increased VAP, when Omy A and FCCP were absent. In contrast, the presence of Omy A or FCCP in non-irradiated samples led to a significant ($P < 0.05$) decrease in VCL, VSL, VAP, LIN, and WOB (**Tables 1A,B**). Moreover, treatments with Omy A and FCCP showed significantly ($P < 0.05$) higher values of BCF (**Table 1C**) and STR in non-irradiated and irradiated samples.

Finally, as shown in **Table 2**, four different motile sperm subpopulations were identified in all treatments (SP1, SP2, SP3, and SP4). Interestingly, irradiation was found to affect the proportions of sperm belonging to each motile subpopulation. Light-stimulation of spermatozoa with red light for 1 min significantly increased ($P < 0.05$) the proportions of sperm belonging to SP1 (**Figure 3A**), which was the subpopulation that exhibited the highest kinematic parameters (**Table 2**). Regardless of whether samples were or not irradiated, the presence of Omy A or FCCP significantly ($P < 0.05$) decreased the proportions of sperm belonging to SP1, SP2, and SP4 (**Figures 3A,B,D**) and increased those of sperm belonging to SP3 (**Figure 3C**), which was the motile subpopulation that exhibited the lowest values in most kinematic parameters (**Table 2**).

Effects of Red Light Stimulation on Mitochondrial Membrane Potential in the Presence or Absence of Either Omy A or FCCP

As shown in **Figure 4A**, irradiation for 1, 5, and 10 min significantly ($P < 0.05$) increased the percentages of spermatozoa with high MMP in samples without Omy A or FCCP. In treatments containing Omy A, irradiation for 1 min or 5 min significantly ($P < 0.05$) augmented the percentages of spermatozoa with high MMP compared to non-irradiated samples. Furthermore, percentages of spermatozoa with high MMP in samples containing FCCP were significantly ($P < 0.05$) higher in samples irradiated for 10 min than in their non-irradiated counterparts. In addition to this, percentages of spermatozoa with high MMP in non-irradiated samples and samples irradiated for 1, 5, or 10 min were significantly lower ($P < 0.05$) when FCCP was present than in the absence of this disruptor (**Supplementary Figure 1**).

As shown in **Figure 4B**, no significant differences in the percentages of sperm with intermediate MMP were observed between non-irradiated and irradiated samples, either in the presence or absence of Omy A and FCCP. In addition, no significant differences in the geometric mean of $JC1_{agg}$ intensity (orange, FL2) of sperm populations with high (**Figure 4C**) and intermediate MMP (**Figure 4D**) were observed between irradiated and non-irradiated samples, either in the presence or absence of Omy A or FCCP. However, geometric mean of the intensity of $JC1_{agg}$ (orange, FL2) in the sperm population with high MMP was significantly ($P < 0.05$) lower in the non-irradiated sample containing FCCP than in that without any inhibitor/disruptor (**Figure 4C**).

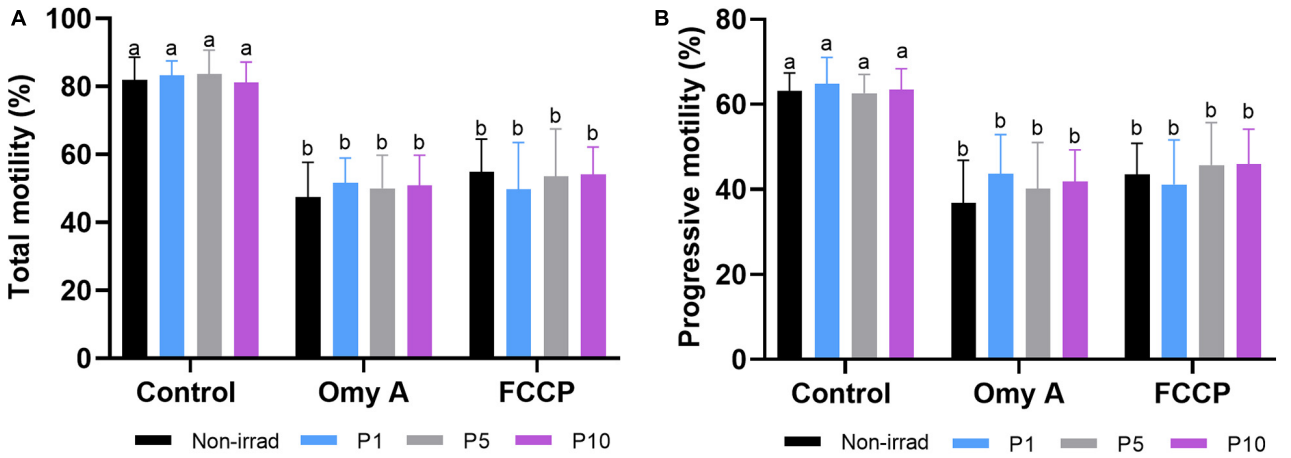

FIGURE 2 | Effects of light-stimulation on the percentages of total **(A)** and progressive **(B)** sperm motility in the presence/absence of oligomycin A (Omy A) or FCCP. Different letters (*a b*) indicate significant differences ($P < 0.05$) between oligomycin A or FCCP with respect to the treatment without the two for a given protocol (i.e., control, P1, P5, or P10). No significant differences were found between the samples exposed to the different irradiation times with respect to non-irradiated sperm. Data are shown as mean ± SD from eight separate experiments.

TABLE 1A | Kinetic parameters (VSL, VCL, and VAP) of donkey sperm in the control and the different light-stimulation patterns in the presence or absence of oligomycin A (Omy A) and FCCP.

Treatments		Kinetic parameters					
		VCL (μm/s)		VSL (μm/s)		VAP (μm/s)	
		Mean ± SD	Q1, median, Q3	Mean ± SD	Q1, median, Q3	Mean ± SD	Q1, median, Q3
Control	Control	130.7 ± 13.5^{Aa}	110.0, 133.0, 147.5	102.1 ± 10.9^{Aa}	89.0, 105.3, 111.6	$117.6 \pm 6, 9^{Aa}$	101.3, 121.0, 131.1
	Omy A	66.0 ± 8.7^{Ab}	55.6, 64.7, 77.1	42.4 ± 8.7^{Ab}	30.8, 44.2, 47.6	46.5 ± 6.0^{Ab}	36.0, 49.1, 53.7
	FCCP	75.8 ± 9.8^{Ab}	69.5, 75.9, 87.8	44.0 ± 9.5^{Ab}	35.1, 46.4, 49.9	49.2 ± 6.9^{Ab}	40.7, 52.2, 57.4
P1	Control	135.2 ± 15.6^{Aa}	110.6, 137.4, 156.4	105.1 ± 13.3^{Aa}	88.6, 107.3, 120.5	126.3 ± 9.9^{Aa}	103.2, 129.0, 138.8
	Omy A	68.4 ± 8.1^{Ab}	59.4, 66.6, 77.1	43.2 ± 7.4^{Ab}	35.2, 46.9, 50.7	47.7 ± 5.5^{Ab}	39.2, 50.4, 55.0
	FCCP	73.4 ± 11.8^{Ab}	63.5, 70.1, 91.5	41.2 ± 10.6^{Ab}	31.9, 45.7, 51.8	46.5 ± 8.9^{Ab}	34.1, 50.8, 58.3
P5	Control	139.6 ± 11.6^{Aa}	123.7, 141.5, 153.4	109.2 ± 8.9^{Aa}	94.9, 108.2, 117.4	130.7 ± 6.2^{Ba}	115.3, 131.8, 142.5
	Omy A	69.2 ± 10.8^{Ab}	55.8, 65.9, 82.6	44.5 ± 10.6^{Ab}	35.1, 46.0, 54.4	49.5 ± 5.5^{Ab}	38.9, 51.1, 60.7
	FCCP	80.4 ± 12.3^{Ab}	69.2, 81.8, 92.2	48.6 ± 11.5^{Ab}	39.4, 49.6, 54.2	53.0 ± 6.4^{Ab}	43.7, 54.8, 59.2
P10	Control	141.2 ± 10.7^{Aa}	132.6, 142.2, 158.7	110.0 ± 11.6^{Aa}	99.5.0, 111.2, 119.5	132.1 ± 6.4^{Aa}	122.4, 133.9, 142.3
	Omy A	66.9 ± 8.1^{Ab}	57.4, 66.2, 76.8	41.9 ± 7.5^{Ab}	34.5, 42.8, 49.8	46.1 ± 5.5^{Ab}	38.4, 47.3, 54.0
	FCCP	78.2 ± 11.7^{Ab}	68.4, 76.9, 90.5	47.1 ± 10.6^{Ab}	37.1, 49.1, 53.7	54.2 ± 6.2^{Ab}	41.4, 53.7, 59.3

Different letters (A,B) indicate significant differences ($P < 0.05$) between the control and the different light stimulation patterns used in the presence or absence of oligomycin A (Omy A) or FCCP. Different letters (a,b) indicate significant differences ($P < 0.05$) between Omy A or FCCP with respect to treatment without the two inhibitors for a given protocol (i.e., control, P1, P5, or P10). Data are shown as mean ± SD, median and interquartile range from eight separate experiments.

Finally, we also evaluated $JC1_{agg}/JC1_{mon}$ ratios of sperm populations with high (**Figure 4E**) and intermediate MMP (**Figure 4F**). No significant differences between non-irradiated and irradiated samples were observed, either in the presence/absence of Omy A/FCCP, or within the same irradiation pattern comparing samples with and without disruptors.

Effects of Red Light Stimulation on Intracellular ROS Levels in the Presence or Absence of Either Omy A or FCCP

Figures 5A,B show the proportions of viable spermatozoa with high intracellular levels of peroxides (% DCF^+/PI^- spermatozoa) and the GMFI of DCF^+ in the population of viable sperm with high levels of peroxides (DCF^+/PI^-). No significant differences between irradiated and non-irradiated samples were observed, either in the presence or absence of Omy A or FCCP. In addition, no significant differences were found within each irradiation pattern when samples with and without disruptors (Omy A and FCCP) were compared.

Percentages of viable sperm with high levels of superoxides (% E^+/YO-PRO-1^- spermatozoa; **Figure 5C**) and GMFI of E^+ in the viable sperm population with high levels of superoxides (E^+/YO-PRO-1^-; **Figure 5D**) did not significantly differ between irradiated and non-irradiated samples, or between treatments with and without disruptors (Omy A and FCCP) within each irradiation pattern.

TABLE 1B | Kinetic parameters (LIN, STR and WOB) of donkey sperm in the control and the different light-stimulation patterns in the presence or absence of oligomycin A (Omy A) and FCCP.

Treatments		Kinetic parameters					
		LIN (%)		STR (%)		WOB (%)	
		Mean ± SD	Q1, median, Q3	Mean ± SD	Q1, median, Q3	Mean ± SD	Q1, median, Q3
Control	Control	77.8 ± 3.4^{Aa}	69.6, 79.7, 84.8	85.2 ± 2.1^{Aa}	78.5.6, 87.1, 90.7	91.3 ± 3.6^{Aa}	88.7, 91.1, 96.2
	Omy A	63.9 ± 7.7^{Ab}	55.0, 64.6, 72.0	90.3 ± 2.4^{Ab}	87.3, 91.7, 92.8	70.6 ± 8.0^{Ab}	63.1, 70.4, 79.6
	FCCP	56.2 ± 7.5^{Ab}	49.3, 59.2, 63.1	88.0 ± 2.9^{Aa}	87.8, 90.4, 90.8	62.9 ± 7.9^{Ab}	56.1, 65.2, 69.6
P1	Control	78.3 ± 2.6^{Aa}	72.9, 77.8, 84.2	84.9 ± 1.8^{Aa}	79.7, 85.2, 90.3	92.1 ± 2.8^{Aa}	91.2, 91.7, 93.3
	Omy A	63.2 ± 6.9^{Ab}	56.9, 62.0, 69.1	90.4 ± 1.4^{Ab}	89.2, 90.5, 91.3	69.8 ± 7.9^{Ab}	63.5, 68.9, 76.3
	FCCP	56.0 ± 7.8^{Ab}	49.4, 54.7, 61.6	88.3 ± 2.2^{Aa}	87.3, 88.5, 90.1	63.3 ± 8.3^{Ab}	56.7, 61.2, 69.8
P5	Control	78.1 ± 3.2^{Aa}	67.7, 81.1, 86.2	84.2 ± 2.2^{Aa}	78.9, 86.8, 90.7	93.0 ± 3.6^{Aa}	89.1, 91.4, 95.8
	Omy A	64.3 ± 6.2^{Ab}	54.6, 67.5, 72.1	89.7 ± 2.4^{Ab}	86.6, 89.8, 92.5	71.5 ± 8.6^{Ab}	63.0, 74.1, 78.5
	FCCP	59.5 ± 9.7^{Ab}	50.1, 56.9, 69.9	90.3 ± 1.4^{Ab}	88.6, 91.1, 91.6	65.7 ± 10.3^{Ab}	55.9, 63.0, 75.5
P10	Control	78.3 ± 3.5^{Aa}	71.0, 77.9, 86.4	83.8 ± 2.7^{Aa}	80.3, 84.8, 90.6	93.1 ± 4.8^{Aa}	88.4, 91.9, 96.0
	Omy A	62.6 ± 8.3^{Ab}	55.3, 60.1, 70.8	90.8 ± 1.6^{Ab}	89.2, 90.9, 92.5	68.8 ± 8.7^{Ab}	61.9, 65.3, 77.7
	FCCP	60.2 ± 10.0^{Ab}	50.9, 58.7, 68.5	90.4 ± 1.1^{Ab}	89.6, 90.3, 90.9	66.5 ± 10.4^{Ab}	57.0, 65.1, 74.3

Different letters (A,B) indicate significant differences ($P < 0.05$) between the control and the different light stimulation patterns used in the presence or absence of oligomycin A (Omy A) or FCCP. Different letters (a,b) indicate significant differences ($P < 0.05$) between Omy A or FCCP with respect to treatment without the two inhibitors for a given protocol (i.e., control, P1, P5, or P10). Data are shown as mean ± SD, median and interquartile range from eight separate experiments.

Effects of Red Light Stimulation on Intracellular Calcium Levels in the Presence or Absence of Either Omy A or FCCP

Percentages of viable sperm with high intracellular calcium levels did not differ between irradiated and non-irradiated samples in the presence/absence of Omy A and FCCP, nor between the presence/absence of disruptors within each irradiation pattern (**Figure 6A**). Similar results were obtained in the case for the GMFI of $Fluo3^+$ in the viable sperm population with high intracellular calcium levels ($Fluo3^+/PI^-$; **Figure 6B**).

TABLE 1C | Kinetic parameters (ALH and BCF) of donkey sperm in the control and the different light-stimulation patterns in the presence or absence of oligomycin A (Omy A) and FCCP.

Treatments		Kinetic parameters			
		ALH (μm)		BCF (Hz)	
		Mean ± SD	Q1, median, Q3	Mean ± SD	Q1, median, Q3
Control	Control	2.5 ± 0.7^{Aa}	1.8, 2.6, 3.3	9.2 ± 1.0^{Aa}	8.1, 9.0, 10.3
	Omy A	2.4 ± 0.3^{Aa}	2.1, 2.4, 2.7	12.9 ± 1.0^{Ab}	10.4, 12.6, 13.5
	FCCP	2.8 ± 0.3^{Aa}	2.5, 2.9, 3.0	13.3 ± 0.7^{Ab}	12.3, 13.3, 13.8
P1	Control	2.6 ± 0.4^{Aa}	1.9, 2.5, 3.2	9.1 ± 1.1^{Aa}	7.7, 8.9, 11.0
	Omy A	2.5 ± 0.2^{Aa}	2.3, 2.5, 2.7	12.7 ± 0.8^{Ab}	11.0, 12.5, 13.1
	FCCP	2.9 ± 0.4^{Aa}	2.5, 2.8, 3.2	12.9 ± 0.9^{Ab}	12.2, 12.7, 13.7
P5	Control	2.6 ± 0.6^{Aa}	2.0, 2.5, 3.4	8.9 ± 1.0^{Aa}	7.7, 8.8, 10.4
	Omy A	2.5 ± 0.4^{Aa}	2.2, 2.4, 2.8	11.8 ± 0.9^{Ab}	10.6, 12.0, 12.9
	FCCP	2.9 ± 0.3^{Aa}	2.6, 3.0, 3.1	13.8 ± 1.0^{Ab}	11.8, 13.6, 14.2
P10	Control	2.7 ± 0.6^{Aa}	2.0, 2.8, 3.5	9.4 ± 0.9^{Aa}	8.2, 9.4, 10.6
	Omy A	2.5 ± 0.3^{Aa}	2.2, 2.4, 2.7	12.3 ± 0.9^{Ab}	11.0, 12.4, 13.3
	FCCP	2.8 ± 0.4^{Aa}	2.4, 2.8, 3.1	13.8 ± 0.8^{Ab}	12.1, 13.7, 14.0

Different letters (A,B) indicate significant differences ($P < 0.05$) between the control and the different light stimulation patterns used in the presence or absence of oligomycin A (Omy A) or FCCP. Different letters (a,b) indicate significant differences ($P < 0.05$) between oligomycin A or FCCP with respect to treatment without the two inhibitors for a given protocol (i.e., P1, P5, or P10). Data are shown as mean ± SD, median and interquartile range from eight separate experiments.

Effects of Red Light Stimulation on Intracellular Levels of ATP and Oxygen Consumption in the Presence or Absence of Either Omy A or FCCP

Figure 7A shows the intracellular levels of ATP observed in non-irradiated and irradiated samples in the presence or absence of Omy A or FCCP. No significant differences were observed between non-irradiated and irradiated samples were observed, either in the presence or absence of oligomycin A. In the presence of FCCP, intracellular ATP levels were significantly ($P < 0.05$) higher in sperm irradiated for 1 min than in those non-irradiated. In addition, samples irradiated for 1 min showed significantly ($P < 0.05$) higher intracellular levels of ATP in the presence than in the absence of FCCP.

Figure 7B shows that light stimulation ($P < 0.05$) significantly increased the O_2 consumption rate in all three protocols (i.e., P1, P5, and P10) compared to the non-irradiated control. In samples containing Omy A, no significant differences between non-irradiated and irradiated samples were observed. However, O_2 consumption rates in non-irradiated and irradiated samples containing Omy A were significantly ($P < 0.05$) lower than in the ones that did not contain this inhibitor. On the other hand, no significant differences between irradiated and non-irradiated samples were observed in samples containing FCCP. However, samples containing FCCP showed significantly ($P < 0.05$) higher O_2 consumption rates

TABLE 2 | Descriptive parameters (mean ± SD, median and interquartile range) of the four sperm subpopulations (SP1, SP2, SP3, and SP4) identified in donkey fresh semen, in the presence or absence of oligomycin A (Omy A) or FCCP.

	SP1		SP2		SP3		SP4	
N	**7,611**		**9,455**		**16,551**		**6,694**	
Parameter	**Mean ± SD**	**Q1, median, Q3**	**Mean ± SD**	**Q1, median, Q3**	**Mean ± SD**	**Q1, median, Q3**	**Mean ± SD**	**Q1, median, Q3**
VCL μm/s)	168.4 ± 13.6	153.1, 168.1, 182.0	114.2 ± 16.1	98.0, 116.4, 132.8	70.2 ± 14.9	54.5, 68.7, 86.3	151.4 ± 19.5	132.3, 155.7, 173.9
VSL μm/s)	132.9 ± 18.0	113.5, 132.9, 150.9	101.7 ± 15.6	84.6, 102.3, 119.7	41.8 ± 9.3	30.5, 43.1, 53.8	54.5 ± 17.8	35.7, 56.0, 74.2
VAP μm/s)	152.4 ± 14.9	137.0, 151.8, 166.8	109.2 ± 16.1	92.1, 111.0, 128.2	47.4 ± 7.6	36.2, 47.8, 58.4	115.0 ± 19.1	98.9, 117.8, 134.2
LIN (%)	78.9 ± 9.2	69.8, 80.7, 88.7	89.1 ± 5.7	85.4, 91.3, 94.7	59.4 ± 13.2	49.8, 61.3, 71.2	35.9 ± 12.1	24.3, 37.4, 48.2
STR (%)	87.1 ± 7.2	81.8, 88.7, 94.4	93.3 ± 4.2	90.5, 95.5, 97.9	86.5 ± 12.2	84.9, 92.6, 95.5	47.3 ± 16.5	33.3, 49.2, 61.8
WOB (%)	90.3 ± 4.3	84.6, 91.1, 95.0	95.1 ± 3.6	92.4, 96.4, 98.8	68.1 ± 10.5	59.5, 68.5, 73.3	75.9 ± 9.1	69.3, 77.9, 84.2
ALH (μm)	3.7 ± 0.6	3.1, 3.6, 4.2	2.1 ± 0.5	1.6, 2.0, 2.5	2.6 ± 0.5	2.1, 2.5, 3.0	4.6 ± 1.1	3.7, 4.6, 5.5
BCF (Hz)	10.9 ± 2.5	9.0, 11.0, 13.0	8.2 ± 2.0	6.8, 8.0, 10.0	11.6 ± 3.1	9.0, 12.0, 14.0	8.0 ± 2.4	6.0, 8.0, 10.0

These data were obtained after classifying sperm cells into motile subpopulations through principal component and cluster analyses.

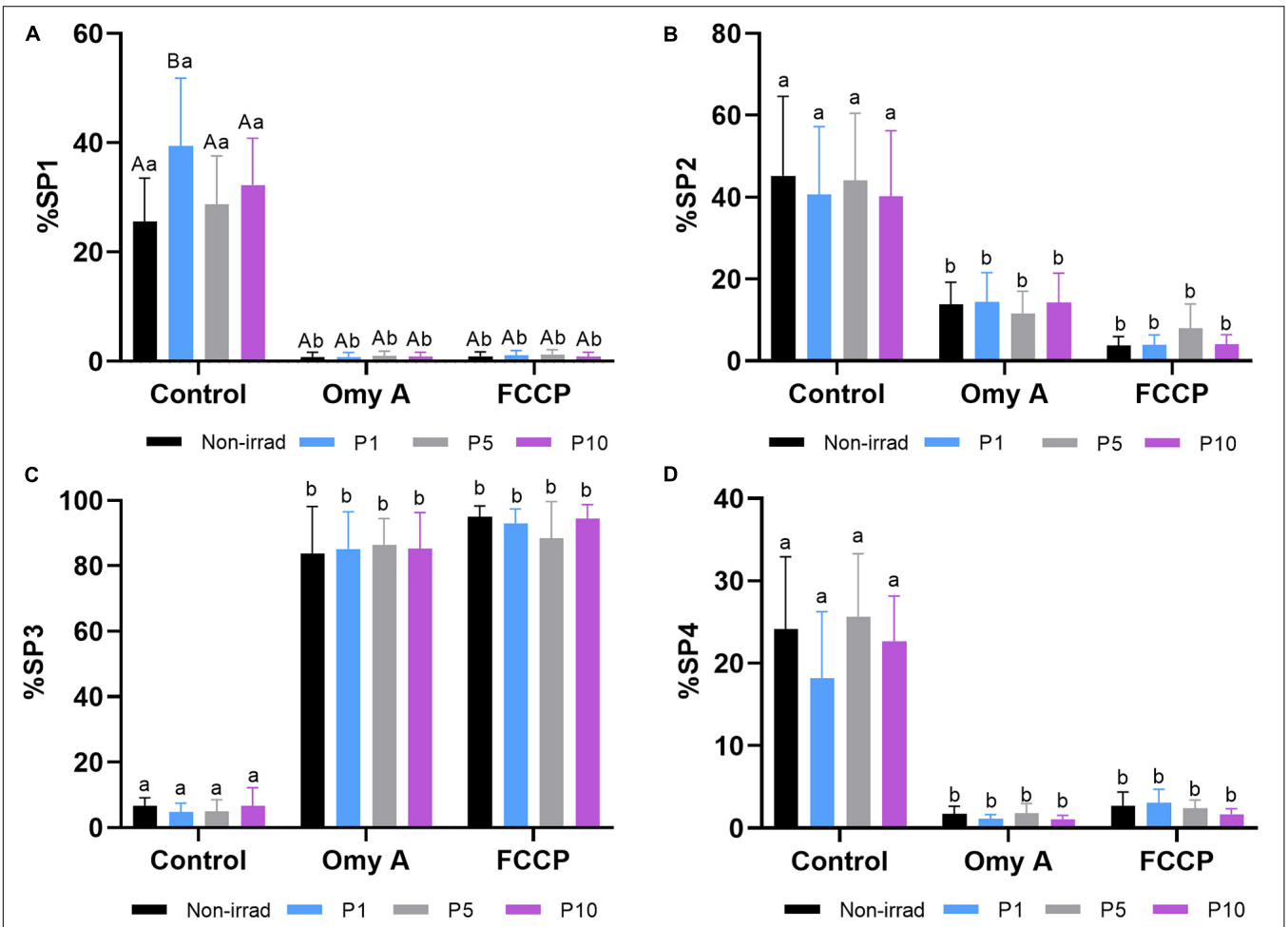

FIGURE 3 | Effects of light stimulation on the structure of the motile sperm subpopulation in the presence/absence of oligomycin A (Omy A) or FCCP. **(A)** Subpopulation 1 (SP1, the fastest and most linear); **(B)** Subpopulation 2 (SP2 presented intermediate values, lower than SP1 and SP4, but more linear than SP4; **(C)** Subpopulation 3 (SP3, the slowest, but more linear than SP4); and **(D)** Subpopulation 4 (SP4 presented intermediate values, higher than SP2, but was the least linear). Different letters (*A,B*) indicate significant differences ($P < 0.05$) between non-irradiated samples and the different light stimulation patterns used in the presence or absence of oligomycin A (Omy A) or FCCP. Different letters (*a,b*) indicate significant differences ($P < 0.05$) between oligomycin A (Omy A) or FCCP with respect to the treatment without the two disruptors for a given protocol (i.e., control, P1, P5, or P10). Data are shown as mean ± SD from eight separate experiments.

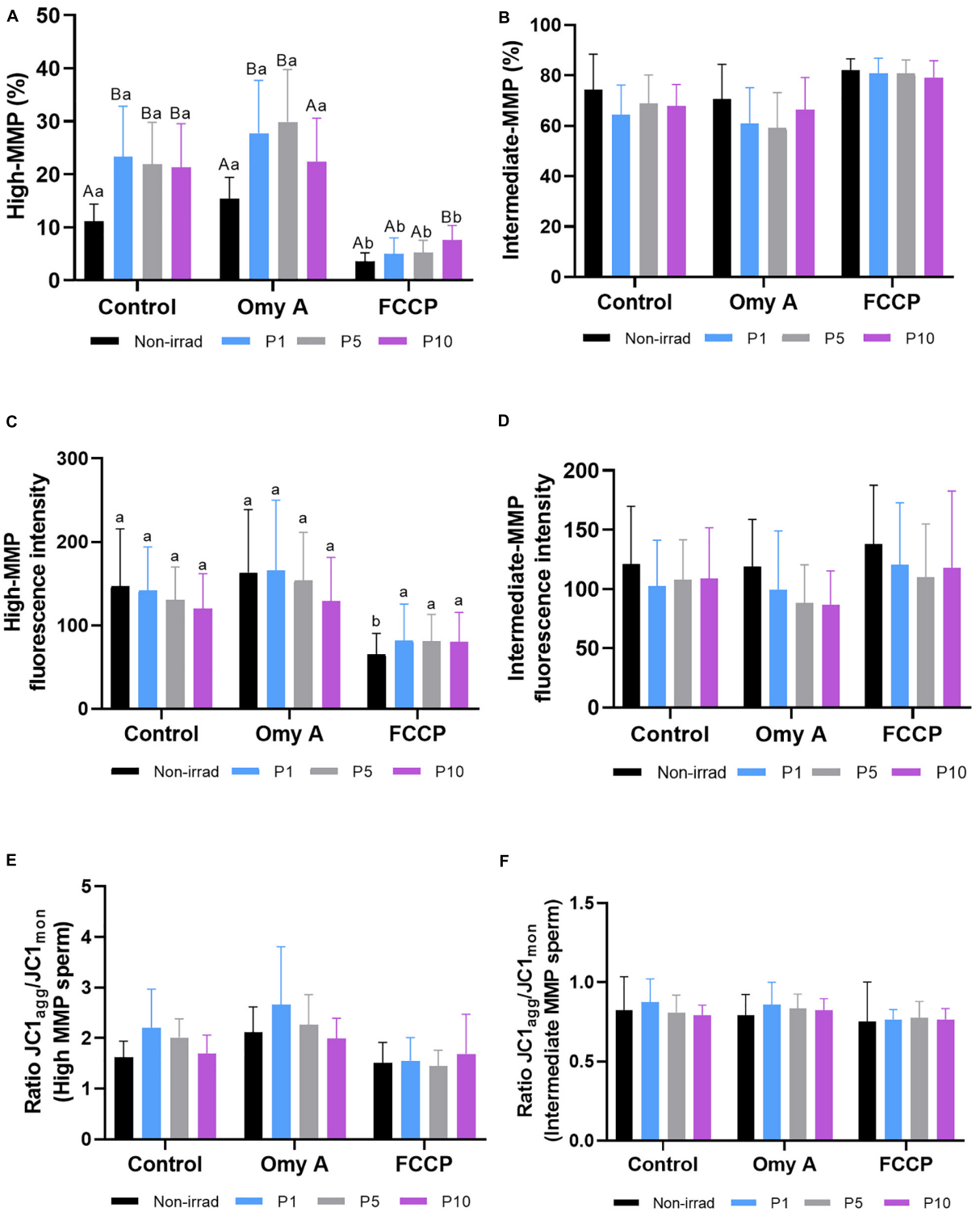

FIGURE 4 | Effects of light stimulation on the mitochondrial membrane potential in the presence/absence of oligomycin A (Omy A) or FCCP. The results are presented as percentages of sperm with high mitochondrial membrane potential (MMP; $JC1_{agg}{}^{++}$; **(A)** and with intermediate mitochondrial membrane potential (MMP; $JC1_{agg}{}^{+}$; **(B)**; geometric mean of the $JC1_{agg}$ fluorescence intensity (GMFI, FL2) in the sperm populations with high **(C)** and intermediate **(D)** MMP; and the $JC1_{agg}/JC1_{mon}$ (GMFI FL2/GMFI FL1) ratios in sperm populations with high **(E)** and intermediate **(F)** MMP in control and irradiation patterns (P1, P5, or P10), in the presence/absence of Omy A. Different letters (*A, B*) indicate significant differences ($P < 0.05$) between non-irradiated samples and the different light-stimulation patterns used in the presence or absence of Omy A or FCCP. Different letters (*a, b*) indicate significant differences ($P < 0.05$) between Omy A or FCCP with respect to the treatment without the two disruptors for a given protocol (i.e., control, P1, P5, or P10). Data are shown as mean ± SD from eight separate experiments.

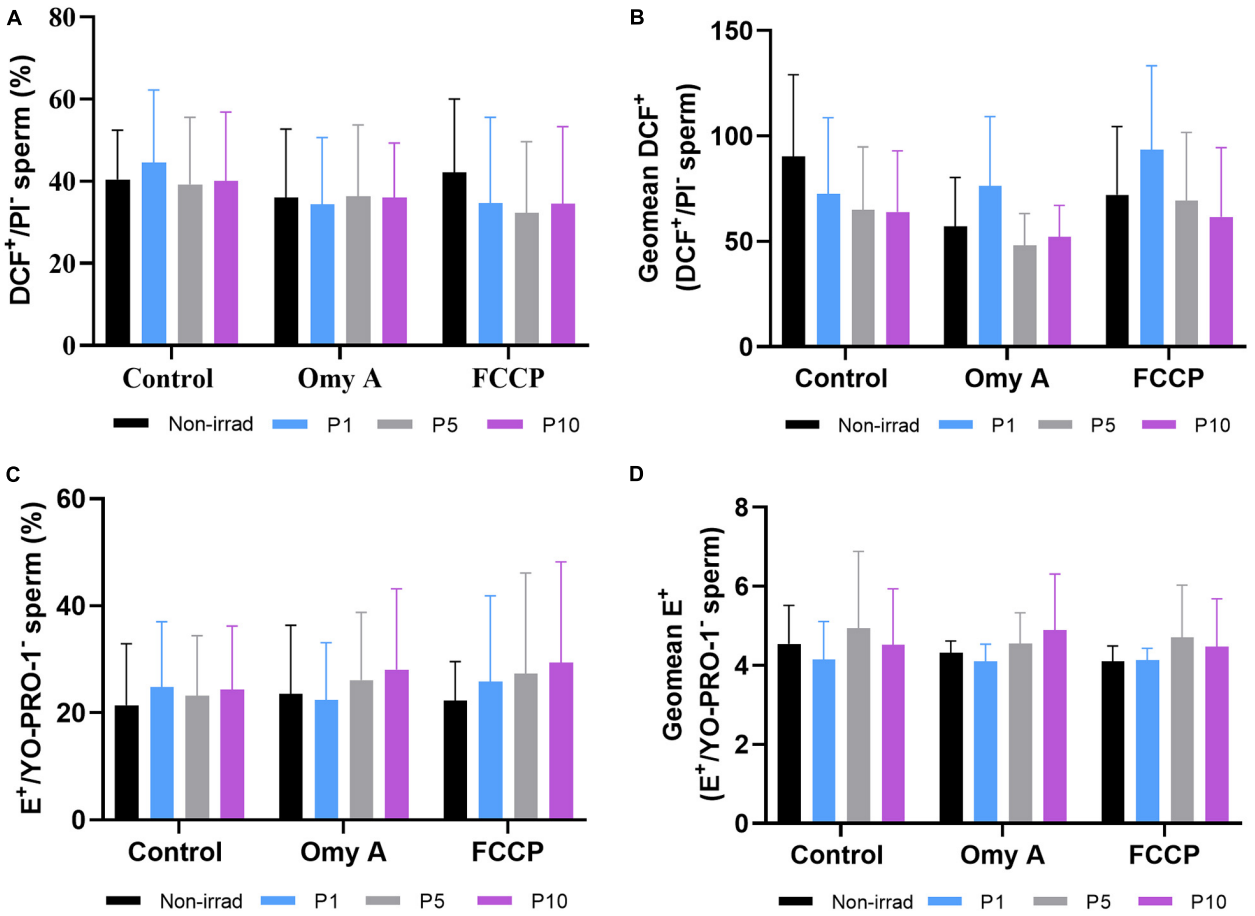

FIGURE 5 | Effects of light-stimulation on the percentages of viable spermatozoa with high peroxide levels (DCF^+/PI^-; **(A)** geometric mean of DCF^+ -intensity (GMFI, FL1 channel) in the population of viable spermatozoa with high peroxide levels **(B)** and percentages of viable spermatozoa with high superoxide levels ($E^+/YO\text{-}PRO\text{-}1^-$; **(C)** and geometric mean of E^+ -intensity (GMFI, FL3 channel) in the population of viable spermatozoa with high superoxide levels **(D)** in the control and irradiated samples in the presence or absence of oligomycin A (Omy A) or FCCP. No significant differences were observed between non-irradiated sperm and the different light-stimulation patterns used in the presence/absence of oligomycin A or FCCP, nor between the results of the samples in the presence of Omy A or FCCP with respect to the treatment without the two disruptors for a given protocol (i.e., control, P1, P5, or P10). Data are shown as mean ± SD from eight separate experiments.

than those without this disruptor, regardless of whether they were irradiated.

Effects of Red Light Stimulation on Cytochrome C Oxidase Activity in the Presence or Absence of Either Omy A or FCCP

As shown in **Figure 8**, irradiation for 1, 5, or 10 min induced a significant increase ($P < 0.05$) in CCO activity compared to non-irradiated samples. Although these effects were observed in both the presence and absence of Omy A or FCCP, the highest CCO activity was observed in sperm irradiated for 5 min in the absence of Omy A/FCCP.

While neither Omy A nor FCCP affected the significant ($P < 0.05$) increase in CCO activity observed in irradiated sperm compared to non-irradiated sperm, samples containing Omy A or FCCP showed significantly ($P < 0.05$) lower CCO activity than when these two molecules were absent from non-irradiated sperm and sperm irradiated for 5 min and 10 min. In contrast, CCO activity in sperm irradiated for 1 min was significantly ($P < 0.05$) lower when Omy A was present than when this inhibitor was absent.

DISCUSSION

The results obtained in the present study with regard to the potential of mitochondrial membrane, sperm kinetic parameters, the structure of motile sperm subpopulations, CCO activity and oxygen consumption rate support that irradiation with red LED light affects mitochondrial activity of donkey sperm. Furthermore, the impact of red light has been found to rely upon the time of exposure (i.e., 1, 5, or 10 min), regardless of the presence of Omy A and FCCP, which is in agreement with

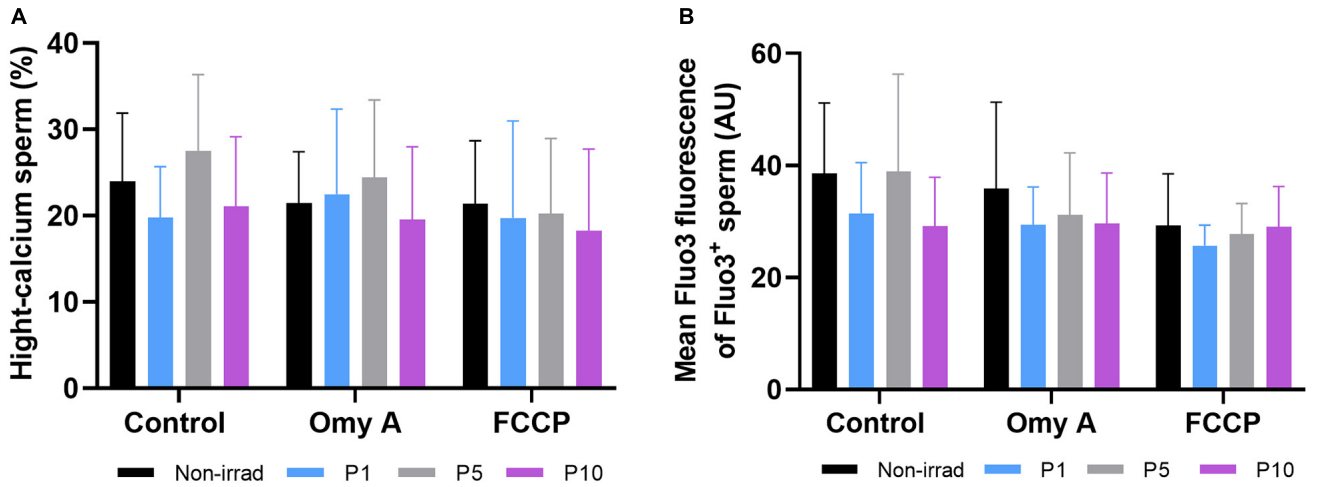

FIGURE 6 | Effects of light-stimulation on percentages of spermatozoa with high intracellular calcium levels ($Fluo3^+$); **(A)** and geometric mean intensity of $Fluo3^+$ **(B)** in the presence/absence of either oligomycin A or FCCP. No significant differences were observed between non-irradiated sperm and the different light stimulation patterns used in the presence or absence of oligomycin A (Omy A) or FCCP, nor between the results of the samples in the presence of Omy A or FCCP with respect to the treatment without the two inhibitors for a given protocol (i.e., control, P1, P5, or P10). Data are shown as mean ± SD from eight separate experiments.

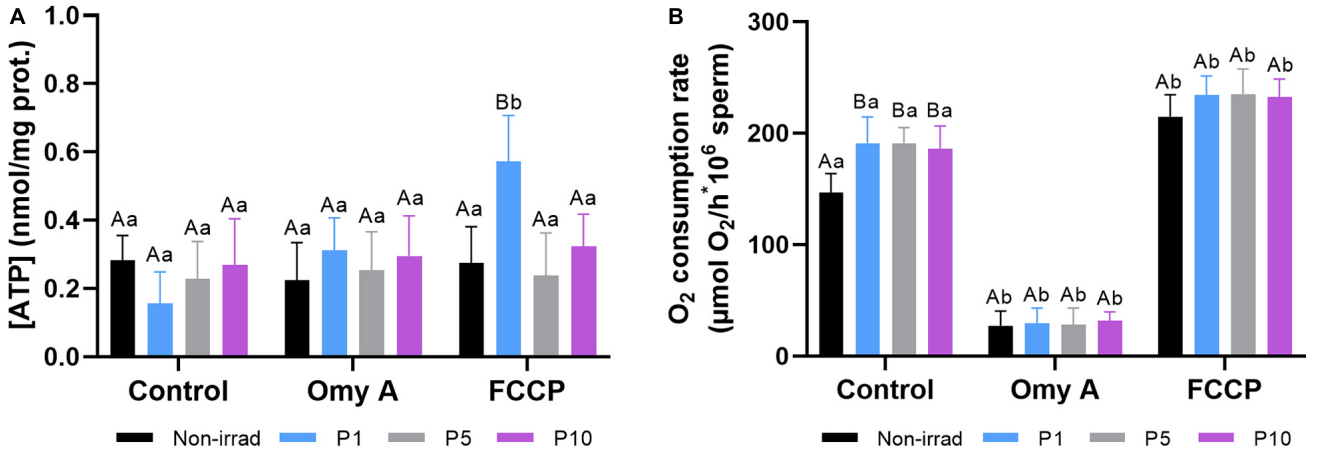

FIGURE 7 | Effects of light-stimulation on intracellular ATP levels **(A)** and O_2 consumption rate **(B)** in the presence/absence of either oligomycin A (Omy A) or FCCP. Different letters (*A, B*) indicate significant differences ($P < 0.05$) between non-irradiated sperm and the different light stimulation patterns used in the presence or absence of Omy A or FCCP. Different letters (*a, b*) indicate significant differences ($P < 0.05$) between Omy A or FCCP with respect to the treatment without the two disruptors for a given protocol (i.e., control, P1, P5, or P10). Data are shown as mean ± SD from eight separate experiments.

previous studies conducted in other mammalian species, such as pigs, dogs, buffalos, humans, donkeys and horses (Corral-Baqués et al., 2009; Abdel-Salam et al., 2011; Salman Yazdi et al., 2014; Yeste et al., 2016; Catalán et al., 2020a,b,c). In this context, it is worth emphasizing that a high individual variation was observed, which indicates that apart from the relevance of the stimulation pattern, time and intensity (Yeste et al., 2016), the sperm response to red light also depend on the functional status of the cell (Catalán et al., 2020a). Although the mechanisms underlying this different response have yet to be elucidated, this work suggests that, in donkey sperm, red light acts on mitochondrial photosensitizers and that the energy supplied to the mitochondrial electron chain following irradiation is related to the time of exposure and intensity. Therefore, the exact level of energy provided to sperm through red light stimulation and the overall sperm function status appear to be on the basis of the different impact observed between treatments and species.

With regard to the effects of red light on the mitochondrial electron chain observed in this work, it is reasonable to surmise that this could be explained by the direct action of red light on mitochondrial photosensitizers (reviewed in Yeste et al., 2018). Indeed, we observed that red light affected the activity of CCO, which is a crucial component of the mitochondrial electron chain and is sensitive to light at a wavelength ranging from 630 to 660 nm (Lynch and Copeland, 1992). These observed

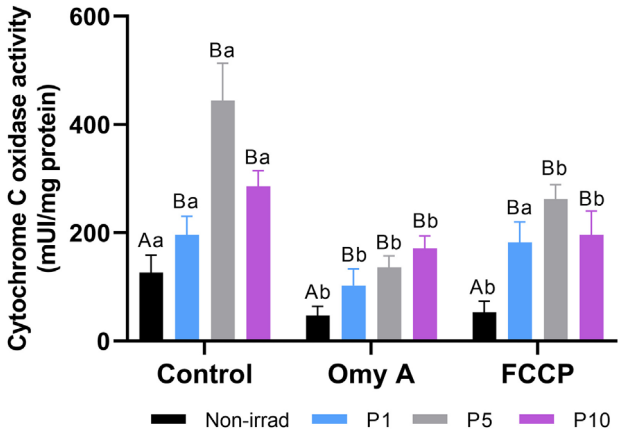

FIGURE 8 | Effects of light-stimulation on cytochrome C oxidase activity in the presence/absence of either oligomycin A (Omy A) or FCCP. Different letters (*A, B*) indicate significant differences ($P < 0.05$) between non-irradiated sperm and the different light stimulation patterns used in the presence or absence of Omy A or FCCP. Different letters (*a, b*) indicate significant differences ($P < 0.05$) between Omy A or FCCP with respect to the treatment without the two inhibitors for a given protocol (i.e., control, P1, P5, or P10). Data are shown as mean ± SD from eight separate experiments.

increases in CCO activity are similar to those reported in ram semen irradiated with He-Ne laser (632.8 nm; Iaffaldano et al., 2016) and in liquid-stored pig semen irradiated with LED (Blanco-Prieto et al., personal communication), which would also support the hypothesis that mitochondrial photosensitizers play a relevant role in the effects of red light upon sperm cells. On the other hand, our results showed that neither irradiation nor the presence of Omy A or FCCP had any detrimental effect on sperm viability, which was evaluated through the $SYBR14^{+}/PI^{-}$ test. These results are in agreement with Yeste et al. (2016) and Pezo et al. (2019), who conducted their studies in liquid-stored pig semen; Catalán et al. (2020a), who evaluated the effects of red light irradiation on fresh and cooled-stored donkey semen; and Catalán et al. (2020b,c) that used frozen-thawed and fresh horse sperm.

As far as the effects of red light on sperm motility are concerned, it is worth mentioning that while no significant differences were observed in the percentages of TMOT and PMOT between non-irradiated and samples irradiated with red light, light-stimulation for 5 min or 10 min in the absence of Omy A/FCCP significantly increased VAP, which is in agreement with previous studies conducted in dogs (Corral-Baqués et al., 2005, 2009), cattle (Siqueira et al., 2016), buffalos (Abdel-Salam et al., 2011), pigs (Yeste et al., 2016), donkeys (Catalán et al., 2020a), and horses (Catalán et al., 2020b,c). We also evaluated the effects of red light on motile sperm subpopulations and we identified four different subpopulations, which is in agreement with that previously reported in the donkey (Miró et al., 2005). Remarkably, we observed that irradiation for 1 min increased the percentages of sperm belonging to SP1, which was the one that included the fastest and most linear motile sperm. Thus, our data suggest that irradiation of fresh donkey sperm with red light modifies the structure of motile sperm subpopulations by increasing the proportions of faster and more linear sperm cells. In addition, our results concur with a previous study conducted on dog semen, in which stimulation with red light (laser) significantly increased the proportions of the fastest sperm subpopulation (Corral-Baqués et al., 2009) and another one carried out with fresh horse sperm where, in a similar fashion to this work, an increase in the most rapid and linear subpopulation was observed (Catalán et al., 2020c). These changes in the characteristics of the motile sperm subpopulations, together with those observed in sperm kinetic parameters, indicate that not only does irradiation with red light increase the speed but also alters the motility pattern of donkey sperm. While there is not, at present, a clear explanation about how red light stimulation affects sperm motility, the aforementioned impact on mitochondrial function could provide some clues. Related to this, it is worth mentioning that the increase observed in VAP and in the proportions of spermatozoa belonging to SP1 was concomitant with a rise in the percentages of sperm with high MMP, determined through JC1. These findings agree with Siqueira et al. (2016), who found that irradiation with a He-Ne laser at a wavelength of 633 nm augmented the percentage of sperm with intermediate MMP. Similar results were found in pig, donkey and horse sperm, since irradiation with red LED light at a wavelength between 620 and 630 nm increased the percentages of sperm with high MMP (Yeste et al., 2016; Catalán et al., 2020a,b,c). Therefore, the current study suggests that stimulation with red light increases mitochondrial activity through endogenous photosensitizers, such as cytochrome C (Begum et al., 2013; Iaffaldano et al., 2016; Yeste et al., 2016; Catalán et al., 2020a,b,c), which could, in turn, lead to greater motility of sperm and higher fertilization potential (Breitbart et al., 1996).

Recent studies indicate that oxygen consumption represents an alternative measure of mitochondrial activity, which could be better than the use MMP markers, such as JC1 (Moscatelli et al., 2017; Meyers et al., 2019). Oxygen consumption rate would also provide an indirect measure of ATP produced by oxidative phosphorylation in mammalian sperm (Meyers et al., 2019). The results obtained in this study showed an increase in oxygen consumption on all irradiated samples (namely, light-stimulated for 1, 5, or 10 min) in the absence of Omy A or FCCP compared to the non-irradiated control. While these results are in agreement with those obtained from the evaluation of some motility parameters, the structure of motile subpopulations, the percentages of viable sperm with high MMP and the activity of cytochrome C oxidase, it is surprising that no link to intracellular levels of ATP was observed, since no differences in this parameter were found when non-irradiated and irradiated samples without oligomycin A/FCCP were compared. Moreover, no relationship between intracellular ATP levels and other mitochondrial parameters was observed in samples irradiated for 1 min in the presence of FCCP. The increase in the potential of the mitochondrial membrane is associated with changes in the consumption of ATP and in the activity of respiratory chain enzymes

(Alberts et al., 2002; Zorova et al., 2018). Related with this, Iaffaldano et al. (2016) observed that light stimulation of frozen-thawed ram sperm with a He-Ne laser increased ATP content and the activity and affinity of cytochrome C oxidase for its substrate (cytochrome C). Interestingly, these authors found that CCO activity and ATP content were positively correlated with each other and with sperm motility, supporting the hypothesis that the effects of red light upon sperm are mediated by mitochondria. However, and as aforementioned, we did not observe that correspondence in the case of donkey sperm. An explanation about why irradiation did not result in a clear increase of intracellular ATP levels could be that ATP in sperm is mainly synthesized through two routes, glycolysis and mitochondrial oxidative phosphorylation, without dismissing other energy sources available to sperm such as β-oxidation (Storey and Keyhani, 1974; Amaral et al., 2013). The precise balance of ATP production from both sources is very dynamic and multifactorial, undergoing rapid changes not only between species, but also within the same cell under different physiological and environmental conditions. The intracellular changes that are related to the complex relationship between mitochondrial oxidative phosphorylation and glycolysis, and that could explain these effects will be later discussed in more detail.

In addition to the aforementioned, the electron chain is known to play a fundamental role in the generation of reactive oxygen species (ROS), since mitochondria are the most important source of ROS generation in eukaryotic cells (Zhao et al., 2019). A previously established hypothesis indicates that light-stimulation increases ROS production by sperm (Cohen et al., 1998; Zan-Bar et al., 2005). Furthermore, cytochrome complexes are also involved in the intrinsic apoptotic pathway (Cai et al., 1998), and it has been surmised that both generation of ROS and modulation of apoptotic-like changes could be crucial to elicit and modulate the achievement of capacitated status by sperm (Ortega-Ferrusola et al., 2009; Aitken et al., 2015). Against this background, one could reasonably suggest that the red light-induced changes in CCO activity observed herein could ultimately affect the lifespan and capacitation status of mammalian sperm. However, our results showed that light-stimulation of fresh donkey sperm did not increase intracellular levels of ROS or calcium, which is a crucial secondary messenger involved in early and late capacitation events (Yeste, 2013; Correia et al., 2015). Thus, our data differ from those observed in donkeys and other species in which irradiation was found to increase intracellular ROS (Cohen et al., 1998; Zan-Bar et al., 2005; Catalán et al., 2020a) and intracellular calcium levels (Lubart et al., 1992; Cohen et al., 1998). These differences could be due to the high individual variability in the sperm response to red light, as well as to differences in the light source, intensity and irradiation pattern, as previous reports found for intracellular levels of ROS (Catalán et al., 2020a) and calcium (Breitbart et al., 1996). Moreover, the existence of a complex homeostasis system aimed at maintaining ROS levels within a physiological range, which would include systems such as the glutathione peroxidase-glutathione reductase complex (GPX/GSR) and enzymes such as intracellular peroxidases (see Peña et al., 2019 for review), would allow sperm to maintain ROS levels in the event of a temporarily induced stress like the one caused by light-stimulation. Nevertheless, further research should be conducted to confirm this hypothesis.

Regarding our results obtained in samples containing Omy A or FCCP, one should note that irradiation in the presence of these two molecules increased the percentages of sperm with high MMP, compared to the non-irradiated control in the presence of these molecules. Furthermore, non-irradiated samples in the presence of FCCP exhibited lower intensity of $JC1_{agg}$ fluorescence in the sperm population with high MMP, which did not occur in irradiated samples. These findings also support that light-stimulation of sperm exerts its effects via MMP. At this point, it is worth mentioning that some studies have recently questioned the use of MMP probes to assess the potential of the mitochondrial membrane due to its non-specific nature (Meyers et al., 2019). These reports point up that MMP probes are cationic and their accumulation rate inside the mitochondria is inversely proportional to the potential of the internal mitochondrial membrane; hence, MMP probes like JC1, which was the one used in this study, may not be reliable as a quantitative measure of MMP without adequate controls. Therefore, these previous studies suggest that high/low MMP controls, such as ATP synthase inhibitors like Omy A and MMP uncouplers like FCCP or DNP, are needed (Meyers et al., 2019). Remarkably, the results obtained in this work with Omy A/FCCP showed this controlling effect, since percentages of sperm with high MMP in samples without disruptors were lower than those containing Omy A, and significantly higher than those containing FCCP. Regarding sperm motility parameters in the presence of these two molecules, they were similar to those found by Ramió-Lluch et al. (2014) and Nesci et al. (2020) in previous studies conducted with pig semen. According to Nesci et al. (2020), the reduced motility observed in treatments containing Omy A or FCCP could result from the decrease in ATP content caused by these two molecules. However, our results indicate that the presence of Omy A and FCCP in irradiated and non-irradiated sperm reduces sperm motility without causing a decrease on overall sperm ATP levels. These findings observed in the presence of Omy A are similar to those seen by Ramió-Lluch et al. (2014), who reported that the control exerted by Omy A-sensitive ATP synthase over pig sperm motility does not seem to be related to its inhibiting effect upon ATP levels. In this context, it is worth mentioning that a previous study reported that mitochondrial respiration of pig sperm incubated in the presence of glucose only contributes to 5% of the total energy produced by the cell, the other 95% being obtained from glycolysis (Marín et al., 2003). Therefore, it is surprising that the relatively low levels of energy produced through ATP synthase affected sperm motility as much as they did in the study of Ramió-Lluch et al. (2014), especially if one bears in mind that these authors did not observe an alteration of overall sperm energy levels. Related with this, in a recent study, Nesci et al. (2020) observed that, despite pig sperm being regarded to rely upon glycolysis, the motility of these cells is highly dependent on the ATP produced through mitochondrial oxidative phosphorylation. In other studies, such as those carried

out by Iaffaldano et al. (2016) on ram sperm and Odet et al. (2013) on mouse sperm, an association between overall ATP content and sperm motility has also been observed. In the case of mice, one should keep in mind that their sperm have been reported to maintain their function through the ATP originated from glycolysis or mitochondrial respiration indistinctly (Pasupuleti, 2007). In addition to this, a recent study published by Balbach et al. (2020) has demonstrated a functional link between these two pathways during mouse sperm capacitation. All these data strongly point to the existence of species-specific differences on the mechanisms by which mammalian spermatozoa produce ATP via glycolysis or oxidative phosphorylation (Rodríguez-Gil and Bonet, 2016). Our results suggest that changes in intracellular ATP levels cannot be taken as a direct indicator of changes affecting mitochondrial function, since glycolysis and probably other metabolic pathways present in sperm also produce ATP; thus, further metabolomics studies in donkey sperm are needed to understand the precise glycolysis/oxidative phosphorylation balance in these cells.

While the evidence reported in this and another study in pigs (Blanco-Prieto et al., personal communication) indicates that the effects of red light on sperm would be related to the direct effect on intracellular light-sensitive proteins, especially the impact on endogenous photosensitizers, such as mitochondrial cytochromes, other pathways or factors that might modulate the effects of red light on mammalian sperm could also be involved (reviewed in Yeste et al., 2018). These pathways or factors include light-sensitive receptors, such as opsins (Pérez-Cerezales et al., 2015) and transient receptor potential proteins (TRP) (De Blas et al., 2009; Bahat and Eisenbach, 2010; Gibbs et al., 2011), whose one of their most probable functions in mammalian sperm is the regulation of thermotaxis (Wu et al., 2010; Pérez-Cerezales et al., 2015). Thermotaxis could be, in fact, an important modulator of light stimulation, since mammalian sperm are sensitive to temperature changes as small as 0.0006°C (Bahat et al., 2012; Pérez-Cerezales et al., 2015). Therefore, it is reasonable to suggest that red light stimulation could also act through this pathway, especially if one takes into consideration that, in this study, the effects of irradiation on MMP and ATP content, which rely on glycolysis/oxidative phosphorylation balance, differed. In addition, one should not discard that signaling transduction pathways triggered when opsins and TRP receptors are activated could change ATP production via glycolysis as well as the balance between glycolysis and oxidative phosphorylation.

CONCLUSION

In conclusion, our results indicate that the effects induced by the stimulation of fresh donkey sperm with red LED light are related to mitochondrial photosensitizers, such as CCO, which modify the activity of the mitochondrial electron chain; the effect of red light on these photosensitizers depends on the time of exposure, among other factors. However, these findings do not exclude that this mitochondrial mechanism could work in conjunction with other pathways, such as thermotaxis, via plasma membrane receptors.

DATA AVAILABILITY STATEMENT

The raw data supporting the conclusions of this article will be made available by the authors, without undue reservation, to any qualified researcher.

ETHICS STATEMENT

All jackasses used in this study were semen donors and no manipulation to animals, apart from semen collection in the authorized center, was made. The animal study was reviewed and approved by the Ethics Committee for Animal and Human Experimentation (CEEAH) of our institution (Autonomous University of Barcelona; authorization code: CEEAH 1424.

AUTHOR CONTRIBUTIONS

MY, JR-G, and JM: conceptualization. JC, MP, LT-R, OB-P, JM, MY, and JR-G: methodology and investigation. JM, MY, and JR-G: validation, project administration, and supervision. JR-G: formal analysis and data curation. JC: writing—original draft preparation. JM and MY: writing—review and editing, funding acquisition, and resources. All authors have read and agreed to the published version of the manuscript.

FUNDING

JC was funded by the National Agency for Research and Development (ANID), Ministry of Education, Chile (Scheme: Becas Chile Doctorado en el Extranjero, PFCHA; Grant: 2017/72180128). The authors also acknowledge the support from the Ministry of Science and Innovation, Spain (Grants: RYC-2014-15581 and AGL2017-88329-R), and the Regional Government of Catalonia, Spain (2017-SGR-1229).

ACKNOWLEDGMENTS

We acknowledge the technical support from Estela Garcia-Bonavila, Sandra Recuero, Ariadna Delgado-Bermúdez, Marc Llavanera, and Yentel Mateo.

SUPPLEMENTARY MATERIAL

The Supplementary Material for this article can be found online at: https://www.frontiersin.org/articles/10.3389/fcell.2020.588621/full#supplementary-material

Supplementary Figure 1 | Representative flow-cytometry dot-plots observed in non-irradiated samples and samples irradiated for 5 min, in the presence/absence of FCCP and Omy A.

REFERENCES

Abdel-Salam, Z., Dessouki, S. H. M., Abdel-Salam, S. A. M., Ibrahim, M. A. M., and Harith, M. A. (2011). Green laser irradiation effects on buffalo semen. *Theriogenology* 75, 988–994. doi: 10.1016/j.theriogenology.2010.11.005

Aitken, R. J., Baker, M. A., and Nixon, B. (2015). Are sperm capacitation and apoptosis the opposite ends of a continuum driven by oxidative stress? *Asian J. Androl.* 17, 633–639. doi: 10.4103/1008-682X.153850

Alberts, B., Johnson, A., Lewis, J., Raff, M., Roberts, K., and Walter, P. (2002). Energy conversion: mitochondria and chloroplasts. *Mol. Biol. Cell* 2002, 753–812. doi: 10.1201/9781315735368-14

Amaral, A., Castillo, J., Estanyol, J. M., Ballescà, J. L., Ramalho-Santos, J., and Oliva, R. (2013). Human sperm tail proteome suggests new endogenous metabolic pathways. *Mol. Cel. Proteom.* 12, 330–342. doi: 10.1074/mcp.M112.020552

Bahat, A., Caplan, S. R., and Eisenbach, M. (2012). Thermotaxis of human sperm cells in extraordinarily shallow temperature gradients over a wide range. *PLoS One* 7:e41915. doi: 10.1371/journal.pone.0041915

Bahat, A., and Eisenbach, M. (2010). Human sperm thermotaxis is mediated by phospholipase C and inositol trisphosphate receptor Ca2+ Channel1. *Biol. Reprod.* 82, 606–616. doi: 10.1095/biolreprod.109.080127

Begum, R., Powner, M. B., Hudson, N., Hogg, C., and Jeffery, G. (2013). Treatment with 670 nm light up regulates cytochrome c oxidase expression and reduces inflammation in an age-related macular degeneration model. *PLoS One* 8:e57828. doi: 10.1371/journal.pone.0057828

Balbach, M., Gervasi, M. G., Hidalgo, D. M., Visconti, P. E., Levin, L. R., and Buck, J. (2020). Metabolic changes in mouse sperm during capacitation†. *Biol. Reprod.* 103, 791–801. doi: 10.1093/biolre/ioaa114

Blanco-Prieto, O., Catalán, J., Lleonart, M., Bonet, S., Yeste, M., and Rodríguez-Gil, J. E. (2019). Red-light stimulation of boar semen prior to artificial insemination improves field fertility in farms: a worldwide survey. *Reprod. Domest. Anim.* 54, 1145–1148. doi: 10.1111/rda.13470

Bradford, M. M. (1976). A rapid and sensitive method for the quantitation of microgram quantities of protein utilizing the principle of protein-dye binding. *Anal. Biochem.* 72, 248–254. doi: 10.1016/0003-2697(76)90527-3

Breitbart, H., Levinshal, T., Cohen, N., Friedmann, H., and Lubart, R. (1996). Changes in Calcium Transport in Mammalian Sperm Mitochondria and Plasma Membrane Irradiated at 633 Nm (HeNe Laser). *J. Photochem. Photobiol. B Biol.* 34, 117–121. doi: 10.1016/1011-1344(95)07281-0

Cai, J., Yang, J., and Jones, D. P. (1998). Mitochondrial control of apoptosis: the role of cytochrome C. *Biochim. Biophys. Acta Bioenerg.* 1366, 139–149. doi: 10.1016/S0005-2728(98)00109-1

Canisso, I. F., Souza, F. A., Ortigoza, J. M., Ribeiro De Carvalho, G., Davies- Morel, M. C., Capistrano, et al. (2008). Freezing of donkey semen (Equus Asinus). *Rev. Inv. Vet. Perú.* 19, 113–125.

Catalán, J., Llavanera, M., Bonilla-Correal, S., Papas, M., Gacem, S., Rodríguez-Gil, J. E., et al. (2020a). Irradiating frozen-thawed stallion sperm with red-light increases their resilience to withstand post-thaw incubation at 38 °C. *Theriogenology* 157, 85–95. doi: 10.1016/j.theriogenology.2020.07.027

Catalán, J., Papas, M., Gacem, S., Mateo-Otero, Y., Rodríguez-Gil, J. E., Miró, J., et al. (2020b). Red-light irradiation of horse spermatozoa increases mitochondrial activity and motility through changes in the motile sperm subpopulation structure. *Biology* 9:254. doi: 10.3390/biology9090254

Catalán, J., Papas, M., Gacem, S., Noto, F., Delgado-Bermúdez, A., Rodríguez-Gil, J. E., et al. (2020c). Effects of red-light irradiation on the function and survival of fresh and liquid-stored donkey semen. *Theriogenology* 149, 88–97. doi: 10.1016/j.theriogenology.2020.03.024

Chida, J., Yamane, K., Takei, T., and Kido, H. (2012). An efficient extraction method for quantitation of adenosine triphosphate in mammalian tissues and cells. *Anal. Chim Acta.* 727, 8–12. doi: 10.1016/j.aca.2012.03.022

Cohen, N., Lubart, R., Rubinstein, S., and Breitbart, H. (1998). Light irradiation of mouse spermatozoa: stimulation of in vitro fertilization and calcium signals. *Photochem. Photobiol.* 68, 407–413. doi: 10.1111/j.1751-1097.1998.tb09700.x

Corral-Baqués, M. I., Rigau, T., Rivera, M., Rodríguez, J. E., and Rigau, J. (2005). Effect of 655-Nm diode laser on dog sperm motility. *Lasers Med. Sci.* 20, 28–34. doi: 10.1007/s10103-005-0332-3

Corral-Baqués, M. I., Rivera, M. M., Rigau, T. J. E., Rodríguez-Gil, J. E., and Rigau, J. (2009). The effect of low-level laser irradiation on dog spermatozoa motility is dependent on laser output power. *Lasers Med. Sci* 24, 703–713. doi: 10.1007/s10103-008-0606-7

Correia, J., Michelangeli, F., and Publicover, S. (2015). Regulation and roles of Ca2+ stores in human sperm. *Reproduction* 150, 65–76. doi: 10.1530/rep-15-0102

Crowe, C. A., Ravenhill, P. J., Hepburn, R. J., and Shepherd, C. H. (2008). A retrospective study of artificial insemination of 251 mares using chilled and fixed time frozen-thawed semen. *Equine Vet. J.* 40, 572–576. doi: 10.2746/042516408X281199

De Blas, G. A., Darszon, A., Ocampo, A. Y., Serrano, C. J., Castellano, L. E., Hernández-González, E. O., et al. (2009). TRPM8, a Versatile Channel in Human Sperm. *PLoS One* 4:e6095. doi: 10.1371/journal.pone.0006095

Garner, D. L., and Johnson, L. A. (1995). Viability assessment of mammalian sperm using SYBR-14 and propidium iodide. *Biol. Reprod.* 53, 276–284. doi: 10.1095/biolreprod53.2.276

Gibbs, G. M., Orta, G., Reddy, T., Koppers, A. J., Martínez-López, P., De La Vega-Beltràn, J. L., et al. (2011). Cysteine-rich secretory protein 4 is an inhibitor of transient receptor potential M8 with a role in establishing sperm function. *Proc. Natl. Acad. Sci. U.S.A.* 108, 7034–7039. doi: 10.1073/pnas.1015935108

Guthrie, H. D., and Welch, G. R. (2006). Determination of intracellular reactive oxygen species and high mitochondrial membrane potential in percoll-treated viable boar sperm using fluorescence-activated flow cytometry1. *J. Anim. Sci.* 84, 2089–2100. doi: 10.2527/jas.2005-766

Hamano, K., Kawanishi, T., Mizuno, A., Suzuki, M., and Takagi, Y. (2016). Involvement of transient receptor potential vanilloid (TRPV) 4 in mouse sperm thermotaxis. *J. Reprod. Dev.* 62, 415–422. doi: 10.1262/jrd.2015-106

Iaffaldano, N., Paventi, G., Pizzuto, R., Di Iorio, M., Bailey, J. L., Manchisi, A., et al. (2016). Helium-neon laser irradiation of cryopreserved ram sperm enhances cytochrome c oxidase activity and ATP levels improving semen quality. *Theriogenology* 86, 778–784. doi: 10.1016/j.theriogenology.2016.02.031

Kadirvel, G., Kumar, S., Kumaresan, A., and Kathiravan, P. (2009). Capacitation status of fresh and frozen-thawed buffalo spermatozoa in relation to cholesterol level. Membrane Fluidity and Intracellular Calcium. *Anim. Reprod. Sci.* 116, 244–253. doi: 10.1016/j.anireprosci.2009.02.003

Kenney, R. M., Bergman, R. V., Cooper, W. L., and Morse, G. W. (1975). Minimal contamination techniques for breeding mares: techniques and priliminary findings. *Proc. Am. Assoc. Equine Pract.* 21, 327–336.

Kessel, D. (1982). Determinants of hematoporphyrin-catalyzed photosensitization. *Photochem. Photobiol.* 36, 99–101. doi: 10.1111/j.1751-1097.1982.tb04347.x

Kowalczyk, A., Czerniawska-Piątkowska, E., and Kuczaj, M. (2019). Factors influencing the popularity of artificial insemination of mares in europe. *Animals* 9:460. doi: 10.3390/ani9070460

Lee, J. A., Spidlen, J., Boyce, K., Cai, J., Crosbie, N., Dalphin, M., et al. (2008). MIFlowCyt: the minimum information about a flow cytometry experiment. *Cytometry A.* 73, 926–930. doi: 10.1002/cyto.a.20623

Lishko, P. V., Kirichok, Y., Ren, D., Navarro, B., Jean-Ju Chung, J.-J., and Clapham, D. E. (2012). The control of male fertility by spermatozoan ion channels. *Annu. Rev. Physiol.* 74, 453–475. doi: 10.1146/annurev-physiol-020911-153258

Loomis, P. R. (2006). Advanced methods for handling and preparation of stallion semen. *Vet. Clin. North Am. Equine Pract.* 22, 663–676. doi: 10.1016/j.cveq.2006.07.002

Lubart, R., Friedmann, H., Levinshal, T., Lavie, R., and Breitbart, H. (1992). Effect of light on calcium transport in bull sperm cells. *J. Photochem. Photobiol. B Biol.* 15, 337–341. doi: 10.1016/1011-1344(92)85139-L

Luna, C., Yeste, M., Rivera Del Alamo, M. M., Domingo, J., Casao, A., Joan, E., et al. (2017). Effect of seminal plasma proteins on the motile sperm subpopulations in ram ejaculates. *Reprod. Fertil. Dev.* 29, 394–405. doi: 10.1071/RD15231

Lynch, S. R., and Copeland, R. A. (1992). Electronic and Vibrational Spectroscopy of the Cytochrome c: cytochrome c oxidase complexes from bovine and paracoccus denitrificans. *Protein Sci.* 1, 1428–1434. doi: 10.1002/pro.5560011104

Marín, S., Chiang, K., Bassilian, S., Lee, W. N., Boros, L. G., Fernandez-Novell, J. M., et al. (2003). Metabolic strategy of boar spermatozoa revealed by metabolomic characterisation. *FEBS Lett.* 554, 342–346. doi: 10.1016/S0014-5793(03)01185-2

Mclean, T. R., Jones, J. W., Svensson, L. G., and Beall, A. C. (1993). Selective topical cooling for myocardial protection. *Vascular* 1, 176–181. doi: 10.1177/096721099300100219

Meyers, S., Bulkeley, E., and Foutouhi, A. (2019). Sperm mitochondrial regulation in motility and fertility in horses. *Reprod. Domest. Anim.* 54, 22–28. doi: 10.1111/rda.13461

Miró, J., Lobo, V., Quintero-Moreno, A., Medrano, A., Peña, A., and Rigau, T. (2005). Sperm motility patterns and metabolism in catalonian donkey semen. *Theriogenology* 63, 1706–1716. doi: 10.1016/j.theriogenology.2004.07.022

Miró, J., Marín, H., Catalán, J., Papas, M., Gacem, S., and Yeste, M. (2020). Seminal plasma, sperm concentration, and Sperm-PMN interaction in the donkey: an in vitro model to study endometrial inflammation at post-insemination. *Int. J. Mol. Sci.* 21:3478. doi: 10.3390/ijms21103478

Miró, J., and Papas, M. (2018). Post–Artificial Insemination Endometrial Inflammation and Its Control in Donkeys. *J. Equine Vet. Sci.* 65, 38–43. doi: 10.1016/J.JEVS.2017.11.007

Moscatelli, N., Spagnolo, B., Pisanello, M., Lemma, E. D., De Vittorio, M., Zara, V., et al. (2017). Single-cell-based evaluation of sperm progressive motility via fluorescent assessment of mitochondria membrane potential. *Sci. Rep.* 7:17931. doi: 10.1038/s41598-017-18123-1

Mundt, N., Spehr, M., and Lishko, P. V. (2018). TRPV4 is the temperature-sensitive ion channel of human sperm. *eLife* 7:e35853. doi: 10.7554/eLife.35853

Murillo, M. M., Carmona-Cuenca, I., Del Castillo, G., Ortiz, C., Roncero, C., Sánchez, A., et al. (2007). Activation of NADPH oxidase by transforming growth factor-β in hepatocytes mediates up-regulation of epidermal growth factor receptor ligands through a nuclear factor-KB-dependent mechanism. *Biochem. J.* 405, 251–259. doi: 10.1042/BJ20061846

Nesci, S., Spinaci, M., Galeati, G., Nerozzi, C., Pagliarani, A., Algieri, C., et al. (2020). Sperm function and mitochondrial activity: an insight on boar sperm metabolism. *Theriogenology* 144, 82–88. doi: 10.1016/j.theriogenology.2020.01.004

Odet, F., Gabel, S., London, R. E., Goldberg, E., and Eddy, M. (2013). Glycolysis and mitochondrial respiration in mouse LDHC null sperm. *Biol. Reprod.* 88:95. doi: 10.1095/biolreprod.113.108530

Ortega-Ferrusola, C., Macías García, B., Gallardo-Bolaños, J. M., González-Fernández, L., Rodríguez-Martinez, H., Tapia, J. A., et al. (2009). Apoptotic markers can be used to forecast the freezeability of stallion spermatozoa. *Anim. Reprod. Sci.* 114, 393–403. doi: 10.1016/j.anireprosci.2008.10.005

Pagl, R., Aurich, J. E., Müller-Schlösser, F., Kankofer, M., and Aurich, C. (2006). Comparison of an extender containing defined milk protein fractions with a skim milk-based extender for storage of equine semen at 5 °C. *Theriogenology* 66, 1115–1122. doi: 10.1016/j.theriogenology.2006.03.006

Pasupuleti, V. (2007). *Role of Glycolysis and Respiration in Sperm Metabolism and Motility*. Master's thesis, Kent State University, Kent, OH.

Peña, F. J., O'Flaherty, C., Ortiz Rodríguez, J. M., Martín Cano, F. E., Gaitskell-Phillips, G. L., Gil, M. C., et al. (2019). Redox regulation and oxidative stress: the particular case of the stallion spermatozoa. *Antioxidants* 8:567. doi: 10.3390/antiox8110567

Pérez-Cerezales, S., Boryshpolets, S., Afanzar, O., Brandis, A., Nevo, R., Kiss, V., et al. (2015). Involvement of opsins in mammalian sperm thermotaxis. *Sci. Rep.* 5:16146. doi: 10.1038/srep16146

Petrunkina, A. M., Waberski, D., Bollwein, H., and Sieme, H. (2010). Identifying non-sperm particles during flow cytometric physiological assessment: a simple approach. *Theriogenology* 73, 995–1000. doi: 10.1016/j.theriogenology.2009.12.006

Pezo, F., Zambrano, F., Uribe, P., Ramírez-Reveco, A., Romero, F., and Sanchéz, R. (2019). LED-based red light photostimulation improves short-term response of cooled boar semen exposed to thermal stress at 37°C. *Andrologia* 51:e13237. doi: 10.1111/and.13237

Pottier, R., and Truscott, T. G. (1986). The photochemistry of haematoporphyrin and related systems. *Int. J. Radiat. Biol.* 50, 421–452. doi: 10.1080/09553008614550851

Ramió-Lluch, L., Yeste, M., Fernández-Novell, J. M., Estrada, E., Rocha, L., Cebrián-Pérez, J. A., et al. (2014). Oligomycin A-induced inhibition of mitochondrial ATP-synthase activity suppresses boar sperm motility and in vitro capacitation achievement without modifying overall sperm energy levels. *Reprod. Fertil. Dev.* 26, 883–897. doi: 10.1071/RD13145

Rodríguez-Gil, J. E., and Bonet, S. (2016). Current knowledge on boar sperm metabolism: Comparison with other mammalian species. *Theriogenology* 85, 4–11. doi: 10.1016/j.theriogenology.2015.05.005

Roy, D., Levi, K., Kiss, V., Nevo, R., and Eisenbach, M. (2020). Rhodopsin and melanopsin coexist in mammalian sperm cells and activate different signaling pathways for thermotaxis. *Sci. Rep.* 10:112. doi: 10.1038/s41598-019-56846-5

Salman Yazdi, R., Bakhshi, S., Jannat Alipoor, F., Akhoond, M. R., Borhani, S., Farrahi, F., et al. (2014). Effect of 830-Nm diode laser irradiation on human sperm motility. *Lasers Med. Sci.* 29, 97–104. doi: 10.1007/s10103-013-1276-7

Singh, A. P., and Rajender, S. (2014). CatSper channel, sperm function and male fertility. *Reprod. Biomed. Online.* 30, 28–38. doi: 10.1016/j.rbmo.2014.09.014

Siqueira, A. F. P., Maria, F. S., Mendes, C. M., Hamilton, T. R. S., Dalmazzo, A., Dreyer, T. R., et al. (2016). Effects of photobiomodulation therapy (PBMT) on bovine sperm function. *Lasers Med. Sci.* 31, 1245–1250. doi: 10.1007/s10103-016-1966-z

Squires, E. L. (2009). Changes in equine reproduction: have they been good or bad for the horse industry? *J. Equine Vet. Sci.* 29, 268–273. doi: 10.1016/j.jevs.2009.04.184

Storey, T., and Keyhani, E. (1974). Energy metabolism of spermatozoa. ii. Comparison of pyruvate and fatty acid oxidation by mitochondria of rabbit epididymal spermatozoa. *Fertil. Steril.* 25, 857–864. doi: 10.1016/s0015-0282(16)40692-8

Sun, X. H., Zhu, Y. Y., Wang, L., Liu, H. L., Ling, Y., Li, Z. L., et al. (2017). The catsper channel and its roles in male fertility: a systematic review. *Reprod. Biol. Endocrinol.* 15:65. doi: 10.1186/s12958-017-0281-2

Varner, D. D. (2016). Strategies for processing semen from subfertile stallions for cooled transport. *Vet. Clin. North Am. Equine Pract.* 32, 547–560. doi: 10.1016/j.cveq.2016.07.007

Vriens, J., Nilius, B., and Voets, T. (2014). Peripheral thermosensation in mammals. *Nat. Rev. Neurosci.* 15, 573–589. doi: 10.1038/nrn3784

Wu, L. J., Sweet, T. B., and Clapham, D. E. (2010). International union of basic and clinical pharmacology. LXXVI. current progress in the mammalian TRP ion channel family. *Pharmacol. Rev.* 62, 381–404. doi: 10.1124/pr.110.002725

Yeste, M. (2013). "Boar spermatozoa within the oviductal environment (II): sperm capacitation," in *Boar Reproduction: Fundamentals and New Biotechnological Trends*, eds S. Bonet, I. Casas, W. V. Holt, and M. Yeste (Berlin: Springer), 281–342.

Yeste, M., Castillo-Martín, C., Bonet, S., and Rodríguez-Gil, J. E. (2018). Impact of light irradiation on preservation and function of mammalian spermatozoa. *Anim. Reprod. Sci.* 194, 19–32. doi: 10.1016/j.anireprosci.2018.02.004

Yeste, M., Codony, F., Estrada, E., Lleonart, M., Balasch, S., Peña, A., et al. (2016). Specific LED-based red light photo-stimulation procedures improve overall sperm function and reproductive performance of boar ejaculates. *Sci. Rep.* 6:22569. doi: 10.1038/srep22569

Yeste, M., Fernández-Novell, J. M., Ramió-Lluch, L., Estrada, E., Rocha, L. G. J. A., Cebrián-Pérez, J. A., et al. (2015). Intracellular calcium movements of boar spermatozoa during 'in vitro' capacitation and subsequent acrosome exocytosis follow a multiple-storage place, extracellular calcium-dependent model. *Andrology* 3, 729–747. doi: 10.1111/andr.12054

Zan-Bar, T., Bartoov, B., Segal, R., Yehuda, R., Lavi, R., Lubart, R., et al. (2005). Influence of visible light and ultraviolet irradiation on motility and fertility of

mammalian and fish sperm. *Photomed. Laser Surg.* 23, 549–555. doi: 10.1089/pho.2005.23.549

Zhao, H., Kalivendi, S., Zhang, H., Joseph, J., Nithipatikom, K., Vásquez-Vivar, J., et al. (2003). Superoxide reacts with hydroethidine but forms a fluorescent product that is distinctly different from ethidium: potential implications in intracellular fluorescence detection of superoxide. *Free Radic. Biol. Med.* 34, 1359–1368. doi: 10.1016/S0891-5849(03)00142-4

Zhao, R. Z., Jiang, S., Zhang, L., and Yu, Z. B. (2019). Mitochondrial electron transport chain, ROS generation and uncoupling (Review). *Int J. Mol. Med.* 44, 3–15. doi: 10.3892/ijmm.2019.4188

Zheng, J. (2013). Molecular mechanism of TRP channels. *Compr. Physiol.* 3, 221–242. doi: 10.1002/cphy.c120001

Zorova, L. D., Popkov, V. A., Plotnikov, E. Y., Silachev, D. N., Pevzner, I. B., Jankauskas, S. S., et al. (2018). Mitochondrial membrane potential. *Anal. Biochem.* 552, 50–59. doi: 10.1016/j.ab.2017.07.009

Conflict of Interest: JR-G and MY were inventors of a patent entitled 'Method and apparatus for improving the quality of mammalian sperm' (European Patent Office, No. 16199093.2; EP-3-323-289-A1), which is owned by Instruments Utils de Laboratori Geniul, SL (Barcelona, Spain).

The remaining authors declare that the research was conducted in the absence of any commercial or financial relationships that could be construed as a potential conflict of interest.

Copyright © 2020 Catalán, Papas, Trujillo-Rojas, Blanco-Prieto, Bonilla-Correal, Rodríguez-Gil, Miró and Yeste. This is an open-access article distributed under the terms of the Creative Commons Attribution License (CC BY). The use, distribution or reproduction in other forums is permitted, provided the original author(s) and the copyright owner(s) are credited and that the original publication in this journal is cited, in accordance with accepted academic practice. No use, distribution or reproduction is permitted which does not comply with these terms.

frontiers in Cell and Developmental Biology

ORIGINAL RESEARCH
published: 23 December 2020
doi: 10.3389/fcell.2020.580019

Role of Phosphorylated Gonadotropin-Regulated Testicular RNA Helicase (GRTH/DDX25) in the Regulation of Germ Cell Specific mRNAs in Chromatoid Bodies During Spermatogenesis

*Rajakumar Anbazhagan[1], Raghuveer Kavarthapu[1], Steven L. Coon[2] and Maria L. Dufau[1]**

[1] *Section on Molecular Endocrinology, Division of Developmental Biology, Eunice Kennedy Shriver National Institute of Child Health and Human Development, National Institutes of Health, Bethesda, MD, United States,* [2] *Molecular Genomics Core, Eunice Kennedy Shriver National Institute of Child Health and Human Development, National Institutes of Health, Bethesda, MD, United States*

OPEN ACCESS

Edited by:
Tomer Avidor-Reiss, The University of Toledo, United States

Reviewed by:
Labib Rouhana, Wright State University, United States
Ravi Kumar Gutti, University of Hyderabad, India
Fei Sun, Shanghai Jiao Tong University, China

***Correspondence:**
Maria L. Dufau
dufaum@mail.nih.gov

Specialty section:
This article was submitted to Cell Growth and Division, a section of the journal Frontiers in Cell and Developmental Biology

Received: *04 July 2020*
Accepted: *11 November 2020*
Published: *23 December 2020*

Citation:
Anbazhagan R, Kavarthapu R, Coon SL and Dufau ML (2020) Role of Phosphorylated Gonadotropin-Regulated Testicular RNA Helicase (GRTH/DDX25) in the Regulation of Germ Cell Specific mRNAs in Chromatoid Bodies During Spermatogenesis. Front. Cell Dev. Biol. 8:580019. doi: 10.3389/fcell.2020.580019

GRTH/DDX25 is a member of the DEAD-box family of RNA helicases that play an essential role in spermatogenesis. GRTH knock-in (KI) mice with the human mutant GRTH gene (R242H) show loss of the phospho-species from cytoplasm with preservation of the non-phospho form in the cytoplasm and nucleus. GRTH KI mice are sterile and lack elongated spermatids and spermatozoa, with spermatogenic arrest at step 8 of round spermatids which contain chromatoid body (CB) markedly reduced in size. We observed an absence of phospho-GRTH in CB of GRTH KI mice. RNA-Seq analysis of mRNA isolated from CB revealed that 1,421 genes show differential abundance, of which 947 genes showed a decrease in abundance and 474 genes showed an increase in abundance in GRTH KI mice. The transcripts related to spermatid development, differentiation, and chromatin remodeling (*Tnp1/2*, *Prm1/2/3*, *Spem1/2*, *Tssk 2/3/6*, *Grth*, *tAce*, and *Upf2*) were reduced, and the transcripts encoding for factors involved in RNA transport, regulation, and surveillance and transcriptional and translational regulation (*Eef1a1, Ppp1cc*, *Pabpc1*, *Ybx3*, *Tent5b*, *H2al1m*, *Dctn2*, and *Dync1h1*) were increased in the CB of KI mice and were further validated by qPCR. In the round spermatids of wild-type mice, mRNAs of *Tnp2*, *Prm2*, and *Grth* were abundantly co-localized with MVH protein in the CB, while in GRTH KI mice these were minimally present. In addition, GRTH binding to *Tnp1/2*,

Prm1/2, *Grth*, and *Tssk6* mRNAs was found to be markedly decreased in KI. These results demonstrate the importance of phospho-GRTH in the maintenance of the structure of CB and its role in the storage and stability of germ cell-specific mRNAs during spermiogenesis.

Keywords: phospho-GRTH, chromatoid bodies, spermatogenesis, transcriptome analysis, TP2 and PRM2

INTRODUCTION

Spermatogenesis is characterized by a complex and highly specialized differentiation program, in which male germ cells show a cohesive expression of an array of testicular genes with a remarkable degree of cellular restructuring involved in a complex events of genomic and epigenetic reorganization to produce mature spermatozoa (Steger, 2001; Sassone-Corsi, 2002; Kimmins and Sassone-Corsi, 2005). During these events, several mRNAs transported from the nucleus to the cytoplasm undergo near-to-complete translational silencing/repression, extensive post-transcriptional processing, and storage at specific cytoplasmic sites, such as the ribonucleoprotein (RNP) granules called chromatoid bodies (CBs), for translation at later stages of spermiogenesis (Steger, 2001; Maclean and Wilkinson, 2005; Kotaja and Sassone-Corsi, 2007). Owing to the importance of accurate RNA regulatory mechanisms in controlling normal spermatogenesis, it is imperative to study the functions of CB which may act as a compartment for mRNA processing pathways.

The CB is a membraneless, perinuclear organelle which primarily contains Piwi-interacting RNA (piRNA), mRNAs, small RNAs, long non-coding RNAs, RNA binding proteins, and other proteins involved in RNA processing of male germ cells which play a critical role in chromatin compaction during sperm elongation (Parvinen, 2005; Sato et al., 2010). CBs temporarily store mRNAs that are transported from the nucleus by gonadotropin-regulated testicular RNA helicase (GRTH/DDX25), where these are translationally repressed, awaiting translation at various stages of spermatid development, and the mRNAs can also undergo degradation (Sheng et al., 2006; Sato et al., 2010). During spermiogenesis, there is a precise control and stability in the quality of transcription and posttranscriptional regulation to secure the correct timing of protein expression in male germ cells/spermatids (Sato et al., 2010). At later stages of spermatid elongation, "CB" splits into two separate structures: one gets discarded along with the residual cytoplasm, and the other forms a ring around the base of the flagellum (Fawcett et al., 1970; Shang et al., 2010; Meikar et al., 2011; Lehtiniemi and Kotaja, 2018). The origin of CBs is highly debatable, the most accepted notion being their emergence from small granules which are associated with the nuclear envelope present nearby the inter-mitochondrial cement (IMC). The IMC is highly electron-dense and has CB-like material found among clusters of mitochondria during male germ cell differentiation (Fawcett et al., 1970; Yokota, 2012; Lehtiniemi and Kotaja, 2018), and it is particularly evident in pachytene spermatocytes. CBs are believed to possess functional similarities to RNA processing bodies (P-bodies) (Franks and Lykke-Andersen, 2008; Luo et al., 2018) and stress granules of somatic cells that maintain RNA regulation (Eulalio et al., 2007; Decker and Parker, 2012). CB contains several components of the RNA-induced silencing complex (Kotaja et al., 2006), mouse Vasa homolog (MVH/DDX4), a germ cell marker (Fujiwara et al., 1994; Noce et al., 2001), piRNA binding protein, and GRTH/DDX25 in high abundance (Sato et al., 2010; Meikar et al., 2014). piRNA and piRNA binding protein constitute a major part of the CB composition, and piRNAs derived from pachytene piRNA clusters and transposable elements. piRNAs are present both in the embryonic and the postnatal male germ cells, and their expression is induced abundantly in late meiotic cells and haploid round spermatids (Meikar et al., 2011, 2014).

GRTH is a member of the DEAD-box family of RNA helicases that play an essential role in the completion of spermatogenesis (Tsai-Morris et al., 2004; Dufau and Tsai-Morris, 2007). In germ cells, there are two species of GRTH, the 56-kDa non-phospho and the 61-kDa phospho forms. Previous studies revealed a missense mutation ($R^{242}H$) of GRTH in Japanese azoospermic men, which resulted in the lack of phospho-GRTH at T239 (pGRTH) (Tsai-Morris et al., 2007, 2012; Raju et al., 2019). GRTH knock-in (KI) transgenic mice (human mutant GRTH gene with $R^{242}H$) lack the 61-kDa phospho-species from the cytoplasm and CBs, while the non-phospho form from the cytoplasm, nucleus, and CBs are not affected. GRTH KI mice are sterile and have testis of reduced size which lack elongated spermatids and spermatozoa, with arrest at step 8 of round spermatids (RS) (Kavarthapu et al., 2019). Of note is the observed marked reduction in the size or complete loss of CBs in the round spermatids, indicating the importance of pGRTH in maintaining the structural integrity of CB (Kavarthapu et al., 2019). GRTH participates in the transport of specific mRNAs from the nucleus to the cytoplasmic sites, including CB, for storage prior to their translation during spermiogenesis (Sheng et al., 2006; Dufau and Tsai-Morris, 2007; Sato et al., 2010).

To understand the precise role of pGRTH in the regulation of germ cell-specific mRNA in CBs during spermiogenesis, CBs isolated from germ cells of WT and GRTH KI mice were analyzed using Illumina RNA-Seq to compare their transcriptome profiles. This study delineates the importance of pGRTH/DDX25 in CB regulation and participation in pathways which are essential for the progression and completion of spermiogenesis.

MATERIALS AND METHODS

Animals

GRTH KI transgenic mice were generated with the human GRTH gene containing the $R^{242}H$ mutation found in Japanese

infertile men as described previously (Kavarthapu et al., 2019). Briefly, WT and GRTH KI transgenic mice were genotyped after confirming the presence/absence of the transgene using two sets of primers Geno F1/Geno R1 and Geno F2/Geno R2 (**Supplementary Table 1**). All the animals were housed in pathogen-free and temperature- and light-controlled conditions (22°C), with 14:10-h light/dark cycle. All studies were approved by the National Institute of Child Health and Human Development Animal Care and Use Committee.

Isolation of CBs From Mouse Testes

Isolation of CBs from adult mouse testes was carried out using the protocol (Meikar and Kotaja, 2014) with minor modifications. Testes from 10 WT and homozygous GRTH KI mice (45 days) (two mice for each sample, $N = 5$) were finely minced and digested in phosphate-buffered saline (PBS) containing 0.5 mg/ml of collagenase with 1 mg/ml glucose for 60 min at room temperature. Digested seminiferous tubules were filtered using a 100-μm cell strainer (BD Biosciences) and centrifuged for 5 min at 300 *g* at 4°C. After two washes in cold PBS, the cells were crosslinked with 0.1% paraformaldehyde (PFA; Thermo Scientific, MA, United States) for 20 min at 22°C. The reaction was stopped by adding 0.25 M glycine, pH 7.0 (Bostonbio, MA, United States). The cells were washed in PBS once, resuspended in RIPA buffer [(Millipore-Merck); 150 mM NaCl, 50 mM Tris–HCl, pH 7.5, 1 mM DTT, 1% Non-idet P40, 0.5% sodium deoxycholate with 1:200 RNase Inhibitor (Thermo Scientific), and protease inhibitor cocktail (Thermo Scientific)], and sonicated (five cycles of 20 s with 45-s intervals). The cell lysate was centrifuged for 10 min at 500 *g* at 4°C. The pellet containing the CBs was suspended in RIPA buffer and sonicated (two cycles of 20 s with 45-s intervals), filtered with a 5-μm filter (Millipore-Merck), and used for CB isolation. Aliquots of germ cells, pellet (PEL), and filtered pellet (FPEL) fractions were collected to monitor the success of the procedure. Fifty microliters of Protein G Dynabeads (Thermo Scientific) was coupled with 8 μg of commercial rabbit polyclonal anti-MVH antibody (cst#8761; Cell Signaling) or control rabbit IgG for 3 h according to the manufacturer's instructions. After two washes with citrate phosphate buffer containing 0.1% Tween, the Dynabeads–IgG complex was stored in RIPA buffer briefly. The FPEL was pre-cleared with 10 μl of washed Protein G Dynabeads (Thermo Scientific) for 30 min at 4°C and used for immunoprecipitation (IP) overnight with rotation at 4°C with the Dynabeads–IgG complex. On the next day, the Dynabeads–IgG–CB complexes were washed three times in 1 ml of RIPA buffer. Crosslinking was reversed in the same buffer (for RNA analysis) or in 1 × Laemmli/SDS sample buffer (for protein analysis) at 70°C for 45 min. Subsequently, the Dynabeads–IgG complex containing CBs was used for RNA isolation.

Immunofluorescence and Electron Microscopy Analysis

To monitor the success of the CB isolation procedure, the CB samples (5 μl) were fixed using a drying-down fixing solution (0.15% TritonX-100 and 1% PFA in PBS; 10 μl/slide) on a precleaned slide and air-dried overnight in a humidified chamber at 22°C. Once the slides were completely dried, these were post-fixed using 2% PFA for 5 min and then washed and treated with 0.2% Triton-X-100 in PBS for 2 min. Then, the slides were blocked using 5% BSA for 1 h in a humidified chamber and immunoprobed using anti-MVH/DDX4 antibody (1:1,000; cst#8761; Cell Signaling) overnight at 4°C. Following incubation with Alexa Fluor 568 secondary antibody (1:500) or Alexa Fluor 488 secondary antibody (1:500) for 1 h at 22°C, the slides were washed with phosphate-buffered saline–Tween® 20 (PBST; twice, 5 min each) and PBS (twice, 5 min each) and mounted with ProLong Diamond antifade reagent (Thermo Scientific). These slides were imaged using a Zeiss LSM 710 confocal microscope (Carl Zeiss, CA, United States) and analyzed using ZenPro software (Carl Zeiss, CA, United States). Immunofluorescent staining of drying-down slide preparations is a reliable method to visualize the CBs. Testicular sections or germ cell preparations obtained from WT and KI mice were immunoprobed using anti-MVH/DDX4 antibody (1:1,000; cst#8761; Cell Signaling) overnight at 4°C. Following incubation with Alexa Fluor 488 secondary antibody (1:500) for 1 h at 22°C, the slides were washed with PBST (twice, 5 min each) and PBS (once, 5 min each) and mounted with ProLong Diamond antifade reagent with DAPI (Thermo Scientific). These slides were imaged using a Ziess Axioplan 2 fluorescence microscope (Carl Zeiss, CA, United States) and were analyzed using ZenPro blue and Axiovision v4.5 software (Carl Zeiss, CA, United States). Electron microscopy studies were carried out as described previously (Kavarthapu et al., 2019). Briefly, testicular tissue isolated from WT and GRTH KI mice were first fixed in 2.5% glutaraldehyde buffer at 4°C overnight, and then the tissues were post-fixed with 1% osmium tetroxide and stained using 2% uranyl acetate, dehydrated, and then embedded in Spurr's epoxy. An EM ultramicrotome (Leica, Wetzlar, Germany) was used for making ultra-thin sections and were post-stained with lead citrate and observed under a JEOL JEM-1400 transmission electron microscope (JEOL USA, Inc., Peabody, MA, United States).

Western Blot Analysis

CBs isolated from the testes of WT and GRTH KI mice were subjected to western blot analysis. The protein G–IgG–CB complex was washed in RIPA buffer and reverse cross-linked at 70°C for 45 min in the 1× Laemmli/SDS sample buffer containing reducing agents. The resulting protein samples were centrifuged at 1,500 *g* for 5 min at 22°C. The supernatants collected were run on 4–12% Bis-Tris gel (Thermo Scientific) and transferred onto a nitrocellulose membrane in an iBlot (Thermo Scientific). The membrane was blocked with 5% skimmed milk powder in tris-buffered saline and then incubated with either of the following primary antibodies: affinity-purified anti-GRTH rabbit polyclonal antibody (1:500 dilution), anti-MVH/DDX4 polyclonal (1:500; cst#8761; Cell Signaling), mouse Argonaute/PIWI family RNA binding protein (MIWI) monoclonal antibody (CB control; 1:500; cst#6915; Cell Signaling), brain and muscle ARNT-like 1 (BMAL1) rabbit

monoclonal antibody (1:500 dilution; cst#14020; Cell Signaling), circadian locomotor output cycles protein kaput (CLOCK) rabbit monoclonal antibody (1:500 dilution; cst#5157; Cell Signaling), Ybx3 mouse monoclonal antibody (1:500 dilution; LS-C105064; LS Bio), PRM1 rabbit polyclonal antibody (1:500 dilution; HPA055150; Millipore Sigma, St. Louis, MO, United States), and PRM2 rabbit monoclonal antibody (1:500 dilution; Sc-30172; Santa Cruz Biotechnology, Dallas, Texas). After the antibody incubation and washing steps, the membranes were incubated with the respective secondary antibodies conjugated with Poly-HRP (1:2,000; Thermo Scientific). Immunosignals were detected by a super-signal chemiluminescence system (Thermo Scientific).

Total RNA Preparation, Library Construction, RNA-Seq (Illumina HiSeq2500)

Total RNA was extracted from reverse cross-linked Dynabeads–IgG–CB complexes using phenol/chloroform/isoamyl alcohol (25:24:1, v/v; Thermo Scientific). RNA quality and quantity were assessed using the RNA Nano 6000 Assay Kit in an Agilent Bioanalyzer 2100 system (Agilent Technologies, Santa Clara, CA, United States). Sequencing libraries were prepared using a TruSeq Stranded mRNA Prep Kit (Illumina), without the polyA selection step. Sequencing was performed *via* a paired-end 75 cycle on Illumina HiSeq 2500 (Molecular Genomics Core, NICHD). The RNA-Seq data have been submitted to the NCBI (https://www.ncbi.nlm.nih.gov/geo), with GEO accession number GSE148897.

RNA-Seq Data and Differences in the Abundance of Transcripts

RNA-Seq reads were trimmed and aligned using STAR to mouse mm10 reference genome sequences using Partek Flow for next-generation sequencing data (http://www.partek.com/partek-flow/). The transcript abundance was quantitated using Partek E/M (mm10-Ensembl Transcripts release 97) annotation model to obtain gene counts. Principal component analysis was done on gene counts to determine the variability in the data set (data not shown). Differences in mRNA/transcript abundance between WT and GRTH KI were generated using DESeq2 (fold change < -1.5 or > 1.5; false discovery rate/$P_{adj} < 0.05$; $P < 0.05$) in Partek Flow.

Gene Ontology Analysis

Gene Ontology (GO) enrichment analysis was performed to identify the functional classes using metascape software. Transcripts were annotated to three main GO categories—biological process (BP), cellular component (CC), and molecular function (MF)—and were represented separately. Kyoto Encyclopedia of Genes and Genomes (KEGG) pathway enrichment analysis was performed on all the transcripts which show differential abundance using metascape to identify the important pathways ($P < 0.05$).

Protein–Protein Interaction Network Analysis Using String/Cytoscape

To better illustrate the interactions among the differentially enriched transcripts, The Search Tool for the Retrieval of Interacting Genes/Proteins (STRING) was used to construct and visualize the PPI network using Cytoscape software (version 3.7.2), and to analyze by network analyzer plugin, cytoHubba app was used to find the top 100 hub genes based on the maximal clique centrality (MCC) algorithm, and the PPI network was constructed. Four different clusters were identified using the MCODE app in Cytoscape and were further assessed based on functional enrichment analysis.

Validation of RNA-Seq Using Real-Time Quantitative PCR Analysis

qRT-PCR was used to validate the differentially enriched transcripts obtained from RNA-Seq transcriptome analysis. Total RNA prepared for RNA sequencing library preparation was used to perform qRT-PCR. One microgram of total RNA was used to prepare cDNA using the Iscript first-strand synthesis kit (Bio-Rad Laboratories, Hercules, CA, United States), and qRT-PCR was performed with Fast SYBR green using a set of specific gene primers (**Supplementary Table 1**) in a 7500 Fast Real-Time PCR machine (Applied Biosystems, Foster City, CA, United States). All reactions were performed in triplicates, and the cycle threshold (Ct) values were normalized to *DDX-4/Vasa/MVH* as the reference gene, and the comparative quantification of mRNA was performed using the $2^{-\Delta\Delta Ct}$ method.

Immunoprecipitation of GRTH Protein–RNA Complex and qRT-PCR Analysis

The CB-enriched fraction (FPEL; 0.5 mg) isolated from the testes of WT and GRTH KI mice was reverse cross-linked and pre-cleared using 50 μl of protein A-agarose beads (Thermo Scientific) and 1 μg of rabbit IgG containing IP binding buffer (Thermo Scientific, United States) for 30 min at 4°C in a rocker. Upon spinning, the resulting pre-cleared supernatant obtained was incubated with 5 μg of anti-GRTH rabbit polyclonal antibody (Kavarthapu et al., 2019) or rabbit IgG at 4°C overnight to co-immunoprecipitate the GRTH–RNP complex. Upon overnight incubation, the GRTH–RNP complex was incubated with 50 μl of protein A-agarose beads and incubated for 2 h at 4°C. The resulting protein–RNP complex was washed with IP binding buffer (four washes), and the total RNA was isolated using the phenol/chloroform/isoamyl alcohol (25:24:1, v/v; Thermo Scientific, Waltham, MA, United States) method. The first-strand cDNA was prepared using iscript first-strand synthesis kit (Bio-Rad Laboratories, Hercules, CA, United States), and qRT-PCR was performed with Fast SYBR green using a set of gene-specific primers (**Supplementary Table 1**) in a 7500 Fast Real-Time PCR machine (Applied Biosystems, Foster City, CA, United States).

In situ Hybridization

A germ cell suspension was obtained by squeezing the seminiferous tubules of WT and GRTH KI mice with fine forceps in 1% PFA containing 100 mM sucrose (RNase free) in a petri dish. The germ cell suspensions were spread onto slides pre-coated/cleaned with 1% PFA with 0.15% Triton X-100 and dried overnight in a humidified chamber. *In situ* hybridization was carried out using a slightly modified procedure (Rajakumar and Senthilkumaran, 2014). In short, the fixed cells were permeabilized with Proteinase K (in PBST) for 10 min and washed twice with PBST (5 min each). Pre-hybridization was carried out using a hybridization buffer: formamide (1:1 v/v) at 55°C for 1 h in a hybridization oven. The respective probes (100 ng) in hybridization buffer/formamide (1:1 v/v) were pre-heated at 85°C for 5 min, cooled on ice for a few minutes, and added onto the slides and incubated for 4 h in a hybridization oven. For post-hybridization washes, wash buffer containing a decreasing concentration of SSC at 60°C was used. The slides were then blocked with a blocking buffer (Thermo Scientific) containing 5% normal goat serum (Sigma) in 1× maleic acid buffer (Thermo Scientific) for 1 h at room temperature in a humidified chamber. The slides were incubated with anti-DIG Rhodamine secondary antibody (1:500) and specific anti-MVH/DDX4 rabbit polyclonal antibody (Cell Signaling, cst#8761; 1:1,000 dilution) in blocking buffer (Thermo Scientific) containing 5% normal goat serum (Sigma) in maleic acid buffer at 4°C overnight. The slides were subsequently washed with DIG wash buffer (twice for 10 min each), PBST (5 min), and PBS (5 min) and incubated with Alexa Fluor 488 for 1 h at room temperature. The slides were washed with PBST (twice, 5 min each), PBS (twice, 5 min each), and mounted with ProLong Diamond antifade reagent with DAPI (Thermo Scientific). These slides were imaged using a Ziess Axioplan 2 fluorescence microscope (Carl Zeiss, CA) and were analyzed using ZenPro blue and Axiovision v4.5 software (Carl Zeiss, CA, United States).

Statistical Analyses

The significance of the differences between groups was determined by Tukey's multiple-comparison test (one-way ANOVA analysis) using the Prism software program (GraphPad Software, Inc., San Diego, CA, United States) and Microsoft Excel (Microsoft).

RESULTS

Analysis of CBs From WT and GRTH KI Mouse Testes

The size of the testis of KI mice was significantly reduced ($P < 0.05$) when compared to that of WT mice (**Supplementary Figure 2**). The CBs were isolated successfully from WT and KI mice (**Figure 1A**). The KI mice have smaller CBs in the testicular sections (**Figure 1B**) and round spermatids (**Figure 1C**). The success of the CB isolation procedure was confirmed using microscopy (**Supplementary Figure 3**). The CBs obtained from the WT group were markedly bigger in size compared to those of GRTH KI mice (**Figure 1D**). Furthermore, EM studies showed smaller and condensed CBs in KI mice, which is evident by a significant reduction in their size/diameter when compared to CBs of WT mice which display an amorphous "nuage" texture

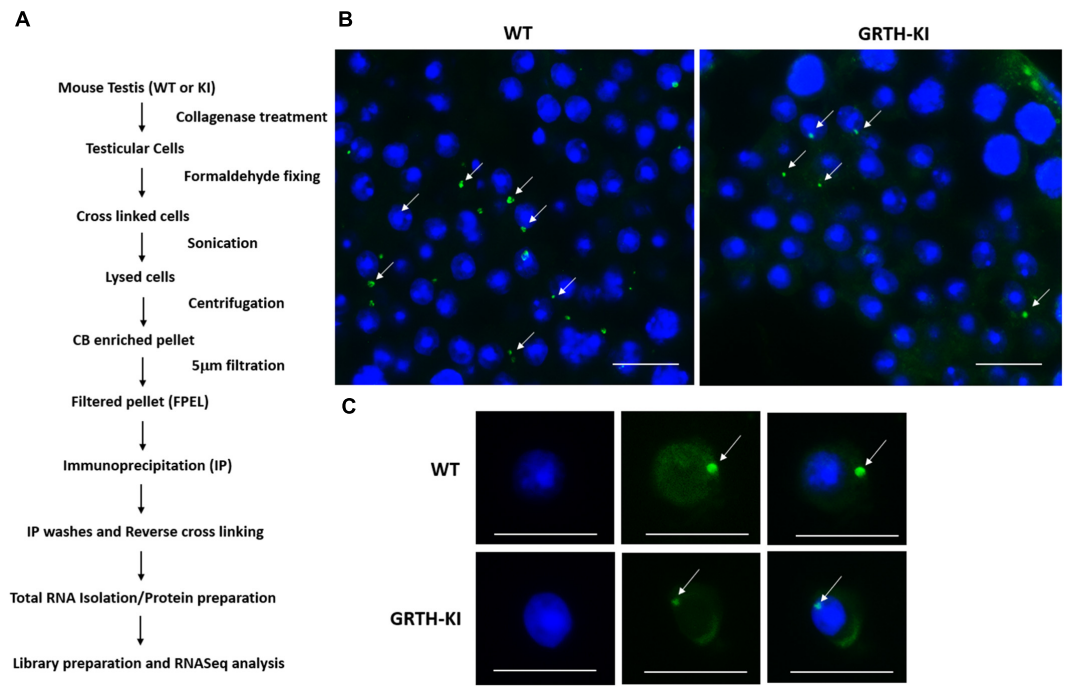

FIGURE 1 | Continued

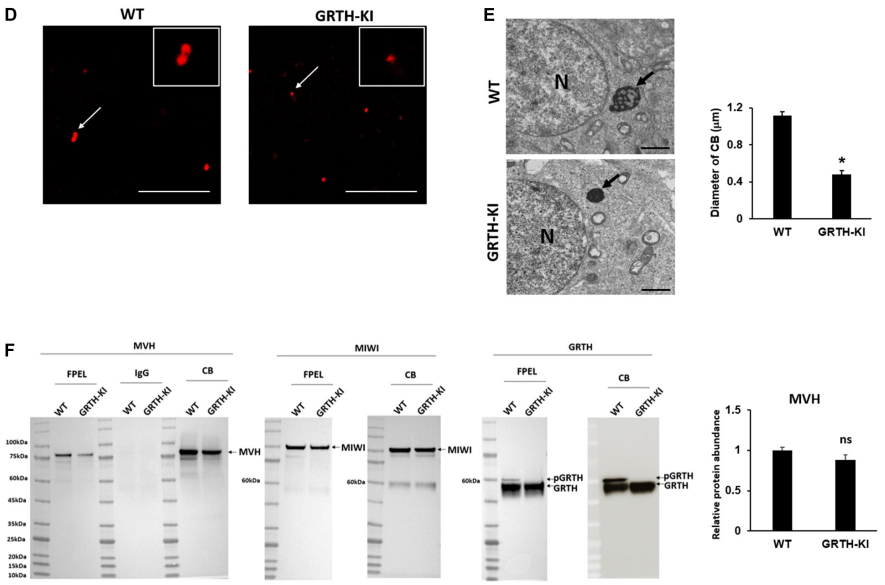

FIGURE 1 | Isolation and characterization of chromatoid bodies (CBs) from wild-type (WT) and knock-in (KI) mice. **(A)** Overview of CB isolation protocol from germ cells of mouse testes. **(B)** Immunofluorescence staining of MVH/DDX4 (green) in the testicular tissue sections of WT and KI mice; CBs are indicated by an arrow. Scale bar, ∼25 μm. **(C)** Immunofluorescence staining of MVH/DDX4 (green) in the round spermatids obtained from WT and KI mice; CBs are indicated by an arrow. Scale bar, ∼10 μm. **(D)** Immunofluorescence staining of MVH/DDX4 as a marker showing that CBs (red) isolated from KI mice are smaller in size compared to WT. Inset shows the detail of CBs indicated by an arrow. Scale bar, ∼25 μm. **(E)** Electron microscopy images from round spermatids showing a lobular structure with an irregular network of the less-dense strands characteristic of the CB clearly visible in WT, while in KI, CBs are markedly reduced in size. Arrows indicate CBs and N indicates the nucleus. *P*-values were calculated by two-tailed Students t-test (*$P < 0.05$). Scale bar, ∼1 μm. **(F)** Western blot analysis showing the complete loss of pGRTH proteins in CBs of KI mice compared to CBs of WT mice, while the levels of MVH, MIWI (CB control), and non-phospho GRTH were unaltered. FPEL, filtered pellet.

(**Figure 1E**). Among proteins extracted from CBs of WT and KI mice, the levels of MVH/DDX4, MIWI (CB control), and non-phospho GRTH were unaltered, while pGRTH protein was completely absent in the CBs of KI mice compared to WT (**Figure 1F**; **Table 1A**; Kavarthapu et al., 2019). In addition, there was no change in the expression of BMAL1, CLOCK, and YBX3 proteins in the CB of WT and KI mice. PRM1/PRM2 expression was not detected in the CB of WT and KI mice (**Supplementary Figure 4**).

Overview of RNA-Seq Data Analysis

RNA-Seq was performed on RNA samples obtained from the CBs of WT and KI mice testes ($N = 5$) to analyze the transcriptomic profiles of CBs in the presence (WT mice) and in the absence of pGRTH (KI mice). Sequencing of CBs from WT and GRTH KI mice yielded 75.6 and 125.9 million reads, respectively. The average Phred score was 38 (with base calling error rate of almost 1 in 10,000), and more than 75% of reads could be mapped to the mouse reference genome. Separation of the GRTH KI and WT genotypes was evident in the hierarchically clustered heat map shown in the transcript abundance profiles (**Figure 2A**).

Differences in Transcript Abundance Analysis Using GO and KEGG Pathways

The transcript levels of several genes involved in spermatogenesis (Tnp1/2, Prm1/2, TSSK 2/3/6, *etc.*) were also significantly reduced in the CB of KI mice similar to that which we found in RNA-seq data from germ cells of KI mice (Kavarthapu et al., 2020; **Supplementary Table 5**). Differences in the transcript abundance

TABLE 1 | (A) List of important proteins with their cellular localization with respect to wild-type and knock-in mice.

List of proteins (WT)	Cytoplasm (WT)	Nucleus (WT)	CB (WT)
GRTH	Yes	Yes	Yes
pGRTH	Yes	No	Yes
MVH	Yes	No	Yes
List of proteins (KI)	**Cytoplasm (KI)**	**Nucleus (KI)**	**CB (KI)**
GRTH	Yes	Yes	Yes
pGRTH	No	No	No
MVH	Yes	No	Yes

(B) Kyoto Encyclopedia of Genes and Genomes pathway enrichment analysis of differentially enriched transcripts showing two essential pathways.

List of KEGG pathways	List of genes
RNA Transport	Eef1a1, Eif4e, Eif4ebp2, Pabpc1, Rasl2-9, Ube2i, Eif4e2, Nup160, Pabpc6, Nup35, 1700009N14Rik, 4930444G20Rik, Paip1, Thoc5, AF366264, Nup133, Pabpc4l, Upf2, Gm5415, Gm9839, Ncbp1
Protein processing in ER	Atf4, Bag1, Hspa1l, Hspa2, Hsp90ab1, Ube2d2a, Dnajc5b, Edem3, Ero1lb, Stt3b, Tram1, Dnajb1, Rpn1, Selenos, Yod1, Sel1l2, Ubqlnl, Mbtps2

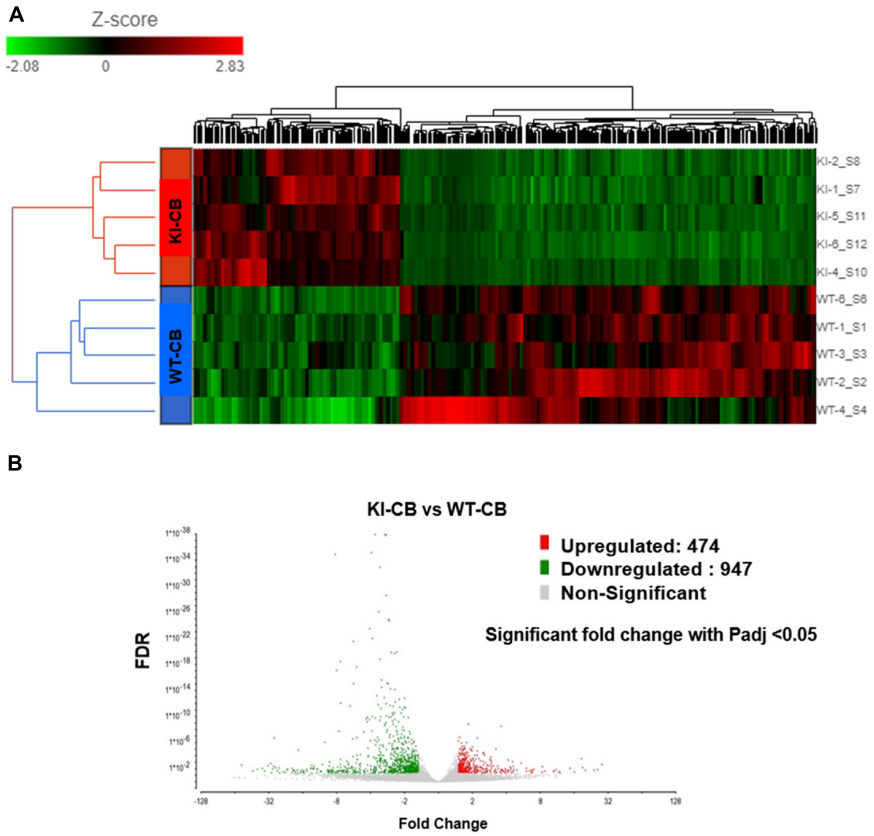

FIGURE 2 | RNA-Seq analysis of RNA extracted from chromatoid bodies of wild-type (WT) and knock-in (KI) mice. **(A)** RNA-Seq data show a clustered heat map with differential abundance of transcripts (WT and KI; fold change < -1.5 or > 1.5; $P_{adj} < 0.05$). The red blocks represent the genes with an increase in abundance, and the green blocks represent a decrease in abundance of genes. The colored bar represents the transcript abundance levels. **(B)** Volcano plot (fold change vs. false discovery rate value) showing 1,421 differentially enriched transcripts from KI and WT groups ($n = 5$ per group). Significantly increased and decreased abundances of transcripts are highlighted in red and green, respectively. The X-axis shows the fold change in transcripts between different samples, and the Y-axis shows the statistical significance of the differences.

between CBs isolated from WT and KI mice were analyzed using DESeq2. In total, 1,421 genes show differential abundance, including 474 genes that showed an increase in abundance and 947 genes with a decrease in abundance ($P_{adj} < 0.05$; **Supplementary Table 6**). Volcano plots (**Figure 2B**) were used to infer the overall distribution of differentially enriched transcripts. The GO functional enrichment analysis was classified into three categories: BP, CC, and MF (**Supplementary Table 7**). Only significant GO categories with $P < 0.05$ were chosen for analysis, and differentially abundant transcripts (top 10) of gene-enriched GO terms were identified. In the BP group, transcripts which show differential abundance were mainly enriched in spermatogenesis, spermatid differentiation, and spermatid development, motility, and fertilization (**Figure 3A**). In the CC group, transcripts which show differential abundance were enriched in sperm principle piece, microtubule organizing center, cation channel complex, *etc*., while in the MF group, transcripts which show differential abundance were enriched in protein kinase binding, voltage-gated cation channel activity, proline-rich region binding, passive transmembrane transporter activity, *etc*. (**Figure 3A**). KEGG pathway enrichment analysis revealed that all the differentially enriched transcripts ($P < 0.05$) were associated with either RNA transport or protein processing in the endoplasmic reticulum pathways (**Figure 3B**; **Table 1B**). We also compared the transcript abundance (fold change) of genes from CB RNA-seq (this study) and germ cells RNA-seq data (expression in fold change) that were previously reported from our laboratory (Kavarthapu et al., 2020). Among 947 genes with a decrease in abundance in CBs of KI mice, we found 272 genes that were downregulated and eight genes that were upregulated in the germ cells of KI mice. Among 474 genes with an increase in abundance in CBs of KI mice, we found 18 genes that were upregulated in the germ cells of KI mice, which were illustrated in the form of Venn diagrams (**Supplementary Figure 8**). The detailed list of genes with fold change between these datasets are given in **Supplementary Table 5**.

PPI Network Analysis Showing Important Network/Pathway Interactions

All 1,421 differentially enriched transcripts ($P_{adj} < 0.05$ and $< -1.5/ > 1.5$ fold) were analyzed using the STRING tool in Cytoscape software to visualize the PPI network. The

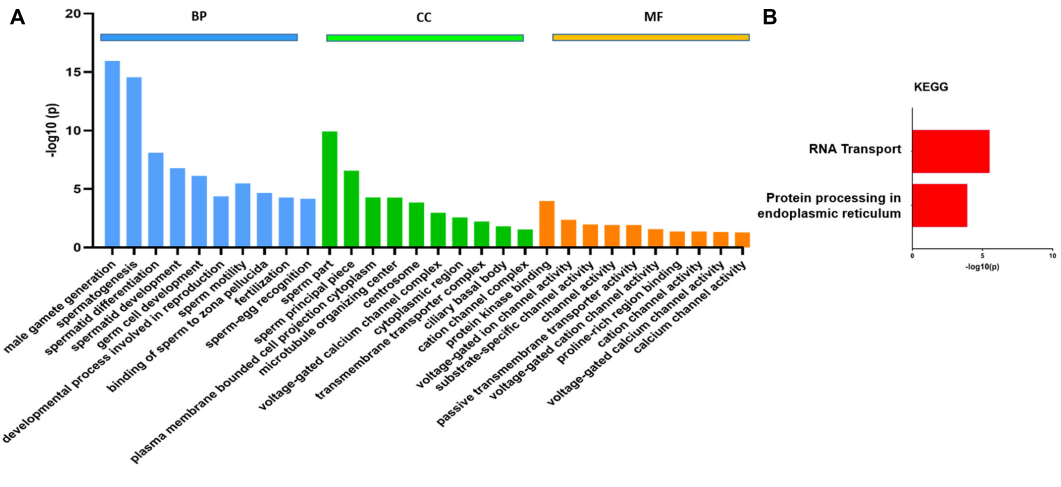

FIGURE 3 | Gene Ontology (GO) analysis in differentially enriched transcripts obtained from RNA-Seq using STRING. **(A)** GO analysis (top 10) of transcripts ($P_{adj} < 0.05$) obtained from chromatoid bodies of wild-type and knock-in mice. The GO results were grouped into different functional categories: cellular component (CC), molecular function (MF), and biological process (BP). The Y-axis represents the number of genes in each GO term. **(B)** Kyoto Encyclopedia of Genes and Genomes enrichment analysis of the top two enriched pathways with -log10 *P*-value on the X-axis.

top 100 hub genes in the PPI network were chosen based on the MCC algorithm using cytoHubba app in Cytoscape (**Figure 4**). A total of 99 nodes and 541 edges were mapped in the PPI network, and all these four important modules (squared) which were interconnected to each other belong to major pathways/processes, including RNA surveillance/transport, spermatogenesis, chromatin condensation/compaction, ubiquitin-proteasome pathway (UPP), centrosome organization, and organelle assembly (**Figure 4**).

RNA-Seq/Differences in Transcript Abundance Validation Using qRT-PCR

To validate the genes that are enriched in RNA-Seq data, specific sets were selected based on GO and KEGG results, and their transcript abundance was analyzed using qRT-PCR. Overall, the qRT-PCR analysis results showed a good correlation with the RNA-Seq/transcriptome analysis results. The transcript levels of *Tnp1/2*, *Prm1/2*, *Spem1, Tssk 3/6*, *Grth*, *tAce*, and *Upf2* involved in spermatid development, differentiation, chromatin compaction, and remodeling were significantly ($P < 0.05$) reduced in the CB of GRTH KI mice compared to that of WT mice (**Figure 5A**). Furthermore, transcripts encoding for factors involved in RNA transport, storage, transcriptional, and translational regulation (*Eef1a1, Ppp1cc*, *Pabpc1*, *Ybx3*, *Tent5b*, *H2al1m*, *Dctn2*, and *Dync1h1*) were found to be increased (**Figure 5B**) in the CB of GRTH KI mice compared to CB of WT mice, confirming the consistency of the RNA-Seq data.

GRTH-IP and RNA Analysis Reveal the Importance of pGRTH Binding to Specific Transcripts in the CBs

Successful GRTH-IP were confirmed using western blot (**Supplementary Figure 9**) prior to isolating GRTH-bound mRNAs. GRTH-IP mRNA binding experiments reveal that GRTH protein binding to specific germ cell mRNAs (*Tnp1/2*, *Prm1/2, Grth*, and *Tssk6)* in CBs was decreased significantly to basal IgG levels ($P < 0.05$) in GRTH KI mice (**Figure 6**). The mRNA binding function in CBs was impacted significantly in GRTH KI mice (lacks pGRTH), which resulted in impaired chromatin compaction and spermatid elongation and stalled spermiogenesis at step 8.

Role of pGRTH in the Storage of *Tnp2*, *Prm2*, and *Grth* mRNAs in the CB of Round Spermatids

The ISH analysis revealed that the presence of *Tnp2*, *Prm2*, and *Grth* mRNAs was more abundant in CBs than in the cytoplasm of round spermatids (**Figures 7A–C**). In WT mouse germ cells, *Tnp2*, *Prm2*, and *Grth* mRNAs (red) and MVH-protein (green) were distinctively noticeable (**Figures 7A–C**), while in GRTH KI mouse germ cells, *Tnp2*, *Prm2*, and *Grth* mRNAs were drastically reduced in CBs, and the sizes of the CBs were smaller, with less distinction through the cytoplasm (**Figures 7A–C**). In GRTH KI mice, the mRNA storage decreases due to lack of pGRTH, which is one of the CB structural proteins. Taken together, these results indicate that loss of pGRTH impaired the storage of these specific mRNAs in the CBs of round spermatids which are later required for their translation and are essential for the progress of spermiogenesis. These findings reveal the importance of CBs in mRNA storage and the role of pGRTH in maintaining their structure during specific stages of spermiogenesis.

DISCUSSION

The GRTH KI mice with loss of pGRTH protein, lacking elongating spermatids due to arrest at step 8 of spermiogenesis,

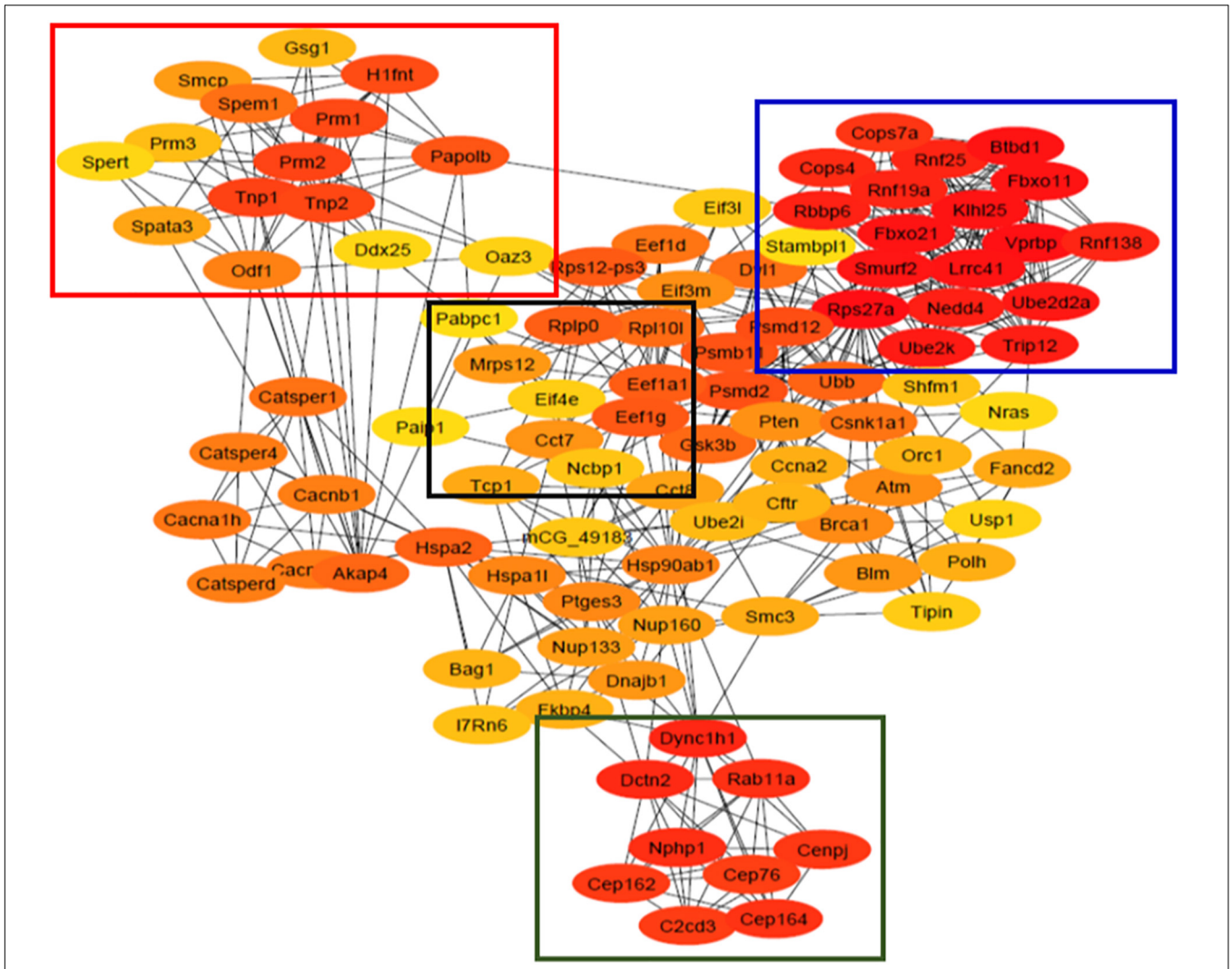

FIGURE 4 | Protein–protein interaction (PPI) network of the top 100 hub genes identified using cytoHubba plugin in Cytoscape software. Four different clusters were obtained from this network using MCODE which belong to genes involved in spermatogenesis (red box), ubiquitination pathway (blue box), RNA transport (black box), and centrosome organization and organelle assembly (green box). The colored nodes represent genes/proteins having high (red) and low (yellow) PPI scores. The edges represent the protein–protein interaction/associations.

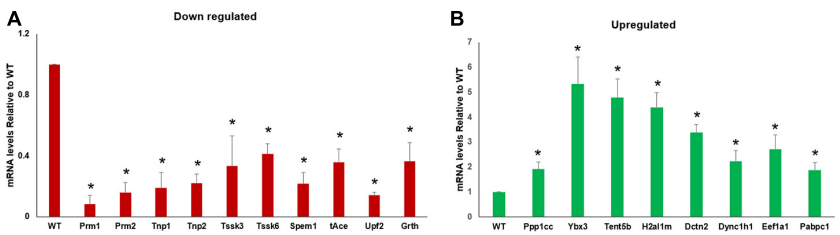

FIGURE 5 | qRT-PCR validation of RNA-Seq data with RNA obtained from chromatoid bodies (CBs) isolated from wild-type (WT) and knock-in (KI) mice. The transcript levels showing decreased **(A)** and increased **(B)** abundances in CBs obtained from KI *vs*. WT mice were normalized using actin. All statistical analyses were performed using Student's *t*-test (*$P < 0.05$), and data represent mean ± SEM of three independent experiments in triplicates.

contain round spermatids with structural changes in the CBs (Kavarthapu et al., 2019). However, studies of specific changes in the CB at the level of the transcriptome were of immediate relevance to link the function of pGRTH and its effects in the subsequent translational events with this site. In this study, we demonstrated the importance of CBs in spermiogenesis

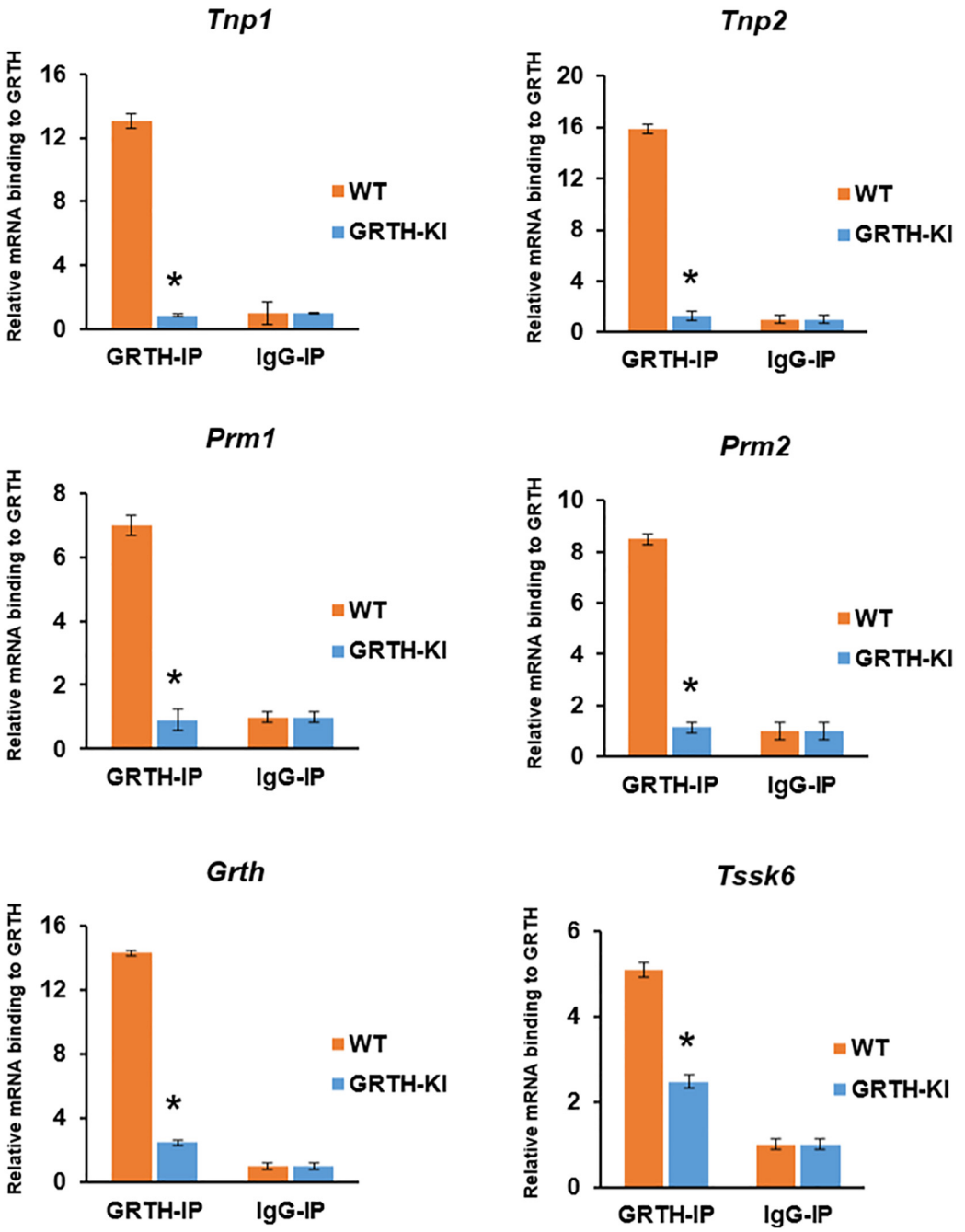

FIGURE 6 | Binding of GRTH to specific germ cell mRNAs in chromatoid bodies (CBs) isolated from wild-type (WT) and knock-in (KI) mice. Relative binding of *Tnp1/2*, *Prm1/2*, *Grth*, and *Tssk6* mRNA to GRTH protein in CB of germ cells in the testes from WT and GRTH-KI mice. All statistical analyses were performed using Student's *t*-test (*$P < 0.05$), and data represent mean ± SEM of three independent experiments in triplicates.

in the presence and in the absence of pGRTH by analyzing the abundance of transcripts of intrinsic importance in the progression of spermatogenesis through an evaluation of transcriptome profiles of CBs from WT and GRTH KI mice together with their association with GRTH protein and localization of selected mRNAs which are involved in the initial and late stages of spermiogenesis.

GRTH is an RNA binding protein involved in the transport of germ cell-specific mRNAs from the nucleus to the cytoplasmic site and is essential for the completion of spermatogenesis (Sheng et al., 2006; Dufau and Tsai-Morris, 2007). GRTH associates with actively translating polyribosomes and regulates the translation of specific germ cell genes likes *Tnp1/2* and *Prm1/2*, which are involved in sperm maturation (Tsai-Morris et al., 2012). The

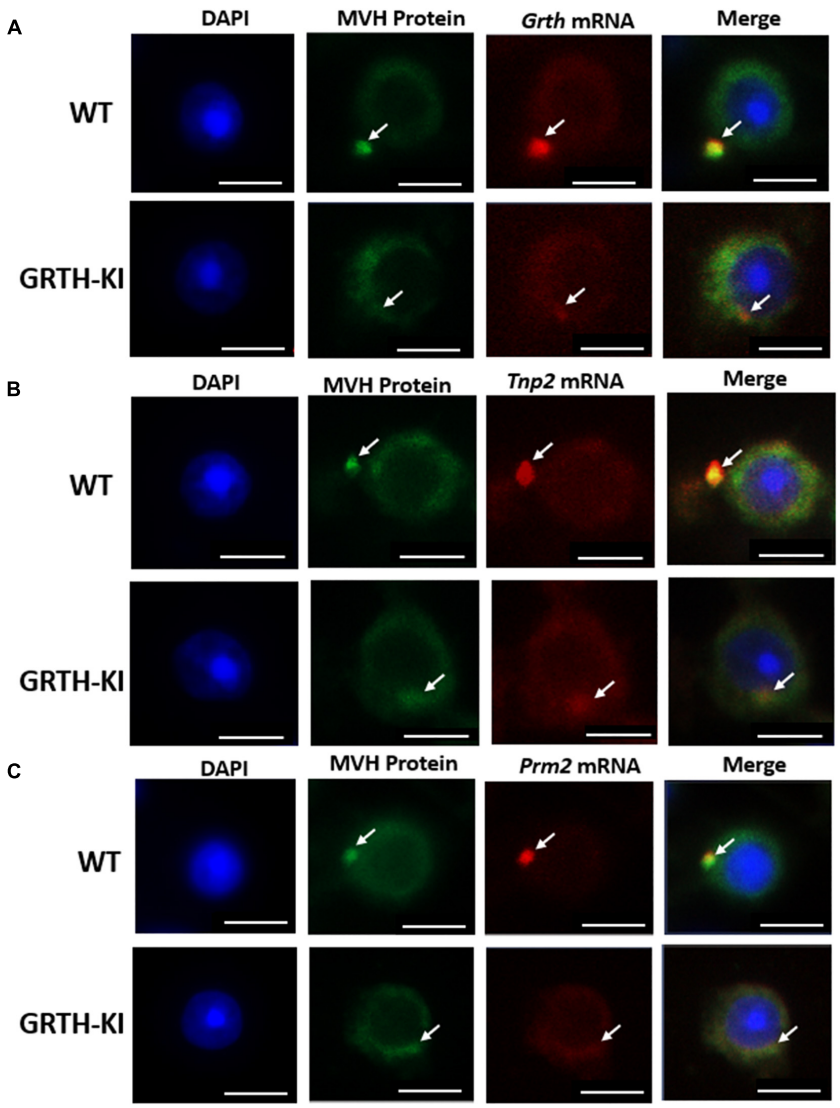

FIGURE 7 | Chromatoid bodies (CBs) accumulate mRNAs involved in spermiogenesis. Fluorescence microscopy showing the *in situ* localization of selected mRNAs (red) with MVH protein (green) in CBs of round spermatids from WT and KI mice. **(A)** *ISH* of *Grth* mRNAs. **(B)** *ISH* of *Tnp2* mRNAs. **(C)** *ISH* of *Prm2* mRNAs. CBs of KI mice are indistinct/smaller in size compared to CBs of WT mice. Co-staining with MVH confirmed their localization in the CB. The nuclei are stained with DAPI (blue). CB is marked by white arrows. Scale bar, ∼5 μm.

pGRTH is shown to regulate the translation of the *Tnp2* gene which occurs in a 3′-UTR-dependent manner (Kavarthapu et al., 2019). During the process of spermiogenesis, RS undergo an elongation process where the histones are first replaced by highly basic proteins TNP1/2 and subsequently by PRM1/2. These chromatin remodeling proteins play a crucial role in hyper-chromatin condensation and reshaping the nucleus of elongating and condensing spermatids (Boa and Bedfors, 2016).

In this study, in a GO enrichment analysis, transcripts which show differential abundance to be prevalent in spermatogenesis, spermatid differentiation, and development are significantly decreased. The germ cell-specific transcripts like *Tnp2*, *Prm2*, and *Grth* in CBs decreased significantly, and this was confirmed by the *in situ* localization of these transcripts in CBs of RS of both WT and GRTH KI mice (**Figure 7**). Furthermore, the association of pGRTH protein with specific germ cell mRNAs (*Tnp1/2*, *Prm1/2*, *Grth*, and *Tssk6)* in CBs was also found to be decreased due to the loss of pGRTH in GRTH KI mice. These results demonstrate the importance of pGRTH as an RNA binding protein for the above-mentioned genes and as a stabilizer of their mRNAs in CBs until translation at the later stages of spermiogenesis. The absence of the phospho form of GRTH in the CBs of KI mice also has a direct impact on the structure of CBs in RS as GRTH is one of the important structural proteins along with other CB markers MVH and MIWI (Sato et al., 2010; Kavarthapu et al., 2019). The expression of MVH and MIWI protein was unaltered in the CBs of KI mice compared to WT. MVH is an essential factor in the piRNA processing pathway (Kuramochi-Miyagawa

et al., 2010; Meikar et al., 2011). Also unchanged in the KI mice are CB transient proteins, CLOCK and BMAL1, with their expression overlapping with CB marker proteins in an RS stage-specific manner (Peruquetti et al., 2012). Targeted ablation of these circadian proteins BMAL1 and CLOCK results in infertility in mice with significant characteristic morphological alterations of CBs (Peruquetti et al., 2012) which are clearly different from those observed in mice lacking pGRTH (KI) (Kavarthapu et al., 2019) and GRTH null mice (Tsai-Morris et al., 2004). From the unaltered levels of CLOCK and BMAL1 proteins in the CB of KI in our present studies, we can exclude pGRTH as a regulator of these proteins.

The RNA profiles of CBs obtained from WT and GRTH KI were distinct, which is apparent from the hierarchically clustered heat map and volcano plots of differentially enriched transcripts, which depict genes with decrease and increase in abundance in CBs of GRTH KI mice. The KEGG pathway enrichment analysis revealed that most of the differentially enriched transcripts were mainly associated with both RNA transport and protein processing in endoplasmic reticulum pathways, which also confirms the impact on RNA transport into the CBs due to the loss of pGRTH in the GRTH KI mice. To compensate for the loss, the genes essential for RNA stability, including *Pabpc*, were increased inside the CBs of GRTH KI mice.

Furthermore, the inter-relation among differentially enriched transcripts and PPI network was constructed. This showed four classes/modules with key hub genes belonging to spermatogenesis, UPP, mRNA metabolism/regulation, and microtubule organization/motility. The UPP genes are implicated in histone ubiquitination and acetylation, which play a crucial role in chromatin remodeling essential for spermatid elongation during spermiogenesis (Lu et al., 2010; Sheng et al., 2014). Recently, our studies in KI mice have shown that loss of pGRTH results in a reduced expression of UPP genes (*Ube2J1*, *Ube2K*, *Ube2W*, *Rnf8*, *Rnf133*, and *Rnf138*) and *Mof/Myst1*, which subsequently impaired the ubiquitination of H2A/B and the acetylation of H4 essential for histone eviction and replacement with transition proteins, followed by protamines during spermiogenesis (Kavarthapu et al., 2020). During elongation of RS, histones were first replaced by transition proteins (TNP1/2), which constitute 90% of the chromatin basic proteins, and then followed by the deposition of the protamines (PRM1/2), which results in hyper-chromatin condensation and compaction of the RS nucleus (Boa and Bedfors, 2016; Schneider et al., 2016; Kavarthapu et al., 2019). The transcripts of *Tnp1/2*, *Prm1/2/3*, *Tssk2/3/6*, and *Spem1/2* were significantly reduced in the CB of GRTH KI mice. The reduction in these transcripts in the CBs is probably due to the decreased mRNA transport and/or mRNA degradation as they are not bound to pGRTH in GRTH KI mice. This eventually led to failure of chromatin remodeling, which is essential for the condensation of chromatin in developing spermatids during spermiogenesis. *Tssk2/6* KO mice are sterile, with defects in spermatogenesis due to post-meiotic chromatin remodeling and intracellular signal transduction defects (Shima et al., 2004; Spiridonov et al., 2005). *Spem1* is exclusively expressed in the round and elongating spermatids, and the loss of this protein causes aberrant cytoplasm removal, sperm deformation, and male infertility (Zheng et al., 2007). Interestingly, mice deficient of *Tnp1/2* (Meistrich et al., 2003; Shirley et al., 2004) and Camk4 (Wu et al., 2000) also show failure of cytoplasmic removal during spermiogenesis. Furthermore, the exchange of basic nuclear proteins is impaired in male germ cells lacking Camk4 (Wu et al., 2000). This explains the impact of the loss of pGRTH on these germ cell-specific transcripts (*Tnp1/2*, *Prm1/2/3*, *Tssk2/3/6*, and *Spem1/2*) and their cumulative effects which result in complete spermatogenic arrest just before spermatid elongation at step 8 in GRTH KI mice. *Upf2*, which is involved in nonsense-mediated mRNA decay, an mRNA surveillance pathway that eliminate transcripts with premature stop codons, was decreased, resulting in inefficient mRNA surveillance in GRTH KI mice. To support the role of CBs in mRNA processing, splicing, regulation, translation, and mRNA turnover, a very high number of poly(A)-binding proteins (Pabp) and Poly (rC) binding protein (Pcbp) are found in CBs (Meikar et al., 2014; Peruquetti, 2015). In the current study, transcripts of *Pabpc 1/6/4l* and *Pcbp 2/3* were reduced significantly in CBs of GRTH KI mice, as the decreased mRNAs in the CB of KI mice require more stabilization from Pabpc and Pcbp proteins. Furthermore, *Pabpc1/4*, *Pcbp1/3* were abundantly expressed in round spermatids prior to their elongation, and hence their transcript levels were abundant in GRTH KI mice. The m7G cap at the 5' end associates with eukaryotic initiation factor 4E (eIF4E) which, through interaction with other factors, regulates gene expression. Transcripts of several initiation factors (*eIF4e2*, 4ebp2, 3l and 3m) together with mRNAs related to the 60S subunit (Rpl10l/Rplp0) were increased and accumulated in CB as mRNAs which could not get transported from the CB to the polyribosomes for translation; these instead remain stored in the CB in GRTH KI mice due to the loss of pGRTH, hence the disruption of RNA quality control and translation machinery in germ cells of GRTH KI mice.

CONCLUSION

In summary, our data demonstrate that pGRTH is required for the maintenance of the CB structure and is crucial for the storage of germ cell-specific mRNAs until their translation in later stages of spermatids during spermiogenesis.

DATA AVAILABILITY STATEMENT

The RNA-Seq data have been submitted to the NCBI (https://www.ncbi.nlm.nih.gov/geo) with GEO accession number GSE148897.

ETHICS STATEMENT

The animal study was reviewed and approved by National Institute of Child Health and Human Development Animal Care and Use Committee.

AUTHOR CONTRIBUTIONS

RA, RK, and MD conceived and planned the experiments. RA performed the experiments and analyzed the data. RA and MD discussed the results and wrote the manuscript. SC contributed to part of the RNA-Seq data analysis. All authors contributed to the article and approved the submitted version.

ACKNOWLEDGMENTS

We thank Dr. Tianwei Li and Dr. James Iben, NICHD Molecular Genomic Core, for their assistance with the HiSeq 2500 RNA-Seq work and Dr. Louis Dye for EM studies. This work was supported by the National Institutes of Health Intramural Research Program through the *Eunice Kennedy Shriver* National Institute of Child Health and Human Development.

SUPPLEMENTARY MATERIAL

The Supplementary Material for this article can be found online at: https://www.frontiersin.org/articles/10.3389/fcell.2020.580019/full#supplementary-material

Supplementary Table 1 | List of primers used for genotyping and validation of differentially enriched transcripts using qRT-PCR.

Supplementary Figure 2 | (A) The size of the testes obtained from wild-type and GRTH knock-in (KI) mice. The testes from homozygous KI mice are smaller compared with those from wild-type mice. **(B)** Mean testis–body weight ratio of WT and GRTH KI mice ($n = 10$). $^*P < 0.05$.

Supplementary Figure 3 | Successful chromatoid body isolation from wild-type and knock-in mice was validated with DDX4 antibody immunofluorescence. Arrows indicate CBs showing DDX4 expression in green.

Supplementary Figure 4 | Western blot analysis showing BMAL1, CLOCK, YBX3, PRM1, and PRM2 expression in the CB samples obtained from wild-type and knock-in mice. MIWI was used as a loading control for CB proteins.

Supplementary Table 5 | Comparison of gene expression (fold change) in germ cells with transcript abundance and fold change from chromatoid bodies (CBs) obtained from WT and KI mice. **(A)** Downregulated/Upregulated genes in germ cells in comparison with a decrease in abundance of genes in CB. **(B)** Upregulated genes in germ cells in comparison with an increase in abundance of genes in CB.

Supplementary Table 6 | Differential abundance of transcripts with ensemble ID, total counts, *P*-value, false discovery rate, and fold change between chromatoid bodies of wild-type and knock-in groups.

Supplementary Table 7 | Gene Ontology enrichment analysis showing functional classes, biological process, cellular component, and molecular function with group ID, category, log *P*-value, and list of gene symbols.

Supplementary Figure 8 | Comparison of gene expression in germ cells with transcript abundance from chromatoid bodies (CBs) obtained from wild-type and knock-in mice. **(A)** Venn diagram showing downregulated genes in germ cells and a decrease in the abundance of genes in CB. **(B)** Venn diagram showing upregulated genes in germ cells and an increase in abundance of genes in CB.

Supplementary Figure 9 | Western blot analysis showing GRTH expression in input samples and GRTH immunoprecipitation samples from the chromatoid bodies obtained from wild-type and knock-in mice.

REFERENCES

Boa, J., and Bedfors, M. T. (2016). Epigenetic regulation of the histone-to-protamine transition during spermiogenesis. *Reproduction* 151, 55–70.

Decker, C. J., and Parker, R. (2012). P-bodies and stress granules: possible roles in the control of translation and mRNA degradation. *Cold Spring Harb. Perspect. Biol.* 4:a012286. doi: 10.1101/cshperspect.a012286

Dufau, M. L., and Tsai-Morris, C. H. (2007). Gonadotropin-regulated testicular helicase (GRTH/DDX25): an essential regulator of spermatogenesis. *Trends Endocrinol. Metab.* 18, 314–320. doi: 10.1016/j.tem.2007.09.001

Eulalio, A., Behm-Ansmant, I., and Izaurralde, E. (2007). P bodies: at the crossroads of post-transcriptional pathways. *Nat. Rev. Mol. Cell Biol.* 8, 9–22. doi: 10.1038/nrm2080

Fawcett, D. W., Leak, L. V., and Heidger, P. M. Jr. (1970). Electron microscopic observations on the structural components of the blood-testis barrier. *J. Reprod. Fertil. Suppl.* 10, 105–122.

Franks, T. M., and Lykke-Andersen, J. (2008). The control of mRNA decapping and P-body formation. *Mol. Cell.* 32, 605–615. doi: 10.1016/j.molcel.2008.11.001

Fujiwara, Y., Komiya, T., Kawabata, H., Sato, M., Fujimoto, H., Furusawa, M., et al. (1994). Isolation of a DEAD-family protein gene that encodes a murine homolog of Drosophila vasa and its specific expression in germ cell lineage. *Proc. Natl. Acad. Sci. U.S.A.* 91, 12258–12262. doi: 10.1073/pnas.91.25.12258

Kavarthapu, R., Anbazhagan, R., Raju, M., Morris, C. T., Pickel, J., and Dufau, M. L. (2019). Targeted knock-in mice with a human mutation in GRTH/DDX25 reveals the essential role of phosphorylated GRTH in spermatid development during spermatogenesis. *Hum. Mol. Genet.* 28, 2561–2572. doi: 10.1093/hmg/ddz079

Kavarthapu, R., Anbazhagan, R., Sharma, A., Shiloach, J., and Dufau, M. L. (2020). Linking phospho-Gonadotropin regulated testicular RNA helicase (GRTH/DDX25) to histone ubiquitination and acetylation essential for spermatid development during spermiogenesis. *Front. Cell Dev. Biol.* 8:310. doi: 10.3389/fcell.2020.00310

Kimmins, S., and Sassone-Corsi, P. (2005). Chromatin remodelling and epigenetic features of germ cells. *Nature* 434, 583–589. doi: 10.1038/nature03368

Kotaja, N., Bhattacharyya, S. N., Jaskiewicz, L., Kimmins, S., Parvinen, M., Filipowicz, W., et al. (2006). The chromatoid body of male germ cells: similarity with processing bodies and presence of Dicer and microRNA pathway components. *Proc. Natl. Acad. Sci. U.S.A.* 103, 2647–2652. doi: 10.1073/pnas.0509333103

Kotaja, N., and Sassone-Corsi, P. (2007). The chromatoid body: a germ-cell-specific RNA-processing centre. *Nat. Rev. Mol. Cell Biol.* 8, 85–90. doi: 10.1038/nrm2081

Kuramochi-Miyagawa, S., Watanabe, T., Gotoh, K., Takamatsu, K., Chuma, S., Kojima-Kita, K., et al. (2010). MVH in piRNA processing and gene silencing of retrotransposons. *Genes Dev.* 24, 887–892. doi: 10.1101/gad.1902110

Lehtiniemi, T., and Kotaja, N. (2018). Germ granule-mediated RNA regulation in male germ cells. *Reproduction* 155, 77–91.

Lu, L. Y., Wu, J., Ye, L., Gavrilina, G. B., Saunders, T. L., and Yu, X. (2010). RNF8-dependent histone modifications regulate nucleosome removal during spermatogenesis. *Dev. Cell* 18, 371–384. doi: 10.1016/j.devcel.2010.01.010

Luo, Y., Na, Z. K., and Slavoff, S. A. (2018). P-bodies: composition, properties, and functions. *Biochemistry* 57, 2424–2431. doi: 10.1021/acs.biochem.7b01162

Maclean, J. A., and Wilkinson, M. F. (2005). Gene regulation in spermatogenesis. *Curr. Top. Dev. Biol.* 71, 131–197.

Meikar, O., Da Ros, M., Korhonen, H., and Kotaja, N. (2011). Chromatoid body and small RNAs in male germ cells. *Reproduction* 142, 195–209. doi: 10.1530/rep-11-0057

Meikar, O., and Kotaja, N. (2014). Isolation of chromatoid bodies from mouse testis as a rich source of short RNAs. *Methods Mol. Biol.* 1173, 11–25. doi: 10.1007/978-1-4939-0931-5_2

Meikar, O., Vagin, V. V., Chalmel, F., Sõstar, K., Lardenois, A., Hammell, M., et al. (2014). An atlas of chromatoid body components. *RNA* 20, 1–3.

Meistrich, M. L., Mohapatra, B., Shirley, C. R., and Zhao, M. (2003). Roles of transition nuclear proteins in spermiogenesis. *Chromosoma* 111, 483–488. doi: 10.1007/s00412-002-0227-z

Noce, T., Okamoto-Ito, S., and Tsunekawa, N. (2001). Vasa homolog genes in mammalian germ cell development. *Cell Struct. Funct.* 26, 131–136. doi: 10.1247/csf.26.131

Parvinen, M. (2005). The chromatoid body in spermatogenesis. *Int. J. Androl.* 28, 189–201. doi: 10.1111/j.1365-2605.2005.00542.x

Peruquetti, R. L. (2015). Perspectives on mammalian chromatoid body research. *Anim. Reprod. Sci.* 159, 8–16. doi: 10.1016/j.anireprosci.2015.05.018

Peruquetti, R. L., de Mateo, S., and Sassone-Corsi, P. (2012). Circadian proteins CLOCK and BMAL1 in the chromatoid body, a RNA processing granule of male germ cells. *PLoS One* 7:e42695. doi: 10.1371/journal.pone.0042695

Rajakumar, A., and Senthilkumaran, B. (2014). Expression analysis of sox3 during testicular development, recrudescence and after hCG induction in catfish, *Clarias batrachus*. *Sex. Dev.* 8, 376–386.

Raju, M., Hassan, S. A., Kavarthapu, R., Anbazhagan, R., and Dufau, M. L. (2019). Characterization of the phosphorylation site of GRTH/DDX25 and protein kinase a binding interface provides structural basis for the design of a non-hormonal male contraceptive. *Sci. Rep.* 9, 1–10.

Sassone-Corsi, P. (2002). Unique chromatin remodeling and transcriptional regulation in spermatogenesis. *Science* 296, 2176–2178. doi: 10.1126/science.1070963

Sato, H., Tsai-Morris, C. H., and Dufau, M. L. (2010). Relevance of gonadotropin-regulated testicular RNA helicase (GRTH/DDX25) in the structural integrity of the chromatoid body during spermatogenesis. *Biochim. Biophys. Acta* 1803, 534–543. doi: 10.1016/j.bbamcr.2010.02.004

Schneider, S., Balbach, M., Jikeli, J. F., Fietz, D., Nettersheim, D., Jostes, S., et al. (2016). Re-visiting the protamine-2 locus: deletion, but not haploinsufciency, renders male mice infertile. *Sci. Rep.* 6:36764.

Shang, P., Baarends, W. M., Hoogerbrugge, J., Ooms, M. P., van Cappellen, W. A., de Jong, A. A., et al. (2010). Functional transformation of the chromatoid body in mouse spermatids requires testis-specific serine/threonine kinases. *J. Cell Sci.* 123, 331–339. doi: 10.1242/jcs.059949

Sheng, K., Liang, X., Huang, S., and Xu, W. (2014). The role of histone ubiquitination during spermatogenesis. *Biomed. Res. Int.* 2014:870695.

Sheng, Y., Tsai-Morris, C. H., Gutti, R., Maeda, Y., and Dufau, M. L. (2006). Gonadotropin-regulated testicular RNA helicase (GRTH/Ddx25) is a transport protein involved in gene-specific mRNA export and protein translation during spermatogenesis. *J. Biol. Chem.* 281, 35048–35056. doi: 10.1074/jbc.m605086200

Shima, J. E., McLean, D. J., McCarrey, J. R., and Griswold, M. D. (2004). The murine testicular transcriptome: characterizing gene expression in the testis during the progression of spermatogenesis. *Biol. Reprod.* 71, 319–330. doi: 10.1095/biolreprod.103.026880

Shirley, C. R., Hayashi, S., Mounsey, S., Yanagimachi, R., and Meistrich, M. L. (2004). Abnormalities and reduced reproductive potential of sperm from Tnp1- and Tnp2-null double mutant mice. *Biol. Reprod.* 71, 1220–1229. doi: 10.1095/biolreprod.104.029363

Spiridonov, N. A., Wong, L., Zerfas, P. M., Starost, M. F., Pack, S. D., Paweletz, C. P., et al. (2005). Identification and characterization of SSTK, a serine/threonine protein kinase essential for male fertility. *Mol. Cell. Biol.* 25, 4250–4261. doi: 10.1128/mcb.25.10.4250-4261.2005

Steger, K. (2001). Haploid spermatids exhibit translationally repressed mRNAs. *Anat. Embryol.* 203, 323–334. doi: 10.1007/s004290100176

Tsai-Morris, C. H., Koh, E., Sheng, Y., Maeda, Y., Gutti, R., Namiki, M., et al. (2007). Polymorphism of the GRTH/DDX25 gene in normal and infertile Japanese men: a missense mutation associated with loss of GRTH phosphorylation. *Mol. Hum. Reprod.* 13, 887–892. doi: 10.1093/molehr/gam065

Tsai-Morris, C. H., Sato, H., Gutti, R., and Dufau, M. L. (2012). Role of gonadotropin regulated testicular RNA helicase (GRTH/Ddx25) on polysomal associated mRNAs in mouse testis. *PLoS One* 7:e32470. doi: 10.1371/journal.pone.0032470

Tsai-Morris, C. H., Sheng, Y., Lee, E., Lei, K. J., and Dufau, M. L. (2004). Gonadotropin regulated testicular RNA helicase (GRTH/DDX25) is essential for spermatid development and completion of spermatogenesis. *Proc. Natl. Acad. Sci. U.S.A.* 101, 6373–6378. doi: 10.1073/pnas.0401855101

Wu, J. Y., Ribar, T. J., Cummings, D. E., Burton, K. A., McKnight, G. S., and Means, A. R. (2000). Spermiogenesis and exchange of basic nuclear proteins are impaired in male germ cells lacking Camk4. *Nat. Genet.* 25, 448–452. doi: 10.1038/78153

Yokota, S. (2012). Nuage proteins: their localization in subcellular structures of spermatogenic cells as revealed by immunoelectron microscopy. *Histochem. Cell Biol.* 138, 1–11. doi: 10.1007/s00418-012-0962-z

Zheng, H., Stratton, C. J., Morozumi, K., Jin, J., Yanagimachi, R., and Yan, W. (2007). Lack of Spem1 causes aberrant cytoplasm removal, sperm deformation, and male infertility. *Proc. Natl. Acad. Sci. U.S.A.* 104, 6852–6857. doi: 10.1073/pnas.0701669104

Conflict of Interest: The authors declare that the research was conducted in the absence of any commercial or financial relationships that could be construed as a potential conflict of interest.

Copyright © 2020 Anbazhagan, Kavarthapu, Coon and Dufau. This is an open-access article distributed under the terms of the Creative Commons Attribution License (CC BY). The use, distribution or reproduction in other forums is permitted, provided the original author(s) and the copyright owner(s) are credited and that the original publication in this journal is cited, in accordance with accepted academic practice. No use, distribution or reproduction is permitted which does not comply with these terms.

frontiers in Cell and Developmental Biology

REVIEW
published: 16 February 2021
doi: 10.3389/fcell.2021.634536

Genes Regulating Spermatogenesis and Sperm Function Associated With Rare Disorders

*Emma Linn, Lillian Ghanem, Hanisha Bhakta, Cory Greer and Matteo Avella**

Department of Biological Science, College of Engineering and Natural Sciences, University of Tulsa, Tulsa, OK, United States

Spermatogenesis is a cell differentiation process that ensures the production of fertilizing sperm, which ultimately fuse with an egg to form a zygote. Normal spermatogenesis relies on Sertoli cells, which preserve cell junctions while providing nutrients for mitosis and meiosis of male germ cells. Several genes regulate normal spermatogenesis, some of which are not exclusively expressed in the testis and control multiple physiological processes in an organism. Loss-of-function mutations in some of these genes result in spermatogenesis and sperm functionality defects, potentially leading to the insurgence of rare genetic disorders. To identify genetic intersections between spermatogenesis and rare diseases, we screened public archives of human genetic conditions available on the Genetic and Rare Diseases Information Center (GARD), the Online Mendelian Inheritance in Man (OMIM), and the Clinical Variant (ClinVar), and after an extensive literature search, we identified 22 distinct genes associated with 21 rare genetic conditions and defective spermatogenesis or sperm function. These protein-coding genes regulate Sertoli cell development and function during spermatogenesis, checkpoint signaling pathways at meiosis, cellular organization and shape definition during spermiogenesis, sperm motility, and capacitation at fertilization. A number of these genes regulate folliculogenesis and oogenesis as well. For each gene, we review the genotype–phenotype association together with associative or causative polymorphisms in humans, and provide a description of the shared molecular mechanisms that regulate gametogenesis and fertilization obtained in transgenic animal models.

Keywords: sperm motility, acrosome, Sertoli, centrosome, infertility, genetic disease

OPEN ACCESS

Edited by:
Tomer Avidor-Reiss, University of Toledo, United States

Reviewed by:
Sigrid Hoyer-Fender, University of Göttingen, Germany
Dorothy Lerit, Emory University, United States

****Correspondence:***
Matteo Avella
maa8422@utulsa.edu

Specialty section:
This article was submitted to Cell Growth and Division, a section of the journal Frontiers in Cell and Developmental Biology

Received: *28 November 2020*
Accepted: *20 January 2021*
Published: *16 February 2021*

Citation:
Linn E, Ghanem L, Bhakta H, Greer C and Avella M (2021) Genes Regulating Spermatogenesis and Sperm Function Associated With Rare Disorders. Front. Cell Dev. Biol. 9:634536. doi: 10.3389/fcell.2021.634536

INTRODUCTION

In sexual reproduction, female and male gametes, the egg and the sperm fuse to generate a new and unique embryo (Bhakta et al., 2019). Fertilization requires proper gametogenesis to ensure healthy, euploid and genetically intact sperm and eggs. At gametogenesis, chiasmata hold homologous chromosomes in opposition on the meiotic spindle during recombination to ensure accurate segregation in the haploid gametes, and defective chromosomal segregation results in embryonic lethality or developmental defects (Lu et al., 2012; Nagaoka et al., 2012). On the male side, spermatogenesis generates structurally defined sperm in the testes; spermatogonia stem cells are unipotent stem cells that self-renew or differentiate into spermatocytes which traverse the Sertoli

cell blood–testis barrier to enter the seminiferous tubules (Law et al., 2019). Here, spermatocytes complete two meiotic divisions to generate round spermatids, and through spermiogenesis, size, shape, and organelle composition of spermatids undergo significant changes, which lead to the formation of fully elongated sperm. At this stage, sperm are immotile and unable to fertilize an egg *in vivo*; to complete their maturation process, sperm must transit through the caput and cauda epididymis, where they acquire the ability to become motile (Da Ros et al., 2015). Finally, in the female reproductive tract, sperm undergo capacitation, which consists of a series of physiological changes that enable the sperm to fertilize an egg. Capacitated sperm can undergo acrosome exocytosis, a step in fertilization that consists of the exocytosis of a sub-Golgi-derived vesicle, the acrosome, that surrounds the nucleus in the apical region of the sperm head. Capacitated sperm are also enabled to bind to the zona pellucida and fertilize the egg (Puga Molina et al., 2018; Ritagliati et al., 2018).

Each step described above is regulated by a number of genes whose targeted deletion in transgenic animal models has been shown to cause defective gametogenesis, fertilization and fertility phenotypes. Here, we review 21 different rare diseases associated with fertility disorders due to mutations in genes controlling molecular pathways that ensure proper gametogenesis and fertilization (**Table 1**). To identify the genetic intersection between defective spermatogenesis and rare diseases, we screened 680 rare genetic conditions affecting humans in the Genetic and Rare Diseases Information Center (GARD), and the Online Mendelian Inheritance in Man (OMIM). We then performed extensive literature search, to narrow down our list to 82 monogenic and 20 polygenic conditions presenting a fertility phenotype associated with the rare disorder. Among the papers screened, we looked specifically for phenotypes pertaining to testes, male germ cell development and differentiation, Sertoli cell development, spermatogonia, spermatogenesis, meiosis checkpoints, centriole, centrosome, acrosome biogenesis and exocytosis, manchette formation, nuclear sperm compaction, sperm head and tail development, sperm motility, sperm capacitation, and hyperactivation. We have identified 21 conditions, caused by deleterious mutations in 22 genes regulating different aspects of sperm development, maturation, and function. Two of these conditions were identified using the Clinical Variant (ClinVar) database (Greer et al., 2021) (**Table 1**). For each gene and the related disorder, we provide a description of the fertility phenotype, the underlying defective molecular mechanism, and the phenotypic characterization of genome-edited animal models.

MECHANISMS REGULATING SERTOLI CELL DEVELOPMENT AND FUNCTION AT SPERMATOGENESIS

Spermatogenesis generates millions of haploid motile sperm from diploid spermatogonia and is a process mediated by a series of concerted molecular interactions between the developing germ cells and the somatic Sertoli cells (Law et al., 2019). Due to the presence of a significant amount of highly unsaturated fatty acids, the continuous cell proliferation, and high enzymatic activity, testes are subject to oxidative stress due to the overexpression of reactive oxygen species, which may compromise sperm count or affect sperm DNA integrity (Aitken, 2020). Key regulators of spermatogenesis are the peroxisomal membrane adrenoleukodystrophy protein (ALDP), the hemojuvelin gene *(HJV),* Polycystic kidney disease (*PKD*) 1 and 2, the Survivor motor neuron 1 (*SMN1)*, which codes for the SMN protein, the Equilibrative Nucleoside Transporter 3 (ENT3), and Gap Junction Protein, Alpha-1 (GJA1), which codes for Connexin 43. ALDP regulates the degradation process of very long-chain fatty acids during spermatogenesis, HJV regulates iron metabolism in the testes, and PKD1 and 2 control male germ cell development by regulating the mTOR signaling pathway, while SMN, CONNEXIN 43 and ENT3 regulate normal Sertoli cell development, maturation and physiology (**Figure 1A**, left).

Very long chain fatty acids (VLCFAs) (fatty acids with $C > 20$) are constituents of cellular lipids (e.g., sphingolipids and glycerophospholipids) and serve as precursors of lipid mediators (van Roermund et al., 2008). VLCFAs converted to VLCFA-CoAs, are transferred into the cell's peroxisomes, and are subjected to β-oxidization into long-chain or acyl-CoAs, which are transported to the mitochondria where they undergo β-oxidization (van Roermund et al., 2008). ALDP is encoded by the ATP Binding Cassette Subfamily D Member 1 (*ABCD1*) located on the X chromosome (Watkins et al., 1995). In humans, loss-of-function mutations in *ABCD1* affect the VLCFA degradation process, leading to a pathogenic accumulation of saturated C24–C26 VLCFAs in the plasma, brain, adrenal grand, and other tissues (Moser, 1997), causing myelopathies, as reported for the ***X-linked adrenoleukodystrophy (X-ALD)*** and the adult form, the Adrenomyeloneuropathy type (Moser, 1997). Typically, onset of adrenomyeloneuropathy type is around the age of 30 years, with patients presenting adrenocortical dysfunction, peripheral neuropathy, poor androgenization, low testosterone and elevated LH and FSH, lesions in interstitial cells of the testes, smaller seminiferous tubules, low ejaculate volumes, oligospermia, or azoospermia, which lead to male infertility (Powers and Schaumburg, 1981; Assies et al., 1997; Aversa et al., 1998). In testes, docosahexaenoic acid (C22:6n-3; DHA) synthesis in round spermatids from linolenic acid is controlled by ELOVL2 and ELOVL5 (Gregory et al., 2013, p. 2) and is mediated by peroxisomal β-oxidation (Rejraji et al., 2006). Mitochondrial and peroxisomal β-oxidation induce generation of reactive oxygen species, whose high levels have been associated with male infertility due to defective spermatogenesis and leukocytospermia (Pasqualotto et al., 2000). Of note, deletion of *Abcd1* in hemizygous male mice does not recapitulate the human phenotypes (Brennemann et al., 1997) and males are fertile (Lu et al., 1997), which raises the prediction of the presence of putative DNA variant modifier(s) in humans that would elicit the pathogenic phenotypes. In particular, an import machinery in peroxisomes regulates the transport of matrix proteins; PEX13 is a main component of this transport machinery and *Pex13* deletion leads to peroxisomal biogenesis defects in transgenic mice; more specifically, conditional knockout of *Pex13* in Sertoli cells leads to a "Sertoli-cell-only" syndrome

TABLE 1 | List of genes regulating different aspects of sperm development and function.

Gene	Description	Fertility Phenotype	Rare Genetic Disease
ABCD1	ATP binding cassette subfamily D member 1 [Source:HGNC Symbol;Acc:HGNC:61]	Sertoli-cell-only syndrome and azoospermia	X-Linked Adrenoleukodystrophy, Adrenomyeloneuropathy Type
ATM	ATM serine/threonine kinase [Source:HGNC Symbol;Acc:HGNC:795]	Meiosis arrest at gametogenesis: development of spermatocytes arrests between the zygotene and pachytene stages; meiosis was disrupted before normal arrest at prophase I and absence of primary oocytes and follicles	Ataxia telangiectasia
BUB1B	BUB1 mitotic checkpoint serine/threonine kinase B [Source:HGNC Symbol;Acc:HGNC:1149]	Impaired proliferation of spermatogonia, abnormal chromosome segregation in spermatocytes, abnormal MII oocyte chromosomal configurations, and meiotic chromosome segregation defects	Premature chromatid separation with mosaic variegated aneuploidy syndrome
CATSPER2	Cation channel sperm associated 2 [Source:HGNC Symbol;Acc:HGNC:18810]	Failure to undergo hyperactivation, failure to fertilize eggs	Deafness infertility syndrome
CFTR	CF transmembrane conductance regulator [Source:HGNC Symbol;Acc:HGNC:1884]	Defective sperm motility, oligospermia, asthenospermia and teratospermia	Cystic fibrosis due to CTFR mutations
CLPP	Caseinolytic mitochondrial matrix peptidase proteolytic subunit [Source:HGNC Symbol;Acc:HGNC:2084]	Severe defects in granulosa cell differentiation and disruption of normal oogenesis and defective cellular biogenesis during early spermatogenesis	Perrault Syndrome type III
DCAF17	DDB1 and CUL4 associated factor 17 [Source:HGNC Symbol;Acc:HGNC:25784]	Defective manchette formation, leading to aberrant sperm morphology and lower motility	Woodhouse Sakati syndrome
DNAH1	Dynein axonemal heavy chain 1 [Source:HGNC Symbol;Acc:HGNC:2940]	Abnormal sperm flagella morphology and defective sperm motility	Primary ciliary dyskinesia type 37
FGD1	FYVE, RhoGEF and PH domain containing 1 [Source:HGNC Symbol;Acc:HGNC:3663]	Aberrant sperm morphology, absence of the acrosome	Aarskog Syndrome
GJA1	Gap junction protein alpha 1 [Source:HGNC Symbol;Acc:HGNC:4274]	Interrupted folliculogenesis after the primary follicle stage, Sertoli-cell-only syndrome	Oculodentodigital dysplasia
GPX4	Glutathione peroxidase 4 [Source:HGNC Symbol;Acc:HGNC:4556]	Decreased sperm progressive motility associated with impaired mitochondrial membrane potential and cellular abnormalities (e.g., hairpin-like flagella bend at the midpiece, swelling of mitochondria) and oligoasthenozoospermia.	Spondylometaphyseal dysplasia, sedaghatian type
HJV	Hemojuvelin BMP co-receptor [Source:HGNC Symbol;Acc:HGNC:4887]	Spermatogenesis defects and hypogonadotropic hypogonadism	Hemochromatosis 2A
NPHP4	Nephrocystin 4 [Source:HGNC Symbol;Acc:HGNC:19104]	Reduced sperm count and motility defects	Nephronophthisis
PKD1	Polycystin 1, transient receptor potential channel interacting [Source:HGNC Symbol;Acc:HGNC:9008]	Cystic testis, Sertoli-cell-only syndrome and azoospermia	Autosomal dominant polycystic kidney disease
PKD2	Polycystin 2, transient receptor potential cation channel [Source:HGNC Symbol;Acc:HGNC:9009]	Cystic testis, Sertoli-cell-only syndrome and azoospermia, defective sperm migration towards eggs *in vivo* (in fruit fly)	Autosomal dominant polycystic kidney disease
P0C1A	POC1 centriolar protein A [Source:HGNC Symbol;Acc:HGNC:24488]	Defective spindle formation, defective meiosis, aneuploidy.	Short Stature, Onychodysplasia, Facial Dysmorphism, and Hypotrichosis Syndrome
P0C1B	POC1 centriolar protein B [Source:HGNC Symbol;Acc:HGNC:30836]	Immotile sperm with aberrant axoneme architecture	Cone Rod Dystrophy type 20
PRKAR1A	Protein kinase cAMP-dependent type I regulatory subunit alpha [Source:HGNC Symbol;Acc:HGNC:9388]	Round spermatids developing large nuclear areas devoid of chromatin, resulting in aberrant sperm morphology with defects in sperm head and tail and inability of sperm to bind to the zona pellucida or fuse with eggs.	Carney complex
SLC22A5	Solute carrier family 22 member 5 [Source:HGNC Symbol;Acc:HGNC:10969]	Anatomically-deformed epididymis and obstructive azoospermia	Acetyl-carnitine deficiency
SLC29A3	Solute carrier family 29 member 3 [Source:HGNC Symbol;Acc:HGNC:23096]	Oligospermia and secondary male infertility due to Sertoli-cell-only syndrome	Histiocytosis-lymphadenopathy plus syndrome
SLC39A4	Solute carrier family 39 member 4 [Source:HGNC Symbol;Acc:HGNC:17129]	Sperm motility possibly due to defective zinc uptake	Acrodermatitis enteropathica
SMN1	Survival of motor neuron 1, telomeric [Source:HGNC Symbol;Acc:HGNC:11117]	Disrupted spermatogenesis due to aberrant splicing in prepubertal testis	Adult-onset spinal muscular atrophy

Deleterious variants in each of these genes have also been associated with monogenic rare disorders. Columns from left to right-(A) Gene name. (B) Class of protein produced by gene. (C) Observed fertilization or gametogenesis phenotype associated with gene mutation. (D) Genetic disorder associated with gene mutation.

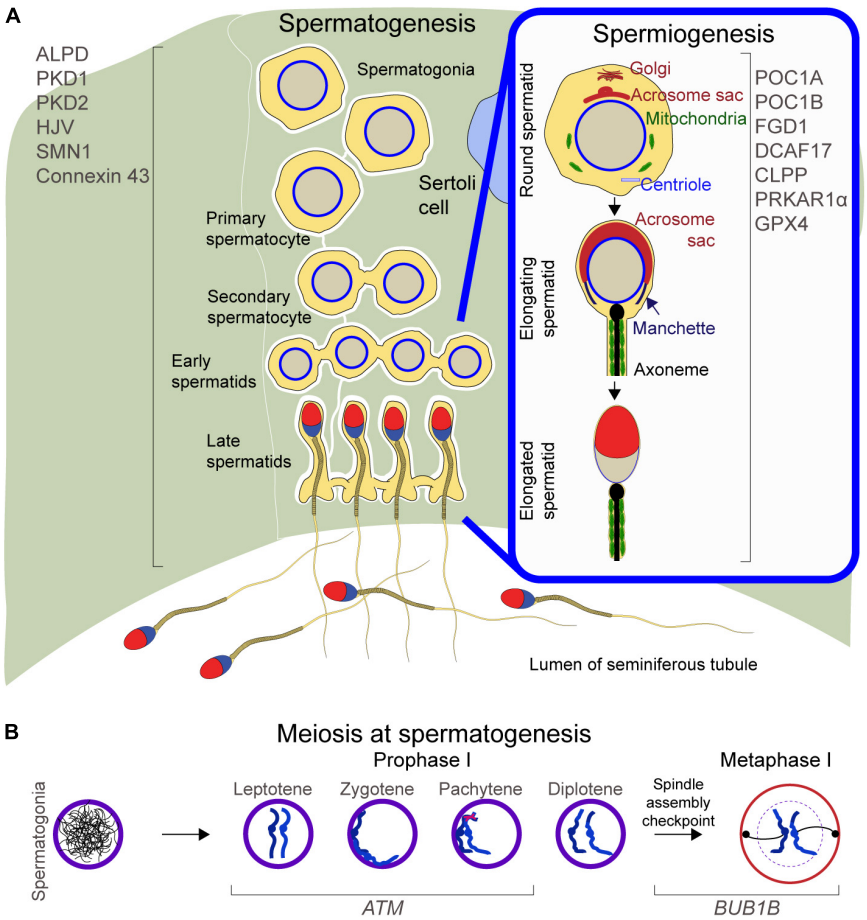

FIGURE 1 | Schematic of spermatogenesis and spermiogenesis: **(A)** Left, proteins regulating spermatogenesis. Right inset, proteins mediating cellular remodeling at spermiogenesis. **(B)** Meiosis during spermatogenesis, with focus on Prophase and Metaphase II and proteins regulating chromosome migration, DNA double strand breaks repair, and spindle assembly checkpoint.

with a significant increase in triglycerides and cholesteryl esters (Nenicu et al., 2009). Also, conditional deletion of *Pex13* in pre-meiotic germ cells impairs the import of peroxisomal matrix proteins in germ cells, leading to interruption of differentiation at the round spermatid stage and azoospermia in male mice (Brauns et al., 2019).

Hemojuvelin gene is involved in iron metabolism and encodes the hemojuvelin protein (Huang et al., 2005). In *Hjv* knockout mice, absence of the hemojuvelin protein causes a reduction in production of hepcidin mRNA. Hepcidin is a regulator of iron metabolism and is able to bind to ferroportin. Upon targeted disruption of *Hjv*, increased levels of ferroportin expression have been reported in several tissues including the liver, spleen, and blastolateral membrane (Huang et al., 2005). Ferroportin is an ion transporter present in cellular membranes of macrophages and endothelial cells of the intestines, and it plays a significant role in nutrient absorption. Iron is transported through cellular membranes by ferroportin, and iron uptake is downregulated by hepcidin binding, indicating that *Hjv* plays a role in preventing iron overload by maintaining physiological hepcidin levels (Huang et al., 2005; Niederkofler et al., 2005). In humans, missense mutations in *HJV* are associated with ***Juvenile Hemochromatosis***, which manifests in teens and young adults with high iron levels throughout the entire body and consequent symptoms such as cardiac deficits, diabetes, and hypogonadism (Papanikolaou et al., 2004). Excess iron levels are observed in knockout *Hjv* mice, particularly in the kidney, liver, heart, pancreas, and testis (Huang et al., 2005). However, cardiac and organ dysfunction, diabetes, hepatic fibrosis, and fertility phenotypes are not observed as are in human hemochromatosis (Huang et al., 2005). Male patients with hemochromatosis experience fertility disorders due to spermatogenesis defects and hypogonadotropic hypogonadism (McDermott and Walsh, 2005; Leichtmann-Bardoogo et al., 2012). Excess iron levels cause oxidative stress, a phenomenon that can hamper the delicate homeostasis required for spermatogenesis (Leichtmann-Bardoogo et al., 2012). Spermatogenesis is protected from iron imbalances by Sertoli cells (Leichtmann-Bardoogo et al., 2012). Sertoli cells store excess iron and redeposit it into new spermatocytes (Leichtmann-Bardoogo et al., 2012). Mice with high iron levels generated by deletion of the genes encoding iron regulatory protein 2 (IRP2) and Human homeostatic iron

regulator protein (HFE) demonstrate iron buildup around the seminiferous tubules, but lower buildup within the tubules, observations that indicate a more autonomous iron regulatory system during spermatogenesis (Leichtmann-Bardoogo et al., 2012). Homozygous knockout *Irp2* mice contain viable sperm in the epididymis and demonstrate normal fertility (Leichtmann-Bardoogo et al., 2012). The same amount of apoptotic cells are observed in knockouts as are wild type mice (Leichtmann-Bardoogo et al., 2012). Observations of sperm were not made and no subsequent studies have utilized this model for iron regulation in the testis. Additionally, the most frequent non-diabetic endocrine symptom of hemochromatosis presents as hypogonadotropic hypogonadism (McDermott and Walsh, 2005). Hypogonadism is caused by accumulation of iron in the pituitary gonadotroph cells, which are responsible for regulating gonadotropins (McDermott and Walsh, 2005). Low levels of TSH, LH, and testosterone manifest, resulting in variable fertility defects (McDermott and Walsh, 2005).

PKD 1 and *2* are two protein-coding genes associated with the insurgence of ***Autosomal dominant polycystic kidney disease (ADPKD)***, a monogenic disorder that results in the bilateral development of renal cysts, leading to end-stage renal disease (Torres et al., 2007). *PKD1* codes for Polycystin-1, an integral membrane protein presenting 11 transmembrane domains and an extracellular region that includes 12 PKD immunoglobulin-like fold domains, known as PKD domains, which typically function as mediators for protein-protein or protein–carbohydrate interactions (Hughes et al., 1995; Mochizuki et al., 1996). *PKD2* codes for Polycystin-2, a non-selective cation/calcium channel. Polycystins form a complex that regulates intracellular levels of Ca^{2+} in different cell types involved in cell–cell and cell–matrix interactions, in the endoplasmic reticulum, or in primary cilia. In primary cilia, the intraflagellar transport motor component KIF3A mediates protein movement in the cilium and is necessary for ciliary formation (Harris and Torres, 2009). Kidney-specific deletion of *Kif3a* disrupts this protein transport and mutant mice develop renal cysts (Lin et al., 2003). Moreover, the polycystin complex serves as a flow-sensor in the cilium mediated by Ca^{2+} influx into the cell that occurs through the polycystin-2 channel. *Pkd1* and *Pkd2* null mice are embryo lethal, due to defects in formation of the kidney, pancreas, heart, and capillary blood vessels, whereas conditional deletion of *Pkd1* leads to the development of cysts in the mouse kidneys (Shibazaki et al., 2008). $Pkd2^{ws25/-}$ mice (an animal model of ADPKD) show hepatic cysts, cardiac defects, and renal failure (Wu et al., 2000). Extra-renal cyst development occurs in male reproductive organs including the testis, epididymis, seminal vesicles, and prostate (Danaci et al., 1998).

In adult human testes, presence of cilia has been reported in the peritubular myoid cells and in differentiating Leydig cells. Of note, cilia are also present in pathological conditions such as in azoospermic patients with Klinefelter syndrome (presenting Sertoli cell-only phenotype) (Nygaard et al., 2015). Atrophic testes typically present peritubular cells that produce aberrant-long cilia (Nygaard et al., 2015). Male fertility phenotypes are not uncommon in ADPKD patients, with individuals presenting necrospermia and testis cysts; one possible molecular mechanism behind such fertility phenotypes may reside within the mechanistic Target of Rapamycin (mTOR) signaling pathway. The mTOR signaling is aberrantly upregulated in ADPKD and rapamycin has been shown to inhibit cyst expansion (Shillingford et al., 2006). In testes, mTOR regulates spermatogonial stem cell maintenance and differentiation, controls the physiology of Sertoli cells, and helps preserve the maintenance of the blood–testis barrier, while nurturing maturing sperm during spermatogenesis (Moreira et al., 2019). Indeed, chronic inhibition of mTOR by rapamycin leads to a partially reversible spermatogenic arrest in adult male mice; this is due to defects in sex body formation and meiotic sex chromosome inactivation, which lead to partially reversible impaired spermatogenesis and male infertility (Zhu et al., 2019). Dysregulation of mTOR signaling in the testes of ADPKD patients could represent the cause of cystic testes and possibly other unreported testis-related fertility phenotypes.

SMN1 codes for the SMN protein, which mediates the assembly of small nuclear ribonucleoproteins (snRNPs), key constituents of the spliceosome machinery (Lefebvre et al., 1995). SMN is expressed in motor neurons, as well as muscle, heart, lung, and intestine tissues (Ottesen et al., 2016). In humans, deletion and missense mutations have been associated with the insurgence of ***Adult Spinal Muscular Atrophy (SMA)***, a group of genetic conditions that gradually abolishes motor neurons that result in muscle weakness, impairment in the control of skeletal muscle activities (e.g., speaking, walking, breathing, and swallowing), and atrophy (Lefebvre et al., 1995). Typically, the severity of SMA is defined by the SMN levels: SMN signals the proper assignment of spliceosomal proteins to the corresponding snRNA (Pellizzoni et al., 2002). Subsequently, SMN dissociates from this complex and the snRNA proceeds to RNA splicing (Pellizzoni et al., 2002). In the mammalian genome, the paralog *SMN2* is unable to rescue the phenotypes due to *SMN1* null mutations (because of skipping of exon 7 at splicing that results in an only partially functioning SMNΔ7 truncated protein) (Lorson et al., 1999). Abnormal splicing of particular genes such as Neurexin 2 *(NRXN2)*, which coordinates synapse development, and Ubiquitin like modifier activating enzyme 1 *(UBA1)*, whose function is to regulate ubiquitin levels, have been proposed to trigger neuromuscular specific phenotypes observed in SMA (See et al., 2014; Wishart et al., 2014).

Homozygous *Smn1 Smn2* double knockout mice present periimplantation lethality (Hsieh-Li et al., 2000). Therefore, extensive research efforts have been made to establish a mouse model with an intermediate form of the disease, in an effort to provide a research tool to better investigate SMA. To this end, expression of human *SMN2* and *SMNΔ7* in the *Smn1* null background in transgenic mice is shown to rescue the embryo-lethal phenotype, with transgenic rescue mice showing spinal cord and skeletal muscle abnormalities similar to phenotypes seen in SMA patients (Hsieh-Li et al., 2000). Another SMA mouse model known as $Smn^{C/C}$ mouse, expresses two copies of a chimeric-hybrid transgene defined by the murine genomic *Smn1* (exons 1-6) and human genomic *SMN2* (spanning exons 7–8) carrying a 42 kb genomic *SMN2* segment (downstream of exon 8)

(Osborne et al., 2012). This mouse generates ∼25–50% of the SMN protein, and presents symptoms of SMA, including small testis, reduced number of post-meiotic cells, and disrupted spermatogenesis (Ottesen et al., 2016). Also, sperm count has been reported as severely reduced (∼10 times lower than normal mice) (Ottesen et al., 2016). $Smn^{C/C}$ testis transcriptome analyses report downregulation of genes expressed in late spermatocytes and spermatids, and an altered expression of genes regulating apoptotic pathways, which may affect pre-pubertal Sertoli cell development (Bao et al., 2015).

The Solute Carrier Family 29 Member 3 (*SLC29A3*) gene encodes ENT3, an intracellular nucleoside transporter. ENT3 localizes to late endosomes, lysosomes, and mitochondria, and it translocates hydrophilic nucleosides across the membrane to regulate DNA synthesis and purinergic signaling (Young et al., 2013, p. 29). In humans, homozygous or compound heterozygous loss of function mutations in *SLC29A3* have been associated with ***Histiocytosis-lymphadenopathy plus syndrome***, a genetic disease that includes 4 previously thought different histiocytic conditions. Resulting conditions include Faisalabad histiocytosis (FHC), Sinus Histiocytosis with Massive Lymphadenopathy (SHML), H syndrome, and Pigmented Hypertrichosis with Insulin-dependent Diabetes mellitus syndrome (PHID) with a broad spectrum of clinical defects involving the skin, pancreas, eyes, musculoskeletal system, or presenting multiple hematological and endocrinological features (Morgan et al., 2010). In particular, H syndrome has been reported to associate with hyperpigmentation, hypertrichosis, hepatosplenomegaly, heart anomalies, hearing loss, low-height, hyperglycemia and hypogonadism (Molho-Pessach et al., 2008, p. 3). Gene deletion of *Slc29a3* in mice recapitulates the defective human phenotypes including hypogonadism (Nair et al., 2019); male mice show severe subfertility, producing small litters (2/3 pups per litter) and secondary infertility, possibly due to endocrinopathy (Nair et al., 2019), although no phenotypic evidence for the mouse gametes is reported. Of note, ENT3 is expressed in mammalian Sertoli cell lines (Kato et al., 2006), implicating a possible role of ENT3 in mammalian spermatogenesis.

GJA1 codes for Connexin 43, a main component of gap junctions, which consists of intercellular channels and ensures diffusion of low-weight molecules between adjacent cells. *GJA1* is expressed in a broad variety of tissues such as brain, eye, muscles, skin, and bones. More than 70 different missense *GJA1* mutations have been associated in humans with misassembled channels or altered channel conduction properties, leading to a genetic condition known as ***Oculodentodigital Dysplasia***, an autosomal dominant disorder with high penetrance and variable expressivity (Paznekas et al., 2003). Typical phenotypes include craniofacial anomalies (e.g., thin nose with hypoplastic alae nasi, small anteverted nares, prominent columnella, and microcephaly), brittle nails and hair abnormalities of hypotrichosis, dysplastic ears and conductive hearing loss, ophthalmic defects (e.g., glaucoma, and optic atrophy), cleft palate, and mandibular overgrowth (Paznekas et al., 2003). Gene deletion in transgenic mice leads to perinatal lethality due to congenital defects in the heart (Reaume et al., 1995, p. 43). Conditional deletion of *Gja1* in mouse testis results in seminiferous tubules presenting only Sertoli cells which surprisingly continue to proliferate even after 20 days of age, and severe reduction of maturing germ cells lead to a Sertoli-cell-only phenotype (Sridharan et al., 2007).

CHECKPOINT SIGNALING PATHWAYS REGULATE DNA DAMAGE RESPONSE AT MEIOSIS

To ensure successful transmission of genetic information to the progeny, meiosis checkpoints halt the beginning of late cell-cycle events until the completion of earlier events (Hartwell and Weinert, 1989). Checkpoints are necessary to activate repair mechanisms upon DNA damage, for genome stability, and to ensure faithful segregation of replicated chromosomes (Hartwell and Weinert, 1989). At meiosis, the Ataxia-Telangiectasia Mutated *(ATM)* and the Bub1-Mitotic Checkpoint Serine/Threonine Kinase B (*BUB1B)* genes regulate cell cycle checkpoint signaling pathways (**Figure 1B**).

ATM encodes a kinase that responds to DNA double strand breaks (DSBs) by regulating the ATM- and Rad3-related (ATR) kinase, a checkpoint kinase required for meiosis progression (Jazayeri et al., 2006; Lange et al., 2011) and for DNA repair in cases of excess DSBs formation (Lange et al., 2011). In humans, missense, frameshift, or nonsense mutations in the *ATM* gene result in the absence of a functional ATM protein and the insurgence of a rare genetic disease defined as ***Ataxia telangiectasia*** (Jacquemin et al., 2012). Symptoms include susceptibility to cancer development, cerebellar impairments causing ataxia, oculomotor apraxia, immune deficits, and fertility impairments (Jacquemin et al., 2012). Gonadal insufficiencies causing infertility originate with meiotic arrest, and meiotic disruptions likely occur in the crossing over stages of prophase I (Xu et al., 1996).

Atm null mice lack round and elongated spermatids (Xu et al., 1996), whereas in females degenerate ovaries do not contain early stage oocytes or development of follicles (Xu et al., 1996). *Atm* is epistatic over the Spo11 Initiator Of Meiotic Double Stranded Breaks gene (*Spo11*), which regulates the formation of DSBs at crossing over (Lange et al., 2011). *Atm* null spermatocytes present an increase in SPO11 expression, likely associated with a higher number of DSBs (Lange et al., 2011). It is believed that the ATM kinase is activated by DSBs, and by phosphorylation it downregulates SPO11, decreasing the generation of DSBs in a negative feedback loop (Lange et al., 2011). *Atm* knockout mice show growth retardation, immune deficits, develop thymic lymphomas, and present testicular and ovarian abnormalities (Xu et al., 1996). Immunostaining of spermatocytes with polyclonal antibodies against the chromosomal core protein COR1 has been performed to follow chromosomal synapse complexes during crossing over (Xu et al., 1996). At meiosis, *ATM* initiates repair of DSBs (Xu et al., 1996; Lange et al., 2011) and absence of ATM is found to correlate with unusually high numbers of univalents, only partially synapsed bivalents, and a delay in observed synapsis (Xu et al., 1996). Also, bivalents are fragmented, causing chromosome fragmentation. In the testes of *Atm* null males, development of spermatocytes halts between

the zygotene and pachytene stages of meiotic prophase, which lead to male infertility (Xu et al., 1996). Null mice present a female fertility phenotype as well: in the null ovaries, no primary oocytes or follicles are observed and meiosis is disrupted before normal arrest at prophase I, which results in female infertility (Xu et al., 1996).

BUB1B codes for a kinase controlling spindle checkpoint function: BUB1B delays the onset of anaphase by acting at the kinetochore and inhibiting the anaphase-promoting complex/cyclosome; this mechanism ensures proper chromosome segregation prior to cell division (Cahill et al., 1998; Taylor et al., 1998; Perera et al., 2007). In humans, deleterious biallelic mutations (missense or frameshift) which inactivate the BUB1B kinase domain are associated with a ***Premature Chromatid Separation Trait***, which leads to ***Mosaic Variegated Aneuploidy Syndrome*** (Limwongse et al., 1999). This autosomal recessive disorder is defined by mosaic aneuploidies (trisomies and monosomies) observed in different chromosomes and tissues. Patients with this condition present aneuploidies in more than 25% of their cells (Rudd et al., 1983), which is associated with variable developmental delay and a wide range of other congenital defects such as intrauterine growth retardation, microcephaly and eye anomalies. Plus, severe risks of malignancy are reported including rhabdomyosarcoma, Wilms tumor, leukemia (Hanks et al., 2004) and ovarian cancer (Feng et al., 2019). Furthermore, *BUB1B* has been associated with infertility due to premature ovarian insufficiency (Chen et al., 2020). Gene deletion of mouse *Bub1b* leads to embryo lethality (Baker et al., 2004); however, through a sophisticated gene deletion strategy, mutant mice homozygous for the 'H' allele ($Bub1b^{H/H}$) were generated and found to be infertile. In these mice, transcription of the 'H' allele leads to a precursor mRNA which is occasionally spliced abnormally (Baker et al., 2004), causing the development of mutant mature *Bub1b* mRNA that is not translated; this reduces the cellular BUB1B protein levels (Baker et al., 2004), leading to male and female infertility. Testis weight of homozygous mutant males is lower than normal controls and sperm count is significantly reduced. Sperm motility, morphology, and ability to bind to the zona are reported as normal, though no data in the original manuscript is shown regarding sperm ability to fuse with the ovulated eggs. Of note, $Bub1b^{H/H}$ ovulates a larger number of eggs (206 eggs) compared to normal (152), but only 6% lead to 2-cell stage embryos (Baker et al., 2004). Also, 5% of spermatocytes in metaphase of meiosis II present abnormal karyotypes; moreover, in follow-up studies, conditional deletion of *Bub1b* in mouse testis impairs proliferation of spermatogonia, induces abnormal chromosome segregation in spermatocytes, and drastically reduces sperm production (over 80%), resulting in male infertility (Perera et al., 2007). Hence, lower expression or full deletion of *Bub1b* in the testes impairs spermatogenesis and fertilization (Baker et al., 2004). In females, $Bub1b^{H/H}$ ovaries are able to ovulate MII oocytes, though ∼70% of ovulated eggs present highly abnormal MII chromosomal configurations, leading to meiotic chromosome segregation defects and female infertility (Baker et al., 2004).

SPERM CELLULAR ORGANIZATION AND SHAPE

In the final stage of spermatogenesis, defined as spermiogenesis, spermatids undergo cellular and nuclear reshaping, organelle reorganization, and tail formation, which results in the development of mature spermatozoa. Centrosomes are formed from centrioles, organelles located near the nuclear envelope of animal cells which are necessary for the proper organization of microtubules, as well as for the positions of the nucleus and other organelles (Avidor-Reiss and Turner, 2019). At spermiogenesis, the manchette, a transient microtubular platform consisting of α- and β-tubulin heterodimers (Lehti and Sironen, 2016), mediates a number of considerable changes in the developing haploid germ cells, which include the development of the sperm tail as well as the condensation and elongation of the sperm head (Gaffney et al., 2011). Mature mammalian sperm are characterized by a strong flagellum to drive them through the female genital tract and are equipped with several mitochondria that generate energy for the flagellum motility (Gaffney et al., 2011); the flagellum axoneme is defined by two central singlet microtubules surrounded by nine microtubule doublets, which in turn are enclosed by nine outer dense fibers (Gaffney et al., 2011). The sperm head presents a condensed haploid nucleus containing tightly packed DNA coiled around protamines (Wykes and Krawetz, 2003). Underlying the anterior plasma membrane of the sperm head is the acrosome, a secretory Golgi-derived subcellular organelle, that contains a number of lytic enzymes, which are not necessary for binding or penetration of the zona pellucida in mice (Buffone et al., 2014). Nonetheless, one of these enzymes, Acrosin, is necessary for zona penetration in hamsters (Hirose et al., 2020) (**Figure 1A**, right panel).

Key molecular players in the definition of cellular structure are POC1 Centriolar Proteins (POC1) A and B (*POC1A* and *B*), FYVE, RhoGEF and PH domain containing 1 (*FGD1* encoding FGD1), DDB1– and Cul4–Associated Factor 17 (*DCAF17*, encoding Cullin-RING E3), Caseinolytic Peptidase P (*CLPP*), and Protein Kinase Camp-Dependent Type I Regulatory Subunit A (*PRKAR1α*). The POC1 Centriolar Protein *(POC1)* A and B (*POC1A* and *B)* play important roles in the elongation and structural stability of the centriole (Geister et al., 2015). FGD1 possibly controls acrosome biogenesis, Cullin-RING E3 regulates manchette formation and nuclear compaction, CLPP regulates mitochondrial activity during early spermatogenesis, and *PRKAR1α* controls normal sperm head and tail development during male germ cell differentiation.

In human sperm, centrosomes are defined by the proximal centriole (PC), surrounded by the pericentriolar material (PCM), and the distal centriole (DC). The sperm DC is located at the base of the axoneme, and an atypical structure is defined when its microtubules are wide-opening outward. During spermatid development, a number of DC centriolar proteins organize into rods (Fishman et al., 2018). In bovine sperm, it has been shown that DC recruits the PCM, to establish a daughter centriole, which localizes to the spindle pole, while remaining attached to the axoneme (Fishman et al., 2018). This structure is an atypical sperm centriole, which serves as the second

centriole of the zygote (Fishman et al., 2018). In humans, missense mutations or deletion of *POC1A* are associated with ***Short Stature, Onychodysplasia, Facial Dysmorphism, and Hypotrichosis Syndrome***, which results in stunted bone and ectodermal tissue development (Sarig et al., 2012). Deleterious mutations in *POC1A* result in an increased number of centrioles and an aberrant Golgi stack assembly, leading to abnormal cellular material trafficking (Sarig et al., 2012). Abnormal Golgi function has been associated with disorders of the bone and skin, and abnormal centriole formation causes severe disruption to Golgi trafficking (Sarig et al., 2012). Ciliary function also regulates chondrocytes differentiation, and *POC1A* deleterious mutations alter this process (Geister et al., 2015). In mice, expression of *Poc1a* is enriched in the seminiferous tubules and Sertoli cells, and LINE-retrotransposon mediated deletion of *Poc1a* (chagun mice) mimic the human disorder and results in male infertility, due to defective meiosis in germ cells (Sarig et al., 2012; Geister et al., 2015). Mutant mouse embryos develop additional centrosomes, and occasionally 3– 4 spindle poles, which likely results in aneuploidy (Geister et al., 2015). In cases where proper spindle formation proceeds, only ∼28% of cells develop primary cilia (Geister et al., 2015). While some spermatocytes are observed in knockout seminiferous tubules, developing germ cells are not generally present (Geister et al., 2015, p. 1). Particularly, in mutant males, secondary spermatocytes and round/elongating spermatids do not develop, which may indicate that cell death occurs in the pre-leptotene stage of spermatogenesis (Geister et al., 2015). Male infertility is due to these early meiotic defects originating with spindle formation (Geister et al., 2015, p. 1).

POC1B together with *POC1A*, maintains centriole structure and ensures proper formation of the mitotic spindle. Studies performed in zebrafish localize *poc1b* expression to the basal bodies of primary cilia in the retina membrane (Roosing et al., 2014). *POC1B* interacts with the FAM161 centrosomal protein A gene *(FAM161A)* to regulate ciliary development in the basal body (Roosing et al., 2014). Knockdown of *poc1b* is induced through a morpholino-oligonucleotide in zebrafish, which prevents the splicing or translation of Exon 2 (Roosing et al., 2014). Truncated poc1b protein interacts significantly less with fam161a and small eyes develop (Roosing et al., 2014). Additional phenotypes commonly observed with ciliopathies are displayed, including a curved body axis and kidney cysts (Roosing et al., 2014). In the free-living ciliate *Tetrahymena thermophila*, and in humans, POC1B is localized to the basal body cartwheel, to the site of new basal body assembly, and to the microtubule cylinder walls; this protein preserves the stability of basal bodies, while ensuring proper ciliary-based motility, and cilia formation (Pearson et al., 2009). *Poc1b* small interfering (si)RNA treated cells demonstrate a 30% decrease in ciliogenesis, alongside shortened and bent cilia development (Pearson et al., 2009). In humans, deletion or missense mutations in *POC1B,* usually affecting exons 6 or 7, cause the loss of association of the basal body to the primary cilium (Roosing et al., 2014). These mutations are associated with autosomal ***Cone Rod Dystrophy type 20*** (Roosing et al., 2014). Defects originating in the ciliary function of retina cause either complete absence of, or the progressive degeneration of, cone function affecting color detection (Roosing et al., 2014). Disease progression may later impair rod function, likely owing to degeneration of cone function (Roosing et al., 2014).

In *Drosophila*, *poc1b* is expressed in spermatogonia and throughout spermatogenesis (Khire et al., 2016). Unlike other ciliary regulatory proteins, POC1B has been found to be upregulated in the maturation of spermatogonia to spermatozoa (Khire et al., 2016). The giant centriole (GC) and the proximal centriolar-like structure (PCL) are two centrioles highly involved in proper centrosome formation (Khire et al., 2016). Downregulation of GC and PCL proteins is observed as spermatids mature to spermatozoa, whereas poc1b is consistently upregulated (Khire et al., 2016). Additionally, POC1B is highly expressed at the center of the PCL (Khire et al., 2016). In spermatocyte, POC1A and B are necessary for GC elongation; in particular, POC1A is shown to be necessary and sufficient for sperm motility, and POC1B for controlling the protein composition PCL (Khire et al., 2016). *Poc1b* mutants show immotile sperm presenting with aberrant axoneme architecture, and early embryos present monopolar spindles lacking microtubule aster (Khire et al., 2016). These mutant phenotypes are rescued by the expression of a *Poc1* transgene. In particular, the transgene consists of a *BamGal4* promoter which can drive the expression of a polycistronic mRNA consisting of an untagged *poc1A* and a GFP-tagged *poc1b* (Khire et al., 2016), specifically in late spermatogonia and early spermatocytes. Trangenic-rescue sperm can fertilize normal oocytes, and embryos show bipolar spindles and microtubule asters (Khire et al., 2016).

The *FGD1* gene encodes the FGD1 protein, a guanine-nucleotide exchange factor (GEF) that is responsible for the activation of the p21 GTPase CDC42 (German Pasteris et al., 1994; Zheng et al., 1996; Kierszenbaum et al., 2003). The FGD1 protein is defined by a proline-rich N-terminus, the GEF and pleckstrin homology (PH) domains, a FYVE-finger domain, and a PH domain (PH2) located at the C terminus of the protein; these latter domains mediate protein signaling and subcellular localization (Zheng et al., 1996). In humans, several mutations in *FGD1* have been associated with the manifestation of ***Aarskog-Scott syndrome*** (Lebel et al., 2002; Orrico et al., 2005; Bottani et al., 2007), an X-linked genetic disease defined by severe a short stature, hypertelorism, shawl scrotum, and brachydactyly, and occasionally intellectual disability (German Pasteris et al., 1994). Moreover, a 31 years old male patient with Aarskog-Scott syndrome is reported with infertility and recurrent miscarriage, possibly due to severe spermatogenesis defects, with 95% of his sperm lacking the acrosome (Meschede et al., 1996). In mice, *Fgd1* expression is localized at sites of active bone formation within osteoblasts, playing a pivotal role during skeletal formation (German Pasteris et al., 1994). In particular, *Fgd1* expression has been described in the subcortical actin cytoskeleton and in the Golgi apparatus (Estrada et al., 2001), the latter defining spermatid polarity and being the source of proacrosomal vesicles during the biogenesis of the acrosome (Kierszenbaum et al., 2003). Although no sperm-specific conditional knockout mouse for *Fgd1* has been reported yet, it is conceivable to speculate a role of *Fgd1* during acrosomal biogenesis (Meschede et al., 1996).

Indeed, a conditional knockout mouse for *Fgd1* would prove useful to inform on the relation between CDC42 and FGD1 at spermatogenesis.

DCAF17, a member of DCAF family genes, encodes substrate receptor proteins for Cullin-RING E3 ubiquitin ligases, enzymes that act as key mediators of post-translational protein regulation in multiple cellular processes. Deleterious variants in *DCAF17* have been identified as the primary cause of ***Woodhouse Sakati syndrome***, a rare autosomal recessive genetic condition characterized by alopecia, hearing impairment, diabetes mellitus, learning disabilities, extrapyramidal manifestations, and hypogonadism (Alazami et al., 2008). Gene deletion of *Dcaf17* in male mice leads to infertility due to aberrant sperm development and morphology due to a defective manchette formation and nuclear compaction during spermiogenesis (Ali et al., 2018, p. 17): *Dcaf17* null males produce a low number of sperm that present abnormal shape and lower motility. Morphology analyses show sperm with deformed and decondensed nuclei with defective nuclear chromatin condensation, with triangular, oval or amorphous head shapes, miss-localized and deformed and detached acrosomes (which were missing in 20% of the sperm), disorganized and disrupted mitochondrial sheaths with disorganized outer dense fibers, and aggregating mitochondria near the deformed nucleus (Ali et al., 2018, p. 17), a phenotype similar to oligoasthenoteratozoospermia in humans. DCAF17 acts as receptor for several Cullin4-based E3 ligase complexes and serves as substrate to the E3 ligase complex for protein ubiquitination (Lee and Zhou, 2007). During sperm development, two proteins, CUL4A and CUL4B function as scaffold proteins for the assembly of the Cullin4-based E3 ligase complex (Jackson and Xiong, 2009). Testicular phenotypes obtained upon gene deletion of *Cul4a* and *Cul4b* resemble the results observed in Dcaf17 knockout testes; this may implicate a collaborative role of CUL4A, CUL4B, and DCAF17 proteins in regulating spermatogenesis via ubiquitin-mediated mechanism for maintenance of protein homeostasis.

CLPP encodes a mitochondrial peptidase conserved in prokaryotes and eukaryotes (Gispert et al., 2013) that is sufficient to digest small polypeptides without ATP requirement (Gispert et al., 2013). For hydrolysis of larger proteins, CLPP rings are secured by the activity of the ATP-dependent Clp protease ATP-binding subunit Clpx (CLPX) enzyme (Voos, 2009; Gispert et al., 2013). CLPP has been identified also as a component of mitochondrial unfolded protein response, a reaction in which CLPP expression increases under accumulation of unfolded proteins (Voos, 2009). The CLPP/CLPX protein complex establishes a proteolytic barrel structure in which target-proteins in the mitochondria are broken down (Gispert et al., 2013). In the mouse, *Clpp* expression is enriched in a variety of tissues, including liver, brain, heart, ovary, and testis (Gispert et al., 2013). In humans, missense *CLPP* mutations cause ***Perrault syndrome type 3***, which is characterized by sudden sensorineural hearing loss, epilepsy, growth retardation (Dursun et al., 2016), ovarian dysgenesis manifesting in amenorrhea, and azoospermia in men (Gispert et al., 2013; Demain et al., 2017). The missense mutations reported likely affect the alpha helices and beta sheets of CLPP, as well as disrupt the hydrophobic cleft of the protein that is responsible for the interaction with CLPX (Jenkinson et al., 2013). Consequent structural abnormalities cause deficits in CLPX functionality, resulting in decreased degradation of misfolded proteins. This excess of abnormal protein content induces poor cell functionality in expressed locations, including sensory hair follicles and developing ovaries (Jenkinson et al., 2013). *Clpp* null mice showed an increased expression of CLPX in the liver, brain, heart, testis, and ovary (Gispert et al., 2013). Analogous to the observed symptoms associated with *CLPP* mutations, increased CLPX expression has been correlated to impaired hearing, motor deficits, and male and female infertility (Gispert et al., 2013). *Clpp* deletion in mouse testes have been shown to lead to halted spermatogenesis before the formation of spermatids, likely due to the presence of misfolded proteins (Gispert et al., 2013; Jenkinson et al., 2013). It is conceivable that absence of CLPP leads to a compensatory effect by inducing the expression of cytosolic protease subunits to enhance degradation. Yet, *Clpp* null seminiferous tubules completely lack spermatids and mature spermatozoa in the testis, and electron microscope analysis shows severe defective cellular organization with no acrosomes or axonemes (Gispert et al., 2013).

PRKAR1A encodes the R1α regulatory subunit of cAMP-dependent protein kinase A (PKA). PKA mediates cellular cAMP signaling in mammals. PKA consists of a tetramer defined by two catalytic subunits and two regulatory subunits, which reversibly bind to cAMP to release the active catalytic subunits (Bossis and Stratakis, 2004). cAMP/PKA mediated-phosphorylation regulates cellular metabolism, proliferation, differentiation, and apoptosis (Bossis and Stratakis, 2004). *PRKAR1A* acts as a tumor suppressor gene, and frameshift mutations result in haploinsufficiency of R1α associated with ***Carney complex*** (Casey et al., 2000). This rare genetic disease is defined by different benign neoplasia, which affects a broad spectrum of tissues including heart, skin, and endocrine tissues, or results in abnormalities of skin complexion and a spotty appearance (Bossis and Stratakis, 2004). Mutant mice carriers for a null mutation in *Prkar1a* present unregulated PKA activity which results in severely reduced male fertility (Burton et al., 2006). Heterozygous mutant males show low sperm count, and mature sperm from the cauda epididymis present aberrant shapes, bended and fragmented tails, detached heads, and an inability to bind to the zona or fuse with zona-free oocytes upon *in vitro* insemination (Burton et al., 2006). It is shown that altered phosphorylation levels of nuclear proteins by PKA lead to stage-I round spermatids developing large nuclear areas devoid of chromatin, resulting in the aberrant phenotype (Burton et al., 2006). Of note, a similar fertility phenotype is observed in Carney complex patients, with sperm presenting abnormal heads and tails comparable to the mutant mice (Burton et al., 2006).

SPERM MOTILITY AND CAPACITATION

Sperm motility and capacitation are key factors that permit the sperm to travel through the female genital tract, transverse the oocyte vestments (which include the cumulus mass and the

zona pellucida, an extracellular glycoprotein matrix surrounding mammalian oocyte), and undergo acrosome exocytosis (Puga Molina et al., 2018; Ritagliati et al., 2018; Bhakta et al., 2019). During sperm capacitation, several modifications including alteration of motility and the induction of acrosomal exocytosis enable sperm to efficiently travel and penetrate the zona pellucida of the egg (Puga Molina et al., 2018). The motility of the sperm is ensured by the flagellar dyneins, the molecular motors that regulate shearing and bending of the sperm flagellum (Neesen et al., 2001). Also, the flagellum is defined by three functional regions, which are the mid-piece, the principal piece, and an end-piece. The principal piece presents the vast majority of characterized ion channels that regulate sperm motility (Lishko and Mannowetz, 2018).

Crucial molecular regulators of sperm motility and capacitation are Dynein Axonemal Heavy Chain 1 (*DNAH1*), the Cystic Fibrosis Transmembrane Conductance Regulator (*CFTR*), the CatSper channel, Glutathione peroxidase 4 (*GPx4*), Nephrocystin 4 (*NPHP4*, coding for Nephroretinin), PKD2, and the solute carrier family 39 member 4 *(SLC39A4,* which encodes a zinc transporter protein known as Zip4).

DNAH1 is a central component of the dynein chains in the flagella of sperm, CFTR and CatSper are ion channels which mediate sperm capacitation prior to fertilization, GPX4 preserves normal mitochondrial function to ensure morphology and sperm progressive motility, Nephroretinin localizes next to the basal bodies of sperm flagella to regulate flagellar motility, PKD2 (described above) regulates directional sperm motility *in vivo* (in *Drosophila*), and ZIP4 regulates zinc uptake which has been reported to be critical during spermatogenesis and in the regulation of sperm motility (in the Japanese eel and in *C. elegans*) (**Figure 2**).

DNAH1 encodes a heavy chain localized to the inner dynein arms of mammalian cilia and flagella. Cilia are comprised of outer and inner dynein arms, which contain light, intermediate, and heavy dynein chains (Neesen et al., 2001). Heavy dynein chains drive the motor function of cilia and flagella through ATP hydrolysis performed in the P loops of the heavy chain. On the N terminus of the heavy chains is located a stem structure which interacts with light and intermediate chains to create bonds and form dynein complexes (Neesen et al., 2001). On the C-terminus, a microtubule binding site serves as a point of attachment for motor function (Neesen et al., 2001). In mice, expression of the *DNAH1* homolog, *Mdhc7,* is observed in developing testis by postnatal day 17. Knockout mice have been generated through disrupting exons responsible for encoding the ATP binding site on dynein heavy chain 7 (Neesen et al., 2001). While heterozygotes do not possess notable impairments to fertility, homozygous knockout males are infertile and fail to produce MDHC7 protein. The majority of mutant sperm are immotile, indicating that the MDHC7 protein is an important component of dynein chains in the sperm flagella (Neesen et al., 2001). However, knockout mouse sperm can fertilize eggs *in vitro*, albeit with low efficiency, though no analyses of sperm-egg binding have been reported (Neesen et al., 2001). In humans, missense or frameshift mutations in *DNAH1* have been associated with ***Primary Ciliary Dyskinesia (PCD)***. PCD manifests as respiratory deficits in affected patients causing sinusitis, bronchitis, and lung damage. Impaired ciliary function disrupts the ability of cilia in the airway to propel mucus

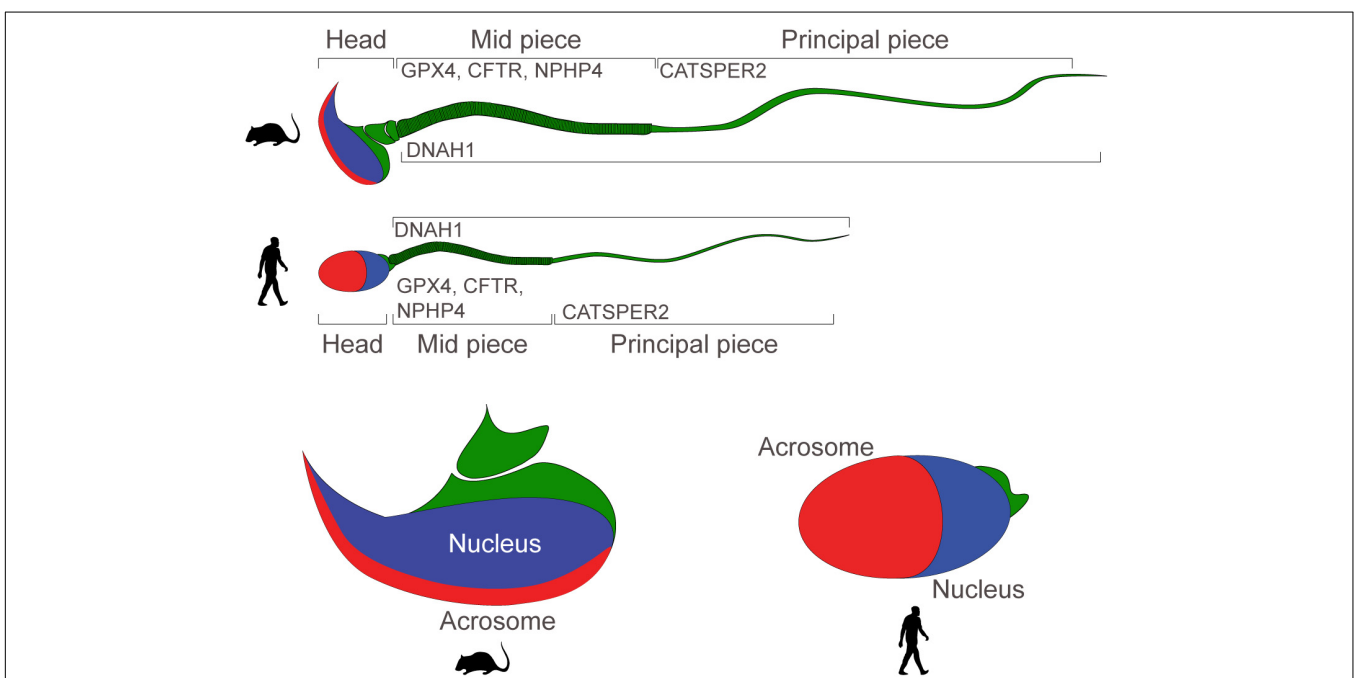

FIGURE 2 | Motility and functionality of mouse and human sperm: schematic portraying the structure of mature mouse and human sperm. Proteins regulating sperm motility and ability to fertilize eggs are expressed in the mid-piece, or in the principal piece. Sperm heads present a nucleus and an acrosome.

(Imtiaz et al., 2015). Impairments to ciliary and flagellar function caused by PCD lead to subfertility in female patients due to reduced functionality of human oviduct cilia. Similarly to mice, infertility associated with PCD in men is correlated with defective sperm motility (Imtiaz et al., 2015); particularly, abnormalities in sperm flagella morphology are observed in patients with homozygous frameshift and nonsense mutations in *DNAH1*. Patients exhibit asthenzoospermia and flagellar morphological abnormalities such as short, coiled, kinked, and absent flagella (Wang et al., 2017). Sperm viability in affected patients ranges from 35 to 75% (Wang et al., 2017).

CFTR, a cAMP-modulated Cl^- channel, controls ion exchange and water secretion/absorption in epithelial tissues. Phosphorylation of the regulatory domain, ATP-binding to the nucleotide-binding domains, or ATP hydrolysis, controls channel activation, and loss-of-function mutations in *CFTR* result in cystic fibrosis (Riordan et al., 1989), the most common genetic disorder in Caucasians (1 individual affected over 3,500 newborns) (Castellani et al., 2009). Absence or defective CFTR leads to reduced epithelia permeability to Cl^-, hence, reduced Cl^- secretion and a decrease of salt on the apical surface ensues, and these conditions fail to recall water to enter the lumen. Also, lack of CFTR leads to non-controlled activities of other channels, such as ENaC, which results in an unregulated absorption of salt from the airway surface liquid. The mucous blanket overlying the epithelia becomes thicker and compresses the cilia, thus delaying mucociliary clearance (Matsui et al., 1998), causing chronic lung infection and inflammation, pancreatic insufficiency, and infertility (Rowe et al., 2005). Indeed, ∼98% of male patients present infertility, mainly due to a congenital bilateral absence of *vas deferens*, leading to obstructive azoospermia (Chillón et al., 1995), although a number of cases have shown non-obstructive azoospermia, oligospermia, asthenospermia, and teratospermia (Chen et al., 2012). Of note, CFTR is expressed in mouse and human sperm (Hernández-González et al., 2007); sperm capacitation is defined by a series of physiological changes that the fertilizing sperm must acquire to fuse with an egg. Mouse and human sperm undergo a capacitation-associated plasma membrane hyperpolarization, which is necessary for the induction of acrosome exocytosis. Of interest, when CFTR is blocked with diphenylamine-2-carboxylic acid, the capacitation-associated hyperpolarization of the sperm membrane is repressed; on the other hand, exposure of sperm to genistein (a CFTR channel activator) induces sperm hyperpolarization under conditions that would not normally support capacitation (Hernández-González et al., 2007). No male germline conditional knockout mouse has been generated thus far, so it has not been possible to test the role of CFTR in spermatogenesis or sperm capacitation prior to fertilization.

CatSper is a flagellar specific and Ca^{2+}-selective channel, which is defined by at least nine different protein –coding genes (*CatSper1–4*, β, γ, δ, ε, and ζ). CatSper1-4 delineates a pore-forming α subunit (Ren et al., 2001; Quill et al., 2003; Qi et al., 2007; Strünker et al., 2011), whereas the transmembrane CatSperβ, CatSperγ, CatSperδ, CatSperε, and cytosolic CatSperζ preserve proper channel structure and function (Liu et al., 2007; Wang et al., 2009; Chung et al., 2011, 2017). CatSper controls sperm hyperactivation by regulating Ca^{2+} signaling through the establishment of nanodomains that are localized throughout the sperm (Chung et al., 2014). Humans homozygous for a deletion in Chromosome 15 spanning *STRC* and *CATSPER2* genes have been associated with ***Deafness-infertility syndrome (DIS)***, which presents itself as an early-onset deafness in males and females with modest symmetric sensorineural hearing loss (Dgany et al., 2002, p. 1); men present normal ejaculate volume, though sperm count, motility, and morphology are affected, which results in asthenoteratozoospermia and male infertility (Dgany et al., 2002, p. 1). Male mice null for 8 of the 9 different protein–coding genes present sperm unable to undergo hyperactivation and fertilize eggs *in vitro* or *in vivo*. In *CatSper*ζ null males, the channel is still functional albeit that CatSper nanodomains are disrupted, resulting in subfertility (Chung et al., 2011, 2014, 2017). CatSper Ca^{2+} nanodomains regulate phosphorylation cascades in the sperm tail, which modify the axonemal motion while initiating the peculiar asymmetric/high-angle bend of hyperactivated tail motility (Chung et al., 2014). Protein tyrosine phosphorylation increases in a time-dependent fashion during sperm capacitation (Visconti et al., 1995), with the majority of tyrosine phosphorylation observed in the axoneme and absence of CatSper leading to an increase of tyrosine phosphorylation, which also mislocalizes to periaxonemal regions (Chung et al., 2014). The inability of sperm to undergo hyperactivation, together with the disruption of the capacitation-initiated tyrosine phosphorylation pathway, makes sperm unable to fertilize eggs *in vivo* or *in vitro* (Chung et al., 2014).

GPX4, a member of the selenoproteins glutathione peroxidase family, uses glutathione as an electron donor to catalyze the reduction of hydroperoxides in membrane lipids (e.g., phospholipids, cholesterol, and cholestryl ester) (Brigelius-Flohé, 1999). GPX4 preserves normal mitochondrial function and suppresses apoptosis, while repairing oxidation damage to cardiolipin (a phospholipid constituting ∼20% of mitochondria lipid composition) in a number of organs, including male gonads. Gene deletion of *GPX4* in null mice leads to post-implantation embryo lethality (E7.5) (Imai et al., 2003). Tamoxifen-inducible inactivation of *GPX4* in neuron-specific conditional knockout newborn mouse pups leads to 12/15-lipoxygenase-derived lipid peroxidation, which in turn triggers apoptosis-inducing factor (AIF)-mediated cell death. Neuron-specific *GPX4* depletion leads to severe neurodegeneration with presence of pyknotic cells in the pyramidal layer of the CA3 region of the hippocampus and pups were euthanized on postnatal day 13 (Seiler et al., 2008). In humans, loss-of-function mutations (i.e., frameshift or nonsense) in the *GPX4* gene are associated with the manifestation of ***Spondylometaphyseal dysplasia Sedaghatian type (SMDS)***. SMDS is a rare disease that leads to neonatal death due to respiratory failure. This genetic condition is defined by severe metaphyseal chondrodysplasia, delayed epiphyseal ossification, platyspondyly, irregular iliac crests, and pulmonary hemorrhage. Moreover, defective development of the central nervous system is observed, and in particular abnormal neuronal migration, agenesis of the corpus callosum, pronounced frontotemporal pachygyria, simplified gyral pattern, partial lissencephaly, and severe cerebellar hypoplasia (Smith et al., 2014). GPX4 expression

is also enriched in the mitochondria of testis and sperm. A spermatocyte-specific *GPX4* knockout mouse line shows male infertility due to oligoasthenozoospermia, and decreased sperm progressive motility associated with impaired mitochondrial membrane potential and cellular abnormalities (e.g., hairpin-like flagella bend at the midpiece, swelling of mitochondria) (Imai et al., 2009). *GPX4* appears to play a role in human spermatogenesis as well: a significant reduction in *GPX4* expression is found in a number of infertile oligospermic men (Imai et al., 2001).

NPHP4 encodes a 1426 amino acid-long protein (also known as Nephroretinin), presenting a proline-rich domain between amino acids 458–514. NPHP4 localizes to the basal bodies of the primary cilia in polarized epithelial tubular cells, in the proximity of the cortical actin cytoskeleton, and to the centrosomes of dividing cells (Mollet et al., 2002). Molecular binding partners of NPHP4 are NPHP1, RP GTPase regulator interacting protein 1 (RPGRIP1) (Roepman et al., 2005), NPHP8 (alias of RPGRIP1L) (Delous et al., 2007) and Retinitis pigmentosa GTPase regulator (RPGR) (Murga-Zamalloa et al., 2010), proteins that regulate ciliary function. Homozygous missense or heterozygous frameshift mutations in *NPHP4* have been associated with ***Nephronophthisis***, an autosomal recessive kidney disease mainly affecting children and young adults (Strauss and Sommers, 1967) that presents with polyuria, polydipsia, and anemia (Wolf, 2015); it has been associated with different syndromes, including the Senior–Loken syndrome (SLSD) with retinitis pigmentosa (RP), Joubert syndrome with RP, cerebellar and brainstem malformations, and intellectual disability (Otto et al., 2002, 2005; Parisi et al., 2004). Mutant mice homozygous for a nonsense mutation in the *Nphp4* gene present male infertility (Won et al., 2011) with reduced sperm counts (98% reduction compared to fertile controls), scarce motility, and virtually absent progressive motility (Won et al., 2011). Electron microscopy of cross-section and longitudinal images of the flagella reveal intact normal nine microtubule doublets encircling a central microtubule pair in the mutant flagellar axoneme. NPHP4 normally localizes next to the basal bodies in the testicular spermatozoa and spermatids, and its absence seems to be the cause of the defective phenotype (Won et al., 2011): these sperm are unable to fertilize eggs *in vitro* or *in vivo* (Won et al., 2011).

Of note, PKD2 (associated with ADPKD, described above) regulates directional sperm motility in *Drosophila*, and null males present normal spermatogenesis but are unable to localize the egg *in vivo* (Gao et al., 2003).

SLC39A4 encodes a zinc transporter protein known as Zip4 which is expressed in the human intestine, colon, ovary, and testis (Küry et al., 2002; Wang et al., 2004; Dufner-Beattie et al., 2007). In humans, missense mutations in *SLC39A4* affecting the ZIP4 transmembrane domains have been associated with ***Acrodermatitis enteropathica*** (***AE***), a genetic condition characterized by concurrent manifestation of diarrhea, dermatitis, alopecia, skin lesions, growth retardation, impaired wound healing, and male hypogonadism together with low sperm count (Maverakis et al., 2007) due to defective cellular zinc uptake. Deletion of *Slc39a4* in mice results in embryonic lethality (by embryonic day 10) (Dufner-Beattie et al., 2007), whereas heterozygous null mice present incomplete lethality prior to weaning. Those that survive show hydrocephalus, incomplete eye development, and growth retardation (Dufner-Beattie et al., 2007). In humans, hormone replacement therapy restores sperm count, improves seminiferous tubule volume, and stimulates spermatogenesis in azoospermic patients (Vicari et al., 1992). The role of zinc in mammalian spermatogenesis and fertilization has not been well described, however, it has been shown that zinc is necessary for proper spermatogenesis in the Japanese eel (*Anguilla japonica*), during which it accumulates in the mitochondria of spermatogonia and developing sperm and regulates sperm motility (Yamaguchi et al., 2009). Also, zinc controls sperm activation in *C. elegans* by inducing immotile spermatids to rapidly develop into mature, motile sperm (Zhao et al., 2018).

SPERM PASSAGE THROUGH THE EPIDIDYMIS

The epididymis is defined by four anatomical regions, the initial segment: the caput, the corpus, and the cauda, the latter being the region connected to the *vas deferens*. Each of these regions present a tissue-enriched gene expression profile that is important to ensure proper concentrations of luminal ions, which are important for the maturation of the fertilizing sperm (Belleannée et al., 2012).

The Solute Carrier Family 22 Member 5 (*SLC22A5*) gene codes for the Organic Cation Transporter 2 (OCTN2), a transporter of organic cations and carnitine (Wu et al., 1999). OCTN2 normally transports an array of organic cations, however, its affinity to carnitine and the ability to transport carnitine increases in the presence of sodium (Wu et al., 1999). OCTN2 is expressed in the kidneys and other tissues including the heart, placenta, brain, testis, and epididymis (Wu et al., 1999; Rodríguez et al., 2002). In humans, homozygous deletions, splice-site, or frameshift mutations in *SLC22A5* have been associated with ***Primary systemic carnitine deficiency*** (***SCD***), an autosomal recessive disorder characterized by negligible cellular uptake of carnitine in different tissues leading to progressive cardiomyopathy, skeletal myopathy, hypoglycaemia, and hyperammonaemia (Nezu et al., 1999). To become functionally mature and capable of fertilizing eggs, mammalian sperm transverse the epididymis, where glycoproteins, lipids and inorganic compounds assist with the maturation of sperm (Gervasi and Visconti, 2017). During sperm transport through the epididymis, carnitine acts as cofactor for the transport of long-chain fatty acid in the mitochondria; here, long-chain fatty acid undergoes beta-oxidation, producing acetyl-CoA, which is important for sperm to acquire motility in the distal epididymis (Dacheux and Dacheux, 2014). A mutant mouse (the juvenile visceral steatosis or *jvs* mouse) homozygous for a missense mutation in *Slc22a5* that abrogates carnitine transport (Nezu et al., 1999), presents an anatomically deformed epididymis and male infertility (Toshimori et al., 1999); in particular, the duct of the proximal epididymis accumulates an anomalous number of immature sperm, which occasionally

causes the rupture of the epididymal epithelium, with sperm being reversed into the stroma (Toshimori et al., 1999). These phenotypic consequences lead to obstructive azoospermia, which is reversible with exogenous administration of L-carnitine (Toshimori et al., 1999).

PKD1 (associated with ADPKD, described above) expression is also enriched in the epididymis (Nie and Arend, 2013). In mice, *Pkd1* null male mice present cystic dilation of the efferent ducts (derivatives of the mesonephric tubules), with the development of the epididymis being severely delayed or arrested (Nie and Arend, 2013).

CONCLUSION

By the age of 25, approximately 5.3% of live-born humans develop genetic diseases (Baird et al., 1988), some of which result from deleterious mutations in genes that also regulate different aspects of gametogenesis and fertilization; plausibly the role of these genes in reproduction may be overlooked, as genetic conditions oftentimes are so severe that associated fertility disorders can go disregarded. Moreover, the clinical manifestation of a number of disorders have been reported after the appearance of a fertility phenotype (Eisenberg et al., 2014, 2016; Tarín et al., 2015). Thus, certain defective fertility phenotypes may represent a marker for future severe conditions. For example, among the conditions reviewed here, ADPKD incidence peak has been reported between the ages of 30 and 40 (Pei and Watnick, 2010); hence, an early diagnosis of male infertility associated with azoospermia or necrospermia (Nie and Arend, 2013, p. 1), or Sertoli cell only syndrome (Nygaard et al., 2015) could represent a possible red flag for a later onset of the ADPKD (Pei and Watnick, 2010) and genetic testing might be required. To understand better the genetic intersection between rare disorders and defective spermatogenesis, one could establish mouse lines expressing the exact mutation that has been associated with the aberrant phenotypes in humans. Indeed, as an increasing number of individual human genomes has lately become available (1000 Genomes Project Consortium et al., 2015; Wang et al., 2020), the functional characterization of novel genes (Kiyozumi et al., 2020; Noda et al., 2020), or putative deleterious variants (Singh and Schimenti, 2015) in transgenic animal models, will allow us to identify more comorbidities between gametogenesis or fertilization defects and rare genetic disorders (Vaquer et al., 2013; Hmeljak and Justice, 2019).

AUTHOR CONTRIBUTIONS

EL and MA conceived the study and wrote the manuscript. EL, LG, HB, and CG performed the database analyses and literature research. All the authors contributed to the article and approved the submitted version.

FUNDING

This study was supported by the Department of Biological Science and by the Office of Research and Sponsored Programs at the University of Tulsa (Faculty Research Grant and Faculty Research Summer Fellowship) to MA, and the University of Tulsa, Tulsa Undergraduate Research Challenge (TURC) program to EL.

ACKNOWLEDGMENTS

We are thankful to our colleagues and fellow students in the lab and in the department for helpful insights and discussions. We apologize to colleagues whose work could not be referenced herein due to space limitations.

REFERENCES

1000 Genomes Project Consortium, Auton, A., Brooks, L. D., Durbin, R. M., Garrison, E. P., Kang, H. M., et al. (2015). A global reference for human genetic variation. *Nature* 526, 68–74. doi: 10.1038/nature15393

Aitken, R. J. (2020). Impact of oxidative stress on male and female germ cells: implications for fertility. *Reprod. Camb. Engl.* 159, R189–R201. doi: 10.1530/REP-19-0452

Alazami, A. M., Al-Saif, A., Al-Semari, A., Bohlega, S., Zlitni, S., Alzahrani, F., et al. (2008). Mutations in C2orf37, encoding a nucleolar protein, cause hypogonadism, alopecia, diabetes mellitus, mental retardation, and extrapyramidal syndrome. *Am. J. Hum. Genet.* 83, 684–691. doi: 10.1016/j.ajhg.2008.10.018

Ali, A., Mistry, B. V., Ahmed, H. A., Abdulla, R., Amer, H. A., Prince, A., et al. (2018). Deletion of DDB1- and CUL4- associated factor-17 (Dcaf17) gene causes spermatogenesis defects and male infertility in mice. *Sci. Rep.* 8:9202. doi: 10.1038/s41598-018-27379-0

Assies, J., Gooren, L. J., Van Geel, B., and Barth, P. G. (1997). Signs of testicular insufficiency in adrenomyeloneuropathy and neurologically asymptomatic X-linked adrenoleukodystrophy: a retrospective study. *Int. J. Androl.* 20, 315–321. doi: 10.1046/j.1365-2605.1997.00066.x

Aversa, A., Palleschi, S., Cruccu, G., Silvestroni, L., Isidori, A., and Fabbri, A. (1998). Rapid decline of fertility in a case of adrenoleukodystrophy. *Hum. Reprod. Oxf. Engl.* 13, 2474–2479. doi: 10.1093/humrep/13.9.2474

Avidor-Reiss, T., and Turner, K. (2019). The evolution of centriole structure: heterochrony, neoteny, and hypermorphosis. *Results Probl. Cell Differ.* 67, 3–15. doi: 10.1007/978-3-030-23173-6_1

Baird, P. A., Anderson, T. W., Newcombe, H. B., and Lowry, R. B. (1988). Genetic disorders in children and young adults: a population study. *Am. J. Hum. Genet.* 42, 677–693.

Baker, D. J., Jeganathan, K. B., Cameron, J. D., Thompson, M., Juneja, S., Kopecka, A., et al. (2004). BubR1 insufficiency causes early onset of aging-associated phenotypes and infertility in mice. *Nat. Genet.* 36, 744–749. doi: 10.1038/ng1382

Bao, J., Tang, C., Yuan, S., Porse, B. T., and Yan, W. (2015). UPF2, a nonsense-mediated mRNA decay factor, is required for prepubertal Sertoli cell development and male fertility by ensuring fidelity of the transcriptome. *Dev. Camb. Engl.* 142, 352–362. doi: 10.1242/dev.115642

Belleannée, C., Thimon, V., and Sullivan, R. (2012). Region-specific gene expression in the epididymis. *Cell Tissue Res.* 349, 717–731. doi: 10.1007/s00441-012-1381-0

Bhakta, H. H., Refai, F. H., and Avella, M. A. (2019). The molecular mechanisms mediating mammalian fertilization. *Development* 146:dev176966. doi: 10.1242/dev.176966

Bossis, I., and Stratakis, C. A. (2004). Minireview: PRKAR1A: normal and abnormal functions. *Endocrinology* 145, 5452–5458. doi: 10.1210/en.2004-0900

Bottani, A., Orrico, A., Galli, L., Karam, O., Haenggeli, C.-A., Ferey, S., et al. (2007). Unilateral focal polymicrogyria in a patient with classical Aarskog-Scott

syndrome due to a novel missense mutation in an evolutionary conserved RhoGEF domain of the faciogenital dysplasia gene FGD1. *Am. J. Med. Genet. A* 143A, 2334–2338. doi: 10.1002/ajmg.a.31733

Brauns, A.-K., Heine, M., Tödter, K., Baumgart-Vogt, E., Lüers, G. H., and Schumacher, U. (2019). A defect in the peroxisomal biogenesis in germ cells induces a spermatogenic arrest at the round spermatid stage in mice. *Sci. Rep.* 9:9553. doi: 10.1038/s41598-019-45991-6

Brennemann, W., Köhler, W., Zierz, S., and Klingmüller, D. (1997). Testicular dysfunction in adrenomyeloneuropathy. *Eur. J. Endocrinol.* 137, 34–39. doi: 10.1530/eje.0.1370034

Brigelius-Flohé, R. (1999). Tissue-specific functions of individual glutathione peroxidases. *Free Radic. Biol. Med.* 27, 951–965. doi: 10.1016/s0891-5849(99)00173-2

Buffone, M. G., Hirohashi, N., and Gerton, G. L. (2014). Unresolved questions concerning mammalian sperm acrosomal exocytosis. *Biol. Reprod.* 90:112. doi: 10.1095/biolreprod.114.117911

Burton, K. A., McDermott, D. A., Wilkes, D., Poulsen, M. N., Nolan, M. A., Goldstein, M., et al. (2006). Haploinsufficiency at the Protein Kinase A RIα gene locus leads to fertility defects in male mice and men. *Mol. Endocrinol. Baltim. Md* 20, 2504–2513. doi: 10.1210/me.2006-0060

Cahill, D. P., Lengauer, C., Yu, J., Riggins, G. J., Willson, J. K. V., Markowitz, S. D., et al. (1998). Mutations of mitotic checkpoint genes in human cancers. *Nature* 392, 300–303. doi: 10.1038/32688

Casey, M., Vaughan, C. J., He, J., Hatcher, C. J., Winter, J. M., Weremowicz, S., et al. (2000). Mutations in the protein kinase A R1alpha regulatory subunit cause familial cardiac myxomas and Carney complex. *J. Clin. Invest.* 106, R31–R38. doi: 10.1172/JCI10841

Castellani, C., Picci, L., Tamanini, A., Girardi, P., Rizzotti, P., and Assael, B. M. (2009). Association between carrier screening and incidence of cystic fibrosis. *JAMA* 302, 2573–2579. doi: 10.1001/jama.2009.1758

Chen, H., Ruan, Y. C., Xu, W. M., Chen, J., and Chan, H. C. (2012). Regulation of male fertility by CFTR and implications in male infertility. *Hum. Reprod. Update* 18, 703–713. doi: 10.1093/humupd/dms027

Chen, Q., Ke, H., Luo, X., Wang, L., Wu, Y., Tang, S., et al. (2020). Rare deleterious BUB1B variants induce premature ovarian insufficiency and early menopause. *Hum. Mol. Genet.* 29, 2698–2707. doi: 10.1093/hmg/ddaa153

Chillón, M., Casals, T., Mercier, B., Bassas, L., Lissens, W., Silber, S., et al. (1995). Mutations in the cystic fibrosis gene in patients with congenital absence of the vas deferens. *N. Engl. J. Med.* 332, 1475–1480. doi: 10.1056/NEJM199506013322204

Chung, J.-J., Miki, K., Kim, D., Shim, S.-H., Shi, H. F., Hwang, J. Y., et al. (2017). CatSperζ regulates the structural continuity of sperm Ca2+ signaling domains and is required for normal fertility. *eLife* 6:e23082. doi: 10.7554/eLife.23082

Chung, J.-J., Navarro, B., Krapivinsky, G., Krapivinsky, L., and Clapham, D. E. (2011). A novel gene required for male fertility and functional CATSPER channel formation in spermatozoa. *Nat. Commun.* 2:153. doi: 10.1038/ncomms1153

Chung, J.-J., Shim, S.-H., Everley, R. A., Gygi, S. P., Zhuang, X., and Clapham, D. E. (2014). Structurally distinct Ca(2+) signaling domains of sperm flagella orchestrate tyrosine phosphorylation and motility. *Cell* 157, 808–822. doi: 10.1016/j.cell.2014.02.056

Da Ros, V. G., Muñoz, M. W., Battistone, M. A., Brukman, N. G., Carvajal, G., Curci, L., et al. (2015). From the epididymis to the egg: participation of CRISP proteins in mammalian fertilization. *Asian J. Androl.* 17, 711–715. doi: 10.4103/1008-682X.155769

Dacheux, J.-L., and Dacheux, F. (2014). New insights into epididymal function in relation to sperm maturation. *Reproduction* 147, R27–R42. doi: 10.1530/REP-13-0420

Danaci, M., Akpolat, T., Baştemir, M., Sarikaya, S., Akan, H., Selçuk, M. B., et al. (1998). The prevalence of seminal vesicle cysts in autosomal dominant polycystic kidney disease. *Nephrol. Dial. Transplant.* 13, 2825–2828. doi: 10.1093/ndt/13.11.2825

Delous, M., Baala, L., Salomon, R., Laclef, C., Vierkotten, J., Tory, K., et al. (2007). The ciliary gene RPGRIP1L is mutated in cerebello-oculo-renal syndrome (Joubert syndrome type B) and Meckel syndrome. *Nat. Genet.* 39, 875–881. doi: 10.1038/ng2039

Demain, L. A. M., Urquhart, J. E., O'Sullivan, J., Williams, S. G., Bhaskar, S. S., Jenkinson, E. M., et al. (2017). Expanding the genotypic spectrum of Perrault syndrome. *Clin. Genet.* 91, 302–312. doi: 10.1111/cge.12776

Dgany, O., Avidan, N., Delaunay, J., Krasnov, T., Shalmon, L., Shalev, H., et al. (2002). Congenital dyserythropoietic anemia type i is caused by mutations in Codanin-1. *Am. J. Hum. Genet.* 71, 1467–1474. doi: 10.1086/344781

Küry, S., Bézieau, S., Giraudet, S., Kharfi, M., Kamoun, R., et al. (2002). Identification of SLC39A4, a gene involved in acrodermatitis enteropathica. *Nat. Genet.* 31, 239–240. doi: 10.1038/ng913

Dufner-Beattie, J., Weaver, B. P., Geiser, J., Bilgen, M., Larson, M., Xu, W., et al. (2007). The mouse acrodermatitis enteropathica gene Slc39a4 (Zip4) is essential for early development and heterozygosity causes hypersensitivity to zinc deficiency. *Hum. Mol. Genet.* 16, 1391–1399. doi: 10.1093/hmg/ddm088

Dursun, F., Mohamoud, H. S. A., Karim, N., Naeem, M., Jelani, M., and Kırmızıbekmez, H. (2016). A novel missense mutation in the Clpp gene causing perrault syndrome type 3 in a Turkish Family. *J. Clin. Res. Pediatr. Endocrinol.* 8, 472–477. doi: 10.4274/jcrpe.2717

Eisenberg, M. L., Li, S., Behr, B., Cullen, M. R., Galusha, D., Lamb, D. J., et al. (2014). Semen quality, infertility and mortality in the USA. *Hum. Reprod. Oxf. Engl.* 29, 1567–1574. doi: 10.1093/humrep/deu106

Eisenberg, M. L., Sundaram, R., Maisog, J., and Buck Louis, G. M. (2016). Diabetes, medical comorbidities and couple fecundity. *Hum. Reprod. Oxf. Engl.* 31, 2369–2376. doi: 10.1093/humrep/dew200

Estrada, L., Caron, E., and Gorski, J. L. (2001). Fgd1, the Cdc42 guanine nucleotide exchange factor responsible for faciogenital dysplasia, is localized to the subcortical actin cytoskeleton and Golgi membrane. *Hum. Mol. Genet.* 10, 485–496. doi: 10.1093/hmg/10.5.485

Feng, H., Gu, Z.-Y., Li, Q., Liu, Q.-H., Yang, X.-Y., and Zhang, J.-J. (2019). Identification of significant genes with poor prognosis in ovarian cancer via bioinformatical analysis. *J. Ovarian Res.* 12, 35. doi: 10.1186/s13048-019-0508-2

Fishman, E. L., Jo, K., Nguyen, Q. P. H., Kong, D., Royfman, R., Cekic, A. R., et al. (2018). A novel atypical sperm centriole is functional during human fertilization. *Nat. Commun.* 9:2210. doi: 10.1038/s41467-018-04678-8

Gaffney, E. A., Gadêlha, H., Smith, D. J., Blake, J. R., and Kirkman-Brown, J. C. (2011). Mammalian sperm motility: observation and theory. *Annu. Rev. Fluid Mech.* 43, 501–528. doi: 10.1146/annurev-fluid-121108-145442

Gao, Z., Ruden, D. M., and Lu, X. (2003). PKD2 cation channel is required for directional sperm movement and male fertility. *Curr. Biol.* 13, 2175–2178. doi: 10.1016/j.cub.2003.11.053

Geister, K. A., Brinkmeier, M. L., Cheung, L. Y., Wendt, J., Oatley, M. J., Burgess, D. L., et al. (2015). LINE-1 mediated insertion into Poc1a (Protein of Centriole 1 A) causes growth insufficiency and male infertility in mice. *PLoS Genet.* 11:e1005569. doi: 10.1371/journal.pgen.1005569

German Pasteris, N., Cadle, A., Logie, L. J., Porteous, M. E. M., Schwartz, C. E., Stevenson, R. E., et al. (1994). Isolation and characterization of the faciogenital dysplasia (Aarskog-Scott syndrome) gene: a putative RhoRac guanine nucleotide exchange factor. *Cell* 79, 669–678. doi: 10.1016/0092-8674(94)90552-5

Gervasi, M. G., and Visconti, P. E. (2017). Molecular changes and signaling events occurring in sperm during epididymal maturation. *Andrology* 5, 204–218. doi: 10.1111/andr.12320

Gispert, S., Parganlija, D., Dröse, S., Wittig, I., Mittelbronn, M., et al. (2013). Loss of mitochondrial peptidase Clpp leads to infertility, hearing loss plus growth retardation via accumulation of CLPX, mtDNA and inflammatory factors. *Hum. Mol. Genet.* 22, 4871–4887. doi: 10.1093/hmg/ddt338

Greer, C., Bhakta, H., Ghanem, L., Refai, F., Linn, E., and Avella, M. (2021). Deleterious variants in genes regulating mammalian reproduction in Neanderthals, Denisovans and extant humans. *Hum. Reprod. Oxf. Engl.* [Epub ahead of print] doi: 10.1093/humrep/deaa347

Gregory, M. K., Cleland, L. G., and James, M. J. (2013). Molecular basis for differential elongation of omega-3 docosapentaenoic acid by the rat Elovl5 and Elovl2. *J. Lipid Res.* 54, 2851–2857. doi: 10.1194/jlr.M041368

Hanks, S., Coleman, K., Reid, S., Plaja, A., Firth, H., Fitzpatrick, D., et al. (2004). Constitutional aneuploidy and cancer predisposition caused by biallelic mutations in BUB1B. *Nat. Genet.* 36, 1159–1161. doi: 10.1038/ng1449

Harris, P. C., and Torres, V. E. (2009). Polycystic kidney disease. *Annu. Rev. Med.* 60, 321–337. doi: 10.1146/annurev.med.60.101707.125712

Hartwell, L. H., and Weinert, T. A. (1989). Checkpoints: controls that ensure the order of cell cycle events. *Science* 246, 629–634. doi: 10.1126/science.2683079

Hernández-González, E. O., Treviño, C. L., Castellano, L. E., Vega-Beltrán, J. L., de la, Ocampo, A. Y., Wertheimer, E., et al. (2007). Involvement of cystic fibrosis

transmembrane conductance regulator in mouse sperm capacitation. *J. Biol. Chem.* 282, 24397–24406. doi: 10.1074/jbc.M701603200

Hirose, M., Honda, A., Fulka, H., Tamura-Nakano, M., Matoba, S., Tomishima, T., et al. (2020). Acrosin is essential for sperm penetration through the zona pellucida in hamsters. *Proc. Natl. Acad. Sci. U.S.A.* 117, 2513–2518. doi: 10.1073/pnas.1917595117

Hmeljak, J., and Justice, M. J. (2019). From gene to treatment: supporting rare disease translational research through model systems. *Dis. Model. Mech.* 12:dmm039271. doi: 10.1242/dmm.039271

Hsieh-Li, H. M., Chang, J.-G., Jong, Y.-J., Wu, M.-H., Wang, N. M., Tsai, C. H., et al. (2000). A mouse model for spinal muscular atrophy. *Nat. Genet.* 24, 66–70. doi: 10.1038/71709

Huang, F. W., Pinkus, J. L., Pinkus, G. S., Fleming, M. D., and Andrews, N. C. (2005). A mouse model of juvenile hemochromatosis. *J. Clin. Invest.* 115, 2187–2191. doi: 10.1172/JCI25049

Hughes, J., Ward, C. J., Peral, B., Aspinwall, R., Clark, K., San Millán, J. L., et al. (1995). The polycystic kidney disease 1 (PKD1) gene encodes a novel protein with multiple cell recognition domains. *Nat. Genet.* 10, 151–160. doi: 10.1038/ng0695-151

Imai, H., Hakkaku, N., Iwamoto, R., Suzuki, J., Suzuki, T., Tajima, Y., et al. (2009). Depletion of selenoprotein GPx4 in spermatocytes causes male infertility in mice. *J. Biol. Chem.* 284, 32522–32532. doi: 10.1074/jbc.M109.016139

Imai, H., Hirao, F., Sakamoto, T., Sekine, K., Mizukura, Y., Saito, M., et al. (2003). Early embryonic lethality caused by targeted disruption of the mouse PHGPx gene. *Biochem. Biophys. Res. Commun.* 305, 278–286. doi: 10.1016/s0006-291x(03)00734-4

Imai, H., Suzuki, K., Ishizaka, K., Ichinose, S., Oshima, H., Okayasu, I., et al. (2001). Failure of the expression of phospholipid hydroperoxide glutathione peroxidase in the spermatozoa of human infertile males. *Biol. Reprod.* 64, 674–683. doi: 10.1095/biolreprod64.2.674

Imtiaz, F., Allam, R., Ramzan, K., and Al-Sayed, M. (2015). Variation in DNAH1 may contribute to primary ciliary dyskinesia. *BMC Med. Genet.* 16:14. doi: 10.1186/s12881-015-0162-5

Jackson, S., and Xiong, Y. (2009). CRL4s: the CUL4-RING E3 ubiquitin ligases. *Trends Biochem. Sci.* 34, 562–570. doi: 10.1016/j.tibs.2009.07.002

Jacquemin, V., Rieunier, G., Jacob, S., Bellanger, D., d'Enghien, C. D., Laugé, A., et al. (2012). Underexpression and abnormal localization of ATM products in ataxia telangiectasia patients bearing ATM missense mutations. *Eur. J. Hum. Genet.* 20, 305–312. doi: 10.1038/ejhg.2011.196

Jazayeri, A., Falck, J., Lukas, C., Bartek, J., Smith, G. C. M., Lukas, J., et al. (2006). ATM- and cell cycle-dependent regulation of ATR in response to DNA double-strand breaks. *Nat. Cell Biol.* 8, 37–45. doi: 10.1038/ncb1337

Jenkinson, E. M., Rehman, A. U., Walsh, T., Clayton-Smith, J., Lee, K., Morell, R. J., et al. (2013). Perrault syndrome is caused by recessive mutations in CLPP, encoding a mitochondrial ATP-Dependent chambered protease. *Am. J. Hum. Genet.* 92, 605–613. doi: 10.1016/j.ajhg.2013.02.013

Kato, R., Maeda, T., Akaike, T., and Tamai, I. (2006). Characterization of novel Na+-dependent nucleobase transport systems at the blood-testis barrier. *Am. J. Physiol. Endocrinol. Metab.* 290, E968–E975. doi: 10.1152/ajpendo.00160.2005

Khire, A., Jo, K. H., Kong, D., Akhshi, T., Blachon, S., Cekic, A. R., et al. (2016). Centriole remodeling during spermiogenesis in Drosophila. *Curr. Biol.* 26, 3183–3189. doi: 10.1016/j.cub.2016.07.006

Kierszenbaum, A. L., Rivkin, E., and Tres, L. L. (2003). Acroplaxome, an F-actin-keratin-containing plate, anchors the acrosome to the nucleus during shaping of the spermatid head. *Mol. Biol. Cell* 14, 4628–4640. doi: 10.1091/mbc.e03-04-0226

Kiyozumi, D., Noda, T., Yamaguchi, R., Tobita, T., Matsumura, T., Shimada, K., et al. (2020). NELL2-mediated lumicrine signaling through OVCH2 is required for male fertility. *Science* 368, 1132–1135. doi: 10.1126/science.aay5134

Lange, J., Pan, J., Cole, F., Thelen, M. P., Jasin, M., and Keeney, S. (2011). ATM controls meiotic double-strand-break formation. *Nature* 479, 237–240. doi: 10.1038/nature10508

Law, N. C., Oatley, M. J., and Oatley, J. M. (2019). Developmental kinetics and transcriptome dynamics of stem cell specification in the spermatogenic lineage. *Nat. Commun.* 10:2787. doi: 10.1038/s41467-019-10596-0

Lebel, R. R., May, M., Pouls, S., Lubs, H. A., Stevenson, R. E., and Schwartz, C. E. (2002). Non-syndromic X-linked mental retardation associated with a missense mutation (P312L) in the FGD1 gene. *Clin. Genet.* 61, 139–145. doi: 10.1034/j.1399-0004.2002.610209.x

Lee, J., and Zhou, P. (2007). DCAFs, the missing link of the CUL4-DDB1 ubiquitin ligase. *Mol. Cell* 26, 775–780. doi: 10.1016/j.molcel.2007.06.001

Lefebvre, S., Bürglen, L., Reboullet, S., Clermont, O., Burlet, P., Viollet, L., et al. (1995). Identification and characterization of a spinal muscular atrophy-determining gene. *Cell* 80, 155–165. doi: 10.1016/0092-8674(95)90460-3

Lehti, M. S., and Sironen, A. (2016). Formation and function of the manchette and flagellum during spermatogenesis. *Reprod. Camb. Engl.* 151, R43–R54. doi: 10.1530/REP-15-0310

Leichtmann-Bardoogo, Y., Cohen, L. A., Weiss, A., Marohn, B., Schubert, S., Meinhardt, A., et al. (2012). Compartmentalization and regulation of iron metabolism proteins protect male germ cells from iron overload. *Am. J. Physiol. Endocrinol. Metab.* 302, E1519–E1530. doi: 10.1152/ajpendo.00007.2012

Limwongse, C., Schwartz, S., Bocian, M., and Robin, N. H. (1999). Child with mosaic variegated aneuploidy and embryonal rhabdomyosarcoma. *Am. J. Med. Genet.* 82, 20–24. doi: 10.1002/(SICI)1096-8628(19990101)82:1<20::AID-AJMG4<3.0.CO;2-5

Lin, F., Hiesberger, T., Cordes, K., Sinclair, A. M., Goldstein, L. S. B., Somlo, S., et al. (2003). Kidney-specific inactivation of the KIF3A subunit of kinesin-II inhibits renal ciliogenesis and produces polycystic kidney disease. *Proc. Natl. Acad. Sci. U.S.A.* 100, 5286–5291. doi: 10.1073/pnas.0836980100

Lishko, P. V., and Mannowetz, N. (2018). CatSper: a unique calcium channel of the sperm flagellum. *Curr. Opin. Physiol.* 2, 109–113. doi: 10.1016/j.cophys.2018.02.004

Liu, J., Xia, J., Cho, K.-H., Clapham, D. E., and Ren, D. (2007). CatSperbeta, a novel transmembrane protein in the CatSper channel complex. *J. Biol. Chem.* 282, 18945–18952. doi: 10.1074/jbc.M701083200

Lorson, C. L., Hahnen, E., Androphy, E. J., and Wirth, B. (1999). A single nucleotide in the SMN gene regulates splicing and is responsible for spinal muscular atrophy. *Proc. Natl. Acad. Sci. U.S.A.* 96, 6307–6311. doi: 10.1073/pnas.96.11.6307

Lu, J.-F., Lawler, A. M., Watkins, P. A., Powers, J. M., Moser, A. B., Moser, H. W., et al. (1997). A mouse model for X-linked adrenoleukodystrophy. *Proc. Natl. Acad. Sci. U.S.A.* 94, 9366–9371.

Lu, S., Zong, C., Fan, W., Yang, M., Li, J., Chapman, A. R., et al. (2012). Probing meiotic recombination and aneuploidy of single sperm cells by whole-genome sequencing. *Science* 338, 1627–1630. doi: 10.1126/science.1229112

Matsui, H., Grubb, B. R., Tarran, R., Randell, S. H., Gatzy, J. T., Davis, C. W., et al. (1998). Evidence for periciliary liquid layer depletion, not abnormal ion composition, in the pathogenesis of cystic fibrosis airways disease. *Cell* 95, 1005–1015. doi: 10.1016/s0092-8674(00)81724-9

Maverakis, E., Fung, M. A., Lynch, P. J., Draznin, M., Michael, D. J., Ruben, B., et al. (2007). Acrodermatitis enteropathica and an overview of zinc metabolism. *J. Am. Acad. Dermatol.* 56, 116–124. doi: 10.1016/j.jaad.2006.08.015

McDermott, J. H., and Walsh, C. H. (2005). Hypogonadism in hereditary hemochromatosis. *J. Clin. Endocrinol. Metab.* 90, 2451–2455. doi: 10.1210/jc.2004-0980

Meschede, D., Rolf, C., Neugebauer, D. C., Horst, J., and Nieschlag, E. (1996). Sperm acrosome defects in a patient with Aarskog-Scott syndrome. *Am. J. Med. Genet.* 66, 340–342.

Mochizuki, T., Wu, G., Hayashi, T., Xenophontos, S. L., Veldhuisen, B., Saris, J. J., et al. (1996). PKD2, a gene for polycystic kidney disease that encodes an integral membrane protein. *Science* 272, 1339–1342. doi: 10.1126/science.272.5266.1339

Molho-Pessach, V., Lerer, I., Abeliovich, D., Agha, Z., Abu Libdeh, A., Broshtilova, V., et al. (2008). The H syndrome is caused by mutations in the nucleoside transporter hENT3. *Am. J. Hum. Genet.* 83, 529–534. doi: 10.1016/j.ajhg.2008.09.013

Mollet, G., Salomon, R., Gribouval, O., Silbermann, F., Bacq, D., Landthaler, G., et al. (2002). The gene mutated in juvenile nephronophthisis type 4 encodes a novel protein that interacts with nephrocystin. *Nat. Genet.* 32, 300–305. doi: 10.1038/ng996

Moreira, B. P., Oliveira, P. F., and Alves, M. G. (2019). Molecular mechanisms controlled by mTOR in male reproductive system. *Int. J. Mol. Sci.* 20:1633. doi: 10.3390/ijms20071633

Morgan, N. V., Morris, M. R., Cangul, H., Gleeson, D., Straatman-Iwanowska, A., Davies, N., et al. (2010). Mutations in SLC29A3, encoding an equilibrative nucleoside transporter ENT3, cause a familial histiocytosis syndrome

(*Faisalabad histiocytosis*) and familial Rosai-Dorfman disease. *PLoS Genet.* 6:e1000833. doi: 10.1371/journal.pgen.1000833

Moser, H. W. (1997). Adrenoleukodystrophy: phenotype, genetics, pathogenesis and therapy. *Brain* 120, 1485–1508. doi: 10.1093/brain/120.8.1485

Murga-Zamalloa, C. A., Desai, N. J., Hildebrandt, F., and Khanna, H. (2010). Interaction of ciliary disease protein retinitis pigmentosa GTPase regulator with nephronophthisis-associated proteins in mammalian retinas. *Mol. Vis.* 16, 1373–1381.

Nagaoka, S. I., Hassold, T. J., and Hunt, P. A. (2012). Human aneuploidy: mechanisms and new insights into an age-old problem. *Nat. Rev. Genet.* 13, 493–504. doi: 10.1038/nrg3245

Nair, S., Strohecker, A. M., Persaud, A. K., Bissa, B., Muruganandan, S., McElroy, C., et al. (2019). Adult stem cell deficits drive Slc29a3 disorders in mice. *Nat. Commun.* 10:2943. doi: 10.1038/s41467-019-10925-3

Neesen, J., Kirschner, R., Ochs, M., Schmiedl, A., Habermann, B., Mueller, C., et al. (2001). Disruption of an inner arm dynein heavy chain gene results in asthenozoospermia and reduced ciliary beat frequency. *Hum. Mol. Genet.* 10, 1117–1128. doi: 10.1093/hmg/10.11.1117

Nenicu, A., Okun, J. G., Hartmann, M. F., Wudy, S. A., Guillou, F., Crane, D. I., et al. (2009). Molecular pathogenesis of male infertility due to peroxisome dysfunction in sertoli cells. *Biol. Reprod.* 81, 682–682. doi: 10.1093/biolreprod/81.s1.682

Nezu, J., Tamai, I., Oku, A., Ohashi, R., Yabuuchi, H., Hashimoto, N., et al. (1999). Primary systemic carnitine deficiency is caused by mutations in a gene encoding sodium ion-dependent carnitine transporter. *Nat. Genet.* 21, 91–94. doi: 10.1038/5030

Nie, X., and Arend, L. J. (2013). Pkd1 is required for male reproductive tract development. *Mech. Dev.* 130, 567–576. doi: 10.1016/j.mod.2013.07.006

Niederkofler, V., Salie, R., and Arber, S. (2005). Hemojuvelin is essential for dietary iron sensing, and its mutation leads to severe iron overload. *J. Clin. Invest.* 115, 2180–2186. doi: 10.1172/JCI25683

Noda, T., Lu, Y., Fujihara, Y., Oura, S., Koyano, T., Kobayashi, S., et al. (2020). Sperm proteins SOF1, TMEM95, and SPACA6 are required for sperm-oocyte fusion in mice. *Proc. Natl. Acad. Sci. U.S.A.* 117, 11493–11502. doi: 10.1073/pnas.1922650117

Nygaard, M. B., Almstrup, K., Lindbæk, L., Christensen, S. T., and Svingen, T. (2015). Cell context-specific expression of primary cilia in the human testis and ciliary coordination of Hedgehog signalling in mouse Leydig cells. *Sci. Rep.* 5:10364. doi: 10.1038/srep10364

Orrico, A., Galli, L., Buoni, S., Hayek, G., Luchetti, A., Lorenzini, S., et al. (2005). Attention-deficit/hyperactivity disorder (ADHD) and variable clinical expression of Aarskog-Scott syndrome due to a novel FGD1 gene mutation (R408Q). *Am. J. Med. Genet. A* 135, 99–102. doi: 10.1002/ajmg.a.30700

Osborne, M., Gomez, D., Feng, Z., McEwen, C., Beltran, J., Cirillo, K., et al. (2012). Characterization of behavioral and neuromuscular junction phenotypes in a novel allelic series of SMA mouse models. *Hum. Mol. Genet.* 21, 4431–4447. doi: 10.1093/hmg/dds285

Ottesen, E. W., Howell, M. D., Singh, N. N., Seo, J., Whitley, E. M., and Singh, R. N. (2016). Severe impairment of male reproductive organ development in a low SMN expressing mouse model of spinal muscular atrophy. *Sci. Rep.* 6:20193. doi: 10.1038/srep20193

Otto, E., Hoefele, J., Ruf, R., Mueller, A. M., Hiller, K. S., Wolf, M. T. F., et al. (2002). A gene mutated in nephronophthisis and retinitis pigmentosa encodes a novel protein, nephroretinin, conserved in evolution. *Am. J. Hum. Genet.* 71, 1161–1167. doi: 10.1086/344395

Otto, E. A., Loeys, B., Khanna, H., Hellemans, J., Sudbrak, R., Fan, S., et al. (2005). Nephrocystin-5, a ciliary IQ domain protein, is mutated in Senior-Loken syndrome and interacts with RPGR and calmodulin. *Nat. Genet.* 37, 282–288. doi: 10.1038/ng1520

Papanikolaou, G., Samuels, M. E., Ludwig, E. H., MacDonald, M. L. E., Franchini, P. L., Dubé, M.-P., et al. (2004). Mutations in HFE2 cause iron overload in chromosome 1q–linked juvenile hemochromatosis. *Nat. Genet.* 36, 77–82. doi: 10.1038/ng1274

Parisi, M. A., Bennett, C. L., Eckert, M. L., Dobyns, W. B., Gleeson, J. G., Shaw, D. W. W., et al. (2004). The NPHP1 gene deletion associated with juvenile nephronophthisis is present in a subset of individuals with joubert syndrome. *Am. J. Hum. Genet.* 75, 82–91. doi: 10.1086/421846

Pasqualotto, F. F., Sharma, R. K., Nelson, D. R., Thomas, A. J., and Agarwal, A. (2000). Relationship between oxidative stress, semen characteristics, and clinical diagnosis in men undergoing infertility investigation. *Fertil. Steril.* 73, 459–464. doi: 10.1016/S0015-0282(99)00567-1

Paznekas, W. A., Boyadjiev, S. A., Shapiro, R. E., Daniels, O., Wollnik, B., Keegan, C. E., et al. (2003). Connexin 43 (GJA1) mutations cause the pleiotropic phenotype of oculodentodigital dysplasia. *Am. J. Hum. Genet.* 72, 408–418. doi: 10.1086/346090

Pearson, C. G., Osborn, D. P. S., Giddings, T. H., Beales, P. L., and Winey, M. (2009). Basal body stability and ciliogenesis requires the conserved component Poc1. *J. Cell Biol.* 187, 905–920. doi: 10.1083/jcb.200908019

Pei, Y., and Watnick, T. (2010). Diagnosis and screening of autosomal dominant polycystic kidney disease. *Adv. Chronic Kid. Dis.* 17, 140–152. doi: 10.1053/j.ackd.2009.12.001

Pellizzoni, L., Yong, J., and Dreyfuss, G. (2002). Essential role for the SMN complex in the specificity of snRNP assembly. *Science* 298, 1775–1779. doi: 10.1126/science.1074962

Perera, D., Tilston, V., Hopwood, J. A., Barchi, M., Boot-Handford, R. P., and Taylor, S. S. (2007). Bub1 maintains centromeric cohesion by activation of the spindle checkpoint. *Dev. Cell* 13, 566–579. doi: 10.1016/j.devcel.2007.08.008

Powers, J. M., and Schaumburg, H. H. (1981). The testis in adreno-leukodystrophy. *Am. J. Pathol.* 102, 90–98.

Puga Molina, L. C., Luque, G. M., Balestrini, P. A., Marín-Briggiler, C. I., Romarowski, A., and Buffone, M. G. (2018). Molecular basis of human sperm capacitation. *Front. Cell Dev. Biol.* 6:72. doi: 10.3389/fcell.2018.00072

Qi, H., Moran, M. M., Navarro, B., Chong, J. A., Krapivinsky, G., Krapivinsky, L., et al. (2007). All four CatSper ion channel proteins are required for male fertility and sperm cell hyperactivated motility. *Proc. Natl. Acad. Sci. U.S.A.* 104, 1219–1223. doi: 10.1073/pnas.0610286104

Quill, T. A., Sugden, S. A., Rossi, K. L., Doolittle, L. K., Hammer, R. E., and Garbers, D. L. (2003). Hyperactivated sperm motility driven by CatSper2 is required for fertilization. *Proc. Natl. Acad. Sci. U.S.A.* 100, 14869–14874. doi: 10.1073/pnas.2136654100

Reaume, A. G., de Sousa, P. A., Kulkarni, S., Langille, B. L., Zhu, D., Davies, T. C., et al. (1995). Cardiac malformation in neonatal mice lacking connexin43. *Science* 267, 1831–1834. doi: 10.1126/science.7892609

Rejraji, H., Sion, B., Prensier, G., Carreras, M., Motta, C., Frenoux, J.-M., et al. (2006). Lipid remodeling of murine epididymosomes and spermatozoa during epididymal maturation. *Biol. Reprod.* 74, 1104–1113. doi: 10.1095/biolreprod.105.049304

Ren, D., Navarro, B., Perez, G., Jackson, A. C., Hsu, S., Shi, Q., et al. (2001). A sperm ion channel required for sperm motility and male fertility. *Nature* 413, 603–609. doi: 10.1038/35098027

Riordan, J. R., Rommens, J. M., Kerem, B., Alon, N., Rozmahel, R., Grzelczak, Z., et al. (1989). Identification of the cystic fibrosis gene: cloning and characterization of complementary DNA. *Science* 245, 1066–1073. doi: 10.1126/science.2475911

Ritagliati, C., Luque, G. M., Stival, C., Baro Graf, C., Buffone, M. G., and Krapf, D. (2018). Lysine acetylation modulates mouse sperm capacitation. *Sci. Rep.* 8:13334. doi: 10.1038/s41598-018-31557-5

Rodríguez, C. M., Labus, J. C., and Hinton, B. T. (2002). Organic cation/carnitine transporter, OCTN2, is differentially expressed in the adult rat epididymis. *Biol. Reprod.* 67, 314–319. doi: 10.1095/biolreprod67.1.314

Roepman, R., Letteboer, S. J. F., Arts, H. H., van Beersum, S. E. C., Lu, X., Krieger, E., et al. (2005). Interaction of nephrocystin-4 and RPGRIP1 is disrupted by nephronophthisis or Leber congenital amaurosis-associated mutations. *Proc. Natl. Acad. Sci. U.S.A.* 102, 18520–18525. doi: 10.1073/pnas.0505774102

Roosing, S., Lamers, I. J. C., de Vrieze, E., van den Born, L. I., Lambertus, S., Arts, H. H., et al. (2014). Disruption of the basal body protein POC1B results in autosomal-recessive cone-rod dystrophy. *Am. J. Hum. Genet.* 95, 131–142. doi: 10.1016/j.ajhg.2014.06.012

Rowe, S. M., Miller, S., and Sorscher, E. J. (2005). Cystic fibrosis. *N. Engl. J. Med.* 352, 1992–2001. doi: 10.1056/NEJMra043184

Rudd, N. L., Teshima, I. E., Martin, R. H., Sisken, J. E., and Weksberg, R. (1983). A dominantly inherited cytogenetic anomaly: a possible cell division mutant. *Hum. Genet.* 65, 117–121. doi: 10.1007/BF00286646

Sarig, O., Nahum, S., Rapaport, D., Ishida-Yamamoto, A., Fuchs-Telem, D., Qiaoli, L., et al. (2012). Short stature, onychodysplasia, facial dysmorphism, and

hypotrichosis syndrome is caused by a POC1A mutation. *Am. J. Hum. Genet.* 91, 337–342. doi: 10.1016/j.ajhg.2012.06.003

See, K., Yadav, P., Giegerich, M., Cheong, P. S., Graf, M., Vyas, H., et al. (2014). SMN deficiency alters Nrxn2 expression and splicing in zebrafish and mouse models of spinal muscular atrophy. *Hum. Mol. Genet.* 23, 1754–1770. doi: 10.1093/hmg/ddt567

Seiler, A., Schneider, M., Förster, H., Roth, S., Wirth, E. K., Culmsee, C., et al. (2008). Glutathione peroxidase 4 senses and translates oxidative stress into 12/15-lipoxygenase dependent- and AIF-mediated cell death. *Cell Metab.* 8, 237–248. doi: 10.1016/j.cmet.2008.07.005

Shibazaki, S., Yu, Z., Nishio, S., Tian, X., Thomson, R. B., Mitobe, M., et al. (2008). Cyst formation and activation of the extracellular regulated kinase pathway after kidney specific inactivation of Pkd1. *Hum. Mol. Genet.* 17, 1505–1516. doi: 10.1093/hmg/ddn039

Shillingford, J. M., Murcia, N. S., Larson, C. H., Low, S. H., Hedgepeth, R., Brown, N., et al. (2006). The mTOR pathway is regulated by polycystin-1, and its inhibition reverses renal cystogenesis in polycystic kidney disease. *Proc. Natl. Acad. Sci. U.S.A.* 103, 5466–5471. doi: 10.1073/pnas.0509694103

Singh, P., and Schimenti, J. C. (2015). The genetics of human infertility by functional interrogation of SNPs in mice. *Proc. Natl. Acad. Sci. U.S.A.* 112, 10431–10436. doi: 10.1073/pnas.1506974112

Smith, A. C., Mears, A. J., Bunker, R., Ahmed, A., MacKenzie, M., Schwartzentruber, J. A., et al. (2014). Mutations in the enzyme glutathione peroxidase 4 cause Sedaghatian-type spondylometaphyseal dysplasia. *J. Med. Genet.* 51, 470–474. doi: 10.1136/jmedgenet-2013-102218

Sridharan, S., Simon, L., Meling, D. D., Cyr, D. G., Gutstein, D. E., Fishman, G. I., et al. (2007). Proliferation of adult sertoli cells following conditional knockout of the gap junctional protein GJA1 (Connexin 43) in mice. *Biol. Reprod.* 76, 804–812. doi: 10.1095/biolreprod.106.059212

Strauss, M. B., and Sommers, S. C. (1967). Medullary cystic disease and familial juvenile nephronophthisis. *N. Engl. J. Med.* 277, 863–864. doi: 10.1056/NEJM196710192771606

Strünker, T., Goodwin, N., Brenker, C., Kashikar, N. D., Weyand, I., Seifert, R., et al. (2011). The CatSper channel mediates progesterone-induced Ca2+ influx in human sperm. *Nature* 471, 382–386. doi: 10.1038/nature09769

Tarín, J. J., García-Pérez, M. A., Hamatani, T., and Cano, A. (2015). Infertility etiologies are genetically and clinically linked with other diseases in single meta-diseases. *Reprod. Biol. Endocrinol.* 13:31. doi: 10.1186/s12958-015-0029-9

Taylor, S. S., Ha, E., and McKeon, F. (1998). The human homologue of Bub3 is required for kinetochore localization of Bub1 and a Mad3/Bub1-related protein kinase. *J. Cell Biol.* 142, 1–11. doi: 10.1083/jcb.142.1.1

Torres, V. E., Harris, P. C., and Pirson, Y. (2007). Autosomal dominant polycystic kidney disease. *Lancet* 369, 1287–1301. doi: 10.1016/S0140-6736(07)60601-1

Toshimori, K., Kuwajima, M., Yoshinaga, K., Wakayama, T., and Shima, K. (1999). Dysfunctions of the epididymis as a result of primary carnitine deficiency in juvenile visceral steatosis mice. *FEBS Lett.* 446, 323–326. doi: 10.1016/S0014-5793(99)00241-0

van Roermund, C. W. T., Visser, W. F., Ijlst, L., van Cruchten, A., Boek, M., Kulik, W., et al. (2008). The human peroxisomal ABC half transporter ALDP functions as a homodimer and accepts acyl-CoA esters. *FASEB J. Off. Publ. Fed. Am. Soc. Exp. Biol.* 22, 4201–4208. doi: 10.1096/fj.08-110866

Vaquer, G., Rivière, F., Mavris, M., Bignami, F., Llinares-Garcia, J., Westermark, K., et al. (2013). Animal models for metabolic, neuromuscular and ophthalmological rare diseases. *Nat. Rev. Drug Discov.* 12, 287–305. doi: 10.1038/nrd3831

Vicari, E., Mongioì, A., Calogero, A. E., Moncada, M. L., Sidoti, G., Polosa, P., et al. (1992). Therapy with human chorionic gonadotrophin alone induces spermatogenesis in men with isolated hypogonadotrophic hypogonadism-long-term follow-up. *Int. J. Androl.* 15, 320–329. doi: 10.1111/j.1365-2605.1992.tb01131.x

Visconti, P. E., Bailey, J. L., Moore, G. D., Pan, D., Olds-Clarke, P., and Kopf, G. S. (1995). Capacitation of mouse spermatozoa. I. Correlation between the capacitation state and protein tyrosine phosphorylation. *Dev. Camb. Engl.* 121, 1129–1137.

Voos, W. (2009). Mitochondrial protein homeostasis: the cooperative roles of chaperones and proteases. *Res. Microbiol.* 160, 718–725. doi: 10.1016/j.resmic.2009.08.003

Wang, F., Kim, B.-E., Dufner-Beattie, J., Petris, M. J., Andrews, G., and Eide, D. J. (2004). Acrodermatitis enteropathica mutations affect transport activity, localization and zinc-responsive trafficking of the mouse ZIP4 zinc transporter. *Hum. Mol. Genet.* 13, 563–571. doi: 10.1093/hmg/ddh049

Wang, H., Liu, J., Cho, K.-H., and Ren, D. (2009). A novel, single, transmembrane protein CATSPERG is associated with CATSPER1 channel protein. *Biol. Reprod.* 81, 539–544. doi: 10.1095/biolreprod.109.077107

Wang, Q., Pierce-Hoffman, E., Cummings, B. B., Alföldi, J., Francioli, L. C., Gauthier, L. D., et al. (2020). Landscape of multi-nucleotide variants in 125,748 human exomes and 15,708 genomes. *Nat. Commun.* 11:2539. doi: 10.1038/s41467-019-12438-5

Wang, X., Jin, H., Han, F., Cui, Y., Chen, J., Yang, C., et al. (2017). Homozygous DNAH1 frameshift mutation causes multiple morphological anomalies of the sperm flagella in Chinese. *Clin. Genet.* 91, 313–321. doi: 10.1111/cge.12857

Watkins, P. A., Gould, S. J., Smith, M. A., Braiterman, L. T., Wei, H. M., Kok, F., et al. (1995). Altered expression of ALDP in X-linked adrenoleukodystrophy. *Am. J. Hum. Genet.* 57, 292–301.

Wishart, T. M., Mutsaers, C. A., Riessland, M., Reimer, M. M., Hunter, G., Hannam, M. L., et al. (2014). Dysregulation of ubiquitin homeostasis and β-catenin signaling promote spinal muscular atrophy. *J. Clin. Invest.* 124, 1821–1834. doi: 10.1172/JCI71318

Wolf, M. T. F. (2015). Nephronophthisis and related syndromes. *Curr. Opin. Pediatr.* 27, 201–211. doi: 10.1097/MOP.0000000000000194

Won, J., de Evsikova, C. M., Smith, R. S., Hicks, W. L., Edwards, M. M., Longo-Guess, C., et al. (2011). NPHP4 is necessary for normal photoreceptor ribbon synapse maintenance and outer segment formation, and for sperm development. *Hum. Mol. Genet.* 20, 482–496. doi: 10.1093/hmg/ddq494

Wu, G., Markowitz, G. S., Li, L., D'Agati, V. D., Factor, S. M., Geng, L., et al. (2000). Cardiac defects and renal failure in mice with targeted mutations in Pkd2. *Nat. Genet.* 24, 75–78. doi: 10.1038/71724

Wu, X., Huang, W., Prasad, P. D., Seth, P., Rajan, D. P., Leibach, F. H., et al. (1999). Functional characteristics and tissue distribution pattern of organic cation transporter 2 (OCTN2), an organic cation/carnitine transporter. *J. Pharmacol. Exp. Ther.* 290, 1482–1492.

Wykes, S. M., and Krawetz, S. A. (2003). The structural organization of sperm chromatin. *J. Biol. Chem.* 278, 29471–29477. doi: 10.1074/jbc.M304545200

Xu, Y., Ashley, T., Brainerd, E. E., Bronson, R. T., Meyn, M. S., and Baltimore, D. (1996). Targeted disruption of ATM leads to growth retardation, chromosomal fragmentation during meiosis, immune defects, and thymic lymphoma. *Genes Dev.* 10, 2411–2422. doi: 10.1101/gad.10.19.2411

Yamaguchi, S., Miura, C., Kikuchi, K., Celino, F. T., Agusa, T., Tanabe, S., et al. (2009). Zinc is an essential trace element for spermatogenesis. *Proc. Natl. Acad. Sci. U.S.A.* 106, 10859–10864. doi: 10.1073/pnas.0900602106

Young, J. D., Yao, S. Y. M., Baldwin, J. M., Cass, C. E., and Baldwin, S. A. (2013). The human concentrative and equilibrative nucleoside transporter families, SLC28 and SLC29. *Mol. Aspects Med.* 34, 529–547. doi: 10.1016/j.mam.2012.05.007

Zhao, Y., Tan, C.-H., Krauchunas, A., Scharf, A., Dietrich, N., Warnhoff, K., et al. (2018). The zinc transporter ZIPT-7.1 regulates sperm activation in nematodes. *PLoS Biol.* 16:e2005069. doi: 10.1371/journal.pbio.2005069

Zheng, Y., Fischer, D. J., Santos, M. F., Tigyi, G., Pasteris, N. G., Gorski, J. L., et al. (1996). The faciogenital dysplasia gene product FGD1 functions as a Cdc42Hs-specific guanine-nucleotide exchange factor. *J. Biol. Chem.* 271, 33169–33172. doi: 10.1074/jbc.271.52.33169

Zhu, Z., Yue, Q., Xie, J., Zhang, S., He, W., Bai, S., et al. (2019). Rapamycin-mediated mTOR inhibition impairs silencing of sex chromosomes and the pachytene piRNA pathway in the mouse testis. *Aging* 11, 185–208. doi: 10.18632/aging.101740

Conflict of Interest: The authors declare that the research was conducted in the absence of any commercial or financial relationships that could be construed as a potential conflict of interest.

Copyright © 2021 Linn, Ghanem, Bhakta, Greer and Avella. This is an open-access article distributed under the terms of the Creative Commons Attribution License (CC BY). The use, distribution or reproduction in other forums is permitted, provided the original author(s) and the copyright owner(s) are credited and that the original publication in this journal is cited, in accordance with accepted academic practice. No use, distribution or reproduction is permitted which does not comply with these terms.

frontiers in Cell and Developmental Biology

METHODS
published: 21 April 2021
doi: 10.3389/fcell.2021.648274

High Efficiency RNA Extraction From Sperm Cells Using Guanidinium Thiocyanate Supplemented With Tris(2-Carboxyethyl)Phosphine

*Martin Roszkowski and Isabelle M. Mansuy**

Laboratory of Neuroepigenetics, Brain Research Institute, Medical Faculty of the University of Zurich, and Institute for Neuroscience, Department of Health Science and Technology of the ETH Zurich, Zurich, Switzerland

The extraction of high-quality ribonucleic acid (RNA) from tissues and cells is a key step in many biological assays. Guanidinium thiocyanate-phenol-chloroform (AGPC) is a widely used and efficient method to obtain pure RNA from most tissues and cells. However, it is not efficient with some cells like sperm cells because they are resistant to chaotropic lysis solutions containing guanidinium thiocyanate such as Buffer RLT+ and Trizol. Here, we show that disulfide bonds are responsible for the chemical resistance of sperm cells to RNA extraction reagents. We show that while β-mercaptoethanol (βME) can increase sperm lysis in Buffer RLT+, it has no effect in Trizol and leaves sperm cells intact. We measured the reduction of disulfide bonds in 2,2′-dithiodipyridine (DTDP) and observed that βME has a pH-dependent activity in chaotropic solutions, suggesting that pH is a limiting factor. We identified tris(2-carboxyethyl)phosphine (TCEP) as an efficient lysis enhancer of AGPC solutions that can retain reducing activity even at acidic pH. Trizol supplemented with TCEP allows the complete and rapid lysis of sperm cells, increasing RNA yield by 100-fold and resulting in RNA with optimal quality for reverse transcription and polymerase chain reaction. Our findings highlight the importance of efficient cell lysis and extraction of various macromolecules for bulk and single-cell assays, and can be applied to other lysis-resistant cells and vesicles, thereby optimizing the amount of required starting material and animals.

Keywords: sperm cell, RNA, lysis and extraction, mouse, disulfide bond, TCEP, guanidinium thiocyanate, pH

OPEN ACCESS

Edited by:
Chih-kuan Tung, North Carolina Agricultural and Technical State University, United States

Reviewed by:
Terje Raudsepp, Texas A&M University, United States
Tawin Iempridee, National Nanotechnology Center, Thailand

***Correspondence:**
Isabelle M. Mansuy
imansuy@ethz.ch;
mansuy@hifo.uzh.ch

Specialty section:
This article was submitted to Cell Growth and Division, a section of the journal Frontiers in Cell and Developmental Biology

Received: *31 December 2020*
Accepted: *30 March 2021*
Published: *21 April 2021*

Citation:
Roszkowski M and Mansuy IM (2021) High Efficiency RNA Extraction From Sperm Cells Using Guanidinium Thiocyanate Supplemented With Tris(2-Carboxyethyl)Phosphine. Front. Cell Dev. Biol. 9:648274. doi: 10.3389/fcell.2021.648274

INTRODUCTION

Ribonucleic acid (RNA) is a macromolecule essential for many biological processes across all known species. It exists in different forms and length, and has numerous functions. In eukaryotes, messenger RNA (mRNA) is a form of coding RNA that is transcribed from genes and serves as template for translation into proteins (Buccitelli and Selbach, 2020). Non-coding RNA is transcribed from intergenic regions, and is not translated into proteins but has various regulatory

Abbreviations: βME, β-mercaptoethanol; RNA, ribonucleic acid; 2-TDP, 2-thiopyridione; AGPC, Guanidinium thiocyanate-phenol-chloroform; PUFA, polyunsaturated fatty acids; TCEP, Tris(2-carboxyethyl)phosphine; DTDP, 2,2′-dithiodipyridine; RT-PCR, reverse transcription polymerase chain reaction; DTT, dithiothreitol; G&T-seq, genome and transcriptome sequencing; ANOVA, analysis of variance.

functions. MicroRNAs and long non-coding RNA are involved in the silencing/degradation of mRNA and in genome regulation, while ribosomal and transfer RNA participate to ribosomal constitution and functions, respectively (Holoch and Moazed, 2015; Quinn and Chang, 2016), and small interfering RNA and Piwi-interacting RNA in genome defense (Landry et al., 2013; Ozata et al., 2019). RNA is present in cells and in extracellular vesicles which mediate signaling in-between cells and across tissues (Baldrich et al., 2019; O'Brien et al., 2020). It has also been causally involved in the transmission of phenotypes from parent to offspring in vertebrates and invertebrates (Krawetz, 2005; Bohacek and Mansuy, 2015; Rechavi and Lev, 2017).

Purification of high-quality RNA is an important step to investigate biological processes, cellular functions and phenotypes in molecular assays. The successful extraction of short and long RNA relies on the separation from DNA, proteins and cellular debris contained in cell lysate. Reverse transcription of purified RNA results in cDNA that can be amplified by polymerase chain reaction (PCR) for quantification of gene and transcript expression for classical qPCR or digital droplet PCR. Next generation sequencing is another method to quantify RNA, now commonly used to identify molecular signatures of tissues or individual cells and assess differential expression (Stark et al., 2019).

RNA can be purified from lysed cells by mainly two methods: acid guanidinium thiocyanate-phenol-chloroform (AGPC) and silica-based extraction columns (Chomczynski and Sacchi, 1987; Boom et al., 1990). AGPC extraction yields RNA of all lengths and is therefore the preferred method to obtain total RNA from cells and tissues (Toni et al., 2018). Its low cost, simplicity and adaptability to various biological material make it the most popular method in basic research. However, with this method, RNA purity and quality largely depend on the expertise of the experimenter and on sample handling. Silica-based columns allow nucleic acids extraction by binding to silica in the presence of chaotropic salts. It is commonly used in commercially available RNA extraction kits such as Qiagen RNAeasy and is amenable to automation for high throughput. Silica-based columns preferentially capture nucleic acids longer than 200 nucleotides but provide poor recovery of short RNA because short RNA tightly bind with silica and are less likely to elute (Ali et al., 2017). The recovered RNA is highly pure but the yield is usually lower when compared to AGPC.

In this study, we report that some cells, particularly mouse sperm cells, are resistant to commercially available AGPC and lysis solutions used for silica-based columns. Sperm cells cannot be properly lysed, which results in poor RNA yield and significant sample loss. Sperm lysis in AGPC is not improved by addition of the reducing agent β-mercaptoethanol (βME) or dithiothreitol (DTT), while βME added to the lysis solution in silica-based column protocols results in cell lysis. We observed that reduction of protein disulfide bonds is necessary for the lysis of sperm heads, and that reduction efficiency is pH-dependent, potentially explaining the difference in sperm lysis efficiency of various solutions. We identify tris(2-carboxyethyl)phosphine (TCEP) as a potent enhancer of AGPC RNA extraction and show that it allows complete lysis of mouse sperm cells.

MATERIALS AND METHODS

Animals

Animal experiments were conducted in strict adherence to the Swiss Law for Animal Protection and were approved by the cantonal veterinary office in Zürich under license number 57/2015 and 83/2018. C57Bl/6J mice were obtained from Janvier (France) and bred in-house to generate male mice (n = 32, 5 months old) for experiments. Mice were housed in groups of 3–5 animals in individually ventilated cages. Animals were kept in a temperature- and humidity-controlled facility on a 12 h reversed light/dark cycle (light on at 20:00, off at 8:00) with food (M/R Haltung Extrudat, Provimi Kliba SA, Switzerland) and water *ad libitum*. Cages were changed weekly.

Mouse Sperm Collection

Epididymidis from both sides was incised by several cuts with a fine scissor and placed in 2 ml M2 medium (M7167-100 ml, Sigma-Aldrich). Sperm cells were incubated at 37°C for 30 min. 1 ml of supernatant containing motile sperm was collected and centrifuged at 2,000 rcf for 5 min. The supernatant was again collected, mixed with 1 ml of somatic cell lysis buffer (0.1% sodium dodecyl sulfate and 0.05% Triton X-100 in MilliQ water) and incubated at 4°C for 10 min. Sperm samples were centrifuged at 2,000 rcf for 5 min, sperm pellets were washed twice in phosphate buffer saline (10010-015, Gibco) then snap-frozen and stored at −80°C until further processing. For lysis experiments, sperm samples were immediately resuspended in 250 µl water, lysis solutions were added and sperm observed under a light microscope.

Cell Lysis

Sperm pellets and small pieces of testis, liver or epididymis were lysed in 1 ml of Trizol (15596026, Life Technologies) or 1 ml of Buffer RLT+ (1053393, Qiagen) depending on the experiments. Lysis buffer was supplemented with 100 mM β-mercaptoethanol (M3148, Sigma-Aldrich), 100 mM dithiothreitol (646563-10X.5ml, Sigma-Aldrich) or 100 mM tris(2-carboxyethyl)phosphine (646547-10 × 1ml, Sigma-Aldrich). Sperm samples were either resuspended in lysis buffer by passage through a 30 G syringe or in the presence of 0.2 mm steel beads (SSB02-RNA, NextAdvance) at 20 Hz for up to 10 min in a TissueLyser II (85300, Qiagen). Since the lysis of sperm cells depends primarily on chemical lysis, we recommend future users a simple homogenization to sufficiently break up the cell pellet to obtain a single-cell suspension using 5 mm steel beads for 2 min (69989, Qiagen). We did not observe any differences between sperm lysis using small or large steel beads. Tissue samples were homogenized in a TissueLyser II using 5 mm steel beads at 20 Hz for 2 min.

RNA Extraction

For RNA extraction by phenol chloroform phase separation, 100 µl of sample lysed in Buffer RLT+ were added to 900 µl Trizol and extracted using the standard Trizol protocol. All centrifugation steps were at 4°C and samples kept on ice unless noted otherwise. In brief, 200 µl chloroform was added to 1 ml lysate, shaken for 15 s and then incubated at room temperature for 3 min. Samples were centrifuged at 12,000 rcf for 15 min. The aqueous phase was transferred to a fresh tube, 10 µl glycogen was added and the tube inverted 4 times for mixing. 500 µl isopropanol was then added and the tube inverted again 4 times. After an incubation at room temperature for 10 min, samples were centrifuged at 12,000 rcf for 10 min. The supernatant was removed and the pellet washed twice in 75% ethanol. After a final centrifugation at 7,500 rcf for 5 min, the supernatant was carefully removed. The pellet was dried in a concentrator (Speed-vac, Eppendorf) at 45°C for 4–6 min. Sperm RNA was resuspended in 20 µl nuclease-free water and tissue RNA in 100 µl nuclease-free water (A7398,500, ITW Reagents). Finally, the solution was incubated at 55°C for 15 min. RNA was stored at −80°C.

RNA Quantification and Characterization

RNA concentration and integrity were analyzed on the 2100 Bioanalyzer (G2939BA, Agilent) with the RNA 6000 Pico Kit (5067-1513, Agilent) according to manufacturer instructions. DNA content was quantified by fluorometry with the Qubit double-strand DNA high sensitivity assay (Q32852, Invitrogen) according to manufacturer instructions. For RT-PCR of long RNAs, RNA samples were first DNase treated with the DNA-free Kit (AM1906, Invitrogen) and reverse-transcribed with the GoScript Reverse Transcription System (A5000, Promega) using random hexamers according to manufacturer instructions. A testis sample without GoScript reverse transcriptase (noRT) and a sample without RNA (no Input) was processed in parallel and served as negative controls. For qPCR of cDNA from long RNAs, 1 µl of cDNA per well was quantified using SYBR Green I Master (04887352001, Roche) and primers for β-actin (Forward (5′–3′): CGATGCCCTGAGGCTCTTTT, reverse (5′–3′): TAGAGGTCTTTACGGATGTCAACG). For end-point PCR of cDNA from long RNAs, 5 ng of cDNA was amplified by GoTaq G2 HS Polymerase (M7405, Promega) for 30 cycles using specific primers for Malat1 (Forward (5′–3′): ATCGATTTAAAGTAAATGGGCTA, reverse (5′–3′): TTACATGCAGGAACATTGACA) and Pgk2 (Forward (5′–3′): AAGTTTGATGAGAATGCTAAAGT, reverse (5′–3′): CCTCCTCCTATAATGGTGACA). PCR products size was assessed by agarose gel electrophoresis. In **Figure 6F**, a part of the gel between the DNA ladder and Malat1 PCR products was cut out because it contained an RT-PCR with a different primer set. For qPCR of miRNAs, RNA samples were reverse transcribed with miScript II RT reagents (218161, Qiagen) using HiFlex buffer. RT-qPCR was performed with QuantiTect SYBR Green PCR Kit (1046470, Qiagen) on a Light Cycler II 480 (Roche) using miScript Primers Assays (Qiagen) for miR-141 (MS00011165, Qiagen), miR-101b (MS00023919, Qiagen) and miR-200c (MS00032543, Qiagen). All samples were run in triplicate. Melt curve analysis confirmed amplification of single products for each primer.

Quantification of Disulfide Bond Reduction

The reduction of disulfide bonds was performed as described previously (Han and Han, 1994). 1 mM 2,2′-dithiodipyridine (43791-1G, Sigma-Aldrich) was prepared in nuclease-free water and stored at 4°C. Lysis buffers were prepared as follows and used for absorption reference measurement: Trizol, Buffer RLT+, 1 M guanidinium thiocyanate (G9277-100g, Sigma-Aldrich) in nuclease-free water, 50 mM β-mercaptoethanol (βME) in nuclease-free water, Trizol supplemented with 50 mM βME (Trizol/βME), Buffer RLT+ supplemented with 50 mM βME (RLT+/βME) and Trizol supplemented with 50 mM TCEP (Trizol/TCEP). The reduction of DTDP was quantified by measuring the absorption of 2-thiopyridione (2-TPD) at 343 nm using an Ultrospec 2000 (80-2106-00, Pharmacia Biotech). 980 µl of lysis solution was prepared in UV-cuvettes and 20 µl of 1 mM DTDP solution added. The solution was briefly mixed by pipetting and absorption measurements started 10 s after DTDP addition. All experiments were repeated three times ($n = 3$).

Data, Statistics and Visualization

Data are represented as mean ± standard error of mean (SEM). Two groups were compared by unpaired *t*-test ($p < 0.05$). For comparisons of qPCR data, groups were analyzed by ordinary one-way analysis of variance (ANOVA, $p < 0.05$). For comparisons in the DTDP assay, groups were analyzed by repeated measures one-way analysis of variance (ANOVA, $p < 0.05$). Significant effects in ANOVA were further analyzed by multiple comparison with Tukey's *post hoc* test (adjusted *p*-value < 0.05). Graphs and statistics were prepared using the software GraphPad Prism 9. Contrast in microscopy pictures of **Figure 5B** was enhanced in Adobe PhotoShop 2021. Chemical reactions were drawn in ChemDraw19.

RESULTS

Mouse Sperm Cells Are Resistant to AGPC RNA Extraction

A sperm cell is composed of a head containing a nucleus that carries the paternal genome and RNA, and a flagellum prolonging the head through a mitochondria-rich midpiece, that provides motility (**Figure 1A**). We incubated mouse sperm cells at room temperature in Trizol, a commercially available AGPC RNA extraction reagent containing guanidinium thiocyanate as chaotropic agent. To separate sperm heads from the midpiece and flagellum, and dissociate cell clumps, we passed the sperm samples 10 times through a 30 G needle at the beginning of Trizol incubation. Despite this treatment, sperm heads remained intact after 5 min of incubation, indicating inefficient lysis (**Figure 1A**). We repeated the procedure and

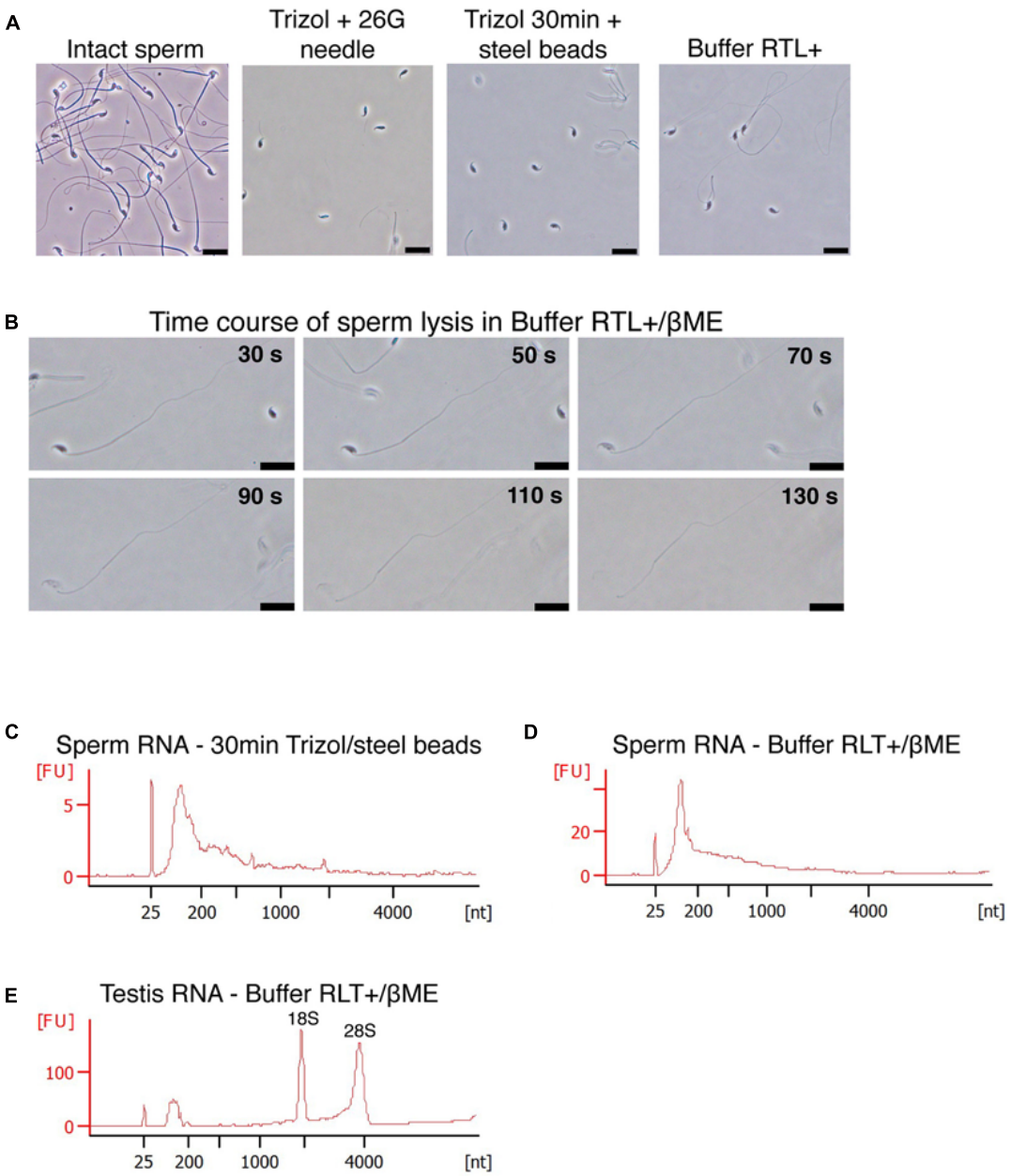

FIGURE 1 | Mouse sperm cells require reducing agents for lysis in chaotropic solutions. **(A)** Mouse sperm is not lysed in Trizol nor Buffer RLT+. Lysis is not improved by mechanical shearing. Scale bars = 20 μm. **(B)** Mouse sperm is rapidly lysed by Buffer RLT+ supplemented with 50 mM βME. Scale bars = 20 μm. **(C–E)** Bioanalyzer electropherograms of RNA concentration in fluorescence units (FU) for a given nucleotide length (nt). Sperm RNA prepared with **(C)** Trizol and homogenized by steel beads, or **(D)** Buffer RLT+ and βME, and **(E)** testes RNA prepared with Buffer RLT+ and βME.

made it more stringent by using longer incubation (30 min) in Trizol and strong homogenization with small steel beads at 20 Hz for 10 min. However, intact sperm heads still remained visible (**Figure 1A**). These results confirm previous observations that 2 M guanidinium does not lyse sperm heads (Flaherty and Breed, 1983).

We examined if other commercially available RNA extraction solutions are more efficient. Buffer RLT+ is a proprietary lysis solution of the Qiagen RNAeasy Mini kit, whose composition is unknown. However, the material safety data sheet suggests that it contains up to 50% guanidinium thiocyanate, thus resembles chaotropic properties of Trizol. Buffer RLT+ did not allow sperm lysis either (**Figure 1A**) even with a prolonged incubation of 18 h at room temperature. However, complete lysis of sperm heads was achieved within 2 min when 100 mM β-mercaptoethanol (βME) was added to Buffer RLT+ at room temperature (**Figure 1B**). βME is a commonly used reducing agent that breaks inter- and

intradisulfide bonds formed between cysteine residues in proteins. The addition of βME is recommended by the manufacturer of the RNAeasy Mini kit to inhibit RNAse, especially when extracting RNA from pancreas and spleen, tissues rich in RNAse.

We extracted RNA from Trizol and Buffer RLT+/βME sperm lysates using a standard phenol-chloroform protocol. To exclude contamination by testicular somatic cells, we prepared sperm samples using a swim-up method followed by treatment with a somatic cell lysis buffer. This approach has previously been shown to yield sperm samples free of somatic cells (Peng et al., 2012; Bianchi et al., 2018). We observed cell debris but no discernible somatic cells in the samples before RNA extraction. We assessed the quality of the extracted RNA by gel electrophoresis. Sperm samples were free of distinct 18S/28S rRNA peaks and had the expected RNA profile (**Figures 1C,D**), whereas RNA from testes had two characteristic peaks at 1,800 and 3,800 nt for 18S and 28S ribosomal RNA, respectively, and are apparent that indicate high-quality RNA (**Figure 1E**), suggesting no contamination by somatic cells.

These results indicate that the standard protocol for AGPC RNA extraction is inappropriate to completely lyse mouse sperm cells and is the main reason for poor RNA yield from these cells, and that using Buffer RLT+/βME instead of AGPC solutions circumvents this issue.

Examining Sperm Lysis Properties and Reduction of Disulfide Bonds

We next examined the reason for the lysis-resistance of sperm outer membrane. Sperm cells are lysed by Buffer RLT+ only if supplemented with βME despite the presence of guanidinium thiocyanate as main chaotropic agent. βME is a widely used reducing agent that disrupts disulfide bonds between thiol groups such as cysteine residues, within and between proteins (**Figure 2A**). During RNA extraction, it inhibits ribonuclease activity and prevents the degradation of RNA released in solution. We tested if adding a reducing agent to AGPC solution results in the successful lysis of sperm cells. Trizol with 100 mM βME however did not lead to the lysis of sperm heads, which remained intact (**Figure 2C**). Similarly, Trizol supplemented with dithiothreitol (DTT, **Figure 2B**) did not induce lysis (**Figure 2C**) even if DTT has been shown to decondense sperm heads by reducing disulfide bonds in protamines (Flaherty and Breed, 1983; Zirkin et al., 1989).

We then examined if the pH of the lysis solution influences the efficiency of sperm lysis. The pH primarily affects the reactivity of reducing agents and an alkaline pH is necessary for efficient reduction of disulfide bonds by βME and DTT (Han and Han, 1994). In contrast, an acidic pH is preferred for protein disulfide bond mapping by mass spectrometry because it preserves disulfide bonds (Lakbub et al., 2018). We measured the pH of several commercially available RNA extraction solutions and observed that Trizol and other AGPC lysis buffers have a pH of 3 while guanidinium thiocyanate in water has a pH of 5 and Buffer RLT+ and lysis buffer from

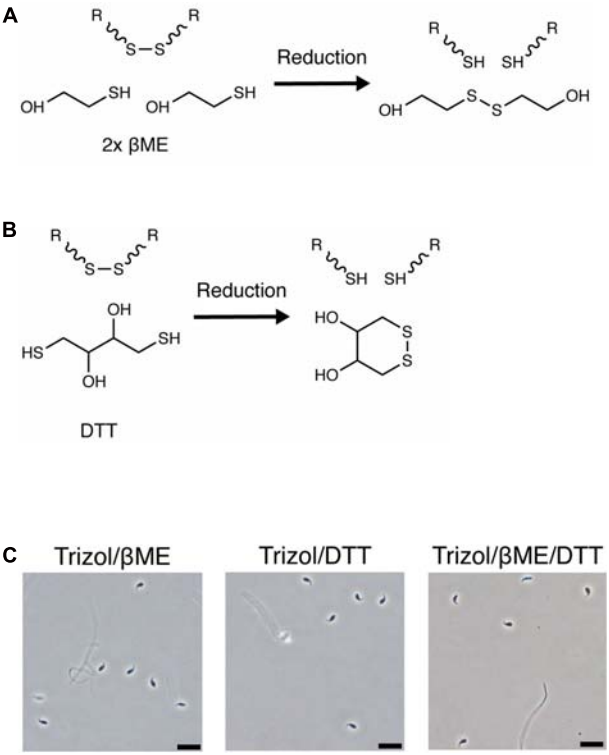

FIGURE 2 | Sperm is not lysed in Trizol supplemented with βME or DTT. **(A,B)** Chemical reduction of a protein disulfide bond by **(A)** βME or **(B)** DTT. **(C)** Mouse sperm is not lysed in Trizol supplemented with 100 mM βME, 100 mM DTT or a combination of both. Scale bars = 20 μm.

TABLE 1 | pH of commercially available lysis solutions for RNA extraction.

Commercial name	RNA extraction method	pH
TRIzol reagent	AGPC	3
QIAzol	AGPC	3
Tri reagent	AGPC	3
TRIsure	AGPC	3
Guanidinium thiocyanate 1 M	AGPC	5
Buffer RLT+	Silica columns	6
mirVana lysis/binding buffer	Silica columns and AGPC	6

mirVana RNA extraction kit using silica-columns have a pH of 6 (**Table 1**). The low pH may explain why βME did not improve lysis by Trizol.

Finally, we confirmed the pH-dependent activity of reducing agents by measuring the amount of 2-thiopyridione (2-TPD) formed after reduction of 2,2′-dithiodipyridine (DTDP) in lysis solutions. DTDP mimics protein disulfide bonds between cysteines and absorbance at 343 nm of 2-TPD in solution indicates the amount of disrupted bonds (**Figure 3A**). Trizol, Buffer RLT+ or 1 M guanidinium thiocyanate did not reduce DTDP. However, Buffer RLT+ supplemented with 50 mM βME led to rapid (within 40 s) and complete reduction of DTDP in water [**Figure 3B**, ANOVA, $F(1.000, 6.000) = 31.6$, $p = 0.0014$]. When added to Trizol, 50 mM βME led to only slow and

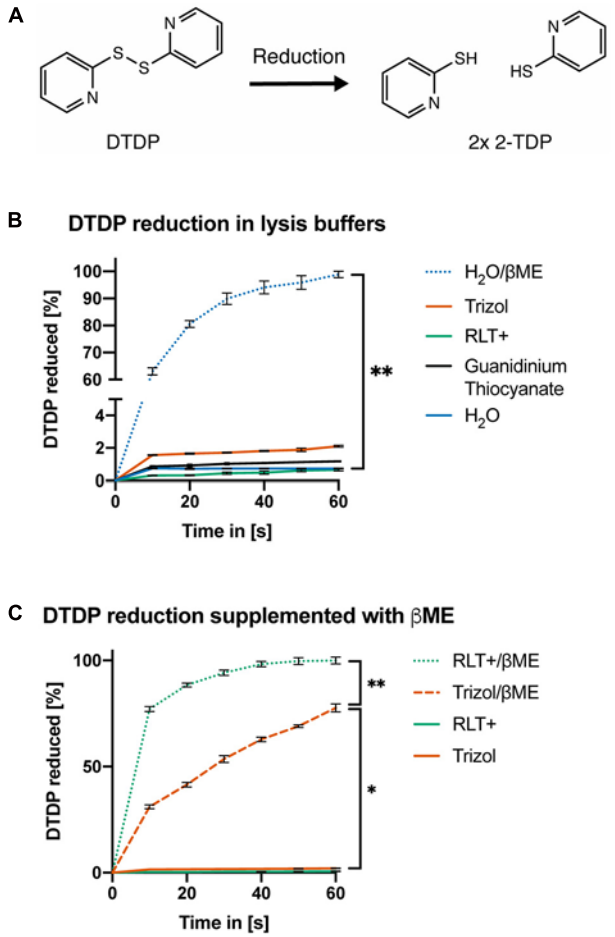

FIGURE 3 | DTDP assay reveals pH-dependent activity of reducing agents. **(A)** Reduction of 2,2′-Dithiodipyridine (DTDP) produces 2-thiopyridione (2-TPD). **(B,C)** Measurement of DTDP reduction in % during 60 s. **(B)** DTDP is not reduced by Trizol, Buffer RLT+, 1 M guanidinium thiocyanate or water. Water supplemented with 50 mM βME reduces DTDP within 60 s. **(C)** Buffer RLT+ supplemented with βME completely reduces DTDP. Trizol supplemented with βME reduces 75% of DTDP in the same time. Each condition was repeated 3 times (n = 3). Data are represented as mean ± standard error of mean (SEM). Significant ANOVAs were followed by Tukey's *post hoc* test, $^{*}p < 0.05$, $^{**}p < 0.01$.

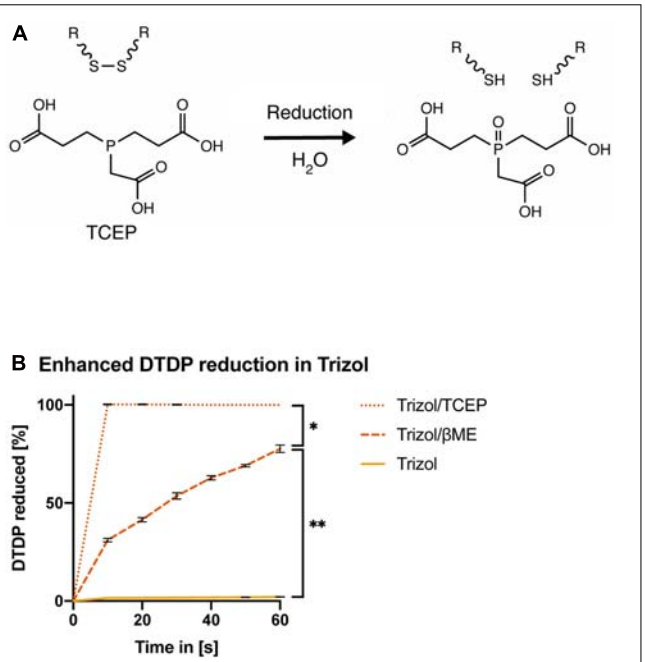

FIGURE 4 | TCEP is a potent reducing agent in AGPC lysis solution. **(A)** Chemical reduction of a protein disulfide bond by TCEP. **(B)** Measurement of DTDP reduction in % during 60 s. DTDP was rapidly reduced in Trizol supplemented with 50 mM TCEP within 10 s. Each condition was repeated 3 times (n = 3). Data are represented as mean ± standard error of mean (SEM). Significant ANOVAs were followed by Tukey's *post hoc* test, $^{*}p < 0.05$, $^{**}p < 0.01$.

incomplete reduction of DTDP, with 25% remaining after 60 s [**Figure 3C**, ANOVA, $F(1.171, 7.026) = 29.94$, $p = 0.0007$].

In summary, the supplementation of acidic AGPC solutions with βME or DTT is not sufficient to lyse mouse sperm, likely because guanidinium thiocyanate cannot reduce disulfide bonds present in the sperm head membrane, and the reactivity of βME is pH dependent.

TCEP Enhances AGPC Lysis

Tris(2-carboxyethyl)phosphine (TCEP) was previously shown to effectively reduce disulfide bonds across a wide pH range from 1.5 to 8.5 (**Figure 4A**; Han and Han, 1994). Therefore, we first assessed if TCEP could be an effective reducing agent for acidic lysis solutions. In contrast to βME, Trizol supplement with 50 mM TCEP rapidly reduced all DTDP within 10 s [**Figure 4B**, ANOVA, $F(1.458, 8.747) = 28.96$, $p = 0.0002$].

Next, we examined if lysis of sperm cells was improved by supplementing AGPC lysis solutions with TCEP. We observed complete lysis of all sperm heads in Trizol with 50 mM TCEP at room temperature within 5 min (**Figures 5A,B**). As expected, complete sperm lysis improved the efficiency of RNA extraction without requiring any adjustment or additional recovery step of the standard AGPC protocol. 1 million sperm cells yielded 30 ng RNA when lysed by Trizol/TCEP, thereby considerably improving RNA yield (**Figure 5C**). Sperm RNA profile had no distinct 18S/28S ribosomal peaks indicating that the source of increased RNA was from sperm cells rather than contamination by somatic cells (**Figure 5D**). Similarly to Buffer RTL+/βME, extraction by Trizol/TCEP from testis tissue yielded high-quality RNA (**Figure 5E**). We observed the likely presence of genomic DNA in the RNA profiles of a sperm sample (**Supplementary Figure 1A**). Subsequent DNA quantification by fluorometry showed the presence of genomic DNA in all sperm RNA samples [**Supplementary Figure 1B**, ANOVA, $F(3, 12) = 18.55$, $p < 0.0001$]. Therefore, all samples were DNAse treated before further use. To exclude RNA degradation, somatic RNA samples were processed in parallel and no substantial decrease in RNA integrity values was observed (**Supplementary Figure 1C**).

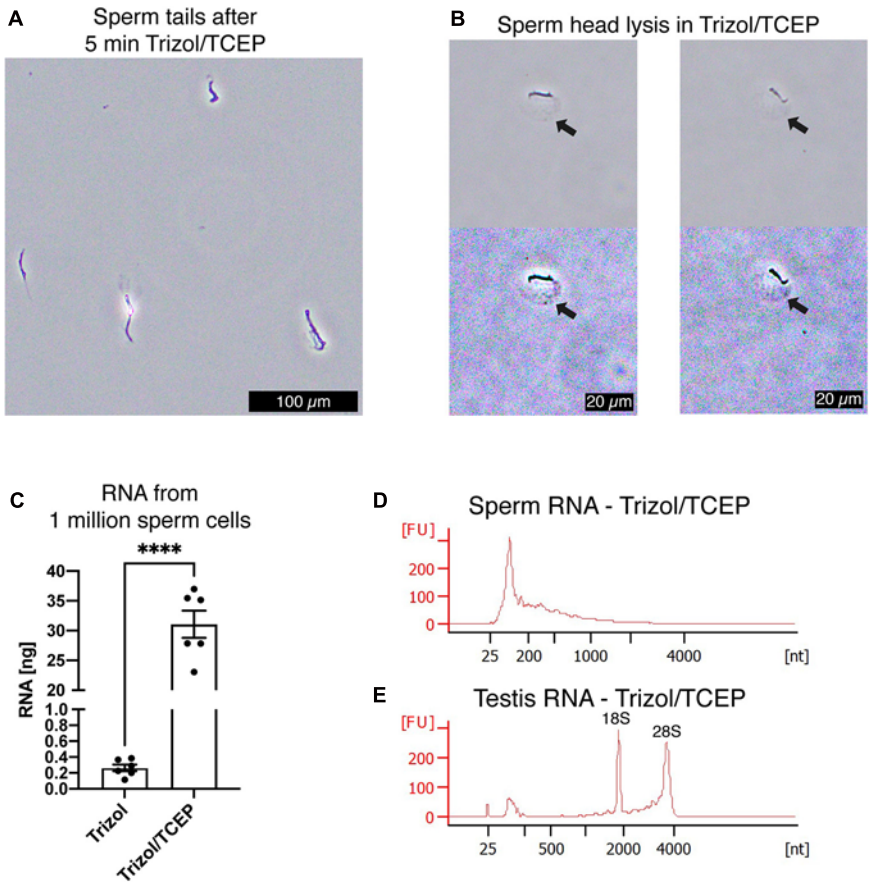

FIGURE 5 | TCEP enhances AGPC lysis and increases sperm RNA yield. **(A)** Mouse sperm cells are rapidly lysed in Trizol supplemented with 50 mM TCEP. Only clumped sperm tails remain visible indicating complete lysis of sperm heads. Scale bar = 100 μm. **(B)** Details of mouse sperm lysis in Trizol/TCEP. In comparison to lysis of mouse sperm in Buffer RLT+/βME, the acrosome remains visible for longer and a distinct swelling of the nucleus containing sperm head is observed (black arrows). In the second row, color contrast of microscopy pictures was increased to highlight the swelling. Scale bars = 20 μm. **(C)** Comparison between RNA yield in ng from 1 millions sperm cells when extracted with only Trizol or Trizol supplemented with TCEP. Trizol/TCEP extraction increased the RNA yield to an average of 30 ng (n = 6 per lysis condition). **(D,E)** Bioanalyzer electropherograms of RNA concentration in fluorescence units (FU) for a given nucleotide length (nt). **(D)** Sperm RNAs extracted from Trizol/TCEP were comprised mostly of RNAs shorter than 200 nt. **(E)** Testis RNA extracted from Trizol/TCEP was comprised of longer RNAs with distinct peaks at 1,800 and 3,800 nt. Data are represented as mean ± standard error of mean (SEM). ****$p < 0.0001$.

Finally, we confirmed that the RNA extracted by Trizol and TCEP was suitable for downstream applications such as reverse transcription polymerase chain reaction (RT-PCR). To determine the differences in RNA yield by quantitative PCR (qPCR), all sperm samples were processed similarly from lysis to final reverse transcription without any adjustment to volumes at the different processing steps. This ensured that initial differences in RNA quantity remained until qPCR and were quantified by reporting the cycle threshold number (Cq). First, we conducted qPCR on miR-141 [**Figure 6A**, ANOVA, $F(3, 12) = 30.42$, $p < 0.0001$], miR-101b [**Figure 6B**, ANOVA, $F(3, 12) = 9.15$, $p = 0.002$], and miR-200c [**Figure 6C**, ANOVA, $F(3, 12) = 25.34$, $p < 0.0001$]. Lower cycle values in qPCR indicate faster amplification and therefore higher RNA concentration in the sample. We observed significantly faster amplification of RNA samples obtained from lysis in Trizol/TCEP and RLT+/TCEP when compared to incomplete lysis (**Figures 6A–C**).

Next, we conducted qPCR on the reference gene β-actin and detected significantly faster amplification in sperm RNA samples obtained from lysis with Trizol/TCEP and RLT+/TCEP [**Figure 6D**, ANOVA, $F(3, 12) = 22.6$, $p < 0.0001$]. Furthermore, we conducted end-point PCR for two less abundant genes, metastasis associated lung adenocarcinoma transcript 1 (Malat1) and germ-cell specific phosphoglycerate kinase 2 (Pgk2). Malat1, a long non-coding RNA expressed in many mouse tissues (Hutchinson et al., 2007), amplified in sperm, testis, epididymis and liver RNA samples extracted by Trizol/TCEP (**Figure 6E**). In contrast, Pgk2 only amplified in sperm and testis samples (**Figure 6F**). In addition, we performed qPCR for Malat1 and Pgk2. However, all sperm samples amplified above 40 cycles and were considered as not detectable (data not shown; Bustin et al., 2009).

In conclusion, the supplementation of AGPC with TCEP enhances the lysis and RNA extraction from sperm cells, and considerably increases the RNA yield from these cells.

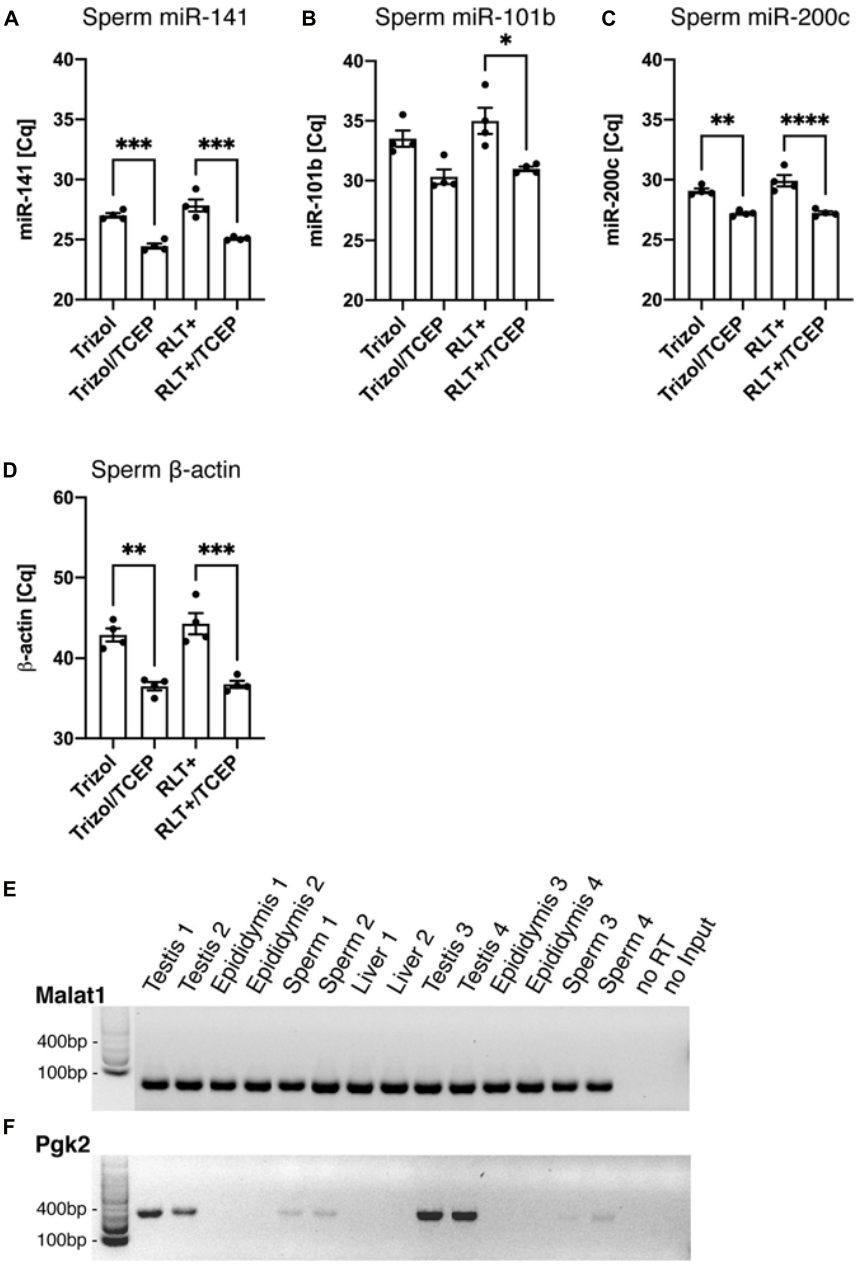

FIGURE 6 | Improved RNA yield quantified by qPCR of specific RNAs. **(A–D)** Quantification of RNA amount by qPCR. Detected cycle thresholds (Cq) are plotted on the y-axis and lower Cq values signify more starting material. **(A–C)** qPCR of miRNAs miR-141, -101b, and -220c. (n = 4 per group). **(D)** qPCR of long RNA β-actin. (n = 4 per group). **(E,F)** Gel images of end-point RT-PCR. **(E)** lncRNA Malat1 is detected by RT-PCR in Trizol/TCEP samples from sperm (n = 4), testis (n = 4), epididymis (n = 4) and liver (n = 2). **(F)** The germ-line specific transcript Pgk2 is only present in sperm and testis. noRT = RNA not reverse transcribed. NoInput = Sample without RNA. Significant ANOVAs were followed by Tukey's *post hoc* test, $^{*}p < 0.05$, $^{**}p < 0.01$, $^{***}p < 0.001$, $^{****}p < 0.0001$.

DISCUSSION

This study shows that mouse sperm cells are resistant to RNA extraction by AGPC and that supplementation with TCEP solves this issue by allowing complete lysis and high RNA yield. The results indicate that a disulfide reducing agent is necessary to lyse sperm cells, suggesting that disulfide bonds confer chemical resistance to sperm cells, in mouse and potentially other species.

The efficiency of AGPC extraction depends on the complete lysis of cells in the presence of chaotropic guanidinium (Gdm^+) and thiocyanate (SCN^-) ions, and additional factors such as mechanical shearing, degrading conditions and osmotic pressure. Gdm^+ and SCN^- ions are strong protein denaturants that partially disrupt accessible hydrophilic bonds, and are commonly used in studies of protein stability and folding (Baldwin, 1996; Mason et al., 2003). They also strongly inhibit the enzymatic

activity of ribonucleases released during cell lysis, thus prevent the degradation of RNA in solution and contribute to the acidification of the lysate (Chang and Li, 2002). An acidic pH is necessary during phenol-chloroform separation where DNA and proteins move to the organic phase while RNA remains in the aqueous phase (Chomczynski and Sacchi, 1987, 2006).

Despite the general applicability and potency of AGPC lysis solutions, we observed that mouse sperm cells are not effectively lysed and require the presence of pH-compatible denaturing agents. Specifically, we show that TCEP improves lysis at acidic pH. TCEP is also used to stabilize extracted RNA, for the reduction of proteomic samples and the preparation of protein:RNA crystallization samples (Rhee and Burke, 2004; Ripin et al., 2019; Thomas et al., 2020).

Sperm cells are specialized cells whose functions are to maintain the paternal genome and transfer it to an oocyte to generate offspring. During the last stages of spermatogenesis, most histones are replaced by protamines in sperm and only 1–8% are retained in mouse and 10–15% in human. Histones are retained principally at genomic regions such as transcription start sites, promoters and enhancers (Jung et al., 2017; Yamaguchi et al., 2018; Lismer et al., 2020). Protamines have different properties to histones, and in contrast to histones, they are highly enriched in disulfide bonds. Intra- and inter-protamine bonds mediate the packaging of DNA into a crystalline-like toroid and stabilize this structure, which requires reducing agents for its decondensation (Hisano et al., 2013; Hutchison et al., 2017). The highly condensed sperm nucleus is surrounded by the acrosome which in mice, has a distinct hook-like shape for cooperative cell motility, and carries enzymes necessary for successful sperm-oocyte fusion (Moore et al., 2002). The acrosome protects the sperm nucleus from the environment of the vagina and uterus during transit to the oviduct. It is primarily composed of proteins, ceramides and sphingomyelins with very long chain (carbon length 24–34) polyunsaturated fatty acids (PUFA) (Robinson et al., 1992). The acrosome composition varies between mouse, rat and human with predominantly very long chain PUFA (C30) in mouse, (C28) in rat and (C16) in human (Zanetti et al., 2010; Craig et al., 2019). Molecular dynamics simulations have shown that the composition regulates the stability and mechanical rigidity of the bilayer membrane, and changes in very long chain PUFA composition have been implicated in reduced sperm quality (Ahumada-Gutierrez et al., 2019; Craig et al., 2019). Our findings suggest a critical role for disulfide bonds in conveying chemical resistance of sperm cells, which has not been described previously.

The resistance of mouse sperm cells to acidic pH may be a form of cellular adaptation to protect sperm cells during transit in the vagina and uterus. While the testicular environment and epididymis are chemically stable in male mice, the uterus and vaginal milieu in females undergo substantial changes during the estrous cycle. The mouse vagina has typically a slightly acidic pH to suppress the growth of undesired bacteria and fungi. Importantly, the acidic environment together with other secreted enzymes contributes to the capacitation of sperm cells. The vaginal pH fluctuates with the estrous cycle and is particularly acidic (pH 4.5) during the estrous phase (Ganesan and Kadalmani, 2016). This is a time when females are the most receptive for copulation (Byers et al., 2012), thus the sperm is naturally exposed to an acidic environment. Its ability to resist such environment therefore allows it to regulate intracellular pH and maintain physiologically relevant functions (Nishigaki et al., 2014).

Since sperm cells are transcriptionally silent, a low RNA yield is expected from these cells. In sperm cells, protein synthesis is suppressed by cleavage of ribosomal RNA and most of the RNA in the cytoplasm is expulsed during spermatogenesis. A single sperm cell likely contains only 10–100 fg RNA (Pessot et al., 1989). Thus, an efficient method for RNA extraction is essential to recover sufficient RNA for RT-PCR and sequencing to avoid pooling several sperm samples. Furthermore, low RNA yield can also confound downstream analyses because RNA species such as miRNAs can be selectively lost during AGPC RNA extraction when using a small number of cells (Kim et al., 2012). With the improved lysis of sperm heads, we obtained on average 30 fg RNA per sperm cell, consistent with previous studies (Krawetz, 2005). This was sufficient to perform qPCR for the quantification of the miRNAs miR-141, -101b, and −200c but long RNA targets such as β-actin, Malat1, and Pgk2 required more amplification cycles. This difference in RNA abundance should be taken into account when selecting targets for RNA quantification in sperm.

While we focused on the lysis of mouse sperm cells, similar issues and resistance to AGPC or other chaotropic solutions have been reported for sperm from other species such as human (Bianchi et al., 2018), bovine (Gilbert et al., 2007) and chicken (Shafeeque et al., 2014), and for extracellular vesicles (Tang et al., 2017) and non-enveloped viruses (Schlegel et al., 2001). Further to RNA, other macromolecules such as DNA, proteins or metabolites will also benefit from the improved lysis method. Further, with the availability of single cell sequencing, the reliable lysis and characterization of each cell becomes even more important. For example, easy to implement protocols such as genome and transcriptome sequencing (G&T-seq) allow parallel sequencing of genomic DNA and RNA from single cells (Macaulay et al., 2015). However, G&T-seq uses Buffer RLT+ without any reducing agent to lyse cells. Supplementing Buffer RLT+ with TCEP may lead to faster and more robust cell lysis. Therefore, our findings can benefit other model organisms and single-cell applications requiring efficient cell lysis.

DATA AVAILABILITY STATEMENT

The original contributions presented in the study are included in the article, further inquiries can be directed to the corresponding author.

ETHICS STATEMENT

The animal study was reviewed and approved by cantonal veterinary office in Zürich.

AUTHOR CONTRIBUTIONS

MR designed, performed, analyzed and interpreted all experimental work. IM supervised and acquired funding for the study. MR and IM wrote the manuscript. Both authors discussed the results and approved the final version of the manuscript.

FUNDING

This work was supported by University of Zurich, ETH Zurich, Swiss National Science Foundation (31003A_175742/1) and Slack-Gyr Foundation. MR received funding from the ETH Zurich Fellowship (ETH-10 15-2). The APC was funded by ETH Zurich.

ACKNOWLEDGMENTS

We thank Dr. Irina-Elena Lazar-Contes and Maria-Andreea Dimitriu for discussions and critical comments on the original draft, Dr. Florentine Veenstra for advice on the DTDP assay, Prof. Johannes Bohacek for conceptual discussions, Dr. Silvia Schelbert for administrative support, and the animal care takers of the Laboratory Animal Services Center.

SUPPLEMENTARY MATERIAL

The Supplementary Material for this article can be found online at: https://www.frontiersin.org/articles/10.3389/fcell.2021.648274/full#supplementary-material

Supplementary Figure 1 | Quantification of residual genomic DNA in sperm RNA samples. **(A,C)** Bioanalyzer electropherograms of RNA concentration in fluorescence units (FU) for a given nucleotide length (nt). **(A)** Unusual peak at 2,000 nt is residual genomic DNA. Subsequent treatment with DNAse removes the peak. **(B)** Quantification of residual genomic DNA by fluorometry and plotted as a ratio against RNA amount per sample. (n = 4 per group). **(C)** Quantification of RNA integrity in somatic RNA shows no decrease of RNA integrity after DNAse treatment. Significant ANOVAs were followed by Tukey's *post hoc* test, $*p < 0.05$, $**p < 0.01$, $***p < 0.001$.

REFERENCES

Ahumada-Gutierrez, H., Peñalva, D. A., Enriz, R. D., Antollini, S. S., and Cascales, J. J. L. (2019). Mechanical properties of bilayers containing sperm sphingomyelins and ceramides with very long-chain polyunsaturated fatty acids. *Chem. Phys. Lipids* 218, 178–186. doi: 10.1016/j.chemphyslip.2018.12.008

Ali, N., Rampazzo, R. D. C. P., Costa, A. D. T., and Krieger, M. A. (2017). Current nucleic acid extraction methods and their implications to point-of-care diagnostics. *Biomed Res. Int.* 2017, 1–13. doi: 10.1155/2017/9306564

Baldrich, P., Rutter, B. D., Karimi, H. Z., Podicheti, R., Meyers, B. C., and Innes, R. W. B. (2019). Plant extracellular vesicles contain diverse small RNA species and are enriched in 10- to 17-nucleotide "Tiny" RNAs. *Plant Cell* 31, 315–324. doi: 10.1105/tpc.18.00872

Baldwin, R. L. (1996). How Hofmeister ion interactions affect protein stability. *Biophys. J.* 71, 2056–2063. doi: 10.1016/S0006-3495(96)79404-3

Bianchi, E., Stermer, A., Boekelheide, K., Sigman, M., Hall, S. J., Reyes, G., et al. (2018). High-quality human and rat spermatozoal RNA isolation for functional genomic studies. *Andrology* 6, 374–383. doi: 10.1111/andr.12471

Bohacek, J., and Mansuy, I. M. (2015). Molecular insights into transgenerational non-genetic inheritance of acquired behaviours. *Nat. Rev. Genet.* 16, 641–652. doi: 10.1038/nrg3964

Boom, R., Sol, C. J. A., Salimans, M. M. M., Jansen, C. L., Wertheim-van Dillen, P. M., and van der Noordaa, J. (1990). Rapid and simple method for purification of nucleic acids. *J. Clin. Microbiol.* 28, 495–503. doi: 10.1128/JCM.28.3.495-503.1990

Buccitelli, C., and Selbach, M. (2020). mRNAs, proteins and the emerging principles of gene expression control. *Nat. Rev. Genet* 21, 630–644. doi: 10.1038/s41576-020-0258-4

Bustin, S. A., Benes, V., Garson, J. A., Hellemans, J., Huggett, J., Kubista, M., et al. (2009). The MIQE guidelines:minimum information for publication of quantitative real-time PCR experiments. *Clin. Chem.* 55, 611–622. doi: 10.1373/clinchem.2008.112797

Byers, S. L., Wiles, M. V., Dunn, S. L., and Taft, R. A. (2012). Mouse estrous cycle identification tool and images. *PLoS One* 7:e35538. doi: 10.1371/journal.pone.0035538

Chang, J. Y., and Li, L. (2002). The unfolding mechanism and the disulfide structures of denatured lysozyme. *FEBS Lett.* 511, 73–78. doi: 10.1016/S0014-5793(01)03284-7

Chomczynski, P., and Sacchi, N. (1987). Single-step method of RNA isolation by acid guanidinium thiocyanate-phenol-chloroform extraction. *Anal. Biochem.* 162, 156–159. doi: 10.1016/0003-2697(87)90021-2

Chomczynski, P., and Sacchi, N. (2006). The single-step method of RNA isolation by acid guanidinium thiocyanate–phenol–chloroform extraction: twenty-something years on. *Nat. Protoc.* 1, 581–585. doi: 10.1038/nprot.2006.83

Craig, L. B., Brush, R. S., Sullivan, M. T., Zavy, M. T., Agbaga, M.-P., and Anderson, R. E. (2019). Decreased very long chain polyunsaturated fatty acids in sperm correlates with sperm quantity and quality. *J. Assist. Reprod. Genet.* 36, 1379–1385. doi: 10.1007/s10815-019-01464-3

Flaherty, S. P., and Breed, W. G. (1983). The sperm head of the plains mouse, Pseudomys australis: ultrastructure and effects of chemical treatments. *Gamete Res.* 8, 231–244. doi: 10.1002/mrd.1120080304

Ganesan, M., and Kadalmani, B. (2016). Phase dependent discrepancy in murine vaginal micro-environment: a correlative analysis of PH, glycogen and serum estrogen upon exposure to lapatinib ditosylate. *Int. J. Pharm. Pharm. Sci.* 8, 404–407.

Gilbert, I., Bissonnette, N., Boissonneault, G., Vallée, M., and Robert, C. (2007). A molecular analysis of the population of mRNA in bovine spermatozoa. *Reproduction* 133, 1073–1086. doi: 10.1530/REP-06-0292

Han, J. C., and Han, G. Y. (1994). A procedure for quantitative determination of Tris(2-Carboxyethyl)phosphine, an odorless reducing agent more stable and effective than dithiothreitol. *Anal. Biochem.* 220, 5–10. doi: 10.1006/abio.1994.1290

Hisano, M., Erkek, S., Dessus-Babus, S., Ramos, L., Stadler, M. B., and Peters, A. H. F. M. (2013). Genome-wide chromatin analysis in mature mouse and human spermatozoa. *Nat. Protoc.* 8, 2449–2470. doi: 10.1038/nprot.2013.145

Holoch, D., and Moazed, D. (2015). RNA-mediated epigenetic regulation of gene expression. *Nat. Rev. Genet.* 16, 71–84. doi: 10.1038/nrg3863

Hutchinson, J. N., Ensminger, A. W., Clemson, C. M., Lynch, C. R., Lawrence, J. B., and Chess, A. (2007). A screen for nuclear transcripts identifies two linked noncoding RNAs associated with SC35 splicing domains. *BMC Genomics* 8:39. doi: 10.1186/1471-2164-8-39

Hutchison, J. M., Rau, D. C., and DeRouchey, J. E. (2017). Role of disulfide bonds on DNA packaging forces in bull sperm chromatin. *Biophys. J.* 113, 1925–1933. doi: 10.1016/j.bpj.2017.08.050

Jung, Y. H., Sauria, M. E. G., Lyu, X., Cheema, M. S., Ausio, J., Taylor, J., et al. (2017). Chromatin states in mouse sperm correlate with embryonic and adult regulatory landscapes. *Cell Rep.* 18, 1366–1382. doi: 10.1016/j.celrep.2017.01.034

Kim, Y.-K., Yeo, J., Kim, B., Ha, M., and Kim, V. N. (2012). Short structured RNAs with low GC content are selectively lost during extraction from a small number of cells. *Mol. Cell* 46, 893–895. doi: 10.1016/j.molcel.2012.05.036

Krawetz, S. A. (2005). Paternal contribution: new insights and future challenges. *Nat. Rev. Genet.* 6, 633–642. doi: 10.1038/nrg1654

Lakbub, J. C., Shipman, J. T., and Desaire, H. (2018). Recent mass spectrometry-based techniques and considerations for disulfide bond characterization in proteins. *Anal. Bioanal. Chem.* 410, 2467–2484. doi: 10.1007/s00216-017-0772-1

Landry, C. D., Kandel, E. R., and Rajasethupathy, P. (2013). New mechanisms in memory storage: piRNAs and epigenetics. *Trends Neurosci.* 36, 535–542. doi: 10.1016/j.tins.2013.05.004

Lismer, A., Siklenka, K., Lafleur, C., Dumeaux, V., and Kimmins, S. (2020). Sperm histone H3 lysine 4 trimethylation is altered in a genetic mouse model of transgenerational epigenetic inheritance. *Nucleic Acids Res.* 48, 11380–11393. doi: 10.1093/nar/gkaa712

Macaulay, I. C., Haerty, W., Kumar, P., Li, Y. I., Hu, T. X., Teng, M. J., et al. (2015). G&T-seq: parallel sequencing of single-cell genomes and transcriptomes. *Nat. Methods* 12, 519–522. doi: 10.1038/nmeth.3370

Mason, P. E., Neilson, G. W., Dempsey, C. E., Barnes, A. C., and Cruickshank, J. M. (2003). The hydration structure of guanidinium and thiocyanate ions: implications for protein stability in aqueous solution. *Proc. Natl. Acad. Sci. U.S.A.* 100, 4557–4561. doi: 10.1073/pnas.0735920100

Moore, H., Dvoráková, K., Jenkins, N., and Breed, W. (2002). Exceptional sperm cooperation in the wood mouse. *Nature* 418, 174–177. doi: 10.1038/nature00832

Nishigaki, T., José, O., González-Cota, A. L., Romero, F., Treviño, C. L., and Darszon, A. (2014). Intracellular pH in sperm physiology. *Biochem. Biophys. Res. Commun.* 450, 1149–1158. doi: 10.1016/j.bbrc.2014.05.100

O'Brien, K., Breyne, K., Ughetto, S., Laurent, L. C., and Breakefield, X. O. (2020). RNA delivery by extracellular vesicles in mammalian cells and its applications. *Nat. Rev. Mol. Cell Biol.* 21, 585–606. doi: 10.1038/s41580-020-0251-y

Ozata, D. M., Gainetdinov, I., Zoch, A., O'Carroll, D., and Zamore, P. D. (2019). PIWI-interacting RNAs: small RNAs with big functions. *Nat. Rev. Genet.* 20, 89–108. doi: 10.1038/s41576-018-0073-3

Peng, H., Shi, J., Zhang, Y., Zhang, H., Liao, S., Li, W., et al. (2012). A novel class of tRNA-derived small RNAs extremely enriched in mature mouse sperm. *Cell Res.* 22, 1609–1612. doi: 10.1038/cr.2012.141

Pessot, C. A., Brito, M., Figueroa, J., Concha, I. I., Yañez, A., and Burzio, L. O. (1989). Presence of RNA in the sperm nucleus. *Biochem. Biophys. Res. Commun.* 158, 272–278. doi: 10.1016/S0006-291X(89)80208-6

Quinn, J. J., and Chang, H. Y. (2016). Unique features of long non-coding RNA biogenesis and function. *Nat. Rev. Genet.* 17, 47–62. doi: 10.1038/nrg.2015.10

Rechavi, O., and Lev, I. (2017). Principles of transgenerational small RNA inheritance in Caenorhabditis elegans. *Curr. Biol.* 27, R720–R730. doi: 10.1016/j.cub.2017.05.043

Rhee, S. S., and Burke, D. H. (2004). Tris(2-carboxyethyl)phosphine stabilization of RNA: comparison with dithiothreitol for use with nucleic acid and thiophosphoryl chemistry. *Anal. Biochem.* 325, 137–143. doi: 10.1016/j.ab.2003.10.019

Ripin, N., Boudet, J., Duszczyk, M. M., Hinniger, A., Faller, M., Krepl, M., et al. (2019). Molecular basis for AU-rich element recognition and dimerization by the HuR C-terminal RRM. *Proc. Natl. Acad. Sci.U.S.A.* 116, 2935–2944. doi: 10.1073/pnas.1808696116

Robinson, B. S., Johnson, D. W., and Poulos, A. (1992). Novel molecular species of sphingomyelin containing 2-hydroxylated polyenoic very-long-chain fatty acids in mammalian testes and spermatozoa. *J. Biol. Chem.* 267, 1746–1751.

Schlegel, A., Immelmann, A., and Kempf, C. (2001). Virus inactivation of plasma-derived proteins by pasteurization in the presence of guanidine hydrochloride. *Transfusion* 41, 382–389. doi: 10.1046/j.1537-2995.2001.41030382.x

Shafeeque, C. M., Singh, R. P., Sharma, S. K., Mohan, J., Sastry, K. V. H., Kolluri, G., et al. (2014). Development of a new method for sperm RNA purification in the chicken. *Anim. Reprod. Sci.* 149, 259–265. doi: 10.1016/j.anireprosci.2014.06.032

Stark, R., Grzelak, M., and Hadfield, J. (2019). RNA sequencing: the teenage years. *Nat. Rev. Genet.* 20, 631–656. doi: 10.1038/s41576-019-0150-2

Tang, Y. T., Huang, Y. Y., Zheng, L., Qin, S. H., Xu, X. P., An, T. X., et al. (2017). Comparison of isolation methods of exosomes and exosomal RNA from cell culture medium and serum. *Int. J. Mol. Med.* 40, 834–844. doi: 10.3892/ijmm.2017.3080

Thomas, S. N., Friedrich, B., Schnaubelt, M., Chan, D. W., Zhang, H., and Aebersold, R. (2020). Orthogonal proteomic platforms and their implications for the stable classification of high-grade serous ovarian cancer subtypes. *iScience* 23:101079. doi: 10.1016/j.isci.2020.101079

Toni, L. S., Garcia, A. M., Jeffrey, D. A., Jiang, X., Stauffer, B. L., Miyamoto, S. D., et al. (2018). Optimization of phenol-chloroform RNA extraction. *MethodsX* 5, 599–608. doi: 10.1016/j.mex.2018.05.011

Yamaguchi, K., Hada, M., Fukuda, Y., Inoue, E., Makino, Y., Katou, Y., et al. (2018). Re-evaluating the localization of sperm-retained histones revealed the modification-dependent accumulation in specific genome regions. *Cell Rep.* 23, 3920–3932. doi: 10.1016/j.celrep.2018.05.094

Zanetti, S. R., de los Ángeles Monclus, M., Rensetti, D. E., Fornés, M. W., and Aveldaño, I. (2010). Ceramides with 2-hydroxylated, very long-chain polyenoic fatty acids in rodents: from testis to fertilization-competent spermatozoa. *Biochimie* 92, 1778–1786. doi: 10.1016/j.biochi.2010.08.012

Zirkin, B. R., Naish, S. J., and Perreault, S. D. (1989). Formation and function of the male pronucleus during mammalian fertilization. *Mol. Biol. Fertili.* 91–114. doi: 10.1016/B978-0-12-622595-2.50011-5

Conflict of Interest: The authors declare that the research was conducted in the absence of any commercial or financial relationships that could be construed as a potential conflict of interest.

Copyright © 2021 Roszkowski and Mansuy. This is an open-access article distributed under the terms of the Creative Commons Attribution License (CC BY). The use, distribution or reproduction in other forums is permitted, provided the original author(s) and the copyright owner(s) are credited and that the original publication in this journal is cited, in accordance with accepted academic practice. No use, distribution or reproduction is permitted which does not comply with these terms.

frontiers in Cell and Developmental Biology

ORIGINAL RESEARCH
published: 22 April 2021
doi: 10.3389/fcell.2021.658891

Fluorescence-Based Ratiometric Analysis of Sperm Centrioles (FRAC) Finds Patient Age and Sperm Morphology Are Associated With Centriole Quality

*Katerina A. Turner[1], Emily L. Fishman[1], Mariam Asadullah[1], Brooke Ott[1], Patrick Dusza[1], Tariq A. Shah[2], Puneet Sindhwani[2], Nagalakshmi Nadiminty[2], Emanuela Molinari[3], Pasquale Patrizio[3], Barbara S. Saltzman[4] and Tomer Avidor-Reiss[1,2]**

[1] Department of Biological Sciences, College of Natural Sciences and Mathematics, University of Toledo, Toledo, OH, United States, [2] Department of Urology, College of Medicine and Life Sciences, University of Toledo, Toledo, OH, United States, [3] Yale Fertility Center, Yale School of Medicine, New Haven, CT, United States, [4] School of Population Health, College of Health and Human Services, University of Toledo, Toledo, OH, United States

OPEN ACCESS

Edited by:
Timothy L. Megraw, Florida State University, United States

Reviewed by:
Giuliano Callaini, University of Siena, Italy
Xin Zhiguo Li, University of Rochester, United States

***Correspondence:**
Tomer Avidor-Reiss
Tomer.AvidorReiss@utoledo.edu

Specialty section:
This article was submitted to Cell Growth and Division, a section of the journal Frontiers in Cell and Developmental Biology

Received: *26 January 2021*
Accepted: *19 March 2021*
Published: *22 April 2021*

Citation:
Turner KA, Fishman EL, Asadullah M, Ott B, Dusza P, Shah TA, Sindhwani P, Nadiminty N, Molinari E, Patrizio P, Saltzman BS and Avidor-Reiss T (2021) Fluorescence-Based Ratiometric Analysis of Sperm Centrioles (FRAC) Finds Patient Age and Sperm Morphology Are Associated With Centriole Quality. Front. Cell Dev. Biol. 9:658891. doi: 10.3389/fcell.2021.658891

A large proportion of infertility and miscarriage causes are unknown. One potential cause is a defective sperm centriole, a subcellular structure essential for sperm motility and embryonic development. Yet, the extent to which centriolar maladies contribute to male infertility is unknown due to the lack of a convenient way to assess centriole quality. We developed a robust, location-based, ratiometric assay to overcome this roadblock, the Fluorescence-based Ratiometric Assessment of Centrioles (FRAC). We performed a case series study with semen samples from 33 patients, separated using differential gradient centrifugation into higher-grade (pellet) and lower-grade (interface) sperm fractions. Using a reference population of higher-grade sperm from infertile men with morphologically standard sperm, we found that 79% of higher-grade sperm of infertile men with substandard sperm morphology have suboptimal centrioles (P = 0.0005). Moreover, tubulin labeling of the sperm distal centriole correlates negatively with age (P = 0.004, R = −0.66). These findings suggest that FRAC is a sensitive method and that patient age and sperm morphology are associated with centriole quality.

Keywords: centriole, infertility, sperm, fluorescence, method, age, teratospermia, miscarriage

INTRODUCTION

Infertility affects 10% of American people, but due to the lack of adequate clinical treatment or access to it, many couples fail to get their desired offspring (Royfman et al., 2020). One reason infertility treatments fail is deficiencies in identifying the underlying causes of male factor reproductive diseases. About 25% of male factor infertility (Pandruvada et al., 2021), 33% of infertility in couples (Smith et al., 2003), 50% of recurrent miscarriages (Garrido-Gimenez and Alijotas-Reig, 2015), and most embryo development defects are unexplained (Reefhuis et al., 2015). Furthermore, intracytoplasmic sperm injection (ICSI) is only successful at leading to clinical pregnancy in 1 out of 2 treated women, and often this requires multiple cycles of treatment (Stern et al., 2010). Therefore,

there is a need to identify novel causes of male infertility and develop an assay to diagnose them (Turner et al., 2020).

Centrioles are essential for the sperm's formation and motility, and the sperm is the sole contributor of centrioles to the zygote (Avidor-Reiss and Fishman, 2019). Recent studies suggest that bovine centrioles play a critical role in coordinating sperm tail and head movement (Khanal et al., 2021). Therefore, sperm centrioles are essential for human fertility (Palermo et al., 1997; Schatten and Sun, 2010; Chemes and Sedo, 2012). The human sperm has two centrioles: a well-established Proximal Centriole (PC) found near the sperm head and a recently discovered atypical Distal Centriole (DC), which is further away from the head and nucleates the axoneme (Fishman et al., 2018). In the testes, the spermatid centrioles undergo a unique "Centriole Remodeling," which results in sperm centrioles having distinct atypical characteristics (Avidor-Reiss, 2018; Leung et al., 2020). The sperm PC has a canonical structure, but a somewhat atypical composition compared to centrioles in other cells. In contrast, the sperm DC has a dramatically atypical structure and composition compared to centrioles in other cells.

The centrioles' essential role in sperm morphology and movement pre-fertilization is well demonstrated and widely accepted (Chemes, 2012). The sperm centriole forms the flagellum (i.e., the sperm tail) and may control the tail's beating shape (Avidor-Reiss et al., 2020). Defects in these functions can result in teratospermia, asthenospermia, or a combination of these phenotypes. Although some of the essential functions of sperm centrioles are known, the canonical PC and atypical DC's precise role in the mature sperm is still unclear. Furthermore, it may not be possible to circumvent infertility stemming from a defective PC or DC using assisted reproductive technology (ART) such as intracytoplasmic sperm injection (ICSI) with ejaculated or testicular sperm (e.g., testicular sperm extraction, TESE) (Avidor-Reiss et al., 2019). Therefore, patients with defective centrioles may be advised that there is not an effective ART treatment for their condition. Because of the potential impact on infertility treatments, there is a need for more comprehensive studies that directly assess the role of human sperm centrioles (Turner et al., 2020).

Sperm centrioles are essential for embryo development in invertebrates and lower vertebrates (O'Connell et al., 2001; Yabe et al., 2007; Blachon et al., 2014; Khire et al., 2016). However, the essential role of human sperm centrioles in post-fertilization events is still debatable. This controversy is due to two significant issues. (1) Most of the studies that suggest the centrioles are essential after fertilization are descriptive and small scale [Level III, Quality of Evidence, (Force, 1989)]. Available literature includes about a dozen case studies, case-control studies, and a few retrospective studies; no prospective studies were reported (Chemes et al., 1999; Alosilla Fonttis et al., 2002; Nakamura et al., 2002; Rawe et al., 2002; Porcu et al., 2003; Emery et al., 2004; Terada et al., 2009; Moretti et al., 2017, 2019; Sha et al., 2017; Garanina et al., 2019). Most of these reports analyzed less than ten infertile patients. Also, the centriole was only directly examined in a few of these studies, and in many, centriolar defects were inferred from gross cell phenotypes. (2) Sperm centrioles are not essential post-fertilization in mice, and pups can be generated from eggs fertilized by isolated sperm nuclei with no centrioles (Kuretake et al., 1996; Yan et al., 2008). However, the dispensability of sperm centrioles observed in mice does not appear to apply to humans (Avidor-Reiss et al., 2019). Recent studies suggest that bovine centrioles play critical and novel roles in the zygote, and their dysfunction leads to aneuploidy (Cavazza et al., 2020; Schneider et al., 2020). Therefore, it is likely that a fraction of human reproductive diseases may be defined as Sperm Centriole Associated Reproductive Disorders (SCARD).

Assessment of sperm morphology is an essential component of semen analysis and for the diagnosis of male factor infertility (WHO, 2010). Abnormal sperm morphology (teratospermia) is estimated to be present in 7–18% of infertile men and, in the great majority of cases, there is no identifiable cause (Thonneau et al., 1991; Sigman et al., 2009; Owolabi et al., 2013; Peter et al., 2016). Yet, sperm morphology assessment is inherently variable and subjective, and its predictive value for pregnancy success is controversial (Shabtaie et al., 2016). However, pregnancy and live birth rates appear to be lower in some cases of teratospermia (Kruger et al., 1988; Grow et al., 1994; Li et al., 2014; Cito et al., 2020). For example, in oligoasthenoteratospermia (OAT), ICSI treatment results in a lower implantation and gestation rate (Pang et al., 1999; Pfeffer et al., 1999; Rubio et al., 2001). Therefore, to better understand the potential for conception with teratospermic sperm samples, it may help to determine whether such sperm have defects in their internal components, such as DNA, RNA, and centrioles. Consequently, there is a need for a robust method to analyze sperm components, including the centrioles (Turner et al., 2020).

Several assays to study human sperm centrioles are available; however, the associated technology is either laborious, not sufficiently specific to centrioles, or subjective. The structure of sperm centrioles has been assessed by *electron microscopy*, an extremely laborious technique that is inadequate for large-scale studies (Chemes et al., 1987; Moretti et al., 2017). Sperm centriolar protein content has been assessed by *western blot* (Hinduja et al., 2010), which measures total protein and is not specific to the centriole; therefore, it cannot conclusively implicate the centriole in infertility. Sperm centriole function has been assessed by *microinjection* of human sperm into oocytes of bovine, rabbit, or hamster, followed by immunofluorescent staining for aster formation (Nakamura et al., 2001; Terada et al., 2004). These assays are useful for studying abnormal sperm centrioles in some infertility cases (Rawe et al., 2002; Terada, 2004); however, this method creates ethical concerns since it generates an embryo using a human gamete and which is then destroyed. Due to these limitations, sperm centriole defects in infertile men have only been demonstrated in small case studies (Nanassy and Carrell, 2008; Chemes, 2012; Moretti et al., 2017; Sha et al., 2017). Therefore, there is a need for a high-throughput, specific, non-subjective, and quantitative method of assessing human sperm centrioles. Fluorescence microscopy provides a high-throughput technique to predict sperm function based on protein markers, and the centrioles can be specifically analyzed (Petrunkina and Harrison, 2013). However, fluorescence microscopy was used only to identify large

defects that include protein mislocalization in small-scale studies (Xu et al., 2008; Sha et al., 2017).

Tubulin and POC1B are structural components of the centriole and axoneme. Tubulin is a heterodimer complex that polymerizes to form the centriole and axoneme wall (Avidor-Reiss and Gopalakrishnan, 2013; Winey and O'Toole, 2014). POC1B is an evolutionarily conserved centriolar protein that forms a luminal scaffold structure in canonical centrioles and novel rod structures in the atypical DC and is essential for centriole stability (Keller et al., 2009; Pearson et al., 2009; Khire et al., 2016; Fishman et al., 2017; Le Guennec et al., 2020). The relationship between the microtubules and POC1B rod structures in the DC is unknown but is likely to have a scaffolding role (Avidor-Reiss and Turner, 2019; Avidor-Reiss et al., 2019).

Advanced paternal age has been consistently implicated in reduced reproductive outcomes and various neurocognitive and developmental conditions in the offspring of humans and other animals (Pizzari et al., 2008; Johnson et al., 2015; Ramasamy et al., 2015; Khandwala et al., 2018). However, the causes for this sperm aging are mostly unknown. One causal factor for sperm aging may be *de novo* mutations in sperm DNA (Kong et al., 2012; Goldmann et al., 2016). However, the contribution of another critical sperm component, the centrioles, to sperm aging is unknown. The centrioles are the only cytoplasmic structure inherited exclusively from the father; they participate in organizing the zygote cytoskeleton and bringing the male and female nuclei together in precise opposition (Sutovsky and Schatten, 2000; Cavazza et al., 2020). As a result, the sperm centrioles are implicated in various reproductive diseases, such as male infertility and early pregnancy failure (Sathananthan, 2009; Chemes and Rawe, 2010; Schatten et al., 2011; Avidor-Reiss et al., 2020). Deterioration of either of the sperm centrioles with patient age may be a novel mechanism for sperm aging.

Here, we developed a quantitative and ratiometric immunofluorescence approach named Fluorescence-based Ratiometric Assessment of Centrioles (FRAC) and performed the most extensive investigation of sperm centriole quality in patients to date using the centriole biomarkers Tubulin and POC1B. We found that infertile men with teratospermia and older men have lower quality centrioles, although the causal relationship between centriolar defects and morphology or age remains unclear. This study opens the door for extensive characterization of the contribution of sperm centrioles to reproductive diseases. Furthermore, rather than providing a binary readout, FRAC quantification of centriole quality provides a range for centrioles quality, which can be combined with other fertility information to specify a more accurate and sensitive fertility prediction. For convenient reading, specific terms (underlined and italicized when they first appear) are described in **Box 1**.

MATERIALS AND METHODS

Overall Project Organization

This project was performed in three consecutive studies over 3 years (November 2016 to September 2019). In each study, sperm centrioles were assessed near the time of collection after the sperm had been separated into a pellet and an interface using differential gradient centrifugation. In study 1 (November 2016 – December 2016), we analyzed the pellet sperm from two proven fertile donors (D1p and D2p) and 12 patients (P1p – P12p) for a total of 14 men obtained from the Yale Fertility Center. In study 2 (May 2018 – September 2018), we received and analyzed the pellet (P13p – P18p) and interface (P13i – P18i) sperm of 7 infertile men from the Urology Clinic at the Regency Medical Center in Toledo. In study 3 (May 2019 – September 2019), we obtained and analyzed the pellet (P19p – P31p) and interface (P19i – P31i) sperm of 12 infertile men from the Urology Clinic at the Regency Medical Center in Toledo. Centrioles were assessed by confocal microscopy using antibody labeling of POC1B and Tubulin. We compared 4 different antibodies against tubulin, including an antibody against acetylated tubulin, and found comparable result in staining of the PC and DC, therefore we choose the sheep antibody because it allowed for more flexibility to stain with antibodies made in rabbit and mouse (Fishman et al., 2018).

Semen Samples

Semen samples from consenting and de-identified donors or consenting infertile men were produced by masturbation and ejaculated into containers at home or in the privacy of a clinic room. The ejaculates were allowed to liquefy for at least 30 min at 37°C, and basic semen analysis was performed following WHO guidelines, including information on semen volume, sperm count, motility, and morphology (WHO, 2010). This information was used to determine which patients had teratospermia or other sperm infertility phenotypes (**Table 1**). Samples were frozen in sperm cryopreservation media (TYB, Irvine Scientific) following the manufacturer's instructions until use, or were used within 5 h of collection (study 2), or were preserved using Sperm CryoProtect (Nidacon, SCP-020) and stored in liquid nitrogen until use (study 3).

Differential Gradient Centrifugation, Washing, Attachment, and Fixation

All samples were separated into interface and pellet sperm using differential gradient centrifugation according to the manufacturer's instructions. The fresh samples were kept at 37°C (study 2). Frozen samples were thawed at 37°C (studies 1 and 3). Then, the samples were layered onto a PureCeption gradient (Origio, ART-2040 and ART-2080) (studies 1 and 2) or a 40/80 PureSperm gradient (Nidacon, PS40-100 and PS80-100) (study 3). The interface was separated from the media and discarded (study 1) or placed in a separate tube (studies 2 and 3) while the pellet remained in the original tube. The interface and pellet sperm were washed using sperm washing media (Origio, ART-1006 (studies 1 and 2) or Nidacon, PSW-100 (study 3). The final pellet of interface sperm and pellet sperm was resuspended in PBS (study 1) or M199 medium (Sigma-Aldrich, M7528) (studies 2 and 3). The total volume of resuspended sperm was 100–600 μL based on the size of the pellet. Approximately 30 μL (study 1), 45 μL (study 2) or 35 μL (study 3) of suspended sperm were

BOX 1 | Definitions.
Centriolar marker or marker – Either of the antibodies against POC1B and Tubulin.
Combined mean ratio range – The combined difference between the patient with highest mean ratio and the patient with lowest mean ratio in the PC, DC, and Ax, and divided by the number of sites.
Fraction – The two groups of sperm generated by differential centrifugations: pellet and interface.
Mean affected individual score (MAIS) – A score describing the average severity of centriole defects in patient populations with low quality centrioles. The numerator is the number of outlier values added together where >2SD is 1 and >3SD is 2. The denominator is the number of affected individuals.
Mean ratio – The mean immunostaining intensity ratio, the mean of the ratios for all sperm in a population from one patient at a location for a marker, usually calculated from 50 to 100 sperm. Each patient had up to 12 mean ratios (PC tubulin, DC tubulin, Ax tubulin, PC POC1B, DC POC1B, and Ax POC1B in the pellet and the interface).
Mean ratio range – The difference between the patients with highest mean ratio and the patients with lowest mean ratio from different men of a group (i.e., 0.57–0.25 = 0.32).
Optimal centrioles – A patient who had all six mean ratios of the pellet fall within the reference range.
Optimal reference population – the 19 men in the reference population that have optimal centrioles.
We studied five populations of sperm: (i) pellet sperm (higher-grade sperm) and (ii) interface sperm (lower-grade sperm) from men with eumorphic sperm; and (iii) pellet sperm and (iv) interface sperm from men with teratospermia; and (iv) pellet sperm from fertile donors.
Ratio – The ratios between the staining intensity of one marker in one location (e.g., PC) over the sum of the intensity of the same marker in all other locations in the same individual sperm (i.e., PC/PC + DC + Ax).
Ratio distribution – The distribution of single sperm ratios from a single sperm fraction from a single man.
Reference population – The pellet sperm from the 22 men with standard sperm morphology; this population includes motility defects and low count.
Reference range – The mean ± 2SD of the reference population for a marker at a given location.
Reference ratio distribution – The percent distribution of the individual sperm ratios from the 19 men from the reference population that were not outliers.
Sample (or semen sample) – the ejaculate or part of it obtained from a sperm donor or patient.
Severe sub-optimal centrioles – A patient who had at least one of the six mean ratios fall more than 3 SDs from the reference range mean.
Sperm location or location – The three sites in the sperm used when quantifying marker intensity: PC, DC, and Ax.
Sub-optimal centrioles – A patient who had at least one of the six mean ratios fall between 2 and 3 SDs from the reference range mean.
Teratospermia – Semen condition where sperm have abnormal morphology.

pipetted into a single well of a Silicone Isolator (EMS 70339-25) on each of 5 Poly Lysine Slides (VWR 16002-116) (study 1), or at least 3 8mm coverslips for each sample (studies 2 and 3). These slides (study 1) or coverslips (studies 2 and 3) were set to rest for 20 min at room temperature, then the excess liquid was removed, and the silicone isolator was removed (study 1). Either 3.7% formaldehyde (study 2) or methanol (studies 1 and 3) was added as a fixative, and samples were left to rest for 15 min at room temperature (study 2) or 5 min at −20°C (studies 1 and 3). Excess fixative was removed. Slides were then washed three times in PBS before mailing in PBS at room temperature to Toledo, where they were stored at 4°C (study 1) or the coverslips were immediately stained after fixation (studies 2 and 3).

Sperm Staining

Staining was performed at the University of Toledo. Samples were permeabilized with 0.3% Triton X100 in PBS for 1 h and blocked with 1% BSA in PBS with 0.3% Triton X100 for 2 h (study 1) or 30 min (studies 2 and 3). Primary antibodies diluted in PBS with 1% BSA and 0.3% Triton were applied to the slide (study 1) or coverslip (studies 2 and 3) and incubated overnight at 4°C. Primary antibodies were anti-POC1B [produced in the lab 10537, 1:100, (Fishman et al., 2018)] and sheep anti-Tubulin (Cytoskeleton, Inc.) (1:600 – 2,000). Slides were then washed in PBS with 0.3% Triton X-1000 3 times for 5 min each. Subsequently, slides were incubated with secondary antibodies and 1 μg/100 μL Hoechst. The secondary antibodies were donkey anti-rabbit DyLight 650 (Thermo Fisher Scientific, SA5-1004; 1:300 – 400) or donkey anti-rabbit Alexa 488 (Jackson ImmunoResearch, 711-545-152; 1:300); and donkey anti-Sheep Cy3 (Jackson ImmunoResearch, 713-165-003; 1:1,200 – 2,000) or donkey anti-Sheep Alexa 555 (Thermo Fisher Scientific, A-21436; 1:1,000). Samples were incubated in this solution at room temperature for 4 h (study 1) or greater than 3 h (studies 2 and 3), then washed in PBS with 0.3% Triton X100 3 times for 5 min each, and PBS 3 times for 5 min each. Coverslips were mounted with ProLong gold (Thermo Fischer Scientific, P10144) and allowed to cure for at least 24 h at room temperature in the dark (study 1),

TABLE 1 | Summary of sperm characteristics from semen analysis.

	Infertile Normal morphology (Range, Mean ± SD, N)	Infertile Abnormal morphology (Range, Mean ± SD, N, P)	Donor Normal morphology (Range, Mean ± SD, N, P)
N	22	9	2
Age	19–46, 33.2 ± 6.6, 17	27–46, 35.6 ± 7.9, 9, 0.42	NA
Sperm number	11.7–418, 222 ± 142, 10	82–579, 154 ± 233, 8, 0.46	NA
Sperm concentration	7.8–209, 66.2 ± 61.2, 20	0.3–193, 47.7 ± 73.6, 9, 0.47	40–228, 134 ± 132.9, 2, 0.19
Progressive motility	13–58, 35.9 ± 18.1, 10	0–36, 15.9 ± 13.1, 8, 0.019	NA
Normal morphology	5–16, 8.2 ± 3.6, 9	0–3, 1.2 ± 1.5, 9, 0.0001	NA

P-value as determined by T-tests comparing Infertile and Donor with Normal morphology. SD, standard deviations; N, number; P, P-value; and NA, not available.

or were mounted with Vectashield (Vector Laboratories, H-1200) and sealed with clear nail polish (studies 2 and 3).

Confocal Microscopy

Slides from all three studies were imaged using a Leica SP8 Confocal microscope in photon counting mode using a 630× magnification, 0.75 zoom, and a format of 4,096 × 4,096 pixels. The scan times was 400 hz with four line averages (study 1) or two frame accumulations and 2 line averages (studies 2 and 3) per scan. We used two sequences. Sequence one activated both a 405 nm laser to collect the DNA staining and the 561 nm laser to collect the tubulin staining; the lasers in this sequence were also used to generate a phase-like picture. Sequence two activated the 633 nm laser (studies 1 and 3) or the 488 nm laser (study 2) to collect the POC1B staining and to generate a phase-like picture. All lasers were kept at less than 5% power. We collected multiple Z sections (10–20) of 0.3 μm thickness from the top of the highest sperm to the bottom of the lowest sperm. We generated a max projection of all the data using the LAX program. Pictures were taken with a gain of 10 and a laser intensity that prevented signal saturation of the centriole markers so we could record both increases and decreases of signal.

Pictures for **Figure 1C** were deconvoluted with HyVolution II from Leica Microsystems. We used the SVI Huygens Essential program with the standard strategy, no auto-crop was used, and the mounting media refractive index was set for Vectashield (1.457).

Staining Quantification

The staining intensities for each marker in the acquired images were quantified in the PC, DC, and Ax of each sperm using a 0.75 μm circle (study 1) or a 0.5 μm × 0.75 μm rectangle (studies 2 and 3) (**Figure 1**). For every sample, every sperm in the view was measured, regardless of an individual's sperm phenotype (except for one man whose centrioles were unidentifiable).

Statistical Analysis

Normal distribution was determined after calculating the skewness and kurtosis by the functions SKEW and KURT in Excel. Pearson Correlation R and best fit were calculated by the function CORREL and the automatic linear regression in Excel, respectively. The Person Correlation R^2 was calculated by RSQ, and the Person Correlation *P*-value was calculated using the function TDIST in Excel. N was calculated using the function COUNT, the T statistic using the equation [R*SQRT(N-2)]/[SQRT(1-R^2)], and the degrees of freedom was calculated by N-2, in Excel. *Z*-tests were calculated on the site https://www.socscistatistics.com/tests/ztest/default2.aspx.

Ethical Approval

The studies involving human participants were reviewed and approved by the University of Toledo's IRB Board and Yale's Human Investigation Committee. The patients/participants provided their written informed consent to participate in this study.

RESULTS

During our initial characterization of protein levels in the sperm centrioles using quantitative immunofluorescence (photon counting), we found that immunofluorescence intensity values alone are not sufficiently sensitive and reproducible to detect differences in staining across multiple studies. This insensitivity is largely due to the inherent variability of staining and imaging within and between samples and appeared to be unrelated to the biological quality of the sperm. Therefore, we developed the Fluorescence-based Ratio Assessment of Centrioles (FRAC) assay that compares the ratios of immunofluorescence intensity. In this assay, the intensity at different *locations* (PC, DC, or Ax) is compared to the total intensity at those locations for each *marker* (tubulin or POC1B) per sperm, generating 6 ratios (2 markers × 3 locations = 6) (**Figure 1**). The use of ratios is advantageous because it has the potential to isolate sperm-specific variables from experimental variation (i.e., lot-to-lot variation in antibodies, reagent potency, human error, changes in microscope laser intensity, and other variables that are difficult to control) (Dunn et al., 1994). To overcome the variability of the sperm present in a patient, we calculated the mean of these ratios from multiple sperm. We will refer to the six *mean ratios* by the marker and location [e.g., "POC1B PC" refers to POC1B PC/(POC1B PC + POC1B DC + POC1B Ax) (**Figure 1D**)].

Population Definitions

We analyzed sperm samples from 31 patients and two donors across three studies between 2016 and 2019 (**Figure 2A**). These 31 patients were all undergoing infertility treatments but had varying diagnoses; their sperm phenotypes were classified as either eumorphic sperm (normal morphology) (n = 22) or teratospermia (poor morphology) based on Kruger's strict criteria (n = 9) (see patient details in **Supplementary Table 1**). Every sample was processed using gradient centrifugation, which resulted in two fractions: a pellet of dense sperm, generally regarded as higher quality, and used for intrauterine insemination, IUI (Karamahmutoglu et al., 2014; Fácio et al., 2016); and an accumulation of lighter sperm at the interface of the gradient phases, which has lower quality sperm (Branigan et al., 1999). The pellet sperm of every sample was collected (n = 31), and the interface from studies 2 and 3 were also collected (n = 19). This centrifugation produced five groups of sperm, each with hypothetically distinct quality levels: (i) the pellet sperm from men without teratospermia (n = 22) (the reference population, **Figure 2A**); (ii) the interface sperm from men without teratospermia (n = 9) (**Figure 2B**); (iii) the pellet sperm from men with teratospermia (n = 8) (**Figure 2C**); (iv) the interface sperm from the men with teratospermia (n = 8) (**Figure 2D**); and (v) the pellet sperm from fertile men with confirmed fertility (n = 2) (**Figure 2A**). These five groups enabled us to characterize the differences in sperm centriole quality between men with and without teratospermia and examine the efficacy of differential centrifugation in isolating sperm with quality centrioles.

We used pellet sperm of infertile men with eumorphic sperm to overcome the limited availability of fertile donor sperm. Since

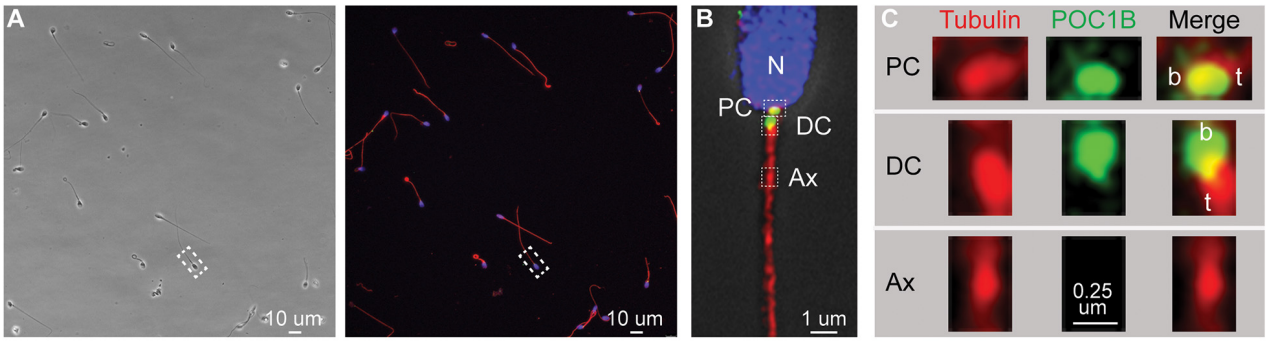

D

$$\text{PC Tubulin} = \frac{\text{PC Tubulin}}{\text{PC Tubulin} + \text{DC Tubulin} + \text{Ax Tubulin}} \qquad \text{PC POC1B} = \frac{\text{PC POC1B}}{\text{PC POC1B} + \text{DC POC1B} + \text{Ax POC1B}}$$

$$\text{DC Tubulin} = \frac{\text{DC Tubulin}}{\text{PC Tubulin} + \text{DC Tubulin} + \text{Ax Tubulin}} \qquad \text{DC POC1B} = \frac{\text{DC POC1B}}{\text{PC POC1B} + \text{DC POC1B} + \text{Ax POC1B}}$$

$$\text{Ax Tubulin} = \frac{\text{Ax Tubulin}}{\text{PC Tubulin} + \text{DC Tubulin} + \text{Ax Tubulin}} \qquad \text{Ax POC1B} = \frac{\text{Ax POC1B}}{\text{PC POC1B} + \text{DC POC1B} + \text{Ax POC1B}}$$

FIGURE 1 | Quantitative imaging of sperm centriole markers. **(A)** An example phase and fluorescent image of a group of pellet spermatozoa. Such a picture ordinarily contains 10–30 spermatozoa. **(B)** Zoom in on one sperm from **(A)** that was deconvolved using HyVolution. Nucleus (N). Three boxes point the approximate location of the PC, DC, and Ax, insets presented in panel **(C)**. **(C)** Zoom in on the Proximal centriole (PC), distal centriole (DC), and axoneme (Ax) of sperm from panel **(B)** labeled with Anti-POC1B and anti-tubulin antibodies. Centriole base (aka proximal end), b; the centriole tip (t) (aka distal end). We consistently find that POC1B labeled more intensely at the proximal end of the tubulin staining. In the PC, this relative position may be because of the presence of microtubular tip extension, known as the centriolar adjunct. In the DC, this relative position may be due to the higher concentration of microtubules at the DC tip. Tubulin staining in the PC and DC is more intense then the nearby axoneme possibly because the PC and DC microtubules were unmasked during centrosome remodeling (Fishman et al., 2018). Because the centrioles are intensely stained with tubulin antibodies, we diluted tubulin antibodies and avoid their exposer to intense laser power that saturates the tubulin labeling. As a result, the axoneme labeling appears punctate. **(D)** The six *mean ratios* by marker and location. The picture is oriented with the PC on the right as describe in Khanal et al. (2021).

the population of sperm in an ejaculate is highly heterogeneous (van der Horst and Maree, 2014), we expected that even the most fertile donors will have some sperm with poor centrioles, and the most infertile patients have some sperm with good centrioles. However, we assumed that sperm centriole defects in infertile men with eumorphic sperm would be minimal, and therefore suitable for generating a reference population. The pellet sperm from the infertile men without teratospermia will be referred to as the *Reference Population* (**Figure 2B**).

The Reference Population

We analyzed the variation of the mean ratios within the reference population to identify outlier values. To identify the samples with a 95% probability of belonging to the reference population we calculated the mean of the ratios in the reference population ± two standard deviations (SDs), which we called the *Reference Range* (Figurer 2A; Wright and Royston, 1999; Boyd, 2010). Therefore, samples with a mean ratio outside the reference range for *any* of the six mean ratio locations/markers were considered outliers and deemed to have *Sub-Optimal Centrioles*. A sample from the reference population was considered to have *Optimal Centrioles* if all six sperm mean ratios were within the reference range. Nineteen of the twenty-two samples (86%) from the reference population had all six mean ratios fall within the reference range and were considered to have optimal sperm centrioles and we defined as the *Optimal Reference Population* (**Figure 2A**). The distribution of the optimal reference population is almost normal (**Figure 2B**). The skewness (the degree of asymmetry of a distribution around its mean) is + /−1 for tubulin of PC, DC, and Ax, as well as for POC1B of PC and DC. Axoneme POC1B skewness was slightly larger, probably because POC1B usually is not found in the axoneme, and the distribution is one-sided. The kurtosis (sharpness of the peak around the mean) is below + /−3 for tubulin of PC, DC, and Ax as well as for POC1B of PC, DC, and Ax.

We determined that three samples from the reference population had sub-optimal sperm centrioles. This result suggested that 14% (3/22) of the reference population samples potentially have sub-optimal centrioles. Two of them, P26p and P28p, had mean ratios between two and three SDs from the mean. The third patient, P30p, had a mean ratio more than three SDs from the mean. P26p, had a semen phenotype of oligospermia (low sperm count), had low PC POC1B; P28p, had a semen phenotype of normospermia (normal semen analysis), had high PC POC1B and low DC POC1B. The third patient, P30p, also had a semen phenotype of normospermia, had high Ax POC1B. This result suggests that there are 4 outlier values to 3 affected individuals, with one that is more than 3 SDs. To evaluate the severity of the low-quality centriole subpopulations we calculated the *Mean Affected Individual Score*

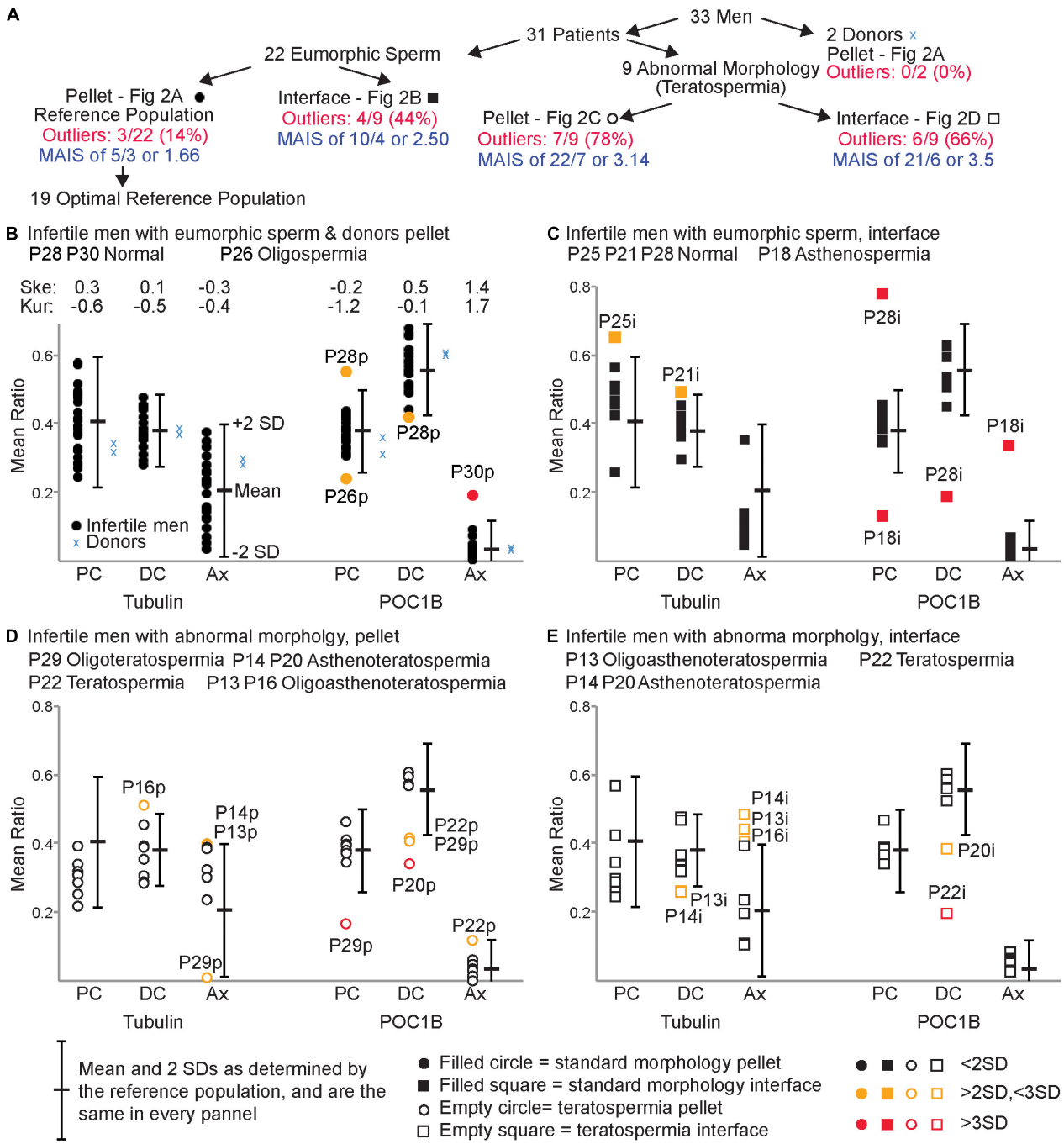

FIGURE 2 | FRAC can identify sperm populations with suboptimal centrioles. **(A)** Breakdown of the 5 populations used. **(B–E)** For each panel, the mean and two standard deviations (SD) of the reference population are indicated to the right of each set of mean ratios. **(B)** Mean ratios of the pellet eumorphic sperm (the reference population) and pellet sperm from donors. The top of the graph indicates the skewness (Ske) and kurtosis (Kur) of the mean ratios of the optimal reference population. **(C)** Mean ratios of the interface eumorphic sperm. **(D)** Mean ratios of the pellet sperm with teratospermia. **(E)** Mean ratios of the interface sperm with teratospermia. Samples that were outside of 2 SD were identified as outliers (colored yellow and labeled). Outliers that were beyond 3 SD are colored red and labeled. The semen analysis results of these outlier patients are identified in the upper left of each graph. MAIS, mean affected individual score.

(MAIS, The numerator is the number of outlier values added together where >2SD is 1 and >3SD is 2. The denominator is the number of affected individuals). The mean affected individual score is 1.66 (5/3).

Finally, we found that all six mean ratios of the two donor men analyzed fell within 2 SDs of the mean (**Figure 2B**). This distribution supports the assumption that the optimal reference population resembles fertile men.

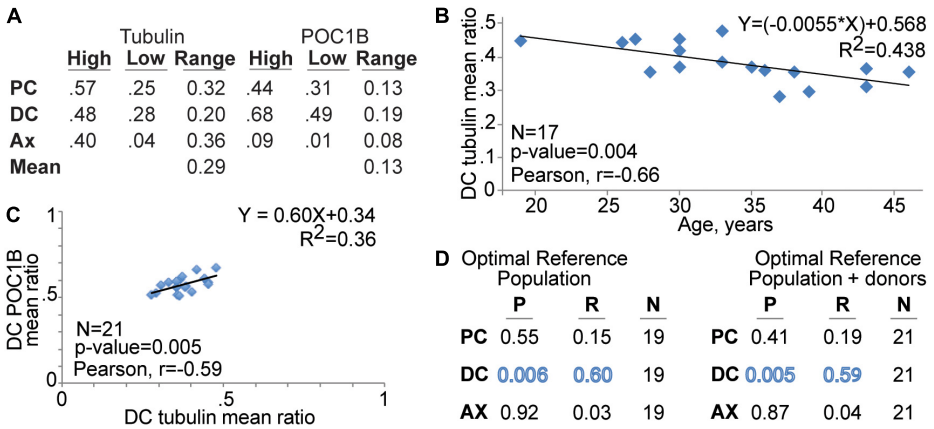

FIGURE 3 | The of DC's tubulin mean ratio corelate with patient age and DC POC1B. **(A)** Tubulin mean ratio range is wider than POC1B mean ratio range. Table shows the centriole marker mean ratio range of the reference population at the PC, DC, and Ax as well as centriole marker combined mean ratio range in the pellet sperm (Mean). **(B)** FRAC finds that the tubulin level in the DC is reduced with patient age. **(C)** Graph depicting the Correlation of DC POC1B and DC tubulin mean ratios in the Optimal Reference Population. **(D)** Table summarizing the correlation *P* value (P), Pearson *R* value (R), and number of men (N) of Tubulin and POC1B patient mean ratios.

Tubulin Ratios Are Negatively Correlated With Patient Age

The quality of a marker is defined by several factors, including range narrowness, sensitivity, and specificity (Utt, 2016). Here, we evaluate the narrowness of the range. We determined the *Mean Ratio Ranges* for the optimal reference population for tubulin and POC1B at each location. The mean ratio ranges were determined by the difference between the highest individual patient's mean ratio and the lowest individual patient's mean (**Figure 3A**). The mean ratio ranges for Tubulin were 0.32 in the PC, 0.20 in the DC, and 0.36 in the Ax. The mean ratio ranges for POC1B were 0.13 in the PC, 0.19 in the DC, and 0.08 in the Ax. Therefore, the *Overall Mean Ratio Range*, the mean of the mean ratio ranges, for tubulin was 0.29, and for POC1B was 0.13. This overall difference is statistically significant ($P = 0.05$), suggesting that the tubulin distribution is a more variable than the POC1B distribution.

To gain insight into a potential explanation for the distribution difference, we looked for an age effect on tubulin and POC1B. We analyzed the 17 men in optimal reference population that provided their age. The mean ratio of tubulin in the DC has a statistically significant ($P = 0.004$) moderate negative correlation with age (Pearson correlation coefficient, $R = -0.66$) (**Figure 3B**). The standard deviation did not change with age ($R = 0.02$, $P = 0.95$). We found no statistically significant and no or weak correlation with age amongst the other five mean ratios ($r = 0.15$–0.24; $P = 0.34$–0.58). The age range in this study was 19–46 (i.e., 27 years difference). The line of best fit between DC tubulin and age ($R^2 = 0.438$) suggests a yearly reduction of ∼1.2% to a total of ∼24% reduction over 20 years. The age effect on DC tubulin may partially explain the wider distribution of tubulin and suggests that DC tubulin is a sensitive marker to other life circumstances.

In canonical centrioles, POC1B forms a scaffold structure that is attached to the microtubules and controls centriole length and stability (Keller et al., 2005; Blachon et al., 2009; Pearson et al., 2009). Therefore, we examined whether the mean ratios of POC1B and tubulin correlate in the pellet of the optimal reference population with normal sperm morphology. We found that, in the DC, POC1B and Tubulin have a significant and modest positive correlation with each other ($P = 0.006$, $R = 0.60$) (**Figure 3C**). No significant correlation was observed between POC1B and Tubulin in the PC or Ax (**Figure 3D**). These data suggest that ∼30% of the DC Tubulin ratio can be predicted by DC POC1B, and vice versa. A similar significant positive correlation was obtained between POC1B and Tubulin when the two donor samples were included with the optimal reference population ($P = 0.005$, $R = 0.59$) (**Figure 3D**).

Interface Sperm of Infertile Men With Eumorphic Sperm Have Sub-Optimal Centrioles

As sperm cells differentiate, they lose cytoplasm and become denser; this difference is used to select the better sperm found in the pellet in differential centrifugation (Oshio et al., 1987; Sakkas, 2013). During sperm differentiation, centrioles are also being remodeled (Fishman et al., 2018). Therefore, we hypothesized that the less dense, and thus less mature, sperm found in the interface would have reduced centriole quality. We tested this hypothesis by comparing the mean ratios of the standard sperm morphology (eumorphic) interface population ($N = 9$) to the reference range (**Figure 2C** and **Table 2**). We found that 44% of samples from these men had outlier mean ratios (4/9). Two, P21i and P25i, had mean ratios between the two and three SDs away from the mean. P21i, who has a semen phenotype of normospermia, had a high level of DC tubulin. P25i, who has a semen phenotype of normospermia, had a high level of PC tubulin. The other two outlier samples, P18i and P28i, had mean ratios outside three SDs from the mean. P18i, who has a semen phenotype of asthenospermia (reduced sperm motility), had low PC POC1B and high Ax POC1B. P28i, who has a semen

TABLE 2 | Summary table comparing the various populations of men examined in the study.

	Infertile Standard Morphology N (patients) (% of population)	Infertile Abnormal Morphology N (patients) (% of population)	*P*-value: Infertile Standard/ Infertile Abnormal	Donor Standard Morphology N (% of population)	*P*-value: Infertile/ donor
Pellet	***N* = 22**	***N* = 9**		***N* = 2**	
2SD	19 (86%)	2 (22%)	0.0005	2 (100%)	0.6527
>2SD	3 (14%)	7 (78%)	0.0005	0	
>2SD, <3SD	2 (P26, P28) (9%)	4 (P13, P16, P22, P14) (44%)	0.0238	0	
>3SD or no staining	1 (P30) (5%)	3 (P20, P27, P29) (33%)	0.03	0	
Interface	***N* = 9**	***N* = 9**		**NA**	
2SD	5 (56%)	3 (33%)	0.3421	NA	
>2SD	4 (44%)	6 (66%)	0.3421	NA	
>2SD, <3SD	2 (P21, P25) (22%)	4 (P13, P14, P16, P20) (44%)	0.31732	NA	
>3SD or no staining	2 (P18, P28) (22%)	2 (P22, P27) (22%)	1	NA	
P-value: pellet/interface					
2SD	0.06288	0.59612			
>2SD	0.06288	0.59612			
>2SD, <3SD	0.32218	1			
>3SD or no staining	0.13104	0.59612			
Total (pellet + interface)	***N* = 9**	***N* = 9**		**NA**	
2SD	3 (33%)	2 (22%)	0.81	NA	
>2SD	6 (67%)	7 (78%)	0.5961	NA	
>2SD, <3SD	3 (P21, P25, P26) (33%)	3 (P13, P14, P16) (33%)	1	NA	
>3SD or no staining	3 (P18, P28, P30) (33%)	4 (P20, P22, P27, P29) (44%)	p.3421	NA	

P-value as determined by Z-test. SD, standard deviations; N, number; P, P-value; and NA, not available.

phenotype of normospermia, had high PC POC1B and low DC POC1B. This patient (P28) seemed to have severely sub-optimal centrioles in both the interface and pellet; he had four outlier values between both sperm populations (pellet and interface), two of which were outside 3 SDs of the mean. These results suggest that the interface sperm of infertile men with eumorphic sperm tend to contain more sperm with reduced quality centrioles than the sperm in the pellet fraction (4/9 versus 3/22, $P = 0.06$) (**Table 2**). The 6 outlier values, with 4 that are more than 3 SDs ($4^*2 + 2^*1 = 10$), in 4 affected individuals yields a mean affected individual score of 2.5 (10/4), which is more severe than the reference population pellet (1.6).

78% of Infertile Men With Teratospermia Have Reduced Centriole Quality

Most reports that suggest that human sperm centrioles have a role post-fertilization are from IVF studies with teratospermia patients (reviewed by Avidor-Reiss et al., 2019). Therefore, we hypothesized that a significant portion of infertile men with morphologically abnormal sperm would have suboptimal sperm centrioles. As such, the objective of this analysis was to test if POC1B and tubulin can identify centriolar differences between sperm populations with and without morphological defects.

We analyzed the mean ratios of the pellet sperm from nine patients with teratospermia and compared them to the reference range (**Figure 2D**). For eight of the nine patients, we were able to detect the sperm centrioles using the antibodies, and we analyzed the mean ratio of their pellet sperm (**Figure 2D**). For one patient, P27, we were not able to detect the PC and DC as discrete entities using either POC1B or tubulin staining in the sperm neck of the pellet or interface populations. Consequently, we were not able to analyze the mean ratios (**Figure 4**); we concluded that the patient's sperm had a major centriole defect or that they are missing. Interestingly, this patient was one of three patients with the most severe sperm phenotypes, oligoasthenoteratospermia (OAT) (low sperm count, low motility, and poor morphology), of the samples we studied as determined by traditional semen analysis.

For the remaining eight of the nine teratospermia patients, we found that six had outlier mean ratios of centriole markers (**Figure 2D**). Four of these patients, P13p, P14p, P16p, and P22p, had mean ratios between two and three SDs from the mean of the reference population. P13p, who has a semen phenotype OAT, had high Ax tubulin. P14p, who has a semen phenotype of asthenoteratospermia, had high Ax tubulin. P16p, who has a semen phenotype of OAT, had high DC tubulin. P22p, who has a semen phenotype of teratospermia, had low DC POC1B and high Ax POC1B. Two of the patients, P20p and P29p, had mean ratios outside three SDs from the mean. P20p, who has a semen phenotype of asthenoteratospermia, had low DC POC1B. P29p, who has a semen phenotype of oligoteratospermia, had low PC and DC POC1B. Interestingly, P13, P27, and P16 all had the same severe sperm phenotype, OAT, but had different severities in their mean ratios, suggesting that semen analysis is insufficient for evaluating sperm quality. These results suggest that the patients with teratospermia have more sub-optimal

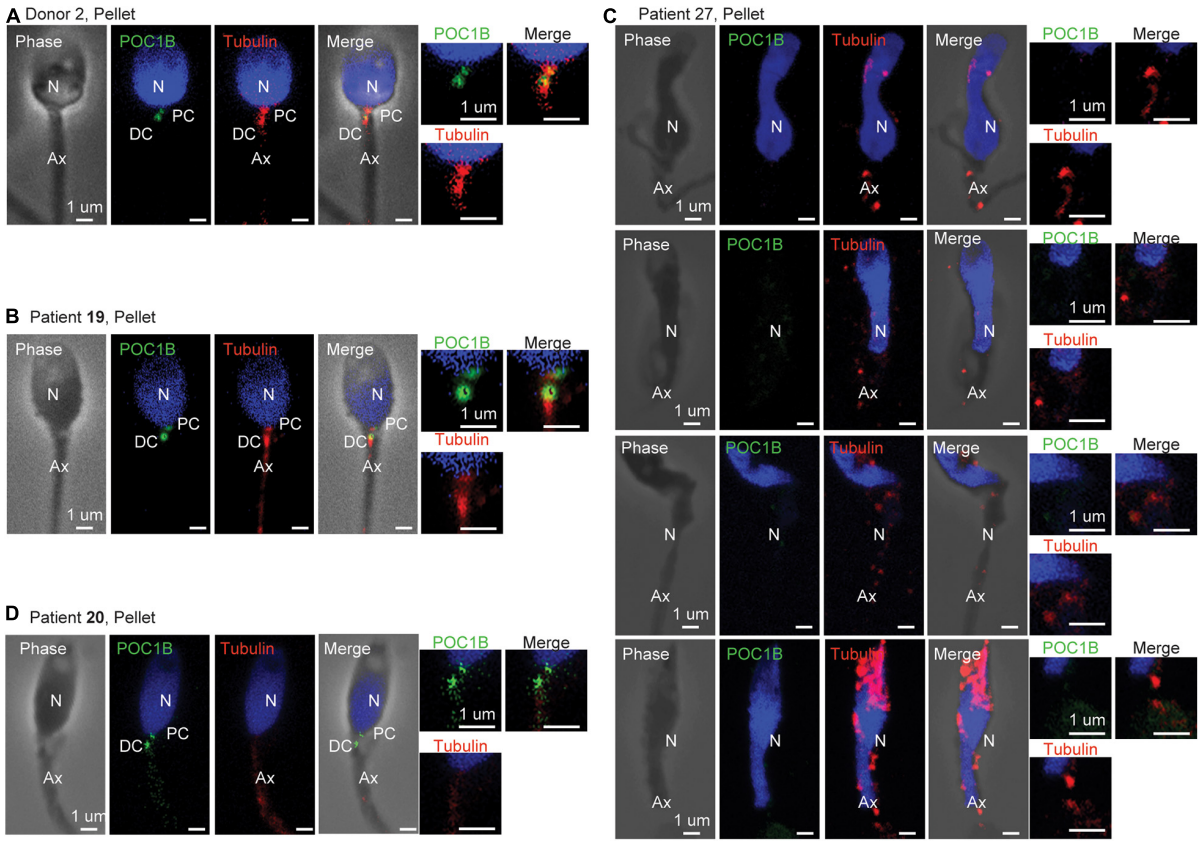

FIGURE 4 | Centriole staining abnormalities. **(A)** Example of standard staining from the pellet sperm of donor 2, who had a standard semen analysis, and whose centriole ratios fell within 2 SDs of the mean for all mean ratios. **(B)** Example of standard staining from the pellet sperm of patient 19, who had a standard semen analysis, and whose centriole ratios fell within 2 SDs of the mean for all mean ratios. **(C)** Example of abnormal staining from the pellet sperm of patient 27, who had a severe oligoasthenoteratospermia phenotype such that the centrioles could not be quantified. **(D)** Example of abnormal staining from the pellet sperm of patient 20, who had an asthenoteratospermia phenotype, and whose centriole ratios fell more than 3 SDs of the mean for distal centriole POC1B. N, nucleus; PC, proximal centriole; DC, distal centriole; Ax, axoneme.

centrioles than patients without teratospermia (7/9, 78%, versus 3/22, 14%, $P = 0.0005$) (**Table 2**).

We designated samples with mean ratios outside three SDs or in samples that we were not able to detect the centrioles, P20p, P27p, and P29p, as samples with *severe sub-optimal centrioles*. It also suggests that there is a statistically significant difference in the number of severe centriolar defects (3/9 versus 1/22, $P = 0.03$) (**Table 2**). This finding supports our hypothesis that sperm with morphological defects are more likely to have lower quality centrioles. This result suggested 14 outlier values (8 + 6) in 7 affected individuals, with 8 that are more than 3 SDs, or a mean affected individual score of 3.14 (22/7), which is more severe than the reference population pellet (1.6) and interphase (2.5).

Differential Centrifugation Is Insufficient to Differentiate Centriole Quality in Teratospermic Men

We found that differential gradient centrifugation of eumorphic sperm results in a pellet enriched for better quality sperm centrioles. We wondered if differential gradient centrifugation has a similar effect on sperm from patients with teratospermia. Therefore, we analyzed interface sperm from men with teratospermia (**Figure 2E**). We found that six of the nine interface sperm samples from men with teratospermia had mean ratios outside the reference range. P13i, P14i, P16i, and P20i had mean ratios between the two and three SDs from the mean of the reference population. P13p, who has a semen phenotype of OAT, had low DC tubulin and high Ax tubulin. P14p, who has a semen phenotype of asthenoteratospermia, had low DC tubulin and high Ax tubulin. P16p, who has a semen phenotype of OAT, had high Ax tubulin. P20i, who has a semen phenotype of asthenoteratospermia, had low DC POC1B. One patient, P22i, had a mean ratio more than three SDs away from the mean of the reference population. P22i, who has a semen phenotype of teratospermia, had a low DC POC1B. Again, we were not able to detect the PC and DC as discrete entities in the interface sperm from patient P27, who has a semen phenotype of OAT, using POC1B or tubulin staining. This result suggests that infertile men with teratospermia have a similar incidence of sub-optimal centrioles in the interface and the pellet fractions (6/9 interface versus 7/9 pellet; p is 1) (**Table 2**). Furthermore, this observation

suggests that sperm selection by differential centrifugation is insufficient for increasing the odds of fertilization in cases of sub-optimal centrioles, thus alternative selection techniques should be investigated. Additionally, this result suggests 12 (6 + 6) outlier values in 6 affected individuals, with 7 that are more than 3 SDs, or a mean affected individual score of 3.50 (21/6), which is more severe than the reference population pellet (1.6) or the interface of the patients with eumorphic sperm (2.5).

The Distribution of a Patient's Sperm Ratios Provides More Insight on Centriole Quality

While the mean ratios of a patient with optimal centrioles are all within the reference ranges, the individual sperm of that patient may fall outside the reference ranges because sperm populations are heterogeneous. The inverse of this is also true: a patient with sub-optimal centrioles may also have some sperm with optimal centriole ratios. Furthermore, because the sperm is heterogenous, means can oversimplify the data, and specifically ignore bimodal data. Therefore, to gain insight into the heterogeneity of the sperm samples, we analyzed the distribution of POC1B ratios in individual sperm of representative men.

The individual ratios from all the pellet sperm 19 men in the optimal reference population served as our standard population, which we termed the *Reference Ratio Distribution* (marked with blue in **Figure 5**). In this reference ratio distribution, POC1B ratios peak at a ratio of 0.3–0.4 for the PC, 0.6–0.7 for the DC, and 0–0.1 for the Ax. The POC1B PC and DC mean ratios had an approximately normal distribution, as the skewness and kurtosis were less than + /−1.0. We then compared it to the staining ratio distributions of a sample of patients that had sub-optimal centrioles, P28p, P28i, P22p, and P22i.

We analyzed the sperm of P28, a patient with eumorphic sperm in the reference population. P28p has sub-optimal higher than the reference ratio distribution peak (0.1) or the pellet sperm (red arrow in **Figure 5D**, middle panel). Centrioles with two outlier mean ratios (**Figure 2B**). P28p had high PC POC1B and low DC POC1B (>2SD, <3SD). We looked at the distribution of all P28p's sperm ratios and found that the PC POC1B ratios peak at 0.5–0.6 (red arrow in **Figure 5A**, left panel), which is higher than the reference ratio distribution (blue arrow in **Figure 5A**). Also, P28p has a smaller peak at 0.9, which is not present in the reference ratio distribution (dashed red arrow, **Figure 4A**, left panel). Interestingly, the peak of DC POC1B ratio mirrors the PC POC1B shift; it was shifted to a lower range of 0.5–0.6 and had an additional peak from 0.1 to 0.3 (red arrows, **Figure 4A**, middle panel). These two peaks indicate the presence of a subpopulation of sperm with a high PC POC1B ratio, and a low DC POC1B ratio. The correlated shifts in the PC and DC raise the possibility that the increased PC POC1B is at the expense of DC POC1B in P28p. The peak of the Ax POC1B ratio was indistinguishable from the reference ratio distribution (**Figure 5A**, right panel).

P28i has the same two outlier mean ratios found in the pellet, high PC POC1B and low DC POC1B, but they are more severe (>3SD) than the pellet fraction (**Figure 2C**). In the interface, the ratio peaks were shifted even further from the reference ratio distribution than the pellet sperm. P28i PC POC1B ratios peaked between 0.9 and 1.0, which is a more exaggerated shift than the pellet population (**Figure 5B**, left panel). Similarly, P28i DC POC1B ratios shifted to lower than their pellet counterpart to 0–0.2 (**Figure 5B**, middle panel). Therefore, this analysis indicates that the P28 interface contains more sperm with sub-optimal centrioles. The peak of the Ax POC1B ratio was not unusual when compared to the reference ratio distribution, similar to P28p (**Figure 5B**, right panel).

Next, we analyzed P22, who has a sperm phenotype of teratospermia. P22 has two mean ratio outliers in the pellet fraction: low DC POC1B and high Ax POC1B (>2SD, <3SD) (**Figure 2D**). In P22p, the DC POC1B ratio has a peak from 0.5 to 0.6 (red arrow in **Figure 5C**, middle panel), which is lower than the reference ratio distribution (blue arrow in **Figure 5C**, middle panel). Additionally, there is a smaller peak at the 0.2 ratio, which is not present in the reference ratio distribution (dashed red arrow, **Figure 5C**, middle panel). The peak of P22p's Ax POC1B ratio was slightly higher, near 0.2–0.3, whereas the reference ratio distribution peak was near 0.1 (red arrow in **Figure 5B**, right panel). These shifted peaks support the possibility that the decreased DC POC1B is due to POC1B leaking from the DC into the Ax in P22p.

P22i has only one outlier mean ratio, low DC POC1B, that it is more severe (>3SD) than the pellet fraction (**Figure 2E**). As expected, the ratio distribution peak in the interface sperm was higher than the reference ratio distribution peak (0.1) or the pellet sperm (red arrow in **Figure 5D**, middle panel). Unexpectedly, even though the mean PC POC1B of P22i fell within the ratio range, the ratio distribution analysis shows very few sperm fall into the reference ratio distribution. Instead, there were two opposing peaks at 0–0.1 and 0.9–1 (the peak for the reference ratio distribution is 0.3–0.5). Therefore, the ratio distribution analysis finds that P22i contains sub-optimal centrioles that are missed by the mean ratio analysis.

DISCUSSION

Fluorescence-based Ratiometric Assessment of Centrioles is the first step toward an assay that can assess sperm centriole quality and reveal their contribution to infertility. We tested two markers: Tubulin and POC1B. However, FRAC can be extended to include other centriole proteins such CETN1, POC5, and CEP135, specific post-translational modifications (e.g., acetylated tubulin), and other subcellular components (e.g., mitochondria, outer dense fibers, manchette, acrosome, nuclear vesicles, etc.). Furthermore, FRAC could be developed for use in other cell types. We demonstrated that an immunofluorescent, localization-based, ratiometric, quantitative assay, such as FRAC, could give reasonably low variability between experiments and enable the identification of outlier samples when comparing distinct sperm populations. We expect that both abnormally low or high levels of any protein at one of the locations (PC, DC, or Ax) may indicate reduced centriole quality, as the deviation of centriole proteins in either direction was associated with sperm dysfunction (Sha et al., 2017; Garanina et al., 2019).

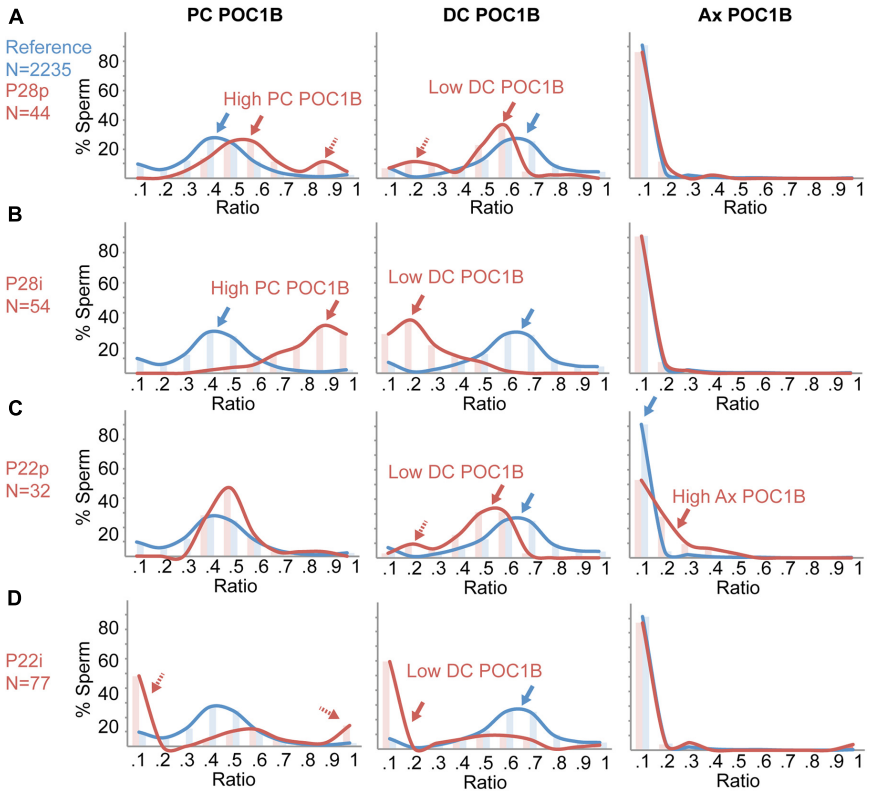

FIGURE 5 | Individual Sperm Ratio Distribution analysis provides additional insight into sperm centriole abnormalities. Histograms of the percent of individual sperm at different ratios of POC1B in the proximal centriole (PC), POC1B distal centriole (DC), and POC1B axoneme (Ax). Reference (blue) is the sperm of the 19 patients within the 22-patient reference population that have optimal centriole quality. **(A)** Ratios of 44 pellet sperm from a patient, P28p (red), that does not have teratospermia but was found to have suboptimal POC1B ratios in the PC and DC. **(B)** Ratios of 54 interface sperm from a patient, P28i (red), that does not have teratospermia but was found to have suboptimal POC1B ratios in the PC and DC. **(C)** Ratios of 32 pellet sperm from a patient, P22p (red), that has teratospermia and was found to have suboptimal POC1B ratios in the DC and Ax. **(D)** Ratios of 77 interface sperm from patient, P22i (red), that has teratospermia and was found to have suboptimal POC1B ratios in the DC. The histogram bins for the ratios on the *x*-axis are 0, –0.1, 0.1 –0.2, 0.2, –0.3, 0.3, –0.4, 0.4, –0.5, 0.5, –0.6, 0.6, –0.7, 0.7, –0.8, 0.8, –0.9, 0.9 – 1.

Tubulin and POC1B are components of distinct centriolar substructures. Tubulin is the structural protein of the microtubule (Downing and Nogales, 1998); POC1B is a structural protein of the centriole lumen (Pearson et al., 2009; Khire et al., 2016; Jo et al., 2019; Atorino et al., 2020; Le Guennec et al., 2020). Therefore, we expect that they report on distinct properties of the sperm centrioles. However, whether these proteins or other centriolar proteins are essential for sperm centriole quality is currently unknown. Future elucidation of essential functions will allow for the development of a minimal set of markers that report on distinct sperm centriole functions and could be used to provide a comprehensive sperm quality report.

Here, we used FRAC with sperm from infertile men, but we expect that the reference range obtained from infertile men with eumorphic sperm would resemble those obtained from fertile men. Since sperm centriole defects are likely to affect only a small portion of infertility cases and the sperm from the two fertile donors falls within the reference range it is likely that other fertile men would also fall within the reference range. However, this expectation needs a more formal demonstration with a larger sample size. Also, at this stage of the investigation, it is not clear if the identified outlier ratios have clinical implications. This clarification can be done in the future by correlating centriole quality with infertility treatment outcomes.

Fluorescence-based Ratiometric Assessment of Centrioles is faster than other techniques currently used to assess sperm centrioles. However, it will need further automation and streamlining to be routinely used in a clinical setting. One way would be to use automated slide immunostaining. Alternatively, image-based flow cytometry could also be used to increase the automation of FRAC. Automation of quantification would be possible by writing an algorithm that scans the major features of the sperm, identifies the centrioles, reads the fluorescence intensity, and outputs mean ratios.

One potential concern regarding FRAC is that it may not identify sperm with an overall reduction or increase in centriole staining since it is based on the relative amount of protein levels. We think this only a minor concern because the two centrioles and the axoneme are different structures with different levels of the same proteins. Therefore, we expect that significant changes in protein expression would result in uneven changes to the various structures. This argument is theoretical and will need

further validation once hypomorphic mutations in the studied proteins are identified.

Fluorescence-based Ratiometric Assessment of Centrioles has the potential to become a useful tool in the clinical evaluation of semen quality. Applying the findings of this study to the sperm of infertile men in general suggests that a considerable fraction of infertile men have lower quality centrioles. Therefore, large-scale studies of sperm centrioles from fertile and infertile men are needed to determine the clinical cut-off values that are associated with sperm centriole-associated reproductive disease (SCARD).

Aging is an important factor in fertility, especially because the average age of paternity is rising in many countries (Bray et al., 2006). Older men have poorer quality semen, and an increased incidence of health problems in their offspring (Mazur and Lipshultz, 2018). However, very little is known about age related changes to the centrioles, which are usually studied in the context of cancer (Tkemaladze and Chichinadze, 2005; Wu et al., 2020). Due to a lack of a convenient way to study sperm centrioles they have only rarely been studied in the context of aging; therefore, little is known about the effect of age on them. Centriole deterioration with age was observed in fruit flies with centrosome misorientation during sperm stem cell division or centrosome amplification in midgut stem cells (Cheng et al., 2008; Park et al., 2014). Also, the centrosomes' position changes with age in endothelial cells of the rabbit aorta (Kiosses and Kalnins, 1993). In light of the rarity of studies on age-related effects on centrioles in general, and on sperm centrioles specifically, our finding that the DC changes with age signifies the importance of studying the impact of age on sperm centrioles.

In summary, we have developed FRAC, a new assay based on image quantification, localization, and ratio calculation, that enables the robust assessment of spermatozoa centrioles. Comparing the mean ratio of centriole and axoneme staining in washed, ejaculated spermatozoa could distinguish between men with just teratospermia, from men with teratospermia and sub-optimal centrioles. The mean ratio of spermatozoa in the ejaculate could be used to stratify whether infertile couples are recommended to use sperm donation rather than ICSI; additionally, women with a lower ovarian reserve may opt to store their eggs until the centriole quality of their male partner increases.

DATA AVAILABILITY STATEMENT

The raw data supporting the conclusions of this article will be made available by the authors, without undue reservation.

ETHICS STATEMENT

The studies involving human participants were reviewed and approved by the University of Toledo's IRB Board and Yale's Human Investigation Committee. The patients/participants provided their written informed consent to participate in this study.

AUTHOR CONTRIBUTIONS

TA-R conceived the manuscript and wrote it. KT wrote the manuscript, produced the figures, and performed the statistical analysis with the consultation of statistician. BS, EF, MA, and BO collected the data. PD improved staining protocol. EM, PP, TS, and PS collected sperm samples, contributed essential expert information, and helped with the comments for the draft manuscript. NN coordinated IRB activity and sample collection procedures. All authors contributed to the article and approved the submitted version.

FUNDING

This work was supported by the Eunice Kennedy Shriver National Institute of Child Health and Human Development (NICHD) grant number R03 HD098314.

ACKNOWLEDGMENTS

We would like to thank Alyssa Sherman, Keith Hoying, Ruben Samroo, Ahmed Hussein, Andrew Gerts, and Rebecca Wynn for their technical help. We would like to thank Gerald Schatten and Calvin Simerly for providing information that was instrumental in initiating this research. We would like to thank Medical Student Research Program (MSRP) of the University of Toledo for sponsoring the work of MA, BO, and PD on this project.

SUPPLEMENTARY MATERIAL

The Supplementary Material for this article can be found online at: https://www.frontiersin.org/articles/10.3389/fcell.2021.658891/full#supplementary-material

Supplementary Table 1 | Patient information. Excel file containing fertility and semen analysis information of all patients.

REFERENCES

Alosilla Fonttis, A., Napolitano, R., and Tomas, M. A. (2002). Successful ICSI in a case of severe asthenozoospermia due to 93% non-specific axonemal alterations and 90% abnormal or absent mitochondrial sheaths. *Reprod. Biomed. Online* 5, 270–272. doi: 10.1016/s1472-6483(10)61831-7

Atorino, E. S., Hata, S., Funaya, C., Neuner, A., and Schiebel, E. (2020). CEP44 ensures the formation of bona fide centriole wall, a requirement for the centriole-to-centrosome conversion. *Nat. Commun.* 11:903. doi: 10.1038/s41467-020-14767-2

Avidor-Reiss, T. (2018). Rapid evolution of sperm produces diverse centriole structures that reveal the most rudimentary structure needed for function. *Cells* 7:67. doi: 10.3390/cells7070067

Avidor-Reiss, T., Carr, A., and Fishman, E. L. (2020). The sperm centrioles. *Mol. Cell. Endocrinol.* 518:110987. doi: 10.1016/j.mce.2020.110987

Avidor-Reiss, T., and Fishman, E. L. (2019). It takes two (centrioles) to tango. *Reproduction* 157, R33–R51. doi: 10.1530/REP-18-0350

Avidor-Reiss, T., and Gopalakrishnan, J. (2013). Building a centriole. *Curr. Opin. Cell. Biol.* 25, 72–77. doi: 10.1016/j.ceb.2012.10.016

Avidor-Reiss, T., Mazur, M., Fishman, E. L., and Sindhwani, P. (2019). The role of sperm centrioles in human reproduction – the known and the unknown. *Front. Cell. Dev. Biol.* 7:188. doi: 10.3389/fcell.2019.00188

Avidor-Reiss, T., and Turner, K. (2019). The evolution of centriole structure: heterochrony, neoteny, and hypermorphosis. *Results Probl. Cell. Differ.* 67, 3–15. doi: 10.1007/978-3-030-23173-6_1

Blachon, S., Cai, X., Roberts, K. A., Yang, K., Polyanovsky, A., Church, A., et al. (2009). A proximal centriole-like structure is present in drosophila spermatids and can serve as a model to study centriole duplication. *Genetics* 182, 133–144. doi: 10.1534/genetics.109.101709

Blachon, S., Khire, A., and Avidor-Reiss, T. (2014). The origin of the second centriole in the zygote of drosophila melanogaster. *Genetics* 197, 199–205. doi: 10.1534/genetics.113.160523

Boyd, J. C. (2010). Defining laboratory reference values and decision limits: populations, intervals, and interpretations. *Asian J. Androl.* 12, 83–90. doi: 10.1038/aja.2009.9

Branigan, E. F., Estes, M. A., and Muller, C. H. (1999). Advanced semen analysis: a simple screening test to predict intrauterine insemination success. *Fertil. Steril.* 71, 547–551. doi: 10.1016/s0015-0282(98)00503-2

Bray, I., Gunnell, D., and Davey Smith, G. (2006). Advanced paternal age: how old is too old? *J. Epidemiol. Community Health* 60, 851–853. doi: 10.1136/jech.2005.045179

Cavazza, T., Politi, A. Z., Aldag, P., Baker, C., Elder, K., Blayney, M., et al. (2020). Parental genome unification is highly erroneous in mammalian embryos. *bioRxiv* 2020:269779. doi: 10.1101/2020.08.27.269779

Chemes, H. E. (2012). "Sperm Centrioles and Their Dual Role in Flagellogenesis and Cell Cycle of the Zygote," in *The Centrosome: Cell and Molecular Mechanisms of Functions and Dysfunctions in Disease*, ed. H. Schatten (Totowa, NJ: Humana Press), 33–48. doi: 10.1007/978-1-62703-035-9_2

Chemes, H. E., Carizza, C., Scarinci, F., Brugo, S., Neuspiller, N., and Schwarsztein, L. (1987). Lack of a head in human spermatozoa from sterile patients: a syndrome associated with impaired fertilization. *Fertil. Steril.* 47, 310–316. doi: 10.1016/s0015-0282(16)50011-9

Chemes, H. E., Puigdomenech, E. T., Carizza, C., Olmedo, S. B., Zanchetti, F., and Hermes, R. (1999). Acephalic spermatozoa and abnormal development of the head-neck attachment: a human syndrome of genetic origin. *Hum. Reprod.* 14, 1811–1818. doi: 10.1093/humrep/14.7.1811

Chemes, H. E., and Rawe, V. Y. (2010). The making of abnormal spermatozoa: cellular and molecular mechanisms underlying pathological spermiogenesis. *Cell. Tissue Res.* 341, 349–357. doi: 10.1007/s00441-010-1007-3

Chemes, H. E., and Sedo, C. A. (2012). Tales of the tail and sperm head aches changing concepts on the prognostic significance of sperm pathologies affecting the head, neck and tail. *Asian J. Androl.* 14, 14–23. doi: 10.1038/aja.2011.168

Cheng, J., Turkel, N., Hemati, N., Fuller, M. T., Hunt, A. J., and Yamashita, Y. M. (2008). Centrosome misorientation reduces stem cell division during ageing. *Nature* 456, 599–604. doi: 10.1038/nature07386

Cito, G., Picone, R., Fucci, R., Giachini, C., Micelli, E., Cocci, A., et al. (2020). Sperm morphology: what implications on the assisted reproductive outcomes? *Andrology* 8, 1867–1874. doi: 10.1111/andr.12883

Downing, K. H., and Nogales, E. (1998). Tubulin and microtubule structure. *Curr. Opin. Cell. Biol.* 10, 16–22.

Dunn, K. W., Mayor, S., Myers, J. N., and Maxfield, F. R. (1994). Applications of ratio fluorescence microscopy in the study of cell physiology. *Faseb. J.* 8, 573–582. doi: 10.1096/fasebj.8.9.8005385

Emery, B. R., Thorp, C., Malo, J. W., and Carrell, D. T. (2004). Pregnancy from intracytoplasmic sperm injection of a sperm head and detached tail. *Fertil. Steril.* 81, 686–688. doi: 10.1016/j.fertnstert.2003.07.025

Fácio, C. L., Previato, L. F., Machado-Paula, L. A., Matheus, P. C., and Araújo, E. F. (2016). Comparison of two sperm processing techniques for low complexity assisted fertilization: sperm washing followed by swim-up and discontinuous density gradient centrifugation. *JBRA Assisted Reproduc.* 20, 206–211. doi: 10.5935/1518-0557.20160040

Fishman, E., Jo, K., Ha, A., Royfman, R., Zinn, A., Krishnamurthy, M., et al. (2017). Atypical centrioles are present in tribolium sperm. *Open Biol.* 7:160334. doi: 10.1098/rsob.160334

Fishman, E. L., Jo, K., Nguyen, Q. P., Kong, D., Royfman, R., Cekic, A. R., et al. (2018). A novel atypical sperm centriole is functional during human fertilization. *Nat. Commun.* 9:2210.

Force, U. P. S. T. (1989). *Guide to clinical preventive services: report of the US Preventive Services Task Force*. Darby, PA: Diane Publishing Company.

Garanina, A. S., Alieva, I. B., Bragina, E. E., Blanchard, E., Arbeille, B., Guerif, F., et al. (2019). The centriolar adjunct(-) appearance and disassembly in spermiogenesis and the potential impact on fertility. *Cells* 8:180. doi: 10.3390/cells8020180

Garrido-Gimenez, C., and Alijotas-Reig, J. (2015). Recurrent miscarriage: causes, evaluation and management. *Postgrad Med. J.* 91, 151–162. doi: 10.1136/postgradmedj-2014-132672

Goldmann, J. M., Wong, W. S., Pinelli, M., Farrah, T., Bodian, D., Stittrich, A. B., et al. (2016). Parent-of-origin-specific signatures of de novo mutations. *Nat. Genet.* 48:935. doi: 10.1038/ng.3597

Grow, D. R., Oehninger, S., Seltman, H. J., Toner, J. P., Swanson, R. J., Kruger, T. F., et al. (1994). Sperm morphology as diagnosed by strict criteria: probing the impact of teratozoospermia on fertilization rate and pregnancy outcome in a large in vitro fertilization population. *Fertil. Steril.* 62, 559–567. doi: 10.1016/s0015-0282(16)56946-5

Hinduja, I., Baliga, N. B., and Zaveri, K. (2010). Correlation of human sperm centrosomal proteins with fertility. *J. Hum. Reprod. Sci.* 3, 95–101. doi: 10.4103/0974-1208.69344

Jo, K. H., Jaiswal, A., Khanal, S., Fishman, E. L., Curry, A. N., and Avidor-Reiss, T. (2019). Poc1B and Sas-6 function together during the atypical centriole formation in drosophila melanogaster. *Cells* 8:841. doi: 10.3390/cells8080841

Johnson, S. L., Dunleavy, J., Gemmell, N. J., and Nakagawa, S. (2015). Consistent age-dependent declines in human semen quality: a systematic review and meta-analysis. *Ageing Res. Rev.* 19, 22–33. doi: 10.1016/j.arr.2014.10.007

Karamahmutoglu, H., Erdem, A., Erdem, M., Mutlu, M. F., Bozkurt, N., Oktem, M., et al. (2014). The gradient technique improves success rates in intrauterine insemination cycles of unexplained subfertile couples when compared to swim up technique; a prospective randomized study. *J. Assist. Reprod. Genet.* 31, 1139–1145. doi: 10.1007/s10815-014-0274-4

Keller, L. C., Geimer, S., Romijn, E., Yates, J. III, Zamora, I., and Marshall, W. F. (2009). Molecular architecture of the centriole proteome: the conserved WD40 domain protein POC1 is required for centriole duplication and length control. *Mol. Biol. Cell.* 20, 1150–1166. doi: 10.1091/mbc.E08-06-0619

Keller, L. C., Romijn, E. P., Zamora, I., Yates, J. R. III, and Marshall, W. F. (2005). Proteomic analysis of isolated chlamydomonas centrioles reveals orthologs of ciliary-disease genes. *Curr. Biol.* 15, 1090–1098. doi: 10.1016/j.cub.2005.05.024

Khanal, S., Leung, M. R., Royfman, A., Fishman, E., Saltzman, B., Gadelha, H., et al. (2021). A dynamic basal complex modulates mammalian sperm movement. *Res. Square* doi: 10.21203/rs.3.rs-136145/v1 **

Khandwala, Y. S., Baker, V. L., Shaw, G. M., Stevenson, D. K., Lu, Y., and Eisenberg, M. L. (2018). Association of paternal age with perinatal outcomes between 2007 and 2016 in the united states: population based cohort study. *BMJ* 363:k4372. doi: 10.1136/bmj.k4372

Khire, A., Jo, K. H., Kong, D., Akhshi, T., Blachon, S., Cekic, A. R., et al. (2016). Centriole remodeling during spermiogenesis in drosophila. *Curr. Biol.* 26, 3183–3189. doi: 10.1016/j.cub.2016.07.006

Kiosses, B. W., and Kalnins, V. I. (1993). Age-related changes in the position of centrosomes in endothelial cells of the rabbit aorta. *Exp. Gerontol.* 28, 69–75. doi: 10.1016/0531-5565(93)90021-5

Kong, A., Frigge, M. L., Masson, G., Besenbacher, S., Sulem, P., Magnusson, G., et al. (2012). Rate of de novo mutations and the importance of father's age to disease risk. *Nature* 488, 471–475.

Kruger, T. F., Acosta, A. A., Simmons, K. F., Swanson, R. J., Matta, J. F., and Oehninger, S. (1988). Predictive value of abnormal sperm morphology in in vitro fertilization. *Fertil. Steril.* 49, 112–117. doi: 10.1016/s0015-0282(16)59660-5

Kuretake, S., Kimura, Y., Hoshi, K., and Yanagimachi, R. (1996). Fertilization and development of mouse oocytes injected with isolated sperm heads. *Biol. Reprod.* 55, 789–795. doi: 10.1095/biolreprod55.4.789

Le Guennec, M., Klena, N., Gambarotto, D., Laporte, M. H., Tassin, A. M., van den Hoek, H., et al. (2020). A helical inner scaffold provides a structural basis for centriole cohesion. *Sci. Adv.* 6:eaaz4137. doi: 10.1126/sciadv.aaz4137

Leung, M. R., Roelofs, M. C., Ravi, R. T., Maitan, P., Henning, H., Zhang, M., et al. (2020). The multi-scale architecture of mammalian sperm flagella and implications for ciliary motility. *bioRxiv* 2020:388975. doi: 10.1101/2020.11.18.388975

Li, B., Ma, Y., Huang, J., Xiao, X., Li, L., Liu, C., et al. (2014). Probing the effect of human normal sperm morphology rate on cycle outcomes and assisted reproductive methods selection. *PloS One* 9:e113392. doi: 10.1371/journal.pone.0113392

Mazur, D. J., and Lipshultz, L. I. (2018). Infertility in the aging male. *Curr. Urol. Rep.* 19:54. doi: 10.1007/s11934-018-0802-3

Moretti, E., Collodel, G., Salvatici, M. C., Belmonte, G., and Signorini, C. (2019). New insights into sperm with total globozoospermia: increased fatty acid oxidation and centrin1 alteration. *Syst. Biol. Reprod. Med.* 65, 390–399. doi: 10.1080/19396368.2019.1626934

Moretti, E., Pascarelli, N. A., Belmonte, G., Renieri, T., and Collodel, G. (2017). Sperm with fibrous sheath dysplasia and anomalies in head-neck junction: focus on centriole and centrin 1. *Andrologia* 49:12701. doi: 10.1111/and.12701

Nakamura, S., Terada, Y., Horiuchi, T., Emuta, C., Murakami, T., Yaegashi, N., et al. (2001). Human sperm aster formation and pronuclear decondensation in bovine eggs following intracytoplasmic sperm injection using a Piezo-driven pipette: a novel assay for human sperm centrosomal function. *Biol. Reprod.* 65, 1359–1363. doi: 10.1095/biolreprod65.5.1359

Nakamura, S., Terada, Y., Horiuchi, T., Emuta, C., Murakami, T., Yaegashi, N., et al. (2002). Analysis of the human sperm centrosomal function and the oocyte activation ability in a case of globozoospermia, by ICSI into bovine oocytes. *Hum. Reprod.* 17, 2930–2934. doi: 10.1093/humrep/17.11.2930

Nanassy, L., and Carrell, D. T. (2008). Paternal effects on early embryogenesis. *J. Exp. Clin. Assist Reprod.* 5:2. doi: 10.1186/1743-1050-5-2

O'Connell, K. F., Caron, C., Kopish, K. R., Hurd, D. D., Kemphues, K. J., Li, Y., et al. (2001). The C. elegans zyg-1 gene encodes a regulator of centrosome duplication with distinct maternal and paternal roles in the embryo. *Cell* 105, 547–558. doi: 10.1016/S0092-8674(01)00338-5

Oshio, S., Kaneko, S., Iizuka, R., and Mohri, H. (1987). Effects of gradient centrifugation on human sperm. *Arch. Androl.* 19, 85–93. doi: 10.3109/01485018708986804

Owolabi, A., Fasubaa, O., and Ogunniyi, S. (2013). Semen quality of male partners of infertile couples in Ile-Ife, nigeria. *Nigerian J. Clin. Prac.* 16, 37–40. doi: 10.4103/1119-3077.106729

Palermo, G. D., Colombero, L. T., and Rosenwaks, Z. (1997). The human sperm centrosome is responsible for normal syngamy and early embryonic development. *Rev. Reprod.* 2, 19–27. doi: 10.1530/revreprod/2.1.19

Pandruvada, S., Royfman, R., Shah, T. A., Sindhwani, P., Dupree, J. M., Schon, S., et al. (2021). Lack of trusted diagnostic tools for undetermined male infertility. *J. Assisted Reproduc. Genet.* 38, 265–276. doi: 10.1007/s10815-020-02037-5

Pang, M. G., Hoegerman, S. F., Cuticchia, A. J., Moon, S. Y., Doncel, G. F., Acosta, A. A., et al. (1999). Detection of aneuploidy for chromosomes 4, 6, 7, 8, 9, 10, 11, 12, 13, 17, 18, 21, X and Y by fluorescence in-situ hybridization in spermatozoa from nine patients with oligoasthenoteratozoospermia undergoing intracytoplasmic sperm injection. *Hum. Reprod.* 14, 1266–1273. doi: 10.1093/humrep/14.5.1266

Park, J.-S., Pyo, J.-H., Na, H.-J., Jeon, H.-J., Kim, Y.-S., Arking, R., et al. (2014). Increased centrosome amplification in aged stem cells of the drosophila midgut. *Biochem. Biophys. Res. Commun.* 450, 961–965. doi: 10.1016/j.bbrc.2014.06.085

Pearson, C. G., Osborn, D. P., Giddings, T. H. Jr., Beales, P. L., and Winey, M. (2009). Basal body stability and ciliogenesis requires the conserved component Poc1. *J. Cell. Biol.* 187, 905–920. doi: 10.1083/jcb.200908019

Peter, A., Temi, A., Olufemi, A., Simidele, O., and Adeniran, A. (2016). Pattern of semen parameters and factors associated with infertility in male partners of infertile couples in nigeria. *Andrology* 5, 2167–2250.

Petrunkina, A. M., and Harrison, R. A. (2013). Fluorescence technologies for evaluating male gamete (dys)function. *Reprod. Domest Anim.* 48, 11–24. doi: 10.1111/rda.12202

Pfeffer, J., Pang, M. G., Hoegerman, S. F., Osgood, C. J., Stacey, M. W., Mayer, J., et al. (1999). Aneuploidy frequencies in semen fractions from ten oligoasthenoteratozoospermic patients donating sperm for intracytoplasmic sperm injection. *Fertil. Steril.* 72, 472–478. doi: 10.1016/s0015-0282(99)00279-4

Pizzari, T., Dean, R., Pacey, A., Moore, H., and Bonsall, M. B. (2008). The evolutionary ecology of pre- and post-meiotic sperm senescence. *Trends Ecol. Evol.* 23, 131–140. doi: 10.1016/j.tree.2007.12.003

Porcu, G. M., Boyer, P., Achard, V., Banet, J., Vasserot, M., Melone, C., et al. (2003). Pregnancies after ICSI using sperm with abnormal head-tail junction from two brothers: case report. *Hum. Reprod.* 18, 562–567. doi: 10.1093/humrep/deg121

Ramasamy, R., Chiba, K., Butler, P., and Lamb, D. J. (2015). Male biological clock: a critical analysis of advanced paternal age. *Fertil. Steril.* 103, 1402–1406. doi: 10.1016/j.fertnstert.2015.03.011

Rawe, V. Y., Terada, Y., Nakamura, S., Chillik, C. F., Olmedo, S. B., and Chemes, H. E. (2002). A pathology of the sperm centriole responsible for defective sperm aster formation, syngamy and cleavage. *Hum. Reprod.* 17, 2344–2349. doi: 10.1093/humrep/17.9.2344

Reefhuis, J., Gilboa, S. M., Anderka, M., Browne, M. L., Feldkamp, M. L., Hobbs, C. A., et al. (2015). The national birth defects prevention study: a review of the methods. *Birth Defects Res A Clin. Mol. Teratol.* 103, 656–669. doi: 10.1002/bdra.23384

Royfman, R., Shah, T. A., Sindhwani, P., Nadiminty, N., and Avidor-Reiss, T. (2020). Sterility, an over looked health condition. *Women* 1, 29–45. doi: 10.3390/women1010003

Rubio, C., Gil-Salom, M., Simón, C., Vidal, F., Rodrigo, L., Mínguez, Y., et al. (2001). Incidence of sperm chromosomal abnormalities in a risk population: relationship with sperm quality and ICSI outcome. *Hum. Reprod.* 16, 2084–2092. doi: 10.1093/humrep/16.10.2084

Sakkas, D. (2013). Novel technologies for selecting the best sperm for in vitro fertilization and intracytoplasmic sperm injection. *Fertil. Steril.* 99, 1023–1029. doi: 10.1016/j.fertnstert.2012.12.025

Sathananthan, A. H. (2009). Human centriole: origin, & how it impacts fertilization, embryogenesis, infertility & cloning. *Indian J. Med. Res.* 129, 348–350.

Schatten, H., Rawe, V. Y., and Sun, Q.-Y. (2011). The sperm centrosome: its role and significance in nature and human assisted reproduction. *J. Reprod. Stem Cell. Biotechnol.* 2, 121–127. doi: 10.1177/205891581100200206

Schatten, H., and Sun, Q. Y. (2010). The role of centrosomes in fertilization, cell division and establishment of asymmetry during embryo development. *Semin. Cell. Dev. Biol.* 21, 174–184. doi: 10.1016/j.semcdb.2010.01.012

Schneider, I., de Ruijter-Villani, M., Hossain, M. J., Stout, T. A. E., and Ellenberg, J. (2020). Non-rodent mammalian zygotes assemble dual spindles despite the presence of paternal centrosomes. *bioRxiv* 2020:342154. doi: 10.1101/2020.10.16.342154

Sha, Y. W., Xu, X., Mei, L. B., Li, P., Su, Z. Y., He, X. Q., et al. (2017). A homozygous CEP135 mutation is associated with multiple morphological abnormalities of the sperm flagella (MMAF). *Gene* 633, 48–53. doi: 10.1016/j.gene.2017.08.033

Shabtaie, S. A., Gerkowicz, S. A., Kohn, T. P., and Ramasamy, R. (2016). Role of abnormal sperm morphology in predicting pregnancy outcomes. *Curr. Urol. Rep.* 17:67. doi: 10.1007/s11934-016-0623-1

Sigman, M., Lipshultz, L., and Howards, S. (2009). Office evaluation of the subfertile male. *Infertil. Male* 4, 153–176. doi: 10.1017/cbo9780511635656.011

Smith, S., Pfeifer, S. M., and Collins, J. A. (2003). Diagnosis and management of female infertility. *JAMA* 290, 1767–1770. doi: 10.1001/jama.290.13.1767

Stern, J. E., Brown, M. B., Luke, B., Wantman, E., Lederman, A., Missmer, S. A., et al. (2010). Calculating cumulative live-birth rates from linked cycles of assisted reproductive technology (ART): data from the Massachusetts SART CORS. *Fertil. Steril.* 94, 1334–1340. doi: 10.1016/j.fertnstert.2009.05.052

Sutovsky, P., and Schatten, G. (2000). Paternal contributions to the mammalian zygote: fertilization after sperm-egg fusion. *Int. Rev. Cytol.* 195, 1–65. doi: 10.1016/s0074-7696(08)62703-5

Terada, Y. (2004). Human sperm centrosomal function during fertilization, a novel assessment for male sterility. *Hum. Cell.* 17, 181–186. doi: 10.1111/j.1749-0774.2004.tb00041.x

Terada, Y., Hasegawa, H., Takahashi, A., Ugajin, T., Yaegashi, N., and Okamura, K. (2009). Successful pregnancy after oocyte activation by a calcium ionophore for a patient with recurrent intracytoplasmic sperm injection failure, with an assessment of oocyte activation and sperm centrosomal function using bovine eggs. *Fertil. Steril.* 91, E935 E11–E935 e14. doi: 10.1016/j.fertnstert.2008.09.043

Terada, Y., Nakamura, S., Simerly, C., Hewitson, L., Murakami, T., Yaegashi, N., et al. (2004). Centrosomal function assessment in human sperm using heterologous ICSI with rabbit eggs: a new male factor infertility assay. *Mol. Reprod. Dev.* 67, 360–365. doi: 10.1002/mrd.20024

Thonneau, P., Marchand, S., Tallec, A., Ferial, M. L., Ducot, B., Lansac, J., et al. (1991). Incidence and main causes of infertility in a resident population (1,850,000) of three French regions (1988-1989). *Hum. Reprod.* 6, 811–816. doi: 10.1093/oxfordjournals.humrep.a137433

Tkemaladze, J. V., and Chichinadze, K. N. (2005). Centriolar mechanisms of differentiation and replicative aging of higher animal cells. *Biochem.* 70, 1288–1303. doi: 10.1007/s10541-005-0261-6

Turner, K. A., Rambhatla, A., Schon, S., Agarwal, A., Krawetz, S. A., Dupree, J. M., et al. (2020). Male infertility is a women's health issue-research and clinical evaluation of male infertility is needed. *Cells* 9:990. doi: 10.3390/cells9040990

Utt, M. D. (2016). Prediction of bull fertility. *Anim. Reprod. Sci.* 169, 37–44. doi: 10.1016/j.anireprosci.2015.12.011

van der Horst, G., and Maree, L. (2014). Sperm form and function in the absence of sperm competition. *Mol. Reprod. Dev.* 81, 204–216. doi: 10.1002/mrd.22277

WHO (2010). *Laboratory Manual for the Examination and Processing of Human Semen.* Geneva: World Health Organization, 7–113.

Winey, M., and O'Toole, E. (2014). Centriole structure. *Phil. Trans. R. Soc. B Biol. Sci.* 369:20130457.

Wright, E. M., and Royston, P. (1999). Calculating reference intervals for laboratory measurements. *Stat. Methods Med. Res.* 8, 93–112. doi: 10.1177/096228029900800202

Wu, Q., Li, B., Liu, L., Sun, S., and Sun, S. (2020). Centrosome dysfunction: a link between senescence and tumor immunity. *Signal Trans. Target Ther.* 5:107. doi: 10.1038/s41392-020-00214-7

Xu, B., Hao, Z., Jha, K. N., Zhang, Z., Urekar, C., Digilio, L., et al. (2008). TSKS concentrates in spermatid centrioles during flagellogenesis. *Dev. Biol.* 319, 201–210. doi: 10.1016/j.ydbio.2008.03.043

Yabe, T., Ge, X., and Pelegri, F. (2007). The zebrafish maternal-effect gene cellular atoll encodes the centriolar component sas-6 and defects in its paternal function promote whole genome duplication. *Dev. Biol.* 312, 44–60. doi: 10.1016/j.ydbio.2007.08.054

Yan, W., Morozumi, K., Zhang, J., Ro, S., Park, C., and Yanagimachi, R. (2008). Birth of mice after intracytoplasmic injection of single purified sperm nuclei and detection of messenger RNAs and MicroRNAs in the sperm nuclei. *Biol. Reprod.* 78, 896–902. doi: 10.1095/biolreprod.107.067033

Conflict of Interest: Provisional patent application number 63/117,056 has been filed.

The authors declare that the research was conducted in the absence of any commercial or financial relationships that could be construed as a potential conflict of interest.

Copyright © 2021 Turner, Fishman, Asadullah, Ott, Dusza, Shah, Sindhwani, Nadiminty, Molinari, Patrizio, Saltzman and Avidor-Reiss. This is an open-access article distributed under the terms of the Creative Commons Attribution License (CC BY). The use, distribution or reproduction in other forums is permitted, provided the original author(s) and the copyright owner(s) are credited and that the original publication in this journal is cited, in accordance with accepted academic practice. No use, distribution or reproduction is permitted which does not comply with these terms.

frontiers in Cell and Developmental Biology

ORIGINAL RESEARCH
published: 23 April 2021
doi: 10.3389/fcell.2021.662903

Genetic Defects in *DNAH2* Underlie Male Infertility With Multiple Morphological Abnormalities of the Sperm Flagella in Humans and Mice

*Jae Yeon Hwang[1†], Shoaib Nawaz[1,2†], Jungmin Choi[3,4†], Huafeng Wang[1], Shabir Hussain[5], Mehboob Nawaz[2], Francesc Lopez-Giraldez[6], Kyungjo Jeong[4], Weilai Dong[3], Jong-Nam Oh[1,7], Kaya Bilguvar[3,6], Shrikant Mane[6], Chang-Kyu Lee[7,8], Christopher Bystroff[9], Richard P. Lifton[10], Wasim Ahmad[2,5] and Jean-Ju Chung[1,11]**

[1] Department of Cellular and Molecular Physiology, Yale School of Medicine, Yale University, New Haven, CT, United States, [2] Department of Biotechnology, Faculty of Biological Sciences, Quaid-i-Azam University, Islamabad, Pakistan, [3] Department of Genetics, Yale School of Medicine, Yale University, New Haven, CT, United States, [4] Department of Biomedical Sciences, Korea University College of Medicine, Seoul, South Korea, [5] Department of Biochemistry, Faculty of Biological Sciences, Quaid-i-Azam University, Islamabad, Pakistan, [6] Yale Center for Genome Analysis, Yale University, New Haven, CT, United States, [7] Department of Agricultural Biotechnology, College of Agriculture and Life Sciences, Seoul National University, Seoul, South Korea, [8] Designed Animal and Transplantation Research Institute, Institutes of Green Bio Science and Technology, Seoul National University, Pyeongchang-gun, South Korea, [9] Department of Biological Sciences, Rensselaer Polytechnic Institute, Troy, NY, United States, [10] Laboratory of Human Genetics and Genomics, The Rockefeller University, New York, NY, United States, [11] Department of Obstetrics, Gynecology and Reproductive Sciences, Yale School of Medicine, Yale University, New Haven, CT, United States

OPEN ACCESS

Edited by:
Tomer Avidor-Reiss, University of Toledo, United States

Reviewed by:
Lin Li, Capital Medical University, China
Pao-Lin Kuo, National Cheng Kung University Hospital, Taiwan
Yanwei Sha, Xiamen University, China

***Correspondence:**
Jean-Ju Chung
jean-ju.chung@yale.edu

† These authors have contributed equally to this work

Specialty section:
This article was submitted to Cell Growth and Division, a section of the journal Frontiers in Cell and Developmental Biology

Received: *01 February 2021*
Accepted: *22 March 2021*
Published: *23 April 2021*

Citation:
Hwang JY, Nawaz S, Choi J, Wang H, Hussain S, Nawaz M, Lopez-Giraldez F, Jeong K, Dong W, Oh J-N, Bilguvar K, Mane S, Lee C-K, Bystroff C, Lifton RP, Ahmad W and Chung J-J (2021) Genetic Defects in DNAH2 Underlie Male Infertility With Multiple Morphological Abnormalities of the Sperm Flagella in Humans and Mice. Front. Cell Dev. Biol. 9:662903. doi: 10.3389/fcell.2021.662903

Asthenozoospermia accounts for over 80% of primary male infertility cases. Reduced sperm motility in asthenozoospermic patients are often accompanied by teratozoospermia, or defective sperm morphology, with varying severity. Multiple morphological abnormalities of the flagella (MMAF) is one of the most severe forms of asthenoteratozoospermia, characterized by heterogeneous flagellar abnormalities. Among various genetic factors known to cause MMAF, multiple variants in the *DNAH2* gene are reported to underlie MMAF in humans. However, the pathogenicity by DNAH2 mutations remains largely unknown. In this study, we identified a novel recessive variant (NM_020877:c.12720G > T;p.W4240C) in *DNAH2* by whole-exome sequencing, which fully co-segregated with the infertile male members in a consanguineous Pakistani family diagnosed with asthenozoospermia. 80–90% of the sperm from the patients are morphologically abnormal, and *in silico* analysis models reveal that the non-synonymous variant substitutes a residue in dynein heavy chain domain and destabilizes DNAH2. To better understand the pathogenicity of various *DNAH2* variants underlying MMAF in general, we functionally characterized *Dnah2*-mutant mice generated by CRISPR/Cas9 genome editing. *Dnah2*-null males, but not females, are infertile. *Dnah2*-null sperm cells display absent, short, bent, coiled, and/or irregular flagella consistent with the MMAF phenotype. We found misexpression of centriolar proteins and delocalization of annulus proteins in *Dnah2*-null spermatids and sperm, suggesting dysregulated flagella development in spermiogenesis. Scanning and transmission electron microscopy analyses revealed that flagella ultrastructure is severely disorganized

in *Dnah2*-null sperm. Absence of DNAH2 compromises the expression of other axonemal components such as DNAH1 and RSPH3. Our results demonstrate that DNAH2 is essential for multiple steps in sperm flagella formation and provide insights into molecular and cellular mechanisms of MMAF pathogenesis.

Keywords: male infertility, asthenozoospermia, WES, *DNAH2*, sperm flagellum, MMAF

INTRODUCTION

Infertility is an important public health concern, affecting approximately 15% of all couples worldwide (Esteves et al., 2011; Mascarenhas et al., 2012). Male factor infertility accounts for approximately half of the infertility cases and results from extremely heterogeneous pathogenesis. Asthenozoospermia (ASZ), which is defined by reduced sperm motility (WHO, 2010), is one of the most prevalent cases of male infertility (Curi et al., 2003). Together with the motility issues, ASZ patients often show sperm morphological defects, including morphological abnormalities of the sperm flagella (MMAF) (Ben Khelifa et al., 2014). MMAF is characterized by sperm with abnormal flagellar morphologies, such as absent, short, bent, coiled, and/or irregular caliber flagella. MMAF is mainly caused by genetic mutations; around 20 MMAF-associated genes have been reported (Toure et al., 2020). The pathogenic mechanisms of MMAF, however, vary depending on genetic mutations. The currently reported MMAF-associated genes explain only 30–60% of the MMAF cases in different cohorts (Toure et al., 2020), indicating heterogeneous genetic etiologies of the disorder. A full picture of the genetic basis of MMAF awaits further genetic exploration.

Sperm flagella and cilia share a highly organized and evolutionarily conserved microtubule-based structure called axoneme (Inaba, 2011; Viswanadha et al., 2017). The axoneme is composed of nine pairs of peripheral microtubule doublets, and a central pair of microtubules ("9+2" arrangement). The peripheral microtubule doublets are connected through the nexin-dynein regulatory complex, and A tubules in each microtubule doublet harbor multiprotein-complexed axonemal components, including radial spokes (RS), and inner and outer dynein arms (IDA and ODA, respectively). IDA and ODA are motor protein complexes that regulate flagella and cilia beating by ATP hydrolysis (Viswanadha et al., 2017). Previous studies have suggested that primary ciliary dyskinesia (PCD, MIM: 244400) by mutations in IDA or ODA components may cause male infertility based on the structural similarity of sperm flagella to motile cilia (Sironen et al., 2020). However, variants in MMAF-causing genes encoding IDA or ODA proteins have been identified in infertile males without PCD symptoms. These MMAF-specific mutations suggest that molecular compositions and the workings of IDA and ODA in sperm flagella, which are yet to be well-characterized, might be distinct to those in motile cilia.

Variants encoding ODA proteins [DNAH8 (MIM: 603337; Liu et al., 2020; Yang et al., 2020) and DNAH17 (MIM: 610063; Whitfield et al., 2019; Sha et al., 2020; Zhang B. et al., 2020; Zhang et al., 2021)] and IDA proteins [DNAH1 (MIM: 603332; Ben Khelifa et al., 2014; Amiri-Yekta et al., 2016; Sha Y. et al., 2017; Wang et al., 2017) and DNAH2 (MIM: 603333; Li et al., 2019)] are reported to cause MMAF in human. *DNAH2* encodes a heavy chain of IDA. Among over 30 single nucleotide variants (SNVs) in *DNAH2* annotated in ClinVar, five variants (four heterozygous and one homozygous) are reported to be pathogenic (Li et al., 2019) but lack functional studies in animal models.

Here, we report a new bi-allelic non-synonymous mutation in *DNAH2* identified from a Pakistani consanguineous family with infertile males diagnosed to oligoasthenozoospermia. Using a mouse model, we found DNAH2 deficiency causes male infertility with MMAF phenotypes and aberrant protein expression of various structural components in sperm flagella. Our findings demonstrate that DNAH2 is essential for sperm flagellar development and structural stabilization, providing an insight into the pathogenicity and variable phenotypic severity of DNAH2-associated MMAF.

MATERIALS AND METHODS

Subjects and Family

Present study was approved by the Institutional Review Board of Quaid-i-Azam University, Islamabad, Pakistan (IRB00003532, IRB protocol# QAU-171) and Yale Center for Mendelian Genomics. A survey was conducted in selected regions of Pakistan to document cases of infertility. The family to participate this study were informed about the nature of work and the possible outcomes of the study. Written informed consent was provided by the family.

Sample Collection and Clinical Investigation

Semen samples were collected from affected individuals after 2–5 days of abstinence from sexual intercourse according to World Health Organization guidelines (WHO, 2010). The samples were analyzed for semen volume, pH, color, and viscosity. Semen samples were subjected to liquefaction at 37°C for 30–60 min. Sperm concentration, motility and morphology were analyzed. For detailed sperm morphology analyses, semen samples were subjected to PAP staining according to protocols approved by WHO (2010). Venous blood from the affected and control members were collected and stored at 4°C. Hormone assay was carried out using automated immunoassay analyzer AIA-360 (Tosoh Bioscience, Inc.). Karyotyping was performed by establishing and harvesting phytohemagglutinin (PHA) after 72 h. Twenty metaphases were then analyzed following Giemsa-Trypsin banding (Howe et al., 2014). Genomic DNA was extracted using QIAamp DNA Mini Kit (Qiagen). To search for the

Y-chromosome microdeletions spanning four regions (AZFa, AZFb, AZFc, and AZFd), PCR was performed using different sets of primer pairs.

Whole-Exome Sequencing and Data Analysis

1.0 μg of blood genomic DNA is sheared to a mean fragment length of about 140 bp using focused acoustic energy (Covaris E210). Exome sequencing was performed by exome capture using the IDT xGen capture probe panel with an additional "spike-in" of ∼2,500 regions, totaling ∼620 kb, of RefGene coding regions that were not included or were poorly covered by the IDT panel. Captured fragments were sequenced using 101 bp paired-end sequencing reads in an Illumina NovaSeq 6000 with a S4 flow cell according to Illumina protocols. Sequencing reads were aligned to human genome build 37 (GRCh37/hg19) using the BWA-MEM (Li, 2013), aggregated into a BAM file, and further processed to produce variants with GATK v3.4 (McKenna et al., 2010) following the GATK Best Practices workflow (van der Auwera et al., 2013). Variants were annotated with ANNOVAR (Wang et al., 2010) and MetaSVM (Dong et al., 2015) was used to predict the deleteriousness of non-synonymous variants. For rare transmitted dominant variants, only loss of function mutations (stop-gains, stop-losses, canonical splice-sites, and frameshift indels) and D-mis mutations (non-synonymous mutations predicted deleterious by MetaSVM) were considered potentially damaging and filtered using the following criteria to reduce false positives: (1) GATK variant quality score recalibration (VQSR) of PASS, (2) MAF $\leq 2 \times 10^{-5}$ in the Genome Aggregation Database (gnomAD) v2.1 (Lek et al., 2016)[1] (calculated based on combined dataset of WES and WGS data from gnomAD database), (3) DP $\geq$ 8 independent reads, (4) GQ score $\geq$20, (5) MQ score $\geq$40, (6) PLdiff/DP $\geq$8, and (7) indels in Low Complexity Regions (LCRs) were also excluded. Transmitted recessive variants were filtered for rare (MAF $\leq 10^{-3}$ in gnomAD) homozygous and compound heterozygous variants using the same criteria described above. Candidate variants were confirmed by PCR amplification followed by Sanger sequencing.

Kinship Analysis

Pairwise proband relatedness and pedigree information of extended family were confirmed using KING v2.2.4 (Manichaikul et al., 2010) by estimating kinship coefficient. Inbreeding coefficient was calculated by homozygosity-by-descent (HBD). The HBD segments in the patients were detected using Beagle v3.3.2 (Browning and Browning, 2011). The criteria of consanguinity are defined as runs of homozygosity in segments of 2 cM or greater length that collectively comprise at least 0.35% of the genome.

Copy Number Variation Analysis

eXome-Hidden Markov Model (XHMM) (Fromer et al., 2012) was run to call CNVs from WES as previously described. GATK DepthOfCoverage was used to calculate mean read depth per targets from the alignment files. The data were normalized by removing the highest variance principal components (variance >70%) and z scores were calculated from the mean read depths. CNVs were called using the Viterbi Hidden Markov model (HMM) and the quality scores were calculated using the forward-backward HMM. After filtering out common CNVs present at allele frequencies greater than 0.1% in 1000 Genomes and 10% in the cohort, high quality CNVs (SQ > 60 where SQ indicates the phred-scaled quality score for the presence of a CNV event within the interval) were subjected to visual inspection.

Genomic DNA PCR

Genomic DNA PCR was performed to confirm the co-segregating variants screened from WES analyses in the family. Genomic DNA extracted from human blood samples were applied for PCR using OneTaq® 2X Master Mix (NEB) with the primer pairs listed in **Supplementary Table 1**. The primer pairs were chosen to amplify genomic region containing screened variants. PCR products were gel-purified and Sanger sequenced using the primers for the targeted PCR amplifications.

Protein Sequence Conservation Analysis

In order to analyze conservation of the mutated residue in each gene, protein sequences of the orthologs were aligned using Clustal Omega (Madeira et al., 2019).

Sequence-Structure Analysis

Sequence analysis was carried out using web-based tools from the National Center for Biological Information (NCBI), including Genome Database Viewer. Phylogenetic analysis and multiple sequence alignments were carried out in the UGENE (Bykova et al., 2016) software package, using PHYLIP (Retief, 2000) and MUSCLE (Edgar, 2004), respectively. Molecular modeling, including homology-based modeling of mutant sequences, was carried out within the software package MOE (Qiao and Guo, 2005) using the AMBER10:EHT force field (Wang et al., 2004), Images were made using Molecular Operating Environment (MOE, Chemical Computing Group Inc.).

Single-Cell RNA-seq Analysis

The raw count matrices for human (GSE109037) and mouse (GSE109033) testis single cell RNA (scRNA)-seq datasets (Hermann et al., 2018) were downloaded from Gene Expression Omnibus (GEO) database[2]. The downloaded raw count matrices were processed for quality control using the Seurat package (ver.3.2.3) (Stuart et al., 2019). Briefly, cells with less than 200 expressed features, higher than 9,000 (GSE109033) or 10,000 (GSE109037) expressed features and higher than 20% (GSE109037) or 25% (GSE109033) mitochondrial transcript fraction were excluded to select single-cells with high quality mRNA profiles. The data was normalized by the total expression, scaled and log transformed. Identification of 2,000 highly variable features was followed by PCA to reduce the number of dimensions representing each cell. Statistically significant 15 PCs were selected based on the JackStraw and Elbow plots and

[1] https://gnomad.broadinstitute.org/

[2] https://www.ncbi.nlm.nih.gov/geo/

provided as input for constructing a K-nearest-neighbors (KNN) graph based on the Euclidean distance in PCA space. Cells were clustered by the Louvain algorithm with a resolution parameter 0.1. Uniform Manifold Approximation and Projection (UMAP) was used to visualize and explore cluster data. Marker genes that define each cluster were identified by comparing each cluster to all other clusters using the MAST (Finak et al., 2015) provided in Seurat package. In order to correct batch effects among samples and experiments, we applied the Harmony package (ver.1.0) (Korsunsky et al., 2019) to the datasets. The Markov Affinity-based Graph Imputation of Cells (MAGIC) algorithm (ver.2.0.3) (van Dijk et al., 2018) was used to denoise and the count matrix and impute the missing data. In these testis datasets from adult human, we identified 23,896 high quality single cells, that were clustered into seven major cell types, including spermatogonia, spermatocytes, early spermatids, late spermatids, peritubular myoid cell, endothelial cell, and macrophage. Similarly, we exploited 30,268 high quality single cells from eight adult and three 6-day postpartum mouse testis tissue samples and subsequently defined 11 major cell populations.

Animals

Mice were treated in accordance with guidelines approved by the Yale Animal Care and Use Committees that reviewed the animal study protocol (20079). Wild-type (WT, C57BL/6) mice were purchased from Charles river laboratories and *Dnah2*-mutant mice (C57BL/6N-Dnah2$^{em1(IMPC)Tcp}$) were purchased from The Center for Phenogenomics. Founders were generated by using CRISPR/Cas9 technique with two guide RNAs (guide RNA1: 5′- GAGTCACACTAACCACCCCA-3′, guide RNA2: 5′- ATCACTACTCACGGTCACAA-3′) and maintained on a C57/B6 background. Genomic DNA from hetero- and homozygous *Dnah2* mutant mice were used for genotyping with PCR (WT allele, forward: 5′-CTTGTATGCACACCTGCCTTA-3′, reverse: 5′-CATTTTCAATGTTTCAGCCTCACT-3′; mutant allele, forward: 5′-ATGCACACCTGCCTTAACTC-3′, reverse: 5′-ACGACACGCTTCTTCTTTGT-3′). Mice were treated with guidelines approved by the Yale Animal Care and Use Committees.

Histological Analyses

Testis, epididymis, trachea, and oviduct were collected from *Dnah2* mutant mice and rinsed with PBS. Rinsed tissues were fixed with 4% PFA in PBS for overnight at 4°C. Fixed tissues were washed in PBS and dehydrated by serial incubations in ethanol to 100%. Dehydrated tissues were embedded into paraffin and sectioned. The sections were deparaffinized and stained with hematoxylin and eosin (H/E). Stained sections were imaged with ac1300–200 μm CMOS camera (Basler AG) equipped in Nikon E200 microscope under 10x phase contrast objective (CFI Plan Achro 10X/0.25 pH1 WF, Nikon).

Sperm Preparation

Epididymal mouse spermatozoa were prepared as described in our previous study (Hwang et al., 2019). Briefly, epididymal sperm were collected in M2 medium (EMD Millipore) or HS medium (135 mM NaCl, 5 mM KCl, 1 mM $MgSO_4$, 2 mM $CaCl_2$, 20 mM HEPES, 5 mM Glucose, 10 mM Lactic acid, and 1 mM sodium pyruvate, pH 7.4) by swim-out method at 37°C for 10 min. Collected sperm were washed and used for the required experiment.

Mouse Sperm Motility Analysis

Non-capacitated epididymal sperm cells were transferred to 37°C chamber (Delta T culture dish controller; Bioptechs) filled with HS medium. Sperm motility were recorded for 4 s with 100 fps using Axio observer Z1 microscope (Carl Zeiss) equipped with a high-speed pco.dege sCMOS camera.

Antibodies and Reagents

Rabbit polyclonal DNAH1 (PA5-57826), DNAH2 (PA5-64309), and DNAH9 (PA5-45744) antibodies were purchased from Thermo Fisher Scientific. Rabbit polyclonal SEPTIN4 antibody (NBP1-90093) was purchased from Novus Biologicals. Monoclonal acetylated tubulin (clone 6-11B-1, T7451), CENTRIN1 (clone 20H5, 04-1624), and γ-tubulin (clone GTU-88, T6557), and rabbit polyclonal SEPTIN12 (HPA041128) antibodies were purchased from MilliporeSigma. In-house rabbit polyclonal RSPH3 antibody was generated in this study by immunizing rabbit with synthesized RSPH3 peptide (TAEASGLYTYSSRPR, Open Biosystems). Antisera from the immunized rabbits were affinity-purified using the peptide immobilized Amino Link Plus resin (Pierce). Goat anti-mouse or rabbit IgG conjugated with Alexa 568 were from Invitrogen. Hoechst dye was purchased from Thermo Fisher Scientific.

Immunocytochemistry of Cauda Epididymal Sperm

Collected mouse sperm cells were washed two times with PBS and attached on glass coverslips by centrifugation at 700 × *g* for 5 min. Coverslips were fixed with acetone at –20°C for 5 min (DNAH1 and acetylated tubulin), methanol at –20°C for 10 min (γ-tubulin), or 4% paraformaldehyde (PFA) in PBS at room temperature (RT) for 10 min. PFA-fixed coverslips were permeabilized with 0.1% (SEPTIN4, SEPTIN12, and CENTRIN1), 0.2% (DNAH9, and RSPH3), or 1% (DNAH2) Triton X-100 in PBS. Permeabilized coverslips were blocked with 10% normal goat serum in PBS (DNAH1, DNAH2, γ-tubulin, CENTRIN1, SEPTIN4, SEPTIN12, RSPH3, and acetylated tubulin) or 5% normal goat serum with 0.2% Triton X-100 in PBS (DNAH9) at RT for 1 h. Blocked coverslips were incubated with primary antibodies, α-DNAH1 (3 μg/ml), α-DNAH2 (0.5 μg/ml), α-DNAH9 (5 μg/ml), α-RSPH3 (10 μg/ml), α-SEPTIN4 (1 μg/ml), α-SEPTIN12 (1:100), α-γ-tubulin (1:400), α-CENTRIN1 (1:100), or α-acetylated tubulin (1:100) in each blocking buffer at 4°C for overnight. The coverslips incubated with primary antibodies were washed with 0.05% (DNAH9) or 0.1% (DNAH2) Triton X-100 in PBS three times or 0.1% Triton X-100 in PBS one time and PBS two times (acetylated tubulin, γ-tubulin, CENTRIN1, SEPTIN4, SEPTIN12, DNAH1, and RSPH3). The samples were stained with secondary antibodies (1:1,000) in 5% (DNAH9) or 10% (DNAH1, DNAH2, γ-tubulin, CENTRIN1, SEPTIN4, SEPTIN12, RSPH3, and acetylated

tubulin) normal goat-serum in PBS for 1 h at RT. Hoechst was used to counterstain sperm nucleus. Immunostained sperm samples were mounted with Vectashield (Vector Laboratories) and imaged with Zeiss LSM710 Elyra P1 using Plan-Apochromat 63X/1.40 oil objective lens.

Immunocytochemistry of Testicular Germ Cells

Mouse seminiferous tubules were dissociated in ice-cold PBS after removing tunica albuginea. The seminiferous tubules were chopped, vortexed gently to isolate testicular cells followed by filtering in cell strainers with 40 μm pores to collect dissociated testicular germ cells. Collected cells were mixed with PFA in 3% concentration in PBS and attached on glass coverslips coated with poly-D-lysine by centrifuge at 250 × *g* for 5 min. The fixed coverslips were permeablized with 0.1% Triton X-100 in PBS for 10 min, blocked with 10% normal goat serum in PBS for an hour, and incubated with CENTRIN1 (1:100) or SEPTIN4 (1 μg/ml) antibodies in blocking solution at 4°C for overnight. The coverslips were washed with PBS two times and incubated with secondary antibodies and Hoechst in blocking solution for an hour at RT. The immunostained coverslips were mounted and imaged as described in sperm immunocytochemistry.

RNA Extraction, cDNA Synthesis, and PCR

Total RNA was extracted from WT, *DNAH2*$^{+/\Delta}$, and *DNAH2*$^{\Delta/\Delta}$ testes using RNeasy mini-kit (QIAGEN). One microgram of total RNA was used to synthesize cDNA samples using iScript cDNA Synthesis kit (Bio-Rad). The cDNAs were applied for PCR using OneTaq® 2X Master Mix (NEB) or quantitative PCR using iTaq Universal SYBR Green Supermix (Bio-Rad). Primer pairs used for the RT-PCR were listed in **Supplementary Table 2**. PCR products were gel-extracted and Sanger sequenced.

Scanning Electron Microscopy

Sperm cells were attached on the glass coverslips and fixed with 2.5% glutaraldehyde (GA) in 0.1M sodium cacodylate buffer (pH 7.4) for 1 h at 4°C and post fixed in 2% osmium tetroxide in 0.1M cacodylate buffer (pH 7.4). The fixed samples were washed with 0.1M cacodylate buffer for three times and dehydrated through a series of ethanol to 100%. The samples were dried using a 300 critical point dryer with liquid carbon dioxide as transitional fluid. The coverslips with dried samples were glued to aluminum stubs and sputter coated with 5 nm platinum using a Cressington 208HR (Ted Pella) rotary sputter coater. Prepared samples were imaged with Hitachi SU-70 scanning electron microscope (Hitachi High-Technologies).

Transmission Electron Microscopy

Collected epididymal sperm cells were washed and pelleted by centrifugation and fixed in 2.5% GA and 2% PFA in 0.1M cacodylate buffer pH 7.4 for 1 h at RT. Fixed sperm pellets were rinsed with 0.1M cacodylate buffer and spud down in 2% agar. The chilled blocks were trimmed, rinsed in the 0.1M cacodylate buffer, and replaced with 0.1% tannic acid in the buffer for 1 h. After rinsing in the buffer, the samples were post-fixed in 1% osmium tetroxide and 1.5% potassium ferrocyanide in 0.1M cacodylate buffer for 1 h. The post-fixed samples were rinsed in the cacodylate buffer and distilled water, followed by en bloc staining in 2% aqueous uranyl acetate for 1 h. Prepared samples were rinsed and dehydrated in an ethanol series to 100%. Dehydrated samples were infiltrated with epoxy resin Embed 812 (Electron Microscopy Sciences), placed in silicone molds and baked for 24 h at 60°C. The hardened blocks were sectioned in 60 nm thickness using Leica UltraCut UC7. The sections were collected on grids coated with formvar/carbon and contrast stained using 2% uranyl acetate and lead citrate. The grids were imaged using FEI Tecnai Biotwin Transmission Electron Microscope (FEI, Hillsboro, OR, United States) at 80 kV. Images were taken using MORADA CCD camera and iTEM (Olympus) software.

Statistical Analysis

Statistical analysis was performed with Student's *t*-test. Differences were considered significant at $^{*}p < 0.05$; $^{**}p < 0.01$; $^{***}p < 0.001$.

RESULTS

Clinical Assessment of the Infertile Males in a Consanguineous Family From Pakistan

A consanguineous family with infertile males was recruited from Pakistan. All the infertile males in this study failed to conceive over 10 years of marriages and unprotected sex (**Table 1**). No PCD-related symptoms were reported by the infertile males. They exhibited normal heights, weights, and secondary characteristics, were not obese, and were free of tuberculosis as children. They had no anatomic defects, ejaculatory failure, or immunological problems, and experienced no environmental exposure to chemical or radioactive elements. Their karyotypes are normal, and they carry no Y chromosome microdeletions. The follicle-stimulating hormone (FSH), luteinizing hormone (LH), prolactin, and testosterone were within normal range in all affected males.

A New Variant in *DNAH2* Causes Oligoasthenozoospermia

The pedigree comprises five generations; three males from the fourth generation (IV-1, IV-2, and IV-3) and one male from the fifth generation (V-1) are infertile (**Figure 1A**). Three affected members (IV-1, IV-3, and V-1) were subjected to clinical analyses and initially diagnosed with oligoasthenozoospermia (OAZ, **Table 1**). Notably, over 80% of sperm cells from the patients were morphologically abnormal by CASA morphological analysis (IV-1, 80%; IV-3, 82%; V-1, 92%). PAP staining revealed morphological abnormalities prominently in the tail, such as near-absent, short, curved, or coiled forms, which is similar to a representative MMAF phenotype, and mild defects in

TABLE 1 | Clinical diagnosis of the infertile patients.

	Normal range	Units	IV-1	IV-3	V-1
Age of patients			50	43	28
Years of marriages			30	23	10
Semen Parameters					
Semen volume	>1.5	ml	3.2	3.7	4
Semen pH	Alkaline		Alkaline	Alkaline	Alkaline
Sperm concentration (10^6/ml)	>15	ml	10	9	7
Morphologically normal sperm	>4	(%)	20	18	8
Motility (a+b+c)	>40	(%)	14	20	10
Progressive motility (a+b)	>32	(%)	4	7	0
Rapid progressive (WHO a)		(%)	1	3	0
Slow progressive (WHO b)		(%)	3	4	0
Non progressive (WHO c)		(%)	10	13	10
Immotile (WHO d)		(%)	86	80	90
Hormones					
FSH	1.7–11.2	mIU/mL	6.5	7.7	5.6
LH	2.1–18.6	mIU/mL	8.9	10.1	7.8
Prolactin	3.6–16.3	ng/ml	9.4	11.3	8.3
Testosterone	62–870	ng/dL	427.5	507.1	618.2

the head shape (**Figure 1B**). To elucidate the genetic basis of this phenotype, we performed WES on the proband (IV-3) and on his nephew (V-1). Analyzing WES data estimated inbreeding co-efficient of 10.52% and 19.39% with the longest HBD segments of 33.86 cM and 49.22 cM for the proband and his nephew, respectively. WES analysis identified three rare damaging variants but only homozygous non-synonymous variant (c.12720G > T;p.W4240C) in *DNAH2* co-segregated with the phenotype (**Figures 1A,C,D**). This variant is predicted as "deleterious" by MetaSVM and absent in all public databases including gnomAD and Browse All Variant Online (Bravo) variant browser[3] (**Table 2**). This novel variant was inherited by all affected, a highly unlikely event to occur by chance (odds in favor of linkage 1,000:1, LOD score of 3.0) within the pedigree. CNVs were not detected from XHMM analysis of the WES.

Human DNAH2 is a paralog of DNAH1 (Kollmar, 2016), the nearest known structure dynein (PDBid:5NUG). The DNAH2 variant in our study encodes a residue residing at the dynein heavy domain at C-terminus, which is highly conserved from human to yeast (**Figures 1C,E**). Structural modeling based on human DNAH1 demonstrates that the DNAH2 mutant residue is in a buried location within the dynein heavy domain (**Figure 1F**). Replacing tryptophan with cysteine of DNAH1 at position 4464, which corresponds to the identified DNAH2 mutation in this study, is predicted to have two destabilizing effects. The mutation of the large tryptophan to the small cysteine would generate an energetically destabilizing void space. Alternatively, the cysteine would pair with a nearby cysteine at position 4454, distorting the structure (**Figure 1G**). Taken together, these data suggest the identified novel *DNAH2* variant is pathogenic and causes male infertility with MMAF-like phenotypes in human, similar to previously reported *DNAH2* variants (**Figure 1C**; Li et al., 2019).

[3]https://bravo.sph.umich.edu/freeze8/hg38/about

Homozygous *Dnah2* Mutant Male Mice Are Infertile

Mutations of genes which encode axonemal IDA, ODA, and RS proteins can cause MMAF (Toure et al., 2020). Infertile males carrying the bi-allelic *DNAH2* variant described in this study also produce sperm with MMAF-like phenotypes (**Figure 1B**). Currently 39 *DNAH2* SNV are annotated in ClinVar (**Supplementary Table 3**). Only five *DNAH2* variants, however, were reported to be pathogenic and cause male infertility with MMAF phenotypes in human (Li et al., 2019). To directly demonstrate the genetic causality and elucidate loss of DNAH2 function in general, we characterized *Dnah2* mutant mice. These mice lack the *Dnah2* genomic region spanning exon 25–28, which is predicted to result in a frameshift and early termination of translation (**Supplementary Figures 1A–C**). RT-PCR result demonstrates that the truncated *Dnah2* mRNAs lacking exon 25–28 are present in testes from homozygous mutant males (**Supplementary Figure 1D**). Yet the mutant mRNA expression is at about 50% level compared to the total *Dnah2* transcripts in heterozygous mutant males ($Dnah2^{+/\Delta}$) (**Supplementary Figure 1E**). These results suggest that $Dnah2^{\Delta/\Delta}$ males cannot generate full-length DNAH2 but potentially a reduced degree of truncated proteins at the C-terminus. Consistently, we validated the absence of the full-length DNAH2 protein in $Dnah2^{\Delta/\Delta}$ sperm by DNHA2 antibody recognizing a C-terminal region located after the deletion (**Figure 2A** and **Supplementary Figure 1F**). Both $Dnah2^{+/\Delta}$ and $Dnah2^{\Delta/\Delta}$ mice showed no gross abnormalities in appearance or survival. $Dnah2^{+/\Delta}$ males and females, and $Dnah2^{\Delta/\Delta}$ females are fertile when mated with WT animals. Homozygous *Dnah2* mutant males, however, are sterile despite their normal sexual behavior. Histological analyses of ciliated epithelia of trachea and oviduct epithelia did not show significant morphological defects in $Dnah2^{\Delta/\Delta}$ mice (**Supplementary Figure 2**). These results demonstrate that homozygous *Dnah2* mutations cause male-specific infertility in mice.

$Dnah2^{\Delta/\Delta}$ Males Present MMAF Phenotypes

To elucidate the etiology of infertility of $Dnah2^{\Delta/\Delta}$ males, we examined the histology of $Dnah2^{\Delta/\Delta}$ testis and mutant sperm morphology (**Figure 2**). Compared to heterozygous mutants, homozygous *Dnah2* mutants had fewer sperm cells in the lumen of seminiferous tubules and epididymis (**Figure 2B**). Sperm cells collected from the cauda epididymis of $Dnah2^{\Delta/\Delta}$ males showed severe morphological defects to a varying degree (**Figures 2C,D**). A majority of the $Dnah2^{\Delta/\Delta}$ sperm flagella were absent (31.1 ± 6.5%), short (9.2 ± 3.7%), bent (11.4 ± 2.2%), coiled (15.9 ± 2.5%), or had an irregular-caliber shape (28.4 ± 6.0%), a typical feature of MMAF. A very small number of sperm cells

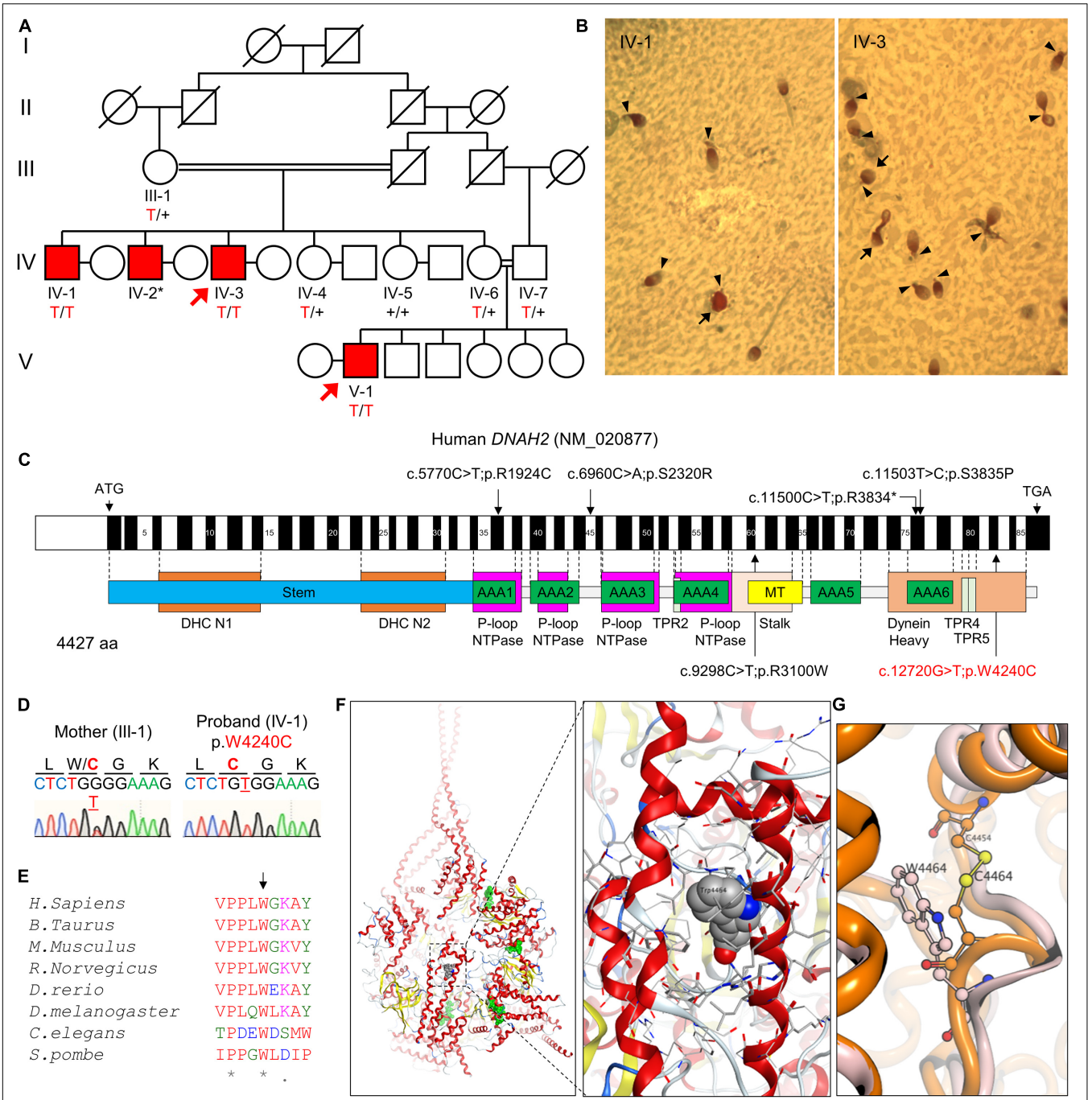

FIGURE 1 | A novel bi-allelic *DNAH2* variant identified from a consanguineous family with oligoasthenozoospermia. **(A)** Pedigree of a consanguineous family with four infertile males (IV-1, IV-2, IV-3, and V-1). WES was performed with IV-3 and V-1 (arrows). Sanger sequencing verified segregation of the variant (red) in the infertile males. A plus (+) indicates a wild-type allele and an asterisk (*) denotes a sample not available for this study. **(B)** PAP-stained semen from patients IV-1 and IV-3. Multiple morphological defects including near absence of a tail or a short tail (arrowheads), and spherical heads (arrows) are prominent from both patients. **(C)** Mapping of the *DNAH2* variant. Mutation of G to T in exon 82 of *DNAH2* cDNA (c.12720G > T; NCBI RefSeq identifier NM_020877) results in a tryptophan-to-cysteine (p.W4240C) substitution in the dynein heavy chain domain. Previously reported pathogenic variants (Li et al., 2019) are also marked (black). **(D)** Chromatograms of the *DNAH2* non-synonymous variant in an infertile sibling (IV-1) and his mother (III-1). The variant is underlined, and the resulting amino acid substitution is marked in red. **(E)** A sequence alignment of the DNAH2 protein across multiple species. The tryptophan at position 4240 (arrow) is conserved in multiple organisms. An asterisk (*) indicates positions fully conserved and a period (.) indicates positions with weakly similar amino acids. **(F,G)** Structural modeling of the DNAH2 mutation from this study. **(F)** Ribbon structure of human DNAH1 (PDB ID: 5NUG), a homolog of human DNAH2. ATP-binding sites are colored in green (*left*). The enlarged area is the region corresponding to that of W4240 in DNAH2 (*right*). DNAH1 W4464, which is homologous to W4240, is represented in a space-filling model. **(G)** Ribbon diagram shows mutation of tryptophan at position 4464 (W4464, orange) to cysteine (W4464C, pink) is predicted to form disulfide bond with nearby C4454 and distort protein backbone structure.

TABLE 2 | Variant detail in the infertility family.

Gene	*DNAH2*	*FZD3*	*MYDGF*
Genome position (Chr-Position)	17-7735087	8-28384879	19-4670172
Transcript position	NM_020877 c.12720G > T	NM_145866 c.602T > C	NM_019107 c.174+1G > T
Mutation type	Non-synonymous	Non-synonymous	Splice donor
Mutation	p.W4240C	p.F201S	c.174+1G > T
ClinVar Allele ID			
dbSNP			rs745851558
gnomAD MAF			0.0000666
Bravo MAF			0.0000319
MetaSVM	D	D	
SIFT	D	D	
PolyPhen	D	D	
CADD	31	26.2	24.4
GTEx TPM in testis*	8.12	5.64	95.44
GTEx Pext in testis#	0.41	1	1
Cosegregation	Yes	No	No

**GTEx TPM: The Genotype-Tissue Expression (GTEx) project V7, Transcripts Per Million. #GTEx Pext: GTEx V7, Proportion Expression across Transcripts.*

had relatively normal-length, though immotile, tails that only vibrated and twitched (**Supplementary Video 1**). In addition, *Dnah2*$^{\Delta/\Delta}$ sperm exhibited mild morphological abnormalities on their head. These sperm characteristics are consistent with the sperm seen in our proband with the identified homozygous *DNAH2* mutation (**Figure 1**). All these results demonstrate that the homozygous *Dnah2* mutation causes MMAF in mice.

DNAH2 Is Required for Normal Flagellar Assembly, Organization, and Expression of Axonemal Proteins

The morphological abnormality led us to examine sperm ultrastructure and molecular organization of flagella (**Figure 3** and **Supplementary Figure 3**). A scanning electron microscopy (SEM) analysis of *Dnah2*$^{\Delta/\Delta}$ sperm demonstrated morphological defects in the midpiece (**Figures 3A,B** and **Supplementary Figure 3A**). Some *Dnah2*$^{\Delta/\Delta}$ sperm lack mitochondria completely. Others have irregular mitochondrial arrangement around the flagellum and/or mitochondria that wrapped around the head (**Supplementary Figure 3A**). Transmission electron microscopy (TEM) images revealed diverse ultrastructural defects in the *Dnah2*$^{\Delta/\Delta}$ flagella (**Figures 3C,D** and **Supplementary Figures 3B–E**). Longitudinal section images showed not only abnormally arranged mitochondria, but also misaligned outer dense fiber (ODF) and microtubule doublets in the midpiece region of *Dnah2*$^{\Delta/\Delta}$ sperm (**Supplementary Figures 3B,C**). It was frequently observed that the longitudinal columns of the fibrous sheath are not fused to the ODFs at positions 3 and 8 or the whole fibrous sheath is missing in the prospective principal piece (**Supplementary Figure 3E**). Electron densities corresponding to both IDA and ODA were observed from the microtubule doublets when the 9+2 arrangement is incomplete in the *Dnah2*$^{\Delta/\Delta}$ axoneme (**Figure 3D**). However, even mutant sperm with relatively normal morphology cannot beat properly, but only vibrate (**Supplementary Video 1**), suggesting axonemal dysfunction in IDAs, ODA, and/or RSs. We hypothesized molecular organization of axoneme is disrupted in sperm lacking DNAH2. Another IDA component, DNAH1, is also absent in the flagella of *Dnah2*$^{\Delta/\Delta}$ sperm (**Figure 3E**), suggesting that DNAH2 interacts with other IDA components during axonemal assembly. In addition, an RS protein, RSPH3, is also absent in sperm lacking DNAH2, indicating its functional association with RS protein localization. By contrast, *Dnah2*$^{\Delta/\Delta}$ sperm cells express acetylated tubulin and DNAH9 on their flagella, indicating DNAH2 deficiency might not affect molecular organization of microtubule doublets and ODA. These results demonstrate that the absence of DNAH2 causes abnormal axonemal structure by disrupting molecular organization of not only IDA but also RS and overall organization defects in flagellar development, underlying MMAF-like sperm phenotypes and male infertility.

DNAH2 Deficiency Dysregulates Developmental Expression and Localization of Basal Body and Annulus Components

A majority of epididymal sperm from *Dnah2*$^{\Delta/\Delta}$ males have short flagella (**Figure 2**), suggesting defects in formation and/or localization of basal body and/or annulus as regulate axoneme elongation and flagellar compartmentalization during spermiogenesis (Avidor-Reiss et al., 2017, 2019). Therefore, we examined expression of centriole and annulus components in epididymal sperm cells (**Figures 4A,B**). In mice, proximal and distal centrioles to comprise the basal body are degenerated gradually in developing spermatids; in mature epididymal sperm, both proximal and distal centrioles are absent at the connecting piece (Manandhar et al., 2005; Avidor-Reiss et al., 2019).

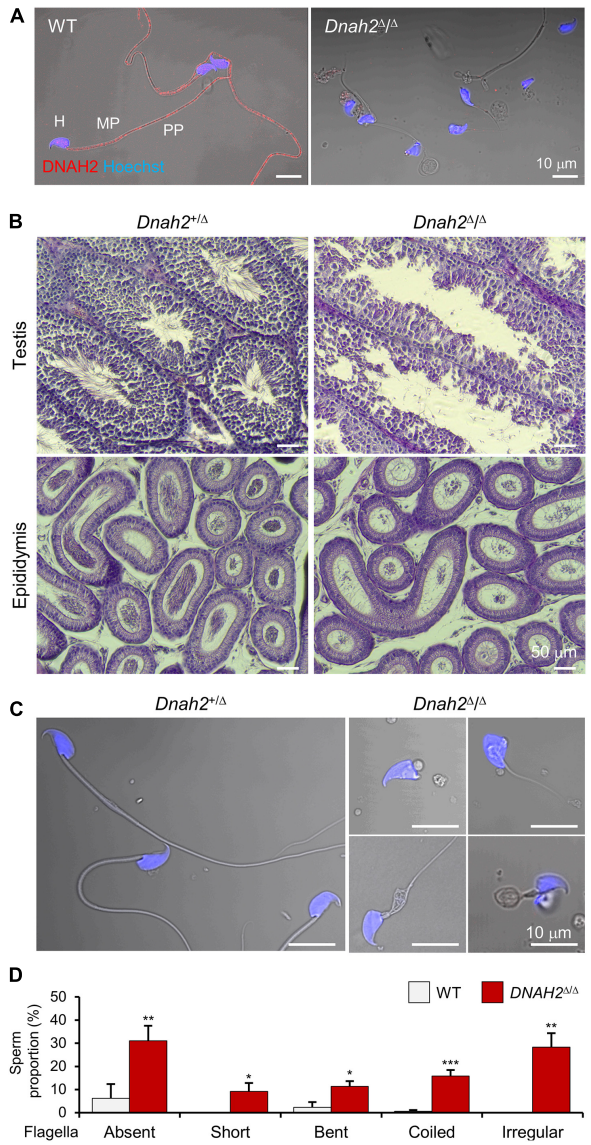

FIGURE 2 | DNAH2 deficiency in mice recapitulates multiple morphological abnormalities of the flagella in humans. **(A)** Confocal images of DNAH2 in WT and *Dnah2*$^{\Delta/\Delta}$ sperm. DNAH2 were immunodetected from WT sperm but not from *Dnah2*$^{\Delta/\Delta}$ sperm. Sperm heads were counterstained with Hoechst. Shown images are confocal images merged to the corresponding DIC images. H, head; MP, midpiece; PP, principal piece. **(B)** Testicular and epididymal histology of *Dnah2*$^{\Delta/\Delta}$ mouse testis and epididymis. H/E stained sections show *Dnah2*$^{\Delta/\Delta}$ males produce less sperm with elongated tails in the lumen of seminiferous tubule in testis (*top*), resulting in fewer sperm cells in the epididymis (*bottom*, corpus). **(C,D)** Multiple morphological defects in epididymal *Dnah2*$^{\Delta/\Delta}$ sperm. **(C)** Morphology of *Dnah2*$^{+/\Delta}$ (*left*) and *Dnah2*$^{\Delta/\Delta}$ (*right*) sperm. Sperm from heterozygous males are morphologically normal. *Dnah2*$^{\Delta/\Delta}$ sperm, however, present MMAF-like phenotypes, such as absent, short, coiled, and irregular-caliber flagella (from *left top*, clockwise direction). Sperm heads were Hoechst-stained (blue). Fluorescence confocal and corresponding DIC images are merged. **(D)** Proportions of sperm with defective flagellar morphologies. Sperm with absent, short, bent, coiled, and irregular-caliber flagella were quantified from WT (gray) and *Dnah2*$^{\Delta/\Delta}$ (red) male mice ($N = 3$, each). Sperm proportions of each pattern were statistically compared between WT and *Dnah2*$^{\Delta/\Delta}$ males. Data is represented as mean ± SEM. $^{*}p < 0.05$; $^{**}p < 0.01$; $^{***}p < 0.001$.

Accordingly, confocal immunostaining revealed that core components of centriole, γ-tubulin and CENTRIN1, are not detected in WT sperm, but remain at connecting piece of *Dnah2*$^{\Delta/\Delta}$ sperm heterogeneously (**Figure 4A**). Next, we examined expression of SEPTIN4 and SEPTIN12, components of the annulus, which compartmentalizes sperm flagella (Avidor-Reiss et al., 2017). SEPTIN4 and SEPTIN12 localize at the junction between the midpiece and principal piece in WT sperm, but their expression and localizations are dysregulated heterogeneously in *Dnah2*$^{\Delta/\Delta}$ sperm like spermatids (**Figure 4B**); a majority of *Dnah2*$^{\Delta/\Delta}$ sperm with short tails express SEPTIN4 and SEPTIN12 near the connecting piece. TEM supports the dysregulated expression and localization of the centriole and/or annulus in *Dnah2*$^{\Delta/\Delta}$ epididymal sperm (**Figures 4C,D**). Although the basal plate and capitulum are present, overall ultrastructure near the connecting piece is severely disorganized in *Dnah2*$^{\Delta/\Delta}$ sperm. Notably, centriole-like structures and/or their traces remain in DNAH2-deficient sperm cells in the cavities, which is likely to correspond to the proximal or distal centriole vaults (PCV and DCV, respectively) in *Dnah2*$^{+/\Delta}$ sperm (red asterisks in **Figure 4D**). In addition, *Dnah2*$^{\Delta/\Delta}$ sperm display annulus-like electron-dense areas much close to the connecting piece which would normally localize at the junction between mitochondria-concentrating midpiece and principal piece in WT sperm (yellow arrows in **Figure 4C**); sometimes the annulus-like structure is even placed before mitochondria appear (yellow arrows in **Figure 4D**). All these results demonstrate that DNAH2 deficiency impairs overall spermiogenesis. We utilized the curated public databases to analyze scRNA-seq datasets in human (GSE109037) and mouse (GSE109033) testes and found that *DNAH2* mRNA expresses the highest in spermatocytes and early spermatids among major cell types in both human and mouse testis (**Figures 5A,B**), supporting the pivotal role of DNAH2 in spermiogenesis.

To better understand DNAH2 function in flagella elongation, especially positioning the basal body and annulus during spermiogenesis, we examined CENTRIN1 and SEPTIN4 in the developing flagella of testicular spermatids from *Dnah2*$^{\Delta/\Delta}$ males (**Figures 5C,D**). Just like *Dnah2*$^{\Delta/\Delta}$ epididymal sperm, after step 8 testicular *Dnah2*$^{\Delta/\Delta}$ spermatids exhibited obvious flagellar defects in positioning of CENTRIN1 and SEPTIN4. Both WT and *Dnah2*$^{\Delta/\Delta}$ spermatids express CENTRIN1 at the junction between nucleus and the elongating tail. However, contrary to a set of paired centrioles to form basal body in WT spermatids, the number of CENTRIN1-containing centrioles varies in *Dnah2*$^{\Delta/\Delta}$ spermatids (**Figure 5C**). The annulus reaches its final position in the elongating spermatids as depicted by SEPTIN4 localization from the proximal to distal flagellum while advancing developmental stages in WT males (**Figure 5D**, *left*). In *Dnah2*$^{\Delta/\Delta}$ spermatids, however, SEPTIN4 expression and localization is variable (**Figure 5D**, *right*). All of these results strongly suggest that DNAH2 deficiency dysregulates the basal body organization and the annulus migration in developing spermatids (**Figure 5E**), proving molecular and cellular mechanisms of MMAF.

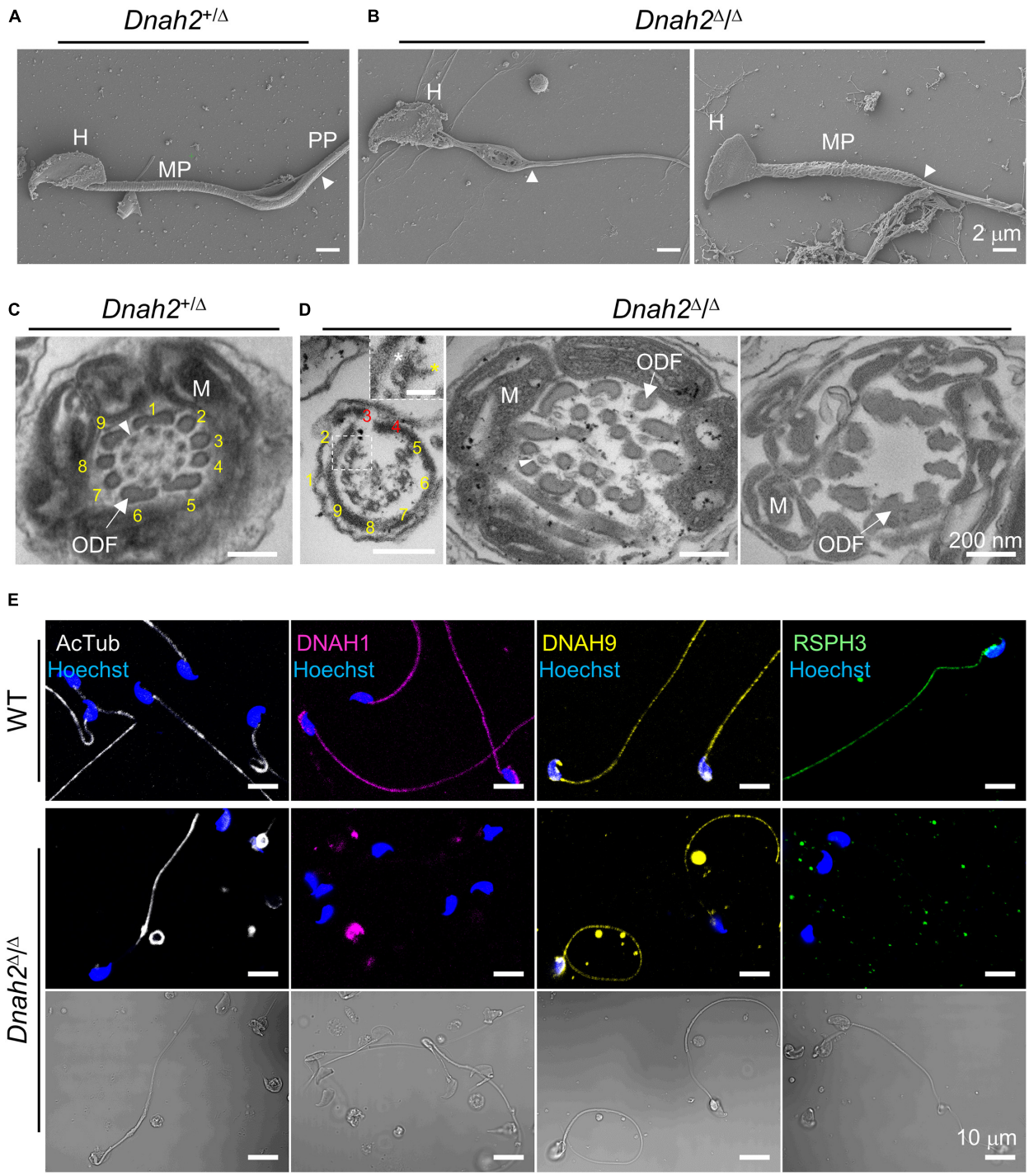

FIGURE 3 | Flagellar ultrastructure is disorganized, and axonemal proteins express abnormally in *Dnah2*-null sperm. **(A,B)** Scanning electron microscopy images of *Dnah2*$^{+/\Delta}$ **(A)** and *Dnah2*$^{\Delta/\Delta}$ **(B)** sperm. *Dnah2*$^{\Delta/\Delta}$ sperm display absence of (*left*) or an irregular (*right*) mitochondrial helical sheath in the midpiece of the sperm tail, along with abnormal head shapes. Arrowheads indicate annulus. H, head; MP, midpiece; and PP, principal piece. **(C,D)** Transmission electron microscopy images of *Dnah2*$^{+/\Delta}$ **(C)** and *Dnah2*$^{\Delta/\Delta}$ **(D)** sperm. Representative cross-section images of TEM reveal conformational defects in the midpiece of *Dnah2*$^{\Delta/\Delta}$ sperm. Incomplete 9+2 axonemal structure (*left*), delocalized outer dense fibers (ODF, arrow) and microtubule doublet (*middle,* arrowhead), and lack of the axonemal components (*right*) were observed in the *Dnah2*$^{\Delta/\Delta}$ sperm. Inner (yellow asterisk) and outer (white asterisk) dynein arm structure were observed from microtubule doublet occasionally (*left*, inset; scale bar = 50 nm). Microtubule doublets are numbered with the absence of the corresponding microtubule doublet in red. M, mitochondria. **(E)** Confocal fluorescence images of axonemal proteins in WT and *Dnah2*$^{\Delta/\Delta}$ sperm. *Dnah2*$^{\Delta/\Delta}$ sperm do not express another IDA component (DNAH1, magenta) and a radial spoke protein (RSPH3, green) but an ODA protein (DNAH9, yellow). Flagella microtubules (AcTub, white) and sperm heads (Hoechst, blue) serve as controls. The corresponding DIC images are shown together for *Dnah2*$^{\Delta/\Delta}$ sperm.

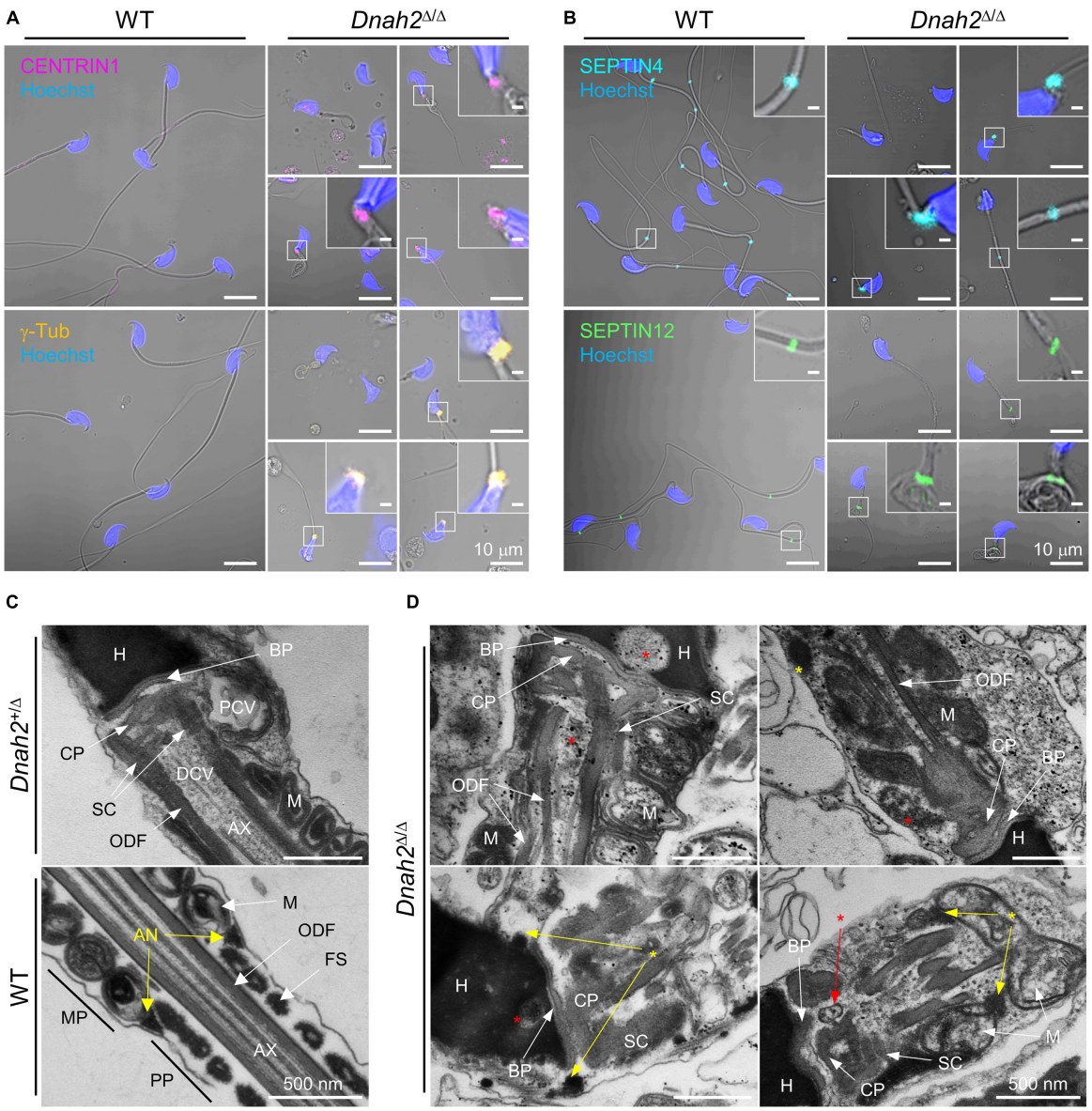

FIGURE 4 | Formation of the basal body and annulus is deregulated in *Dnah2*$^{\Delta/\Delta}$ epididymal sperm. **(A,B)** Confocal images of immunostained centriolar **(A)** and annulus **(B)** proteins in WT (*left*) and *Dnah2*$^{\Delta/\Delta}$ (*right*) epididymal sperm. Centriolar proteins, CENTRIN1 (*top*) and γ-Tubulin (*bottom*), lacking in mouse epididymal sperm, are aberrantly detected near the connecting piece of *Dnah2*$^{\Delta/\Delta}$ sperm **(A)**. Annulus components, SEPTIN4 (*top*) and SEPTIN12 (*bottom*), is localized heterogeneously along the flagella in *Dnah2*$^{\Delta/\Delta}$ sperm **(B)**. Hoechst was used for counter staining. Merged fluorescence and corresponding DIC images are shown **(A,B)**. Magnified insets are represented (scale bars = 1 μm). **(C,D)** Transmission electron microscopy of normal **(C)** and *Dnah2*$^{\Delta/\Delta}$ **(D)** epididymal sperm. *Dnah2*$^{+/\Delta}$ (*top*) and WT (bottom) sperm were used for controls to show ultrastructure of connecting piece lacking centrioles and annulus, respectively **(C)**. Centriole-like structure or the traces are detected (red asterisks) and annulus-like electron-dense area (yellow asterisks) is localized heterogeneously near the connecting piece in *Dnah2*$^{\Delta/\Delta}$ sperm **(D)**. Nu, nucleus; BP, basal plate; CP, capitulum; SC, segmented column; PCV, proximal centriolar vault; DCV, distal centriolar vault; AN, annulus; AX, axoneme; M, mitochondria; ODF, outer dense fiber; MP, midpiece; PP, principal piece.

DISCUSSION

Variants in *DNAH2* Underlying Primary Male Infertility in Human

DNAH2 encodes a 4,427 amino acid long conserved protein which is an IDA component in the axoneme (Chapelin et al., 1997; Viswanadha et al., 2017). DNAH2 is composed of a microtubule binding domain, ATPase domains (AAA domains) (**Figure 1**). The AAA domains hydrolyze ATP and enable DNAH2 to regulate beating of motile cilia and sperm flagella as a motor protein (Cho and Vale, 2012; Toure et al., 2020). A previous study identified pathogenic DNAH2 mutations in AAA1 (p.R1924C) and AAA6 domains (p.S3835P and p.R3834*) from MMAF patients (Li et al., 2019). DNAH2 protein levels were

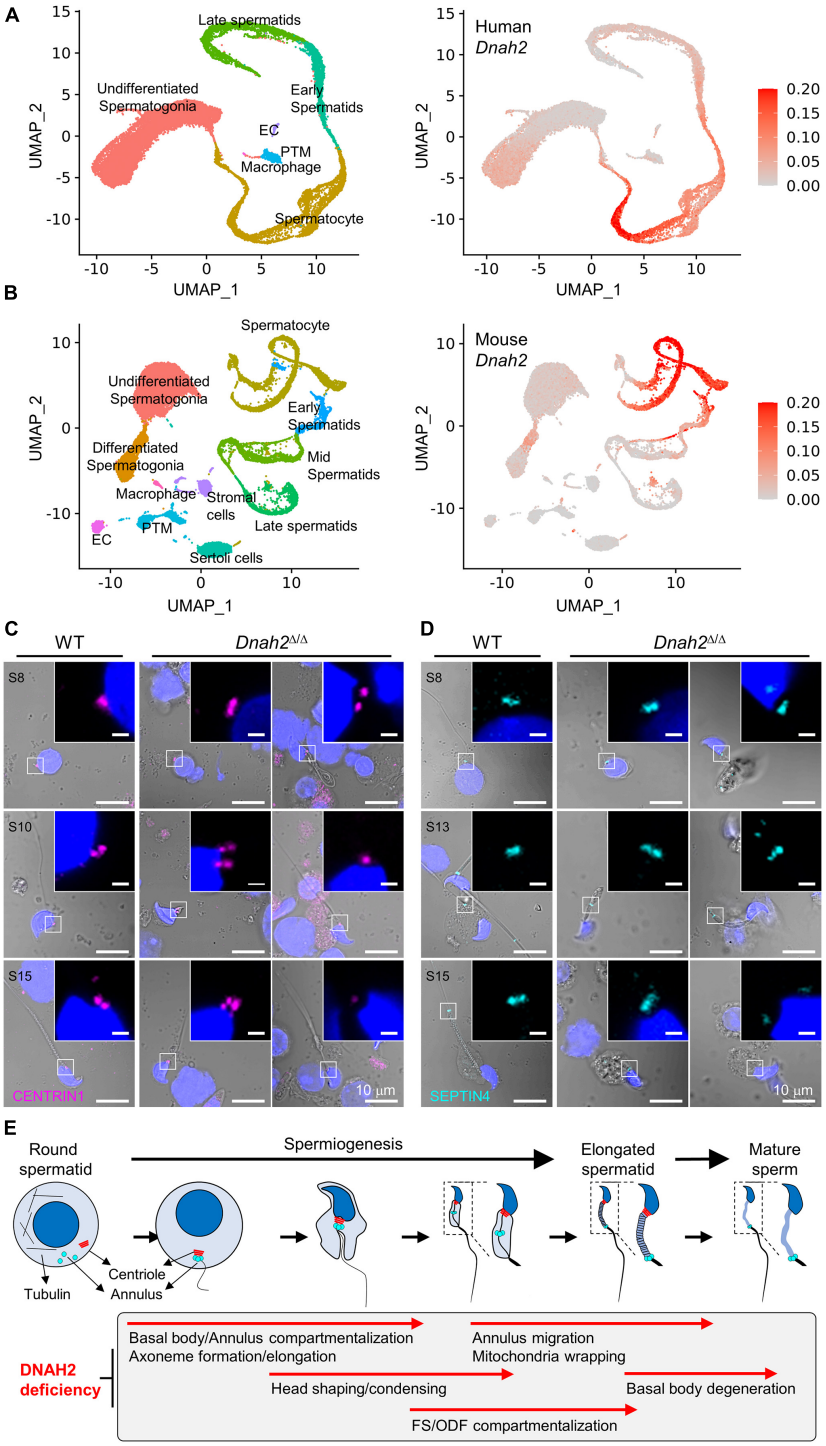

FIGURE 5 | DNAH2 deficiency dysregulates the expression and localization of the basal body and annulus components in developing spermatids. **(A,B)** *DNAH2* mRNA expression in human **(A)** and mouse **(B)** testicular cells. Human (GSE109037) and mouse (GSE109033) testis single-cell RNA (scRNA)-seq datasets were analyzed. UMAP plots represents 7 and 11 clusters of testicular cells in human and mouse (*left*) and *DNAH2* mRNA expression in individual cells (*right*). EC, endothelial cell; PTM, peritubular myoid cell. **(C,D)** Confocal images of centriole (CENTRIN1, **C**) and annulus (SEPTIN4, **D**) proteins in WT and *Dnah2*$^{\Delta/\Delta}$ spermatids in different developmental step (S). The number of centrioles and localization of the annulus are impaired heterogeneously in *Dnah2*$^{\Delta/\Delta}$ spermatids. Hoechst was used for counter staining. Merged fluorescence and corresponding DIC images are shown. Magnified insets are shown with fluorescence images (scale bars = 1 mm, **C,D**). **(E)** A schematic cartoon depicting impaired cellular events by DNAH2 deficiency during sperm development. Testicular germ cells from round to elongated spermatids and mature sperm are drawn (*top*) and the corresponding morphological and structural changes are described in a gray box (*bottom*). DNAH2 deficiency compromises flagella elongation and compartmentalization in developing spermatids, which causes in MMAF in mature sperm eventually.

reduced in sperm from these patients, and the remaining mutant DNAH2 is likely to interfere with normal DNAH2 function, suggesting important roles for AAA domains in DNAH2 function and stability. The novel *DNAH2* variant identified in this study (NM_020877:c.12720G > T;p.W4240C) localizes at the genomic region encoding C-terminal dynein heavy chain. This domain at C-term of DNAH2 contains the AAA6 domain and structurally retains the ATP binding site without a p-loop motif (pfam03028). Our protein modeling predicts that the identified p.W4240C mutation could alter the ATP binding and ATP hydrolysis ability in the mutant DNAH2, likely causing male infertility with MMAF-like phenotype in these Pakistani patients.

Loss-of-Function Mutations in *DNAH2*, an Evolutionarily Conserved IDA-Encoding Gene, Cause MMAF in Human and Mouse

DNAH1 and *DNAH2* are paralogs and are evolutionarily conserved across ciliated eukaryotes. They encode IDA heavy chains in motile cilia and sperm flagella. Previous studies demonstrate pathogenic *DNAH1* or *DNAH2* variants cause male infertility and MMAF without obvious PCD symptoms. Two DNAH1 mutations (p.P3909Rfs*33 and p.G3930Afs*120) at the DHC domain at C-terminus were identified from males with MMAF-phenotypes (Ben Khelifa et al., 2014; Wang et al., 2017), similar to DNAH2 mutations at the corresponding domain (**Figure 1**; Li et al., 2019). Thus, *DNAH1* and *DNAH2* might coordinate flagella development and movement in humans. By contrast, sperm phenotypes by DNAH1 mutations are different from DNAH2 in mice. DNAH1 deficiency in mice did not induce MMAF (Neesen et al., 2001). *Dnah1*-null males are infertile due to severely reduced motility, but the mutant sperm have normal flagellar ultrastructure. This phenotypic difference illuminates that DNAH2 is more than a component of IDA in mice and is involved in overall sperm flagella development compared to the limited function of DNAH1 to IDA. Taken together, *DNAH2* is an MMAF-causing IDA encoding gene conserved in humans and mice.

Etiology and Developmental Mechanisms of MMAF Elucidated by *Dnah2* Loss-of-Function in Mice

The dynein arm is typically composed of light, intermediate, and heavy chain proteins (Viswanadha et al., 2017). Currently known MMAF-associated genes encode IDA (DNAH1 and DNAH2) and ODA (DNAH8 and DNAH17) heavy chains and their mutations do not seem to cause PCD (Toure et al., 2020). A previous study revealed that DNAH8 and DNAH17 express specifically in sperm flagella, but the other ODA heavy chains, DNAH5, DNAH9, and DNAH11, express in airway cilia (Whitfield et al., 2019). The protein expression patterns indicate that sperm ODA are composed of specific ODA proteins. MMAF patients with mutations at *DNAH8* and *DNAH17* do not express DNAH17 and DNAH8, respectively. Yet, the ODA ultrastructure observed through TEM in these patients was relatively normal in their sperm (Whitfield et al., 2019; Liu et al., 2020). Similarly, we found that *Dnah2*-null sperm lack both DNAH1 and DNAH2 proteins but retain electron densities corresponding IDA structure (**Figure 3** and **Supplementary Figure 3**). We did not observe a difference in gross morphology of cilia in tracheal or oviductal epithelia from *Dnah2* knockout mice (**Supplementary Figure 2**). Therefore, it is plausible that DNAH2 functions more specifically in flagella, while DNAH2 contributes to ciliary function awaits further studies.

We found DNAH2 deficiency in mice causes MMAF phenotypes and mildly abnormal heads (**Figures 2–4** and **Supplementary Figure 3**), indicating defects in flagella elongation and head shaping during spermiogenesis. The basal body, originating from mother and daughter centrioles, is a platform for microtubule elongation to form the axoneme in ciliates (Werner et al., 2017). Recent studies identify that mutations of centriolar proteins, DZIP1 and CEP135, from MMAF patients (Sha Y. W. et al., 2017; Lv et al., 2020), highlighting that defective basal body compromises flagellar development. Unexpectedly, we found some *Dnah2*$^{\Delta/\Delta}$ spermatids have more than two centrioles. Considering that *DNAH2* expresses predominantly in spermatocytes (**Figure 5**) and that centrosome duplication occurs in spermatocytes (Alfaro et al., 2021), DNAH2 might be involved in basal body formation in earlier steps in male germ cell development. The proximal region of cilium, called the transition zone, is a specific molecular diffusion barrier to restrict protein entry into cilium. The annulus, SEPTIN-complexed flagellar ring structure, functions as a barrier just like the transition zone in cilium (Avidor-Reiss et al., 2017). Notably, the annulus is initially localized close to the proximal region of the elongating flagella and gradually migrates to the distal part. Immunostaining and TEM images reveal that DNAH2 deficiency impairs the annulus migration in spermatids, resulting in heterogeneous localization in the epididymal sperm. Although how the annulus migrates along the flagella is not well characterized, the defective annulus localization suggests the DNAH2 could be a motor protein to play a role in annulus migration in developing spermatids.

Intraflagellar transporters (IFTs) are essential for proper sperm tail assembly as well as head formation (Lehti and Sironen, 2016). The manchette, sheaths of microtubules extending tailward from the nucleus, is involved in the trafficking of Golgi-derived cargos to the flagellum (Kierszenbaum et al., 2011). DNAH2 might associate with the IFTs and the manchette in developing spermatids. Consistent with this idea, recent human genetic and mouse knockout studies have demonstrated that mutations in IFT components (Liu et al., 2017; Zhang S. et al., 2020) and manchette-associated molecules (O'Donnell et al., 2012; Lehti et al., 2013) result in morphological defects in sperm flagella and heads similar to those seen in *Dnah2*-null sperm (**Figure 3** and **Supplementary Figure 3**). In *Dnah2*-null spermatids, IFT and manchette-mediated transport of axonemal and peri-axonemal components to flagella might have been dysregulated, supported by the loss of DNAH1 and RSPH3. This dysregulation would result in cargo accumulation in the cytoplasm of spermatids, resulting in abnormal head morphology, disorganized 9+2 axoneme, and delocalized peri-axonemal components.

In summary, we identified a novel *DNAH2* variant that segregated with male infertility in a consanguineous family of Pakistani origin. Our genetic, clinical and *in silico* analyses in human subjects and loss-of-function studies in a mouse model elucidate the general pathogenic mechanisms of DNAH2 mutations in the flagellar assembly and beating. DNAH2 deficiency in mice causes male-specific infertility resembling MMAF sperm phenotypes, thus directly establishing DNAH2 as a causative gene to MMAF. Moreover, DNAH2 deficiency not only impairs molecular organization of the axoneme but also other sperm flagellar structures, suggesting the involvement of the dynein complex in sperm flagellar assembly. Our study provides new knowledge to clinicians and genetic counselors for understanding the genetic etiology of MMAF and better planning of assisted reproductive technology for male patients experiencing MMAF-related infertility.

DATA AVAILABILITY STATEMENT

The datasets presented in this study can be found in online repositories. The names of the repository/repositories and accession number(s) can be found below: https://www.ncbi.nlm.nih.gov/gap/?term=phs000744.

ETHICS STATEMENT

The studies involving human participants were reviewed and approved by the Institutional Review Board of Quaid-i-Azam University, Islamabad, Pakistan. The patients/participants provided their written informed consent to participate in this study. The animal study was reviewed and approved by Yale Animal Care and Use.

AUTHOR CONTRIBUTIONS

J-JC and WA conceived and supervised the project. JH and HW performed mouse characterization experiments. SN recruited patients and analyzed patient samples with help from SH and MN. SN and J-NO prepared the DNA samples for WES. JC, FL-G, KB, and SM generated WES data. SN, JC, FL-G, and WD analyzed WES data. JC and KJ analyzed scRNA-seq data. CB modeled protein structures. J-JC, WA, C-KL, and RL provided resources. J-JC administrated entire study. JH, SN, JC, and J-JC wrote the manuscript with the inputs from all other authors. All authors contributed to the article and approved the submitted version.

FUNDING

This work was supported by start-up funds from Yale University School of Medicine, Grantham Foundation, and National Institute of Child Health and Human Development (R01HD096745, https://www.nichd.nih.gov) to J-JC; Pakistan Academy of Sciences (PAS-171, https://www.paspk.org) to WA; and National Human Genome Research Institute: UM1HG006504, https://www.genome.gov) to the Yale Center for Mendelian Genomics. SN was supported by Pakistan Higher Education Commission International Research Support Initiative Program (https://www.hec.gov.pk/english/scholarshipsgrants/IRSIP). J-NO was supported by Seoul National University Long-term Study Abroad Scholarship Award (http://oia.snu.ac.kr). JH is supported by Postdoctoral Fellowship from Male Contraceptive Initiative (https://www.malecontraceptive.org/male-contraception-funding). The Genome Sequencing Program Coordinating Center (U24 HG008956, https://www.genome.gov/Funded-Programs-Projects/NHGRI-Genome-Sequencing-Program/Genome-Sequencing-Program-Coordinating-Center-GSPCC) contributed to cross-program scientific initiatives and provided logistical and general study coordination. The content is solely the responsibility of the authors and does not necessarily represent the official views of the National Institutes of Health. The funders had no role in study design, data collection and analysis, decision to publish, or preparation of the manuscript.

ACKNOWLEDGMENTS

The research is in part supported by a Korea University Medical Center Grant. DNAH2 mutant mouse line was originated from The Centre for Phenogenomics (TCP) and provided by The Canadian Mouse Mutant Repository at The Hospital for Sick Children. The authors highly appreciate participation of the family members in the study presented here. We also thank Case Porter and Miriam Hill for their help in PCR and Sanger sequencing, the Yale Center for Cellular and Molecular Imaging for assistance in scanning and transmission electron microscopy, Luke McGoldrick for critical reading of the initial draft of the manuscript, and Byoung-Il Bae for sharing CENTRIN1 and γ-tubulin antibodies.

SUPPLEMENTARY MATERIAL

The Supplementary Material for this article can be found online at: https://www.frontiersin.org/articles/10.3389/fcell.2021.662903/full#supplementary-material

REFERENCES

Alfaro, E., Lopez-Jimenez, P., Gonzalez-Martinez, J., Malumbres, M., Suja, J. A., and Gomez, R. (2021). PLK1 regulates centrosome migration and spindle dynamics in male mouse meiosis. *EMBO Rep.* e51030.

Amiri-Yekta, A., Coutton, C., Kherraf, Z. E., Karaouzene, T., Le Tanno, P., Sanati, M. H., et al. (2016). Whole-exome sequencing of familial cases of multiple morphological abnormalities of the sperm flagella (MMAF) reveals new DNAH1 mutations. *Hum. Reprod.* 31, 2872–2880. doi: 10.1093/humrep/dew262

Avidor-Reiss, T., Ha, A., and Basiri, M. L. (2017). Transition zone migration: a mechanism for cytoplasmic ciliogenesis and postaxonemal centriole elongation. *Cold Spring Harb. Perspect. Biol.* 9:a028142. doi: 10.1101/cshperspect.a028142

Avidor-Reiss, T., Mazur, M., Fishman, E. L., and Sindhwani, P. (2019). The role of sperm centrioles in human reproduction - the known and the unknown. *Front. Cell Dev. Biol.* 7:188. doi: 10.3389/fcell.2019.00188

Ben Khelifa, M., Coutton, C., Zouari, R., Karaouzene, T., Rendu, J., Bidart, M., et al. (2014). Mutations in DNAH1, which encodes an inner arm heavy chain dynein, lead to male infertility from multiple morphological abnormalities of the sperm flagella. *Am. J. Hum. Genet.* 94, 95–104. doi: 10.1016/j.ajhg.2013.11.017

Browning, B. L., and Browning, S. R. (2011). A fast, powerful method for detecting identity by descent. *Am. J. Hum. Genet.* 88, 173–182. doi: 10.1016/j.ajhg.2011.01.010

Bykova, I., Golosova, O., Bakulina, A., Afonnikov, D., Kandrov, D., Palyanov, A., et al. (2016). "UGENE: a toolkit for teaching students," in *Proceedings of the Mathematical Modeling and High Performance Computing in Bioinformatics, Biomedicine and Biotechnology (MM-HPC-BBB-2016)*, Novosibirsk, 29–29.

Chapelin, C., Duriez, B., Magnino, F., Goossens, M., Escudier, E., and Amselem, S. (1997). Isolation of several human axonemal dynein heavy chain genes: genomic structure of the catalytic site, phylogenetic analysis and chromosomal assignment. *FEBS Lett.* 412, 325–330. doi: 10.1016/s0014-5793(97)00800-4

Cho, C., and Vale, R. D. (2012). The mechanism of dynein motility: insight from crystal structures of the motor domain. *Biochim. Biophys. Acta* 1823, 182–191. doi: 10.1016/j.bbamcr.2011.10.009

Curi, S. M., Ariagno, J. I., Chenlo, P. H., Mendeluk, G. R., Pugliese, M. N., Sardi Segovia, L. M., et al. (2003). Asthenozoospermia: analysis of a large population. *Arch. Androl.* 49, 343–349. doi: 10.1080/713828220

Dong, C., Wei, P., Jian, X., Gibbs, R., Boerwinkle, E., Wang, K., et al. (2015). Comparison and integration of deleteriousness prediction methods for nonsynonymous SNVs in whole exome sequencing studies. *Hum. Mol. Genet.* 24, 2125–2137. doi: 10.1093/hmg/ddu733

Edgar, R. C. (2004). MUSCLE: multiple sequence alignment with high accuracy and high throughput. *Nucleic Acids Res.* 32, 1792–1797. doi: 10.1093/nar/gkh340

Esteves, S. C., Miyaoka, R., and Agarwal, A. (2011). An update on the clinical assessment of the infertile male. [corrected]. *Clinics (Sao Paulo)* 66, 691–700. doi: 10.1590/s1807-59322011000400026

Finak, G., Mcdavid, A., Yajima, M., Deng, J., Gersuk, V., Shalek, A. K., et al. (2015). MAST: a flexible statistical framework for assessing transcriptional changes and characterizing heterogeneity in single-cell RNA sequencing data. *Genome Biol.* 16:278.

Fromer, M., Moran, J. L., Chambert, K., Banks, E., Bergen, S. E., Ruderfer, D. M., et al. (2012). Discovery and statistical genotyping of copy-number variation from whole-exome sequencing depth. *Am. J. Hum. Genet.* 91, 597–607. doi: 10.1016/j.ajhg.2012.08.005

Hermann, B. P., Cheng, K., Singh, A., Roa-De La Cruz, L., Mutoji, K. N., Chen, I. C., et al. (2018). The mammalian spermatogenesis single-cell transcriptome, from spermatogonial stem cells to spermatids. *Cell Rep.* 25, 1650–1667.e8.

Howe, B., Umrigar, A., and Tsien, F. (2014). Chromosome preparation from cultured cells. *J. Vis. Exp.* 2014:e50203. doi: 10.3791/50203

Hwang, J. Y., Mannowetz, N., Zhang, Y., Everley, R. A., Gygi, S. P., Bewersdorf, J., et al. (2019). Dual sensing of physiologic pH and calcium by EFCAB9 regulates sperm motility. *Cell* 177, 1480–1494.e19.

Inaba, K. (2011). Sperm flagella: comparative and phylogenetic perspectives of protein components. *Mol. Hum. Reprod.* 17, 524–538. doi: 10.1093/molehr/gar034

Kierszenbaum, A. L., Rivkin, E., and Tres, L. L. (2011). Cytoskeletal track selection during cargo transport in spermatids is relevant to male fertility. *Spermatogenesis* 1, 221–230. doi: 10.4161/spmg.1.3.18018

Kollmar, M. (2016). Fine-tuning motile cilia and flagella: evolution of the dynein motor proteins from plants to humans at high resolution. *Mol. Biol. Evol.* 33, 3249–3267. doi: 10.1093/molbev/msw213

Korsunsky, I., Millard, N., Fan, J., Slowikowski, K., Zhang, F., Wei, K., et al. (2019). Fast, sensitive and accurate integration of single-cell data with Harmony. *Nat. Methods* 16, 1289–1296. doi: 10.1038/s41592-019-0619-0

Lehti, M. S., Kotaja, N., and Sironen, A. (2013). KIF3A is essential for sperm tail formation and manchette function. *Mol. Cell. Endocrinol.* 377, 44–55. doi: 10.1016/j.mce.2013.06.030

Lehti, M. S., and Sironen, A. (2016). Formation and function of the manchette and flagellum during spermatogenesis. *Reproduction* 151, R43–R54.

Lek, M., Karczewski, K. J., Minikel, E. V., Samocha, K. E., Banks, E., Fennell, T., et al. (2016). Analysis of protein-coding genetic variation in 60,706 humans. *Nature* 536, 285–291.

Li, H. (2013). Aligning sequence reads, clone sequences and assembly contigs with BWA-MEM. *arXiv*[Preprint]. arXiv:1303.3997

Li, Y., Sha, Y., Wang, X., Ding, L., Liu, W., Ji, Z., et al. (2019). DNAH2 is a novel candidate gene associated with multiple morphological abnormalities of the sperm flagella. *Clin. Genet.* 95, 590–600. doi: 10.1111/cge.13525

Liu, C., Miyata, H., Gao, Y., Sha, Y., Tang, S., Xu, Z., et al. (2020). Bi-allelic DNAH8 variants lead to multiple morphological abnormalities of the sperm flagella and primary male infertility. *Am. J. Hum. Genet.* 107, 330–341.

Liu, H., Li, W., Zhang, Y., Zhang, Z., Shang, X., Zhang, L., et al. (2017). IFT25, an intraflagellar transporter protein dispensable for ciliogenesis in somatic cells, is essential for sperm flagella formation. *Biol. Reprod.* 96, 993–1006. doi: 10.1093/biolre/iox029

Lv, M., Liu, W., Chi, W., Ni, X., Wang, J., Cheng, H., et al. (2020). Homozygous mutations in DZIP1 can induce asthenoteratospermia with severe MMAF. *J. Med. Genet.* 57, 445–453. doi: 10.1136/jmedgenet-2019-106479

Madeira, F., Park, Y. M., Lee, J., Buso, N., Gur, T., Madhusoodanan, N., et al. (2019). The EMBL-EBI search and sequence analysis tools APIs in 2019. *Nucleic Acids Res.* 47, W636–W641.

Manandhar, G., Schatten, H., and Sutovsky, P. (2005). Centrosome reduction during gametogenesis and its significance. *Biol. Reprod.* 72, 2–13. doi: 10.1095/biolreprod.104.031245

Manichaikul, A., Mychaleckyj, J. C., Rich, S. S., Daly, K., Sale, M., and Chen, W. M. (2010). Robust relationship inference in genome-wide association studies. *Bioinformatics* 26, 2867–2873. doi: 10.1093/bioinformatics/btq559

Mascarenhas, M. N., Cheung, H., Mathers, C. D., and Stevens, G. A. (2012). Measuring infertility in populations: constructing a standard definition for use with demographic and reproductive health surveys. *Popul. Health Metr.* 10:17.

McKenna, A., Hanna, M., Banks, E., Sivachenko, A., Cibulskis, K., Kernytsky, A., et al. (2010). The genome analysis toolkit: a mapreduce framework for analyzing next-generation DNA sequencing data. *Genome Res.* 20, 1297–1303. doi: 10.1101/gr.107524.110

Neesen, J., Kirschner, R., Ochs, M., Schmiedl, A., Habermann, B., Mueller, C., et al. (2001). Disruption of an inner arm dynein heavy chain gene results in asthenozoospermia and reduced ciliary beat frequency. *Hum. Mol. Genet.* 10, 1117–1128. doi: 10.1093/hmg/10.11.1117

O'Donnell, L., Rhodes, D., Smith, S. J., Merriner, D. J., Clark, B. J., Borg, C., et al. (2012). An essential role for katanin p80 and microtubule severing in male gamete production. *PLoS Genet.* 8:e1002698. doi: 10.1371/journal.pgen.1002698

Price, A. L., Patterson, N. J., Plenge, R. M., Weinblatt, M. E., Shadick, N. A., and Reich, D. (2006). Principal components analysis corrects for stratification in genome-wide association studies. *Nat. Genet.* 38, 904–909. doi: 10.1038/ng1847

Qiao, Y., and Guo, S. (2005). Concise applications of molecular modeling software-MOE. *Comput. Appl. Chem.* 2:157–160.

Retief, J. D. (2000). Phylogenetic analysis using PHYLIP. *Methods Mol. Biol.* 132, 243–258. doi: 10.1385/1-59259-192-2:243

Sha, Y., Wei, X., Ding, L., Mei, L., Huang, X., Lin, S., et al. (2020). DNAH17 is associated with asthenozoospermia and multiple morphological abnormalities of sperm flagella. *Ann. Hum. Genet.* 84, 271–279. doi: 10.1111/ahg.12369

Sha, Y., Yang, X., Mei, L., Ji, Z., Wang, X., Ding, L., et al. (2017). DNAH1 gene mutations and their potential association with dysplasia of the sperm fibrous sheath and infertility in the Han Chinese population. *Fertil. Steril.* 107, 1312–1318.e2.

Sha, Y. W., Xu, X., Mei, L. B., Li, P., Su, Z. Y., He, X. Q., et al. (2017). A homozygous CEP135 mutation is associated with multiple morphological abnormalities of the sperm flagella (MMAF). *Gene* 633, 48–53. doi: 10.1016/j.gene.2017.08.033

Sironen, A., Shoemark, A., Patel, M., Loebinger, M. R., and Mitchison, H. M. (2020). Sperm defects in primary ciliary dyskinesia and related causes of male infertility. *Cell. Mol. Life Sci.* 77, 2029–2048. doi: 10.1007/s00018-019-03389-7

Stuart, T., Butler, A., Hoffman, P., Hafemeister, C., Papalexi, E., Mauck, W. M. I. I. I., et al. (2019). Comprehensive integration of single-cell data. *Cell* 177, 1888–1902.e21.

Toure, A., Martinez, G., Kherraf, Z. E., Cazin, C., Beurois, J., Arnoult, C., et al. (2020). The genetic architecture of morphological abnormalities of the sperm tail. *Hum. Genet.* 140, 21–42. doi: 10.1007/s00439-020-02113-x

van der Auwera, G. A., Carneiro, M. O., Hartl, C., Poplin, R., Del Angel, G., Levy-Moonshine, A., et al. (2013). From FastQ data to high confidence variant calls: the genome analysis toolkit best practices pipeline. *Curr. Protoc. Bioinformatics* 43, 11.10.1–11.10.33.

van Dijk, D., Sharma, R., Nainys, J., Yim, K., Kathail, P., Carr, A. J., et al. (2018). Recovering gene interactions from single-cell data using data diffusion. *Cell* 174, 716–729.e27.

Viswanadha, R., Sale, W. S., and Porter, M. E. (2017). Ciliary motility: regulation of axonemal dynein motors. *Cold Spring Harb. Perspect. Biol.* 9:a018325. doi: 10.1101/cshperspect.a018325

Wang, J., Wolf, R. M., Caldwell, J. W., Kollman, P. A., and Case, D. A. (2004). Development and testing of a general amber force field. *J. Comput. Chem.* 25, 1157–1174. doi: 10.1002/jcc.20035

Wang, K., Li, M., and Hakonarson, H. (2010). ANNOVAR: functional annotation of genetic variants from high-throughput sequencing data. *Nucleic Acids Res.* 38:e164. doi: 10.1093/nar/gkq603

Wang, X., Jin, H., Han, F., Cui, Y., Chen, J., Yang, C., et al. (2017). Homozygous DNAH1 frameshift mutation causes multiple morphological anomalies of the sperm flagella in Chinese. *Clin. Genet.* 91, 313–321. doi: 10.1111/cge.12857

Werner, S., Pimenta-Marques, A., and Bettencourt-Dias, M. (2017). Maintaining centrosomes and cilia. *J. Cell Sci.* 130, 3789–3800. doi: 10.1242/jcs.203505

Whitfield, M., Thomas, L., Bequignon, E., Schmitt, A., Stouvenel, L., Montantin, G., et al. (2019). Mutations in DNAH17, encoding a sperm-specific axonemal outer dynein arm heavy chain, cause isolated male infertility due to asthenozoospermia. *Am. J. Hum. Genet.* 105, 198–212. doi: 10.1016/j.ajhg.2019.04.015

WHO (2010). *WHO Laboratory Manual for the Examination and Processing of Human Semen*. Geneva: WHO.

Yang, Y., Jiang, C., Zhang, X., Liu, X., Li, J., Qiao, X., et al. (2020). Loss-of-function mutation in DNAH8 induces asthenoteratospermia associated with multiple morphological abnormalities of the sperm flagella. *Clin. Genet.* 98, 396–401. doi: 10.1111/cge.13815

Zhang, B., Khan, I., Liu, C., Ma, A., Khan, A., Zhang, Y., et al. (2021). Novel loss-of-function variants in DNAH17 cause multiple morphological abnormalities of the sperm flagella in humans and mice. *Clin. Genet.* 99, 176–186. doi: 10.1111/cge.13866

Zhang, B., Ma, H., Khan, T., Ma, A., Li, T., Zhang, H., et al. (2020). A DNAH17 missense variant causes flagella destabilization and asthenozoospermia. *J. Exp. Med.* 217:e20182365.

Zhang, S., Liu, Y., Huang, Q., Yuan, S., Liu, H., Shi, L., et al. (2020). Murine germ cell-specific disruption of Ift172 causes defects in spermiogenesis and male fertility. *Reproduction* 159, 409–421.

Conflict of Interest: The authors declare that the research was conducted in the absence of any commercial or financial relationships that could be construed as a potential conflict of interest.

Copyright © 2021 Hwang, Nawaz, Choi, Wang, Hussain, Nawaz, Lopez-Giraldez, Jeong, Dong, Oh, Bilguvar, Mane, Lee, Bystroff, Lifton, Ahmad and Chung. This is an open-access article distributed under the terms of the Creative Commons Attribution License (CC BY). The use, distribution or reproduction in other forums is permitted, provided the original author(s) and the copyright owner(s) are credited and that the original publication in this journal is cited, in accordance with accepted academic practice. No use, distribution or reproduction is permitted which does not comply with these terms.

frontiers in Cell and Developmental Biology

ORIGINAL RESEARCH
published: 28 May 2021
doi: 10.3389/fcell.2021.676910

Essential Role of CFAP53 in Sperm Flagellum Biogenesis

Bingbing Wu[1,2†], Xiaochen Yu[3,4,5,6,7†], Chao Liu[1], Lina Wang[8], Tao Huang[3,4,5,6,7], Gang Lu[3,4,5,6,7,9], Zi-Jiang Chen[3,4,5,6,7,9], Wei Li[1,2] and Hongbin Liu[3,4,5,6,7,9*]*

[1] State Key Laboratory of Stem Cell and Reproductive Biology, Institute of Zoology, Stem Cell and Regenerative Medicine Innovation Institute, Chinese Academy of Sciences, Beijing, China, [2] College of Life Sciences, University of Chinese Academy of Sciences, Beijing, China, [3] Center for Reproductive Medicine, Cheeloo College of Medicine, Shandong University, Jinan, China, [4] Key laboratory of Reproductive Endocrinology of the Ministry of Education, Shandong University, Jinan, China, [5] Shandong Key Laboratory of Reproductive Medicine, Jinan, China, [6] Shandong Provincial Clinical Research Center for Reproductive Health, Jinan, China, [7] National Research Center for Assisted Reproductive Technology and Reproductive Genetics, Shandong University, Jinan, China, [8] Department of Respiratory Medicine, National Clinical Research Center of Respiratory Diseases, Beijing Children's Hospital, Capital Medical University, National Center for Children's Health, Beijing, China, [9] CUHK-SDU Joint Laboratory on Reproductive Genetics, School of Biomedical Sciences, The Chinese University of Hong Kong, Hong Kong, Hong Kong

OPEN ACCESS

Edited by:
Tomer Avidor-Reiss, University of Toledo, United States

Reviewed by:
Sigrid Hoyer-Fender, University of Göttingen, Germany
Maria Eugenia Teves, Virginia Commonwealth University, United States

***Correspondence:**
Wei Li
leways@ioz.ac.cn
Hongbin Liu
hongbin_sduivf@aliyun.com

[†] *These authors have contributed equally to this work*

Specialty section:
This article was submitted to Cell Growth and Division, a section of the journal Frontiers in Cell and Developmental Biology

Received: *06 March 2021*
Accepted: *30 April 2021*
Published: *28 May 2021*

Citation:
Wu B, Yu X, Liu C, Wang L, Huang T, Lu G, Chen Z-J, Li W and Liu H (2021) Essential Role of CFAP53 in Sperm Flagellum Biogenesis. Front. Cell Dev. Biol. 9:676910. doi: 10.3389/fcell.2021.676910

The sperm flagellum is essential for male fertility. Despite vigorous research progress toward understanding the pathogenesis of flagellum-related diseases, much remains unknown about the mechanisms underlying the flagellum biogenesis itself. Here, we show that the cilia and flagella associated protein 53 (*Cfap53*) gene is predominantly expressed in testes, and it is essential for sperm flagellum biogenesis. The knockout of this gene resulted in complete infertility in male mice but not in the females. CFAP53 localized to the manchette and sperm tail during spermiogenesis, the knockout of this gene impaired flagellum biogenesis. Furthermore, we identified two manchette and sperm tail-associated proteins that interacted with CFAP53 during spermiogenesis. Together, our results suggest that CFAP53 is an essential protein for sperm flagellum biogenesis, and its mutations might be associated with multiple morphological abnormalities of the flagella (MMAF).

Keywords: male infertility, flagellum, CFAP53, intramanchette transport, intraflagellar transport

INTRODUCTION

Infertility is a widespread human health issue, affecting 10–15% of couples worldwide, and male factors account for around 50% of these cases (Boivin et al., 2007; Tüttelmann et al., 2018). Male infertility is clinically diagnosed as azoospermia, decreased sperm concentration (oligozoospermia), reduced percentage of morphologically normal sperm (teratozoospermia), or lower sperm motility (asthenozoospermia) (Coutton et al., 2015; Ray et al., 2017; Tüttelmann et al., 2018). Spermatozoa are polarized cells composed of two main parts, the head and the flagellum. The flagellum makes up about 90% of the length of the sperm and is essential for sperm motility (Burgess et al., 2003; Mortimer, 2018), and it contains axoneme and peri-axonemal structures, such as the mitochondrial sheath, outer dense fibers, and the fibrous sheath (Lehti and Sironen, 2017; Mortimer, 2018), and the presence of these structures allows the flagellum to be divided into the connecting piece, midpiece, principal piece, and endpiece (Lehti and Sironen, 2017). Defects in the formation of flagellum disrupt sperm morphology and motility, leading to male infertility

(Chemes and Rawe, 2010; Sironen et al., 2020; Turner et al., 2020). Great progress has been made in our understanding of the pathogenesis of flagella-related diseases in recent years, but the pathogenic genes and mechanisms of flagellum biogenesis are far from being fully understood.

The flagellum needs to be integrated with the head in order to function properly during fertilization, and a very complex structure called the sperm head-tail coupling apparatus (HTCA) is necessary for the integration of the sperm head and the flagellum, and defects in this structure result in acephalic spermatozoa syndrome (Wu et al., 2020). Recently, *SUN5*, *PMFBP1*, *HOOK1*, *BRDT*, *TSGA10*, and *CEP112* have been found to be involved in the assembly of the HTCA, and mutations in these genes are associated with acephalic spermatozoa syndrome (Zhu et al., 2016, 2018; Li et al., 2017; Chen et al., 2018; Sha et al., 2018, 2020a; Shang et al., 2018). Abnormalities of the axoneme and accessory structures mainly result in asthenozoospermia, which is associated with morphological flagellar defects such as abnormal tails, irregular mitochondrial sheaths, and irregular residual cytoplasm (Escalier and Touré, 2012; Tu et al., 2020). Previous studies have identified several flagella-associated genes, including *AKAP3*, *AKAP4*, *TTC21A*, *TTC29*, *FSIP2*, *DNAH1*, *DNAH2*, *DNAH6*, *DNAH8*, *DNAH17*, and *DZIP1*, that are involved in sperm flagellum biogenesis (Turner et al., 2001; Ben Khelifa et al., 2014; Martinez et al., 2018; Li Y. et al., 2019; Liu C. et al., 2019; Liu W. et al., 2019; Tu et al., 2019; Liu et al., 2020b; Lv et al., 2020; Sha et al., 2020b). Mutations in these genes cause multiple morphological abnormalities of the flagella (MMAF), which is characterized as sperm without flagella or with short, coiled, or otherwise irregular flagella (Ben Khelifa et al., 2014; Touré et al., 2020). There are two evolutionarily conserved bidirectional transport platforms that are involved in sperm flagellum biogenesis, including intramanchette transport (IMT) and intraflagellar transport (IFT) (Kierszenbaum, 2001, 2002; San Agustin et al., 2015). IMT and IFT share similar cytoskeletal components, namely microtubules and F-actin, that provide tracks for the transport of structural proteins to the developing tail (Kierszenbaum et al., 2011a), and mutations in *TTC21A*, *TTC29*, *SPEF2*, and *CFAP69*, which have been reported to disrupt sperm flagellar protein transport, also lead to MMAF (Dong et al., 2018; Liu C. et al., 2019; Liu W. et al., 2019; Sha et al., 2019; Liu et al., 2020a).

The cilia and flagella associated protein (CFAP) family, such as *CFAP58*, *CFAP61*, *CFAP69*, *CFAP65*, *CFAP43*, *CFAP44*, *CFAP70*, and *CFAP251*, is associated with flagellum biogenesis and morphogenesis (Tang et al., 2017; Dong et al., 2018; Beurois et al., 2019; Li W. et al., 2019; He et al., 2020; Huang et al., 2020; Li et al., 2020). Previous studies have indicated that the functional role of CFAP53 (also named the coiled-coil domain containing protein CCDC11) is involved in the biogenesis and motility of motile cilia (Perles et al., 2012; Narasimhan et al., 2015; Noël et al., 2016; Silva et al., 2016), and CFAP53 is localized not only to the base of the nodal cilia, but also along the axoneme of the tracheal cilia (Ide et al., 2020). However, the exact localization and function of CFAP53 during spermiogenesis is still poorly understood. In the present study, we used a *Cfap53* knockout mouse model to study the underlying mechanism of CFAP53 in sperm flagellum biogenesis. We demonstrated that CFAP53 is localized to the manchette and the sperm tail of spermatids, and we found that depletion of CFAP53 led to defects in sperm flagellum biogenesis and sperm head shaping.

Moreover, we identified two proteins that interacted with CFAP53 during spermiogenesis, namely intraflagellar transport protein 88 (IFT88) and coiled-coil domain containing 42 (CCDC42). Thus, in addition to uncovering the essential role of CFAP53 in sperm flagellum biogenesis, we also show that CFAP53 might participate in the biogenesis of the sperm flagellum by collaborating with the IMT and IFT pathways.

RESULTS

Cfap53 Knockout Leads to Male Infertility

To identify the biological function of CFAP53, we first examined its expression pattern in different tissues and found that it was predominantly expressed in testis (**Figure 1A**). Further immunoblotting of mouse testis lysates prepared from different days after birth was carried out. CFAP53 was first detected in testis at postnatal day 7 (P7), and the level increased continuously from postnatal P14 onward, with the highest levels detected in adult testes (**Figure 1B**). This time course corresponded with the onset of meiosis, suggesting that CFAP53 might have an essential role in spermatogenesis.

To characterize the potential functions of CFAP53 during spermatogenesis, *Cfap53* knockout mice were created using the CRISPR-Cas9 system from Cyagen Biosciences. Exon 4 to exon 6 of the *Cfap53* gene was selected as the target site (**Figure 1C**). The founder animals were genotyped by genomic DNA sequencing and further confirmed by polymerase chain reaction. Two primers were designed to identify the *Cfap53* knockout mice (**Figure 1C**), the size of the *Cfap53* locus in $Cfap53^{+/+}$ mice was 918 bp, while the size of the locus in $Cfap53^{-/-}$ mice was 630 bp (**Figure 1D**). Immunoblotting detection of CFAP53 indicated that the CFAP53 was successfully eliminated in $Cfap53^{-/-}$ mice (**Figure 1H**). Because we cannot obtain adult homozygous $Cfap53^{-/-}$ mice in the C57BL/6J (C57) background, the heterozygous *Cfap53* mutated mice in the C57 background were further crossed with wild-type (WT) ICR mice, and the resulting heterozygotes were interbred to obtain homozygous $Cfap53^{-/-}$ mice in the C57/ICR background. The offspring genotypes deviated from Mendelian ratios (115:237:60 for $Cfap53^{+/+}$: $Cfap53^{+/-}$: $Cfap53^{-/-}$), suggesting an increased prenatal lethal rate in $Cfap53^{-/-}$ mice. We analyzed 25 $Cfap53^{-/-}$ mice, and 48% (12/25) of them presented with situs inversus totalis (SIT) and nearly 8% (2/25) had situs inversus abdominalis (SIA). In addition, 32% (8/25) of the $Cfap53^{-/-}$ mice developed hydrocephalus (**Supplementary Figure 1**).

A total of 72% (43/60) of the $Cfap53^{-/-}$ mice that survived after birth died within 6 weeks, while 25% (15/60) of the $Cfap53^{-/-}$ mice lived longer than 8 weeks of age (**Figure 1E**).

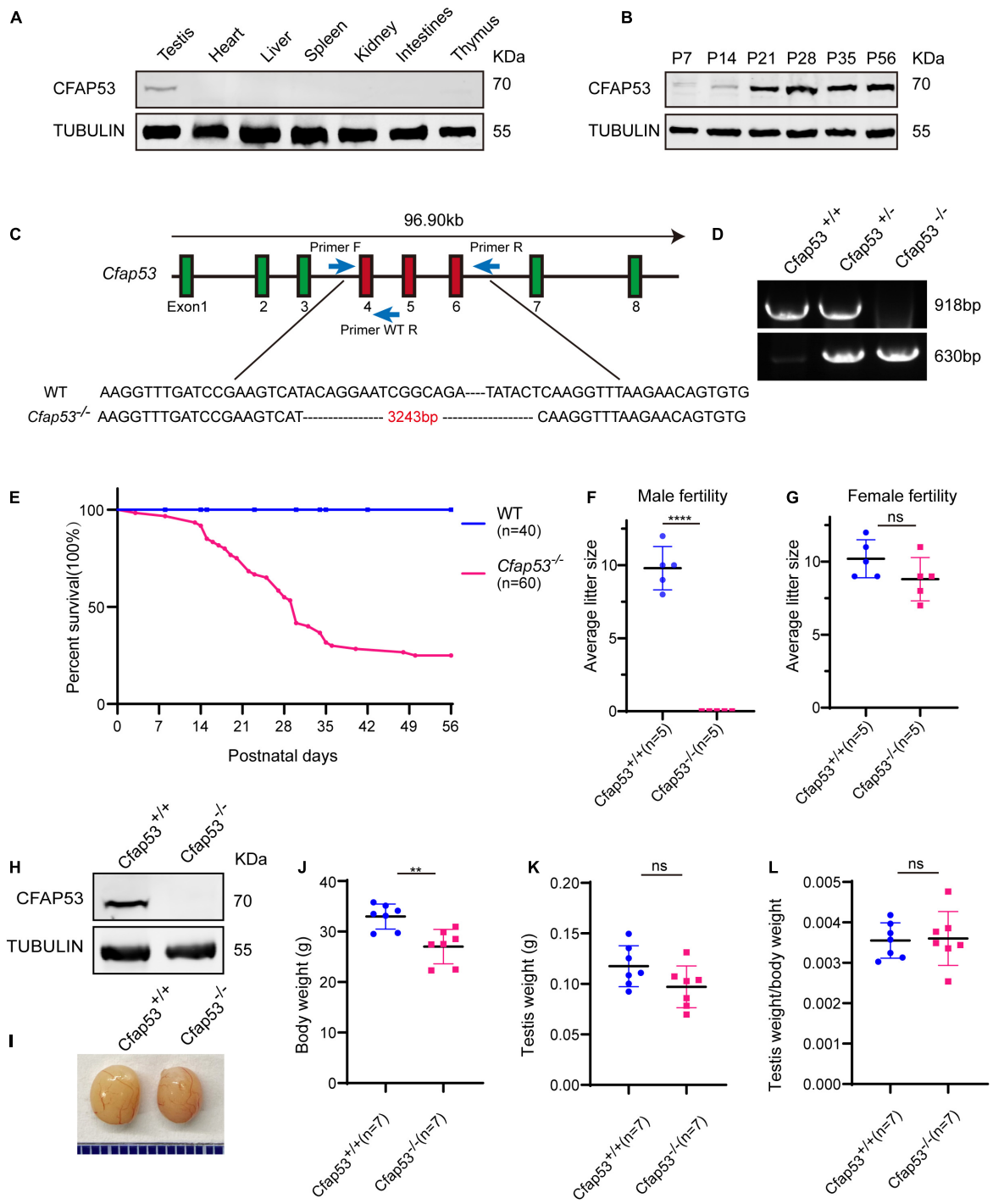

FIGURE 1 | The generation of *Cfap53* knockout mice. **(A)** CFAP53 was predominately expressed in testis. Immunoblotting of CFAP53 was performed in testis, heart, liver, spleen, kidney, intestines, and thymus with Tubulin serving as the control. **(B)** CFAP53 was expressed starting in P7 testes. Tubulin served as the control. **(C)** The generation of *Cfap53* knockout mice lacking exons 4–6. **(D)** Genotyping of *Cfap53* knockout mice. **(E)** Survival rate of postnatal $Cfap53^{-/-}$ mice (n = 60). **(F)** The average litter size of $Cfap53^{+/+}$ and $Cfap53^{-/-}$ male mice at 3 months (n = 5 independent experiments). $Cfap53^{-/-}$ male mice were completely sterile. Data are presented as the mean ± SD. ****$P < 0.0001$. **(G)** The average litter size of $Cfap53^{+/+}$ and $Cfap53^{-/-}$ female mice at 3 months (n = 5 independent experiments). $Cfap53^{-/-}$ female mice were fertile. Data are presented as the mean ± SD. **(H)** Immunoblotting of CFAP53 in $Cfap53^{+/+}$ and $Cfap53^{-/-}$ testes. Tubulin served as the control. **(I)** The testis sizes of $Cfap53^{+/+}$ and $Cfap53^{-/-}$ mice were similar to each other. Data are presented as the mean ± SD. **(J)** The body weights of $Cfap53^{-/-}$ male mice were lower compared to $Cfap53^{+/+}$ male mice (n = 7 independent experiments). Data are presented as the mean ± SD. **$P < 0.01$. **(K)** The testis weights of $Cfap53^{+/+}$ and $Cfap53^{-/-}$ male mice (n = 7 independent experiments). Data are presented as the mean ± SD. **(L)** The ratio of testis weight/body weight in $Cfap53^{+/+}$ and $Cfap53^{-/-}$ male mice (n = 7 independent experiments). Data are presented as the mean ± SD.

We further examined the fertility of *Cfap53* male and female knockout mice. *Cfap53* male knockout mice exhibited normal mounting behaviors and produced coital plugs, but $Cfap53^{-/-}$ male mice failed to produce any offspring after mating with WT adult female mice. In contrast, $Cfap53^{-/-}$ female mice generated offspring after mating with WT males (**Figures 1F,G**). Thus, the disruption in *Cfap53* resulted in male infertility but did not affect the fertility of $Cfap53^{-/-}$ female mice.

The Knockout of *Cfap53* Results in MMAF

To further investigate the cause of male infertility, we first observed the adult $Cfap53^{-/-}$ testis structure at both the gross and histological levels. The body weight of $Cfap53^{-/-}$ male mice was reduced compared to $Cfap53^{+/+}$ male mice (**Figure 1J**), while there were no significant differences in the testis size, testis weight, or testis/body weight ratio between $Cfap53^{-/-}$ and $Cfap53^{+/+}$ male mice (**Figures 1I,K,L**). We then observed the transverse sections of the $Cfap53^{-/-}$ cauda epididymis by hematoxylin and eosin (H&E) staining and found that there was a complete lack of spermatozoa or only a few spermatozoa in the epididymal lumen of $Cfap53^{-/-}$ mice (**Figure 2A**, red arrowhead). We examined the spermatozoa released from the caudal epididymis and found the sperm count in the *Cfap53* knockout mice to be significantly decreased compared with WT mice (**Figure 2B**). To determine the morphological characteristics of the spermatozoa, we performed single-sperm fluorescence of lectin peanut agglutinin (PNA), which is used to visualize the acrosomes of spermatozoa. The $Cfap53^{-/-}$ caudal epididymis only contained malformed spermatozoa exhibiting the prominent MMAF phenotype of short, coiled, or absent flagella compared with $Cfap53^{+/+}$ mice. In addition to the flagella abnormality, $Cfap53^{-/-}$ mice had abnormal sperm heads (**Figure 2C**). The ratio of spermatozoa with abnormal heads and flagella is shown in **Figure 2D**. Abnormal sperm head with short tail and normal sperm head with curly tail were the major defect categories. Immunofluorescence analysis with MitoTracker, which is used to visualize mitochondria, showed that the mitochondrial sheath was malformed in the $Cfap53^{-/-}$ spermatozoa (**Supplementary Figure 2**).

CFAP53 Is Required for Spermatogenesis

To address the question of why *Cfap53* knockout results in MMAF, we conducted Periodic acid–Schiff (PAS) staining to determine the stages of spermatogenesis in $Cfap53^{-/-}$ and WT testes. The most prominent defects were observed in the spermatids at the stages of spermatogenesis, where abnormally elongated and constricted sperm head shapes were identified (**Figure 3A**, asterisks). In addition, some dead cells could be detected in the $Cfap53^{-/-}$ seminiferous tubules (**Figure 3A**). To clarify the detailed morphological effects of the *Cfap53* mutation on the structure of sperm heads, we analyzed the process of sperm head shaping between $Cfap53^{-/-}$ and $Cfap53^{+/+}$ mice. Notably, from step 1 to step 8 the acrosome and nucleus morphology in $Cfap53^{-/-}$ spermatids was normal compared with $Cfap53^{+/+}$ spermatids. Head shaping started at step 9 to step 10, and the morphology of the elongated $Cfap53^{-/-}$ spermatid heads was normal compared with that of $Cfap53^{+/+}$ mice, whereas abnormal club-shaped heads (**Figure 3B**) were seen in step 11 spermatids in $Cfap53^{-/-}$ mice. This phenomenon became more apparent between step 11 and step 16 (**Figure 3B**). Taken together, these results indicate that CFAP53 is required for normal spermatogenesis.

H&E staining was used to further observe the morphological changes of the seminiferous tubules. The seminiferous tubules of $Cfap53^{+/+}$ mice had a tubular lumen with flagella appearing from the developing spermatids. In contrast, the flagella were absent in the seminiferous tubules of $Cfap53^{-/-}$ mice (**Figure 4A**). Immunofluorescence staining for α/β-tubulin, the specific flagellum marker, further confirmed the defects in flagellum biogenesis resulting from the knockout of *Cfap53* (**Figure 4B**). These observations clearly suggest that CFAP53 plays an important role in flagellum biogenesis.

CFAP53 Is Required for Sperm Flagellum Biogenesis and Manchette Function

In order to determine the causes of the abnormal sperm morphology in $Cfap53^{-/-}$ mice, we investigated the effect of *Cfap53* knockout on flagellum biogenesis using the antibody against acetylated tubulin, a flagellum-specific marker. Unlike the well-defined flagellum of the control group, the axoneme was absent in step 2–3 spermatids in $Cfap53^{-/-}$ mice (**Figure 4C**, asterisks). In steps 4–6, abnormally formed flagella were found in $Cfap53^{-/-}$ testis sections (**Figure 4C**, arrowhead). The presence of long and abnormal spermatid heads suggested defects in the function of the manchette, which is involved in sperm head shaping. Immunofluorescence staining for α/β-tubulin antibody showed that manchette formation was normal in step 8 to step 10 spermatids in $Cfap53^{-/-}$ mice, while step 11 to step 13 spermatids of $Cfap53^{-/-}$ mice had abnormally long manchettes compared with WT controls (**Figure 4D**). We performed transmission electron microscopy to study the organization of the sperm manchette in detail in $Cfap53^{-/-}$ mice. During the chromatin condensation period starting from step 11 spermatids, the manchette of $Cfap53^{-/-}$ mice appeared abnormally long and the perinuclear ring constricted the sperm nucleus, causing severe defects in sperm head formation (**Figure 4E**). Thus, deletion of *Cfap53* causes severe defects in sperm flagellum biogenesis and manchette function.

CFAP53 Localizes to the Manchette and the Sperm Tail

In order to determine the functional role of CFAP53 during spermiogenesis, we investigated the subcellular localization of CFAP53 during spermatogenesis in mice using an anti-CFAP53 antibody. The CFAP53 signal was first observed as two adjacent dots nearby the nucleus in spermatocytes and early round spermatids (**Figure 5A**), and these results were

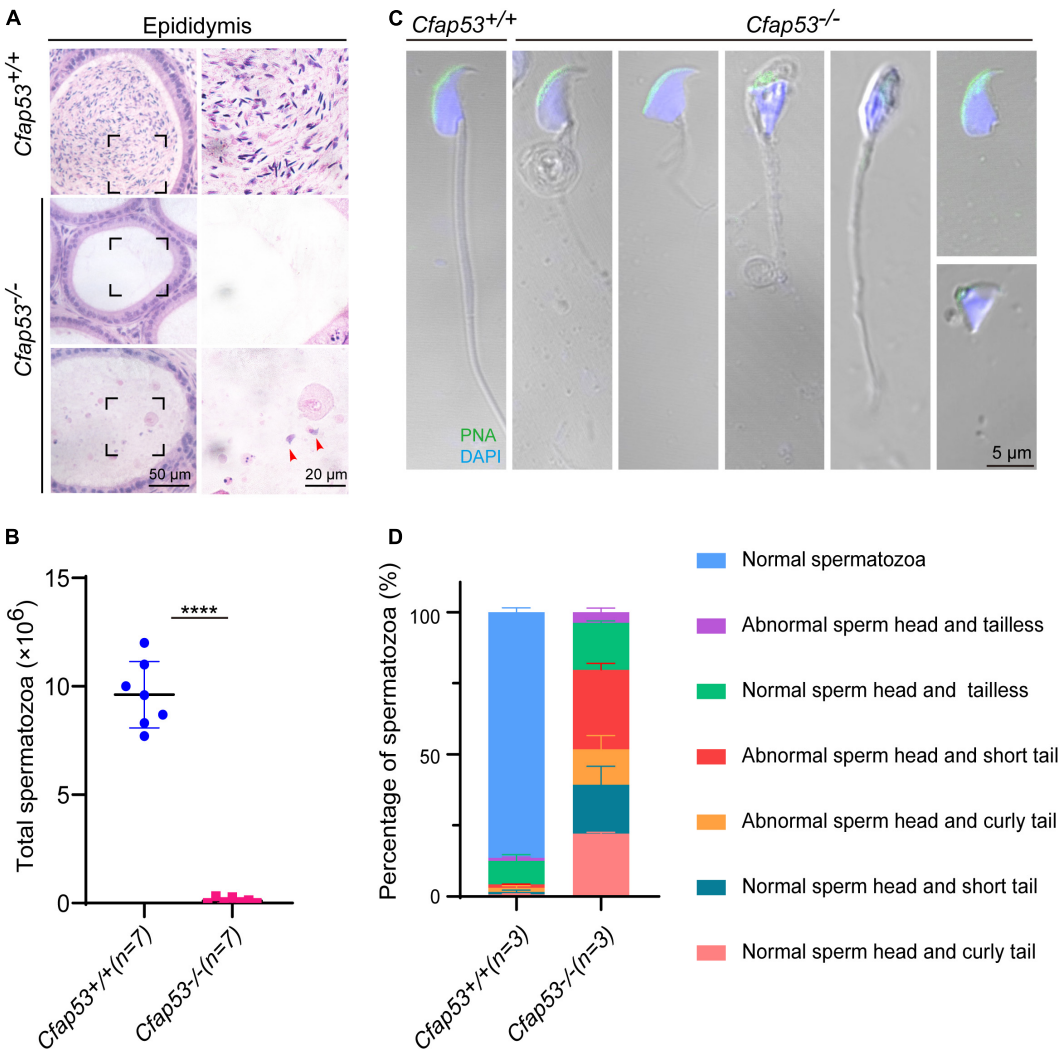

FIGURE 2 | CFAP53 knockout results in MMAF. **(A)** H&E staining of the caudal epididymis from *Cfap53*$^{+/+}$ and *Cfap53*$^{-/-}$ male mice. **(B)** The sperm counts in the caudal epididymis were significantly decreased in the *Cfap53*$^{-/-}$ male mice (n = 7 independent experiments). Data are presented as the mean ± SD. ****$P < 0.0001$. **(C)** PNA staining of *Cfap53*$^{+/+}$ and *Cfap53*$^{-/-}$ spermatozoa, indicating abnormal spermatozoa such as abnormal head and coiled, short, or absent flagella. **(D)** Quantification of different categories of abnormal spermatozoa (n = 3 independent experiments). Data are presented as the mean ± SD. The statistical significance of the differences between the mean values for the different genotypes was measured by Student's t-test with a paired two-tailed distribution.

consistent with the protein expression patterns (**Figure 1B**). During the elongation of the spermatids (step 9–step 14), CFAP53 could be detected as a skirt-like structure that encircled the elongating spermatid head, and the protein was subsequently located to the sperm tail around step 14–step 15. Compared to *Cfap53*$^{+/+}$ mice, there was no CFAP53 staining detected in the germ cells of *Cfap53*$^{-/-}$ male mice (**Figure 5A**). To determine whether CFAP53 associates with microtubular structures, the localization of CFAP53 in the elongating and elongated spermatid was subsequently co-stained with antibodies against α-tubulin (a manchette marker) and against CFAP53. In the elongating spermatid CFAP53 colocalized with the manchette microtubules. CFAP53 was further identified at the sperm tail, whereas α-tubulin marked the whole tail in the elongated spermatids (**Figure 5B**). Taken together, these results indicate that CFAP53 might participate in manchette formation and flagellum biogenesis.

CFAP53 Interacts With IFT88 and CCDC42

Sperm flagellum biogenesis requires protein delivery to the assembly sites via IMT and IFT (Lehti and Sironen, 2016). Because an interacting protein of CFAP53, Kinesin II subunit KIF3A, is required for intraflagellar transport (Marszalek et al., 1999; Lehti et al., 2013), together with the evidence of CFAP53's localization and function during spermiogenesis, we speculated that CFAP53 might participate in flagellum biogenesis by regulating IFT and/or IMT. According to STRING database

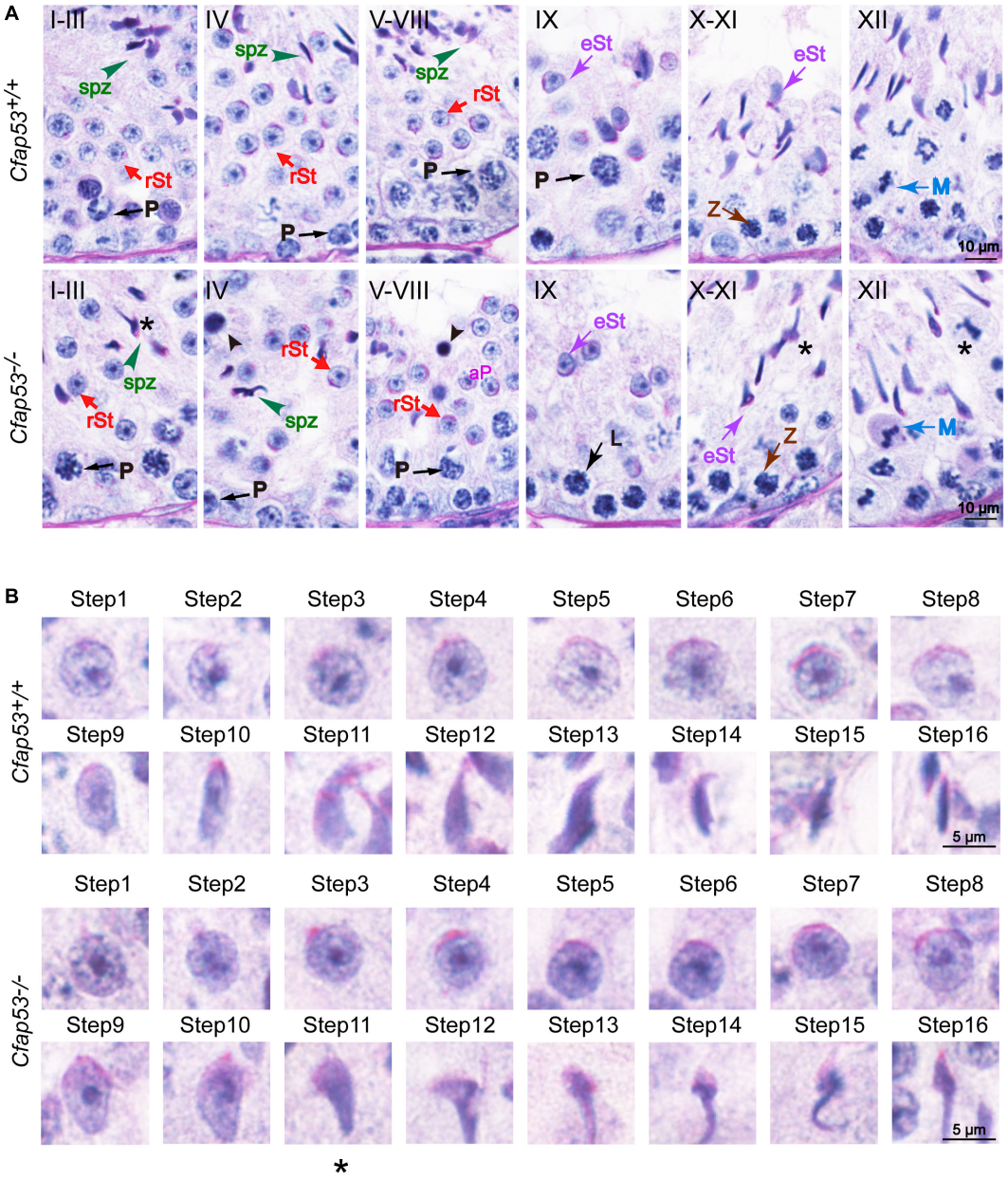

FIGURE 3 | Spermatogenesis defects of *Cfap53*$^{-/-}$ mice. **(A)** PAS staining of testes sections from *Cfap53*$^{+/+}$ and *Cfap53*$^{-/-}$ mice. Defects in the nuclear shape of several elongating spermatids were clearly evident in the *Cfap53*$^{-/-}$ seminiferous tubule (asterisks). Apoptotic bodies were detected in *Cfap53*$^{-/-}$ testes sections (black arrowheads). P: pachytene spermatocyte, L: leptotene spermatocyte, Z: zygotene spermatocyte, M: meiotic spermatocyte, rST: round spermatid, eST: elongating spermatid, spz: spermatozoa. **(B)** The PAS staining of spermatids at different steps from *Cfap53*$^{+/+}$ and *Cfap53*$^{-/-}$ mice. From step 1 to step 10 spermatids, the head morphology was roughly normal in *Cfap53*$^{-/-}$ mice. Abnormal, club-shaped heads (asterisk) were first seen in step 11 spermatids in *Cfap53*$^{-/-}$ mice.

(Szklarczyk et al., 2019), we analyzed KIF3A potential partners, and found that IFT88 and IFT20 are likely interact with this protein (**Supplementary Figure 3**). Both of them belong to the IFT family, they are involved in protein transport, and their depletion affects sperm flagellum biogenesis (Kierszenbaum et al., 2011b; Zhang et al., 2016). CCDC42 localize to the manchette, the sperm connecting piece, and the sperm tail during spermatogenesis, which is also involved in IMT, and it is essential for sperm flagellum biogenesis (Pasek et al., 2016; Tapia Contreras and Hoyer-Fender, 2019). Accordingly, these proteins were chosen to determine their potential interactions with CFAP53 by coimmunoprecipitation (co-IP) assays. To determine their relationship with CFAP53, HEK293T cells were co-transfected with MYC-tagged CFAP53 and IFT88-GFP,

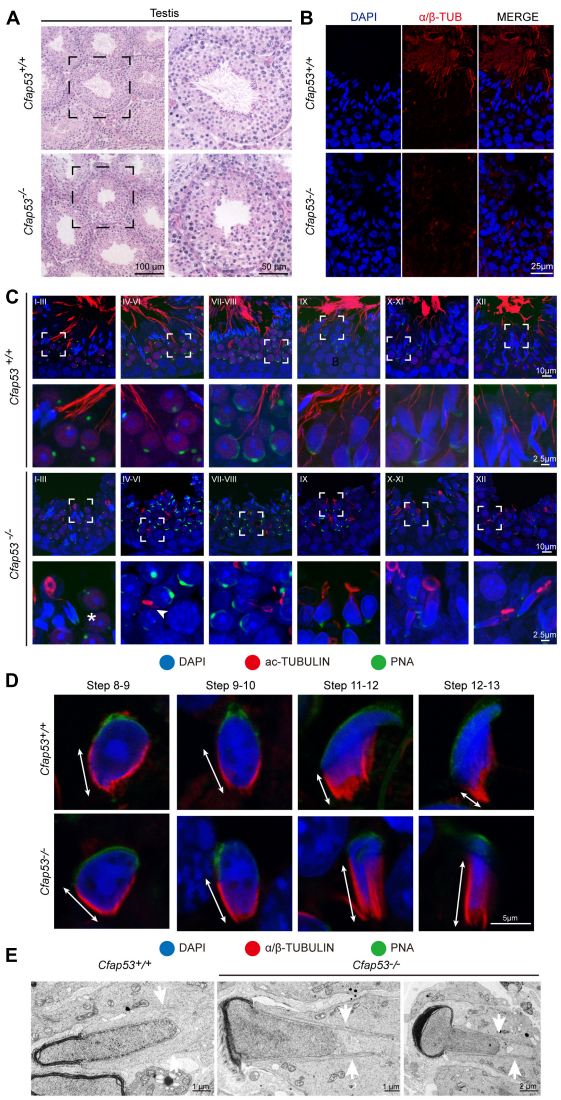

FIGURE 4 | Sperm flagellum biogenesis defects and abnormal manchettes in *Cfap53*$^{-/-}$ mice. **(A)** H&E staining of testes sections from *Cfap53*$^{+/+}$ and *Cfap53*$^{-/-}$ male mice. **(B)** Immunofluorescence of anti-α/β-tubulin (red) antibodies in testes sections from *Cfap53*$^{-/-}$ male mice show flagellar defects. **(C)** Comparison of flagellum biogenesis in testes sections from *Cfap53*$^{+/+}$ and *Cfap53*$^{-/-}$ mice at different stages. Sperm flagella were stained with anti-Acetylated tubulin (red), the acrosome was stained with PNA lectin histochemistry (green), and the nucleus was stained with DAPI (blue). Flagellum formation was first observed at stages I-III of the seminiferous epithelial cycle in *Cfap53*$^{+/+}$ mice, while sperm tails were not detected (asterisks) at stages I-III in testes sections in *Cfap53*$^{-/-}$ mice. From stages IV–VI, sperm flagellum biogenesis defects were clearly seen in *Cfap53*$^{-/-}$ testis sections (arrowhead). **(D)** Comparison of manchette formation between *Cfap53*$^{+/+}$ and *Cfap53*$^{-/-}$ spermatids at different steps. The manchette was stained with anti-α/β-tubulin (red), the acrosome was stained with PNA lectin histochemistry (green), and the nucleus was stained with DAPI (blue). The distance from the perinuclear ring to the caudal side of the nucleus is indicated by white arrows. During steps 12 and 13, the distance was reduced in *Cfap53*$^{+/+}$ spermatids, while the manchette of *Cfap53*$^{-/-}$ spermatids displayed abnormal elongation. **(E)** Transmission electron microscope images of *Cfap53*$^{-/-}$ step 11–13 spermatids showing the perinuclear ring constricting the sperm nucleus and causing abnormal sperm head formation. White arrows indicate the manchette microtubules.

CCDC42-GFP, or GFP-tagged empty vector as a control, and we found that both IFT88 and CCDC42 were coimmunoprecipitated with CFAP53-MYC (**Figures 6A–C**), while we did not detect any interaction between IFT20-FLAG and CFAP53-MYC using the same strategy (**Figure 6D**). Both IFT88 and CCDC42 localize to the manchette, the sperm connecting piece, and the sperm tail during spermatogenesis (Kierszenbaum et al., 2011b; Pasek et al., 2016; Tapia Contreras and Hoyer-Fender, 2019). Because the antibody against CCDC42 does not function for immunofluorescence, we focused on IFT88. Similar to the knockout of *Cfap53*, spermatozoa in the *Ift88* mutant mouse had absent, short, or irregular tails with malformed sperm heads (Kierszenbaum et al., 2011b; San Agustin et al., 2015). In order to further investigate the effect of *Cfap53* knockout on IFT88 localization and its potential interaction with CFAP53 during sperm development, we co-stained the differentiating spermatids with antibodies against IFT88 and CFAP53. We found that IFT88 located to the manchette, the HTCA, and the sperm tail as previously reported (Kierszenbaum et al., 2011b; San Agustin et al., 2015). CFAP53 co-localized with IFT88 in the manchette of the elongating spermatid and in the sperm tail of the elongated spermatid (**Figure 6G**). We next detected IFT88 localization in the different steps of spermatid development in *Cfap53*$^{+/+}$ and *Cfap53*$^{-/-}$ mice. The IFT88 signal was first observed in the tail of round spermatids and continued to be detected in the elongated spermatid. Although the spermatids morphology of *Cfap53*$^{-/-}$ mice is abnormal, IFT88 signal was still present in these cells and its subcellular localization was not affected (**Figure 6H**). To further examine their relationship, we performed immunoblotting of CCDC42, IFT88 and IFT20 in the testes of *Cfap53*$^{+/+}$ and *Cfap53*$^{-/-}$ mice, and we found that the expression levels of CCDC42, IFT88 and IFT20 were all significantly reduced in the testes of *Cfap53*$^{-/-}$ mice (**Figures 6E,F**).

DISCUSSION

In this study, we have identified the essential role of CFAP53 in spermatogenesis and male fertility by generating *Cfap53* knockout mice with the deletion of exons 4–6. Sperm flagellum biogenesis begins in early round spermatids, where the axoneme extends from the distal centriole (Lehti and Sironen, 2017). It has been reported that the expression of many genes that are necessary for sperm flagellum biogenesis is significantly increased at approximately 12 days after birth (Horowitz et al., 2005), and we found that CFAP53 expression was upregulated in the testes between 7 and 14 days after birth (**Figure 1B**), which was consistent with the timing of axoneme formation. Previous studies have shown that CFAP53 is located at the basal body and on centriolar satellites in retinal pigment epithelial cells and on the ciliary axonemes in zebrafish kidneys and human respiratory cells (Narasimhan et al., 2015; Silva et al., 2016). In mice, CFAP53 is located at the base of the nodal cilia and the tracheal cilia, as well as along the axonemes of the tracheal cilia (Ide et al., 2020). Depletion of CFAP53 disrupts the subcellular organization

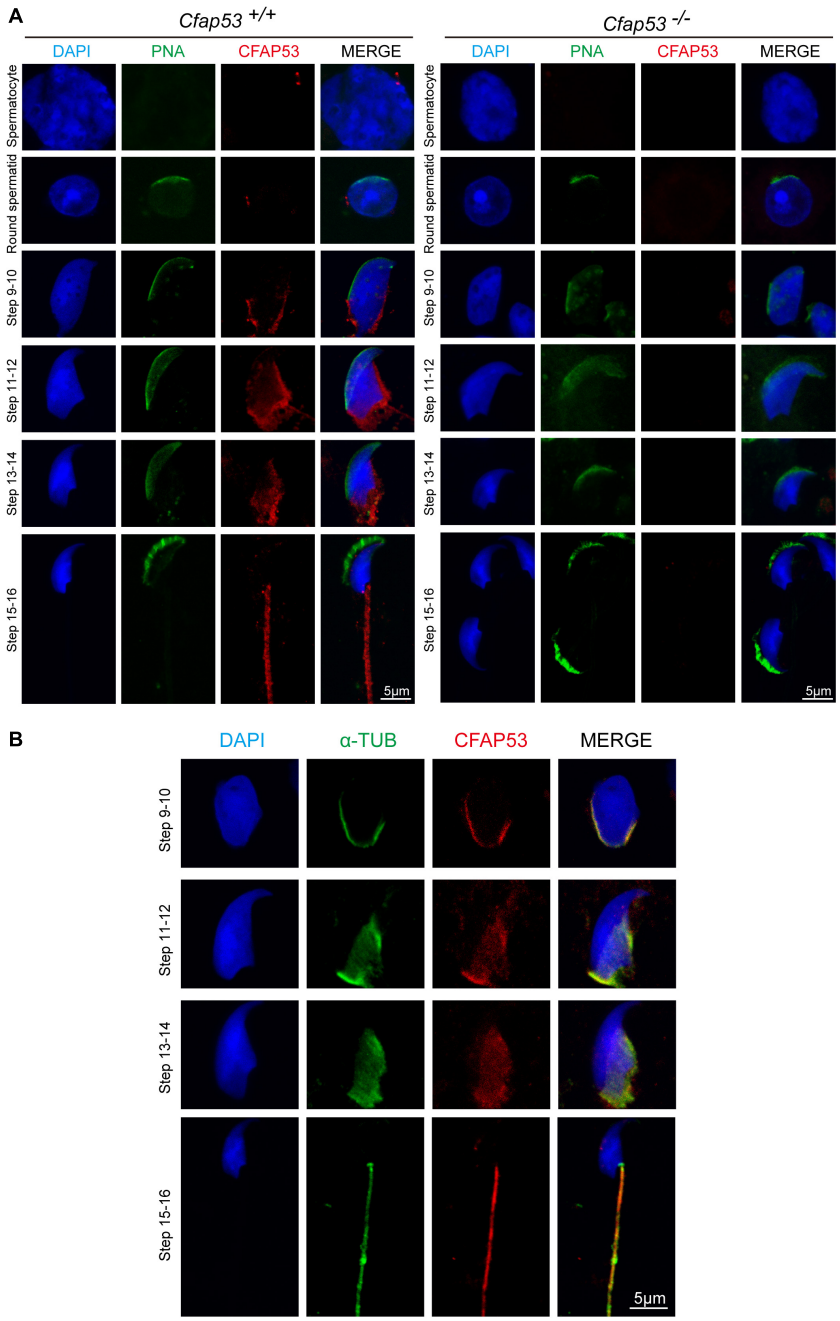

FIGURE 5 | Localization of CFAP53 in developing germ cells. **(A)** Testicular germ cells were prepared from *Cfap53*$^{+/+}$ and *Cfap53*$^{-/-}$ adult mouse testis, and immunofluorescence staining was performed with antibodies to CFAP53 (red). The acrosome was stained with PNA lectin histochemistry (green), and the nucleus was stained with DAPI (blue). **(B)** Testicular spermatids of WT adult mouse testes were stained with antibodies against α-tubulin (green) and CFAP53 (red). The nucleus was stained with DAPI (blue). In step 9–14 spermatids, CFAP53 was detected at the manchette. In 15–16 spermatids, CFAP53 was located at the sperm tail.

of satellite proteins and lead to primary cilium assembly abnormalities (Silva et al., 2016), and knockout of CFAP53 disrupts ciliogenesis in human tracheal epithelial multiciliated cells, in *Xenopus* epidermal multiciliated cells, and in zebrafish Kupffer's vesicle and pronephros (Narasimhan et al., 2015; Noël et al., 2016; Silva et al., 2016). The mammalian sperm flagellum contains an axoneme composed of a 9 + 2 microtubule arrangement, which is similar to that of motile cilia. Our study further showed that axoneme formation was impaired in early round spermatids in *Cfap53*$^{-/-}$ mice (**Figure 4C**), thus demonstrating that CFAP53 is essential for sperm flagellum biogenesis.

We found that CFAP53 localized on the manchette and tail during spermiogenesis, and it could interact with IFT88

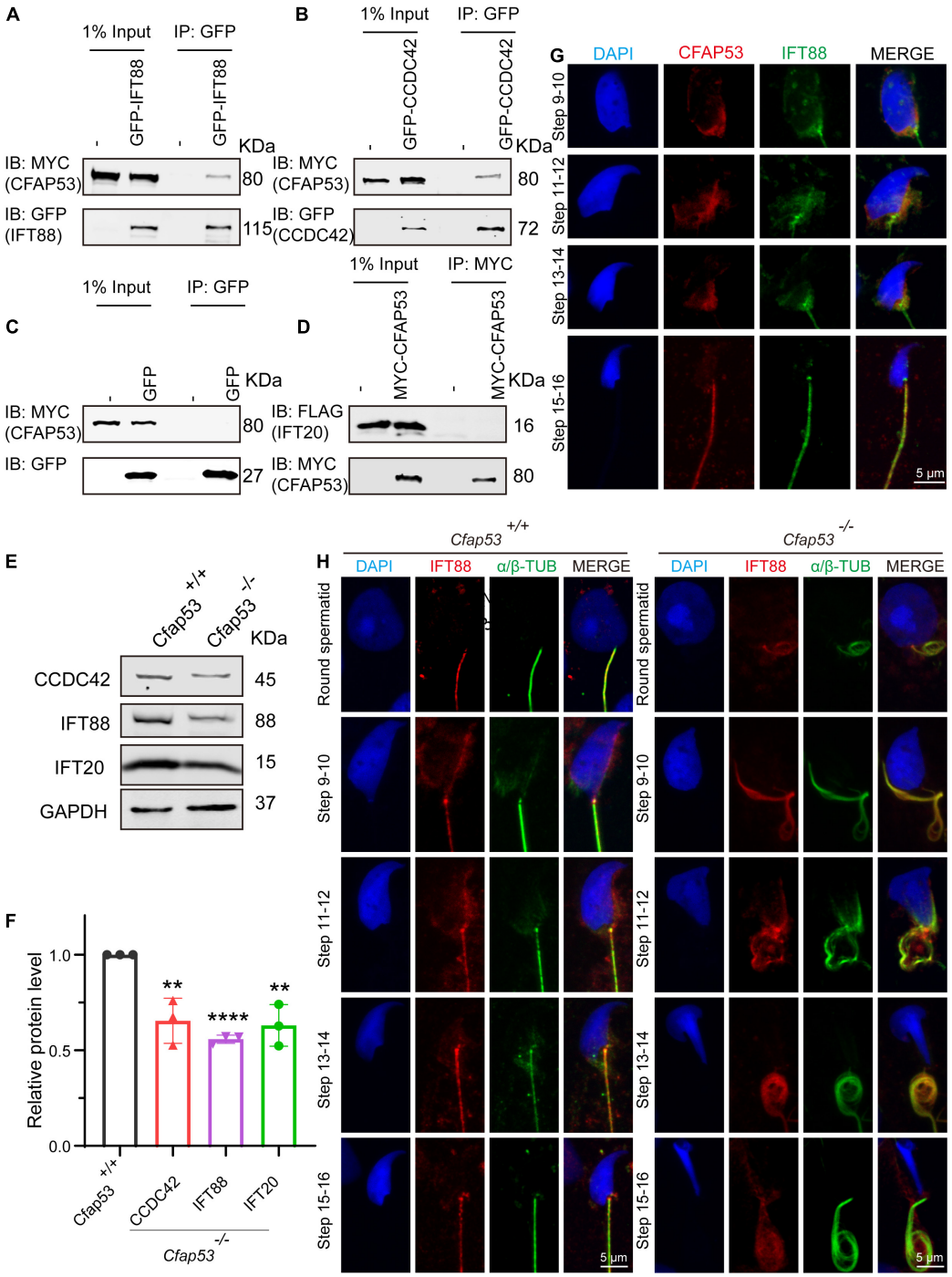

FIGURE 6 | CFAP53 interacts with IFT88 and CCDC42. **(A,B)** CFAP53 interacts with IFT88 and CCDC42. *pCS2-Myc-Cfap53* and *pEGFP-GFP-Ift88* or *pEGFP-GFP-Ccdc42* were co-transfected into HEK293T cells. At 48 h after transfection, the cells were collected for immunoprecipitation (IP) with anti-GFP antibody and analyzed with anti-MYC and anti-GFP antibodies. **(C)** *pCS2-Myc-Cfap53* and Empty vector were co-transfected into HEK293T cells. At 48 h after transfection, the cells were collected for IP with anti-GFP antibody and analyzed with anti-MYC and anti-GFP antibodies. **(D)** *pCS2-Myc-Cfap53* and *pRK-Flag-Ift20* were co-transfected into HEK293T cells. At 48 h after transfection, the cells were collected for IP with anti-MYC antibody and analyzed with anti-MYC and anti-FLAG antibodies. **(E)** Western blot analysis showing CCDC42, IFT88, and IFT20 protein levels in *Cfap53*$^{+/+}$ and *Cfap53*$^{-/-}$ mouse testis lysates. GAPDH served as the loading control. **(F)** Quantification of the relative protein levels of CCDC42, IFT88 and IFT20 using the Odyssey software and compared with the control group ($n = 3$ independent experiments). Data are presented as the mean ± SD. The statistical significance of the differences between the mean values for the different genotypes was measured by Student's *t*-test with a paired, two-tailed distribution. $^{**}P < 0.01$ and $^{****}P < 0.0001$. **(G)** The immunofluorescence analysis of IFT88 (green) and CFAP53 (red) was performed in testicular germ cells. The nucleus was stained with DAPI (blue). **(H)** Immunofluorescence staining with antibodies against IFT88 (red) and α/β-tubulin (green) in spermatids at different developmental stages from *Cfap53*$^{+/+}$ and *Cfap53*$^{-/-}$ adult mice. The nucleus was stained with DAPI (blue).

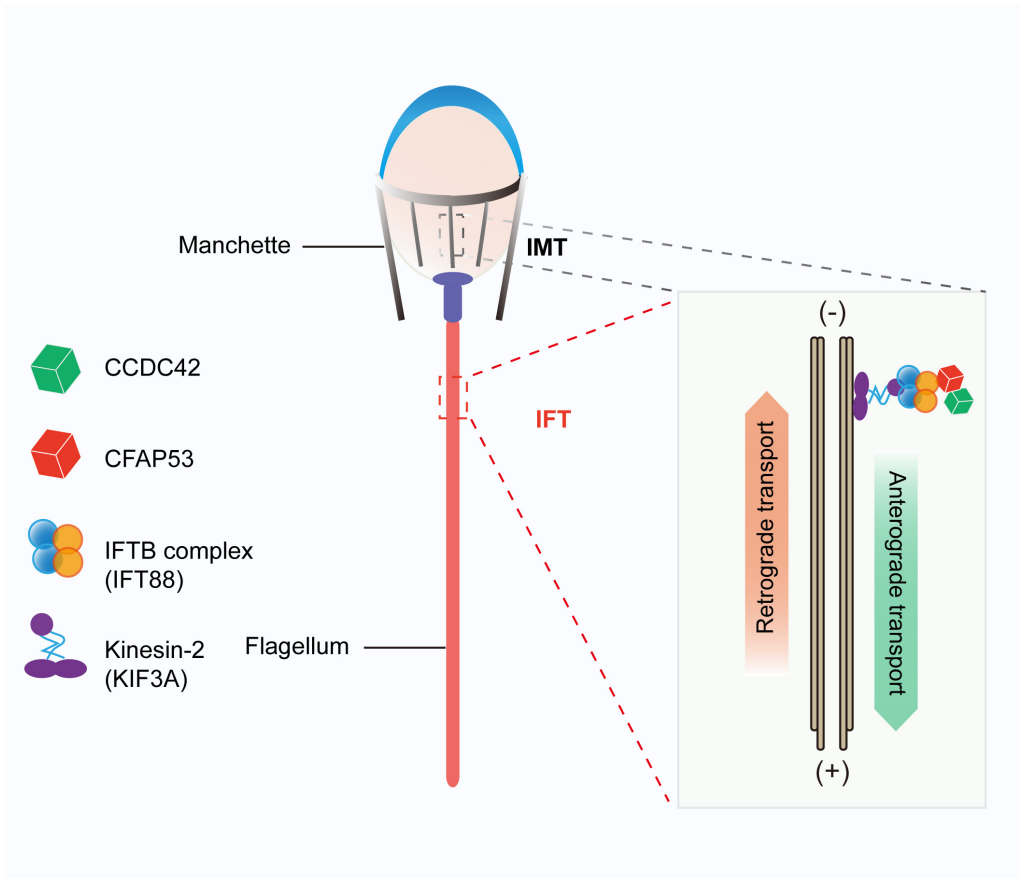

FIGURE 7 | Proposed model for the functional role of CFAP53 during flagellum biogenesis. CFAP53 works as a cargo protein, and it is involved in the stabilization of other cargo proteins, such as CCDC42, that need to be transported to the developing sperm tail. During transport, CFAP53 interacts with IFT complex B member IFT88 and kinesin-2 motor subunit KIF3A for targeting to its destination.

and CCDC42, both of which colocalized to the same positions during spermiogenesis (**Figures 6A,B,G**). In addition, it has been reported that CFAP53 also interacts with KIF3A (Lehti et al., 2013). All of these partner proteins are related to manchette and flagellum biogenesis, with the manchette being one of the transient skirt-like microtubular structures that are required for the formation of sperm flagella and the shaping of the head during spermatid elongation (Kierszenbaum and Tres, 2004; Lehti and Sironen, 2016). It has been proposed that flagellar structure proteins and motor proteins are transported through the manchette via IMT to the base of the sperm flagellum and via IFT to the developing sperm flagellum (Kierszenbaum et al., 2011a; Lehti and Sironen, 2016). Both IMT and IFT provide the bidirectional movement of multicomponent transport systems powered by molecular motors along the microtubules, and both are essential for axoneme assembly (Lehti and Sironen, 2017). Molecular motors (kinesin-2 and dynein 2) move cargo proteins associated with protein rafts consisting of IFT proteins (Kierszenbaum, 2002; Avidor-Reiss and Leroux, 2015), and KIF3A, the motor subunit of kinesin-2, works as an anterograde motor for transporting IFT complex B during the development of the sperm tail (Marszalek et al., 1999; Lehti et al., 2013). KIF3A localizes to the manchette, the basal body, and the axoneme of spermatids, and disruption of KIF3A affects the formation of the manchette and further disrupts the delivery of proteins to the sperm tail (Lehti et al., 2013). IFT88 is an IFT complex B protein that is regarded as a member of the IMT machinery. Notably, the reproductive phenotype of *Ift88* knockout male mice was similar to what we observed in *Cfap53* knockout mice (San Agustin et al., 2015). Thus, CFAP53 might function in collaboration with IFT88 and KIF3A in flagellum biogenesis via IMT and IFT (**Figure 7**).

Previous studies have shown that *Ccdc42* knockout male mice have abnormal head shapes and axoneme assembly defects, and it was speculated that CCDC42 might be a passenger protein transported via the manchette toward the developing tail (Pasek et al., 2016; Tapia Contreras and Hoyer-Fender, 2019). As a partner protein of CCDC42 and IFT88, once CFAP53 was depleted the expression levels of these two partner proteins were also decreased significantly (**Figures 6E,F**). These results raise the question of whether CFAP53 works as a cargo protein or as a component of the IFT and IMT machineries. Given that CFAP53 also localized on sperm flagella, we speculate that CFPA53 might work as a cargo protein and it may be involved in the stabilization of other cargo proteins, such as CCDC42, that are transported by

IFT or IMT (**Figure 7**). Since the irrelevant protein, IFT20, was also decreased in the testes of *Cfap53*$^{-/-}$ mice (**Figures 6E,F**), the decreasing of these proteins might be due to the defect of flagellum biogenesis. Accordingly, our current conclusions might be further expanded to other flagellum-associated proteins, and the depletion of some cargo proteins that need to be transported by either IMT or IFT should have similar phenotypes due to flagellum biogenesis defects, and at least some of the MMAF might be caused by this mechanism.

MATERIALS AND METHODS

Animals

The mouse *Cfap53* gene (Transcript: ENSMUSG00000035394) is 96.90 kb and contains 8 exons and is located on chromosome 18. Exon 4 to exon 6 was chosen as the target site, and *Cfap53* knockout mice were generated using the CRISPR-Cas9 system from Cyagen Biosciences. The gRNA and Cas9 mRNA were co-injected into fertilized eggs of C57BL/6 mice to generate a targeted line with a 3,243 bp base deletion, AAG GTT TGA TCC GAA GTC AT – 3243 bp – CAA GGT TTA AGA ACA GTG TG. The founder animals were genotyped by genomic DNA sequencing. For *Cfap53* knockout mice, the specific primers were Forward: 5′-GAG GGA ATA GGT TTC TGG GTA GGT G-3′ and Reverse: 5′-ACC CTT CTG GTC CCT CAG TCA TCT-3′, yielding a 630 bp fragment. For *Cfap53* WT mice, the specific primers were Forward: 5′-GAG GGA ATA GGT TTC TGG GTA GG TG-3′ and Reverse: 5′-AGC AGC AGT GAA ACT TCA AAC ATG G-3′, yielding a 918 bp fragment. All of the animal experiments were performed according to approved Institutional Animal Care and Use Committee (IACUC) protocols (#08-133) of the Institute of Zoology, Chinese Academy of Sciences.

Plasmids

Mouse *Cfap53* was obtained from mouse testis cDNA and cloned into the pCMV-Myc vector using the Clon Express Ultra One Step Cloning Kit (C115, Vazyme). Mouse *Ccdc42* and *Ift88* were obtained from mouse testis cDNA and cloned into the pEGFP-C1 vector using the Clon Express Ultra One Step Cloning Kit (C115, Vazyme). Mouse *Ift20* was obtained from mouse testis cDNA and cloned into the pRK vector using the Clon Express Ultra One Step Cloning Kit (C115, Vazyme).

Antibodies

Mouse anti-CFAP53 polyclonal antibody (aa 216–358) was generated by Dia-an Biotech (Wuhan, China) and was used at a 1:10 dilution for immunofluorescence and 1:200 dilution for western blotting. Mouse anti-GFP antibody (1:1,000 dilution, M20004L, Abmart), rabbit anti-MYC antibody (1:1,000 dilution, BE2011, EASYBIO), mouse anti-FLAG antibody (1:1,000 dilution, F1804, Sigma), and rabbit anti-CCDC42 antibody (1:500 dilution, abin2785068, antibodies-online) were used for western blotting. Rabbit anti-α-tubulin antibody (AC007, ABclonal) was used at a 1:100 dilution for immunofluorescence and at a 1:10,000 dilution for western blotting. IFT88 polyclonal antibody (13967-1-AP, Proteintech) was used at a 1:50 dilution for immunofluorescence and at a 1:1,000 dilution for western blotting. Mouse anti-α/β-tubulin antibody (1:100, ab44928, Abcam) and mouse anti-acetylated-a-tubulin antibody (T7451, 1:1,000 dilution, Sigma-Aldrich) were used for immunofluorescence. The secondary antibodies were goat anti-rabbit FITC (1:200, ZF-0311, Zhong Shan Jin Qiao), goat anti-rabbit TRITC (1:200 dilution, ZF-0316, Zhong Shan Jin Qiao), goat anti-mouse FITC (1:200 dilution, ZF-0312, Zhong Shan Jin Qiao), and goat anti-mouse TRITC (1:200 dilution, ZF-0313, Zhong Shan Jin Qiao). The Alexa Fluor 488 conjugate of lectin PNA (1:400 dilution, L21409, Thermo Fisher) and MitoTracker Deep Red 633 (1:1,500 dilution, M22426, Thermo Fisher Scientific) were used for immunofluorescence.

Immunoprecipitation

Transfected HEK293T cells were lysed in ELB buffer [50 mM HEPES, 250 mM NaCl, 0.1% NP-40, 1 mM PMSF, and complete EDTA-free protease inhibitor cocktail (Roche)] for 30 min on ice and centrifuged at 12,000 × *g* for 15 min. For immunoprecipitation, cell lysates were incubated with anti-GFP antibody overnight at 4°C and then incubated with protein A-Sepharose (GE, 17-1279-03) for 3 h at 4°C Thereafter, the precipitants were washed four times with ELB buffer, and the immune complexes were eluted with sample buffer containing 1% SDS for 10 min at 95°C and analyzed by immunoblotting.

Immunoblotting

Proteins obtained from lysates or immunoprecipitates were separated by SDS-PAGE and electrotransferred onto a nitrocellulose membrane. The membrane was blocked in 5% skim milk (BD, 232100) and then incubated with corresponding primary antibodies and detected by Alexa Fluor 680 or 800-conjugated goat anti-mouse or Alexa Fluor 680 or 800-conjugated goat anti-rabbit secondary antibodies. Finally, they were scanned using the ODYSSEY Sa Infrared Imaging System (LI-COR Biosciences, Lincoln, NE, RRID:SCR_014579).

Mouse Sperm Collection

The caudal epididymides were dissected from the *Cfap53* WT and knockout mice. Spermatozoa were squeezed out from the caudal epididymis and released in 1 ml phosphate buffered saline (PBS) for 30 min at 37°C under 5% CO_2 for sperm counting and immunofluorescence experiments.

Tissue Collection and Histological Analysis

The testes and caudal epididymides from at least five *Cfap53* WT and five knockout mice were dissected immediately after euthanasia. All samples were immediately fixed in 4% (mass/vol) paraformaldehyde (PFA; Solarbio, P1110) for up to 24 h, dehydrated in 70% (vol/vol) ethanol, and embedded in paraffin. For histological analysis, the 5 μm sections were mounted on glass slides and stained with H&E. For PAS staining, testes were fixed with Bouin's fixatives (Polysciences). Slides were stained with PAS and H&E after deparaffinization, and the stages of the seminiferous epithelium cycle and spermatid development were determined.

Immunofluorescence of the Testicular Germ Cells

The mouse testis was immediately dissected and fixed with 2% paraformaldehyde in 0.05% PBST (PBS with 0.05% Triton X-100) at room temperature for 5 min. The fixed sample was placed on a slide glass and squashed by placing a cover slip on top and pressing down. The sample was immediately flash frozen in liquid nitrogen, and the slides were stored at −80°C for further immunofluorescence experiments (Wellard et al., 2018). After removing the coverslips, the slides were washed with PBS three times and then treated with 0.1% Triton X-100 for 10 min, rinsed three times in PBS, and blocked with 5% bovine serum albumin (Amresco, AP0027). The primary antibody was added to the sections and incubated at 4°C overnight, followed by incubation with the secondary antibody. The nuclei were stained with DAPI. The immunofluorescence images were taken immediately using an LSM 780 microscope (Zeiss) or SP8 microscope (Leica).

Immunofluorescence in Testes

The testes of *Cfap53* WT and knockout mice were fixed in 4% PFA at 4°C overnight, dehydrated in 70% (vol/vol) ethanol, and embedded in paraffin. For histological analysis, the 5 μm sections were mounted on glass slides, then deparaffinized and rehydrated, followed by antigen retrieval in 10 mM sodium citrate buffer (pH 6.0) for 15 min and washing three times in PBS, pH 7.4. After blocking with 5% BSA containing 0.1% Triton X-100, the primary antibodies were added to the sections and incubated at 4°C overnight, followed by incubation with the secondary antibody. The nuclei were stained with DAPI, and images were acquired on an SP8 microscope (Leica).

Transmission Electron Microscopy

The testes from at least three *Cfap53* WT and knockout mice were dissected and pre-fixed in 2.5% (vol/vol) glutaraldehyde in 0.1 M cacodylate buffer at 4°C overnight. After washing in 0.1 M cacodylate buffer, samples were cut into small pieces of approximately 1 mm^3, then immersed in 1% OsO_4 for 1 h at 4°C. Samples were dehydrated through a graded acetone series and embedded in resin for staining. Ultrathin sections were cut on an ultramicrotome and double stained with uranyl acetate and lead citrate, and images were acquired and analyzed using a JEM-1400 transmission electron microscope.

Statistical Analysis

All of the experiments were repeated at least three times, and the results are presented as the mean ± SD. The statistical significance of the differences between the mean values for the different genotypes was measured by the Student's *t*-test with a paired, two-tailed distribution. The data were considered significant for $P < 0.05$.

DATA AVAILABILITY STATEMENT

The original contributions presented in the study are included in the article/**Supplementary Material**, further inquiries can be directed to the corresponding authors.

ETHICS STATEMENT

All of the animal experiments were performed according to approved Institutional Animal Care and Use Committee (IACUC) protocols (#08-133) of the Institute of Zoology, Chinese Academy of Sciences.

AUTHOR CONTRIBUTIONS

WL and HL designed the study and wrote the manuscript. BW performed most of the experiments and analyzed the data. XY performed the experiments and assisted in writing the manuscript. CL, LW, and TH performed some of the immunofluorescence experiments. GL, Z-JC, WL, and HL supervised the project. All authors assisted in data collection, interpreted the data, provided critical input to the manuscript, and approved the final manuscript.

FUNDING

This work was funded by the National Key R&D Program of China (2016YFA0500901), the National Natural Science Foundation of China (grant 81925015), the Strategic Priority Research Program of the Chinese Academy of Sciences (grant XDA16020701), and Qilu Young Scholars Program of Shandong University.

ACKNOWLEDGMENTS

We would like to thank the State Key Laboratory of Membrane Biology, Institute of Zoology, Chinese Academy of Sciences, for our electron microscopy work. We were grateful to Pengyan Xia for his help in preparing the electron microscopy sample. This work has previously appeared online in bioRxiv (Wu et al., 2021).

SUPPLEMENTARY MATERIAL

The Supplementary Material for this article can be found online at: https://www.frontiersin.org/articles/10.3389/fcell.2021.676910/full#supplementary-material

Supplementary Figure 1 | Left–right body asymmetry defects and hydrocephalus in *Cfap53*$^{-/-}$ mice. **(A)** *Cfap53*$^{-/-}$ mice presented with situs inversus totalis (SIT), situs inversus abdominalis (SIA), and situs solitus (SS). L1-5 (white numbers): lung lobes, Lv1-3 (white numbers): liver lobes, St: stomach, Sp: spleen. **(B)** Summary of the phenotypes detected in *Cfap53*$^{-/-}$ mice.

Supplementary Figure 2 | Mitochondrial sheath defects in *Cfap53*$^{-/-}$ spermatozoa. The immunofluorescence analysis for α/β-tubulin (green) and MitoTracker (red) was performed in *Cfap53*$^{+/+}$ and *Cfap53*$^{-/-}$ spermatozoa. The nucleus was stained with DAPI (blue).

Supplementary Figure 3 | Predicted KIF3A partners. STRING version 11 predicted the protein-protein interaction networks.

REFERENCES

Avidor-Reiss, T., and Leroux, M. R. (2015). Shared and distinct mechanisms of compartmentalized and cytosolic ciliogenesis. *Curr. Biol.* 25, R1143–R1150. doi: 10.1016/j.cub.2015.11.001

Ben Khelifa, M., Coutton, C., Zouari, R., Karaouzène, T., Rendu, J., Bidart, M., et al. (2014). Mutations in DNAH1, which encodes an inner arm heavy chain dynein, lead to male infertility from multiple morphological abnormalities of the sperm flagella. *Am. J. Hum. Genet.* 94, 95–104. doi: 10.1016/j.ajhg.2013.11.017

Beurois, J., Martinez, G., Cazin, C., Kherraf, Z.-E., Amiri-Yekta, A., Thierry-Mieg, N., et al. (2019). CFAP70 mutations lead to male infertility due to severe astheno-teratozoospermia. *Case Rep.* 34, 2071–2079. doi: 10.1093/humrep/dez166

Boivin, J., Bunting, L., Collins, J. A., and Nygren, K. G. (2007). International estimates of infertility prevalence and treatment-seeking: potential need and demand for infertility medical care. *Hum. Reprod.* 22, 1506–1512. doi: 10.1093/humrep/dem046

Burgess, S. A., Walker, M. L., Sakakibara, H., Knight, P. J., and Oiwa, K. J. N. (2003). Dynein structure and power stroke. *Nature* 421, 715–718. doi: 10.1038/nature01377

Chemes, H. E., and Rawe, V. Y. (2010). The making of abnormal spermatozoa: cellular and molecular mechanisms underlying pathological spermiogenesis. *Cell Tissue Res.* 341, 349–357. doi: 10.1007/s00441-010-1007-3

Chen, H., Zhu, Y., Zhu, Z., Zhi, E., Lu, K., Wang, X., et al. (2018). Detection of heterozygous mutation in hook microtubule-tethering protein 1 in three patients with decapitated and decaudated spermatozoa syndrome. *J. Med. Genet.* 55, 150–157. doi: 10.1136/jmedgenet-2016-104404

Coutton, C., Escoffier, J., Martinez, G., Arnoult, C., and Ray, P. F. (2015). Teratozoospermia: spotlight on the main genetic actors in the human. *Hum. Reprod. Update* 21, 455–485. doi: 10.1093/humupd/dmv020

Dong, F. N., Amiri-Yekta, A., Martinez, G., Saut, A., Tek, J., Stouvenel, L., et al. (2018). Absence of CFAP69 causes male infertility due to multiple morphological abnormalities of the flagella in human and mouse. *Am. J. Hum. Genet.* 102, 636–648. doi: 10.1016/j.ajhg.2018.03.007

Escalier, D., and Touré, A. (2012). Morphological defects of sperm flagellum implicated in human male infertility. *Med. Sci. (Paris)* 28, 503–511. doi: 10.1051/medsci/2012285015

He, X., Liu, C., Yang, X., Lv, M., Ni, X., Li, Q., et al. (2020). Bi-allelic loss-of-function variants in CFAP58 Cause flagellar axoneme and mitochondrial sheath defects and asthenoteratozoospermia in humans and mice. *Am. J. Hum. Genet.* 107, 514–526. doi: 10.1016/j.ajhg.2020.07.010

Horowitz, E., Zhang, Z., Jones, B. H., Moss, S. B., Ho, C., Wood, J. R., et al. (2005). Patterns of expression of sperm flagellar genes: early expression of genes encoding axonemal proteins during the spermatogenic cycle and shared features of promoters of genes encoding central apparatus proteins. *Mol. Hum. Reprod.* 11, 307–317. doi: 10.1093/molehr/gah163

Huang, T., Yin, Y., Liu, C., Li, M., Yu, X., Wang, X., et al. (2020). Absence of murine CFAP61 causes male infertility due to multiple morphological abnormalities of the flagella. *Sci. Bull.* 65, 854–864. doi: 10.1016/j.scib.2020.01.023

Ide, T., Twan, W. K., Lu, H., Ikawa, Y., Lim, L. X., Henninger, N., et al. (2020). CFAP53 regulates mammalian cilia-type motility patterns through differential localization and recruitment of axonemal dynein components. *PLoS Genet.* 16:e1009232. doi: 10.1371/journal.pgen.1009232

Kierszenbaum, A. L. (2001). Spermatid manchette: plugging proteins to zero into the sperm tail. *Mol. Reprod. Dev.* 59, 347–349. doi: 10.1002/mrd.1040

Kierszenbaum, A. L. (2002). Intramanchette transport (IMT): managing the making of the spermatid head, centrosome, and tail. *Mol Reprod Dev* 63, 1–4. doi: 10.1002/mrd.10179

Kierszenbaum, A. L., Rivkin, E., and Tres, L. L. (2011a). Cytoskeletal track selection during cargo transport in spermatids is relevant to male fertility. *Spermatogenesis* 1, 221–230. doi: 10.4161/spmg.1.3.18018

Kierszenbaum, A. L., Rivkin, E., Tres, L. L., Yoder, B. K., Haycraft, C. J., Bornens, M., et al. (2011b). GMAP210 and IFT88 are present in the spermatid golgi apparatus and participate in the development of the acrosome-acroplaxome complex, head-tail coupling apparatus and tail. *Dev. Dyn.* 240, 723–736. doi: 10.1002/dvdy.22563

Kierszenbaum, A. L., and Tres, L. L. (2004). The acrosome-acroplaxome-manchette complex and the shaping of the spermatid head. *Arch. Histol. Cytol.* 67, 271–284. doi: 10.1679/aohc.67.271

Lehti, M. S., Kotaja, N., and Sironen, A. (2013). KIF3A is essential for sperm tail formation and manchette function. *Mol. Cell. Endocrinol.* 377, 44–55. doi: 10.1016/j.mce.2013.06.030

Lehti, M. S., and Sironen, A. (2016). Formation and function of the manchette and flagellum during spermatogenesis. *Reproduction* 151, R43–R54. doi: 10.1530/REP-15-0310

Lehti, M. S., and Sironen, A. (2017). Formation and function of sperm tail structures in association with sperm motility defects. *Biol. Reprod.* 97, 522–536. doi: 10.1093/biolre/iox096

Li, L., Sha, Y., Wang, X., Li, P., Wang, J., Kee, K., et al. (2017). Whole-exome sequencing identified a homozygous BRDT mutation in a patient with acephalic spermatozoa. *Oncotarget* 8, 19914–19922. doi: 10.18632/oncotarget.15251

Li, W., He, X., Yang, S., Liu, C., Wu, H., Liu, W., et al. (2019). Biallelic mutations of CFAP251 cause sperm flagellar defects and human male infertility. *J. Hum. Genet.* 64, 49–54. doi: 10.1038/s10038-018-0520-1

Li, W., Wu, H., Li, F., Tian, S., Kherraf, Z.-E., Zhang, J., et al. (2020). Biallelic mutations in CFAP65 cause male infertility with multiple morphological abnormalities of the sperm flagella in humans and mice. *J. Med. Genet.* 57, 89–95. doi: 10.1136/jmedgenet-2019-106344

Li, Y., Sha, Y., Wang, X., Ding, L., Liu, W., Ji, Z., et al. (2019). DNAH2 is a novel candidate gene associated with multiple morphological abnormalities of the sperm flagella. *Clin. Genet.* 95, 590–600. doi: 10.1111/cge.13525

Liu, C., He, X., Liu, W., Yang, S., Wang, L., Li, W., et al. (2019). Bi-allelic mutations in TTC29 cause male subfertility with asthenoteratospermia in humans and mice. *Am. J. Hum. Genet.* 105, 1168–1181. doi: 10.1016/j.ajhg.2019.10.010

Liu, C., Lv, M., He, X., Zhu, Y., Amiri-Yekta, A., Li, W., et al. (2020a). Homozygous mutations in SPEF2 induce multiple morphological abnormalities of the sperm flagella and male infertility. *J. Med. Genet.* 57, 31–37. doi: 10.1136/jmedgenet-2019-106011

Liu, C., Miyata, H., Gao, Y., Sha, Y., Tang, S., Xu, Z., et al. (2020b). Bi-allelic DNAH8 variants lead to multiple morphological abnormalities of the sperm flagella and primary male infertility. *Am. J. Hum. Genet.* 107, 330–341. doi: 10.1016/j.ajhg.2020.06.004

Liu, W., He, X., Yang, S., Zouari, R., Wang, J., Wu, H., et al. (2019). Bi-allelic mutations in TTC21A induce asthenoteratospermia in humans and mice. *Am. J. Hum. Genet.* 104, 738–748. doi: 10.1016/j.ajhg.2019.02.020

Lv, M., Liu, W., Chi, W., Ni, X., Wang, J., Cheng, H., et al. (2020). Homozygous mutations in DZIP1 can induce asthenoteratospermia with severe MMAF. *J. Med. Genet.* 57, 445–453. doi: 10.1136/jmedgenet-2019-106479

Marszalek, J. R., Ruiz-Lozano, P., Roberts, E., Chien, K. R., and Goldstein, L. S. (1999). Situs inversus and embryonic ciliary morphogenesis defects in mouse mutants lacking the KIF3A subunit of kinesin-II. *Proc. Natl. Acad. Sci. U.S.A.* 96, 5043–5048. doi: 10.1073/pnas.96.9.5043

Martinez, G., Kherraf, Z. E., Zouari, R., Fourati Ben Mustapha, S., Saut, A., Pernet-Gallay, K., et al. (2018). Whole-exome sequencing identifies mutations in FSIP2 as a recurrent cause of multiple morphological abnormalities of the sperm flagella. *Hum. Reprod.* 33, 1973–1984. doi: 10.1093/humrep/dey264

Mortimer, D. (2018). The functional anatomy of the human spermatozoon: relating ultrastructure and function. *Mol. Hum. Reprod.* 24, 567–592. doi: 10.1093/molehr/gay040

Narasimhan, V., Hjeij, R., Vij, S., Loges, N. T., Wallmeier, J., Koerner-Rettberg, C., et al. (2015). Mutations in CCDC11, which encodes a coiled-coil containing ciliary protein, causes situs inversus due to dysmotility of monocilia in the left-right organizer. *Hum. Mutat.* 36, 307–318. doi: 10.1002/humu.22738

Noël, E. S., Momenah, T. S., Al-Dagriri, K., Al-Suwaid, A., Al-Shahrani, S., Jiang, H., et al. (2016). A zebrafish loss-of-function model for human CFAP53 mutations reveals its specific role in laterality organ function. *Hum. Mutat.* 37, 194–200. doi: 10.1002/humu.22928

Pasek, R. C., Malarkey, E., Berbari, N. F., Sharma, N., Kesterson, R. A., Tres, L. L., et al. (2016). Coiled-coil domain containing 42 (Ccdc42) is necessary for proper sperm development and male fertility in the mouse. *Dev. Biol.* 412, 208–218. doi: 10.1016/j.ydbio.2016.01.042

Perles, Z., Cinnamon, Y., Ta-Shma, A., Shaag, A., Einbinder, T., Rein, A. J. J. T., et al. (2012). A human laterality disorder associated with recessiveCCDC11mutation. *J. Med. Genet.* 49, 386–390. doi: 10.1136/jmedgenet-2011-100457

Ray, P. F., Toure, A., Metzler-Guillemain, C., Mitchell, M. J., Arnoult, C., and Coutton, C. (2017). Genetic abnormalities leading to qualitative defects of sperm morphology or function. *Clin. Genet.* 91, 217–232. doi: 10.1111/cge.12905

San Agustin, J. T., Pazour, G. J., and Witman, G. B. (2015). Intraflagellar transport is essential for mammalian spermiogenesis but is absent in mature sperm. *Mol. Biol. Cell* 26, 4358–4372. doi: 10.1091/mbc.E15-08-0578

Sha, Y., Liu, W., Wei, X., Zhu, X., Luo, X., Liang, L., et al. (2019). Biallelic mutations in sperm flagellum 2 cause human multiple morphological abnormalities of the sperm flagella (MMAF) phenotype. *Clin. Genet.* 96, 385–393. doi: 10.1111/cge.13602

Sha, Y., Wang, X., Yuan, J., Zhu, X., Su, Z., Zhang, X., et al. (2020a). Loss-of-function mutations in centrosomal protein 112 is associated with human acephalic spermatozoa phenotype. *Clin. Genet.* 97, 321–328. doi: 10.1111/cge.13662

Sha, Y., Wei, X., Ding, L., Mei, L., Huang, X., Lin, S., et al. (2020b). DNAH17 is associated with asthenozoospermia and multiple morphological abnormalities of sperm flagella. *Ann. Hum. Genet.* 84, 271–279. doi: 10.1111/ahg.12369

Sha, Y. W., Sha, Y. K., Ji, Z. Y., Mei, L. B., Ding, L., Zhang, Q., et al. (2018). TSGA10 is a novel candidate gene associated with acephalic spermatozoa. *Clin. Genet.* 93, 776–783. doi: 10.1111/cge.13140

Shang, Y., Yan, J., Tang, W., Liu, C., Xiao, S., Guo, Y., et al. (2018). Mechanistic insights into acephalic spermatozoa syndrome-associated mutations in the human SUN5 gene. *J. Biol. Chem.* 293, 2395–2407. doi: 10.1074/jbc.RA117.000861

Silva, E., Betleja, E., John, E., Spear, P., Moresco, J. J., Zhang, S., et al. (2016). Ccdc11 is a novel centriolar satellite protein essential for ciliogenesis and establishment of left-right asymmetry. *Mol. Biol. Cell* 27, 48–63. doi: 10.1091/mbc.E15-07-0474

Sironen, A., Shoemark, A., Patel, M., Loebinger, M. R., and Mitchison, H. M. (2020). Sperm defects in primary ciliary dyskinesia and related causes of male infertility. *Cell. Mol. Life Sci.* 77, 2029–2048. doi: 10.1007/s00018-019-03389-7

Szklarczyk, D., Gable, A. L., Lyon, D., Junge, A., Wyder, S., Huerta-Cepas, J., et al. (2019). STRING v11: protein-protein association networks with increased coverage, supporting functional discovery in genome-wide experimental datasets. *Nucleic Acids Res.* 47, D607–D613. doi: 10.1093/nar/gky1131

Tang, S., Wang, X., Li, W., Yang, X., Li, Z., Liu, W., et al. (2017). Biallelic mutations in CFAP43 and CFAP44 cause male infertility with multiple morphological abnormalities of the sperm flagella. *Am. J. Hum. Genet.* 100, 854–864. doi: 10.1016/j.ajhg.2017.04.012

Tapia Contreras, C., and Hoyer-Fender, S. (2019). CCDC42 localizes to manchette, HTCA and tail and interacts with ODF1 and ODF2 in the formation of the male germ cell cytoskeleton. *Front. Cell. Dev. Biol.* 7:151. doi: 10.3389/fcell.2019.00151

Touré, A., Martinez, G., Kherraf, Z. E., Cazin, C., Beurois, J., Arnoult, C., et al. (2020). The genetic architecture of morphological abnormalities of the sperm tail. *Hum. Genet.* 140, 21–42. doi: 10.1007/s00439-020-02113-x

Tu, C., Nie, H., Meng, L., Yuan, S., He, W., Luo, A., et al. (2019). Identification of DNAH6 mutations in infertile men with multiple morphological abnormalities of the sperm flagella. *Sci. Rep.* 9:15864. doi: 10.1038/s41598-019-52436-7

Tu, C., Wang, W., Hu, T., Lu, G., Lin, G., and Tan, Y.-Q. (2020). Genetic underpinnings of asthenozoospermia. *Best Pract. Res. Clin. Endocrinol. Metab.* 34:101472. doi: 10.1016/j.beem.2020.101472

Turner, K. A., Rambhatla, A., Schon, S., Agarwal, A., Krawetz, S. A., Dupree, J. M., et al. (2020). Male infertility is a women's health issue-research and clinical evaluation of male infertility is needed. *Cells* 9:990. doi: 10.3390/cells9040990

Turner, R. M., Musse, M. P., Mandal, A., Klotz, K., Jayes, F. C., Herr, J. C., et al. (2001). Molecular genetic analysis of two human sperm fibrous sheath proteins, AKAP4 and AKAP3, in men with dysplasia of the fibrous sheath. *J. Androl.* 22, 302–315.

Tüttelmann, F., Ruckert, C., and Röpke, A. (2018). Disorders of spermatogenesis: perspectives for novel genetic diagnostics after 20 years of unchanged routine. *Med. Genet.* 30, 12–20. doi: 10.1007/s11825-018-0181-7

Wellard, S. R., Hopkins, J., and Jordan, P. W. (2018). A seminiferous tubule squash technique for the cytological analysis of spermatogenesis using the mouse model. *JoVE* 132:e56453. doi: 10.3791/56453

Wu, B., Gao, H., Liu, C., and Li, W. (2020). The coupling apparatus of the sperm head and tail. *Biol. Reprod.* 102, 988–998. doi: 10.1093/biolre/ioaa016

Wu, B., Yu, X., Liu, C., Wang, L., Huang, T., Lu, G., et al. (2021). Essential role of CFAP53 in sperm flagellum biogenesis. *bioRxiv* [Preprint]. doi: 10.1101/2021.02.04.429673

Zhang, Z., Li, W., Zhang, Y., Zhang, L., Teves, M. E., Liu, H., et al. (2016). Intraflagellar transport protein IFT20 is essential for male fertility and spermiogenesis in mice. *Mol. Biol. Cell* 27, 3705–3716. doi: 10.1091/mbc.E16-05-0318

Zhu, F., Liu, C., Wang, F., Yang, X., Zhang, J., Wu, H., et al. (2018). Mutations in PMFBP1 cause acephalic spermatozoa syndrome. *Am. J. Hum. Genet.* 103, 188–199. doi: 10.1016/j.ajhg.2018.06.010

Zhu, F., Wang, F., Yang, X., Zhang, J., Wu, H., Zhang, Z., et al. (2016). Biallelic SUN5 mutations cause autosomal-recessive acephalic spermatozoa syndrome. *Am. J. Hum. Genet.* 99, 942–949. doi: 10.1016/j.ajhg.2016.11.002

Conflict of Interest: The authors declare that the research was conducted in the absence of any commercial or financial relationships that could be construed as a potential conflict of interest.

Copyright © 2021 Wu, Yu, Liu, Wang, Huang, Lu, Chen, Li and Liu. This is an open-access article distributed under the terms of the Creative Commons Attribution License (CC BY). The use, distribution or reproduction in other forums is permitted, provided the original author(s) and the copyright owner(s) are credited and that the original publication in this journal is cited, in accordance with accepted academic practice. No use, distribution or reproduction is permitted which does not comply with these terms.

frontiers in Cell and Developmental Biology

REVIEW
published: 20 July 2021
doi: 10.3389/fcell.2021.710825

Modelling Motility: The Mathematics of Spermatozoa

Eamonn A. Gaffney[1†], *Kenta Ishimoto*[2†] *and Benjamin J. Walker*[1*†]

[1] *Wolfson Centre for Mathematical Biology, Mathematical Institute, University of Oxford, Oxford, United Kingdom,* [2] *Research Institute for Mathematical Sciences, Kyoto University, Kyoto, Japan*

In one of the first examples of how mechanics can inform axonemal mechanism, Machin's study in the 1950s highlighted that observations of sperm motility cannot be explained by molecular motors in the cell membrane, but would instead require motors distributed along the flagellum. Ever since, mechanics and hydrodynamics have been recognised as important in explaining the dynamics, regulation, and guidance of sperm. More recently, the digitisation of sperm videomicroscopy, coupled with numerous modelling and methodological advances, has been bringing forth a new era of scientific discovery in this field. In this review, we survey these advances before highlighting the opportunities that have been generated for both recent research and the development of further open questions, in terms of the detailed characterisation of the sperm flagellum beat and its mechanics, together with the associated impact on cell behaviour. In particular, diverse examples are explored within this theme, ranging from how collective behaviours emerge from individual cell responses, including how these responses are impacted by the local microenvironment, to the integration of separate advances in the fields of flagellar analysis and flagellar mechanics.

Keywords: sperm, flagellum, mechanics, modelling, computer-assisted beat-pattern analysis

OPEN ACCESS

Edited by:
Tomer Avidor-Reiss, University of Toledo, United States

Reviewed by:
Lisa Fauci, Tulane University, United States
Gerhard Gompper, Helmholtz-Verband Deutscher Forschungszentren (HZ), Germany
Charles Lindemann, Oakland University, United States

***Correspondence:**
Benjamin J. Walker
benjamin.walker@maths.ox.ac.uk

† These authors have contributed equally to this work

Specialty section:
This article was submitted to Cell Growth and Division, a section of the journal Frontiers in Cell and Developmental Biology

Received: *17 May 2021*
Accepted: *25 June 2021*
Published: *20 July 2021*

Citation:
Gaffney EA, Ishimoto K and Walker BJ (2021) Modelling Motility: The Mathematics of Spermatozoa. Front. Cell Dev. Biol. 9:710825. doi: 10.3389/fcell.2021.710825

1. OBSERVATION AND THEORY OF SPERM MOTILITY: AN INTRODUCTION

The fundamental function of a spermatozoon is the fertilisation of an egg in spite of tremendous challenges, whether that be the hostile environments and barriers of the female reproductive tract for internal fertilisers, or harsh osmotic conditions and background fluid flows for external fertilisers. Sufficient motility is thus a core functional necessity of the sperm cell and the attention of extensive study. However, although sperm motility due to a beating flagellum was first observed by van Leeuwenhoek in the 1670s (Lonergan, 2018), the internal structure of the sperm flagellum was only revealed with the advent of electron microscopy, with studies beginning in the 1950s (Fawcett and Porter, 1954; Afzelius, 1959). Even with this methodological step change, it was not at all clear at the time how the complex flagellar structure underlay the mechanism that drives sperm motility. Indeed, this significantly preceded the elucidation of the underlying mechanism of motility, via sliding microtubule filaments driven by dynein molecular motors along the flagellum, which was conclusively demonstrated by Summers and Gibbons (1971). Nonetheless, Machin (1958)'s theoretical study demonstrated that the active processes driving the flagellum could not solely be due to forcing in the cell membrane, reasoning that the wave amplitude of the elastic flagellum would be too damped by drag, even in a low-viscosity fluid such as a water-based physiological electrolyte. As such, Machin's theoretical study was among the first to highlight the importance of mechanics, and its quantification, in understanding how sperm swim.

More generally, the need for a mechanical perspective on the swimming of spermatozoa was recognised in the 1950s, with initial application to sea urchin sperm based on microscopic imaging (Gray and Hancock, 1955). These pioneer studies have been extended and generalised in numerous directions over the past six to seven decades, with recent refinement in particular driven by improvements in the digital microscopy of the flagellum beat and increased computational power, overcoming many of the technological limitations of previous studies. In particular, after briefly summarising classical computational techniques and whole-cell microscopy, this review will survey current advances in the methodologies that underpin flagellar data analysis and theoretical flagellar mechanics, highlighting the diverse opportunities for future research that are emerging as a result.

1.1. Flagellar Mechanics

1.1.1. Classical Fluid Dynamics

The swimming of sperm is characterised by physical scales where viscosity dominates inertia, the complete opposite to human swimming (Taylor, 1951). Hence, whilst everyday intuition does not apply to the microscale world of sperm swimming, the underlying fluid mechanics is in fact much simpler in this case. Indeed, at each instant in time, the fluid dynamics can be determined solely from the instantaneous velocity of the flagellum, independent of the history of the flagellar beat pattern. It is also *linear*, which in this context means that, *ceteris paribus,* doubling the frequency of flagellar beating will also double the swimming speed. The existence of such simple relations has enabled numerous rapid developments of Gray and Hancock (1955)'s seminal method, known as *resistive force theory* (**Figure 1C**), establishing quantitative links between the flagellar beat pattern and both the sperm's swimming speed and behaviour (for example, Rikmenspoel, 1965; Brokaw, 1972b; Suarez et al., 1991; Elgeti et al., 2010; Ishijima, 2011; Curtis et al., 2012). A key component of this theory is the notion of anisotropic drag, with approximately twice as much force being required to push the flagellum in its normal direction compared to its tangential direction (Gray and Hancock, 1955). This ultimately gives rise to the propulsion of a swimming spermatozoon (**Figure 1**) and can be observed by performing the simple experiment of moving a thin stick through syrup parallel and perpendicular to its length.

In particular, Gray and Hancock's resistive force theory framework assumes complete knowledge of the flagellar beat pattern, which is then used to predict the cell behaviour, rather than considering the fundamental question of how the beat pattern forms. Nonetheless, it provides a fundamental understanding of how beat patterns govern cell behaviour and also the energetics of motility, the latter by enabling the calculation of the mechanical energy and power required for sperm swimming (Ishimoto et al., 2018; Gallagher et al., 2019). It has a major advantage over other approaches due to its remarkable simplicity, though it accordingly makes numerous important assumptions. One pertinent example is that the surrounding medium is Newtonian in nature, such as water or a water-based physiological electrolyte, a common assumption more generally that we will later discuss in detail. A second and perhaps defining assumption, giving rise to the alternative name *local drag theory*, is that of locality, in that the viscous forces experienced at one point of the flagellum are taken to depend only on the velocity of the flagellum relative to the background fluid at that point. This, however, knowingly neglects the presence of, and any interactions with, not only the other parts of the flagellum but also the head of the sperm.

Hence, the level of accuracy in this resistive force theory is highly contingent on context, in that it should not be expected to retain accuracy for large cell bodies, highly curved flagella, nor multiple flagella, for example. Further, one should not expect much accuracy in its predictions of viscous drag close to the distal flagellum nor when the cell is swimming close to surfaces, since neither a finite length flagellum nor surface effects are included in the basic framework. The latter caveat is particularly of note for sperm microscopy, with imaging typically performed close to a coverslip owing to the fact that sperm are less likely to swim out of the focal plane in this setting, resultant of their well-known surface accumulation behaviours near flat boundaries. Despite this, high-accuracy resistive force theory for swimming bull sperm next to a plane has been reported (Friedrich et al., 2010), though with the notable caveat that a parameter within the theory was fitted to obtain the accuracy, whereas all parameters are theoretically fixed by physical principles in terms of the fluid viscosity and flagellum shape.

Whilst resistive force theory can, and has been, generalised to rigorously include surface effects (Brenner, 1962; Katz et al., 1975; Walker et al., 2019a), the resulting theory can be cumbersome to apply, losing the fundamental advantage of resistive force theory's simplicity that has allowed it to persist even to the present day. In particular, when relating flagellar beating to cell behaviour, there is a spectrum of classical methodologies to choose from that improve upon the limited accuracy and flexibility of resistive force theory, at least for Newtonian fluids (Gaffney et al., 2011). Furthermore, in contrast to resistive force theory, these improvements can also be used to determine the fluid flow induced by the sperm flagellum beating (**Figure 2A**). The most accurate and flexible is *computational fluid dynamics,* which is limited in accuracy only by computational resource, machine precision constraints, and the accuracy of the underlying physics, such as the common and broadly appropriate assumption of neglecting inertia on the grounds that it is subordinate to viscous effects and induces only tiny errors. The most common of such approaches for sperm motility are the *boundary element methods* (Pozrikidis, 2002), which have been extensively exploited to study sperm dynamics (for example Phanthien et al., 1987; Ramia et al., 1993; Ishimoto and Gaffney, 2014; Ishimoto et al., 2016; Walker et al., 2019b). However, such methodologies suffer from a relatively complex formulation, in terms of both the underlying mathematics and scientific computation.

An intermediate on the spectrum of accuracy, flexibility, and simplicity for methodologies is *slender-body theory*, which represents the flagellum via a curve of negligible cross-sectional radius, as developed by Keller and Rubinow (1976), Johnson (1980), and Tornberg and Shelley (2004), with numerous applications to sperm (Higdon, 1979; Johnson and Brokaw, 1979;

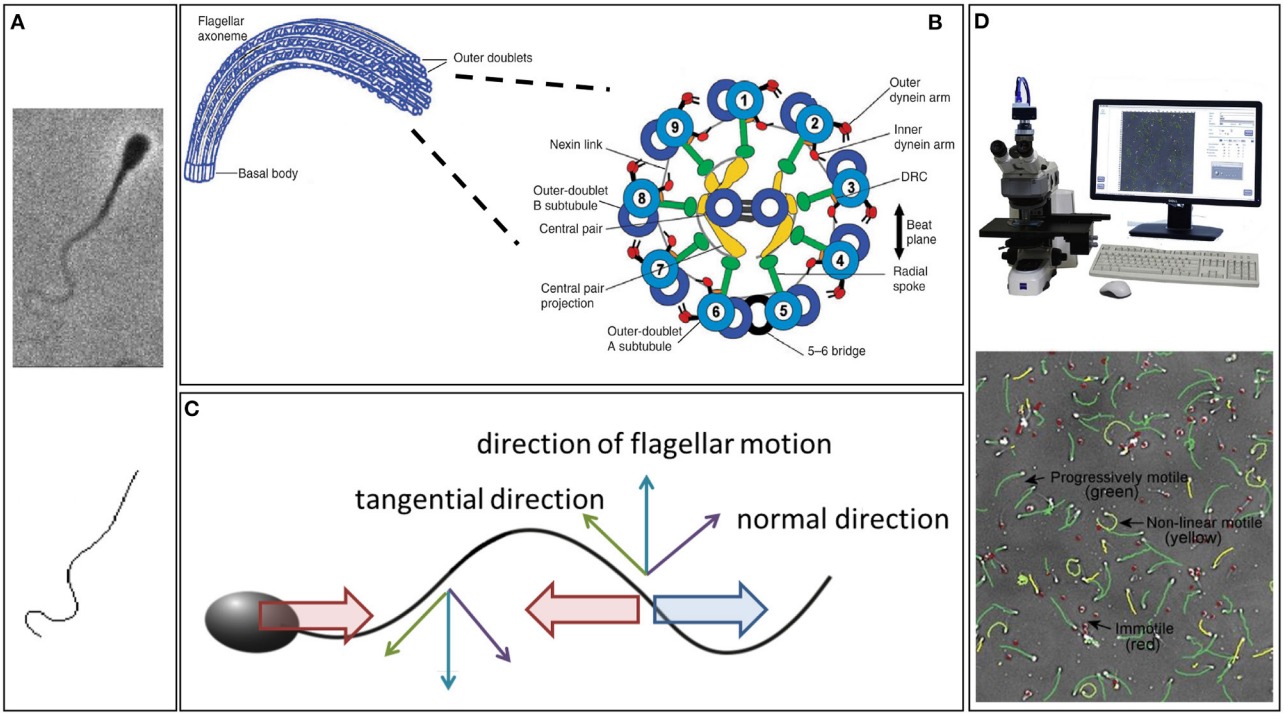

FIGURE 1 | (A) An example of a phase contrast image of a swimming bull sperm (upper), with the digital capture of its flagellum (lower). **(B)** The internal structure of the flagellum, showing the dynein molecular motors. Their contraction induces a couple that acts to slide the microtubule doublets relative to each other, which, combined with the fact the microtubule doublets are constrained at the flagellum-cell body junction, induces flagellar bending (Summers and Gibbons, 1971; Brokaw, 1972a). **(C)** Resistive force theory, which simply relates local flagellum velocity, in the tangential and normal directions, to the forces exerted on the surrounding fluid. The thin upward blue arrow is the flagellum velocity, with the tangential and normal components represented by green and purple thin arrows, respectively. Noting that twice as much force per unit length is required to move the flagellum through the fluid perpendicular to itself compared to tangentially, the upwards-moving flagellum thus exerts a net force on the fluid in the horizontal direction to the right (large blue arrow); similarly for the thin downward blue arrow for the downwards flagellum velocity. Hence, an equal and opposite drag force acts leftwards on the flagellum (leftward red arrow). If the sperm was stationary this would violate Newton's second law, since the inertial term (mass × acceleration) is negligible, entailing that the total force on the cell must be zero. Thus, the sperm must move to the left at a speed that ensures that the additional drag from this motion (rightward red arrow) balances out the leftward force on the flagellum. Analogous reasoning can be used to find the sperm's vertical and angular velocities in terms of the flagellar beat pattern and, thus, the sperm trajectory can be constructed from knowledge of its beat pattern. **(D)** An example CASA system and cell tracking. **(A)** is republished from Walker et al. (2020b) with permission, under the terms of the Creative Commons Attribution License https://creativecommons.org/licenses/by/4.0/. **(B)** is republished with the permission of The Company of Biologists Ltd from Lindemann and Lesich (2010), permission conveyed through the Copyright Clearance Center, Inc. **(D)** is reprinted from Amann and Waberski (2014), with permission from Elsevier.

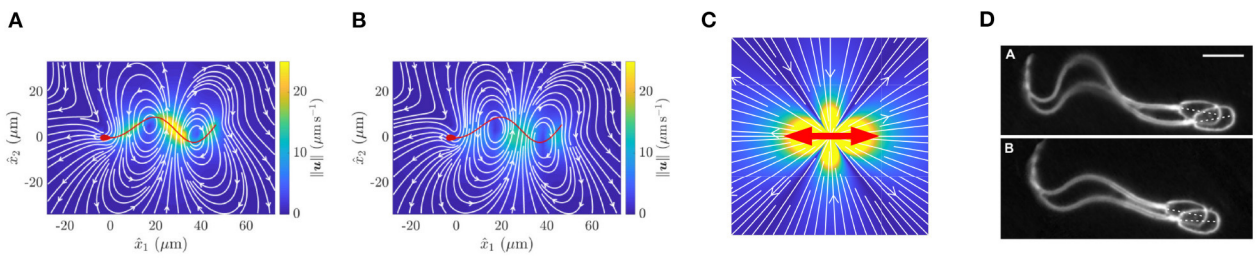

FIGURE 2 | Fluid flow around a virtual spermatozoon, computed via **(A)** the boundary element method and **(B)** a coarse-grained model. **(C)** Flow induced by a point dipole model. The red arrows show the directions of force applied to the fluid, whilst color corresponds to flow velocity. **(D)** Pairwise swimming of bull spermatozoa. **(A,B)** reprinted from Walker et al. (2019b), Copyright (2019) by the American Physical Society. **(D)** republished with permission of the Company of Biologists Ltd from Woolley et al. (2009); permission conveyed through the Copyright Clearance Centre.

Dresdner et al., 1980). Especially when coupled with the use of boundary element methods for the cell body (Smith et al., 2009a), this incurs only very small errors in predictions of the viscous drag, except at the distal end of the flagellum, and can readily accommodate a single flat surface. However, slender-body theory does not readily generalise to multiple swimmers, more

complex confining geometries, or a non-trivial rheology of the surrounding fluid.

An interesting and useful generalisation of the boundary element method that has emerged in the past 20 years is the *regularised boundary integral method* (Cortez, 2001; Cortez et al., 2005), which differs from the original approach in a subtle way. In the original theory, in its most simple "single-layer" form, one can interpret the solution as the flows and forces induced by a collection of point forces in the fluid (Pozrikidis, 1992). True point forces present numerous challenges for computational algorithms, so the regularised boundary element method instead considers a collection of regularised forces, where the force is spread out in space, rather than acting at a single point, though this spread is highly localised. This leads to substantially simpler algorithms, generally at the cost of a limited but uncertain loss of accuracy, which depends on the fine details of how the force is spread out.

More generally, this framework has been extended to a regularised boundary integral method with singularities other than Stokeslets, with early examples developed by Ainley et al. (2008) and Smith (2009). There is also a further generalisation for sperm that we refer to as *regularised slender-body theory*, where the singularities are placed on the flagellum centreline. Compared to standard slender-body theory, this generalisation inherits ease of implementation at the expense of an uncertain loss of accuracy, and has also found substantial application in the modelling of sperm motility (Gillies et al., 2009; Smith et al., 2009a; Cortez and Nicholas, 2012).

1.1.2. Elastohydrodynamics and Emergent Beat Patterns

As exemplified by Machin's study, there is more to the theory of sperm motility than simply how the flagellar beat pattern dictates the cell movement and the flow of fluid around the cell; there is the key question of how the flagellum beat pattern is generated. This is not independent of the surrounding fluid, with the viscous drag playing a fundamental role, as can be seen from differences in beat pattern between sperm surrounded by media of distinct viscosities (Suarez et al., 1991; Smith et al., 2009b). This dependence is further emphasised by the change in mechanical power output, which, for human sperm, increases by a factor of four on comparing swimming in a watery medium and a methylcellulose mucus analogue (Ishimoto et al., 2018), with the regulation of the dynein forces thereby also being modified by viscosity and, more generally, the resistance of the surrounding fluid. This is additionally supported by the observation that sperm flagella can synchronise when they are sufficiently close within media that present a high viscous and elastic resistance (Tung et al., 2017), demonstrating that the forces induced by the medium can effect the timing of the flagella beating.

Hence, the formation of the sperm beat pattern is multifacted, with its study requiring detailed consideration of the spermatazoan mechanical response to drag from the surrounding fluid, its own passive flagellar restoring forces, and the active forces and couples generated by its internal molecular motors. In turn, this entails that such a programme of research may be readily broken down into two distinct parts. The first is the fluid-flagellum interaction problem: given known active forces and torques, how does a flagellum beat and move in a viscous fluid environment where, as usual, fluid inertia is negligible? The second looks to query how to model the dynein molecular motors (**Figure 1B**), the forces and torques they exert, and their regulation, each of which may be coupled to the shape of the flagellum.

The first aspect of this programme concerns modelling the coupling of an elastic deforming filament to the flow of a viscous fluid. This is known as the *elastohydrodynamical problem*, predominantly considered in the inertia-free context appropriate for spermatozoa, which, here, is an excellent approximation. Most commonly, and up until relatively recently, the elastohydrodynamical problem has been pursued using the resistive force theory approximation (Rikmenspoel, 1971, 1978a; Brokaw, 1972b; Lindemann, 1994a; Fu et al., 2008, 2009; Gadêlha et al., 2010). Accordingly, this inherits all the inaccuracies, limitations, and lack of broad applicability described for resistive force theories, whilst moving beyond such local hydrodynamic theory has been, and broadly remains, a methodological challenge. One non-local approach has been the use of immersed boundary methods (Dillon et al., 2007), though these are very computationally demanding for elastic filaments, as opposed to two-dimensional sheets, whilst a further approach has been to use particle-based models with rod-and-spring representations of the flagellum (Elgeti et al., 2010). Tornberg and Shelley (2004) also demonstrated how slender-body techniques could be utilised for the elastohydrodynamic problem for filaments, though this has not been widely adopted in studying sperm motility. In contrast, a technique that has been adopted in this context takes advantage of regularised slender-body theory (Olson et al., 2013; Simons et al., 2014, 2015). However, once coupled with a sperm head and a confining surface, the inclusion of elastohydrodynamics within this methodology is observed to be very demanding in terms of computational resource (Ishimoto and Gaffney, 2018a). Seeking to overcome this computational hurdle, more-recent work has focussed on the development of algorithms that can solve elastohydrodynamical problems with much greater computational efficiency, as we shall touch upon later in Section 2.

The second component of the above programme—modelling molecular motor activity and its regulation—is a complex, multiphysics, multiscale problem that is subject to multiple competing theories and significant numbers of parameters that are not independently measured, as well as substantial inter-cell variation. There have been diverse studies by many authors that focus on how to represent the dynein dynamics, with examples including curvature control (Brokaw, 1975; Hines and Blum, 1978), multistate molecular motor models (Murase et al., 1989; Camalet and Jülicher, 2000; Dillon et al., 2007; Riedel-Kruse and Hilfinger, 2007), and Lindemann's geometric clutch hypothesis (Lindemann, 1994a,b, 2002), together with the latter's mathematical reincarnation by Bayly and Wilson (2014, 2015).

All such dynein models have been limited by the use resistive force theory, or the constraints of a 2D immersed boundary method in the case of Dillon et al. (2007). However, whilst

such models are unquestionably hindered by the difficulties of the elastohydrodynamical problem, reviewing their scientific development is beyond the scope of this current review, but is lucidly detailed by Lindemann and Lesich (2010).

1.2. Computer-Assisted Sperm Analysis

Sperm microscopy presents difficulties in the high frequency of the flagellar beat pattern relative to the sensitivity of the human eye and the small diameter of the flagellum, which approaches the conventional resolution of light optics (Gray, 1955). To circumvent these challenges, early imaging modalities typically relied on darkfield microscopy and, before the emergence of sufficiently high frame rate cameras, stroboscopic illumination (Gray, 1955; Rikmenspoel et al., 1960; Sleigh, 1962). This technique was refined by Rikmenspoel to achieve cinemicroscopy with flagella imaged at 200 frames per second by the mid 1960s (Rikmenspoel, 1965), progressing to 400 frames per second Rikmenspoel (1978b) as well as being adopted by Sleigh, amongst others, for studies of both cilia and flagella (Sleigh, 1974; Sanderson and Sleigh, 1981). Another popular approach emerged with the Nobel prize winning revolution of phase-contrast microscopy, which was developed in the 1930 and 1940s (Zernike, 1955). It enables remarkable spatial resolution at the cellular and sub-cellular scale and has been widely exploited for the imaging of the slender flagella of sperm cells (for example Katz et al., 1978; Overstreet et al., 1979; **Figure 1A**, upper).

However, the conversion between imaging capability on the one hand and meaningful summary statistics of sperm motility on the other required labour-intensive manual analysis of time exposure photomicrographs (Overstreet et al., 1979) or frame-by-frame by-hand analysis of cine films (Rikmenspoel, 1965, 1978b; Katz et al., 1978), as reviewed by Amann and Katz (2004). The laborious nature of studying sperm with such methods was alleviated with the emergence of *Computer-Assisted Sperm Analysis (CASA)* and *Computer-Assisted Sperm Motility Analysis (CASA-Mot)*, **Figure 1D**, in the 1980s, as summarised by Davis and Katz (1989). The technology finds extensive application in theriogenology and andrology, as well as reproductive toxicology and semen marketing for livestock breeding (Mortimer, 1997; Mortimer et al., 1998; Amann and Waberski, 2014), though its use in clinical diagnostics is far from fully accepted (Gallagher et al., 2018).

Whilst CASA-Mot generates numerous and standardised measures of sperm swimming, such as speeds, yaw, and trajectory curvature (WHO, 2010), it almost exclusively focuses on the spermatozoon head and its trajectory. However, with the flagellum and its waveform being fundamental for sperm motility, the beat pattern has been the subject of extensive scientific enquiry since its discovery, though the details of even the shapes formed during its complex and varied beating patterns remain elusive. Indeed, since the advent of appropriate microscopy techniques, the standard approach to quantifying the shapes of beating flagella has been simple: trace out, by hand, the visible flagellum in each captured frame of microscopy data (Ishijima et al., 2002; Vernon and Woolley, 2002, 2004). Understandably, the significant time and human investment required to gain even moderate quantities of digitised beating data in this way limited the scope and power of kinematic analysis. Recent developments, which we later summarise, have naturally striven to overcome this, with a sample automated digitisation shown in **Figure 1A**.

Such modern methods promise to greatly increase the quantity and fidelity of flagellar data available to the community. Realising the full potential of this data, however, will itself necessitate significant complimentary developments in the mathematical modelling of motility and related theories. This need spans many aspects of sperm motility analysis, from the removal of the restriction to Newtonian fluid media to overcoming the drawbacks of standard elastohydrodynamical algorithms. Hence, in what follows, we will survey both a number of recent efforts to address some of these challenges and the opportunities for further and future development that these methodological advances unveil.

2. THE EVOLVING METHODOLOGICAL LANDSCAPE

2.1. Population-Level Modelling

2.1.1. Interacting Swimmers

It has long been known that sperm cells swim together, as exemplified by the microscopy of Woolley et al. (2009), reproduced in **Figure 2D**. In the middle of the last century, the importance of hydrodynamic interactions between cells was suggested by the now classical theoretical analysis of Taylor (1951). Since then, innumerable studies have sought to explore the role of hydrodynamics in the collective swimming of spermatozoa, but the fine details of these interactions remain uncovered. Indeed, the pairwise swimming of even two individuals is not fully elucidated, a necessary precursor to the accurate population-level modelling of swimming sperm. Nevertheless, multiple approaches have been utilised to investigate, with associated levels of approximation, the motion of collections of spermatozoa.

The coarsest model of a single swimmer is the so-called *point-dipole* model (Lauga, 2020), which, in essence, simplifies the cell down to a single point, with the surrounding flow being modelled by two opposing forces, as shown in **Figure 2C**. This representation effectively averages the more complex time-varying flow around a spermatozoon, shown in **Figure 2A**, in doing so almost entirely neglecting the morphology of the swimming cell. These models inherently afford great simplicity and scalability, whilst providing an accurate picture of the hydrodynamics of a swimmer when viewed from the far field, the combination of which has resulted in their widespread use. Despite their apparent crudeness, their utility has been repeatedly highlighted, not least by the ability of these simple representations to explain the attractive hydrodynamic interactions between cells that swim in parallel to one another (Lauga and Powers, 2009), though this does not guarantee the emergence of experimentally noted pairwise swimming.

Arguably representing the opposite end of the modelling spectrum, the computationally intensive *boundary element methods* enable the complex spermatozoan shape to be represented numerically (Pozrikidis, 2002), giving rise to accurate quantifications of the fluid flow around spermatozoa

and the accompanying hydrodynamic interactions. For example, this methodology was used to produce the intricate instantaneous flow field displayed in **Figure 2A**, significantly distinct in character from the time-averaged flow field of **Figure 2C**. This accurate approach was recently used to simulate the motion of two identical model sperm with planar flagellar waveforms (Walker et al., 2019b), which concluded that two cells swimming side-by-side are attracted towards eventual collision, whilst those that are above and below one another (with respect to the plane of the flagellar beat) can swim stably at a certain distance apart. This simulation study highlights the subtle and intricate details of the hydrodynamic interactions between swimming sperm, though such a high fidelity simulation cannot be reasonably extended to population-level analyses due to the overwhelming numerical cost.

An intermediate approach, seeking to balance accuracy and efficiency, involves coarse graining the flow around a spermatozoon, representing the dynamics of the fluid by a small number of simple flow constituents (Ishimoto et al., 2017). The details of this method are somewhat involved, though their success in improving accuracy over the minimal point-dipole is easily evidenced, as can be seen by comparing the flow fields of the point-dipole (**Figure 2C**) and the coarse-grained approach (**Figure 2B**). This methodology can be applied to sperm in multiplicity (Ishimoto et al., 2018), enabling theoretical studies of small populations of spermatozoa with heightened accuracy and efficiency when compared with point-dipole and boundary element methods, respectively.

A subtlety in the common use of each these methods, however, is that they often rely on knowledge of the flagellar beat. The extension of swimmer-swimmer interactions to an elastohydrodynamic setting, where the shape of the flagellum is influenced by its elastic properties as well as interactions with the surrounding fluid, remains challenging. However, the exploration of this coupling, has, and continues to be, the subject of much active research, from early models of *swimming sheets* (Fauci and McDonald, 1995) to more recent theoretical analyses (Elfring and Lauga, 2009, 2011), the latter works highlighting the enhancement of flagellar synchronisation by elasticity. Elastohydrodynamic modelling has since been extended to consider planar motions of flagella (Llopis et al., 2013; Goldstein et al., 2016; Taketoshi et al., 2020), with Taketoshi et al. (2020) extending the boundary element method to include flagellar elasticity. This latter work again explored pairwise dynamics, numerically concluding that spermatozoa enjoy increased swimming speed when beating in synchrony, in contrast to the similar but conditional results of the prescribed-beat study of Walker et al. (2019b). Further, three-dimensional studies have also been initiated (Simons et al., 2015), though there remains significant scope for the investigation of the effects of rheology, confinement, multiplicity, and the details of the driving force behind the spermatozoan beat.

2.1.2. Collective Behaviours

With spermatozoa often present in vast numbers (Zinaman et al., 2000), it is unsurprising that a wide variety of collective behaviours have been observed. Shown in **Figure 3A**, a particularly remarkable example is the phenomenon of *sperm trains*, collections of up to around ten cells that adhere to one another at the head, which occur in some species of rodent (Moore and Taggart, 1995; Moore et al., 2002). These are thought to form due to the hook-like morphology of the spermatozoon head in these organisms, whilst pairwise adhered swimming has been reported to confer increased swimming speed over lone cells in *Monodelphis domestica*, upwards of 20%. This is in agreement with the elastohydrodynamic simulations of Cripe et al. (2016), which considered the motion of two flagella adhered at the base, though these results are significantly dependent on parameters such as interflagellar distance and the angle between the adhered flagella.

Further, in some monotreme, ants, and other species, it has been observed that spermatozoa can form a large bundle-like structure, as showcased in **Figure 3B**, containing more than 100 cells (Djakiew and Jones, 1983; Burnett and Heinze, 2014; Pearcy et al., 2014). These *sperm bundles*, as well as sperm trains, have also been studied from the point of view of elastohydrodynamics (Yang et al., 2008, 2010; Schoeller et al., 2020), with head-head adhesive interactions also having been modelled by Fisher et al. (2014), the latter being noted to be of significance for the competitive viability of such entrained collections of spermatozoa. An additional modelling study suggests the importance of spermatozoan head geometry in the stability and motility of these aggregates (Pearce et al., 2018), with hydrodynamic interactions more generally being highly dependent on cellular morphology. It is important to note, however, that the adhesion that gives rise to these clusters does not appear necessary for their formation in general, with Tung et al. (2017) having reported the aggregation of spermatozoa in the absence of clear adhesion; rather, the observed groupings were transient, with sperm transitioning between clusters over time.

Other collective phenomenon include *sperm vortices*, swirling structures that can arise due to asymmetric flagellar beating of certain species near a substrate (Riedel et al., 2005; Yang et al., 2014b), and *sperm turbulence*, which can be found in dense suspensions both experimentally and theoretically (Creppy et al., 2015, 2016; Schoeller and Keaveny, 2018). This structured turbulence, pictured in **Figure 3C**, appears reminiscent of well known bacterial turbulence (Wensink et al., 2012) and the collective dynamics of active rods (Saintillan and Shelley, 2007), though the statistical features of these phenomena differ slightly.

2.2. The Sperm Microenvironment

Further to the presence of nearby swimmers, more-fundamental aspects of the spermatozoan microenvironment can impact significantly on the motion and behaviours of the swimming cell. For instance, the chemical components of the surrounding environment also can affect the motility of sperm, in particular inducing turning and chemotactic guidance, as first demonstrated by Miller (1966) in hydroids. Studies of the associated flagellar kinematics followed relatively shortly, with the demonstration that chemotactic turning is concomitant with asymmetric flagellar beat patterns (Miller and Brokaw, 1970), again in hydroids. The functional significance of chemotaxis in

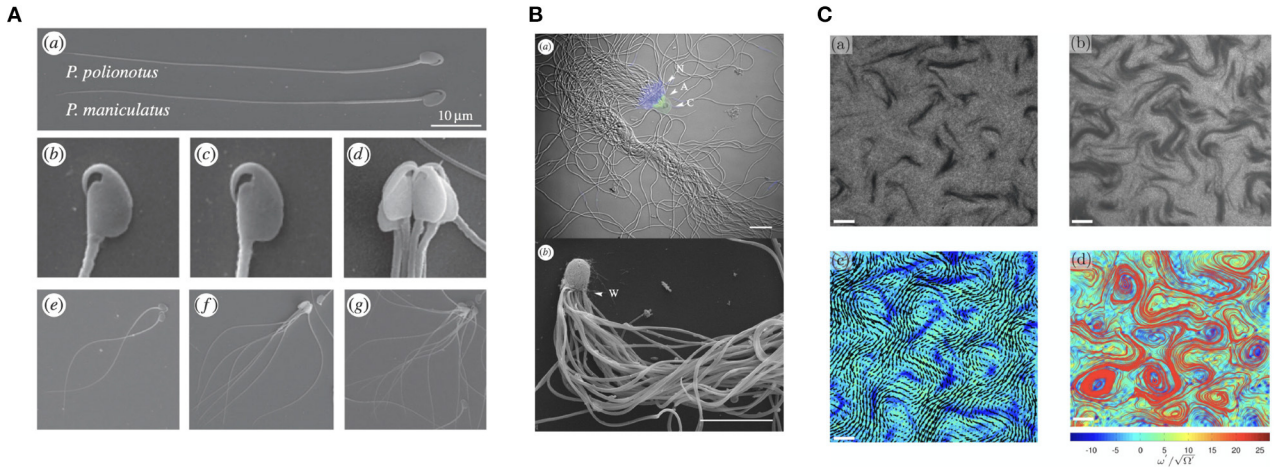

FIGURE 3 | Varieties of sperm collective behaviors. **(A)** A multiswimmer sperm train and the hook-like morphology of some murine spermatozoa. **(B)** Crowded sperm bundles of potentially hundreds of individual swimmers. **(C)** The emergence of sperm turbulence, found in dense suspensions. **(A)** is republished from Fisher et al. (2014), with permission under the terms of the Creative Commons Attribution License http://creativecommons.org/licenses/by/3.0/. **(B)** is republished with the permission of The Royal Society (U.K.) from Pearcy et al. (2014); permission conveyed through the Copyright Clearance Center, Inc. **(C)** is reprinted from Creppy et al. (2015), Copyright (2019) by the American Physical Society.

terms of animal sperm guidance to the egg was first reported in Ward et al. (1985)'s study of sea urchin, whilst the first direct support of the underlying mechanism, in terms of the modulation of intra-cellular calcium, was presented by Cook et al. (1994). The time taken to begin to directly evidence the underlying mechanism of sperm chemotaxis via its impact on intracellular calcium emphasises the challenge in elucidating the systems biology of sperm guidance (Kaupp et al., 2003), as does the observation that this is still not fully resolved to date (Priego-Espinosa et al., 2020).

Nonetheless, it is fully recognised that chemotaxis is a key mechanism of sperm guidance (Eisenbach and Giojalas, 2006; Friedrich and Jülicher, 2007; Cosson, 2015; Jikeli et al., 2015; Hussain et al., 2016; Kaupp and Alvarez, 2016) that is of particular relevance for external fertilisers, where chemoattractants are released from the ovum, in turn inducing a modulation of the sperm flagellar waveform that promotes guidance towards an egg (Shiba et al., 2008). These chemoattractants can be advected by the flow induced by the flagellum and the background fluid, with the latter inducing a spread over a wide region, potentially enabling long range signalling (Riffell and Zimmer, 2007; Zimmer and Riffell, 2011). For instance, fluid shear in marine environments can induce a filamentous region with a strong concentration of molecules extending from the egg (Bell and Crimaldi, 2015). In turn, this can promote sperm cell chemotaxis at larger distances from the egg, with theoretical modelling showing that the moderate shear rate of coastal waters is optimal for sperm-egg encounter rate (Lange and Friedrich, 2021). Nonetheless, the study of the impact of chemoattractants and their transport on sperm behaviour presents numerous significant challenges that are yet to be wholly addressed, including even the measurement of chemoattractants *in vivo*.

Perhaps more fundamentally, the microenvironment can impose mechanical constraints on swimming. In the remainder of this section, we will consider two such factors: the geometrical confinement experienced by the swimmer, such as in a microdevice or the female reproductive tract, and the properties of the fluid media in which it swims, with different media giving rise to greatly distinct beating gaits.

2.2.1. Confinement

A typical, but not ubiquitous, limitation of optical microscopy is that data is acquired in a single focal plane. As free-swimming spermatozoa need not move in this same plane, the acquisition of swimming data can be challenging. This has led to sperm being imaged in confined environments, such as near a substrate or coverslip, which serves to limit the swimmer motion out of the focal plane, enabling swimmer behaviour to be captured in high fidelity. This arises due to the tendency of sperm to swim near a boundary, well-known to occur for glass substrates for over half a century (Rothschild, 1963). Simple theoretical arguments, using the aforementioned point-particle models, predict this behaviour, with hydrodynamic interactions drawing the swimmer close to the boundary Lauga (2020). However, these models fail to capture the fine but significant details of the hydrodynamic interactions between the boundary and a spermatozoon, with the details of the flagellar waveform known to have a crucial impact on the realisation of accumulation behaviours via hydrodynamics alone (Smith et al., 2009a; Ishimoto and Gaffney, 2014).

In addition to the potentially subtle effects of hydrodynamics, there are further mechanical interactions between boundaries and swimmers. Example such mechanisms are contact and adhesive forces, which, much like in the case of swimmer-swimmer interactions, have not been well explored in theoretical studies, though numerical works have documented the interplay between adhesion and hyperactivated beating patterns in realising detachment from a surface (Curtis et al., 2012; Simons et al., 2014; Ishimoto and Gaffney, 2016).

A further, often experimentally undesirable impact of boundary proximity is modification of the flagellar beat. A drastic change in beating was reported by Woolley (2003), with a three-dimensional helical motion of the flagellum being suppressed to a two-dimensional planar gait due to interactions of the spermatozoon with the boundary. This tendency of boundaries serving to reduce non-planar components of beating has also be affirmed by more recent observations (Su et al., 2012; Bukatin et al., 2015; Nosrati et al., 2015). From a theoretical perspective, elastohydrodynamic studies have sought to investigate this phenomenon (Fauci and McDonald, 1995; Elgeti et al., 2010; Huang et al., 2018; Ishimoto and Gaffney, 2018a), concluding that the flagellar waveform can be modified by hydrodynamic interactions with boundaries, though further experimental investigation is required in order to clarify the effects of boundaries on the flagellar gait.

In applications, and certainly *in vivo*, the geometry of confinement need not be as simple as a plane wall. In microdevices, sperm often experience interactions with sharp corners, which give rise to both scattering and accumulation behaviours (Kantsler et al., 2013; Nosrati et al., 2016; Bukatin et al., 2020). Elastohydrodynamic simulations of swimmers near such corners have recently been conducted (Montenegro-Johnson et al., 2015; Rode et al., 2019), though with assumed two-dimensional flagellar waveforms. Experimentally, more complex geometry has been examined, for example in sperm sorters (Denissenko et al., 2012; Tung et al., 2014; Kamal and Keaveny, 2018), though this complexity has inhibited numerical exploration of the same intricate environments. For instance, unexplored theoretically to the best of our knowledge, remarkable *in vivo* experiments of Yang and Lu (2011) exemplify the drastic effects that severe confinement can have on sperm motility in Drosophila, whose long sperm are able to move rapidly in the contorted female reproductive tract whilst being practically immobile in free artificial media (Pitnick et al., 1995; Lu, 2013).

2.2.2. Rheology

A key influence on the waveform exhibited by a spermatozoon is the viscosity of the surrounding fluid, as the balance between elastic and viscous forces changes. A prominent effect is on the amplitude of the flagellar waveform, with high viscosity leading to flagella that appear to bend more readily, which has also been seen in theoretical studies (Fu et al., 2007; Gadêlha et al., 2010). A similar effect occurs as the result of reduced stiffness towards the distal end of the flagellum (Gadêlha and Gaffney, 2019).

Additionally, swimmer dynamics may also be drastically altered by more complex fluid rheology (Smith et al., 2009b; Hyakutake et al., 2019), such as the potentially elastic nature of a fluid due to solvent molecules, broadly termed *viscoelasticity*, in contrast to usual watery medium, termed a Newtonian fluid, as discussed in the previous sections. A complex fluid that cannot be described simply by the Newtonian model is called a non-Newtonian fluid. One of the simplest models for a non-Newtonian medium is a linear Maxwell fluid, which contains a single parameter that encodes a relaxation time due to the elastic property of the medium. In the linear Maxwell fluid model, the rheology of the fluid does not directly influence the hydrodynamic interactions (Fulford et al., 1998; Ishimoto et al., 2017), though does impact on the forces felt by a swimming cell (Ishimoto and Gaffney, 2016). More generally, swimming in non-Newtonian media can result in non-trivial changes to the speed of progression and the emergent waveforms, exemplified in **Figure 4**. In turn, these potentially result in large departures from normal Newtonian behaviour, both in individual and collective dynamics (Li and Ardekani, 2016; Thomases and Guy, 2017; Ishimoto and Gaffney, 2018b; Ishimoto et al., 2018), with a particular example being the enhancement of coherent multiswimmer structures in a non-Newtonian fluid (Tung et al., 2017).

Ultimately, the investigation of swimming in complex fluids requires significant advances in modelling methods and numerical schemes, with non-Newtonian fluids being generally more difficult to study. This affects not only simulation at scale, necessary for investigating collective behaviours, but also the study of individual swimmers, which remains challenging.

2.3. Computer-Assisted Beat-Pattern Analysis

2.3.1. Digitising the Flagellar Beat

As summarised in section 1, the task of studying the flagellar beat has classically been laborious, requiring vast amounts of researcher time to trace flagellar shapes from microscopy. To overcome this barrier to large-scale quantitative analysis, a host of computer-assisted methods have been developed, reducing or removing the need for researcher interaction with the raw dataset. One early approach utilised a television camera and video digitiser for the processing of rephotographed microscopy images, with manual intervention for dust spots and film scratches (Rikmenspoel and Isles, 1985). A further early approach was that of Baba and Mogami (1985), which used pixel intensity measurements to trace out a flagellum from an initially selected basal point. Both approaches were a significant improvement on previous manual techniques and allowed sufficient accuracy for the quantification of flagellar curvature. In particular, the associated software developed from Baba and Mogami (1985)'s study, BohBohsoft, has persisted and enabled numerous studies requiring flagellar digitisation, such as Wood et al. (2005) and Shiba et al. (2008).

More recently, a wide range of refined semi-automatic schemes, requiring further-reduced user input, and even fully automatic unsupervised methods, have become available for tracing out a slender flagellum-like object from videomicroscopy. A selection of these approaches are tailored to the morphology and characteristics of spermatozoa (Smith et al., 2009a; Yang et al., 2014a; Hansen et al., 2018; Gallagher et al., 2019), whilst others are somewhat more general (Hongsheng et al., 2009; Goldstein et al., 2010; Xu et al., 2014; Xiao et al., 2016; Walker et al., 2019c); an example output of one of the latter techniques is reproduced in **Figure 1A**. The development of these software tools and approaches, in combination with improvements in the fidelity of videomicroscopy, has newly enabled studies at scale of the details of flagellar beating in a variety of organisms, including

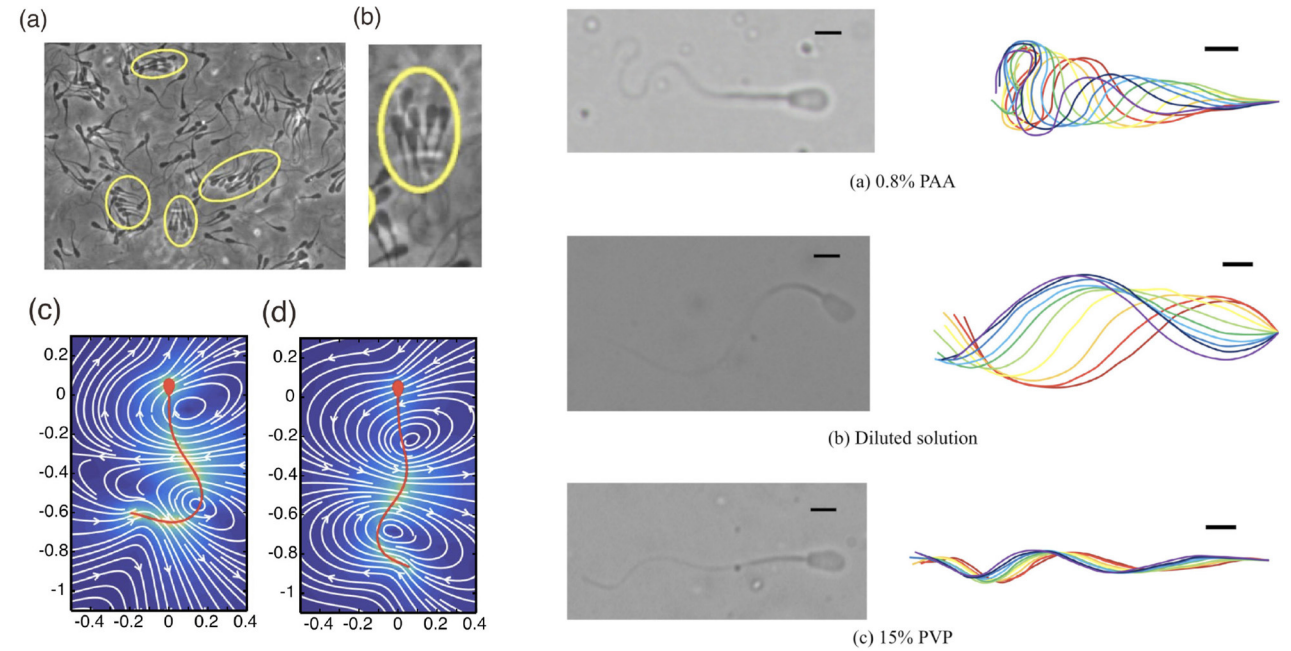

FIGURE 4 | Different waveforms in different environments. **(A)** (a,b) Bull sperm cluster in a viscoelastic medium (Tung et al., 2017) and the flow of (c) low and (d) high viscous medium around human sperm cells (Ishimoto and Gaffney, 2018b). **(B)** Different waveforms seen in bull sperm cells in different rheological media (Hyakutake et al., 2019) **(A)** (a,b) republished from the works of Tung et al. (2017) and **(A)** (c,d) republished from the works of Ishimoto and Gaffney (2018b), all with permission under the terms of the Creative Commons Attribution License http://creativecommons.org/licenses/by/4.0/. **(B)** reprinted from Hyakutake et al. (2019) with permission from Elsevier.

bovine and human spermatozoa (Gallagher et al., 2019; Walker et al., 2019d, 2020b), each analysing hundreds of individual swimmers, with the potential for significant future application and extension.

2.3.2. Summary Statistics

This marked increase in the availability of flagellar beating data, which does not form part of a traditional CASA or CASA-Mot frameworks, motivates the development of a new generation of semen analysis techniques, as noted in the thorough review of Gallagher et al. (2018). Recent methods have sought to incorporate simple summary measures of the flagellar beat, augmenting traditional CASA and CASA-Mot statistics with quantities such as wavelength and beat frequency (Gallagher et al., 2019; Walker et al., 2019d). However, whilst the simplicity of these descriptors is attractive and they can be readily computed, they each implicitly assume particular characteristics of the flagellar beat, which, as we will see, need not hold in practice.

The first and perhaps most subtle assumption is well illustrated by the notion of wavelength, and concerns the problem of definition. To illustrate this, consider the waving motion of a simple travelling sine wave, familiarly written as $y = \sin(kx - t)$ for position x and time t. This has a characteristic and well defined wavelength, here given via the quantity k. Whilst similar such sinusoidal patterns have been classically used to caricature the flagellar beat, the true beating motion of a sperm cell is readily observed to not be quite so simple, as can be seen in **Figure 4B**. Further focussing on the upper panel of **Figure 4B**, it is clear that the concept of wavelength lacks unambiguous meaning in this context, with there being no familiar repeating shape as we move along the flagellum, as would be the case for a simple sine wave. As such, measurements, interpretation, and related discussions of wavelength should be treated with great care, with one study's notion of wavelength not necessarily synonymous with that defined in another analysis. Analogously, this carries over to similarly derived flagellum-wide quantities, such as beat amplitude.

The second commonplace assumption is somewhat more intuitive, and highlights a relatively unexplored aspect of flagellar beating: the evolution of beating over time. For example, though we might report the frequency of the flagellar beat as a single value, the actual frequency may be evolving with time. Of particular note, the recent study of Achikanu et al. (2019) tracked sperm motion over a considerable time period, identifying sustained behavioural switching that is more significant than we have hinted at here, highlighting the significance of careful temporal considerations of the spermatozoan beat and its descriptors.

2.3.3. Whole-Flagellum Analysis

Whilst even refined and well defined summary statistics provide a readily digestible characterisation of a flagellar waveform, they necessarily omit much of the detailed beat pattern data

available. Common techniques such as principal component analysis (PCA) can encode such complex waveform information in a number of coefficients and so-called modes, though at the expense of easy interpretation and simple methods of comparison between swimmers.

Two recent works, however, have sought to address the second of these two drawbacks, applying PCA not just to individual swimmers, but to whole cohorts of swimming cells in order to capture population-level beating information. One, that of Walker et al. (2020b), computed time-dependent PCA coefficients and applied standard hypothesis testing techniques to these quantitative measures, enabling statistical comparison between samples of bovine spermatozoa via the details of their beating, coining the term *computer-assisted beat-pattern analysis* (CABA).

Complementary to this, Guasto et al. (2020) utilised the PCA modes derived for the sperm of different species, from marine invertebrates to human, to compare the shape of the spermatozoan beat, which led to the suggestion of the importance of selective environmental pressure on shaping spermatozoan motility. With these methodological developments being so recent, there remains significant scope for the broader application of data-rich quantitative approaches to spermatozoan motility, from the statistical comparison of samples to querying flagellar form and function via computer-assisted beat-pattern analysis.

2.4. Elastohydrodynamic Advances

The computational simulation of flagellar elasticity and hydrodynamics is well-known to be a prohibitively difficult task (du Roure et al., 2019), requiring hours on large computing resources to perform even a single simulation (Ishimoto and Gaffney, 2018a). Recently, in an attempt to remove this obstacle to elastohydrodynamics, a new coarse-grained approach was proposed by Moreau et al. (2018). Indeed, this method successfully reduced computation times in 2D simulations down to seconds on laptop computers, improving efficiency by multiple orders of magnitude. The key advance of this framework was to computationally represent the elastic flagellum as a series of connected straight segments and then sum up the drag forces and elastic moments on each straight piece. This led to a simple and flexible set-up that could be rapidly simulated and readily extended to a variety of contexts.

Such was the increase in simulation speed and utility of the approach, this methodology has already been extended by multiple groups to include improved hydrodynamics (Hall-McNair et al., 2019; Walker et al., 2019a) and utilised for exploratory study (Neal et al., 2020). In the latter, tailored to spermatozoa, Neal et al. (2020) leveraged the computational efficiency afforded by this methodological advance to explore the effects of multiple parameters on the swimming efficiency of spermatozoa, concluding in particular that an inactive flagellar endpiece can increase the efficiency of swimming. Recent work has also lifted this approach into 3D (Walker et al., 2020a), which again realised orders of magnitude improvements in computational speed over contemporary 3D methodologies (Olson et al., 2013; Ishimoto and Gaffney, 2018a; Carichino and Olson, 2019). The full extent of these advances is yet to be realised, with the potential to greatly expand the scope of both theoretical and data-driven research into the dynamics of the flagellum.

3. NEXT-GENERATION INVESTIGATION

3.1. Refining Mathematical Models

3.1.1. Subcellular Investigation

Advances in capability have naturally afforded advances in scope. For instance, the vast majority of existing theoretical research into spermatozoan motility incorporates known flagellar waveforms into computational models, deducing quantities such a swimming speed or efficiency. However, with elastohydrodynamic methods becoming more popular and, as noted, significantly more efficient, there is novel opportunity to move past kinematics, considering instead the molecular motor dynamics internal to the flagellum. In particular, the prospect now exists for much more extensive exploratory computational studies of this subcellular process, for which many hypotheses exists but none have been universally validated or agreed upon (Hines and Blum, 1978; Lindemann, 1994a; Riedel-Kruse and Hilfinger, 2007). There is also broad scope for the further investigation of the impacts of calcium dynamics on flagellar waveforms, having been recently considered theoretically (Olson, 2013; Carichino and Olson, 2019) and suggested to significantly modulate, or even disable, the flagellar beat (Corkidi et al., 2017; Sanchez-Cardenas et al., 2018).

However, of particular pertinence to regulatory models but pervasive more generally, the biologically realistic parameterisation of flagellar models represents an ongoing challenge for the community, with key measurements lacking for many of the relevant mechanical parameters. Indeed, whilst efforts have identified some material properties of flagella, such as bending and shearing resistance in some organisms (Minoura et al., 1999; Pelle et al., 2009), measurements of many quantities, such as torsional resistance, lateral compressibility, and lateral extensibility, are absent. Due to this lack of appropriate data, theoretical studies are commonly limited to simply estimating material parameters, such as is the case in the aforementioned work of Bayly and Wilson (2014), to Table 4 of which we direct the reader in order to illustrate the scale and scope of the absence of known material quantities, even in the context of Bayly and Wilson's idealised flagellar model. Hence, the detailed measurement of material properties of flagella, guided by and addressing the pressing needs of the theoretical community, represents a pertinent goal for future experimental investigation. Complimentary to this, and likely best realised via the strengthening of collaborative links between experimental and theoretical disciplines, additional efforts are warranted to make appropriate use of available measurements in mathematical models, with studies having often neglected realistic parameterisation, and therefore biologically relevant enquiry, in favour of more abstract exploration.

3.1.2. External Influences

In addition to the detailed consideration of internal factors, future theoretical studies may realise high-fidelity coupling of external influences to the flagellar beat, such as fluid flows, which

are the root of rheotaxis in spermatozoa, and chemoattractant-induced taxis (Miki and Clapham, 2013; Kantsler et al., 2014; Ishimoto and Gaffney, 2015; Hussain et al., 2016). For example, such investigations provide the opportunity to couple the aforementioned improvements in computational elastohydrodynamics and our understanding of molecular motor regulation to study the emergence of asymmetric beat patterns and sperm turning due to guidance cues (Alvarez et al., 2014; Bukatin et al., 2015), including the potential role of flagellar buckling (Gadêlha et al., 2010; Bukatin et al., 2015; Ishimoto and Gaffney, 2018a; Kumar et al., 2019).

Other aspects of the spermatozoan microenvironment also present notable challenges to the mathematical modelling community. For instance, theoretical study that accurately reflects the complex rheology of the female reproductive tract, which is potentially non-Newtonian and displays elastic properties, remains a particularly significant and unresolved challenge for the modelling community, with much contemporary research instead being of more direct relevance to tightly controlled *in vitro* systems. Any advances in this area would also be of much wider pertinence, with rheology being a major confounding factor in the study of cilia and flagella in many contexts, such as those involved in mucociliary clearance and development.

A further complicating factor of *in vivo* systems is their geometry and form, which present a theoretical and computational barrier to mathematical analysis. Whilst exact methodologies are available for studying the fluid flow in the simplest geometries, such as half-spaces or basic channels, similar such tools do not exist for the intricate morphologies found in biology. Whilst recent methods for numerical simulation seek to overcome this problem, such as the mesh-free approach of Gallagher and Smith (2018), accurate and detailed consideration of the shape of pertinent fluid environments remains lacking, requiring marked advances in the field of fluid mechanics as well as coupling to high-resolution imaging and rheological measurements.

3.2. Flagellar Analysis in 3D

Much of the flagellar analysis from videomicroscopy that we have described has been relevant to the most common output of such videomicroscopy: two-dimensional images. However, with the beating of spermatozoa not always being planar, a natural extension of these approaches is to three-dimensional flagellar motion. Indeed, three-dimensional beating data of high quality is becoming increasingly available in general (Su et al., 2013; Wilson et al., 2013; Silva-Villalobos et al., 2014; Hernandez-Herrera et al., 2018; Walker and Wheeler, 2019; Hansen et al., 2020), with holographic imaging having recently been used to study spermatozoa (Daloglu and Ozcan, 2017; Daloglu et al., 2018; Muschol et al., 2018). We showcase sample 3D imaging from Gadêlha et al. (2020) in **Figure 5**, though we note that the work of Gadêlha et al. (2020) has recently been retracted for reasons unrelated to the imaging reproduced here (Shilatifard and Yeagle, 2020; Gadêlha et al., 2021). With this increase in the availability of high-fidelity data, which we only expect to further develop in the coming years, the complimentary approaches of CASA and CABA can be readily extended to motion in three dimensions, broadening the scope of quantitative sperm analysis. This promises to enable new insights via kinematic evaluation of the flagellar beat in unrivalled detail, along with providing a means for further intersample and interspecies comparison that is applicable to general, non-planar motion. That being said, whilst the extension to three dimensions may represent the next generation of spermatozoan investigation, there also remains significant and rich scope for a host of statistical evaluation and analysis of even two-dimensional beating data, only recently available in appropriate quantities.

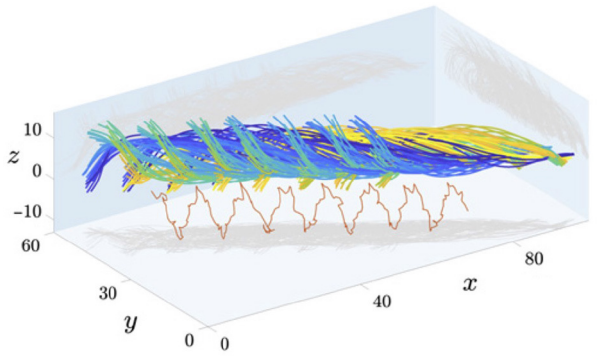

FIGURE 5 | Captured data of the 3D beating of human spermatozoa near a coverslip, with different timepoints shown in different colours. Axes have units of micrometres and a projection of the mid-flagellar point is shown in red. Figure reproduced from the work of Gadêlha and Gaffney (2019), Gadêlha et al. (2020); Shilatifard and Yeagle (2020), with permission under the terms of the Creative Commons Attribution License http://creativecommons.org/licenses/by/4.0/.

3.3. Towards Denser Populations

To date, the detailed study of flagellar kinematics has largely been restricted to lone individuals, with confounding factors present in both the imaging and analysis of multiple flagellated swimmers. This even carries over to theoretical study, where few works have considered multiswimmer settings in high fidelity (Walker et al., 2019b; Taketoshi et al., 2020). Indeed, only small numbers of swimmers, as few as two, are able to be considered without severe simplification. With crowded microenvironments being the norm for many spermatozoa, the next generation of experimental and theoretical analyses should seek to extend our multiswimmer understanding, from interrogating the details of polyswimmer synchrony, as observed by Woolley et al. (2009), to complex population-level interactions. The significant noted advances in both imaging techniques and digital processing will facilitate such developments, with the potential to generate unmatched quantities of data to drive investigative and exploratory study.

Another avenue for promising development is that of coarse-grained dynamics. Whilst the details of cellular geometry and flagellar beating can lead to distinct behaviours at the level of the individual swimmer, it is unclear how such effects scale up to populations. The approach of coarse graining, exemplified in **Figure 2B** for fluid flow but potentially applicable to other aspects

of the problem, such as cell-cell interactions, may represent a viable method for capturing individual effects and thereby scaling up recent computational works, translating microscale mechanisms to complex multiswimmer environments.

3.4. Integrated Approaches

When considered in isolation, recent advances in imaging techniques and mathematical methods have each opened up new directions for exploring the world of a spermatozoon. Perhaps their most promising contribution, however, lies in their potential for synergy. In particular, the combination of high fidelity 3D imaging with modern hydrodynamic methods that afford efficiency, accuracy, and practical simplicity promises to lead to data-driven computational mechanical analyses in three dimensions, with similar explorations so far limited to two dimensions (Friedrich et al., 2010). In turn, this will enable the accurate and ready quantification of the forces and moments exerted on a beating flagellum, with the potential to further our understanding of the nature of active beating in spermatozoa.

Further, the advent of fast methods for the simulation of flagellar elastohydrodynamics brings with it the newfound possibility of realising parameter estimation in the context of swimming spermatozoa. In essence, parameter estimation techniques typically perform numerous simulations of a mathematical model, the results of which are then compared against data to provide refined estimates of model parameters and enable sophisticated model selection. Such methods can be impractical when the costs of simulation are high, much as they have previously been for flagellar elastohydrodynamics. Hence, with individual flagellar simulations having been sped up from many hours to only a few seconds (Moreau et al., 2018; Hall-McNair et al., 2019; Walker et al., 2019a, 2020a) or being performed in parallel (Larson et al., 2021), parameter estimation methods may now be readily applied in combination with datasets of spermatozoan beating, enabling the systematic calibration and assessment of computational models of the flagellum. In turn, this has the potential to be a rich new direction for quantitative analysis, informing biological enquiry and further refining the successful model-experiment cycle of spermatozoon study.

4. SUMMARY

Our understanding of sperm motility mechanics has evolved dramatically since the inaugural studies of the 1950s, with extensive developments in the microscopy and data analysis of sperm swimming, together with advances in the theory and associated computational tools for flagellar beating in Newtonian fluids, as well as an elucidation of the underlying molecular motor mechanisms.

In the first part of this review, we introduced the mechanical interaction between the flagellum and the fluid, in particular the difference in the magnitude of the drag force perpendicular and parallel to the movement of the flagellum, which ultimately drives sperm swimming. More generally, we reviewed the spectrum of theories for flagellar-fluid mechanical interactions in Newtonian fluids, ranging from the simplest *resistive force theory* to the highly accurate but computationally expensive *boundary element methods*. We also surveyed the recent extensive gains in incorporating flagellar elastic responses within this framework, generating *elastohydrodynamic* models. In turn, these developments raise numerous opportunities for analysing the formation of the flagellar beat pattern and how it can be modulated by diverse features of the sperm microenvironment, such as background flows, chemoattractants, and confining geometries. The restriction to Newtonian media throughout the above also serves to emphasise the extensive need for developing the mechanics of sperm swimming in rheological fluids.

Concomitant to such theoretical developments, we have also highlighted the extensive progress that has been made in the digital imaging, video processing, and data analysis of the flagellar waveform. These advances have begun to allow population level data about the flagellum to be extracted from videomicroscopy, as well as high-resolution temporal and 3D spatial information. We have detailed how this presents many opportunities, for instance in using flagellar data for hypothesis testing at population levels, as well as raising a fundamental challenge for the field in parameter estimation and in integrating the many recent and diverse advances, both theoretical and observational, to further our understanding of the sperm flagellum. In summary, our survey has highlighted that the past 70 years of astonishing progress in the mechanics of sperm motility still leaves an immature field, with numerous opportunities and challenges remaining at the interfaces of applied mathematics, physics, and sperm cell and systems biology for the next 70 years.

AUTHOR CONTRIBUTIONS

EG, KI, and BW designed, drafted, and revised this review. All authors contributed to the article and approved the submitted version.

FUNDING

BW is supported by the UK Engineering and Physical Sciences Research Council (EPSRC), grant EP/N509711/1. KI is supported by JSPS-KAKENHI for Young Researchers (18K13456) and JST, PRESTO Grant no. JPMJPR1921.

REFERENCES

Achikanu, C., Correia, J., Guidobaldi, H. A., Giojalas, L. C., Barratt, C. L., Da Silva, S. M., et al. (2019). Continuous behavioural 'switching' in human spermatozoa and its regulation by Ca2+-mobilising stimuli. *Mol. Hum. Reprod.* 25, 423–432. doi: 10.1093/molehr/gaz034

Afzelius, B. (1959). Electron microscopy of the sperm tail-results obtained with a new fixative. *J. Biophys. Biochem. Cytol.* 5, 269. doi: 10.1083/jcb.5.2.269

Ainley, J., Durkin, S., Embid, R., Boindala, P., and Cortez, R. (2008). The method of images for regularized Stokeslets. *J. Comput. Phys.* 227, 4600–4616. doi: 10.1016/j.jcp.2008.01.032

Alvarez, L., Friedrich, B. M., Gompper, G., and Kaupp, U. B. (2014). The computational sperm cell. *Trends Cell Biol.* 24, 198–207. doi: 10.1016/j.tcb.2013.10.004

Amann, R. P., and Katz, D. F. (2004). Andrology lab corner: reflections on CASA after 25 years. *J. Androl.* 25, 317–325. doi: 10.1002/j.1939-4640.2004.tb02793.x

Amann, R. P., and Waberski, D. (2014). Computer-assisted sperm analysis (CASA): capabilities and potential developments. *Theriogenology* 81, 5.e3–17.e3. doi: 10.1016/j.theriogenology.2013.09.004

Baba, S. A., and Mogami, Y. (1985). An approach to digital image analysis of bending shapes of eukaryotic flagella and cilia. *Cell Motil.* 5, 475–489. doi: 10.1002/cm.970050605

Bayly, P. V., and Wilson, K. S. (2014). Equations of interdoublet separation during flagella motion reveal mechanisms of wave propagation and instability. *Biophys. J.* 107, 1756–1772. doi: 10.1016/j.bpj.2014.07.064

Bayly, P. V., and Wilson, K. S. (2015). Analysis of unstable modes distinguishes mathematical models of flagellar motion. *J. R. Soc. Interface* 12, 20150124. doi: 10.1098/rsif.2015.0124

Bell, A. F., and Crimaldi, J. P. (2015). Effect of steady and unsteady flow on chemoattractant plume formation and sperm taxis. *J. Mar. Syst.* 148:236–248. doi: 10.1016/j.jmarsys.2015.03.008

Brenner, H. (1962). Effect of finite boundaries on the Stokes resistance of an arbitrary particle. *J. Fluid Mech.* 12, 35. doi: 10.1017/S0022112062000026

Brokaw, C. (1972a). Flagellar movement-a sliding filament model-an explanation is suggested for spontaneous propagation of bending waves By Flagella. *Science* 178:455. doi: 10.1126/science.178.4060.455

Brokaw, C. J. (1972b). Computer simulation of flagellar movement I. Demonstration of stable bend propagation and bend initiation by the sliding filament model. *Biophys. J.* 12, 564–586. doi: 10.1016/S0006-3495(72)86104-6

Brokaw, C. J. (1975). Computer simulation of flagellar movement. III models incorporating cross bridge kinetics. *J. Mechanochem. Cell Motil.* 3:77.

Bukatin, A., Denissenko, P., and Kantsler, V. (2020). Self-organization and multi-line transport of human spermatozoa in rectangular microchannels due to cell-cell interactions. *Sci. Rep.* 10, 1–8. doi: 10.1038/s41598-020-66803-2

Bukatin, A., Kukhtevich, I., Stoop, N., Dunkel, J., and Kantsler, V. (2015). Bimodal rheotactic behavior reflects flagellar beat asymmetry in human sperm cells. *Proc. Natl. Acad. Sci. U.S.A.* 112, 15904–15909. doi: 10.1073/pnas.1515159112

Burnett, W. E., and Heinze, J. (2014). Sperm bundles in the seminal vesicles of sexually mature lasius ant males. *PLoS ONE* 9:e93383. doi: 10.1371/journal.pone.0093383

Camalet, S., and Jülicher, F. (2000). Generic aspects of axonemal beating. *New J. Phys.* 2:24. doi: 10.1088/1367-2630/2/1/324

Carichino, L., and Olson, S. D. (2019). Emergent three-dimensional sperm motility: coupling calcium dynamics and preferred curvature in a Kirchhoff rod model. *Math. Med. Biol.* 36, 439–469. doi: 10.1093/imammb/dqy015

Cook, S., Brokaw, C., Muller, C., and Babcock, D. (1994). Sperm chemotaxis egg peptides control cytosolic calcium to regulate flagellar responses. *Dev. Biol.* 165, 10–19. doi: 10.1006/dbio.1994.1229

Corkidi, G., Montoya, F., Hernández-Herrera, P., Ríos-Herrera, W., Müller, M., Treviño, C., et al. (2017). Are there intracellular Ca2+ oscillations correlated with flagellar beating in human sperm? a three vs. two-dimensional analysis. *Mol. Hum. Reprod.* 23, 583–593. doi: 10.1093/molehr/gax039

Cortez, R. (2001). The method of regularized Stokeslets. *SIAM J. Sci. Comput.* 23, 1204–1225. doi: 10.1137/S106482750038146X

Cortez, R., Fauci, L., and Medovikov, A. (2005). The method of regularized Stokeslets in three dimensions: analysis, validation, and application to helical swimming. *Phys. Fluids* 17, 031504. doi: 10.1063/1.1830486

Cortez, R., and Nicholas, M. (2012). Slender body theory for Stokes flows with regularized forces. *Commun. Appl. Math. Comput. Sci.* 7, 33–62. doi: 10.2140/camcos.2012.7.33

Cosson, J. J. (2015). *Flagellar Mechanics and Sperm Guidance*. Sharjah: Bentham Science Publishers.

Creppy, A., Plouraboué, F., Praud, O., Druart, X., Cazin, S., Yu, H., et al. (2016). Symmetry-breaking phase transitions in highly concentrated semen. *J. R. Soc. Interface* 13, 20160575. doi: 10.1098/rsif.2016.0575

Creppy, A., Praud, O., Druart, X., Kohnke, P. L., and Plouraboué, F. (2015). Turbulence of swarming sperm. *Phys. Rev. E* 92, 032722. doi: 10.1103/PhysRevE.92.032722

Cripe, P., Richfield, O., and Simons, J. (2016). Sperm pairing and measures of efficiency in planar swimming models. *Spora J. Biomath.* 2, 5. doi: 10.30707/SPORA2.1Cripe

Curtis, M. P., Kirkman-Brown, J. C., Connolly, T. J., and Gaffney, E. A. (2012). Modelling a tethered mammalian sperm cell undergoing hyperactivation. *J. Theor. Biol.* 309, 1–10. doi: 10.1016/j.jtbi.2012.05.035

Daloglu, M. U., Luo, W., Shabbir, F., Lin, F., Kim, K., Lee, I., et al. (2018). Label-free 3D computational imaging of spermatozoon locomotion, head spin and flagellum beating over a large volume. *Light Sci. Appl.* 7, 17121. doi: 10.1038/lsa.2017.121

Daloglu, M. U., and Ozcan, A. (2017). Computational imaging of sperm locomotion. *Biol. Reprod.* 97, 182–188. doi: 10.1093/biolre/iox086

Davis, R. O., and Katz, D. F. (1989). Computer-aided sperm analysis (CASA): image digitization and processing. *Biomater. Artif. Cells Artif. Organs* 17, 93–116. doi: 10.3109/10731198909118272

Denissenko, P., Kantsler, V., Smith, D. J., and Kirkman-Brown, J. (2012). Human spermatozoa migration in microchannels reveals boundary-following navigation. *Proc. Natl. Acad. Sci. U.S.A.* 109, 8007–8010. doi: 10.1073/pnas.1202934109

Dillon, R. H., Fauci, L. J., Omoto, C., and Yang, X. (2007). Fluid dynamic models of flagellar and ciliary beating. *Ann. N.Y. Acad. Sci.* 1101, 494–505. doi: 10.1196/annals.1389.016

Djakiew, D., and Jones, R. (1983). Sperm maturation, fluid transport, and secretion and absorption of protein in the epididymis of the echidna, tachyglossus aculeatus. *Reproduction* 68, 445–456. doi: 10.1530/jrf.0.0680445

Dresdner, R., Katz, D., and Berger, S. (1980). The propulsion by large-amplitude waves of uniflagellar microorganisms of finite length. *J. Fluid Mech.* 97, 591–621. doi: 10.1017/S0022112080002716

du Roure, O., Lindner, A., Nazockdast, E. N., and Shelley, M. J. (2019). Dynamics of flexible fibers in viscous flows and fluids. *Ann. Rev. Fluid Mech.* 51, 539–572. doi: 10.1146/annurev-fluid-122316-045153

Eisenbach, M., and Giojalas, L. (2006). Sperm guidance in mammals-an unpaved road to the egg. *Nat. Rev. Mol. Cell Biol.* 7, 276–285. doi: 10.1038/nrm1893

Elfring, G. J., and Lauga, E. (2009). Hydrodynamic phase locking of swimming microorganisms. *Phys. Rev. Lett.* 103:088101. doi: 10.1103/PhysRevLett.103.088101

Elfring, G. J., and Lauga, E. (2011). Synchronization of flexible sheets. *J. Fluid Mech.* 674, 163–173. doi: 10.1017/S0022112011000814

Elgeti, J., Kaupp, U. B., and Gompper, G. (2010). Hydrodynamics of sperm cells near surfaces. *Biophys. J.* 99, 1018–1026. doi: 10.1016/j.bpj.2010.05.015

Fauci, L. J., and McDonald, A. (1995). Sperm motility in the presence of boundaries. *Bull. Math. Biol.* 57, 679–699. doi: 10.1016/S0092-8240(05)80768-2

Fawcett, D., and Porter, K. (1954). A study of the fine structure of ciliated epithelia. *J. Morphol.* 94, 221–282. doi: 10.1002/jmor.1050940202

Fisher, H. S., Giomi, L., Hoekstra, H. E., and Mahadevan, L. (2014). The dynamics of sperm cooperation in a competitive environment. *Proc. R. Soc. B Biol. Sci.* 281, 20140296. doi: 10.1098/rspb.2014.0296

Friedrich, B. M., and Jülicher, F. (2007). Chemotaxis of sperm cells. *Proc. Natl. Acad. Sci. U.S.A.* 104, 13256–13261. doi: 10.1073/pnas.0703530104

Friedrich, B. M., Riedel-Kruse, I. H., Howard, J., and Julicher, F. (2010). High-precision tracking of sperm swimming fine structure provides strong test of resistive force theory. *J. Exper. Biol.* 213, 1226–1234. doi: 10.1242/jeb.039800

Fu, H. C., Powers, T. R., and Wolgemuth, C. W. (2007). Theory of swimming filaments in viscoelastic media. *Phys. Rev. Lett.* 99:258101. doi: 10.1103/PhysRevLett.99.258101

Fu, H. C., Wolgemuth, C. W., and Powers, T. R. (2008). Beating patterns of filaments in viscoelastic fluids. *Phys. Rev. E* 78:041913. doi: 10.1103/PhysRevE.78.041913

Fu, H. C., Wolgemuth, C. W., and Powers, T. R. (2009). Swimming speeds of filaments in nonlinearly viscoelastic fluids. *Phys. Fluids* 21:033102. doi: 10.1063/1.3086320

Fulford, G. R., Katz, D. F., and Powell, R. L. (1998). Swimming of spermatozoa in a linear viscoelastic fluid. *Biorheology* 35, 295–309. doi: 10.1016/S0006-355X(99)80012-2

Gadêlha, H., and Gaffney, E. A. (2019). Flagellar ultrastructure suppresses buckling instabilities and enables mammalian sperm navigation in high-viscosity media. *J. R. Soc. Interface* 16, 20180668. doi: 10.1098/rsif.2018.0668

Gadêlha, H., Gaffney, E. A., Smith, D. J., and Kirkman-Brown, J. C. (2010). Nonlinear instability in flagellar dynamics: a novel modulation mechanism in sperm migration? *J. R. Soc. Interface* 7, 1689–1697. doi: 10.1098/rsif.2010.0136

Gadêlha, H., Hernández-Herrera, P., Montoya, F., Darszon, A., and Corkidi, G. (2020). Human sperm uses asymmetric and anisotropic flagellar controls to regulate swimming symmetry and cell steering. *Sci. Adv.* 6: eaba5168. doi: 10.1126/sciadv.aba5168

Gadêlha, H., Hernández-Herrera, P., Montoya, F., Darszon, A., and Corkidi, G. (2021). Retraction of the research article: "human sperm uses asymmetric and anisotropic flagellar controls to regulate swimming symmetry and cell steering". *Sci. Adv.* 7:eaau9116. doi: 10.1126/sciadv.aau9116

Gaffney, E. A., Gadêlha, H., Smith, D. J., Blake, J. R., and Kirkman-Brown, J. C. (2011). Mammalian sperm motility: observation and theory. *Ann. Rev. Fluid Mech.* 43, 501–528. doi: 10.1146/annurev-fluid-121108-145442

Gallagher, M. T., Cupples, G., Ooi, E. H., Kirkman-Brown, J. C., and Smith, D. J. (2019). Rapid sperm capture: high-throughput flagellar waveform analysis. *Hum. Reprod.* 34, 1173–1185. doi: 10.1093/humrep/dez056

Gallagher, M. T., and Smith, D. J. (2018). Meshfree and efficient modeling of swimming cells. *Phys. Rev. Fluids* 3:053101. doi: 10.1103/PhysRevFluids.3.053101

Gallagher, M. T., Smith, D. J., and Kirkman-Brown, J. C. (2018). CASA: tracking the past and plotting the future. *Reprod. Fertil. Dev.* 30, 867. doi: 10.1071/RD17420

Gillies, E. A., Cannon, R. M., Green, R. B., and Pacey, A. A. (2009). Hydrodynamic propulsion of human sperm. *J. Fluid Mech.* 625, 445–474. doi: 10.1017/S0022112008005685

Goldstein, R. E., Lauga, E., Pesci, A. I., and Proctor, M. R. E. (2016). Elastohydrodynamic synchronization of adjacent beating flagella. *Phys. Rev. Fluids* 1, 073201. doi: 10.1103/PhysRevFluids.1.073201

Goldstein, T., Bresson, X., and Osher, S. (2010). Geometric applications of the split bregman method: segmentation and surface reconstruction. *J. Sci. Comput.* 45, 272–293. doi: 10.1007/s10915-009-9331-z

Gray, J. (1955). The Movement of sea-urchin spermatozoa. *J. Exper. Biol.* 32, 775–800. doi: 10.1242/jeb.32.4.775

Gray, J., and Hancock, G. J. (1955). The propulsion of sea-urchin spermatozoa. *J. Exper. Biol.* 32, 802–814. doi: 10.1242/jeb.32.4.802

Guasto, J. S., Estrada, J. B., Menolascina, F., Burton, L. J., Patel, M., Franck, C., et al. (2020). Flagellar kinematics reveals the role of environment in shaping sperm motility. *J. R. Soc. Interface* 17, 20200525. doi: 10.1098/rsif.2020.0525

Hall-McNair, A. L., Montenegro-Johnson, T. D., Gadêlha, H., Smith, D. J., and Gallagher, M. T. (2019). Efficient implementation of elastohydrodynamics via integral operators. *Phys. Rev. Fluids* 4, 1–24. doi: 10.1103/PhysRevFluids.4.113101

Hansen, J., Rassmann, S., Jikeli, J., and Wachten, D. (2018). SpermQ-a simple analysis software to comprehensively study flagellar beating and sperm steering. *Cells* 8, 10. doi: 10.3390/cells8010010

Hansen, J. N., Gong, A., Wachten, D., Pascal, R., Turpin, A., Jikeli, J. F., et al. (2020). Multifocal imaging for precise, label-free tracking of fast biological processes in 3D. *bioRxiv*. doi: 10.1101/2020.05.16.099390

Hernandez-Herrera, P., Montoya, F., Rendon-Mancha, J. M., Darszon, A., and Corkidi, G. (2018). 3-D+t human sperm flagellum tracing in low SNR fluorescence images. *IEEE Trans. Med. Imaging* 37, 2236–2247. doi: 10.1109/TMI.2018.2840047

Higdon, J. J. L. (1979). A hydrodynamic analysis of flagellar propulsion. *J. Fluid Mech.* 90, 685. doi: 10.1017/S0022112079002482

Hines, M., and Blum, J. (1978). Bend propagation in flagella. I. Derivation of equations of motion and their simulation. *Biophys. J.* 23, 41–57. doi: 10.1016/S0006-3495(78)85431-9

Hongsheng, L. I, Tian, S., Smith, M. B., Fujiwara, I., Vavylonis, D., and Xiaolei, H. (2009). "Automated actin filament segmentation, tracking and tip elongation measurements based on open active contour models," in *2009 IEEE International Symposium on Biomedical Imaging: From Nano to Macro* (New York, NY: IEEE), 1302–1305.

Huang, J., Carichino, L., and Olson, S. D. (2018). Hydrodynamic interactions of actuated elastic filaments near a planar wall with applications to sperm motility. *J. Coupled Syst. Multiscale Dyn.* 6, 163–175. doi: 10.1166/jcsmd.2018.1166

Hussain, Y. H., Guasto, J. S., Zimmer, R. K., Stocker, R., and Riffell, J. A. (2016). Sperm chemotaxis promotes individual fertilization success in sea urchins. *J. Exper. Biol.* 219, 1458–1466. doi: 10.1242/jeb.134924

Hyakutake, T., Sato, K., and Sugita, K. (2019). Study of bovine sperm motility in shear-thinning viscoelastic fluids. *J. Biomech.* 88, 130–137. doi: 10.1016/j.jbiomech.2019.03.035

Ishijima, S. (2011). Dynamics of flagellar force generated by a hyperactivated spermatozoon. *Reproduction* 142, 409–415. doi: 10.1530/REP-10-0445

Ishijima, S., Baba, S. A., Mohri, H., and Suarez, S. S. (2002). Quantitative analysis of flagellar movement in hyperactivated and acrosome-reacted golden hamster spermatozoa. *Mol. Reprod. Dev.* 61, 376–384. doi: 10.1002/mrd.10017

Ishimoto, K., Cosson, J., and Gaffney, E. (2016). A simulation study of sperm motility hydrodynamics near fish eggs and spheres. *J. Theor. Biol.* 389:187–197. doi: 10.1016/j.jtbi.2015.10.013

Ishimoto, K., Gadêlha, H., Gaffney, E. A., Smith, D. J., and Kirkman-Brown, J. (2017). Coarse-graining the fluid flow around a human sperm. *Phys. Rev. Lett.* 118, 124501. doi: 10.1103/PhysRevLett.118.124501

Ishimoto, K., Gadêlha, H., Gaffney, E. A., Smith, D. J., and Kirkman-Brown, J. (2018). Human sperm swimming in a high viscosity mucus analogue. *J. Theor. Biol.* 446:1–10. doi: 10.1016/j.jtbi.2018.02.013

Ishimoto, K., and Gaffney, E. A. (2014). A study of spermatozoan swimming stability near a surface. *J. Theor. Biol.* 360:187–199. doi: 10.1016/j.jtbi.2014.06.034

Ishimoto, K., and Gaffney, E. A. (2015). Fluid flow and sperm guidance: a simulation study of hydrodynamic sperm rheotaxis. *J. R. Soc. Interface* 12, 20150172. doi: 10.1098/rsif.2015.0172

Ishimoto, K., and Gaffney, E. A. (2016). Mechanical tuning of mammalian sperm behaviour by hyperactivation, rheology and substrate adhesion: a numerical exploration. *J. R. Soc. Interface* 13, 20160633. doi: 10.1098/rsif.2016.0633

Ishimoto, K., and Gaffney, E. A. (2018a). An elastohydrodynamical simulation study of filament and spermatozoan swimming driven by internal couples. *IMA J. Appl. Math.* 83, 655–679. doi: 10.1093/imamat/hxy025

Ishimoto, K., and Gaffney, E. A. (2018b). Hydrodynamic clustering of human sperm in viscoelastic fluids. *Sci. Rep.* 8, 1–11. doi: 10.1038/s41598-018-33584-8

Jikeli, J. F., Alvarez, L., Friedrich, B. M., Wilson, L. G., Pascal, R., Colin, R., et al. (2015). Sperm navigation along helical paths in 3D chemoattractant landscapes. *Nat. Commun.* 6, 7985. doi: 10.1038/ncomms8985

Johnson, R. (1980). An improved slender-body theory for stokes flow. *J. Fluid Mech.* 99:411–431. doi: 10.1017/S0022112080000687

Johnson, R. E., and Brokaw, C. J. (1979). Flagellar hydrodynamics. A comparison between resistive-force theory and slender-body theory. *Biophys. J.* 25, 113–127. doi: 10.1016/S0006-3495(79)85281-9

Kamal, A., and Keaveny, E. E. (2018). Enhanced locomotion, effective diffusion and trapping of undulatory micro-swimmers in heterogeneous environments. *J. R. Soc. Interface* 15, 20180592. doi: 10.1098/rsif.2018.0592

Kantsler, V., Dunkel, J., Blayney, M., and Goldstein, R. E. (2014). Rheotaxis facilitates upstream navigation of mammalian sperm cells. *eLife* 3:e03521. doi: 10.7554/eLife.02403

Kantsler, V., Dunkel, J., Polin, M., and Goldstein, R. E. (2013). Ciliary contact interactions dominate surface scattering of swimming eukaryotes. *Proc. Natl. Acad. Sci. U.S.A.* 110, 1187–1192. doi: 10.1073/pnas.1210548110

Katz, D. F., Blake, J. R., and Paveri-Fontana, S. L. (1975). On the movement of slender bodies near plane boundaries at low Reynolds number. *J. Fluid Mech.* 72, 529. doi: 10.1017/S0022112075003126

Katz, D. F., Mills, R. N., and Pritchett, T. R. (1978). The movement of human spermatozoa in cervical mucus. *Reproduction* 53, 259–265. doi: 10.1530/jrf.0.0530259

Kaupp, U., Solzin, J., Hildebrand, E., Brown, J., Helbig, A., Hagen, V., et al. (2003). The signal flow and motor response controling chemotaxis of sea urchin sperm. *Nat. Cell Biol.* 5, 109–117. doi: 10.1038/ncb915

Kaupp, U. B., and Alvarez, L. (2016). Sperm as microswimmers-navigation and sensing at the physical limit. *Eur. Phys. J. Spec. Top.* 225, 2119–2139. doi: 10.1140/epjst/e2016-60097-1

Keller, J. B., and Rubinow, S. I. (1976). Slender-body theory for slow viscous flow. *J. Fluid Mech.* 75, 705–714. doi: 10.1017/S0022112076000475

Kumar, M., Walkama, D. M., Guasto, J. S., and Ardekani, A. M. (2019). Flow-induced buckling dynamics of sperm flagella. *Phys. Rev. E* 100, 063107. doi: 10.1103/PhysRevE.100.063107

Lange, S., and Friedrich, B. M. (2021). Sperm chemotaxis in marine species is optimal at physiological flow rates according theory of filament surfing. *PLoS Comput. Biol*. 17:e1008826. doi: 10.1371/journal.pcbi.1008826

Larson, K., Olson, S. D., and Matzavinos, A. (2021). A bayesian framework to estimate fluid and material parameters in micro-swimmer models. *Bull. Math. Biol*. 83, 1–25. doi: 10.1007/s11538-020-00852-6

Lauga, E. (2020). *The Fluid Dynamics of Cell Motility, Vol. 62*. Cambridge: Cambridge University Press.

Lauga, E., and Powers, T. R. (2009). The hydrodynamics of swimming microorganisms. *Rep. Prog. Phys*. 72:096601. doi: 10.1088/0034-4885/72/9/096601

Li, G., and Ardekani, A. M. (2016). Collective motion of microorganisms in a viscoelastic fluid. *Phys. Rev. Lett*. 117:118001. doi: 10.1103/PhysRevLett.117.118001

Lindemann, C. B. (1994a). A 'geometric clutch' hypothesis to explain oscillations of the axoneme of cilia and flagella. *J. Theor. Biol*. 168, 175–189. doi: 10.1006/jtbi.1994.1097

Lindemann, C. B. (1994b). A model of flagellar and ciliary functioning which uses the forces transverse to the axoneme as the regulator of dynein activation. *Cell Motil. Cytoskeleton* 29, 141–154. doi: 10.1002/cm.970290206

Lindemann, C. B. (2002). Geometric clutch model version 3: the role of the inner and outer arm dyneins in the ciliary beat. *Cell Motil. Cytoskeleton* 52, 242–254. doi: 10.1002/cm.10049

Lindemann, C. B., and Lesich, K. A. (2010). Flagellar and ciliary beating: the proven and the possible. *J. Cell Sci*. 123, 519–528. doi: 10.1242/jcs.051326

Llopis, I., Pagonabarraga, I., Cosentino Lagomarsino, M., and Lowe, C. P. (2013). Cooperative motion of intrinsic and actuated semiflexible swimmers. *Phys. Rev. E* 87:032720. doi: 10.1103/PhysRevE.87.032720

Lonergan, P. (2018). Review: historical and futuristic developments in bovine semen technology. *Animal* 12, s4–s18. doi: 10.1017/S175173111800071X

Lu, X. (2013). "Chapter seven-fluorescent imaging of drosophila melanogaster sperm in the reproductive tract: a new model of flagellar motility," in *Methods in Enzymology, Cilia, Part B, Vol. 525*, ed W. F. Marshall (Amsterdam: Academic Press), 131–148.

Machin, K. E. (1958). Wave propagation along flagella. *J. Exper. Biol*. 35, 796–806. doi: 10.1242/jeb.35.4.796

Miki, K., and Clapham, D. E. (2013). Rheotaxis guides mammalian sperm. *Curr. Biol*. 23, 443–452. doi: 10.1016/j.cub.2013.02.007

Miller, R. (1966). Chemotaxis during fertilization in hydroid campanularia. *J. Exper. Zool*. 162, 23–44. doi: 10.1002/jez.1401620104

Miller, R. L., and Brokaw, C. J. (1970). Chemotactic turning behaviour of tubularia spermatozoa. *J. Exper. Biol*. 52, 699–706. doi: 10.1242/jeb.52.3.699

Minoura, I., Yagi, T., and Kamiya, R. (1999). Direct measurement of inter-doublet elasticity in flagellar axonemes. *Cell Struct. Funct*. 24, 27–33. doi: 10.1247/csf.24.27

Montenegro-Johnson, T., Gadêlha, H., and Smith, D. J. (2015). Spermatozoa scattering by a microchannel feature: an elastohydrodynamic model. *R. Soc. Open Sci*. 2:140475. doi: 10.1098/rsos.140475

Moore, H., Dvoráková, K., Jenkins, N., and Breed, W. (2002). Exceptional sperm cooperation in the wood mouse. *Nature* 418, 174–177. doi: 10.1038/nature00832

Moore, H. D., and Taggart, D. (1995). Sperm pairing in the opossum increases the efficiency of sperm movement in a viscous environment. *Biol. Reprod*. 52, 947–953. doi: 10.1095/biolreprod52.4.947

Moreau, C., Giraldi, L., and Gadêlha, H. (2018). The asymptotic coarse-graining formulation of slender-rods, bio-filaments and flagella. *J. R. Soc. Interface* 15, 20180235. doi: 10.1098/rsif.2018.0235

Mortimer, S. T. (1997). A critical review of the physiological importance and analysis of sperm movement in mammals. *Hum. Reprod. Update* 3, 403–439. doi: 10.1093/humupd/3.5.403

Mortimer, S. T., Swan, M. A., and Mortimer, D. (1998). Effect of seminal plasma on capacitation and hyperactivation in human spermatozoa. *Hum. Reprod*. 13, 2139–2146. doi: 10.1093/humrep/13.8.2139

Murase, M., Hines, M., and Blum, J. J. (1989). Properties of an excitable dynein model for bend propagation in cilia and flagella. *J. Theor. Biol*. 139:413–430. doi: 10.1016/S0022-5193(89)80219-X

Muschol, M., Wenders, C., and Wennemuth, G. (2018). Four-dimensional analysis by high-speed holographic imaging reveals a chiral memory of sperm flagella. *PLoS ONE* 13:e0199678. doi: 10.1371/journal.pone.0199678

Neal, C. V., Hall-McNair, A. L., Kirkman-Brown, J., Smith, D. J., and Gallagher, M. T. (2020). Doing more with less: the flagellar end piece enhances the propulsive effectiveness of human spermatozoa. *Phys. Rev. Fluids* 5:073101. doi: 10.1103/PhysRevFluids.5.073101

Nosrati, R., Driouchi, A., Yip, C. M., and Sinton, D. (2015). Two-dimensional slither swimming of sperm within a micrometre of a surface. *Nat. Commun*. 6, 8703. doi: 10.1038/ncomms9703

Nosrati, R., Graham, P. J., Liu, Q., and Sinton, D. (2016). Predominance of sperm motion in corners. *Sci. Rep*. 6, 1–9. doi: 10.1038/srep26669

Olson, S. D. (2013). Fluid dynamic model of invertebrate sperm chemotactic motility with varying calcium inputs. *J. Biomech*. 46, 329–337. doi: 10.1016/j.jbiomech.2012.11.025

Olson, S. D., Lim, S., and Cortez, R. (2013). Modeling the dynamics of an elastic rod with intrinsic curvature and twist using a regularized Stokes formulation. *J. Comput. Phys*. 238, 169–187. doi: 10.1016/j.jcp.2012.12.026

Overstreet, J., Katz, D., Hanson, F., and Fonseca, J. (1979). Simple inexpensive method for objective assessment of human sperm movement characteristics. *Fertil. Steril*. 31, 162–172. doi: 10.1016/S0015-0282(16)43817-3

Pearce, D. J., Hoogerbrugge, L., Hook, K. A., Fisher, H. S., and Giomi, L. (2018). Cellular geometry controls the efficiency of motile sperm aggregates. *J. R. Soc. Interface* 15, 20180702. doi: 10.1098/rsif.2018.0702

Pearcy, M., Delescaille, N., Lybaert, P., and Aron, S. (2014). Team swimming in ant spermatozoa. *Biol. Lett*. 10:20140308. doi: 10.1098/rsbl.2014.0308

Pelle, D. W., Brokaw, C. J., Lesich, K. A., and Lindemann, C. B. (2009). Mechanical properties of the passive sea urchin sperm flagellum. *Cell Motil. Cytoskeleton* 66, 721–735. doi: 10.1002/cm.20401

Phanthien, N., Trancong, T., and Ramia, M. (1987). A boundary-element analysis of flagellar propulsion. *J. Fluid Mech*. 184, 533–549. doi: 10.1017/S0022112087003008

Pitnick, S., Spicer, G. S., and Markow, T. A. (1995). How long is a giant sperm? *Nature* 375, 109. doi: 10.1038/375109a0

Pozrikidis, C. (1992). *Boundary Integral and Singularity Methods for Linearized Viscous Flow*. Cambridge: Cambridge University Press.

Pozrikidis, C. (2002). *A Practical Guide to Boundary Element Methods with the Software Library BEMLIB*. Boca Raton, FL: CRC Press.

Priego-Espinosa, D. A., Darszon, A., Guerrero, A., Gonzalez-Cota, A. L., Nishigaki, T., Martinez-Mekler, G., et al. (2020). Modular analysis of the control of flagellar Ca2+-spike trains produced by CatSper and Ca-V channels in sea urchin sperm. *PLoS Comput. Biol*. 16:e1007605. doi: 10.1371/journal.pcbi.1007605

Ramia, M., Tullock, D. L., and Phan-Thien, N. (1993). The role of hydrodynamic interaction in the locomotion of microorganisms. *Biophys. J*. 65, 755–778. doi: 10.1016/S0006-3495(93)81129-9

Riedel, I. H., Kruse, K., and Howard, J. (2005). A self-organized vortex array of hydrodynamically entrained sperm cells. *Science* 309, 300–303. doi: 10.1126/science.1110329

Riedel-Kruse, I. H., and Hilfinger, A. (2007). How molecular motors shape the flagellar beat. *HFSP J*. 1, 192–208. doi: 10.2976/1.2773861

Riffell, J. A., and Zimmer, R. K. (2007). Sex and flow: the consequences of fluid shear for sperm-egg interactions. *J. Exper. Biol*. 210, 3644–3660. doi: 10.1242/jeb.008516

Rikmenspoel, R. (1965). Tail movement of bull spermatozoa. *Obs. Model Calculations Biophys. J*. 5, 365–392. doi: 10.1016/S0006-3495(65)86723-6

Rikmenspoel, R. (1971). Contractile mechanisms in flagella. *Biophys. J*. 11, 446–463. doi: 10.1016/S0006-3495(71)86227-6

Rikmenspoel, R. (1978a). Equation of motion for sperm flagella. *Biophys. J*. 23, 177–206. doi: 10.1016/S0006-3495(78)85442-3

Rikmenspoel, R. (1978b). Movement of sea urchin sperm flagella. *J. Cell Biol*. 76, 310–322. doi: 10.1083/jcb.76.2.310

Rikmenspoel, R., and Isles, C. (1985). Digitized precision measurements of the movements of sea urchin sperm flagella. *Biophys. J*. 47, 395–410. doi: 10.1016/S0006-3495(85)83931-X

Rikmenspoel, R., Vanherpen, G., and Eijkhout, P. (1960). Cinematographic observations of the movements of bull sperm cells. *Phys. Med. Biol*. 5, 167–181. doi: 10.1088/0031-9155/5/2/306

Rode, S., Elgeti, J., and Gompper, G. (2019). Sperm motility in modulated microchannels. *New J. Phys*. 21:013016. doi: 10.1088/1367-2630/aaf544

Rothschild, L. (1963). Non-random distribution of bull spermatozoa in a drop of sperm suspension. *Nature* 198, 1221–1222. doi: 10.1038/1981221a0

Saintillan, D., and Shelley, M. J. (2007). Orientational order and instabilities in suspensions of self-locomoting rods. *Phys. Rev. Lett*. 99:058102. doi: 10.1103/PhysRevLett.99.058102

Sanchez-Cardenas, C., Montoya, F., Navarrete, F., Hernandez-Cruz, A., Corkidi, G., Visconti, P., et al. (2018). Intracellular Ca2+ threshold reversibly switches flagellar beat off and on. *Biol. Reprod*. 99, 1010–1021. doi: 10.1093/biolre/ioy132

Sanderson, M., and Sleigh, M. (1981). Ciliary activity of cultured rabbit tracheal epithelium-beat pattern and metachrony. *J. Cell Sci*. 47, 331–347. doi: 10.1242/jcs.47.1.331

Schoeller, S. F., Holt, W. V., and Keaveny, E. E. (2020). Collective dynamics of sperm cells. *Philos. Trans. R. Soc. B* 375, 20190384. doi: 10.1098/rstb.2019.0384

Schoeller, S. F., and Keaveny, E. E. (2018). From flagellar undulations to collective motion: predicting the dynamics of sperm suspensions. *J. R. Soc. Interface* 15:20170834. doi: 10.1098/rsif.2017.0834

Shiba, K., Baba, S. A., Inoue, T., and Yoshida, M. (2008). Ca2+ bursts occur around a local minimal concentration of attractant and trigger sperm chemotactic response. *Proc. Natl. Acad. Sci. U.S.A*. 105, 19312–19317. doi: 10.1073/pnas.0808580105

Shilatifard, A., and Yeagle, P. (2020). Editorial expression of concern. *Sci. Adv*. 6, 1171. doi: 10.1126/sciadv.abe3154

Silva-Villalobos, F., Pimentel, J. A., Darszon, A., and Corkidi, G. (2014). "Imaging of the 3D dynamics of flagellar beating in human sperm," in *2014 36th Annual International Conference of the IEEE Engineering in Medicine and Biology Society* (New York, NY: IEEE), 190–193.

Simons, J., Fauci, L., and Cortez, R. (2015). A fully three-dimensional model of the interaction of driven elastic filaments in a Stokes flow with applications to sperm motility. *J. Biomech*. 48, 1639–1651. doi: 10.1016/j.jbiomech.2015.01.050

Simons, J., Olson, S., Cortez, R., and Fauci, L. (2014). The dynamics of sperm detachment from epithelium in a coupled fluid-biochemical model of hyperactivated motility. *J. Theor. Biol*. 354, 81–94. doi: 10.1016/j.jtbi.2014.03.024

Sleigh, M. (1962). *The Biology of Cilia and Flagella*. Oxford: Pergamon Press, Ltd.

Sleigh, M. (1974). "Patterns of movement of cilia and flagella," in *Cilia and Flagella*, ed M. Sleigh (London: Academic Press), 79–92.

Smith, D., Gaffney, E., Blake, J., and Kirkman-Brown, J. (2009a). Human sperm accumulation near surfaces: a simulation study. *J. Fluid Mech*. 621, 289–320. doi: 10.1017/S0022112008004953

Smith, D. J. (2009). A boundary element regularized Stokeslet method applied to cilia- and flagella-driven flow. *Proc. R. Soc. A Math. Phys. Eng. Sci*. 465, 3605–3626. doi: 10.1098/rspa.2009.0295

Smith, D. J., Gaffney, E., Gadêlha, H., Kapur, N., and Kirkman-Brown, J. (2009b). Bend propagation in the flagella of migrating human sperm, and its modulation by viscosity. *Cell Motil. Cytoskeleton* 66, 220–236. doi: 10.1002/cm.20345

Su, T.-W., Choi, I., Feng, J., Huang, K., McLeod, E., and Ozcan, A. (2013). Sperm trajectories form chiral ribbons. *Sci. Rep*. 3, 1664. doi: 10.1038/srep01664

Su, T.-W., Xue, L., and Ozcan, A. (2012). High-throughput lensfree 3d tracking of human sperms reveals rare statistics of helical trajectories. *Proc. Natl Acad. Sci. U.S.A*. 109, 16018–16022. doi: 10.1073/pnas.1212506109

Suarez, S., Katz, D., Owen, D., Andrew, J., and Powell, R. (1991). Evidence for the function of hyperactivated motility in sperm. *Biol. Reprod*. 44, 375–381. doi: 10.1095/biolreprod44.2.375

Summers, K., and Gibbons, I. (1971). Adenosine triphosphate-induced sliding of tubules in trypsin-treated flagella of sea-urchin sperm. *Proc. Natl. Acad. Sci. U.S.A*. 68, 3092–3096. doi: 10.1073/pnas.68.12.3092

Taketoshi, N., Omori, T., and Ishikawa, T. (2020). Elasto-hydrodynamic interaction of two swimming spermatozoa. *Phys. Fluids* 32, 101901. doi: 10.1063/5.0022107

Taylor, G. (1951). Analysis of the swimming of microscopic organisms. *Proc. R. Soc. Lond. Ser. A Math. Phys. Sci*. 209, 447–461. doi: 10.1098/rspa.1951.0218

Thomases, B., and Guy, R. D. (2017). The role of body flexibility in stroke enhancements for finite-length undulatory swimmers in viscoelastic fluids. *J. Fluid Mech*. 825, 109–132. doi: 10.1017/jfm.2017.383

Tornberg, A. K., and Shelley, M. J. (2004). Simulating the dynamics and interactions of flexible fibers in Stokes flows. *J. Comput. Phys*. 196, 8–40. doi: 10.1016/j.jcp.2003.10.017

Tung, C.-,k., Lin, C., Harvey, B., Fiore, A. G., Ardon, F., Wu, M., et al. (2017). Fluid viscoelasticity promotes collective swimming of sperm. *Sci. Rep*. 7, 3152. doi: 10.1038/s41598-017-03341-4

Tung, C.-K., Ardon, F., Fiore, A. G., Suarez, S. S., and Wu, M. (2014). Cooperative roles of biological flow and surface topography in guiding sperm migration revealed by a microfluidic model. *Lab. Chip* 14, 1348–1356. doi: 10.1039/C3LC51297E

Vernon, G. G., and Woolley, D. M. (2002). Microtubule displacements at the tips of living flagella. *Cell Motil. Cytoskeleton* 52, 151–160. doi: 10.1002/cm.10041

Vernon, G. G., and Woolley, D. M. (2004). Basal sliding and the mechanics of oscillation in a mammalian sperm flagellum. *Biophys. J*. 87, 3934–3944. doi: 10.1529/biophysj.104.042648

Walker, B. J., Ishimoto, K., Gadêlha, H., and Gaffney, E. A. (2019a). Filament mechanics in a half-space via regularised Stokeslet segments. *J. Fluid Mech*. 879, 808–833. doi: 10.1017/jfm.2019.723

Walker, B. J., Ishimoto, K., and Gaffney, E. A. (2019b). Pairwise hydrodynamic interactions of synchronized spermatozoa. *Phys. Rev. Fluids* 4:093101. doi: 10.1103/PhysRevFluids.4.093101

Walker, B. J., Ishimoto, K., and Gaffney, E. A. (2020a). Efficient simulation of filament elastohydrodynamics in three dimensions. *Phys. Rev. Fluids* 5:123103. doi: 10.1103/PhysRevFluids.5.123103

Walker, B. J., Ishimoto, K., and Wheeler, R. J. (2019c). Automated identification of flagella from videomicroscopy via the medial axis transform. *Sci. Rep*. 9, 5015. doi: 10.1038/s41598-019-41459-9

Walker, B. J., Phuyal, S., Ishimoto, K., Tung, C.-K., and Gaffney, E. A. (2020b). Computer-assisted beat-pattern analysis and the flagellar waveforms of bovine spermatozoa. *R. Soc. Open Sci*. 7:200769. doi: 10.1098/rsos.200769

Walker, B. J., and Wheeler, R. J. (2019). High-speed multifocal plane fluorescence microscopy for three-dimensional visualisation of beating flagella. *J. Cell Sci*. 132:jcs231795. doi: 10.1242/jcs.231795

Walker, B. J., Wheeler, R. J., Ishimoto, K., and Gaffney, E. A. (2019d). Boundary behaviours of *Leishmania mexicana*: a hydrodynamic simulation study. *J. Theor. Biol*. 462:311–320. doi: 10.1016/j.jtbi.2018.11.016

Ward, G. E., Brokaw, C. J., Garbers, D. L., and Vacquier, V. D. (1985). Chemotaxis of Arbacia punctulata spermatozoa to resact, a peptide from the egg jelly layer. *J. Cell Biol*. 101, 2324–2329. doi: 10.1083/jcb.101.6.2324

Wensink, H. H., Dunkel, J., Heidenreich, S., Drescher, K., Goldstein, R. E., Löwen, H., et al. (2012). Meso-scale turbulence in living fluids. *Proc. Natl. Acad. Sci. U.S.A*. 109, 14308–14313. doi: 10.1073/pnas.1202032109

WHO (2010). *WHO Laboratory Manual for the Examination and Processing of Human Semen*. Technical Report, Geneva.

Wilson, L. G., Carter, L. M., and Reece, S. E. (2013). High-speed holographic microscopy of malaria parasites reveals ambidextrous flagellar waveforms. *Proc. Natl. Acad. Sci. U.S.A*. 110, 18769–18774. doi: 10.1073/pnas.1309934110

Wood, C. D., Nishigaki, T., Furuta, T., Baba, S. A., and Darszon, A. (2005). Real-time analysis of the role of Ca2+ in flagellar movement and motility in single sea urchin sperm. *J. Cell Biol*. 169, 725–731. doi: 10.1083/jcb.200411001

Woolley, D. (2003). Motility of spermatozoa at surfaces. *Reproduction* 126, 259–270. doi: 10.1530/rep.0.1260259

Woolley, D. M., Crockett, R. F., Groom, W. D. I., and Revell, S. G. (2009). A study of synchronisation between the flagella of bull spermatozoa, with related observations. *J. Exper. Biol*. 212, 2215–2223. doi: 10.1242/jeb.028266

Xiao, X., Geyer, V. F., Bowne-Anderson, H., Howard, J., and Sbalzarini, I. F. (2016). Automatic optimal filament segmentation with sub-pixel accuracy using generalized linear models and B-spline level-sets. *Med. Image Anal*. 32, 157–172. doi: 10.1016/j.media.2016.03.007

Xu, T., Vavylonis, D., and Huang, X. (2014). 3D actin network centerline extraction with multiple active contours. *Med. Image Anal*. 18, 272–284. doi: 10.1016/j.media.2013.10.015

Yang, H.-F., Descombes, X., Prigent, S., Malandain, G., Druart, X., and Plouraboue, F. (2014a). "Head tracking and flagellum tracing for sperm motility analysis," in *2014 IEEE 11th International Symposium on Biomedical Imaging (ISBI)* (New York, NY: IEEE), 310–313.

Yang, Y., Elgeti, J., and Gompper, G. (2008). Cooperation of sperm in two dimensions: Synchronization, attraction, and aggregation

through hydrodynamic interactions. *Phys. Rev. E* 78:061903. doi: 10.1103/PhysRevE.78.061903

Yang, Y., and Lu, X. (2011). Drosophila sperm motility in the reproductive tract1. *Biol. Reprod*. 84, 1005–1015. doi: 10.1095/biolreprod.110.088773

Yang, Y., Marceau, V., and Gompper, G. (2010). Swarm behavior of self-propelled rods and swimming flagella. *Phys. Rev. E* 82:031904. doi: 10.1103/PhysRevE.82.031904

Yang, Y., Qiu, F., and Gompper, G. (2014b). Self-organized vortices of circling self-propelled particles and curved active flagella. *Phys. Rev. E* 89:012720. doi: 10.1103/PhysRevE.89.012720

Zernike, F. (1955). How I discovered phase contrast. *Science* 121, 345–349. doi: 10.1126/science.121.3141.345

Zimmer, R. K., and Riffell, J. A. (2011). Sperm chemotaxis, fluid shear, and the evolution of sexual reproduction. *Proc. Natl. Acad. Sci. U.S.A.* 108, 13200–13205. doi: 10.1073/pnas.1018666108

Zinaman, M. J., Brown, C. C., Selevan, S. G., and Clegg, E. D. (2000). Semen quality and human fertility: a prospective study with healthy couples. *J. Androl.* 21, 145–153.

Conflict of Interest: The authors declare that the research was conducted in the absence of any commercial or financial relationships that could be construed as a potential conflict of interest.

Copyright © 2021 Gaffney, Ishimoto and Walker. This is an open-access article distributed under the terms of the Creative Commons Attribution License (CC BY). The use, distribution or reproduction in other forums is permitted, provided the original author(s) and the copyright owner(s) are credited and that the original publication in this journal is cited, in accordance with accepted academic practice. No use, distribution or reproduction is permitted which does not comply with these terms.

frontiers in Cell and Developmental Biology

ORIGINAL RESEARCH
published: 28 September 2021
doi: 10.3389/fcell.2021.733653

Conserved Mechanism of Bicarbonate-Induced Sensitization of CatSper Channels in Human and Mouse Sperm

*Juan J. Ferreira[1,2], Pascale Lybaert[3], Lis C. Puga-Molina[1] and Celia M. Santi[1,2]**

[1] Department of Obstetrics and Gynecology, Washington University School of Medicine, St. Louis, MO, United States, [2] Department of Neuroscience, Washington University School of Medicine, St. Louis, MO, United States, [3] Research Laboratory on Human Reproduction, Faculté de Médecine, Université Libre de Bruxelles, Bruxelles, Belgium

OPEN ACCESS

Edited by:
Tomer Avidor-Reiss, University of Toledo, United States

Reviewed by:
Pablo Visconti, University of Massachusetts Amherst, United States
Jean-Ju Lucia Chung, Yale Medicine, United States

***Correspondence:**
Celia M. Santi
santic@wustl.edu

Specialty section:
This article was submitted to Cell Growth and Division, a section of the journal Frontiers in Cell and Developmental Biology

Received: *30 June 2021*
Accepted: *30 August 2021*
Published: *28 September 2021*

Citation:
Ferreira JJ, Lybaert P, Puga-Molina LC and Santi CM (2021) Conserved Mechanism of Bicarbonate-Induced Sensitization of CatSper Channels in Human and Mouse Sperm. Front. Cell Dev. Biol. 9:733653. doi: 10.3389/fcell.2021.733653

To fertilize an egg, mammalian sperm must undergo capacitation in the female genital tract. A key contributor to capacitation is the calcium (Ca^{2+}) channel CatSper, which is activated by membrane depolarization and intracellular alkalinization. In mouse epididymal sperm, membrane depolarization by exposure to high KCl triggers Ca^{2+} entry through CatSper only in alkaline conditions (pH 8.6) or after *in vitro* incubation with bicarbonate (HCO_3^-) and bovine serum albumin (capacitating conditions). However, in ejaculated human sperm, membrane depolarization triggers Ca^{2+} entry through CatSper in non-capacitating conditions and at lower pH (< pH 7.4) than is required in mouse sperm. Here, we aimed to determine the mechanism(s) by which CatSper is activated in mouse and human sperm. We exposed ejaculated mouse and human sperm to high KCl to depolarize the membrane and found that intracellular Ca^{2+} concentration increased at pH 7.4 in sperm from both species. Conversely, intracellular Ca^{2+} concentration did not increase under these conditions in mouse epididymal or human epididymal sperm. Furthermore, pre-incubation with HCO_3^- triggered an intracellular Ca^{2+} concentration increase in response to KCl in human epididymal sperm. Treatment with protein kinase A (PKA) inhibitors during exposure to HCO_3^- inhibited Ca^{2+} concentration increases in mouse epididymal sperm and in both mouse and human ejaculated sperm. Finally, we show that soluble adenylyl cyclase and increased intracellular pH are required for the intracellular Ca^{2+} concentration increase in both human and mouse sperm. In summary, our results suggest that a conserved mechanism of activation of CatSper channels is present in both human and mouse sperm. In this mechanism, HCO_3^- in semen activates the soluble adenylyl cyclase/protein kinase A pathway, which leads to increased intracellular pH and sensitizes CatSper channels to respond to membrane depolarization to allow Ca^{2+} influx. This indirect mechanism of CatSper sensitization might be an early event capacitation that occurs as soon as the sperm contact the semen.

Keywords: sperm, CatSper channels, CAMP/PKA, capacitation, fertilization, hyperactivation, sperm motility, calcium

INTRODUCTION

After ejaculation, human and mouse sperm cannot fertilize an egg until they undergo a maturation process in the female genital tract known as capacitation (Austin, 1951, 1952; Chang, 1951). Capacitation induces two phenotypic changes in sperm. First, they become hyperactive, in which the frequency and pattern of flagellar beating changes to help sperm detach from the oviduct walls and penetrate the egg (Yanagimachi, 1970; Demott and Suarez, 1992; Suarez et al., 1993). Second, capacitated sperm undergo regulated exocytosis of the acrosomal content, releasing enzymes that help the sperm penetrate the zona pellucida surrounding the egg and exposing the sperm sites that will fuse with the egg (Stival et al., 2016; Hirohashi and Yanagimachi, 2018).

Capacitation involves several molecular events such as hyperpolarization of the plasma membrane (Zeng et al., 1995; Santi et al., 2010; de la Vega-Beltran et al., 2012; Chavez et al., 2013; López-González et al., 2014) and increases in intracellular pH, cyclic AMP (cAMP) concentration, protein kinase A (PKA) activity, tyrosine phosphorylation (Visconti et al., 1995; Battistone et al., 2013; Puga Molina et al., 2018), and intracellular calcium concentration ($[Ca^{2+}]_i$) (Baldi et al., 1991; Suarez et al., 1993; Breitbart, 2002a,b; Luque et al., 2018). Some of these events take place as soon as as the sperm are ejaculated, whereas others occur over a longer period of time in the female tract or in a medium that support *in vitro* capacitation (Visconti, 2009).

The increase in $[Ca^{2+}]_i$ during capacitation occurs via activity of the sperm-specific Ca^{2+} channel, CatSper (Ren et al., 2001; Carlson et al., 2003; Xia et al., 2007; Strunker et al., 2011; Alasmari et al., 2013; Smith et al., 2013; Chavez et al., 2014; Vyklicka and Lishko, 2020), which is activated by both membrane depolarization and alkalinization (Kirichok et al., 2006). However, some data have suggested that how CatSper is activated in response to membrane depolarization differs between mouse and human sperm (Lishko et al., 2011). In experiments with mouse sperm, membrane depolarization induced Ca^{2+} entry through CatSper channels only in alkaline media or after *in vitro* capacitation (incubation with bicarbonate and bovine serum albumin) (Carlson et al., 2003; Chavez et al., 2014). Conversely, in experiments with human sperm, membrane depolarization triggered $[Ca^{2+}]_i$ increase in neutral media and in non-capacitated conditions. These differences may reflect species-specific differences in CatSper regulation. Alternatively, these differences could be due to the fact that most of the mouse experiments were done with epidydimal sperm, which have not been exposed to semen, whereas most of the human experiments were done with ejaculated sperm, which have been exposed to semen.

Here, we aimed to determine the mechanism(s) by which CatSper is activated in mouse and human sperm. Our findings indicate that CatSper is activated similarly in mouse and human epididymal sperm and is activated similarly in mouse and human ejaculated sperm. Specifically, we provide evidence that – in both mouse and human sperm – exposure to bicarbonate (HCO_3^-), which is a major semen component, activates the soluble adenylyl cyclase/PKA pathway and increases intracellular pH. This increase in intracellular pH sensitizes CatSper to increase $[Ca^{2+}]_i$ in response to membrane depolarization.

MATERIALS AND METHODS

Mice

All mouse procedures were reviewed and approved by the Institutional Animal Care and Use Committee of Washington University in St. Louis (St. Louis, MO, United States) (protocol # 20-0126) and were performed according to the National Institutes of Health Guiding Principles for the care and use of laboratory animals. *CatSper* knock-out mice (in which the second exon encoding the first putative transmembrane domain was replaced with an IRESLacZ sequence followed by a neomycin resistance gene in 129S4/SvJae-derived J1 ES cells, Ren et al. (2001) were obtained from Jackson Laboratory. C57BL/6 males were used as wild-type controls. Soluble adenylyl cyclase (sAC) knock-out mice were generously provided by Lonni Levin and J Buck (Buck et al., 1999; Hess et al., 2005).

Human Participants

This study conformed with the Declaration of Helsinki (except for registration in a database) and was approved by the Washington University in St. Louis Institutional Review Board (protocol #201706077). All subjects signed written informed consent forms approved by the Washington University in St. Louis Institutional Review Board.

Preparation of Mouse Caudal Epididymal Sperm

Adult (60–90 days old) males were euthanized by cervical dislocation, and the cauda epididymis was removed and incubated in non-capacitated or capacitated HS media (defined below), pH 7.4, for 15–20 min or 90 min, respectively, at 37°C. After incubation, the motile sperm were removed for use in experiments.

Preparation of Mouse Ejaculated Spermatozoa

Mouse ejaculated spermatozoa were isolated as described previously (Li et al., 2015). Briefly, each adult male (60–90 days old) was placed in a cage with a female in estrus before sunrise (3–5 am). Mice were watched under a red light to determine when coitus occurred. Five to ten minutes after coitus was complete, the females were euthanized, and their uteri dissected out. Sperm were retrieved by washing the uterus with 500 μl of non-capacitated HS media, yielding an average of 10.64 ± 6.85 (SD) million sperm per milliliter. Ejaculated mouse sperm did not appear to be capacitated, as the percentages of hyperactivated and acrosome-reacted sperm were similar to the percentages in non-capacitated epididymal sperm (data not shown).

Preparation of Human Epididymal Sperm

Small (1 cm) vas deferens pieces were obtained from healthy donors undergoing elective vasectomy procedures under local

anesthesia. Specimens were kept in non-capacitated HS media at room temperature and flushed within an hour after surgery with non-capacitated recording solution (described below) within 1 h of obtaining the sample.

Preparation of Human Ejaculated Sperm

Freshly ejaculated semen samples were obtained by masturbation after two days of abstinence from healthy donors with normal semen parameters as defined by the World Health Organization (≥32% progressive motility; ≥40% total motility; ≥15 × 10^6 cells/ml). Within two hours, sperm were purified by the swim-up technique at 37°C in a VWR Borosilicate Glass tube with 2 ml of non-capacitated recording solution and 1 ml of sample at the bottom. Sperm were allowed to swim out of the semen for an hour, then collected in recording solution. Human sperm were capacitated by adding 25 mM HCO_3^- (Sigma-Aldrich) and 5 mg/ml BSA to the non-capacitating recording solution and incubating the cells for 18–24 h at 37^{o}C and 5% CO_2.

Ca^{2+} Imaging

After swim up, motile sperm were incubated with 2–4 μM Fluo-4 AM (catalog number F-4201, Life Technologies) and 0.05% Pluronic F-127 (catalog number P3000MP, Life Technologies) in HS media at 37°C for 45 min (human sperm) or 90 min (mouse sperm). Then, sperm were centrifuged at 325 RCF for 5–10 min and resuspended in the corresponding media. Sperm were allowed to attach to the recording chamber floor for 5 min. Mouse sperm were then overlaid with a coverslip coated with1 mg/ml Laminin Mouse Protein, Natural (catalog number 23017015, Gibco®), 0.1% (w/v) Poly-L-lysine in water (catalog number P8920-100ml, Sigma-Aldrich), or Cell-Tak (catalog number 354240, Corning Labware, Bedford, MA, United States). Laminin-coated cover slips were incubated at 4^{o}C for at least 12 hrs before the experiment. Human sperm were overlaid with a coverslip coated with 0.1% Poly-L-lysine or 1 mg/ml Cell-Tak. Non-capacitated sperm were not exposed to HCO_3^- at any time before the recordings. A perfusion device with an estimated exchange time of 10 s was used to apply test solutions. Sperm were pre-incubated with 15 mM (mouse) or 25 mM (human) HCO_3^- for 20 min before recording. Then, HCO_3^- was washed out for 2–4 min so that, at time "0" when the recording was started, no HCO_3^- was present in the recording solution. PKA inhibitors and sAC inhibitor were added only during the pre-incubation period and were not present at the time of stimulation with KCl. Ionomycin (5 μM) and HS plus 2 mM $CaCl_2$ were added at the end of the recordings as references of maximum fluorescence (F_{Iono}).

Imaging was performed with a Leica DMi8 microscope equipped with a Zyla Andor sCMOS camera, and images were collected for 1.5 ms every 5–10 s over 10–30 min. Images were analyzed with Image J software. Fluorescence (F) of Fluo-4 changes was normalized to $F_{Iono}(F/F_{iono})$ after background subtraction. Calcium imaging data are presented as the average ± the standard deviation. The regions of interest were selected automatically and corroborated with ImageJ software. Pclamp 10 and Sigmaplot 12 were used to analyze data. Experiments were done at room temperature. Sperm in which the peak $[Ca^{2+}]_i$ reached 10% or more of the $[Ca^{2+}]_i$ in the presence of Ionomycin were considered to have responded to the stimuli.

Intracellular pH Measurements

Sperm samples were incubated for 60 min in the presence or absence of the soluble adenylyl cyclase inhibitor TDI-10229 (donated by Lonnie Levin and Johen Buck's labs) (Balbach et al., 2021) in capacitating TYH media or in non-capacitating HS media. After incubation, sperm pH was evaluated as previously described (Gunderson et al., 2021). Briefly, samples were incubated for 10 min with 0.5 μM BCECF-AM, washed, and resuspended in non-capacitating TYH media, media plus 15 mM bicarbonate, or media plus 15 mM $HCO_3^-$and 5 μM TDI-10229. For each condition, high potassium-buffered solutions were used to calibrate the pH by adding 5 μM nigericin to equilibrate intracellular and extracellular pH and create a pH calibration curve. Fluorescence of BCECF was recorded as individual cellular events on a FACSCanto II TM cytometer (Becton Dickinson) (excitation 505 nm, emission 530 nm). Sperm intracellular pH was calculated by linearly interpolating the median of the histogram of BCECF fluorescence of the unknown sample to the calibration curve.

Solutions

Non-capacitating HS medium (in mM): 135 NaCl, 5 KCl, 2 $CaCl_2$, 1 $MgSO_4$, 20 HEPES, 5 Glucose, 10 lactic acid (catalog number L13242, Alfa Aesar, Lancashire, United Kingdom), 1 sodium pyruvate (catalog number P2256, Sigma-Aldrich, Saint Louis, MO) at pH7.4 or as indicated. **Capacitated HS medium:** Same as non-capacitating HS medium plus 5 mg/ml bovine serum albumin (BSA, catalog number A2153, Sigma-Aldrich, Saint Louis, MO) and 15 mM $NaHCO_3$ (catalog number S5761, Sigma-Aldrich) (Chavez et al., 2014). **50 mM KCl HS** (in mM): 90 NaCl, 50 KCl, 2 $CaCl_2$, 1 $MgSO_4$, 20 HEPES, 5 glucose, 10 lactic acid, 1 sodium pyruvate in pH as indicated. **Recording solution** (in mM): 110 NaCl, 4 KCl, 2 $CaCl_2$, 1 $MgCl_2$, 20 HEPES, 5 glucose, 10 lactic acid, 1 sodium pyruvate at pH as indicated. **KCl Recording solution** (in mM): 65 NaCl, 50 KCl, 2 $CaCl_2$, 1 $MgCl_2$, 20 HEPES, 5 glucose, 10 lactic acid, 1 sodium pyruvate at pH as indicated. **TYH medium (in mM):**135 NaCl, 4.7 KCl, 1.7 CaCl2, 1.2 KH2PO4, 1.2 MgSO4, 5.6 glucose, 0.56 pyruvate, 10 HEPES, pH 7.4 adjusted at 37°C with NaOH.

pH of the solutions after addition of HCO_3^- was measured with a Sartorious PB-10 basic bench top pH meter, with automatic temperature compensation.

Other Reagents

Dimethyl sulfoxide (DMSO) (catalog number D8418, Sigma-Aldrich); CatSper inhibitor Mibefradil (catalog number 2198, Tocris Bioscience, Bristol, United Kingdom); PKI (Protein Kinase A inhibitor fragment 14-22, myristoylated trifluoroacetate salt,

catalog number P9115; Sigma Aldrich); KT5720 (CAS number 108068-98-0, Cayman Chemicals).

RESULTS

Mouse and Human Sperm at Similar Stages of Maturation Show Similar Increases in Intracellular Calcium Concentration ($[Ca^{2+}]_i$) in Response to Membrane Depolarization

We first repeated previous experiments on mouse epididymal sperm (Chavez et al., 2014) and confirmed that, at pH 7.4, KCl induced an increase in $[Ca^{2+}]_i$ in 12% of sperm in non-capacitating conditions and 61% of sperm in capacitating conditions (bicarbonate $[HCO_3^-]$ plus bovine serum albumin). In this and all subsequent experiments, sperm in which the peak $[Ca^{2+}]_i$ reached 10% or more of the $[Ca^{2+}]_i$ in the presence of Ionomycin were considered to have responded. As expected, bypassing the increase in pH that occurs during capacitation by incubating the sperm at alkaline pH (pH 8.6) allowed 77% of the non-capacitated sperm to respond to KCl. The top row of **Figure 1** shows representative traces of the most prevalent response in each condition.

We next performed similar experiments with human ejaculated sperm, which have been most commonly used to study sperm Ca^{2+} signaling and CatSper activation. For these experiments, we first tested pH 7.4 as in the mouse sperm experiments but found that it caused Ca^{2+} responses with varying kinetics (not shown). Thus, we instead used pH 6.8 and pH 8.0 because they yielded consistent and reproducible Ca^{2+} responses similar to those obtained with mouse sperm at pH 7.4 and pH 8.6. In ejaculated human sperm at pH 6.8, membrane depolarization with KCl triggered an increase in $[Ca^{2+}]_i$ in 67% of sperm in non-capacitating conditions and 60% of sperm in capacitating conditions. As with mouse epididymal sperm, bypassing the increase in pH that occurs during capacitation with alkaline pH (pH 8.0) allowed a high percentage (81%) of sperm to respond to KCl. The bottom row of **Figure 1** shows representative traces of the most prevalent response in each condition. We conclude that, at low pH in non-capacitating conditions, epididymal mouse and ejaculated human sperm sharply differ in their abilities to increase $[Ca^{2+}]_i$ in response to KCl-mediated depolarization.

To determine whether sperm from the two species at similar stages of maturation would respond to KCl-induced membrane depolarization similarly, we compared epididymal mouse sperm to epididymal human sperm and compared ejaculated mouse sperm to ejaculated human sperm. In each case, we assessed response by measuring the percentage of sperm that responded to the KCl stimulus. Additionally, given that the slope of the $[Ca^{2+}]_i$ increase is a good indicator of the number of CatSper channels that are open in response to membrane depolarization (Wennemuth et al., 2003), we compared the rate of $[Ca^{2+}]_i$ increase in the responsive sperm during the first 20 s of the depolarization-evoked response.

In non-capacitating conditions, 12% of mouse epididymal sperm increased $[Ca^{2+}]_i$ in response to high external KCl at pH 7.4 (**Figures 2A,G**). Similarly, 8% of human epididymal sperm increased $[Ca^{2+}]_i$ in response to high external KCl pH 6.8 (**Figures 2C,G**). In contrast, 42% of mouse ejaculated sperm and

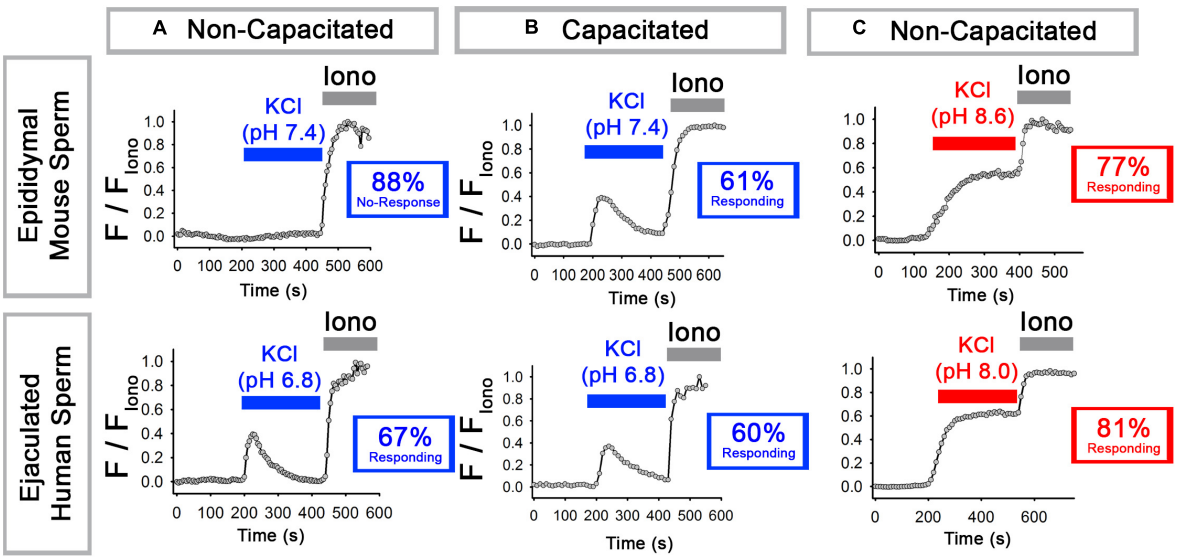

FIGURE 1 | Epididymal mouse sperm and ejaculated human sperm show different $[Ca^{2+}]_i$ responses to KCl. **(A,B)** Representative traces of the most prevalent $[Ca^{2+}]_i$ responses to 50 mM KCl at (top) pH 7.4 in epididymal mouse sperm and (bottom) at pH 6.8 in ejaculated human sperm in **(A)** non-capacitating and **(B)** capacitating conditions. **(C)** Representative traces of the most prevalent $[Ca^{2+}]_i$ responses to 50 mM KCl at (top) pH 8.6 in epididymal mouse sperm and (bottom) at pH 8.0 ejaculated human sperm in non-capacitating conditions. Numbers in boxes indicate the percentage of sperm that did or did not respond (see Results and Methods for how "responding" was defined).

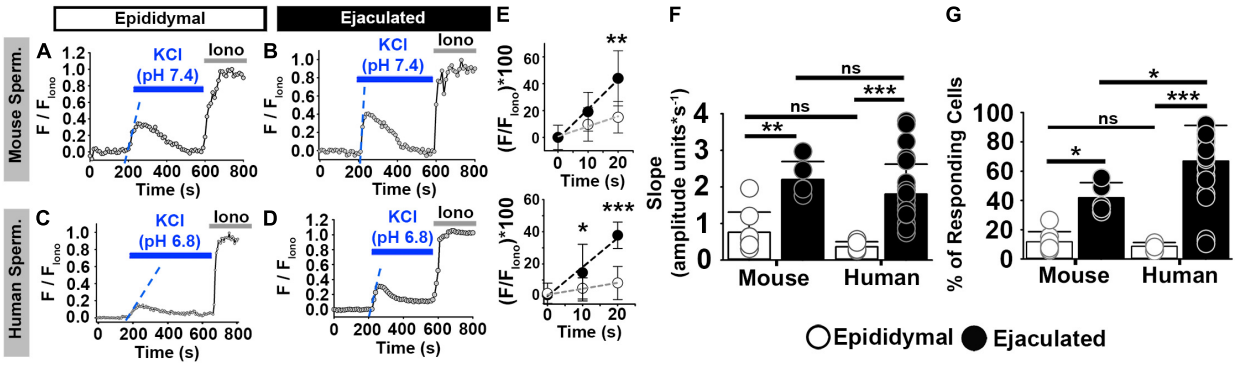

FIGURE 2 | Mouse and human sperm at similar stages of maturation show similar increases in $[Ca^{2+}]_i$ in response to KCl. **(A–D)** $[Ca^{2+}]_i$ traces from the epididymal and ejaculated sperm responsive to KCl in non-capacitated conditions. **(E)** Linear fit of the averaged normalized fluorescence in the first 20 s after KCl addition [blue dashed lines in panels **(A–D)**] in responding sperm. **(F)** Graph of the slope values of the best-fit regression lines. Mean values were as follows: epididymal mouse sperm, 0.76 ± 0.547 amplitude units * s^{-1} (8 mice, 307 sperm); ejaculated mouse sperm, 2.20 ± 0.494 amplitude units *s^{-1} (5 mice, 170 sperm); epididymal human sperm, 0.36 ± 0.137 amplitude units *s^{-1} (5 samples, 191 sperm); and ejaculated human sperm, 1.80% ± 0.82 amplitude units *s^{-1} (26 samples, 1836 sperm). **(G)** Graph of the percentage of responsive sperm. Mean values were as follows: epididymal mouse sperm, 11.80% ± 6.9 (8 mice, 307 sperm); ejaculated mouse sperm, 41.9% ± 10.2 (5 mice, 170 sperm); epididymal human sperm, 8.72% ± 2.54 (5 samples, 191 sperm); and ejaculated human sperm, 66.94% ± 24.30 (26 samples, 1836 sperm). *$P < 0.050$, **$P < 0.010$, ***$P < 0.001$, and ns, non-significant by one-way ANOVA. Error bars indicate standard deviation. Iono = 5 μM Ionomycin + 2 mM Ca^{2+}.

67% of human ejaculated sperm increased $[Ca^{2+}]_i$ in response to high external KCl (**Figures 2B,D,G**). In both mouse and human sperm, a significantly higher percentage of ejaculated sperm responded than did epididymal sperm (**Figure 2G**). When we examined only those sperm in each condition that responded, we found that the rate of $[Ca^{2+}]_i$ increase was significantly higher in ejaculated mouse and human sperm than in epididymal mouse and human sperm, respectively (**Figures 2E,F**).

In capacitating conditions, mouse epididymal sperm showed $[Ca^{2+}]_i$ increases in response to high external KCl at low pH, and both non-capacitated and capacitated sperm from human and mouse species showed $[Ca^{2+}]_i$ increases in response to high external KCl at high pH (**Supplementary Figure 1**; Wennemuth et al., 2000; Chavez et al., 2014). As expected (Xia et al., 2007; Chavez et al., 2014), capacitated epididymal sperm from CatSper knockout mice did not show $[Ca^{2+}]_i$ increases in response to high external KCl (**Supplementary Figure 1C**). Similarly, in ejaculated human sperm, the $[Ca^{2+}]_i$ increase in response to high external KCl was inhibited by the CatSper channel blocker Mibefradil (**Supplementary Figure 1F**). Together, these results indicate that human and mouse ejaculated sperm show comparable $[Ca^{2+}]_i$ increases in response to membrane depolarization by high extracellular KCl. This depolarization similarly activates CatSper channels in mouse and human sperm at similar maturational stages.

Bicarbonate (HCO_3^-) Increases $[Ca^{2+}]_i$ Responses to Neutral and Alkaline Depolarization in Both Mouse and Human Epididymal Sperm

The main difference between epididymal and ejaculated sperm is that ejaculated sperm are exposed to semen. Thus, we aimed to identify the component in semen that was responsible for the differences in $[Ca^{2+}]_i$ increases in response to membrane depolarization between epididymal and ejaculated sperm. We focused on bicarbonate (HCO_3^-) because it is a major component of semen (Okamura et al., 1985) and influences sperm function and intracellular Ca^{2+} regulation (Austin, 1952; Austin and Bishop, 1958; Wennemuth et al., 2003; Chavez et al., 2014). For example, Wennemuth et al. showed that a pulse of HCO_3^- facilitated Ca^{2+} increase in mouse sperm by enhancing the rate of depolarization-evoked $[Ca^{2+}]_i$ increase (Wennemuth et al., 2003). Additionally, de la Vega-Beltran et al. (2012) and Chavez et al. (2014) showed that exposure to HCO_3^- and bovine serum albumin triggered Ca^{2+} responses in mouse sperm, and Orta et al. (2018) showed that CatSper activity was modulated by HCO_3^- in mouse sperm.

To assess the effect of HCO_3^-, we pre-incubated mouse epididymal sperm without or with 15 mM HCO_3^- (a concentration similar to that in seminal fluid) (Okamura et al., 1985) for 20 min. Whereas 12% of sperm not exposed to HCO_3^- showed increased $[Ca^{2+}]_i$ in response to high extracellular KCl at pH 7.4 (**Figures 3A,G**), 48% of sperm exposed to HCO_3^- showed increased $[Ca^{2+}]_i$ in response to high extracellular KCl at pH 7.4 (**Figures 3B,G**). Exposure to HCO_3^- also increased the percentage of cells showing increased $[Ca^{2+}]_i$ in response to high extracellular KCl at pH 8.6 (**Figures 3C,D,G**). When we only examined the responding sperm in each condition, we found that pre-incubation with HCO_3^- enhanced the rate of depolarization-evoked $[Ca^{2+}]_i$ increase in mouse epididymal sperm (**Figures 3E,F**), indicating an increase in the number of open CatSper channels in response to KCl depolarization. These $[Ca^{2+}]_i$ increases were not observed in sperm from CatSper knock-out mice (**Figure 3G**). Importantly, 15 mM HCO_3^- did not significantly increase the pH of the HS media or the recording solution (**Supplementary Figure 2**). Moreover, HCO_3^- was not present in the chamber during the recordings.

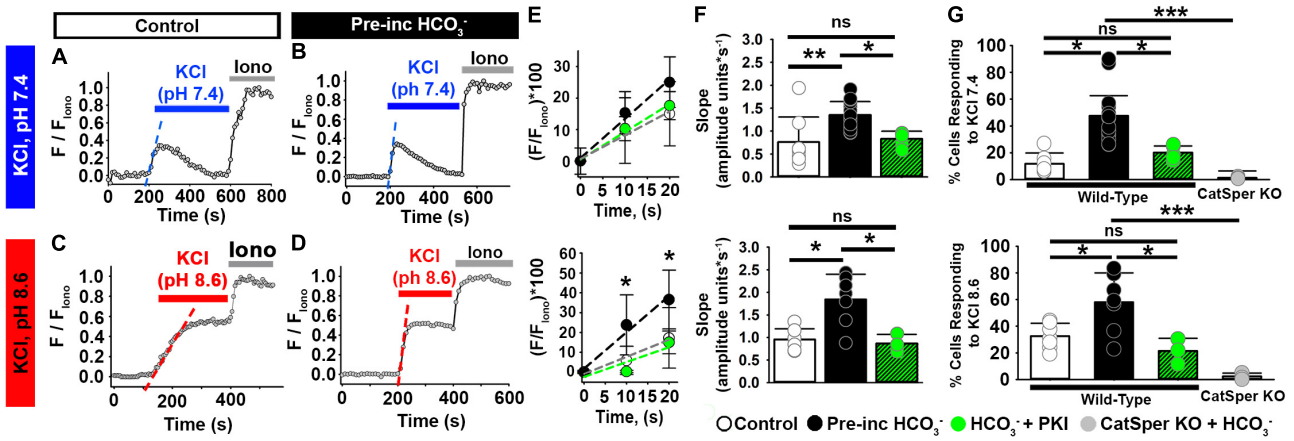

FIGURE 3 | HCO_3^- enhances the depolarization-evoked responses from mouse epididymal NC sperm and its effect is inhibited by the PKA inhibitor PKI. **(A–D)** Representative traces of $[Ca^{2+}]_i$ responses to 50 mM KCl at **(A,B)** pH 7.4 and **(C,D)** pH 8.6 in mouse epididymal sperm in non-capacitating conditions. **(E)** Linear fit of the averaged normalized fluorescence in the first 20 s after KCl addition [blue or red dashed lines in panels **(A–D)**] in responding sperm. **(F)** Graph of the slope values of the best-fit regression line for each condition. Mean values at pH 7.4 were as follows: control, 0.76 ± 0.547 amplitude units * s^{-1} (8 mice, 307 sperm); HCO_3^-, 1.35 ± 0.297 amplitude units *s^{-1} (15 mice, 1035 sperm); and HCO_3^- + PKI, 0.83 ± 0.166 amplitude units *s^{-1} (5 mice, 264 sperm). Mean values at pH 8.6 were as follows: control, 0.95 ± 0.237 amplitude units * s^{-1} (7 mice, 243 sperm); HCO_3^-, 1.84 ± 0.556 amplitude units *s^{-1} (7 mice, 281 sperm); and HCO_3^- + PKI, 0.86 ± 0.203 amplitude units *s^{-1} (3 mice, 126 sperm). **(G)** Graph of the percentage of responsive sperm. Mean values at pH 7.4 were as follows: control, 11.80% ± 6.9 (8 mice, 307 sperm); HCO_3^-, 47.6% ± 19.39 (15 mice, 1035 sperm); HCO_3^- + PKI, 20.1% ± 5.30 (5 mice, 264 sperm); and HCO_3^- in CatSper KO mice, 1.37% ± 0.623 (5 mice, 137 sperm). Mean values at pH 8.6 were as follows: control, 32.6% ± 9.58 (7 mice, 243 sperm); HCO_3^-, 58.0% ± 21.940 (7 mice, 281 sperm); HCO_3^- + PKI, 21.45% ± 9.513 (3 mice, 126 sperm); and HCO_3^- in CatSper KO mice, 2.34% ± 2.524 (3 mice, 95 sperm). *$P < 0.050$, **$P < 0.010$, ***$P < 0.001$, and ns, non-significant by one-way ANOVA. Error bars indicate standard deviation. Iono = 5 μM Ionomycin + 2 mM Ca^{2+}.

To assess the effect of HCO_3^- on $[Ca^{2+}]_i$ responses in non-capacitated human epididymal sperm, we incubated them in the presence or absence of HCO_3^- for 20–30 min and then exposed them to high external KCl. High external KCl at pH 6.8 induced $[Ca^{2+}]_i$ increases in 9% of the human epididymal sperm in control conditions (**Figures 4A,E**). In contrast, high external KCl at pH 6.8 induced $[Ca^{2+}]_i$ increases in 37% of sperm pre-incubated with HCO_3^- (**Figures 4B,E**). Pre-incubation with HCO_3^- also significantly increased the rate of depolarization-evoked $[Ca^{2+}]_i$ increase in human epididymal sperm (**Figures 4C,D**), indicating an increase in the number of open CatSper channels in response to KCl depolarization. These results indicate that $[Ca^{2+}]_i$ responses to membrane depolarization depend on HCO_3^- in both mouse and human sperm.

HCO_3^- Activates the cAMP/PKA Pathway and Sensitizes CatSper to Membrane Depolarization in Sperm From Both Mice and Humans

One of the early events of sperm capacitation, which can occur as soon as sperm are ejaculated, is HCO_3^--induced activation of soluble adenylyl cyclase (sAC), leading to increased intracellular cyclic adenosine monophosphate (cAMP) and activation of protein kinase A (PKA) (Chen et al., 2000; Hess et al., 2005; Xie et al., 2006; Visconti, 2009). Given a report suggesting that CatSper channels are modulated by PKA (Orta et al., 2018), we wondered whether the effect of HCO_3^- on the Ca^{2+} responses in epididymal sperm depended on PKA activation. Recent work from Orta et al. showed that the PKA inhibitor PKI reduced HCO_3^--induced $[Ca^{2+}]_i$ increases in mouse epididymal sperm without directly blocking mouse CatSper currents (Orta et al., 2018). Thus, we incubated mouse epididymal sperm in HCO_3^- in the absence or presence of 10 μM PKI for 20 min before recording, then stimulated them with KCl in the absence of HCO_3^- or PKI. Compared to sperm not pre-treated with PKI, significantly fewer sperm pre-treated with PKI showed an increase in $[Ca^{2+}]_i$ in response to high external KCl at both pH 7.4 and pH 8.6 (**Figure 3G**). The rate of $[Ca^{2+}]_i$ increase of the responsive cells was also significantly lower in cells pre-incubated with HCO_3^- in the presence than in the absence of PKI (**Figures 3E,F**).

We next asked whether the cAMP/PKA pathway was also involved in $[Ca^{2+}]_i$ increases induced by external KCl in ejaculated mouse sperm. At pH 7.4 (**Figures 5 A,B**), treatment with PKI reduced the percentage of ejaculated mouse sperm that showed increased $[Ca^{2+}]_i$ in response to high extracellular KCl from 42 to 16% (**Figure 5G**, top panel). PKI also significantly reduced the rate of $[Ca^{2+}]_i$ increase in the responsive sperm (**Figures 5E,F**). Likewise, at pH 8.6 (**Figures 5 C,D**), treatment with PKI reduced the percentage of ejaculated sperm that showed increased $[Ca^{2+}]_i$ in response to high extracellular KCl from 71 to 32% (**Figure 5G**, bottom panel). PKI also significantly reduced the rate of $[Ca^{2+}]_i$ increase in the responsive sperm (**Figures 5E,F**). These results indicated that PKI reduced the number of CatSper channels that opened in response to membrane depolarization in mouse ejaculated sperm.

We wanted to determine whether PKA was required for the $[Ca^{2+}]_i$ increase in ejaculated human sperm. However, because

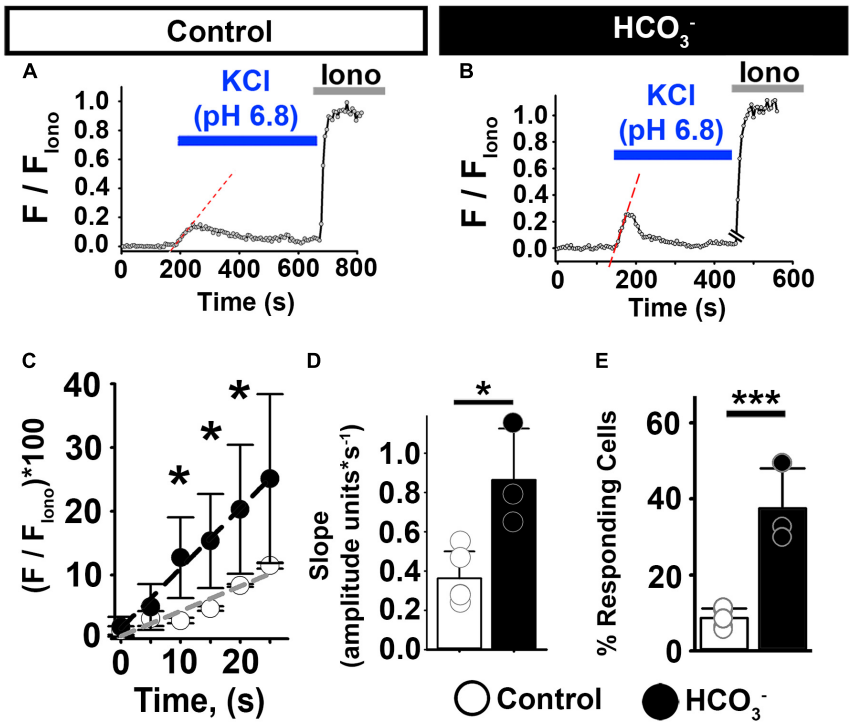

FIGURE 4 | HCO_3^- enhances $[Ca^{2+}]_i$ responses to KCl in human epididymal sperm. **(A,B)** Representative traces of $[Ca^{2+}]_i$ responses to 50 mM KCl at pH 6.8 in epididymal human sperm in non-capacitating conditions **(A)** without and **(B)** after pre-incubation with HCO_3^-. **(C)** Linear fit of the averaged normalized fluorescence in the first 20 s after KCl addition. **(D)** Graph of slope values of the best-fit regression line for each condition. Mean values were as follows: control, 0.36 ± 0.137 amplitude units * s^{-1} (4 samples, 62 sperm); and HCO_3^-, 0.86 ± 0.260 amplitude units *s^{-1} (3 samples, 52 sperm). **(E)** Graph of the percentage of responsive sperm. Mean values were as follows: control, 8.72% ± 2.54 (4samples, 62 sperm); and pre-incubation with HCO_3^-, 37.5% ± 10.54 (3 samples, 52 sperm). *$P < 0.050$, ***$P < 0.001$ by independent t-test. Error bars indicate standard deviation. Iono = 5 μM Ionomycin + 2 mM Ca^{2+}.

PKI has been reported to directly inhibit human CatSper currents (47), we instead used KT5720, a PKA inhibitor that does not directly inhibit human CatSper currents (Wang et al., 2020). Pre-incubation of ejaculated human sperm with HCO_3^- in the presence of 50 μM KT5720 reduced the percentage of sperm responding from 67 to 32% (**Figures 6A–D,G**). Additionally, KT5720 significantly decreased the rate of $[Ca^{2+}]_i$ increase in responsive sperm (**Figures 6E,F**). These results indicate that the cAMP/PKA pathway is involved in the $[Ca^{2+}]_i$ responses to membrane depolarization in ejaculated sperm from both mice and humans.

Activation of Soluble Adenylyl Cyclase Is Involved in $[Ca^{2+}]_i$ Increases Induced by Bicarbonate

As mentioned above, HCO_3^- regulates the production of cAMP and PKA activity through stimulation of a soluble adenylyl cyclase (sAC) (Chen et al., 2000; Hess et al., 2005; Xie et al., 2006; Visconti, 2009). Moreover, KCl-induced Ca^{2+} entry is impaired in sAC (*Adcy10*) knock-out mice (Xie et al., 2006). To determine whether sAC was required for the depolarization-induced $[Ca^{2+}]_i$ increase in sperm, we took two approaches. First, in a genetic approach, we isolated epididymal sperm from sAC knockout mice. HCO_3^- had no effect on the percentages of sperm from sAC knockout mice that increased $[Ca^{2+}]_i$ in response to extracellular KCl (**Figure 7H**). Likewise, HCO_3^- had no effect on the rate of $[Ca^{2+}]_i$ increase in responding sperm from sAC knockout mice (**Figures 7F,G**).

Second, in a pharmacologic approach, we treated epididymal sperm from wild-type mice with the sAC-specific inhibitor TDI-10229 (Balbach et al., 2021) and found that it prevented an increase in the percentage of sperm responding to high extracellular KCl (**Figures 7C,H**). Treatment with TDI-10229 also reduced the rate of $[Ca^{2+}]_i$ increase in responsive sperm (**Figures 7A,B,D,E**). Likewise, TDI-10229 prevented the increase in the percentage of ejaculated human sperm responding to high extracellular KCl (**Figure 8G**) and reduced the rate of $[Ca^{2+}]_i$ increase in the responsive sperm (**Figures 8A–F**). Together, these data indicate that activation of CatSper channels by membrane depolarization is facilitated by activation of the HCO_3^--sAC-cAMP/PKA pathway in both mouse and human sperm.

The Effect of HCO_3^- Is Mediated by an Increase in Intracellular pH Induced by sAC Activation

Several studies have revealed that HCO_3^- raises sperm intracellular pH (pH_i) (Demarco et al., 2003; Chavez et al., 2019; Matamoros-Volante and Trevino, 2020) and that HCO_3^-

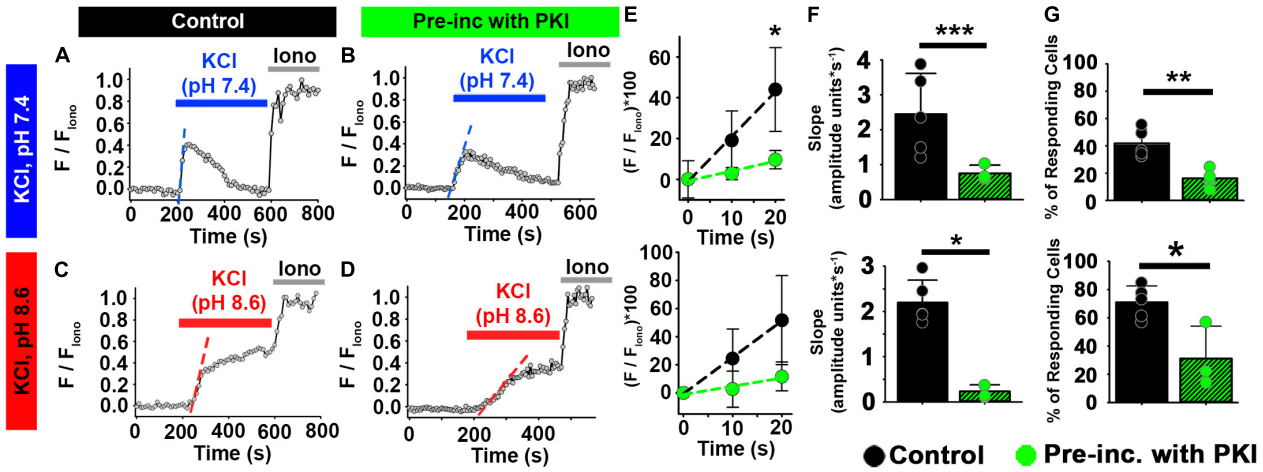

FIGURE 5 | PKA inhibition impairs the effect of HCO_3^- on depolarization-evoked Ca^{2+} responses in ejaculated mouse sperm. **(A–D)** Representative traces of $[Ca^{2+}]_i$ responses to 50 mM KCl at pH 7.4 and pH 8.6 in ejaculated mouse sperm in **(A,C)** control conditions and **(B,D)** after pre-incubation with 10 μM PKI. **(E)** Linear fit of the averaged normalized fluorescence in the first 20 s after KCl addition. **(F)** Graph of slope values of the best-fit regression line for each condition. Mean values at pH 7.4 were as follows: control, 2.20 ± 0.494 amplitude units * s^{-1} (5 mice, 137 sperm); and PKI pre-incubation, 0.237 ± 0.144 amplitude units *s^{-1} (4 mice, 86 sperm). Mean values at pH 8.6 were as follows: control, 2.45 ± 1.161 amplitude units * s^{-1} (5 mice, 107 sperm); and PKI pre-incubation, 0.753 ± 0.232 amplitude units *s^{-1} (3 mice, 81 sperm). **(G)** Graph of the percentage of responsive sperm. Mean values at pH 7.4 were as follows: control, 41.92% ± 10.22 (5 mice, 137 sperm); and PKI pre-incubation, 16.30% ± 7.01 (4 mice, 82 sperm). Mean values at pH 8.6 were as follows: control, 70.96% ± 11.50 (5 mice, 107 sperm); and PKI pre-incubation, 31.22% ± 22.80 (3 mice, 81 sperm). *$P < 0.050$, **$P < 0.010$, and ***$P < 0.001$ by independent *t*-test. Error bars indicate standard deviation. Iono = 5 μM Ionomycin + 2 mM Ca^{2+}.

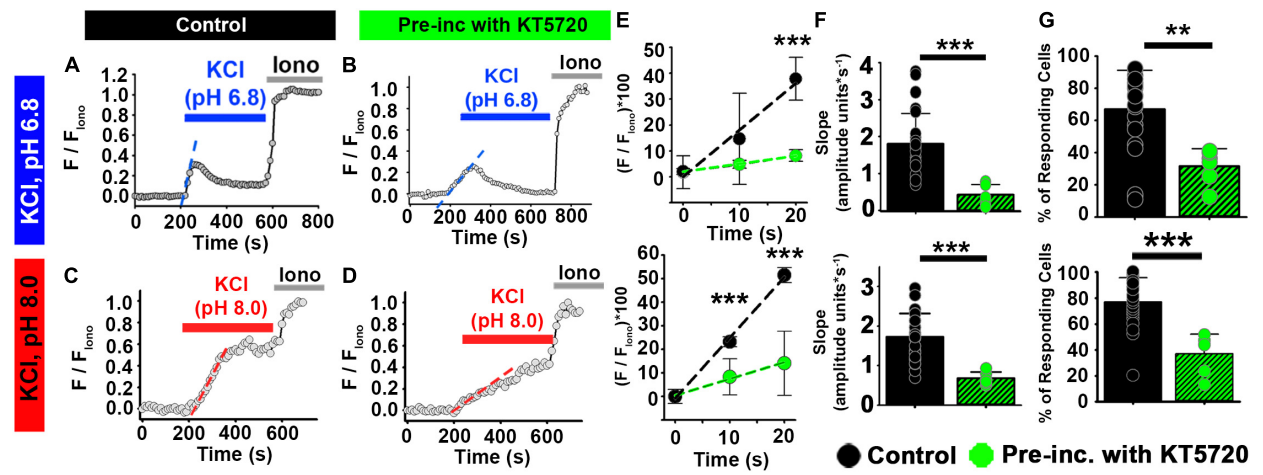

FIGURE 6 | PKA inhibitor KT5720 impairs the effect of HCO_3^- on depolarization-evoked Ca^{2+} responses in ejaculated human sperm. **(A–D)** Representative traces of $[Ca^{2+}]_i$ responses to 50 mM KCl at **(A,B)** pH 6.8 and **(C,D)** pH 8.0 in ejaculated human sperm in non-capacitating conditions in **(A,C)** control and **(B,D)** after pre-incubation with KT5720. **(E)** Linear fit of the averaged normalized fluorescence in the first 20 s after KCl addition. **(F)** Graph of slope values of the best-fit regression line for each condition. Mean values at pH 6.8 were as follows: control, 1.80 ± 0.82 amplitude units * s^{-1} (26 samples, 1836 sperm); and KT5720 pre-incubation, 0.426 ± 0.277 amplitude units *s^{-1} (6 samples, 624 sperm). Mean values at pH 8.0 were as follows: control, 1.73 ± 0.594 amplitude units * s^{-1} (26 samples, 3036 sperm); and KT5720 pre-incubation, 0.678 ± 0.162 amplitude units *s^{-1} (5 samples, 974 sperm). **(G)** Graph of the percentage of responsive sperm. Mean values at pH 6.8 were as follows: control, 66.94% ± 24.30 (26 samples, 1836 sperm); and KT5720 pre-incubation, 31.57% ± 10.87 (6 samples, 624 sperm). Mean values at pH 8.6 were as follows: control, 77.04% ± 18.67 (26 samples, 3036 sperm); and KT5720 pre-incubation, 36.90% ± - 15.33 (6 samples, 974 sperm). **$P < 0.010$, ***$P < 0.001$ by independent *t*-test. Error bars indicate standard deviation. Iono = 5 μM Ionomycin + 2 mM Ca^{2+}.

can activate CatSper channels in mouse sperm (Orta et al., 2018). Therefore, we investigated whether the $[Ca^{2+}]_i$ changes induced by HCO_3^- were due to a change in pH_i. We found that addition of HCO_3^- to the media (which only raised the media pH by 0.1 unit; **Supplementary Figure 2**) caused a 0.4–0.5 unit increase in non-capacitated mouse epididymal sperm pH_i within 1–2 min (**Figure 9A**). This increase in pH_i was similar to the increase in pH_i seen in capacitated mouse sperm and was completely inhibited by incubation with the sAC inhibitor TDI-10229 (**Figure 9B**).

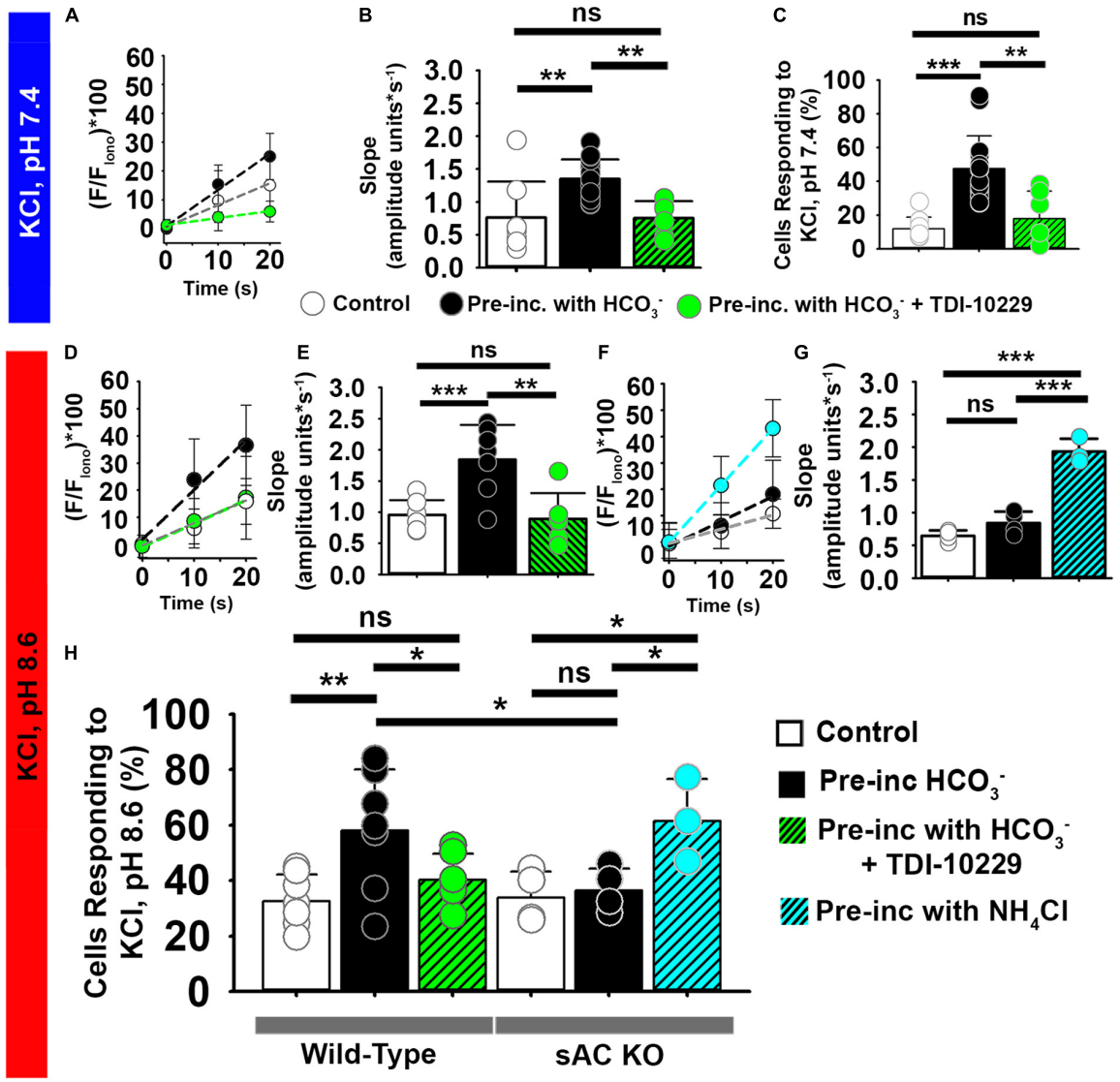

FIGURE 7 | The soluble adenylyl cyclase (sAC) is required for $[Ca^{2+}]_i$ increases evoked by KCl after HCO_3^- sensitization in epididymal mouse sperm. **(A,D,F)** Linear fit of the averaged normalized fluorescence in the first 20 s after KCl addition at **(A)** pH 7.4 and **(D,F)** pH 8.6. Data were obtained from epididymal **(A,D)** wild-type mouse sperm and from **(G)** sAC KO mouse sperm in control conditions (white) and after pre-incubation with HCO_3^- (black), HCO_3^- + PKA inhibitor TDI-10229 (Green), or NH_4Cl (Blue). **(B)** Graph of slope values of the best-fit regression line for each condition. Mean values at pH 7.4 were as follows: control, 0.76 ± 0.547 amplitude units * s^{-1} (8 mice, 307 sperm); incubation with HCO_3^-, 1.35 ± 0.297 amplitude units *s^{-1} (15 mice, 1035 sperm); and incubation with TDI-10229, 0.75 ± 0.259 amplitude units *s^{-1} (6 mice, 364 sperm). **(C)** Graph of the percentage of responsive sperm. Mean values at pH 7.4 were as follows: control, 11.80% ± 6.9 (8 mice, 307 sperm); HCO_3^-, 47.6% ± 19.39 (15 mice, 1035 sperm); and HCO_3^- + TDI-10229,17.8% ± 16.33 (6 mice, 364 sperm). **(E)** Slope values per animal of the best-fit linear regression of the rise in KCl at pH 8.6 in different conditions. Mean values at pH 8.6 were as follows: control, 0.95 ± 0.237 amplitude units * s^{-1} (7 mice, 243 sperm); HCO_3^-, 1.84 ± 0.556 amplitude units *s^{-1} (7 mice, 281 sperm); and HCO_3^- + TDI-10229, 0.88 ± 0.413 amplitude units *s^{-1} (6 mice, 126 sperm). **(G)** Graph of slope values of the best-fit regression line for each condition in the sAC KO mice. Mean values at pH 8.6 were as follows: control, 0.645 ± 0.084 amplitude units * s^{-1} (4 mice, 123 sperm); HCO_3^-, 0.840 ± 0.173 amplitude units *s^{-1} (4 mice, 109 sperm); and NH_4Cl, 1.932 ± 0.197 amplitude units *s^{-1} (3 mice, 74 sperm). **(H)** Graph of the percentage of responsive sperm. Mean values for wild-type at pH 8.6 were as follows: control, 32.62% ± 9.58 (7 mice, 243 sperm); HCO_3^-, 58.05% ± 21.94 (7 mice, 281 sperm); and HCO_3^- + TDI-10229, 40.25% ± 9.51 (6 mice, 126 sperm). Mean values for sAC knockout at pH 8.6 were as follows: control, 33.80% ± 9.44 (4 mice, 91 sperm); HCO_3^-, 36.36% ± 7.96 (4 mice, 83 sperm); and NH_4Cl, 61.47% ± 15.20 (3 mice, 74 sperm). *$P < 0.050$, **$P < 0.010$, ***$P < 0.001$, and ns, non-significant by one-way ANOVA. Error bars indicate standard deviation. Iono = 5 μM Ionomycin + 2 mM Ca^{2+}.

Finally, we asked whether we could bypass the need for sAC by treating sperm with 20 mM NH_4Cl, which increases pH_i. This treatment increased the percent of sperm from sAC knock-out mice that increased $[Ca^{2+}]_i$ in response to high extracellular KCl from 33.8 to 61.5% (**Figure 7H**). These data indicate that the change in pH_i induced by sAC/PKA activation is responsible for sensitizing CatSper channels to membrane depolarization.

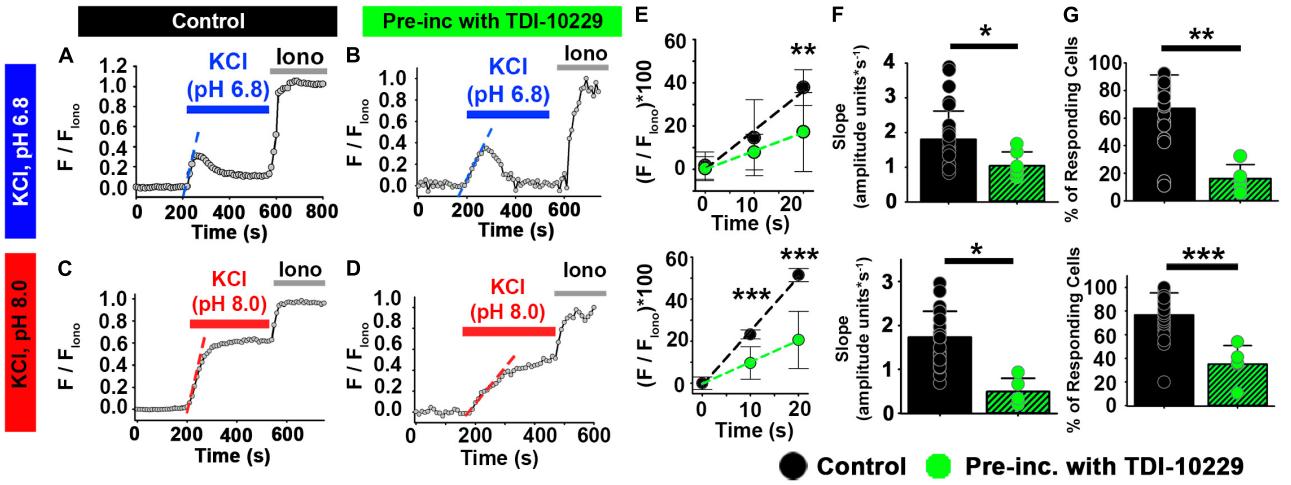

FIGURE 8 | The sACspecific inhibitor TDI-10229 impairs $[Ca^{2+}]i$ responses to KCl in ejaculated human sperm. **(A–D)** Representative traces of $[Ca^{2+}]_i$ responses to 50 mM KCl at **(A,B)** pH 6.8 and **(C,D)** pH 8.0 in ejaculated human sperm in non-capacitating conditions in **(A,C)** control and **(B,D)** after pre-incubation with TDI-10229. **(E)** Linear fit of the averaged normalized fluorescence in the first 20 s after KCl addition at pH 6.8 and pH 8.0. **(F)** Graph of slope values of the best-fit regression line for each condition. Mean values at pH 6.8 were as follows: control, 1.80 ± 0.82 amplitude units * s^{-1} (26 samples, 1836 sperm); and TDI-10229 incubation, 0.426 ± 0.276 amplitude units *s^{-1} (5 samples, 2279 sperm). Mean values at pH 8.0 were as follows: control, 1.73 ± 0.594 amplitude units * s^{-1} (26 samples, 3036 sperm); and TDI-10229 incubation, 0.491 ± 0.305 amplitude units *s^{-1} (5 samples, 2279 sperm). **(G)** Graph of the percentage of responsive sperm. Mean values at pH 6.8 were as follows: control, 66.94% ± 24.30 (26 samples, 1836 sperm); and TDI-10229 pre-incubation, 16.18% ± 10.10 (5 samples, 2279 sperm). Mean values at pH 8.0 were as follows: control, 77.04% ± 18.67 (26 samples, 3036 sperm); and TDI-10229 pre-incubation, 35.43% ± 15.77 (5 samples, 2279 sperm). *$P < 0.050$, **$P < 0.010$, and ***$P < 0.001$ by independent *t*-test. Error bars indicate standard deviation. Iono = 5 μM Ionomycin + 2 mM Ca^{2+}.

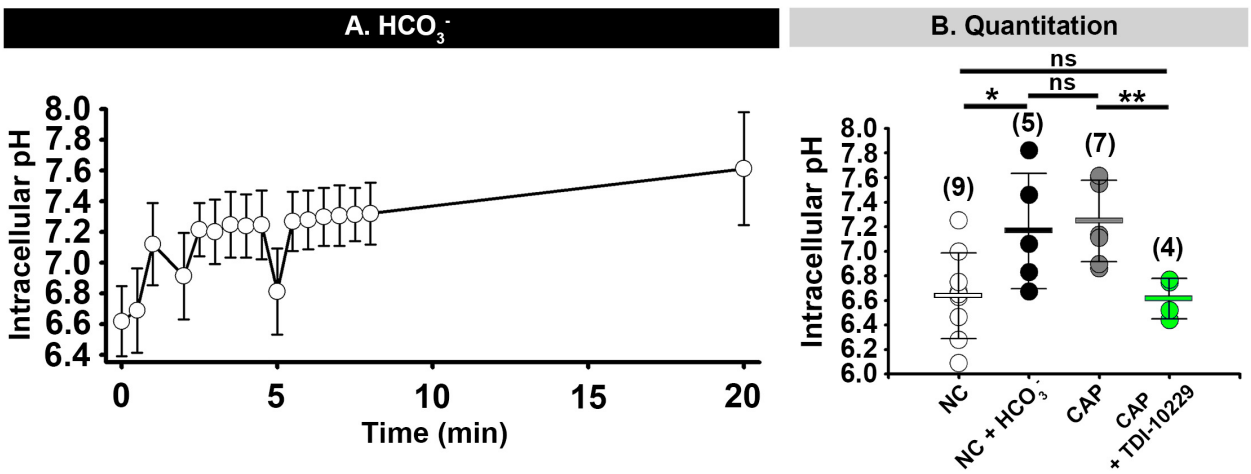

FIGURE 9 | HCO_3^-- induced increase of intracellular pH depends on sAC activity. **(A)** Mean and standard deviation values of intracellular pH in mouse epididymal sperm after addition of 15 mM HCO_3^- at 0 min) (*n* = 3 mice). **(B)** Graph showing sperm intracellular pH values after 60 min incubation in the indicated conditions. NC, non-capacitating; CAP, capacitating. Horizontal bars indicate mean and standard deviation. Mean values for intracellular pH were as follows: NC, 6.64 ± 0.349 (9 mice); NC + HCO_3^-, 7.17 ± 0.469 (5 mice); CAP, 7.25 ± 0.331 (7 mice); and CAP + TDI10229, 6.62 ± 0.164 (4 mice) respectively. Numbers in parentheses are numbers of animals. *$P < 0.05$ and **$P < 0.01$ by one-way ANOVA. ns, non-significant.

DISCUSSION

Together, our data indicate that the model shown in **Figure 10** is responsible for CatSper sensitization to membrane depolarization in both mouse and human sperm. First, ejaculated sperm from both mice and humans showed substantial $[Ca^{2+}]_i$ increases in response to high external KCl at pH 7.4 and pH 6.8, respectively. The greater $[Ca^{2+}]_i$ responses in ejaculated sperm than in epididymal sperm were reflected both by increases in the percentage of responsive sperm and by faster rates of $[Ca^{2+}]_i$ increase in the responsive sperm. Second, although $[Ca^{2+}]_i$ did not increase in response to high external KCl at low pH in either mouse epididymal or human epididymal sperm, $[Ca^{2+}]_i$ increases occurred in mouse epididymal and human epididymal

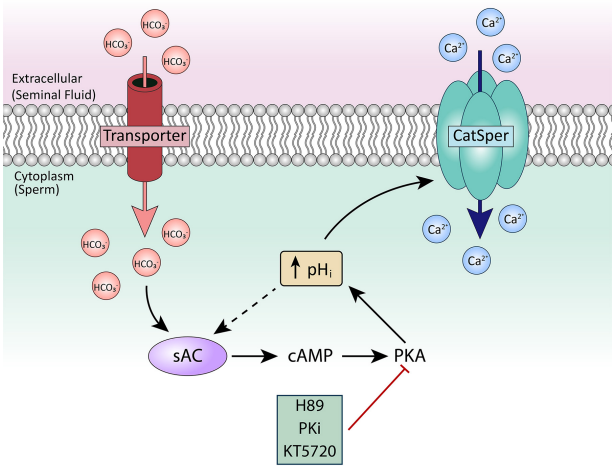

FIGURE 10 | Proposed model for CatSper activation in ejaculated human and mouse sperm. After ejaculation, sperm are exposed to HCO_3^- in the seminal fluid. HCO_3^- activates sAC, leading to production of cAMP, which activates PKA. PKA stimulates alkalinization of the cytoplasm, which sensitizes CatSper to respond to membrane depolarization.

sperm exposed to HCO_3^-. This result indicates that exposure to semen, which contains HCO_3^-, is important for CatSper activation. Third, PKA inhibitors prevented the increases in $[Ca^{2+}]_i$ in response to high external KCl in both mouse and human ejaculated sperm and mouse epididymal sperm pre-incubated with HCO_3^-. These PKA inhibitors reduced both the percentage of responsive sperm and the rate of $[Ca^{2+}]_i$ increase in the responsive sperm. Finally, both genetic ablation of sAC and its pharmacological inhibition prevented the $[Ca^{2+}]_i$ increases induced by HCO_3^-. Thus, our data reveal that CatSper is activated by KCl-induced membrane depolarization similarly in mouse and human sperm at similar stages. Moreover, our data suggest that regulation of CatSper activation by cAMP/PKA starts when the sperm cells encounter the seminal fluid.

Our data help resolve a question in the field regarding CatSper. Although CatSper is known to be the principal Ca^{2+} channel controlling sperm motility in numerous species (Lishko and Mannowetz, 2018), whether the mechanisms of activation are conserved has been unclear. For example, in sea urchin, mouse, and human sperm, CatSper channels are activated by membrane depolarization and by increases in intracellular pH (Kirichok et al., 2006; Seifert et al., 2015; Hwang et al., 2019), suggesting conserved mechanisms. Conversely, human CatSper activity is modulated by nanomolar concentrations of progesterone and prostaglandins both in epididymal and ejaculated samples (Lishko et al., 2011; Strunker et al., 2011), whereas mouse CatSper seems not to be modulated by these hormones (Lishko et al., 2011). Previous work from many labs has shown that HCO_3^- modulates Ca^{2+} entry in mouse and human sperm (Wennemuth et al., 2003; Bedu-Addo et al., 2005; Chavez et al., 2014; Luque et al., 2018). Recently, mouse CatSper was proposed to be activated by HCO_3^- through activation of sAC and PKA (Orta et al., 2018), whereas this mechanism was thought not to apply to human CatSper (Wang et al., 2020). Our work resolves this issue by comparing CatSper activation in mouse and human sperm before and after ejaculation. Thus, our data illustrate the importance of comparing sperm from similar stages of maturation and after similar environmental exposures.

In contrast with our results, Wang et al. (2020) recently reported that CatSper was not modulated by PKA. Several differences in the approach and interpretation of data could explain the different outcomes. First, most of the experiments done by Wang et al. used progesterone to induce Ca^{2+} responses in human sperm. We did not examine the effect of HCO_3^- on the progesterone response, which might differ from the effect of HCO_3^- on the KCl depolarization response. In the few experiments done by Wang et al. using KCl at pH 8.6, they measured the amplitude of $[Ca^{2+}]_i$ and not the rate of $[Ca^{2+}]_i$ increase. We argue that the rate of $[Ca^{2+}]_i$ increase is a better indicator of the effect of HCO_3^- on the depolarizing-evoked Ca^{2+} responses than the absolute amplitude. The amplitude of the response might be affected by Ca^{2+} extrusion and intracellular Ca^{2+} buffers, which can vary upon changes in membrane potential, pH_i, or both.

Second, Wang et al. suggested that the effect of HCO_3^- on CatSper activation could be non-specific and due to HCO_3^--induced changes in the pH of the media and the cytosol (Wang et al., 2020). Specifically, the authors showed that addition of 50 mM HCO_3^- significantly changed the pH of the recording solutions over 120 min, and these changes in pH of the media could change the sperm pH_i. We performed similar experiments measuring the pH of all of our solutions 30 min (the timeline of our experiments) after adding 15, 25, or 50 mM HCO_3^-. Although 50 mM HCO_3^- substantially increased the pH, 15 mM HCO_3^- only increased the pH of the solutions by 0.05–0.1 units after 30 min (**Supplementary Figure 2**). In addition, we washed HCO_3^- out during stimulation with KCl. We also showed that, in non-capacitated sperm, the pH_i increased by 0.5–0.8 units after 10 min incubation in 15 mM HCO_3^-. Thus, HCO_3^- caused the sperm pH_i to increase 5–10-fold more than the media pH. Thus, any changes to external pH were not likely to be responsible for the pH_i changes of 0.5–0.6 units we observed after applying HCO_3^-.

Third, we used different experimental systems than Wang et al. Most notably, Wang et al. performed experiments on sperm populations with a multi-well plate reader (Fluostar Omega, BMG Labtech) in which solutions cannot be changed. Concentrations of ions and drugs can be modified only by adding concentrated solutions such as 50 mM HCO_3^- and 98.5 mM KCl to yield final concentrations of approximately 25 mM HCO_3^- and 50 mM KCl. Given the diffusion of the ions in the first minute of the recordings, a considerable number of cells could have been exposed to the higher concentrations of HCO_3^- and KCl. Therefore, the effects on Ca^{2+} signals reported at 25 mM HCO_3^- and KCl at pH 8.6 could be underestimated, as many cells could have been exposed to a saturating stimulus of 98.5 mM KCl and 50 mM HCO_3^- in the controls at the moment of injection. In contrast, we measured $[Ca^{2+}]_i$ in individual cells, and our system allowed the exchange of solutions without exposing the cells to

high concentrations of HCO_3^- and KCl, and without changes in the osmolarity of the solutions.

Our results are consistent with others' observations that the sAC and PKA pathways are important in regulating sperm capacitation in many species and that these pathways act, at least in part, by regulating pH_i (Puga Molina et al., 2017; Chavez et al., 2019; Matamoros-Volante and Trevino, 2020; Balbach et al., 2021). Carlson et al. showed no changes in pH_i induced by HCO_3^- in mouse sperm. However, those experiments only tested the effect of HCO_3^- during the first 30–60 s of HCO_3^- application (Carlson et al., 2007). Notably, the changes in pH_i that we measured after applying HCO_3^- occurred in the same temporal window as the activation of PKA (1–2 min) (Buffone et al., 2014).

Our observation that the HCO_3^--induced change in pH_i was inhibited by a specific sAC inhibitor (Balbach et al., 2020, 2021) suggests that the main mechanism of pH_i increase is through the sAC/cAMP/PKA pathway. This increase in pHi might further activate sAC, as Xie et al. showed that sAC activity increases upon intracellular alkalinization (Xie et al., 2006). Further work is needed to determine whether PKA solely regulates CatSper through pH_i or also through other mechanisms. Adonal work is also needed to identify the molecular mechanism responsible for the increase in pH_i induced by PKA.

DATA AVAILABILITY STATEMENT

The raw data supporting the conclusions of this article will be made available by the authors, without undue reservation.

ETHICS STATEMENT

The studies involving human participants were reviewed and approved by University in St. Louis Institutional Review Board (protocol #201706077). The patients/participants provided their written informed consent to participate in this study. The animal study was reviewed and approved by Institutional Animal Care and UseCommittee of Washington University in St. Louis (St. Louis, MO) (protocol # 20-0126).

AUTHOR CONTRIBUTIONS

JJF designed, performed, analyzed data, and interpreted the results. PL designed and analyzed experiments. LCP-M designed, performed, analyzed experiments. CMS analyzed data and interpreted the results. JJF and LCP-M prepared the figures. JJF and CMS drafted the manuscript. JJF, PL, LCP-M, and CMS edited, revised, and approved the final version of the manuscript. All authors contributed to the article and approved the submitted version

FUNDING

This work was supported by: NIH, NICHD R01 grant # R01HD069631 to CMS.

ACKNOWLEDGMENTS

We thank Deborah Frank for editing the manuscript, Anthony Bartley for designing **Figure10**, and Lonny Levin and Jochen Buck for generous donation of sAC knockout mice and the sAC inhibitor TDI-10229.

SUPPLEMENTARY MATERIAL

The Supplementary Material for this article can be found online at: https://www.frontiersin.org/articles/10.3389/fcell.2021.733653/full#supplementary-material

REFERENCES

Alasmari, W., Costello, S., Correia, J., Oxenham, S. K., Morris, J., Fernandes, L., et al. (2013). Ca2+ signals generated by CatSper and Ca2+ stores regulate different behaviors in human sperm. *J. Biol. Chem.* 288, 6248–6258. doi: 10.1074/jbc.M112.439356

Austin, C. R. (1951). Observations on the penetration of the sperm in the mammalian egg. *Aust. J. Sci. Res. B* 4, 581–596. doi: 10.1071/BI9510581

Austin, C. R. (1952). The capacitation of the mammalian sperm. *Nature* 170:326. doi: 10.1038/170326a0

Austin, C. R., and Bishop, M. W. (1958). Capacitation of mammalian spermatozoa. *Nature* 181:851. doi: 10.1038/181851a0

Balbach, M., Fushimi, M., Huggins, D. J., Steegborn, C., Meinke, P. T., Levin, L. R., et al. (2020). Optimization of lead compounds into on-demand, nonhormonal contraceptives: leveraging a public-private drug discovery institute collaborationdagger. *Biol. Reprod.* 103, 176–182. doi: 10.1093/biolre/ioaa052

Balbach, M., Ghanem, L., Rossetti, T., Kaur, N., Ritagliati, C., Ferreira, J., et al. (2021). Soluble adenylyl cyclase inhibition prevents human sperm functions essential for fertilization. *bioRxiv* [Preprint]. doi: 10.1093/molehr/gaab054

Baldi, E., Casano, R., Falsetti, C., Krausz, C., Maggi, M., and Forti, G. (1991). Intracellular calcium accumulation and responsiveness to progesterone in capacitating human spermatozoa. *J. Androl.* 12, 323–330. doi: <doi>

Battistone, M. A., Da Ros, V. G., Salicioni, A. M., Navarrete, F. A., Krapf, D., Visconti, P. E., et al. (2013). Functional human sperm capacitation requires both bicarbonate-dependent Pka activation and down-regulation of Ser/Thr phosphatases by Src family kinases. *Mol. Hum. Reprod.* 19, 570–580. doi: 10.1093/molehr/gat033

Bedu-Addo, K., Lefievre, L., Moseley, F. L., Barratt, C. L., and Publicover, S. J. (2005). Bicarbonate and bovine serum albumin reversibly 'switch' capacitation-induced events in human spermatozoa. *Mol. Hum. Reprod.* 11, 683–691. doi: 10.1093/molehr/gah226

Breitbart, H. (2002a). Intracellular calcium regulation in sperm capacitation and acrosomal reaction. *Mol. Cell. Endocrinol.* 187, 139–144. doi: 10.1016/S0303-7207(01)00704-3

Breitbart, H. (2002b). Role and regulation of intracellular calcium in acrosomal exocytosis. *J. Reprod. Immunol.* 53, 151–159. doi: 10.1016/S0165-0378(01)00085-7

Buck, J., Sinclair, M. L., Schapal, L., Cann, M. J., and Levin, L. R. (1999). Cytosolic adenylyl cyclase defines a unique signaling molecule in mammals. *Proc. Natl. Acad. Sci. U.S.A.* 96, 79–84. doi: 10.1073/pnas.96.1.79

Buffone, M. G., Wertheimer, E. V., Visconti, P. E., and Krapf, D. (2014). Central role of soluble adenylyl cyclase and cAMP in sperm physiology. *Biochim. Biophys. Acta* 1842, 2610–2620. doi: 10.1016/j.bbadis.2014.07.013

Carlson, A. E., Hille, B., and Babcock, D. F. (2007). External Ca2+ acts upstream of adenylyl cyclase SACY in the bicarbonate signaled activation of sperm motility. *Dev. Biol.* 312, 183–192. doi: 10.1016/j.ydbio.2007.09.017

Carlson, A. E., Westenbroek, R. E., Quill, T., Ren, D., Clapham, D. E., Hille, B., et al. (2003). CatSper1 required for evoked Ca2+ entry and control of flagellar function in sperm. *Proc. Natl. Acad. Sci. U.S.A.* 100, 14864–14868. doi: 10.1073/pnas.2536658100

Chang, M. C. (1951). Fertilizing capacity of spermatozoa deposited into the fallopian tubes. *Nature* 168, 697–698. doi: 10.1038/168697b0

Chavez, J. C., Darszon, A., Trevino, C. L., and Nishigaki, T. (2019). Quantitative intracellular pH determinations in single live mammalian spermatozoa using the ratiometric dye SNARF-5F. *Front. Cell Dev. Biol.* 7:366. doi: 10.3389/fcell.2019.00366

Chavez, J. C., de la Vega-Beltran, J. L., Escoffier, J., Visconti, P. E., Trevino, C. L., Darszon, A., et al. (2013). Ion permeabilities in mouse sperm reveal an external trigger for SLO3-dependent hyperpolarization. *PLoS One* 8:e60578. doi: 10.1371/journal.pone.0060578

Chavez, J. C., Ferreira, J. J., Butler, A., De La Vega Beltran, J. L., Trevino, C. L., Darszon, A., et al. (2014). SLO3 K+ channels control calcium entry through CATSPER channels in sperm. *J. Biol. Chem.* 289, 32266–32275. doi: 10.1074/jbc.M114.607556

Chen, Y., Cann, M. J., Litvin, T. N., Iourgenko, V., Sinclair, M. L., Levin, L. R., et al. (2000). Soluble adenylyl cyclase as an evolutionarily conserved bicarbonate sensor. *Science* 289, 625–628. doi: 10.1126/science.289.5479.625

de la Vega-Beltran, J. L., Sanchez-Cardenas, C., Krapf, D., Hernandez-Gonzalez, E. O., Wertheimer, E., Trevino, C. L., et al. (2012). Mouse sperm membrane potential hyperpolarization is necessary and sufficient to prepare sperm for the acrosome reaction. *J. Biol. Chem.* 287, 44384–44393. doi: 10.1074/jbc.M112.393488

Demarco, I. A., Espinosa, F., Edwards, J., Sosnik, J., de la Vega-Beltran, J. L., Hockensmith, J. W., et al. (2003). Involvement of a Na+/HCO-3 cotransporter in mouse sperm capacitation. *J. Biol. Chem.* 278, 7001–7009. doi: 10.1074/jbc.M206284200

Demott, R. P., and Suarez, S. S. (1992). Hyperactivated sperm progress in the mouse oviduct. *Biol. Reprod.* 46, 779–785. doi: 10.1095/biolreprod46.5.779

Gunderson, S. J., Puga Molina, L. C., Spies, N., Balestrini, P. A., Buffone, M. G., Jungheim, E. S., et al. (2021). Machine-learning algorithm incorporating capacitated sperm intracellular pH predicts conventional in vitro fertilization success in normospermic patients. *Fertil. Steril.* 115, 930–939. doi: 10.1016/j.fertnstert.2020.10.038

Hess, K. C., Jones, B. H., Marquez, B., Chen, Y., Ord, T. S., Kamenetsky, M., et al. (2005). The "soluble" adenylyl cyclase in sperm mediates multiple signaling events required for fertilization. *Dev. Cell* 9, 249–259. doi: 10.1016/j.devcel.2005.06.007

Hirohashi, N., and Yanagimachi, R. (2018). Sperm acrosome reaction: its site and role in fertilization. *Biol. Reprod.* 99, 127–133. doi: 10.1093/biolre/ioy045

Hwang, J. Y., Mannowetz, N., Zhang, Y., Everley, R. A., Gygi, S. P., Bewersdorf, J., et al. (2019). Dual sensing of physiologic pH and calcium by EFCAB9 regulates sperm motility. *Cell* 177, 1480.e19–1494.e19. doi: 10.1016/j.cell.2019.03.047

Kirichok, Y., Navarro, B., and Clapham, D. E. (2006). Whole-cell patch-clamp measurements of spermatozoa reveal an alkaline-activated Ca2+ channel. *Nature* 439, 737–740. doi: 10.1038/nature04417

Li, H., Hung, P. H., and Suarez, S. S. (2015). Ejaculated mouse sperm enter cumulus-oocyte complexes more efficiently in vitro than epididymal sperm. *PLoS One* 10:e0127753. doi: 10.1371/journal.pone.0127753

Lishko, P. V., Botchkina, I. L., and Kirichok, Y. (2011). Progesterone activates the principal Ca2+ channel of human sperm. *Nature* 471, 387–391. doi: 10.1038/nature09767

Lishko, P. V., and Mannowetz, N. (2018). CatSper: a unique calcium channel of the sperm flagellum. *Curr. Opin. Physiol.* 2, 109–113. doi: 10.1016/j.cophys.2018.02.004

López-González, I., Torres-Rodríguez, P., Sánchez-Carranza, O., Solís-López, A., Santi, C. M., Darszon, A., et al. (2014). Membrane hyperpolarization during human sperm capacitation. *MHR Basic Sci. Reprod. Med.* 20, 619–629. doi: 10.1093/molehr/gau029

Luque, G. M., Dalotto-Moreno, T., Martin-Hidalgo, D., Ritagliati, C., Puga Molina, L. C., Romarowski, A., et al. (2018). Only a subpopulation of mouse sperm displays a rapid increase in intracellular calcium during capacitation. *J. Cell. Physiol.* 233, 9685–9700. doi: 10.1002/jcp.26883

Matamoros-Volante, A., and Trevino, C. L. (2020). Capacitation-associated alkalization in human sperm is differentially controlled at the subcellular level. *J. Cell Sci.* 133:jcs238816. doi: 10.1242/jcs.238816

Okamura, N., Tajima, Y., Soejima, A., Masuda, H., and Sugita, Y. (1985). Sodium-bicarbonate in seminal plasma stimulates the motility of mammalian spermatozoa through direct activation of adenylate-cyclase. *J. Biol. Chem.* 260, 9699–9705. doi: 10.1016/S0021-9258(17)39295-5

Orta, G., de la Vega-Beltran, J. L., Martin-Hidalgo, D., Santi, C. M., Visconti, P. E., and Darszon, A. (2018). CatSper channels are regulated by protein kinase A. *J. Biol. Chem.* 293, 16830–16841. doi: 10.1074/jbc.RA117.001566

Puga Molina, L. C., Pinto, N. A., Torres, N. I., Gonzalez-Cota, A. L., Luque, G. M., Balestrini, P. A., et al. (2018). Cftr/EnaC-dependent regulation of membrane potential during human sperm capacitation is initiated by bicarbonate uptake through Nbc. *J. Biol. Chem.* 293, 9924–9936. doi: 10.1074/jbc.RA118.003166

Puga Molina, L. C., Pinto, N. A., Torres Rodriguez, P., Romarowski, A., Vicens Sanchez, A., Visconti, P. E., et al. (2017). Essential Role of CFTR in PKA-dependent phosphorylation, alkalinization, and hyperpolarization during human sperm capacitation. *J. Cell. Physiol.* 232, 1404–1414. doi: 10.1002/jcp.25634

Ren, D., Navarro, B., Perez, G., Jackson, A. C., Hsu, S., Shi, Q., et al. (2001). A sperm ion channel required for sperm motility and male fertility. *Nature* 413, 603–609. doi: 10.1038/35098027

Santi, C. M., Martinez-Lopez, P., de la Vega-Beltran, J. L., Butler, A., Alisio, A., Darszon, A., et al. (2010). The SLO3 sperm-specific potassium channel plays a vital role in male fertility. *FEBS Lett.* 584, 1041–1046. doi: 10.1016/j.febslet.2010.02.005

Seifert, R., Flick, M., Bonigk, W., Alvarez, L., Trotschel, C., Poetsch, A., et al. (2015). The CatSper channel controls chemosensation in sea urchin sperm. *EMBO J.* 34, 379–392. doi: 10.15252/embj.201489376

Smith, J. F., Syritsyna, O., Fellous, M., Serres, C., Mannowetz, N., Kirichok, Y., et al. (2013). Disruption of the principal, progesterone-activated sperm Ca2+ channel in a CatSper2-deficient infertile patient. *Proc. Natl. Acad. Sci. U.S.A.* 110, 6823–6828. doi: 10.1073/pnas.1216588110

Stival, C., Puga Molina, L. D. C., Paudel, B., Buffone, M. G., Visconti, P. E., and Krapf, D. (2016). Sperm capacitation and acrosome reaction in mammalian sperm. *Adv. Anat. Embryol. Cell Biol.* 220, 93–106. doi: 10.1007/978-3-319-30567-7_5

Strunker, T., Goodwin, N., Brenker, C., Kashikar, N. D., Weyand, I., Seifert, R., et al. (2011). The CatSper channel mediates progesterone-induced Ca2+ influx in human sperm. *Nature* 471, 382–386. doi: 10.1038/nature09769

Suarez, S. S., Varosi, S. M., and Dai, X. (1993). Intracellular calcium increases with hyperactivation in intact, moving hamster sperm and oscillates with the flagellar beat cycle. *Proc. Natl. Acad. Sci. U.S.A.* 90, 4660–4664. doi: 10.1073/pnas.90.10.4660

Visconti, P. E. (2009). Understanding the molecular basis of sperm capacitation through kinase design. *Proc. Natl. Acad. Sci. U.S.A.* 106, 667–668. doi: 10.1073/pnas.0811895106

Visconti, P. E., Moore, G. D., Bailey, J. L., Leclerc, P., Connors, S. A., Pan, D., et al. (1995). Capacitation of mouse spermatozoa. II. Protein tyrosine phosphorylation and capacitation are regulated by a camp-dependent pathway. *Development* 121, 1139–1150. doi: 10.1242/dev.121.4.1139

Vyklicka, L., and Lishko, P. V. (2020). Dissecting the signaling pathways involved in the function of sperm flagellum. *Curr. Opin. Cell Biol.* 63, 154–161. doi: 10.1016/j.ceb.2020.01.015

Wang, T., Young, S., Krenz, H., Tuttelmann, F., Ropke, A., Krallmann, C., et al. (2020). The Ca(2+) channel CatSper is not activated by camp/Pka signaling but directly affected by chemicals used to probe the action of cAMP and PKA. *J. Biol. Chem.* 295, 13181–13193. doi: 10.1074/jbc.RA120.013218

Wennemuth, G., Carlson, A. E., Harper, A. J., and Babcock, D. F. (2003). Bicarbonate actions on flagellar and Ca2+ -channel responses: initial events in sperm activation. *Development* 130, 1317–1326. doi: 10.1242/dev.00353

Wennemuth, G., Westenbroek, R. E., Xu, T., Hille, B., and Babcock, D. F. (2000). CaV2.2 and CaV2.3 (N- and R-type) Ca2+ channels in depolarization-evoked

entry of Ca2+ into mouse sperm. *J. Biol. Chem.* 275, 21210–21217. doi: 10.1074/jbc.M002068200

Xia, J., Reigada, D., Mitchell, C. H., and Ren, D. (2007). Catsper channel-mediated Ca2+ entry into mouse sperm triggers a tail-to-head propagation. *Biol. Reprod.* 77, 551–559. doi: 10.1095/biolreprod.107.061358

Xie, F., Garcia, M. A., Carlson, A. E., Schuh, S. M., Babcock, D. F., Jaiswal, B. S., et al. (2006). Soluble adenylyl cyclase (sAC) is indispensable for sperm function and fertilization. *Dev. Biol.* 296, 353–362. doi: 10.1016/j.ydbio.2006.05.038

Yanagimachi, R. (1970). The movement of golden hamster spermatozoa before and after capacitation. *J. Reprod. Fertil.* 23, 193–196. doi: 10.1530/jrf.0.0230193

Zeng, Y., Clark, E. N., and Florman, H. M. (1995). Sperm membrane potential: hyperpolarization during capacitation regulates zona pellucida-dependent acrosomal secretion. *Dev. Biol.* 171, 554–563. doi: 10.1006/dbio.1995.1304

Conflict of Interest: The authors declare that the research was conducted in the absence of any commercial or financial relationships that could be construed as a potential conflict of interest.

Publisher's Note: All claims expressed in this article are solely those of the authors and do not necessarily represent those of their affiliated organizations, or those of the publisher, the editors and the reviewers. Any product that may be evaluated in this article, or claim that may be made by its manufacturer, is not guaranteed or endorsed by the publisher.

Copyright © 2021 Ferreira, Lybaert, Puga-Molina and Santi. This is an open-access article distributed under the terms of the Creative Commons Attribution License (CC BY). The use, distribution or reproduction in other forums is permitted, provided the original author(s) and the copyright owner(s) are credited and that the original publication in this journal is cited, in accordance with accepted academic practice. No use, distribution or reproduction is permitted which does not comply with these terms.

frontiers in Cell and Developmental Biology

BRIEF RESEARCH REPORT
published: 29 September 2021
doi: 10.3389/fcell.2021.727264

Microtubule Organizing Centers Contain Testis-Specific γ-TuRC Proteins in Spermatids of Drosophila

*Elham Alzyoud[1,2], Viktor Vedelek[1], Zsuzsánna Réthi-Nagy[2,3], Zoltán Lipinszki[3] and Rita Sinka[1]**

[1] Department of Genetics, University of Szeged, Szeged, Hungary, [2] Faculty of Science and Informatics, Doctoral School of Biology, University of Szeged, Szeged, Hungary, [3] Biological Research Centre, Institute of Biochemistry, MTA SZBK Lendület Laboratory of Cell Cycle Regulation, Eötvös Loránd Research Network (ELKH), Szeged, Hungary

OPEN ACCESS

Edited by:
Chih-kuan Tung,
North Carolina Agricultural and Technical State University, United States

Reviewed by:
Paul Conduit,
UMR 7592 Institut Jacques Monod (IJM), France
Brian Galletta,
National Heart, Lung, and Blood Institute (NHLBI), United States

***Correspondence:**
Rita Sinka
rsinka@bio.u-szeged.hu

Specialty section:
This article was submitted to Cell Growth and Division, a section of the journal Frontiers in Cell and Developmental Biology

Received: 18 June 2021
Accepted: 10 September 2021
Published: 29 September 2021

Citation:
Alzyoud E, Vedelek V, Réthi-Nagy Z, Lipinszki Z and Sinka R (2021) Microtubule Organizing Centers Contain Testis-Specific γ-TuRC Proteins in Spermatids of Drosophila. Front. Cell Dev. Biol. 9:727264. doi: 10.3389/fcell.2021.727264

Microtubule nucleation in eukaryotes is primarily promoted by γ-tubulin and the evolutionary conserved protein complex, γ-Tubulin Ring Complex (γ-TuRC). γ-TuRC is part of the centrosome and basal body, which are the best-known microtubule-organizing centers. Centrosomes undergo intensive and dynamic changes during spermatogenesis, as they turn into basal bodies, a prerequisite for axoneme formation during spermatogenesis. Here we describe the existence of a novel, tissue-specific γ-TuRC in Drosophila. We characterize three genes encoding testis-specific components of γ-TuRC (t-γ-TuRC) and find that presence of t-γ-TuRC is essential to male fertility. We show the diverse subcellular distribution of the t-γ-TuRC proteins during post-meiotic development, at first at the centriole adjunct and then also on the anterior tip of the nucleus, and finally, they appear in the tail region, close to the mitochondria. We also prove the physical interactions between the t-γ-TuRC members, γ-tubulin and Mozart1. Our results further indicate heterogeneity in γ-TuRC composition during spermatogenesis and suggest that the different post-meiotic microtubule organizing centers are orchestrated by testis-specific gene products, including t-γ-TuRC.

Keywords: Drosophila, spermatogenesis, γ-TuRC, microtubules, MTOC, basal body, mitochondria

INTRODUCTION

Microtubule-organizing centers and microtubule cytoskeleton contribute to the process of cellular differentiation, cell division and the organization of flagella and cilia. The centrosome is the best-understood and main microtubule-organizing center (MTOC) of eukaryotic dividing cells, and is composed of two centrioles surrounded by pericentriolar material (Wiese and Zheng, 1999; Lattao et al., 2017). Apart from the centrosome, other non-centrosomal MTOCs (ncMTOCs) exist to fulfil specific functions on the mitochondria, Golgi, nuclear envelope, or cell cortex. Both the centrosome and the ncMTOCs can recruit the multiprotein γ-TuRC to the nucleation site. γ-tubulin exists in two evolutionary conserved complexes: the γ-Tubulin Small Complex (γ-TuSC) and γ-TuRC (Wiese and Zheng, 1999; Tillery et al., 2018). Despite the importance of γ-TuRC in γ-Tubulin binding and microtubule nucleation, the core γ-TuRC proteins are represented by only one ortholog in different species so far. The stabilization of the core γ-TuRC was suggested by binding

with additional γ-TuRC interacting proteins, such as Mozart1 (Mzt1) and Mozart2, Nedd1 or the γ-TuRC tethering CDK5RAP2 (Liu et al., 2021). In Drosophila γ-TuSC is composed of two γ-tubulins and two Grip proteins, Grip84 and Grip91; while γ-TuRC comprises multiple γ-TuSC proteins and three or four additional Grip proteins, Grip75, Grip128, Grip163, and Grip71 (Gunawardane et al., 2000; Veìrollet et al., 2006). It was shown that both the CDK5RAP2 ortholog Cnn and the recently identified Mzt1 can bind to components of the core γ-TuRC in Drosophila (Zhang and Megraw, 2007; Tovey et al., 2018). The testis-specific isoform of Cnn, CnnT was shown to support the formation of MTOCs on the mitochondrial surface, while Mzt1 was shown to concentrate on the centriole adjunct of spermatids (Chen et al., 2017; Tovey et al., 2018).

Gene duplication is a major mechanism in molecular evolution, providing the possibility of neofunctionalization and subfunctionalization of the duplicated genes. Many metabolic enzymes and protein-degradation-related genes have been shown to have duplicated retrogenes with testis-specific transcript enrichment patterns in the late stages of spermatogenesis (Porcelli et al., 2007; Belote and Zhong, 2009; White-Cooper and Bausek, 2010).

Testis-specific gene products contribute to specialized sperm-specific organelle formation in late spermiogenesis, such as the elongated mitochondria, the acrosome or centriole adjunct (Dallai et al., 2016; Vedelek et al., 2016; Chen et al., 2017; Laurinyecz et al., 2019). As the spermatids begin to elongate, the nebenkern unfurls and forms two mitochondrial derivatives, which elongate with the cooperation of cytoplasmic non-axonemal microtubules and run along the sperm tail (Noguchi et al., 2011). Centrosomes transform into basal bodies and the centrioles become exceptionally long during spermatocyte maturation, eventually giving rise to a 1.8 mm long flagellar axonemes after the meiotic divisions (Fabian and Brill, 2012). Several basal body or centriole adjunct components of the spermatids are not present in the mature sperm, suggesting their intensive reduction in late spermiogenesis (e.g., γ-Tubulin, Sas4, Sas6) (Raynaud-Messina et al., 2001; Blachon et al., 2014). Since sperm elongation and nuclear shaping largely depend on the microtubule cytoskeleton, microtubule nucleation must be strictly regulated to guarantee the correct formation of microtubule networks in the different stages of sperm development. Interestingly, many Drosophila mutants for centrosome, basal body or centriole adjunct components are viable, but male sterile, suggesting that male germline development is very sensitive to alterations in these organelles, making it an ideal system to study the components of MTOCs through cell differentiation.

In this study, we describe the presence and dynamic post-meiotic protein localization of alternative γ-TuRCs during spermatogenesis in *Drosophila melanogaster*. We identified three testis-specific γ-TuRC (t-γ-TuRC) proteins, t-Grip84, t-Grip91, and t-Grip128 and we show that from the round spermatid stage onward, the three t-γ-TuRC proteins start to localize at the centriole adjunct, then also to the nuclear tip, and finally surrounding the mitochondria of the elongating cyst. We demonstrate that the identified complexes colocalize and bind directly to both γ-tubulin and Mzt1, suggesting a transition of these proteins between the somatic and testis-specific complex. Our work proves the existence of different types of γ-TuRCs in the spermatogenesis of *Drosophila melanogaster*.

RESULTS

Identification and Phenotypic Characterization of t-γ-TuRC Members

We previously conducted a transcriptomic analysis of the different regions of Drosophila testis and identified members of several protein families (including γ-tubulin-containing complexes) with high transcript accumulation in the basal end of the testis (Vedelek et al., 2018). Transcripts of the somatic γ-TuRC genes (Grip84, Grip91, Grip75, Grip128, Grip163, and Grip71) are present mainly in the apical end of the testis, based on RNA sequencing data (**Figure 1A**; Vedelek et al., 2018). Interestingly, we identified three testis-specific Grip paralogs (CG7716 (t-Grip84), CG18109 (t-Grip91), and CG32232 (t-Grip128)) with high transcript accumulation in the basal end of the testis, suggesting that they are components of an uncharacterized testis-specific γ-TuRC (**Figure 1A**). We compared the somatic and testis-specific γ-TuRC proteins by protein sequence alignment and also we constructed a phylogenetic tree to visualize the relation between the γ-TuRC proteins (**Figure 1A**; **Supplementary Figure 1**).

To investigate the function of the t-γ-TuRC coding genes, we analyzed their mutant phenotype. We collected the available mutants of *t-Grip84* (*t-Grip84*^{MB07394} (thereafter *t-Grip84*^{ms}), *t-Grip84*^{MI12921}), *t-Grip91* (*t-Grip91*^{MI05374} (thereafter *t-Grip91*^{ms})) and generated a null mutant allele for *t-Grip128* using CRISPR-Cas9 gene editing (*t-Grip128*$^{\Delta 65}$). By measuring the relative gene expression in homozygous *t-Grip84*^{ms}, *t-Grip91*^{ms} and *t-Grip128*$^{\Delta 65}$ testis, we found a dramatic reduction of the gene products in all three mutants (**Supplementary Figure 2A**). Despite containing a deletion of 3359 bp, which removes the start codon and most of the coding region (1–891aa) of *t-Grip128*, homozygous *t-Grip128*$^{\Delta 65}$ males are fertile, suggesting that *t-Grip128* is not essential for normal male fertility (**Figure 1B** and **Supplementary Figure 2B**). We tested the age-dependent fertility of *t-Grip128*$^{\Delta 65}$ mutants and found a comparable number of offspring in the control, suggesting a redundant role in male fertility for *t-Grip128* (**Supplementary Figure 2C**). However, both *t-Grip84*^{ms} and *t-Grip84*^{MI12921} are male-sterile, while *t-Grip91*^{ms} males are semi-sterile in homozygotes and hemizygotes (**Figure 1B** and **Supplementary Figure 2B**). We found empty seminal vesicles, lacking mature sperm in *t-Grip84*^{ms}, whereas a reduced number of sperms is present in *t-Grip91*^{ms} seminal vesicles (**Figures 1C–E**).

During cyst elongation, long axonemes form parallel with the elongated mitochondria, in close connection with the elongated nucleus, followed by cyst individualization which is orchestrated by actin-containing individualization complexes (IC). To understand the function of t-γ-TuRC proteins during spermatogenesis, we investigated the morphology of the *t-Grip84*^{ms} and *t-Grip91*^{ms} mutant testes. We analyzed the

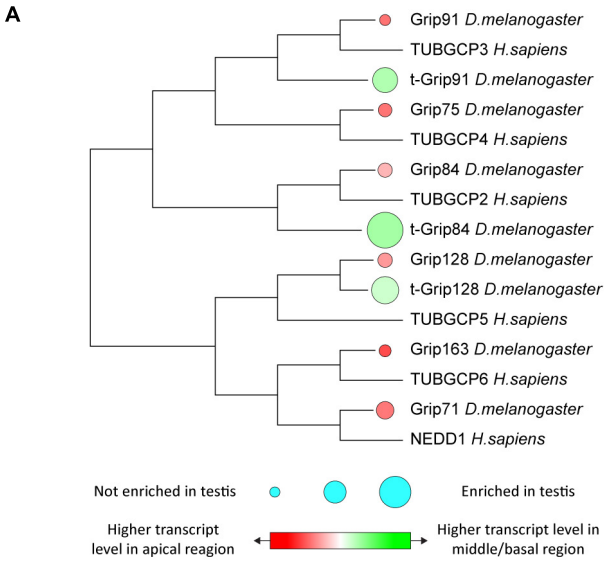

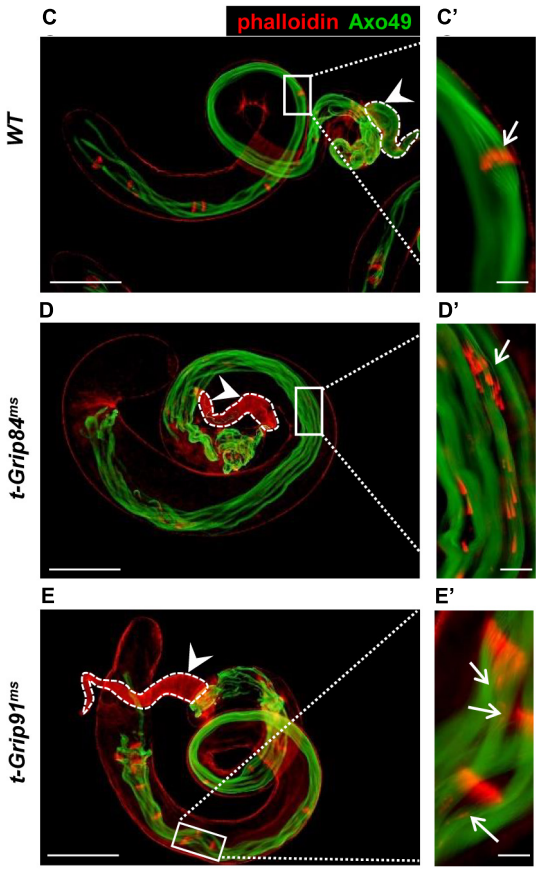

B

Gene	Mutant allele	Homozygous Phenotype	Hemizygous Phenotype
t-Grip84	*t-Grip84^{MB07394} (t-Grip84^{ms})*	male-sterile	male-sterile
	t-Grip84^{MI12921}	male-sterile	male-sterile
t-Grip91	*t-Grip91^{MI05374} (t-Grip91^{ms})*	male-semi-sterile	male-semi-sterile *
t-Grip128	*t-Grip128$^{\Delta 65}$*	fertile	fertile

FIGURE 1 | Identification and phenotypic characterization of t-γ-TuRC members. **(A)** The phylogenetic tree shows conservation among Drosophila and human γ-TuRC proteins. Transcript accumulation in the apical region (red) and basal region (green) and testis enrichment of γ-TuRC members are labelled. **(B)** Phenotypic characterization of t-γ-TuRC mutants. *70% of *t-Grip91^{ms}* males are sterile. (See also **Supplementary Figures 2B,C**). **(C–E)** Polyglycylated elongated axonemes are visualized by AXO49 staining (green) and individualization complexes stained with Phalloidin (red). Axoneme elongation of *t-Grip84^{ms}* and *t-Grip91^{ms}* mutants is similar to WT. **(C')** Movement of the investment cones are synchronized (arrow) and **(C)** seminal vesicle is filled with mature sperm (arrowhead) in WT testis. **(D',E')** Scattered investment cones (arrows) and **(D,E)** empty seminal vesicles (arrowhead) are present in *t-Grip84^{ms}* and *t-Grip91^{ms}* mutants. Scale bars: C-E 100 μm, **(C'–E')** 20 μm.

different developmental stages of spermatogenesis and found that the mitotic and meiotic divisions were normal in both t-γ-TuRC mutants, resulting in wild type round spermatids with equal-sized nebenkern and nucleus, in a 1:1 ratio (**Supplementary Figures 2D–G**). First, we tested the presence and distribution of polyglycylated tubulin, a hallmark of the fully elongated, developed axoneme of the spermatid at the onset of individualization (Bre et al., 1996). We found that, similar to the wild type, the axonemes of both mutants contain polyglycylated tubulin, suggesting normal cyst elongation and axoneme formation (**Figures 1C–E**). Next, we tested the individualization of the spermatids (**Figures 1C–E**). Visualization of the actin cones of the IC revealed that, although the formation of the actin cones is not disturbed, they become severely dispersed in the sterile *t-Grip84^{ms}*. We observed a weaker phenotype in *t-Grip91^{ms}* mutant cysts, but abnormally distributed actin cones were still present (**Figures 1C'–E'** and **Supplementary Figure 2H**). These results strongly suggest that t-γ-TuRC is not essential during the early stages of spermatogenesis or for the formation of the axoneme, and the asynchronous movement of the ICs of the elongated spermatids is probably a secondary consequence of the disturbed spermiogenesis.

Localization of t-γ-TuRC Members During Spermatogenesis

To better understand the expression pattern and subcellular distribution of the t-γ-TuRC components, we generated transgenic proteins fused with different protein tags. We established *t-Grip84-mCherry* (*t-Grip84-mCh*), *t-Grip84-GFP, HA-t-Grip91*, and *HA-t-Grip128* transgenic lines, under the control of their own promoters (genomic locus surrounding the 5′ end of the coding region of each gene). We were able to rescue the male sterility with the tagged version of *t-Grip84* or *t-Grip91,* indicating the functionality of the transgenes (**Supplementary Figure 2B**). The presence of the t-γ-TuRC proteins could only be detected after the meiotic divisions, exclusively in the germline cells of the cysts. t-Grip84-mCh or

t-Grip84-GFP, HA-t-Grip91, and HA-t-Grip128 signals appear first in the round spermatids and localize to the centriole adjunct during nuclear elongation (**Figures 2A–C,H Supplementary Figures 3A,C**). Centriole adjunct localization of the t-γ-TuRC proteins was further confirmed by simultaneous labelling of t-Grip84-mCh/t-Grip84-GFP, HA-t-Grip91, and HA-t-Grip128 with γ-tubulin. We concluded that t-γ-TuRC members colocalize with γ-tubulin and with each other at the centriole adjunct (**Figures 2A–C** and **Supplementary Figure 3A**). The centriole adjunct localization of t-γ-TuRC persists in the elongating spermatid stage but diminishes in the fully elongated cysts (**Supplementary Figure 3B**). We observed additional localization signals of the t-γ-TuRC proteins through the development of the cysts, on the anterior tip of the elongating nuclei and on the tail region, near the mitochondria of the late elongating spermatids (**Figures 2D–G** and **Supplementary Figures 3D,E**). We confirmed HA-t-Grip91, HA-t-Grip128 and t-Grip84-GFP potential mitochondrial association by staining with Mitotracker or coexpressing with the mitochondrial outer membrane protein Tom20-mCh (**Figures 2D–F**) (Zhang et al., 2016). Interestingly, Mzt1, the Grip91- and Grip128-interacting protein is known to exhibit a partly similar localization pattern to the newly identified t-γ-TuRC members (Tovey et al., 2018). To test the colocalization of Mzt1 and the t-γ-TuRC proteins, we engineered an endogenous promoter-driven GFP-Mzt1 transgene. We confirmed the previously published centrosomal and centriole adjunct localization of GFP-Mzt1 (**Figure 2H**; **Supplementary Figure 3F**) (Tovey et al., 2018). We also found additional GFP-Mzt1 accumulation in a close association with the mitochondria during the meiotic division of spermatocytes using the mitochondrial marker Tom20-mCh (**Figure 2H** and **Supplementary Figure 4A**). We could not detect GFP-Mzt1 signal on the surface of the mitochondria of the onion stage and early elongating spermatids (**Supplementary Figures 4B,C**; Tovey et al., 2018). We found GFP-Mzt1 colocalization with all three t-γ-TuRC proteins after meiosis, from the round spermatid stage (**Figures 2G,H** and **Supplementary Figure 3D**). Similarly to the localization of t-γ-TuRC proteins, the GFP-Mzt1 signal was detected at the centriole adjunct, the tip of the nuclei, and additionally resides closely to the mitochondria of the late elongating spermatids (**Figure 2G**; **Supplementary Figures 3D**, **4B–D**). This kind of diverse and overlapping distribution of t-γ-TuRC members and Mzt1 in spermatids strongly supports the existence and necessity of multiple MTOCs in post-meiotic stages of Drosophila spermatogenesis.

Next, we tested the mutual dependence of the diverse localization of the t-γ-TuRC proteins. We found that neither HA-t-Grip91 nor t-Grip84-GFP localizes to the centriole adjunct or nuclear tip in the round or early elongating spermatids of *t-Grip84*^{ms} or *t-Grip91*^{ms} mutants, respectively (**Figures 3A–C**; **Supplementary Figures 5H,I**). Afterward, we analyzed the distribution of γ-tubulin and Mzt1, the two potential interactor proteins of the complex in the mutants. We found that both γ-tubulin and GFP-Mzt1 are present on the centrosome of spermatocytes in *t-Grip84*^{ms} and *t-Grip91*^{ms} mutants, however, from the round spermatid stage onward, their localizations disappear and, they become cytoplasmic (**Supplementary Figures 3F–N** and **Figures 3D–I**). These results provide additional evidence that t-γ-TuRC function is restricted to the post-meiotic stages and is not essential for centrosomal recruitment of the γ-TuRC interacting proteins. These findings raised the question of whether the lack of *t-Grip84* or *t-Grip91* resulted in a general disintegration of the centriole adjunct and basal body. We tested the localization of three basal body proteins, the centriole/pericentriolar material protein PACT, the centriole component Ana1 and Asterless in *t-Grip84*^{ms} and *t-Grip91*^{ms} mutants to assess the impact of the lack of t-γ-TuRC proteins (Martinez-Campos et al., 2004; Fu et al., 2016; Galletta et al., 2020). GFP-PACT, Ana1 and Asterless were found on the basal body of *t-Grip84*^{ms} and *t-Grip91*^{ms} mutant spermatids. However, we observed their nuclear scattering during the later stages of individualization, as well as the partial detachment of the GFP-PACT, Ana1 and Asterless labelled basal body from the nucleus in both mutants (**Figures 3J–L** and **Supplementary Figures 5A–K**).

The t-γ-TuRC members influence each other's localization and despite normal axoneme assembly, basal body attachment to the nucleus and integrity of the cysts is disturbed in the *t-Grip84*^{ms} and *t-Grip91*^{ms} mutants. Taken together, these results suggest that the observed abnormalities in the mutants are not due to the disappearance of centriole adjunct or general failure of sperm development.

Composition of the t-γ-TuRC

Together, the above observations suggested that an alternative γ-TuRC could assemble in the post-meiotic stages of spermatogenesis, but its molecular composition remained partly unclear. To address this issue, we first performed a yeast two-hybrid (Y2H) analysis to test the interactions between t-γ-TuRC proteins in every combination and with full-length γ-tubulin and Mzt1 (**Figure 4A**). Due to the large size of the proteins, we divided all three t-γ-TuRC proteins into an N-terminal and a C-terminal part (**Supplementary Figure 6A**). We found that t-Grip84-N, t-Grip91-N, and t-Grip128-C bind to the ubiquitously expressed γ-Tub23C. We showed that Mzt1 binds exclusively to the N-terminal of t-Grip91 (**Figures 4A,B**). Interaction of the N-terminal of both somatic Grip91 and Grip128 with Mzt1 was previously reported, however, the precise location of this interaction during spermatogenesis was not investigated (Tovey et al., 2018). Our results suggest that N-terminus of t-Grip91 could be responsible for the t-γ-TuRC interaction of Mzt1 in the post-meiotic stages. We found that t-Grip84-N interacts with both t-Grip91-N and t-Grip91-C. Moreover, t-Grip91-C shows binding with t-Grip84-C and t-Grip128-C. t-Grip91-N also shows binding with both t-Grip128-N and t-Grip128-C in Y2H assays (**Figures 4A,B**). To confirm the positive Y2H results, we performed direct binding experiments, in which we individually expressed, purified, and immobilized the GST-tagged version of the N- or C-terminal parts of the t-γ-TuRC proteins (bait). Bait proteins were mixed with ^{35}S-methionine-labelled candidates, produced with a coupled *in vitro* transcription-translation (IVTT) system followed by autoradiography to detect physical interactions. Results of the *in vitro* binding experiments supported the

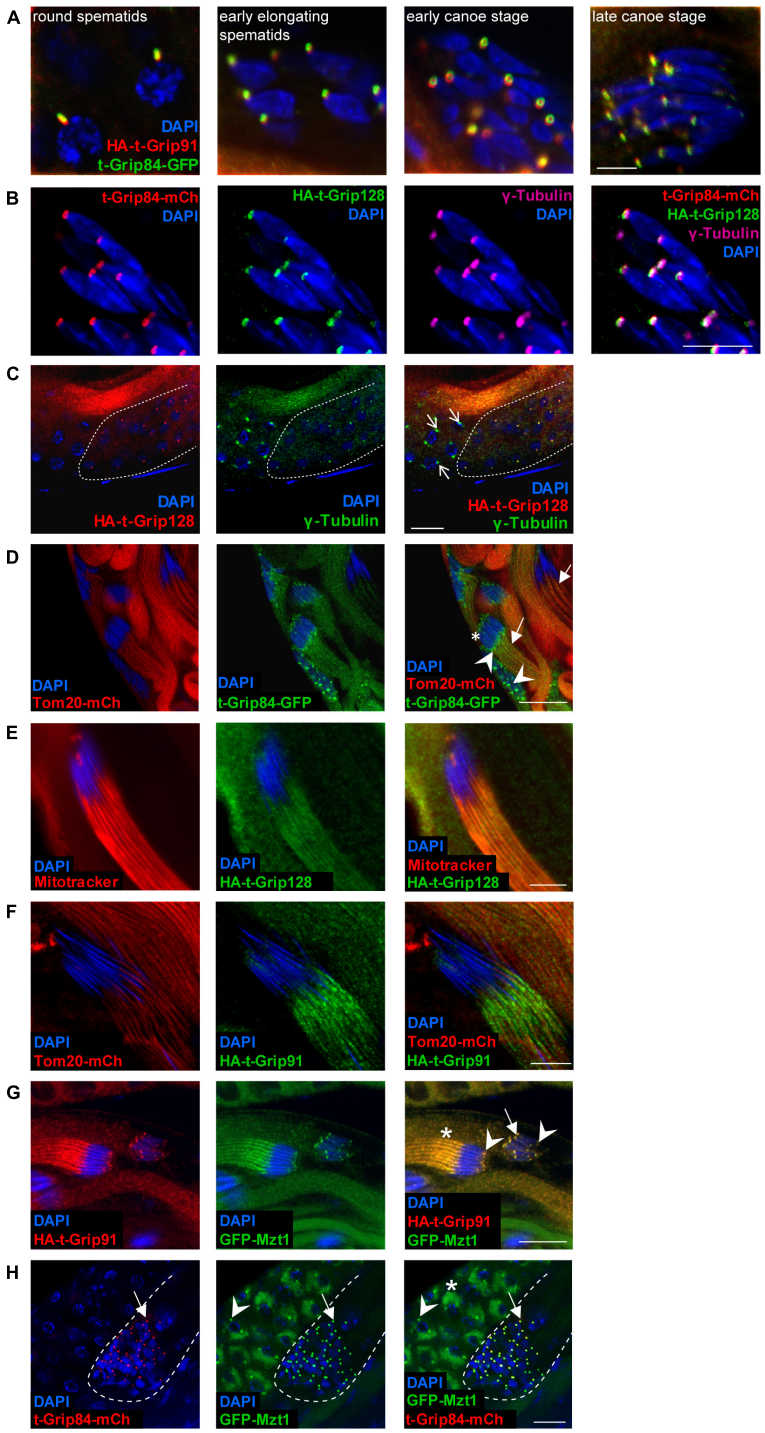

FIGURE 2 | Localization of t-γ-TuRC proteins during spermatogenesis. **(A)** HA-t-Grip91 (red) colocalizing with t-Grip84-GFP (green) in round spermatids, early elongating, early canoe and late canoe stage spermatids. **(B)** t-Grip84-mCh (red), colocalizing with HA-t-Grip128 (green), and also with γ-tubulin (magenta) at the centriole adjunct in canoe stage elongating spermatids. Nuclei are visualized by DAPI (blue). **(C)** HA-t-Grip128 (red) is not present on the centrosome of meiotic spermatocytes (arrow), but present and show an overlapping pattern with γ-Tubulin (green) in round spermatids (the cyst highlighted with dashed line). **(D)** In addition to the centriole adjunct localization (arrowhead) t-Grip84-GFP is localizing to the nuclear tip (asterisk) and close proximity to the mitochondria, labelled by Tom20-mCh (arrows) in the elongating cysts. **(E,F)** HA-t-Grip128 and HA-t-Grip91 are localizing close to the mitochondria (stained with Mitotracker (red) and labelled by Tom20-mCh, respectively) of the late elongating spermatids. **(G)** HA-t-Grip91 (red) colocalizing with GFP-Mzt1 (green) on the centriole adjunct (arrow) and at the tip of the nuclei (arrowhead) in the canoe stage and near the mitochondria (asterisk) in the needle stage spermatids. **(H)** t-Grip84-mCh and GFP-Mzt1 are colocalizing on the centriole adjunct (arrow) in the post-meiotic cysts (highlighted by the white dashed lines), while GFP-Mzt1 is present on the centrosome (arrowhead) and close to the mitochondria (star) of meiotic spermatocytes. Scale bars: A 5 μm, **(C,D,G,H)** 20 μm, **(B,E,F)** 10 μm.

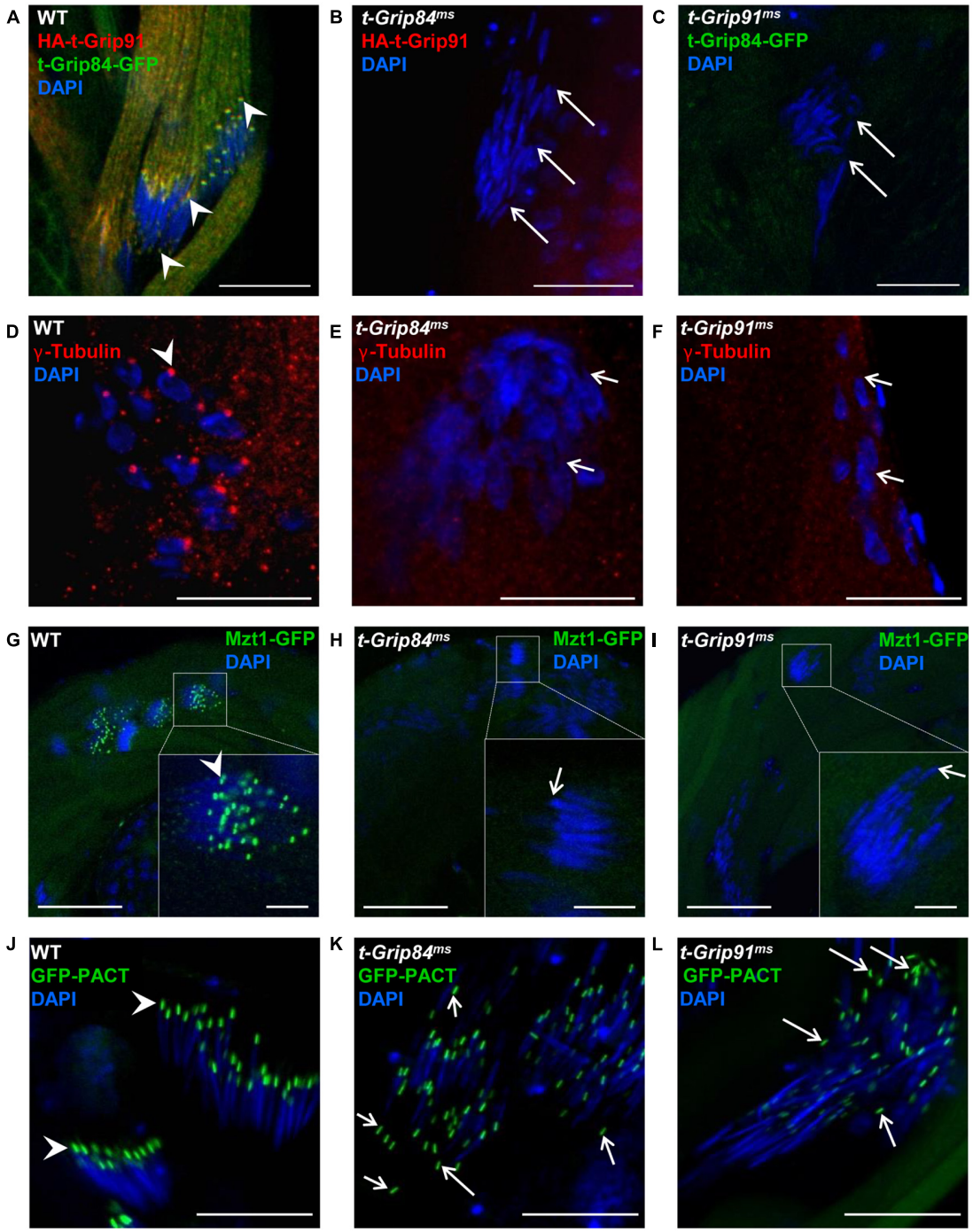

FIGURE 3 | Localization of centriole adjunct components in t-γ-TuRC mutants. **(A–C)** HA-t-Grip91 and t-Grip84-GFP are colocalized on the centriole adjunct and nuclear tip (arrows) in WT spermatids, while HA-t-Grip91 became cytoplasmic in *t-Grip84*^{ms} and t-Grip84-GFP in *t-Grip91*^{ms} mutant spermatids. **(D–I)** γ-tubulin (red, arrowhead) and Mzt1-GFP (green, arrowhead) are mislocalized in *t-Grip84*^{ms} and *t-Grip91*^{ms} mutants. **(J–L)** GFP-PACT is on the basal body in WT, *t-Grip84*^{ms} and *t-Grip91*^{ms} elongating spermatids, but GFP-PACT signal detached from the nucleus in *t-Grip84*^{ms} and *t-Grip91*^{ms} spermatids (arrows). Statistical analysis is in **Supplementary Figure 5D**. Scale bars: **(A–F)** and **(J–L)** 20 μm, G-I 50 μm, insets 10 μm.

Y2H findings (**Figure 4C** and **Supplementary Figure 6**). Consequently, we proved with two independent experimental systems that all three t-γ-TuRC proteins could bind with γ-tubulin, but only the N-terminal t-Grip91 shows interaction with Mzt1. Furthermore, the diverse binding of the core t-γ-TuRC proteins with each other implies the possibility of

a variable t-γ-TuRC composition, which could contribute to the different localization of the complexes in the late stages of spermatogenesis.

DISCUSSION

It is understood, that the multiprotein γ-TuRC is a template for microtubule nucleation in various parts of the cell (Tovey and Conduit, 2018). In this study, we have shown that *Drosophila melanogaster* encodes three t-γ-TuRC proteins, t-Grip84, t-Grip91, and t-Grip128 and we identified and characterized the classical mutants of *t-Grip84* and *t-Grip91* and *t-Grip128*. We found that *t-Grip84^{ms}* and *t-Grip91^{ms}* are male sterile, while *t-Grip128$^{\Delta 65}$* males are fertile. It is also known, that *Grip84*, *Grip91* and *γ-tub23C* mutants are lethal, while *Grip75* and *Grip128* mutants are female and male sterile, suggesting that γ-TuSC is essential at each developmental stage and γ-TuRC components have a modulator function in somatic cells (Sunkel et al., 1995; Barbosa, 2000; Bourbon et al., 2002; Vogt, 2006). The male sterility of *Grip75* and *Grip128* mutants manifest in the late post-meiotic stages of spermatogenesis, similar to *t-Grip84^{ms}* and *t-Grip91^{ms}* mutants, indicating that the late stages of spermatogenesis are particularly sensitive to alterations in γ-TuRC composition, likely due to the lack of transcriptional compensation mechanisms following meiosis.

The scattered and detached individualization complexes and centrioles in the *t-Grip84^{ms}* and *t-Grip91^{ms}* mutants suggest that t-γ-TuRC contribute to the establishment or maintenance of the stable connection between the nucleus and cilia.

The necessity of *Grip128* could explain the normal fertility of *t-Grip128$^{\Delta 65}$* males, where the product of *Grip128* is probably sufficient for normal sperm development and fertility.

t-γ-TuRC members show a dynamic post-meiotic protein localization pattern in the developing spermatids. We found that from the round spermatid stage onward the three t-γ-TuRC proteins begin to localize at the centriole adjunct, then also to the nuclear tip, and then finally to the surface of the mitochondria of the late elongating cyst, where they colocalize with γ-tubulin and Mzt1 (Chen et al., 2017; Tovey et al., 2018). It was recently shown that γ-Tubulin localizes both to the nuclear tip and the centriole adjunct of the elongating spermatids and could contribute to the nuclear elongation (Riparbelli et al., 2020). The centriole adjunct and apical tip localization of t-γ-TuRC proteins and γ-Tubulin itself indicate that they could contribute to the organization of the perinuclear microtubule network, and to stabilizing the attachment of the axoneme to the nucleus. One may imagine that an MTOC at the nuclear tip could promote nuclear elongation, as well as the organization of the acroblast, the precursor of the acrosome.

This diverse t-γ-TuRC composition implies the possibility of multiple t-γ-TuRCs with diverse localization abilities during the post-meiotic stages of spermatogenesis. It is tempting to speculate that, despite both Mzt1 and γ-tubulin binding to the somatic γ-TuRC prior to the meiotic stages, following meiosis, Mzt1, and probably γ-tubulin, can also be recruited to different MTOCs by the t-γ-TuRC (**Supplementary Figure 7**).

Two lines of evidence support the hypothesis that the testis-specific splice variant, centrosomin (CnnT), orchestrates the formation of the mitochondrial MTOC by recruitment of γ-TuRCs to the elongating mitochondria. Firstly, CnnT is able to recruit the γ-TuRC proteins GCP2 and GCP5 to the mitochondria in HEK293 cells. Secondly, CnnT itself localizes on the surface of spermatid mitochondria, converting mitochondria into MTOCs during spermatid development (Chen et al., 2017). Taking these results together with earlier findings and the phenotype of the mutants, we suggest that t-Grip128, Mzt1 and CnnT could have moderator or redundant roles, in contrast to t-Grip84, t-Grip91, Grip75, and Grip128, which likely have more fundamental roles in spermatid development (Vogt, 2006; Chen et al., 2017; Tovey et al., 2018). Additional experiments are necessary to test whether CnnT is a direct binding partner of t-γ-TuRC in the post-meiotic stages and to test the significance of the mitochondrial association of t-γ-TuRC and its interactor proteins in the late elongating spermatids.

Targeting γ-tubulin to the elongating spermatids is not dependent on Grip75 or Grip128, despite the γ-tubulin binding capacity of both proteins (Vogt, 2006). While all tested γ-TuRC and t-γ-TuRC proteins could bind to γ-tubulin *in vitro*, the localization of γ-tubulin is disturbed only in the post-meiotic cysts of the *t-Grip84^{ms}* and *t*-Grip91^{ms} mutants. This strongly suggests that t-Grip84 and t-Grip91 are fundamental in the centriole adjunct, nuclear tip and mitochondrial recruitment of γ-tubulin in the post-meiotic stages. Based on the late spermatogenesis phenotype of *Grip75* and *Grip128* mutants, and the fact that Grip163 (GCP6) was shown to be part of the Drosophila sperm proteome, we can imagine that some of the somatic γ-TuRC proteins could be present in the t-γ-TuRC and inherited through the sperm following fertilization (Vogt, 2006; Wasbrough et al., 2010). We believe that our results open up a new avenue to understanding the composition of alternative γ-TuRCs in different specialized cell types, such as the spermatids, and the function of MTOCs' heterogeneity.

MATERIALS AND METHODS

Fly Stocks, Mutants the Sperm Following, and Fertility Test

Flies were maintained on cornmeal agar medium at 25°C in standard lab conditions. Fly stocks used in this study were obtained from Bloomington Drosophila Stock Center, unless stated otherwise. GFP-PACT line was obtained from Jordan Raff's and Tom20-mCherry from Hong Xu's laboratory (Martinez-Campos et al., 2004; Zhang et al., 2016). *w^{1118}* used as wild type control (3605, BDSC). Mi{MIC}CG7716^{MI12921} (58006, BDSC), Mi{ET1}CG7716^{MB07394} (26394, BDSC), Df(3L)BSC375, (24399, BDSC), Mi{MIC}CG18109^{MI05374} (42318, BDSC), and Df(2L)osp29 (3078, BDSC) mutant stocks were used in this study. The *pCFD4-Grip128-gRNA* line was crossed with the Cas9 source line, y1 M{nos-Cas9.P}ZH-2Aw- (BDSC 54591) to generate deletions in the *t-Grip128* gene. The deletions were identified by PCR and sequencing, and *t-Grip128$^{\Delta 65}$* line was

A

	t-Grip84-N	t-Grip84-C	t-Grip91-N	t-Grip91-C	t-Grip128-N	t-Grip128-C
γ-Tub23-C	+	-	+	-	-	+
Mzt1	-	-	+	-	-	-
t-Grip84-N			+	+	-	-
t-Grip84-C			-	+	-	-
t-Grip91-N					+	+
t-Grip91-C					-	+

B

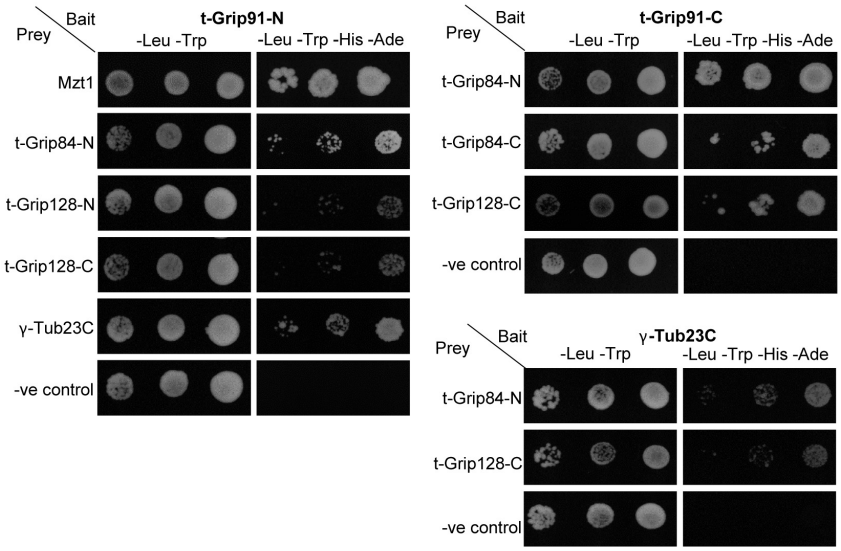

C

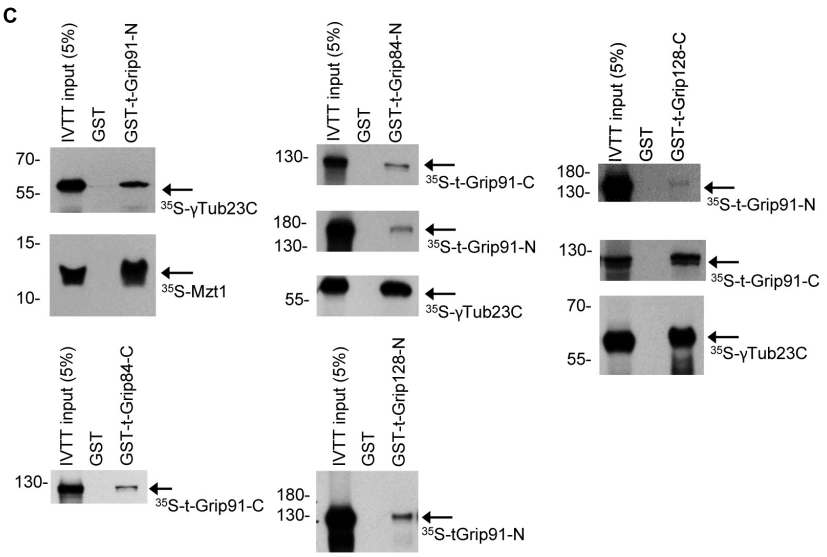

FIGURE 4 | Interaction between the t-γ-TuRC and partner proteins. **(A)** Summary of Y2H analysis between N-and C-terminal t-γ-TuRC proteins with each other and with γ-Tub23-C and Mzt1. **(B)** Mated yeast were plated as 10-fold serial dilutions (left to right) on -Leu, -Trp medium that selective for the bait and prey plasmids and -Leu, -Trp, -His, -Ade medium that selective for the bait, prey, and the interaction between the tested proteins. Negative control (-ve control) is the empty prey with the corresponding bait vector. **(C)** Autoradiography showing the interactions between purified GST-t-γ-TuRC protein fragments and ^{35}S-methionine-labelled interacting proteins produced in IVTT reaction.

established. Transgenic constructs for t-Grip84-GFP, t-Grip84-mCh, HA-t-Grip91, HA-t-Grip128 and GFP-Mzt1 were injected into P{CaryP}attP40 (BDSC 25709) or P{CaryP}attP2 (BDSC 8622) fly lines. For fertility tests, individual males were crossed with three w^{1118} virgin females. 14 days after crossing, the hatched progeny was counted in every tube. Experiments were on four occasions with > 10 males per condition.

DNA Constructs

To make *t-Grip128*$^{\Delta 65}$ null mutant alleles, two sgRNAs (t-Grip128_CRISPR1 AAAACAAGTCTTAAACTCA, t-Grip128_CRISPR2 GATTCCGTCTAAGTTGAGT) were cloned into pCFD4 vector (Addgene, 49411) at Bbs1 site to create a deletion of 3,359 bp and stable transgenic lines were established as described in Port and Bullock (2016) and Port et al. (2014). t-Grip84-mCh, t-Grip84-GFP, HA-t-Grip91, HA-t-Grip128, and GFP-Mzt1 constructs were made by amplifying the 5′ upstream regions (2,134 bp of *t-Grip84*, 970 bp of *t-Grip91*, 2,213 bp of *t-Grip128* and 1,581 bp of *Mzt1*) from genomic DNA, the coding sequence of t-γ-TuRC proteins and Mzt1 from w^{1118} testis cDNA (NEB, M0530S).

The purified PCR products (K0502, Thermo Fisher) were cloned into pUASTattB-mCherry, pUASTattB-GFP or pUASTattB-3xHA vectors using HiFi DNA Assembly Master Mix (E2621S, NEB) (Gibson et al., 2009). For YTH analysis t-Grip84s (1–399 aa N-term, 400–728 aa C-term), t-Grip128s (1–550 aa N-term, 551–975 aa C-term) and full-length Mzt1 were cloned into pGAD424. t-Grip91s (1–966 aa N-term, 967–1932 aa C-term) were cloned into pGBT9 and the full-length γ-Tubulin23C was cloned into pGAD424 and pGBT9 vectors, using HiFi DNA Assembly Master Mix (E2621S, NEB) (**Supplementary Figure 6A**). N- and C-terminal parts of t-Grip84, t-Grip91 and t-Grip128 were inserted into the pDEST15 (11802014, Thermo Fisher) vector by Gateway cloning (11791-020, Thermo Fisher). To generate prey proteins for *in vitro* binding N- and C-terminal parts of t-Grip84, t-Grip91 and t-Grip128 were cloned into pJET1.2 plasmid downstream of the T7 promoter using CloneJET PCR Cloning Kit (K1231, Thermo Fisher). cDNA of Mzt1, γ-Tub23C were obtained from the Drosophila Gold collection (DGRC). Primers used in cloning are listed in **Supplementary Figure 8**.

Staining and Microscopy

Dissection and staining of testis were performed as described by White-cooper (2004). Rat anti-HA (1:100) (11867423001, Roche), mouse anti-pan polyglycylated Tubulin (1:5,000) (clone AXO 49, MABS276, Merck), mouse anti-γ-Tubulin (1:5,000) (clone GTU-88, T6557, Sigma), rabbit anti-Ana1 (1:5,000) (Fu et al., 2016), rabbit anti-Asl (1:1,000) (Fu et al., 2016) primary antibodies were used. Secondary antibodies Alexa Fluor 488 (A-11029, A-21208) Alexa Fluor 546 (A-11030, A-11081, A-11010, A32754), and Alexa Fluor 647 (A-21052) conjugated anti-mouse, anti-rat, and anti-rabbit antibodies (Thermo Fisher), respectively, were used (1:400). Texas Red1-X Phalloidin (T7471, Life Technologies) was used at a 1:250 dilution. 4′,6-diamidino-2-phenylindole (DAPI) was used at 1 μg/ml concentration (D1306, Thermo Fisher). Mitotracker Red CMXRos (0.5 μM in PBS) (M7512, Thermo Fisher) and Hoechst (1:500 in PBS) (H3570, Thermo Fisher) were used on freshly dissected testes for a 20 min incubation period. Fixed samples were mounted in SlowFade Gold antifade reagent (S36967, Life Technologies). Images were taken using an Olympus BX51 fluorescent microscope or an Olympus Fluoview Fv10i Confocal microscope.

Yeast Two-Hybrid Assay

Yeast two-hybrid assay was carried out using the Matchmaker two-hybrid system (K1605, Clontech). One of the baits pGBT9: N- and C- terminal parts of t-Grip91 and full-length γ-Tub23C was cotransformed with one of the preys pGAD424: N- and C- terminal parts of t-Grip84, t-Grip91, t-Grip128, full-length Mzt1 and γ-Tub23C into PJ69 yeast cells (James et al., 1996). Individual colonies were streaked out on yeast synthetic double drop-out plates that lacked tryptophan and leucine (Y0750, Merck). After growing, they were inoculated on quadruple dropout plates lack tryptophan, leucine, histidine, and adenine (Y2021, Merck) containing 10 mM 3-amino-1, 2, 4-aminotrizole (3-AT) (A8056, Sigma).

Recombinant Protein Production

Recombinant GST-tagged bait proteins were expressed, purified, and immobilized onto glutathione sepharose beads as described previously (17-0756-01, GE Healthcare) (Karman et al., 2020).

In vitro Transcription-Translation (IVTT) and *in vitro* Binding

^{35}S-methionine-labelled prey proteins (N-terminal and C-terminal parts of t-Grip91, full-length Mzt1 and γ-Tub23C) were produced *in vitro* using the TnT T7 Quick Coupled IVTT kit (L1170, Promega). Detailed protocol of IVTT and the GST-binding assay was described previously (Karman et al., 2020).

Quantitative RT-PCR

Total RNA was purified from 25 pairs of testes, for *t-Grip84*^{ms}, *t-Grip91*^{ms}, *t-Grip128*$^{\Delta 65}$ and WT using Quick-RNA MiniPrep kit (R1054, Zymo Research). For the first-strand cDNA synthesis, RevertAid First Strand cDNA Synthesis Kit (K1670, Thermo Fisher) was used according to the manufacturer's instructions. Maxima SYBR Green/ROX qPCR Master Mix (K0222, Thermo Fisher) was used for the real-time quantitative PCR reaction, according to the manufacturer's instructions. Reactions were run on three occasion times in triplicates in the Rotor-Gene Q Real-Time PCR Detection System (QIAGEN) with the following reaction conditions: 95°C 10 min, 50 cycles of 95°C 15 s, 54°C 30 s, 72°C 30 s. Gene-specific and *rp49* specific primers were used and are listed in **Supplementary Figure 8**.

Alignments, Quantification and Statistical Analysis

Pairwise sequence alignments for paralogs were made by Clustal Omega 1.2.4. Alignments were visualised using Unipro UGENE 1.31.1. Domain predictions were highlighted based on Pfam predictions. The phylogenetic tree was constructed by MEGA X with the maximum likelihood method. Data analysis and graph production were carried out using Origin

9.0 (OriginLab Corporation, Northampton, MA, United States). One-way ANOVA followed by Tukey's HSD test were used to produce comparisons between WT and mutants (**Supplementary Figures 2A–C,G,H**, **5D**).

DATA AVAILABILITY STATEMENT

The raw data supporting the conclusions of this article will be made available by the authors, without undue reservation.

AUTHOR CONTRIBUTIONS

RS contributed to the conception and design of the study and wrote the first draft of the manuscript. EA, VV, ZR-N, ZL, and RS performed the experiments. EA and ZL wrote sections of the manuscript. All authors contributed to manuscript revision, read, and approved the submitted version.

FUNDING

This work was supported by the Government of Hungary (Stipendium Hungaricum Scholarship) to EA and (Ph.D. scholarship) to ZR-N, Ministry for National Economy of Hungary (GINOP-2.3.2-15-2016-00001 and GINOP-2.3.2-15-2016-00032) to ZL and RS, Hungarian Academy of Sciences [Lendület Grant (LP2017-7/2017)] to ZL and National Research, Development and Innovation Office (K132155) to RS.

ACKNOWLEDGMENTS

We are grateful to the *Drosophila* Genomics Resource Center (supported by NIH grant 2P40OD010949) for the Gold collection cDNA clones as well as FlyBase, the *Drosophila* genetic and genomic database (supported by NIH grant U41 HG000739 and British Medical Research Council grant MR/N030117/1). We are indebted to Jordan Raff, Hong Xu, Ildikó Unk, and David M. Glover for fly stocks and reagents. We also thank Ferenc Jankovics and József Mihály for discussion and critical reading of the manuscript.

SUPPLEMENTARY MATERIAL

The Supplementary Material for this article can be found online at: https://www.frontiersin.org/articles/10.3389/fcell.2021.727264/full#supplementary-material

REFERENCES

Barbosa, V. (2000). Mutation of a *Drosophila* gamma tubulin ring complex subunit encoded by discs degenerate-4 differentially disrupts centrosomal protein localization. *Genes Dev.* 14, 3126–3139. doi: 10.1101/gad.182800

Belote, J. M., and Zhong, L. (2009). Duplicated proteasome subunit genes in *Drosophila* and their roles in spermatogenesis. *Heredity (Edinb.)* 103, 23–31. doi: 10.1038/hdy.2009.23

Blachon, S., Khire, A., and Avidor-Reiss, T. (2014). The origin of the second centriole in the zygote of *Drosophila melanogaster*. *Genetics* 197, 199–205. doi: 10.1534/genetics.113.160523

Bourbon, H.-M., Gonzy-Treboul, G., Peronnet, F., Alin, M.-F., Ardourel, C., Benassayag, C., et al. (2002). A P-insertion screen identifying novel X-linked essential genes in *Drosophila*. *Mech. Dev.* 110, 71–83. doi: 10.1016/S0925-4773(01)00566-4

Bre, M. H., Redeker, V., Quibell, M., Darmanaden-Delorme, J., Bressac, C., Cosson, J., et al. (1996). Axonemal tubulin polyglycylation probed with two monoclonal antibodies: widespread evolutionary distribution, appearance during spermatozoan maturation and possible function in motility. *J. Cell Sci.* 109, 727–738. doi: 10.1242/jcs.109.4.727

Chen, J. V., Buchwalter, R. A., Kao, L.-R., and Megraw, T. L. (2017). A splice variant of centrosomin converts mitochondria to microtubule-organizing centers. *Curr. Biol.* 27, 1928.e–1940.e. doi: 10.1016/j.cub.2017.05.090

Dallai, R., Paoli, F., Mercati, D., and Lupetti, P. (2016). The centriole adjunct of insects: need to update the definition. *Tissue Cell* 48, 104–113. doi: 10.1016/j.tice.2016.02.001

Fabian, L., and Brill, J. A. (2012). *Drosophila* spermiogenesis. *Spermatogenesis* 2:3, 197–212. doi: 10.4161/spmg.21798

Fu, J., Lipinszki, Z., Rangone, H., Min, M., Mykura, C., Chao-Chu, J., et al. (2016). Conserved molecular interactions in centriole-to-centrosome conversion. *Nat. Cell Biol.* 18, 87–99. doi: 10.1038/ncb3274

Galletta, B. J., Ortega, J. M., Smith, S. L., Fagerstrom, C. J., Fear, J. M., Mahadevaraju, S., et al. (2020). Sperm head-tail linkage requires restriction of pericentriolar material to the proximal centriole end. *Dev. Cell* 53, 86.e–101.e. doi: 10.1016/j.devcel.2020.02.006

Gibson, D. G., Young, L., Chuang, R.-Y., Venter, J. C., Hutchison, C. A., and Smith, H. O. (2009). Enzymatic assembly of DNA molecules up to several hundred kilobases. *Nat. Methods* 6, 343–345. doi: 10.1038/nmeth.1318

Gunawardane, R. N., Martin, O. C., Cao, K., Zhang, L., Dej, K., Iwamatsu, A., et al. (2000). Characterization and reconstitution of *Drosophila* γ-tubulin ring complex subunits. *J. Cell Biol.* 151, 1513–1524. doi: 10.1083/jcb.151.7.1513

James, P., Halladay, J., and Craig, E. A. (1996). Genomic libraries and a host strain designed for highly efficient two-hybrid selection in yeast. *Genetics* 144, 1425–1436. doi: 10.1093/genetics/144.4.1425

Karman, Z., Rethi-Nagy, Z., Abraham, E., Fabri-Ordogh, L., Csonka, A., Vilmos, P., et al. (2020). Novel perspectives of target-binding by the evolutionarily conserved PP4 phosphatase. *Open Biol.* 10, 200343. doi: 10.1098/rsob.200343

Lattao, R., Kovács, L., and Glover, D. M. (2017). The centrioles,centrosomes, basal bodies, and cilia of *Drosophila melanogaster*. *Genetics* 206, 33–53. doi: 10.1534/genetics.116.198168

Laurinyecz, B., Vedelek, V., Kovács, A. L., Szilasi, K., Lipinszki, Z., Slezák, C., et al. (2019). Sperm-Leucylaminopeptidases are required for male fertility as structural components of mitochondrial paracrystalline material in *Drosophila melanogaster* sperm. *PLoS Genet.* 15:e1007987. doi: 10.1371/journal.pgen.1007987

Liu, P., Würtz, M., Zupa, E., Pfeffer, S., and Schiebel, E. (2021). Microtubule nucleation: the waltz between γ-tubulin ring complex and associated proteins. *Curr. Opin. Cell Biol.* 68, 124–131. doi: 10.1016/j.ceb.2020.10.004

Martinez-Campos, M., Basto, R., Baker, J., Kernan, M., and Raff, J. W. (2004). The *Drosophila* pericentrin-like protein is essential for cilia/flagella function, but appears to be dispensable for mitosis. *J. Cell Biol.* 165, 673–683. doi: 10.1083/jcb.200402130

Noguchi, T., Koizumi, M., and Hayashi, S. (2011). Sustained elongation of sperm tail promoted by local remodeling of giant mitochondria in *Drosophila*. *Curr. Biol.* 21, 805–814. doi: 10.1016/j.cub.2011.04.016

Porcelli, D., Barsanti, P., Pesole, G., and Caggese, C. (2007). The nuclear OXPHOS genes in insecta: a common evolutionary origin, a common cis-regulatory motif, a common destiny for gene duplicates. *BMC Evol. Biol.* 7:215. doi: 10.1186/1471-2148-7-215

Port, F., and Bullock, S. L. (2016). "Creating heritable mutations in *Drosophila* with CRISPR-Cas9," in *Methods in Molecular Biology*, Vol. 1478, ed. C. Dahmann (New York, NY: Humana Press), 145–160. doi: 10.1007/978-1-4939-6371-3_7

Port, F., Chen, H.-M., Lee, T., and Bullock, S. L. (2014). Optimized CRISPR/Cas tools for efficient germline and somatic genome engineering in *Drosophila*. *Proc. Natl. Acad. Sci. U.S.A.* 111, E2967–E2976. doi: 10.1073/pnas.1405500111

Raynaud-Messina, B., Debec, A., Tollon, Y., Garès, M., and Wright, M. (2001). Differential properties of the two *Drosophila* γ-tubulin isotypes. *Eur. J. Cell Biol.* 80, 643–649. doi: 10.1078/0171-9335-00195

Riparbelli, M. G., Persico, V., and Callaini, G. (2020). The microtubule cytoskeleton during the early *Drosophila* spermiogenesis. *Cells* 9:2684. doi: 10.3390/cells9122684

Sunkel, C. E., Gomes, R., Sampaio, P., Perdigão, J., and González, C. (1995). Gamma-tubulin is required for the structure and function of the microtubule organizing centre in *Drosophila* neuroblasts. *EMBO J.* 14, 28–36. doi: 10.1002/j.1460-2075.1995.tb06972.x

Tillery, M., Blake-Hedges, C., Zheng, Y., Buchwalter, R., and Megraw, T. (2018). Centrosomal and Non-Centrosomal Microtubule-Organizing Centers (MTOCs) in *Drosophila melanogaster*. *Cells* 7:121. doi: 10.3390/cells7090121

Tovey, C. A., and Conduit, P. T. (2018). Microtubule nucleation by γ-tubulin complexes and beyond. *Essays Biochem.* 62, 765–780. doi: 10.1042/EBC20180028

Tovey, C. A., Tubman, C. E., Hamrud, E., Zhu, Z., Dyas, A. E., Butterfield, A. N., et al. (2018). γ-TuRC heterogeneity revealed by analysis of Mozart1. *Curr. Biol.* 28, 2314.e–2323.e. doi: 10.1016/j.cub.2018.05.044

Vedelek, V., Bodai, L., Grézal, G., Kovács, B., Boros, I. M., Laurinyecz, B., et al. (2018). Analysis of *Drosophila melanogaster* testis transcriptome. *BMC Genomics* 19:697. doi: 10.1186/s12864-018-5085-z

Vedelek, V., Laurinyecz, B., Kovács, A. L., Juhász, G., and Sinka, R. (2016). Testis-specific bb8 is essential in the development of spermatid mitochondria. *PLoS One* 11:e0161289. doi: 10.1371/journal.pone.0161289

Veìrollet, C., Colombieì, N., Daubon, T., Bourbon, H.-M., Wright, M., and Raynaud-Messina, B. (2006). *Drosophila melanogaster* γ-TuRC is dispensable for targeting γ-tubulin to the centrosome and microtubule nucleation. *J. Cell Biol.* 172, 517–528. doi: 10.1083/jcb.200511071

Vogt, N. (2006). The TuRC components Grip75 and Grip128 have an essential microtubule-anchoring function in the *Drosophila* germline. *Development* 133, 3963–3972. doi: 10.1242/dev.02570

Wasbrough, E. R., Dorus, S., Hester, S., Howard-Murkin, J., Lilley, K., Wilkin, E., et al. (2010). The *Drosophila melanogaster* sperm proteome-II (DmSP-II). *J. Proteomics* 73, 2171–2185. doi: 10.1016/j.jprot.2010.09.002

White-cooper, H. (2004). Analysis of meiosis and morphogenesis. *Drosoph. Cytogenet. Protoc.* 247:468.

White-Cooper, H., and Bausek, N. (2010). Evolution and spermatogenesis. *Philos. Trans. R. Soc. B Biol. Sci.* 365, 1465–1480. doi: 10.1098/rstb.2009.0323

Wiese, C., and Zheng, Y. (1999). Gamma-tubulin complexes and their interaction with microtubule-organizing centers. *Curr. Opin. Struct. Biol.* 9, 250–259. doi: 10.1016/S0959-440X(99)80035-9

Zhang, J., and Megraw, T. L. (2007). Proper recruitment of gamma-tubulin and D-TACC/Msps to embryonic *Drosophila* centrosomes requires Centrosomin Motif 1. *Mol. Biol. Cell* 18, 4037–4049. doi: 10.1091/mbc.e07-05-0474

Zhang, Y., Chen, Y., Gucek, M., and Xu, H. (2016). The mitochondrial outer membrane protein MDI promotes local protein synthesis and mtDNA replication. *EMBO J.* 35, 1045–1057. doi: 10.15252/embj.201592994

Conflict of Interest: The authors declare that the research was conducted in the absence of any commercial or financial relationships that could be construed as a potential conflict of interest.

Publisher's Note: All claims expressed in this article are solely those of the authors and do not necessarily represent those of their affiliated organizations, or those of the publisher, the editors and the reviewers. Any product that may be evaluated in this article, or claim that may be made by its manufacturer, is not guaranteed or endorsed by the publisher.

Copyright © 2021 Alzyoud, Vedelek, Réthi-Nagy, Lipinszki and Sinka. This is an open-access article distributed under the terms of the Creative Commons Attribution License (CC BY). The use, distribution or reproduction in other forums is permitted, provided the original author(s) and the copyright owner(s) are credited and that the original publication in this journal is cited, in accordance with accepted academic practice. No use, distribution or reproduction is permitted which does not comply with these terms.

frontiers in Cell and Developmental Biology

ORIGINAL RESEARCH
published: 18 October 2021
doi: 10.3389/fcell.2021.761627

Tex13a Optimizes Sperm Motility *via* Its Potential Roles in mRNA Turnover

Yinchuan Li[1†], Panpan Mi[1†], Xue Chen[1†], Jiabao Wu[2], Xiaohua Liu[2], Yunge Tang[2], Jinmei Cheng[1], Yingying Huang[1], Weibing Qin[2], C. Yan Cheng[3*] and Fei Sun[1*]*

[1] Institute of Reproductive Medicine, Medical School of Nantong University, Nantong, China, [2] NHC Key Laboratory of Male Reproduction and Genetics, Guangdong Provincial Reproductive Science Institute (Guangdong Provincial Fertility Hospital), Guangzhou, China, [3] The Mary M. Wohlford Laboratory for Male Contraceptive Research, Center for Biomedical Research, Population Council, New York, NY, United States

OPEN ACCESS

Edited by:
Chih-kuan Tung,
North Carolina Agricultural and Technical State University, United States

Reviewed by:
Sergio Minucci,
Università della Campania Luigi Vanvitelli, Italy
Eloi Garí,
Universitat de Lleida, Spain

***Correspondence:**
Weibing Qin
guardqin@163.com
C. Yan Cheng
ccheng@rockefeller.edu
Fei Sun
sunfei@ntu.edu.cn
orcid.org/0000-0002-0870-8375

[†]These authors share first authorship

Specialty section:
This article was submitted to Cell Growth and Division, a section of the journal Frontiers in Cell and Developmental Biology

Received: 20 August 2021
Accepted: 22 September 2021
Published: 18 October 2021

Citation:
Li Y, Mi P, Chen X, Wu J, Liu X, Tang Y, Cheng J, Huang Y, Qin W, Cheng CY and Sun F (2021) Tex13a Optimizes Sperm Motility via Its Potential Roles in mRNA Turnover. Front. Cell Dev. Biol. 9:761627. doi: 10.3389/fcell.2021.761627

mRNAs have been found to undergo substantial selective degradation during the late stages of spermiogenesis. However, the mechanisms regulating this biological process are unknown. In this report, we have identified *Tex13a*, a spermatid-specific gene that interacts with the CCR4–NOT complex and is implicated in the targeted degradation of mRNAs encoding particular structural components of sperm. Deletion of *Tex13a* led to a delayed decay of these mRNAs, lowered the levels of house-keeping genes, and ultimately lowered several key parameters associated with the control of sperm motility, such as the path velocity (VAP, average path velocity), track speed (VCL, velocity curvilinear), and rapid progression.

Keywords: Tex13a, CCR4–NOT, Cnot1, spermiogenesis, sperm motility, knock-out

INTRODUCTION

Dozens of genes have been reported to be transcribed enormously in round spermatids during spermiogenesis due to nucleus condensation and transcription termination, for later use during the late steps of elongating spermatids (ESs) (Kleene, 1989, 1996; Iguchi et al., 2006). Short truncated 3′-UTR, alternative splicing, changes in the site of polyadenylation, and increased rates of transcription in round spermatids for delayed translation have been adopted potentially to enhance the half-time of these mRNAs (Braun, 1998; Walker et al., 1999; Steger, 2001; Kleene, 2003; Liu et al., 2007; Cullinane et al., 2015; Li et al., 2016). However, it is unclear how these mRNAs are degraded once they have completed their roles and turned into junk RNAs during late ESs. The majority of published papers, on the other hand, relate to piRNA, the chromatoid body, and nonsense-mediated mRNA decay (NMD) in round spermatids (Meikar et al., 2011; Peruquetti, 2015; Jones and Wilkinson, 2017; MacDonald and Grozdanov, 2017). piRNAs have also been reported to play an important part in massive mRNA decay in the late spermatids (Gou et al., 2015). Similarly, CCR4–NOT was also reported to participate in the mRNA degradation in the late spermatids. For example, Cnot7, a nuclease of the CCR4–NOT complex, was knocked out in testis, resulting in significant germ cell defects and male infertility (Berthet et al., 2004). The CCR4–NOT complex is a multifunctional machinery that contains two different types of deadenylase enzymes that effectively shorten mRNA poly(A) tails (Bartlam and Yamamoto, 2010; Ukleja et al., 2016). However, the possible roles of the CCR4–NOT complex in modulating ESs largely remain unknown.

Three types of nucleases and multiple signaling pathways are involved in the breakdown of RNA (Garneau et al., 2007; Houseley and Tollervey, 2009; Arraiano et al., 2013). These nucleases and pathways usually play redundant roles in the cells. Among these pathways, the CCR4–NOT

complex can effectively degrade poly(A) tails of mRNAs and initiate the early as well as the rate-limiting step of mRNA turnover (Wahle and Winkler, 2013). The CCR4–NOT complex, as a core and non-specific scissor for poly(A) tail, normally requires the help of other special partners, such as 3′-UTR regulatory elements and a variety of *trans*-acting factors, to trigger targeted decay of specific mRNAs (Mayya and Duchaine, 2019; Chalabi Hagkarim and Grand, 2020). Cnot1 is the largest subunit of the core CCR4–NOT complex and provides the backbone for other subunits to associate together (Temme et al., 2014; Chalabi Hagkarim and Grand, 2020). DND1 has been shown to bind Cnot1 and mediate the degradation of specific mRNAs in spermatogonia (Yamaji et al., 2017).

In this report, we have identified Tex13a, a spermatid-specific partner of CCR4–NOT complex, that can potentially bind to Cnot1 and alter the degradation of particular mRNAs encoding structural components of late ESs. Tex13a was initially revealed to repress transcription (Kwon et al., 2014, 2016; Kim et al., 2021). *Tex13* family is composed of four different members: *Tex13a*, *Tex13b*, *Tex13c1*, and *Tex13d* being transcribed specifically or predominantly in male mouse germ cells (Bellil et al., 2021; Kim et al., 2021). Tex13b was found to be highly expressed in spermatogonia, and Tex13d was found to be highly expressed in meiotic phase spermatocytes. Tex13a and Tex13c were found to be highly expressed in post-meiotic spermatids, which were ideal for exploring their roles in spermiogenesis. The C-terminal zf-RanBP2 domain of Tex13a can bind a consensus AGGUAA of single-stranded RNA (Nguyen et al., 2011). In this report, *Tex13a* was deleted and single-cell RNA sequencing (scRNA-seq) was adopted to monitor the transcriptomic changes during the late steps of ESs. Additionally, the phenotypes of *Tex13a* deletion and the changes of sperm motility were also evaluated in both Tex13a-KO and WT male mice.

MATERIALS AND METHODS

Mice and Tex13a-KO Models

Male C57BL/6N mice (10–12 weeks old) were used for this study and animals were maintained under standard conditions. All animal protocols and experiments were approved by the University of Nantong Animal Care and Use Committee and the Animal Care and Use Office. Tex13a-KO C57BL/6N mice models were developed by Shanghai Model Organisms with CRISPR/Cas9. All the reading frames of Tex13a were deleted.

Single-Cell Library Preparation and scRNA-Seq Data Analysis

Three unilaterally decapsulated testes from three mice from either Tex13a-KO or Tex13a-WT groups were pooled. The cell suspension preparation, cell capture, and library preparation were carried out according to previous reports (Dura et al., 2019; Li et al., 2021). scRNA-seq libraries were prepared by following the protocol of GEXSCOPE^{TM} Single-Cell RNA Library Kit (Singleron Biotechnologies, Nanjing, China). Briefly, mixed single-cell suspensions were loaded onto the microfluidic devices. Barcode beads were loaded onto the microfluidic device after the cells had settled into the wells. The cells were incubated with the lysis buffer for 20 min to facilitate the release of mRNA, which were then captured by the barcode beads. The beads were washed with 6× SSC twice after retrieval, and the captured mRNA was reverse-transcribed. The beads coated with cDNA were then amplified by PCR. The amplified DNA was purified followed by assessing its quality by Agilent BioAnalyzer using high-sensitivity chip. The purified cDNA was then pooled and used for the standard Nextera tagmentation and amplification reactions (Nextera XT, Illumina) using a custom primer instead of an i5 index primer to amplify only those specific fragments that contained the cell barcodes and UMIs. The libraries were sequenced on the Illumina HiSeq X using 150-bp paired-end reads.

The raw data analysis pipeline was conducted essentially according to our previous report (Li et al., 2021). Briefly, the raw data were processed by FastQC (V0.11.7) for quality evaluation, whereas fastp (v1) was used for trimming and STAR aligner (v2.5.3a) was used for alignment, while feature Counts (v1.6.2) were used for transcript counting. The cell barcodes and UMIs of the transcripts without polyT tails were extracted after they were filtered out. Adapters and polyA tails were thereafter trimmed before the second read was mapped to the UCSC mm10 reference genome with ensemble version 92 gene annotation. The reads with the same cell barcode, UMIs, and genes were grouped to calculate the number of UMIs generated per gene per cell. The cells from Tex13a-KO and WT testes were integrated and filtered under Seurat 3.2.3 (Stuart et al., 2019). The batch effects were thereafter removed by sctransform 0.3.1 embedded in the Seurat package. All the cell clusters were divided in an unbiased manner.

To identify the differentially expressed genes, the function FindMarkers of Seurat was used (test.use = "bimod," logfc.threshold = 0.1). Upregulated genes ($p \leq 0.05$, p_val_adj ≤ 0.05, logFC ≥ 0.2, and PCT1 ≥ 0.2) and downregulated genes ($p \leq 0.05$, p_val_adj ≤ 0.05, logFC ≤ -0.2, and PCT2 ≥ 0.2) were filtered as the differentially expressed genes between Tex13a-KO and WT.

The gene set enrichment was performed following the competitive gene set enrichment test CAMERA embedded in the SingleSeqGset (version 0.1.2.9000) R package (Wu and Smyth, 2012; Cillo et al., 2020). mRNA surveillance pathway, deadenylation-dependent mRNA decay, and RNA degradation were derived from PathCards of GeneCards (Belinky et al., 2015). All other gene sets or pathways used were obtained from C5 ontology gene sets of GSEA (Subramanian et al., 2005).

GST Pull-Down Assay, Western Blot, and Hematoxylin–Eosin Staining

GST-tagged segments of the five domains have been indicated in **Figure 2A**; GST-tagged Tex13a and empty vector encoding GST (pGEX4t-1) were expressed, respectively, in BL21(DE3) induced by 0.5 mM IPTG for 2 h. GST-tagged proteins were isolated by Glutathione Sepharose 4B beads (GE Health). His6-HA-tagged full-length Tex13a was similarly expressed in BL21(DE3), isolated with Ni-NTA Sepharose FF column (GE Health, Piscataway, NJ, United States), and desalted by dialysis. GST-tagged recombinant

proteins bound in Glutathione Sepharose 4B beads were mixed with His6-HA-tagged Tex13a in the mild lysis buffer [50 mM Tris (pH 7.4), 150 mM NaCl, 0.1% TRITON X-100] with proteinase inhibitor cocktail on ice for 3 h. Following washing, the different bound proteins on Glutathione Sepharose 4B beads were diluted with reduced glutathione and were subjected to SDS-PAGE electrophoresis. SDS-PAGE gels were either transferred to PVDF membrane for Western blots analysis or stained by Coomassie brilliant blue. GST-tagged Tex13a beads were incubated for 3 h on ice with testis homogenates diluted in the abovementioned mild lysis buffer. The bound proteins were subjected to Western blotting.

For Western blot analysis, 40-μg protein samples were subjected to SDS-PAGE, and then transferred to PVDF membranes. After blocking with skimmed milk, the membrane was incubated with primary antibodies anti-HA (1:2,000, KM8004, Sungene Biotech, Tianjin, China) and anti-Cnot1 (1:500, 14276-1-AP, Proteintech, Wuhan, China) overnight at 4°C. The membrane was then incubated with the following secondary antibodies for 30 min: goat anti-rabbit IgG H&L (Alexa Fluor 790, Abcam) and goat anti-mouse IgG H&L (Alexa Fluor 791, Abcam). The membranes were thereafter detected on an Odyssey infrared imaging system (LI-COR Biosciences, Lincoln, NE, United States).

Formalin-fixed paraffin-embedded mouse testis sections of 5 μm thickness were used for HE staining.

Sperm Motility Assay

Male mice aged 3–10 months were used to extract sperm from the caudal epididymis. HS solution containing 25 mM $NaHCO_3$ was used to dilute and release the sperm for motility detection. Sperm samples were injected into 80-μm-deep chambers (Hamilton-Throne, Beverly, MA, United States) and analyzed on a computer-assisted sperm analysis (CASA) system (Hamilton-Throne, Beverly, MA, United States) on a Zeiss microscope with a 10× objective (Oberkochen, German). Statistical analysis was performed *via* the unpaired *t*-test incorporated in GraphPad Prism 8. The sperm samples from 14 KO mice and 13 WT mice were analyzed.

Data Availability

The raw scRNA-Seq data and disposed data have been deposited in the GEO database (GSE183626).

RESULTS

Tex13a-KO Led to a Delayed Degradation of mRNAs Encoding Structural Components of Elongating Spermatids

Tex13a is an X-linked gene with two exons in the mouse, both of which were knocked out by CRISPR/Cas9-mediated genome editing (**Supplementary Figure 1A**). In line with an earlier report (Lu et al., 2019), Tex13a-KO mice were fertile and no visible phenotype was found upon examining of the testis slices stained by HE (**Supplementary Figure 1B**).

To further delineate the function of *Tex13a*, scRNA-seq was performed in wild-type (WT) and *Tex13a* knocked-out (KO) mice. One cluster of spermatogonia, two clusters of spermatocytes, one mixed cell cluster of spermatocyte and early spermatids (Sd1), and nine clusters of haploid spermatids were divided (**Supplementary Figure 2A**). The well-known cell markers of each cluster were plotted in **Figure 1A**. Moreover, by examining the differentially expressed genes (DEGs) during the middle and late steps of spermatids (Sd5-Sd10) in between WT and KO, we found that Sd10_WT and Sd10_KO had more significant DEGs, which were enriched in proteasomal proteins, catabolic process, and protein translation pathways (**Supplementary Figures 2B–D**).

CAMERA enrichment analysis was performed for comparing the overall changes in each gene set or signaling pathway between Tex13a-KO and WT mice (Wu and Smyth, 2012; Cillo et al., 2020). CAMERA enrichment analysis of C5 (CC) pathway gene sets (GSEA) revealed that the gene sets involved in the structural components of sperm tail and head (sperm connecting piece, manchette, centriole, axonemal dynein complex, nuclear pore nuclear basket, outer dynein arm, zona pellucida receptor complex, mitochondrial crista, radial spoke, nuclear pore nuclear basket, PML body, heterochromatin, and chaperonin-containing T complex) were significantly upregulated. Meanwhile, components of the ribosomes were downregulated in the last detectable step of ESs (Sd10) by scRNA-seq (**Figure 1B**). CAMERA enrichment analysis of C5 (MF) and C5 (BP) pathway gene sets (GSEA) further indicated the existence of extensive alterations of the transcriptome in Sd10 ESs (**Figures 1C,D**). Furthermore, a 50 hallmark gene sets enrichment analysis revealed that the pathways of various house-keeping genes were globally lower in Sd10_KO than in Sd10_WT, potentially due to competition between junk mRNAs and house-keeping gene transcripts (**Figure 1E**), which will be discussed further later. Most of the differentially expressed gene sets emerged in Sd10 and some were also found in Sd9, which coincided with the highest expression level of Tex13a in Sd9 and Sd10 (**Figure 1F**). Therefore, Tex13a could be involved in the regulation of overall RNA metabolism during the late ESs.

Tex13a Was Revealed to Be a Testis-Specific Component of the CCR4–NOT Complex

To further verify the involvement of Tex13a in the RNA metabolism, we analyzed the potential association of Tex13a with the CCR4–NOT complex, which serves as a key RNA machine participating in the initial step of RNA degradation. Among the several important components of the CCR4–NOT complex, Cnot1 was the largest and main structural component with five domains (Chalabi Hagkarim and Grand, 2020). The five domains annotated by Pfam have been shown in **Figure 2A**. Tex13a was difficult to be detected by Western blot or immunofluorescence for heterologous expression of HA-tagged Tex13a in cell lines (data not shown). As a result, the full-length Tex13a in fusion with His6-HA tags at the N-terminus and the five recombinant

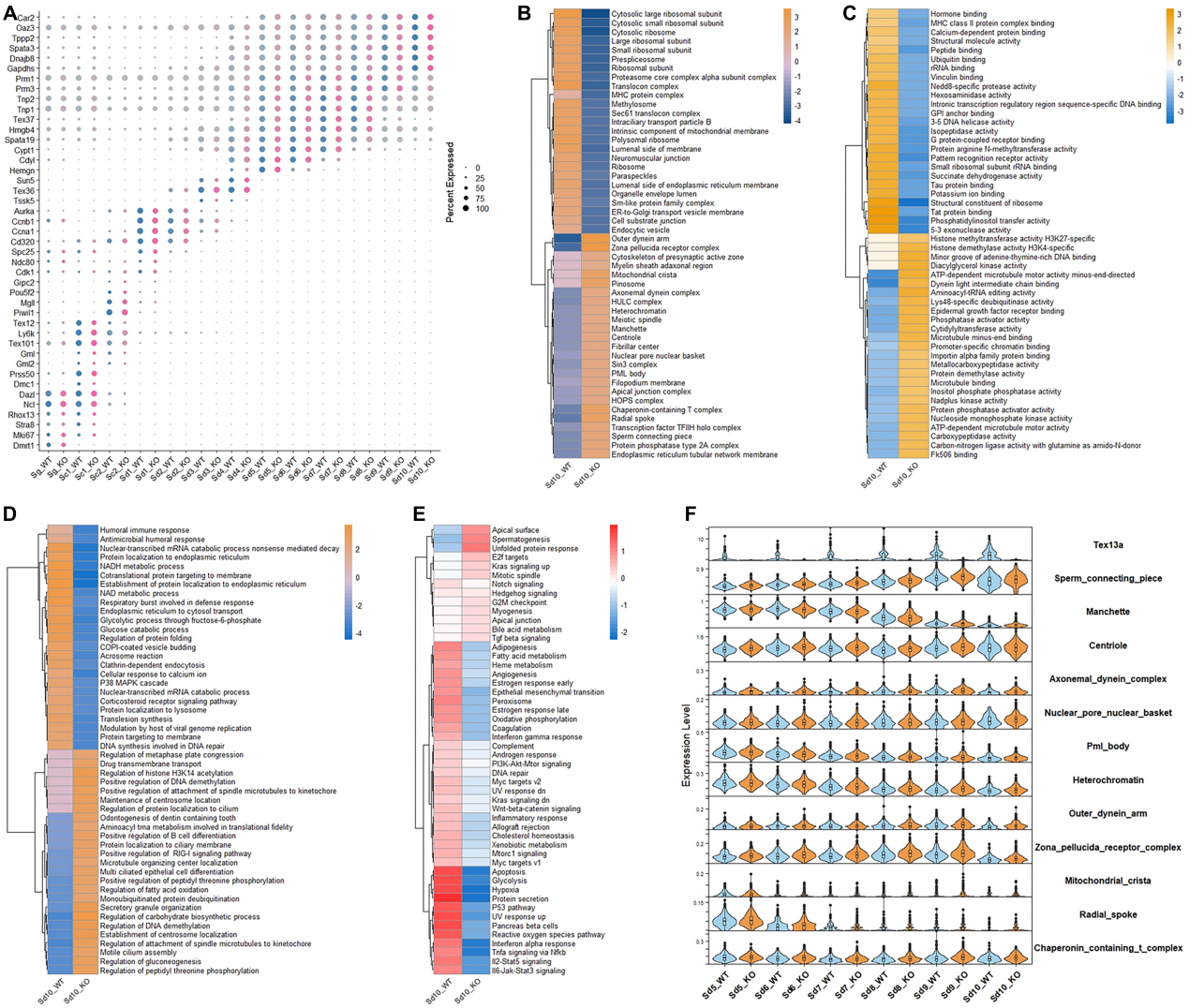

FIGURE 1 | The altered gene expression patterns in the elongating spermatids in Tex13-KO and WT mouse. **(A)** The cell markers of all the germ cell clusters in WT and Tex13a KO mouse testes. **(B)** Top 25 upregulated and downregulated pathways of C5 (CC) (GSEA) in elongating spermatid Sd10 from WT and Tex13a KO mouse testes. **(C)** Top 25 upregulated and downregulated pathways of C5 (MF) (GSEA) in elongating spermatid Sd10. **(D)** Top 25 upregulated and downregulated pathways of C5 (BP) (GSEA) in Sd10_WT and Sd10_KO. **(E)** The relative expression level of 50 hallmark signaling pathways (GSEA) in Sd10_WT and Sd10_KO. **(F)** The expression profiles in Sd5–Sd10 of selected upregulated pathways in Sd10_KO.

segments in fusion with GST corresponding to the five domains were constructed, expressed, and extracted from *E. coli* for GST pull-down analysis (**Figures 2A,B**). As expected, GST pull-down showed a direct interaction of Tex13a with Cnot1. The interaction was found to be mediated by the C-terminal HEAT domain (pfam domain PF04054) of Cnot1 (**Figure 2C**). In turn, GST-Tex13a also pulled down endogenous Cnot1 from the mouse testis homogenates (**Figure 2D**). As a feedback effect, Tex13a deletion led to the upregulation of deadenylation-dependent mRNA decay and CCR4–NOT pathways, but without changing the level of the RNA degradation pathway (**Figure 2E**). We proposed a novel interacting model of Tex13a and CCR4–NOT complex based on the consensus AGGUAA motif bound by Tex13a and the interaction of Tex13a with Cnot1, which gave the CCR4–NOT complex the potential to cause targeted mRNA degradation in late steps of ESs (**Figure 2F**).

Tex13a Deletion Altered the Sperm Motility

The delayed degradation of RNAs of sperm structural components did not result in a visible phenotype in the morphology of the mature sperm and fertility (Lu et al., 2019). Additionally, it remarkably altered the different parameters of sperm motility, such as path velocity (VAP, average path velocity) (p = 0.01372), track speed (VCL, velocity curvilinear) (p = 0.0009073), and rapid progression (p = 0.0001580) as well as the sperm total concentration (p = 0.02968) (**Figure 3**). However,

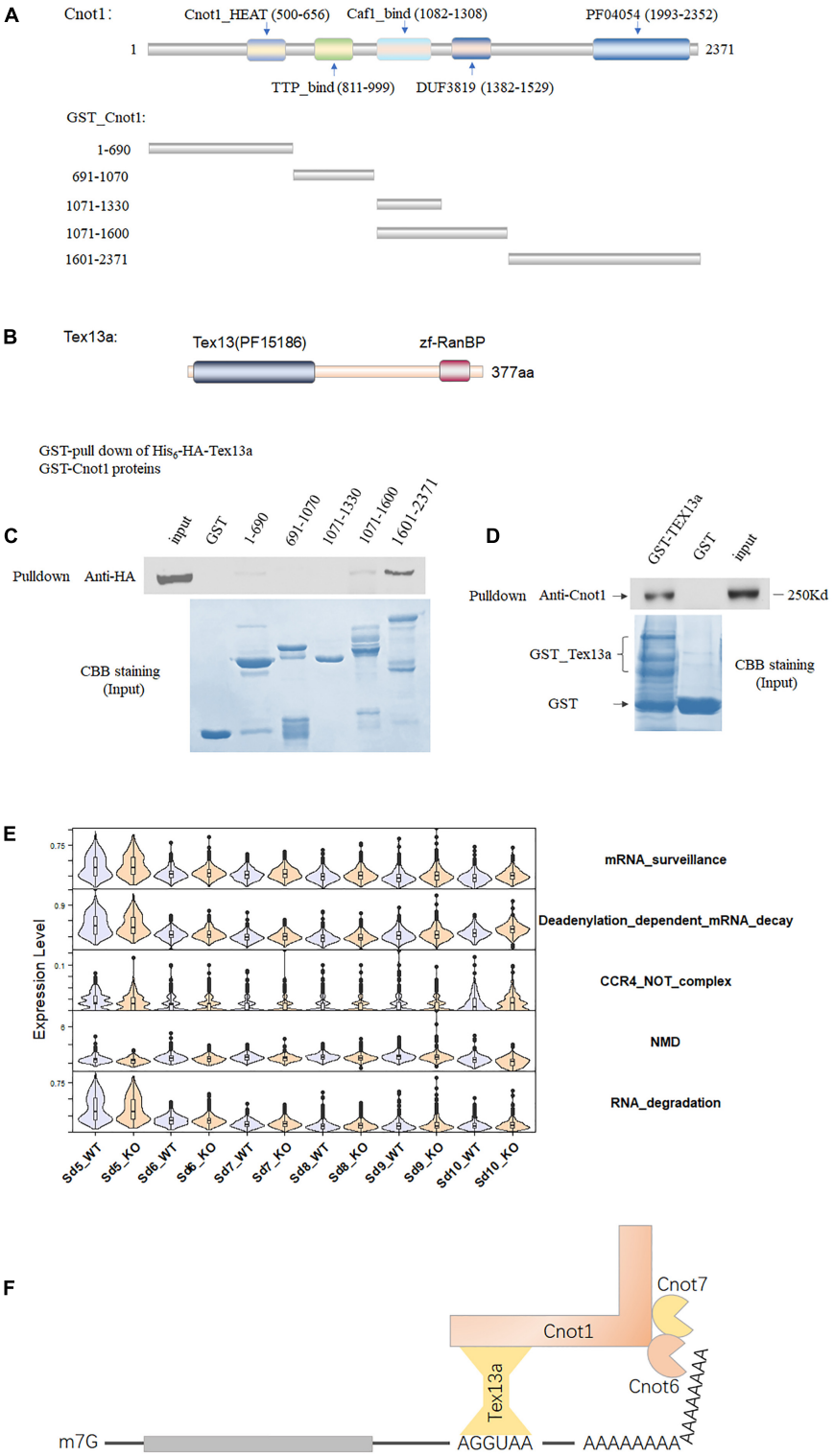

FIGURE 2 | The association of Tex13a with the CCR4–NOT complex. **(A)** The five domains of Cnot1, the five truncated segments of Cnot1 in fusion with GST in the N-terminus facilitated recombinant protein expression. **(B)** Diagram showing the domains of Tex13a. **(C)** GST pull-down analysis of His6-HA-Tex13a with the five recombinant GST-tagged segments of Cnot1 *in vitro*. Recombinant proteins were stained with Coomassie brilliant blue (CBB) staining. **(D)** Endogenous Cnot1 of mouse testes was pulled down by recombinant GST_Tex13a. **(E)** The expression profiles of four RNA metabolism-related pathways from Sd5 to Sd10 in between WT and KO. **(F)** A proposed interaction model of Tex13a with CCR4–NOT complex.

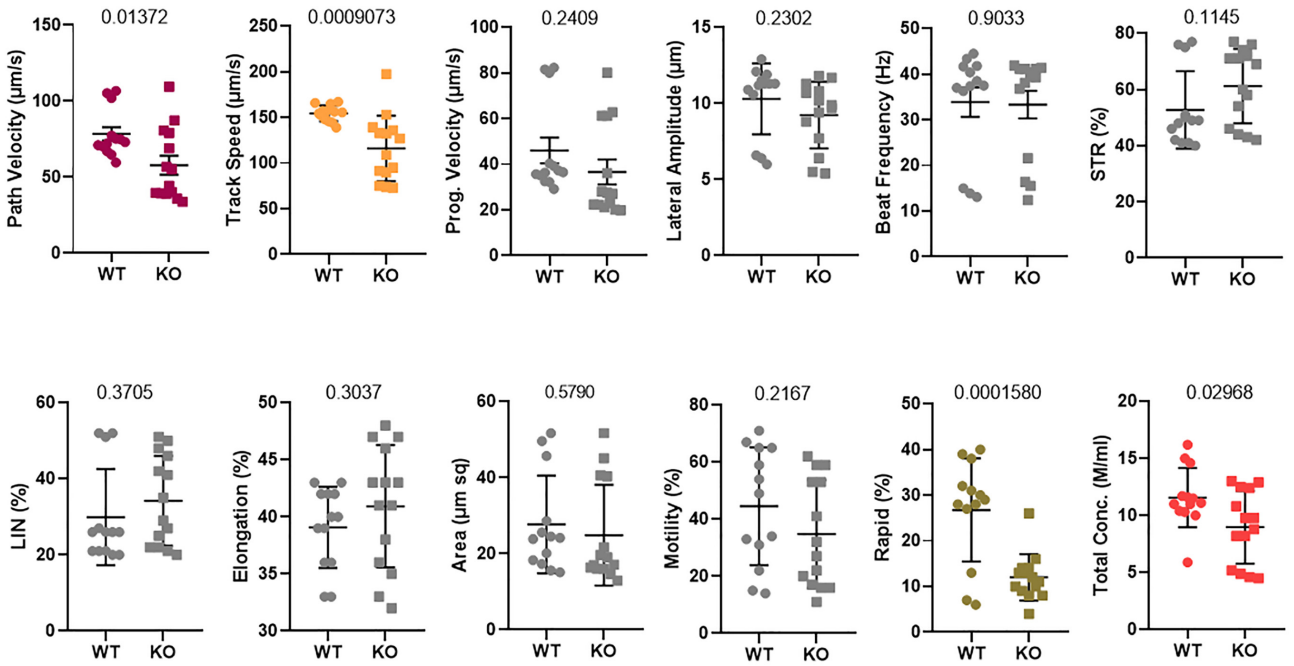

FIGURE 3 | Sperm motility was analyzed using a computer-assisted sperm analysis (CASA) system. Twelve different parameters were assayed and compared between WT and Tex13a_KO mice. *p*-value was displayed above each image.

the beat frequency was not changed. Therefore, the rapid motility was significantly altered in Tex13-KO mouse sperm. Hence, a significant reduction of rapid motility could be considered as a typical phenotype marker of *Tex13a* deletion.

DISCUSSION

Various mRNAs can accumulate during the late stages of ESs, causing delayed translation. These junk RNAs should be eliminated as soon as their tasks are completed. This was demonstrated by an abrupt degradation of mRNAs in Sd10 and a transitory upregulation of CCR4–NOT pathway genes in the late steps of ESs (**Figure 2E**). Chromatid bodies have been regarded as an important center for the RNA metabolic process *via* regulating NMD in spermatids (MacDonald, 2019). NMD is involved in the surveillance and degradation of aberrant RNAs *via* affecting NMD pathways, though it is also capable of degrading a subset of functional intact RNAs (He and Jacobson, 2015; Jones and Wilkinson, 2017). Deadenylation, the rate-limiting step of mRNA degradation, initiates all major mRNA decay pathways identified so far in eukaryotes (Chen and Shyu, 2011). Thereafter, following shortening of the poly(A) tail, the mRNAs can be degraded in a 3′–5′ direction by the exosomes, or, alternatively, deadenylation is followed by decapping (a backup way) and degradation in a 5′–3′ direction (Parker and Song, 2004; Houseley and Tollervey, 2009). Mammalian mRNA deadenylation involves two consecutive phases mediated by the PAN2-PAN3 for long poly(A) and the CCR4–NOT complexes for short poly(A) (Bartlam and Yamamoto, 2010; Wahle and Winkler, 2013). Therefore, degradation of the intact mRNAs during the late steps of ESs were likely initiated by deadenylation, and NMD might not serve as a major degradation pathway, which was also evidenced by the decreased level of NMD in Sd10 (**Figure 2F**). The C-terminal module of CNOT1 contains a rigid scaffold consisting of two perpendicular stacks of HEAT-like repeats (Boland et al., 2013). Moreover, based on the interacting details of Tex13a with Cnot1 C-terminus, the binding model of Cnot2 and Cnot3 with Cnot1 C-terminus can provide a useful clue (Boland et al., 2013), but the application of crystallography might be required in the future investigations.

As to the converse co-relationship between spermatid-specific gene levels and house-keeping genes in late steps of ESs (**Figures 1B,E**), a possible explanation could be that the timely degradation of junk RNAs possibly made space for low-level house-keeping genes due to the limited spaces for storage. "Promiscuous" transcription has been reported to exist in haploid spermatids; an array of genes were found to be transcribed extremely high while the other genes were transcribed at lower levels (Schmidt and Schibler, 1995; White-Cooper and Davidson, 2011). Such low-level transcripts were possibly more vulnerable to be downregulated by delayed degradation of junk mRNAs during spermiogenesis. Most of such genes have been derived from the general pathways involved in the various house-keeping roles (**Figure 1E**). However, more detailed information about the exact RNA motif and mRNAs targeted by Tex13a *in vivo* are needed in the future. For example, identification of new approaches regulating RNA–protein interactions as CLIP can be used for monitoring the RNA motifs bound by Tex13 family members (Nechay and Kleiner, 2020; Masuda et al., 2021).

In terms of the role of Tex13a in the mRNA turnover, only sperm motility alteration might not significantly affect the fertility when Tex13a was deleted, because no alternation of litter size and fertility was recorded (Lu et al., 2019). This is in line with the previous studies that have indicated that only sperm motility is less predictive for evaluating male fertility (Broekhuijse et al., 2012; Wang and Swerdloff, 2014; Boe-Hansen and Satake, 2019). Additionally, the detailed information about parameters of the percentage of spermatozoa with the cytoplasmic droplets (distal cytoplasmic droplets and proximal cytoplasmic droplets), sperm head (length, width, perimeter, and area), midpiece and tail (length and abnormalities), acrosome integrity, plasma membrane integrity, mitochondria activity, DNA damage, histones, chromatin defects, ROS levels, calcium channel activity, pH, and acrosome reaction can also be helpful in complete phenotyping of Tex13a_KO in future studies. The genes derived from the skeletal structures, energy metabolism, mitochondria, and calcium channels may affect the sperm dynamics more directly. Furthermore, animal pairing experiments might also be worth establishing to test the sperm penetration rate *in vitro*, pregnancy rate, farrowing rate and litter size. In this report, we only displayed the changes of sperm motility parameters to verify the potential role of Tex13a in the turnover of mRNAs associated with the different structural components of sperm, many of which were directly related to sperm motility parameters. Screening of differentially expressed genes in protein level related to sperm motility should also be carried out in future studies.

It also needs to be highlighted that the weak phenotype in the spermiogenesis in Tex13a-KO mice may be compensated by other members of the *Tex13* family (Lu et al., 2019). Therefore, Tex13c, which was expressed in late steps of spermatids, also should be paid more attention (Kim et al., 2021).

In summary, *Tex13a* deletion resulted in a delayed degradation of mRNAs of spermiogenesis-related structural components, which potentially resulted in the reduction of house-keeping genes. Sperm motility was also affected, especially the rapid motility was significantly reduced. Interestingly, Tex13a was able to bind Cnot1, a core component of the CCR4–NOT complex, which may affect the decay of particular junk mRNAs during the late steps of ESs.

DATA AVAILABILITY STATEMENT

The datasets presented in this study can be found in online repositories. The names of the repository/repositories and accession number(s) can be found in the article/**Supplementary Material**.

ETHICS STATEMENT

The animal study was reviewed and approved by University of Nantong Animal Care and Use Committee and the Animal Care and Use Office.

AUTHOR CONTRIBUTIONS

FS, CC, YT, and WQ performed supervision, funding acquisition, project administration, and methodology. PM performed sperm motility, HE staining, and genotyping. XC performed DNA cloning, recombinant protein isolation, GST pull-down, and Western blot. JW and XL provided technical assistance, data curation, and project supervision. JC and YH performed animal model preparation. YL performed data analysis, designed experiment, and wrote the manuscript. All authors contributed to the article and approved the final manuscript.

FUNDING

We thank the following funders for supporting this project: the National Key Research and Development Program of China (No. 2018YFC1003500 to FS), the open project of NHC Key Laboratory of Male Reproduction and Genetics in Guangzhou (No. KF201806 to YL), and the National Natural Science Foundation of China (No. 31271448 to YL).

ACKNOWLEDGMENTS

We thank Chen Chen and Professor Xuhui Zeng from Nantong University in helping with the sperm motility assessment. We also thank Shengxinbaodian in helping with the data analysis.

SUPPLEMENTARY MATERIAL

The Supplementary Material for this article can be found online at: https://www.frontiersin.org/articles/10.3389/fcell.2021.761627/full#supplementary-material

REFERENCES

Arraiano, C. M., Mauxion, F., Viegas, S. C., Matos, R. G., and Seraphin, B. (2013). Intracellular ribonucleases involved in transcript processing and decay: precision tools for RNA. *Biochim. et Biophys. Acta.* 1829, 491–513. doi: 10.1016/j.bbagrm.2013.03.009

Bartlam, M., and Yamamoto, T. (2010). The structural basis for deadenylation by the CCR4-NOT complex. *Protein Cell* 1, 443–452. doi: 10.1007/s13238-010-0060-8

Belinky, F., Nativ, N., Stelzer, G., Zimmerman, S., Iny Stein, T., Safran, M., et al. (2015). PathCards: multi-source consolidation of human biological pathways. *Database J. Biol. Databases Curation* 2015:bav006.

Bellil, H., Ghieh, F., Hermel, E., Mandon-Pepin, B., and Vialard, F. (2021). Human testis-expressed (TEX) genes: a review focused on spermatogenesis and male fertility. *Basic Clin. Androl.* 31:9.

Berthet, C., Morera, A. M., Asensio, M. J., Chauvin, M. A., Morel, A. P., Dijoud, F., et al. (2004). CCR4-associated factor CAF1 is an essential factor for

spermatogenesis. *Mol. Cell. Biol.* 24, 5808–5820. doi: 10.1128/mcb.24.13.5808-5820.2004

Boe-Hansen, G. B., and Satake, N. (2019). An update on boar semen assessments by flow cytometry and CASA. *Theriogenology* 137, 93–103. doi: 10.1016/j.theriogenology.2019.05.043

Boland, A., Chen, Y., Raisch, T., Jonas, S., Kuzuoglu-Ozturk, D., Wohlbold, L., et al. (2013). Structure and assembly of the NOT module of the human CCR4-NOT complex. *Nat. Struct. Mol. Biol.* 20, 1289–1297. doi: 10.1038/nsmb.2681

Braun, R. E. (1998). Post-transcriptional control of gene expression during spermatogenesis. *Sem. Cell Dev. Biol.* 9, 483–489. doi: 10.1006/scdb.1998.0226

Broekhuijse, M. L., Sostaric, E., Feitsma, H., and Gadella, B. M. (2012). The value of microscopic semen motility assessment at collection for a commercial artificial insemination center, a retrospective study on factors explaining variation in pig fertility. *Theriogenology* 77, 1466–1479.e3.

Chalabi Hagkarim, N., and Grand, R. J. (2020). The Regulatory properties of the Ccr4-not complex. *Cells* 9:2379. doi: 10.3390/cells9112379

Chen, C. Y., and Shyu, A. B. (2011). Mechanisms of deadenylation-dependent decay. *Wiley Interdiscipl. Rev. RNA* 2, 167–183. doi: 10.1002/wrna.40

Cillo, A. R., Kurten, C. H. L., Tabib, T., Qi, Z., Onkar, S., Wang, T., et al. (2020). Immune landscape of viral- and carcinogen-driven head and neck cancer. *Immunity* 52, 183–199.e9.

Cullinane, D. L., Chowdhury, T. A., and Kleene, K. C. (2015). Mechanisms of translational repression of the Smcp mRNA in round spermatids. *Reproduction* 149, 43–54. doi: 10.1530/rep-14-0394

Dura, B., Choi, J. Y., Zhang, K., Damsky, W., Thakral, D., Bosenberg, M., et al. (2019). scFTD-seq: freeze-thaw lysis based, portable approach toward highly distributed single-cell 3' mRNA profiling. *Nucleic Acids Res.* 47:e16. doi: 10.1093/nar/gky1173

Garneau, N. L., Wilusz, J., and Wilusz, C. J. (2007). The highways and byways of mRNA decay. *Nat. Rev. Mol. Cell Biol.* 8, 113–126. doi: 10.1038/nrm2104

Gou, L. T., Dai, P., Yang, J. H., Xue, Y., Hu, Y. P., Zhou, Y., et al. (2015). Pachytene piRNAs instruct massive mRNA elimination during late spermiogenesis. *Cell Res.* 25:266. doi: 10.1038/cr.2015.14

He, F., and Jacobson, A. (2015). Nonsense-mediated mRNA decay: degradation of defective transcripts is only part of the story. *Ann. Rev. Genet.* 49, 339–366. doi: 10.1146/annurev-genet-112414-054639

Houseley, J., and Tollervey, D. (2009). The many pathways of RNA degradation. *Cell* 136, 763–776. doi: 10.1016/j.cell.2009.01.019

Iguchi, N., Tobias, J. W., and Hecht, N. B. (2006). Expression profiling reveals meiotic male germ cell mRNAs that are translationally up- and down-regulated. *Proc. Natl. Acad. Sci. U.S.A.* 103, 7712–7717. doi: 10.1073/pnas.0510999103

Jones, S. H., and Wilkinson, M. (2017). RNA decay, evolution, and the testis. *RNA Biol.* 14, 146–155. doi: 10.1080/15476286.2016.1265199

Kim, D., Hong, S. H., Han, G., and Cho, C. (2021). Analysis of mouse male germ cell-specific or -predominant Tex13 family genes encoding proteins with transcriptional repressor activity. *Mol. Biol. Rep.* 48, 3017–3022. doi: 10.1007/s11033-021-06265-5

Kleene, K. C. (1989). Poly(A) shortening accompanies the activation of translation of five mRNAs during spermiogenesis in the mouse. *Development* 106, 367–373. doi: 10.1242/dev.106.2.367

Kleene, K. C. (1996). Patterns of translational regulation in the mammalian testis. *Mol. Reprodu. Dev.* 43, 268–281. doi: 10.1002/(sici)1098-2795(199602)43:2<268::aid-mrd17>3.0.co;2-#

Kleene, K. C. (2003). Patterns, mechanisms, and functions of translation regulation in mammalian spermatogenic cells. *Cytogenetic Genome Res.* 103, 217–224. doi: 10.1159/000076807

Kwon, J. T., Jin, S., Choi, H., Kim, J., Jeong, J., Kim, J., et al. (2014). Identification and characterization of germ cell genes expressed in the F9 testicular teratoma stem cell line. *PLoS One* 9:e103837. doi: 10.1371/journal.pone.0103837

Kwon, J. T., Jin, S., Choi, H., Kim, J., Jeong, J., Kim, J., et al. (2016). TEX13 is a novel male germ cell-specific nuclear protein potentially involved in transcriptional repression. *FEBS Lett.* 590, 3526–3537. doi: 10.1002/1873-3468.12433

Li, W., Park, J. Y., Zheng, D., Hoque, M., Yehia, G., and Tian, B. (2016). Alternative cleavage and polyadenylation in spermatogenesis connects chromatin regulation with post-transcriptional control. *BMC Biol.* 14:6.

Li, Y., Mi, P., Chen, X., Wu, J., Qin, W., Shen, Y., et al. (2021). Dynamic profiles and transcriptional preferences of histone modifications during spermiogenesis. *Endocrinology* 162:bqaa210.

Liu, D., Brockman, J. M., Dass, B., Hutchins, L. N., Singh, P., McCarrey, J. R., et al. (2007). Systematic variation in mRNA 3′-processing signals during mouse spermatogenesis. *Nucleic Acids Res.* 35, 234–246. doi: 10.1093/nar/gkl919

Lu, Y., Oura, S., Matsumura, T., Oji, A., Sakurai, N., Fujihara, Y., et al. (2019). CRISPR/Cas9-mediated genome editing reveals 30 testis-enriched genes dispensable for male fertility in micedagger. *Biol. Reprodu.* 101, 501–511. doi: 10.1093/biolre/ioz103

MacDonald, C. C. (2019). Tissue-specific mechanisms of alternative polyadenylation: testis, brain, and beyond (2018 update). *Wiley Interdiscipl. Rev. RNA.* 10:e1526.

MacDonald, C. C., and Grozdanov, P. N. (2017). Nonsense in the testis: multiple roles for nonsense-mediated decay revealed in male reproduction. *Biol. Reprodu.* 96, 939–947. doi: 10.1093/biolre/iox033

Masuda, A., Kawachi, T., and Ohno, K. (2021). Rapidly growing protein-centric technologies to extensively identify protein-RNA interactions: application to the analysis of co-transcriptional RNA processing. *Int. J. Mol. Sci.* 22:5312. doi: 10.3390/ijms22105312

Mayya, V. K., and Duchaine, T. F. (2019). Ciphers and executioners: how 3′-untranslated regions determine the fate of messenger RNAs. *Front. Genet.* 10:6.

Meikar, O., Da Ros, M., Korhonen, H., and Kotaja, N. (2011). Chromatoid body and small RNAs in male germ cells. *Reproduction* 142, 195–209. doi: 10.1530/rep-11-0057

Nechay, M., and Kleiner, R. E. (2020). High-throughput approaches to profile RNA-protein interactions. *Curr. Opin. Chem. Biol.* 54, 37–44. doi: 10.1016/j.cbpa.2019.11.002

Nguyen, C. D., Mansfield, R. E., Leung, W., Vaz, P. M., Loughlin, F. E., Grant, R. P., et al. (2011). Characterization of a family of RanBP2-type zinc fingers that can recognize single-stranded RNA. *J. Mol. Biol.* 407, 273–283. doi: 10.1016/j.jmb.2010.12.041

Parker, R., and Song, H. (2004). The enzymes and control of eukaryotic mRNA turnover. *Nat. Struct. Mol. Biol.* 11, 121–127. doi: 10.1038/nsmb724

Peruquetti, R. L. (2015). Perspectives on mammalian chromatoid body research. *Animal Reprodu. Sci.* 159, 8–16. doi: 10.1016/j.anireprosci.2015.05.018

Schmidt, E. E., and Schibler, U. (1995). High accumulation of components of the RNA polymerase II transcription machinery in rodent spermatids. *Development* 121, 2373–2383. doi: 10.1242/dev.121.8.2373

Steger, K. (2001). Haploid spermatids exhibit translationally repressed mRNAs. *Anat. Embryol.* 203, 323–334. doi: 10.1007/s004290100176

Stuart, T., Butler, A., Hoffman, P., Hafemeister, C., Papalexi, E., Mauck, W. M. III, et al. (2019). Comprehensive integration of single-cell data. *Cell* 177, 1888–1902.e21.

Subramanian, A., Tamayo, P., Mootha, V. K., Mukherjee, S., Ebert, B. L., Gillette, M. A., et al. (2005). Gene set enrichment analysis: a knowledge-based approach for interpreting genome-wide expression profiles. *Proc. Natl. Acad. Sci. U.S.A.* 102, 15545–15550. doi: 10.1073/pnas.0506580102

Temme, C., Simonelig, M., and Wahle, E. (2014). Deadenylation of mRNA by the CCR4-NOT complex in drosophila: molecular and developmental aspects. *Front. Genet.* 5:143.

Ukleja, M., Valpuesta, J. M., Dziembowski, A., and Cuellar, J. (2016). Beyond the known functions of the CCR4-NOT complex in gene expression regulatory mechanisms: New structural insights to unravel CCR4-NOT mRNA processing machinery. *Bio Essays News Rev. Mol. Cell. Dev. Biol.* 38, 1048–1058. doi: 10.1002/bies.201600092

Wahle, E., and Winkler, G. S. (2013). RNA decay machines: deadenylation by the Ccr4-not and Pan2-Pan3 complexes. *Biochim. et Biophys. Acta.* 1829, 561–570. doi: 10.1016/j.bbagrm.2013.01.003

Walker, W. H., Delfino, F. J., and Habener, J. F. (1999). RNA processing and the control of spermatogenesis. *Front. Hormone Res.* 25:34–58. doi: 10.1159/000060996

Wang, C., and Swerdloff, R. S. (2014). Limitations of semen analysis as a test of male fertility and anticipated needs from newer tests. *Fertil. Steril.* 102, 1502–1507. doi: 10.1016/j.fertnstert.2014.10.021

White-Cooper, H., and Davidson, I. (2011). Unique aspects of transcription regulation in male germ cells. *Cold Spring Harbor Perspect. Biol.* 3:a002626. doi: 10.1101/cshperspect.a002626

Wu, D., and Smyth, G. K. (2012). Camera: a competitive gene set test accounting for inter-gene correlation. *Nucleic Acids Res.* 40:e133. doi: 10.1093/nar/gks461

Yamaji, M., Jishage, M., Meyer, C., Suryawanshi, H., Der, E., Yamaji, M., et al. (2017). DND1 maintains germline stem cells via recruitment of the CCR4-NOT complex to target mRNAs. *Nature* 543, 568–572. doi: 10.1038/nature 21690

Conflict of Interest: The authors declare that the research was conducted in the absence of any commercial or financial relationships that could be construed as a potential conflict of interest.

Publisher's Note: All claims expressed in this article are solely those of the authors and do not necessarily represent those of their affiliated organizations, or those of the publisher, the editors and the reviewers. Any product that may be evaluated in this article, or claim that may be made by its manufacturer, is not guaranteed or endorsed by the publisher.

Copyright © 2021 Li, Mi, Chen, Wu, Liu, Tang, Cheng, Huang, Qin, Cheng and Sun. This is an open-access article distributed under the terms of the Creative Commons Attribution License (CC BY). The use, distribution or reproduction in other forums is permitted, provided the original author(s) and the copyright owner(s) are credited and that the original publication in this journal is cited, in accordance with accepted academic practice. No use, distribution or reproduction is permitted which does not comply with these terms.

frontiers in Cell and Developmental Biology

ORIGINAL RESEARCH
published: 04 November 2021
doi: 10.3389/fcell.2021.749559

Loss of Profilin3 Impairs Spermiogenesis by Affecting Acrosome Biogenesis, Autophagy, Manchette Development and Mitochondrial Organization

*Naila Umer[1], Lena Arévalo[1], Sharang Phadke[1†], Keerthika Lohanadan[2], Gregor Kirfel[2], Dominik Sons[3], Denise Sofia[4], Walter Witke[4] and Hubert Schorle[1]**

[1] Department of Developmental Pathology, Institute of Pathology, University Hospital Bonn, Bonn, Germany, [2] Institute for Cell Biology, University of Bonn, Bonn, Germany, [3] Department of Membrane Biochemistry, Life and Medical Sciences (LIMES) Institute, University of Bonn, Bonn, Germany, [4] Institute of Genetics, University of Bonn, Bonn, Germany

OPEN ACCESS

Edited by:
Tzviya Zeev-Ben-Mordehai, Utrecht University, Netherlands

Reviewed by:
Yi-Jang Lee, National Yang Ming Chiao Tung University, Taiwan
Mariano G. Buffone, Instituto de Biología y Medicina Experimental (IBYME-CONICET), Argentina

***Correspondence:**
Hubert Schorle
Hubert.Schorle@ukbonn.de

†Present address:
Sharang Phadke, Department of Medicine III, University Hospital RWTH Aachen, Aachen, Germany

Specialty section:
This article was submitted to Cell Growth and Division, a section of the journal Frontiers in Cell and Developmental Biology

Received: *29 July 2021*
Accepted: *28 September 2021*
Published: *04 November 2021*

Citation:
Umer N, Arévalo L, Phadke S, Lohanadan K, Kirfel G, Sons D, Sofia D, Witke W and Schorle H (2021) Loss of Profilin3 Impairs Spermiogenesis by Affecting Acrosome Biogenesis, Autophagy, Manchette Development and Mitochondrial Organization. Front. Cell Dev. Biol. 9:749559. doi: 10.3389/fcell.2021.749559

Profilins (PFNs) are key regulatory proteins for the actin polymerization in cells and are encoded in mouse and humans by four *Pfn* genes. PFNs are involved in cell mobility, cell growth, neurogenesis, and metastasis of tumor cells. The testes-specific PFN3 is localized in the acroplaxome–manchette complex of developing spermatozoa. We demonstrate that PFN3 further localizes in the Golgi complex and proacrosomal vesicles during spermiogenesis, suggesting a role in vesicle transport for acrosome formation. Using CRISPR/Cas9 genome editing, we generated mice deficient for *Pfn3*. $Pfn3^{-/-}$ males are subfertile, displaying a type II globozoospermia. We revealed that $Pfn3^{-/-}$ sperm display abnormal manchette development leading to an amorphous sperm head shape. Additionally, $Pfn3^{-/-}$ sperm showed reduced sperm motility resulting from flagellum deformities. We show that acrosome biogenesis is impaired starting from the Golgi phase, and mature sperm seems to suffer from a cytoplasm removal defect. An RNA-seq analysis revealed an upregulation of *Trim27* and downregulation of *Atg2a*. As a consequence, mTOR was activated and AMPK was suppressed, resulting in the inhibition of autophagy. This dysregulation of AMPK/ mTOR affected the autophagic flux, which is hallmarked by LC3B accumulation and increased SQSTM1 protein levels. Autophagy is involved in proacrosomal vesicle fusion and transport to form the acrosome. We conclude that this disruption leads to the observed malformation of the acrosome. TRIM27 is associated with PFN3 as determined by co-immunoprecipitation from testis extracts. Further, actin-related protein ARPM1 was absent in the nuclear fraction of $Pfn3^{-/-}$ testes and sperm. This suggests that lack of PFN3 leads to destabilization of the PFN3–ARPM1 complex, resulting in the degradation of ARPM1. Interestingly, in the $Pfn3^{-/-}$ testes, we detected increased protein levels of essential actin regulatory proteins, cofilin-1 (CFL1), cofilin-2 (CFL2), and actin depolymerizing factor (ADF). Taken together, our results reveal the importance for PFN3 in male fertility and implicate this protein as a candidate for male factor infertility in humans.

Keywords: profilin 3, acrosome biogenesis, sperm biology, globozoospermia, autophagy, male fertility

INTRODUCTION

Spermatogenesis is defined as the process of producing mature spermatozoa from spermatogonia. It comprises three phases, (i) spermatocytogenesis (mitotic), (ii) meiotic, and (iii) spermiogenesis. After a series of successive mitotic and meiotic divisions, spermiogenesis is the last step, where spermatozoa are reshaped to their final appearance. During spermiogenesis, haploid round spermatids are transformed into elongated spermatozoa (Oakberg, 1956; Agnew, 1997). This is achieved by a series of cellular reconstruction processes such as formation of the acrosome and tail, replacement of histones and protamine-induced DNA hypercondensation, removal of most of the cytoplasm, and rearrangement of mitochondria along the neck and tail region of the sperm. All mammalian spermatozoa are divided into two basic units based on their function—the head and the flagellum. Both units are shaped and assembled during spermiogenesis, which is the cytomorphogenic phase of spermatogenesis (Khawar et al., 2019). The acrosome is derived from the Golgi and is a secretory vesicle with an acidic pH, containing lysosomal hydrolases and other proteins such as acrosin and acrosin-binding proteins (Tang et al., 1982; Martínez-Menárguez et al., 1996). There are two main pathways that participate in acrosome formation, namely, (i) biosynthetic pathway—a route from trans-Golgi and (ii) endocytic pathway—a route from the endosome (Berruti and Paiardi, 2015). Acrosome biogenesis consists of four phases—(i) Golgi, (ii) cap, (iii) acrosomal, and (iv) maturation (Ramalho-Santos et al., 2001; Moreno and Alvarado, 2006). During the Golgi phase, proacrosomal granules fuse to form a single spherical acrosomal vesicle (Leblond and Clermont, 1952). In the cap phase, the acrosomal granule forms a head cap-like structure. Initially, there is transport of vesicles from Golgi to the acrosome. However, during the cap phase, the Golgi apparatus of the spermatid migrates to the front side of the cell, ending the transport of glycoproteins via the Golgi biosynthetic pathway (Tang et al., 1982; Ramalho-Santos et al., 2001). During the acrosomal phase, the head cap-like structure is elongated along the dorsal edge of the cell. In the final/maturation phase, the acrosome spreads over the anterior half in parallel to the elongation of the sperm head.

In spermatozoa, acrosomal abnormalities result in severe morphogenetic deformations leading to subfertility or infertility. In humans, this disorder is known as globozoospermia, affecting $>0.1\%$ of the infertile male population (Dam et al., 2007). Two types of globozoospermia have been described: type I globozoospermia, where all spermatozoa lack an acrosome and display a round head shape, and type II globozoospermia, where 20–60% spermatozoa lack an acrosome and display a round head shape (Bartoov et al., 1980). Acrosome formation is driven by proteins known to be involved in autophagy. There, the microtubule-associated protein LC3B plays an important role in autophagosome formation and is a widely used biomarker to detect autophagic flux. Further, autophagy-related genes such as *Atg7* (Wang et al., 2014), *Atg9* (Yefimova et al., 2019), and *Atg5* (Huang et al., 2020) are important for the acrosome biogenesis and male fertility. Autophagy itself is regulated, among others, by members of the TRIM protein family (Di Rienzo et al., 2020). In colorectal cancer cells, it has been shown that the overexpression of *Trim27* results in the activation of AKT signaling (Zhang et al., 2018). AKT is a serine threonine kinase, a downstream class of PI3K, and an activator of mTOR (Hahn-Windgassen et al., 2005). In turn, activated mTOR inhibits AMPK signaling, which leads to the suppression of autophagy (Liang et al., 2018).

The flagellum of the mammalian spermatozoa contains mitochondria, a fibrous sheath and central bundle of microtubules called axoneme (Lindemann and Lesich, 2016). The acroplaxome is a cytoskeletal scaffold present in the subacrosomal space within the spermatid. The function of the acroplaxome is the stabilization and anchoring of the acrosome during sperm nuclear elongation (Kierszenbaum and Tres, 2004). The manchette is a transient skirt-like structure present on the exterior pole of the developing spermatozoa. It is essential for the formation of a microtubular platform between the perinuclear ring surrounding the nucleus and the elongated sperm axoneme (Behnen et al., 2009). The exogenous clutching forces generated by F-actin hoops present in the apical region of the sperm nucleus coupled with endogenous modulating mechanism of the acrosome–acroplaxome–manchette complex are thought to play a role in the shaping of the spermatid head (Kierszenbaum and Tres, 2004). Spermiogenesis involves the extensive reshaping of the sperm head by the interaction of F-actin filaments with actin-interacting proteins such as profilins (PFNs) and cofilins (CFLs).

Two of the four known profilin gene family members *Pfn3* and *Pfn4* are expressed in the testes. Contrary to PFN1 and PFN2, PFN3 affected the kinetics of actin polymerization to a lesser extent, suggesting alternative and additional roles of PFN3. During the early steps of spermiogenesis, PFN3 is mainly observed in the acroplaxome of round spermatids and later detected in elongating spermatids at the acroplaxome–manchette complex (Behnen et al., 2009). However, the exact intracellular localization of PFN3 is not yet determined.

To understand the role of PFN3 in male fertility, we used CRISPR/Cas9 to generate *Pfn3*-deficient mice. Lack of *Pfn3* leads to male subfertility with sperm displaying impaired acrosome biogenesis due to defective transport of Golgi vesicles, malformed acrosomes, amorphous head shape, and manchette and flagellum deformities. These defects are reminiscent to type II globozoospermia. Using an RNA-seq analysis, we found *Trim27* upregulated in *Pfn3*-deficient mice. As a consequence, mTOR signaling was activated and AMPK was suppressed, leading to the accumulation of LC3B and SQSTM1 proteins, indicating a disturbance of the autophagic flux. Co-immunoprecipitation confirmed PFN3 interaction with TRIM27 from testis extracts. Further defects include loss of ARPM1 protein in the nuclear fraction of sperm and upregulation of actin-binding proteins ADF and CFL. Interestingly, in the mid-piece of the sperm flagellum, actin organization seemed not affected. These results suggest a surprising role of PFN3, an actin-related protein. Its main role seems to be the control of the *Trim27*-dependent signaling pathways, orchestrating acrosome formation, while the contribution to manchette formation seems rather minor.

MATERIALS AND METHODS

Ethics Statement

Animal care, breeding setup, and experimental procedures were approved according to the German law of animal protection and in agreement with the approval of the local institutional animal care committees (Landesamt für Natur, Umwelt und Verbraucherschutz, North Rhine-Westphalia, approval ID: AZ84- 02.04.2013.A429).

Designing CRISPR Guide RNA and Plasmid Construction

Guide RNAs (gRNAs) specific for *Pfn3* were designed using the online tool from Feng Zhang's lab[1] (Hsu et al., 2013). Designed gRNAs were annealed and cloned into pX330-U6-Chimeric_BB-CBh-hSpCas9 (plasmid # 42230 obtained from Addgene) (Cong et al., 2013) as described previously (Ran et al., 2013).

Functionality of gRNAs Into mES Cells

The functionality of gRNAs was checked using E14Tg2a mES cells (kind gift of Christof Niehrs, IMB Mainz, Germany). On gelatinized cell culture dishes with standard ES cell medium without antibiotics, 3×10^5 cells per well were seeded at 37°C and 7.5% CO_2. After 3 h, cells were transfected with Lipofectamine 2000, pX330 containing gRNAs in a ratio of 1:3, according to the manufacturers' protocol (Thermo Fisher Scientific, Waltham, United States). To remove DNA–Lipofectamine complexes, the medium was changed after 6–8 h to standard ES media.

Generation of Pfn3 KO Mice

Superovulation was done by intraperitoneal injections of PMS (pregnant mare's serum, 5 IU) and hCG (human chorionic gonadotropin, 5 IU) in C57BL/6J female mice and two females mated with one C57BL/6J male. At 0.5 dpc, zygotes from the oviducts were isolated and microinjection was done using an inverted microscope (Leica, Wetzlar, Germany) equipped with micromanipulators (Narishige, Japan) and piezo unit (Eppendorf, Hamburg, Germany). Injection pipettes (PIEZO 8-15-NS, Origio, Charlottesville, United States) were filled with Fluorinert (FC-770, Sigma-Aldrich, Taufkirchen, Germany) for appropriate piezo pulse propagation. Co-injection of Cas9 mRNA (100 ng/μl) (Sigma-Aldrich) and *in vitro*-transcribed single-guide RNAs (sgRNAs) (50 ng/μl each) were achieved into the cytoplasm of zygotes, as described previously (Yang et al., 2014). The zygotes that survived after microinjection were kept for 3 days in KSOM medium in a CO_2 incubator. Resulting blastocysts were transferred into the uteri of pseudo-pregnant foster recipients. The alleles were registered with mouse genome informatics and received the following IDs: $Pfn3^{em1Hsc}$ MGI:6384215, $Pfn3^{em2Hsc}$ MGI:6384216, and $Pfn3^{em3Hsc}$ MGI:6384217.

Genotyping PCR

Genomic DNA was extracted from mice following the phenol/chloroform method and subjected for PCR. Gene-specific primers were used for PCR. PCR products were sequenced to identify the locus-specific deletions mediated by CRISPR/Cas9 genome editing. Primer list is given in the **Supplementary Data** (**Supplementary Table 1**).

Fertility Analysis

For fertility analysis, total five–seven WT and KO male mice aged 10 to 12 weeks were individually housed with sexually mature WT C57BL/6J females in a controlled breeding experiment. Females were observed for the presence of vaginal plugs and pregnancies. The average litter size from pregnant females were calculated.

Morphological Analysis

Pfn3 knockouts were used for gross morphological analyses including body weight, testis weight, epididymis weight, and appearance of testes as compared to heterozygous and wild-type littermates ($n = 13$ animals/genotype).

Epididymis Sperm Assessment

Mice epididymal sperm were extracted by multiple incisions of the cauda followed by a swim out for 30–60 min in M2 medium. Using a Neubauer hemocytometer, sperm count was determined ($n = 13$). A sperm vitality analysis was performed using eosin and nigrosine (E&N) staining, and sperm membrane integrity was accessed by hypo-osmotic swelling test (HOS test); 200 spermatozoa were calculated from three animals per genotype (WT, heterozygous, and knockouts) in a repetition, and results were expressed as percentage of live-to-dead sperm ratio. For all experiments, sexually mature males with an age of 2–6 months were used.

Nuclear Morphology Analysis

For nuclear morphology analysis, after swim out, sperm cells were fixed and washed three times in 2% paraformaldehyde (PFA). After fixation, sample was diluted in a fixative and spread evenly on a glass slide and allowed to air dry. Slides were counterstained with DAPI (Carl Roth, Karlsruhe, Germany) as described previously (Skinner et al., 2019). Images were taken on the Leica DM5500 B/JVC KY-F75U digital camera. Images were analyzed using the ImageJ plugin "Nuclear morphology analysis v1.15.3" according to the developer's instructions.

Immunohistochemistry

The testes were fixed in Bouin's solution for 4–24 h, washed with 70% ethanol to remove excess Bouin, embedded in paraffin, and sectioned at 5-μm thickness. Immunohistochemistry (IHC) was done in the Lab Vision PT module (Thermo Fisher Scientific) and Autostainer 480S (Medac, Hamburg, Germany) as published previously (Nettersheim et al., 2013). The primary antibodies against PFN3 (BEG6 kind gift of Prof. Dr. W. Witke), LC3B (ab58610, Abcam), p-mTOR (Cat#2971, Cell Signaling), RAB5 (PA-5-29022), and ARPM1 (27580-1-AP) were used.

Protein Extraction and Western Blot Analysis

For the crude protein extracts, the testes were homogenized into 500–900 μl RIPA buffer (Thermo Fisher Scientific, Waltham,

[1] http://crispr.mit.edu

United States) using a Dounce homogenizer (Sartorius, Göttingen, Germany). The homogenized mixture was kept on ice for 15 min followed by 15 min of centrifugation at 4°C and 13,000 rpm. In order to load equal amounts of protein, supernatant was used to measure the protein concentration using the Pierce BCA Protein Assay Kit (Thermo Fisher Scientific, Waltham, United States). Cytoplasmic and nuclear fractions were separated as described previously (Hara et al., 2008). SDS gel followed by western blot was performed as described previously (Nettersheim et al., 2016) with primary antibodies against PFN3 (BEG6 kind gift of Prof. Dr. W. Witke), CFL1, CFL2, and ADF (kind gift of Prof. Dr. W. Witke), and ARPM1 (27580-1-AP, ProteinTech), ATG2A (Cat#PA5-77794, Thermo Fisher Scientific), TRIM27 (12205-1-AP), LC3B (ab58610, Abcam), SQSTM1 (Cat#5114, Cell Signaling), mTOR (Cat#2972, Cell Signaling), p-mTOR (Cat#2971, Cell Signaling), and AMPK (Cat#5831, Cell Signaling) were used.

Immunoprecipitation

Protein immunoprecipitation (IP) was performed on whole adult testis lysate. Testis tissue was homogenized in RIPA buffer followed by sonication at high speed for five cycles of 30-s ON/30-s OFF with a Bioruptor® sonication device, and protein extraction was done as described above. Co-IP was performed using Dynabeads® M-280 Sheep Anti-Rabbit IgG as described by the manufacturer's protocol. The captured and eluted proteins were separated by SDS-PAGE and transferred to nitrocellulose membranes in preparation for immunoblot analysis.

cDNA Synthesis and Real-Time PCR

RNA was extracted from testes tissue after removal of the tunica albuginea using TRIzol reagent according to manufacturer's protocol (Life Technologies, Carlsbad, United States). The concentration and purity of isolated RNA was measured by a NanoDrop instrument (Peqlab, Erlangen, Germany). After DNAseI treatment of RNA, cDNA was synthesized using RevertAid First Strand cDNA Synthesis Kit (Fermentas, St. Leon-Rot, Germany). Quantitative reverse transcription polymerase chain reaction (qRT-PCR) was performed on ViiA 7 Real-Time PCR System (Applied Biosystems, distributed by Life Technologies) using Maxima SYBR Green qPCR Master Mix (Life Technologies) as described previously (Jostes et al., 2017). At the end of each PCR run, a melting point analysis was performed. GAPDH was used as reference gene for data normalization.

RNA-Seq Analysis

RNA integrity (RIN) was determined by the sequencing facility (UKB sequencing core facility) using the RNA Nano 6000 Assay Kit with the Agilent Bioanalyzer 2100 system (Agilent Technologies, Santa Clara, CA, United States). RIN values ranged from 8.2 to 10 for all samples. RNA sample quality control and library preparation were performed by the sequencing facility (UKB sequencing core facility), using the QuantSeq 3'-mRNA Library Prep (Lexogen). RNA-seq was performed on the Illumina HiSeq 2500 V4 platform, producing > 10 million, 50-bp 3'-end reads per sample.

All samples were mapped to the mouse genome (GRCm38.89). Mapping was done using HISAT2 2.1 (Kim et al., 2015). Transcript quantification and annotation was done using StringTie 1.3.3 (Pertea et al., 2015). Gene annotation information for the mouse genome was retrieved from the Ensembl FTP server[2] (GRCm38.89). We used the python script (preDE.py) included in the StringTie package to prepare gene-level count matrices for analysis of differential gene expression.

Differential expression was tested with DESeq2 1.16.1 (Love et al., 2014). Pseudogenes were removed from the count matrices based on "biotype" annotation information extracted from Biomart (R-package biomaRt) (Durinck et al., 2005). Low counts were removed by the independent filtering process implemented in DESeq2 (Bourgon et al., 2010). The adjusted *p*-value (Benjamini–Hochberg method) cutoff for DE was set at <0.05, and log2 fold change of expression (LFC) cutoff was set at >1.5.

The datasets presented in this study can be found in online repositories. The names of the repository/repositories and accession number(s) can be found at: https://www.ncbi.nlm.nih.gov/geo/, GSE171068.

Transmission Electron Microscopy

Epididymal sperm and testis tissue were washed in phosphate buffered saline (PBS) and fixed in 1.5% glutaraldehyde in 0.1 M cacodylate buffer (pH 7.4). Sperm cells were rinsed in 0.1 M cacodylate buffer and fixed in 2% osmium tetroxide again followed by an additional washing in 0.1 M cacodylate buffer. Afterward, dehydration was performed by an increasing ethanol concentration, terminated by two incubations in propylene oxide for 15 min, and an interim staining in 0.5% uranyl acetate. Samples were stored in propylene oxide and EPON mixture (1:1) overnight and followed by embedding in EPON for 24 h at 70°C. Ultrathin sections were picked up on grids, stained with 3.5% uranyl acetate for 25 min and lead citrate solution for 7 min, and images were taken on the Philips CM 10 TEM. For immunogold labeling, prior to fixation in glutaraldehyde, sections were incubated with PFN3 antibody (1:50) for 1 h. Followed by washing, gold-conjugated anti-rabbit IgG (10 nm) secondary antibody (1:50) was incubated for 1 h. In the negative control, primary antibody was omitted. Finally, the sections were post-stained with uranyl acetate.

Scanning Electron Microscopy

Sperm cells were fixed in primary fixative for 30 min at 4°C: 1% glutaraldehyde and 0.4% formaldehyde in 0.1 M sodium cacodylate buffer (pH 7.2). After washing the samples three times in 0.1 M sodium cacodylate buffer for 5 min, they were post-fixed with 1% OsO_4 in 0.1 M sodium cacodylate buffer for 30 min followed by three washing steps. Images were taken using a Verios 460L (FEI, Eindhoven, Netherlands) (Nussdorfer et al., 2018) equipped with a STEM 3 detector.

[2]https://ftp.ensembl.org/

Immunofluorescence Staining

Immunofluorescence staining was performed on testis sections using peanut agglutinin (PNA)- fluorescein isothiocyanate (FITC) Alexa Fluor 488 conjugate (Molecular Probes, Invitrogen), anti-mouse GM130 (610823, BD Biosciences, United States), and anti-rabbit TGN46 (JF1-024, Thermo Fischer Scientific) to check the acrosome biogenesis and *cis*- and *trans*-Golgi structural organization, respectively; 5-μm testis tissue sections were taken on slides. Deparaffinization on Bouin's fixed paraffin-embedded testis tissue was performed by immersing them in xylol for two times, followed by dehydration steps in 100, 95, and 70% alcohol. After washing with PBS twice, tissue sample was permeabilized in 0.1% Triton X-100 for 5 min at 37°C, followed by blocking in 1% bovine serum albumin (BSA) for 1 h at room temperature. Tissue sections were incubated with diluted PNA-FITC in PBS at room temperature for 30 min; next, slides were washed in PBS for two times. Tissue sections were incubated with GM130 and TGN46 antibodies diluted at 2 μg/ml in 0.1% BSA at 4°C for overnight, followed by PBS washing, and respective secondary antibodies were used for 1 h at room temperature. Tissue sections were mounted with ROTI®Mount FluorCare DAPI (Carl Roth, Karlsruhe, Germany). Images were taken within 24 h using an LSM 710 (Zeiss, Oberkochen, Germany).

For sperm immunofluorescence, after swim out, sperms were washed two–three times in PBS followed by fixation in 4% paraformaldehyde for 20 min at room temperature. After washing with PBS, spermatozoa were incubated with PNA-FITC and Mito Red (5 nM, 53271; Sigma Aldrich) diluted in PBS at room temperature for 30 min. For manchette staining, germ cell population was isolated from testes as described previously (Li W. et al., 2015), and staining with anti-alpha tubulin antibody (clone DM1A Alexa Flour 488 conjugate; 16-232 Sigma Aldrich) was performed as described previously (Rotgers et al., 2015). Next, spermatozoa were plated onto Superfrost Plus Microscope Slides (Thermo Fisher Scientific), mounted with ROTI®Mount FluorCare DAPI (Carl Roth, Karlsruhe, Germany). Images were taken within 24 h using an LSM 710 (Zeiss, Oberkochen, Germany).

STED Imaging

Epididymal sperm cells after swim out were diluted into PBS (1:10); 400 μl of diluted sperm were loaded on poly-L-lysine (CAS 25988-63-0, Sigma Aldrich)-coated coverslips in a six-well plate and air dried for 30 min at 37°C. After removing the PBS, sperm cells were fixed in 4% PFA followed by quenching with 50 mM NH_4Cl for 15 min. Sperm cells were permeabilized by 0.02% Triton X-100 for 3 min followed by washing with PBS, incubation for 1 h at RT with Phalloidin ATTO647 (1/1,000 in 3% BSA, ab176759, Abcam), and mounting with ProLong Gold Antifade (#P36930, Life Technologies). STED micrographs were acquired using a four-channel easy3D super-resolution STED optics module (Abberior Instruments, Göttingen, Germany) coupled with an Olympus IX73 confocal microscope (Olympus, Tokyo, Japan) and equipped with an UPlanSApo × 100 (1.4 NA) objective (Olympus, Tokyo, Japan) (Mikuličić et al., 2019), available in the LIMES Imaging Facility.

Sperm Motility Analysis

Epididymal sperm were incubated in TYH medium at 37°C for 20 min, after swim out sperm cells were diluted into the TYH medium supplemented with BSA. The diluted cell suspension was placed onto the pre-warmed (37°C) slide, and video was recorded using the Basler Microscopy ace camera (acA 1920-155uc) at 300 frames, streaming video using pylon Viewer (v.5.0.11.10913, Basler AG, Ahrensburg, Germany). Sperm motility was evaluated by using the OpenCASA program as described previously (Alquézar-Baeta et al., 2019).

Acrosomal Reaction

Sperm were isolated from cauda epididymis and allowed to swim out in M2 medium for 10 min. Capacitation was induced by incubating in HTF medium for 90 min at 37°C, 5% CO_2. To induce acrosome reaction, calcium ionophore A23187 (10 μM, c7522; Sigma Aldrich) was added. After 15 min, sperm were spread on glass slides, air dried, and fixed in methanol for 3 min at RT. Followed by PBS washing, sperm were subjected to Coomassie brilliant blue staining (2% *w*/*v* G250) for 3 min as described previously (Liu et al., 2019). Followed by PBS washing two times for 2–3 min each, mounting was performed by using ROTI®Mount FluorCare (HP 21.1 Carl Roth). Two hundred spermatozoa for each genotype ($n = 3$) were assessed by a bright field microscope.

Statistics

The mean of all values for a particular data set has been represented in graphical form. Error bars have been used to denote standard deviation. Student's *T*-test (two-tailed unpaired and one-tailed paired) and ANOVA (Tukey's *post hoc*) were performed to ascertain the significance of the variability in data. *P*-value less than 0.05 ($p < 0.05^{*}$, $<0.005^{**}$, 0.001^{***}) was considered as statistically significant.

RESULTS

Ultrastructural Analysis of PFN3 Localization in Mouse Testes

We examined the distribution of PFN3 at ultrastructural level during spermiogenesis with a PFN3 polyclonal antibody and a gold-conjugated secondary antibody using immunoelectron microscopy. With immunogold labeling, we were able to determine localization of PFN3 in sub-domains of cellular compartments at the *cis*- and *trans*- Golgi network, the acroplaxome, mitochondria, and the manchette. In the Golgi phase, the electron dense giant acrosomal granule forms from the numerous Golgi-derived proacrosomal vesicles (**Supplementary Figure 1A**). Gold particles were detected representing PFN3 in the *cis*- and *trans*-part of the Golgi network adjacent to the nuclear pole of the round spermatid (**Figure 1A** and **Supplementary Figures 1B,C,E,F**, arrows). The *cis*-part is

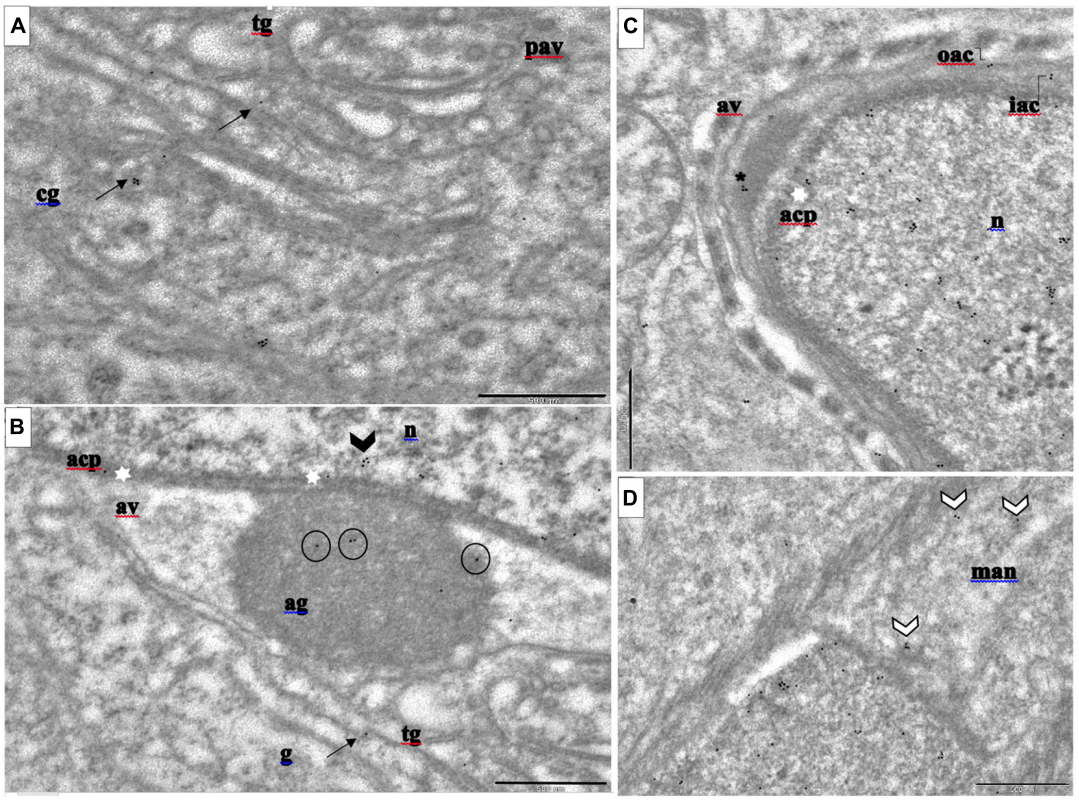

FIGURE 1 | Immunogold labeling of PFN3 in developing mouse spermatid during acrosome biogenesis. **(A)** *cis*- and *trans*-Golgi network; immunogold particles in cg and tg = black arrows. **(B)** Golgi phase; immunogold labeling highlighted in ag = circles, acp = white stars, and n = arrow head. **(C)** Cap phase; immunogold particles highlighted in av = asterisk. **(D)** Man immunogold labeling = white arrow heads. cg, cis-Golgi; tg, trans-Golgi; ag, acrosomal granule; n, nucleus; acp, acroplaxome; av, acrosomal vesicle. Scale bar = 500 nm. **(A,B)** are from the same image (ref.to **Supplementary Figure 2A**).

responsible for organizing and sorting of proteins imported from the endoplasmic reticulum (ER) and transported to the *trans*-part of the Golgi network where they are modified and exported as proacrosomal vesicles (**Supplementary Figure 1E**). Immunogold labelling was detected in the acrosomal granule (**Figure 1B**, circle), a giant structure attached to the middle of the acroplaxome (**Figure 1B**, white stars) of developing spermatozoa. We detected gold traces in the mitochondria, which are responsible for providing energy for flagellum propelling and germ cell differentiation (**Supplementary Figures 1D,E**, white arrows). Some of the gold particles were detected in the inner membrane of acrosome–acroplaxome interface, suggesting that PFN3 contributes to the attachment of acrosomal granule (**Supplementary Figure 1E**, white stars). In the cap phase (**Supplementary Figure 1G**), we detected PFN3 in the acrosomal vesicles (**Figure 1C** and **Supplementary Figures 1H,I**, asterisk), which are responsible for the formation of acrosome. In addition, we detected few gold traces in the nucleus (**Figures 1B,C** and **Supplementary Figures 1H–M**), suggesting that PFN3 might play a role in sperm nuclear shaping. Immunogold labelling also showed PFN3 localization in inner and outer membranes at the leading edge of the acrosome (**Supplementary Figures 1H,I,K**, elbow). Gold traces were also detected in highly specialized structures of elongating spermatozoa such as the manchette (**Figure 1D** and **Supplementary Figures 1J,M**, white arrow heads), the acroplaxome marginal ring (**Supplementary Figure 1O**, double arrows), as well as flagellum formation (**Supplementary Figures 1N,Q,T**). Cross sections of the flagellum showed gold traces in the mitochondria, which are gathered around the axoneme (**Supplementary Figures 1U–W**) to form the mitochondrial sheath in the sperm mid-piece (**Supplementary Figure 1W**). So, PFN3 is detected in the Golgi sub-domains, the acroplaxome–manchette complex, and the mitochondria, suggesting a role for PFN3 in acrosome biogenesis, sperm head shaping, and tail formation. The negative control is given in the **Supplementary Data** (**Supplementary Figures 1Y,Z**).

Pfn3-Deficient Male Mice Display Sub-Fertility and Low Sperm Quantity and Quality

We generated *Pfn3*-deficient mice by injecting Cas9 mRNA and two sgRNAs into the cytoplasm of fertilized eggs targeting the exon of the gene (**Figure 2A**). Six pups carrying CRISPR/Cas9-induced mutations were identified (**Supplementary Figure 2A**) and three mouse lines, *Pfn3*Δ254, *Pfn3*Δ41, and *Pfn3*Δ29 harboring deletions of 254, 41, and 29 bp, respectively, were

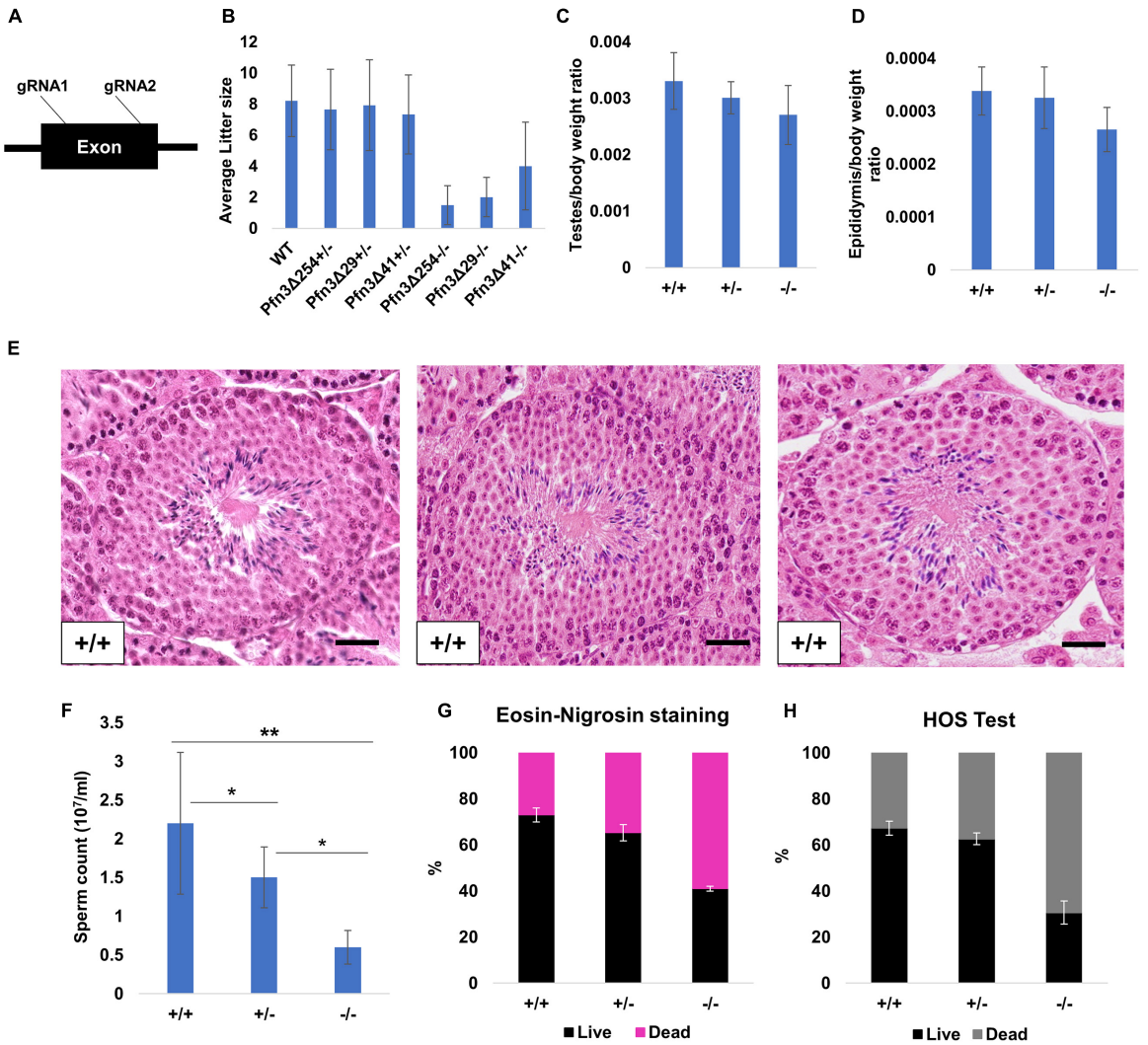

FIGURE 2 | Generation and characterization of *Pfn3*-deficient mice. **(A)** Schematic representation of *Pfn3* genomic locus with targeting sites of designed gRNAs. **(B)** Mating statistics of wild-type, *Pfn3*Δ254, *Pfn3*Δ41, and *Pfn3*Δ29 heterozygous and homozygous (n = 5/*Pfn3*-deficient mouse model) males. Successful mating of heterozygous and homozygous males with wild-type females was indicated by the presence of a vaginal plug at 0.5 dpc. **(C,D)** Relative weights of testes and cauda epididymis are comparable between all three genotypes of *Pfn3*Δ254 (n = 13). **(E)** H & E staining on $Pfn3^{+/+}$, $Pfn3^{+/-}$, and $Pfn3^{-/-}$ testes section. **(F)** Sperm count comparison in $Pfn3^{+/+}$, $Pfn3^{+/-}$, and $Pfn3^{-/-}$ littermates (n = 13). **(G)** Eosin and nigrosine staining on biological replicates (n = 3) of $Pfn3^{+/+}$, $Pfn3^{+/-}$, and $Pfn3^{-/-}$ sperm. **(H)** Hypo-osmotic swelling test on biological replicates (n = 3) of $Pfn3^{+/+}$, $Pfn3^{+/-}$, and $Pfn3^{-/-}$ sperm. At least 200 spermatozoa were evaluated per sample.

established by backcrossing with C57BL/6 mice. All deletions result in null alleles since they encode for frame shifts in the PFN3 reading frame leading to premature translational termination (**Supplementary Figure 2C**). qRT-PCR, western blotting, and IHC confirmed the deletion of *Pfn3* in the *Pfn3*-deficient mice (**Supplementary Figure 2D**). Western blotting displayed a signal in testis/post-natal testis (day 28). All other tissues tested were negative for PFN3. Similarly, IHC produced a signal for PFN3 in the testis but not in the brain and kidney sections. These results indicate the specificity of the PFN3 antibody (**Supplementary Figure 2E**). IHC of WT testis section using anti-PFN3 antibody showed a strong expression of PFN3 in the nuclear region of elongated spermatids (**Supplementary Figure 2D**). In addition, IF using PFN3 antibody on purified germ cells revealed that PFN3 is localized to the cytoplasm of round spermatids. As round spermatids develop into elongating spermatids, PFN3 is localized in a punctuated manner around the acrosomal region (**Supplementary Figure 2F**). In non-acrosome-reacted spermatozoa, PFN3 is located in the acrosome and the nucleus. In acrosome-reacted spermatozoa, PFN3 can be detected in the head region (**Supplementary Figure 2G**). Males heterozygous for either *Pfn3*Δ254, *Pfn3*Δ41, and *Pfn3*Δ29 produced an average litter size of 7.6, 7.9, and 7.3, respectively (**Figure 2B**), which is comparable to wild-type mice with a mean litter size of 8.2 (Biggers et al., 1962). Homozygous *Pfn3* male mice are sub-fertile since they produced an average litter

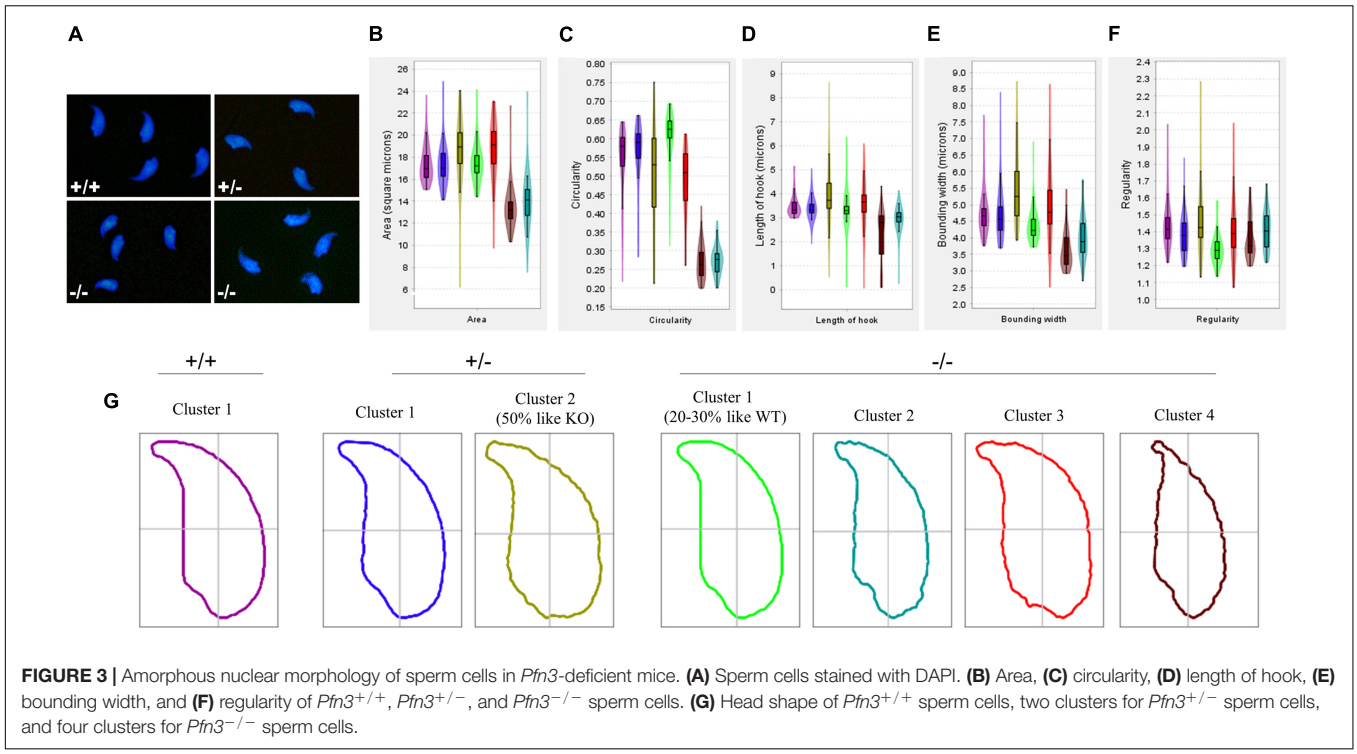

FIGURE 3 | Amorphous nuclear morphology of sperm cells in *Pfn3*-deficient mice. **(A)** Sperm cells stained with DAPI. **(B)** Area, **(C)** circularity, **(D)** length of hook, **(E)** bounding width, and **(F)** regularity of $Pfn3^{+/+}$, $Pfn3^{+/-}$, and $Pfn3^{-/-}$ sperm cells. **(G)** Head shape of $Pfn3^{+/+}$ sperm cells, two clusters for $Pfn3^{+/-}$ sperm cells, and four clusters for $Pfn3^{-/-}$ sperm cells.

TABLE 1 | Motility parameters were analyzed for $Pfn3^{+/+}$, $Pfn3^{+/-}$, and $Pfn3^{-/-}$ sperms using OpenCASA software (n = 3/genotype).

	VSL mean (μm/s)	VCL mean (μm/s)	VAP mean (μm/s)	Progressive motility (%)	Motility (%)
$Pfn3^{+/+}$	62.33 ± 1.2	218.5 ± 11.5	122.3 ± 4.7	47.2 ± 1.7	59 ± 5.9
$Pfn3^{+/-}$	58.46 ± 1.9	187 ± 5	107 ± 5.2	45.65 ± 9.9	52.11 ± 7.8
$Pfn3^{-/-}$	49.57 ± 13.8	170.857 ± 49.14	91.39 ± 25.03	32.388 ± 7.4*	34.91 ± 7.9**

Data is presented as mean ± SD using ANOVA (Tukey's post hoc test). VSL, straight-line velocity (μm/s); VCL, curvilinear velocity (μm/s); VAP, average path velocity (μ m/s).

size of 1.5, 2, and 4 for *Pfn3*Δ254, *Pfn3*Δ41, and *Pfn3*Δ29, respectively (**Figure 2B**).

Adult *Pfn3*-deficient males for either *Pfn3*Δ254, *Pfn3*Δ41, or *Pfn3*Δ29 mated with females normally as vaginal plugs were clearly detectable. Relative weights of the testes and epididymis of *Pfn3*-deficient mice (*Pfn3*Δ254) were slightly reduced; however, that reduction was not significant (**Figures 2C,D**). Histological analysis using hematoxylin and eosin H & E) staining on $Pfn3^{+/+}$, $Pfn3^{+/-}$, and $Pfn3^{-/-}$ testes sections showed normal morphology of seminiferous tubules (**Figure 2E**). This suggests that deletion of *Pfn3* left the gross morphology of the testes and epididymis unaffected.

However, $Pfn3^{+/-}$ and $Pfn3^{-/-}$ males showed a significant reduction in sperm count (**Figure 2F**). Next, E&N staining was performed to assess the vitality of spermatozoa. E&N distinguish live (whitish in color, arrow head) from dead sperm (pink in color, arrow in **Supplementary Figure 2K**). A percentage of live sperm in the range of 60–80% is considered normal, borderline 40–60%, and below 40% is considered abnormal. E&N staining showed that in heterozygous males, the percentage of viable sperm is in the normal range, while in case of *Pfn3*-deficient mice, the percentage of viable sperm was at borderline (∼40%) (**Figure 2G**). Further, the HOS test was performed to check the integrity of sperm membrane, where intact (live) sperm displays a swelling of the tail (**Supplementary Figure 2M**). The percentage of hypo-osmotic reactive sperm for $Pfn3^{-/-}$ mice was again at borderline (**Figure 2H**). Male mice for *Pfn3*Δ41 and *Pfn3*Δ29 have the same phenotype as *Pfn3*Δ254 mice (**Supplementary Figures 2H–N**). In conclusion, loss of *Pfn3* impinges not only on sperm quantity but also sperm quality.

Sperm Head Morphology Is Altered in Pfn3-Deficient Mice

We next used geometric morphometric analysis to analyze sperm head shape in detail. DAPI-stained sperm cells showed altered head shape for $Pfn3^{-/-}$ compared to control (**Figure 3A**). An analysis of 994 nuclei revealed (334 $Pfn3^{+/+}$, 289 $Pfn3^{+/-}$, and 371 $Pfn3^{-/-}$) that *Pfn3*-deficient sperm shows alterations in area (**Figure 3B**), circularity (**Figure 3C**), length of hook (**Figure 3D**), bounding width (**Figure 3E**), and regularity (**Figure 3F**). Next, clustering was performed to categorize the sperm heads. Of note, 50% of heterozygous sperm nuclei are similar to WT, while 50% have abnormal morphology similar to *Pfn3*-deficient sperm

nuclei (**Figure 3G**). This finding suggests a gene–dosage effect, which, however, does not seem to affect the mating success of $Pfn3^{+/-}$ males. Interestingly, 70–80% of *Pfn3*-deficient sperms showed irregular/round head morphology. Our analysis clearly shows that PFN3 plays a role in shaping of the sperm head during spermiogenesis.

Sperm Motility Is Reduced in Pfn3-Deficient Mice

To analyze the swimming properties of *Pfn3*-deficient sperm, we performed computer-assisted semen analysis (CASA). Compared to WT and Het sperm samples (**Table 1**) $Pfn3^{-/-}$ sperm showed significantly reduced progressive and total motility. The other sperm motility parameters such as curvilinear velocity (VCL), straight-line velocity (VSL), and average path velocity (VAP) are reduced, but the difference is not significant when compared to sperm samples of controls. Of note, the observed reduction in sperm motility most likely is the reason of the decreased sperm count in *Pfn3*-deficient mice.

Impaired Acrosome Biogenesis in Pfn3-Deficient Mice

PFN3 is detected in actin-rich structures such as acrosome–acroplaxome and Golgi complex, suggesting a role in acrosome biogenesis. In order to investigate the development of acrosome, we used PNA-FITC fluorescence labeling on testes sections. In tubules of wild-type (**Figure 4A**) and heterozygous males (**Figure 4B**), Golgi-phase spermatids showed developing acrosomes forming a homogenous single cluster on the apical face of cell nuclei. In mutant spermatids, PNA staining was scattered, suggesting a less uniform acrosomal compartment (**Figure 4C**). This abnormal formation of the acrosome was further observed in the next step, the cap phase. Here, the acrosome forms a cap-like structure covering the anterior half on round spermatids as seen in WT (**Figure 4D**) and heterozygous (**Figure 4E**) sections. In $Pfn3^{-/-}$, the cap structures were more unevenly distributed in round spermatids (**Figure 4F**). In the acrosomal phase, as spermatids started to elongate during sperm head remodeling, these defects were more prominent, and the acrosomal content failed to form an arrow-like shape in elongating spermatids of $Pfn3^{-/-}$ mice (**Figure 4I**), compared to WT (**Figure 4G**) and heterozygous (**Figure 4H**). These results indicate that loss of PFN3 impairs acrosomal biogenesis already at the Golgi phase.

To understand the impaired acrosome biogenesis more in detail, an ultrastructure analysis using transmission electron microscopy (TEM) was performed on developing spermatids. In the Golgi phase, proacrosomal granules originate from the *trans*-Golgi and fuse to form a single, large acrosome vesicle attaching itself in the middle of the acroplaxome on the nuclear surface as seen in WT (**Supplementary Figure 3A**) and heterozygous cells (**Supplementary Figure 3B**). However, sections of *Pfn3*-deficient testes showed that the proacrosomal vesicle fail to attach in the middle of the acroplaxome and did not form a dense giant vesicle (**Supplementary Figure 3C**). In the cap phase, the proacrosomal granule starts to develop and flattens over the nucleus, forming the acrosomal cap, displayed in WT (**Supplementary Figure 3D**) and heterozygous spermatids (**Supplementary Figure 3E**). However, in *Pfn3*-deficient testes, the acrosomal vesicle fails to form a continuous cap-like structure and present as a detached granule from the acroplaxome (**Supplementary Figure 3F**). In the acrosome phase, the cap continues to develop as an arrow-like cover spanning the anterior two-third of the nucleus as indicated in WT (**Supplementary Figure 3G**) and heterozygous spermatids (**Supplementary Figure 3H**). Finally, at the end of maturation phase, acrosome formation is completed (**Supplementary Figures 3I,J**). In *Pfn3*-deficient sperm, during the acrosomal and maturation phases, the acrosomal granule fails to develop further (**Supplementary Figures 3K,L**).

In order to see the acrosomal defect in mature sperm, we next analyzed epididymal sperm cells of *Pfn3*-deficient males using TEM and immunofluorescence staining (PNA-FITC). An ultrastructural analysis and acrosomal labelling revealed malformation of the acrosomal region in epididymal sperms of $Pfn3^{-/-}$ mice. Sperm cells present with elongating projections (highlighted by arrows), detached acrosome, abnormal acrosomal covering, and impaired removal of cytoplasm (**Figure 4J**). Similarly, mature sperm stained with PNA showed malformation of the acrosome in addition to abnormal sperm head morphology (**Figure 4K**). Imaging of 200 spermatozoa revealed that, in $Pfn3^{-/-}$ male mice, 51–56% of spermatozoa display malformed acrosome compared to heterozygous (18%) and WT (16%) spermatozoa (**Figures 4L,M**).

Significant Decrease of Acrosome-Reacted Sperm in Pfn3-Deficient Mice

As a consequence of the malformed acrosome, we reasoned that the acrosomal reaction (AR) could be impaired. We used the A23187 to induce AR. Acrosomal status was evaluated using Coomassie staining; intact acrosomes were stained dark blue as a crescent-like shape on the top of the sperm head (**Figure 5A**, white arrows), whereas acrosome-reacted sperm showed that the crescent-like shape (acrosome) on the top of the sperm head was not present (**Figure 5A**, white arrow heads). The rate of A23187-induced AR was significantly reduced in *Pfn3*-deficient sperm. Upon exposure to A23187, more than 60% of sperm from $Pfn3^{+/+}$ mice and ∼60% of sperm from $Pfn3^{+/-}$ mice (**Figure 5B**) underwent acrosome exocytosis, whereas the AR occurred only in 37.5% of sperm from $Pfn3^{-/-}$ mice (**Figure 5B**). This result indicates that the observed acrosome malformation impairs the acrosome exocytosis.

Disrupted Golgi Network in Pfn3-Deficient Mice

In order to investigate the underlying mechanism of impaired acrosome biogenesis in *Pfn3*-deficient mice, we performed immunofluorescence (IF) staining by using GM130 and TGN46 antibodies, markers for *cis*- and *trans*-Golgi network, respectively. GM130 plays a crucial role in vesicle tethering, fusion, and maintaining *cis*-Golgi structural integrity (Tiwari et al., 2019),

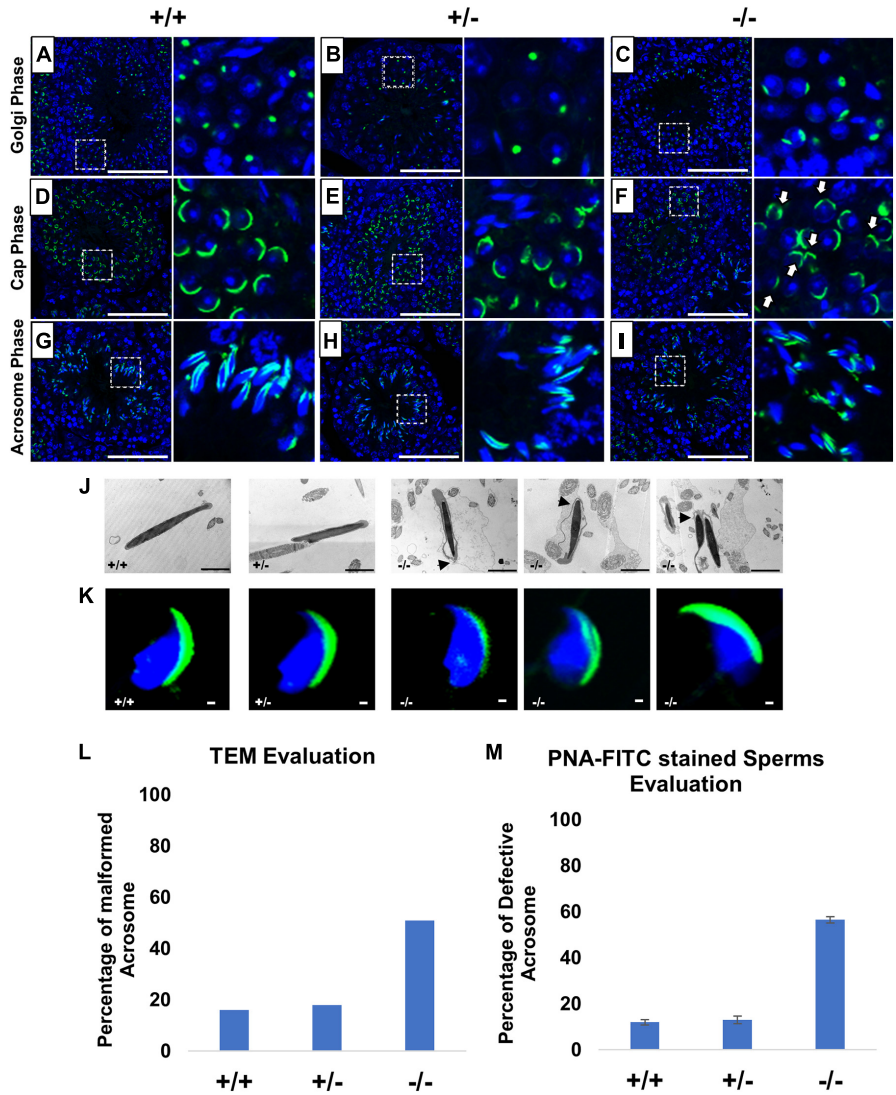

FIGURE 4 | Impaired acrosome biogenesis in *Pfn3*-deficient mice. Adult testis sections of $Pfn3^{+/+}$ (left panel), $Pfn3^{+/-}$ (middle panel), and *Pfn3*-deficient (right panel) mice; the developing acrosome was labeled with PNA-FITC (green) and cell nuclei were stained with DAPI (blue); inset panel showed the Golgi/cap/acrosomal phase of the tubules displayed in the main panel ($n = 3$). In the Golgi phase, proacrosomal granule (green) labeled by PNA-FITC for **(A)** $Pfn3^{+/+}$, **(B)** $Pfn3^{+/-}$, and **(C)** $Pfn3^{-/-}$ round spermatozoa. In the cap phase, acrosomal caps (green) stained for **(D)** $Pfn3^{+/+}$, **(E)** $Pfn3^{+/-}$, and **(F)** $Pfn3^{-/-}$ round spermatozoa (white arrows show fragmented cap structures). In the acrosome phase, PNA-FITC-labeled acrosomal area on **(G)** $Pfn3^{+/+}$, **(H)** $Pfn3^{+/-}$, and **(I)** $Pfn3^{-/-}$ elongated spermatids. Scale bar = 20 μm. **(J)** Ultrastructure analysis using TEM revealed the acrosomal structures of $Pfn3^{+/+}$, $Pfn3^{+/-}$, and $Pfn3^{-/-}$ sperm cells. Scale bar = 2 μm. **(K)** Immunofluorescence staining using PNA-FITC (green) on epididymal sperm cells of $Pfn3^{+/+}$, $Pfn3^{+/-}$, and $Pfn3^{-/-}$ mice ($n = 3$). Scale bar = 20 μm. **(L)** TEM evaluation shows the percentage of malformed acrosomes in $Pfn3^{+/+}$, $Pfn3^{+/-}$, and $Pfn3^{-/-}$ sperm cells ($n = 2$). **(M)** A graph represents the PNA-stained defective acrosome percentage of $Pfn3^{+/+}$, $Pfn3^{+/-}$, and $Pfn3^{-/-}$ sperm cells ($n = 3$). Two hundred spermatozoa were counted per genotype.

while TGN46 is important for formation of exocytic vesicles and secretion from the *trans*-part of the Golgi network (Huang et al., 2019). IF revealed *cis*- and *trans*-Golgi predominantly concentrated at one pole of the $Pfn3^{+/+}$ (**Figures 6A,D**) and $Pfn3^{+/-}$ (**Figures 6B,E**) spermatids, whereas the $Pfn3^{-/-}$ spermatids showed defects and disorganization in *cis*- (**Figure 6C**) and *trans*-Golgi network (**Figure 6F**). These results indicate that loss of *Pfn3* leads to disruption of the Golgi sub-domains causing defects in Golgi-derived proacrosomal vesicles leading to acrosome malformations.

Berruti and Paiardi (2015) published that in addition to the Golgi-derived biosynthetic pathway, the endocytic pathway contributes to acrosome biogenesis. In order to check whether loss of PFN3 affects the endocytic pathway, we performed IHC staining using anti-Rab5 antibody on testis sections for all three genotypes. Rab5 is a marker for early endosomes and a key factor in early endosome transport. The Rab5-mediated endo-lysosomal trafficking pathway is responsible for maturation of early endosomes to late endosomes. Interestingly, we did not observe any difference in the Rab5 staining of

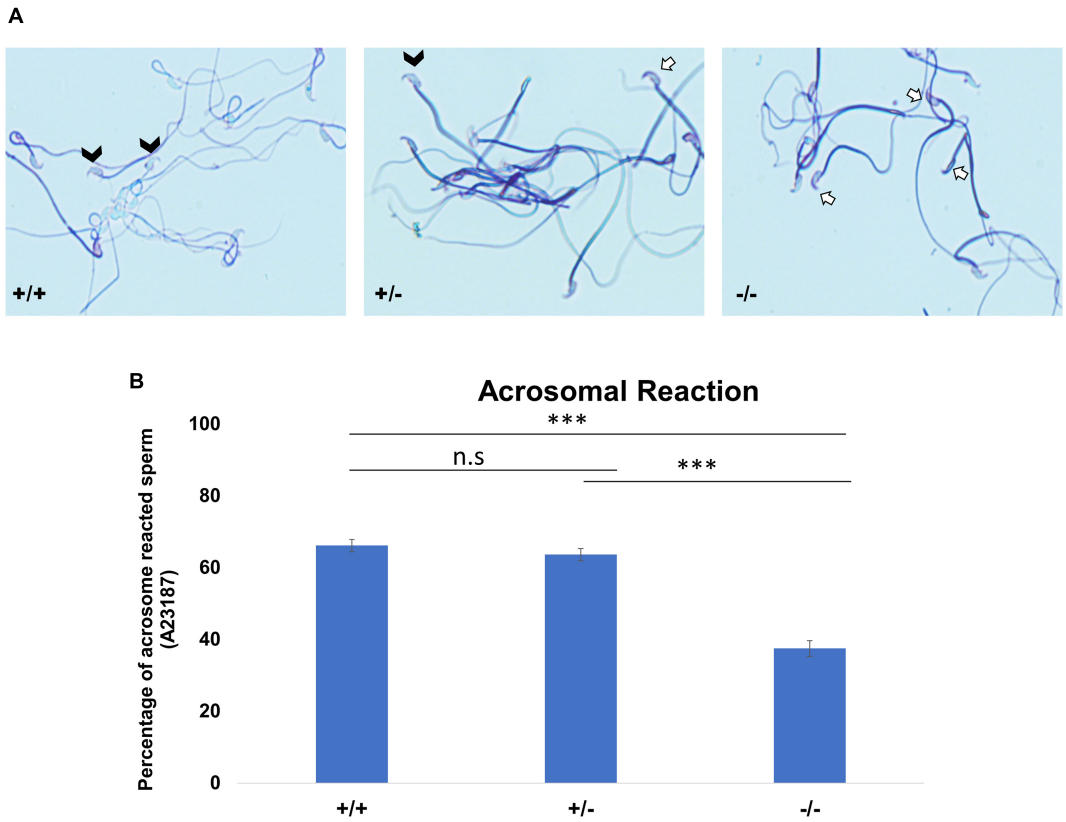

FIGURE 5 | The acrosomal reaction (AR) using calcium ionophore. **(A)** Coomassie-stained sperm cells of *Pfn3*$^{+/+}$, *Pfn3*$^{+/-}$, and *Pfn3*$^{-/-}$. Black arrow heads indicate successful acrosomal reaction took place. A white arrow indicates a crescent-shape acrosome on sperm head, indicating acrosomal reaction did not take place. **(B)** Percentage of acrosomal-reacted sperm for *Pfn3*$^{+/+}$, *Pfn3*$^{+/-}$, and *Pfn3*$^{-/-}$ (n = 3 biological replicates/genotype, ***$p < 0.0005$, Student's t-test, one tail, paired).

Pfn3$^{-/-}$ testis sections as compared to the *Pfn3*$^{+/-}$ and *Pfn3*$^{+/+}$ testis sections (**Supplementary Figure 4**). This result suggests that in *Pfn3*-deficient mice, the endocytic pathway is not affected.

RNA-Seq Revealed Alterations in the Expression Levels of Germ Cell Development-Related Genes in Pfn3$^{-/-}$ Mice

Since the function of PFN3 is only beginning to be understood, we set out to identify whether deletion of *Pfn3* impinges on global gene expression and performed RNA-sequencing on total RNA isolated from testes of *Pfn3*$^{+/+}$, *Pfn3*$^{+/-}$, and *Pfn3*$^{-/-}$ mice. RNA-sequencing identified 38 significantly differentially expressed (DE) genes with log2 fold change > 1.5 in *Pfn3*$^{-/-}$ as compared to control (**Figure 7A**). In total, 27 genes were found to be upregulated and 11 genes to be downregulated in *Pfn3*$^{-/-}$ testes compared to wild type (**Figure 7B**). In order to check that the results observed are not skewed due to a defect in spermiogenesis in the PFN3-deficient mice, we tested for expression levels of marker genes indicative for Leydig cells, Sertoli cells, and spermatogonia. Box plots of marker genes for the different cell types are given in the **Supplementary Data** (**Supplementary Figure 5**) and reveal that the overall quantity and development of sperm cells are not affected in *Pfn3*$^{-/-}$ mice. Tukey's multiple-comparison ANOVA was used to check for statistics, and all groups showed non-significant difference. Quantitative real-time PCR was used to validate the results for 13 of the DE genes, which are related to male fertility. *Cfl1*, *Trim27*, *B3gnt9*, *Mul1*, and *Hhatl* were upregulated, while *Exosc1*, *Srsf9*, *Atg2a*, *Copa*, *Slc25a36*, *Sap30*, *Dpm2*, and *Qrich1* were downregulated in *Pfn3*$^{-/-}$ mice (**Figure 7C**). These results indicated that deletion of *Pfn3* disrupts the expression of genes involved in actin cytoskeletal dynamics, regulation of autophagy, and mitochondrial and Golgi network structural integrity.

Autophagic Flux and AMPK/mTOR Signaling Pathway Are Affected in Pfn3-Deficient Mice

The RNA-seq analysis revealed *Trim27* as the most upregulated gene in *Pfn3*-deficient mice. The overexpression of *Trim27* leads to activation of AKT signaling (Zhang et al., 2018). AKT in turn is an activator of mTOR (Hahn-Windgassen et al., 2005). Autophagy is regulated by AMPK/mTOR signaling pathways,

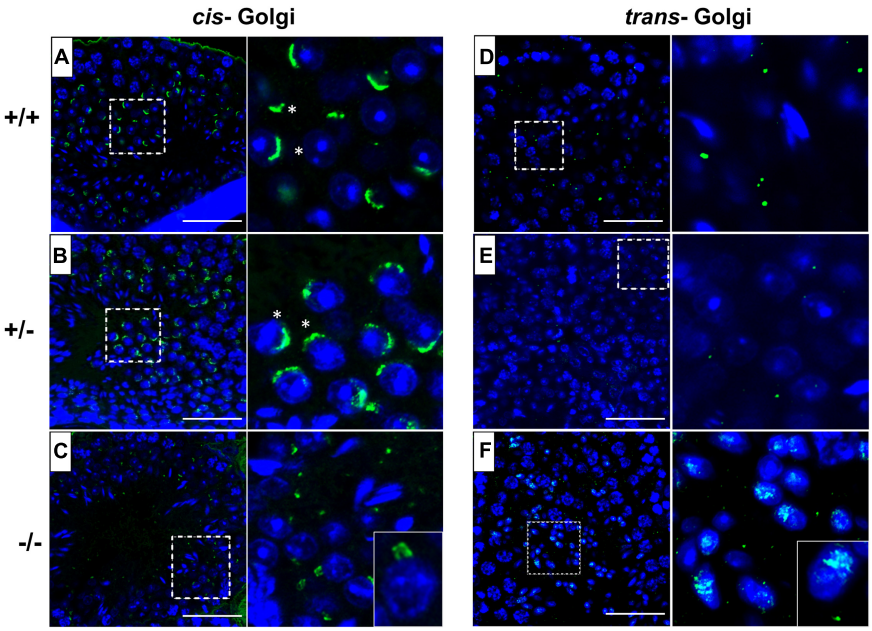

FIGURE 6 | *Pfn3*$^{+/+}$, *Pfn3*$^{+/-}$, and *Pfn3*$^{-/-}$ testis sections stained for the *cis*- (GM130 antibody) and *trans*- (TGN46 antibody) Golgi compartment (green) and nuclei (DAPI, blue) ($n = 3$). **(A)** WT and **(B)** heterozygous, and **(C)** *Pfn3*$^{-/-}$ spermatozoa stained for *cis*-Golgi compartment (asterisks). **(D)** WT, **(E)** heterozygous, and **(F)** *Pfn3*$^{-/-}$ spermatozoa stained for *trans*-Golgi network. Scale bar = 50 μm.

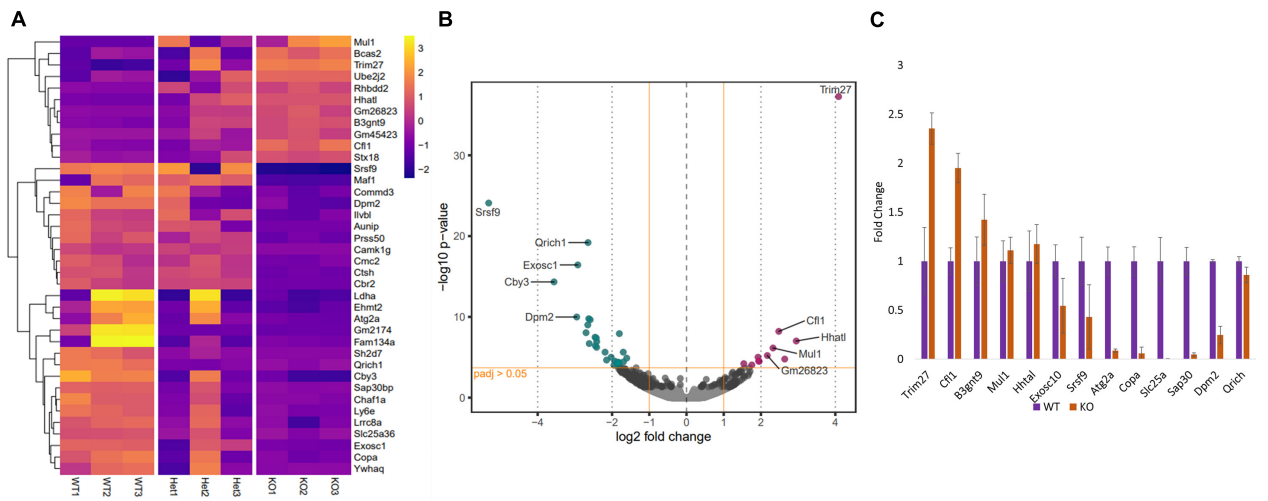

FIGURE 7 | Changes in gene expression profile of *Pfn3*-deficient mice. **(A)** Heat map visualization of top 38 differentially expressed (DE) genes obtained by RNA-seq on *Pfn3*$^{+/+}$, *Pfn3*$^{+/-}$, and *Pfn3*$^{-/-}$ testes. **(B)** Volcano plots displaying DE genes for *Pfn3*$^{+/+}$ vs. *Pfn3*$^{-/-}$ [adjusted p-value < 0.05; log2 fold change of expression (LFC) > 1.5]. **(C)** DE genes obtained by RNA-seq were verified by qRT-PCR on *Pfn3*$^{+/+}$, *Pfn3*$^{+/-}$, and *Pfn3*$^{-/-}$ testicular RNA ($n = 3$ biological replicates/genotype).

with AMPK being stimulating and mTOR being repressive (Liang et al., 2018). Next, we were interested to determine whether the signaling pathways downstream of *Trim27* responsible for regulation of autophagy are affected in *Pfn3*-deficient mice. Indeed, immunoblotting showed increased protein levels for mTOR and phospho-mTOR, while the level of phospho-AMPKα was reduced (**Figure 8A**). Increased level of phospho-mTOR was validated by IHC in *Pfn3*-deficient mice (**Figure 8B**). So, these data suggest that loss of *Pfn3* leads to an upregulation of *Trim27*, which results in the activation of mTOR signaling (Hahn-Windgassen et al., 2005; Liang et al., 2018; Zhang et al., 2018), causing a decrease in p-AMPKα resulting in the disruption of autophagy. Furthermore, the autophagic gene *Atg2a* was expressed at lower levels in *Pfn3*-deficient mice. *Atg2a* is involved

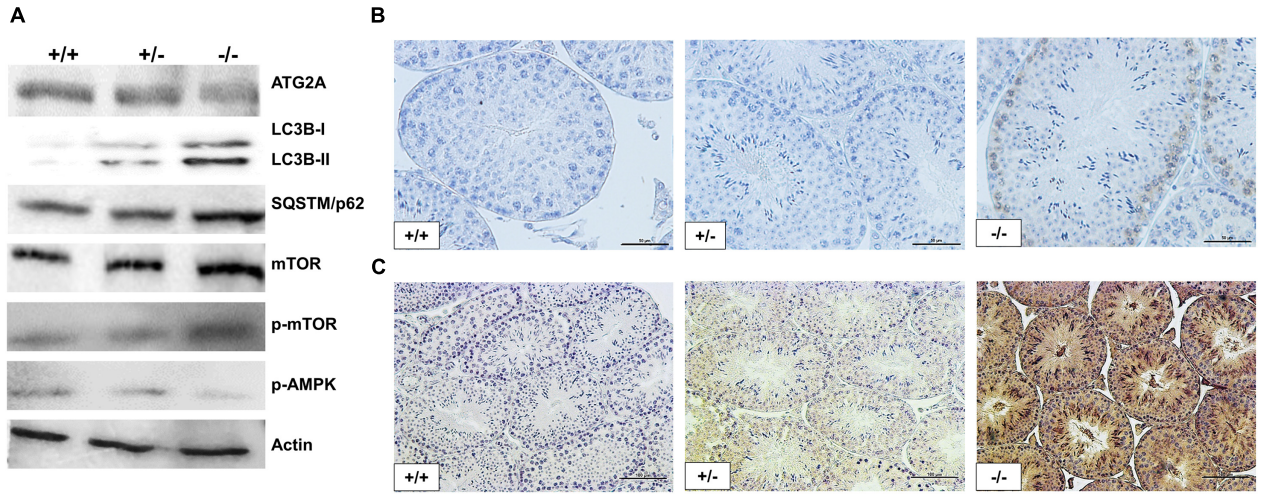

FIGURE 8 | Disruption in autophagic flux and AMPK/mTOR signaling pathway of *Pfn3*-deficient mice. **(A)** Immunoblot analysis against ATG2A, LC3B, SQSTM1, mTOR, phospho-mTOR, and phospho-AMPKα on protein lysates from $Pfn3^{+/+}$, $Pfn3^{+/-}$, and $Pfn3^{-/-}$ testes. **(B)** Immunohistochemical staining against phospho-mTOR on $Pfn3^{+/+}$, $Pfn3^{+/-}$, and $Pfn3^{-/-}$ testis sections (top row). **(C)** Immunohistochemical staining against LC3B on $Pfn3^{+/+}$, $Pfn3^{+/-}$, and $Pfn3^{-/-}$ testis sections (bottom row). Staining of testicular tissue sections from $Pfn3^{+/+}$ (left column), $Pfn3^{+/-}$ (middle column), and $Pfn3^{-/-}$ (right column) animals is shown. Scale bar = 100 μm.

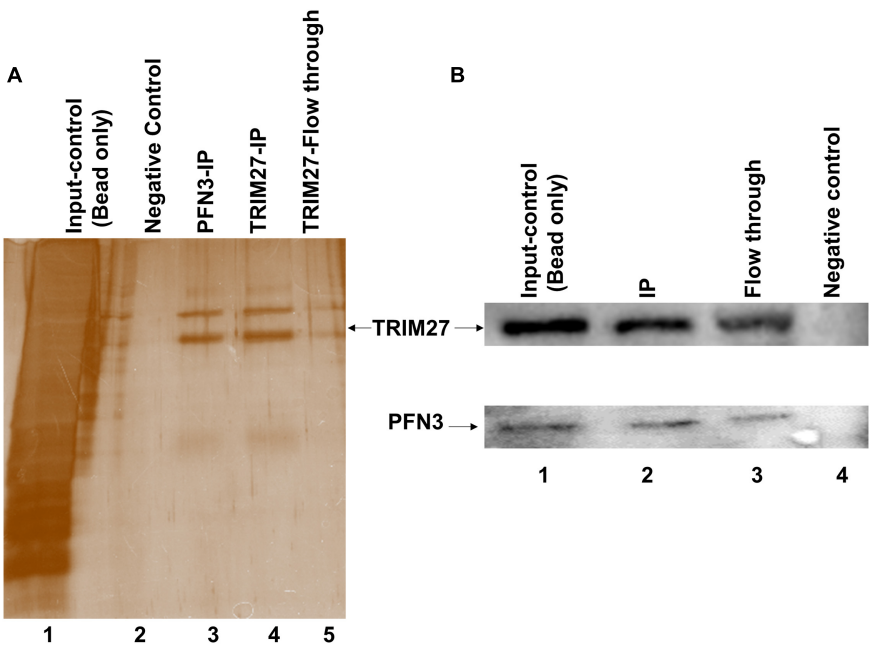

FIGURE 9 | Co-immunoprecipitation using anti-PFN3 and anti-TRIM27 antibody on testis lysates. **(A)** Silver-stained SDS-PAGE; lane 1: input control (protein lysate), lane 2: negative control (only antibody), lane 3: IP using PFN3 antibody, lane 4: IP using PFN3 antibody, and lane 5: flow through. **(B)** Western blot showed PFN3 and TRIM27 proteins. Lane 1: input control. Lane 2: immunoblot of reciprocal IP for TRIM27 (band observed at ∼58 kDa) and PFN3 protein levels (band observed at ∼14 kDa) using anti-PFN3 and anti-TRIM27 antibodies, respectively. Lane 3: flow through. Lane 4: negative control.

in the phagophore elongation leading to the formation of the autophagosome (Bozic et al., 2020). The elongation step is completed by the conjugation of LC3B, known as microtubule-associated protein and a widely used marker for autophagosomes (Tang et al., 2017). LC3B is a core protein in the autophagic flux where it functions as an autophagic cargo by interacting with an autophagic substrate SQSTM1/p62 (Tang et al., 2017). It is well established that depletion of *Atg2a* results in blocking of autophagic flux leading to accumulation of LC3B and SQSTM1 (Bozic et al., 2020). Therefore, we analyzed LC3B and SQSTM1

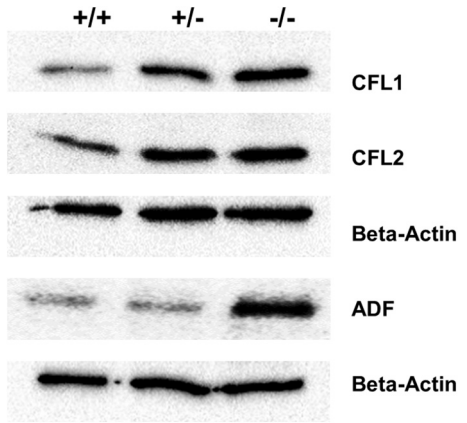

FIGURE 10 | Immunoblotting against ADF, CFL1, and CFL2 on protein lysates from *Pfn3*$^{+/+}$, *Pfn3*$^{+/-}$, and *Pfn3*$^{-/-}$ testes.

protein levels. Interestingly, in *Pfn3*-deficient testes, levels of LC3B were increased as shown by WB and IHC (**Figures 8A,C**, respectively). We further found an accumulation of SQSTM1 in *Pfn3*-deficient testes using WB (**Figure 8A**). Quantification of protein levels (**Supplementary Figure 6**) revealed an increase in LC3B, P62, p-mTOR, and mTOR levels and reduction of ATG2a and AMPK. So, we hypothesized that deletion of *Pfn3* results in upregulation of *Trim27*, which leads to mTOR-mediated inhibition of autophagy hallmarked by lower levels of *Atg2a*. As a consequence, autophagic flux stalls, indicated by accumulation of LC3B and SQSTM1. This might cause the disturbance of the acrosome formation in *Pfn3*-deficient mice.

PFN3 Interacts With TRIM27

Next, we used co-immunoprecipitation (Co-IP) to test whether PFN3 and TRIM27 interact. From whole-testis lysate, a PFN3-specific antibody pulled down TRIM27 (**Figure 9A**, lane 3) and the IP with a TRIM27 antibody was able to capture and elute PFN3 (not shown). The specificity of the assay was confirmed by using protein extraction buffer as a negative control (**Figure 9A**, lane 2); whole-testis lysate was used as an input control (**Figure 9A**, lane 1). To validate this interaction, reciprocal antibodies on immunoblot (**Figure 9B**) showed PFN3 (∼14 kDa) and TRIM27 (∼58 kDa) proteins from input control (lane1), Co-IP (lane 2), flow through (lane 3), and negative control.

Pfn3-Deficient Mice Exhibit Increased Protein Levels of ADF/CFL Variants Compared to WT

Furthermore, the expression of cofilin1 (*Cfl1*) was upregulated in *Pfn3*-deficient testes. We decided to check protein levels using WB for the cofilin traditional proteins (CFL1, CFL2, and ADF) known as actin-binding proteins. The level of ADF protein was increased in *Pfn3*$^{-/-}$ testes, while CFL1 and CFL2 (**Figure 10**) protein levels were already increased in heterozygous testes.

PFN3 Binding Protein Is Lost in Nuclear Fraction of Sperm

PFN3 is detected in a complex with ARPM1, specifically in the sperm nucleus, however, not in the cytoplasm (Hara et al., 2008). In sperm cytoplasm of *Pfn3*$^{-/-}$ mice, a moderate signal of ARPM1 can still be detected (**Supplementary Figure 7A**). We performed WB using anti-ARPM1antibody on proteins isolated from cytoplasmic and nuclear fractions of both testes and sperm. Western blot showed that ARPM1 could not be detected in the nuclear fraction of *Pfn3*-deficient testes and sperm, while cytoplasmic ARPM1 protein levels in testes are slightly reduced in *Pfn3*-deficient mice (**Supplementary Figure 7A**).

These findings were further confirmed by immunohistochemistry; the nucleus of spermatozoa in testes of *Pfn3*-deficient mice were devoid of ARPM1 (**Supplementary Figure 7B**). This finding suggests that loss of PFN3 destabilizes the PFN3–ARPM1 complex, leading to loss of ARPM1 in the nuclei of *Pfn3*-deficient sperm.

F-Actin Organization Is Not Altered in Pfn3-Deficient Sperm

Pfn3 binds to actin monomers and plays a role in actin polymerization. Actin is mainly located in the mid-piece of sperm flagellum, suggesting a role in sperm motility, elasticity, and membrane integrity. F-actin is present as a helical structure (Gervasi et al., 2018), which is in parallel with the organization of the mitochondrial sheath in mouse sperm (Amaral et al., 2013). We wanted to see whether the *Pfn3* deletion affects the actin cytoskeleton organization in the sperms. Phalloidin ATTO647 fluorescence staining revealed that actin assembly was not altered in the mid-piece of *Pfn3*$^{-/-}$ sperm (**Supplementary Figure 8**).

Abnormal Manchette Development in Pfn3-Deficient Mice

We found that PFN3 localized in the manchette complex of the developing spermatid. The manchette is a transient structure on the posterior part of the sperm head and is involved in nuclear shaping and protein transport for sperm flagellum formation. The manchette is first detected in step 8, when round spermatids start to elongate by nuclear polarization and the nuclear shape changes from spherical to slightly elongated. After shaping the sperm head, the manchette disappears at step 13 (Okuda et al., 2017).

In order to investigate whether the abnormal head morphology of *Pfn3*-deficient sperm was due to the alteration in manchette structure or formation, we performed an immunofluorescence staining using alpha tubulin for step-by-step comparison on the germ cell population isolated from testes. Tubulin staining revealed that in WT and heterozygous spermatids (**Figures 11A,B**), manchette was forming the proper skirt-like structure while the manchette was not properly covering and constricted overly at the posterior region in *Pfn3*-deficient round spermatids (**Figure 11C**). This abnormal manchette development is more obvious in the later steps of development (steps 9–13) in *Pfn3*-deficient spermatids. We conclude that deletion of PFN3 leads to disruption of manchette

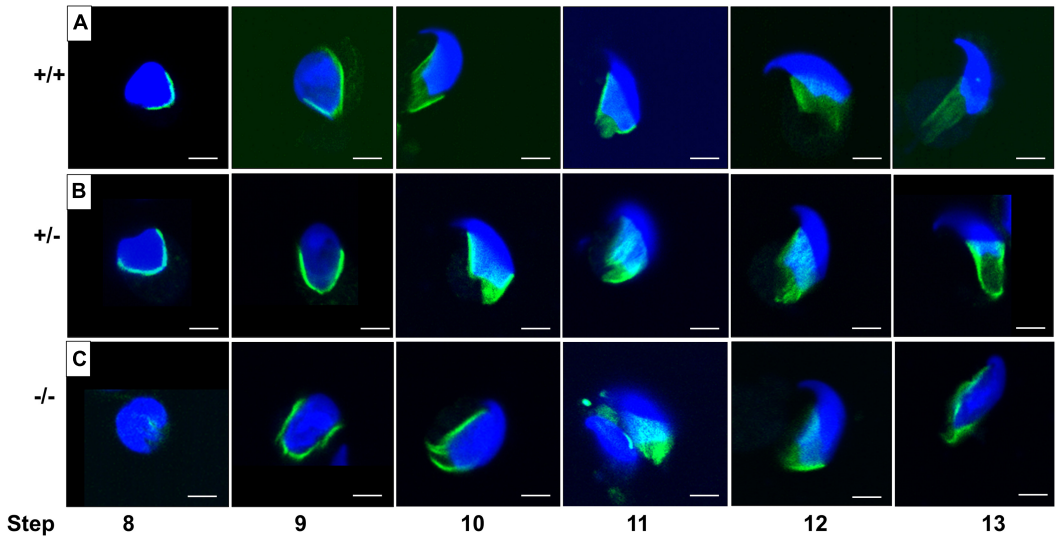

FIGURE 11 | Manchette structure stained by using α-tubulin antibody (green) on germ cell population isolated from **(A)** *Pfn3*$^{+/+}$, **(B)** *Pfn3*$^{+/-}$, and **(C)** *Pfn3*$^{-/-}$ testes (*n* = 3/genotype). Nuclei were stained with DAPI (blue). Scale bar = 20 μm.

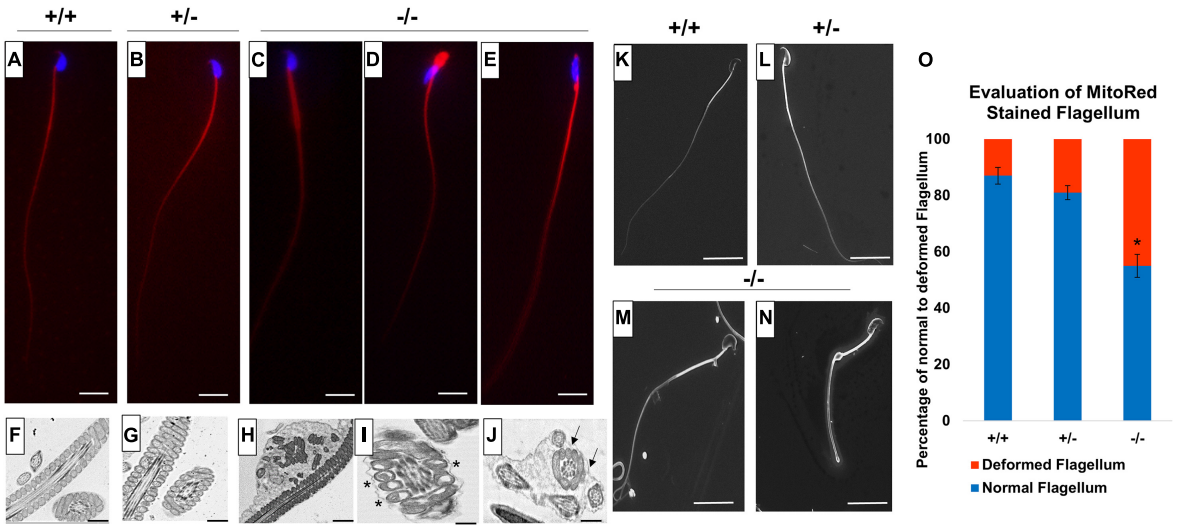

FIGURE 12 | Flagellum analysis on mature sperm cells from *Pfn3*$^{+/+}$, *Pfn3*$^{+/-}$, and *Pfn3*$^{-/-}$ mice. Mito Red staining (red) of sperm flagellum on **(A)** *Pfn3*$^{+/+}$; **(B)** *Pfn3*$^{+/-}$; and **(C–E)** *Pfn3*$^{-/-}$ sperm cells isolated from cauda epididymis. Scale bar = 10 μm. Ultrastructural analysis using TEM on **(F)** *Pfn3*$^{+/+}$; **(G)** *Pfn3*$^{+/-}$; and **(H–J)** *Pfn3*$^{-/-}$ sperm cells isolated from cauda epididymis. Vacuolated mitochondria are shown by asterisk, and fibrous sheet that contained more than one axoneme–mitochondrial complex is shown by arrows. Scale bar = 5 μm. Surface analysis using SEM on **(K)** *Pfn3*$^{+/+}$, **(L)** *Pfn3*$^{+/-}$, and **(M,N)** *Pfn3*$^{-/-}$ mature sperm cells isolated from cauda epididymis. Scale bar = 50 μm. **(O)** Statistical analysis of Mito Red-stained flagellum of *Pfn3*$^{+/+}$, *Pfn3*$^{+/-}$, and *Pfn3*$^{-/-}$ sperm cells. Data is presented as mean ± SD using ANOVA (Tukey's *post hoc*) (*$p < 0.05$).

formation, which in turn contributes to the abnormal shape of the sperm head in *Pfn3*-deficient sperm.

Pfn3-Deficient Sperm Display Flagellar Deformities

Since we detected low sperm motility in *Pfn3*-deficient mice, we analyzed sperm flagella structure. We used Mito Red immunostaining to assess the mitochondrial sheath in the mid-piece of sperm flagella. While Mito Red uniformly stained the mitochondrial sheath in spermatozoa of WT (**Figure 12A**) and heterozygous (**Figure 12B**), *Pfn3*-deficient sperm flagella showed a variety of aberrations spanning from abnormally thick mid-piece (**Figure 12C**), slightly tapered bent thick neck (**Figure 12D**), and cytoplasmic droplets with amorphous sperm heads (**Figure 12E**). This suggests that loss of PFN3 resulted in flagellar deformities due to mitochondrial disorganization.

Next, we performed TEM on mature sperm isolated from cauda epididymis to analyze whether the mid-piece of

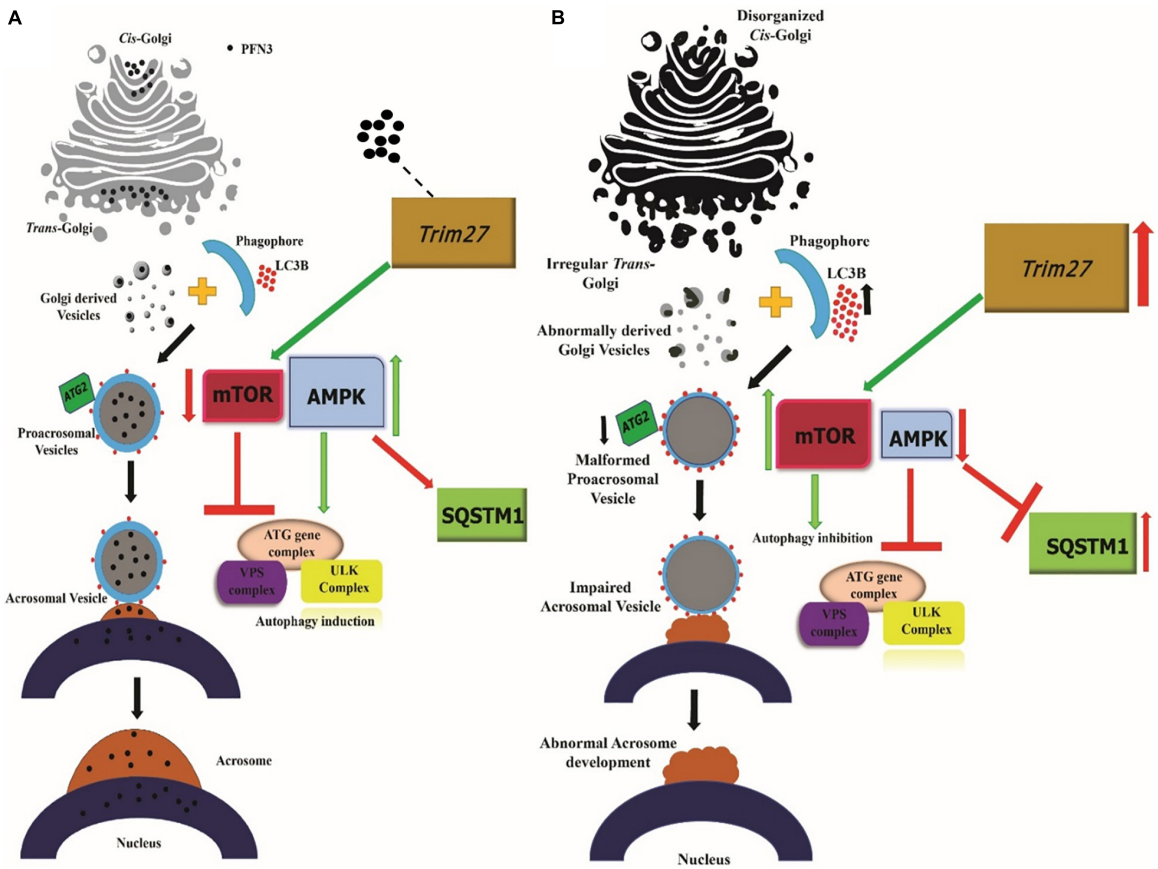

FIGURE 13 | Working hypothesis on the PFN3 role in acrosome biogenesis. **(A)** Schematic illustration of the *Pfn3* presence in Golgi network responsible for proacrosomal formation associated with the autophagy mechanism. **(B)** Schematic illustration depicting the disrupted autophagy mechanism and acrosome formation in the absence of *Pfn3*. Black dots = PFN3.

sperm have normal axonemal and mitochondrial structure. TEM of *Pfn3*-deficient sperm showed several ultrastructural defects, like plasma membrane not covering uniformly the mitochondrial sheet (**Figure 12H**), disorganized or vacuolated mitochondria (**Figure 12I**, asterisk), axonemal fibrous sheet enclosed two or more mitochondria and axonemal flagellar complex (**Figure 12J**) compared to WT (**Figure 12F**), and heterozygous sperm ultrastructure (**Figure 12G**). Scanning electron microscopy (SEM) showed similar sperm abnormalities in *Pfn3*-deficient mice, thick sperm mid-pieces with distal cytoplasmic droplets (**Figures 12M,N**) compared to WT (**Figure 12K**) and heterozygous sperm (**Figure 12L**). This result correlates with the previous (Mito Red and TEM ultrastructural sperm analysis) findings. These findings showed that sperm from *Pfn3*-deficient mice display an abnormal morphology of mitochondrial and axonemal fibrous sheet. Statistical analysis revealed that the percentage of deformed sperm flagella in *Pfn3*-deficient mice (∼55%) compared to WT and heterozygous sperms was significantly higher (**Figure 12O**). We speculate that these defects contribute to the reduced sperm motility. Altogether, our results indicate that loss of PFN3 located in mitochondria resulted in sperm flagellar defects and further support a cytoplasm removal defect.

DISCUSSION

Pfn3 has multiple physiological roles in sperm formation and function. In this study, we have shown that deletion of *Pfn3* results in male subfertility hallmarked by reduced sperm count/vitality with sperm displaying type II globozoospermia. *Pfn3*-deficient mice display an impaired acrosome biogenesis followed by malformed acrosomal covering on mature spermatozoa including cytoplasm removal defects, abnormal manchette development contributing to amorphous head shape of sperm, and flagellar deformities resulting in reduced sperm motility. In addition, loss of *Pfn3* disturbs the morphology of Golgi sub-domains, resulting in abnormal formation of Golgi-derived vesicles. Furthermore, we found by co-IP that PFN3 interaction with TRIM27 plays a role in autophagy for acrosome development. Mechanistically, we found a deregulation of autophagy master regulators (*Trim27*, AMPK, mTOR, *Atg2a*, LC3B, and SQSTM1), which seem to relate the disruption of acrosome formation in *Pfn3*-deficient germ cells.

The first and foremost effect of deleting *Pfn3* was impaired acrosome development due to defective vesicle transport from Golgi. Golgi complexes were disorganized and not oriented correctly, leading to an impaired post Golgi trafficking. Acrosome

labeling in *Pfn3*-deficient testes revealed that acrosome biogenesis was affected in the Golgi phase of development. The underlying defect was the failure of proacrosomal granule formation and fusion. Loss of *Pfn3* affected the transport of vesicles released from Golgi complexes in *Pfn3*-deficient mice. It is known that profilin1 is found in the Golgi compartment (Dong et al., 2000) and profilin2 is associated with proteins that play a role in membrane trafficking (Gareus et al., 2006).

The formation of the acrosome uses elements of the autophagy machinery that are involved in the fusion/transportation of Golgi-derived proacrosomal vesicles (Wang et al., 2014). We demonstrate that deletion of *Pfn3* leads to upregulation of *Trim27*, which leads to the activation of mTOR. This, in turn, leads to repression of AMPK. Together, higher mTOR and lower AMPK lead to an attenuation of autophagy hallmarked by lower levels of *Atg2a.* As a consequence, autophagic flux stalls, indicated by accumulation of LC3B and SQSTM1. This causes the developmental arrest of the acrosome formation in *Pfn3*-deficient mice. Disruption of autophagic flux leading to failure of proacrosomal granule formation is also reported in mice deficient for *Sirt1* (Liu et al., 2017) and *Atg7* (Wang et al., 2014). Interestingly, in *Atg7* mutants, LC3B levels are increased, but AMPK and mTOR levels remain unaffected (Wang et al., 2014). However, in *Sirt1* mutants, autophagic flux is partially disrupted by the accumulation of acetylated LC3B in the nucleus (Liu et al., 2017). This suggest that ATG7 and SIRT1 act further downstream in the autophagic cascade compared to *Pfn3*.

We demonstrate that loss of *Pfn3* leads to an upregulation of *Trim27*. So, we speculate that *Pfn3* directly or indirectly interacts with or is tethered to *Trim27* to modulate its activity during spermiogenesis. In fact, the interaction was demonstrated using co-immunoprecipitation. So, we hypothesize that a lack of *Pfn3* unleashes *Trim27* leading to i) enhanced expression of *Trim27*, which initiates a cascade resulting in ii) impaired acrosome development.

In addition, acrosome labelling and evaluation of transmission electron microscopy showed malformed/fragmented acrosomes in 50–60% of mature epididymal *Pfn3*-deficient sperm. Besides defective acrosome morphology of mature spermatozoa, 70% of *Pfn3*-deficient sperms showed amorphous head shape lacking the typical hook area and circularity. We demonstrated that the development of the manchette is disturbed in *Pfn3*-deficient sperm. Defective manchette development leading to abnormal shaping of sperm head is also reported in *Katnb1*, *Sun4*, *Lrguk1*, *Kif3A*, *Hook1*, and *Kash* mutants. Intriguingly, these genes interact with the microtubule network and the proteins are localized in the microtubular manchette (Mendoza-Lujambio et al., 2002; O'Donnell et al., 2012; Lehti et al., 2013; Gunes et al., 2020). The manchette is connected to the nucleus by fuzzy material/linkers, which indicates that manchette and nucleus possess a structural relationship through which they exert forces on each other for the shaping of sperm head (Russell et al., 1991). This suggests that loss of microtubular proteins in the manchette disturbs the structural relationship between manchette and nucleus resulting in abnormal sperm head development. The fact that PFN3 is localized to the microtubules of the manchette, and loss of PFN3 results in manchette deformities, suggests that PFN3 contributes to the organization and remodeling of the manchette for sperm head shaping.

The fact that the sperm count is significantly reduced is most likely due to the observed motility defect.

Further, *Pfn3*-deficient sperm showed significant reduction in progressive motility as well as cytoplasmic removal defects. Vacuolated mitochondria result in the deformities in the flagellum leading to the reduced motility. Sperm motility is the outcome of flagellar movement of sperm tail, gained by ATP-driven energy produced by mitochondrion located in sperm mid-piece (Tourmente et al., 2015). Sperm flagellum deformities lead to poor sperm motility and abnormal flagellum structure, as seen in other mouse KO models such as TSSK4, QRICH2, and CABYR (Lehti and Sironen, 2017; Shen et al., 2019). This suggests that deformities of the flagellum led to the reduced motility in $Pfn3^{-/-}$ mice, however, caused by a yet unexplained mechanism.

To our surprise, we observed unaltered F-actin organization in *Pfn3*-deficient sperm. This suggests that the role of *Pfn3* in actin polymerization is rather minor.

Hara et al. (2008) showed that, in the nuclei of spermatids, ARPM1 binds to PFN3, while cytoplasmic ARPM1 does not. The ARPM1–PFN3 complex contributes to spermatid head shaping (Hara et al., 2008). We found that a lack of PFN3 led to the loss of ARPM1 in spermatid nuclei. We hypothesized that PFN3 is required for the stabilization or localization of ARPM1 in nuclei of the spermatids. So, the abnormal sperm nuclear morphology observed in *Pfn3*-deficient mice might be a consequence of a lack of testes-specific PFN3–ARPM1 complex. In addition, ARPM1 protein was detected in the cytoplasm of testes since ARPM1–PFN3 complex is only restricted to sperm nucleus, which further confirms the findings of Hara et al. (2008).

Further, *Srsf9*, *Slc25a36*, *Prss50*, and *Copa* are downregulated in our *Pfn3*-deficient mice. Bansal et al. (2015) reported that patients with reduced sperm motility known as asthenozoospermia display lower levels of *Srsf9*. Additionally, *Slc25a36* is a member of the solute carrier super family and is known to regulate mitochondrial function. It is reported by Xin et al. (2019) that *Slc25a36* deficiency led to impaired mitochondria and decreased mitochondrial membrane potential. PRSS50 and COPA are involved in male fertility and Golgi trafficking, respectively, (Sleutels et al., 2012; Custer et al., 2019). Downregulation of PRSS50 resulted in reduced male fertility (Sleutels et al., 2012). Moreover, knockdown of COPA impairs Golgi–ER trafficking (Tang et al., 2015). We reported severely reduced male fertility and sperm motility, malformed mitochondria, and disturbed Golgi-derived vesicles in *Pfn3*-deficient mice. In addition, we observed that *Mul1* is upregulated in *Pfn3*-deficient testes. *Mul1* is essential for maintaining the mitochondrial morphology (Li J. et al., 2015). We found vacuolated mitochondria in sperm flagellum of *Pfn3*-deficient mice. These findings suggest that loss of *Pfn3* results in differentially expressed genes leading to reduced sperm motility and flagellar deformities.

Taken together, our findings demonstrate that *Pfn3* affects multiple processes during spermiogenesis. We summarize our findings related to the role of PFN3 in vesicle transport from Golgi to nucleus for acrosome biogenesis in **Figure 13**. A lack of PFN3 causes a disruption of Golgi sub-domains leading to

impaired acrosome biogenesis. On a molecular level, loss of PFN3 leads to upregulation of *Trim27*, resulting in deregulation of mTOR and AMPK signaling, leading to a disruption of autophagic flux. Furthermore, we show that loss of *Pfn3* causes abnormal manchette development and loss of ARPM1 in sperm nucleus. We detected vacuolated mitochondria in the flagellum. This might lead to reduced sperm motility in *Pfn3*-deficient mice. In conclusion, our study highlights the requirement of *Pfn3* during spermiogenesis specifically in acrosome biogenesis and adds this gene to the growing catalog of genes potentially involved in human male infertility.

DATA AVAILABILITY STATEMENT

RNA-seq data from this study have been submitted to the NCBI Gene Expression Omnibus (GEO; https://www.ncbi.nlm.nih.gov/geo/) under accession no. GSE171068.

ETHICS STATEMENT

The animal study was reviewed and approved by Landesamt für Natur, Umwelt und Verbraucherschutz, North Rhine-Westphalia, approval ID: AZ84- 02.04.2013.A429.

AUTHOR CONTRIBUTIONS

NU and HS conceived and designed the project. NU generated the knockouts and performed the detailed experimental analyses. SP and DoS performed basic analyses. LA contributed to RNA-seq analysis. DeS contributed to IF staining of PFN3. KL and GK contributed to scanning electron microscopy. DoS carried out STED microscopy. NU wrote the manuscript. HS supervised the manuscript. All authors contributed to the article and approved the submitted version.

FUNDING

This study was funded by grants by the German Academic Exchange Program (DAAD) to NU (91646787).

SUPPLEMENTARY MATERIAL

The Supplementary Material for this article can be found online at: https://www.frontiersin.org/articles/10.3389/fcell.2021.749559/full#supplementary-material

REFERENCES

Agnew, D. J. (1997). Review — the CCAMLR ecosystem monitoring programme. *Antarctic Sci.* 9, 235–242. doi: 10.1098/rstb.2006.1954

Alquézar-Baeta, C., Gimeno-Martos, S., Miguel-Jiménez, S., Santolaria, P., Yániz, J., Palacín, I., et al. (2019). OpenCASA: a new open-source and scalable tool for sperm quality analysis. *PLoS Comput. Biol.* 15:e1006691. doi: 10.1371/journal.pcbi.1006691

Amaral, A., Lourenço, B., Marques, M., and Ramalho-Santos, J. (2013). Mitochondria functionality and sperm quality. *Reproduction* 146, R163–R174.

Bansal, S. K., Gupta, N., Sankhwar, S. N., and Rajender, S. (2015). Differential genes expression between fertile and infertile spermatozoa revealed by transcriptome analysis. *PLoS One* 10:e0127007. doi: 10.1371/journal.pone.0127007

Bartoov, B., Eltes, F., Weissenberg, R., and Lunenfeld, B. (1980). Morphological characterization of abnormal human spermatozoa using transmission electron microscopy. *Arch. Androl.* 5, 305–322.

Behnen, M., Murk, K., Kursula, P., Cappallo-Obermann, H., Rothkegel, M., Kierszenbaum, A. L., et al. (2009). Testis-expressed profilins 3 and 4 show distinct functional characteristics and localize in the acroplaxome-manchette complex in spermatids. *BMC Cell Biol.* 10:34. doi: 10.1186/1471-2121-10-34

Berruti, G., and Paiardi, C. (2015). USP8/UBPy-regulated sorting and the development of sperm acrosome: the recruitment of MET. *Reproduction* 149, 633–644. doi: 10.1530/REP-14-0671

Biggers, J. D., Finn, C. A., and Mclaren, A. (1962). Long-term reproductive performance of female mice. i. effect of removing one ovary. *J. Reprod. Fertility* 3, 303–312. doi: 10.1530/jrf.0.0030303

Bourgon, R., Gentleman, R., and Huber, W. (2010). Reply to Talloen et al.: independent filtering is a generic approach that needs domain specific adaptation. *Proc. Natl. Acad. Sci.* 107, E175–E175.

Bozic, M., van den Bekerom, L., Milne, B. A., Goodman, N., Roberston, L., Prescott, A. R., et al. (2020). A conserved ATG2-GABARAP family interaction is critical for phagophore formation. *EMBO Rep.* 21:e48412. doi: 10.15252/embr.201948412

Cong, L., Ran, F. A., Cox, D., Lin, S., Barretto, R., Habib, N., et al. (2013). Multiplex genome engineering using CRISPR/Cas systems. *Science* 339, 819–823.

Custer, S. K., Foster, J. N., Astroski, J. W., and Androphy, E. J. (2019). Abnormal Golgi morphology and decreased COPI function in cells with low levels of SMN. *Brain Res.* 1706, 135–146. doi: 10.1016/j.brainres.2018.11.005

Dam, A. H. D. M., Feenstra, I., Westphal, J. R., Ramos, L., van Golde, R. J. T., and Kremer, J. A. M. (2007). Globozoospermia revisited. *Hum. Reprod. Update* 13, 63–75. doi: 10.1093/humupd/dml047

Di Rienzo, M., Romagnoli, A., Antonioli, M., Piacentini, M., and Fimia, G. M. (2020). TRIM proteins in autophagy: selective sensors in cell damage and innate immune responses. *Cell Death Differentiation* 27, 887–902. doi: 10.1038/s41418-020-0495-2

Dong, J., Radau, B., Otto, A., Müller, E. C., Lindschau, C., and Westermann, P. (2000). Profilin i attached to the golgi is required for the formation of constitutive transport vesicles at the trans-Golgi network. *Biochim. Biophys. Acta Mol. Cell Res.* 1497, 253–260. doi: 10.1016/s0167-4889(00)00056-2

Durinck, S., Moreau, Y., Kasprzyk, A., Davis, S., De Moor, B., Brazma, A., et al. (2005). BioMart and Bioconductor: a powerful link between biological databases and microarray data analysis. *Bioinformatics* 21, 3439–3440. doi: 10.1093/bioinformatics/bti525

Gareus, R., Di Nardo, A., Rybin, V., and Witke, W. (2006). Mouse profilin 2 regulates endocytosis and competes with SH3 ligand binding to dynamin 1. *J. Biol. Chem.* 281, 2803–2811. doi: 10.1074/jbc.M503528200

Gervasi, M. G., Xu, X., Carbajal-Gonzalez, B., Buffone, M. G., Visconti, P. E., and Krapf, D. (2018). The actin cytoskeleton of the mouse sperm flagellum is organized in a helical structure. *J. Cell Sci.* 131:jcs215897. doi: 10.1242/jcs.215897

Gunes, S., Sengupta, P., Henkel, R., Alguraigari, A., Sinigaglia, M. M., Kayal, M., et al. (2020). Microtubular dysfunction and male infertility. *World J. Men's Health* 38, 9–23.

Hahn-Windgassen, A., Nogueira, V., Chen, C. C., Skeen, J. E., Sonenberg, N., and Hay, N. (2005). Akt activates the mammalian target of rapamycin by regulating cellular ATP level and AMPK activity. *J. Biol. Chem.* 280, 32081–32089.

Hara, Y., Yamagata, K., Oguchi, K., and Baba, T. (2008). Nuclear localization of profilin III-ArpM1 complex in mouse spermiogenesis. *FEBS Lett.* 582, 2998–3004. doi: 10.1016/j.febslet.2008.07.058

Hsu, P. D., Scott, D. A., Weinstein, J. A., Ran, F. A., Konermann, S., Agarwala, V., et al. (2013). DNA targeting specificity of RNA-guided Cas9 nucleases. *Nat. Biotechnol.* 31, 827–832. doi: 10.1038/nbt.2647

Huang, Q., Liu, Y., Zhang, S., Yap, Y. T., Li, W., Zhang, D., et al. (2020). Autophagy core protein ATG5 is required for elongating spermatid development, sperm individualization and normal fertility in male mice. *Autophagy* 17, 1753–1767. doi: 10.1080/15548627.2020.1783822

Huang, Y., Ma, T., Lau, P. K., Wang, J., Zhao, T., Du, S., et al. (2019). Visualization of protein sorting at the trans-golgi network and endosomes through super-resolution imaging. *Front. Cell Dev. Biol.* 7:181. doi: 10.3389/fcell.2019.00181

Jostes, S., Nettersheim, D., Fellermeyer, M., Schneider, S., Hafezi, F., Honecker, F., et al. (2017). The bromodomain inhibitor JQ1 triggers growth arrest and apoptosis in testicular germ cell tumours in vitro and in vivo. *J. Cell Mol. Med.* 21, 1300–1314. doi: 10.1111/jcmm.13059

Khawar, M. B., Gao, H., and Li, W. (2019). Mechanism of acrosome biogenesis in mammals. *Front. Cell Dev. Biol.* 7:195.

Kierszenbaum, A. L., and Tres, L. L. (2004). The acrosome-acroplaxome-manchette complex and the shaping of the spermatid head. *Arch. Histol. Cytol.* 67, 271–284. doi: 10.1679/aohc.67.271

Kim, D., Langmead, B., and Salzberg, S. L. (2015). HISAT: a fast spliced aligner with low memory requirements. *Nat. Methods* 12, 357–360. doi: 10.1038/nmeth.3317

Leblond, C. P., and Clermont, Y. (1952). Definition of the stages of the cycle of the seminiferous epithelium in the rat. *Ann. N. Y. Acad. Sci.* 55, 548–573. doi: 10.1111/j.1749-6632.1952.tb26576.x

Lehti, M. S., and Sironen, A. (2017). Formation and function of sperm tail structures in association with sperm motility defects. *Biol. Reprod.* 97, 522–536. doi: 10.1093/biolre/iox096

Lehti, M. S., Kotaja, N., and Sironen, A. (2013). KIF3A is essential for sperm tail formation and manchette function. *Mol. Cell. Endocrinol.* 377, 44–55. doi: 10.1016/j.mce.2013.06.030

Li, J., Qi, W., Chen, G., Feng, D., Liu, J., Ma, B., et al. (2015). Mitochondrial outer-membrane E3 ligase MUL1 ubiquitinates ULK1 and regulates selenite-induced mitophagy. *Autophagy* 11, 1216–1229. doi: 10.1080/15548627.2015.1017180

Li, W., Tang, W., Teves, M. E., Zhang, Z., Zhang, L., Li, H., et al. (2015). A MEIG1/PACRG complex in the manchette is essential for building the sperm flagella. *Development* 142, 921–930. doi: 10.1242/dev.119834

Liang, P., Jiang, B., Li, Y., Liu, Z., Zhang, P., Zhang, M., et al. (2018). Autophagy promotes angiogenesis via AMPK/Akt/mTOR signaling during the recovery of heat-denatured endothelial cells. *Cell Death Dis.* 9:1152. doi: 10.1038/s41419-018-1194-5

Lindemann, C. B., and Lesich, K. A. (2016). Functional anatomy of the mammalian sperm flagellum. *Cytoskeleton* 73, 652–669. doi: 10.1002/cm.21338

Liu, C., Song, Z., Wang, L., Yu, H., Liu, W., Shang, Y., et al. (2017). Sirt1 regulates acrosome biogenesis by modulating autophagic flux during spermiogenesis in mice. *Development* 144, 441–451. doi: 10.1242/dev.147074

Liu, F., Liu, X., Liu, X., Li, T., Zhu, P., Liu, Z., et al. (2019). Integrated analyses of phenotype and quantitative proteome of CMTM4 deficient mice reveal its association with male fertility. *Mol. Cell. Proteomics* 18, 1070–1084. doi: 10.1074/mcp.RA119.001416

Love, M. I., Huber, W., and Anders, S. (2014). Moderated estimation of fold change and dispersion for RNA-seq data with DESeq2. *Genome Biol.* 15:550. doi: 10.1186/s13059-014-0550-8

Martínez-Menárguez, J. A., Geuze, H. J., and Ballesta, J. (1996). Evidence for a nonlysosomal origin of the acrosome. *J. Histochem. Cytochem.* 44, 313–320. doi: 10.1177/44.4.8601690

Mendoza-Lujambio, I., Burfeind, P., Dixkens, C., Meinhardt, A., Hoyer-Fender, S., Engel, W., et al. (2002). The Hook1 gene is non-functional in the abnormal spermatozoon head shape (azh) mutant mouse. *Hum. Mol. Genet.* 11, 1647–1658. doi: 10.1093/hmg/11.14.1647

Mikuličić, S., Finke, J., Boukhallouk, F., Wüstenhagen, E., Sons, D., Homsi, Y., et al. (2019). ADAM17-dependent signaling is required for oncogenic human papillomavirus entry platform assembly. *ELife* 8:e44345. doi: 10.7554/eLife.44345

Moreno, R. D., and Alvarado, C. P. (2006). The mammalian acrosome as a secretory lysosome: new and old evidence. *Mol. Reprod. Dev.* 73, 1430–1434. doi: 10.1002/mrd.20581

Nettersheim, D., Heukamp, L. C., Fronhoffs, F., Grewe, M. J., Haas, N., Waha, A., et al. (2013). Analysis of TET expression/activity and 5mC oxidation during normal and malignant germ cell development. *PLoS One* 8:e82881. doi: 10.1371/journal.pone.0082881

Nettersheim, D., Jostes, S., Fabry, M., Honecker, F., Schumacher, V., Kirfel, J., et al. (2016). A signaling cascade including ARID1A, GADD45B and DUSP1 induces apoptosis and affects the cell cycle of germ cell cancers after romidepsin treatment. *Oncotarget* 7, 74931–74946. doi: 10.18632/oncotarget.11647

Nussdorfer, P., Cilenšek, I., Zorn, B., and Petroviè, D. (2018). Adapted methods for scanning electron microscopy (SEM) in assessment of human sperm morphology. *Bosn. J. Basic Med. Sci.* 18, 43–48. doi: 10.17305/bjbms.2017.2173

O'Donnell, L., Rhodes, D., Smith, S. J., Merriner, D. J., Clark, B. J., Borg, C., et al. (2012). An essential role for Katanin p80 and microtubule severing in male gamete production. *PLoS Genet.* 8:e1002698. doi: 10.1371/journal.pgen.1002698

Oakberg, E. F. (1956). A description of spermiogenesis in the mouse and its use in analysis of the cycle of the seminiferous epithelium and germ cell renewal. *Am. J. Anat*. 391–413. doi: 10.1002/aja.1000990303

Okuda, H., DeBoer, K., O'Connor, A. E., Merriner, D. J., Jamsai, D., and O'Bryan, M. K. (2017). LRGUK1 is part of a multiprotein complex required for manchette function and male fertility. *FASEB J.* 31, 1141–1152. doi: 10.1096/fj.201600909R

Pertea, M., Pertea, G. M., Antonescu, C. M., Chang, T. C., Mendell, J. T., and Salzberg, S. L. (2015). StringTie enables improved reconstruction of a transcriptome from RNA-seq reads. *Nat. Biotechnol.* 31, 1141–1152. doi: 10.1038/nbt.3122

Ramalho-Santos, J., Moreno, R. D., Wessel, G. M., Chan, E. K. L., and Schatten, G. (2001). Membrane trafficking machinery components associated with the mammalian acrosome during spermiogenesis. *Exp. Cell Res.* 267, 45–60. doi: 10.1006/excr.2000.5119

Ran, F. A., Hsu, P. D., Wright, J., Agarwala, V., Scott, D. A., and Zhang, F. (2013). Genome engineering using the CRISPR-Cas9 system. *Nat. Protoc.* 8, 2281–2308.

Rotgers, E., Cisneros-Montalvo, S., Jahnukainen, K., Sandholm, J., Toppari, J., and Nurmio, M. (2015). A detailed protocol for a rapid analysis of testicular cell populations using flow cytometry. *Andrology* 3, 947–955. doi: 10.1111/andr.12066

Russell, L. D., Russell, J. A., MacGregor, G. R., and Meistrich, M. L. (1991). Linkage of manchette microtubules to the nuclear envelope and observations of the role of the manchette in nuclear shaping during spermiogenesis in rodents. *Am. J. Anat.* 192, 97–120. doi: 10.1002/aja.1001920202

Shen, Y., Zhang, F., Li, F., Jiang, X., Yang, Y., Li, X., et al. (2019). Loss-of-function mutations in QRICH2 cause male infertility with multiple morphological abnormalities of the sperm flagella. *Nat. Commun.* 10:433.

Skinner, B. M., Rathje, C. C., Bacon, J., Johnson, E. E. P., Larson, E. L., Kopania, E. E. K., et al. (2019). A high-throughput method for unbiased quantitation and categorization of nuclear morphology. *Biol. Reprod.* 100, 1250–1260. doi: 10.1093/biolre/ioz013

Sleutels, F., Soochit, W., Bartkuhn, M., Heath, H., Dienstbach, S., Bergmaier, P., et al. (2012). The male germ cell gene regulator CTCFL is functionally different from CTCF and binds CTCF-like consensus sites in a nucleosome composition-dependent manner. *Epigenetics Chromatin* 5:8. doi: 10.1186/1756-8935-5-8

Tang, F. L., Liu, W., Hu, J. X., Erion, J. R., Ye, J., Mei, L., et al. (2015). VPS35 deficiency or mutation causes dopaminergic neuronal loss by impairing mitochondrial fusion and function. *Cell Rep.* 12, 1631–1643.

Tang, X. M., Lalli, M. F., and Clermont, Y. (1982). A cytochemical study of the Golgi apparatus of the spermatid during spermiogenesis in the rat. *Am. J. Anat.* 163, 283–294. doi: 10.1002/aja.1001630402

Tang, Z., Takahashi, Y., Chen, C., Liu, Y., He, H., Tsotakos, N., et al. (2017). Atg2A/B deficiency switches cytoprotective autophagy to non-canonical caspase-8 activation and apoptosis. *Cell Death Differ.* 24, 2127–2138. doi: 10.1038/cdd.2017.133

Tiwari, N., Graham, M., Liu, X., Yue, X., Zhu, L., Meshram, D., et al. (2019). Golgin45-Syntaxin5 interaction contributes to structural integrity of the golgi stack. *Sci. Rep.* 9:12465. doi: 10.1038/s41598-019-48875-x

Tourmente, M., Villar-Moya, P., Rial, E., and Roldan, E. R. S. (2015). Differences in ATP generation via glycolysis and oxidative phosphorylation and relationships

with sperm motility in mouse species. *J. Biol. Chem.* 290, 20613–20626. doi: 10.1074/jbc.M115.664813

Wang, H., Wan, H., Li, X., Liu, W., Chen, Q., Wang, Y., et al. (2014). Atg7 is required for acrosome biogenesis during spermatogenesis in mice. *Cell Res.* 24, 852–869. doi: 10.1038/cr.2014.70

Xin, Y., Wang, Y., Zhong, L., Shi, B., Liang, H., and Han, J. (2019). Slc25a36 modulates pluripotency of mouse embryonic stem cells by regulating mitochondrial function and glutathione level. *Biochem. J.* 476, 1585–1604.

Yang, H., Wang, H., and Jaenisch, R. (2014). Generating genetically modified mice using CRISPR/Cas-mediated genome engineering. *Nat. Protoc.* 9, 1956–1968.

Yefimova, M., Buschiazzo, A., Burel, A., Lavault, M. T., Pimentel, C., Jouve, G., et al. (2019). Autophagy is increased in cryptorchid testis resulting in abnormal spermatozoa. *Asian J. Androl.* 21, 570–576. doi: 10.4103/aja.aja_12_19

Zhang, Y., Feng, Y., Ji, D., Wang, Q., Qian, W., Wang, S., et al. (2018). TRIM27 functions as an oncogene by activating epithelial-mesenchymal transition and p-AKT in colorectal cancer. *Int. J. Oncol.* 53, 620–632. doi: 10.3892/ijo.2018.4408

Conflict of Interest: The authors declare that the research was conducted in the absence of any commercial or financial relationships that could be construed as a potential conflict of interest.

Publisher's Note: All claims expressed in this article are solely those of the authors and do not necessarily represent those of their affiliated organizations, or those of the publisher, the editors and the reviewers. Any product that may be evaluated in this article, or claim that may be made by its manufacturer, is not guaranteed or endorsed by the publisher.

Copyright © 2021 Umer, Arévalo, Phadke, Lohanadan, Kirfel, Sons, Sofia, Witke and Schorle. This is an open-access article distributed under the terms of the Creative Commons Attribution License (CC BY). The use, distribution or reproduction in other forums is permitted, provided the original author(s) and the copyright owner(s) are credited and that the original publication in this journal is cited, in accordance with accepted academic practice. No use, distribution or reproduction is permitted which does not comply with these terms.

frontiers in Cell and Developmental Biology

ORIGINAL RESEARCH
published: 17 November 2021
doi: 10.3389/fcell.2021.772254

Bicarbonate-Stimulated Membrane Reorganization in Stallion Spermatozoa

Paula Piccolo Maitan[1,2†], Elizabeth G. Bromfield[3,4†], Romy Hoogendijk[1], Miguel Ricardo Leung[5], Tzviya Zeev-Ben-Mordehai[5], Chris H. van de Lest[3], Jeroen W. A. Jansen[3], Bart Leemans[1], José Domingos Guimarães[2], Tom A. E. Stout[1], Bart M. Gadella[3,6*] and Heiko Henning[1]*

[1]Department of Clinical Sciences, Faculty of Veterinary Medicine, Utrecht University, Utrecht, Netherlands, [2]Department of Veterinary Medicine, Universidade Federal de Viçosa, Viçosa, Brazil, [3]Department of Biomolecular Health Science, Faculty of Veterinary Medicine, Utrecht University, Utrecht, Netherlands, [4]Priority Research Centre for Reproductive Science, The University of Newcastle, Callaghan, NSW, Australia, [5]Cryo-Electron Microscopy, Bijvoet Centre for Biomolecular Research, Utrecht University, Utrecht, Netherlands, [6]Department of Population Health Science, Faculty of Veterinary Medicine, Utrecht University, Utrecht, Netherlands

OPEN ACCESS

Edited by:
Hongmin Qin,
Texas A&M University, United States

Reviewed by:
Satoshi Kishigami,
University of Yamanashi, Japan
Dibyajyoti Talukdar,
College of Veterinary Sciences and Animal Husbandry, Selesih, India

***Correspondence:**
Elizabeth G. Bromfield
elizabeth.bromfield@newcastle.edu.au
Bart M. Gadella
B.M.Gadella@uu.nl

†These authors have contributed equally to this work

Specialty section:
This article was submitted to Cell Growth and Division, a section of the journal Frontiers in Cell and Developmental Biology

Received: *07 September 2021*
Accepted: *25 October 2021*
Published: *17 November 2021*

Citation:
Maitan PP, Bromfield EG, Hoogendijk R, Leung MR, Zeev-Ben-Mordehai T, van de Lest CH, Jansen JWA, Leemans B, Guimarães JD, Stout TAE, Gadella BM and Henning H (2021) Bicarbonate-Stimulated Membrane Reorganization in Stallion Spermatozoa. Front. Cell Dev. Biol. 9:772254. doi: 10.3389/fcell.2021.772254

Classical *in vitro* fertilization (IVF) is still poorly successful in horses. This lack of success is thought to be due primarily to inadequate capacitation of stallion spermatozoa under *in vitro* conditions. In species in which IVF is successful, bicarbonate, calcium, and albumin are considered the key components that enable a gradual reorganization of the sperm plasma membrane that allows the spermatozoa to undergo an acrosome reaction and fertilize the oocyte. The aim of this work was to comprehensively examine contributors to stallion sperm capacitation by investigating bicarbonate-induced membrane remodelling steps, and elucidating the contribution of cAMP signalling to these events. In the presence of capacitating media containing bicarbonate, a significant increase in plasma membrane fluidity was readily detected using merocyanine 540 staining in the majority of viable spermatozoa within 15 min of bicarbonate exposure. Specific inhibition of soluble adenylyl cyclase (sAC) in the presence of bicarbonate by LRE1 significantly reduced the number of viable sperm with high membrane fluidity. This suggests a vital role for sAC-mediated cAMP production in the regulation of membrane fluidity. Cryo-electron tomography of viable cells with high membrane fluidity revealed a range of membrane remodelling intermediates, including destabilized membranes and zones with close apposition of the plasma membrane and the outer acrosomal membrane. However, lipidomic analysis of equivalent viable spermatozoa with high membrane fluidity demonstrated that this phenomenon was neither accompanied by a gross change in the phospholipid composition of stallion sperm membranes nor detectable sterol efflux ($p > 0.05$). After an early increase in membrane fluidity, a significant and cAMP-dependent increase in viable sperm with phosphatidylserine (PS), but not phosphatidylethanolamine (PE) exposure was noted. While the events observed partly resemble findings from the *in vitro* capacitation of sperm from other mammalian species, the lack of cholesterol removal appears to be an equine-specific phenomenon. This research will assist in the development of a defined medium for the capacitation of stallion sperm and will facilitate progress toward a functional IVF protocol for horse gametes.

Keywords: spermatozoa, capacitation, membrane, lipid, bicarbonate (HCO_3–), fertilization, equine, adenylyl cyclase

INTRODUCTION

To fertilize an oocyte, spermatozoa must undergo a process called capacitation, which begins when the spermatozoa enter the female reproductive tract, or are exposed to specific *in vitro* capacitation media. Capacitation was originally defined as the physiological membrane changes that take place inside the female reproductive tract and that enable spermatozoa to acquire fertilizing capacity (Chang 1951; Austin 1952). Since the development of *in vitro* fertilization (IVF), the definition of capacitation has been refined and is now considered to involve the consecutive activation of signalling pathways that induce physiological and biochemical modifications that prime the sperm cell for fertilization *in vitro* (Gervasi and Visconti, 2016). However, classical *in vitro* capacitation techniques (i.e., the inclusion of bicarbonate in the medium) achieve varying degrees of success in different species (Bailey, 2010). In horses, classical IVF (gamete co-incubation) is still a very poorly successful technique that has only ever yielded two foals, both born in France in the early 1990s (Palmer et al., 1991) and live foal production has not been reproduced. The fact that *in vitro* matured oocytes transferred to the oviduct of an inseminated mare yield a similar percentage of embryos to spontaneous ovulation (Hinrichs et al., 2002) and that *in vitro* treated sperm fail to penetrate both *in vivo* and *in vitro* matured oocytes (Tremoleda et al., 2003), suggests that the deficit in equine IVF may reside in an inability to adequately induce capacitation of stallion sperm under *in vitro* conditions.

The changes during capacitation render the sperm able to 1) bind to the oocyte extracellular matrix, the zona pellucida (ZP), and undergo an acrosome reaction (Saling et al., 1978; Saling and Storey, 1979; Topper et al., 1999); 2) acquire hyperactivation (Ho and Suarez, 2001); and 3) fuse with the oocyte plasma membrane (Evans and Florman, 2002). For capacitation to occur, the sperm must be held in environment (*in vivo* or *in vitro*) that contains bicarbonate (HCO_3^-), calcium (Ca^{2+}), and albumin. These three factors are known to induce capacitation in many species, including mice (Visconti et al., 1995a; Visconti et al., 1995b), humans (Osheroff et al., 1999), and pigs (Flesch and Gadella, 2000). Besides inducing changes in membrane potential, these conditions alter cyclic adenosine monophosphate (cAMP) levels, intracellular pH (Leemans et al., 2019a), and intracellular Ca^{2+} (Gervasi and Visconti, 2016). Additionally, this capacitation-inducing environment leads to the removal of decapacitation factors from the surface of the sperm plasma membrane, leading to a "reorganization" of the plasma membrane lipid components and activation of several intracellular pathways (Gadella and Harrison, 2000; Flesch et al., 2001). Besides these three main elements, some species-specific factors for capacitation have also been identified. In cattle for example, heparin-like molecules such as glycosaminoglycans are essential for triggering capacitation (Parrish et al., 1988). However, no specific molecule has been identified as essential to triggering capacitation in stallion spermatozoa (Leemans et al., 2019b).

In the cauda epididymis, the HCO_3^- concentration is very low (<1 mM), whereas when spermatozoa reach the fertilization site in the female genital tract the concentration is much higher (>15 mM) (Harrison, 1996). The rise in HCO_3^- activates the sAC/cAMP/protein kinase A (PKA) pathway leading to an increase in membrane fluidity, and reorganization of the lipids in the plasma membrane, including the translocation of phosphatidylserine (PS) and phosphatidylethanolamine (PE) to the outer leaflet of the sperm plasma membrane (Flesch and Gadella, 2000; Gadella and Harrison, 2002). The translocation of these phospholipids during capacitation depends on the activation of PKA, which occurs after an increase in cAMP levels as a result of sAC activity (Visconti et al., 1995a). Phosphodiesterase (PDE) enzymes that metabolize cAMP to 5′-AMP (Nelson and Cox, 2004) also play a role in regulation of this process. As such, PDE inhibitors, such as caffeine, can maintain high levels of cAMP in the cell, thereby promoting capacitation, and spontaneous acrosome reaction with a consequent increase in sperm motility (Stephens et al., 2013). Another way to raise intracellular cAMP levels is by adding cell-permeable cAMP-analogues to the medium (Fraser, 1981; Visconti et al., 1995b; O'Flaherty et al., 2004).

Adenylyl cyclases (ACs) and their product, cAMP, have been implicated in several cellular signalling pathways in various cell types. In spermatozoa, the presence of sAC and transmembrane AC has primarily been studied in man and the mouse (Uguz et al., 1994; Harrison and Miller, 2000; Lefievre et al., 2000; Baxendale and Fraser, 2003; Spehr et al., 2004; Tardif et al., 2004; Wertheimer et al., 2013). In stallion sperm, there is limited data on the nature of the expressed ACs and their involvement in the specific steps of capacitation, the acrosome reaction, and hyperactivated motility. It is thought that bicarbonate, and thus bicarbonate-mediated activation of the sAC, is essential for cAMP upregulation and consequent initiation of capacitation in stallion sperm (Bromfield et al., 2014). However, recently the contribution of cAMP (generated by ACs) to hyperactivation in stallion spermatozoa has been questioned because cAMP upregulation was not detected under capacitating conditions (Leemans et al., 2019a). Based on these contrasting observations it is of vital interest to understand the extent to which ACs contribute to capacitation-related phenomena in stallion spermatozoa.

The current study aimed to investigate and clarify several aspects of stallion sperm capacitation as triggered by the presence of bicarbonate, calcium, and albumin. Specifically, membrane re-organization after the initiation of sperm capacitation was investigated using lipidomics, cryo-electron tomography, flow cytometry, and complementary biochemical strategies. To this end, PS and PE exposure in viable sperm were monitored by flow cytometry and PS exposure by live imaging. Finally, pharmacological assays were performed to determine which AC is responsible for the increase in membrane fluidity of stallion sperm under *in vitro* conditions.

MATERIALS AND METHODS

Chemicals and Fluorescent Probes

All chemicals were purchased from Sigma-Aldrich (Zwijndrecht, Netherlands) unless otherwise stated. (±)-2-(1*H*-benzimidazol-2-

ylthio) propanoicacid2-[(5-bromo-2 hydroxyphenyl)methylene] hydrazide (KH7) was from Sanbio (13243-10, Uden, Netherlands), 6-chloro-N4-cyclopropyl-N4-[(thiophen-3-yl) methyl]pyrimidine-2,4-diamine (LRE1; HY-100524) was obtained from MedChemExpress (NJ, United States). Annexin–V-FLUOS was purchased from Merck (11828681001, Darmstadt, Germany), lectin from *Arachis hypogea* (peanut) conjugated to Alexa Fluor™ 647 (PNA-AlexaFluor 647) was obtained from ThermoFisher Scientific (L32460; Waltham, MA, United States), and sodium; 3-[(2E)-2-[(E)-4-(1,3-dibutyl-4,6-dioxo-2-sulfanylidene-1,3-diazinan-5-ylidene) but-2-enylidene]-1,3-benzoxazol-3-yl] propane-1-sulfonate (merocyanine 540 abbreviated here to M540) was from Molecular Probes (M24571, Eugene, OR, United States). 4-(5-(4-Methylpiperazin-1-yl)-1H,1′H-[2,5′-bibenzo [d]imidazol]-2′-yl) phenol trihydrochloride (Hoechst 33258; 8861405) and 5.5‘,6.6‘-tetrachloro-1,1‘,3,3‘-tetraethylbenzimidazol-carbocyanine iodide (JC-1; T4069) were obtained from Sigma-Aldrich, and duramycin-cy5 was from Molecular Targeting Technologies, Inc., (D- 1002, West Chester, PS, United States). ADCY10 Polyclonal Antibody was purchased from Bioss Antibodies Inc., (bs-3916R, Woburn, MA, United States) and Goat anti-Rabbit IgG conjugated to Alexa Fluor™ 488 was from Life Technologies (A-11008, Bleiswijk, Netherlands). The semen extender was a commercial skim milk-based product (INRA 96) purchased from IVM technologies (016441, l'Aigle, France).

Media for Sperm Incubation

The basic variant of Tyrode's medium ($Tyr_{Control}$) consisted of 111 mM NaCl, 20 mM HEPES, 5 mM glucose, 3.1 mM KCl, 0.4 mM $MgSO_4$, 0.3 mM KH_2PO_4, 100 μg/ml gentamycin sulfate, 1.0 mM sodium pyruvate, 21.7 mM sodium lactate. In the bicarbonate containing variant (Tyr_{Bic}) a defined amount of NaCl was replaced by 30 mM of $NaHCO_3$. The pH was adjusted to 7.40 ± 0.05 at room temperature with NaOH or HCl and the osmolality to 300 ± 5 mOsmol/kg. All media were passed through a polyethersulfone syringe filter (PES membrane, pore size 0.22 μm; Merck Millipore, Amsterdam, Netherlands) for sterile filtration. Both media contained 1 mg/ml of bovine serum albumin (BSA; A6002, Sigma-Aldrich) and 2 mM of Ca^{2+} supplemented as $CaCl_2$. The bicarbonate containing medium (Tyr_{Bic}) and its variants were kept in an incubator with 5% CO_2 and 100% humidity at 37°C for at least 24 h for equilibration prior to experimentation. Incubations of spermatozoa in bicarbonate containing media took place in the same incubator used for equilibration. Incubations of spermatozoa in control medium ($Tyr_{Control}$) were carried out in a metal heating block at 37°C.

Semen Collection and Dilution

Semen was collected using an artificial vagina (Hanover model) from stallions attending the Faculty of Veterinary Medicine at Utrecht University for routine breeding soundness examination, or from stallions located at nearby horse farms (Stal Schep and Stal van Vliet) with the written consent of the owners. After collection, semen was filtered through gauze to remove the gel fraction and gross debris. A smear of raw semen with Aniline Blue-Eosin was prepared to assess sperm morphology. Sample concentration was measured with a Bürker Türk haemocytometer and ejaculates were diluted in INRA 96® to a concentration of 30×10^6 spermatozoa/mL. Motility was checked objectively using a computer-assisted semen analysis (CASA) system (SpermVision 3.5, Minitüb, Tiefenbach, Germany) as described by Brogan et al. (2015). Only samples with greater than or equal to 70% (total) motile sperm in the diluted semen were used for experiments. Diluted semen was kept at room temperature until further processing. For each experiment, semen from a minimum of three different stallions was used, with the exact number of replicates stated in each figure caption.

Semen Preparation for Experiments

Density gradient centrifugation was performed to separate the spermatozoa from the semen extender and seminal plasma prior to experimentation. Diluted semen (6 ml) was layered on top of a discontinuous gradient consisting of 2 ml of isotonic 70% Percoll®-saline solution and 4 ml of isotonic 35% Percoll®-saline solution in a 15-ml centrifugation tube, as described by Harrison et al. (1993). Tubes were centrifuged for 20 min at room temperature; 10 min at 300 g followed by 10 min at 750 g, without stopping in between. After centrifugation, the supernatant was removed and the remaining pellet was resuspended in 1 ml of $Tyr_{Control}$ without $CaCl_2$ and BSA. The sperm concentration was adjusted to 30×10^6 sperm/mL, unless otherwise stated. The sperm suspension was used within 30 min of preparation.

Flow Cytometry Analysis

Flow Cytometer

A FACS Canto II flow cytometer (BD Biosciences, Breda, Netherlands) was used to assess membrane changes in stallion spermatozoa. The machine was equipped with laser lines at 405 nm (30 mW), 488 nm (20 mW), and 633 nm (17 mW). A gate on forward and side scatter characteristics identified the single sperm population. For each sample, data from 10,000 individual spermatozoa were acquired at medium speed (35 μL ± 5 μL/min). Signals for the fluorescent dyes were collected through a 450/50 nm filter (Hoechst 33258), 530/30 nm filter (JC-1 monomers, Annexin-V-FLUOS), 585/42 nm (JC-1 aggregates, M540), and a 660/20 nm (PNA-Alexa Fluor™ 647, Duramycin-Cy5). Data were analyzed using FCS Express (version 3 and 7, De Novo Software, Glendale, CA, United States). Spectral overlap between dyes was compensated post acquisition.

General Stimulation of cAMP-Dependent Pathways

Where indicated, a final concentration of 1 mM caffeine (2,760, Sigma-Aldrich) and/or 1 mM N^6,2′-O-Dibutyryladenosine 3′,5′-cyclic monophosphate sodium salt (db-cAMP; D0260, Sigma-Aldrich) were added to $Tyr_{Control}$ and Tyr_{Bic} prior to experimentation.

Assessment of Viability, Acrosome Integrity, and Membrane Fluidity

Ten microliter Percoll-washed sperm aliquots were added to FACS tubes containing 490 μL of either $Tyr_{Control}$ or Tyr_{Bic}. All media contained Hoechst 33258 and PNA-AlexaFluor 647.

Samples were then incubated for 15, 30, and 60 min. Fifteen minutes before measurements took place, 2 μL M540 (stock solution: 750 mM in DMSO) was added to the tube and the incubation continued. FACS tubes were capped prior to removal from the incubator and transported in a metal heating block at 37°C to the flow cytometer. The transport time was less than 30 s. Before analysis on the flow cytometer, samples were briefly vortexed.

Assessment of PS or PE Exposure

PS exposure was detected with the probe Annexin-V-FLUOS. Spermatozoa were incubated in 500 μL $Tyr_{Control}$ or Tyr_{Bic} with Hoechst 33258 and PNA-AlexaFluor™ 647. Fifteen minutes before a measurement, 100 μL of the tube's content was transferred to a new, prewarmed tube and 2 μL of Annexin-V-FLUOS was added. The Annexin-V staining was carried out in the presence or absence of 0.2 μL M540. PE exposure was detected with duramycin-Cy5. Samples were incubated in 500 μL $Tyr_{Control}$ or Tyr_{Bic} with Hoechst 33258 and PNA-AlexaFluor488 (stock solution: 0.25 mg/ml in aqua dest). Five minutes before a measurement, 2 μL of duramycin-Cy5 (stock solution: 0.5 mg/ml in 1% DMSO in aqua dest) was added.

Assessment of Mitochondrial Transmembrane Potential

Spermatozoa were incubated in 500 μL $Tyr_{Control}$ or Tyr_{Bic} with Hoechst 33258 and PNA-AlexaFluor 647. Fifteen minutes before a measurement was due, 2 μM JC-1 (stock solution: 250 μM in DMSO) was added to a tube and the content briefly mixed.

Inhibition of sAC with KH7 or LRE1

Three different concentrations of either KH7 or LRE1 (10, 60, and 120 μM) were tested in $Tyr_{Control}$ and Tyr_{Bic} media. Concentrations were based on previous published work on mouse and stallion spermatozoa (Hess et al., 2005; McPartlin and Visconti, 2011). These inhibitors were added to the sperm suspension directly after Percoll centrifugation. In these experiments $Tyr_{Control}$ and Tyr_{Bic} were also supplemented from the beginning with the respective KH7 or LRE1 concentration. Samples processed in presence of DMSO served as solvent controls. Tubes were incubated for 15, 30, and 60 min. All media contained Hoechst 33258 and PNA-AlexaFluor 647. Merocyanine 540 or JC-1 were added 15 min prior to the measurements on the flow cytometer.

Immunolabelling of Soluble Adenylyl Cyclase

Sperm Preparation for Immunocytochemistry and Immunoblotting

For this experiment, stallion and boar spermatozoa (from AIM Varkens KI Netherlands) were used to compare the subcellular localization of sAC in the sperm cell. Boar spermatozoa were used as a control because these cells have previously been reported to have high sAC activity (Leemans et al., 2019a). This experiment used one ejaculate from three different animals from each species (n = 3 biological replicates). For both species, the spermatozoa were separated from the semen extender and seminal plasma by density gradient centrifugation. Diluted semen (9 ml) was layered on top of 3 ml of 35% Percoll®-saline in a 15-ml centrifugation tube and centrifuged at 750 x g for 10 min at room temperature. After centrifugation, the supernatant was removed. The remaining pellet was resuspended in Dulbecco's PBS (DPBS). For immunolocalization experiments, 500 μL of the sperm preparation was incubated with 500 μL of 4% paraformaldehyde for 15 min at room temperature for fixation. After fixation, the samples were centrifuged for 5 min at 600 x g. The supernatant was removed, the pellet diluted in DPBS and another centrifugation was performed.

Immunofluorescent Labelling of sAC

Next, the samples were settled onto Superfrost™ (Thermo Fisher) glass slides for 1 h at room temperature, after which slides were washed once before the addition of a 0.2% Triton X-100 solution for cell permeabilization (10 min at room temperature). Cells were then blocked with 3% BSA/PBS for 1 h and washed once in DPBS. Anti-ADCY10 primary antibody (Bioss Antibodies; bs_3916R) was applied (final concentration 10 μg/ml) and slides were incubated overnight and then washed twice with DPBS. Next, the secondary antibody [goat anti-mouse IgG (H + L), Alexa Fluor 488] was added and slides were incubated for 1 h at room temperature. Hoechst 33342 and PNA-AlexaFluor647 were also included to stain the nuclei and the acrosome of the sperm, respectively. After the incubation, slides were washed with PBS and later covered with 5 μL of Vectashield (Vector Laboratories, California, United States) and a coverslip that was sealed on with nail varnish. Vectashield was added to prevent the fluorescence from bleaching. For cell imaging, a laser scanning confocal microscope (LEICA SPE II DMI 4000, Leica Microsystems, Wetzlar, Germany) was used. On the LEICA SPE II DMI 4000, Hoechst33342 which labels all DNA was excited with the 405 nm laser and the secondary antibody (conjugated to Alexa Fluor 488) for detection of the ADCY10, was excited with the 488 nm laser. PNA-AlexaFluor647 was excited using a 633 nm laser for acrosome detection.

Immunoblot Detection of sAC

To prepare samples for immunoblotting, DPBS was removed *via* centrifugation, and replaced with 500 μL of sodium-dodecylsulphate (SDS) extraction buffer (0.375 M Tris pH 6.8, 2% w/v SDS, 10% w/v sucrose, protease inhibitor cocktail). Samples were boiled at 100°C for 5 min and insoluble material was removed by centrifugation (17,000 g, 10 min); soluble protein remaining in the supernatant was quantified using a BCA protein assay kit (ThermoFisher Scientific). Equivalent amounts of protein lysates (10 μg for both boar and stallion samples) were boiled in SDS-polyacrylamide gel electrophoresis (PAGE) sample buffer (2% v/v beta-mercapto-ethanol, 2% w/v SDS, and 10% w/v sucrose in 0.375 M Tris, pH 6.8, with bromophenol blue) at 100°C for 5 min, prior to being resolved by SDS-PAGE (150 V, 1 h) and transferred to nitrocellulose membranes (350 mA, 1.5 h). Membranes were then blocked in 3% BSA diluted in Tris-buffered saline (TBS) supplemented with 0.1% (v/v) Tween-20 (TBST), and then incubated with anti-ADCY10 (Bioss

Antibodies; bs_3916R) diluted in 1% BSA/TBST (final concentration 2 μg/ml). Immunoblots were washed 3 × 10 min at room temperature with TBST before being probed with appropriate horse-radish peroxidase (HRP)-conjugated secondary antibodies. After three further washes, labelled proteins were detected using an enhanced chemiluminescence kit (ECL-detection kit; Supersignal West Pico, Pierce, Rockford IL, United States). All immunoblots were re-probed with anti-GAPDH antibodies and appropriate secondary antibodies to check for equivalent protein loading.

Live Imaging of Annexin-V Staining Patterns

A live imaging approach was used to demonstrate whether Annexin-V staining was present in viable stallion sperm under capacitating conditions. To this end, 10 μL of Percoll-washed sperm (120×10^6 sperm/mL) was incubated in 500 μL of either Tyr_{Bic} or Tyr_{Bic} supplemented with 1 mM caffeine. Previous experiments indicated that these conditions yielded the highest abundance of Annexin-V positive spermatozoa. Both media contained Hoechst 33258 and PNA-AlexaFluor647, as described for flow cytometry. Samples were evaluated after total incubation times of 30 and 60 min, respectively. 15 min before measurements took place, 100 μL of the sample was transferred to a pre-warmed Eppendorf tube, and 2 μL of Annexin-V FLUOS was added. Live imaging was performed on a NIKON STORM/A1Rsi/TIRF microscope (Nikon, NY, United States), with a preheated stage at 37 °C. After incubation, the samples were centrifuged for 2 min at 1000 x *g* and then resuspended in 10 μL of the respective medium. Next, a 1 μL droplet was placed in a FluoroDish (FD35-100, World Precision Instruments, Friedberg, Germany) and covered with a round coverslip (diameter: 8 mm). Pre-warmed mineral oil was placed around the coverslip to prevent the sample from drying. The autofocus function of the microscope was used to locate the imaging plane. General imaging settings in the acquisition software were: 40x objective, scan speed ½; image size 1,024 × 1,024 pixels, pinhole 5.0 and zoom 1. At least five large scans were performed in a 2 × 2 panel series with laser lines at 405 nm, 488 nm, and 647 nm and corresponding detection channels for the dyes (Hoechst 33258, Annexin-V-FLUOS, AlexaFluor 647, DIC). Images were analyzed with NIS Elements Viewer software (Nikon, NY, United States). An automated detection of the different fluorescent signals in each cell was performed. Subsequently, the staining patterns were validated visually and the location of Annexin V staining (PS exposure) was determined. At least 200 viable cells were scored for each medium.

Sperm Sorting for Lipidomics and Cryo-Electron Tomography

Stallion spermatozoa were sorted on a FACS Influx (Becton Dickinson, San Jose, Canada). A total of 4×10^7 spermatozoa were incubated for 60 min in either 0.5 ml $Tyr_{Control}$ or Tyr_{Bic} media supplemented with 2 μL Hoechst 33258. M540 was added 15 min before sorting. Hoechst 33258 was excited with a 405 nm Laser. Emission was captured with a 460/50 nm filter. M540 was excited with a 561 nm laser, and emission was captured with a 585/42 nm filter. Spermatozoa were analyzed at a rate of between 8,000 and 10,000 events per second. Only events with forward and side scatter characteristics of single spermatozoa were considered for further analysis. During sorting, the sample-input tube on the FACS Influx was kept at 38°C to maintain the sample's temperature during the entire sorting procedure. Phosphate-buffered saline served as sheath fluid. Two subpopulations were sorted: 1) viable spermatozoa (Hoechst 33258 negative) with low membrane fluidity (M540 fluorescence low) from $Tyr_{Control}$, and 2) viable spermatozoa with high membrane fluidity (M540 fluorescence high) from Tyr_{Bic}. A total of 250,000 spermatozoa from a specific subpopulation were sorted into a single tube. The sorting time per tube ranged from 8 min to 15 min. Immediately after sorting, the tube was centrifuged at 11,000 x *g* for 10 min and the supernatant discarded.

Cryo-Electron Tomography

Pellets of sorted spermatozoa were diluted to ~3×10^6 cells/mL in phosphate buffered saline. Approximately 3 μL of cell suspension was applied to glow-discharged Quantifoil R 2/1 200-mesh holey carbon grids. Approximately 1 μL of BSA-gold (Aurion, Wageningen, Netherlands) was added, after which grids were blotted manually from the back for 3–4 s and immediately plunged into a 37% liquid ethane/propane mix cooled to liquid nitrogen temperature. Grids were stored under liquid nitrogen until imaging. Imaging was performed on a Talos Arctica (ThermoFisher) operated at 200 kV and equipped with a post-column energy filter (Gatan) in zero-loss imaging mode with a 20-eV energy-selecting slit. All images were recorded on a ~ 4k × 4k K2 Summit direct electron detector (Gatan) in counting mode with dose-fractionation. Tilt series were collected with SerialEM, using a grouped dose-symmetric tilt scheme covering an angular range of ± 56° in 2° increments. Tilt series were acquired with a Volta phase plate (VPP) at a target defocus of −0.75 μm and with a pixel size of 3.514 Å. The total dose was limited to <100 $e^-/Å^2$. Frames were aligned using Motioncor2 1.2.1. Tomograms were reconstructed in IMOD 4.10.25 using weighted back-projection. Contrast Transfer Function (CTF) correction was not performed because tilt series were acquired close to focus with the VPP. For segmentation and presentation, 6x-binned tomograms were reconstructed with a simultaneous iterative reconstruction technique (SIRT)-like filter corresponding to 20 iterations. Membrane thickness and intermembrane distances from at least five selected tomograms for each sample group were measured in Fiji (Schindelin et al., 2012). For all selected tomograms, ten measurements were performed for each compartment (plasma membrane, intermembrane distance and outer acrosomal membrane when possible). Measurement locations were spaced by at least 100 nm.

Lipid Analysis

Lipid Extraction From Stallion Spermatozoa

After pelleting the sorted spermatozoa (6 biological replicates and two technical replicates), the supernatant was discarded. The cell pellets were held for 10 min in a box with constant N_2 gas supply

to eliminate oxygen and then stored at −20°C. For mass spectrometry the technical replicates were pooled together to form a total cell pellet of 5,00,000 sperm cells for each biological sample (to aid in the detection of poorly abundant lipids) and these cell samples (n = 6) were then transferred to glass vials for lipid extraction. A 1:1 chloroform/methanol (C/M) solution containing three reference lipids: 0.5 μM sitosterol; 0.05 μM 3-keto cholesterol and 0.5 μM 1,2-dimyristoyl-sn-glycero-3-phosphocholine (DMPC) was added to each sample for a total volume of 200 μL. Sperm lipids were extracted in this solution by incubating samples for 30 min at room temperature with gentle mixing. Samples were then centrifuged at 2000 x g for 10 min and supernatants containing the organic phase were transferred to new mass spectrometry grade glass inserts and vials. Samples were then dried under nitrogen and resuspended in 30 μL of 1:1 C/M prior to use for mass spectrometry. Remaining 1:1 C/M with the reference lipids was used as a control.

Detection of Cholesterol and Desmosterol

Extracted lipids were loaded on a C8-column (2.6 μm Kinetex C8 100 Å, 150 × 3.0 mm, Phenomenex, Torrance, CA, United States) maintained at 40°C and eluted at a flow rate of 0.6 ml/min. A gradient elution was performed from methanol/water (1/1; v/v) to methanol/iso-propanol (4/1; v/v) in 2 min, followed by isocratic elution with the latter solvent for an additional 7 min. A 1 min re-equilibration time was used between runs. The column outlet of the LC (Dionex HPG-3200RS UPLC; Thermo Fisher Scientific, Waltham, MA, United States) was connected to the atmospheric pressure chemical ionization source of an LTQ-XL mass spectrometer (Thermo Fisher Scientific). Full scan spectra were collected in positive ionization mode in the range from 200 to 1100Da.

Detection of Phospholipids

Lipid extracts in 1:1 C/M were injected (5 μL in triplicate) onto a hydrophilic interaction liquid chromatography (HILIC) column (2.6 μm HILIC 100 Å, 50 × 4.6 mm, Phenomenex, Torrance, CA, United States). Lipid classes were separated by gradient elution on an Infinity II 1290 UPLC (Agilent, Santa Clara, CA, United States) at a constant flow rate of 1 ml/min. Acetonitrile/acetone (9:1, v/v) was used as solvent A and Solvent B consisted of a mixture of acetonitrile/H_2O (7:3, v/v) with 10 mM ammonium formate. Both solvents contained 0.1% formic acid. The gradient used was (time in min, %B): (0, 0), (1, 50), (3, 50), (3.1, 100), (4, 100). The column flow was connected to a heated electrospray ionization (H-ESI) source of an Orbitrap Fusion mass spectrometer (ThermoScientific) operated at −3,600 V in the negative ionization mode. Temperatures for the vaporizer and ion transfer tube were 275°C and 380°C, respectively. Full scan MS1 measurements in the mass range from 420 to 1150 u were collected in the Orbitrap at a resolution of 1,20,000. Data-dependent MS2 experiments were performed in parallel to the Orbitrap MS1 scanning by fragmentation through higher-energy collisional dissociation, set at 30 V, using the dual-stage linear ion trap to generate up to 30 spectra per second.

Data Analysis

Acquired raw datafiles were converted to mzML files by msConvert (part of ProteoWizard v3.0.913) and processed with the R package xcms v2.99.3. Annotation of lipids was performed by matching measured MS1 m/z values with theoretical m/z values as described in Molenaar et al. (2019). Peak intensities of the annotated lipids were deisotoped and corrected for recovery from the internal standard. Resulting data are included in **Supplementary File S1**.

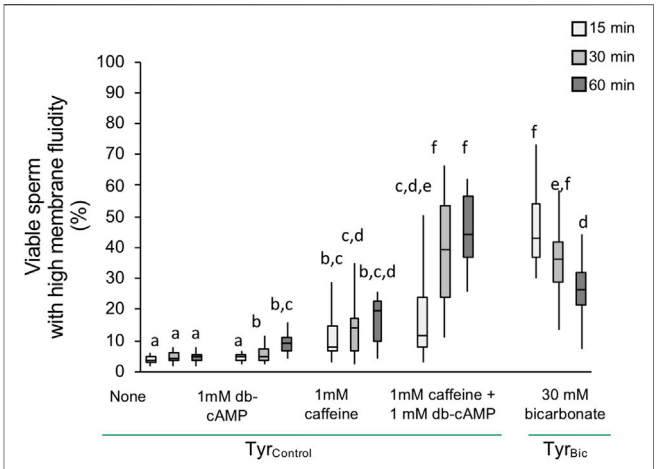

FIGURE 1 | An increase in plasma membrane fluidity in viable stallion spermatozoa is dependent on cAMP signalling. Spermatozoa were in incubated in Tyrodes (Tyr) medium either in the presence of 30 mM bicarbonate (Tyr$_{Bic}$) or its absence (Tyr$_{Control}$). An increase in plasma membrane fluidity, i.e. increased merocyanine 540 staining, in viable (Hoechst 33258 negative) spermatozoa was induced by bicarbonate within 15 min. A similar, but delayed, increase was evoked by 1 mM caffeine and 1 mM bd-cAMP (n = 8 stallions; $p < 0.05$).

Statistics

Data were analyzed using the Statistical Analysis System software (SAS®, version 9.4; SAS Inst. Inc., Cary, NC, United States). Parameters were tested for normal distribution using the Shapiro-Wilk test. Where applicable, a multivariate analysis of variance (ANOVA) for repeated measurements was performed. Comparisons between individual treatments or time points were carried out using Student's t-test for paired observations. All data are presented as mean ± standard deviation (SD). Differences were considered significant when $p \leq 0.05$.

RESULTS

Bicarbonate Induces an Increase in Membrane Fluidity in Viable Sperm

Initial experiments were conducted to confirm that the experimental conditions would stimulate an increase in membrane fluidity (as previously demonstrated by Rathi et al. (2001)). Our results indicated that incubating stallion spermatozoa in Tyr$_{Bic}$ medium resulted in a significantly increased population of viable spermatozoa with high membrane fluidity after a 15 min incubation time (**Figure 1**). In the absence of bicarbonate no change was observed. The combination of a cAMP analogue (db-cAMP) and a PDE

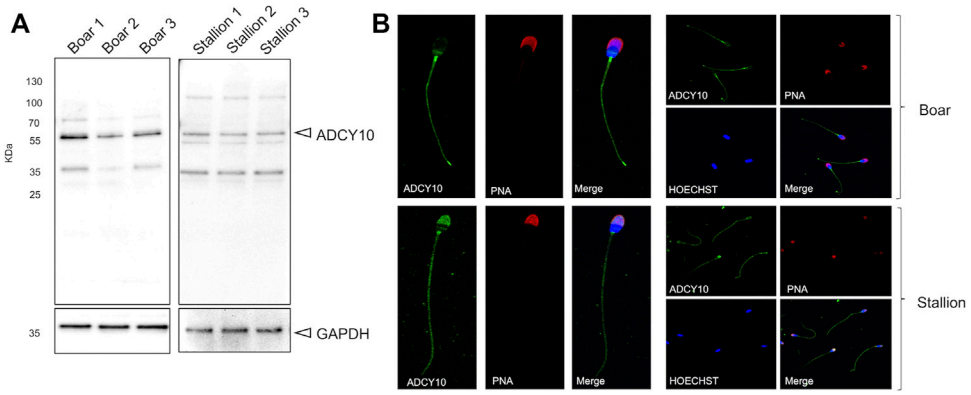

FIGURE 2 | Detection and localization of ADCY10 in stallion and boar spermatozoa. Native semen samples were processed for immunoblotting and immunofluorescence with a polyclonal antibody against ADCY10. **(A)** Immunoblot of anti-ADCY10 in boar semen samples (n = 3 boars) and stallion semen samples (n = 3 stallions). GAPDH was used as a loading control. **(B)** Representative images for the localization of ADCY10 in boar spermatozoa and stallion spermatozoa (n = 3 boars; n = 3 stallions). Samples were counterstained with PNA-AlexaFluor™ 647 (to visualize sperm acrosomes) and Hoechst 33342 (to visualize the nucleus).

inhibitor (caffeine) was able to mimic the bicarbonate effect and induced an equally large population of viable sperm with high membrane fluidity (**Figure 1**; **Supplementary Figure S1I**). Nonetheless, the response was slower than for Tyr_{Bic} and it took at least 30 min before this population was detectable (**Figure 1**). It is thought that bicarbonate is essential for cAMP upregulation and in other eutherian mammals this response is mediated by adenylyl cyclase. Indeed, in spermatozoa, the presence of soluble adenylyl cyclase (sAC) has primarily been studied in human and mouse sperm (Uguz et al., 1994; Harrison and Miller, 2000; Lefievre et al., 2000; Baxendale and Fraser, 2003; Spehr et al., 2004; Tardif et al., 2004; Wertheimer et al., 2013). In stallion sperm, there is limited available data regarding the nature of sACs and its involvement in the specific steps of capacitation. Thus, the following studies were designed to determine whether the impact of bicarbonate on stallion sperm membrane fluidity is mediated by sAC.

Detection of sAC in Stallion and Boar Sperm

To investigate the presence and localization of sAC in stallion spermatozoa, immunoblotting and immunofluorescence with an anti-ADCY10 antibody was performed. The results were compared sAC localization in boar sperm, where it is known to have high activity (Leemans et al., 2019b), and shares 87.03% sequence similarity to equine ADCY10. Immunoblotting demonstrated that the sAC is present in both boar and stallion spermatozoa as an immunoreactive band at approximately 55 kDa (**Figure 2A**). This is the predicted size of the testis-specific form of sAC. In both species, some additional bands were detected at approx. 35 and 50 kDa. Immunofluorescent labelling of sAC revealed that this adenylyl cyclase is distributed along the tail of spermatozoa from both species, with bright labelling noted in the endpiece of the tail. However, a higher signal intensity for both species was noted in the neck region. In the sperm head, species-specific staining patterns were observed with sAC localized over the whole acrosomal area in stallion spermatozoa, whereas the sAC signal was limited to a distinct band across the post-equatorial region of boar spermatozoa (**Figure 2B**). Secondary controls where Anti-ADCY10 was omitted revealed no non-specific fluorescence (**Supplementary Figure S1**).

Inhibition of sAC Prevents an Increase in Membrane Fluidity

Following confirmation that sAC was present in stallion spermatozoa, the effect of sAC inhibition was then assessed in this species. Indirect inhibition of sAC with the inhibitor KH7 in the presence of bicarbonate (Tyr_{Bic}) appeared to be effective in a large proportion of viable spermatozoa at concentrations of 60 and 120 μM (**Supplementary Figure S2A**). However, off-target effects were also observed, with KH7 at 60 and 120 μM resulting in an increase in viable sperm populations with high membrane fluidity in $Tyr_{Control}$ but abolishing the high mitochondrial transmembrane potential in virtually all spermatozoa (**Supplementary Figures S2B–D**). Further observations confirmed that spermatozoa stopped tail beating within 1 min after exposure to KH7 at all concentrations. This is in line with a previous report suggesting that KH7 acts as a mitochondrial uncoupler (Jakobsen et al., 2018). Given these challenges, a direct inhibitor of sAC, LRE1, which specifically competes with the bicarbonate binding site of sAC (Ramos-Espiritu et al., 2016), was used in equivalent experiments. Using LRE1, the expected increase in membrane fluidity could be prevented in most of the viable spermatozoa after incubation for 15 min in the presence of 30 mM bicarbonate (Tyr_{Bic}; **Figure 3A**). The strength of the inhibition lessened over time, but was still significant after 60 min of incubation (**Figure 3A**). A small, but significant increase in the percentage of viable spermatozoa with high membrane fluidity was noted in the absence of bicarbonate ($Tyr_{Control}$). However, this population stayed below 10% (**Figure 3B**). In contrast to the observations for KH7, there were no adverse effects of LRE1 in Tyr_{Bic} or

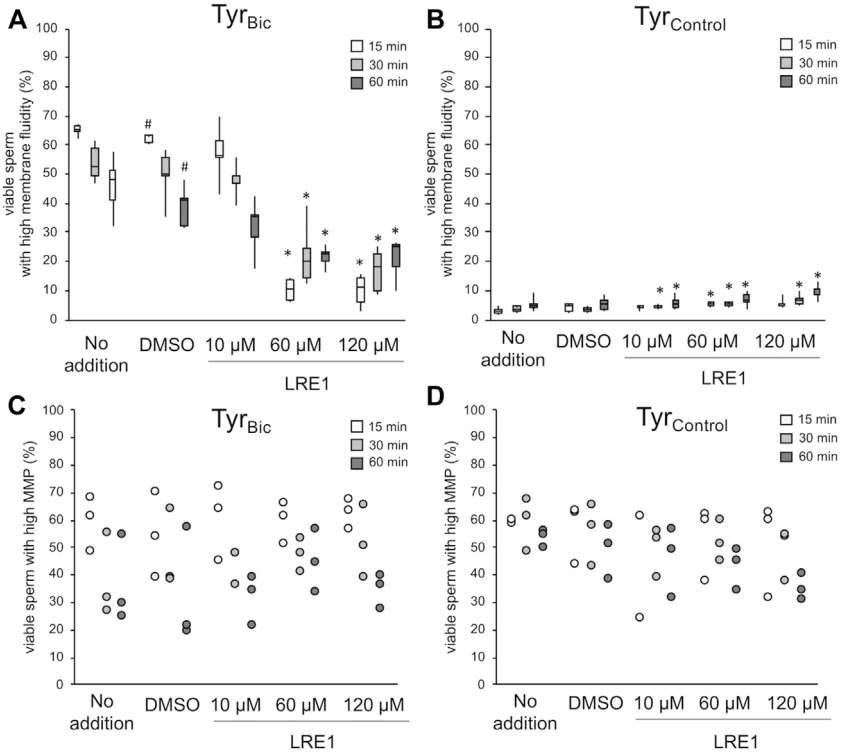

FIGURE 3 | LRE1 blocks sAC activity with no off-target effects on mitochondrial membrane potential. Spermatozoa were incubated either in presence of 30 mM bicarbonate (Tyr_{Bic}) or its absence ($Tyr_{Control}$). Media contained either no further additions, DMSO (solvent control), or an increasing concentration of LRE1 to directly block sAC activity. An increase in plasma membrane fluidity, i.e., increased merocyanine 540 staining, in viable (Hoechst 33258 negative) sperm was monitored in absence or presence of LRE1 [**(A,B)**; $n = 6$ stallions]. A hash symbol (#) indicates significant differences between DMSO exposed samples and samples without any additions ($p < 0.05$). An asterisk (*) indicates significant differences between DMSO exposed samples and samples treated with LRE1 ($p < 0.05$). In a subset of samples, the percentage of viable sperm with high mitochondrial transmembrane potential (MMP) was monitored using the probe JC-1 [**(C,D)**; $n = 3$ stallions].

$Tyr_{Control}$ on the percentage of spermatozoa with high mitochondrial membrane potential, and the cells remained motile (**Figures 3C,D**).

Cryo-EM Reveals Membrane Reorganization in the Acrosomal Area of Viable Sperm with High Membrane Fluidity

To visualize structural changes associated with high membrane fluidity, we imaged whole, unfixed, unstained stallion sperm using cryo-electron tomography (cryo-ET). Cryo-ET yields three-dimensional reconstructions of subcellular structures within the context of fully-hydrated cells, avoiding artefacts from dehydration and chemical fixation. To establish baseline membrane morphology, we imaged non-sorted spermatozoa that had been incubated for 60 min in $Tyr_{Control}$ (**Figures 4A,B**). In these non-capacitated cells, the plasma membrane (PM) and outer acrosomal membrane (OAM) were smooth and parallel (10/12 tomograms, each from a different cell, from two stallions), with a regular intermembrane distance of ~11 ± 2 nm. To directly correlate structural changes to membrane fluidity, we imaged flow-sorted viable sperm with either low or high M540 staining. The majority of sorted, viable sperm with low membrane fluidity were similar to non-sorted control cells, with the PM and OAM both intact, smooth, and running parallel to each other (13/19 tomograms, each from a different cell, from three stallions) (**Figures 4C,D**). In contrast, most of the sorted, viable spermatozoa with high membrane fluidity showed evidence of membrane destabilization (23/26 tomograms, each from a different cell, from three stallions). A range of phenotypes could be distinguished. Some cells showed a clear approximation of the PM and OAM (**Figure 4E**), in particular at sites where the OAM becomes discontinuous and bends upwards towards the OM (**Figure 4F**) (6 tomograms, each from a different cell). This was reflected by a reduced average intermembrane distance (**Figure 4G**). Finally, in some spermatozoa the presence of membrane vesicles was observed in regions close to sites of membrane disruption (**Supplementary Figure S1**).

Membrane Reorganization is Not Accompanied by a Change in Sperm Lipid Composition

Given that the cryo-ET analysis revealed modulated membrane organization in sperm cells with high membrane fluidity, we next sought to determine whether changes in membrane organization were reflective of changes in either the phospholipidome or

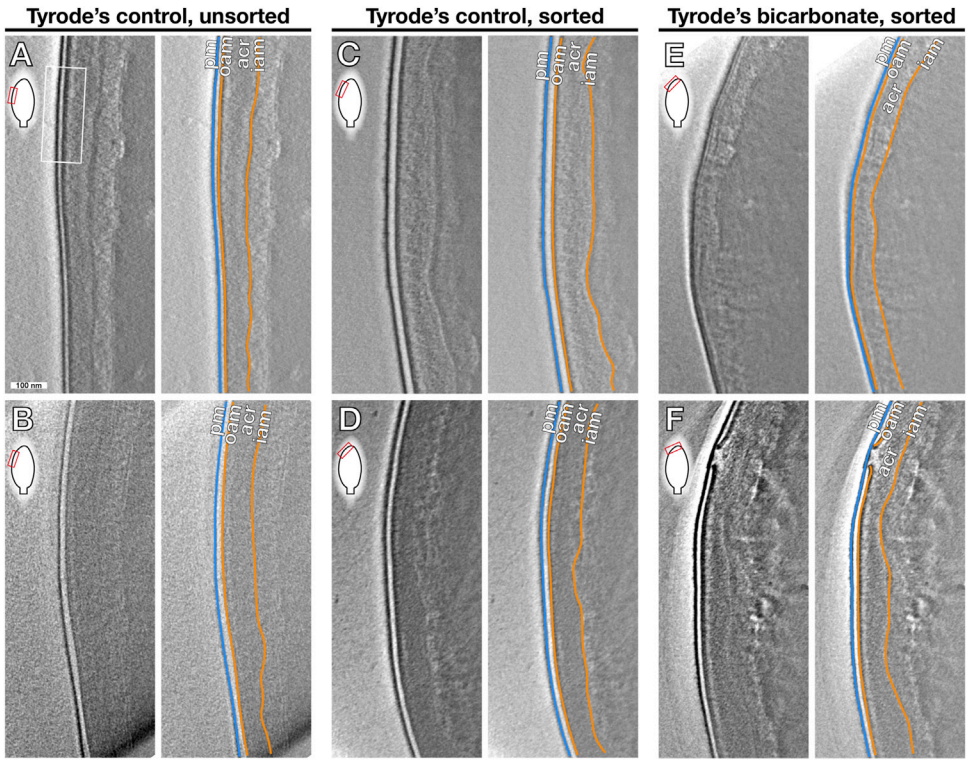

G

	pm thickness (nm)	oam thickness (nm)	intermembrane distance (nm)
Tyrode's control, unsorted	6 ± 1	9 ± 1	11 ± 1 [a]
Tyrode's control, sorted	6 ± 1	9 ± 2	11 ± 2 [a]
Tyrode's bicarbonate, sorted	6 ± 1		6 ± 1 [b]

FIGURE 4 | Sperm membrane reorganization detected by Cryo-ET after incubation with bicarbonate. Spermatozoa were incubated either in the presence of 30 mM bicarbonate (Tyr_{Bic}) or its absence ($Tyr_{Control}$) for 60 min and then FACS-sorted to inspect membrane reorganization using cryo-electron tomography (cryo-ET). To mark structures identified by cryo-ET, the membranes are colour coded to indicate the plasma membrane (PM) (blue), outer acrosomal membrane (OAM), and inner acrosomal membrane (IAM) (orange) that surround the acrosomal content. Red boxes indicate the approximate region of the sperm head featured in the frames. Unsorted spermatozoa in $Tyr_{Control}$ typically demonstrated an intact PM and OAM that were smooth and ran parallel to each other along the sperm head **(A,B)**. This was also observed in a majority of FACS-sorted viable, "low fluidity" cells in TyrControl **(C,D)** (n = 3 stallions). However, sorted viable, "high fluidity" sperm cells incubated in Tyr_{Bic} mostly showed evidence of membrane remodelling and destabilization, including closer approximation of the PM and OAM **(E)** in particular at **(F)** points of apparent rupture of the OAM **(F)**, leading to a decrease in apparent intermembrane distance **(G)** (n = 3 stallions).

alterations in cholesterol efflux caused by bicarbonate treatment. While lipidomic analysis of FACS-sorted spermatozoa revealed 15 distinct phospholipid and glycolipid classes (**Figure 5A**) consisting of >150 unique phospholipid/glycolipid species (**Supplementary File S1**), no significant differences in the relative intensity of these lipid classes, or in individual molecular species, were detected between low and high membrane fluidity stallion sperm samples (n = 6 stallions; **Figure 5A**). Similarly, when the levels of cholesterol and desmosterol were measured in the same samples, equivalent pmole amounts/sample (~500,000 sperm cells) were detected in low and high membrane fluidity sorted cell populations (**Figure 5B**). The absence of differences in lipid composition between the high and low membrane fluidity sperm subpopulations indicates that differences in membrane fluidity are not caused by compositional differences in sperm membrane lipids. Therefore, further experiments were carried out to investigate whether or not the organization of lipids in the sperm membrane were altered in a cAMP-dependent manner.

Flow Cytometry Detects PS, but Not PE Exposure in Viable Stallion Sperm After Bicarbonate Stimulation

In the sperm cells of most species studied, rearrangement of the sperm lipid membrane bilayer is essential to increase its fluidity prior to fertilization (Visconti et al., 1995a; Gadella and Harrison, 2000; Cross, 2003). The following experiment was performed to understand whether the exposure of PS and PE phospholipids is required for the activation of the sAC/cAMP/PKA pathway leading to an increase in membrane fluidity as previously described in boar sperm (Flesch and Gadella, 2000). In a preliminary experiment we observed that M540 staining may have a small, but significant impact on the number of

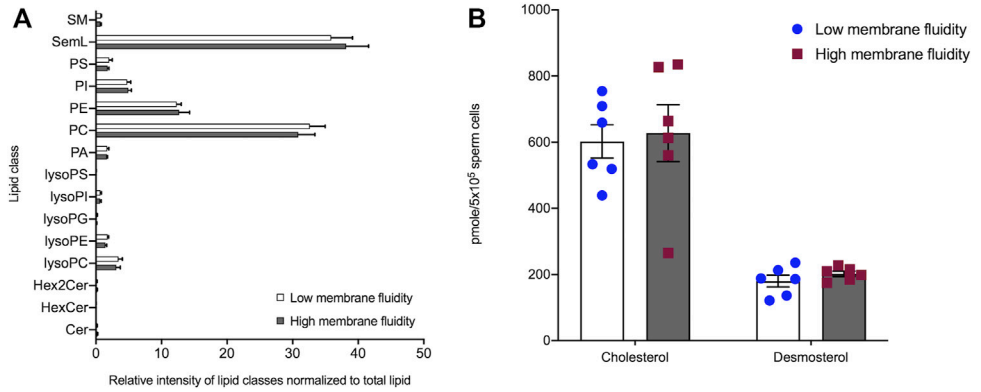

FIGURE 5 | Lipidomic analysis of stallion sperm populations with low- and high-membrane fluidity selected by FACS-sorting. Stallion spermatozoa were incubated for 60 min in either $Tyr_{Control}$ or Tyr_{BIC} medium supplemented with Hoechst 33258. Fifteen minutes prior to FACS sorting M540 was added to each population. Using a FACS Influx, stallion sperm cells were sorted into two subpopulations; viable sperm with low membrane fluidity (Hoechst negative, M540 "low"); and viable sperm with high membrane fluidity (Hoechst negative, M540 "high"). Samples were then processed for either phospholipid and glycolipid analysis or quantitation of cholesterol and desmosterol. Phospholipid and glycolipid analysis revealed 15 classes of phospholipids present in stallion spermatozoa **(A)** with a relative abundance of seminolipid (SemL) and phosphatidylcholine (PC). No significant differences were found between spermatozoa with high membrane fluidity or low membrane fluidity (n = 6 stallions). **(B)** Similarly, the comparison of cholesterol and desmosterol levels in low and high membrane fluidity populations revealed no significant difference in major sterol content in stallion spermatozoa (n = 6 stallions). Abbreviations: SM, sphingomyelins; SemL, seminolipids; PS, phosphatidylserines; PI, phosphatidylinositols; PE, phosphatidylethanolamines; PC, phosphatidylcholines; PA, phosphatidic acids; lysoPS, lysophosphatidylserines; lysoPI, lysophosphatidylinositols; lysoPG, lysophosphatidylglycerols; lysoPE, lysophosphatidylethanolamines; lysoPC, lysophosphatidylcholines; Hex2Cer, dihexosylceramides; HexCer, hexocylceramides; Cer, ceramides.

viable spermatozoa detected as Annexin-V positive (data not shown). Consequently, the following results for PS and PE exposure in viable spermatozoa were obtained in the absence of M540 staining so as not to bias the analysis (**Figure 6**). Samples with M540 staining were run in parallel to ensure that most of the viable spermatozoa were showing increased membrane fluidity. Annexin-V labelling demonstrated that PS exposure could be detected in Tyr_{Bic} in a subset of viable spermatozoa (**Figure 6A**). However, exposure of PE in viable spermatozoa was barely observed (**Figure 6B**).

Bicarbonate was required to significantly increase the proportion of viable sperm with PS exposure after 30 and 60 min incubation ($Tyr_{Control}$ (no addition) **Figure 6C** versus Tyr_{Bic} (no addition) **Figure 6E**). Maximal PS exposure in Tyr_{Bic} (no addition) was reached after 60 min incubation (**Figure 6E**). Caffeine, db-cAMP, and the combination of both compounds were able to increase the population of viable spermatozoa with PS exposure after 15 min and/or 30 min in Tyr_{Bic}, but not after 60 min (**Figure 6E**). In the absence of bicarbonate ($Tyr_{Control}$), either caffeine or the combination of caffeine and db-cAMP initiated an increase in the percentage of viable sperm with PS exposure (**Figure 6C**). Values in $Tyr_{Control}$ with db-cAMP and caffeine were identical to those from Tyr_{Bic} (no addition; **Figures 6C,E**). The exposure of PE in viable sperm was always limited to less than 5% of the spermatozoa and could not be stimulated by db-cAMP, caffeine, or the combination of the two compounds (**Figures 6D,F**).

Live Imaging Revealed Distinctly Different Staining Patterns for Annexin V in Viable Stallion Sperm

As flow cytometry cannot specify where Annexin-V binds within cells, live imaging was used to visualize Annexin-V staining patterns in stallion sperm under capacitating conditions in Tyr_{Bic}. Three main Annexin-V staining patterns were observed in viable stallion spermatozoa (**Figure 7**; arrow indicated). The dominant pattern was an homogenous labelling of the acrosomal area in the sperm head (**Figure 7A**), followed by a labelling of the entire head and midpiece (**Figure 7C**). A smaller subset of spermatozoa stained Annexin-V positive over the whole sperm head (**Figures 7B,D**). Statistical analysis revealed significant differences in the abundance of these three staining patterns (i.e., number of cells for each Annexin-V labelling pattern), but not significant influence of time or treatment on the number of cells demonstrating each pattern.

DISCUSSION

Failure of *in vitro* capacitation of stallion sperm has been cited as a major limiting factor in the development of conventional IVF in the horse (Tremoleda et al., 2003). This means that equine IVF in practice is currently achieved *via* intracytoplasmic sperm injection (ICSI), a time-consuming process that requires highly-trained individuals and expensive equipment (Stout and Griffiths, 2021). Although previous studies have reported successful induction of sperm-zona pellucida interaction between equine gametes (Macías-García et al., 2015), media developed to support gamete interaction have not yielded repeatable IVF success (Choi et al., 1994; Dell'Aquila et al., 1997a; Dell'Aquila et al., 1997b; Alm et al., 2001; Hinrichs et al., 2002; Mugnier et al., 2009). Unlike other mammalian species such as the mouse and the boar, stallion sperm membrane physiology and lipid biochemistry have not been meticulously explored to understand essential species-specific events required for capacitation.

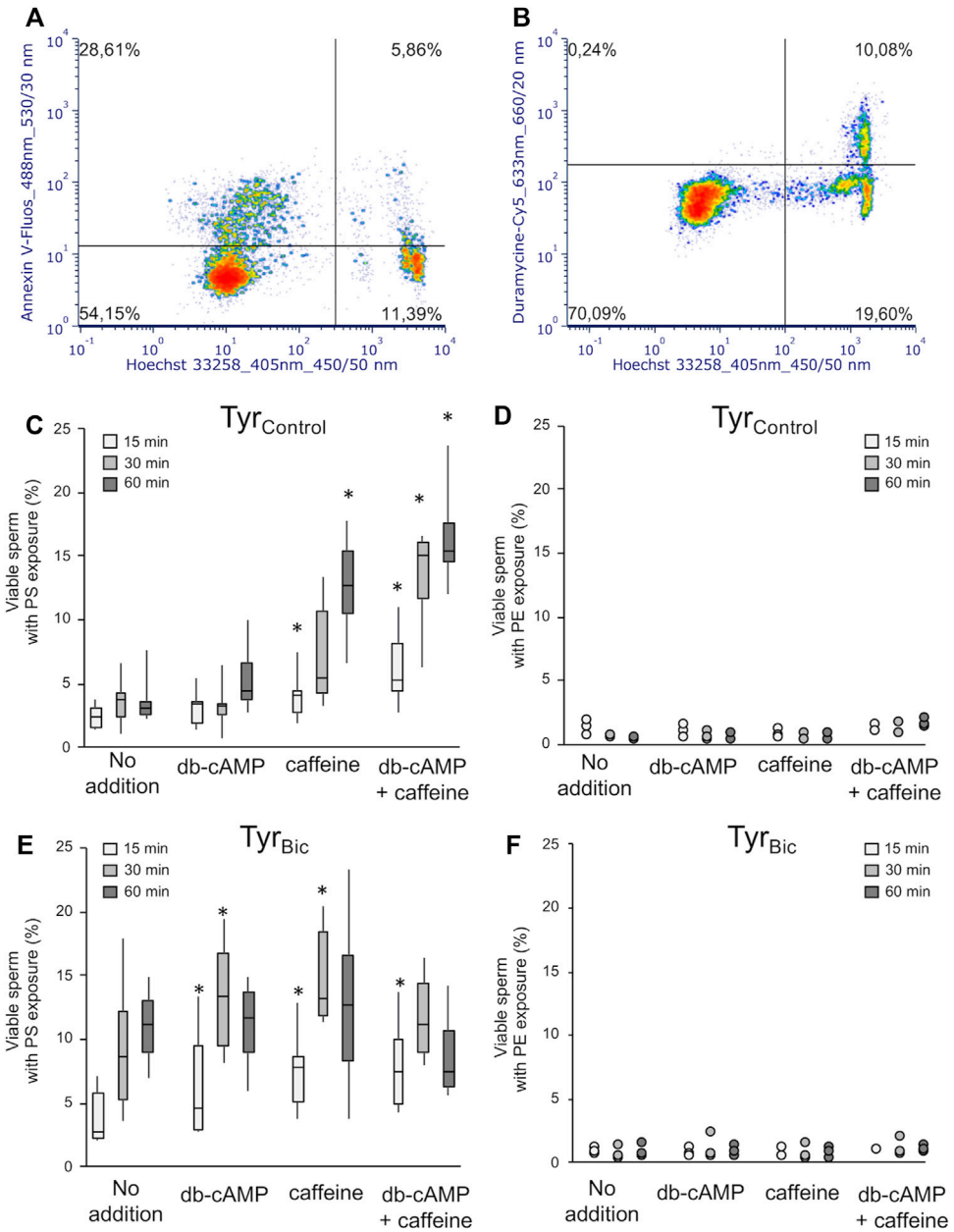

FIGURE 6 | Viable stallion spermatozoa demonstrate exposed PS, but not PE upon direct or indirect elevation of intracellular cAMP levels. Spermatozoa were incubated either in the presence of 30 mM bicarbonate (Tyr_{Bic}) or its absence ($Tyr_{Control}$). Media contained either no further additions, 1 mM db-cAMP, 1 mM caffeine, or a combination of 1 mM each of db-cAMP and caffeine. PS exposure to the outer lipid monolayer of the sperm plasma membrane in viable (Hoechst 33258 negative) sperm was detected using Annexin V-Fluos [**(A,C,E)**; $n = 6$ stallions]. An asterisk (*) indicates significant differences between samples with no addition and samples exposed to db-cAMP and/or caffeine ($p < 0.05$). PE exposure residues was monitored using duramycine-Cy5 [**(B,D,F)**; $n = 3$ stallions].

Rather than seeking to develop a new capacitation medium, our study aimed to improve understanding of well-described capacitation events, such as bicarbonate-driven membrane destabilization, through the use of advanced technologies including cryo-electron tomography, phospholipidomics, and live imaging. Many of these techniques have not previously been applied to study capacitation in stallion spermatozoa. Assessing stallion sperm capacitation in more intricate detail yielded new insight into the timing of and requirements for capacitation. Specifically, we now know that the membrane remodelling induced by bicarbonate promotes rapid fluidization of the membrane (within 15 min of bicarbonate exposure) that is driven, at least in part, by sAC. Moreover, this extensive bicarbonate-induced membrane reorganization that can be visualized by cryo-electron tomography does not require overt changes in the overall phospholipid composition of

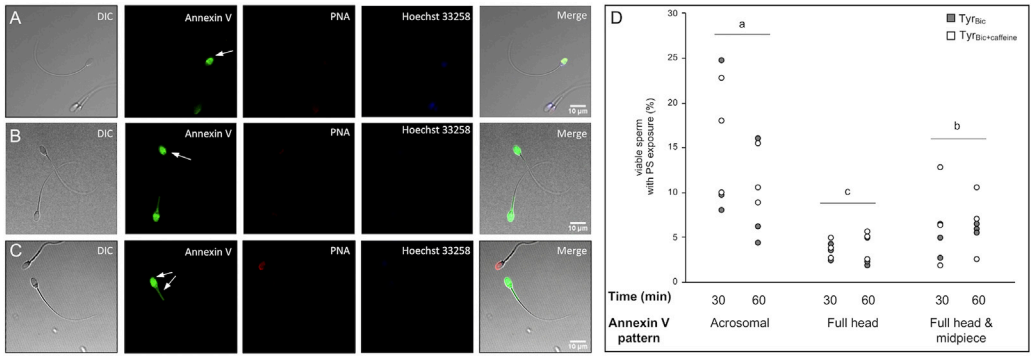

FIGURE 7 | Patterns of phosphatidylserine-exposure in viable stallion sperm. Spermatozoa were incubated either in the presence of 30 mM bicarbonate (Tyr$_{Bic}$) or Tyr$_{Bic}$ containing 1 mM caffeine (Tyr$_{Bic+caffeine}$). An exposure of phosphatidylserine (PS) in viable (Hoechst 33258 negative) sperm was detected using Annexin V-Fluos (n = 3 stallions). PNA-Alexa Fluor647 was included as an additional marker for acrosome integrity. Staining patterns for Annexin V were observed in the acrosomal area [**(A)**, arrow], across the complete head region [**(B)**, arrow] or in the complete head and the midpiece [**(C)**, arrows]. The frequency of each pattern in the viable sperm population was determined after 30 and 60 min incubation time **(D)**. Differing letters **(A–C)** indicate significant differences between the abundance of each labelling pattern for Annexin V. There were no significant differences between timepoints (n = 12 samples per pattern; $p < 0.05$).

the membrane, nor does it involve detectable sterol efflux. These results are in stark contrast to the membrane fluidization process in boar spermatozoa where a redox-dependent sterol efflux facilitates downstream membrane changes (Boerke et al., 2013). We will further discuss the peculiarities of the capacitation of stallion spermatozoa and how future research could be designed to further understand this process and aid development of equine assisted reproduction.

To become capable of fertilizing an oocyte, sperm cells must pass through capacitation steps that permit the plasma membrane to transition to a metastable, fusible state (Gadella and Harrison, 2002; Maitan et al., 2021). *In vitro*, this process can be achieved using capacitating media in which bicarbonate is a key element. An early alteration induced by bicarbonate in sperm membranes is an increase in membrane phospholipid packing disorder that can be detected by the fluorescent amphiphilic probe M540 (Harrison, 1996). Indeed, the increase in the live, M540 positive sperm population induced by Tyr$_{Bic}$ media in our study indicates that this capacitation step can be rapidly achieved in a large proportion of stallion sperm by exposure to bicarbonate. Moreover, when intracellular cAMP levels were increased by the inclusion of db-cAMP and caffeine, this M540 response could be further amplified. This confirms earlier reports that this step in capacitation is important for stallion sperm, as it is for sperm from other mammalian species (pig: Harrison, 1996; stallion: Rathi et al., 2001; dog: Steckler et al., 2015). By inhibiting sAC using LRE1, we demonstrated the involvement of sAC in the regulation of cyclicAMP that underpins the bicarbonate-membrane fluidity response; the incubation of stallion sperm with LRE1 resulted in a dose-dependent decrease in membrane fluidity. In contrast to boar spermatozoa, sAC was localized across the acrosomal region of stallion spermatozoa suggesting that the precise role of sAC in stallion sperm may differ to boar sperm (Leemans et al., 2019b). sAC has previously been linked to the capacitation-related rearrangements of lipids in human sperm (de Vries et al., 2003), as well as to tyrosine phosphorylation (Wertheimer et al., 2013).

Having confirmed that bicarbonate can induce a significant, sAC-regulated, M540 response in stallion spermatozoa, we examined the nature of the increased membrane fluidity using a combination of fluorescence-assisted cell sorting and cryo-electron tomography. This approach allowed us to distinguish between viable "low membrane fluidity" cells and viable "high membrane fluidity" cells and to determine how they differ morphologically. Stallion spermatozoa from the "high membrane fluidity" population consistently showed evidence of membrane destabilization, including vesiculation, rupture, and/or swelling. In contrast, the "low membrane fluidity" cells mostly had intact membranes. Importantly, these observations were not an artifact of the sorting process. Although the sorted "low fluidity" population had more cells with disrupted membranes than the non-sorted control, the majority of sperm had intact membranes, as opposed to the sorted "high fluidity" population in which most cells showed signs of membrane destabilization. Furthermore, sorted "low fluidity" and non-sorted control cells were very similar in terms of membrane morphology, with smooth and regularly-spaced PM and OAM. These observations indicate that extensive membrane remodelling takes place in response to bicarbonate, and is an important step on the path to the acrosome reaction.

Given the membrane destabilization observed in the tomograms, we anticipated that this lipid remodelling was likely to be accompanied by changes in phospholipid and/or sterol content in the sperm membranes. However, investigation of the phospholipidome of FACS sorted "high membrane fluidity" and "low membrane fluidity" spermatozoa revealed no significant differences in the abundance of phospholipid classes or sub-species. Moreover, no significant difference in the content of cholesterol or desmosterol, the key sterols in sperm membranes, were detected between the two defined cell populations. These observations do not align with our previous understanding of sperm membrane remodelling in which the

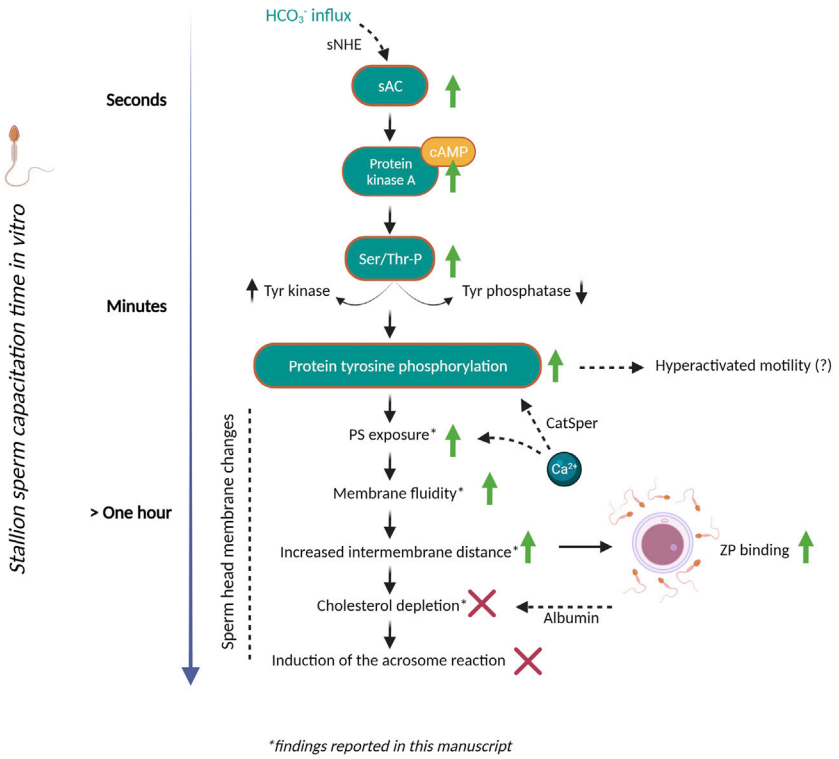

FIGURE 8 | Steps towards stallion sperm capacitation *in vitro* and ongoing challenges. A number of changes must take place in the sperm head membrane to permit interactions with the oocyte. In the stallion we now know that the bicarbonate induced membrane fluidity changes that facilitate downstream sperm functions are regulated by soluble adenylyl cyclase. This leads to an increase in cyclicAMP levels, the regulation of tyrosine kinases and phosphatases and an increase in protein tyrosine phosphorylation (as reported in independent studies). We have demonstrated here that a population of stallion sperm cells also expose phosphatidylserine (PS) in the outer leaflet of the plasma membrane during this process but remain viable. Using cryo-electron tomography we have observed distinct changes in the stallion sperm membrane (such as altered intermembrane distance) in response to bicarbonate. However, these morphological membrane changes were not accompanied by a significant change in membrane phospholipid composition, nor cholesterol efflux. The lack of cholesterol efflux may be a unique aspect of stallion sperm capacitation that differs from other species studied, such as the boar. However, these data may indicate that bicarbonate-enriched capacitation media is insufficient to permit a complete capacitation of stallion sperm cells. Indeed, the field lacks a reliable method to induce acrosomal exocytosis *in vitro*. This incomplete capacitation may underpin our inability to conduct IVF in the horse. Further research should be focused around elucidating the "slower" aspects of the capacitation process that permit the acrosome reaction and sperm-egg fusion. Abbreviations: HCO_3^-, bicarbonate; sNHE, sperm-specific Na^+/H^+ exchanger; sAC, soluble adenylyl cyclase; cAMP, cyclic adenosine monophosphate; PKA, protein kinase A; Ser/Thr-P, serine/threonine phosphorylation; Tyr, tyrosine. This figure was created with BioRender.com.

addition of albumin to capacitating media supported cholesterol efflux from bicarbonate responsive cells (Flesch and Gadella, 2000). In some species, depletion of cholesterol from the plasma membrane occurs after the formation of oxysterols, which activate sterol transporter proteins (such as albumin; Brouwers et al., 2011; Boerke et al., 2013). While the measurement of oxysterols in stallion sperm remains to be performed, the retention of membrane cholesterol in stallion sperm cells implies that bicarbonate-induced membrane remodelling is likely to occur through novel mechanisms in this species. Importantly, an inability to withdraw membrane cholesterol from stallion spermatozoa has also been noted in independent studies (Macías-García et al., 2015). An alternate explanation may be that bicarbonate-enriched media such as Tyr_{Bic} are insufficient to trigger observable cholesterol removal from stallion sperm membranes. While the latter remains to be explored, Tyr_{Bic} is known to be sufficient to induce several downstream events of stallion sperm capacitation, such as responsiveness to acrosome reaction inducing stimuli. The acrosome reaction is however thought to be permitted by cholesterol efflux (Cross, 1998; Boerke et al., 2008). It is possible that in stallion spermatozoa, membrane remodelling can occur despite the retention of sterols. However, these aspects should be explored further in detailed lipidomic studies focused on understanding cholesterol acceptors that may be unique to stallion spermatozoa. Nonetheless, this observation marks a distinct aspect of stallion sperm capacitation that should be considered when designing future IVF media for equine gametes.

In some species, the increase in membrane phospholipid disorder that is detected by M540 leads to an activation of a phospholipid scramblase which in turn collapses the lipid asymmetry across the plasma membrane. As a result, PE and PS are translocated to the outer surface of spermatozoa and can be detected using fluorescent probes (Williamson and Schlegel, 1994; Gadella and Harrison, 2002). Incubating boar

sperm for 2 h in a bicarbonate containing medium has previously revealed exposure of PS in a substantial subpopulation of intact cells, reaching a maximum at 60 min of incubation (Gadella and Harrison, 2002). Similarly, incubating human sperm with bicarbonate for 4 h resulted in steady state labelling of PS with Annexin V after 90 min of incubation (de Vries et al., 2003). However, some contradictory evidence gathered for boar spermatozoa has also suggested that PS externalization may identify the non-viable sperm population (Kurz et al., 2005). In our experiments, 60 min of incubation in Tyr_{Bic} medium, induced exposure of PS in only 12% of stallion spermatozoa. However, inclusion of a viability stain confirmed that this population consisted of live cells. In stallion spermatozoa, the PS exposure was found to take place at the external surface of the plasma membrane after 30 min of incubation with bicarbonate and thus, temporally, may follow the collapse (or scrambling) of the plasma membrane phospholipid asymmetry that appears to occur following only 15 min of incubation in Tyr_{Bic}. Changes in the transbilayer movement of phospholipids are also controlled through the cAMP-dependent phosphorylation pathway that results in the increase in M540 positive cells (Gadella and Harrison, 2000; Harrison and Miller, 2000). Caffeine, whether in combination with db-cAMP or not, also induced an increase in the percentage of live, M540 and Annexin-V positive cells.

With respect to the Annexin-V staining, fluorescence in the acrosome region only was more prevalent than other staining patterns in media containing bicarbonate. Gadella and Harrison (2002) previously demonstrated in boar sperm cells that Annexin V labelling was restricted to the anterior acrosomal region of the sperm head. Moreover, they demonstrated that Annexin-V labelling of the midpiece of the sperm cell was indicative of propidium iodide positive cells (dead or dying). The three staining patterns we observed for Annexin-V in stallion sperm suggest a sequential evolution of PS exposure, with the first step in membrane remodelling resulting in externalization of PS in the acrosomal region. Notably, as some Annexin-V stained cells were also labelled positively for PNA, these cells may have possessed compromised acrosome integrity, potentially allowing annexin V to interact with the inner acrosomal membrane. Thus, this could represent the second step in the evolution of PS exposure. However, the acrosomal status of these cells needs to be further examined in a quantitative manner. In accordance with the previous literature in boar sperm, the midpiece staining pattern we observed in live stallion sperm may indicate that these cells are in a final stage of PS exposure that will end in cell death if fertilization does not take place soon. This is in accordance with previous proposals that capacitation and cell death are interconnected processes in sperm cells (Aitken, 2011; Aitken and Drevet, 2020).

Contrasting the finding that a very high percentage of viable stallion spermatozoa become M540 positive in the presence of bicarbonate, with the very low percentage of viable sperm that exhibit PS exposure leads us to question whether PS exposure is a critical requirement for capacitation of stallion sperm. This is one of the first manuscripts to report on Annexin-V labelling to assess PS exposure by live imaging rather than confocal microscopy. Thus, a comparative study assessing whether PS exposure is indeed a hallmark of capacitation in other species should be performed using live cell technologies. For stallion spermatozoa, a live imaging time series will assist in understanding the sequence of Annexin-V staining patterns, and any potential link with PNA staining patterns and the acrosome reaction.

In conclusion, a large percentage of stallion spermatozoa demonstrate changes in phospholipid disorder (detected with M540) in bicarbonate containing media, whereas only a relatively small population of viable spermatozoa expose PS. The observation of three different Annexin-V staining patterns for live stallion spermatozoa may warrant further investigation with respect to whether these represent sequential steps in membrane remodelling. However, it is important to note that while this manuscript highlight potential equine-specific features, further work with direct comparative studies is required to accurately delineate species-specific effects from the effects of capacitation media and other factors that dictate the ability of stallion sperm cells to capacitate. Overall, this study reveals several intricacies of the bicarbonate-induced membrane remodelling response in stallion spermatozoa, a key finding being that this remodelling occurs despite retention of membrane sterols and all other lipid components (summarised in **Figure 8**). Further investigation into sAC inhibition and alternative cholesterol acceptors should help to further delineate key steps in the preparation of equine spermatozoa for fertilization.

DATA AVAILABILITY STATEMENT

The original contributions presented in the study are included in the article/**Supplementary Material**, further inquiries can be directed to the corresponding authors. Raw data is publicly available at the following link: https://public.yoda.uu.nl/dgk/UU01/LRWWGJ.html.

ETHICS STATEMENT

The animal study was reviewed and approved by The Institutional Animal Care and Use Committee of Utrecht University. Written informed consent was obtained from the owners for the participation of their animals in this study.

AUTHOR CONTRIBUTIONS

PM performed the experiments included in this article, wrote key sections of the draft, and analyzed the data. HH conceived the study and contributed to supervision, data analysis and interpretation, article writing, figure preparation and editing. EGB contributed to article writing, data acquisition, experiments, figure preparation and article editing, and data interpretation. ML, RH, BL, JJ, CHvL, TZ, BMG, and JG contributed to data acquisition, experiments, and/or data analysis. TAES and BMG contributed to supervision, article editing, funding acquisition, and data interpretation. All authors contributed to article edits.

FUNDING

This work was funded by Research Foundation Flanders (FWO-Flanders grant number 12I0517N) to BL; EU COST Action 16119 (CellFit) to BMG and BL and an NWO Start-Up Grant 740.018.007 to T.Zx. The authors also gratefully acknowledge the following funding bodies: CAPES (Coordenação de Aperfeiçoamento de Pessoal de Nível Superior); CNPq (Conselho Nacional de Desenvolvimento Científico e Tecnológico) and the NHMRC (National Health and Medical Research Council, Australia) for supporting the international research periods of PM and EGB at Utrecht University.

ACKNOWLEDGMENTS

The authors gratefully acknowledge Dr. Richard Wubbolts and Dr. Ger Arkesteijn for their expert assistance with live cell imaging and flow cytometry.

SUPPLEMENTARY MATERIAL

The Supplementary Material for this article can be found online at: https://www.frontiersin.org/articles/10.3389/fcell.2021.772254/full#supplementary-material

Supplementary Figure S1 | Stallion sperm membrane reorganization detected by Cryo-EM after incubation with bicarbonate. Spermatozoa were incubated either in the presence of 30 mM bicarbonate (TyrBic) or its absence (TyrControl) for 60 minutes and then FACS-sorted to inspect membrane reorganization using cryo-electron microscopy (cryo-EM). To delineate structures in the cryo-EM frames, the membranes are colour coded to indicate the plasma membrane (PM) (blue), outer acrosomal membrane (OAM) and inner acrosomal membranes (IAM) (orange). Red boxes indicate the sperm cell regions depicted in the frames. Unsorted sperm cells in TyrControl medium demonstrated an intact PM and OAM with a consistent intermembrane distance (A, B). This was also demonstrated in sorted sperm cells in TyrControl (C, D). However, frames from sorted sperm cells incubated in TyrBic reveal rupture of the OAM (E, F) and vesiculation of the PM (E) (n = 3 stallions). (G, H) Boar and stallion sperm cell secondary antibody only controls were prepared where the anti-ADCY10 antibody was replaced by 1% BSA/PBS and cells were then counterstained with Hoechst 33258 and PNA (n = 3 stallions/boars). (I) Percentage of live, M540 positive sperm in different base media with 30 mM bicarbonate (TyrBic). Media were supplemented with either 1 mM db-cAMP, 1 mM caffeine, or both to increase intracellular cAMP levels. Different small letters indicate effects of the supplements in a given medium and at a given time ($p < 0.05$). All values are presented as mean ± SD.

Supplementary Figure S2 | 58 negative) sperm was monitored in the absence or presence of KH7 KH7 has an off-target effect on sperm mitochondrial membrane potential during inhibition of sAC. Spermatozoa were incubated either in the presence of 30 mM bicarbonate (TyrBic) or its absence (TyrControl). Media contained either no further additions, DMSO (a solvent control), or increasing concentrations of KH7 to indirectly block sAC activity. An increase in plasma membrane fluidity, i.e., increased merocyanine 540 staining, in viable (Hoechst 332[**(A, B)**; n = 6 stallions]. A hash symbol (#) indicates significant differences between DMSO exposed samples and samples without any addition ($P < 0.05$). An asterisk (*) indicates significant differences between DMSO exposed samples and samples treated with KH7 ($P < 0.05$). In a subset of samples, the percentage of viable sperm with high mitochondrial transmembrane potential (MMP) was monitored with the probe JC-1 [**(C, D)**; n = 3 stallions]. Concentrations of 60 μM and 120 μM KH7 significantly reduced the percentage of sperm with high MMP compared to control samples (DMSO; $p < 0.05$).

REFERENCES

Aitken, R. J. (2011). The Capacitation-Apoptosis Highway: Oxysterols and Mammalian Sperm Function. *Biol. Reprod.* 85, 9–12. doi:10.1095/biolreprod.111.092528

Aitken, R. J., and Drevet, J. R. (2020). The Importance of Oxidative Stress in Determining the Functionality of Mammalian Spermatozoa: A Two-Edged Sword. *Antioxidants* 9 (2), 111. doi:10.3390/antiox9020111

Alm, H., Torner, H., Blottner, S., Nurnberg, G., and Kanitz, W. (2001). Effect of Sperm Cryopreservation and Treatment With Calcium Ionophore or Heparin on *In Vitro* Fertilization of Horse Oocytes. *Theriogenology* 56, 817–829. doi:10.1016/S0093-691X(01)00610-0

Austin, C. R. (1952). The 'Capacitation' of the Mammalian Sperm. *Nature* 170, 326. doi:10.1038/170326a0

Bailey, J. L. (2010). Factors Regulating Sperm Capacitation. *Syst. Biol. Reprod. Med.* 56, 334–348. doi:10.3109/19396368.2010.512377

Baxendale, R. W., and Fraser, L. R. (2003). Evidence for Multiple Distinctly Localized Adenylyl Cyclase Isoforms in Mammalian Spermatozoa. *Mol. Reprod. Dev.* 66, 181–189. doi:10.1002/mrd.10344

Boerke, A., Browers, J. F., Olkkonen, V. M., Lest, C. H. A., Sostaric, E., Schoevers, E. J., et al. (2013). Involvement of Bicarbonate-Induced Radical Signaling in Oxysterol Formation and Sterol Depletion of Capacitating Mammalian Sperm During *In Vitro* Fertilization. *Biol. Reprod.* 88, 1–18. doi:10.1095/biolreprod.112.101253

Boerke, A., Tsai, P. S., Garcia-Gil, N., Brewis, I. A., and Gadella, B. M. (2008). Capacitation Dependent Reorganization of Microdomains in the Apical Sperm Head Plasma Membrane: Functional Relationship with Zona Binding and the Zona-Induced Acrosome Reaction. *Theriogenology* 70, 1188–1196. doi:10.1016/j.theriogenology.2008.06.021

Brogan, P. T., Beitsma, M., Henning, H., Gadella, B. M., and Stout, T. A. E. (2015). Liquid Storage of Equine Semen: Assessing the Effect of D-Penicillamine on Longevity of Ejaculated and Epididymal Stallion Sperm. *Anim. Reprod. Sci.* 159, 155–162. doi:10.1016/j.anireprosci.2015.06.011

Bromfield, E. G., Aitken, R. J., Gibb, Z., Lambourne, S. R., and Nixon, B. (2014). Capacitation in the Presence of Methyl-β-Cyclodextrin Results in Enhanced Zona Pellucida-Binding Ability of Stallion Spermatozoa. *Reproduction* 147, 153–166. doi:10.1530/REP-13-0393

Browers, J. F., Boerke, A., Silva, P. F. N., Garcia-Gil, N., van Gestel, R. A., Helms, J. B., et al. (2011). Mass Spectrometric Detection of Cholesterol Oxidation in Bovine Sperm. *Biol. Reprod.* 85, 128–136. doi:10.1095/biolreprod.111.091207

Chang, M. C. (1951). Fertilizing Capacity of Spermatozoa Deposited into the Fallopian Tubes. *Nature* 168, 697–698. doi:10.1038/168697b0

Choi, Y. H., Okada, Y., Hochi, S., Braun, J., Sato, K., and Oguri, N. (1994). *In-Vitro* Fertilization Rate of Horse Oocytes with Partially Removed Zonae. *Theriogenology* 42, 795–802. doi:10.1016/0093-691X(94)90448-R

Cross, N. L. (1998). Role of Cholesterol in Sperm Capacitation. *Biol. Reprod.* 59, 7–11. doi:10.1095/biolreprod59.1.7

Cross, N. L. (2003). Decrease in Order of Human Sperm Lipids during Capacitation. *Biol. Reprod.* 69, 529–534. doi:10.1095/biolreprod.102.013052

Dell'Aquila, M. E., Cho, Y. S., Minoia, P., Traina, V., Fusco, S., Lacalandra, G. M., et al. (1997a). Intracytoplasmic Sperm Injection (ICSI) Versus Conventional IVF on Abottoir Derived and In Vitro-Matured Equine Oocytes. *Theriogenology* 47, 1139–1156. doi:10.1016/S0093-691X(97)00095-2

Dell'Aquila, M. E., Cho, Y. S., Minoia, P., Traina, V., Lacalandra, G. M., and Maritato, F. (1997b). Effects of Follicular Fluid Supplementation of *In-Vitro* Maturation Medium on the Fertilization and Development of Equine Oocytes After *In-Vitro* Fertilization or Intracytoplasmic Sperm Injection. *Hum. Reprod.* 12, 2766–2772. doi:10.1093/humrep/12.12.2766

de Vries, K. J., Wiedmer, T., Sims, P. J., and Gadella, B. M. (2003). Caspase Independent Exposure of Aminophospholipids and Tyrosine Phosphorylation in Bicarbonate Responsive Human Sperm Cells. *Biol. Reprod.* 68, 2122–2134. doi:10.1095/biolreprod.102.012500

Evans, J. P., and Florman, H. M. (2002). The State of the union: the Cell Biology of Fertilization. *Nat. Cel. Biol.* 4, S57–S63. doi:10.1038/nm-fertilitys5710.1038/ncb-nm-fertilitys57

Flesch, F. M., and Gadella, B. M. (2000). Dynamics of the Mammalian Sperm Plasma Membrane in the Process of Fertilization. *Biochim. Biophys. Acta (Bba) - Rev. Biomembranes* 1469, 197–235. doi:10.1016/s0304-4157(00)00018-6

Fraser, L. R. (1981). Dibutyryl Cyclic AMP Decreases Capacitation Time *In Vitro* in Mouse Spermatozoa. *Reproduction* 62, 63–72. doi:10.1530/jrf.0.0620063

Gadella, B. M., and Harrison, R. A. P. (2000). The Capacitating Agent Bicarbonate Induces Protein Kinase A-dependent Changes in Phospholipid Transbilayer Behavior in the Sperm Plasma Membrane. *Development* 127, 2407–2420. doi:10.1242/dev.127.11.2407

Gadella, B. M., and Harrison, R. A. P. (2002). Capacitation Induces Cyclic Adenosine 3′,5′-monophosphate-dependent, but Apoptosis-Unrelated, Exposure of Aminophospholipids at the Apical Head Plasma Membrane of Boar Sperm Cells. *Biol. Reprod.* 67, 340–350. doi:10.1095/biolreprod67.1.340

Gervasi, M. G., and Visconti, P. E. (2016). Chang's Meaning of Capacitation: A Molecular Perspective. *Mol. Reprod. Dev.* 83, 860–874. doi:10.1002/mrd.22663

Harrison, R. (1996). Capacitation Mechanisms, and the Role of Capacitation as Seen in Eutherian Mammals. *Reprod. Fertil. Dev.* 8, 581–594. doi:10.1071/RD9960581

Harrison, R. A. P., Mairet, B., and Miller, N. G. A. (1993). Flow Cytometric Studies of Bicarbonate-Mediated Ca2+ Influx in Boar Sperm Populations. *Mol. Reprod. Dev.* 35, 197–208. doi:10.1002/mrd.1080350214

Harrison, R. A. P., and Miller, N. G. A. (2000). Camp-dependent Protein Kinase Control of Plasma Membrane Lipid Architecture in Boar Sperm. *Mol. Reprod. Dev.* 55, 220–228. doi:10.1002/(SICI)1098-2795(200002)55:2<220:AID-MRD12>3.0.CO;2-I

Hess, K. C., Jones, B. H., Marquez, B., Chen, Y., Ord, T. S., Kamenetsky, M., et al. (2005). The "soluble" Adenylyl Cyclase in Sperm Mediates Multiple Signaling Events Required for Fertilization. *Dev. Cel.* 9, 249–259. doi:10.1016/j.devcel.2005.06.007

Hinrichs, K., Love, C. C., Brinsko, S. P., Choi, Y. H., and Varner, D. D. (2002). *In Vitro* Fertilization of In Vitro-Matured Equine Oocytes: Effect of Maturation Medium, Duration of Maturation, and Sperm Calcium Ionophore Treatment, and Comparison with Rates of Fertilization *In Vivo* after Oviductal Transfer. *Biol. Reprod.* 67, 256–262. doi:10.1095/biolreprod67.1.256

Ho, H., and Suarez, S. (2001). Hyperactivation of Mammalian Spermatozoa: Function and Regulation. *Reproduction* 122, 519–526. doi:10.1530/rep.0.1220519

Jakobsen, E., Lange, S. C., Andersen, J. V., Desler, C., Kihl, H. F., Hohnholt, M. C., et al. (2018). The Inhibitors of Soluble Adenylate Cyclase 2-OHE, KH7, and Bithionol Compromise Mitochondrial ATP Production by Distinct Mechanisms. *Biochem. Pharmacol.* 155, 92–101. doi:10.1016/j.bcp.2018.06.023

Kurz, A., Viertel, D., Herrmann, A., and Müller, K. (2005). Localization of Phosphatidylserine in Boar Sperm Cell Membranes During Capacitation and Acrosome Reaction. *Reproduction* 130, 615–626. doi:10.1530/rep.1.00561

Leemans, B., Stout, T. A. E., De Schauwer, C., Heras, S., Nelis, H., Hoogewijs, M., et al. (2019b). Update on Mammalian Sperm Capacitation: How Much Does the Horse Differ from Other Species? *Reproduction* 157, R181–R197. doi:10.1530/rep-18-0541

Leemans, B., Stout, T. A. E., Soom, A. V., and Gadella, B. M. (2019a). pH-dependent Effects of Procaine on Equine Gamete Activation. *Biol. Reprod.* 101, 1056–1074. doi:10.1093/biolre/ioz131

Lefièvre, L., de Lamirande, E., and Gagnon, C. (2000). The Cyclic GMP-specific Phosphodiesterase Inhibitor, Sildenafil, Stimulates Human Sperm Motility and Capacitation but Not Acrosome Reaction. *J. Androl.* 21, 929–937. doi:10.1002/j.1939-4640.2000.tb03424.xj

Macías-García, B., Gonzalez-Fernandez, L., Loux, S.C., Rocha, A.M., Guimarães, T., Pena, F.J., et al. (2015). Effect of Calcium, Bicarbonate, and Albumin on Capacitation-Related Events in Equine Sperm. *Reproduction* 149, 87–99. doi:10.1530/REP-14-0457

Maitan, P., Bromfield, E. G., Stout, T. A. E., Gadella, B. M., and Leemans, B. (2021). A Stallion Spermatozoon's Journey through the Mare's Genital Tract: *In Vivo* and *In Vitro* Aspects of Sperm Capacitation. *Ani. Repro. Sci.* 14 106848 doi:10.1016/j.anireprosci.2021.106848

Mcpartlin, L. A., Visconti, P. E., and Bedford-Guaus, S. J. (2011). Guanine-Nucleotide Exchange Factors (RAPGEF3/RAPGEF4) Induce Sperm Membrane Depolarization and Acrosoma Exocytosis in Capacitated Stallion Sperm. *Biol. Reprod.* 85, 179–188. doi:10.1095/biolreprod.110.085555

Molenaar, M. R., Jeucken, A., Wassenaar, T. A., van de Lest, C. H. A., Brouwers, J. F., and Helms, J. B. (2019). LION/web: A Web-Based Ontology Enrichment Tool for Lipidomic Data Analysis. *Gigascience* 8, 1–10. doi:10.1093/gigascience/giz061

Mugnier, S., Kervella, M., Douet, C., Canepa, S., Pascal, G., Deleuze, S., et al. (2009). The Secretions of Oviduct Epithelial Cells Increase the Equine *In Vitro* Fertilization Rate: Are Osteopontin, Atrial Natriuretic Peptide A and Oviductin Involved? *Reprod. Biol. Endocrinol.* 7, 129. doi:10.1186/1477-7827-7-129

Nelson, D. L., and Cox, M. M. (2004). *Lehninger Principles of Biochemistry*. 4th ed. W. H. Freeman.

O'Flaherty, C., de Lamirande, E., and Gagnon, C. (2004). Phosphorylation of the Arginine-X-X-(Serine/Threonine) Motif in Human Sperm Proteins during Capacitation: Modulation and Protein Kinase A Dependency. *Mol. Hum. Reprod.* 10, 355–363. doi:10.1093/molehr/gah046

Osheroff, J. E., Visconti, P. E., Valenzuela, J. P., Travis, A. J., Alvarez, J., and Kopf, G. S. (1999). Regulation of Human Sperm Capacitation by a Cholesterol Efflux-Stimulated Signal Transduction Pathway Leading to Protein Kinase A-Mediated Up-Regulation of Protein Tyrosine Phosphorylation. *Mol. Hum. Reprod.* 5, 1017–1026. doi:10.1093/molehr/5.11.1017

Palmer, E., Bézard, J., Magistrini, M., and Duchamp, G. (1991). *In Vitro* fertilization in the Horse. A Retrospective Study. *J. Reprod. Fertil. Suppl.* 44, 375–384.

Parrish, J. J., Susko-Parrish, J., Winer, M. A., and First, N. L. (1988). Capacitation of Bovine Sperm by Heparin. *Biol. Reprod.* 38, 1171–1180. doi:10.1095/biolreprod38.5.1171

Ramos-Espiritu, L., Kleinboelting, S., Navarrete, F. A., Alvau, A., Visconti, P. E., Valsecchi, F., et al. (2016). Discovery of LRE1 as a Specific and Allosteric Inhibitor of Soluble Adenylyl Cyclase. *Nat. Chem. Biol.* 12, 838–844. doi:10.1038/nchembio.2151

Rathi, R., Colenbrander, B., Bevers, M. M., and Gadella, B. M. (2001). Evaluation of *In Vitro* Capacitation of Stallion Spermatozoa. *Biol. Reprod.* 65, 462–470. doi:10.1095/biolreprod65.2.462

Saling, P. M., and Storey, B. T. (1979). Mouse Gamete Interactions during Fertilization *In Vitro*. Chlortetracycline as a Fluorescent Probe for the Mouse Sperm Acrosome Reaction. *J. Cel. Biol.* 83, 544–555. doi:10.1083/jcb.83.3.544

Saling, P. M., Storey, B. T., and Wolf, D. P. (1978). Calcium-dependent Binding of Mouse Epididymal Spermatozoa to the Zona Pellucida. *Dev. Biol.* 65, 515–525. doi:10.1016/0012-1606(78)90046-5

Schindelin, J., Arganda-Carreras, I., Frise, E., Kaynig, V., Longair, M., Pietzsch, T., et al. (2012). Fiji: An Open-Source Platform for Biological-Image Analysis. *Nat. Methods* 9, 676–682. doi:10.1038/nmeth.2019

Spehr, M., Schwane, K., Riffell, J. A., Barbour, J., Zimmer, R. K., Neuhaus, E. M., et al. (2004). Particulate Adenylate Cyclase Plays a Key Role in Human Sperm Olfactory Receptor-Mediated Chemotaxis. *J. Biol. Chem.* 279, 40194–40203. doi:10.1074/jbc.M403913200

Steckler, D., Stout, T. A. E., Durandt, C., and Nöthling, J. O. (2015). Validation of Merocyanine 540 Staining as a Technique for Assessing Capacitation-Related Membrane Destabilization of Fresh Dog Sperm. *Theriogenology* 83, 1451–1460. doi:10.1016/j.theriogenology.2015.01.019

Stephens, T. D., Brooks, R. M., Carrington, J. L., Cheng, L., Carrington, A. C., Porr, C. A., et al. (2013). Effects of Pentoxifylline, Caffeine, and Taurine on post-thaw Motility and Longevity of Equine Frozen Semen. *J. Equine Vet. Sci.* 33, 615–621. doi:10.1016/j.jevs.2012.10.004

Stout, T. A. E., and Griffiths, H. (2021). Clinical Insights: Assisted Reproductive Techniques: More Than a Solution to Subfertility? *Equine Vet. J.* 53, 1084–1087. doi:10.1111/evj.13510

Tardif, S., Lefièvre, L., Gagnon, C., and Bailey, J. L. (2004). Implication of cAMP during Porcine Sperm Capacitation and Protein Tyrosine Phosphorylation. *Mol. Reprod. Dev.* 69, 428–435. doi:10.1002/mrd.20178

Topper, E. K., Killian, G. J., Way, A., Engel, B., and Woelders, H. (1999). Influence of Capacitation and Fluids from the Male and Female Genital Tract on the Zona Binding Ability of Bull Spermatozoa. *Reproduction* 115, 175–183. doi:10.1530/jrf.0.1150175

Tremoleda, J. L., Stout, T., Gadella, B. M., and Colenbrander, B. (2003). Sperm-oocyte Interaction during *In Vitro* Fertilization in the Horse. *Reprod. Fert. Dev.* 16, 263. doi:10.1071/rdv16n1ab286

Uguz, C., Vredenburgh, W. L., and Parrish, J. J. (1994). Heparin-Induced Capacitation but Not Intracellular Alkalinization of Bovine Sperm Is Inhibited by Rp-Adenosine-3′,5′-Cyclic Monophosphorothioate. *Biol. Reprod.* 51, 1031–1039. doi:10.1095/biolreprod51.5.1031

Visconti, P. E., Bailey, J. L., Moore, G. D., Pan, D., Olds-clarke, P., and Kopf, G. S. (1995a). Capacitation of Mouse Spermatozoa. I. Correlation between the Capacitation State and Protein Tyrosine Phosphorylation. *Development* 121, 1129–1137. doi:10.1242/dev.121.4.1129

Visconti, P. E., Moore, G. D., Bailey, J. L., Leclerc, P., Connors, S. A., Pan, D., et al. (1995b). Capacitation of Mouse Spermatozoa. II. Protein Tyrosine Phosphorylation and Capacitation Are Regulated by a cAMP-dependent Pathway. *Development* 121, 1139–1150. doi:10.1242/dev.121.4.1139

Wertheimer, E., Krapf, D., De La Vega-Beltran, J. L., Sánchez-Cárdenas, C., Navarrete, F., Haddad, D., et al. (2013). Compartmentalization of Distinct CAMP Signaling Pathways in Mammalian Sperm. *J. Biol. Chem.* 288, 35307–35320. doi:10.1074/jbc.M113.489476

Williamson, P., and Schlegel, R. A. (1994). Back and Forth: The Regulation and Function of Transbilayer Phospholipid Movement in Eukaryotic Cells. *Mol. Membr. Biol.* 11, 199–216. doi:10.3109/09687689409160430

Conflict of Interest: The authors declare that the research was conducted in the absence of any commercial or financial relationships that could be construed as a potential conflict of interest.

Publisher's Note: All claims expressed in this article are solely those of the authors and do not necessarily represent those of their affiliated organizations, or those of the publisher, the editors and the reviewers. Any product that may be evaluated in this article, or claim that may be made by its manufacturer, is not guaranteed or endorsed by the publisher.

Copyright © 2021 Maitan, Bromfield, Hoogendijk, Leung, Zeev-Ben-Mordehai, van de Lest, Jansen, Leemans, Guimarães, Stout, Gadella and Henning. This is an open-access article distributed under the terms of the Creative Commons Attribution License (CC BY). The use, distribution or reproduction in other forums is permitted, provided the original author(s) and the copyright owner(s) are credited and that the original publication in this journal is cited, in accordance with accepted academic practice. No use, distribution or reproduction is permitted which does not comply with these terms.

frontiers | Frontiers in Cell and Developmental Biology

ORIGINAL RESEARCH
published: 25 April 2022
doi: 10.3389/fcell.2022.757042

TMPRSS12 Functions in Meiosis and Spermiogenesis and Is Required for Male Fertility in Mice

*Jingjing Zhang[1,2†], Xinli Zhou[1†], Danyang Wan[1], Li Yu[1], Xu Chen[1], Tong Yan[1], Zhu Wu[1], Meimei Zheng[1,3], Feng Zhu[1,4] and Hui Zhu[1]**

[1]State Key Laboratory of Reproductive Medicine, Department of Histology and Embryology, Nanjing Medical University, Nanjing, China, [2]Department of Prenatal Diagnosis, Women's Hospital of Nanjing Medical University, Nanjing Maternity and Child Health Care Hospital, Nanjing, China, [3]Reproductive Medicine Center of No. 960 Hospital of PLA, Jinan, China, [4]Department of Pathology, The First People's Hospital of Changzhou, Changzhou, China

Serine proteases are involved in many physiological activities as initiators of proteolytic cascades, and some members have been reported to play roles in male reproduction. Transmembrane serine protease 12 (TMPRSS12) has been shown to regulate sperm motility and uterotubal junction migration in mice, but its role in the testis remains unknown. In this study, we verified that TMPRSS12 was expressed in the spermatocytes and spermatids of testis and the acrosome of sperm. Mice deficient in *Tmprss12* exhibited male sterility. In meiosis, TMPRSS12 was demonstrated to regulate synapsis and double-strand break repair; spermatocytes of *Tmprss12*$^{-/-}$ mice underwent impaired meiosis and subsequent apoptosis, resulting in reduced sperm counts. During spermiogenesis, TMPRSS12 was found to function in the development of mitochondria; abnormal mitochondrial structure in *Tmprss12*$^{-/-}$ sperm led to reduced availability of ATP, impacting sperm motility. The differential protein expression profiles of testes in *Tmprss12*$^{-/-}$ and wild-type mice and further molecule identification revealed potential targets of TMPRSS12 related to meiosis and mitochondrial function. Besides, TMPRSS12 was also found to be involved in a series of sperm functions, including capacitation, acrosome reaction and sperm-egg interaction. These data imply that TMPRSS12 plays a role in multiple aspects of male reproduction.

Keywords: TMPRSS12, meiosis, spermiogenesis, serine protease, male infertility

OPEN ACCESS

Edited by:
Chih-kuan Tung, North Carolina Agricultural and Technical State University, United States

Reviewed by:
Srinivasan Vijayaraghavan, Kent State University, United States
Fei Sun, Shanghai Jiao Tong University, China

****Correspondence:***
Hui Zhu
njzhuhui@njmu.edu.cn

†These authors have contributed equally to this work and share first authorship

Specialty section:
This article was submitted to Cell Growth and Division, a section of the journal Frontiers in Cell and Developmental Biology

Received: *11 August 2021*
Accepted: *05 April 2022*
Published: *25 April 2022*

Citation:
Zhang J, Zhou X, Wan D, Yu L, Chen X, Yan T, Wu Z, Zheng M, Zhu F and Zhu H (2022) TMPRSS12 Functions in Meiosis and Spermiogenesis and Is Required for Male Fertility in Mice. Front. Cell Dev. Biol. 10:757042. doi: 10.3389/fcell.2022.757042

INTRODUCTION

Sperm are the ultimate executors of male reproduction, and a sufficient quantity and quality of sperm guarantee male fertility. Sperm production in the testis, i.e., spermatogenesis, involves spermatogonia self-renewal, spermatocyte meiosis and spermatid differentiation (spermiogenesis), which ultimately form sperm with appropriate morphology, structure, and molecular reserve (Neto et al., 2016). These sperm are then released into the epididymis for further functional maturation. The generation and functional maturation of sperm necessitate a large number of proteins expressed in a certain time sequence and in a specific way to participate or play a regulatory role.

Proteases have attracted the attention of researchers, and they cleave peptide bonds to activate protein precursors and produce various active peptides or functional proteins, which further participate in different physiological processes (Barrett et al., 2001; Barrett, 2004; Chalmel and Rolland, 2015). One of the representatives is serine proteases (PRSSs), which account for

approximately one-third of all known proteases (Hedstrom, 2002). Among PRSSs, trypsin-like serine proteases are the largest group, and they are responsible for numerous biological processes, such as digestion, haemostasis, apoptosis, signal transduction, reproduction, and immune response (Hedstrom, 2002; Page and Di Cera, 2008). Many trypsin-like serine proteases have been demonstrated to play important roles in spermatogenesis and/or sperm function. For example, PRSS41, PRSS42 and PRSS43 are involved in spermatocyte meiosis and germ cell apoptosis (Yoneda et al., 2013; Yoneda and Kimura, 2013). PRSS55 is essential for the structural differentiation and energy metabolism of sperm (Shang et al., 2018; Kobayashi et al., 2020; Zhu et al., 2021). PRSS37 affects sperm migration from the uterus into the oviduct and sperm-zona binding (Shen B. et al., 2013).

We focused on a special trypsin-like serine protease, transmembrane serine protease (TMPRSS). Besides a trypsin-like serine protease domain that is essential for catalysis, TMPRSS also contains a transmembrane structure that functions in signal transduction (Hooper et al., 2001). Although the identified TMPRSS members and their reports are far fewer than those of PRSS, the potential role of TMPRSSs in physiology and pathology has been shown (Antalis et al., 2011). Most of the known TMPRSS members are expressed in specific tissues, and their functions have obvious tissue specificity. For example, TMPRSS3 is predominantly expressed in the inner ear. Cell membrane-bound TMRPSS3 is an essential component for hair cell homeostasis and survival, and mutation of the *Tmprss3* gene can cause nonsyndromic recessive deafness (Guipponi et al., 2008; Fasquelle et al., 2011). TMPRSS6 is expressed in the liver and plays an essential role in regulating the expression of the main regulator of iron homeostasis hepcidin; mutations in *Tmprss6* induce high hepcidin levels, which cause iron-refractory iron deficiency anemia (Finberg et al., 2008; Nai et al., 2016; Al-Jamea et al., 2021). TMPRSS10 is most abundant in cardiac myocytes of the atrium and activates atrial natriuretic peptide (ANP) to regulate blood pressure, and deficiency in TMPRSS10 is reported to cause spontaneous hypertension (Yan et al., 2000; Li B. et al., 2017). These results indicate that TMPRSS members specifically expressed in the testis are very likely to be important for spermatogenesis and male reproduction.

To gain insights into the complicated protein networks involved in spermatogenesis and sperm function, human testis and human sperm proteome databases were constructed in our laboratory through the use of a proteomic research platform, and many novel candidate spermatogenesis-/sperm function-related proteins were obtained (Liu et al., 2013; Wang et al., 2013). The TMPRSS family member TMPRSS12 was identified in both the testis and sperm protein profiles, suggesting its potential important role in testicular spermatogenesis and sperm function. According to recently published transcriptomic data, *Tmprss12* was exclusively expressed in testis tissue and located from spermatocytes to round spermatids (da Cruz et al., 2016; Li H. et al., 2017). In addition, we identified 2 heterozygous mutations (c.634G > C [p. Gly212Arg]) in 300 unrelated infertile men with dyszoospermia, and the mutation site was predicted to be potentially deleterious by searching the Polyphen2 and SIFT databases (**Supplementary Figure 1**). All these results indicated a relationship between TMPRSS12 and male reproduction.

Larasati et al. first explored the function of TMPRSS12 using a *Tmprss12* knockout (KO) mouse model, and they found that *Tmprss12*$^{-/-}$ mice were male sterile and demonstrated that TMPRSS12 regulated sperm motility and ADAM3-related sperm migration to the oviduct (Larasati et al., 2020). The above study focused on the effect of TMPRSS12 on sperm function. Nevertheless, *Tmprss12* expression begins at the stage of zygotene spermatocytes in the testis according to the report of Larasati et al., which is consistent with the reported expressive feature of *Tmprss12* obtained by transcriptome sequencing (da Cruz et al., 2016; Li B. et al., 2017). Thus, TMPRSS12 might function in spermatogenesis. Therefore, our study aimed to use *Tmprss12*$^{-/-}$ mice to reveal the function and mechanism of TMPRSS12 in spermatogenesis. Our results provide detailed information that TMPRSS12 affects spermatogenesis, which elucidate the role of TMPRSS12 in male reproduction more comprehensively.

MATERIALS AND METHODS

Animals

Tmprss12$^{-/-}$ mice were generated on the C57BL/6 background via Cas9/RNA-mediated gene targeting as described previously (Shen C. et al., 2013). All the mice were housed under specific pathogen free condition with unlimited access to food and water. The constant room was maintained at the temperature of 22–24°C with a light:dark cycle of 12:12. All the research involving animal experiments were approved by the ethics committees of Nanjing Medical University.

RNA Isolation, cDNA Synthesized, PCR and Quantitative Real-Time PCR Analyses

Total RNA was extracted from the sample by using Trizol reagent (Invitrogen, 15596-026) according to the manufacturer's instructions. mRNA was reverse transcribed to cDNA using HiScript II Q Select RT SuperMix for qPCR (Vazyme, R232-01). PCR (polymerase chain reaction) was performed using 2 × Taq Plus Master Mix (Vazyme, P212-01), with primers specific for mouse *Tmprss12*. The PCR products were analyzed by agarose gel electrophoresis using mouse *Actin* as an internal control. Quantitative real-time PCR of cDNA was carried out using AceQ qPCR SYBR Green Master Mix (Vazyme, Q141-02) according to the manufacturer's instructions with an ABI Q5 real-time PCR System (Applied Biosystems, Thermo Fisher Scientific). The primer sequences used for these experiments are listed in **Supplementary Table 1**.

Western Blot Analysis

Protein extracts from mouse tissues or sperms were separated on 10% SDS-PAGE gels and transferred onto nitrocellulose membranes (Bio-Rad, 1620177). Membranes were blocked

with 5% nonfat milk and then incubated overnight with the primary antibodies: anti-TMPRSS12 (Santa Cruz Biotechnology, sc-249059; 1:500), anti-TEKTIN-T (Proteintech, 13518-1-AP; 1: 500), anti-IQCG (Bioss, bs-9022R; 1:500), anti-CLIP170 (Proteintech, 23839-1-AP; 1:2,000), anti-MEIG1 (Bioss, bs-18778R; 1:500), anti-AGFG1 (ZENBIO, 513500; 1:1,000), anti-KLC3 (Santa Cruz Biotechnology, sc-398332E-7; 1:500), anti-COX2 (ZENBIO, 381136; 1:1,000), anti-COX3 (ZENBIO, 381270; 1:1,000), anti-MTATP (Proteintech, 55313-AP; 1:500), anti-MTCYB (Proteintech, 55090-1-AP; 1:500), anti-BAX (Proteintech, 50599-2-Ig; 1:5,000), anti-BCL2 (Proteintech, 12789-1-AP; 1: 2,000), anti-CASPASE3 (Proteintech, 19677-1-AP; 1:1,000), anti-HELLS (Abclonal, A5831; 1:1,000), anti-RAD51 (Abclonal, A6268; 1:500), anti-BCCIP (Abclonal, A8586; 1:500), anti-MGST1 (Abclonal, A16399; 1:1,000), anti-PGAM2 (Abclonal, A7917; 1:1,000), anti-β-ACTIN (Biogot, AP0060; 1:10,000), anti-α-TUBULIN (Biogot, BS1482M; 1: 10,000). The washed membranes were incubated with the secondary antibodies according to the appropriate concentration. The specific protein bands were detected by an ECL kit (Thermo, 32109) and Bio-Rad gel imaging system.

Assessment of Fertility

Three adult *Tmprss12*$^{-/-}$ mice and wild-type (WT) mice were used for fertility tests. Each male was matched with two females. Male and female mice were paired in this manner for 6 months and the number of live-born pups for each pairing was recorded.

Computer Assisted Sperm Analysis

The sperm count and motility was quantified by Computer Assisted Sperm Analysis detection with the IVOS II™ system (Hamilton Thorne, United States). Briefly, sperm from *Tmprss12*$^{-/-}$ and WT mice were extracted from the cauda epididymis and incubated in human tubal fluid (HTF) culture medium (Easy Check, M1130) at 37°C. The sperm suspension was added to a counting chamber for analysis.

Histological Analysis

Testes from adult mice were fixed in modified Davidson's fluid, embedded in paraffin and cut into 5-μm sections. Periodic acid-Schiff (PAS) staining was performed for testis sections according to the manufacturer's protocol (Thermo, 87007) to determine the stage of spermatogenesis. Each stage with a distinct ordering of cell associations along the length of the seminiferous tubules was designated by Roman numerals, and approximately 200 tubules from each section were analyzed under microscopy (ZEISS, Germany). For sperm morphology analysis, sperm was washed three times in phosphate buffered saline (PBS) and transferred to slides. After immobilization with 4% PFA, sperm was stained with hematoxylin-eosin (HE) (Beyotime, C0105S). At least 200 sperm cells were analyzed per sample.

Immunofluorescence Analysis

The prepared sections were blocked in 1% bovine serum album for 2 hours and then incubated with the goat polyclonal anti-TMPRSS12 (1:100, sc-249059; Santa Cruz Biotechnology) overnight at 4°C. The sections were incubated with fluorescently labeled secondary antibodies at room temperature for 2 h. After being counterstained with DAPI, the slides were viewed with a LSM700 confocal microscope (Zeiss, Germany).

Terminal Deoxynucleotidyl Transferase dUTP Nick End Labeling Assays

Apoptosis detection of spermatogenic tubules and cells was conducted using a terminal deoxynucleotidyl transferase nick-end labeling (TUNEL) BrightRed Apoptosis Detection Kit (Vazyme, A113-01), following the manufacturer's directions. Briefly, the testis sections were equilibrated with TdT buffer for 20 min at room temperature. TdT buffer was removed and terminal transferase reaction mix was added. The reaction was performed for 1 h at 37°C. Sections were washed with PBS and then counterstained with DAPI. Slides were viewed under a LSM700 confocal microscope (Zeiss, Germany).

MI Chromosome Spread

Chromosome spreads of prophase I spermatocytes were performed as previously described (Peters et al., 1997; Kolas et al., 2005). In brief, seminiferous tubules were separated, cut into pieces with scissors, and incubated in hypotonic buffer (0.45% NaCl) for 40 min. Cell suspensions were fixed with 1% paraformaldehyde containing 0.15% Triton X-100 and 0.5 M sodium borate and then air-dried on slides. Samples were blocked with 1x ADB (1% normal donkey serum, 0.03% BSA, and 0.05% Triton X-100) for 1 h and then incubated with primary antibodies at 37°C for 12–16 h. After being blocked with 1x ADB for 5–6 h at room temperature, the samples incubated in fluorescently labeled secondary antibodies at 37 °C for 1.5 h. The slides were viewed under a LSM700 confocal microscope (Zeiss, Germany). Primary antibodies were as follows: SYCP1 (1:100, NB300-229; Novus Biologicals), SYCP3 (1:500, ab97672; Abcam), γH2AX (1:500, ab2893; Abcam).

Electron Microscopy Observation

Sperm samples separated from cauda epididymis were fixed in 0.1 M phosphate buffer (pH7.3) containing 2.5% glutaraldehyde and 4% (vol/vol) glutaraldehyde with 2% (wt/vol) OsO4 and then embedded in Araldite. Transmission electron microscopy was performed by the Electron Microscopy Laboratory of Nanjing Medical University. Transmission electron microscopy imaging was conducted on a JEM-1010 transmission electron microscope (JEOL, United States, Inc.).

Sperm ATP Assay

According to the manufacturer's instructions (Beyotime, S0027), sperm samples were washed twice, resuspended in lysis buffer, vortexed and then placed on ice. ATP was measured by luminometric methods using commercially available luciferin/luciferase reagents in luminometer (TD-20/20, Turner Designs). An average of 5×10^7 sperm were used for ATP analysis.

Mitochondrial Membrane Potential Assay

The JC-1 mitochondrial membrane potential detection kit (Beyotime, C2003S) was used to determinate the MMP.

Briefly, sperm were incubated with JC-1 staining working fluid in the dark at 37°C for 20 min. After washed by PBS, the sperms were analyzed by an LSM700 confocal microscope (Zeiss, Germany) and flow cytometer. JC-1 monomers give green fluorescence while JC-1 aggregates produce red fluorescence. MMP was analyzed by relative ratio of red/green fluorescence.

Assays of Extracellular Acidification and Oxygen Consumption

Extracellular acidification and oxygen consumption were analysed by a glycolysis assay kit (Abcam, ab197244) and extracellular oxygen consumption assay kit (Abcam, ab197243), respectively, according to the manufacturer's instructions. Briefly, sperm were plated at 50,000 cells per well in a 96-well plate, and then test reagent was added to the sample wells. For the oxygen consumption assay, two drops of prewarmed high-sensitivity mineral oil were added to each well before measurement. Fluorescence (Ex 360 nm Em 620 nm for the extracellular acidification assay; Ex 380 nm Em 645 nm for the oxygen consumption assay) was measured every 6 min for 1 h by using a microplate reader (BioTek Synergy Mx, United States).

2-D Gel Electrophoresis Combined with Matrix-Assisted Laser Desorption/ Ionization Time-of-Flight Tandem Mass Spectrometry (MALDI-TOF/TOF MS/MS)

Testes proteins were extracted from WT and *Tmprss12*$^{-/-}$ mice in lysis buffer. The protein was loaded and separated by gel rehydration on 24-cm immobilized, PH3-10, nonlinear gradient strips for 2-D according to the previously described (Guo et al., 2010). After isoelectric focusing carried out in an IPGphor apparatus (GE Healthcare, San Francisco, CA, United States), the samples for second-dimension were separated in 12% polyacrylamide gels by an Ettan-Dalt 6 system (GE Healthcare). Subsequently, the gels were stained with silver staining. The sliver-stained gels were scanned and analyzed using 2D Elite Image Master software (GE Healthcare). The protein spots, which were shown >2-fold difference ($p < 0.05$, Student's *t*-test) between WT and *Tmprss12*$^{-/-}$ testes, were excised, dehydrated in ACN, and dried at room temperature. The protein spots were digested according to our previous described (Guo et al., 2010). The digests were immediately spotted onto 400-μm anchor chips (Bruker Daltonics). The protein spots were subsequently subjected to identification by MALDI-TOF/TOF analysis. All the samples were analyzed in a time-of-flight Biflex IV mass spectrometer (Bruker Daltonics). Tandem mass spectra were given by an Ultraflex II mass spectrometer (Bruker Daltonics) in LIFT mode and processed using FlexAnalysis software (version 2.4; Bruker Daltonics). Each acquired tandem mass spectrometry (MS/MS) queries were performed using the Mascot (version 2.1, Matrix Science, London, United Kingdom) search engine in the Uniport-House mouse database. All MS/MS identifications by Mascot were manually verified for spectral quality and y and b ion series matches.

Statistical Analysis

All experiments were repeated at least three times. Significance was tested by using Two-way ANOVA or Student's *t* test using Prism software (GraphPad Software, La Jolla, CA, United States). Values of $p < 0.05$ were considered to be statistically significant. All data are reported as means ± the standard deviation of the mean (SD).

RESULTS

TMPRSS12 Is Specifically Expressed in Testicular Spermatocytes and Spermatids as Well as Sperm

The expression of *Tmprss12* was assayed by RT-PCR performed with 11 mouse tissues, including heart, liver, spleen, lung, kidney, brain, muscle, testis, epididymis, uterus and ovary tissues. As shown in **Figure 1A**, *Tmprss12* was exclusively expressed in testis tissue. By PCR and western blot detection, we found at the mRNA and protein levels that TMPRSS12 was first detected in the testes of 10-day-old mice, and its expression remained constant after 14 days of age (**Figures 1B,C**). We further detected the expression characteristics of TMPRSS12 in mouse testes by immunofluorescence analysis. The results demonstrated TMPRSS12 expression in germ cells within the seminiferous tubules and showed that its expression was initiated from spermatocytes and remained until step 12 elongated spermatids (**Figure 1D**). We also confirmed the expression of TMPRSS12 in mature sperm by PCR and western blot analysis (**Figures 1E,F**), and the immunofluorescence results showed positive signals of TMPRSS12 located in the acrosome (**Figure 1G**). The above results suggested the potential important role of TMPRSS12 in male reproductive function, which very likely influenced meiosis, spermiogenesis and acrosome-related sperm function.

Targeted Disruption of TMPRSS12 Results in Male Infertility

To investigate whether TMPRSS12 is required for male fertility, *Tmprss12* knockout mice were generated using the CRISPR/Cas9 system. The injection of a single guide RNA targeting *Tmprss12* exon 2 produced knockout mice harbouring a 2-bp deletion. A representative image of the Sanger sequencing results for the verification of the *Tmprss12*$^{-/-}$ mouse is shown in **Figure 2A**. We confirmed the lack of TMPRSS12 in the testes and sperm of *Tmprss12*$^{-/-}$ mice by western blot and immunofluorescence assays (**Figures 2B–D**).

Mating tests were performed and continuous monitoring was conducted for 6 months to analyse the fertility of the mice. The female *Tmprss12*$^{-/-}$ mice were fertile with litter sizes comparable to those of WT females. However, *Tmprss12*$^{-/-}$ males were infertile and produced no litters (**Figure 2E**). These results suggest that TMPRSS12 is required for male reproduction.

Tmprss12$^{-/-}$ Mice Have Decreased Sperm Count and Reduced Sperm Motility

To explore the possible reasons for infertility in *Tmprss12*$^{-/-}$ mice, we first detected the sperm parameter by Computer

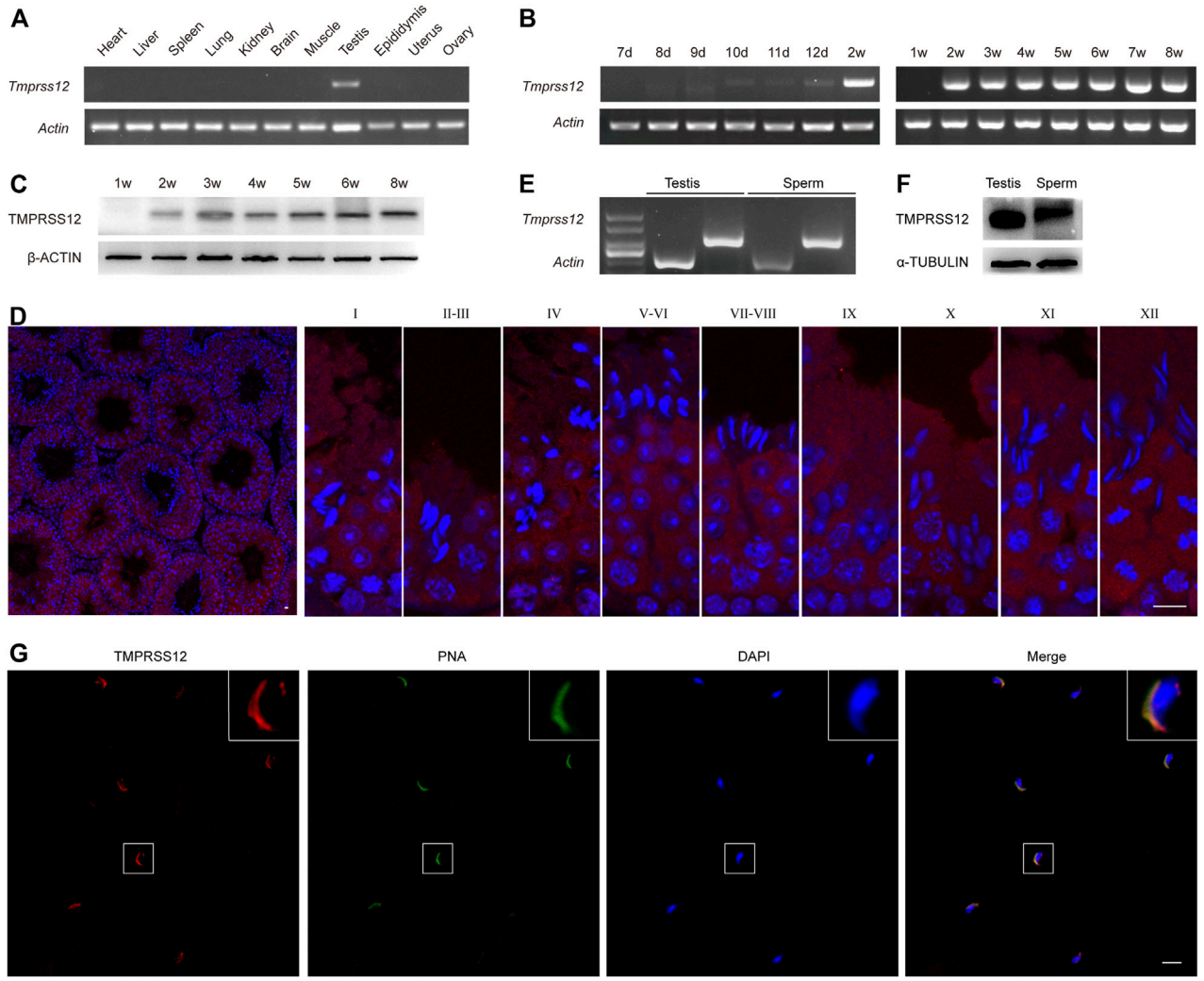

FIGURE 1 | TMPRSS12 is expressed in testicular spermatocytes and spermatids as well as sperm. **(A)** Expression of *Tmprss12* mRNA in various tissues from adult mice was detected by RT-PCR. TMPRSS12 was specifically expressed in the testis. *Actin* was used as an internal control. **(B)** Expression of testicular *Tmprss12* mRNA at the indicated time points after birth was examined by RT-PCR, showing that its expression first appeared in 10-day-old mice. *Actin* was used as an internal control. **(C)** Western blot of TMPRSS12 from the testes of mice at different weeks of age. TMPRSS12 was observed in 2-week-old mice and continued until adulthood. β-ACTIN was used as an internal control. **(D)** Immunofluorescence staining of testis sections from adult mice for TMPRSS12 (red), with nuclei counterstained by DAPI (blue). Each image exhibits a stage of the seminiferous epithelial cycle, and they are denoted by Roman numerals at the top of each image. The expression of TMPRSS12 initiated from spermatocytes and remained until step 12 elongated spermatids. Scale bar: 10 μm. **(E)** Expression of *Tmprss12* was examined by RT-PCR using RNA isolated from mouse sperm. *Actin* was used as an internal control. **(F)** Western blot of TMPRSS12 in mouse sperm. α-TUBULIN was used as an internal control. **(G)** Immunofluorescence staining of mouse sperm for TMPRSS12 (red). The nuclei and acrosomes of sperm were labelled with DAPI (blue) and PNA (green), respectively. The images in the upper right corner are enlarged views of the sperm. Scale bar: 20 μm.

Assisted Sperm Analysis (CASA). The results showed that the sperm count and motility were significantly decreased in *Tmprss12*$^{-/-}$ mice compared to WT mice (**Figure 3A**).

The weight and size of the testis did not differ significantly, and the gross morphology and histology of the testis and sperm were similar between the WT and *Tmprss12*$^{-/-}$ mice (**Figures 3B–D**). Moreover, we paid close attention to the spermatogenesis of *Tmprss12*$^{-/-}$ testes by counting spermatogenic cells at all stages (**Figure 3E**). The counts of pachytene spermatocytes, diplotene spermatocytes, round spermatids and elongated spermatids all decreased significantly in *Tmprss12*$^{-/-}$ mice compared with WT mice, which probably led to the decreased sperm count in *Tmprss12*$^{-/-}$ mice.

Increased Apoptosis and Disrupted Meiosis of Spermatocytes in the Testes of *Tmprss12*$^{-/-}$ Mice

To assess the reasons for the decrease in germ cells, we first evaluated the state of spermatogenic cells in the testes of *Tmprss12*$^{-/-}$ and WT mice. Terminal deoxynucleotidyl transferase nick-end labelling (TUNEL) assays were performed

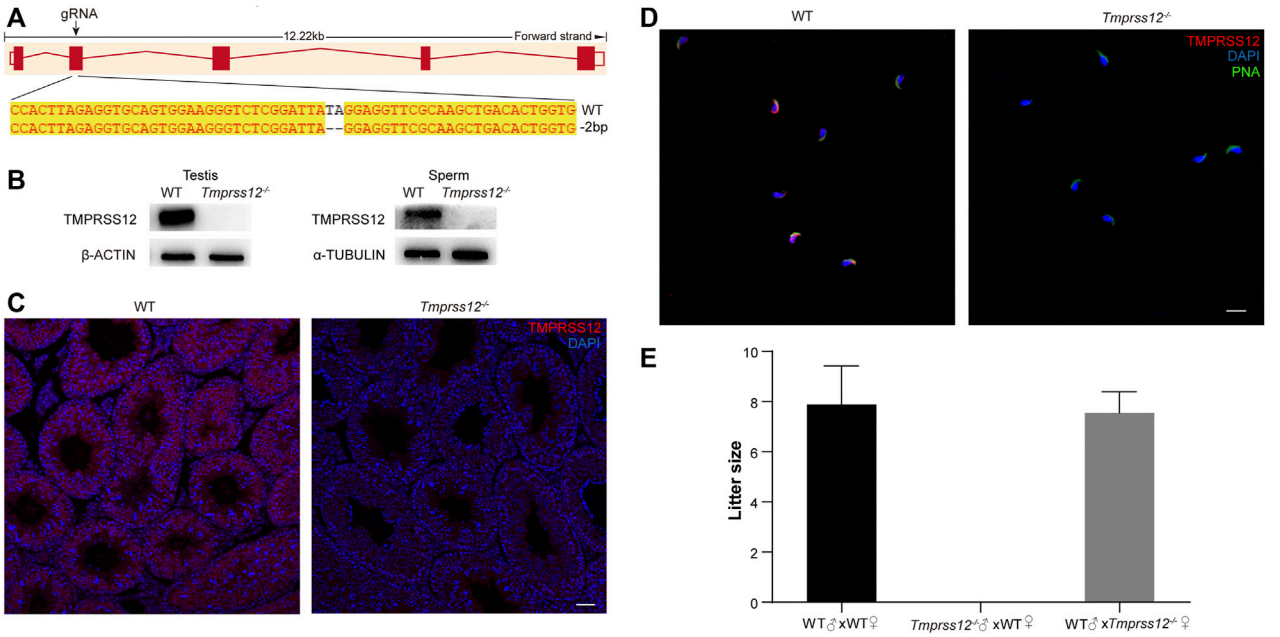

FIGURE 2 | *Tmprss12* knockout mice display male sterility. **(A)** Schematic strategies for the generation of *Tmprss12*$^{-/-}$ mice using CRISPR/Cas9 technology. Image of Sanger sequencing results showing a 2-bp deletion in exon 2. **(B)** Western blot of the testes and sperm from WT and *Tmprss12*$^{-/-}$ mice to verify the validation of *Tmprss12* knockout. β-ACTIN and α-TUBULIN were used as internal controls. **(C)** TMPRSS12 expression in the testes of WT and *Tmprss12*$^{-/-}$ mice was evaluated through immunofluorescence analysis. No TMPRSS12 signal was detected in *Tmprss12*$^{-/-}$ mice. Scale bar: 50 μm. **(D)** TMPRSS12 expression in the sperm of WT and *Tmprss12*$^{-/-}$ mice was determined by immunofluorescence analysis. A positive signal was not observed in *Tmprss12*$^{-/-}$ sperm. Scale bar: 20 μm. **(E)** Number of pups per litter produced by *Tmprss12*$^{-/-}$ mice and WT mice. *Tmprss12*$^{-/-}$ male mice are infertile (n = 3). Data are the mean ± s.d.

to detect apoptotic cells in the testes of these two groups. We found that the numbers of apoptotic germ cells increased remarkably in *Tmprss12*$^{-/-}$ mice compared with WT mice and the apoptotic cells were mainly spermatocytes (**Figures 4A,B**).

In spermatogenesis, meiosis is an important biological process that produces haploid germ cells. Abnormal meiosis interferes with the spermatocyte state and affects the progress of spermatogenesis. Based on our findings that spermatocyte apoptosis increased and the number of spermatogenic cells after the zygotene stage decreased, it is reasonable to speculate that TMPRSS12 may be involved in meiosis. Therefore, we examined the key biological events of meiosis in *Tmprss12*$^{-/-}$ testes. We assessed chromosomal synapsis by immunofluorescence analysis using antibodies against SYCP1 and SYCP3, which are components of the synaptonemal complex (SC). Chromosome spreads from WT testes showed that the fluorescence signal of anti-SYCP3 in the pachytene stage completely overlapped with that of anti-SYCP1 around the SC, including 19 pairs of autosomes and partial synapsed sex chromosomes in the pseudoautosomal region (PAR). In the pachytene spermatocytes of *Tmprss12*$^{-/-}$ testes, chromothripsis, no synapsed sex chromosomes, and abnormal SYCP1 signals in non-PAR were observed (**Figure 4C**). We quantified the spermatocytes of WT and *Tmprss12*$^{-/-}$ testes and found that spermatocytes with abnormal synapses were significantly higher in *Tmprss12*$^{-/-}$ mice than in WT mice (**Figure 4D**).

In addition, we monitored the meiotic recombination of homologues in spermatocytes. Recombination is initiated by DNA double-strand break (DSB) formation in leptotene spermatocytes. DSBs could be marked by the presence of phosphorylated H2AX (γH2AX). In normal meiosis, γH2AX is present on autosomal chromatin and distributed throughout the nucleus in leptotene spermatocytes, persists into the zygotene stage and is restricted to only the sex chromosomes at the pachytene stage. As shown in **Figure 4E**, γH2AX disappeared from autosomes following meiotic DSB repair and was restricted to the sex chromosomes in the pachytene stages of WT spermatocytes, but the γH2AX signal was distributed in *Tmprss12*$^{-/-}$ pachytene spermatocytes and was not restricted to sex chromosomes, suggesting failure in the repair of meiotic DSBs. Moreover, the results of quantifying the abnormal spermatocytes in the two groups were significantly different (**Figure 4F**).

Increased Sperm Apoptosis in *Tmprss12*$^{-/-}$ Mice

We further explored whether the apoptotic state of sperm was also involved in the decreased sperm count of *Tmprss12*$^{-/-}$ mice. Mitochondrial membrane potential (MMP) reduction is an important indicator of early apoptosis. Therefore, we examined the MMP of sperm in *Tmprss12*$^{-/-}$ mice. JC-1 dye was used to monitor the MMP, which was lower in *Tmprss12*$^{-/-}$ mice than WT mice (**Figures 5A–C**). Furthermore, we detected key molecules in classic apoptosis pathways, including BAX, BCL-2 and CASPASE3 (Yang and Cortopassi, 1998; Antonsson et al., 2000; Barroso et al., 2006; Brunelle and Letai, 2009). The expression levels of BAX and CASPASE3 were increased while that of BCL-2 was decreased in

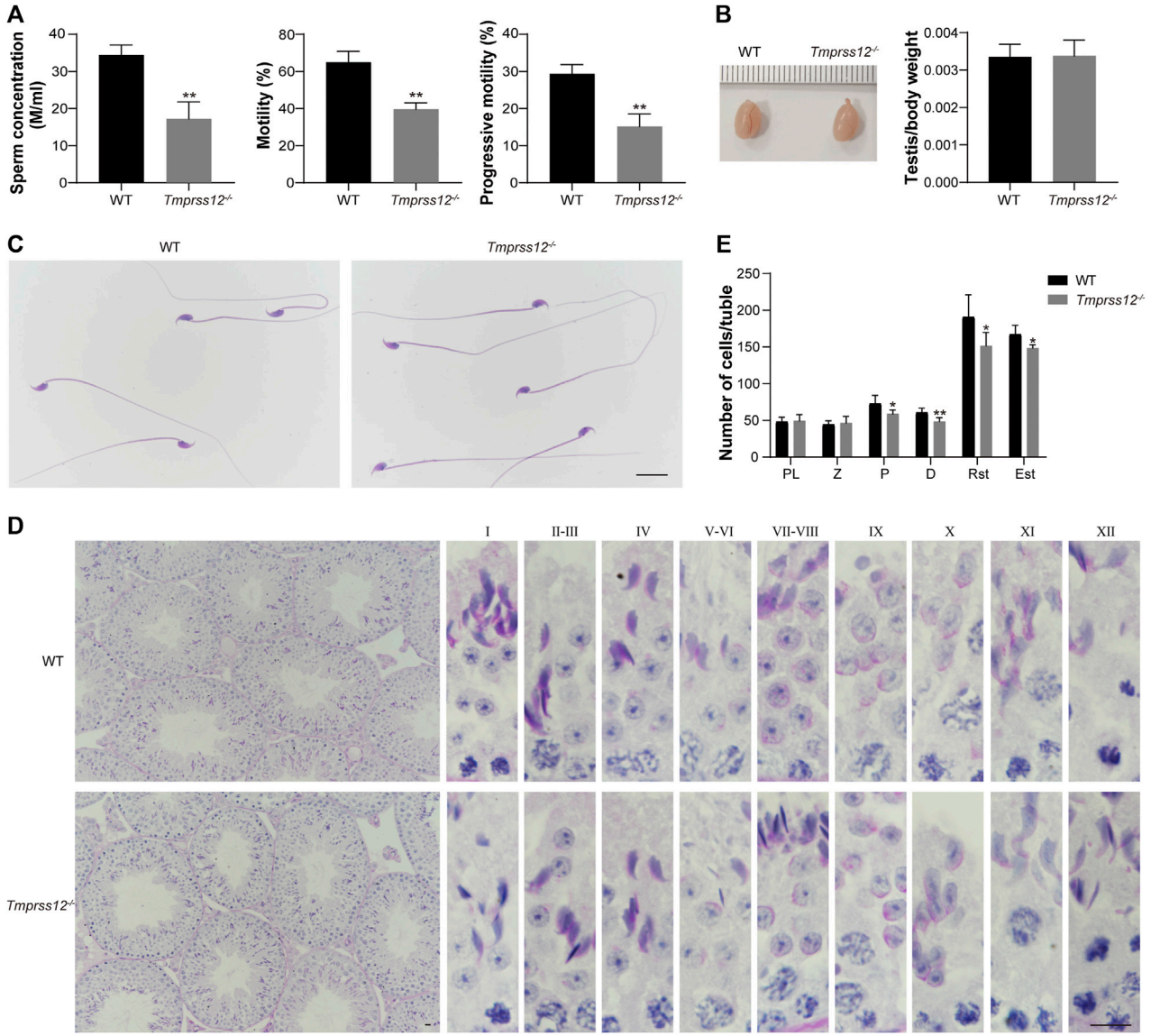

FIGURE 3 | *Tmprss12* knockout mice exhibit oligoasthenospermia, with decreased spermatogenic cells in testes. **(A)** Computer assisted sperm analysis (CASA) showed that the sperm concentration was reduced and motility and progressive motility were decreased in *Tmprss12*$^{-/-}$ mice ($n = 3$). Data are the mean ± s.d. $^{**}p < 0.01$. **(B)** Gross morphology of testes from WT and *Tmprss12*$^{-/-}$ mice and relative testis weight to body weight in the two groups showed no significant difference ($n = 3$). Data are the mean ± s.d. **(C)** The sperm morphology of WT and *Tmprss12*$^{-/-}$ mice. The sperm of *Tmprss12*$^{-/-}$ mice showed no obvious abnormality. Scale bar: 20 μm. **(D)** Periodic acid-Schiff staining of testis sections from WT and *Tmprss12*$^{-/-}$ mice. Complete spermatogenic tubules and orderly arranged spermatogenic cells could be seen in the testes of *Tmprss12*$^{-/-}$ mice. Scale bar: 10 μm. **(E)** Reduced number of spermatogenic cells in *Tmprss12*$^{-/-}$ testes. Numbers of spermatogenic cells per tubule are shown. 10 tubules cross sections for each stage were counted. Compared with the WT, the number of pachytene spermatocytes, diplotene spermatocytes and spermatids of *Tmprss12*$^{-/-}$ mice decreased significantly ($n = 6$). Data are the mean ± s.d. $^{*}p < 0.05$, $^{**}p < 0.01$.

Tmprss12$^{-/-}$ mice, which indicated increased sperm apoptosis when TMPRSS12 was deficient (**Figures 5D,E**).

Abnormal Mitochondrial Structure and Impaired ATP Synthesis in the Sperm of *Tmprss12*$^{-/-}$ Mice

The CASA analysis revealed that the sperm motility of *Tmprss12*$^{-/-}$ male mice was significantly lower than that of WT mice. To explore the reason for the decreased sperm motility, we further observed the ultrastructure of sperm in *Tmprss12*$^{-/-}$ and WT mice under a transmission electron microscope. The results showed that the inner mitochondrial membrane cristae were blurred or absent in *Tmprss12*$^{-/-}$ mice. According to the statistical analysis, the number of sperms with abnormal mitochondria in *Tmprss12*$^{-/-}$ mice was significantly higher than that in WT mice (**Figures 6A,B**).

Mitochondria are the energy metabolism centres of cells and the main sites of oxidative phosphorylation for producing ATP.

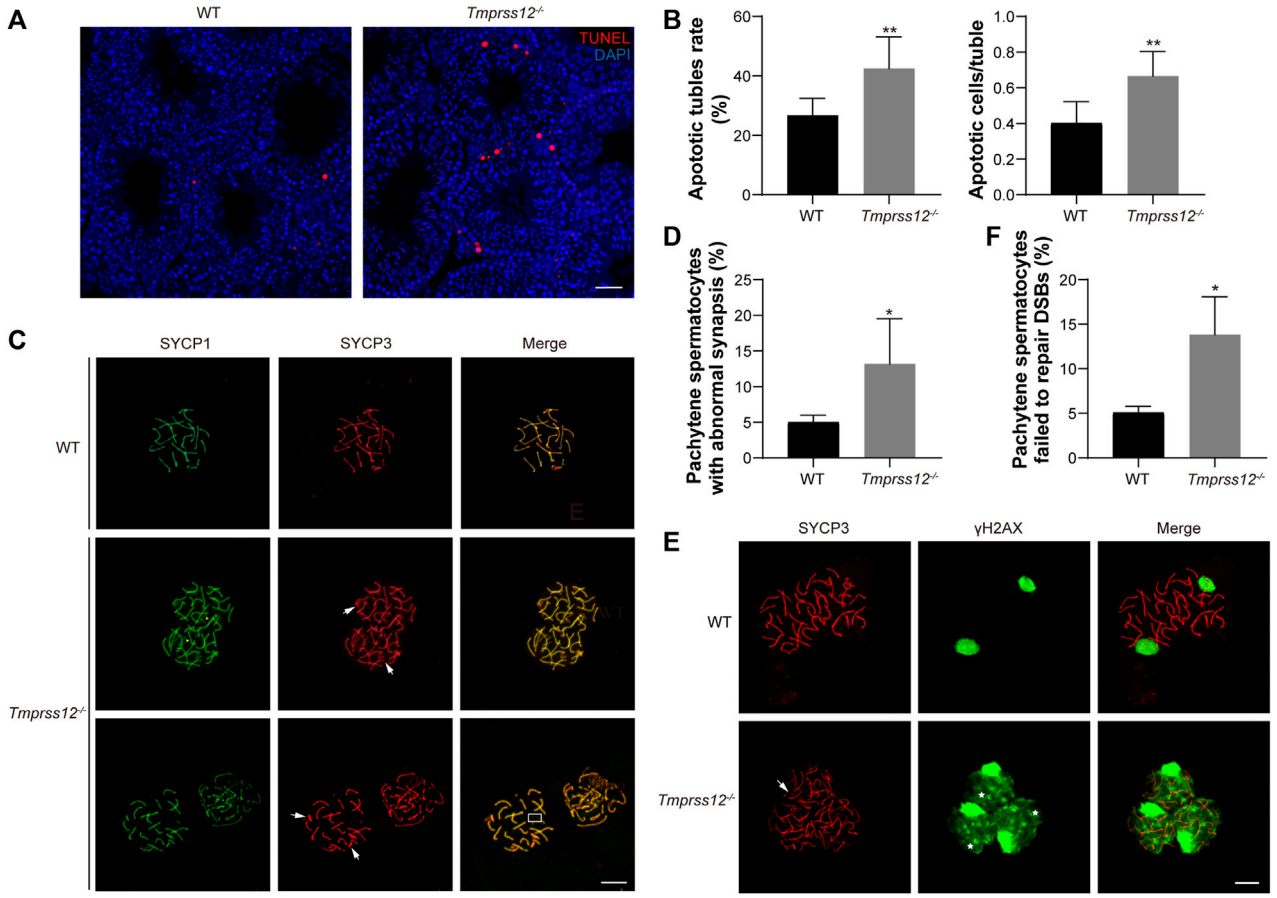

FIGURE 4 | *Tmprss12* deletion leads to damaged synapsis and DSB repair in meiosis. **(A)** Terminal deoxynucleotidyl transferase nick-end-labelling (TUNEL) staining (red) in the testes. Apoptosis in *Tmprss12*$^{-/-}$ mice was significantly increased, and the apoptotic cells were mainly spermatocytes. Nuclei are stained with DAPI (blue). Scale bar: 50 μm. **(B)** Analysis of the apoptotic tubule rate and the number of apoptotic cells per tubule. All spermatogenic tubules from testis sections of the same size in two groups were observed. The data showed increased apoptosis in *Tmprss12*$^{-/-}$ mouse testes (n = 3). Data are the mean ± s.d. $^{**}p < 0.01$. **(C)** Immunofluorescence staining of SYCP1 and SYCP3 on spermatocyte spreads produced from WT and *Tmprss12*$^{-/-}$ mouse testes. Chromothripsis (white arrows), no synapsed sex chromosomes (boxed area), and abnormal SYCP1 signals in non-PAR (yellow arrows) were observed in *Tmprss12*$^{-/-}$ mice. Scale bars: 10 μm. **(D)** Percentage of pachynema spermatocytes with abnormal synapses. The quantitative value was increased in *Tmprss12*$^{-/-}$ mice (n = 3). Data are the mean ± s.d. $^{*}p < 0.05$. **(E)** Immunofluorescence staining of SYCP3 and γH2AX on spermatocyte spreads produced from adult WT and *Tmprss12*$^{-/-}$ mouse testes. In *Tmprss12*$^{-/-}$ images, white arrows indicate chromothripsis, and asterisks indicate the abnormal γH2AX signal. Scale bars: 10 μm. **(F)** Statistical analysis showing that the percentage of pachytene spermatocytes with abnormal DSB repair was increased compared with that in WT mice (n = 3). Data are the mean ± s.d. $^{*}p < 0.05$.

Thus, we detected the sperm ATP content, glycolysis, oxygen consumption and the key markers of the oxidative phosphorylation process in mitochondria. The decreased ATP content in the sperm of *Tmprss12*$^{-/-}$ mice is shown in **Figure 6C**. Extracellular acidification revealed that the sperm of *Tmprss12*$^{-/-}$ mice had glycolysis levels similar to those of WT mice (**Figure 6D**). However, the oxygen consumption assay showed that the oxygen consumption of sperm of *Tmprss12*$^{-/-}$ mice was reduced compared with that of the sperm of WT mice (**Figure 6E**). COX2, COX3, MTATP and MTCYB are the key markers of the oxidative phosphorylation process in mitochondria (Feng et al., 2008; Heidari et al., 2016). The mRNA and protein levels of MTATP and MTCYB in the sperm of *Tmprss12*$^{-/-}$ mice were reduced compared with those in WT mice (**Figure 6F,G**; **Supplementary Figure 2**). The above results suggested that an abnormal ultrastructure of mitochondria and impaired ATP synthesis in sperm are potential causes of decreased sperm motility.

Impaired Mitochondrial Development During Spermiogenesis in *Tmprss12*$^{-/-}$ Mice

To investigate whether the abnormal mitochondrial structure is caused by damaged spermiogenesis, we detected special molecules involved in spermiogenesis in the testes, including TEKTIN-T, IQCG, CLIP-170, MEIG1, AGFG1, and KLC3. TEKTIN-T and IQCG are essential for sperm flagellum formation (Tanaka et al., 2004; Li et al., 2014). CLIP-170 and MEIG1 are critical for manchette structures (Akhmanova et al., 2005; Zhang et al., 2009). AGFG1 is involved in acrosomal development (Kang-Decker et al., 2001). KLC3 plays an

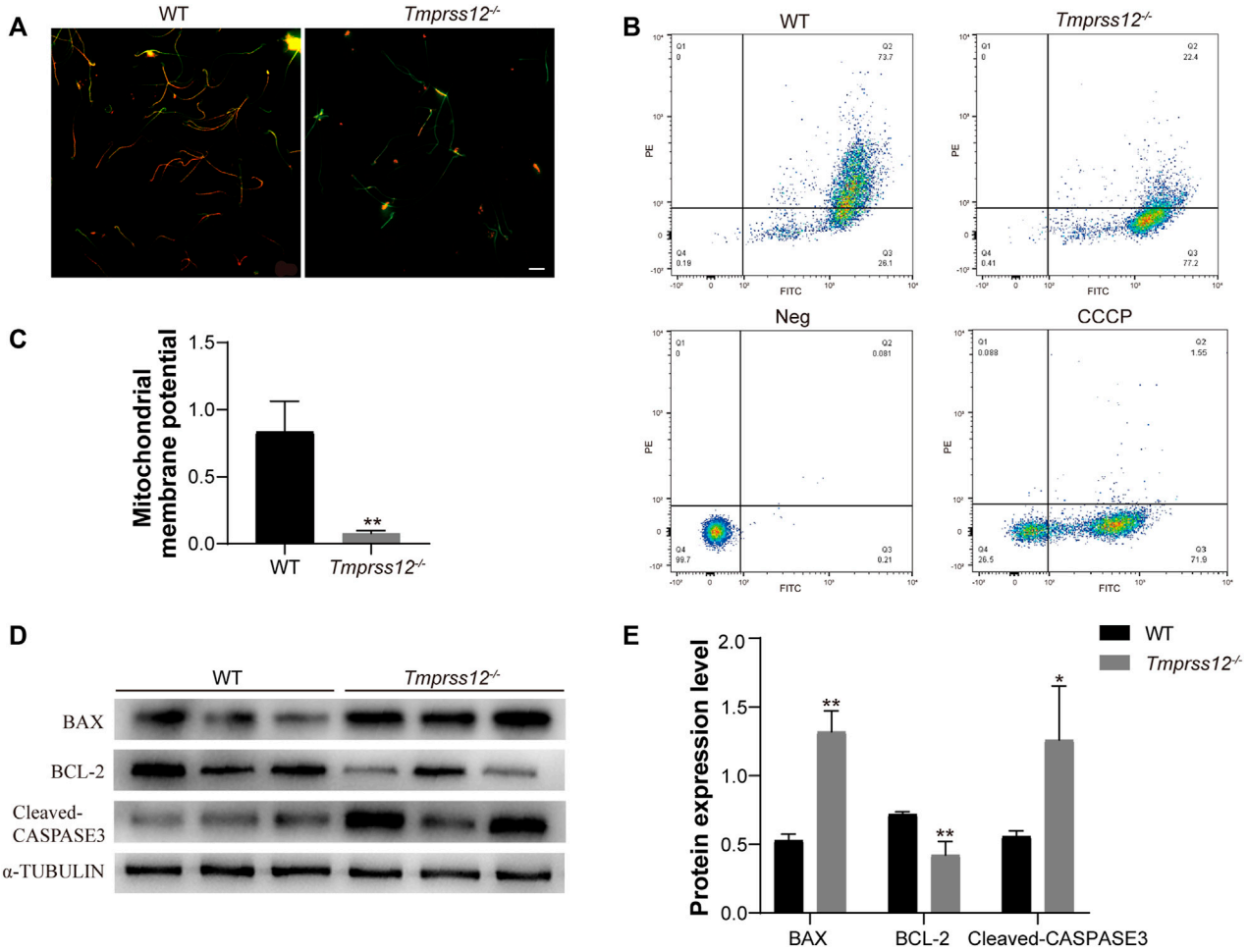

FIGURE 5 | *Tmprss12* deletion causes increased sperm apoptosis. **(A)** Fluorescence microscopy observation of sperm after JC-1 staining between WT and *Tmprss12*$^{-/-}$ mice. The red fluorescent sperm were normal, and the green sperm had a low mitochondrial membrane potential (MMP). Scale bars: 20 μm. **(B)** Sperm from WT and *Tmprss12*$^{-/-}$ mice stained with JC-1 dye were checked for their corresponding MMP through flow cytometry analysis. Q2, red-stain sperm; Q3, green-stain sperm. Neg and carbonyl cyanide 3-chlorophenylhydrazone (CCCP) were used as a negative control and positive control, respectively. **(C)** MMP was analysed by the relative ratio of red/green fluorescence. The sperm of *Tmprss12*$^{-/-}$ mice showed low MMP levels ($n = 3$). Data are the mean ± s.d. $^{*}p < 0.05$. **(D)** Western blot of apoptosis-related molecules from sperm of WT and *Tmprss12*$^{-/-}$ mice. α-TUBULIN was used as an internal control. **(E)** Grey intensity analysis showing the expression level of the above markers. The expression levels of BAX and CASPASE3 were increased while BCL-2 was decreased in *Tmprss12*$^{-/-}$ mice ($n = 3$). Data are the mean ± s.d. $^{*}p < 0.05$.

important role in mitochondrial migration and sperm tail midpiece formation (Zhang et al., 2012). Real-time PCR and western blot both showed that the expression of KLC3 decreased in the testes of *Tmprss12*$^{-/-}$ mice (**Figures 7A,B**; **Supplementary Figure 3**).

Absence of *Tmprss12* Affects the Expression of Some Proteins in Mouse Testes

As a serine protease, TMPRSS12 should theoretically regulate target proteins to play a specific role in spermatogenesis. To further investigate the mechanism of TMPRSS12 in male reproduction, we used 2-D electrophoresis combined with MALDI-TOF-TOF MS/MS to construct differential protein expression profiles of testes in *Tmprss12*$^{-/-}$ and WT mice (**Supplementary Figure 4**). A total of 64 spots with 2-fold or more differential expression between two groups were identified using MALDI-TOF-TOF MS/MS. As a result, 54 unique proteins were identified successfully, including 39 proteins with decreased expression and 15 proteins with increased expression in *Tmprss12*$^{-/-}$ mice (**Supplementary Table 2**). We analysed the molecular functions of these differentially expressed proteins by IPA (Ingenuity Pathway Analysis) and found that these proteins were mainly related to meiosis, apoptosis, mitochondrial function and cell adhesion (**Figure 8A**).

To certify the expression levels of differential proteins, some proteins related to key events were selected for an expression analysis by western blot. For example, lymphoid-specific helicase

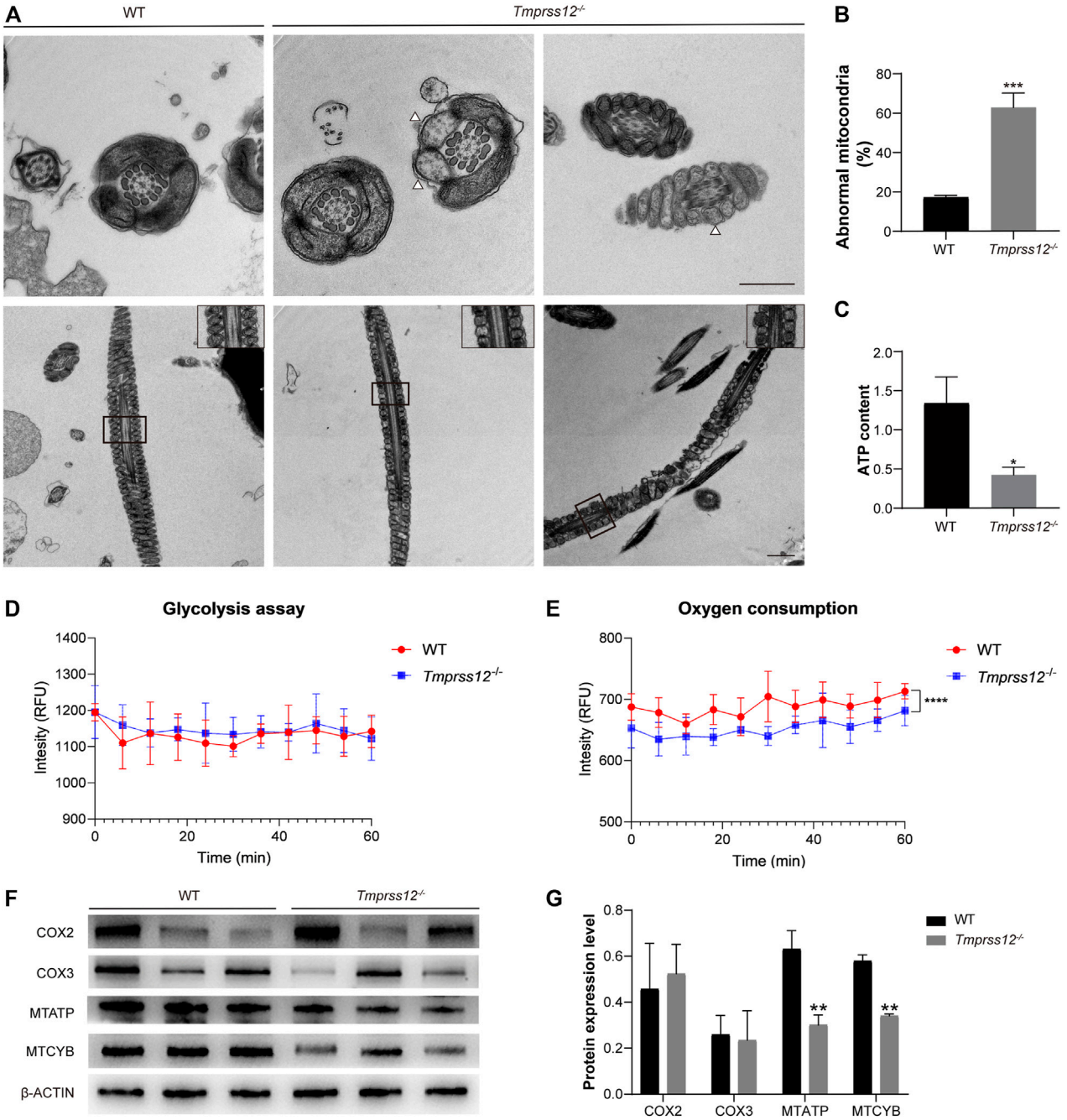

FIGURE 6 | Impaired mitochondrial structure and function in the sperm of *Tmprss12*$^{-/-}$ mice. **(A)** Transmission electron microscopy (TEM) images of the sperm ultrastructure are shown, revealing blurred or absent inner mitochondrial membrane (IMM) cristae (white arrows). The images in the upper right corner of the second row are enlarged views of the mitochondria. Scale bars: 1 μm. **(B)** Percentage of mitochondria with an abnormal structure. The percentage was increased in *Tmprss12*$^{-/-}$ mice ($n = 4$). Data are the mean ± s.d. $^{***}p < 0.001$. **(C)** Tested ATP contents of sperm between WT and *Tmprss12*$^{-/-}$ mice. There were no energy substrates in the sperm isolation buffer and background ATP was consumed before detection. The ATP level was significantly lower in *Tmprss12*$^{-/-}$ mice ($n = 3$). Data are the mean ± s.d. $^{*}p < 0.05$. **(D)** Glycolysis assay measured as cytoplasmic acidification. Sperm of WT and *Tmprss12*$^{-/-}$ mice were extracted from the cauda epididymis and suspended in respiration buffer, followed by glycolysis measurement for 60 min via fluorescent emission. There was no significant difference in glycolysis between sperm of WT and *Tmprss12*$^{-/-}$ mice ($n = 3$). Data are the mean ± s.d. **(E)** Oxygen consumption analysis. Sperm of WT and *Tmprss12*$^{-/-}$ mice were extracted from the cauda epididymis and suspended in PBS. Then fluorescent emission was measured and compared during 60 min via fluorescence spectroscopy. *Tmprss12*$^{-/-}$ sperm showed lower oxygen consumption than WT sperm ($n = 3$). Data are the mean ± s.d. $^{****}p < 0.0001$. **(F)** Western blot of key markers in the mitochondrial electron transfer chain from sperm of WT and *Tmprss12*$^{-/-}$ mice. β-ACTIN was used as an internal control. **(G)** Grey intensity analysis showing the expression level of the above markers. The expression levels of MTATP and MTCYB were decreased in *Tmprss12*$^{-/-}$ mice ($n = 3$). Data are the mean ± s.d. $^{**}p < 0.01$.

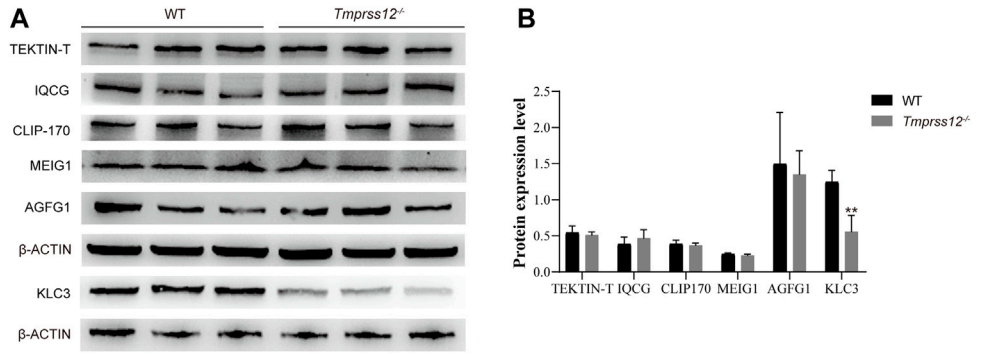

FIGURE 7 | Mitochondrial development in testicular spermatids was impaired in *Tmprss12* knockout mice. **(A)** Western blot of special molecules involved in spermiogenesis from the testes of WT and *Tmprss12*$^{-/-}$ mice. β-ACTIN was used as an internal control. **(B)** Grey intensity analysis showing that the expression level of KLC3 decreased in *Tmprss12*$^{-/-}$ mice (n = 3). Data are the mean ± s.d. $^{*}p < 0.05$.

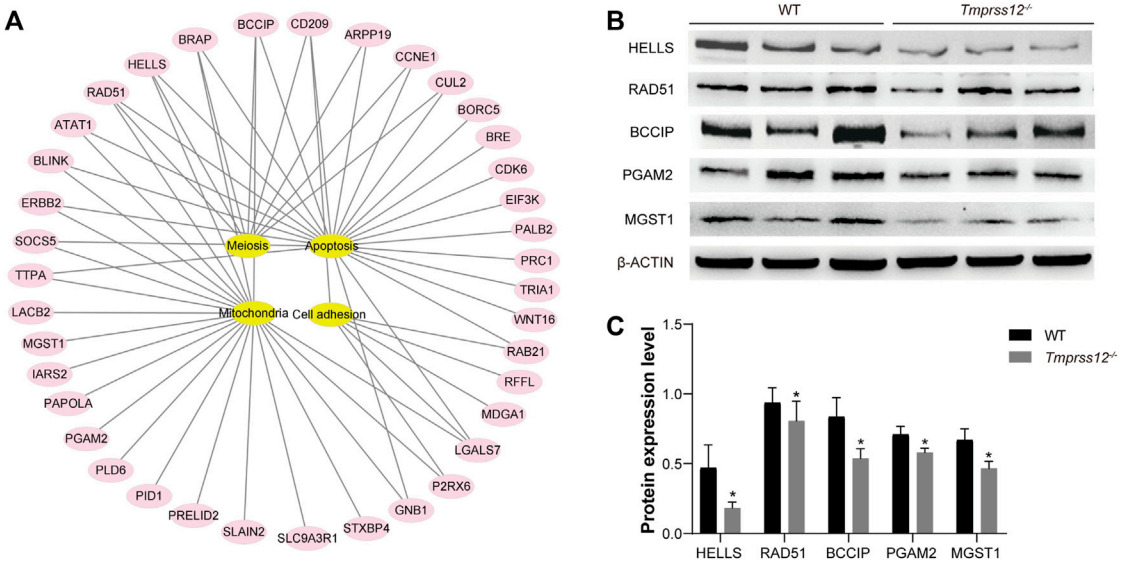

FIGURE 8 | Analysis of differential protein expression profiles of testes from WT and *Tmprss12*$^{-/-}$ mice. **(A)** Proteins showing a difference of more than 2-fold were analysed according to IPA (ingenuity pathway analysis), and they were mainly related to meiosis, apoptosis, mitochondrial function and cell adhesion. **(B)** Verification of the expression levels of some differential proteins related to key events in WT and *Tmprss12*$^{-/-}$ mouse testes by western blot. β-ACTIN was used as an internal control. **(C)** Grey intensity analysis showing the expression level of the above proteins. The results were consistent with the differential expression profiles (n = 3). Data are the mean ± s.d. $^{*}p < 0.05$.

(HELLS) has been proven to be essential for meiotic progression, especially in chromosomal synapses (Zeng et al., 2011; Kollarovic et al., 2020). Recombinase RAD51 is necessary for DSB repair and homologous recombination (Hinch et al., 2020). BCCIP interacts with RAD51 to stimulate DNA pairing activity in homologous recombination (Kelso et al., 2017). PGAM2 activity could modulate mitochondrial function (Okuda et al., 2013). MGST1 is a glutathione transferase located in mitochondrial membranes that protects mitochondria against oxidative stress to ensure their normal biological function (Zhang et al., 2001; Johansson et al., 2010; Schaffert, 2011). The western blot results showed that the expression trend of these proteins was consistent with the differential expression profiles (**Figures 8B,C**).

DISCUSSION

Mammalian reproduction is a complicated and finely regulated process. For males, spermatogenesis takes place in the testis, and the mature sperm must capacitate, migrate to the oviduct ampulla, penetrate the cumulus oophorus cells and zona pellucida and finally fuse with oocytes. Many testis-predominant proteins involved in the process have been studied to explore the biological characteristics and regulatory mechanism of spermatogenesis and sperm function.

Because it activates various proteins, serine protease is considered a relative upstream regulator in physiological processes (Bugge et al., 2009; Shen B. et al., 2013), and it has attracted the attention of researchers in various fields. Many

serine protease members have been found to be involved in different stages of spermatogenesis and/or sperm function (Mbikay et al., 1997; Kawano, et al., 2010; Yoneda and Kimura, 2013; Yoneda et al., 2013; Shen C. et al., 2013; Shang et al., 2018; Kobayashi et al., 2020; Holcomb et al., 2020; Zhu et al., 2021). Compared with PRSS proteins, fewer TMPRSS members have been identified and studied. At present, only one member, TMPRSS12, has been found to be specifically expressed in the testis and sperm (Liu et al., 2013; Wang et al., 2013).

Larasati et al. first generated *Tmprss12*$^{-/-}$ mice and demonstrated that *Tmprss12*$^{-/-}$ males were sterile. They found that *Tmprss12*$^{-/-}$ mice had reduced sperm motility, ZP binding defects and low IVF rates and their spermatozoa failed to migrate through the uterotubal junction (Larasati et al., 2020). The study preliminarily confirmed that TMPRSS12 was related to sperm function. Similar to the above study, our results also confirmed that *Tmprss12*$^{-/-}$ mice were sterile and had low sperm motility and *in vitro* fertilization rates (**Supplementary Figure 5**).

In this study, we focused on the role of TMPRSS12 in testis spermatogenesis; therefore, we detailed the expression and location of TMPRSS12 in the testis. TMPRSS12 was first detected in the testes of 10-day-old mice, and its expression remained constant after 14 days of age. TMPRSS12 was expressed over a long time range in adult mouse testes from spermatocytes to spermatids. These results suggested that TMPRSS12 might function in meiosis and spermiogenesis in spermatogenesis. Using *Tmprss12*$^{-/-}$ mice, we studied spermatogenesis in the testis. First, the increased TUNEL-positive cells in spermatocytes and decreased counts of spermatogenic cells in *Tmprss12*$^{-/-}$ testes were observed, which could provide an explanation for the decreased sperm count observed in this study. The above data indicated that the loss of TMPRSS12 might influence the biological process of meiosis, which corresponds with its expression in spermatocytes. It is well known that meiosis is an important biological process in spermatogenesis. During meiosis, pairing of homologous chromosomes, synapsis, recombination and chromosome segregation are conserved events (Zickler and Kleckner, 1999; Page and Hawley, 2004). In WT pachynema, 19 pairs of autosomes and partial synapsed sex chromosomes in the pseudoautosomal region (PAR) were observed. However, we found that *Tmprss12*$^{-/-}$ mice had chromothripsis, no synapsed sex chromosomes, and abnormal SYCP1 signalling in non-PAR, thus demonstrating abnormal synapsis in these mice (de Vries et al., 2005). We also studied DSB repair during meiosis. DSBs are marked by the presence of phosphorylated H2AX (γH2AX) (Mahadevaiah et al., 2001). While γH2AX labelling successively disappeared from the autosomes and was restricted to the sex chromosomes in the pachynema of WT mice, the γH2AX signal remained and surrounded most of the chromosomes in a cloud-like manner in *Tmprss12*$^{-/-}$ mice, which indicated that DSBs were not efficiently repaired. Thus, our findings demonstrated that meiosis progress was arrested in some spermatocytes when TMPRSS12 was lost, which resulted in increased apoptosis of spermatocytes.

As a protease, TMPRSS12 theoretically plays its role by influencing the expression and function of some proteins. In this study, we explored the downstream proteins targeted by TMPRSS12 through proteomics methods to elucidate the mechanism. A series of potential targeted proteins involved in meiosis were identified, and some of them were verified by our experimental results, including HELLS, BCCIP, and RAD51. HELLS is a member of the SNF2 family of chromatin remodelling proteins. HELLS-deficient spermatocytes exhibit abnormal meiosis, including extensive asynapsis of the autosomal chromatin compartment and failure to form the sex body, resulting in pachytene spermatocyte arrest and apoptosis (Zeng et al., 2011; Kollarovic et al., 2020). The observed decrease in HELLS in *Tmprss12*$^{-/-}$ mice disturbed the synapsis of homologous chromosomes. Recombinase RAD51 and its paralog DMC1 localized at DNA DSB sites in the meiotic prophase and played a key role in the repair of DSBs (Hinch et al., 2020). BCCIP binds DNA and physically and functionally interacts with RAD51 to stimulate its homologous DNA pairing activity in homologous recombination (Kelso et al., 2017). We confirmed the decreased expression of BCCIP and RAD51 in *Tmprss12*$^{-/-}$ mice, which influenced the repair of chromosomal lesions, such as DSBs. Because homologous recombination is a DNA repair pathway, defects in this repair pathway may cause chromosomal aberrations and meiosis arrest.

Normal spermatogenesis in the testis not only ensures an adequate sperm count but also guarantees sperm quality. During the process of spermiogenesis, round spermatids undergo dramatic morphological, molecular and cellular alterations, thus laying a foundation for the generation of functional sperm (Ozturk et al., 2017; Zakrzewski et al., 2021). Due to its predominant expression in spermatids, TMPRSS12 very likely participates in spermiogenesis. Unique molecules involved in spermiogenesis were detected, and KLC3, which plays a role in the development of sperm tail midpieces and mitochondrial transport during spermiogenesis (Zhang et al., 2012), was found to have a low expression level in *Tmprss12*$^{-/-}$ mice. To explore the relationship between TMPRSS12 and mitochondria, we observed the morphology and ultrastructure of sperm. The *Tmprss12*$^{-/-}$ mice had a normal morphology, which is consistent with the findings of Larasati et al. (2020). Ultrastructure analysis showed the normal head shape and microtubule structure of the tail in *Tmprss12*$^{-/-}$ sperm, which were the same as those found by Larasati et al. However, we found blurred or absent inner mitochondrial membrane (IMM) cristaes in the sperm of *Tmprss12*$^{-/-}$ mice. By double-blind counting and statistical analysis, we demonstrated that the percentage of mitochondria with abnormal structures was significantly increased in *Tmprss12*$^{-/-}$ mice, and we speculated that mitochondrial function was disturbed. Thus, we measured the oxygen consumption level of sperm and detected several key markers related to ATP synthesis in the mitochondria, including COX2, COX3, MTATP and MTCYB (Feng et al., 2008; Heidari et al., 2016). The reduction in oxygen consumption and the decreased expression of MTATP and MTCYB suggested that the dysfunction of aerobic oxidation in mitochondria affected the energy production and motor function of sperm in *Tmprss12*$^{-/-}$ mice. In this study, we identified two potential targeted proteins (PGAM2 and MGST1) of TMPRSS12 that are related to the

function of mitochondria (Zhang et al., 2001; Johansson et al., 2010; Schaffert, 2011; Okuda et al., 2013). However, the exact mechanism by which TMPRSS12 affects mitochondrial development and function needs to be explored further.

It is worth mentioning that MMP detection was also performed in our study, and a decrease in MMP was observed in *Tmprss12*$^{-/-}$ mice, indicating that the mitochondria were unable to maintain normal physiological functions to synthesize ATP. This result verified the influence of TMPRSS12 on mitochondrial function. In addition, we detected the apoptosis status of the sperm because a decline in MMP is an important event in early apoptosis. The results demonstrated that the expression levels of BCL-2 decreased and BAX and CASPASE3 increased, indicating that the deletion of TMPRSS12 might activate mitochondrial apoptotic pathways in sperm, which influence the counts of sperm in the epididymis. This is also one of the reasons for oligospermia in *Tmprss12*$^{-/-}$ mice.

Although this study focused on spermatogenesis, we also noticed the effect of TMPRSS12 on sperm function. Similar to the study by Larasati et al. (2020), our data showed that TMPRSS12 was expressed in the acrosomal region of sperm. This specific location in sperm suggested the potential role of TMPRSS12 in acrosomal reactions, sperm-egg interactions, etc. Larasati et al. interpreted the role of TMPRSS12 in uterotubal junction migration in mice. We performed additional research on sperm function. CTC staining results showed that the rate of sperm capacitation and the acrosome reaction of *Tmprss12*$^{-/-}$ mouse sperm decreased significantly (**Supplementary Figure 6**). In addition, *in vivo* and *in vitro* fertilization experiments were conducted. The results showed that the *in vivo* fertilization rate was 0 and the *in vitro* fertilization rate was severely reduced in *Tmprss12*$^{-/-}$ mice (**Supplementary Figures 5, 7**), suggesting that the decreased sperm motility and the impaired sperm-egg interaction synergically affected the fertilization results of these mice. It is worth noting that Larasati et al. found very little expression of mature ADAM3 in *Tmprss12* KO spermatozoa (Larasati et al., 2020). Since ADAM3 is an essential protein for sperm-egg interactions (Inoue et al., 2011), this result also supports the involvement of TMPRSS12 in sperm-egg interactions. However, the mechanism of TMPRSS12 in regulating sperm function requires further investigation.

In summary, we confirmed the important role of TMPRSS12 in spermatogenesis and preliminarily identified its potential targets. By affecting specific molecules, TMPRSS12 regulates chromosomal synapse and DSB repair during spermatocyte meiosis and influences mitochondrial development during spermiogenesis, resulting in decreased sperm counts and quality. Our study provides a more complete explanation for male sterility in *Tmprss12*$^{-/-}$ mice. The involvement of TMPRSS12 in many aspects of male reproduction suggests its key role. Considering the oligospermia, asthenospermia and infertility phenotype exhibited by *Tmprss12*$^{-/-}$ mice and the deleterious missense mutation of *Tmprss12* found in infertile men with dyszoospermia, *Tmprss12* is likely to be a potential pathogenic gene in these patients. TMPRSS12 and its downstream molecules could become potential targets for the clinical diagnosis and treatment of infertility. In the future, further research is required to confirm whether potential deleterious mutations affect TMPRSS12 protein function.

DATA AVAILABILITY STATEMENT

The datasets presented in this study can be found in online repositories. The data presented in the study are deposited in the PRIDE repository, accession number PXD028014.

ETHICS STATEMENT

The animal study was reviewed and approved by the ethics committees of Nanjing Medical University.

AUTHOR CONTRIBUTIONS

HZ have designed the study. JZ, XZ, DW, TY, LY, ZW, MZ, and FZ performed the experiments. JZ, XZ, XC, and HZ analyzed the data. JZ wrote the original draft. XZ, DW, and LY produced figures and edited the manuscript. HZ critically revised the manuscript and supervised the study.

FUNDING

This study was supported by grants from the National Natural Science Foundation of China (31671552, 31871164, 82071702); Natural Science Foundation of Jiangsu Province (BK20181370).

SUPPLEMENTARY MATERIAL

The Supplementary Material for this article can be found online at: https://www.frontiersin.org/articles/10.3389/fcell.2022.757042/full#supplementary-material

REFERENCES

Akhmanova, A., Mausset-Bonnefont, A.-L., van Cappellen, W., Keijzer, N., Hoogenraad, C. C., and Stepanova, T. (2005). The Microtubule Plus-End-Tracking Protein CLIP-170 Associates with the Spermatid Manchette and Is Essential for Spermatogenesis. *Genes Dev.* 19, 2501–2515. doi:10.1101/gad.344505

Al-Jamea, L. H., Woodman, A., Heiba, N. M., Elshazly, S. A., Khalaf, N. B., Fathallah, D. M., et al. (2021). Genetic Analysis of TMPRSS6 Gene in Saudi Female Patients with Iron Deficiency Anemia. *Hematol. Oncol. Stem Cel Ther* 14, 41–50. doi:10.1016/j.hemonc.2020.04.007

Antalis, T. M., Bugge, T. H., and Wu, Q. (2011). Membrane-anchored Serine Proteases in Health and Disease. *Prog. Mol. Biol. Transl Sci.* 99, 1–50. doi:10.1016/B978-0-12-385504-6.00001-4

Antonsson, B., Montessuit, S., Lauper, S., Eskes, R., and Martinou, J. C. (2000). Bax Oligomerization Is Required for Channel-Forming Activity in Liposomes and to Trigger Cytochrome C Release from Mitochondria. *Biochem. J.* 345 Pt 2, 271–278. doi:10.1042/bj3450271

Barrett, A. J. (2004). Bioinformatics of Proteases in the MEROPS Database. *Curr. Opin. Drug Discov. Devel* 7, 334–341.

Barrett, A. J., Rawlings, N. D., and O'Brien, E. A. (2001). The MEROPS Database as a Protease Information System. *J. Struct. Biol.* 134, 95–102. doi:10.1006/jsbi.2000.4332

Barroso, G., Taylor, S., Morshedi, M., Manzur, F., Gavino, F., and Oehninger, S. (2006). Mitochondrial Membrane Potential Integrity and Plasma Membrane Translocation of Phosphatidylserine as Early Apoptotic Markers: a Comparison of Two Different Sperm Subpopulations. *Fertil. Steril* 85, 149–154. doi:10.1016/j.fertnstert.2005.06.046

Brunelle, J. K., and Letai, A. (2009). Control of Mitochondrial Apoptosis by the Bcl-2 Family. *J. Cel Sci* 122, 437–441. doi:10.1242/jcs.031682

Bugge, T. H., Antalis, T. M., and Wu, Q. (2009). Type II Transmembrane Serine Proteases. *J. Biol. Chem.* 284, 23177–23181. doi:10.1074/jbc.R109.021006

Chalmel, F., and Rolland, A. D. (2015). Linking Transcriptomics and Proteomics in Spermatogenesis. *Reproduction* 150, R149–R157. doi:10.1530/REP-15-0073

da Cruz, I., Rodriguez-Casuriaga, R., Santinaque, F. F., Farias, J., Curti, G., Capoano, C. A., et al. (2016). Transcriptome Analysis of Highly Purified Mouse Spermatogenic Cell Populations: Gene Expression Signatures Switch from Meiotic-To Postmeiotic-Related Processes at Pachytene Stage. *BMC Genomics* 17, 294. doi:10.1186/s12864-016-2618-1

de Vries, F. A., de Boer, E., van den Bosch, M., Baarends, W. M., Ooms, M., Yuan, L., et al. (2005). Mouse Sycp1 Functions in Synaptonemal Complex Assembly, Meiotic Recombination, and XY Body Formation. *Genes Dev.* 19, 1376–1389. doi:10.1101/gad.329705

Fasquelle, L., Scott, H. S., Lenoir, M., Wang, J., Rebillard, G., Gaboyard, S., et al. (2011). Tmprss3, a Transmembrane Serine Protease Deficient in Human DFNB8/10 Deafness, Is Critical for Cochlear Hair Cell Survival at the Onset of Hearing. *J. Biol. Chem.* 286, 17383–17397. doi:10.1074/jbc.M110.190652

Feng, C. Q., Song, Y. B., Zou, Y. G., and Mao, X. M. (2008). Mutation of MTCYB and MTATP6 Is Associated with Asthenospermia. *Zhonghua Nan Ke Xue* 14, 321–323. doi:10.3969/j.issn.1009-3591.2008.04.007

Finberg, K. E., Heeney, M. M., Campagna, D. R., Aydinok, Y., Pearson, H. A., Hartman, K. R., et al. (2008). Mutations in TMPRSS6 Cause Iron-Refractory Iron Deficiency Anemia (IRIDA). *Nat. Genet.* 40, 569–571. doi:10.1038/ng.130

Guipponi, M., Toh, M. Y., Tan, J., Park, D., Hanson, K., Ballana, E., et al. (2008). An Integrated Genetic and Functional Analysis of the Role of Type II Transmembrane Serine Proteases (TMPRSSs) in Hearing Loss. *Hum. Mutat.* 29, 130–141. doi:10.1002/humu.20617

Guo, X., Zhao, C., Wang, F., Zhu, Y., Cui, Y., Zhou, Z., et al. (2010). Investigation of Human Testis Protein Heterogeneity Using 2-dimensional Electrophoresis. *J. Androl.* 31, 419–429. doi:10.2164/jandrol.109.007534

Hedstrom, L. (2002). Serine Protease Mechanism and Specificity. *Chem. Rev.* 102, 4501–4524. doi:10.1021/cr000033x

Heidari, M. M., Khatami, M., Danafar, A., Dianat, T., Farahmand, G., and Talebi, A. R. (2016). Mitochondrial Genetic Variation in Iranian Infertile Men with Varicocele. *Int. J. Fertil. Steril* 10, 303–309. doi:10.22074/ijfs.2016.5047

Hinch, A. G., Becker, P. W., Li, T., Moralli, D., Zhang, G., Bycroft, C., et al. (2020). The Configuration of RPA, RAD51, and DMC1 Binding in Meiosis Reveals the Nature of Critical Recombination Intermediates. *Mol. Cel* 79, 689–701 e10. doi:10.1016/j.molcel.2020.06.015

Holcomb, R. J., Oura, S., Nozawa, K., Kent, K., Yu, Z., Robertson, M. J., et al. (2020). The Testis-specific Serine Proteases PRSS44, PRSS46, and PRSS54 Are Dispensable for Male Mouse Fertilitydagger. *Biol. Reprod.* 102, 84–91. doi:10.1093/biolre/ioz158

Hooper, J. D., Clements, J. A., Quigley, J. P., and Antalis, T. M. (2001). Type II Transmembrane Serine Proteases. Insights into an Emerging Class of Cell Surface Proteolytic Enzymes. *J. Biol. Chem.* 276, 857–860. doi:10.1074/jbc.R000020200

Inoue, N., Ikawa, M., and Okabe, M. (2011). The Mechanism of Sperm-Egg Interaction and the Involvement of IZUMO1 in Fusion. *Asian J. Androl.* 13, 81–87. doi:10.1038/aja.2010.70

Johansson, K., Jarvliden, J., Gogvadze, V., and Morgenstern, R. (2010). Multiple Roles of Microsomal Glutathione Transferase 1 in Cellular protection: a Mechanistic Study. *Free Radic. Biol. Med.* 49, 1638–1645. doi:10.1016/j.freeradbiomed.2010.08.013

Kang-Decker, N., Mantchev, G. T., Juneja, S. C., McNiven, M. A., and van Deursen, J. M. (2001). Lack of Acrosome Formation in Hrb-Deficient Mice. *Science* 294, 1531–1533. doi:10.1126/science.1063665

Kelso, A. A., Goodson, S. D., Watts, L. E., Ledford, L. L., Waldvogel, S. M., Diehl, J. N., et al. (2017). The Beta-Isoform of BCCIP Promotes ADP Release from the RAD51 Presynaptic Filament and Enhances Homologous DNA Pairing. *Nucleic Acids Res.* 45, 711–725. doi:10.1093/nar/gkw877

Kobayashi, K., Endo, T., Matsumura, T., Lu, Y., Yu, Z., Matzuk, M. M., et al. (2020). Prss55 but Not Prss51 Is Required for Male Fertility in Micedagger. *Biol. Reprod.* 103, 223–234. doi:10.1093/biolre/ioaa041

Kolas, N. K., Svetlanov, A., Lenzi, M. L., Macaluso, F. P., Lipkin, S. M., Liskay, R. M., et al. (2005). Localization of MMR Proteins on Meiotic Chromosomes in Mice Indicates Distinct Functions during Prophase I. *J. Cel Biol* 171, 447–458. doi:10.1083/jcb.200506170

Kollarovic, G., Topping, C. E., Shaw, E. P., and Chambers, A. L. (2020). The Human HELLS Chromatin Remodelling Protein Promotes End Resection to Facilitate Homologous Recombination and Contributes to DSB Repair within Heterochromatin. *Nucleic Acids Res.* 48, 1872–1885. doi:10.1093/nar/gkz1146

Larasati, T., Noda, T., Fujihara, Y., Shimada, K., Tobita, T., Yu, Z., et al. (2020). Tmprss12 Is Required for Sperm Motility and Uterotubal junction Migration in Micedagger. *Biol. Reprod.* 103, 254–263. doi:10.1093/biolre/ioaa060

Li, B., Qing, T., Zhu, J., Wen, Z., Yu, Y., Fukumura, R., et al. (2017). A Comprehensive Mouse Transcriptomic BodyMap across 17 Tissues by RNA-Seq. *Sci. Rep.* 7, 4200. doi:10.1038/s41598-017-04520-z

Li, H., Zhang, Y., and Wu, Q. (2017). Role of Corin in the Regulation of Blood Pressure. *Curr. Opin. Nephrol. Hypertens.* 26, 67–73. doi:10.1097/MNH.0000000000000297

Li, R. K., Tan, J. L., Chen, L. T., Feng, J. S., Liang, W. X., Guo, X. J., et al. (2014). Iqcg Is Essential for Sperm Flagellum Formation in Mice. *PLoS One* 9, e98053. doi:10.1371/journal.pone.0098053

Liu, M., Hu, Z., Qi, L., Wang, J., Zhou, T., Guo, Y., et al. (2013). Scanning of Novel Cancer/testis Proteins by Human Testis Proteomic Analysis. *Proteomics* 13, 1200–1210. doi:10.1002/pmic.201200489

Mahadevaiah, S. K., Turner, J. M., Baudat, F., Rogakou, E. P., de Boer, P., Blanco-Rodriguez, J., et al. (2001). Recombinational DNA Double-Strand Breaks in Mice Precede Synapsis. *Nat. Genet.* 27, 271–276. doi:10.1038/85830

Mbikay, M., Tadros, H., Ishida, N., Lerner, C. P., De Lamirande, E., Chen, A., et al. (1997). Impaired Fertility in Mice Deficient for the Testicular Germ-Cell Protease PC4. *Proc. Natl. Acad. Sci. U S A.* 94, 6842–6846. doi:10.1073/pnas.94.13.6842

Nai, A., Rubio, A., Campanella, A., Gourbeyre, O., Artuso, I., Bordini, J., et al. (2016). Limiting Hepatic Bmp-Smad Signaling by Matriptase-2 Is Required for Erythropoietin-Mediated Hepcidin Suppression in Mice. *Blood* 127, 2327–2336. doi:10.1182/blood-2015-11-681494

Neto, F. T., Bach, P. V., Najari, B. B., Li, P. S., and Goldstein, M. (2016). Spermatogenesis in Humans and its Affecting Factors. *Semin. Cel Dev Biol* 59, 10–26. doi:10.1016/j.semcdb.2016.04.009

Okuda, J., Niizuma, S., Shioi, T., Kato, T., Inuzuka, Y., Kawashima, T., et al. (2013). Persistent Overexpression of Phosphoglycerate Mutase, a Glycolytic Enzyme, Modifies Energy Metabolism and Reduces Stress Resistance of Heart in Mice. *PLoS One* 8, e72173. doi:10.1371/journal.pone.0072173

Ozturk, N., Steger, K., and Schagdarsurengin, U. (2017). The Impact of Autophagy in Spermiogenesis. *Asian J. Androl.* 19, 617–618. doi:10.4103/1008-682X.190324

Page, M. J., and Di Cera, E. (2008). Serine Peptidases: Classification, Structure and Function. *Cell Mol Life Sci* 65, 1220–1236. doi:10.1007/s00018-008-7565-9

Page, S. L., and Hawley, R. S. (2004). The Genetics and Molecular Biology of the Synaptonemal Complex. *Annu. Rev. Cel Dev Biol* 20, 525–558. doi:10.1146/annurev.cellbio.19.111301.155141

Peters, A. H., Plug, A. W., van Vugt, M. J., and de Boer, P. (1997). A Drying-Down Technique for the Spreading of Mammalian Meiocytes from the Male and Female Germline. *Chromosome Res.* 5, 66–68. doi:10.1023/a:1018445520117

Schaffert, C. S. (2011). Role of MGST1 in Reactive Intermediate-Induced Injury. *World J. Gastroenterol.* 17, 2552–2557. doi:10.3748/wjg.v17.i20.2552

Shang, X., Shen, C., Liu, J., Tang, L., Zhang, H., Wang, Y., et al. (2018). Serine Protease PRSS55 Is Crucial for Male Mouse Fertility via Affecting Sperm

Migration and Sperm-Egg Binding. *Cel Mol Life Sci* 75, 4371–4384. doi:10.1007/s00018-018-2878-9

Shen, B., Zhang, J., Wu, H., Wang, J., Ma, K., Li, Z., et al. (2013). Generation of Gene-Modified Mice via Cas9/RNA-Mediated Gene Targeting. *Cell Res* 23, 720–723. doi:10.1038/cr.2013.46

Shen, C., Kuang, Y., Liu, J., Feng, J., Chen, X., Wu, W., et al. (2013). Prss37 Is Required for Male Fertility in the Mouse. *Biol. Reprod.* 88, 123. doi:10.1095/biolreprod.112.107086

Tanaka, H., Iguchi, N., Toyama, Y., Kitamura, K., Takahashi, T., Kaseda, K., et al. (2004). Mice Deficient in the Axonemal Protein Tektin-T Exhibit Male Infertility and Immotile-Cilium Syndrome Due to Impaired Inner Arm Dynein Function. *Mol. Cel Biol* 24, 7958–7964. doi:10.1128/MCB.24.18.7958-7964.2004

Wang, G., Guo, Y., Zhou, T., Shi, X., Yu, J., Yang, Y., et al. (2013). In-depth Proteomic Analysis of the Human Sperm Reveals Complex Protein Compositions. *J. Proteomics* 79, 114–122. doi:10.1016/j.jprot.2012.12.008

Yan, W., Wu, F., Morser, J., and Wu, Q. (2000). Corin, a Transmembrane Cardiac Serine Protease, Acts as a Pro-atrial Natriuretic Peptide-Converting Enzyme. *Proc. Natl. Acad. Sci. U S A.* 97, 8525–8529. doi:10.1073/pnas.150149097

Yang, J. C., and Cortopassi, G. A. (1998). Induction of the Mitochondrial Permeability Transition Causes Release of the Apoptogenic Factor Cytochrome C. *Free Radic. Biol. Med.* 24, 624–631. doi:10.1016/s0891-5849(97)00367-5

Yoneda, R., and Kimura, A. P. (2013). A Testis-specific Serine Protease, Prss41/Tessp-1, Is Necessary for the Progression of Meiosis during Murine *In Vitro* Spermatogenesis. *Biochem. Biophys. Res. Commun.* 441, 120–125. doi:10.1016/j.bbrc.2013.10.028

Yoneda, R., Takahashi, T., Matsui, H., Takano, N., Hasebe, Y., Ogiwara, K., et al. (2013). Three Testis-specific Paralogous Serine Proteases Play Different Roles in Murine Spermatogenesis and Are Involved in Germ Cell Survival during Meiosis. *Biol. Reprod.* 88, 118. doi:10.1095/biolreprod.112.106328

Zakrzewski, P., Lenartowska, M., and Buss, F. (2021). Diverse Functions of Myosin VI in Spermiogenesis. *Histochem. Cel Biol* 155, 323–340. doi:10.1007/s00418-020-01954-x

Zeng, W., Baumann, C., Schmidtmann, A., Honaramooz, A., Tang, L., Bondareva, A., et al. (2011). Lymphoid-specific Helicase (HELLS) Is Essential for Meiotic Progression in Mouse Spermatocytes. *Biol. Reprod.* 84, 1235–1241. doi:10.1095/biolreprod.110.085720

Zhang, J., Yu, L., Fu, Q., Gao, J., Xie, Y., Chen, J., et al. (2001). Mouse Phosphoglycerate Mutase M and B Isozymes: cDNA Cloning, Enzyme Activity Assay and Mapping. *Gene* 264, 273–279. doi:10.1016/s0378-1119(00)00597-7

Zhang, Y., Ou, Y., Cheng, M., Saadi, H. S., Thundathil, J. C., and van der Hoorn, F. A. (2012). KLC3 Is Involved in Sperm Tail Midpiece Formation and Sperm Function. *Dev. Biol.* 366, 101–110. doi:10.1016/j.ydbio.2012.04.026

Zhang, Z., Shen, X., Gude, D. R., Wilkinson, B. M., Justice, M. J., Flickinger, C. J., et al. (2009). MEIG1 Is Essential for Spermiogenesis in Mice. *Proc. Natl. Acad. Sci. U S A.* 106, 17055–17060. doi:10.1073/pnas.0906414106

Zhu, F., Li, W., Zhou, X., Chen, X., Zheng, M., Cui, Y., et al. (2021). PRSS55 Plays an Important Role in the Structural Differentiation and Energy Metabolism of Sperm and Is Required for Male Fertility in Mice. *J. Cel Mol Med* 25, 2040–2051. doi:10.1111/jcmm.16116

Zickler, D., and Kleckner, N. (1999). Meiotic Chromosomes: Integrating Structure and Function. *Annu. Rev. Genet.* 33, 603–754. doi:10.1146/annurev.genet.33.1.603

Conflict of Interest: The authors declare that the research was conducted in the absence of any commercial or financial relationships that could be construed as a potential conflict of interest.

Publisher's Note: All claims expressed in this article are solely those of the authors and do not necessarily represent those of their affiliated organizations, or those of the publisher, the editors, and the reviewers. Any product that may be evaluated in this article, or claim that may be made by its manufacturer, is not guaranteed or endorsed by the publisher.

Copyright © 2022 Zhang, Zhou, Wan, Yu, Chen, Yan, Wu, Zheng, Zhu and Zhu. This is an open-access article distributed under the terms of the Creative Commons Attribution License (CC BY). The use, distribution or reproduction in other forums is permitted, provided the original author(s) and the copyright owner(s) are credited and that the original publication in this journal is cited, in accordance with accepted academic practice. No use, distribution or reproduction is permitted which does not comply with these terms.

Advantages of publishing in Frontiers

OPEN ACCESS
Articles are free to read for greatest visibility and readership

FAST PUBLICATION
Around 90 days from submission to decision

HIGH QUALITY PEER-REVIEW
Rigorous, collaborative, and constructive peer-review

TRANSPARENT PEER-REVIEW
Editors and reviewers acknowledged by name on published articles

Frontiers
Avenue du Tribunal-Fédéral 34
1005 Lausanne | Switzerland

Visit us: www.frontiersin.org
Contact us: frontiersin.org/about/contact

REPRODUCIBILITY OF RESEARCH
Support open data and methods to enhance research reproducibility

DIGITAL PUBLISHING
Articles designed for optimal readership across devices

FOLLOW US
@frontiersin

IMPACT METRICS
Advanced article metrics track visibility across digital media

EXTENSIVE PROMOTION
Marketing and promotion of impactful research

LOOP RESEARCH NETWORK
Our network increases your article's readership